Fourth Edition

Powder Technology Handbook

Edited by
Ko Higashitani
Hisao Makino
Shuji Matsusaka



CRC Press
Taylor & Francis Group

Powder Technology Handbook

Fourth Edition



Taylor & Francis
Taylor & Francis Group
http://taylorandfrancis.com

Powder Technology Handbook

Fourth Edition

Edited by
Ko Higashitani, Hisao Makino, and Shuji Matsusaka


CRC Press
Taylor & Francis Group
Boca Raton London New York

CRC Press is an imprint of the
Taylor & Francis Group, an **informa** business

CRC Press
Taylor & Francis Group
6000 Broken Sound Parkway NW, Suite 300
Boca Raton, FL 33487-2742

© 2020 by Taylor & Francis Group, LLC
CRC Press is an imprint of Taylor & Francis Group, an Informa business

No claim to original U.S. Government works

Printed on acid-free paper

International Standard Book Number-13: 978-0-367-86280-0 (Hardback)

This book contains information obtained from authentic and highly regarded sources. Reasonable efforts have been made to publish reliable data and information, but the author and publisher cannot assume responsibility for the validity of all materials or the consequences of their use. The authors and publishers have attempted to trace the copyright holders of all material reproduced in this publication and apologize to copyright holders if permission to publish in this form has not been obtained. If any copyright material has not been acknowledged, please write and let us know so we may rectify in any future reprint.

Except as permitted under U.S. Copyright Law, no part of this book may be reprinted, reproduced, transmitted, or utilized in any form by any electronic, mechanical, or other means, now known or hereafter invented, including photocopying, microfilming, and recording, or in any information storage or retrieval system, without written permission from the publishers.

For permission to photocopy or use material electronically from this work, please access www.copyright.com (http://www.copyright.com/) or contact the Copyright Clearance Center, Inc. (CCC), 222 Rosewood Drive, Danvers, MA 01923, 978-750-8400. CCC is a not-for-profit organization that provides licenses and registration for a variety of users. For organizations that have been granted a photocopy license by the CCC, a separate system of payment has been arranged.

Trademark Notice: Product or corporate names may be trademarks or registered trademarks, and are used only for identification and explanation without intent to infringe.

Visit the Taylor & Francis Web site at
http://www.taylorandfrancis.com

and the CRC Press Web site at
http://www.crcpress.com

Preface to the Fourth Edition

Powder Technology Handbook has been published, aiming to provide the necessary and sufficient methodologies of powder and particle handling technology, not only for fundamental scientific researchers but also for practical industrial engineers.

The first edition was published in 1988, and then successive editions have been updated almost every ten years to meet the expanding demands of the contemporary powder and particle technology: the second edition in 1997, the third edition in 2007.

More than 10 years have passed since the third edition was published. During the last decade, unprecedented progress and advancement have been made in the fundamental and applied fields: the details of conventional technologies are able to be analyzed by sophisticated methodologies and large-scale simulations; well-characterized functional particles, especially nanoparticles, were able to be synthesized and constructed into many advanced functional materials, such as, electric, magnetic, optical, pharmaceutical, cosmetic, food, pigment and various chemical materials; the risk and hazards of particles and nanoparticles to the human body and society have been evoked, and so on.

It seems that the field of powder and particle technology is now in the new phase. In order to meet the needs of the times, this edition was updated by adding new chapters and by inviting not only active Japanese researchers but also internationally distinguished researchers from abroad as the contributors of new and conventional chapters. Because of these ambitious approaches to the fourth edition, the volume of contents expanded greatly so that the style of the book must be changed. Hence, we are sure that this book contains the contemporary and comprehensive information on powder and particle handling technology that will be extremely useful not only for newcomers but also for professional engineers and researchers in the field of powder and particle science and technology.

We would like to thank all the contributors who wrote the manuscripts with enthusiasm, and also the original authors cited in the manuscripts. We especially express our thanks to the following advisory board members who advised us from various points of view.

Professor Hiroaki Masuda of Kyoto University

Professor Kikuo Okuyama of Hiroshima University

Professor Hidehiro Kamiya of Tokyo University of Agriculture and Technology

We also acknowledge the constant and patient support of publishing team members of Taylor & Francis/CRC Press, especially, the editorial staff, Allison Shatkin and Camilla Michael.

Ko Higashitani
Hisao Makino
Shuji Matsusaka



Taylor & Francis
Taylor & Francis Group
http://taylorandfrancis.com

Preface to the Third Edition

Powders and particles are extending their applications in recent developing fields such as the information market, including mobile phones, copy machines, and electronic displays, as well as pharmaceuticals, cosmetics, foods, chemicals, and many other fundamental engineering fields. Nanoparticles are also promising research subjects for the development of more effective applications of various particles. They need powder technology in their preparation, characterization, measurement, and functional treatment and for totally systematic handling.

Since the first edition published in 1988 and the second edition in 1997, the *Powder Technology Handbook* has been accepted in many fields of engineering. Because of this acceptance and the encouragement of Russell Dekker, we agreed to update the book and present this third edition.

This new edition has been substantially revised and expanded. The content has been updated, not only by adding newly developed areas such as simulations, surface analysis, and nanoparticles, but also by introducing new young authors. Some sections are combined, so that the readers can easily refer to the subject.

We hope this handbook will serve as a strong guide to the field of powder and particle technology.

Special acknowledgment is given to all contributors and also to all the original authors whose valuable work is cited in this handbook. We also extend acknowledgment to Dr. Matsusaka, associate professor of Kyoto University, for his collaboration on the editing work.

With this, our third edition, we thank our new editorial staff: Kari Budyk, Tao Woolfe, and others at Taylor & Francis Books (formerly Marcel Dekker) for their laborious editing and production work.

Hiroaki Masuda
Ko Higashitani
Hideto Yoshida



Taylor & Francis
Taylor & Francis Group
http://taylorandfrancis.com

Preface to the Second Edition

Since first published in 1988, the *Powder Technology Handbook* has been accepted as a reference in many areas of engineering. Because of this acceptance and the support of Russell Dekker, the Chief Publishing Officer of our publisher, we agreed to update the book and present this second edition.

This entire book has been substantially revised. American and European authors have been invited to join the Japanese authors who participated in writing the first edition, giving the book a wider viewpoint. In response to reviews for the first edition, the contents have been reorganized. New sections have been added to treat the recent advances in computer simulation (V.19) and working atmospheres and hazards (VII.1–VII.3). This second edition contains a more detailed table of contents so that readers can understand the whole range of the handbook.

It is hoped that this handbook will serve as a strong guide to the field of particle technology.

Special acknowledgment is given to Dr. Koichi Iinoya, professor emeritus of Kyoto University, for his advisory work. This second edition is dedicated to him on the occasion of his 80th year of age. We are indebted to Joseph Stubenrauch and others at Marcel Dekker, Inc., for their laborious editing work.

Keishi Gotoh
Hiroaki Masuda
Ko Higashitani



Taylor & Francis
Taylor & Francis Group
http://taylorandfrancis.com

Preface to the First Edition

Particulate or powder technology deals with a variety of particles, from submicrometer to large grains and gravels and from liquid mist or droplets to bubbles, as well as solid particles and aggregates. It also deals with two-phase (solid–gas, solid–liquid, and liquid–gas) and three-phase (solid– liquid–gas) mixtures and is related to work in the medical, biological, pharmaceutical, chemical, mining, metallurgical, mechanical, civil, food and agricultural science, and engineering fields. Many natural and artificial phenomena encountered in our daily lives may be explained by knowledge of powder technology.

The first book on particle technology in general was probably *Micromeritics* by J. M. Dalavalle, published in 1943; the second may be *Particulate Technology* by C. Orr, published in 1966. There are also various books on specific fields in powder technology. In Japan, the first handbook was published in 1965 and the second appeared in 1986.

Particulate or powder technology is a fundamental engineering field involving newly developed high or evolutionary technology. Submicrometer particles, for example, are a focus of practical applications.

This handbook has been developed from the second Japanese handbook, although the contents have been revised and updated. It provides a comprehensive understanding of powder technology. Although many investigators have contributed, the various manuscripts have, as much possible, been edited in a unified fashion, so as not to become a mere collection of monographs: Keishi Gotoh has edited the sections on dry powders and Ko Higashitani those on wet powders. Koichi Iinoya assumes the entire responsibility as editor in chief.

Special acknowledgment is given to all contributors who prepared their manuscripts on time. The editors also acknowledge all original authors whose valuable work is cited in this handbook. We are indebted to Nikkan Kougyo Shimbunsha Publishers, who kindly supplied us with the original drawings of all figures used in the Japanese edition. The work of a number of students in relettering the artwork is gratefully acknowledged.

Once again, this handbook provides a comprehensive understanding of powder technology as a sort of encyclopedia and it is hoped that it will be valuable as a guide to this invaluable engineering field. We are indebted to Ms. Lila Harris and others at Marcel Dekker, Inc., for their laborious editing work.

Koichi Iinoya
Keishi Gotoh
Ko Higashitani



Taylor & Francis
Taylor & Francis Group
http://taylorandfrancis.com

Editors

Ko Higashitani, PhD, is an emeritus professor of Kyoto University. He earned a BS degree from Kyoto University in 1968, and a PhD degree from the University of Wisconsin-Madison, USA in 1973 in the field of Chemical Engineering. After he worked in Kyushu Institute of Technology, he moved to Kyoto University as a professor of Chemical Engineering. Dr. Higashitani is on the Editorial Board of *Powder Technology*, the International Advisory Board of *Particuology* and the Honorary Editor-in-Chief of *Advanced Powder Technology*, and he was the Executive Editor of *Chemical Engineering Science*, the Editor-in-Chief of *Advanced Powder Technology*, on the Editorial Board of *KONA Powder and Particle Journal* and the Editor-in-Chief of *Kagaku Kogaku Ronbunshu* (Chemical Engineering Journal in Japanese).

His present major research interest is the correlation between macroscopic behaviors of colloidal particles in solutions, such as, the particle formation, the coagulation, dispersion, deposition and detachment of colloidal particles, with the molecular-scale characteristics of particles and particle surfaces which can be evaluated by the atomic force microscope.

Hisao Makino, PhD, is a Research Advisor of the Central Research Institute of Electric Power Industry, Japan (CRIEPI) and a Visiting Professor of Kyushu University and Gunma University. He is also the Vice President of the Association of Powder Process Industry and Engineering, Japan and the Vice President of the Japan Institute of Energy. Dr. Makino earned his BSc, MSc degrees and PhD from Kyoto University. His main research subject is the development of solid fossil fuel utilization technology including coal and biomass for power generation. His current interests are high temperature combustion and the gasification reaction of pulverized fossil fuel, dust collection technology and control technology of greenhouse gas emissions from thermal power stations.

Shuji Matsusaka, PhD, is a Professor of Chemical Engineering at Kyoto University. He earned his BSc and MSc degrees from Hiroshima University and PhD from Kyoto University. He has held important positions in academic organizations in areas of powder technology, aerosol science and electrostatics. He has been the editor-in-chief of *Advanced Powder Technology* since 2013. Dr. Matsusaka's current research interests are characterizing particle electrification, adhesion and flowability, as well as handling micro-particles and nano-particles in gases.



Taylor & Francis
Taylor & Francis Group
http://taylorandfrancis.com

Contributors

Tooru Andoh
Kobe Gakuin University
Kobe, Japan

Tina Bonakdar
University of Leeds
Leeds, United Kingdom

Xizhong Chen
Chinese Academy of Sciences
Beijing, China

Luke Andrew Connal
Australian National University
Canberra, Australia

Vincent S. J. Craig
Australian National University
Canberra, Australia

Ritsu Dobashi
The University of Tokyo
Tokyo, Japan

Shigehisa Endoh
National Institute of Advanced Industrial Science and Technology
Tsukuba, Japan

Yoshiyuki Endo
Sumitomo Chemical Co. Ltd.
Osaka, Japan

Elizaveta Forbes
Commonwealth Scientific & Industrial Research Organisation (CSIRO)
Canberra, Australia

George Vincent Franks
University of Melbourne
Melbourne, Australia

Masayoshi Fuji
Nagoya Institute of Technology
Tajimi, Japan

Fumihiko Fujii
Kobe Gakuin University
Kobe, Japan

Toshiyuki Fujimoto
Muroran Institute of Technology
Muroran, Japan

Toyohisa Fujita
Guangxi University
Nanning, China

Kakeru Fujiwara
Yamagata University
Yonezawa, Japan

Tomonori Fukasawa
Hiroshima University
Higashi-Hiroshima, Japan

Kunihiro Fukui
Hiroshima University
Higashi-Hiroshima, Japan

Wei Gao
Dalian University of Technology
Dalian, China

Jakub M. Gac
Warsaw University of Technology
Warsaw, Poland

Mojtaba Ghadiri
University of Leeds
Leeds, United Kingdom

Kuniaki Gotoh
Okayama University
Okayama, Japan

Jusuke Hidaka
Shiraishi Kogyo Kaisha Ltd.
Osaka, Japan

Ko Higashitani
Kyoto University
Kyoto, Japan

Shanwei Hu
Chinese Academy of Sciences
Beijing, China

Hideki Ichikawa
Kobe Gakuin University
Kobe, Japan

Kenji Iimura
University of Hyogo
Himeji, Japan

Eiji Iritani
Nagoya University
Nagoya, Japan

Naoyuki Ishida
Okayama University
Okayama, Japan

Hidehiro Kamiya
Tokyo University of Agriculture and Technology
Koganei, Japan

Chikao Kanaoka
Kanazawa University
Kanazawa, Japan

Junya Kano
Tohoku University
Sendai, Japan

Yoshiyuki Komoda
Kobe University
Kobe, Japan

Ryoichi Kurose
Kyoto University
Kyoto, Japan

Xinhua Liu
Chinese Academy of Sciences
Beijing, China

Bona Lu
Chinese Academy of Sciences
Beijing, China

Hisao Makino
Central Research Institute of Electric Power Industry
Yokosuka, Japan

Hiroaki Masuda
Kyoto University
Kyoto, Japan

Shuji Matsusaka
Kyoto University
Kyoto, Japan

Minoru Miyahara
Kyoto University
Kyoto, Japan

Takamasa Mori
Hosei University
Koganei, Japan

Yasushige Mori
Doshisha University
Kyotanabe, Japan

Yasuo Morimoto
University of Occupational and Environmental Health
Kitakyushu, Japan

Kazuo Murase
Chuo University
Tokyo, Japan

Toshihiko Myojo
University of Occupational and Environmental Health
Kitakyushu, Japan

Sadegh Nadimi
University of Leeds
Leeds, United Kingdom

Makio Naito
Osaka University
Ibaraki, Japan

Koichi Nakaso
Okayama University
Okayama, Japan

Wei Sung Ng
University of Melbourne
Melbourne, Australia

Takashi Ogi
Hiroshima University
Higashi-Hiroshima, Japan

Kikuo Okuyama
Hiroshima University
Higashi-Hiroshima, Japan

Jun Oshitani
Okayama University of Science
Okayama, Japan

Yosufumi Otsubo
Chiba University
Chiba, Japan

Mehrdad Pasha
University of Leeds
Leeds, United Kingdom

Wolfgang Peukert
Friedrich-Alexander-Universität Erlangen-Nürnberg
Erlangen, Germany

Sotiris E. Pratsinis
Eidgenosische Technische Hochschule
Zurich, Switzerland

Stefan Romeis
Friedrich-Alexander-Universität Erlangen-Nürnberg
Erlangen, Germany

Fumio Saito
Tohoku University
Sendai, Japan

Mikio Sakai
The University of Tokyo
Tokyo, Japan

Isao Sekiguchi
Chuo University
Tokyo, Japan

Takafumi Seto
Kanazawa University
Kanazawa, Japan

Manabu Shimada
Hiroshima University
Higashi-Hiroshima, Japan

Hiroyuki Shinto
Fukuoka University
Fukuoka, Japan

Hiromi Shirai
Central Research Institute of Electric Power Industry
Yokosuka, Japan

Yoshiyuki Shirakawa
Doshisha University
Kyotanabe, Japan

Hisao Suzuki
Shizuoka University
Hamamatsu, Japan

Michitaka Suzuki
University of Hyogo
Himeji, Japan

Hiroshi Takahashi
Muroran Institute of Technology
Muroran, Japan

Minoru Takahashi
Nagoya Institute of Technology
Tajimi, Japan

Chika Takai
Gifu University
Gifu, Japan

Takashi Takei
Tokyo Metropolitan University
Hachioji, Japan

Hirofumi Takeuchi
Gifu Pharmaceutical University
Gifu, Japan

Kenji Tanno
Central Research Institute of Electric Power Industry
Yokosuka, Japan

Ken-ichiro Tanoue
Yamaguchi University
Ube, Japan

Junichi Tatami
Yokohama National University
Yokohama, Japan

Yuji Tatemoto
Shizuoka University
Hamamatsu, Japan

Yuji Tomita
Kyushu Institute of Technology
Kitakyushu, Japan

JunIchiro Tsubaki
Nagoya Industrial Science Research Institute
Nagoya, Japan

Yutaka Tsuji
Osaka University
Suita, Japan

Ryoichi Yamamoto
Kyoto University
Kyoto, Japan

Toyokazu Yokoyama
Hosokawa Micron Corporation
Hirakata, Japan

Hideto Yoshida
Hiroshima University
Higashi-Hiroshima, Japan

Jun Yoshida
Ohsaki Research Institute
Tokyo, Japan

Hiroki Yotsumoto
National Institute of Advanced Industrial Science and Technology
Tsukuba, Japan

Shinichi Yuu
Ootake R. and D. Consultant Office
Fukuoka, Japan

Johannes Walter
Friedrich-Alexander-Universität Erlangen-Nürnberg
Erlangen, Germany

Limin Wang
Chinese Academy of Sciences
Beijing, China

Satoru Watano
Osaka Prefecture University
Sakai, Japan

Richard A. Williams
Heriot-Watt University
Edinburgh, United Kingdom

Umair Zafar
University of Leeds
Leeds, United Kingdom

Qiwu Zhang
Wuhan University of Technology
Wuhan, China

Contents

PART 1 Particle Characterization and Standard Powder

Chapter 1.1 Particle Size 3

JunIchiro Tsubaki

1.1.1 Definition of Particle Diameter 3
1.1.2 Particle Size Distribution 3
1.1.3 Average Particle Size 5
References 7

Chapter 1.2 Size Measurement 9

Yasushige Mori

1.2.1 Introduction 9
1.2.2 Classification of Particle Size Analysis Methods 10
1.2.3 Counting Analysis 10
1.2.4 Fractionation Analysis 13
1.2.5 Ensemble Analysis 16
1.2.6 Others 18
1.2.7 Summary 18
References 18

Chapter 1.3 Particle Shape Characterization 19

Shigehisa Endoh

1.3.1 Introduction 19
1.3.2 Representative Size 19
1.3.3 Geometrical Shape Descriptors 20
1.3.4 Dynamic Equivalent Shape 24
1.3.5 Concluding Remarks 25
References 25

Chapter 1.4 Particle Density 27

Yoshiyuki Endo

1.4.1 Definition of Particle Density 27
1.4.2 Measurement Method of Particle Density 27
1.4.3 Measurement Method of Bulk Density 30
References 31

Chapter 1.5 Hardness, Stiffness and Toughness of Particles 33

Mojtaba Ghadiri, Mehrdad Pasha, and Umair Zafar

1.5.1 Indentation Hardness 33
1.5.2 Measurement of Hardness 34
1.5.3 Measurement of Stiffness 37

1.5.4 Measurement of Toughness 37
References 40

Chapter 1.6 Surface Properties and Analysis 41

Masayoshi Fuji and Chika Takai

1.6.1 Surface Structures and Properties 41
1.6.2 Surface Characterization 45
References 51

Chapter 1.7 Characterization by Atomic Force Microscope 53

Naoyuki Ishida and Vincent S. J. Craig

1.7.1 Principle of AFM 53
1.7.2 Surface Characterization by AFM 54
1.7.3 Measurements of Interaction Forces by AFM 55
References 58

Chapter 1.8 Specific Properties of Nanoparticles 59

Wolfgang Peukert and Johannes Walter

1.8.1 Property Function and Disperse Properties 59
1.8.2 Transport Properties 60
1.8.3 Particle Interactions 60
1.8.4 Thermophysical Properties 61
1.8.5 Mechanical Properties 62
1.8.6 Optical Properties 63
1.8.7 Electrical Properties 63
1.8.8 Magnetic Properties 64
1.8.9 Catalytic Particles 65
References 67

Chapter 1.9 Standard Powders and Particles 69

Hideto Yoshida

References 72

PART 2 Fundamental Properties of Particles

Chapter 2.1 Optical Properties 75

Yasushige Mori

2.1.1 Definitions 75
2.1.2 Light Scattering 75
2.1.3 Light Extinction 77
2.1.4 Dynamic Light Scattering 77
2.1.5 Photophoresis 78
References 78

Chapter 2.2 Electrification and Electrophoresis 81

Shuji Matsusaka and Hiroaki Masuda (2.2.1)
Hiroyuki Shinto and Tomonori Fukasawa (2.2.2)

2.2.1 In Gaseous State 81

2.2.2 In Liquid State 83
References 89

Chapter 2.3 Magnetic Properties 91

Toyohisa Fujita

2.3.1 Magnetic Force on a Particle 91
2.3.2 Ferromagnetic Properties of a Small Particle 93
2.3.3 Magnetism of Various Materials 94
References 96

Chapter 2.4 Diffusion of Particles 97

Toshiyuki Fujimoto and Kikuo Okuyama (2.4.1)
Shinichi Yuu (2.4.2)

2.4.1 Thermal Diffusion 97
2.4.2 Turbulent Diffusion 100
References 103

Chapter 2.5 Particle Motion in Fluid 105

Shinichi Yuu

2.5.1 Introduction 105
2.5.2 Motion of a Single Particle 105
2.5.3 PARTICLE Motion in Shear Flow 107
References 107

Chapter 2.6 Particle Sedimentation 109

Shinichi Yuu

2.6.1 Introduction 109
2.6.2 Terminal Settling Velocity 109
2.6.3 Settling of Two Spherical Particles 111
2.6.4 Rate of Sedimentation in Concentrated Suspension 111
References 112

Chapter 2.7 Adhesive Force of Single Particle 113

Kuniaki Gotoh (2.7.1)
Naoyuki Ishida (2.7.2)
Shuji Matsusaka (2.7.3)

2.7.1 In Gaseous State 113
2.7.2 In Liquid State 116
2.7.3 Measurement of Adhesive Force 117
References 119

Chapter 2.8 Particle Deposition and Reentrainment 121

Manabu Shimada (2.8.1)
Shuji Matsusaka and Hiroaki Masuda (2.8.2)

2.8.1 Particle Deposition 121
2.8.2 Particle Reentrainment 124
References 127

Chapter 2.9 Agglomeration (Coagulation) 129

Takafumi Seto and Kikuo Okuyama (2.9.1)
Ko Higashitani (2.9.2)

2.9.1 In Gaseous State 129
2.9.2 In Liquid State 133
References 137

Chapter 2.10 Viscosity of Slurry 139

Yoshiyuki Komoda

2.10.1 Introduction 139
2.10.2 Basic Flow Characteristics 139
2.10.3 Time-Dependent Flow Characteristics 139
2.10.4 Viscosity Equations for Suspensions of Spherical Particles of Narrow Particle Size Distribution 140
2.10.5 Effect of Particle Size Distribution on Slurry Viscosity 141
2.10.6 Shear Thinning or Thickening Behavior of Slurry 141
2.10.7 Measurement of Slurry Viscosity by a Capillary Viscometer 141
2.10.8 Measurement of Slurry Viscosity by a Rotating Viscometer 142
References 142

Chapter 2.11 Particle Impact Breakage 145

Mojtaba Ghadiri

2.11.1 Impact Force 145
2.11.2 Mode of Breakage 146
2.11.3 Analysis of Breakage for the Brittle Failure Mode 146
2.11.4 Analysis of Breakage for the Semi-Brittle Failure Mode 147
2.11.5 Analysis of Breakage of Agglomerates 148
References 148

Chapter 2.12 Sintering 151

Takafumi Seto and Kikuo Okuyama

2.12.1 Mechanisms of Solid-Phase Sintering 151
2.12.2 Modeling of Sintering of Agglomerates 151
2.12.3 Sintering Process of Nanoparticles 152
2.12.4 Sintering Process of Packed Powder 153
References 154

Chapter 2.13 Mechanochemistry 155

Qiwu Zhang and Fumio Saito

2.13.1 Introduction 155
2.13.2 Phase Transformation 155
2.13.3 Solid State Reaction 155
2.13.4 Mechanochemical Doping 160
2.13.5 Mechanical Synthesis of Hydrated Compounds 160
2.13.6 Decomposition of Halogenated Polymers 161
2.13.7 Material Processing with Mechanical Activation Followed by Chemical or Physical Treatment 162
References 164

Chapter 2.14 Ignition and Combustion Reaction 167

Hisao Makino and Ryoichi Kurose

2.14.1 Combustion Profile 167
2.14.2 Devolatilization and Ignition 167
2.14.3 Gaseous Combustion 168
2.14.4 Solid Combustion 169
References 169

Chapter 2.15 Solubility and Dissolution Rate 171

Hirofumi Takeuchi

2.15.1 Solubility of a Solid 171
2.15.2 Solubility Changes as Properties of Solvent or Solute Change 171
2.15.3 Dissolution Rate Analysis: Theory and Methods 172
2.15.4 Methods to Improve the Solubilization of Powdered Materials 174
References 176

PART 3 Properties of Powders and Powder Beds

Chapter 3.1 Specific Surface Area 179

Takashi Takei

3.1.1 Definition of Specific Surface Area 179
3.1.2 Estimation of Surface Area by Gas Adsorption 179
3.1.3 Methodology of Gas Adsorption 181
3.1.4 Estimation of Surface Area by Gas Flow (Permeametry) 182
References 183

Chapter 3.2 Adsorption Characteristics 185

Takashi Takei

3.2.1 Introduction 185
3.2.2 Adsorption Measurement 185
3.2.3 Theory of Adsorption Isotherms 186
3.2.4 Estimation of Surface Properties by Adsorption Method 188
References 190

Chapter 3.3 Moisture Content 193

Satoru Watano

3.3.1 Bound Water and Adhesive Water 193
3.3.2 Method to Determine Moisture Content in Particulate System 194
References 194

Chapter 3.4 Electrical Properties 195

Ken-ichiro Tanoue and Hiroaki Masuda (3.4.1)
Yasufumi Otsubo (3.4.2)

3.4.1 In Gaseous State 195
3.4.2 In Nonaqueous Solutions 199
References 202

Chapter 3.5 Packing Properties 203

Michitaka Suzuki

3.5.1 Packing of Equal-Size Spheres 203
3.5.2 Packing of Multi-Size Particles 205
3.5.3 Effect of Particle Shape on Void Fraction 207
References 209

Chapter 3.6 Capillarity of Porous Media 211

Minoru Miyahara

3.6.1 Common Phenomenon: Young–Laplace Effect 211
3.6.2 Nitrogen Adsorption Method 211
3.6.3 Mercury Intrusion Method (Mercury Porosimetry) 214
3.6.4 Other Techniques of Interest 214
References 215

Chapter 3.7 Permeation (Flow through Porous Media) 217

Chikao Kanaoka

3.7.1 Resistance to Flow Through a Porous Media 217
3.7.2 Pressure Drop Across a Fibrous Mat 219
References 221

Chapter 3.8 Mechanical Properties of a Powder Bed 223

Michitaka Suzuki

3.8.1 Shearing Strength of a Powder Bed 223
3.8.2 Adhesion of a Powder Bed 225
3.8.3 Yielding Characteristics of a Powder Bed 226
References 229

Chapter 3.9 Fluidity of Powder 231

Toyokazu Yokoyama

3.9.1 Definition of Fluidity 231
3.9.2 Measurement of Fluidity 231
3.9.3 Factors Affecting Fluidity 234
3.9.4 Improvement of Fluidity 235
References 235

Chapter 3.10 Blockage in Storage Vessels 237

Hiroshi Takahashi and Jun Yoshida

3.10.1 Typical Phenomena 237
3.10.2 Mechanisms and Flow Criteria 237
3.10.3 Experimental Study 240
3.10.4 Methods of Preventing Blockage 241
References 241

Chapter 3.11 Segregation of Particles 243

Kuniaki Gotoh

3.11.1 Segregation Phenomena and its Factors 243
3.11.2 Mechanism of Segregation 243

3.11.3 Surface Segregation 244
3.11.4 Interlayer Segregation 246
3.11.5 Method to Prevent Segregation 247
References 247

Chapter 3.12 Vibrational and Acoustic Characteristics 249

Jusuke Hidaka

3.12.1 Behavior of a Particle on a Vibrating Plate 249
3.12.2 Behavior of a Vibrating Powder Bed 250
3.12.3 Generating Mechanism of Impact Sound Between Two Particles 252
3.12.4 Frictional Sound from a Granular Bed 253
3.12.5 Vibration of a Small Particle in a Sound Wave 256
3.12.6 Attenuation of Sound in a Suspension of Particles 256
References 257

PART 4 Particle Generation and Modification

Chapter 4.1 Aerosol Particle Generation 261

Jakub M. Gac and Sotiris E. Pratsinis

4.1.1 Atomization of Fluids 261
4.1.2 Condensation Methods 265
4.1.3 Powder Dispersion 267
References 268

Chapter 4.2 Generation of Particles by Reactions 269

Kakeru Fujiwara and Sotiris E. Pratsinis (4.2.1)
Hisao Suzuki (4.2.2)

4.2.1 Gas-Phase (Aerosol) Techniques 269
4.2.2 Liquid-Phase Techniques 273
References 277

Chapter 4.3 Crystallization 279

Yoshiyuki Shirakawa

4.3.1 Introduction 279
4.3.2 Solid-Liquid Equilibrium and Supersaturated Solution 279
4.3.3 Nucleation Rate 280
4.3.4 Crystal Growth Rate 281
4.3.5 Control of Powder Properties in Crystallization Processes 281
4.3.6 Synthesis of Composite Particles 282
References 284

Chapter 4.4 Design and Formation of Composite Particles 285

Hideki Ichikawa, Tooru Andoh, and Fumihiko Fujii

4.4.1 Typical Structure of Composite Particles 285
4.4.2 Process 285
4.4.3 Materials 286
4.4.4 Examples of Particulate Design and Preparation of Composite Particles 287
References 296

Chapter 4.5 Electrical Charge Control 299

Takashi Ogi and Kikuo Okuyama (4.5.1.1)
Shuji Matsusaka (4.5.1.2)
Ko Higashitani (4.5.2.1)
Hidehiro Kamiya (4.5.2.2)

4.5.1 In Gaseous State 299
4.5.2 In Liquid State 305
References 309

Chapter 4.6 Surface Modification 311

Makio Naito (4.6.1), (4.6.3)
Hidehiro Kamiya (4.6.2)

4.6.1 Purpose of Surface Modification and Its Methods 311
4.6.2 Chemical Methods 311
4.6.3 Physical Methods 314
References 315

PART 5 Powder Handlings and Simulations

Chapter 5.1 Crushing and Grinding 319

Fumio Saito

5.1.1 Introduction 319
5.1.2 Basic Approach for Understanding Grinding Phenomena 319
5.1.3 Comminution of Materials 324
References 334

Chapter 5.2 Dispersion of Particles 337

Kuniaki Gotoh (5.2.1)
Ko Higashitani (5.2.2)

5.2.1 In Gaseous State 337
5.2.2 Dispersion in Liquids 341
References 345

Chapter 5.3 Classification 347

Hideto Yoshida and Kunihiro Fukui

5.3.1 Basis of Classification 347
5.3.2 Dry Classification 348
5.3.3 Wet Classification 351
5.3.4 Screening 359
References 362

Chapter 5.4 Storage (Silo) 363

Jun Yoshida

5.4.1 Storing Bulk Solids 363
5.4.2 Basic Structure and Functions 363

5.4.3 Classification of Silos 364
5.4.4 Behavior of Bulk Solids in Silos 364
5.4.5 Planning Silos 365
5.4.6 Structural Design 366
5.4.7 Trouble in Silos 368
References 369

Chapter 5.5 Feeding 371

Shuji Matsusaka

5.5.1 Introduction 371
5.5.2 Type of Feeders 371
References 374

Chapter 5.6 Transportation 375

Yuji Tomita (5.6.1)
Yoshiyuki Komoda (5.6.2)

5.6.1 Transportation in the Gaseous State 375
5.6.2 Transportation in the Liquid State 381
References 382

Chapter 5.7 Fluidization and Fluidized Bed 385

Xinhua Liu and Shanwei Hu (5.7.1)
Xinhua Liu, Bona Lu, Xizhong Chen and Limin Wang (5.7.2)

5.7.1 Overview of Fluidization 385
5.7.2 Computational Methods for Fluidization 389
References 398

Chapter 5.8 Mixing 401

Satoru Watano

5.8.1 Introduction 401
5.8.2 Mixing Mechanism 401
5.8.3 Mixing Indices and Mixing Rate 401
5.8.4 Evaluation of Mixing Condition 402
5.8.5 Characterization of Mixing Equipment 407
References 409

Chapter 5.9 Slurry Conditioning 411

JunIchiro Tsubaki and Takamasa Mori

5.9.1 Slurry Characterization 411
5.9.2 Slurry Preparation 414
References 415

Chapter 5.10 Granulation 417

Kazuo Murase and Isao Sekiguchi

5.10.1 Growth Mechanisms of Wet Granulation 417
5.10.2 Mechanical Properties of Wet Granules 418
5.10.3 Testing Methods for Evaluating the Agglomerate Granulation of Wet Powders 420
5.10.4 Granulators 423
References 426

Chapter 5.11 Kneading and Plastic Forming 429

Minoru Takahashi and Masayoshi Fuji

5.11.1 Kneading 429
5.11.2 Plastic Forming 430
References 432

Chapter 5.12 Drying 433

Yuji Tatemoto

5.12.1 Fundamental of Drying 433
5.12.2 Dryer Selection and Design 434
References 438

Chapter 5.13 Combustion 439

Hisao Makino and Kenji Tanno

5.13.1 Introduction 439
5.13.2 Control of the Combustion Process 439
5.13.3 Combustion Burner 441
5.13.4 Furnace and Kiln 442
References 443

Chapter 5.14 Dust Collection 445

Chikao Kanaoka

5.14.1 Flow-Through-Type Dust Collectors 446
5.14.2 Obstacle-Type Dust Collectors 449
5.14.3 Barrier-Type Dust Collectors 452
5.14.4 Miscellaneous 453
References 453

Chapter 5.15 Electrostatic Separation 455

Ken-ichiro Tanoue and Hiroaki Masuda

5.15.1 Separation Mechanism 455
5.15.2 Separation Machines 457
References 460

Chapter 5.16 Magnetic Separation 461

Toyohisa Fujita

5.16.1 Classification of Magnetic Separators 461
5.16.2 Static Magnetic Field Separators 461
5.16.3 Application of Magnetic Separation 466
5.16.4 Magnetohydrostatic Separation 469
5.16.5 Electromagnetic-Induction-Type Separation 470
References 471

Chapter 5.17 Dry Dense Medium Separation 473

Jun Oshitani

5.17.1 Basis of Separation 473
5.17.2 Application of Separation 475
References 475

Chapter 5.18 Gravity Thickening 477

Eiji Iritani

5.18.1 Pretreatment 477
5.18.2 Ideal Settling Basin 477
5.18.3 Settling Curve 477
5.18.4 Kynch Theory 478
5.18.5 Design of Continuous Thickener 479
References 480

Chapter 5.19 Filtration 481

Eiji Iritani

5.19.1 Basis of Cake Filtration Theory 481
5.19.2 Constant-Pressure and Constant-Rate Filtration 484
5.19.3 Internal Structure of Compressible Filter Cake 485
5.19.4 Filtration of Non-Newtonian Fluid–Solid Mixtures 486
5.19.5 Filtration Equipment 486
References 488

Chapter 5.20 Expression 489

Eiji Iritani

5.20.1 Basis of Expression 489
5.20.2 Modified Terzaghi Model 489
5.20.3 Secondary Consolidation 491
5.20.4 Simplified Analysis 492
5.20.5 Expression Equipment 492
References 493

Chapter 5.21 Flotation 495

Wei Sung Ng, George Vincent Franks, Elizaveta Forbes, Luke Andrew Connal and Hiroki Yotsumoto

5.21.1 Fundamentals of Flotation 495
5.21.2 Minerals Separation 498
5.21.3 Flotation Reagents 499
5.21.4 Flotation Equipment 500
5.21.5 Plant Practice 503
5.21.6 Challenges in Flotation 505
5.21.7 Emerging Technologies 505
References 506

Chapter 5.22 Electrostatic Powder Coating 509

Ken-ichiro Tanoue

5.22.1 Coating Machines 509
5.22.2 Powder Feeding Machine 510
5.22.3 Powder Coating Booth 510
5.22.4 Numerical Simulation for Electrostatic Powder Coating 511
References 512

Chapter 5.23 Multipurpose Equipment 515

Hisao Makino and Hiromi Shirai (5.23.1, 5.23.2)
Junichi Tatami (5.23.3)

5.23.1 Fixed Beds 515
5.23.2 Moving Beds 516
5.23.3 Rotary Kiln 518
References 519

Chapter 5.24 Nanoparticle Handling and Formulation 521

Wolfgang Peukert and Stefan Romeis

5.24.1 Introduction and Overview 521
5.24.2 Formation of Nanoparticles 522
5.24.3 Dispersion of Nanoparticles 522
5.24.4 Nanoparticle Stabilization 523
5.24.5 From Surfaces to Properties – The Effect of Surface Modification 527
5.24.6 Nanoparticle Handling in Classical Unit Operations of Powder Processing 529
5.24.7 Processing of Functional Thin Films from Liquids 531
5.24.8 Conclusions 532
References 532

Chapter 5.25 Simulation of Powders and Particles in Dry and Wet Phases 535

Junya Kano and Jusuke Hidaka (5.25.1)
Mikio Sakai (5.25.2)
Yutaka Tsuji (5.25.3)
Mojtaba Ghadiri, Tina Bonakdar and Sadegh Nadimi (5.25.4)
Kenji Iimura and Ko Higashitani (5.25.5)
Ryoichi Yamamoto (5.25.6)

5.25.1 Powder Simulation Using Discrete Element Method (DEM) 535
5.25.2 Recent Advances in DEM Simulations for Industrial Applications 542
5.25.3 Particle Motion in Fluid 543
5.25.4 Breakage of Particles in Gas Phase 545
5.25.5 Breakage of Aggregates in Liquid Phase 549
5.25.6 Direct Numerical Simulations of Colloidal Particles in a Liquid 551
References 557

PART 6 Process Instrumentation

Chapter 6.1 Powder Sampling 563

Hiroaki Masuda

6.1.1 Sampling Equipment 563
6.1.2 Analysis of Sampling 564
References 566

Chapter 6.2 Particle Sampling in Gas Flow 567

Hideto Yoshida (6.2.1, 6.2.2)
Hisao Makino (6.2.3)

6.2.1 Anisokinetic Sampling Error 567
6.2.2 Sampling in Stationary Air 568

6.2.3 Practical Applications of Particle Sampling 570
References 573

Chapter 6.3 Concentration and Flow Rate Measurement 575

Shuji Matsusaka

6.3.1 Particle Concentration in Suspensions 575
6.3.2 Powder Flow Rate 577
References 579

Chapter 6.4 Level Measurement of Powder Bed 581

Shuji Matsusaka

6.4.1 Level Meters and Level Switches 581
6.4.2 Mechanical Methods 581
6.4.3 Electrical Methods 582
6.4.4 Ultrasonic Wave Level Meters 583
6.4.5 Radiometric Method 583
6.4.6 Pneumatic and Other Methods 583
References 584

Chapter 6.5 Temperature Measurement of Powder 585

Koichi Nakaso and Kuniaki Gotoh

6.5.1 Temperature Measurement by Contact-Type Thermometers 585
6.5.2 Temperature Measurement by Non-Contact-Type Thermometers 586
References 588

Chapter 6.6 On-Line Measurement of Moisture Content 589

Satoru Watano

6.6.1 Introduction 589
6.6.2 Electric Methods 589
6.6.3 Optical Moisture Sensor 591
6.6.4 Continuous Monitoring and Control of Moisture Content 593
References 594

Chapter 6.7 Tomography 595

Richard A. Williams

6.7.1 Introduction 595
6.7.2 Sensor Selection and Specification 596
6.7.3 Examples of Powder and Slurry Processing Applications 597
References 600

PART 7 Working Atmospheres-Risks, Hazards and Protection

Chapter 7.1 Health Effects Due to Particle Matter 603

Yasuo Morimoto and Toshihiko Myojo

7.1.1 Introduction 603
7.1.2 Respiratory System 603

7.1.3 Penetration and Deposition of Particles in the Respiratory Tract 603
7.1.4 Rate of Deposited Particles 604
7.1.5 Health Effects of Inhaled Particles 604
7.1.6 Threshold Limit Value 605
References 606

Chapter 7.2 Risks of Nanoparticles 607

Toshihiko Myojo (7.2.1–7.2.3)
Hidehiro Kamiya (7.2.4)

7.2.1 Introduction 607
7.2.2 Concept of Risk Assessment and Management of Nanomaterials 607
7.2.3 Risk Management Using Control Banding of Nanomaterials 608
7.2.4 Specific Risk and Measurement of PM2.5 609
References 611

Chapter 7.3 Respiratory Protective Devices for Particulate Matter 613

Toshihiko Myojo

7.3.1 Introduction 613
7.3.2 Types of Respirators 613
7.3.3 Protection Factor 615
7.3.4 Fit Check and Fit Test of Respirators 615
7.3.5 Selection, Use, and Maintenance of Respirators 616
References 616

Chapter 7.4 Dust Explosion 617

Ritsu Dobashi and Wei Gao

7.4.1 What is Dust Explosion? 617
7.4.2 Flame Propagation Mechanism in Dust Explosion 617
7.4.3 Risk of Dust Explosion 621
7.4.4 Prevention and Mitigation of Accidental Dust 627
References 632

Index 633

Part 1

Particle Characterization and Standard Powder



Taylor & Francis
Taylor & Francis Group
http://taylorandfrancis.com

1.1 Particle Size

JunIchiro Tsubaki

1.1.1 DEFINITION OF PARTICLE DIAMETER

Particle size data are essential to anyone treating powders. If particles are spherical, it is easy to define the particle size because the diameter is the unique expression of their size. In general, particles are not spherical but irregular in shape. Hence, the particle size is expressed in terms of various kinds of definitions. Major definitions of particle size are listed in Table 1.1.1.

The definitions frequently used are the sieve diameter, the laser scattering diameter, the diffusion diameter, the Stokes' diameter, the equivalent area diameter and the Feret's diameter. The sieve diameter is popular for coarse particles larger than several ten-micron meters. The laser scattering diameter is the most common because the particle size analyzers based on the laser scattering theory are very widely used. As particles less than 1 μm are usually measured with the dynamic laser scattering method, the diffusion diameter is popular. The Stokes' diameter has the clearest physical meaning, because it is determined from the settling velocity almost without mathematical assumptions. The sedimentation method is a precise particle size analyzer, and is important. In the case of analyzing the particle images, the particle size is commonly expressed with the equivalent area diameter or Feret's.

1.1.2 PARTICLE SIZE DISTRIBUTION

Size Distribution

When a characteristic diameter shown in Table 1.1.1 is measured for the total number of particles N and the number of particles dN between the diameters x and $x+dx$, the density size distribution $q_0(x)$ is defined as

$$q_0(x) = \frac{dN}{N}\frac{1}{dx} \tag{1.1.1}$$

where

$$\int_0^\infty q_0(x)dx = 1 \tag{1.1.2}$$

TABLE 1.1.1 Definition of Characteristic Diameters of Particles

		Characteristic Diameters	Physical Meaning
Definitions by Size-Dependent Behavior		Sieve diameter	The width of the minimum square aperture through which the particle will pass.
	Equivalent Diameters	Laser scattering diameter	Diameter of a sphere giving the same laser scattering pattern as the particle. The sphere has the same refractive index as the particle.
		Diffusion diameter	Diameter of a sphere giving the same diffusion coefficient as the particle.
		Stokes' diameter	Diameter of a sphere giving the same settling velocity as the particle. The sphere has the same density as the particle.
		Equivalent volume diameter	Diameter of a sphere having the same volume as the particle.
Geometrical Definitions		Equivalent surface area diameter	Diameter of a sphere having the same surface area as the particle.
		Equivalent specific surface area diameter	Diameter of a sphere having the same specific surface area as the particle.
		Equivalent area diameter (Heywood diameter)	Diameter of a circle having the same projected area as the particle.
		Equivalent perimeter diameter	Diameter of a circle having the same projected perimeter as the particle.
	Three-Axis Diameters	Thickness	The minimum distance between two parallel planes which are tangential to opposite surface of the particle, one plane being the plane of maximum stability.
		Breadth	The minimum distance between two parallel planes which are perpendicular to the planes defining the thickness and tangential to opposite sides of the particle.
		Width	The distance between two parallel planes which are perpendicular to the planes defining the thickness and the breadth and tangential to opposite sides of the particle.
	Statistical Diameters	Feret's diameter	The distance between two parallel lines which are tangential to the projected outline of the particle.
		Martin's diameter	The chord length of the projected outline of the particle. The two projected areas divided by the chord are same.
		Unrolled diameter	The mean chord length through the center of gravity of the particle.

The cumulative distribution $Q_0(x)$ is given as

$$Q_0(x) = \int_0^x q_0(x)dx \tag{1.1.3}$$

Therefore,

$$\frac{dQ_0(x)}{\mathrm{d}x} = q_0(x) \tag{1.1.4}$$

$q_0(x)$ and $Q_0(x)$ are the number basis distributions. In the case of mass or volume basis, the total mass M and fractional mass dM are used instead of N and dN, respectively, and the subscript r changes from 0 to 3, such as $q_3(x)$, $Q_3(x)$. In general, the subscripts $r=0$, 1, 2 and 3 represent the number, length, area and mass or volume basis, respectively. A density distribution $q_r(x)$ can be converted to another distribution $q_s(x)$ having the subscript of s by

$$q_s(x) = \frac{x^{s-r}q_r(x)dx}{\int_0^\infty x^{s-r}q_r(x)dx} \tag{1.1.5}$$

When the particle size distributes in a wide range, the distribution is plotted against ln$x$ instead of x and defined as

$$Q_r(\ln x) = Q_r(x) \tag{1.1.6}$$

$$q_r^*(\ln x) = \frac{dQ_r(x)}{d\ln x} = xq_r(x) \tag{1.1.7}$$

The density distribution represented with a logarithmic abscissa is distinguished by superscript*.

The discrete expressions, which give the histograms of size distribution, $\overline{q}_{r,i}$, $\overline{q}^*_{r,i}$, are given by

$$\overline{q}_{r,i} = \frac{\Delta Q_{r,i}}{\Delta x_i} = \frac{Q_r(x_i) - Q_r(x_{i-1})}{x_i - x_{i-1}} \tag{1.1.8}$$

$$\overline{q}^*_{r,i} = \frac{\Delta Q_{r,i}}{\Delta \ln x_i} = \frac{Q_r(x_i) - Q_r(x_{i-1})}{\ln(x_i/x_{i-1})} \tag{1.1.9}$$

Normal Distribution

The normal or Gaussian distribution function is defined as

$$q_r(x) = \frac{1}{\sigma\sqrt{2\pi}}\exp\left[-\frac{(x-x_{50})^2}{2\sigma^2}\right] \tag{1.1.10}$$

where

x_{50} is the 50% or median diameter defined as $Q_r(x_{50}) = 0.5$.

σ is the standard deviation expressing the dispersion distribution, and is defined by

$$\sigma = x_{84.1} - x_{50} = x_{50} - x_{15.9} \tag{1.1.11}$$

Log-Normal Distribution

The log-normal distribution function is given by substituting $\ln x$ and $\ln\sigma_g$ for x and σ in Equation (1.1.10) respectively, as follows:

$$q_r^*(\ln x) = \frac{1}{\ln\sigma_g \cdot \sqrt{2\pi}}\exp\left[-\frac{(\ln x - \ln x_{50})^2}{2\ln^2\sigma_g}\right] \tag{1.1.12}$$

where σ_g is the geometric standard deviation given as,

$$\sigma_g = \frac{x_{84.1}}{x_{50}} = \frac{x_{50}}{x_{15.9}} \tag{1.1.13}$$

If a size distribution obeys the log-normal form, the distribution converted by Equation (1.1.5) also obeys the log-normal form. Their geometric standard deviations are the same, and the median diameters are different but can convert each other. In the case of the volume and number distributions, the corresponding median diameters, $x_{50,3}$ and $x_{50,0}$, can convert each other by Hatch's Equation.

$$\ln x_{50,3} = \ln x_{50,0} + 3\ln^2\sigma_g \tag{1.1.14}$$

Rosin-Rammler (Weibull) Distribution

The Rosin-Rammler or Weibull distribution function is written as

$$Q_r(x) = 1 - \exp\left(-bx^n\right) \text{ or}$$
$$Q_r(x) = 1 - \exp\left[-\left(\frac{x}{x_e}\right)^n\right] \tag{1.1.15}$$

where

b is a constant equal to x_e^{-n}.

x_e is the absolute size constant defined by $Q_r(x_e) = 1 - e^{-1} = 0.632$ that is, $x_e = x_{63.2}$.

n is the distribution constant expressing the dispersion of particle size.

The density distribution is written as

$$q_r(x) = nbx^{n-1}\exp(-bx^n) \text{ or}$$
$$q_r(x) = \frac{1}{x}\left(\frac{x}{x_e}\right)^n \exp\left[-\left(\frac{x}{x_e}\right)^n\right] \tag{1.1.16}$$

TABLE 1.1.2 Calculation of the Histogram and the Cumulative Distribution

1	2	3	4	5	6	7	8
i	x_i	ΔM_i	$Q_{3,i}$	Δx_i	$\bar{q}_{3,i}$	$\Delta \ln x_i$	$(\bar{q}_{3,i})$
	(mm)	($\times 10^{-3}$kg)	(%)	(mm)	(%mm^{-1})		(%)
0	0.063		0				
1	0.09	0.1	0.1	0.027	3.7	0.357	0.3
2	0.125	0.27	0.37	0.035	7.7	0.329	0.8
3	0.18	1.03	1.4	0.055	18.7	0.365	2.8
4	0.25	2.2	3.6	0.07	31.4	0.329	6.7
5	0.355	5.4	9	0.105	51.4	0.351	15.4
6	0.5	9.3	18.3	0.145	64.1	0.342	27.2
7	0.71	13.7	32	0.21	65.2	0.351	39.1
8	1	17	49	0.29	58.6	0.342	49.6
9	1.4	17	66	0.4	42.5	0.336	50.5
10	2	14.6	80.6	0.6	24.3	0.357	40.9
11	2.8	9.9	90.5	0.8	12.4	0.336	29.4
12	4	5.6	96.1	1.2	4.7	0.357	15.7
13	5.6	2.4	98.5	1.6	1.5	0.336	7.1
14	8	1.1	99.6	2.4	0.5	0.357	3.1
15	11.2	0.3	99.9	3.2	0.1	0.336	0.9
16	16	0.1	100	4.8	0.0	0.357	0.3

Graphical Representation[1]

As an example, a set of data obtained by a sieving test is given in Table 1.1.2. The corresponding size distributions are illustrated in Figure 1.1.1 with a linear abscissa and Figure 1.1.2 with a logarithmic abscissa. $Q_{3,i}$ in Table 1.1.2 is plotted on a log-normal and Rosin-Rammler probability paper as shown in Figure 1.1.3. Since the plots are on a straight line on a log-normal probability graph, the particle size distribution obeys the log-normal function of $x_{50} = 1.0\,\text{mm}$ and $x_{84.1} = 2.2\,\text{mm}$. If we are able to read the values of $x_{15.9}$ and either one of x_{50} or $x_{84.1}$ from the figure, σ_g can be calculated: $x_{50} = 1.0\,\text{mm}$ and $x_{84.1} = 2.2\,\text{mm}$, and so $\sigma_g = 2.2$. The dotted line in Figure 1.1.3 is the number distribution converted from measured volume distribution by Hatch's equation.

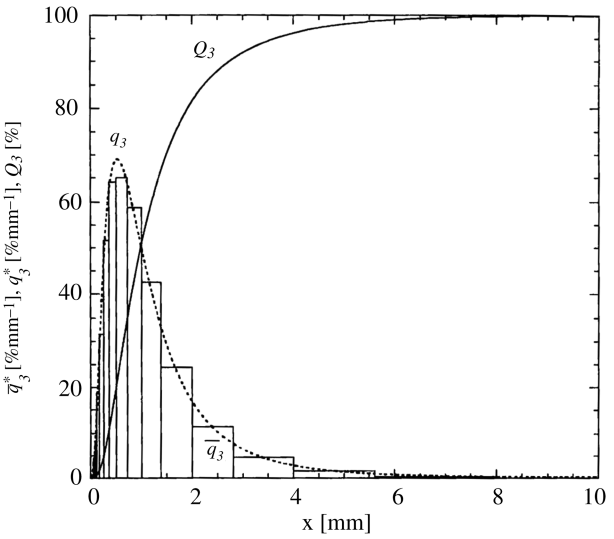


FIGURE 1.1.1 A graphical representation of particle size distribution with a linear abscissa.

Definition of Characteristic Diameters of Particles

1.1.3 AVERAGE PARTICLE SIZE[2]

All average particle diameters except the geometric mean diameter are defined by

$$\bar{x}_{k,r} = \sqrt[k]{M_{k,r}} = \sqrt[k]{\frac{M_{k+r,0}}{M_{r,0}}} = \sqrt[k]{\frac{M_{k+r-3,3}}{M_{r-3,3}}} \tag{1.1.17}$$

where $M_{k,r}$ is the complete k-th moment of a $q_r(x)$-distribution

$$M_{k,r} = \int_0^\infty x^k q_r(x)\,dx \tag{1.1.18}$$

The geometric mean diameter is defined as

$$\ln \bar{x}_{geo,r} = \int_0^\infty \ln x \cdot q_r(x)\,dx \tag{1.1.19}$$

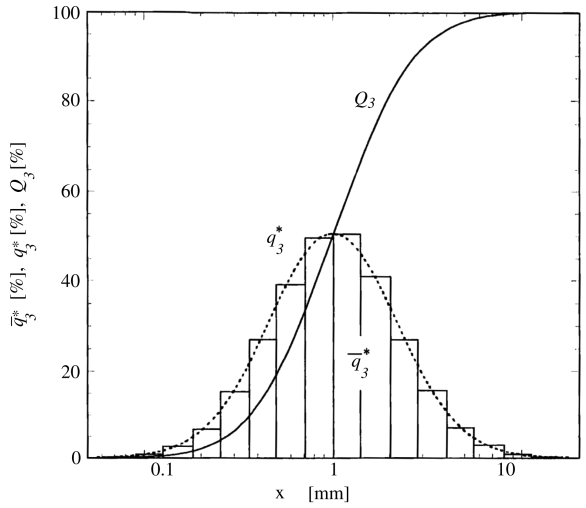


FIGURE 1.1.2 A graphical representation of particle size distribution with a logarithmic abscissa.

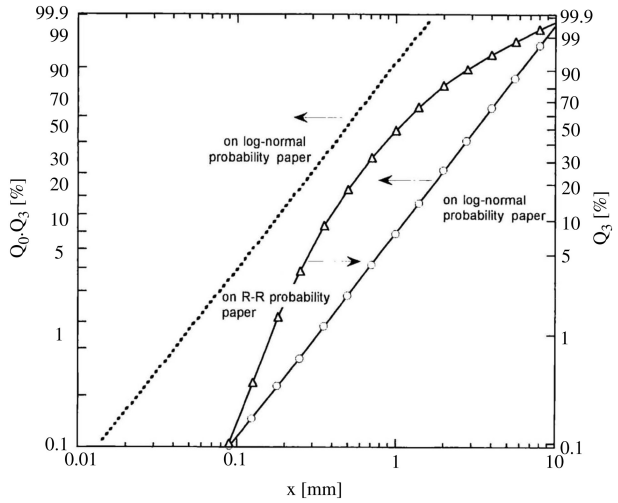


FIGURE 1.1.3 Cumulative distributions on a log-normal and Rosin–Rammler distribution graph.

Although a lot of average diameters can be defined, those listed in Table 1.1.3 are generally used. If a density distribution is given as a histogram, $M_{k,r}$ is calculated by the following equations. Equation (1.1.18) is rewritten as follows if $k \neq -1$.

$$M_{k,r} = \sum_{i=1}^{m} \overline{q}_{r,i} \int_{x_{i-1}}^{x_i} x^k dx$$

$$= \frac{1}{k+1} \sum_{i=1}^{m} \overline{q}_{r,i} \left(x_i^{k+1} - x_{i-1}^{k+1} \right) \qquad (1.1.20)$$

$$= \frac{1}{k+1} \sum_{i=1}^{m} \Delta Q_{r,i} \left(\frac{x_i^{k+1} - x_{i-1}^{k+1}}{x_i - x_{i-1}} \right)$$

If $k = -1$,

$$M_{-1,r} = \sum_{i=1}^{m} \overline{q}_{r,i} \ln \frac{x_i}{x_{i-1}} = \sum_{i=1}^{m} \Delta Q_{r,i} \frac{\ln \frac{x_i}{x_{i-1}}}{x_i - x_{i-1}} \qquad (1.1.21)$$

Equation (1.1.19) is rewritten as follows:

$$\ln \overline{x}_{geo,r} = \sum_{i=1}^{m} \overline{q}_{r,i} \int_{x_{i-1}}^{x_i} \ln x dx$$

$$= \sum_{i=1}^{m} \frac{\overline{q}_{r,i}}{x_i - x_{i-1}} = \sum_{i=1}^{m} \frac{\Delta Q_{r,i}}{\left(x_i - x_{i-1} \right)^2} \qquad (1.1.22)$$

The values of the average diameters can be calculated from the data in Table 1.1.2. The results are given in Table 1.1.3.

The spread of a size distribution is represented by its variance, which is the square of the standard deviation, σ^2. The variance of a $q_r(x)$-distribution is defined as:

$$\sigma^2 = \int_0^\infty \left(x - \overline{x}_{1,r} \right)^2 q_r(x) dx = M_{2,r} - \left(M_{1,r} \right)^2. \qquad (1.1.23)$$

From a histogram:

$$\sigma^2 = \frac{1}{3} \left[\sum_{i=1}^{m} \overline{q}_{r,i} \left(x_i^3 - x_{i-1}^3 \right) \right]$$

$$- \frac{1}{4} \left[\sum_{i=1}^{m} \overline{q}_{r,i} \left(x_i^2 - x_{i-1}^2 \right) \right]^2$$

$$= \frac{1}{3} \left[\sum_{i=1}^{m} \Delta Q_{r,i} \left(\frac{x_i^3 - x_{i-1}^3}{x_i - x_{i-1}} \right) \right] \qquad (1.1.24)$$

$$- \frac{1}{4} \left[\sum_{i=1}^{m} \Delta Q_{r,i} \left(x_i + x_{i-1} \right) \right]^2$$

The standard deviation of the particle sizes given in Table 1.1.2 is calculated as $\sigma = 1.29\,\text{mm}$ by Equation (1.1.24).

NOTATION

i: number of the size class with upper particle size, x_i
k: power of x
m: total number of size classes
$M_{k,r}$: complete k-th moment of a $q_r(x)$-distribution
n: distribution constant
N: number of particles
$q_r(x)$: density distribution
q_r: $= q_r(x)$
$q_r^*(\ln x)$: density distribution in a representation with a logarithmic abscissa

TABLE 1.1.3 Cumulative Distributions on a Log-Normal and Rosin–Rammler Distribution Graph

Average Diameters	Symbols	Examples of Table 1.1.2 [mm]
Arithmetic average length diameter (Weighted average number diameter)	$\overline{x}_{1,0}$	0.228
Arithmetic average surface diameter	$\overline{x}_{2,0}$	0.303
Arithmetic average volume diameter	$\overline{x}_{3,0}$	0.410
Weighted average length diameter	$\overline{x}_{1,1}$	0.402
Weighted average surface diameter, Sauter-diameter	$\overline{x}_{1,2}$	0.749
Weighted average volume diameter	$\overline{x}_{1,3}$	1.40
Harmonic mean diameter	$\overline{x}_{1,r}$	0.147 ($r=0$)
		0.749 ($r=3$)
Geometric mean diameter	$\overline{x}_{geo,r}$	3.98 ($r=3$)

q_r^*: $= q_r^*(x)$
$\overline{q}_{r,i}$: average density distribution of the class Δx_i, histogram
$\overline{q}_{r,i}^*$: average density distribution of the class $\Delta \ln x_i$, histogram
$Q_r(x)$: cumulative distribution
Q_r: $= Q_r(x)$
$\Delta Q_{r,i}$: $= Q_r(x_i) - Q_r(x_{i-1})$
x: particle size, diameter of a sphere
x_e: absolute size constant
x_i: upper size of a particle size interval
x_{i-1}: lower size of a particle size interval
Δx_i: $= x_i - x_{i-1}$, width of the particle size interval
$x_{15.9}, x_{50}, x_{63.2}, x_{84.1}$: defined as $Q_r(x_{15.9}) = 0.159$, $Q_r(x_{50}) = 0.5$, $Q_r(x_{63.2}) = 0.632$, $Q_r(x_{84.1}) = 0.841$
$x_{50,3}$: median particle size of a cumulative volume distribution
$x_{50,0}$: median particle size of a cumulative number distribution
r, s: type of quantity of a distribution, $r, s = 0, 1, 2, 3$
σ: standard deviation
σ_g: geometrical standard deviation of log-normal distribution

REFERENCES

1. ISO 9276-1 (JIS Z 8819-1), Representation of results of particle size analysis-Part 1: Graphical representation.
2. ISO 9276-2 (JIS Z 8819-2), Representation of results of particle size analysis-Part 2: Calculation of average particle size/diameters and moments from particle size distributions.



Taylor & Francis
Taylor & Francis Group
http://taylorandfrancis.com

1.2 Size Measurement

Yasushige Mori

1.2.1 INTRODUCTION

The equivalent diameter, D_ρ, of a sphere is defined by the product between particle size, X, and the adjustment factor, F.

$$D_\rho = FX \tag{1.2.1}$$

where the value of F, which is unity for spherical particles, depends on the detecting physical principles and the measuring instruments. Hence, the average particle sizes calculated from the data obtained by the sedimentation, light scattering, and diffusion measurements will not necessarily coincide each other. The differences obtained may provide the valuable fingerprint of particles which may characterize their specific properties.

Table 1.2.1 shows some common expressions defined for the size of irregular particles, which are classified into two groups. The first nine expressions, which are classified as a geometric diameter, are obtained from the shape information of particles by microscopy, image analysis, and other methods. The rest of the expressions are obtained from the dependency of physical interactions toward particles, such as movement of particles in the gravitational or electrical field, Brownian motion, or electromagnetic interaction. Figure 1.2.1 shows the dependence of the physical properties of a particle on the particle size. The electrical mobility and Brownian diffusion increase with decreasing particle size. This means those physical properties can be used for the size measurement technique of small particles. On the other hand, the light scattering intensity or terminal settling velocity increases with particle size. This is the reason why the methods are used for relatively larger particles.

The particle size distribution (PSD) will be determined from many particles with different sizes. There are several types of PSD such as the number of particles (number-based PSD), the volume of particles (volume-based PSD), or the light scattering intensity of particles (optical-based PSD). It can be converted mathematically to other types of PSD, if all particles are spheres. In the case of irregular particles, however, this PSD conversion is impossible. Hence, one can only compare with the results of particle size measurements, which were done using the same definition of size and the same type of PSD. For example, when particles of the test sample are measured by microscope and analyzed with particle size as Feret diameter, the PSD is obtained as a number-based PSD. On the other side, the PSD of the same test sample is calculated based on the volume of particles using Stokes' diameter from the results measured by the sedimentation method. When comparing those two PSDs, they might be not agreed with each other, even if the number-based PSD was converted to the volume-based PSD mathematically.

In this chapter, theory will be minimal and only typical methods or instruments of size measurement will be discussed. As for the other methods, the corresponding reference books are simply referred.[1–4]

TABLE 1.2.1 Several Expressions of Particle Size of Irregular Particles

Average length	The average diameter of the longest chords measured along the upper surface of a particle in the position of rest
Average breadth	The average diameter at right angles to the diameter of average length along the upper surface of a particle in its position of rest
Feret diameter	The distance between two parallel tangents on opposite sides of the image of a particle in its position of rest
Martin diameter	The diameter which divides the particles profile into two equal areas measured in the direction of scan when the particle is in a position of rest
Projected area diameter (Haywood diameter)	The diameter of the circle having the same area as the projected image of the particle in the position of rest
Particle sieve diameter	The width of the minimum square aperture through which the particle will pass
Specific surface diameter	The diameter of the sphere having the same ratio of external surface area to volume as the particle
Equivalent surface area diameter	The diameter of the sphere having the same surface area as the particle
Equivalent volume diameter	The diameter of the sphere having the same volume as the particle
Stokes diameter	The diameter of the sphere having the same density and terminal settling velocity as the particle in the same liquid under creeping flow conditions
Equivalent aerodynamic diameter	The diameter of the sphere with 1 kg/m^3 density having the same terminal settling velocity as the particle in gas
Equivalent electrical mobility diameter	The diameter of the sphere having the same electrical mobility as the particle
Equivalent diffusion (or hydrodynamic) diameter	The diameter of the sphere having the same diffusion coefficient as the particle
Equivalent light scattering diameter	The diameter of a homogeneous sphere of a reference substance (e.g. latex) which scatters defined incident light with the same radiation efficiency into a defined solid angle element

1.2.2 CLASSIFICATION OF PARTICLE SIZE ANALYSIS METHODS

The methods of particle size analysis can be grouped as follows:

Counting analysis:

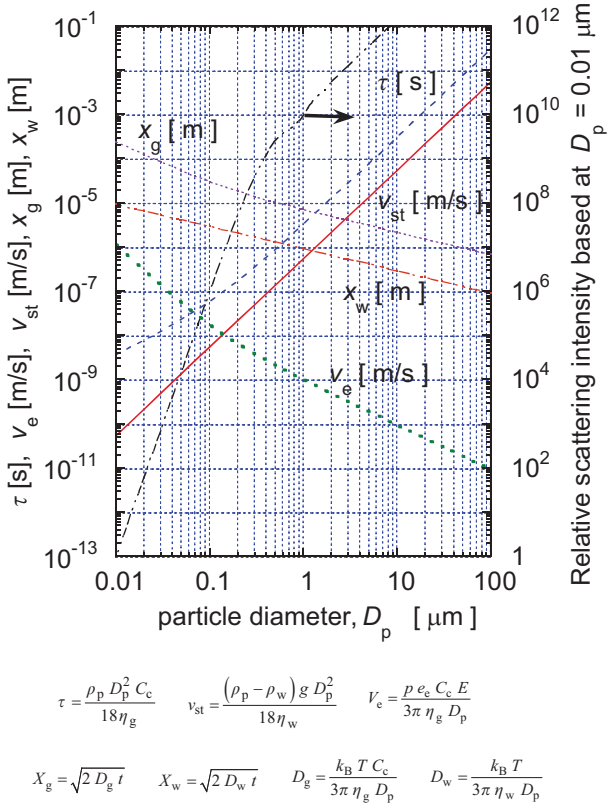
In this analysis, each particle can be measured for size one by one, and the PSD based on number is usually obtained. However, a large number of particles must be counted to obtain the representative result for an actual sample. Typical methods in this category are listed in Table 1.2.2.

Fractionation analysis:

In this analysis, the sample is separated into nearly monodispersed fractions prior to quantifying the particles. Some methods in this category are coupled with on-line or off-line ensemble or counting analysis. This analysis has higher reliability than the counting analysis and higher resolution than the ensemble analysis, although the PSD could depend on the recovery problem at the fraction step, on the quantifying method, and on the measurement of the particle concentration of the fraction. The typical methods in this category are listed in Table 1.2.3.

Ensemble analysis:

In this analysis, a large number of particles are measured simultaneously and the size information from many particles is obtained as one physical signal. The PSD is extracted from this signal using the mathematical model based on the physical principle of the measuring method, and could strongly depend on the analytical algorithm of calculation. The typical methods in this category are listed in Table 1.2.4.



$$\tau = \frac{\rho_p D_p^2 C_c}{18\eta_g} \qquad v_{st} = \frac{(\rho_p - \rho_w) g D_p^2}{18\eta_w} \qquad V_e = \frac{p e_e C_c E}{3\pi \eta_g D_p}$$

$$X_g = \sqrt{2 D_g t} \qquad X_w = \sqrt{2 D_w t} \qquad D_g = \frac{k_B T C_c}{3\pi \eta_g D_p} \qquad D_w = \frac{k_B T}{3\pi \eta_w D_p}$$

FIGURE 1.2.1 Dependence of Physical Properties of Particle on Particle Size. τ: relaxation time of particle in air (ρ_p=1000 kg m^{-3}), V_{st}: terminal settling velocity of particle in water expressed by Equation 1.2.4 (ρ_p=2000 kg m^{-3}, ρ_w=1000 kg m^{-3}), V_e: electrical mobility of particle in air expressed by Equation 1.2.7 (number of elementary charges, p=1, electric field, E=1 V m^{-1}), X_g: root mean square moving distance of particle in air by Brownian diffusion for one second, X_w: root mean square moving distance of particle in water by Brownian diffusion for one second. C_c: Cunningham correction, η: viscosity, subscript, g: air, w: water, p: particle

1.2.3 COUNTING ANALYSIS

The most important procedure in this analysis is how many particles should be counted to get the reliable PSD. The standard deviation, s, of a cumulative undersize distribution of the number-based PSD, $Q_0(x_i)\left(0 \le Q_0(x_i) \le 1\right)$, at any particle diameter x_i can be calculated using the mathematics of binomial distribution.[2]

$$s^2 = \frac{Q_0(x_i)\{1 - Q_0(x_i)\}}{N} \tag{1.2.2}$$

TABLE 1.2.2 Several Particle Size Measurement Methods Grouped in Counting Analysis

Method	Size Range [μm]	Equivalent Diameter	Base of Size Distribution
Image analysis (optical)	3–	geometric	number
Image analysis (SEM)	0.01–500	geometric	number
Image analysis (TEM)	0.001–5	geometric	number
Light scattering	0.1–100	light scattering	number
Light extinction	1–500	geometric	number
Time-of-fight	0.5–200	aerodynamic	number
Electro sensing zone	0.5–1000	volume	number
Particle tracking	0.05–1	diffusion	number

TABLE 1.2.3 Several Particle Size Measurement Methods Grouped in Fractionation Analysis

Method	Size Range [μm]	Equivalent Diameter	Base of Size Distribution
Sieving	5–	sieve	volume
Sedimentation (gravity)	0.5–200	Stokes	volume or optical
Sedimentation (centrifugal)	0.005–10	Stokes	volume or optical
Chromatographic	0.01–10	volume	optical
Inertial impaction	0.01–50	aerodynamic	volume
Electrical mobility classification	0.002–1	electrical mobility	number
Diffusion battery	0.01–1	diffusion	number

TABLE 1.2.4 Several Particle Size Measurement Methods Grouped in Ensemble Analysis

Method	Size Range [μm]	Equivalent Diameter	Base of Size Distribution
Dynamic light scattering	0.005–1	diffusion	optical
Laser diffraction / scattering	0.1–1000	light scattering	volume
Small angle x-ray scattering	0.001–0.3	x-ray scattering	x-ray scattering
Acoustic	0.01–2000	ultrasound attenuation	volume
Induced gradient	0.02–0.3	diffusion	volume

TABLE 1.2.5 Values of u_0 and Confidence Level (1–α)

confidence level (1 – α) [%]	50	75	80	90	95	97.5	99	99.5
u_0	0.67	1.15	1.28	1.64	1.96	2.24	2.57	2.81

TABLE 1.2.6 *r*-value for Quantity Type of PSD

Type of Quantity of PSD	Number	Length	Area	Volume
r	0	1	2	3

where N is the total number of particles of all size classes. The standard deviation, s, is the maximum when $Q_0(x_i) = 0.5$; s will always be less than 2%, which is an acceptable error for most instances, if $N \geq 625$ particles.

For the volume- or mass-based PSDs, the general calculation of the standard deviation is not simple. When the PSD is expressed by a log-normal distribution, the number of particles, N^*, should be counted to obtain the mean diameter, $\bar{x}_\beta$, under the condition of confidence level, (1–α), and relative error, δ_0, from the number-based PSD.[5]

$$N^* = \left(\frac{u_0 \beta \sigma}{\delta_0}\right)^2 \left(2\sigma^2 c^2 + 1\right) \tag{1.2.3}$$

where $c = r + \beta/2$, $\sigma = \ln \sigma_g$, and u_0, r, and β are given in Tables 1.2.5, 1.2.6, and 1.2.7, respectively. σ_g is the geometric standard deviation of PSD. Hence, if the following mean diameters are obtained from the number-based PSD (r=0) with $\sigma_g = 1.53$ within $(1-\alpha) = 95\%$ and δ_0=0.03 (3%), the number of particles is counted over 840 for the number mean diameter (β=1). However, the number of particles is counted over 12600 or 118000 for the mean volume diameter (β=3) or mass median diameter (β=5) under the same condition, respectively. Hence, to make a comparison between the number-based and the volume-based PSDs, an enormous number of particles should be counted. Otherwise, one particle with large volume could be omitted easily from statistical viewpoint. For example, when a sample has 999 particles of 1 μm in diameter and one 10 μm particle, the omission of one 10 μm particle results in neglecting approximately 50% of the mass. Hence, very accurate assessment of the largest particles in the sample is essential for the mass-based PSD.

TABLE 1.2.7 β-value for Various Mean Diameters

Mean Diameter	Number Mean Diameter	Mean Volume Diameter	Surface Mean Diameter (mean volume-surface diameter)	Mass Median Diameter	Volume Mean Diameter
β	1	3	5	6	7

Static Image Analysis Method

The microscopic method is important because the absolute range of sizes and the degree of dispersion is directly obtained. As this method nowadays combines with a high performance computer, a large number of particles could be measured for a relatively short time and the shape or morphology analysis could be done simultaneously during the size analysis. The most important point especially in this method is the sample preparation technique: how to disperse particles and prevent the particle aggregation and segregation at the sample preparation on the observing substrate. Another important note for irregular-shaped particles is that particle imaging can vary significantly depending on the orientation of the particles on the observing substrate.

The optical microscope may be used to measure particle size down to about 3 μm. When particles are of this size, the light diffraction at particle edges makes the particle size and shape unclear. A Scanning Electron Microscopy (SEM) or a Transmission Electron Microscopy (TEM) should be used for the image below a few micrometers, instead of the optical microscope. Because SEM detects the backscatter electron beam, particles are dispersed onto a metal substrate and made conductive by coating with a thin layer of carbon in a vacuum evaporator to prevent the surface charge on the particles. In TEM, particles are deposited on a very thin film which is transparent to the electron beam. This film is supported on metal grids or frames.

Dynamic Image Analysis Method

The size of moving particles in a liquid or gas and on a conveyor is detected by the image capture such as a Charge Coupled Device (CCD) or Complementary Metal Oxide Semiconductor (CMOS) device, and analyzed as the projected area diameter. The most important point for this method is to disperse particles so that they don't overlap each other, as in case of the static image analysis method, as well as their sharp images at the image capture point.

The resolution of the image by a dynamic image analysis method depends not only on the optical system, such as the lens magnification and camera resolution, but also on the lighting system and the velocity of the particles. In the image analysis method, the particle edge is defined by the suitable threshold level, checking whether the particle edge in the moving direction is unclear or not. It is strongly recommended that the threshold level should be adjusted by comparing the processed binary images with the original images, to ensure that the binary images are a reliable representation of the original images. In the case of particles in liquid, the edge image of the particle becomes sometimes unclear when the difference of refractive indexes between particles and surrounding medium decreases. In order to make a clear image of the edge in this case, it is strongly recommended to use the medium whose refractive index is not near of particles.

Light Scattering Method

Particles in air or liquid are forced to flow into the measuring zone of their scattering light. The intensity of scattered light of each particle is converted to its size using some calibration or assumptions for the scattering behavior. The typical instrument of this method is called an Optical Particle Counter. Either white light or laser is used as the light source. The particle concentration should be diluted for the measurement of an individual particle like a flow cytometry. Compared with the dynamic image analysis method, this method has an advantage to be able to measure smaller particles, because the scattering intensity of one particle is used instead of the detection of the projected area of a particle. On the other hand, the disadvantage of this method is that the higher dilution of the sample and longer measuring time are needed. Recently, the method was expanded to using a two-dimensional image from a one-dimensional image by the stream line of the suspension, where the number-based PSD can be obtained in a short measuring time.

Condensation Particle Counter or Condensation Nucleus Counter is used for the concentration measurement of aerosols. When particles become small enough not to detect their scattering intensity, they flow through a chamber with saturated vapor, such as the vapors of 1-butanol or 2-propanol. The vapor condenses on the particle surface, and then particles become large enough to detect their light scattering signal. This instrument counts only the number of particles, but does not measure the particle size. So it is usually used combining with the fractionation analysis, such as the electrical mobility classification method.

Light Extinction Method

This method is known as Focused Beam Reflectance Method or Time of Transition Technique. When a particle suspension is scanned by the focused laser beam, the reflected light on the particle surface is measured. This measured time of reflection together with the scanning speed of the laser beam is used to evaluate the size information of particles. Because this evaluated length for one particle varies statistically from zero to

the maximum length of the particle, and moving particles are not randomly oriented, no adequate model exists to determine the particle size from the experimental data at present. Moreover, there is no method to estimate the probability of multiple counting of particles. However, the advantage of this technique is that the time-varying PSD can be monitored in the inline processes.

Time-of-Flight Method

In this method, aerosol particles are rapidly accelerated through a nozzle and focused by a clean sheath of air. At the short distance after the exit of the nozzle, a particle passes two focused laser beams whose distance is about 0.1–1 mm, and makes a short pulse of scattered light in each beam. The time interval between the two pulses gives the time-of-flight of each particle, and then the aerodynamic diameter can be calculated from this measured time. Nowadays, this technique is combined with the mass spectrometer, which makes the chemical composition of individual particles measurable, as well as their size. This is useful for determining the characteristic of airborne particles for environmental science.

Electro Sensing Zone Method

Suspensions of dilute concentration of particles in a conductive liquid are employed in this method. Particles pass through an orifice of a given size by the pressure difference, as shown in Figure 1.2.2. A constant DC voltage is applied between two electrodes located at either side of the orifice. The tube with the orifice is called as an aperture tube. When a particle passes through the orifice, a pulse change of current is detected by the impedance change, and the particle volume can be known from the pulse height of the current. Many pulses are counted to obtain volume-based PSD. The measurable particle size range by this method is from 0.6 to 1200 μm, although several orifices of different sizes have to be used to achieve this size range, because each orifice can sense only particles with the size range from 2% to 60% of the orifice diameter. The main problems of this method are the blockage of the orifice hole by large particles, the multiple passages of particles at the same time, and the detection limit of 2% to 60% of the orifice size. In spite of these problems, this method has high precision, high resolution, and full traceability if the proper calibration is properly done with the standard reference material beforehand.

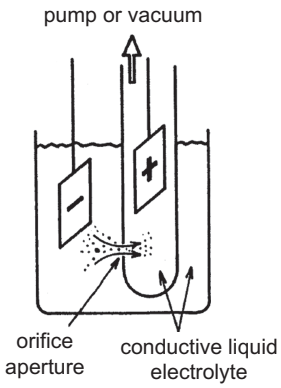


FIGURE 1.2.2 Principle of electro sensing zone method.

Recently, the instrument with a changeable pinhole in polymer film instead of the aperture in glass tube was developed. Particles with a size range from ten nanometers to a few micrometers can be measured in this instrument. When the diameter of a pinhole decreases, however, the high electrolyte solution needs in order to detect a pulse current for the signal that a particle passes through a pinhole. Such a high electrolyte solution rises to the agglomeration of particles, and then the measurement of PSD is much more difficult to compare with the ordinary method, even if the adequate surfactant is used to prevent particle agglomeration.

Particle Tracking Method

A laser beam irradiates particles in liquid, and light scattered from each particle is collected by an ultramicroscopy and visualized by a suitable detector, such as a CCD or CMOS device. By recording a series of sequential images, a computer tracks individual particles in time and space, allowing analysis of their movements. By tracking individual particles of random Brownian motion, from frame to frame, the average spatial displacement of the particles per unit time can be calculated, and the diffusion coefficient of a particle can be estimated by this displacement. And then the diffusion (i.e. hydrodynamic) diameter of the particles can be calculated through the Stokes-Einstein formula.

When the sample has a monodispersed or narrow PSD, this method can work well by checking how long one particle can be traced. When the PSD becomes wide, however, the tracking data of many particles need the accuracy of the measurement and it is very difficult to detect the light from smaller particles because the light intensity of the size range to be able to measure in this method is usually proportional to about 4–6 orders of magnitude of particle diameter.

1.2.4 FRACTIONATION ANALYSIS

This fractionation analysis is typified by procedures that permit the extraction of a certain size class from the feed sample followed by a measurement of the percentage by mass or number of the removed size class relative to the feed concentration.

Sieving Method

Sieving is well known as the oldest form of this analysis. Sieving consists of a plate or a mesh of intersecting wires with numerous openings of a fixed size. The sample powder is placed on the sieve and then shaken, so that particles of a size smaller than the holes pass through. To speed up the analysis, several sieves are placed on top of each other, the coarsest at the top and the rest shaken until the residue on each sieve contains particles, which cannot pass through the lower sieve. A Ro-tap shaker machine with horizontal rotary and vertical

tapping motion is highly effective for strong adhesive particles. When particles highly agglomerate, air-swept sieves or wet sieves are effective.

The error of the sieving method mainly comes from a large deviation of opening size. Hence, sieve calibration is necessary at frequent intervals of use if size analysis is to be accurate. Several approaches have been used, including microscopy and sieving with standard powders. The latter is more tedious, but for woven sieves, it gives a better measure of three-dimensional aperture sizes and calibrates the sieve in terms of volume diameter using the actual procedure used for size measurement.

As sieving is a rate process and the passage of a particle through an aperture is a statistical procedure, sieving accuracy (i.e. the time of sieving) depends also on PSD spread of sizes, the number and mass of particles on the sieve surface, the particle shape, the method of shaking, and the percentage of open area. This means PSD obtained from sieving method depend on the operation conditions and an operator. The sieving process is simple but its result needs the accuracy check due to the above notes.

Sedimentation Method

Sedimentation method is based on the settling of a single sphere under gravitational or centrifugal fields. This method is classified according to the following operating and measuring parameters: feed inlet way of sample, detection system, and applied external force field as shown in Figure 1.2.3. The feed inlet way of sample means how to start the measurement, i.e. the line start where the sample suspension feeds on the top of a clear solution, or the homogeneous start where the homogeneous particle concentration of the sample suspension is used at the start of measurement. For the detection systems, the particle concentration is detected at a known depth below the surface of the solution (incremental detection system), or the particle mass deposited on the bottom is detected (cumulative detection system). And gravitational or centrifugal forces are used for the external force field depending on particle size range to measure.

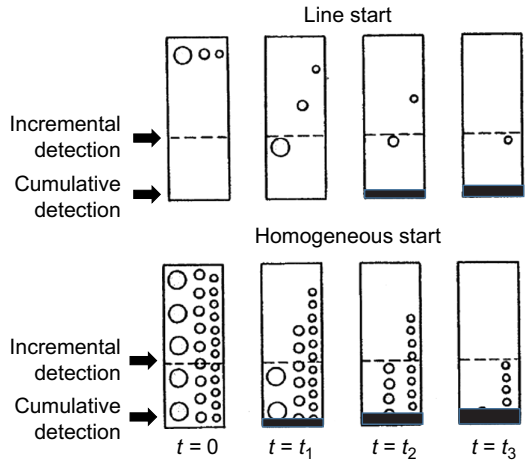


FIGURE 1.2.3 Schematics of operation for sedimentation method.

The larger, heavier particles settle faster than the smaller, lighter ones. Thus, after a certain time, some particles disappear from the upper part of the vessel and are concentrated or sediment at the bottom according to the terminal settling velocity, v_{st}, expressed by Stokes' law in gravitational force field.

$$v_{st} = \frac{H}{t} = \frac{\left(\rho_p - \rho_f\right) g\, D_{st}^2}{18\,\eta_f} \tag{1.2.4}$$

where

ρ_p and ρ_f are the density of particle and liquid, respectively.
η_f is liquid viscosity
g is gravitational acceleration constant.

As the velocity of particles reaches the terminal settling velocity at a short time, the particle diameter can be determined as Stokes diameter, D_{st}, when a particle settles to the depth, H, at time, t, from starting measurement. In the centrifugal force field, the terminal settling velocity depends on not only rotational speed but also the distance from the center of rotation. Stokes diameter, D_{st}, can be expressed as the following equation.

$$D_{st} = \sqrt{\frac{18\,\eta_f \ln\left(R_d/R_f\right)}{\left(\rho_p - \rho_f\right)\omega^2\, t}} \tag{1.2.5}$$

where

R_d and R_f are the distance of the detection point and the surface of the liquid from the center of rotation, respectively.
ω is angular velocity of centrifuge.

At the homogeneous start and incremental detection system, the particle concentration decreases at a known depth below the surface of the liquid, and is measured by light or X-ray extinction, liquid pressure, or apparent density of suspension. This concentration is for smaller particles than what the Stokes' diameter calculated at measuring time and the detection depth. When the suspension is sampled from a known depth at distinct time intervals, the particle concentration of the sample can be calculated from the sampled volume and the solid content after drying the sample. This detection system is used in Andreasen pipet method, which can be understood on the principle of the sedimentation method.

On the other hand, in the case of the line start and incremental detection system, the concentration only detects for the particles of the Stokes' diameter at measuring time and the detection depth.

In the cumulative detection system, the signal at the bottom of the vessel increase with time, which is usually detected by means of a balance, and then this signal is directly converted to the cumulative undersize distribution.

Chromatographic Method

Chromatographic method is trying to use for particle size analysis. Field Flow Fractionation (FFF), Hydrodynamic Chromatography (HDC), and Size Exclusion Chromatography (SEC) are listed as this method. However, the separation principles of those techniques are essentially different from each other as shown in Figure 1.2.4.

The separation column for FFF in Figure 1.2.4 (a) a is rectangle without packing materials inside. The external force is applied perpendicularly to the laminar flow in the column, and can be chosen such as centrifugal, electrical, magnetic, and thermal forces, or perpendicular flow. Particles are accumulated near the wall (accumulation wall) of the column by the extremal force and particle diffusion occurs due to this concentration gradient. As the diffusion effect of small particles is much larger than that of a large particle, small particles migrate to the higher-velocity flow, and then exit faster than large particles.

In HDC, a small tube (Figure 1.2.4 [b]) or a column packed nonporous large particles (Figure 1.2.4 [c]) is used as a separation column. Particle separation occurs due to the hydrodynamic interaction of the laminar flow profile in the column and the cross section of the particle. Large particles whose diameters interact with the higher-velocity central stream lines of the parabolic laminar flow profile move faster through the column or the tube (thick particle exclusion layer), whereas small particles whose diameters interact only with the slower profiles near the surfaces (thin particle exclusion layer) move slower.

SEC in Figure 1.2.4 (d) is also known as Gel Permeation Chromatography (GPC). The separation mechanism is similar to HDC, although the porous large particles are used for the alternative of nonporous large particles in the column. If the particles are too large not to enter any pores (if particles have particle exclusion layer), then they move together with liquid flow and exit at the almost same residence time as liquid. If the particles permeate into the pore, it means they stay in the column for a longer time, and then exit late. UV-vis spectroscopy, refractometer, or DLS is used for a detection device in all techniques for this method.

Size resolution of FFF is good from the view point of the retention time (the residence time in the instrument), but the retention time of the same size particles fluctuates widely because this technique belongs to chromatography essentially. Even worse, the quantitative capability of PSD is poor because particles deposit on a wall of the column and the amount of deposition depends on particle size. For these reasons, the quantitative discussion for PSD is difficult. Size resolution and quantitative capability of PSD for HDC and SEC is not generally as good as FFF.

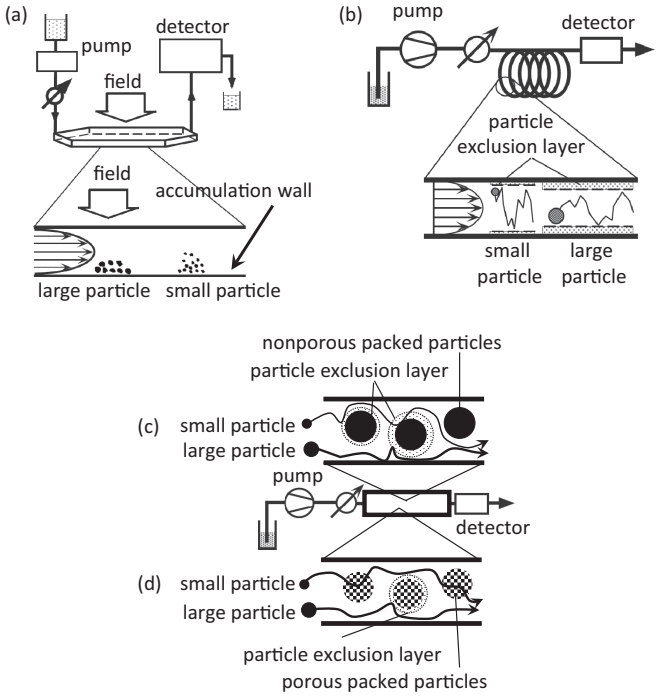


FIGURE 1.2.4 Separation principle of chromatographic method. (a) Field Flow Fractionation (FFF), (b) Capillary Type Hydrodynamic Chromatography (HDC), (c) Column Type Hydrodynamic Chromatography (HDC), (d) Size Exclusion Chromatography (SEC).

Inertial Impaction Method

In impactors, the particles in gas are passed through a nozzle and made to interact normally with a plane surface. The resulting particle trajectories can be calculated using the equation of motion of a particle in a flow field. Above a certain size of particle, termed the cut size, particles will strike the surface with the potential for collection. Particles smaller than the cut size will follow the flow of gas, not touch the surface, and have low potential for collection. The collection efficiency at the impaction surface is expressed in terms of the Stokes number (*Stk*),

$$Stk = \frac{C_c\, D_{aer}^2\, U_0}{18\,\eta_g\, R} \tag{1.2.6}$$

where

D_{aer} is the aerodynamic diameter
C_c is the Cunningham correction
U_o is the velocity of the gas at the nozzle
η_g is the gas viscosity
R is the radius or half-width of the nozzle.

Impaction surfaces are calibrated by determining the collection efficiency as a function of the Stokes number. When the square root of the Stokes number increases above 0.47 at a given impactor geometry and operating condition, the collection efficiency increases rapidly. Then the instrument is designed according to this result. The diameter calculated from the Stokes number at 50% collection efficiency is defined as the cut size D_{aer}.

Thus, by reducing the value of the nozzle radius for the identical gas flow, the impaction velocity increases and the

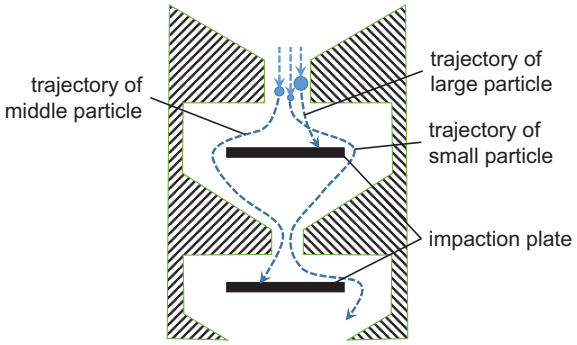


FIGURE 1.2.5 Schematic of cascade-impactor with two stages.

cut size is reduced. In this way, multiple impaction stages can be designed within one instrument to collect a variety of sizes. This instrument is termed a Cascade-Impactor, and Figure 1.2.5 shows the two stages type Cascade-Impactor. A mass-based PSD can be determined by weighing the amount of particles on each surface using a microbalance or a quartz crystal microbalance (QCM).

Electrical Mobility Classification Method

For fine particles with below 1 μm size in gases, electrical mobility analyzers are widely used. The velocity V_e of a charged spherical particle in an electric field is given by

$$V_e = \frac{p\, e_e\, C_c\, E}{3\pi \eta_g\, D_{em}} = B_e\, E \tag{1.2.7}$$

where

E is the strength of the electric field
e_e is the elementary charge
p is the number of elementary charges carried by a particle
C_c is the Cunningham correction
η_g is the gas viscosity
D_{em} is the particle diameter
B_e is the electrical mobility.

The velocity of the particle is inversely proportional to diameter and can be varied by changing the strength of the electric field, i.e. the applied voltage.

Figure 1.2.6 shows schematic of a typical system of this method, which is called Differential Mobility Analyzer (DMA). As aerosols generally have an unknown electric charge, they are discharged to yield Boltzmann distribution of charges around zero by using a radioactive source. And they are introduced into a laminar flow of air in a chamber where the constant electro field is applied between the outer pipe and the centered rod. Particles having the same electric mobility move along the same trajectory, and then are extracted through a narrow slit, which is located near the end of the centered rod for the electrode. Changing the electric field of the analyzer changes the mobility of particles extracted, and the number of particles is detected by an electrometer or a Condensation Nuclei Counter, which obtains the electrical

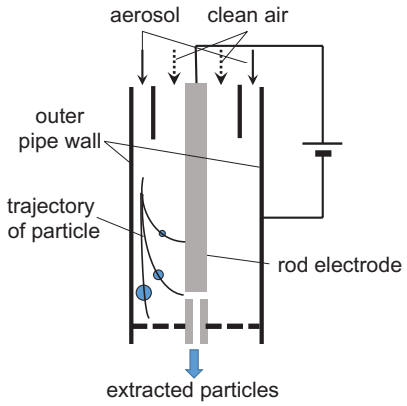


FIGURE 1.2.6 Schematic of differential mobility analyzer.

mobility distribution of aerosol. PSD is estimated after the correction of the charge distribution.

1.2.5 ENSEMBLE ANALYSIS

Ensemble analysis measures the interaction of an assembly of particles and interpret the signal in terms of PSD of the assembly.

Dynamic Light Scattering Method

In this method, the particle diameter determines how fast a particle moves in suspension through Brownian motion. When a laser beam is passed into a suspension under Brownian motion and the scattered light fluctuations measured at a certain scattering angle to the incident beam. The scattering angle is typically, 90° for dilution sample and ca. 170° for relatively high concentration suspension. In most Dynamic Light Scattering (DLS) instruments, the autocorrelation function of this scattered light fluctuation is recorded as a function of time. This system is often called a Photon Correlation Spectroscopy (PCS). Particle size can be obtained by fitting the autocorrelation function to an exponential decay function depending on the diffusion coefficient of particles, the scattering angle, and the wavelength of a laser. This yields an average size by using the Stokes-Einstein relationship. And the polydispersity factor, that is, some indication of the spread of sizes around the average value is calculated simultaneously, which is named as the cumulants method.

Some instruments have a frequency analysis system instead of autocorrelation function analysis, where the signal from the detector is sampled at regular intervals. The sampled values are then subjected to Fast Fourier Transformation (FFT) to yield a frequency power spectrum. The complete PSD is calculated by using the iterative fitting of the experimental power spectrum obtained using a number of predefined size and frequency channels. Moreover, different designs, some using fiber optics and some multi-angle systems, are available in DLS method.

DLS method is a low resolution method that is not capable of resolving narrowly spaced peaks in the particle size distribution. The original signal obtained by DLS method is based

on the scattered intensity. Many DLS instruments have the software to convert to volume-based or number-based PSD from the scattered intensity-weighted signal. In most calculation techniques, however, this involves the smoothing of the scattered-intensity-based PSD, which introduces uncertainties. Another issue which affects all calculation techniques is the highly nonlinear dependence of the scattering intensity on the particle size. Therefore, transformation of scattered-intensity-based PSD to volume-based or number-based PSD is not recommended.

Laser Diffraction/Scattering Method

This method was formerly called Low-Angle Laser Light-Scattering (LALLS) instruments, and is now applied to many commercial instruments. The principle of this method is that light scattered from particles in a collimated laser beam is collected by an array of detectors in the focal plane with the collecting lens. Because the light intensity scattered from one spherical particle can be calculated by the Fraunhofer and Mie equations, which depend on particle size, refractive indexes of particle and medium, and the scattering angle, diffraction and scattering pattern of the assembly of particles could be obtained if the volume-based PSD is known. Hence, the measured diffraction and scattering pattern has to be deconvoluted to estimate PSD using the calculated light-scattering pattern of the single particle.

The device usages are limited within a few percent mass concentration and extensively useable in off-line and on-line applications. For online applications in dense slurries, they require a dilution pre-analysis step, although multiple scattering studies have been made but not widely applied. The high advantages of this method are to operate easily and to get highly reproducible data. However, as each instrument differs such as the designs of the sensor/array to measure the scattering pattern of particles, of the mathematical deconvolution routine, of the method of extending the lower limit of 0.1 μm, and of the method of extending the upper limit to 3000 μm, the result from one instrument may not be the same result from another instrument, even if these are different product types from the same manufacture. It is also noted that their general tendency is to oversize the coarse end of PSD and assign an excess of particles to the fine end of PSD, which results in broadening PSD. Hence, PSD would be wider when measuring a sample with sharp PSD. Moreover, the fragment of small particle size below a few micrometers really depends on the refractive index of particles, especially the imaginary part of the refractive index of particles.

Small Angle X-Ray Scattering Method

Small Angle X-Ray Scattering (SAXS) method has the same measuring principle as the laser diffraction/scattering method, where the monochromatic X-ray (typically 0.154 nm CuKα line) is used instead of a laser with 400–700 nm wavelength. Although the scattering in SAXS method is related to the difference in electron density between particles and their dispersion medium, it is easy understanding that SAXS can measure very small particles of a few nanometers in diameter from the comparison of the wave length between SAXS and laser diffraction/scattering methods. As the conversion to PSD is sensitive to the noise disturbance and is still now developing, the mean particle size is estimated using the equation called Guinier diameter, although several computer algorithms exist for the determination of PSDs. The X-ray scattering pattern can be also used to estimate the shape or the internal structure of particles such as pores and local differences in the chemical composition.

Acoustic Method

In this method, the attenuation of ultrasound or the retardation of ultrasound velocity by particles in a liquid is measured by changing the ultrasound frequency. The measured pattern as a function of ultrasound frequency is then converted to PSD by the mathematical model, using a matrix which contains the attenuation pattern in defined-size classes. In order to make this matrix, various properties of both particles and liquid have to be known, such as density, coefficient of thermal expansion, heat capacity, and viscosity. This calculation is also simplified through an assumption of some kind of model PSD such as a normal or a log-normal distribution.

When the charged particles in a liquid are oscillated by the pressure change due to the transport of the sound wave, the electric field in the suspension vibrate as a result, and the electrodes placed at different locations measure an electric potential. This effect of the mutual interaction of sound and electric field is called the Colloid Vibration Potential (CVP) effect, and the dynamic mobility of colloid is determined, which depends on the particle size and zeta potential. This mutual interaction of sound and electric field is reversible. This means that charged particles move, when an alternating electric field is applied between electrodes in the suspension. Then sound waves are generated due to moving particles, and the dynamic mobility of particles is analyzed. This effect is called the Electro-kinetic Sonic Amplitude (ESA) effect. Both effects are usually applied to measure zeta potential of particles in suspension.

The advantage of this method is the broad range of particle concentration from 0.1 to 70% in volume can be measured with zeta potential of particles. However, if the volume percentage is over 5 %, the particle-particle interaction and the overlap of acoustical fields of different particles may become significant, so that the adaptation of the model is required to compensate for these effects.

Induced Gradient Method

When the particle size deceases to below several tens of nanometers, the scattering intensity from a particle, which is called Rayleigh scattering, quickly decreases by six orders of particle size, and the pattern of scattered light intensity comes to be independent of a scattered angle and a particle size. Therefore, when DLS or PTA is used for the analysis

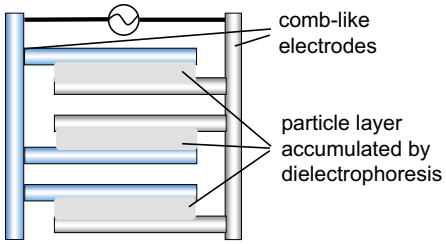


FIGURE 1.2.7 The particle accumulation state among the electrodes by dielectrophoresis. From this state, the electric field is turned off, and then particles diffuse by Brownian motion.

of a few nm size particles, the scattered light intensity is not enough to be measured. If a laser diffraction/scattering method is used, no dependency of the scattered intensity on a scattered angle results in trouble to calculate PSD. Under such a measuring condition, this method could be powerful. This method utilizes the phenomena of dielectrophoresis by applying the alternating electric field to gather particles as shown in Figure 1.2.7, and then the time-varying diffracted light intensity from the accumulated particles due to particle diffusion is measured when the electric field is turned off. The diffusion (i.e. hydrodynamic) diameter is calculated from this diffracted light intensity change, and also the volume-based PSD is estimated by the software. One of the disadvantages is that some materials such as conducting particles cannot be measured, because the dielectrophoresis phenomena do not work on them.

1.2.6 OTHERS

Surface Area Method

The surface area method can be used to measure only the average size of a powder, not estimate PSD. Generally, this method is done to dry powders by two approaches. For dense and smooth particles with insignificant internal porosity, the permeability method gives the mean specific surface diameter using the permeability equation such as the Kozeny-Carman equation. The lowest size, which could be applied to this method, is several micrometers. Another approach is the gas adsorption method, in which the internal and external surface area is evaluated using the BET equation, although the particle size is underestimated if particles have the internal surface significantly. The BET method is useful to discuss the effect of the particle size on the characteristics of particle surface, such as the surface reaction or absorption on the particle surface.

X-Ray Diffraction Method

X-ray Diffraction (XRD) is widely used as a technique to analyze the crystalline structure of materials. The principle of XRD has been known for many decades and is based on the Bragg low, which relates to the lattice spacing with the observed angles from the X-ray scatters by crystalline materials. When the size of crystalline materials decreases, the lattice spacing of the edge of materials may change to be somewhere shorter or longer. This means X-ray diffraction peaks of particles or powder are not sharp and broadened. This broadening is caused by the crystal size and the defect of crystalline materials. Hence, the crystal size can be estimated by applying the Scherrer equation to the broadening of XRD peaks, if the defect of crystalline materials is not significant. The size calculated from XRD method is the average size of crystal, not the particle diameter. However, when the particle size become a nanometer, most of particles are monocrystalline. In this situation, the size calculated from XRD method could equal to a particle diameter.

1.2.7 SUMMARY

This chapter outlines the particle size analysis in the 2010s. It does not provide the details of each method or the ranges of choice that are available even for one manufacturer's instrument. Today, most instruments are modular and have options that can be selected for specific needs. For more information of these methods, refer to the books in the reference, as well as the ISO documents prepared by TC 24 and TC 229.

REFERENCES

1. Barth, H. G. (ed.), *Modern Methods of Particle Size Analysis*, John Wiley & Sons, New York, 1984.
2. Allen, T., *Particle Size Measurement*, 5th ed., Chapman & Hall, New York, 1997.
3. Xu, R., *Particle Characterization: Light Scattering Methods*, Kluwer Academic Publishers, Dordrecht, 2000.
4. Merkus, H. G., *Particle Size Measurement*, Springer, Alphen aan den Rijn, 2009.
5. Masuda, H., Iinoya, K., *J. Chem. Eng. Jpn*., 4, 60–67, 1971.

1.3 Particle Shape Characterization

Shigehisa Endoh

1.3.1 INTRODUCTION

Particles have various shapes depending on their manufacturing method and mechanical properties. Unlike a sphere or a rectangular parallelepiped, which are the objects with clear geometrical definitions, powder particles are very complicated objects with no definite form. It is generally very difficult to describe their shapes. They have therefore been conventionally described and classified by the use of various terms.

On the other hand, along with recent rapid advances in computer and information technologies, the image-processing technology has remarkably progressed in both software and hardware, making it easy to obtain image information and geometrical features of particles. Accordingly, various quantitative methods for expressing particle shape have been proposed and adopted.

The particle shape description or expression is classified by several criteria. In the most primitive manner, the descriptions are classified into either *quantitative* or *qualitative* method. In the *qualitative* description, the shape is expressed by several terms, such as "spherical," "granular," "blocky," "flaky," "platy," "prismodal," "rodlike," "acicular," "fibrous," "irregular" and so on.[1,2] The verbal description is sometimes convenient to express irregular shape and makes it easy to understand the shape visually. But how are a platy shape and a flaky shape distinguished? Under present conditions, this distinction must depend on human visual judgments in many cases. Therefore, the quantitative descriptions of a particle shape will be necessary.

The *quantitative shape descriptors* can be calculated from 2- or 3-dimensional geometrical properties, and/or by comparing with physical properties of reference shape.

The following are required for the shape descriptor[3]:

- Rotation invariance: Values of the descriptor should be the same in any orientation.
- Scale invariance: Values of the descriptor should be the same for identical shapes of different size.
- Reflection invariance: Values of the descriptor should be the same for reflected images.
- Independence: If the elements of the descriptors are independent, some can be discarded without the need to recalculate the other.
- Uniqueness: One shape should always produce the same set of descriptors, and one set of descriptors should describe only one shape.
- Parsimony: It is desirable that the descriptors are thrifty in the number of terms used to describe a shape.

The form and property of particles are essentially 3-dimensional, but the shape of a 2-dimensional image is mainly treated here, as shown in Figure 1.3.1[4].

1.3.2 REPRESENTATIVE SIZE

If a given particle has the k-dimensional quantity of geometric property Q_k, the perimeter P for 1-dimension (1D), the surface area S and projected area A for 2-dimension (2D), the volume V for 3-dimension (3D), the equivalent diameter x_β of a sphere having the same quantity can generally be expressed by the following equation:

$$x_\beta = \left(Q_k / \phi_\beta\right)^{1/k} \tag{1.3.1}$$

where the coefficient ϕ_β is called the geometrical shape factor. From the mathematical relations for a sphere, the equivalent diameters and the factors are given as follows[2]:

- volume equivalent diameter;

$$x_V = \sqrt[3]{6V/\pi},\ \phi_V = 6/\pi \tag{1.3.2}$$

- Surface equivalent diameter;

$$x_S = \sqrt{S/\pi},\ \phi_S = \pi \tag{1.3.3}$$

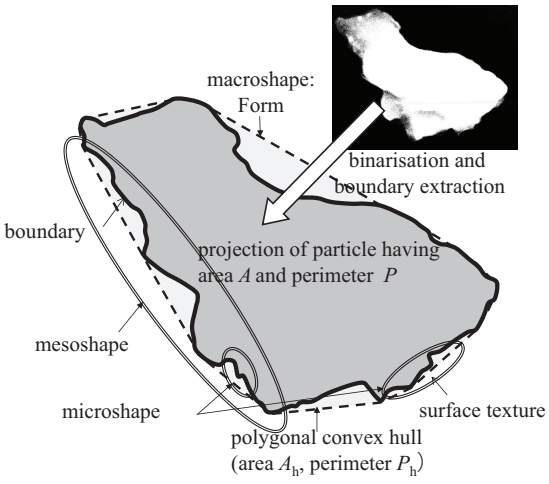


FIGURE 1.3.1 Digitized 2D-image of particle.

- projected area equivalent diameter (Heywood diameter);

$$x_A = \sqrt{4A/\pi},\ \phi_A = \pi/4 \tag{1.3.4}$$

- perimeter equivalent diameter;

$$x_P = P/\pi \tag{1.3.5}$$

When particles have similar shapes, the averages of volume and surface area are given by the following expressions, respectively:

$$\overline{V} = \phi_\beta M_{3,0} \tag{1.3.6}$$

$$\overline{S} = \phi_\gamma M_{2,0} \tag{1.3.7}$$

where $M_{k,0}$ is the complete k-th moment of number distribution density $q_0(x_\beta)$ of x_β, which is defined by the following equation:

$$M_{k,0} = \int x_\beta^k q_0(x_\beta) dx_\beta \tag{1.3.8}$$

Accordingly, a volume related specific surface is as follows:

$$S_V = \frac{\overline{S}}{\overline{V}} = \frac{\phi_S M_{2,0}}{\phi_V M_{3,0}} = \frac{\phi_{23}}{M_{1,2}} \tag{1.3.9}$$

where ϕ_{23} is a specific surface area shape factor given by the ratio between ϕ_S and ϕ_V. $M_{1,2}$ which is a ratio of $M_{3,0}$ to $M_{2,0}$, is called the Sauter-diameter $\overline{x}_{VS}(=\overline{x}_{1,2})$ (an average weighted surface diameter):

$$\overline{x}_{VS} = M_{1,2}(=M_{3,0}/M_{2,0}) = \int x_\beta q_2(x_\beta)\, dx_\beta \tag{1.3.10}$$

where $q_2(x_\beta)$ is area distribution density. The specific surface area shape factor of spheres is given as $\phi_{23} = 6$ and the specific surface area as $S_V = 6/x_\beta$. Hence, by applying a correction coefficient ϕ_C, i.e. Carman's shape factor, S_v for a general particle is given by $S_V = 6/\phi_C x_\beta$.

A 2D image of the particle gives the Feret diameter x_F, which is a distance between parallel tangents as shown in Figure 1.3.2. Since the Feret diameter changes with the tangent angles $x_F(\theta)$, it is the statistical diameter and its average value $\overline{x}_F$, which is employed as a representative diameter, is given by:

$$\overline{x}_F = \frac{1}{\pi}\int_0^\pi x_F(\theta) d\theta \tag{1.3.11}$$

The maximum and minimum Feret diameters give the "length" and "breadth," respectively. The unrolled diameter $x_R(\theta)$ is also defined as a diameter passing through the center of gravity (CG) of the image, as shown in Figure 1.3.2. The average diameter is given by:

$$\overline{x}_R = \frac{1}{\pi}\int_0^\pi x_R(\theta) d\theta \tag{1.3.12}$$

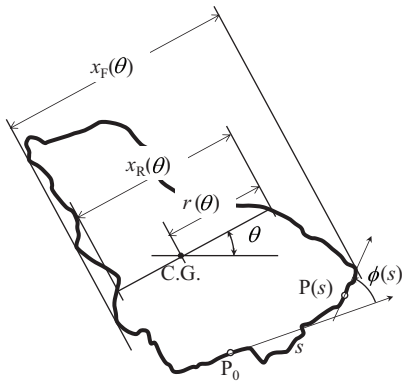


FIGURE 1.3.2 Statistical diameters and angular function.

1.3.3 GEOMETRICAL SHAPE DESCRIPTORS

Quantitative descriptors for the geometry of particle image can be also classified into three categories based on the scale of the inspection of form, as shown in Figure 1.3.1[4,5]:

(a) Macroscopic descriptor: expressing overall form, and referring to "proportion," or "elongation" of the particle image. The Fourier descriptors of lower order harmonic number also give overall form features.
(b) Mesoscopic descriptor: expressing details of form and profile outline, and defining space filling feature (or bulkiness), concavity, and robustness of the particle.
(c) Microscopic descriptor: expressing surface structure and texture, giving roundness and Fractal dimension of the image. The Fourier descriptors of higher order also express surface properties.

1.3.3.1 Macroscopic Descriptors

The definitions and classification of shape descriptors expressing macroscopic shape properties are calculated from macroscopic geometrical features, such as representative diameter, axis lengths, thickness, and so on.

1) Proportion:

Parameter describes the anisotropy or elongation of a particle. It is given by the ratio of lengths of axes (length L, breadth B, thickness T)[6]:

$$\text{elongation} = L/B \quad \text{or} \quad = L'/B' \tag{1.3.13}$$

$$\text{flatness} = B/T \quad \text{or} \quad L/T \tag{1.3.14}$$

where L and B' are the maximum and minimum Feret diameters (x_{Fmax} and x_{Fmin}) respectively, and B and L' are the Feret diameters perpendicular to L and B' respectively, as shown in Figure 1.3.3[4].

The axial ratio of the radius-equivalent ellipse is known as the Legendre ellipse of inertia shown in Figure 1.3.4. This

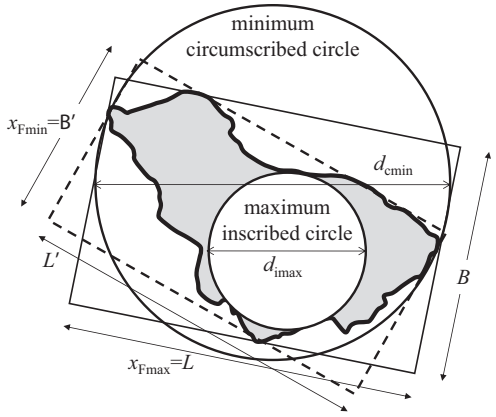


FIGURE 1.3.3 Geodesic length and width of fibrous particle (very long particle).

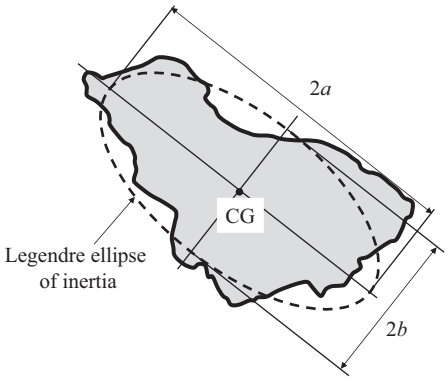


FIGURE 1.3.4 Inscribed and circumscribed circles and their diameters; Feret boxes and Feret diameters.

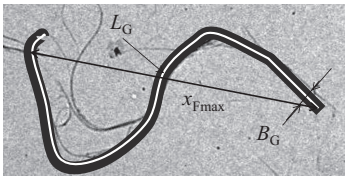


FIGURE 1.3.5 Legendre ellipse of inertia.

image has the same geometrical moments up to the second order as the original particle silhouette, which is referred as "anisometry," and also gives the proportional property[6]:

$$\text{anisometry} \quad K = \sqrt{I_1 / I_2} = a / b \quad (I_1 > I_2) \tag{1.3.15}$$

where I_1 and I_2 are the major and minor principle inertia moments of the particle silhouette, and the axis lengths a and b are given by $a = \sqrt{I_1 / A}$ and $b = \sqrt{I_2 / A}$, respectively.

For fibrous particle as shown in Figure 1.3.5, the elongation is defined by the following equation[7]:

$$\text{elongation} = L_G / B_G \tag{1.3.16}$$

where L_G and B_G are the geodesic length and breadth of a fibrous particle, as shown in Figure 1.3.4[4].

2) Index given by the ratio of characteristic particle diameters:

Circularity ψ_{AP} is defined by the ratio of the perimeter P_{Circle} of a circle to the projected area of the same particle P, which represents the degree of similarity to a circle. The circularity is also given the ratio of the Heywood diameter x_A to the perimeter equivalent diameter x_P, as follows:

$$\psi_{AP} = P_{Circle} / P = x_A / x_P \tag{1.3.17}$$

For the 3D description, the Wadell's sphericity ψ_S, which is defined by the ratio of the surface area of a sphere of the same volume, S_{Sphere}, to that of a given particle S, represents the degree of sphericity of the particle, as follows[8]:

$$\psi_S = S_{Sphere} / S \tag{1.3.18}$$

ψ_S is approximately obtained by the ratio x_A/d_{cmin}, where d_{cmin} is the diameter of the minimum circumscribed circle shown in Figure 1.3.5.[4] The other kinds of shape descriptors are given by the ratios of characteristic particle diameters[9]:

$$\psi_{AF} = x_A / \overline{x_F}, \ \psi_{RA} = \overline{x_R} / x_A, \ \psi_{RP} = \overline{x_R} / x_P \tag{1.3.19}$$

The coefficient of variation of the statistical diameter σ_β defined by Equation 1.3.20 is considered to be the shape descriptor representing the deviation from a circle with the mean size.

$$\sigma_\beta = \frac{1}{\overline{x_\beta}} \sqrt{\frac{1}{\pi} \int_0^\pi \left(x_\beta(\theta) - \overline{x_\beta} \right)^2 d\theta} \tag{1.3.20}$$

where the subscript β means the Feret diameter (β=F) or the unrolled diameter (β=R).

This descriptor implies the degree of circularity of particles.

1.3.3.2 Mesoscopic Descriptors

1) Space filling factor:

The descriptor, which is called "bulkiness" or "bulkiness factor," expresses the bulky space occupied by a particle, and it also indicates the degree of compactness. The bulkiness is defined as the ratio of the particle area to the area of either circumscribed rectangle or circumscribed circle defined in Figure 1.3.5, as follows[10]:

$$f_{bR} = A / LB \tag{1.3.21}$$

$$f_{bC} = 4A / \pi d_{cmin}^2 \tag{1.3.22}$$

The bulkiness is corresponding to the "solidity" defined as the ratio of the particle area to the circumscribed convex hull area A_h defined in Figure 1.3.1, as follows [11]:

$$\text{Solidity} = A / A_h \tag{1.3.23}$$

The projected area relative to the area of the Legendre ellipse of inertia can be defined also as a the space filling factor, as follows[12]:

$$f_{bE} = A / \pi ab \tag{1.3.24}$$

where a and b are the major and minor radii of the ellipse defined in Figure 1.3.4, respectively.

In 3D inspection, circumscribed polyhedron (rectangular prism) or sphere is employed and the factor is given by the ratio between the volumes. The irregularity index d_{imax} / d_{cmin} defined by the ratio of diameters of the inscribed maximum circle to that of the circumscribed minimum circle gives bulky property, as shown in Figure 1.3.5.

For fibrous particle, "curl" is defined by the following equation [7]:

$$\text{Curl} = L(= x_{F\max}) / L_G \tag{1.3.25}$$

2) Concavity and robustness:

The descriptor is based on mathematical relation. The descriptor ψ_{FP} is defined by the ratio of average Feret diameter to the equivalent perimeter one:

$$\psi_{FP} = \bar{x}_F / x_P \tag{1.3.26}$$

ψ_{FP} for a shape without any convex portions on the surface is unity, thus the descriptor ψ_{FP} can be used to assess the surface concavity [9].

The descriptors indicating the degree of convex or concavity on the surface of the image are proposed, as follows:

$$\text{Convexity} = P / P_h \tag{1.3.27}$$

$$\text{Concavity} = (A_h - A) / A_h \tag{1.3.28}$$

where P_h is the perimeter of the convex circumscribed polygon shown in Figure 1.3.1[11].

The image processing technique gives the morphological descriptors (Figure 1.3.6). The robustness factor is:

$$\Omega_1 = 2\omega_1 / \sqrt{A} \tag{1.3.29}$$

where ω_1 is the numbers of erosions in image processing necessary to completely eliminate the image.

The largest concavity factor is:

$$\Omega_2 = 2\omega_2 / \sqrt{A} \tag{1.3.30}$$

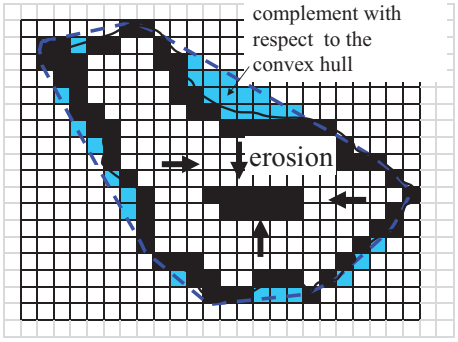


FIGURE 1.3.6 Erosion of binary image of particle and the complement with respect to the convex hull.

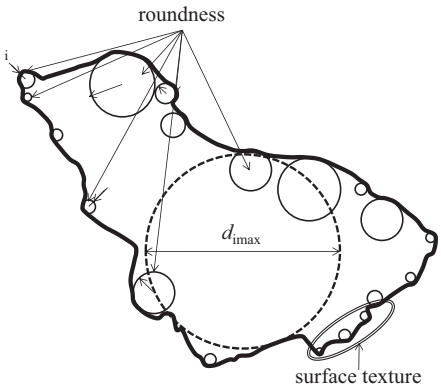


FIGURE 1.3.7 Surface structure and roundness.

where ω_2 is the numbers of erosions necessary to eliminate the complement with respect to the convex hull.

Robustness is correlated to the elongation. The plot of Ω_1 vs. Ω_2 is used for shape screening.[7,13]

3) Surface roughness:

Hausner's surface index is given by a reciprocal of circularity ψ_{AP10}[10]:

$$C = 1/\psi_{AP}^2 = P^2 / 4\pi A \tag{1.3.31}$$

If the convex portion of the silhouette outline of a particle is an arc, the roundness is defined by the ratio of the average value of the curvature radii of the corners and edges to the radius of maximum inscribed circle $d_{imax}/2$, as shown in Figure 1.3.7[8]:

$$Rn = \frac{2\sum \rho_i}{N d_{imax}} \tag{1.3.32}$$

where ρ_i is the curvature radius of the corner i and N is the number of corners.

1.3.3.3 Application of Fourier Analysis – The Fourier Descriptor

The Morphology of a particle can be expressed by Fourier descriptor. The Fourier descriptor is a set of Fourier coefficient $A_k(=2|C_k|)$, or pairs of the amplitude A_k and phase angle α_k of the Fourier coefficients that can be obtained by the Fourier transformation of the projected image function $F(\Theta)$:

$$C_k = \frac{a_k - jb_k}{2} = \frac{1}{2\pi}\int_0^{2\pi} F(\Theta)\exp(-jk\Theta)d\Theta \tag{1.3.33}$$

$$A_k = \sqrt{a_k^2 + b_k^2}$$

$$a_k = \tan^{-1}(b_k / a_k) \tag{1.3.34}$$

for the harmonic order $k = 0, \pm 1, \pm 2, \cdots, j = \sqrt{-1}$. The composite values of the Fourier coefficients and their statistical values are referred to as the Fourier descriptor, also. A_k's for the lower harmonic order give the macroscopic form the feature,[14–24] that is, A_2 corresponds to the elongation (i.e. aspect ratio), and A_3 and A_4 mean the triangularity and squareness, respectively.

The Fourier descriptor is distinguished from other shape descriptors in the representation of the measured image. The representation of the original form $F(\Theta)$ can be guaranteed within the number of coordinate points N measured or interpolated for the Fourier transformation, as follows:

$$F(\Theta) = \frac{a_0}{2} + \sum_{k=1}^{N/2-1} A_k \cos(k\Theta - a_k) \tag{1.3.35}$$

The outline of the particle image can be described by several functions, such as redial length r(θ), angular bend function ϕ(s) etc, (Figure 1.3.2). The Fourier descriptors are obtained by Fourier transformation of those functions, as follows.

1) The radial Fourier descriptor; Polar coordinate method:

In the polar coordinate method, the radius vector $\boldsymbol{r}(\theta)$ from the center of gravity (CG) to the boundary of the image as a function of an angle θ of counterclockwise rotation about CG is transformed into the Fourier space (Figure 1.3.2).[14–17] The radial length $r(\theta)\left(=|\boldsymbol{r}(\theta)|\right)$ is given by the Fourier series, as follows:

$$r(\theta) = r_0 + \sum_{k=1}^{N/2-1} A_k \cos(k\theta - a_k) \tag{1.3.36}$$

$$r_0 = \frac{1}{2\pi}\int_0^{2\pi} r(\theta)d\theta \tag{1.3.37}$$

Some of the geometrical quantities, such as area and mean unrolled diameter are given by the Fourier coefficient in polar coordinates. The mean radial length is $r_0\left(=\bar{x}_R/2\right)$ given by Equation 1.3.37 and the area A is given by:

$$A = \pi\left[r_0^2 + \sum_{k=1}^{N/2-1} A_k^2\right] \tag{1.3.38}$$

The Fourier descriptors of the Polar coordinate method can be defined as follows:

$$IRR = (x_A/2r_0)^2 = \psi_{RA}{}^{-2} \tag{1.3.39}$$

$$\text{Randance} = \mu_2/r_0{}^2 = \sum A_k{}^{*2} \tag{1.3.40}$$

$$\text{Skewness} = \mu_3/r_0{}^3 \tag{1.3.41}$$

where $A_k{}^*$ is the normalized amplitude A_k/A_0 and μ_m is the m-th moment around the mean radius r_0, as follows:

$$\mu_m = \int\left[r(\theta) - r_0\right]^m d\theta/2\pi \tag{1.3.42}$$

IRR corresponds to the equivalent dimensionless area diameter and is a measure for irregularity. Dimensionless moments $\mu_2/r_{02}{}^2$ and $\mu_3/r_{03}{}^3$ are called Randance and Skewness. This method, however, cannot be applied unless the radius vector $\boldsymbol{r}(\theta)$ becomes a single-valued function of θ.

2) The angular bend function method; ZR Fourier descriptor:

The ZR Fourier descriptors are derived by the Fourier transformation of the angular bend function $\phi(s)$, which is the direction change (angle of deviation) of the outline tangent at the point P(s) of the arc length s from the starting point P_0 (Figure 1.3.2).[18–21] The normalized angular bend function $\phi^*(t)$ is meaningful in comparison between different size particles, by defining:

$$\phi^*(t) = \phi(s) - t = \phi(Pt/2\pi) - t \tag{1.3.43}$$

where t is a normalized argument with the perimeter P, as follows:

$$t = 2\pi(s/P) \tag{1.3.44}$$

$\phi^*(t)$ is subjected to the Fourier transformation:

$$\phi^*(t) = \mu_0 + \sum_{k=1}^{\infty}\left(a_k \cos kt + b_k \sin kt\right) \tag{1.3.45}$$

The profile of the particle image can be approximated by polygon, then, the Fourier descriptors are derived:

$$\mu_0 = \pi + \frac{1}{P}\sum_{j=1}^{m} s_j \Delta\phi_j \tag{1.3.46}$$

$$a_k = \frac{1}{k\pi}\sum_{j=1}^{m}\Delta\phi_j\cos(kt_j) \tag{1.3.47}$$

$$b_k = \frac{1}{k\pi}\sum_{j=1}^{m}\Delta\phi_j\sin(kt_j) \tag{1.3.48}$$

where s_j is the arc length of jth vertex from starting point, $\Delta\phi_j$ is the change of slope at vertex j and m is the total number of sides of the polygon.

The angular bend function method can be applied to every shape, even if the radial function $r(\theta)$ is not unique with θ. In some cases, however, the starting point and the endpoint of the represented profile do not coincide.[20]

3) The Radius Vector method

In the case where $r(\theta)$ does not become a single-valued function, the modified function by considering the rotational direction of radius vector is introduced and subjected to the Fourier transformation.[22] The modified radial function is defined as:

$$R(\theta') = r(\theta')f_D(\theta') \tag{1.3.49}$$

where $f_D(\theta')$ indicates the rotational direction of radius vector. The function gives $f_D(\theta') = +1$ for the counterclockwise rotational direction and $f_D(\theta') = -1$ for the clockwise rotational direction, respectively. θ' is a cumulative value of angle variations at θ from the starting point, such as $\theta' = \sum|\Delta\theta|$.

The (x, y) coordinates can be transformed into the Fourier spectrum.[23,24]

1.3.3.4 Fractal Dimensions

Fractal dimensions[25] are applied to the quantification of particle shape.[26] Generally, the fractal dimension is defined as follows. The geometrical quantity Q_k of a k-dimensional pattern (topological dimension k) measured by a certain scale η is proportional to the number of element for k-dimensional volume N.

$$Q_k = \eta N \tag{1.3.50}$$

If the scale η and N is given by the following relation:

$$N = \eta^{-D_f}, \quad D_f \neq k \tag{1.3.51}$$

the pattern is *fractal*, which means statistical self similarity, and D_f is called a *fractal dimension*.

As shown in Figure 1.3.8, the perimeter P can be estimated by dividing the contour by the linear scale of length η. When the number of the linear scale N to cover the contour is plotted against η on amphi-logarithmic sheet, the relation is expressed in Formula (1.3.52). The fractal dimension D_f is its slope:

$$\log P = (1-D_f)\log\eta + c \tag{1.3.52}$$

With the influence of the concavity and convexity on the surface, D_f for the perimeter of the outline ($k=1$) becomes

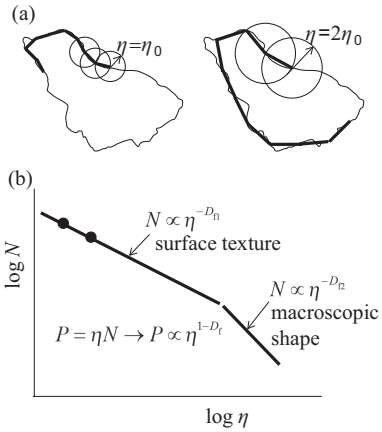


FIGURE 1.3.8 Estimation of perimeter with changing liner element length h.

$1 < D_f < 2$. The D_f value of a particle with a smooth surface is close to unity, whereas the fractal dimension is higher for complicated curves.[7,27,28] Therefore, it is believed that the fractal dimension quantitatively expresses the complexity of the surface and structure of the surface.

Usually, log$N$-logη plot for the profile with a fractal structure shows the relation as shown in Figure 1.3.8(b), that is, the linear relation divided into two regions, or more. The region of scale larger than some break point is referring to the macroscopic morphology, on the other hand, the smaller region corresponds to the microscopic surface properties, such as surface texture.

When a 2D pattern of a binary image ($k=2$) seems to be fractal, the correlation function $C(r)$ of density between the patterns with a distance r satisfies the following relation,[29,30]

$$C(r) = < f(r+r')\cdot f(r') > \propto r^{-y} \tag{1.3.53}$$

where <> expresses an average operation, y is the slope of log$C(r)$-log$r$ plot and $f(r')$ is an image function at a point r', which takes 0 or 1. The fractal dimension is given by the following expression.

$$D_f = k - y \tag{1.3.54}$$

1.3.4 DYNAMIC EQUIVALENT SHAPE

1.3.4.1 Drag Force Shape Factor

Stokes' fluid drag force F_D, which acts on an irregular shaped particle moving at a relative velocity v in a fluid with a viscosity μ, is given by the following expression.

$$F_D = 3\pi\mu v x_\beta K_\beta \tag{1.3.55}$$

where

x_β is the characteristic particle diameter and the coefficient
K_β is the drag force shape factor.

The F_D value of irregular shaped particle varies depending on the orientation to fluid flow, and thus the drag shape factor K_β depends on the orientation of the particle. Also, the value of K_β depends on the characteristic particle diameter employed in the equation.

Stokes diameter x_{st} is generally given using the volume shape factor as follows:

$$x_{st}^2 = \frac{6}{\pi}\frac{\phi_V}{K_\beta}x_\beta^2 \tag{1.3.56}$$

If the drag shape factors with the axes of an ellipsoid orthogonal and parallel to the flow are $K_{\beta a}$ and $K_{\beta c}$, respectively, the factor for random orientation can be given by the following equation[31]:

$$3/\bar{K}_\beta = (1/K_{\beta a} + 2/K_{\beta c}) \tag{1.3.57}$$

1.3.4.2 Dynamic Shape Factor

The dynamic shape factor κ is defined as follows[32]:

$$\kappa = \frac{\text{fluid drag force acting on a particle}}{\text{drag force to a sphere with equal volume}} \tag{1.3.58}$$

κ is equal to the drag force shape factor of the equivalent volume diameter K_V. It is also given by the ratio of the volume equivalent diameter and the Stokes diameter, as follows:

$$\kappa = (x_V/x_{st})^2 \tag{1.3.59}$$

Also, according to $(\phi_V/\kappa)x_V^2 = (\phi_A/K_A)x_A^2$, the following relation is obtained:

$$\kappa = \frac{\pi}{6\phi_A}\left(\frac{x_V}{x_A}\right)^2 K_A = \left(\frac{\pi}{6\phi_A}\right)^{1/3} K_A \tag{1.3.60}$$

κ of a spheroid is shown in Figure 1.3.9.[2,33,34]

The Wadell sphericity is related with dynamic shape factor in the following expression:

$$\psi_S = (K_A/\kappa)^2 = (6\phi_A/\pi)^{2/3} \tag{1.3.61}$$

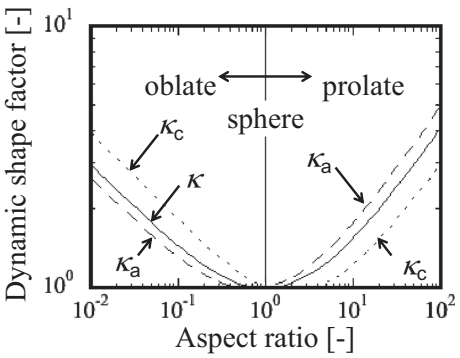


FIGURE 1.3.9 Dynamic shape factor of spheroid.

The dynamic shape factor of agglomerates with porosity ε is given by the volume shape factor $\phi_{V,agst}$ base on the Stokes diameter of aggregate x_{agst}, as follows[35]:

$$\kappa = \frac{(x_V/x_{agst})^2}{(1-\varepsilon)} = \left(\frac{6}{\pi}\right)^{2/3}\frac{\phi_{V,agst}^2}{(1-\varepsilon)} \tag{1.3.62}$$

For the blocky and chainlike aggregate composed by n particles, empirical relationships for κ are obtained, as follows[36]:

$$\begin{aligned}\kappa &\approx 1.232, \text{ (blocky, } 5 \le n \le 23)\\ \kappa &\approx 0.863n^{1/3}, \text{ (chainlike, } n \le 8)\end{aligned} \tag{1.3.63}$$

1.3.5 CONCLUDING REMARKS

The shape descriptors presented here are mainly classified into two categories based on the scale of inspection. The descriptors derived from geometric quantities represents overall or mesoscopic feature of shape. Those descriptors are convenient to treat the shape, however, they are not unique with the shapes. This means that the form cannot be reconstructed using the overall or mesoscopic descriptor.

On the other hand, the harmonic analysis, such as the Fourier transformation, for several images of the particle is useful. The harmonic spectrum extracted from the image function describes not only overall shape feature but microscopic shape. Further, the shape reconstruction can be done using the Fourier coefficients. Appropriate Fourier descriptors should be selected for particle shape characterization.

In this chapter, classification and distinction of particles based on shape have not been treated, but these are significant in practical powder processing. The statistical methods and artificial neural networks are effective tools for particle characterization.[21,37,38]

The property of the particle is essentially 3D. A few descriptors for 3D shape have been proposed and used in restricted fields. The 3D morphological analysis including 3D measuring technique should be developed.

REFERENCES

1. Allen, T., *Particle Measurement*, p. 107, Chapman and Hall Ltd., London (1981)
2. Endoh, S., *J. Powder Technol., Japan*, **29**, 854 (1992), idem., *ibid*., **35**, 383 (1998)
3. Chan, L. C. L., and N. W. Page, *Part. Part. Syst. Charact*., **14**, 67 (1997)
4. Endoh, S., *J. Powder Technol*., *Japan*, **46**, 819 (1992)
5. ISO 9276-6:2008 Representation of results of particle size analysis — Part 6: The descriptive and quantitative representation of particle shape and morphology
6. Heywood, H., *Trans. Inst. Chem. Engrs*., **25S,** 14 (1947)
7. Pons, M. N. et al., *Powder Technol*., **103**, 44 (1999)
8. Wadell, H., *J. Geo*., **40**, 443 (1932), idem., *ibid*., **43**, 250 (1935), idem., *J. Franklin Inst*., **217**, 459 (1934)
9. Tsubaki, J., and G. Jimbo, *Powder Technol*., **22**, 161 (1979)
10. Hausner, H. H., *Planseeber. Pulvermetall*., **14**, 75 (1966)
11. Faris, N. et al., *Powder Technol*., **133**, 54 (2003)

12. Medaria, A. I., *Powder Technol*., **4**, 117 (1970/71)
13. Vocak, M. et al., *Powder Technol*., **97**, 1 (1998)
14. Schwarcz, H. P., and K. C. Shane, *Sedimentology*, **13**, 213 (1969)
15. Meloy, T. P., *Powder Technol*., **16**, 233 (1977)
16. Luerkins, D. W. et al., *Powder Technol*., **31**, 209 (1982)
17. Beddow, J. K. et al., *Powder Technol*., **18**, 19 (1977)
18. Zahn, C. T. et al., *IEEE Trans. Compt*., **C-21**, 269 (1972)
19. Fong, S. T. et al., *Powder Technol*., **22**, 17 (1979)
20. Koga, J. et al., *Report IPCR*, **56**, 63 (1980)
21. Hundal, H. S. et al., *Powder Technol*., **91**, 217 (1997)
22. Gotoh, K., *Powder Technol*., **23**, 131 (1979)
23. Shibata, T. et al., *J. Powder Technol., Japan*, **24**, 217 (1987)
24. Browman, E. T. et al., *Geotechnique*, **51**, 545 (2001)
25. Mandelbrot, B. B., *Fractoal, Form, Chance and Dimension,* Freeman, San Francisco. CA (1977)
26. Kaye, B. H., *Powder Technol*., **21**, 1 (1978)
27. Kaye, B. H., *Part. Charact*., **1**, 14 (1984)
28. Suzuki, M et al., *J. Powder Technol., Japan*, **25**, 287 (1988)
29. Meakin, P., *J. Colloid and Interface Sci*., **96**, 415 (1983)
30. Meakin, P., *Phys. Rev. A*, **29**, 997 (1984)
31. Blumberg, P. N. et al., *AIChE J*., **14**, 331 (1968)
32. Fuchs, N. A., *The Mechanics of Aerosol*, p. 40, Pargamon Press, London (1964)
33. Gans. R., Sitzber math-physk Klasse Akad. Wiss., *München*, **41**, 191 (1911)
34. Endoh, S., *Handbook of Powder Technology* (Powder Technol. Soc. Japan Ed.), p. 37, Asakura-shoten, Tokyo (2014)
35. Kosaka, Y. et al., *J. Colloid. Interface Sci*., **84**, 91 (1981)
36. Stober, W., *Fine Particles* (B. Y. H. Liu Ed.), p. 363, Academic Press, New York and London (1970)
37. Chien, Y. T., Interactive Pattern Recognition, p.32, Marcel Dekker, New York and Basel (1978)
38. Endoh, S. et al., *Kagaku Kogaku Ronbunshu*, **8**, 476 (1982)

1.4 Particle Density

Yoshiyuki Endo

1.4.1 DEFINITION OF PARTICLE DENSITY

The density of particles and powder is a physical property as important as the particle size. Although the density is defined as the ratio of mass to volume, the density of the particles does not necessarily agree with that of the particle material, as a particle occasionally includes closed voids, as shown in Figure 1.4.1. The density defined for particles and powder is as follows:

True Density, ρ_s

This density is defined as the ratio of the mass of the particle to its actual volume excluding inside closed voids, i.e. the density of material composing the particle. If the particles are ground so fine as to make the voids disappear, the true density can be measured.

Particle Density, ρ_p

This is defined as the particle mass divided by the particle volume, including the closed voids inside. If the particle does not contain any void, the particle density equals the true density. If an open pore (see Figure 1.4.1) does not have a large enough orifice for the surrounding gas or liquid molecules to enter, the open pore behaves strictly like a closed void. In this case, practically, the particle volume includes such open pores. Therefore the measurement values of the particle density may be slightly different depending on the molecular size of liquid or gas used for measurement.

Bulk Density, ρ_B

The bulk density ρ_b is defined for powder or particle beds. It is defined as the ratio of the mass of the powder bed in a container to the volume of the bed, including the empty voids between primary particles. The porosity or void fraction ε is defined as the fraction of the volume of voids over the total volume of the bed. If the values of ρ_p and ρ_b are measured, ε can be determined by

$$\varepsilon = 1 - \left(\rho_b / \rho_p\right) \tag{1.4.1}$$

For fine particles, porosity ε of the particle bed changes easily by aeration, vibration, tapping, and other external forces. The change in the porosity generally increases with smaller particles within the range of the tightest packing to the most loosely packed state. Thus the bulk density ρ_b has various values according to Equation (1.4.1).

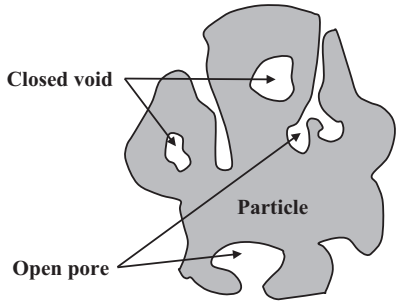


FIGURE 1.4.1 Illustration of a cross section of a particle.

1.4.2 MEASUREMENT METHOD OF PARTICLE DENSITY

The measurement of particle density consists of measuring its mass and volume. The measurement methods can be categorized into two as below:

The first is the method of measuring the particle density in a powdery state. The mass of the powder can be accurately measured with an electronic balance, and volume of particles composing the powder is determined from the increase in liquid volume upon adding the particles to the liquid, or in the case of a gaseous medium, it is determined from the increased amount of gas volume or pressure.

The second is the method of measuring the density of aerosol particles. The mass of an electrically charged particle suspended in gas is measured on the basis of the balance between gravity (or centrifugal force) and electrostatic force acting on the particle. If size and shape of the particle are known, the particle volume is calculated. Besides this, there is a method of measuring mass concentration of aerosol and its particle size distribution on a number basis at the same time.

1.4.2.1 Particle Density Measurement in a Powdery State

Pycnometer Method Using a Liquid

This is the most representative method using a liquid medium. The pycnometer (Figure 1.4.2) is a glass flask with a close-fitting ground glass stopper with a capillary hole through it. This fine hole releases the excess liquid after closing a top-filled pycnometer and enables a given volume of liquid to be determined with high accuracy. The pycnometer volume is generally about 50 ml. In this method,[1–3] each of the following

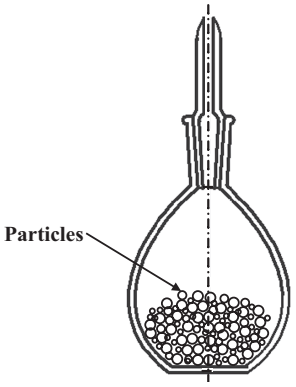


FIGURE 1.4.2 Pycnometer.

mass is measured: empty pycnometer m_0, pycnometer filled with liquid up to a fixed volume m_{l0}, pycnometer plus the sample particles m_{s0}, and pycnometer plus the sample particles and filled with liquid up to the fixed volume m_{sl0}. The particle density ρ_p is given by

$$\rho_p = \frac{(m_{s0} - m_0)}{(m_{l0} - m_0)/\rho_l - (m_{sl0} - m_{s0})/\rho_l} = \frac{\rho_l (m_{s0} - m_0)}{(m_{l0} - m_0) - (m_{sl0} - m_{s0})} \tag{1.4.2}$$

where ρ_l is the liquid density. In this method, one has to use a nonvolatile liquid in which the particles are lyophilic and insoluble. Air bubbles that adhere onto the particle surface can be effectively removed by heating or boiling the liquid under diminished pressure.[3]

Constant Gas Volume Method

In this method, gas such as air or helium is used instead of liquid. The density of almost any particle can be measured because, in contrast with the liquid pycnometer method, there is no problem of particle solubility in the fluid medium. The volume of particles composing a powder is determined from the increased amount of gas volume or pressure. There are several devices to change the gas volume and/or pressure.[1,4–7] Basically, these operate much under the same principle. Some of the devices are called "gas pycnometer."

Figure 1.4.3 shows the basic principle of constant gas volume method.[5] First, without any powder sample in the cylinder, the piston is moved from position A to position B. In this compression process, the volume and the pressure of gas in the cylinder change as follows:

$$V + V_0 \rightarrow V$$

$$P_a \rightarrow P_a + \Delta P_1 \tag{1.4.3}$$

where V_0 is the cylinder volume between positions A and B, and V is the volume between the position B and the bottom of

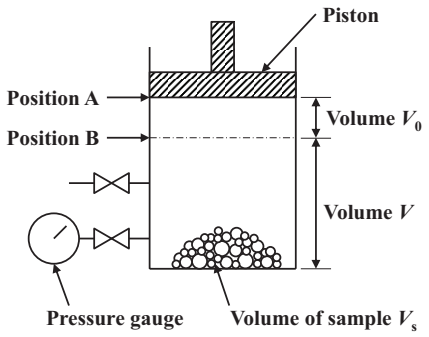


FIGURE 1.4.3 Constant gas volume method.

the cylinder. According to Boyle's law, the following relation holds:

$$P_a (V + V_0) = (P_a + \Delta P_1) V \tag{1.4.4}$$

This may be rewritten as

$$V = V_0 (P_a / \Delta P_1) \tag{1.4.5}$$

Second, after introducing a powder sample having known mass m_s into the cylinder, the above procedure is repeated. The changes in volume and pressure are

$$V + V_0 - V_s \rightarrow V - V_s$$

$$P_a \rightarrow P_a + \Delta P_2 \tag{1.4.6}$$

Thus the following equation is obtained:

$$V - V_s = V_0 (P_a / \Delta P_2) \tag{1.4.7}$$

From Equations 1.4.5 and 1.4.7, the particle volume V_s becomes

$$V_s = V_0 \left[\frac{P_a}{\Delta P_1} - \frac{P_a}{\Delta P_2} \right] \tag{1.4.8}$$

Thus the particle density ρ_p is obtained as the ratio of m_s to v_s.

1.4.2.2 Particle Density Measurement of Particles Suspended in Gas

Method Based on Balance between Electrostatic Force and Gravity

First, a test aerosol is passed through a bipolar charger having an ion source such as Am-241, Kr-85, or Po-210 to be in Boltzmann equilibrium charge distribution, and then introduced into a differential mobility analyzer (DMA)[8,9] to obtain either positively or negatively charged particles having a certain electrical mobility. The particles (e.g. having positive charge) are introduced into a small cell surrounded with two horizontal parallel electrodes in Figure 1.4.4,[10] which is the well-known Millikan cell. The distance between the

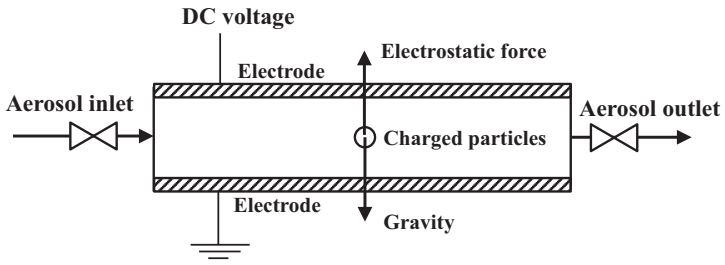


FIGURE 1.4.4 Millikan cell consisting of horizontal parallel electrodes.

electrodes h is about 2 mm. The particles are trapped in the cell by closing the inlet and outlet valves. One can stop a particle suspended inside the cell from sedimenting by applying the DC voltage V between the electrodes. At the moment, as upward Coulomb's force and gravity balance each other out, the following equation is fulfilled:

$$n_p eE = \frac{\pi}{6} x_{ve}{}^3 \left(\rho_p - \rho_f\right) g \tag{1.4.9}$$

where

- n_p is the number of elementary charges,
- e is the elementary charge $(= 1.60 \times 10^{-19}\ \mathrm{C})$,
- E is the electric field strength $\left(E = V / h\right)$,
- ρ_f is the density of gas (usually air),
- g is the acceleration of gravity $\left(= 9.8 \mathrm{m/s^2}\right)$,
- x_{ve} is called the equivalent volume diameter; the diameter of a sphere having the same volume as the irregularly shaped particle. If the particle is spherical, x_{ve} equals the diameter of the sphere.

The particles from the DMA outlet contain not only particles of $n_p = 1$ but also $n_p = 2,3,\ldots$ a little. In these particles, the particle having $n_p = 1$ is smallest, because the DMA outlet particles have the same electrical mobility Z_p [e.g. ref. [11]]:

$$Z_p = \frac{n_p eC\left(x_{me}\right)}{3\pi\mu x_{me}} = \frac{n_p eC\left(x_{ve}\right)}{3\pi\mu x_{ve}\kappa} \tag{1.4.10}$$

where

- C is the Cunningham slip correction factor,
- μ is the fluid viscosity,
- x_{me} is the mobility equivalent diameter,
- κ is the dynamic shape factor, which is defined as the ratio of the actual fluid drag force of the non-spherical particle to the fluid drag force of a sphere having the same volume and velocity as the non-spherical particle.

Among the particles introduced into the cell, the particle having $n_p = 1$ sediments most slowly as mentioned above, when the electric field is interrupted. This particle is selected for the measurement. For spherical particles, x_{ve} is calculated from Equation (1.4.10), because of $\kappa = 1$ for spheres. One applies the voltage V between the electrodes so as to stop this particle from sedimenting in the gas. Thus the particle density ρ_p is determined using Equation (1.4.9).

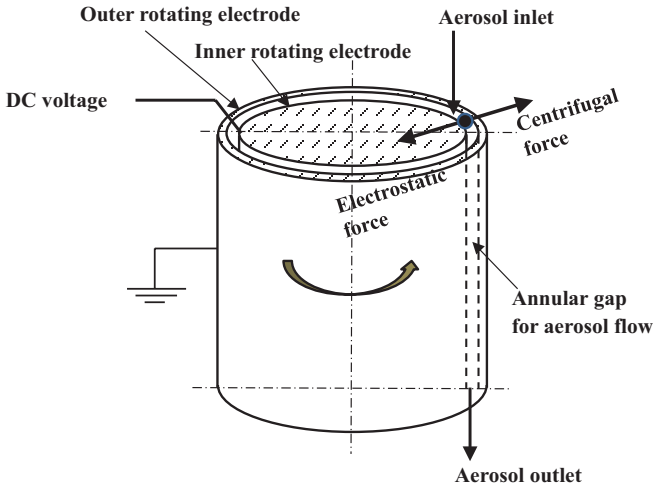


FIGURE 1.4.5 Principle of aerosol particle mass (APM) analyzer.

For irregular particles ($\kappa > 1$), some literature values of κ are available, e.g. cube: 1.08, quartz: 1.36, silica: 1.57 and talc: 2.04.[12,13] If κ is known, x_{ve} can be obtained from Equation (1.4.10), and ρ_p is determined using Equation (1.4.9). Even if κ for irregular particles is unknown, we can define "effective density" assuming $\kappa = 1$ i.e. $x_{ve} = x_{me}$. The effective density ρ_{eff} can be calculated substituting the mobility equivalent diameter x_{me} obtained from Equation (1.4.10) for x_{ve} in Equation (1.4.9).

Even for powder, the particle density can be measured by this method, if it can be dispersed into primary particles in air. When the particle size is smaller than about 500 nm, this method is unqualified, because Brownian motion (haphazard random movement) of the particle intensifies.

Method Based on Balance between Electrostatic Force and Centrifugal Force

For fine particles smaller than about 500 nm in diameter, centrifugal force is applicable instead of gravity, using rotating coaxial cylindrical electrodes (see Figure 1.4.5). In this case, Equation (1.4.9) is rewritten as follows:

$$n_p eE = \frac{\pi}{6} x_{ve}{}^3 \rho_p \omega^2 r \tag{1.4.11}$$

where

ω is the angular velocity of the coaxial cylindrical electrodes,

r is the radial distance from the axis of rotation to the annular gap,

E is the electric field strength in the annular gap h.

The device to realize this Equation is called "Aerosol Particle Mass (APM) Analyzer."[14,15] The main dimensions of the APM are outer and inner radii of 52 and 50 mm (h = 2 mm) and height of 250 mm. It is reasonable to assume that E and r are constant within the annular gap, because the gap distance h is small compared with r.

As a similar device, there is the "Centrifugal Particle Mass Analyzer (CPMA)."[16,17] Two cylindrical electrodes of the APM rotate at the same speed, but in the CPMA, the inner electrode rotates slightly faster than the outer. Both devices have almost the same structure except for this difference. Here we will explain the APM.

Before the APM, test aerosol particles are passed through a bipolar charger to be in Boltzmann equilibrium charge distribution, and then classified with the DMA to obtain particles having a certain electrical mobility. If the particles are sufficiently small, most charged particles have charge of n_p=1, and also x_{ve} is determined from Equation (1.4.10) for sphere ($\kappa = 1$). These particles feed into the APM operating at a constant rotational speed. The particles leaving the APM, which means the particles that fulfill Equation (1.4.11), are counted with Condensation Nuclei Counter (CNC)[8] connected with the APM outlet. Specifically, by gradually changing the DC voltage V between the electrodes, the number of particles is scanned with the CNC. Thus, the voltage V_m at the largest particle number can be found. Substituting $E = V_m / h$ for Equation (1.4.11), the particle density ρ_p is determined. If κ for irregular particle is unknown, above-mentioned effective density ρ_{eff} can be calculated assuming $\kappa = 1$.

In this measurement, it is desirable to calibrate the APM beforehand using spheres of known density such as polystyrene latex (PSL) particles.

Piezoelectric Microbalance Method

Piezoelectric Microbalance (Kanomax USA Inc., PIEZOBALANCE Dust Monitor®) is the device for measuring aerosol mass concentration m (mg/m^3) in the air.[18] This is based on the principle that piezoelectric crystal vibration reduces with mass of particles deposited onto the vibrating crystal. The measurable range is 0.01 to 10 mg/m^3 with airborne particles having diameters between 0.1 and 10 μm.

On the other hand, the number basis particle size distribution can be measured using a DMA-CNC system.[8,9] The distribution is given as the function of count mean diameter x_g and geometric standard deviation σ_g, and also, the particle number concentration n (particles/m^3) is obtained.

When the mass concentration m and the number basis size distribution (x_g, σ_g, and n) are measured at the same time, the following equation holds:

$$m = \frac{\pi}{6} x_v^3 \rho_p n = \frac{\pi}{6} \rho_p n x_g^3 \exp\left[4.5\left(\ln\sigma_g\right)^2\right] \quad (1.4.12)$$

where x_v is the diameter of average volume or mass. The right side of the above equation is obtained, using the relation $x_v = x_g \exp\left[1.5\left(\ln\sigma_g\right)^2\right]$ [e.g. Reference 13].

Thus, the particle density ρ_p is determined by Equation (1.4.12). If the particles are not spherical, ρ_p obtained from Equation (1.4.12) is inexact. However, the ρ_p can be used roughly as effective density, if the shape is assumed to be close to sphere.

1.4.3 MEASUREMENT METHOD OF BULK DENSITY

For fine particles, the value of bulk density varies within the range of the most loosely packed state to the most tightly packed state. When measuring the bulk density, the particle packing condition would have to be selected suitably according to the utilization purpose of the bulk density value.

For densely packing condition, the tapping method is usually used.[19–22] Figure 1.4.6 shows an example of the tapping apparatus. After tapping, mass and volume of particle bed in the measuring cap (e.g. 100 cm^3) is measured to calculate the bulk density. Besides this, there is the compression method using weight plunger.[23] However, this is occasionally undesirable. When static friction is large between the measuring cup inner wall and compressed powder, uniform densification of the powder bed does not take place, e.g. upper layer is dense, while bottom layer stays as it was loose.

A loosely packed powder bed is prepared by the method where the powder pours into a measuring cap (e.g. 100 cm^3) through a specified funnel and/or a mesh screen.[21,24–26] After packing, mass and volume of the powder bed in the measuring cap is measured. The device called "Scott Volumeter" is typical of this method.[25]

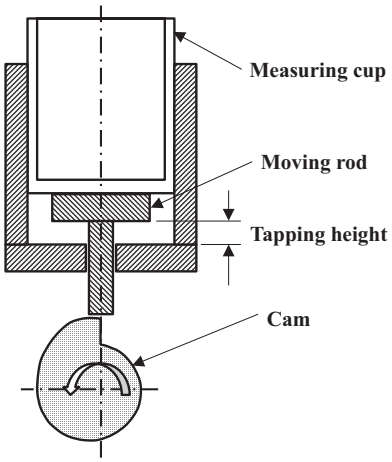


FIGURE 1.4.6 Tapping apparatus.

REFERENCES

1. JIS R 1620. 1995. Testing Methods for Particle Density of Fine Ceramic Powder.
2. ISO 11508. 1998. Soil Quality-Determination of Particle Density.
3. ASTM D854-14. 2014. Standard Test Methods for Specific Gravity of Soil Solids by Water Pycnometer.
4. Ayral, A., Phalippou, J., Woignier, T., Skeletal, *J. Mater. Sci*., 27, 1166–1170, 1992.
5. Tamari, S., *Meas. Sci. Technol*., 15, 549–558, 2004.
6. ISO 12154. 2014. Determination of Density by Volumetric Displacement-Skeleton Density by Gas Pycnometry.
7. ASTM D5550-14. 2014. Standard Test Method for Specific Gravity of Soil Solids by Gas Pycnometer.
8. Lui, B. Y. H., Pui, D. Y. H., *J. Colloid Interface Sci*. 47, 155–171, 1974.
9. Knutson, E. O., Whitby, K. T., *J. Aerosol. Sci*., 6, 443–451, 1975.
10. Kousaka, Y, Okuyama, K., Endo, Y., *J. Chem. Eng. Jpn*., 14, 214–218, 1981.
11. Kasper, G., *Aerosol Sci. Technol*., 1, 187–199, 1982.
12. Davies, C. N., *J. Aerosol Sci*., 10, 477–513, 1979.
13. Hinds, W. C., *Aerosol Technology, Properties, Behavior, and Measurement of Airborne Particles*, 2nd Ed., John Wiley and Sons, New York, 1999, pp. 51–53 or 98.
14. Ehara, K., Hagwood, C., Coakley. K. J., *J. Aerosol Sci*., 27, 217–234, 1996.
15. McMurry, P. H., Wang, X, Park, K., Ehara, K., *Aerosol Sci. Technol*., 36, 227–238, 2002.
16. Olfert, J. S., Collings, N., *J. Aerosol Sci*., 36, 1338–1352, 2005.
17. Johnson, T. J., Symonds, J. P. R., Olfert, J. S., *Aerosol Sci. Technol*., 47, 1215–1225, 2013.
18. Olin, J. G., Sem, G. J., *Atmos. Environ*., 5, 653–668, 1971.
19. ISO 3953. 2011. Metallic Powders-Determination of Tap Density.
20. ASTM B527-15. 2015. Standard Test Method for Tap Density of Metal Powders and Compounds.
21. JIS R 1628. 1997. Test Methods for Bulk Density of Fine Ceramic Powder.
22. JIS Z 2512. 2012. Metallic Powders -Determination of Tap Density.
23. ASTM D1895-96 Method C. 2010. Standard Test Methods for Apparent Density, Bulk Factor, and Pourability of Plastic Materials.
24. ISO 3923-1. 2008. Metallic Powders -Determination of Apparent Density-Part 1: Funnel Method.
25. ASTM B329-14. 2014. Standard Test Method for Apparent Density of Metal Powders and Compounds Using the Scott Volumeter.
26. Carr, R. L., *Chem. Eng*., 18, 163–168, 1965.



Taylor & Francis
Taylor & Francis Group
http://taylorandfrancis.com

1.5 Hardness, Stiffness and Toughness of Particles

Mojtaba Ghadiri, Mehrdad Pasha, and Umair Zafar

Hardness, stiffness and toughness represent the resistance of solid materials to plastic and elastic deformations and crack propagation, respectively. They are important in processes such as comminution, tabletting, polishing, abrasive and erosive wear and attrition, as they define the mode and pattern of mechanical failure. Their characterisation is highly desirable for product and process improvement and optimisation.

1.5.1 INDENTATION HARDNESS

The stress required for plastic deformation can be quantified directly only for a number of well-defined geometric shapes, such as spherical, conical and pyramidal objects[1] by, for example, compression of a particle between two platens. For non-spherical particles the indentation hardness is easier to measure (as compared to the deformation stress) from which the resistance to plastic deformation can be inferred. Hardness is related to a number of fundamental properties of solids, such as the yield stress, work hardening rate and anisotropy, and is influenced by the geometry of the deformed region.[2,3]

Indentation hardness is commonly defined as the resistive pressure, H, when a permanent impression is made. It is measured after a certain amount of plastic strain has been induced, typically between 8% and 10%,[4] and is therefore affected by anisotropy in the structure and the work hardening process. However, it is still useful to relate indentation hardness to yield stress, and the ratio of hardness over yield stress is commonly defined as the constrain factor.[5] This factor is usually much greater than unity, because the plastic deformation in a hardness test is constrained by the surrounding region which is under elastic deformation.

The indentation hardness and constraint factor depend on the properties of the deformed material, the indenter geometry,[6] and the coefficient of friction.[7,8] The material properties of concern here are the elastic modulus, yield stress, rate of work-hardening and anisotropy. The yield stress is a function of temperature and strain rate.[9,10] As temperature is decreased, the dislocation mobility is reduced and hence the yield stress increases. A similar behavior is observed when the strain rate is increased and a power function can be used to quantify the relationship between hardness and strain rate.[11]

The hardness is related to the yield stress and work hardening by considering the characteristics of the uniaxial stress-strain curve for several types of material failure. Figures 1.5.1a and b represent materials that do not work-harden; elastic deformation is included in Figure 1.5.1b, whilst ideal plastic behavior is shown in Figure 1.5.1a. The effect of work-hardening is included with and without an elastic deformation in Figures 1.5.1d and c, respectively. The elastic deformation and rate of work-hardening have a very strong influence on the value of the constraint factor, and this is analyzed by the theoretical models of indentation hardness as outlined below.

Rigid-Perfectly Plastic Indentation

A general treatment of the indentation process for this case has been described by Hill,[12] based on the wedge cutting mechanism. Here, the deformation process is represented by Figure 1.5.1a. The deformation for a blunt indenter has also been analyzed by approximating the process to the deformation by a rigid flat punch penetrating a semi-infinite rigid-perfectly plastic medium.[7]

According to the wedge cutting mechanism, the indentation is treated as cutting by a smooth wedge, where it is assumed that slip occurs along planes of maximum shear. In this case, a simple relationship exists between the yield stress, Y, and hardness, H:

$$\phi = H / Y \cong 3 \tag{1.5.1}$$

Tabor[4] tested various ductile metals and found that the experimental results for perfectly plastic deformation show a good agreement with the above theory. However, the above simple relationship does not apply to anisotropic and work-hardening materials.[13] Furthermore, the experimental observations made by Samuels and Mulhearn[14] have shown that the wedge-cutting mechanism operates only when the wedge angle is less than 30°. For wedge angles greater than 30°, the plastic deformation occurs by radial compression producing hemispherical surfaces of constant strain, where Hill's theory of expansion of a spherical cavity is more applicable (see below).

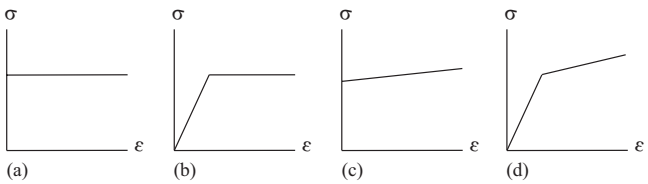


FIGURE 1.5.1 Characteristic uniaxial stress-strain curves: (a) rigid-perfectly plastic, (b) elastic-perfectly plastic, (c) rigid-plastic with work-hardening and (d) elastic-plastic with work-hardening.

Elastic-Perfectly Plastic Indentation

The deformation characteristics are shown in Figure 1.5.1b. The expansion of a spherical cavity in an infinite elastic-plastic medium has been used to describe the process of indentation, where the mean pressure, p, at which the cavity expands, is given by Hill:[12]

$$\frac{p}{Y} = \frac{2}{3}\left\{1 + \mathrm{Ln}\left(\frac{E}{3(1-\nu)Y}\right)\right\} \tag{1.5.2}$$

where

E is Young's modulus,
ν is Poisson's ratio,

The contact pressure, p, is equivalent to the hardness of the flat surface, H, and the above model has been widely used to interpret the problems associated with elastic-plastic indentation.

Following Hill's approach, Marsh[15] has proposed a similar expression for the expansion of a hemispherical cavity, where the constraint around the plastic zone is less than that of around a spherical cavity. It can be seen from Equation (1.5.2) that p/Y (or H/Y) is a function of E/Y. Tabor[8] has presented the hardness of a wide range of materials on such a coordinate system. The onset of plastic flow occurs at a ratio of p/Y of about 1, and the rigid-perfectly plastic theory predicts $p/Y = 3$.

Indentation is often made with a conical or pyramidal shape indenter where the angle of indenter affects the indentation pressure. A model of indentation hardness for this case has been presented by Johnson[6] based on the spherical cavity expansion as:

$$\frac{H}{Y} = \frac{2}{3}\left(1 + \mathrm{Ln}\frac{E\cot\theta}{3Y}\right) \tag{1.5.3}$$

where θ is the indenter semi-angle. For a spherical indenter, $\cot\theta$ may be replaced by a/R, where a is the radius of the impression and R is the indenter radius. This is a simple correlation between the indentation hardness and the indenter angle. However, Equation (1.5.3) is not valid for very sharp indenters having a narrow apex angle.[16,17]

Work-Hardening Model

For materials which exhibit significant work-hardening, the hardness is much larger than the yield stress. This is because hardness is conventionally measured at a strain of about 8%, where significant work-hardening can take place.[5] It is possible to use the analysis of expansion of a spherical cavity, and to incorporate the effect of work-hardening, whose characteristics are shown in Figures 1.5.1c and d. Here, the stress after yielding can be expressed in the form of:

$$\sigma = Y + \Pi \tag{1.5.4}$$

where Π is the *augmented* stress associated with work-hardening, and it is a function of strain, ε. Π is normally approximated by a linear relationship of the form:

$$\Pi = \Pi' \times (\varepsilon - \varepsilon_o), \ \varepsilon > \varepsilon_o \tag{1.5.5}$$

where Π' is the rate constant of hardening, and ε_o is the strain corresponding to the onset of work-hardening. For an incompressible material, i.e. no change of volume ($\nu = 0.5$), a simple relationship between the resistive pressure and the rate of work-hardening has been given by Bishop, Hill and Mott:[18]

$$H = p = \frac{2}{3}Y\left\{1 + \mathrm{Ln}\left(\frac{2E}{3Y}\right)\right\} + \frac{2\pi^2}{27}\Pi' \tag{1.5.6}$$

An alternative approach to determine the constraint factor for work-hardening materials has been suggested by Tabor,[5] where the constraint factor is described as the ratio of the indentation hardness to the representative *uniaxial flow stress*, Y_R, at an effective strain ε_R.

$$\phi = H / Y_R \tag{1.5.7}$$

For a Vickers indenter, the average effective strain produced by the indenter is between 8% and 10%.[4] The flow stress at this value of strain is taken to calculate the constraint factor from Equation (1.5.7). This approach produces significantly different values for ϕ, and does not include the yield stress and work-hardening in an explicit way.

In summary, the relationship between the hardness and yield stress is illustrated in Figure 1.5.2. It is clear that the material is subjected to more constraint as its morphology changes from the amorphous state to the crystalline state.

1.5.2 MEASUREMENT OF HARDNESS

Measurement and theory of hardness testing have been developed in the field of material testing, where it has been possible to carry out hardness tests on relatively large specimens. With recent advancements in the field of nano-testing and atomic force microscopy (AFM), characterisation of hardness on micron and sub-micron sized specimens is now possible.[19–21] Care should be considered when comparing the measured hardness values at micro and macro scales for materials such as polycrystalline (see Figure 1.5.3), as they refer to different measures of hardness.[22]

The measurement of hardness started with scratch testing of flat surfaces by various particles having varying degree of hardness, i.e. Mohs hardness test (see e.g. ref.[23]). This method provided a qualitative indication of resistance to plastic flow, but it was too complex for analysis to obtain quantitative results. The method of indentation hardness testing evolved by the use of well-defined indenter geometry, such as spherical, pyramidal or conical shapes. Tabor's[4] pioneering work established the basis of understanding of the deformation processes involved in the indentation. There are a number of common test methods available using different indenter

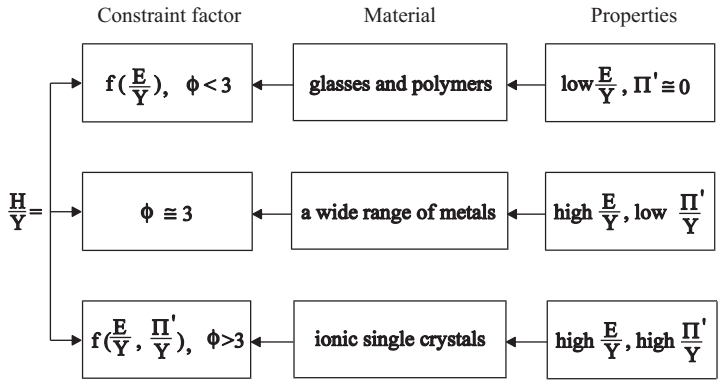


FIGURE 1.5.2 Relationship between hardness and yield stress.

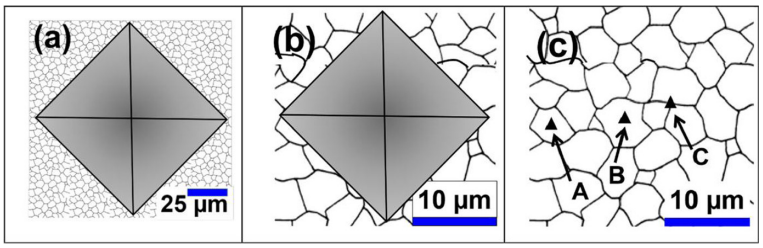


FIGURE 1.5.3 Scheme of indentation hardness of a polycrystalline material at (a) macroscale; (b) microscale; and (c) nanoscale.

shapes: Brinell, using a 10 mm sphere of steel or tungsten carbide; Vickers, using a diamond pyramid; Knoop, using also a diamond pyramid, and Rockwell, using diamond cone with a spherical tip and steel spheres.[8,24] In all these tests, a load is applied to the surface under testing by slowly penetrating the indenter at the right angle into the specimen. The hardness number is calculated from the applied load, the projected area of the impression, and by taking account of the shape of the indenter. The relevant formula for hardness numbers may be found for example from Fischer-Cripps.[24]

The above techniques cannot be easily applied to the measurement of hardness of particles unless the particle is large, i.e. above a few millimetres. However, the recent advancement of nano-test and atomic force microscopy methods have enabled a full characterization of mechanical properties, i.e. elastic modulus, hardness, yield stress, and fracture toughness.[20,25] Because of the small size of impression, which can be sub-micrometre, almost all nano-indentation methods measure the resistance of material to penetration (i.e. the applied load) as a function of depth of penetration, from which an 'effective' hardness can be inferred.

A schematic diagram of a typical nano-test device is shown in Figure 1.5.4. There are several designs (see e.g. ref.[26–29]) or other commercial instruments. The design shown here was originally developed by Pollock, Maugis and Barquins[30] and is now manufactured by Micro Materials Ltd, Wrexham, UK. The device measures the movement of a calibrated diamond indenter penetrating into a specimen surface at a controlled loading rate or depth rate. It uses a pendulum pivoted on bearings which are essentially frictionless. A coil is mounted at the top of the pendulum so that when a coil current is present

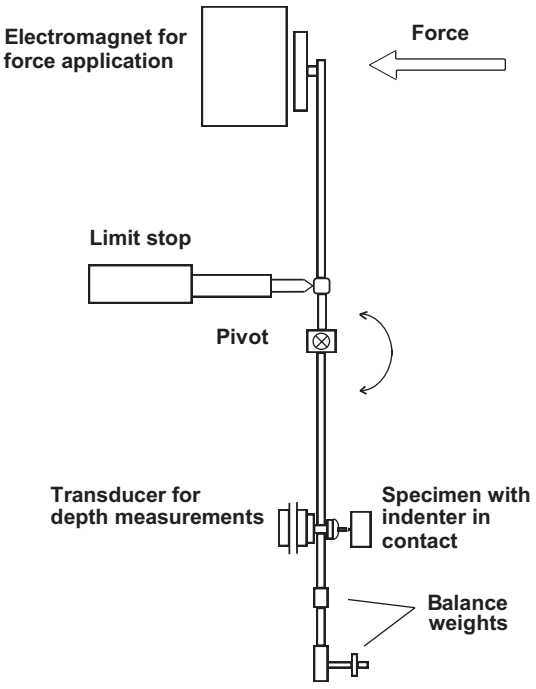


FIGURE 1.5.4 Schematic diagram of the nanoindenter device.

the coil is attracted towards a permanent magnet, producing motion of the indenter towards the specimen and into the specimen surface. The displacement of the diamond is measured by means of a parallel plate capacitor, one plate of which is attached to the diamond holder; when the diamond moves, the capacitance changes, and this change is measured by means

of a capacitance bridge. The most commonly used indenter is a Berkovitch diamond, a three-sided pyramid, which is particularly suitable for nanoindentation work because it can be machined down very accurately to a very sharp tip. However, 90° trigonal and spherical indenters have also been used. The above device is capable of measuring load and displacement with typical resolutions around 3 nN and better than 0.1 nm, respectively.

In a nanoindentation test, the specimen is first brought in contact with the indenter; then the load or depth is increased at a prescribed rate until the desired maximum load or depth is reached, and then it is decreased back to zero at the same rate. Therefore a continuous recording of the penetration depth and the applied load is made, from which an effective hardness modulus may be inferred at a specified strain rate by invoking a relation between the penetration depth and the indentation area. For coated material however, it has been shown that the penetration depth should not exceed from 5% to 10% thickness of the film.[31,32] A typical depth/load cycle is shown in Figure 1.5.5. During the unloading part of the cycle, the elastic deformation of the sample recovers, and therefore the unloading curve is not horizontal. The maximum depth and characteristics of the unloading curve are used to calculate the hardness. It is also possible to evaluate the elastic modulus from the unloading curve. Two distinct regions can be observed here: the initial unloading stage bearing all the features of an elastic unloading, and a highly non-linear stage towards the end of the unloading cycle. Reasons for this non-linearity are complex; changes in the contact area arising from an increase in the apical angle of the impression are thought to be responsible.[33,34] There are several methods for the evaluation of hardness from such data (e.g. see ref.[33,35]). The method described below is based on the analysis of Oliver and Pharr,[35] and is one of the most widely used methods.

At the initiation of unloading (Figure 1.5.5), the elastic component of the deformation starts to recover so that contact between the material surface and the indenter is still maintained. As the load is decreased the elastic displacement continues to recover until at zero loads the displacement reaches a final value, h_f. At the peak load, F_{max}, the displacement is h_{max}. A schematic diagram depicting a cross-sectional view of an indentation is shown in Figure 1.5.6. The total displacement, h, can be described at any time during loading as

$$h = h_C + h_S \tag{1.5.8}$$

where

h_C is the contact depth, i.e. the vertical distance along which contact is made, corresponding to the contact size, a,

h_S is the elastic displacement of the surface at the perimeter of the contact.

In this analysis, hardness, H, can be determined by

$$H = \frac{F_{max}}{A} \tag{1.5.9}$$

where A is the projected area of the impression. Now, from the geometry of the indenter

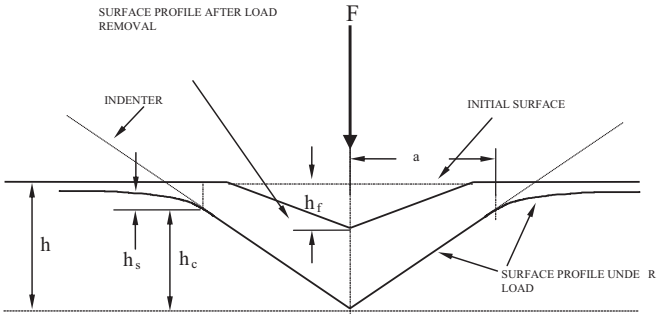


FIGURE 1.5.6 A schematic diagram depicting a cross-sectional view on an indentation.

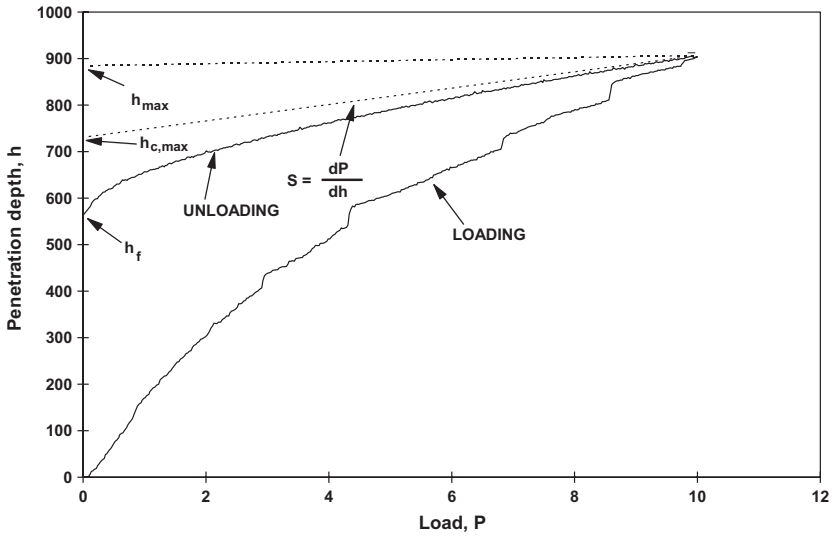


FIGURE 1.5.5 Typical loading/unloading curve in a nanoindentation test.

$$A = kh_{c,max}^2 \tag{1.5.10}$$

with k being the indenter shape factor, and $h_{c,max}$ the contact depth at F_{max}. Now, to determine the contact depth from the experimental data, it can be noted that

$$h_{c,max} = h_{max} - h_{s,max} \tag{1.5.11}$$

which follows directly from Equation (1.5.8). h_{max} is experimentally measured, and $h_{s,max}$ can be ascertained from the unloading data by the use of an expression derived by Oliver and Pharr[35] from Sneddon's[36] solution for the elastic contact of indenters of different shapes. This expression is given by

$$h_{s,max} = \varepsilon \frac{F_{max}}{S} \tag{1.5.12}$$

where

S is the stiffness at load F_{max} (as shown in Figure 1.5.5),
ε is a constant which depends upon indenter geometry.

The value of ε for a Berkovitch indenter cannot be determined analytically; however, it has been shown that the Berkovitch indenter behaves very much like a paraboloid of revolution for which a solution for the parameter ε exists, i.e. $\varepsilon \approx 0.75$.[37] In practice, the stiffness, S, is obtained by fitting the unloading data to a power law relation of the form

$$F = \alpha \left(h - h_f\right)^m \tag{1.5.13}$$

where

$(h–h_f)$ is the elastic displacement of the indentation during unloading,
α and m are constants.

The values of α, m, and h_f are all determined by a non-linear curve fitting procedure. Equation (1.5.13) can then be differentiated analytically with respect to $(h–h_f)$ to obtain the value of stiffness

$$S = \frac{dF}{d\left(h - h_f\right)} \tag{1.5.14}$$

which can then be evaluated at the peak load, F_{max}. Then, by first substituting the value of stiffness obtained from Equation (1.5.14) into (1.5.12), the value of $h_{s,max}$ is calculated. The Equations (1.5.11, 1.5.10 and 1.5.9) are then used to determine the hardness.

1.5.3 MEASUREMENT OF STIFFNESS

Particles subjected to mechanical stresses below the critical level for plastic yielding undergo elastic deformation. The resistance to elastic deformation is represented by the ratio of load over the extent of deformation, termed stiffness. As in the case of plastic deformation, for non-spherical particles the contact geometry is too complex for characterizing the stiffness by standard techniques. The approach outlined above for indentation hardness measurement can also be used to evaluate the stiffness. For materials obeying Hooke's law, the stiffness can be calculated from Young's modulus, and this in turn can be determined from the unloading portion of the depth-load data (as shown in Figure 1.5.5) by the use of Sneddon's analysis. This analysis is independent of indenter geometry,[37] and is therefore applicable to results obtained with the Berkovitch indenter:

$$E_r = \frac{\sqrt{\pi}}{2} \frac{S}{\sqrt{A}} \tag{1.5.15}$$

where S is calculated from Equation (1.5.14); A is the contact area given by Equation (1.5.10); and E_r is the reduced modulus defined by

$$\frac{1}{E_r} = \frac{(1-\nu^2)}{E} + \frac{(1-\nu_i^2)}{E_i} \tag{1.5.16}$$

where E and ν are Young's modulus and Poisson's ratio of the specimen, and E_i and ν_i are the same parameters for the diamond indenter. Since Young's modulus of the indenter is two orders of magnitude greater than that of the test materials, the reduced modulus is effectively Young's modulus of the specimen. In conclusion, the above approach enables the determination of hardness and Young's modulus at the micro and nano-scale levels. However, great care is needed for the experimental procedure and interpretation of the data because of the scale of operation.

1.5.4 MEASUREMENT OF TOUGHNESS

Fracture toughness represents the resistance of solid materials to crack propagation. The basis of its measurement lies in the principles of linear elastic fracture mechanics and the Griffith energy balance for crack propagation.[38] For large specimens, the measurement of fracture toughness is made using a uniform stress field. A number of methods have been developed in the past for measuring the fracture toughness such as the Chevron notch bar (CNB), single-edge notch beam (SENB), single-edge V-notched beam (SEVNB), single-edge pre-cracked beam (SEPB) and three-point bend test. A review of these methods is given by Zhu and Joyce[39] and Mukhopadhyay, Datta and Chakraborty.[40] The three-point bend test is a common method of measuring the fracture toughness of relatively large specimens, as shown in Figure 1.5.7, where a crack of length, c, is made much shorter than the specimen depth, d, providing uniform tension at the crack tip. In this case the fracture toughness is calculated based on the simple beam theory and is given by:[38]

$$K = m(3Fb / d^2)(\pi\, c)^{1/2} \tag{1.5.17}$$

where m is a factor which depends on c/d and has a limiting value of 1.12.

For small particles the measurement of fracture toughness using the above-mentioned method may not be possible. Instead, the indentation methods can be used to measure the fracture toughness as described below (see e.g. ref.[41,42]).

Indentation Fracture Toughness

In indentation fracture by a sharp indenter causing plastic deformation, there is a critical size of indentation, r_c, above which fracture is initiated:[43]

$$r_c \cong \alpha \frac{E\Gamma}{Y^2} \tag{1.5.18}$$

where

- α is a constant,
- E is Young's modulus,
- Γ is the fracture surface energy,
- Y is the yield stress in a uniaxial compression test.

This critical size reflects the influence of the mechanical properties. The yield stress is related to the hardness, as $Y = H/\phi$, where ϕ is the constraint factor. The fracture surface energy and Young's modulus are related to the fracture toughness based on the Linear Elastic Fracture Mechanics. For the case of plane strain:

$$E\Gamma = K_c^2(1-\nu^2) \tag{1.5.19}$$

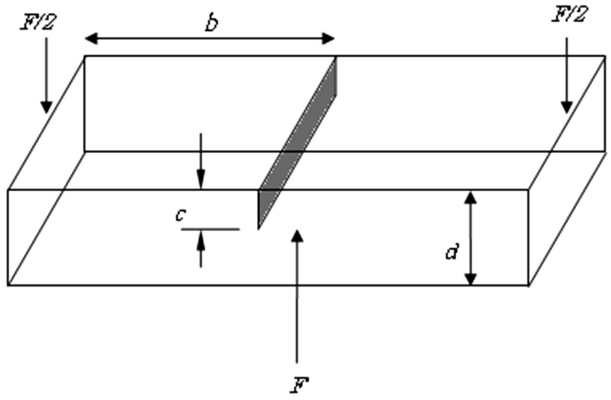


FIGURE 1.5.7 Three-point bend test.

where ν is Poisson's ratio. Considering that ν^2 is much smaller than unity, the critical size can be written approximately in the following form:

$$r_c \approx \alpha' \left(\frac{K_c}{H}\right)^2 \tag{1.5.20}$$

When the surface is indented by a sharp indenter, the plastic zone size increases until a critical size is reached, above which cracks propagate. From the indentation fracture mechanics, it can be shown that the size of the stress field scales with $\sqrt{r_c}$. Therefore the crack length is controlled by r_c, which in turn is related to K_c. On indentation, two distinct types of radial cracks can be generated, median and Palmqvist cracks, as shown in Figure 1.5.8. The fracture toughness can then be determined from the relationship of the crack length with applied load. A large number of correlations are available and reviewed by Ponton and Rawlings.[42] The correlations due to Laugier[44,45] for the two crack types may be unified in form by Equation (1.5.21).

$$K_c = x_v \left(\frac{a}{l}\right)^k \left(\frac{E}{H_v}\right)^n \frac{P}{c^{3/2}} \tag{1.5.21}$$

where x_v is a calibration factor, (a/l) is the ratio of impression size to crack length as defined in Figure 1.5.8, c $(=a+l)$ is the crack size as measured from the center of the impression, P is the load, and k and n are power indices. For median cracks: $x_v = 0.011$, $k = 0$, and $n = 2/3$, whilst for Palmqvist cracks: $x_v = 0.0143$, $k = 1/2$ and $n = 2/3$.

The main advantage of measuring fracture toughness by indentation is that no special specimen geometry is required. However, since it relies upon the indentations producing a radial or median crack system with well-formed surface traces, its applicability is limited to materials which exhibit brittle and semi-brittle fracture during indentation. In a typical test a number of different loads are applied and the indent size and crack length as shown in Figure 1.5.8 are measured. A plot of crack length, c, as a function of $P^{2/3}$ should produce a straight line, the slope of which would give K_c.

As an example, the results of measurement of fracture toughness of paracetamol and α-lactose monohydrate crystals by nanoindentation are shown below. Figure 1.5.9 shows indentations on the (100) face of lactose crystals.

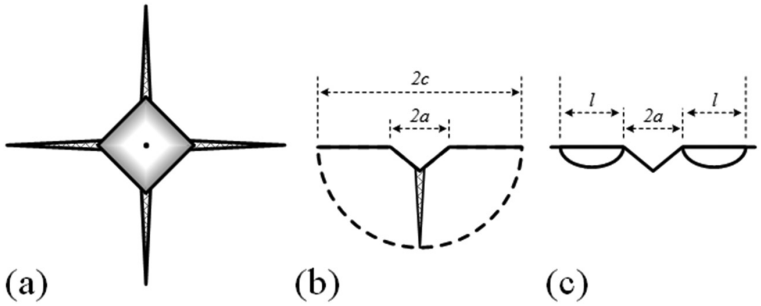


FIGURE 1.5.8 Indentation crack geometry: (a) Berkovitch impression; cross-section view of (b) radial crack and (c) median crack systems.

The relationships between crack length and load are shown in Figure 1.5.10 for indentations in lab-produced crystals of paracetamol and lactose. Error bars of one standard deviation of the mean are also included in the figure. The load-crack length relationship given previously, i.e. $P/c^{3/2} \approx$ constant, has been added for comparison. The values of the intercept, b, as indicated in the figure, have been chosen to be slightly different from the values of the intercept for the best fits of the experimental data to show the close agreement in the slopes of the lines. It is clear that the load-crack length data for both materials approximate reasonably well the expected relationship. The results of fracture toughness for both paracetamol and α-lactose monohydrate are shown in Figure 1.5.11 as plots of fracture toughness against load. Here, the equation proposed by Laugier[44,45] has been used to calculate K_c, as this correlation has been developed for materials which are well-behaved in their indentation response and it takes into account the role of plastic deformation in driving the crack growth.

Care needs to be taken into account for the effect of indenter geometry. Most correlations reported in the literature are based on the Vickers indentation with four associated radial cracks whilst with Berkovitch (three-sided pyramid) indentations a smaller number of cracks are produced and with Knoop indenter the cracks are forced to propagate along preferred direction. Dukino and Swain[46] compared measurements of fracture toughness obtained from Berkovitch and Vickers indentations, and proposed a method to relate the two measurements.

The mechanical properties addressed in this chapter are influential in processes in which solid particles experience large stresses to cause deformation and breakage, such as comminution and tabletting. It should be noted these properties are dependent on temperature and strain rate, particularly for semi-brittle failure mode, as crack propagation is preceded by plastic deformation. However their characterization at the prevailing high temperature or high strain rate is not

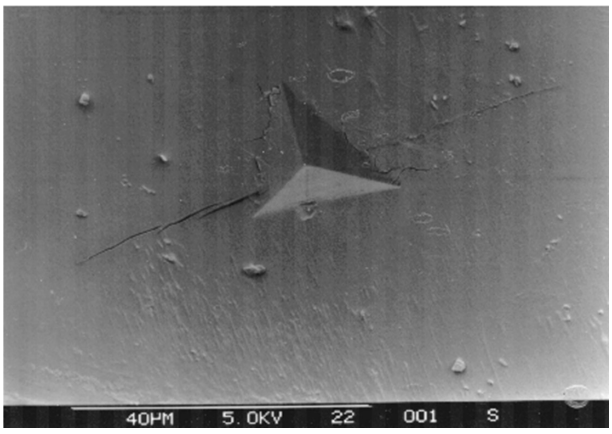


FIGURE 1.5.9 SEM micrograph of a nanoindentation in the (100) face of lab-produced lactose. Applied force: 100 mN. Indenter: Berkovitch pyramid.

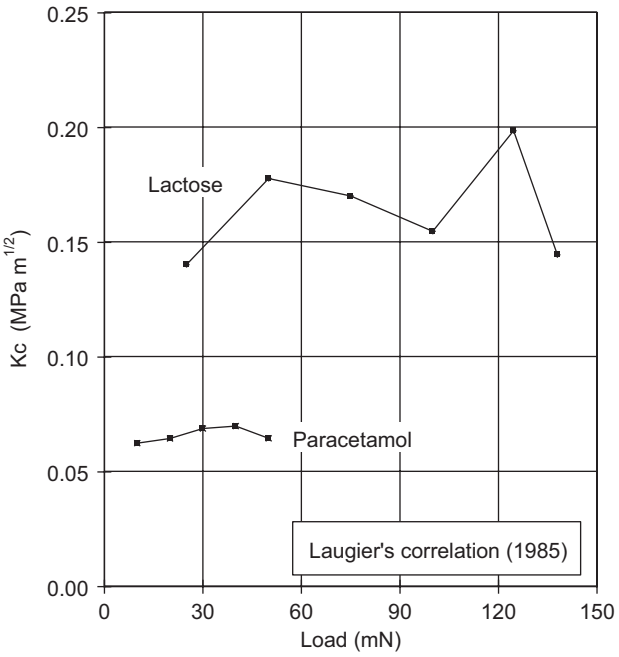


FIGURE 1.5.11 Plots of fracture toughness against load for paracetamol and lactose crystals.

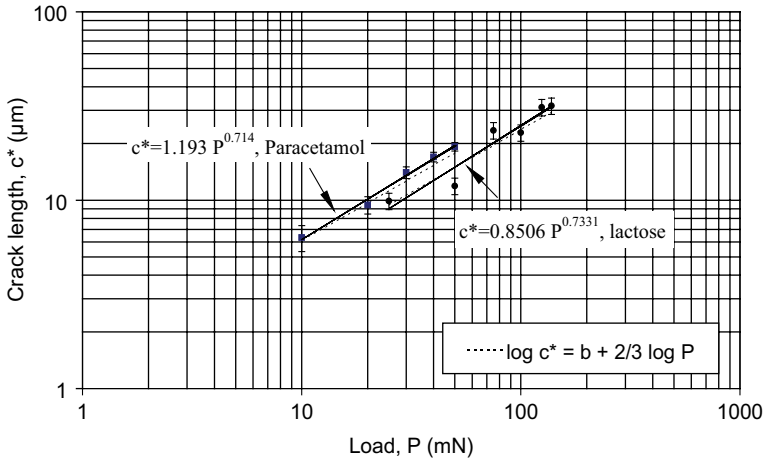


FIGURE 1.5.10 Relationship between crack length and load from nanoindentation experiments on paracetamol and lactose crystals.

easy. The application of hardness, stiffness and toughness for analysis of particle breakage is addressed in Chapter 2.11. An issue of interest is the critical particle size below which there is insufficient elastic strain energy for crack propagation to occur. Several models have been proposed (see e.g. ref.[47–50]). All these models, although based on different considerations and assumptions, follow the same general form. In the case of α-lactose monohydrate and paracetamol used as an example here, the values of r_c are calculated as 0.5 μm and 2.4 μm, respectively, which seems reasonable.

REFERENCES

1. Chaudhri, M.M., *J. Mater. Sci.*, 19, 3028–3042, 1984.
2. Czichos, H., Saito, T., Smith, L.E., *Springer handbook of metrology and testing*, Springer, Berlin Heidelberg, 2011.
3. Herrmann, K., *Hardness testing: Principles and applications.* Materials Park, Ohio, ASM International, 2011.
4. Tabor, D., *Proc. R. Soc. London*, *Ser. A*, 192, 247–274, 1948.
5. Tabor, D., *Indentation hardness and its measurement: Some cautionary* in: Microindentation techniques in material science and engineering, Blau, P.J., Lawn, B.R., Eds., ASTM International, Philadelphia, 1986.
6. Johnson, K.L., *J. Mech. Phys. Solids*, 18, 2, 115–126, 1970.
7. Gilman, J.J., *Hardness-a strength microprobe*, Westbrook, J.H., Conrad, H., Eds., American Society for Metals, Geauga County, OH, 1973.
8. Tabor, D., *Rev. Phys. Tech.*, 1, 145, 1970.
9. Soares, G.C., Rodrigues, M.C.M., Santos, L.D., *Mater. Res. IBERO-Am. J. Mater.*, 20, 141–151, 2017.
10. Hull, D., Bacon, D.J., *Introduction to dislocations*, Pergamon Press, Oxford, New York, 1984.
11. Grau, P., Berg, G., Meinhard, H., Mosch, S., *J. Am. Ceram. Soc.*, 81, 1557–1564, 1998.
12. Hill, R., *The mathematical theory of plasticity*, Clarendon Press, Oxford, New York, 1998.
13. Gao, X.L., Jing, X.N., Subhash, G., *Int. J. Solids Struct.*, 43, 2193–2208, 2006.
14. Samuels, L.E., Mulhearn, T.O., *J. Mech. Phys. Solids*, 5, 125–134, 1957.
15. March, D.M., *Proc. R. Soc. London*, 420–435, 1964.
16. Hirst, W., Howse, M.G.J.W., *Proc. R. Soc. London*, 311, 429–444, 1969.
17. Atkins, A.G., Tabor, D., *J. Mech. Phys. Solids*, 13, 149–164, 1965.
18. Bishop, R.F., Hill, R., Mott, N.F., *Proc. Phys. Soc. London*, 57, 147, 1945.
19. Fischer-Cripps, A.C., *Vacuum*, 58, 569–585, 2000.
20. Butt, H.-J., Cappella, B., Kappl, M., *Surf. Sci. Report*, 59, 1–152, 2005.
21. Passeri, D., Bettucci, A., Biagioni, A., Rossi, M., et al., *Rev. Sci Instrum.*, 79, 066105, 2008.
22. Broitman, E. *Tribol. Lett.*, 65, 23, 2017.
23. Tabor, D., *Proc. Phys. Soc. London*, *Sect. B*, 67, 249–257, 1954.
24. Fischer-Cripps, A.C., *Nanoindentation*, Springer, New York, 2013.
25. Arteaga, P.A., Ghadiri, M., Lawson, N.S., Pollock, H.M., *Tribol. Int.*, 26, 305–310, 1993.
26. Micro Materials Ltd. Nanotest vantage. Wrexham LL13 7YL, UK.
27. Hysitron Inc. Hysitron TI TriboIndenter. Minneapolis, MN 55344, US.
28. Nanomechanics Inc. iNano Nanoindenter. Oak Ridge, TN 37830, US.
29. CSEN Instruments. Nano-hardness tester. CH-2007 Neuchâtel, Switzerland.
30. Pollock, H.M., Maugis, D., Barquins, M., *Microindentation techniques in materials science and engineering*, Blau, P., Lawn, B., Eds., ASTM STP, Philadelphia, PA, 1986.
31. Zocco, A., Perrone, A., Broitman, E., Czigany, Z., Hultman, L., Anderle, M., Laidani, N., *Diam. Relat. Mater.*, 11, 98–104, 2002.
32. Gamonpilas, C., Busso, E.P., *Mater. Sci. Eng. A*, 380, 52–61, 2004.
33. Doerner, M.F., Nix, W.D., *J. Mater. Res.*, 1, 601–609, 1986.
34. Ion, R.H., Pollock, H.M., *J. Mater. Sci.*, 25, 1444–1454, 1990.
35. Oliver, W.C., Pharr, G.M., *J. Mater. Res.*, 7, 1564–1583, 1992.
36. Sneddon, I.N., *Int. J. Eng. Sci.*, 3, 47–57, 1965.
37. Pharr, G.M., Oliver, W.C., Brotzen, F.R., *J.Mater. Res.*, 7, 613–617, 1992.
38. Lawn, B.R., *Fracture of brittle solids.*, Cambridge University Press, Cambridge, New York, 1975.
39. Zhu, X.-K., Joyce, J.A., *Eng. Fract. Mech.*, 85, 1–46, 2012.
40. Mukhopadhyay, A.K., Datta, S.K., Chakraborty, D., *Ceram. Int.*, 25, 447–454, 1999.
41. Chicot, D., Pertuz, A., Roudet, F., Staia, M., et al., *Mater. Sci. Technol.*, 20, 877–884, 2004.
42. Ponton, C.B., Rawlings, R.D., *Mater. Sci. Technol.*, 5, 865–872, 1989.
43. Puttick, K.E., *J. Phys. D. Appl. Phys.*, 11, 595–604, 1978.
44. Laugier, M.T., *J. Mater. Sci. Lett.*, 4, 1539–1541, 1985.
45. Laugier, M.T., *J. Mater. Sci. Lett.*, 6, 355–356, 1987.
46. Dukino, R.D., Swain, M.V., *J. Am. Ceram. Soc.*, 75, 3299–3304, 1992.
47. Lawn, B.R., Evans, A.G., *J. Mater. Sci.*, 12, 2195–2199, 1977.
48. Kendall, K., *Nature*, 272(5655), 710–711, 1978.
49. Hagan, J.T., *J. Mater. Sci.*, 16, 2909–2911, 1981.
50. Puttick, K.E., *J. Phys. D. Appl. Phys.*, 13, 2249–2262, 1980.

1.6 Surface Properties and Analysis

Masayoshi Fuji and Chika Takai

1.6.1 SURFACE STRUCTURES AND PROPERTIES

1.6.1.1 Particle Surface and Character

A material that does not have flowability at temperatures below its melting point can exist as a solid in various shapes. The significant feature is the degree of the unsaturation of the chemical bond to which the internal structure terminates when the surface of the solid is looked at on the microscopic scale. It is not possible to diffuse because the activation energy of the surface diffusivity is generally high, when the adjacent potential energy is different by atoms, ions, or molecules that compose the surface. Therefore, a feature of the solid surface is that it is not able to produce a uniform energy like the liquid surface. Various characteristics of a solid surface are strongly influenced by these two features.

The population of atoms, ions, and molecules that compose the fine particle surface increases in comparison with the particulate inside. In this case, a lot of peculiar characteristics begin to appear in fine particles.[1] Especially, the property concerning handling the powder begins to strongly depend on the character of the particulate surface.[2] Therefore, how one can know the character of the particulate surface and control it are the major technologies in all fields where the powder has an effect. Here, we describe in detail an important matter for understanding the character of the particulate surface.

1.6.1.2 Surface Relaxation

Various surface relaxations appear for the stabilization because the solid surface has broken chemical bonds and exists in an unstable state. These relaxations are different depending on the kind of chemical bond, such as covalent bond, ionic bond, and metallic bond, and the kind of material. In this section we separately describe chemical relaxation with a chemical change and physical relaxation with a structural change. Moreover, because the solid is usually handled in the atmosphere, we also describe the stabilization of the surface by water adsorption.

1.6.1.3 Physical Surface Relaxation

An atom, ion, or molecule on the surface receives an unsymmetrical interaction force, because chemical bonds have been cut on the crystal surface. Therefore, these positions change from the position forecast from the internal crystal lattice. In the case of a surface of alkali halides, which are ionic crystals, the anion or the cation is displaced to a position that is positive or negative in the vertical direction against the surface from the position expected from the lattice location. Figure 1.6.1 shows such an example. In the surface layer of the (100) face of NaCl, Cl^-, which is the anion, is polarized with the Na^+ ion on the circumference and, as a result, displaces from the surface to the outside. The cations internally displace.

The electrical double layer is formed as a result and the surface has been stabilized. That is, a center position for both ions does not exist on the same face. Moreover, the distance between the position of the first layer as the average of both ions and the position of the second layer is compressed neater than interlayer distances in the crystal. It is assumed that such displacement is caused from the first layer to the fifth layer in NaCl.[3] A similar phenomenon in other materials is listed in Table 1.6.1. In the (100) face of MgO, whose bond energy is larger than the alkali halide though it is classified into the same ionic crystal system, the interionic distance of the first surface layer and the second layer is compressed to about 85% of the interlayer distance in the crystal. The physical surface relaxation phenomenon is presumed to be different depending on

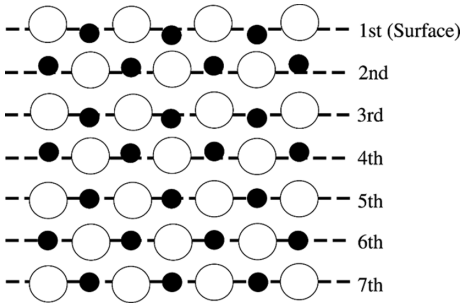


FIGURE 1.6.1 Physical relaxation model for (100) face of alkali halide alkali. Open circle is anion. Closed circle is cation. Dotted line indicates the position of inner crystal lattice.

TABLE 1.6.1 Physical Surface Relaxation

	Crystal Structure	(110)	(001)	(111)
Cu	face-centered cubic	0.900	0.997	0.954
Al	face-centered cubic	0.900	1.00	1.021
Fe	body-centered cubic	1.00	0.986	0.85
NaF	rock-salt	—	0.972	—
NaCl	rock-salt	—	0.970	—
NaBr	rock-salt	—	0.972	—
MgO	rock-salt	—	0.85	—

* The data indicate the ratio of the length between surface layer and 2nd layer and the length between atoms in bulk.

the difference in the ion species, the coordination number, the crystal face, and the bond energy for the crystal with the same ionic bond.[4] A similar relaxation is also caused on the surface of a metallic crystal. The surface relaxation is high in the crystal face; therefore, the atomic density is small, as shown in Table 1.6.1. The change region is assumed to be from the surface to about two layers. The (2×1) structure in the Si(001) face and the (7×7) structure in the Si(111) are well known.[5,6,7]

1.6.1.4 Chemical Surface Relaxation

Because a chemical bond is unsaturated in the solid surface as previously described, the reactiveness is high. When the solid is exposed to an atmosphere, the surface, where the reactivity is high, chemically reacts with the reactive gas in the atmosphere, that is, oxygen, carbon dioxide, or water vapor, and forms a surface composition different from the chemical composition of the bulk. The metallic surface is oxidized by atmospheric oxygen and water vapor, and corrosion is a daily phenomenon. Moreover, oxygen in the air is chemically adsorbed and an oxide is also formed on the surface of the nitride. This oxide surface further chemically adsorbs the water vapor, and the oxide is also formed on the surface of nitride and boride. In addition, the oxide surface changes into a surface of hydroxyl groups by chemisorption of the water vapor. Examples of the chemisorption of oxygen on a metallic surface and the nitride surface are as follows.

$$2Fe + O_2 \rightarrow 2FeO \tag{1.6.1}$$

$$4AlN + 3O_2 \rightarrow 2Al_2O_3 + 2N_2 \tag{1.6.2}$$

$$Si_3N_4 + 3O_2 \rightarrow 3SiO_2 + 2N_2 \tag{1.6.3}$$

$$2TiB_2 + 6H_2O \rightarrow 2TiO_2 + 2B_2H_6 + O_2 \tag{1.6.4}$$

$$\equiv Si - O - Si \equiv + H_2O \rightarrow 2 \equiv Si - OH \tag{1.6.5}$$

$$Si_3N_4 + 6H_2O \rightarrow 3SiO_2 + 4NH_3 \tag{1.6.6}$$

The material chemically adsorbs the atmospheric carbon dioxide and forms a carbonic acid salt. For instance, carbonate and a surface hydroxyl group are formed with the carbon dioxide and water vapor in air on MgO, CaO, and the surface of the MgO–ZnO complex oxide. Water vapor is easily chemically adsorbed in general, and the surface becomes covered by hydroxyl groups on the oxide surface. Figure 1.6.2 shows the chemisorptions of water vapor on the surface of MgO having a simple crystal structure as one example. The chemisorption of water vapor has the ability to adsorb only on the surface layer and adsorb into a layer in the solid. Not only the first surface layer but even the inside of the solid MgO can absorb.

The surface hydroxyl group is desorbed by heating. The desorption behavior not only differs depending on the oxide type, but also changes depending on synthetic method and the thermal hysteresis of the sample. Figure 1.6.3 shows the change in the amount of the surface hydroxyl groups by heating various oxides.[8–11] The physical adsorption of the water vapor occurs on the polar surface when the solid has been left in the atmosphere and the surface free energy has decreased. The adsorption layer is formed from about two molecular layers at the relative humidity about 60% on the hydrophilic surface such as glass. Figure 1.6.4 shows water vapor adsorption isotherms for silica glass surfaces. The silica surface is stabilized by the existence of these adsorbed water molecules, and the dynamic, chemical, and electrical properties

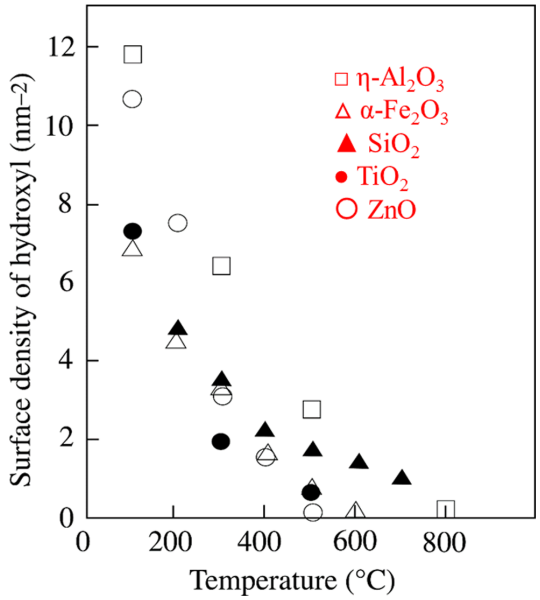


FIGURE 1.6.3 Changes of surface density of hydroxyl on several oxides with heat-treatment.

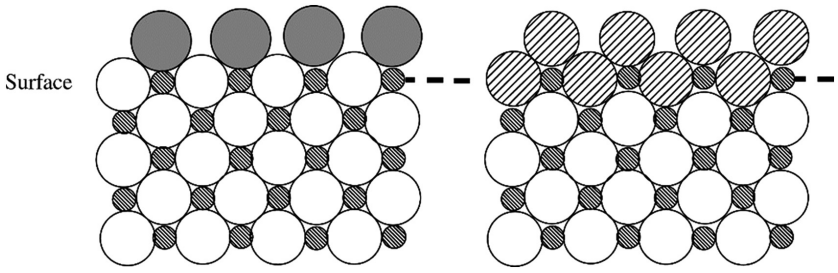


FIGURE 1.6.2 Chemical adsorption of water molecules on MgO (100). Closed circle, open circle, gray colored circle, and hatched circle represent Mg^{2+}, O^{2-}, H_2O, OH, respectively.

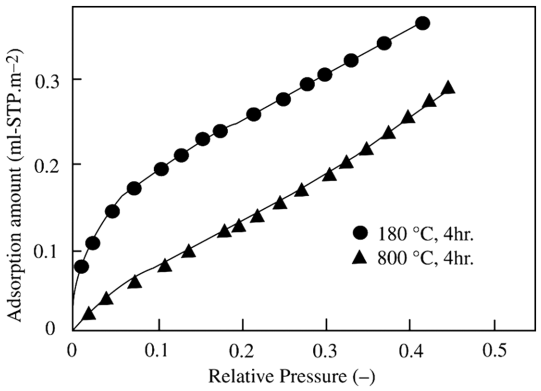


FIGURE 1.6.4 Water vapor adsorption isotherms on silica glass.

of the material are significantly influenced. Moreover, it is known that the adhesive force between particles changes and produces a remarkable influence on the aggregation and the solidifying properties of the powder.[12–14]

1.6.1.5 Surface Acidity and Basicity

Influence of the Element

For the chemical property of the oxide surface, one of the important characteristics for practical use might be the solid acid and base. The acidity and the basicity of the oxide surface are predictable to some degree based on the chemical property of the atom composition. Figure 1.6.5 shows the relation to electronegativity (χ_1) of the partial charge and the metal ion on the oxide oxygen.[15] It is understood that the negative charge density of oxygen becomes smaller when the electronegativity of the metal ion is high and shows acidity. The electronegativity of the metal ion is shown here by the following equation:

$$\chi_i = (1+2z)\chi_0 \tag{1.6.7}$$

where

z is the charge,

χ_0 is the electronegativity of the metal atom.

Auroux et al. found a linear relation, as shown in Figure 1.6.6, from the heat of adsorption measurement of CO_2 by some oxides and the ratios of the charge/metal ion radius. When the ratio of the charge/metal ion radius is low, and the ionicity of chemical bond is high, the basicity is strong.[16]

Influence of Partially Chemical Structure

The strength of the acid and the base changes depending on the chemical structural difference, even if it is a single chemical composition. As for the free surface hydroxyl group observed on the Al_2O_3 surface, two or more structures are possible based on the relation of the coordination number. If the net charge of the hydroxyl of each structure is requested, one can use it becomes as Table 1.6.2. It is expected that the higher the amount of the positive charge, the stronger the acidity. The complex oxide, which consists

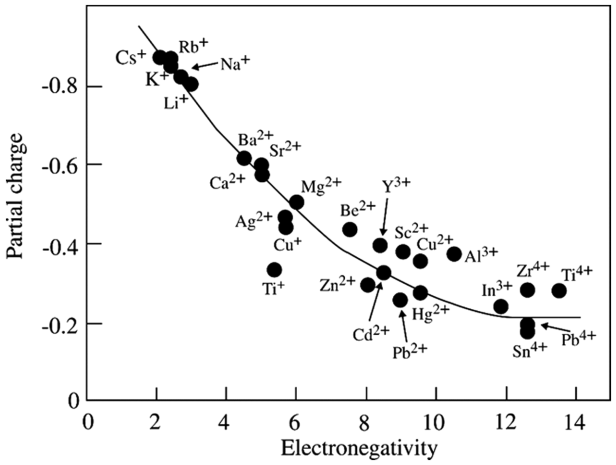


FIGURE 1.6.5 Relationship between partial charge of oxide surface and electronegativity of metal ion.

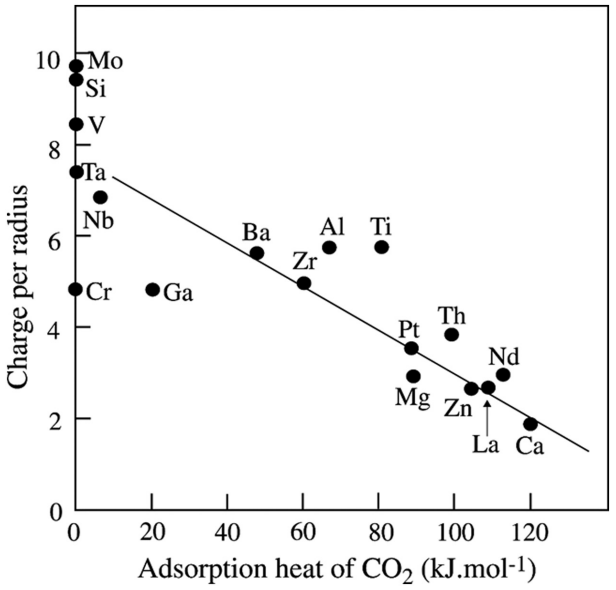


FIGURE 1.6.6 Relationship between adsorption heat of CO_2 and ratio of surface charge and radius of ion.

TABLE 1.6.2 Net Charges of Hydroxl Group on Alumina Surface

H	H	H	H	H
|	|	|	|	|
O	O	O	O	O
|	|	/\	/\	/I\
AI	AI	AI AI	AI AI	AI AI AI
[O]	[T]	[O] [O]	[T] [O]	[O] [O] [O]
–0.5	–0.25	0	+0.25	+0.5

Note: O, octahedral coordination; T, tetrahedral coordination.

TABLE 1.6.3 Isoelectric Point of Various Powders

Material	Isoelectric Point	Material	Isoelectric Point
WO_3	>0.5	γ-Al_2O_3	7.4–8.6
SiO_2	1.8	Y_2O_3	9.0
SiC	3.4	α-Fe_2O_3	9.04
Au	4.3	α-$A1_2O_3$	9.1
$Al(OH)_3$	5.0–5.2	ZnO	9.3
SnO_2	6.6	CuO	9.4
α-FeO(OH)	6.7	BeO	10.2
TiO_2	6.7	La_2O_3	10.4
CeO_2	6.75	ZrO_2	10–11
Cr2O3	7.0	$Ni(OH)_2$	11.1
γ-FeO(OH)	7.4	$Co(OH)_2$	11.4
$Zn(OH)_2$	7.8	MgO	12.4 ± 0.3

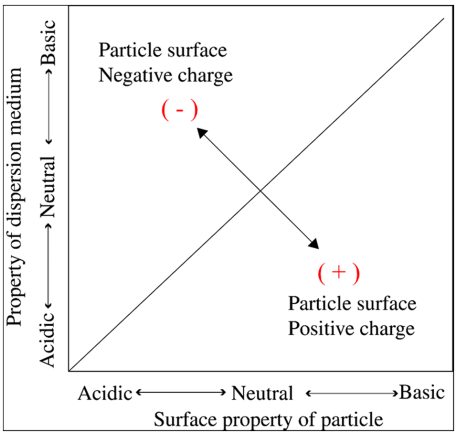


FIGURE 1.6.7 Acidic and basic properties of particle surface in nonaqueous dispersion medium.

of the oxide and contains more than two kinds of metals, occasionally shows an acidity which does not appear in a single oxide. Tanabe et al. reported that the acid appearance of the complex oxide can be explained according to the coordination number and each electric charge of the metal ion and oxygen.[17] Moreover, the acid strength of the complex oxide is found to correlate to the average of the electronegativity of the composition metal ion.[18] Recently, the acid and the base on the surface were also explained by the quantum chemical calculation using the cluster model, by which an oxide part is cut out.[19]

Influence of Surface Acidity and Basicity on Dispersion

The surface hydroxyl group receives the proton or dissociates and positively electrifies the particle surface or negatively in water.

$$M-OH+H^+ + OH^- \rightarrow M-OH^{2+} + OH^- \qquad (1.6.8)$$

$$M-OH+H^+ + OH^- \rightarrow M-O^- + H_2O + H^+ \qquad (1.6.9)$$

The charge of the particulate surface strongly influences the dispersibility of the particle in a liquid. The character of the proton receipt or the dissociation of the hydroxyl depends on the acidity and basicity. Therefore, the difference in the positive and negative charges of the surface and the amount of the charge is caused by the oxide type. The typical oxide isoelectric point is shown in Table 1.6.3.[20] When the oxide powder is dispersed in the medium, it is influenced by dissociation according to which type of the above equation by the character of the H^+ or OH^- acceptor. That is, the state of the interfacial interaction is determined by the relative intensity of an acid, the base character of the powder, and the acid and base characteristics of the medium. The principle of this interfacial phenomenon is shown in Figure 1.6.7. For instance, when the acidity of the powder surface is strong and the medium is basic, the particle gives the medium H^+ and the surface is charged negatively. On the other hand, when the basicity of the particulate surface is strong and the medium is acidic, the particulate surface receives H^+ from the medium, and the surface is charged positively. When acidity and the basicity of the particulate surface and the dispersion medium are the same strength, the particle is not charged.

Enhanced Surface Properties on Particle

Various surface relaxations and the physical adsorption of water occur, and the stabilization of the surface energy is achieved as on an actual solid surface. The surface inhomogeneity may exist as a step, a kink, a defect, or a dislocation, plus the adsorption impurities; therefore, the state of the actual surface is more complex. The exposure ratio of the crystal face and the number of heterogeneity sites on the surface differ and depend on the preparation conditions of the solid. The surface structures on the top and the edge increase when the particle becomes a fine particle. Many of these unsaturated bonds are skillfully used as active sites, as with solid catalysts. The ratio of the surface of the atom to the entire atom that composes the particle increases when the particle of a salt crystal with six coordinations becomes small, as shown in Figure 1.6.8. For instance, when the ratio of particle size to atomic diameter becomes 50 or less, it is understood that the ratio of the surface of the atom rapidly increases. Moreover, when the solid is used as a material, it is necessary to process the solid. With respect to processing factors such as generated heat and chemical reaction, the surface layer of the particle is different from the inside; that is, a processing-altered layer is formed on the surface, and defects and dislocations are generated. On the other hand, it is thought that the amorphous solid of glass, for instance, is solidified without making the supercooled liquid a crystal. Therefore, there is no regular array of atoms, ions, or molecules observed in the crystal. The surface of melted glass is a smooth plane because of the surface tension as well as the liquid. When the cooling solidification is done, the surface smoothness is maintained. Because the mobility of the material is high in the melt, the element by which the surface energy is decreased is concentrated at the surface. Especially, alkaline components easily gather on the

surface. Moreover, because the melt is at a high temperature, it seems that the vaporization of the element and the alteration of the element along with the disappearance, by the reaction with the reactive gas in the atmosphere, have occurred on the surface. As mentioned above, the actual surface is complex. However, with an understanding of the major characteristics it is possible to predict how it will react by carefully considering the generation process of the powder and the matters explained here.

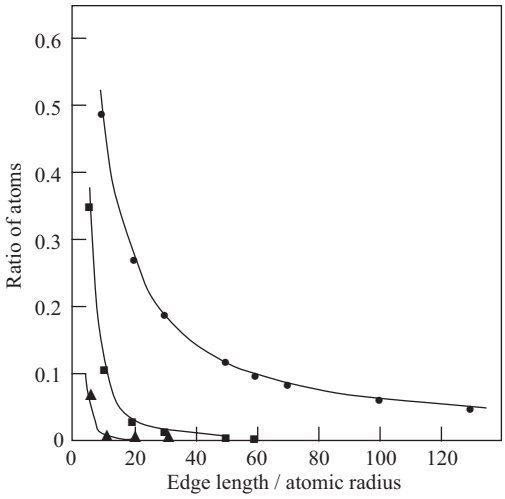


FIGURE 1.6.8 Ratio of edge length of cubic sodium chloride crystal and number of atoms.

1.6.2 SURFACE CHARACTERIZATION

Classification of Surface Characterization

The characterization methods for particulate surfaces are shown in Table 1.6.4. The characterization methods, separate for the dry and the wet processes, are roughly classified; a strict classification is difficult. Many solid surface analyses based on the spectrum can be used to determine composition and chemical conditions. The methods as shown in Table 1.6.4 are a part of all measurements. For a powder sample, various physical properties are generally measured as the powder sample undergoes compression molding as a disk. When the powder sample is measured using these methods, it is necessary to note the relative size difference between the particle size and the equipment, such as the beam diameter of the probe, penetration depth of the probe, escape depth of the response signal, and diffusion effects of the response signal. It cannot be judged whether the information is for the powder surface or the entire powder. Moreover, the surface roughness of the powder sample that undergoes compression molding influences the detection efficiency. The level of qualitative measurement is generally appropriate to this method. It is easy for the composition analysis in the wet process to analyze the chemical composition of the entire particle. On the other hand, various instruments are necessary, as only the surface is dissolved to determine information on the surface. However, this method has enough ability to qualitatively analyze the ion, which undergoes segregation to the particulate surface. The analysis of surface functional groups, surface acidity and basicity, wettability, and roughness and porosity, and their measurements are described below.

TABLE 1.6.4 Classification of Particle Surface Analysis

	For Dry Powder and/or Dry Process	For Wet Powder and/or Wet Process
Composition, chemical condition	Magic angle spinning nuclear magnetic resonance: MAS-NMR X-ray fluorescence: XRF X-ray photoelectron spectroscopy: XPS Secondary ion mass spectrometry: SIMS Electron spin resonance: ESR	Inductively couple plasma: ICP Atomic absorption spectrometry: AAS
Functional groups	Chemical reaction method Infrared spectroscopy: IR Thermogravimetric and differential thermal analysis: TG/DTA	Chemical reaction method Zeta potential measurement
Acidity and basicity	Gas adsorption, adsorption heat: IR Temperature-programmed desorption: TPD Thermal desorption spectroscopy: TDS	Adsorption (CV, titration etc.) ultraviolet and visible spectrophotometry: UV Titration Heat of immersion
Wettability	Contact angle measurement by direct observation of droplet, wet velocity, or AFM, gas adsorption, heat of adsorption Inverted gas chromatography	Heat of immersion, Preferential dispersion test Hansen solubility parameter: HSP
Roughness and porosity	Gas adsorption Scanning electron microscope: SEM Transmission electron microscope: TEM Atomic force microscope: AFM X-ray Computerized tomography: X-CT	Adsorption AFM Magnetic resonance imaging: MRI

Surface Functional Groups

The analysis method of a surface functional group is chiefly accomplished with a method based on a chemical reaction, spectroscopy methods such as infrared (IR) and nuclear magnetic resonance (NMR) spectroscopy, and methods that combine both approaches. Here, the measurement method of the surface hydroxyl group is explained. A similar method can be applied for other functional groups. The ignition loss method, Grignard reagent method,[21] alkyl silane reagent method,[22–24] and so forth, are chemical reaction methods for surface hydroxyl group determination. The D_2O displacement method, which uses IR spectroscopy, is a kind of chemical reaction method.[25,26] The chemical reaction method and the analysis methods that use IR spectroscopy are discussed below.

The basis of the ignition loss method for an oxide powder is a chemical reaction due to dehydration between the surface hydroxyl groups by heating. The chemical reactions for silica are as follows:

$$\equiv Si-OH + HO-Si \equiv \rightarrow \equiv Si-O-Si \equiv + H_2O \qquad (1.6.10)$$

Therefore, if the water molecule generated along with heating is measured by a suitable method, the amount of the hydroxyl can be estimated. The weight change according to heating or the water capacity generated along with heating is then measured. In the method of applying gas chromatography, the generated water is measured with a thermal conductivity detector. It is possible to measure not only the hydroxyl, which exists in the powder surface, but also the water, which exists inside the particle, and this method is very simple and easy.[16]

It explains the characterization of the surface hydroxyl group on the oxide that uses the chemical reaction method. The chemical reaction method is classified based on the name of the molecule used for the evaluation, such as the Grignard reagent method and the silane method. The Grignard reagent method measures CH_4 generated by the reaction shown in Equation (1.6.11).

$$\equiv Si-OH + CH_3MgI \rightarrow \equiv Si-O-MgI + CH_4 \qquad (1.6.11)$$

The reagents that can be used for the chemical reaction method are shown in Table 1.6.5.

The surface hydroxyl group gives clear IR spectroscopy results. Therefore, IR spectroscopy analysis is an extremely effective evaluation method of the surface hydroxyl group to

TABLE 1.6.5 Reagents Used for Determination of Surface Hydroxyls

Reagent	Molecular Formula	Detected Molecule
Diazomethane	CH_2N_2	N_2
Lithium aluminium hydride	$LiAlH_4$	H_2
Trimethylchlorosilane	CH_3ClSi	HCl

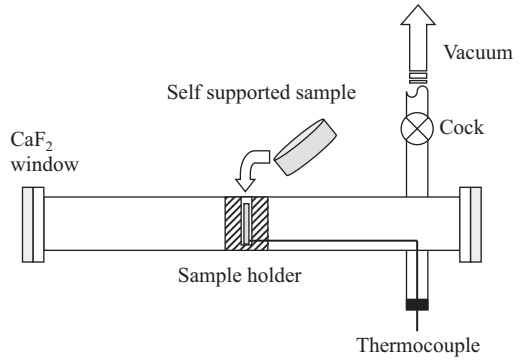


FIGURE 1.6.9 An optical cell of *in situ* measurement for IR spectra.

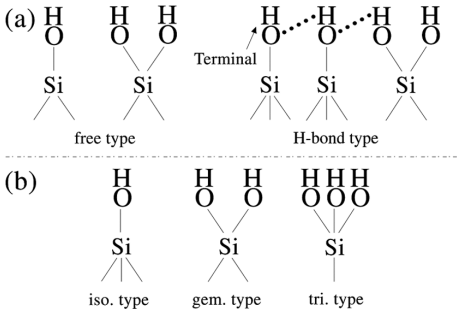


FIGURE 1.6.10 Classification of surface silanol (a) according to chemical state, (b) according to chemical structure.

observe the O–H stretching vibration (3000 to 3800 cm^{-1}). The O–H stretching vibration of the physisorbed water exists in this wave-number region. Therefore, a cell that can do the degassing operation and the heating operation in the system, as shown in Figure 1.6.9, is used.[27,28] The type of surface hydroxyl group that can be identified by IR analysis, as shown in Figure 1.6.10A, is the H-bonded hydroxyl, which forms the hydrogen bond and the free-type hydroxyl, which does not form the hydrogen bond. There is much research about surface hydroxyl groups. It is believed that three types of hydroxyls with different chemical structures, as shown in Figure 1.6.10B, exist on the surface of SiO_2.[29] The iso-type hydroxyl and the gem-type hydroxyl have a narrow absorption at about 3750 cm^{-1}. It is difficult to distinguish them by IR spectroscopy.[30,31] These can be distinguished using ^{29}Si solid-state NMR spectroscopy.[32–34] Reports concerning the existence of the tri-type hydroxyl are very few.[35,36] As for the H-bonded hydroxyl, a wide peak, which centers on about 3600 cm^{-1}, has been observed. In addition, the H-bonded hydroxyl marked by the arrow in Figure 1.6.10A is called the terminal hydroxyl and has an absorption at about 3720 cm^{-1}.[37] The wave number of the OH stretching vibration changes when the kind of atom that bonds the hydroxyls changes. The relation between the electronegativity of the atom that unites the hydroxyls and the OH stretching vibration is shown in Figure 1.6.11.[38] In addition, two or more infrared absorption spectra appear when the oxygen coordination number is different, even if the chemical composition is the same. Figure 1.6.12 shows the structure and

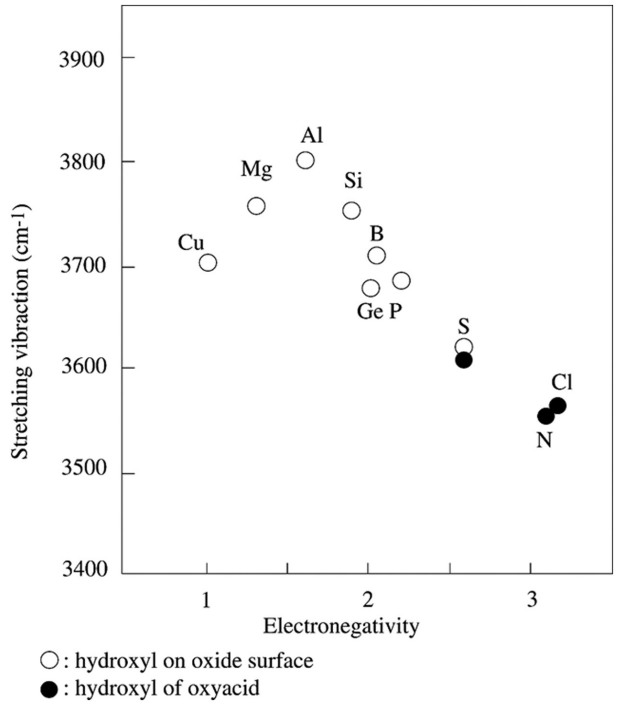


FIGURE 1.6.11 Relation between electronegativity of atom with hydroxyl and stretching vibration of free hydroxyl.

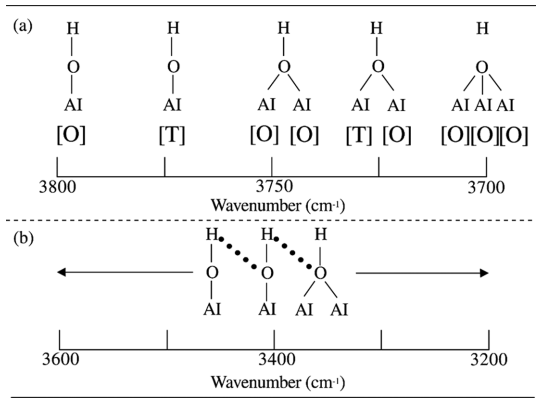


FIGURE 1.6.12 Structures and stretching frequencies of hydroxyl observed in alumina surface: (a) free hydroxyl, (b) hydrogen-bonded hydroxyl. O, octahedral coordination; T, tetrahedral coordination.

absorption spectrum of the surface hydroxyl group observed on the surface of Al_2O_3.[39,40] Moreover, the dehydration behavior caused by heating of the surface hydroxyl group differs depending not only on the oxide type but also on the preparation method and the hysteresis of the sample.

IR spectroscopy is used to measure the strength of the adsorption site and to identify the adsorption site. The history of the research on the observations of the adsorbed molecular state, which uses the infrared spectroscopy and interaction with the surface, is long. Especially, many of the interactions of the surface hydroxyl group and the adsorbed molecule have been determined for the oxide.[41] Kiseleve et al.[42] found the relationship between the heat of formation of the hydrogen bond between the organic molecule and the hydroxyl, and wave number shifts of the O–H stretching vibration by adsorption from the heat of adsorption measurement of the organic molecule and the IR spectroscopy measurement for silica. These results are shown in Figure 1.6.13. Because the solvent molecule, in addition to the adsorbed molecule, exists in the liquid-phase adsorption, this adsorption behavior is more complex than gas-phase adsorption. However, the interaction between the surface hydroxyl group and the adsorbed molecule can be examined by IR spectroscopy and calorimetry, as well as by gas-phase adsorption.[43,44]

The cleavage reaction of (M–O–M) on the oxide surface in addition to the reaction of the surface hydroxyl group is an important characteristic of the powder surface. Because the reactiveness to water is the same as the mechanism of surface hydroxyl group generation, it is considered an index of the chemical stability of the water molecule on the surface. Moreover, some reactivities with other molecules have been reported. Morrow et al.[45] observed the dissociation of NH_3 to the siloxane linkage (≡Si–O–Si≡) and adsorption from the change in the IR absorption spectrum of the NH_3 adsorption on silica gel. Bunker et al.[46] found the structure of reactivity siloxane that tetrahedron SiO_4 share the edge from the analysis of the IR absorption spectrum. SiO_2 is a coupled structure of the SiO_4 tetrahedron. The ring structure with three types of distortion shown in Figure 1.6.14 is reported in IR spectroscopy[47] and Raman spectroscopy.[48] Especially important, the structure that the SiO_4 tetrahedron shares the edge and the D2 structure has a big distortion. Therefore, it is confirmed that various molecules easily have a dissociation adsorption on the surface with these structures.[49–51] The wave number corresponding to these structures and the calculation value of the strain energy are shown in Table 1.6.6.[52] It is expected that the amount of siloxane of such reactiveness differs according to the production method and the hysteresis of the silica.

Surface Acidity and Basicity

The strength of the acid–base of the solid surface applies to the definition of the H_0 function and H_- function, which shows the strength of the acidity/basicity of a uniform solvent. That is, the acid strength of the solid surface is defined by H_0, and the base strength is defined by H_-. For instance, when indicator B of basicity is adsorbed on the acid site of the solid surface, a part of the indicator is made a proton with the acid site. The strength H_0 of these acid sites is shown in Equation (1.6.12) by the value of pK_{BH+} of BH^+. which is the conjugate acid of indicator B when the concentration C_{BH+} of indicator BH^+ made a proton is equal to the concentration C_B of indicator B not made a proton.

$$H_0 = pK_{BH+} - \log\left(C_{BH+}/C_B\right) \tag{1.6.12}$$

Therefore, the acid strength indicated by the H_0 value shows the ability to change into the conjugate acid by the acid sites which give the protons half of the base indicator B of the neutral which the acid site on the surface adsorbs. In Lewis's

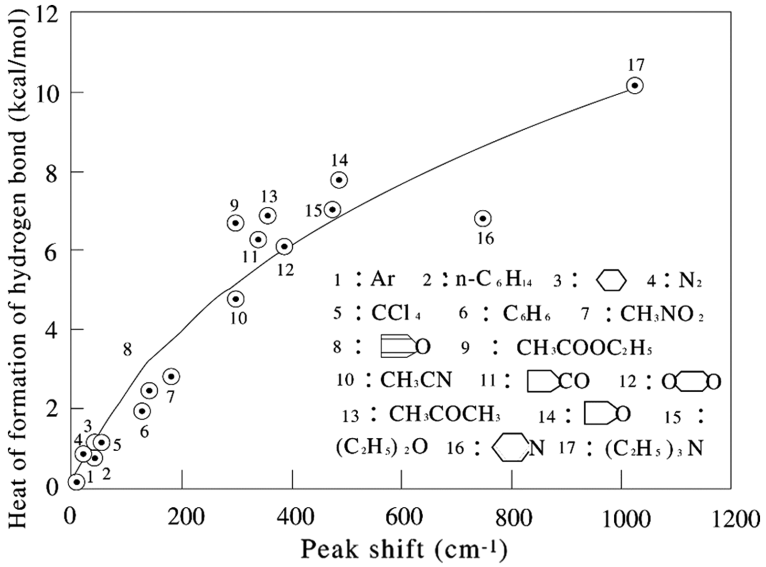


FIGURE 1.6.13 Relation between binding formation heat of various molecules and silanols and peak shift values of surface hydroxyl by adsorption.

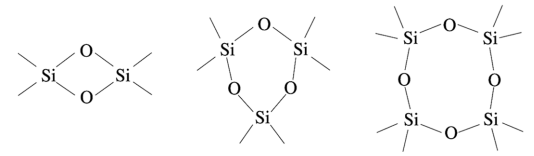
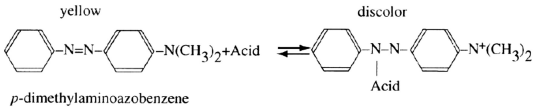


FIGURE 1.6.14 Distortion ring structures into silica.

TABLE 1.6.6 Infrared and Raman Absorption and Strain Energy of the Structure of [SiO_4] in Silica

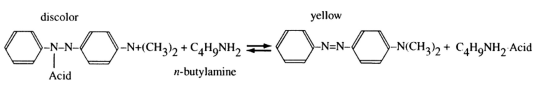
Ring Structure	Absorption Spectrum	Spectroscopy	Strain Energy
4-membered	888/908 cm^{-1}	Infrared	58 kJ/mol (Si–O)
6-membered	605 cm^{-1} (D_2)	Raman	17 kJ/mol (Si–O)
8-membered	490 cm^{-1} (D_1)	Raman	—

definition, the H_0 value shows the ability that the electron pair can be received from half of the adsorbed base indicator B. The investigation of base strength is similar to the investigation of acid strength. When indicator BH, which defines base strength, adsorbs on the solid surface, H^+ is pulled out by the basic site, and a part of indicator BH becomes the state of B^-. The strength H_- of the basic site is shown by the pK_{BH} value of indicator BH when concentration C_{B-} of B^- is equal to the concentration C_{BH} of BH from which H^+ is not pulled out. However, because the measurement of the ratio of the concentration (C_{BH+}/C_B) and (C_{BH}/C_{B-}) of the indicator on the solid surface is difficult, the following techniques are actually used. Because it is possible to apply it to both the acid and the base, the evaluation method of the acid site is described here. Many indicators of basicity in which the charge neutrality becomes a conjugate acid by receiving H^+ are known as Hammett indicators. Here, each pK_a value of these conjugate acids is assumed to be b, c, d, and e ($b < c < d < e$). The indicator $pK_a = b$ is also assumed not to be changed by the acid structure at the acid site, nor is the indicator $pK_a = c$ assumed to have been changed by the acid structure. At this time, it is understood that the acid strength H_0 value of the surface acid site is between b and c. The indicator causes a discoloration, and the change occurs in the UV spectra when the indicator is changed into the acid structure by the solid acid site. Therefore, the strength and the amount of the acid site are measurable by using these phenomena. An example of the determination of the acid site by the discoloration of the indicator is shown as follows. *p*-dimethylaminoazobenzene (yellow), which is the indicator, is adsorbed on the solid acid site and becomes red with the following acid structures:



(1.6.13)

n-butylamine, which is a stronger basicity molecule than the indicator, is dropped by the following procedure. Then, *n*-butylamine causes the exchange adsorption as the indicator of the acid structure which has been adsorbed according to the next equation, and the indicator returns to the former yellow color.



(1.6.14)

TABLE 1.6.7 Indicators Used for Acid Strength Measurements

Indicator	Basic Color	Acid Color	pK_{3H+}	H_2SO_4 wt. %
Neutral red	Colorless	Red	+6.8	8×10^{-8}
Methyl red	Yellow	Red	+4.8	—
Phenylazonaphthylamine	Yellow	Red	+4.0	5×10^{-5}
p-Dimethlaminoazobenzene	Yellow	Red	+3.3	3×10^{-4}
2-Amino-5-azotoluene	Yellow	Red	+2.0	0.005
Benzeneazodiphenylamine	Yellow	Purple	+1.5	0.02
4-Dimethylaminoazo-1-naphthalene	Yellow	Red	+1.2	0.03
Crystal violet	Blue	Purple	+0.8	0.1
p-Nitrobenzeneazo-(*p*′-nitro)-diphenylamine	Yellow	Purple	+0.43	—
Dicinnamalacetone	Yellow	Red	–3.0	48
Benzalacetophenone	Colorless	Yellow	–5.6	71
Anthraquinone	Colorless	Yellow	–8.2	90
p–Nitrotoluene	290 μm	350 μm	–10.5	99.9
2,4-Dinitrotoluene	255 μm	320 μm	–12.8	106

TABLE 1.6.8 Indicators Used for Base Strength Measurements

Indicator	Acid Color	Basic Color	pK_{BH}
Bromothymol blue	Yellow	Blue	7.2
Phenolphthalein	Colorless	Pink	9.3
2,4,6-Trinitroaniline	Yellow	Tango	12.2
2,4-Dinitroaniline	Yellow	Purple	15.0
4-Chloro-2-nitroaniline	Yellow	Orange	17.2
4-Nitroaniline	Yellow	Orange	18.4
4-Chloroaniline	Colorless	Pink	26.5

Acid strength is understood from the difference in the base strength of the indicator used. Moreover, the amount of the acid site can be obtained according to the amount of *n*-butylamine necessary to erase the color of the acid structure. The reacted indicator is made the acid structure, and discolor, even if the acid sites are a Brønsted acid site or a Lewis acid site. It is possible to do the same for the evaluation of basicity. Indicators to examine acidity and basicity are shown in Tables 1.6.7 and 1.6.8, respectively.[53]

In this procedure, it is necessary to leave it for a long time at the time of each *n*-butylamine dropping to achieve an adsorption equilibrium and confirm that the color of the acid structure disappears. Therefore, a long time is required for the measurement. The Benesi method in which this fault is improved is widely used. In the Benesi method, many sample solutions, which have different dosages of *n*-butylamine, are prepared. After the sorption equilibrium isotherm of *n*-butylamine, various indicators are added for each sample. The discoloration of these indicators to the acid structure is examined, and the acid strength distribution is measured. The intensity distribution of the basic site in the solid surface is obtained by the same principle. That is, one only has to use an acid molecule such as benzoic acid as a titration reagent instead of *n*-butylamine, and the indicator for the H^- measurement is used.

Adsorption of the basic gaseous molecule is caused on the acid site, and the absorbed amount corresponds to the acidity. The adsorptive interaction of the basicity molecule that adsorbs on a strong acid site is strong, and desorption is difficult at low temperature. Therefore, the desorption temperature of the adsorbed base molecule is closely related to the strength of the acid site. Several measurement examples are given as follows. The base molecules that adsorb onto the surface, and then the physisorbed and hydrogen-bonded molecules are removed at a suitable temperature when basicity gases such as ammonia, pyridine, and alkylamines are used. The amount of the base molecules, which chemically adsorb on the acid site, is measured as follows. The temperature gradually rises while removing the desorption gas, and the amount of chemisorption at each temperature is measured; or the temperature continuously rises while removing the desorption gas, and the intensity distribution of the acid site is obtained as the desorption spectrum of the base molecule. The amount of the desorption base as the amount of chemisorptions is measured by the weight method with a balance or by gas chromatography. That is, the kind of site where the adsorption activity is different is distinguished from the number of desorption peaks in the temperature-programmed desorption method. Moreover, the chemical bonding state and strength of the acid site are obtained from the difference in the desorption temperature, and the amount of the acid site is obtained from the amount of each desorption.

The activation energy of desorption assumes it is almost equal to the heat of adsorption, and it is used as an index of the strength of the acid. The next equation, for the temperature-programmed desorption method, shows a relation between the programming rate (V_t) and desorption peak temperature (T_m), by which the maximum elimination kinetics is given when the gas, in which the strength of the acid site is uniform, and when detached is not adsorbed again.

$$2\log T_m - \log V_t = E_d / (2.303RT_m) + \log(E_d / AR) \quad (1.6.15)$$

A is a frequency factor, E_d is the activation energy, and R is the gas constant. The sample with the same absorbed amount of the base probe molecule is prepared, the programming rate is changed, and the desorption peak temperature T_m corresponding to the changes is obtained. The activation energy, E_d, is obtained from the slope of the straight line of the plot of $2\log T_m - \log V_t$ to $1/T_m$. As for the features of the gas absorption method, the solvent has no influence, and the surface acidity at various temperatures can be measured. Moreover, as another advantage, the amount of the initial adsorption can be easily controlled, and a catalytic reaction mechanism and

kinetics data might be able to be comparatively facilitated. On the other hand, strong physisorption and chemisorption on powder surfaces cannot be distinguished, which is a disadvantage. In addition, because the diffusion process of the gas cannot be disregarded and re-adsorption of desorption gas occurs, obtaining an accurate kinetic parameter might be difficult. Moreover, when the amount of the acid site is measured using ammonia and *n*-butylamine is considered, as the adsorption mechanism to the acid site is the same, the amount obtained with ammonia might be large. It is considered that the pore distribution and the distance between acid sites are closely related to this difference.

The evaluation of the acid–base site where IR spectroscopy was used is subsequently introduced. The amounts of the Brønsted acid site and the Lewis acid site are measured from the strength of IR spectroscopy of the chemically adsorbed base molecules. The IR absorption spectrum of pyridine, which adsorbs on the Brønsted acid site and the Lewis acid site, is shown in Figure 1.6.15.[54] The infrared absorption spectrum in the 1400 to 1700 cm^{-1} region is derived from the in-plane vibration of the pyridine ring. The wave number is remarkably different according to whether the adsorbed pyridine forms a hydrogen bond, a coordinate bond, or an ionic bond. The infrared absorption spectrum features of the adsorbed pyridine are shown in Table 1.6.9. Moreover, the acid site type can be identified according to the IR absorption spectrum of the adsorption ammonia. The reason for this is that the IR absorption of the deformation vibration of H–N–H changes depending on the kind of adsorption site. As for the ammonium ion (NH^{4+}) and ammonia, which formed

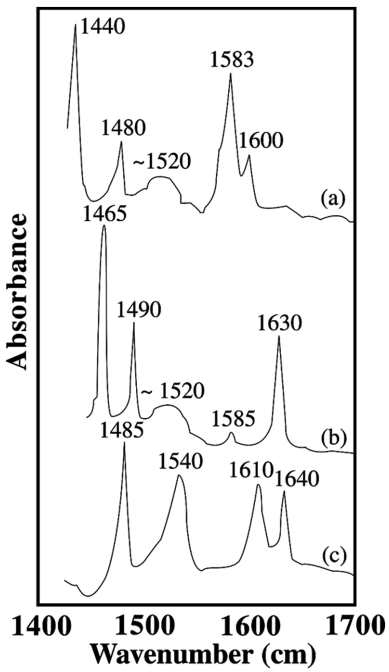


FIGURE 1.6.15 Infrared absorption spectrum of pyridine: (a) CCl_4 solution of pyridine, (b) CCl_4 solution of pyridine: BH_3, (c) chloroform solution of (pyridine:H)+Cl^-. The absorption band at 1520 is wide and is an absorption peak of the CCl_4 solvent.

TABLE 1.6.9 IR Absorption Band Assigned Pyridine Molecules Adsorbed on Acidic Surface

Hydrogen Bonded	Coordinately Bonded	Ionically Bonded
1400–1447 (VS)	1470–1465 (VS)	
1480–1490 (W)	1471–1503 (W-S)	1478–1500(VS)
	1525–1542 (S)	1562–1580 (W)
1580–1600(S)	1592–1633 (S)	1600–1620 (S)
		1634–1640 (S)

Note: Absorbance strength: VS, very strong; S, strong; W, weak.

the coordinate bond, absorption appears at about 1400 cm^{-1} and at about 1620 cm^{-1}, respectively. The former is a Brønsted acid site, and the latter is a Lewis acid site.[55,56]

There is a method of measuring the thermal transformation when the probe molecule directly adsorbs on the acid–base site. Because a suitable basic or acidic molecule can be used, the adsorbate and the temperature of the heat of adsorption measurement can be arbitrarily selected according to the calorimeter; acid strength can be obtained under various conditions. For the heat of adsorption measurement, a suitable amount of sample is first placed in the cell, and the heating exhaust processing is done under optimum conditions. The sample is placed in the calorimeter with the heating exhaust processing done. The adsorbate is introduced after it reaches the thermal equilibrium state and the generated heat of adsorption is measured. The absorbed amount is obtained at the same time. In general, because the change in the heat of adsorption is large in the region where the absorbed amount is low, a little probe gas is introduced. The heat of adsorption is converted into the amount of 1 mol adsorbate, and a graph of absorbed amount (V) versus heat of adsorption (q) is obtained. If $\Delta V/\Delta q$ is obtained from the graph based on the V–q curve, and $\Delta V/\Delta q$ is plotted for q, the intensity distribution curve of the acid–base is obtained.

Wettability

For the large particle shown in Figure 1.6.16, the contact angle can be directly measured with a microscope.[57] Moreover, the contact angle is directly obtained by attaching the particle to the AFM probe for the single particle micron scale.[58] However, it is difficult to directly measure the contact angle in a general powder. It assumes as follows, and the contact angle is calculated. It is considered that a minute space in the packed bed of the powder shown in Figure 1.6.17 is formed with the capillary having a uniform cylindrical shape. The contact angle can be measured according to the velocity of the liquid as it infiltrates into this capillary. The following equation holds when the radius of the cylindrical capillary in the powder-packed bed is assumed to be r.

$$\frac{dx}{dt} = \frac{ry\cos\theta}{4\eta x} - \frac{r^2\rho g}{8\eta} \tag{1.6.16}$$

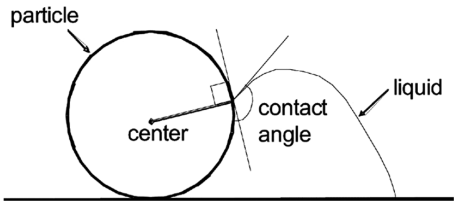


FIGURE 1.6.16 Contact angle measurement for large particle.

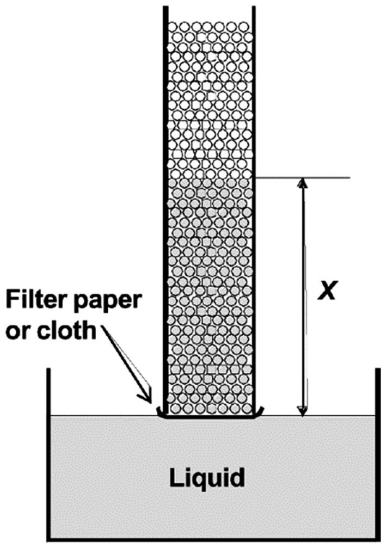


FIGURE 1.6.17 Contact angle estimated from wet velocity of powder bed.

Here

- x is the height to which the capillary rises,
- t is the time,
- γ is the liquid surface tension,
- η is the viscosity of the liquid,
- ρ is the density,
- g is gravitational acceleration,
- θ is the contact angle.

The first term on the right in Equation (1.6.16) is the contribution of the capillary force. The second term is the contribution of gravity. When the second term can be neglected, the following equation is obtained by integrating Equation (1.6.16).

$$x^2 = \frac{r\gamma \cos\theta}{2\eta} t \qquad (1.6.17)$$

Therefore, the capillary radius r in the powder-packed bed is obtained from the straight line relation between x^2 and t beforehand by using the liquid which has contact angle $\theta = 0$ where the powder is wet. The contact angle θ is then obtained by measuring the relation between x^2 and t for the powder with a target liquid. Moreover, the wettability evaluation of the powder is determined from the preference dispersing test of the powder in various liquids or mixed solvents. Additionally, the wettability can be judged according to the analysis of the adsorption isotherm, heat of adsorption, and heat of immersion.[59]

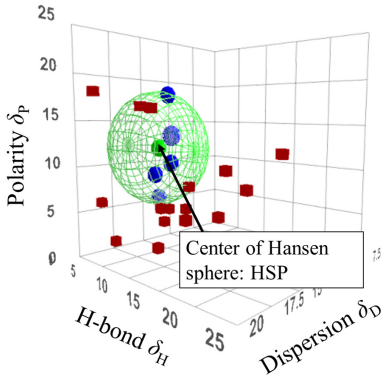


FIGURE 1.6.18 Hansen sphere drawn including high dispersibility excluding low dispersibility solvents. Center of the Hansen sphere is defined as HSP. ●: high dispersibility solvents, ■: low dispersibility solvents.

Hansen solubility parameter (HSP), δ, was proposed by Hansen[60] to predict solubility among polymers, organic solvents, additives, etc. which are divided into three parameters: dispersion (δ_d), polarity (δ_p), hydrogen bonding (δ_h). Given this theory to expand to particles, it is possible to predict particle wettability. Briefly, dispersibility of suspensions where test particles were dispersed in HSP-known solvents are judged as high or low by kind of dispersion test such as sedimentation test.[61–65] The HSP of the used solvents are shown on δ_d-δ_p-δ_h three-dimensional coordinate system. A similar way to predict solubility, a Hansen sphere is drawn including high dispersibility solvents excluding low dispersibility solvents as shown in Figure 1.6.18. To draw a Hansen sphere, commercial software (HSPiP) is applicable.[66] The center of the sphere is HSP value of particles.

REFERENCES

1. Kubo, R., *Phys. Lett.*, 1, 49–50, 1962.
2. Chikazawa, M., Takei, T., *Gypsum Lime*, 228, 255–267, 1990.
3. Benson, G. C., Claxton, T. A., *J. Chem. Phys.*, 48, 1356–1364, 1968.
4. Nakamatsu, H., Sudo, A., Kawai, S., *Surf. Sci.*, 194, 265–271, 1988.
5. Taroni, A., Haneman, D., *Surf. Sci.*, 10, 215–221, 1968.
6. Schlier, R. E., Farnsword, H. E., *J. Chem. Phys.*, 30, 917–925, 1959.
7. Pandey, K. C., *Phys. Rev. Lett.*, 49, 223–229, 1982.
8. Morimoto, T., Nagao, M., Tokuda, F., *Bull. Chem. Soc. Jpn.*, 41, 1533–1539, 1968.
9. Morimoto, T., Naono, H., *Bull. Chem. Soc. Jpn.*, 46, 2000–2006, 1973.
10. Naono, H., Kodama, T., Morimoto, T., *Bull. Chem. Soc. Jpn.*, 48, 1123–1129, 1975.
11. Zhuravlve, L. T., *Langmuir*, 3, 316–322, 1987.
12. Chikazawa, M., Kanazawa, T., *J. Soc. Powder Technol. Jpn.*, 14, 18–25, 1977.
13. Harnb, N., Hawkins, A. E., Opalinski, I., *Trans. IchemE*, 74, 605–626, 1996.

14. Chikazawa, M., Kanazawa, T., Yamaguchi, T., *KONA (Powder Particle)*, 2, 54–61, 1984.
15. Ozaki, A., *Shokubai-kougaku-kouza 10*, Chijinsyoten, Tokyo, 1972, p. 778.
16. Auroux, A., Gervasini, A., *J. Phys. Chem.*, 94, 6371–6376, 1990.
17. Tanabe, T., Sumiyoshi, T., Shibata, K., Kiyoura, T., et al., *Bull. Chem. Soc. Jpn.*, 47, 1064–1070, 1974.
18. Shibata, K., Kiyoura, T., Kitagawa, J., Sumiyoshi, T., et al., *Bull. Chem. Soc. Jpn.*, 46, 2985–2991, 1973.
19. Yoshida, S., Kawakami, H., *Hyomen*, 21, 737–743, 1983.
20. Yoon, R. H., Salman, T., Donnay, G., *J. Colloid Interface Sci.*, 70, 483–489, 1979.
21. Fripiat, J. J., Uytterhoeven, J., *J. Phys. Chem.*, 66, 800–806, 1962.
22. Kanazawa, T., Chikazawa, M., Takei, T., Mukasa, K., *J. Ceram. Soc. Jpn.*, 92, 11, 654–660, 1984.
23. Hair, M. L., Hertl, W., *J. Phys. Chem.*, 73, 2372–2378, 1969.
24. Van Der Voort, P., Gillis-D'hamers, I., Vansant, E. F., *J. Chem. Soc. Faraday Trans.*, 86, 3751–3757, 1990.
25. Madeley, J. D., Richmond, R. C., Anorg, Z., *Allg. Chem.*, 389, 92–98, 1972.
26. Davydov, V. Ya., Kiserev, A. V., Kiserev, S. A., Polotnyuk, V. O. V., *J. Colloid Interface Sci.*, 74, 378–386, 1980.
27. Yates, Jr., J. T., Madey, T. E., *Vibrational Spectroscopy of Molecules on Surfaces*. Plenum, New York, 1987, p. 116.
28. Kondo, J., Domen, K., *Shokubai (Catalysts Catalysis)*, 32, 206–212, 1990.
29. Iler, R. K., *The Chemistry of Silica*, John Wiley & Sons, New York, 1979, p. 622.
30. Hoffmann, P., Knozinger, E., *Surf. Sci.*, 188, 181–187, 1987.
31. Ferrari, A. M., Ugliengo, P., Garrone, E., *J. Phys. Chem.*, 97, 2671–2677, 1993.
32. Sindrof, D. W., Maciel, G. E., *J. Am. Chem. Soc.*, 105, 1487–1493, 1983.
33. Leonardelli, S., Facchini, L., Fretigny, C., Tougne, P., et al., *J. Am. Chem. Soc.*, 114, 6412–6418, 1992.
34. Hayashi, S., *J. Soc. Powder Technol. Jpn.*, 32, 573–579, 1995.
35. Takei, T., *J. Jpn. Soc. Colour Mater.*, 69, 623–631, 1996.
36. Hauuka, S., Root, A., *Langmuir*, 98, 1695–1701, 1994.
37. Morrow, B. A., Cody, I. A., Lee, L. S. M., *J. Phys. Chem.*, 80, 2761–2767, 1976.
38. Smirnov, E. P., Tsyganenko, A. A., *React. Kinet. Catal. Lett.*, 7, 425–431, 1977.
39. Knozinger, H., Ratnasamy, P., *Catal. Rev. Sci. Eng.*, 17, 31–37, 1978.
40. Ballinger, T. H., Yates, Jr., J. T., *Langmuir*, 7, 3041–3047, 1991.
41. Little, L. H., in *Infrared Spectra of Adsorbed Species*, Kagaku-doujin, Kyoto, 1971, pp. 246–308.
42. Curthoys, G., Davydov, V. Y., Kiselev, A. V., Kiselev, S. A., *J. Colloid Interface Sci.*, 48, 58–64, 1974.
43. Korn, M., Killmann, E., Eisenlauer, J., *J. Colloid Interface Sci.*, 76, 7–13,1980.
44. Zhao, Z., Zhang, L., Lin, Y., *J. Colloid Interface Sci.*, 166, 23–29, 1994.
45. Morrow, B. A., Cody, I. A., *J. Phys. Chem.*, 80, 1998–2004, 1976.
46. Bunker, B. C., Haaland, D. M., Ward, K. J., Michalske, T. A., et al., *Surf. Sci.*, 210, 406–421, 1989.
47. Chiang, C., Zegarski, B. R., Dubois, L. H., *J. Phys. Chem.*, 97, 6948–6956, 1993.
48. Krol, D. M., van Lierop, J. G., *J. Non-Cryst. Solids*, 63, 131–137, 1984.
49. Bunker, B. C., Haaland, D. M., Michalske, T. A., Smith, W. L., *Surf. Sci.*, 222, 95–101, 1989.
50. Grabbe, A., Michalske, T. A., Smith, W. L., *J. Phys. Chem.*, 99, 4648–4656, 1995.
51. Wallance, S., West, J. K., Hench, L. L., *J. Non-Cryst. Solids*, 152, 101–107, 1993.
52. O'Keeffe, M., Gibbs, G. V., *J. Chem. Phys.*, 81, 876–884, 1984.
53. Chikazawa, M., Fuji, M., *J. Powder Soc., Japan*, 33, 427, 1996.
54. Little, L. H., in *Infrared Spectra of Adsorbed Species*, Kagaku-doujin, Kyoto, 1971, pp. 202–203.
55. Mapes, J. E., Eischens, R. P., *J. Phys. Chem.*, 58, 809–815, 1954.
56. Pliskin, W. A., Eischens, R. P., *J. Phys. Chem.*, 59, 1156–1162, 1955.
57. Fuji, M., Fujimori, H., Takei, T., Watanabe, T., et al., *J. Phys. Chem. B*, 102, 10498–10504, 1998.
58. Preuss, M., Butt, H.-J., *J. Colloid Interface Sci.*, 208, 468–477, 1998.
59. Fuji, M., Takei, T., Watanabe, T., Chikazawa, M., *Colloid Surf. A*, 154, 13–24, 1999.
60. Hansen, C. M., *Hansen Solubility Parameters - A User's Handbook*, CRC Press, Boca Raton, FL, 2000.
61. Nakamura, D., Shigetoh, K, Suzumura, A., *J. Eur. Ceram. Soc.*, 37, 1175–1185, 2017
62. Nakamura, D., Hirano, M., Ohta, R., *Chem. Commun.*, 53, 4096, 2017.
63. Sobisch, T., Lerche, D., *Colloid Polym. Sci.*, 278, 369–374, 2000.
64. Sobisch, T., Lerche, D., *Powder Technol.*, 174, 46–49, 2007.
65. Nishimura, N., Takeda, S., Teranishi, T., Hayashi, H., et al., *Mater. Trans.*, 56, 12, 2006–2009, 2015.
66. https://www.hansen-solubility.com/

1.7 Characterization by Atomic Force Microscope

Naoyuki Ishida and Vincent S. J. Craig

Rapid developments in nanotechnology have led many industrial processes to handle nanosized materials including nanoparticles in order to take advantage of their specific functions. When handling nanoscale materials, it is of utmost importance to characterize them with molecular scale resolution with regards to geometry and surface properties in order to control the quality of products produced.

The development of a series of scanning probe microscopes (SPM) instigated by the invention of the scanning tunneling microscope (STM) in 1982 is regarded as a cornerstone of progress in nanoscience and nanotechnology. The appearance of STM provided unprecedented access to single atoms on surfaces of conducting and semiconducting materials. The atomic force microscopy (AFM), invented as an adaptation of SPM by Binning et al. in 1986[1], extended atomic level imaging to non-conducting surfaces by introducing the optical lever method and combining it with stylus probes and feedback control incorporated from the STM.

Since its invention, AFM has become a powerful tool in a wide range of research areas in science and engineering including powder technology as a technique to explore surface structures and properties. The widespread adoption of AFM can be attributed to particular advantages of the AFM; firstly the AFM can be operated in various environmental conditions, including liquids and gases, without vacuum, secondly the AFM enables *in situ* measurements, and thirdly with AFM surface observations and interaction force measurements with high-resolution are relatively easy to obtain. In addition to surface imaging, AFM can be employed to measure interaction forces between surfaces, which are critical in many applications of powder technology. In this chapter, we provide an overview of the principles of AFM and the rapid advances in AFM applications for surface characterization and force measurements.

1.7.1 PRINCIPLE OF AFM

The basic composition of an AFM instrument is illustrated in Figure 1.7.1. The main elements which compose an AFM system include; the probe, laser, photodetector, piezoelectric scanner, and controller. The probe has a very sharp tip (the typical radius of commercial tips is 2–20 nm) attached to the end of a microfabricated cantilever, usually made either of Si or Si_3N_4. The spring constant of commercial probes ranges typically from 0.01 to 100 N/m. A laser beam reflected from the back of the cantilever is detected with a four-segment photodiode detector. By the positions of the incident beam at the detector, vertical deflections and lateral distortions of the cantilever can be evaluated. Scanning of the probe over the sample surface is carried out with the piezoelectric scanner, which expands or shrinks in response to applied voltages. Commercial AFMs have a system either to move the probe attached on the scanner over the sample (in which case the sample remains stationary) or move the sample on the scanner under the probe (the probe is stationary). The controller evaluates the signals from the photodetector to adjust the z-displacement of the piezo scanner, i.e. moves the sample or the probe upward and downward, to keep the feedback control parameter constant. The mapping of the resulting z-piezo movements in the x and y dimensions provides the various images of the sample surface.

In the past, two different methods have been employed to obtain surface topographic images. One is contact mode, in which the probe scans over a sample surface whilst constantly in contact with the surface. As the cantilever deflects upward or downward following the undulations of the sample surface, the feedback loop adjusts the z-position of the piezo scanner to maintain a constant degree of deflection during the scan. By mapping the z-displacement of a calibrated piezo scanner, a height image of the surface can be obtained. The other mode is dynamic mode, also known as non-contact mode or tapping mode. In the dynamic mode, the cantilever is oscillated at a frequency close to the resonance frequency during scanning. As the amplitude of the oscillation changes due to the distance between the probe and the sample, the feedback system adjusts the z-position of the piezo scanner to maintain a constant amplitude. The dynamic mode is more commonly used nowadays, because it allows observations with

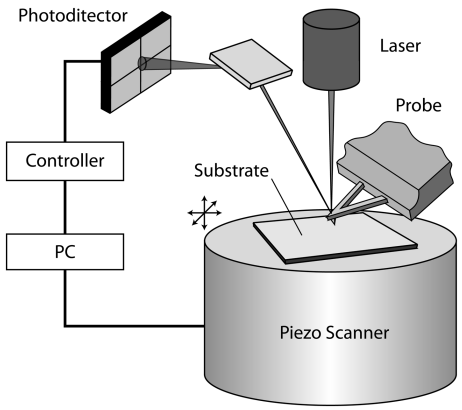


FIGURE 1.7.1 Schematic drawing of the atomic force microscope.

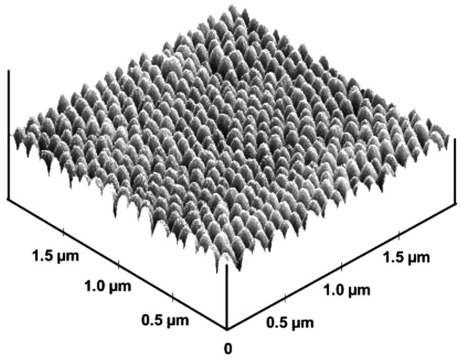


FIGURE 1.7.2 AFM height image of the silica particles of 110 nm in size deposited on a silica substrate. (Reprinted from Götzinger and Peukert, *Langmuir*, 20, 5298–5303, 2004, with permission. Copyright (2004) American Chemical Society.)

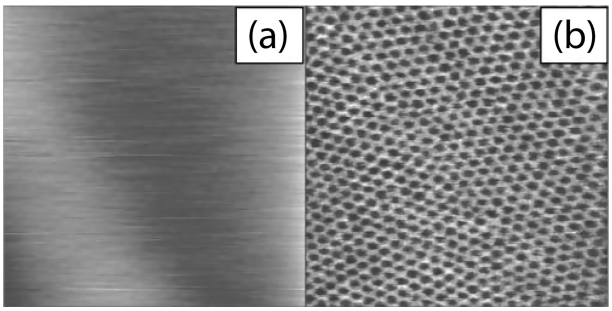


FIGURE 1.7.3 AFM height image (a) and corresponding phase image (b) of a hydrogenated poly(butadiene-b-ethyleneoxide) film on a silicon wafer prepared by spin coating. (Reprinted from Reiter et al., *Phys. Rev. Lett.*, 87, 226101, 2001, with permission. Copyright (2001) The American Physical Society.)

limited damage to the sample and the probe, which is particularly beneficial for observations of soft surfaces. In addition, using frequency-modulation AFM (FM-AFM), which is the advanced version of the dynamic mode AFM, one can obtain atomic-scale images even for surfaces immersed in a liquid phase.[2]

1.7.2 SURFACE CHARACTERIZATION BY AFM

As previously mentioned, one of the advantages of the AFM technique is that the images can be obtained *in situ* in both gaseous and liquid environments without the need for any conductive coatings and vacuum, unlike electron microscopy. Therefore, height imaging by AFM is used not only to observe the morphology of flat surfaces but also to evaluate the size and the shape of particles by depositing them onto a flat surface as shown in Figure 1.7.2, as a handy technique for characterization. On the other hand, when the size of the samples to be observed is small enough to be comparable to the size of the probe tip, as in the case of nanoparticles, the accuracy of the image width of the surface feature decreases significantly in AFM imaging. This is because the geometry and the width of the AFM tip broaden the image for the x and y dimensions.[3] In this case, the true images should be reconstructed by a deconvolution of the obtained images, which is usually performed by using an image processing software. Alternatively, the image size in the vertical (z) dimension is sometimes used when the particle is not deformable and one particle on the flat surface can be identified. In any case, however, the size evaluation by AFM imaging should be conducted carefully.

Surface roughness is one of the most important quantitative factors that one can derive from the height images. AFM essentially excels in measuring the surface roughness at the nanoscale, having a resolution far exceeding that of other stylus-based and optical methods. In AFM imaging, the root mean square (RMS) roughness is commonly used as an indicator of the magnitude of the surface roughness. While surface roughness itself is a particularly important parameter when particle interactions[5] and adhesion[6] are evaluated, a change in the roughness values often also provides important information about other surface properties such as the morphological changes taking place in the molecules present on the surfaces as a result of environmental conditions.[7]

Another important advantage of the AFM imaging is that except for the topological images, the distribution of various properties of the sample surfaces can be visualized by utilizing its feedback principle. Thus far, a number of imaging modes have been developed based on the two previously mentioned primary imaging modes, namely, contact mode and dynamic mode. Phase imaging is probably the most extensively used imaging mode. This mode allows one to evaluate the viscoelastic properties of the material surfaces, which are not clearly detected in the height images in most cases. In phase imaging, the shifts of the oscillation phase between the signal for driving the probe and the actual detected signal are monitored during scanning with the dynamic mode. The shifts can be correlated to the differences in the surface properties such as elasticity and adhesion. Thus, by mapping the degree of the shifts over the surfaces, information about the variations in the surface viscoelastic properties can be obtained, which is complementary to the information derived from the height image as shown in Figure 1.7.3.[8,9]

Lateral force microscopy (LFM), also called as friction force microscopy, allows the visualization of the relative strength of the lateral (frictional) force between the tip and the sample surface. The LFM and height images can be obtained simultaneously by the contact mode. During the scanning of the tip over a sample surface, the cantilever twists because of the frictional force between them. The degree of the cantilever twists can be detected by the lateral displacement of the laser on the photodetector. The mapping of the lateral output signals provides a distribution of the relative strength of the friction over the surface. The frictional properties of various materials including polymers,[10] metal oxides,[11] and carbon materials[12] have been investigated by using LFM.

An assessment of the nanoscopic distribution of electrical and magnetic properties on the material surfaces is of significant interest in many fields in material science and engineering. The sensing of electrical properties can be conducted by

applying a DC bias between a probe with a conductive coating and the sample during scanning. Conductive AFM (CAFM) is a current sensing mode that is carried out during the contact mode imaging. The current between the probe tip and the sample is measured simultaneously via an electric current amplifier. CAFM is essentially useful for studying conductive nanomaterials such as nanoparticles[13] and nanorods,[14] as well as relatively resistive materials such as organic semiconductors.[15,16] On the other hand, Kelvin probe force microscopy is utilized for visualizing the surface potential, which is derived from the tapping mode. Recently, this technique has also been applied for an evaluation of the nanoscopic electric potential of various hybrid nanodevices.[17,18] The magnetic force gradient can be imaged by magnetic force microscopy (MFM), in which the magnetized tip scans a magnetic sample. A variety of magnetic particles have been studied by MFM, including magnetite[19] and iron oxide[20] nanoparticles.

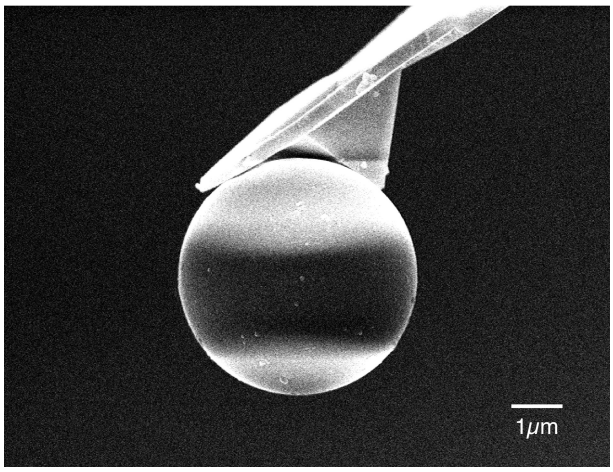


FIGURE 1.7.4 Scanning electron microscope image of a colloid probe.

1.7.3 MEASUREMENTS OF INTERACTION FORCES BY AFM

Principle of Force Measurements

Understanding the interaction forces between two opposing surfaces in air and in liquid provides a basis for evaluating and controlling particle behavior in various processes. The invention of the surface force apparatus (SFA)[21] enabled the direct measurement of interaction forces both in air and in liquid with molecular level resolution, has led to remarkable progress in understanding surface forces in detail. Following the SFA, the application of AFM to force measurement has further extended the possibility of force measurements to new fields of research. Despite the greater accuracy of the SFA, it is limited in the range of surfaces that can be employed by instrumental requirements. Typically, the surfaces should be thin (micrometer), transparent sheets of atomically smooth materials over a relatively large area of several square centimeters, which is practically restricted to mica and silica. On the other hand, AFM can be used on a much wider variety of materials and has therefore found applications in a wider variety of research fields. In addition, the introduction of the colloid probe technique[22,23] allowed quantitative evaluations of forces between macroscopic surfaces. In the colloid probe technique, a spherical particle with the typical diameter of 2–40 μm is attached to the end of a probe tip as shown in Figure 1.7.4, and the force is measured between this particle and a flat surface. This method made force measurements using the AFM comparable to those with the SFA.

In order to apply the AFM to force measurements, the probe or the sample substrate is moved vertically (z-direction) to alter the distance between the probe and the surface. During scanning, the probe tip-substrate interaction force is determined from the vertical deflection of the probe cantilever. Figure 1.7.5 shows a schematic representation of typical deflection versus piezo translation one can obtain by a force measurement between charged solid surfaces in an aqueous solution and its transformation into force versus separation

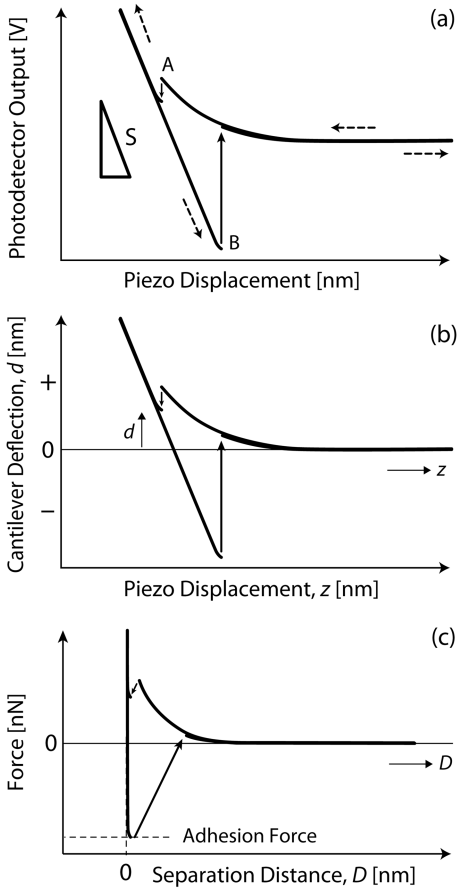


FIGURE 1.7.5 Typical force data by AFM measurements. (a) The raw data, (b) cantilever deflection-sample displacement data obtained from (a), and (c) the force-separation distance curve converted from (b).

data. In most commercial AFMs, approaching the probe to the flat substrate, bringing the surfaces into contact, and retracting the probe from the substrate constitutes one measurement cycle. Positive deflection (force) value usually indicates repulsive force. During the measurement, the deflection

of the cantilever is recorded by the photodetector output voltage V as a function of the relative displacement of the sample or the probe. In the case of the force in Figure 1.7.5(a), a repulsive force between the surfaces is detected at large surface separation, then the surfaces are brought into contact due to an attraction acting at a shorter range, shown as point A in the figure. If the attraction is a strong function of separation, the surfaces often "jump-in" to contact, due to the instability of the cantilever. This occurs when the slope of the interaction force F along the separation distance D exceeds the spring constant of the cantilever k, i.e.

$$\frac{dF}{dD} \geq k \tag{1.7.1}$$

When the surfaces are in firm contact, the change in cantilever deflection equals the change in displacement as indicated by a linear region often called the "constant compliance region." As the surfaces are separated, an adhesion force may be seen between the surfaces. In this case, the cantilever usually undergoes a jump-out to zero interaction force, which is marked by point B in the figure. This is the reverse effect of the jump-in.

Unlike the SFA, the AFM usually contains no device or system to directly measure the separation distance between the interacting surfaces. Therefore, the force versus distance relationship has to be calculated from the photodiode voltage vs. piezo displacement curve, which is obtained directly from the AFM.[22] The cantilever deflection d is calculated from the slope S of the constant compliance region shown in Figure 1.7.5(a) as

$$d = V / S \tag{1.7.2}$$

If the separation is set to zero at the constant compliance region as shown in Figure 1.7.5(b), the separation distance D at each point of the data is simply calculated by

$$D = z + d \tag{1.7.3}$$

where z is the piezo displacement at each point. Then, the force-distance relationship can be obtained by multiplying d with the spring constant of the cantilever as shown in Figure 1.7.5(c). When a colloid probe is used, the obtained value of the interaction force F is commonly divided by the particle radius R, because the value of $F/2\pi R$ is equal to the interaction energy between parallel planes par unit area by Derjaguin approximation.

It should be noted that an accurate zero distance cannot be guaranteed by this method, although it is the dominant means used to determine the separation distance in AFM measurements. In particular, if there is an adsorbed layer of any kind of molecules on the surfaces and if the molecules are not excluded when the surfaces are brought into contact, a certain offset of the distance should be expected. Therefore, the distance D should be regarded as the relative distance from the point of closest approach in the AFM force measurements and this should be kept in mind when precise distances between the surfaces need to be considered. Additionally, most surfaces have some degree of roughness and this complicates both the definition of zero separation and the practical determination of zero separation in a force measurement.[5]

Force Measurements in Gas and Liquid Phase

The AFM measurements in gas phase are conducted mainly to obtain adhesion forces between solid surfaces. The adhesion forces due to capillary force have been evaluated with changing multiple factors including roughness, deformability, hydrophilicity, geometrical shape the size of the surfaces employed.[24–26] The dependency of the capillary force on the relative humidity is somewhat complicated as there has been some discrepancy in the data published thus far.

The colloid probe method has been employed in studies of electrostatic charging of single particles. Both model spherical particles[27,28] and particles used in applications such as printer toner particles[29] have been used. Fitting the adhesion force between the particles and sample plates to theoretical models has allowed the charge density on particles to be estimated.

Developments in direct force measurements in liquids with the SFA and the AFM have not only provided an experimental basis for Derjaguin-Landau-Verwey-Overbeek (DLVO) theory, but also have extended our understanding of the forces to those that lie outside of the DLVO paradigm, which are often called non-DLVO forces. Hydration force is one of the most important non-DLVO forces.[30] The hydration force is the monotonically repulsive force with the range of about 1–5 nm typically acting between charged surfaces in aqueous electrolyte solutions, particularly at high concentrations. This force can be attributed to the energy required to remove hydrated ions from surface when they are brought into contact. The range of force between negatively-charged surfaces was found to increase following the hydration enthalpy of the cations, in the order of $Li^+ \sim Na^+ > K^+ > Cs^+$,[30,31] as indicted in Figure 1.7.6.

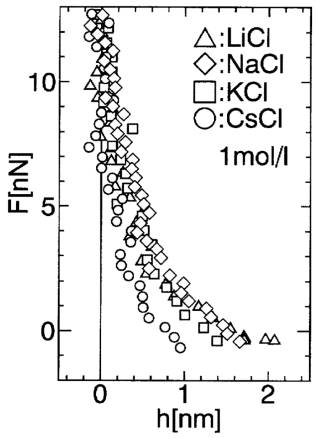


FIGURE 1.7.6 Forces measured between an AFM tip and a mica surface in 1 M electrolyte solutions of monovalent cations. (Reprinted from Higashitani and Ishimura, *J. Chem. Eng. Jpn.*, 30, 52–58, 1997, with permission. Copyright (1997) The Society of Chemical Engineers, Japan.)

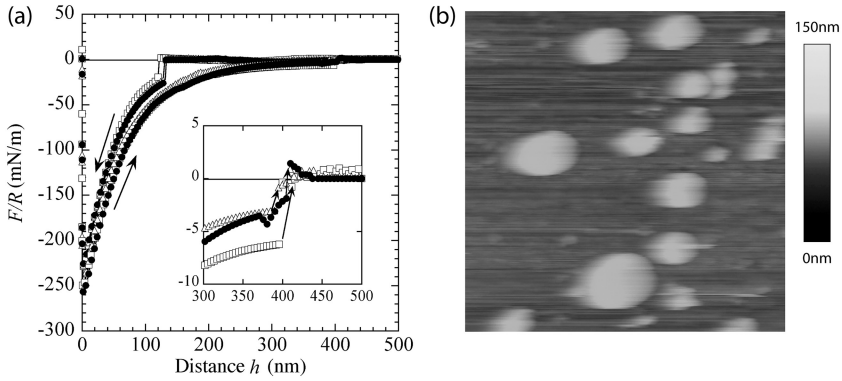


FIGURE 1.7.7 Typical approaching and retracting force curves between the silica surfaces hydrophobized with octadecyltrichlorosilane (OTS) measured in water (a) and a tapping-mode AFM image ($3 \times 3\ \mu m^2$) of the substrate hydrophobized with OTS obtained in water (b). The steps that appear in the approaching and retracting force curves in (a) are considered to represent the force changes when a bridging of nanobubbles between the surfaces forms and disappears. The nanobubbles on the surface are observed as domain-like structures (bright regions) in the image in (b).

Hydrophobic attraction is a strong and long-range attractive force between hydrophobic surfaces in aqueous solutions. The origin of the hydrophobic attraction, however, was much disputed because the experimentally observed forces sometimes have an inconceivably long range, that reaches up to several hundreds of nanometers,[32] which no conventional thermodynamics can explain. Gradually, however, the contribution of numerous studies investigating the hydrophobic attraction has revealed the origin of the measured force and multiple phenomena have been found to apply depending on the system. Bridging of nanobubbles is now recognized as the main cause of the very long-range forces, particularly when the surfaces are highly hydrophobic and robust.[9,32] (Figure 1.7.7[a]). When hydrophobic surfaces are prepared by physical adsorption of surfactants or amphiphiles, electrostatic forces can arise as they tend to form domains of aggregates on the surfaces.[33]

The interactions of surfaces in non-aqueous solvents have also been measured by AFM, though the number of studies is much less than those in aqueous solution. In non-aqueous solvents, the solvation and structuring of liquid molecules adjacent to surfaces gives rise to specific interactions at short-range, referred to as solvation forces.[34] Solvent mixtures often produce complex interaction forces. A trace amount of water present in cyclohexane was found to condense between silica surfaces and give rise to an extraordinary long-range capillary force, the range of which was up to 250 nm[35] as shown in Figure 1.7.8.

The flexibility of AFM for materials used in force measurements enables to use fluid interfaces such as air bubbles and oil droplets as surfaces by attaching a small bubble or oil droplet to a hydrophobic plate in a liquid cell.[36,37] Not only bubble-particle and oil-particle interactions, but forces between two fluid interfaces in solution, such as bubble-bubble and oil-oil, has been successfully developed by attaching a small bubble or an oil droplet on the top of a specially microfabricated cantilever.[38,39]

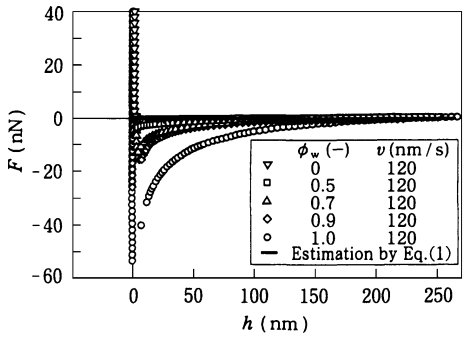


FIGURE 1.7.8 Interaction forces between silica surfaces in cyclohexane with various amounts of water. In the plot, ϕ_w denotes the mixing ratio of water-saturated cyclohexane (contains 68 ppm of water) to dried cyclohexane. (Reprinted from Kanda et al., *J. Soc. Powder Technol., Jpn*, 38, 316–322, 2001, with permission. Copyright (2002) The Society of Powder Technology, Japan.)

In addition to "static" interactions described above, the hydrodynamic force can be studied using AFM. Most AFM studies related to the hydrodynamic force seem to have focused on the boundary slip condition of Newtonian liquids over a solid wall. By utilizing the AFM colloid probe technique to measure the hydrodynamic drag force, the slip was found to occur with a varying slip length of up to ~20 nm, depending on the liquid viscosity and the shear rate, on hydrophobic surfaces.[40] The measurement of friction by AFM can be conducted by scanning a probe over a surface with a constant normal load and measuring the twisting of the cantilever. From the magnitude of the twist, the lateral force can be determined as a function of the normal load. Using this method, the friction between silica surfaces in aqueous electrolyte solutions was found to follow the order of hydration of cations ($Li^+ > Na^+ > Cs^+$),[41] which can be attributed to the lateral mobility of the water molecule in the hydration shell of adsorbed cations.

REFERENCES

1. Binnig, G., Quate, C. F., Gerber, C., *Phys. Rev. Lett.*, 56, 930–933, 1986.
2. Fukuma, T., Ueda, Y., Yoshioka, S., Asakawa, H., *Phys. Rev. Lett.*, 104, 016101, 2010.
3. Keller, D., *Surf. Sci.*, 253, 353–364, 1991.
4. Götzinger, M., Peukert, W., *Langmuir*, 20, 5298–5303, 2004.
5. Parsons, D. F., Walsh, R. B., Craig, V. S. J., *J. Chem. Phys.*, 140, 164701, 2014.
6. Farshchi-Tabrizi, M., Kappl, M., Cheng, Y., Gutmann, J., et al., *Langmuir*, 22, 2171–84, 2006.
7. Ishida, N., Biggs, S., *Langmuir*, 23, 11083–11088, 2007.
8. Reiter, G., Castelein, G., Sommer, J.-U., Röttele, A., et al., *Phys. Rev. Lett.*, 87, 226101, 2001.
9. Ishida, N., Inoue, T., Miyahara, M., Higashitani, K., *Langmuir*, 16, 6377–6380, 2000.
10. Hammerschmidt, J. A., Gladfelter, W. L., Haugstad, G., *Macromolecules*, 32, 3360–3367, 1999.
11. Hähner, G., Marti, A., Spencer, N. D., *Tribol. Lett.*, 3, 359–365, 1997.
12. Ruan, J. A., Bhushan, B., *J. Appl. Phys.*, 76, 5022–5035, 1994.
13. Raccosta, S., Baldacchini, C., Rita Bizzarri, A., Cannistraro, S., *Appl. Phys. Lett.*, 102, 203704, 2013.
14. Beinik, I., Kratzer, M., Wachauer, A., Wang, L., et al., *J. Appl. Phys.*, 110, 052005, 2011.
15. Kelley, T. W., Frisbie, C. D., *J. Phys. Chem. B*, 105, 4538–4540, 2001.
16. Nakamura, M., Yanagisawa, H., Kuratani, S., Iizuka, M., et al., *Thin Solid Films*, 438, 360–364, 2003.
17. Li, W., Dong, H., Guo, X., Li, N., et al., *J. Mater. Chem. A*, 2, 20105–20111, 2014.
18. Yoo, H., Bae, C., Yang, Y., Lee, S., et al., *Nano Lett.*, 14, 4413–4417, 2014.
19. Sievers, S., Braun, K.-F., Eberbeck, D., Gustafsson, S., et al., *Small*, 8, 2675–2679, 2012.
20. Zhang, Y., Yang, M., Ozkan, M., Ozkan, C. S., *Biotechnol. Progr.*, 25, 923–928, 2009.
21. Tabor, D., Winterton, R. H. S., *Nature*, 219, 1120–1121, 1968.
22. Ducker, W. A., Senden, T. J., Pashley, R. M., *Nature*, 353, 239–241, 1991.
23. Butt, H.-J., *Biophys. J.*, 60, 1438–1444, 1991.
24. Harrison, A. J., Corti, D. S., Beaudoin, S. P., *Particul. Sci. Technol.*, 33, 526–538, 2015.
25. Fuji, M., Machida, K., Takei, T., Watanabe, T., et al., *J. Phys. Chem. B*, 102, 8782–8787, 1998.
26. Jones, R., Pollock, H. M., Jamie A. S. Cleaver, A., et al., *Langmuir*, 18, 8045–8055, 2002.
27. Gady, B., Schleef, D., Reifenberger, R., Rimai, D., et al., *Phys. Rev. B*, 53, 8065–8070, 1996.
28. Mizes, H., Ott, M., Eklund, E., Hays, D., *Colloids Surf., A*, 165, 11–23, 2000.
29. Zhou, H., Götzinger, M., Peukert, W., *Powder Technol.*, 135–136, 82–91, 2003.
30. Pashley, R. M., *J. Colloid Interface Sci.*, 83, 531–546, 1981.
31. Higashitani, K., Ishimura, K., *J. Chem. Eng. Jpn.*, 30, 52–58, 1997.
32. Ishida, N., Sakamoto, M., Miyahara, M., Higashitani, K., *Langmuir*, 16, 5681–5687, 2000.
33. Zhang, J., Yoon, R.-H., Mao, M., Ducker, W. A., *Langmuir*, 21, 5831–5841, 2005.
34. Franz, V., Butt, H.-J., *J. Phys. Chem. B*, 106, 1703–1708, 2002.
35. Kanda, Y., Nishimura, T., Higashitani, K., *J. Soc. Powder Technol., Jpn*, 38, 316–322, 2001.
36. Fielden, M. L., Hayes, R. A., Ralston, J., *Langmuir*, 12, 3721–3727, 1996.
37. Hartley, P. G., Grieser, F., Mulvaney, P., Stevens, G. W., *Langmuir*, 15, 7282–7289, 1999.
38. Dagastine, R. R., Manica, R., Carnie, S. L., Chan, D. Y. C., et al., *Science*, 313, 210–213, 2006.
39. Vakarelski, I. U., Manica, R., Tang, X., O'Shea, S. J., et al., *Proc. Natl. Acad. Sci. U.S.A.*, 107, 11177–11182, 2010.
40. Craig, V. S. J., Neto, C., Williams, D. R. M., *Phys. Rev. Lett.*, 87, 054504, 2001.
41. Donose, B. C., Vakarelski, I. U., Higashitani, K., *Langmuir*, 21, 1834–1839, 2005.

1.8 Specific Properties of Nanoparticles

Wolfgang Peukert and Johannes Walter

1.8.1 PROPERTY FUNCTION AND DISPERSE PROPERTIES

Properties of particles in general, and of nanoparticles in particular, depend on the chemical composition and on the dispersity of the material. The dispersity is characterized by the particle size distribution (PSD), the particles' shape, their morphology in terms of internal structure (amorphous, crystalline, pore size distributions and all sorts of structural and electronic defects) and their interfacial properties. This relation we call, in accordance with Hans Rumpf who coined the term already in the 1960s, the "property function":[1]

$$\text{Product property} = f\left(\text{dispersity, chemical composition}\right) \tag{1.8.1}$$

Dispersity includes:

- particle size and shape and their respective distribution.
- particle morphology including defects.
- particle surface properties.

Thus, the property function relates the nanoparticulate structure (size, shape, morphology and surface) to the product properties (structure-property function). Several examples will be discussed in the following sections. Not only single particles but also particle ensembles in the form of agglomerates, thin films or filter cakes are included in this consideration.

Modern products are often characterized by several properties which have to be achieved simultaneously. Transparent and scratch resistant coatings on a car or sun blockers, which are transparent for visible light and UV absorbing, may serve as well-known examples. Thus, a multi-functional product space evolves which must be created through design of the related structures using the respective process technology. Further, it is helpful to distinguish between handling properties and end-use properties. The former is related to properties, which are important for the formation and processing of particles and will be discussed in more detail in Chapter 5.24. The end-use properties of nanoparticles are more in the focus of this chapter. It must be noted that we can only provide a rough overview of the field with few selected examples due to space restrictions. Several books and monographs have been published for nanoparticles with more detailed information.[2–4]

In this chapter, we consider particles which have at least one dimension well below 100 nm. By this definition we include not only quasi-spherical particles, but also nanofibers such as carbon nanotubes with diameters of 1 nm and lengths of several μm as well as nanoplatelets such as graphene or other novel 2D materials whose monolayer thickness is below 1 nm with much larger lateral dimensions. Particles of arbitrary shape are typically characterized by equivalent properties and sizes, e.g. diameter of a sphere of equal volume, chord length, surface or cross-section or diameter of a sphere with equal hydrodynamic behavior.[5]

A number of techniques are available for nanoparticle size characterization such as Scanning Mobility Particle Sizer (SMPS) coupled to Condensation Particle Counter (CPC) for size analysis of particles in the gas phase[6] or Dynamic Light Scattering (DLS),[7,8] Field Flow Fractionation (FFF)[9,10] or ultrasound spectroscopy[11] for analysis in the liquid phase. In recent years, Analytical Ultracentrifugation (AUC) was boosted to new levels by the development of in situ multi-wavelength UV-V is spectroscopy in the centrifuge.[5,12–14] This technique can now be considered a new "gold standard" due to its outstanding resolution, accuracy and reproducibility. The technique is based on measuring sedimentation and diffusional transport (see Section 1.8.2) in strong centrifugal fields and works in the size range from below 1 nm up to almost 1 μm. AUC is now being extended towards multidimensional analysis for the simultaneous characterization of size and shape, size and density or size and optical properties. To give just two recent examples: (i) particle size and spectral information can be used to derive band gap vs. size dependencies for semiconducting quantum dots,[15,16] (ii) particle size and ligand shell thickness on the surface of the nanoparticles can be determined from size and density information.[17,18] Further, quantitative shape analysis was demonstrated for graphene oxide and several types of nanorods.[19–21] In comparison to tedious Transmission Electron Microscopy (TEM), Scanning Electron Microscopy (SEM) or Atomic Force Microscopy (AFM) image analysis, AUC is much faster as particles are measured directly in dispersion and more reliable due to the superior sampling statistics.

Besides AUC, few techniques are known which are able to measure particle properties beyond size, i.e. particle shape or particle surface composition. For shape, image analysis by TEM, SEM or AFM are the most important techniques. The primary particle size as well as the number, surface area and volume distributions of loose nanoparticle agglomerates can be measured by a combination of Differential Mobility Analyzer (DMA) and CPC coupled to a unipolar charger combined with an electrometer in the gas phase.[22]

Nanoparticle surface properties are of ultimate importance due to the high specific surface area of nanoparticles. Although considerable progress was made in recent years, they are by far not sufficiently understood in terms of equilibrium and

transient composition as well as morphology due to the lack of reliable characterization techniques. Particles charge can be measured in the gas phase by differential mobility analysis, whereas the zeta-potential as an estimate of the surface potential in liquids can be obtained in diluted systems from optical techniques measuring the electrophoretic mobility, or from electro-acoustics even for dense and opaque dispersions up to concentrations of 40 vol.%.[11] Nonlinear optical techniques such as Second Harmonic Generation (SHG) are inherently surface sensitive and give direct access to the surface potential, adsorption and chemisorption processes at particle surfaces.[23,24] Recently, also more complex situations were analyzed including amphoteric particles[25] or ligand exchange of adsorbents.[26]

1.8.2 TRANSPORT PROPERTIES

In general, the motion of particles in fluids can be described by either deterministic motion based on Newton's second law or stochastic motion. Nanoparticles have low inertia and thus follow the streamlines of convective flows. However, for nanoparticles (here defined by hydrodynamic diameters below 100 nm), the diffusion coefficient given by

$$D = \frac{k_B T}{f} = \frac{k_B T}{3\pi\eta x} \tag{1.8.2}$$

is sufficiently large that nanoparticles undergo stochastic Brownian motion which can be modeled by solving the Langevin equation:

$$m\frac{dw}{dt} = -F_d + F(t) \tag{1.8.3}$$

k_B is Boltzmann's constant,
T is the absolute temperature in Kelvin,
f is the friction coefficient,
η is the viscosity of the solvent,
x is the hydrodynamic diameter,
m is the mass of the particle,
w is the particle velocity,
$F(t)$ is a stochastic Brownian force at time t.

The diffusion coefficient can be derived from a solution of the Langevin equation. The first term on the right-hand side is the Stokesian drag force being valid for $Re = u{\cdot}x{\cdot}\rho/\eta < 1$, which holds true for all nanoparticles. u is the relative velocity taking into account the fluid velocity. This way, it can be shown that the thermal energy kT equals the kinetic energy of the particle (in a quiescent fluid):

$$\frac{3}{2}kT = \frac{1}{2}mw^2 \tag{1.8.4}$$

The above holds true for all nanoparticles in liquids and for nanoparticles which are larger than the mean free path λ in the gas phase. Particles in the free molecular regime, which is defined by the Knudsen number, $Kn = \lambda/x < 1$, travel on rectilinear trajectories between two collisions with the gas molecules. The drag force acting on the particles is then corrected by the Cunningham factor Cu:

$$Cu = 1 + Kn\left[2.514 + 0.8\exp\left(\frac{-0.55}{Kn}\right)\right] \tag{1.8.5}$$

$$F_d = \frac{3\pi\eta x}{Cu}\cdot w \tag{1.8.6}$$

Gas transport in nanoporous particles such as Molecular Organic Frameworks (MOFs), zeolites or nanoparticulate films occurs by Knudsen diffusion and flow is characterized in such a case by molecular-wall collisions only.

Due to the Brownian motion, nanoparticles easily collide with each other leading to agglomeration. The agglomeration can be considered as a second order process where its frequency is proportional to the square of the particle concentration. Coagulation often leads to fractal aggregates (see Chapter 4.1). The control of coagulation is very difficult in the gas phase and more easily achieved in the liquid phase by tuning the particle-particle interactions via electrostatic, steric or electro-steric means (see Chapter 5.24).

1.8.3 PARTICLE INTERACTIONS

The most relevant particle interactions for nanoparticles are van der Waals forces, electrostatic interactions and steric interactions mediated by adsorbed (macro-)molecules. In this section we discuss van der Waals forces whereas electrostatic interactions are discussed in Chapter 2.9.2. The molecular origin of van der Waals forces is based on fluctuating dipoles leading to the so-called dispersion interaction. Two approaches exist: The older Hamaker approach assumes additivity of forces and can often be used for engineering approximations. The younger and physically correct Lifshitz theory uses quantum field theory and leads to so-called Lifshitz integrals which are functions of the frequency-dependent dielectric functions of the particles and of the fluid in which the particles are dispersed. It has to be noted that the dielectric permittivity is the macroscopic analog of the molecular polarizability. Van der Waals interactions are always attractive in the gas phase. In the liquid phase, van der Waals forces are mostly attractive but can vanish by index-matching, i.e. by dispersing particles in a liquid with similar dielectric properties. In rare cases, van der Waals forces can be made repulsive for two different particles by choosing a liquid whose dielectric permittivity lies between those of the two particles.

The high relevance of van der Waals forces between particles becomes obvious by the following scaling argument. Since the van der Waals forces between two equal particles at close distance scale with the particle diameter, the ratio of attractive van der Waals force F_{vdW} and weight force F_G scales with the inverse square of the particle diameter x:

$$\frac{F_{vdW}}{F_G} = \frac{Ax}{24a^2}\cdot\frac{6}{\pi x^3\rho} = \frac{A}{4\pi x^2\rho a^2} \sim x^{-2}. \tag{1.8.7}$$

A denotes the Hamaker constant, *a* is the particle-particle distance and the other variables have their usual meaning. For typical values of the Hamaker constant and smooth particle surfaces of 1 μm in diameter, the van der Waals attraction is about 1 million times larger than the particle weight and increases accordingly for smaller particles. This means that the behavior of nanoparticles, and thus the success of nanotechnology in general, is only possible by careful control of these attractive van der Waals forces. Van der Waals interactions are responsible for many phenomena observed for nanoparticles such as low packing density of nanoparticulate layers, their tendency for agglomeration and their adhesion to fibers in a filter for product recovery or environmental protection.

1.8.4 THERMOPHYSICAL PROPERTIES

Several properties of nanoparticles, including size-dependent melting and sintering, solubility and evaporation as well as elastic and some catalytic properties (see Sections 1.8.5 and 1.8.9) can be explained by the ratio of surface to volume. With decreasing particle size, the relative portion of surface atoms or molecules increases. Particles with diameters below roughly 1 nm or the novel 2D materials (e.g. graphene) exclusively consist of surface atoms, whereas the relative amount of surface atoms is mostly negligible for sizes above 100 nm, i.e. the particle property depends on the materials properties of the bulk.

Kelvin Effect

Atoms and molecules located at the surface are less coordinated than those in the inner of the particle and have thus a lower binding energy, leading to higher surface mobility and the related colligative properties. This effect is reflected in the Kelvin equation[27] which is derived from the Gibbs fundamental equation[28] by a balance of volume and surface energy for a spherical "droplet" of radius *r* and surface energy γ:

$$RT \ln \frac{c(r)}{c_\infty} = \frac{2\gamma V}{r} \tag{1.8.8}$$

V is the droplet volume and the concentration *c(r)* is the solubility of the nanoparticle in a solvent relative to c_∞, which is the solubility of the bulk material. The equation can be applied to evaporation by replacing the concentration by the respective vapor pressures. In meso- and nanoporous systems, the Kelvin equation is modified for cylindrical pores (the factor 2 in Equation [1.8.8] is replaced by 1) and used to estimate the vapor pressure depression, i.e. for estimation of capillary condensation.

Of course, the Kelvin equation can only be a rough but helpful approximation for non-spherical particles, such as crystalline nanoparticles with edges and corners. However, the arguments for the higher mobility of atoms at corners and edges hold true as well.

Ostwald Ripening

Ostwald Ripening is an important effect in liquids which is observed for many nanoparticulate systems including semiconductors of extremely low bulk solubility at the lower nanoscale[29,30] and in pharmaceutical nanotechnology where the effect can be observed for sizes of several 100 nm.[31,32] As most nanoparticle systems are distributed in size, smaller particles will have a higher solubility than the bigger ones, i.e. the larger particles will grow at the expense of the smaller ones. Ripening may not only lead to a change in particle size but may also induce changes in particle shape, e.g. the spontaneous decay of noble metal nanorods such as silver. Here, internal defects ending at the surface of the nanorods trigger the decay.[33] In pharmaceutical applications, the change in the polymorph habitus of the crystals is an unwanted effect. Ostwald's step rule states that in general it is not the most stable but the least stable polymorph that crystallizes first. Therefore, Ostwald suggested that the solid first formed by crystallization of a solution or a melt would be the least stable polymorph. During crystallization and ripening metastable forms of organic crystal can easily form and be transformed later to more stable ones.[34,35] These effects are described on the basis of thermodynamics and structural relationships of the crystal. In equilibrium, the crystal shape should obey Wulff's construction,[36] i.e. the overall surface energy is minimized by the equilibrium shape of the crystal.

Sintering

Sintering is an important effect in the gas phase synthesis of nanoparticles (see Chapter 4.1) and in the formation of ceramics, for instance. The scaling laws of sintering are dependent on the respective mechanism. The most important ones are viscous sintering for amorphous and glassy particles, surface, volume or grain boundary diffusion, or evaporation and recondensation. The dimensionless neck radius *R* is a function of temperature and time *t* and strongly depends on the particle radius *r*:

$$\left(\frac{R}{r}\right)^m = \frac{f(T)}{r^n} t \tag{1.8.9}$$

The parameter *n* ranges between 1 and 4 depending on the respective mechanism, whereas *m* lies between 2 and 7.[37]

A relatively recent experimental and theoretical study on vitreous nanoparticle sintering did lead to the following expression for the characteristic sintering time t_S using Friedlander's kinetic equation for the evolution of the particle surface *S*:[38,39]

$$\frac{dS}{dt} = -\frac{1}{t_s}\left(S - S_f\right) \text{ with}$$
$$t_s = \frac{\left(1-(1/e)\right) r_f^2}{2^{2/3} k_s} \exp\left(\frac{E_A}{k_B T}\right) \tag{1.8.10}$$

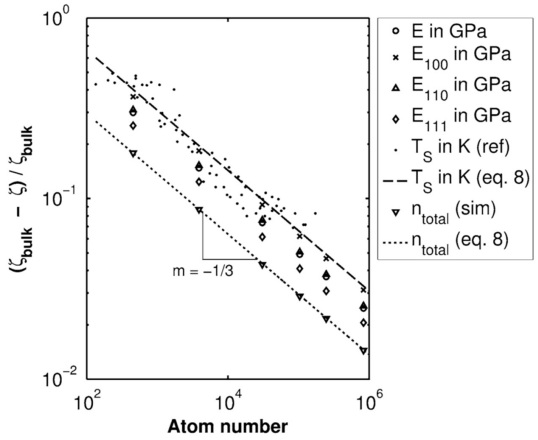


FIGURE 1.8.1 Deviation of particle properties ξ relative to the respective bulk property ξ_{bulk} for gold nanoparticles as a function of the number of atoms per particle. All properties investigated can be described by Equation 8 in [41] using adjusted scaling parameters k (for gold it ranges from $k=1.38$ for n_{total} to $k=3.05$ for T_S). This suggests that all quantities are coupled by the increasing surface to volume ratio with decreasing particle size and the accompanied decrease in surface coordination. The data for the melting temperature were taken from Buffat and Borel.[40] (Reprinted from Armstrong and Peukert, *J. Nanopart. Res.*, 14, 1288, 2012. With permission. Copyright 2012).

For the case of silica, the kinetic constant $k_s = 3.510^{-4}$ m^2/s and the activation energy $E_A = 3.8$ eV were determined for temperatures between 1300°C and 1600°C. S_f and r_f denote the surface area and particle radius after complete coalescence, respectively.

A famous example of size-dependent melting of gold was published by Buffat and Borel in 1976,[40] the data scale with the inverse third power of the atom number in the particles as shown in Figure 1.8.1. This depicts the importance of the surface-to-volume ratio.

Figure 1.8.1 also shows the size-dependent Young's modulus which obviously obeys the same scaling law. Mechanical properties of nanoparticles will be discussed in the following section.

1.8.5 MECHANICAL PROPERTIES

Mechanical properties of nanoparticles are of interest for all fields of application where particles in contact play a role, e.g. adhesion, compaction, tableting and powder storage, filtration or powder flow. These phenomena and related processes can be modeled by Discrete Element Simulations (DEM, see Chapter 5.25) but need quantitative mechanical particle properties as input parameters. These are, however, too seldom known.

So far, the mechanical properties of nanostructured materials, which exhibit at least one relevant length scale below 100 nm (in most cases "nanostructured" refers to the grain size), have mainly been studied.[42,43] Reported synthesis routes for nanostructured materials include the top-down routes mechanical alloying, nanomilling and severe plastic deformation or bottom-up routes like inert gas condensation, plasma synthesis and spark erosion. For nanostructured materials, a significant portion of all atoms is in grain boundaries, which gives rise to special mechanical properties: For metals a decrease of the Young's modulus has been reported. An increase of the yield strength approximately scales with the grain size d according to the well-known Hall-Petch relation ($\sim d^{-n}$, $0.3 \le n \le 0.7$), also improved toughness and reduced elastic modulus and ductility have been reported for such materials.[44] Often defects mask intrinsic material properties: in most cases there is still a widespread disagreement and contradicting data is often reported. One striking example is the so-called inverse Hall-Petch effect. Both the existence and possible physical mechanisms of a deviation from the well-known Hall-Petch mechanism below a critical grain size (in the order of 10 nm) is still a matter of debate.[45] In the field of nanoscale ceramics, the systems ZrO_2, TiO_2, $BaTiO_3$ and SiC have been extensively studied. Especially superplasticity of ceramics has seen scientific attention. At elevated temperatures ($T/T_m > 0.5$) and small strain rates (as compared to deformation of metals) nanoscaled ceramics can be deformed to large extents without breakage. Grain boundary "sliding" (i.e. translation and rotation of individual grains) is generally accepted as the deformation mechanism. However, the physical mechanisms of grain motion are still unknown.

Far less is known about the mechanical properties of individual nanoparticles. Although electron microscopy supported testing platforms are becoming more widespread,[46] our current understanding is mainly hampered by a lack of suitable experimental data. In most performed studies, however, samples which show uniaxial or plain stress/strain fields are being investigated. Hence, mainly focused ion beam machined pillars and micro-tensile specimens are being tested today. The influence of the ion beam milling on the behavior of the sample is still being discussed. One noteworthy exception is in situ tensile testing of individual carbon nanotubes which has now been performed for over a decade.[47,48] In the few available studies dealing with nanoparticles (including theoretical and experimental work) it has been suggested that the free particle surfaces induce similar effects like grain boundaries, i.e. the formation and storage of defects within the individual particle (or grain) becomes energetically less favorable. Furthermore, the surface (or grain boundary) acts as a sink for defects. This has been seen for example in mechanical alloying of metals[49] or the deformation of silicon particles made by aerosol techniques.[50–52] Whisker behavior has been reported for these particles, i.e. sudden yielding near the theoretical strength of the material which is accompanied by a burst of dislocations.[53] Similar effects have also been reported in alumina particles or freestanding gold structures. For the smallest particles (below 10 nm) and in special cases (e.g. the embedded atom method for metallic bonds allows to simulate rather large ensembles), where mechanical data is experimentally not accessible, molecular dynamics studies can be performed.[41] A reduction of the Young's modulus which scales with the amount of surface atoms (comparable to sintering of nanoparticles[54]) has been shown, see Equation (1.8.11) and Figure 1.8.1.

$$E(x) = E_{\text{bulk}}\left(1 - \frac{\lambda}{N^{\frac{1}{3}}}\right)$$
$$= E_{\text{bulk}}\left(1 - \frac{\lambda}{x\left(\frac{\pi\rho_{\text{bulk}}}{6M_a}\right)^{\frac{1}{3}}}\right). \quad (1.8.11)$$

Here

E is the Young's modulus for a particle of diameter x, while E_{bulk} is the modulus for the continuum,

ρ_{bulk} denotes the bulk density and M_a is the atomic mass.

Mechanical properties of nanoparticles are especially relevant for comminution: the release of energy from the elastic strain fields drives the formation and propagation of cracks. The particle strength strongly increases with decreasing particle size, an effect which depends on the decreasing defect density inside of the particle as fracture is mostly induced at defect sites.[55] For wet grinding of crystalline materials (oxides) in stirred media mills, the lower limit to comminution, i.e. the minimal achievable particle size, is directly connected to the activity of defects. Particle sizes as small as 10 nm have been achieved, e.g. for alumina and tin oxide.[56,57] In these small crystals, defects are not stable anymore since internal defects such as dislocations are attracted by the surfaces due to image forces. Furthermore, cracks can be initiated by the formation of voids due to activity of dislocations or grain boundary sliding. For amorphous materials which are perceived as brittle at macroscopic length scale, the so-called brittle-to-ductile transition marks a critical particle/specimen size where yielding occurs instead of cracking.[58]

1.8.6 OPTICAL PROPERTIES

The interaction of particles with electro-magnetic waves is governed by the Maxwell equations. Light can be scattered, absorbed or diffracted. Mie's theory provides a general solution for spherical particles. Nanoparticles with dimensions smaller than the wavelength of the visible light (400–800 nm) behave like dipoles in the polarizing electro-magnetic field (Rayleigh scattering). The scattering cross-section of the light scattered from a small dielectric sphere of refractive index n (averaged over all angles) is given as a special solution of Mie's theory and is given by:

$$\sigma_s = \frac{2\pi^5}{3}\frac{x^6}{\lambda^4}\left(\frac{n^2-1}{n^2+2}\right)^2 \quad (1.8.12)$$

x is the particle diameter and λ is given here as the wavelength of the incident light. The scattering intensity scales with the square of the particle volume. Thus, the scattered light intensity of ultrasmall particles is quite small, i.e. dispersions of nanoparticles become transparent. DLS instruments make use of Rayleigh scattering for size analysis. A major limitation here is that the smaller particles may be easily hidden by stronger scattering of the larger particles, making it difficult to measure wider or multimodal distributions.

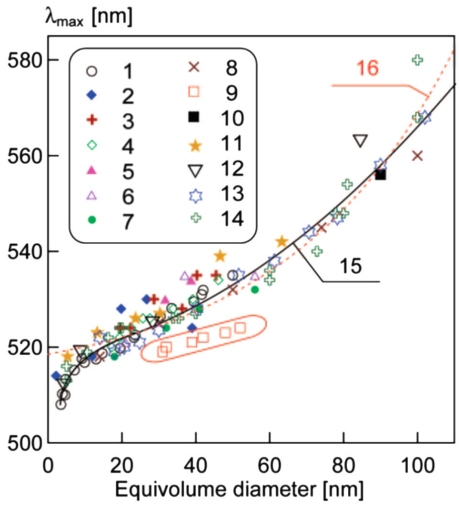


FIGURE 1.8.2 Position of the surface plasmon resonance peak (λ_{max}) as a function of the mean equivolume particle diameter for gold nanoparticles in water. The symbols designate experimental data taken from different works. Solid line 15 was calculated by Equation 4 in [66], dashed line 16 corresponds to Equation 9 in [67]. (Reprinted from Khlebtsov, *Anal. Chem.*, 80, 6620–6625, 2008. With permission. Copyright (2008) American Chemical Society.)

In the field of nanotechnology, the size- and shape-dependent light absorption of noble metal nanoparticles such as gold or silver is of particular importance. The electro-magnetic waves interact with the free electrons in the metal particles. The resulting plasmon resonances give rise to size-dependent absorption in the visible regime, depicted exemplarily in Figure 1.8.2 for gold nanoparticles. For instance, these phenomena have been used empirically in the past for tuning the colors in windows. For other shapes than spheres, e.g. nanorods, two distinct absorption maxima are observed due to the resonances in transversal and longitudinal direction. To date, noble metal nanoparticles and related alloys are used in the evolving field of plasmonics.[59] Applications range from sensors in bionanotechnology[60] including surface enhanced Raman spectroscopy,[61] energy conversion[62,63] to future possibilities for light management and building opto-electronic circuits for computers operating with light.[64] A comprehensive overview for the characterization of single particles by spectroscopy techniques has been published by Olson et al.[65]

Light absorption and also emission can be tuned by quantum-confined semiconductors. These aspects are discussed in the following section.

1.8.7 ELECTRICAL PROPERTIES

For small semiconductor nanoparticles the energy levels are not continuous as it would be in the bulk but are discrete instead. Due to the confinement of the electronic wave function to the physical dimensions of the particles, a finite density

of states is observed. This effect is known as quantum confinement and the corresponding (quasi-spherical) nanoparticles are therefore referred to as quantum dots. As the energy spectrum is discrete for quantum confined particles, the band gap is found to be a function of the particle's radius R. The particle radius-dependent band gap energy $E(R)$ can be estimated by the effective mass approximation of Brus:[68]

$$E(R) \simeq E_g + \frac{\hbar^2 \pi^2}{2R^2}\left[\frac{1}{m_e} + \frac{1}{m_h}\right] - \frac{1.8e^2}{\in R} + \text{smaller terms} \quad (1.8.13)$$

The first term is a quantum mechanical term reflecting the simple case of a confined particle in a box, which scales with R^{-2} and depends on the effective masses of electrons m_e and holes m_h. The second term is the Coulomb interaction of electron-hole pairs and E_g is the band gap energy of the bulk. This rough approximation can be refined by quantum chemical simulations, such as tight binding models or full electron density functional theory. Figure 1.8.3 depicts the emission spectra of CdSe quantum dots of different size as well as the size band gap correlation for various semiconductor nanoparticles.

The size-dependency of the band gap for small direct semiconductor nanoparticles can be used to determine their PSD based on a simple measurement of the sample's absorption spectrum.[73] For that purpose, the spectrum is deconvoluted starting at its upper end. This procedure has been validated carefully against TEM or AUC, e.g. for CdTe,[16] $CuInS_2$,[72] PbS,[73] PbSe,[73] ZnO[78] and ZnS,[78] and is very helpful for quality control of particle synthesis as in situ measurements can be easily realized. In addition to absorption, photoluminescence is an important property of quantum dots as it shifts with size as well. Thus, the emission properties of a semiconductor nanoparticle, e.g. for application in sensing, display technology or communication, can be easily altered by size variation.

Besides band gap, physical properties like conductivity or resistivity are observed to change at the nanoscale level. The manifold electrical properties of nanoparticles open a variety of applications in industry and academia. Energy conversion and storage, computer and display technology, sensing as well as medical applications are just a few to be named.

Not only semiconductor nanoparticles exhibit unique properties as there is always a substantial variation of fundamental electrical and optical properties observed with reduced size when the energy spacing between the electronic levels exceeds the thermal energy. In particular, carbon allotropes show interesting electrical properties which can be changed by varying their morphology. For a bulk material, the conductivity does not depend upon its dimensions. However, for carbon nanotubes it is found that conductivity changes when altering cross sections. It is further observed that conductivity varies when shear forces are applied to nanotubes. Moreover, conductivity of a multi-walled carbon nanotube is different compared to that of single nanotube. Depending on their chirality, carbon nanotubes can act as semiconductor or conductor, even though graphite is known to be a good conductor. Unique electrical properties are also reported for 2D carbon allotropes such as graphene, where promising applications in transparent conductive films or GHz transistors are discussed[79,80]. In most of these cases, synthesis, formulation and handling of nanoparticles are of utmost importance for quality control in the later applications (see the discussions in Chapter 5.24).

1.8.8 MAGNETIC PROPERTIES

Magnetic nanoparticles find wide application in industry, including magnetic recording media, biomedicine and separation technologies based on magnetic beads.[81–86] The desired magnetic properties of the nanoparticulate system depend strongly on its desired field of application. In the case of magnetic hard drives, particles need to possess stable, switchable magnetic states to allow for robust and energy efficient data storage. In contrast, superparamagnetic behavior at room temperature is preferred for particles applied in biomedicine.

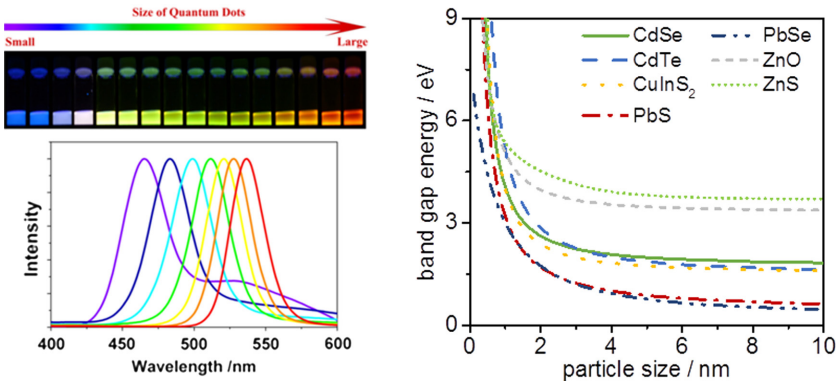


FIGURE 1.8.3 (Left) Sixteen emission colors from small (blue) to large (red) CdSe quantum dots excited by a near-ultraviolet lamp (top) and photoluminescence spectra of selected CdSe quantum dots (bottom). (Reprinted from Bera, et al., *Drug Delivery Nanoparticles Formulation and Characterization*, Pathak, Y. V., Thassu, D., Eds. CRC Press, Boca Raton, FL, 2009, pp. 349–366. With permission.) (Right) Size band gap correlation derived by fitting experimental data for CdSe,[70,71] CdTe,[16] $CuInS_2$,[72] PbS,[73] PbSe,[73] ZnO[74] and ZnS[75,76] nanoparticles.

Superparamagnetic nanoparticles based on a core consisting of iron oxides (SPION) are used for magnetic resonance imaging (MRI), tumor therapy or cardiovascular disease. Such nanoparticle systems are coated with biocompatible materials and can be easily targeted through external magnets. They can further be functionalized with drugs, proteins or plasmids for medical drug targeting.

Superparamagnetism appears in small ferromagnetic nanoparticles which are single-domain, where magnetization can randomly flip direction at room temperature. Thus, superparamagnetic nanoparticles will show only net magnetization in the presence of an external field, while ferromagnetic nanoparticles will maintain a net magnetization. The reaction of ferromagnetic materials on an applied field is described by a hysteresis loop, being characterized by two main quantities, the remanence and coercivity. The coercivity is related to the width of the hysteresis loop and is a measure of the ability of a ferromagnetic material to withstand an external magnetic field without becoming demagnetized.

Figure 1.8.4 depicts the coercivity as a function of particle size. It becomes apparent that the number of magnetic domains in a particle will decrease with its size, while the coercivity increases to a maximum and decreases towards zero for a superparamagnetic nanoparticle. The critical size of the single domain is described by the magnetic domain theory and is determined by several factors, which include the value of the magnetic saturation, the strength of the crystal anisotropy and exchange forces, surface or domain-wall energy and the shape of the particles.[88]

Superparamagnetism is observed for example for cobalt, nickel, iron, iron oxide (magnetite), nickel and cobalt nanoparticles, when diameters are below 3–50 nm, depending on the respective material. However, cobalt and nickel, both highly magnetic elements, are toxic and susceptible to oxidation. Therefore, they have to be coated, e.g. by a shell of silica which can be further functionalized for the respective application.

1.8.9 CATALYTIC PARTICLES

Heterogeneous catalysis is widely employed in the chemical industry for the production of chemicals, energy harvesting, conversion and storage as well as environmental technology. Typically, heterogeneous catalysts consist of finely dispersed nanoparticles anchored onto a more or less complex catalyst support in form of porous carrier particles or monoliths. The compositional and structural complexity of such nanoparticulate systems offers many degrees of freedom for tuning their catalytic performance.[89] The catalytic performance depends on the reactivity, selectivity and stability of the catalytic system.

Exemplarily, we highlight here only very few examples from systematic and particle size-dependent studies of gas phase reactions with noble metal model catalysts. The catalytic activity is a function of the binding energy of gas phase adsorbates on the nanoparticles and of the relative thermodynamic stabilities of the reaction intermediates which in turn depend on the local configuration of the adsorption site, and on particle size and shape. While the effect of local configuration of the adsorption site was found to be adsorbate specific, the reduction of the nanoparticle size results in a pronounced decrease of binding energy for both adsorbates and appears to be a general trend. This is depicted in Figure 1.8.5 for the case of CO adsorption on well-defined palladium nanoparticles on Pd/Fe_3O_4 (111)/Pt model.[89] The heat of adsorption decreases with smaller particle size for which two microscopic effects are discussed: (i) weakening of the chemisorptive interaction as a result of the decreasing average coordination number of atoms with higher surface-to-volume ratio (similar to the effects shown in Figure 1.8.1 and (ii) reduction of the van der Waals attraction with decreasing particle size.

Besides reactivity and selectivity, stability issues are of major importance in nanoparticle catalysis. Thermodynamics drives atoms into more stable and less-energetic states in larger particles. For instance, silver atoms are more stable in silver nanoparticles <4 nm when these are attached to CeO_{2-x} (111) and Fe_3O_4 (111) rather than to MgO (100) (see Figure 1.8.6). The differences get smaller with larger particles and completely vanish for particles >6 nm. Accordingly, sintering rates of silver nanoparticles are smaller on CeO_2 or Fe_3O_4 than on MgO.

The data are consistent with the following model:[90] the more weakly the surface metal atom is attached to the nanoparticle, the more strongly it binds small adsorbates. Its strength of attachment to the nanoparticle is dominated by the number of metal-metal bonds which bind it there, but also

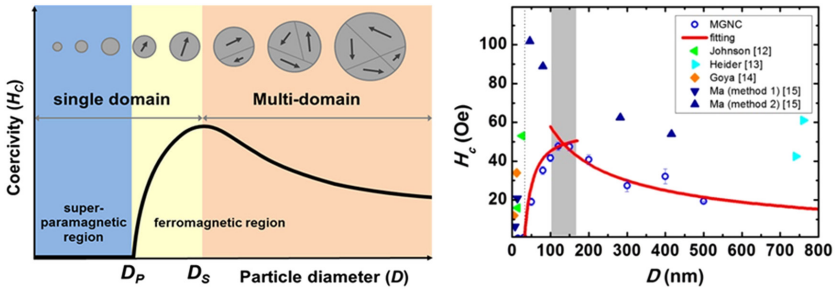


FIGURE 1.8.4 (Left) Schematic representation of the coercivity H_C change as a function of particle size. D_s is the critical size of multidomain/single domain transition, D_P is the critical particle size of ferromagnetic/superparamagnetic transition.[87] (Right) Variation of coercivity as a function of particle diameter D of magnetite (Fe_3O_4) multi-granule nanoclusters (MGNC).[87]

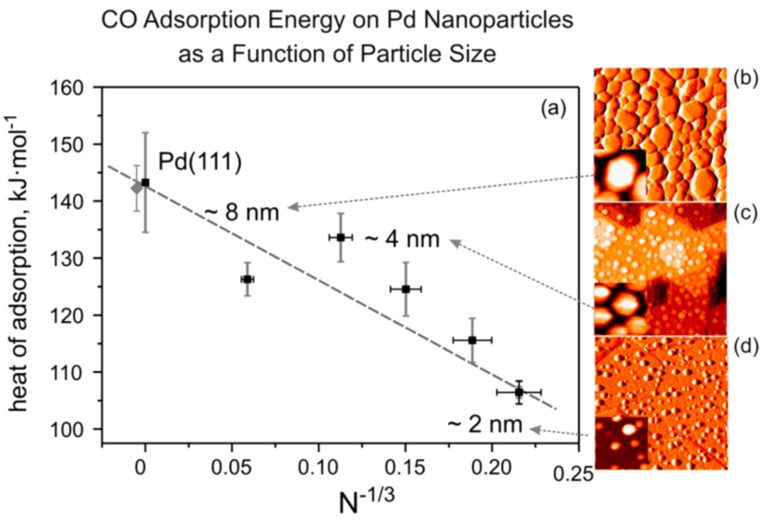


FIGURE 1.8.5 (a) Initial heat of adsorption of CO as function of palladium particle size, (b)–(d) STM images of $Pd/Fe_3O_4/Pt$ (111) model catalyst. (Reprinted from Schauermann et al., *Acc. Chem. Res.*, 46, 1673–1681, 2013. With permission Copyright (2013) American Chemical Society.)

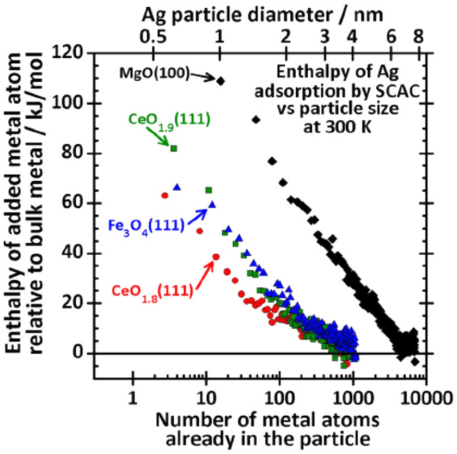


FIGURE 1.8.6 Measured heat of silver atom adsorption from the vapor phase on silver nanoparticles sitting on the respective surfaces. (Reprinted from Campbell, C. T., *Acc. Chem. Res.*, 46, 1712–1719, 2013. With permission. Copyright (2013) American Chemical Society.)

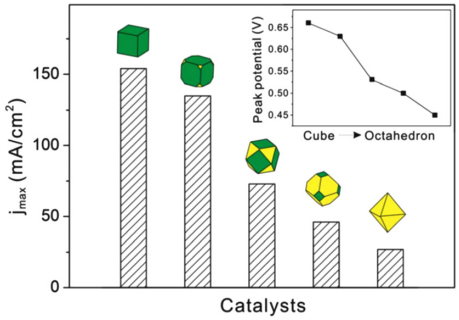


FIGURE 1.8.7 Maximum current densities of formic acid oxidation over palladium cubes, truncated cubes, cuboctahedrons, truncated octahedrons, and octahedrons enclosed by (111) and (100) facets in different proportions. The inset shows their corresponding peak potentials. (Reproduced from Jin et al., *Energ. Environ. Sci.*, 5, 6352–6357, 2012. With permission from The Royal Society of Chemistry.)

by the strength of metal/oxide interfacial bonding. This same combination of bond strengths controls sintering rates as well: the less stable a surface metal atom is in the nanoparticle, the greater is the thermodynamic driving force for it to sinter and the faster is its sintering rate. These correlations provide key insights into how and why specific structural properties of catalyst nanoparticles dictate their catalytic properties. For example, they explain why supported silver (and also gold) catalysts must contain nanoparticles smaller than about 6 nm to have high activity for combustion and selective oxidation reactions. Only below about 6 nm, metal atoms are so weakly attached to the catalyst that they bind oxygen sufficiently strongly to enable the activation of O_2.[90] For palladium nanocrystals it was shown that the performance for formic acid oxidation depends on the surface structure.[91] Figure 1.8.7 depicts the maximum current densities for structures with different proportions of {111} to {100} facets. It was found that nanocubes with slight truncation at the corners are the best choice for formic acid oxidation.

The shown phenomena of adsorption, catalytic activity, ripening and sintering obviously obey similar scaling rules as shown already in Figure 1.8.1 for the melting points of nanoparticles and for Young's modulus of the metals nanoparticles. A key parameter is always the number of low-coordinated surface atoms which is proportional to increasing specific surface area with decreasing particle size.

The shown structure-property relationships are rare examples extracted from simple model catalysts. In technical applications, catalyst particles and support surface structures are typically widely distributed in terms of size, shape and surface topology. It is also known that active catalysts change their size, shape and composition during catalytic conversion.

In particular, defects such as steps, kinks or stacking faults can play a prominent role as shown, for instance, for Cu/ZnO/Al_2O_3 methanol catalysts.[92] The preparation of defective nanoparticle-based catalysts and the control of their highly dynamic changes under real-life conditions is one of the grant challenges for the application nanoparticle science and technology in heterogeneous catalysis.

REFERENCES

1. Rumpf, H., Über die Eigenschaften von Nutzstäuben. *Staub-Reinhalt. der Luft*, 27, 3–13, 1967.
2. Naito, M., Yokoyama, T., Hosokawa, K., Nogi, K., *Nanoparticle Technology Handbook*, Elsevier Science, Amsterdam, 2018.
3. Aliofkhazraei, M., *Handbook of Nanoparticles*, Springer International Publishing, Heidelberg, 2015.
4. Schmid, G., *Nanoparticles: From Theory to Application*, Wiley, Weinheim, 2010.
5. Walter, J., Löhr, K., Karabudak, E., Reis, W., et al., *ACS Nano*, 8, 8871–8886, 2014.
6. Wang, S. C., Flagan, R. C., *Aerosol Sci. Technol.*, 13, 230–240, 1990.
7. Pecora, R., *J. Nanopart. Res.*, 2, 123–131, 2000.
8. Hoo, C. M., Starostin, N., West, P., Mecartney, M. L., *J. Nanopart. Res.*, 10, 89–96, 2008.
9. Giddings, J. C., *Science*, 260, 1456–1465, 1993.
10. Giddings, J. C., *Separ. Sci.*, 1, 123–125, 1966.
11. Dukhin, A. S., Goetz, P. J., *Characterization of Liquids, Nano- and Microparticulates, and Porous Bodies Using Ultrasound*, Elsevier Science, Amsterdam, 2010.
12. Mächtle, W., Börger, L., *Analytical Ultracentrifugation of Polymers and Nanoparticles*. Springer-Verlag, Berlin, 2006.
13. Pearson, J., Walter, J., Peukert, W., Cölfen, H., *Anal. Chem.*, 90, 1280–1291, 2018.
14. Karabudak, E., Cölfen, H., *Analytical Ultracentrifugation: Instrumentation, Software, and Applications*, Uchiyama, S., Arisaka, F., Stafford, W. F., Laue, T., Eds. Springer, Tokyo, 2016, pp. 63–80.
15. Akdas, T., Walter, J., Segets, D., Distaso, M., et al., *Nanoscale*, 7, 18105–18118, 2015.
16. Karabudak, E., Brookes, E., Lesnyak, V., Gaponik, N., et al., *Angew. Chem. Int. Ed.*, 55, 11770–11774, 2016.
17. Walter, J., Gorbet, G., Akdas, T., Segets, D., et al., *Analyst*, 142, 206–217, 2018.
18. Carney, R. P., Kim, J. Y., Qian, H., Jin, R., et al., *Nat. Commun.*, 2, 335, 2011.
19. Walter, J., Nacken, T. J., Damm, C., Thajudeen, T., et al., *Small*, 11, 814–825, 2015.
20. Fagan, J. A., Zheng, M., Rastogi, V., Simpson, J. R., et al., *ACS Nano*, 7, 3373–3387, 2013.
21. Thajudeen, T., Walter, J., Srikantharajah, R., Lübbert, C., et al., *Nanoscale Horiz.*, 2, 253–260, 2017.
22. Wang, J., Shin, W. G., Mertler, M., Sachweh, B., et al., *Aerosol Sci. Technol.*, 44, 97–108, 2010.
23. Eisenthal, K. B., *Chem. Rev.*, 106, 1462–1477, 2006.
24. Schürer, B., Wunderlich, S., Sauerbeck, C., Peschel, U., et al., *Phys. Rev. B*, 82, 241404, 2010.
25. Sauerbeck, C., Braunschweig, B., Peukert, W., *J. Phys. Chem. C*, 118, 10033–10042, 2014.
26. Dinkel, R., Braunschweig, B., Peukert, W., *J. Phys. Chem. C*, 120, 1673–1682, 2016.
27. Thomson, W., *London, Edinburgh Dublin Philos. Mag. J. Sci.*, 42, 448–452, 1871.
28. Gibbs, J. W., *Graphical Methods in the Thermodynamics of Fluids*, Connecticut Academy, New Haven, 1873.
29. Talapin, D. V., Rogach, A. L., Haase, M., Weller, H., *J. Phys. Chem. B.*, 105, 12278–12285, 2001.
30. Haderlein, M., Segets, D., Gröschel, M., Pflug, L., et al., *Chem. Eng. J.*, 260, 706–715, 2015.
31. Liu, Y., Kathan, K., Saad, W., Prud'homme, R. K., *Phys. Rev. Lett.*, 98, 036102, 2007.
32. Iggland, M., Mazzotti, M., *Cryst. Growth Des.*, 12, 1489–1500, 2012.
33. Damm, C., Segets, D., Yang, G., Vieweg, B. F., et al., *Small*, 7, 147–156, 2011.
34. Mersmann, A., *Crystallization Technology Handbook*, CRC Press, New York, 2001.
35. Mullin, J. W., *Crystallization*, Elsevier Science, Oxford, 2001.
36. Wulff, G., *Cryst. Mater.*, 34, 449, 1901.
37. Kingery, W. D., Bowen, H. K., Uhlmann, D. R., *Introduction to Ceramics*, Wiley, New York, 1976.
38. Kirchhof, M. J., Förster, H., Schmid, H. J., Peukert, W., *J. Aerosol Sci.*, 45, 26–39, 2012.
39. Friedlander, S. K., Wu, M. K., *Phys. Rev. B*, 49, 3622–3624, 1994.
40. Buffat, P., Borel, J. P., *Phys. Rev. A*, 13, 2287–2298, 1976.
41. Armstrong, P., Peukert, W., *J. Nanopart. Res.*, 14, 1288, 2012.
42. Meyers, M. A., Mishra, A., Benson, D. J., *Prog. Mater. Sci.*, 51, 427–556, 2006.
43. Gleiter, H., *Prog. Mater. Sci.*, 33, 223–315, 1989.
44. Meyers, M. A., Andrade, U. R., Chokshi, A. H., *Metall. Mater. Trans. A*, 26, 2881–2893, 1995.
45. Carlton, C. E., Ferreira, P. J., *Acta Mater.*, 55, 3749–3756, 2007.
46. Legros, R., Gianola, D. S., Motz, C., *MRS Bull.*, 35, 354–360, 2010.
47. Wang, Z. L., Poncharal, P., Heer, W. A. D., *J. Phys. Chem. Solids*, 61, 1025–1030, 2000.
48. Huang, J. Y., Chen, S., Wang, Z. Q., Kempa, K., et al., *Nature*, 439, 281, 2006.
49. Koch, C. C., *Nanostruct. Mater.*, 9, 13–22, 1997.
50. Mook, W. M., Nowak, J. D., Perrey, C. R., Carter, C. B., et al., *Phys. Rev. B*, 75, 214112, 2007.
51. Gerberich, W. W., Mook, W. M., Perrey, C. R., Carter, C. B., et al., *J. Mech. Phys. Solids*, 51, 979–992, 2003.
52. Deneen, J. N., Mook, W. M., Minor, A. M., Gerberich, W. W., et al., *J. Mater. Sci.: Mater. Med.*, 41, 4477–4483, 2006.
53. Brenner, S. S., *J. Appl. Phys.*, 28, 1023, 1957.
54. Kirchhof, M. J., Förster, H., Schmid, H.-J., Peukert, W., *J. Aerosol Sci.*, 45, 26–39, 2012.
55. Bernotat, S., Schönert, K., Size reduction. In *Ullmann's Encyclopedia of Industrial Chemistry*, Wiley-VCH Verlag GmbH & Co. KGaA, Weinheim, 5.1–5.39, 2000.
56. Knieke, C., Sommer, M., Peukert, W., *Powder Technol.*, 195, 25–30, 2009.
57. Knieke, C., Romeis, S., Peukert, W., *AIChE J.*, 57, 1751–1758, 2011.
58. Kendall, K., *Nature*, 272, 710–711, 1978.
59. Cortie, M. B., McDonagh, A. M., *Chem. Rev.*, 111, 3713–3735, 2011.
60. Anker, J. N., Hall, W. P., Lyandres, O., Shah, N. C., et al., *Nat. Mater.*, 7, 442, 2008.
61. Howes, P. D., Rana, S., Stevens, M. M., *Chem. Soc. Rev.*, 43, 3835–3853, 2014.
62. Linic, S., Christopher, P., Ingram, D. B., *Nat. Mater.*, 10, 911, 2011.
63. Catchpole, K. R., Polman, A., *Opt. Express*, 16, 21793–21800, 2008.

64. Ozbay, E., *Science*, 311, 189–193, 2006.
65. Olson, J., Dominguez-Medina, S., Hoggard, A., Wang, L.-Y., et al., *Chem. Soc. Rev.*, 44, 40–57, 2015.
66. Khlebtsov, N. G., *Anal. Chem.*, 80, 6620–6625, 2008.
67. Haiss, W., Thanh, N. T. K., Aveyard, J., Fernig, D. G., *Anal. Chem.*, 79, 4215–4221, 2007.
68. Brus, L., *J. Phys. Chem.*, 90, 2555–2560, 1986.
69. Bera, D., Qian, L., Holloway, P. H., *Drug Delivery Nanoparticles Formulation and Characterization*, Pathak, Y. V., Thassu, D., Eds. CRC Press, Boca Raton, FL, 2009, pp. 349–366.
70. Soloviev, V. N., Eichhöfer, A., Fenske, D., Banin, U., *J. Am. Chem. Soc.*, 122, 2673–2674, 2000.
71. Yu, W. W., Qu, L., Guo, W., Peng, X., *Chem. Mater.*, 15, 2854–2860, 2003.
72. Akdas, T., Haderlein, M., Walter, J., Apeleo Zubiri, B., et al., *RSC Adv.*, 7, 10057–10063, 2017.
73. Segets, D., Lucas, J. M., Klupp Taylor, R. N., Scheele, M., et al., *ACS Nano*, 6, 9021–9032, 2012.
74. Viswanatha, R., Sapra, S., Satpati, B., Satyam, P. V., et al., *J. Mater. Chem.*, 14, 661–668, 2004.
75. Nanda, J., Sapra, S., Sarma, D. D., Chandrasekharan, N., et al., *Chem. Mater.*, 12, 1018–1024, 2000.
76. Sapra, S., Sarma, D. D., *Phys. Rev. B*, 69, 125304, 2004.
77. Segets, D., Gradl, J., Taylor, R. K., Vassilev, V., et al., *ACS Nano*, 3, 1703–1710, 2009.
78. Segets, D., Komada, S., Butz, B., Spiecker, E., et al., *J. Nanopart. Res.*, 15, 1486, 2013.
79. Huang, X., Qi, X., Boey, F., Zhang, H., *Chem. Soc. Rev.*, 41, 666–686, 2012.
80. Sun, X., Sun, H., Li, H., Peng, H., *Adv. Mater.*, 25, 5153–5176, 2013.
81. Niemeyer, C. M., *Angew. Chem. Int. Edit.*, 40, 4128–4158, 2001.
82. Neuberger, T., Schöpf, B., Hofmann, H., Hofmann, M., et al., *J. Magn. Magn. Mater.*, 293, 483–496, 2005.
83. Faraji, M., Yamini, Y., Rezaee, M., *J. Iran Chem. Soc.*, 7, 1–37, 2010.
84. Tartaj, P., Morales, M. D. D., Veintemillas-Verdaguer, S., Gonzalez-Carreno, T., et al., *J. Phys. D: Appl. Phys.*, 36, R182–R197, 2003.
85. Alexiou, C., Tietze, R., Schreiber, E., Jurgons, R., et al., *J. Magn. Magn. Mater.*, 323, 1404–1407, 2011.
86. Nirschl, H., Keller, K., *Upscaling of Bio-Nano-Processes: Selective Bioseparation by Magnetic Particles.* Springer, Heidelberg, 2014.
87. Sung Lee, J., Myung Cha, J., Young Yoon, H., Lee, J.-K., et al., *Sci. Rep.*, 5, 12135, 2015.
88. Akbarzadeh, A., Samiei, M., Davaran, S., *Nanoscale Res. Lett.*, 7, 144, 2012.
89. Schauermann, S., Nilius, N., Shaikhutdinov, S., Freund, H.-J., *Acc. Chem. Res.*, 46, 1673–1681, 2013.
90. Campbell, C. T., *Acc. Chem. Res.*, 46, 1712–1719, 2013.
91. Jin, M., Zhang, H., Xie, Z., Xia, Y., *Energ. Environ. Sci.*, 5, 6352–6357, 2012.
92. Behrens, M., Studt, F., Kasatkin, I., Kühl, S., et al., *Science*, 336, 893–897, 2012.

1.9 Standard Powders and Particles

Hideto Yoshida

There are several standard particles currently in scientific use. For example, uniformly sized spherical polystyrene latex particles are used as a calibration standard in electron microscope studies. Natural pollens and spores are also mono-sized and nearly spherical, but they are sometimes swelled by moisture and have irregular surfaces. For example, the diameter of lycopodium particles measured by a microscope is about 30 μm, whereas it is about 24 μm when a liquid sedimentation method is used, because of their surface irregularities. A specially made precipitated calcium carbonate is also mono-sized and is cubic in shape.

Standard powders for industrial use generally have fairly narrow size distributions. In the United States, AC fine and coarse dusts are defined by the Society of Automotive Engineers and are utilized for performance tests of automobile air cleaners. They have the same size distributions as Japanese Standard Powders (JIS Z 8901) No.2 and No.3 or No.7 and No.8, respectively.

Japan has also defined many types of standard powders and particles for industrial tests as the JIS Z 8901. They are sold by the Association of Powder Process Industry and Engineering (APPIE), Japan. Figure 1.9.1 shows some information on their size distributions, and Table 1.9.1 lists the materials they are prepared from and applications. The No.8 Kanto loam powder is used mainly for the performance tests of automobile engine air cleaners in Japan, because it is easily dispersed in air by a mechanical or an air jet type powder disperser shown in Figures 1.9.2 and 1.9.3, respectively. Nearly mono-size glass beads and white fused alumina are also defined as JIS Z 8901, and their sizes are shown in Tables 1.9.2 and 1.9.3.

Table 1.9.4 presents several reference powders for certified size distributions, defined in Europe, and Table 1.9.5 presents several reference powders for the same purpose in the United States.

Recently, Japan also defined two types of standard powders, MBP1-10 and MBP10-100. For the MBP1-10 and 10–100 particles, the size ranges of particles are from 1 to 10 μm and 10 to 100 μm, respectively. They consist of barium titanate glass beads and their sizes are controlled to nearly log-normal distributions within the requested size range. Table 1.9.6 shows some of their physical properties and Figure 1.9.4 shows photographs of the test particles.

Figures 1.9.5 and 1.9.6 show particle size distributions, that were carefully measured by a scanning electron microscope with a particle count more than about 50000 particles. The symbols Q_0 and Q_3 indicate number and mass based cumulative size distributions. The particle size distribution includes the uncertainty region based on statistical theory. The committee of APPIE, Japan, recognizes these particles as a standard reference particle in Japan.[1,2]

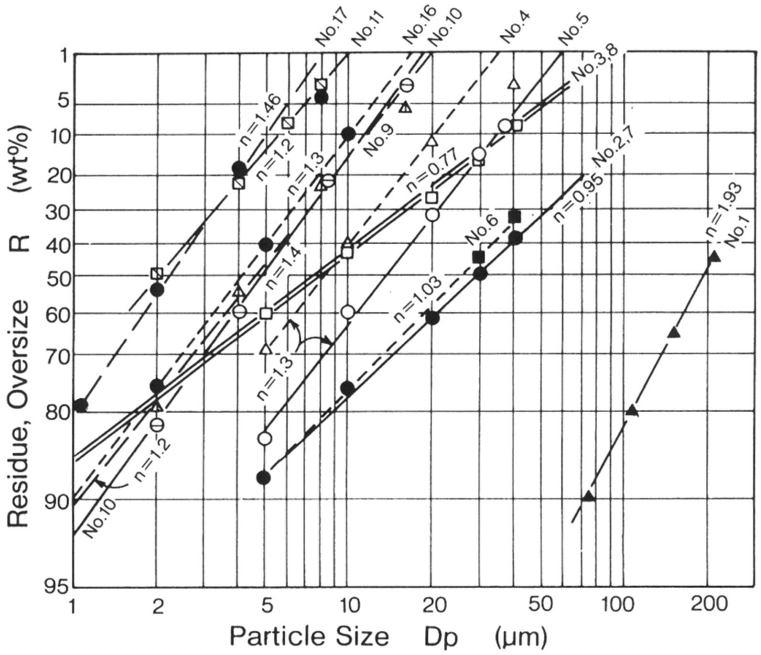


FIGURE 1.9.1 Size distributions of standard test powders (JIS Z 8901).

TABLE 1.9.1 Materials and Application Examples of Standard Particles (JIS Z8901)

Type	Material	Test Application Examples
No.1	Silica sand (coarse)	Abrasion or life test of machine; performance test of chemical plant
No.2	Silica sand (medium)	Abrasion or life test of machine
No.3	Silica sand (fine)	Abrasion or life test of machine
No.4	Talc (fine)	Dust collector performance test
No.5	Flyash (fine)	Dust collector performance test
No.6	Portland cement	Airtightness test of car lamps
No.7	Kanto loam (medium)	Dust collector performance test; abrasion or life test of machine
No.8	Kanto loam (fine)	Dust collector performance test; abrasion or life test of machine
No.9	Talc (ultrafine)	Performance test of high-efficiency dust collector air filter
No.10	Flyash (ultrafine)	Performance test of high-efficiency dust collector air filter
No.11	Kanto loam (ultrafine)	Performance test of high-efficiency dust collector air filter
No.12	Carbon Black (ultrafine)	Performance test of high-efficiency dust collector
No.15	Mixed dust	Prefilter performance test
No.16	Calcium carbonate (fine)	Performance test of dust collector and air classifier
No.17	Calcium carbonate (ultrafine)	Performance test of dust collector and air classifier

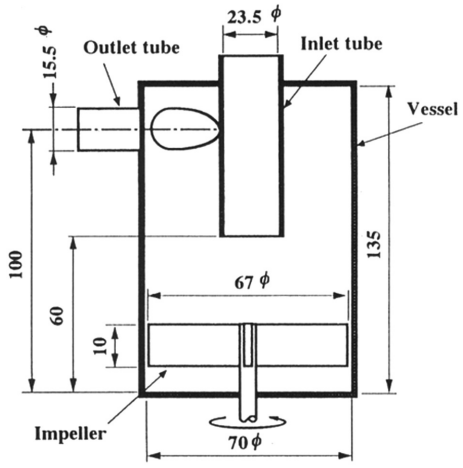


FIGURE 1.9.2 Mixer-type disperser.

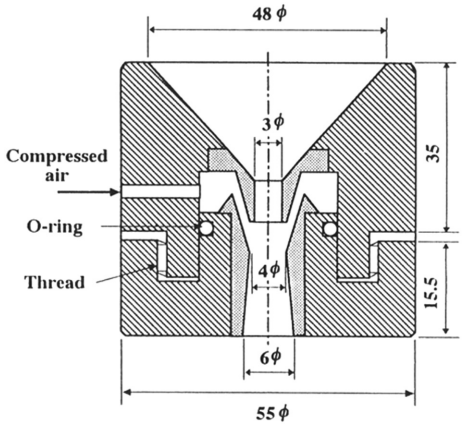


FIGURE 1.9.3 Nozzle-jet-type disperser.

TABLE 1.9.2 Size Distribution of Glass Beads Standard Powders in Japan (JIS Z 8901)

		Oversize in Mass Basis		
No.	Code[a]	90% Size (μm)	50% Median Size (μm)	10% Size (μm)
1	GBL30	>26	30 ± 1.0	<34
2	GBL40	>37	41 ± 1.0	<45
3	GBL60	>55	59 ± 1.0	<63
4	GBL100	>95	100 ± 1.0	<105
5	GBM20	>18	22 ± 1.0	<26
6	GBM30	>26	30 ± 1.0	<34
7	GBM40	>37	41 ± 1.0	<45

[a] GBL: sodalime silicate glass (ρ_p = 2.1–2.5 g/cm^3); GBM: barium titanate glass (ρ_p = 4.0–4.2 g/cm^3)

TABLE 1.9.3 Size Distributions of White Fused Alumina Standard Powder in Japan (JIS Z 8901)

	Oversize in Mass Basis		
No.	92% Size (μm)	50% Median Size (μm)	3% Size (μm)
1	>0.8	2 ± 0.4	<5
2	>2.0	4 ± 0.5	<11
3	>4.5	8 ± 0.6	<20
4	>9.0	14 ± 1	<31
5	>20	30 ± 2	<58
6	>40	57 ± 3	<103

Note: ρ_p = 3.9–4.0 g/cm^3

TABLE 1.9.4 IRMM—SMT in Europe (BCR Before 1995)

CRM No.	Description		Size Range (μm)	Unit Size	Price (ECU)
066	Quartz Powder	Stokes diam	0.35–3.50	10 g	125
067	Quartz Powder	Stokes diam	2.4–32	10 g	125
068	Quartz Sand	Vol. diam	160–630	100 g	125
069	Quartz Powder	Stokes diam	14–90	10 g	125
070	Quartz Powder	Stokes diam	1.2–20	10 g	125
130	Quartz Powder	Vol. diam	50–220	50 g	125
131	Quartz Powder	Vol. diam	480–1800	200 g	125
132	Quartz Gravel	Vol. diam	1400–5000	700 g	125
165	Latex	Sphere	2.223 ± 0.013	1 vial	100
166	Latex	Sphere	4.821 ± 0.019	1 vial	100
167	Latex	Sphere	9.475 ± 0.018	1 vial	100

CRM No.	Description	Specific Surface Area	Unit Size ($m^2 \cdot g^{-1}$)	Price (ECU)
169	Alpha Alumina	0.104 ± 0.012	60	100
170	Alpha Alumina	1.05 ± 0.05	50	100
171	Alumina	2.95 ± 0.13	50	100
172	Quartz	2.56 ± 0.10	10	100
173	Rutile Titania	8.23 ± 0.21	46	100
175	Tungsten	0.181 ± 0.031	200	100

Note: Joint Research Centre Institute for Reference Materials and Measurements (IRMM), Retieseweg, B-2440 Geel, Belgium. Attention: Management of Reference.
Materials (MRM) Unit. Tel.: 32 14 57 17 19, Fax: 32 14 59 04 06.
Standards, Measurements and Testing (SMT) Program.

TABLE 1.9.5 NIST-SRM (301) in the United States (1996)

SRM No.	Description	Particle Size (μm)	Unit Issued	Price (US $)	Certif. Date
114p	Portland cement	45 μm oversize 8.24%	Set (20)	114.00	May 94
659	Silicon nitride (particle size)	0.2–10	Set (5)	207.00	Mar. 92
1003b	Glass (particle size)	10–60	25 g	159.00	Sept. 93
1004a	Glass (particle size)	40–170	70 g	154.00	Dec. 93
1017b	Glass (particle size)	100–310	70 g	252.00	Aug. 95
1018b	Glass (particle size)	225–780	74 g	In prep.	–
1019a	Glass (particle size)	760–2160	200 g	179.00	Oct. 84
1690	Polystylene (particle size)	0.895	5 ml	391.00	Dec. 82
1691	Polystylene (particle size)	0.269	5 ml	39.00	May 84
1692	Polystylene (particle size)	2.982	5 ml	384.00	May 91
1960	Polystylene (particle size)	9.89	5 ml	805.00	Apr. 85
1961	Polystylene (particle size)	29.64	5 ml	806.00	Jan. 87
1963	Polystylene (particle size)	0.1007	5 ml	504.00	Nov. 93
1965	Polystylene (particle size)	9.94	1 slide	147.00	Jan. 87
1978	Zirconium oxide (particle size)	0.33–2.19	5 g	203.00	Oct. 93
8570	LGCGM calcined kaolin (surf. area)	10.3–10.9 m^2/g	10 g (25 g)	90.00	Sept. 94
8571	LGCGM alumina (surf. area)	153.2–158.7 m^2/g	10 g (25 g)	90.00	Sept. 94
8572	LGCGM silica (surf. area)	277.6–291.2 m^2/g	25 g	90.00	Sept. 94

Note: Purchase orders (in English) for all NIST SRMs/RMs should be directed to: National Institute of Standards and Technology (NIST). Standard Reference Materials Program (SRM), Room 204, Building 202, Gaithersburg, MD 20899-000l, USA; Tel.: (301) 975-6766, Fax: (301) 948-3730, e-mail: SRMINFO@enh.nist.gov.

TABLE 1.9.6 Physical Properties of Test Particles

	MBP1-10 n = 56728	MBP10-100 n = 51002
D_{p50} (μm) (mass base)	4.70	37.00
$\sigma = \ln\sigma_g$ (-)	0.312	0.395
σ_g (-)	1.37	1.48
ρ_p (g/cm^3)	4.19	4.10

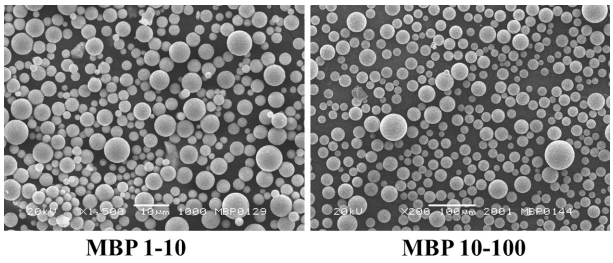


FIGURE 1.9.4 Photographs of reference particles.

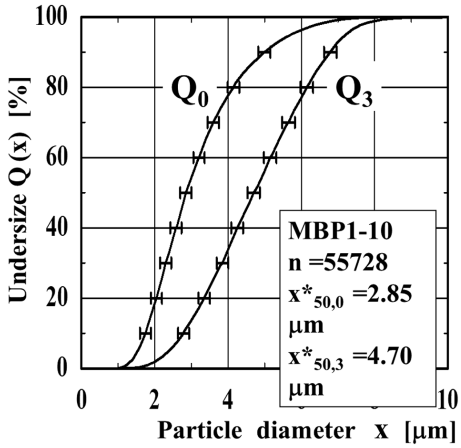


FIGURE 1.9.5 Particle size distribution with uncertainty region (MBP1-10).

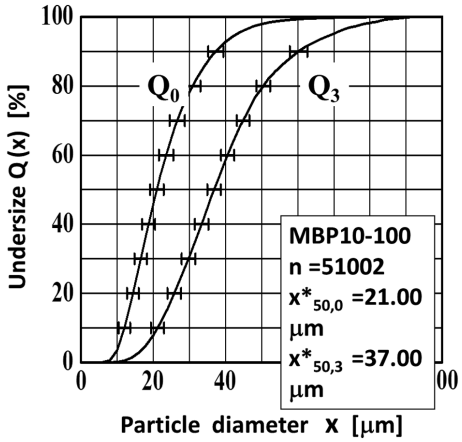


FIGURE 1.9.6 Particle size distribution with uncertainty region (MBP10-100).

REFERENCES

1. Yoshida, H., Masuda, H., et al. *Adv. Powder Technol.*, 12, 79–94, 2001.
2. Yoshida, H., Masuda, H., et al. *Adv. Powder Technol.*, 14, 17–31, 2003.

Part 2

Fundamental Properties of Particles



Taylor & Francis
Taylor & Francis Group
http://taylorandfrancis.com

2.1 Optical Properties

Yasushige Mori

2.1.1 DEFINITIONS

Light is electromagnetic radiation in the wavelength range from 3 nm to 30 μm. Visible light is the part of electromagnetic radiation to which the human eye is sensitive, and the wavelength of it ranges from 400 nm to 750 nm. When a light beam illuminates a particle having a dielectric constant different from unity, a part of the light will be reflected on the surface of particle, and the rest of the light will pass into the particle, as shown in Figure 2.1.1. The part of the light passed into the particle will go out as refraction, and the rest will be absorbed. When the particle size is much larger than the wavelength of the incident light, the light beam is diffracted near the particle. The scattering phenomenon of light includes diffraction, deflection, and refraction of light. The net results of the absorption and scattering caused by the particle are known as the extinction of incident light. In describing such optical phenomena, the size parameter α defined by the following expression may be important:

$$\alpha = \pi D_p / \lambda \tag{2.1.1}$$

where

D_p is the particle diameter,
λ is the wavelength of the incident light.

Another important definition is the refractive index. The refractive index of the medium is given by the ratio of the velocity of light in a vacuum, c, to that in the medium, v:

$$m_0 = c / v \tag{2.1.2}$$

This value is always larger than unity.

For an absorbing material having appreciable electrical conductivity, the refractive index is expressed as a complex number:

$$m_m = n_1 - i\, n_2 \quad \left(i = \sqrt{-1}\right) \tag{2.1.3}$$

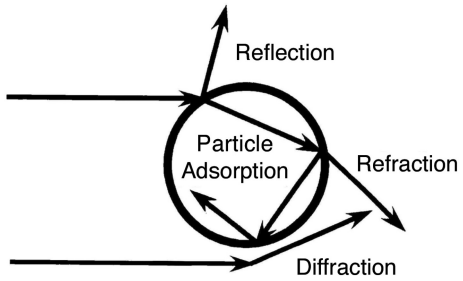


FIGURE 2.1.1 Scattering geometry.

The imaginary part n_2 is zero for nonabsorbing particles, as n_2 expresses the property of absorption of light. m is defined as the ratio of the complex refractive index of the absorbing material, m_m, and the refractive index of the medium, m_0, via

$$m = m_m / m_0 \tag{2.1.4}$$

2.1.2 LIGHT SCATTERING

Mie used electromagnetic theory to obtain the rigorous solution of light scattering by a uniform and spherical particle.[1] When unipolarized light of intensity I_0 illuminates a particle as shown in Figure 2.1.2, the scattering intensity at a distance r in the direction θ from the particle is given as

$$I = \frac{\lambda^2}{8\pi^2 r^2}\left(i_1 + i_2\right) I_0 \tag{2.1.5}$$

where i_1 and i_2 are the Mie intensity parameters for scattered light with perpendicular and parallel polarization against the observed plain, respectively. These parameters are expressed in the following equations as functions of m, α, and θ.[2]

$$i_1 = \left| \sum_{n=1}^{\infty} \frac{2n+1}{n(n+1)} \left\{ a_n\, \pi_n + b_n\, \tau_n \right\} \right|^2 \tag{2.1.6}$$

$$i_2 = \left| \sum_{n=1}^{\infty} \frac{2n+1}{n(n+1)} \left\{ b_n\, \pi_n + a_n\, \tau_n \right\} \right|^2 \tag{2.1.7}$$

$$a_n = \frac{\psi_n(\alpha)\psi_n'(m\alpha) - m\psi_n'(\alpha)\psi_n(m\alpha)}{\zeta_n(\alpha)\psi_n'(m\alpha) - m\zeta_n'(\alpha)\psi_n(m\alpha)} \tag{2.1.8}$$

$$b_n = \frac{m\psi_n(\alpha)\psi_n'(m\alpha) - \psi_n'(\alpha)\psi_n(m\alpha)}{m\zeta_n(\alpha)\psi_n'(m\alpha) - \zeta_n'(\alpha)\psi_n(m\alpha)} \tag{2.1.9}$$

where ψ_n' and ζ_n' means the first derivative of ψ_n and ζ_n, respectively. The functions ψ_n and ζ_n are related to the Bessel (J_n) and second-order Hankel $\left(H_n^{(2)}\right)$ functions via

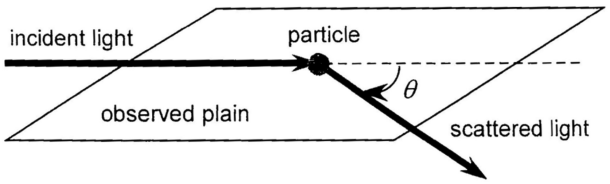


FIGURE 2.1.2 Scattering and diffraction of light.

$$\psi_n(x) = \sqrt{\frac{\pi\alpha}{2}} J_{n+1/2}(x) \tag{2.1.10}$$

$$\zeta_n(x) = \left(\frac{x\pi}{2}\right)^{1/2} H^{(2)}_{n+\frac{1}{2}}(x) \tag{2.1.11}$$

where x is equal to α or $m\alpha$.

Figure 2.1.3 shows the angular distribution of scattered intensity calculated for uniform spheres with size parameter α and $m = 1.2$. The intensity of scattered light becomes a minimum at a scattering angle between 90° and 150°. Figures 2.1.4 (a) and (b) show the effect of the ratio of the refractive index m on the intensity of scattered light for $\alpha = 2$ and 5, respectively. The dependency of the scattering angle on the intensity of scattered light can be roughly estimated when fused silica ($m = 1.05$), polystyrene latex, alumina, quartz, soda lime glass ($m = 1.2$), barium titanate glass ($m = 1.5$), and titania ($m = 2.0$) particles with $\alpha = 2$ or 5 are dispersed in water. For absorbing particles having the imaginary part of refractive index n_2, the fluctuation of the scattered intensity decreases with the value of n_2.

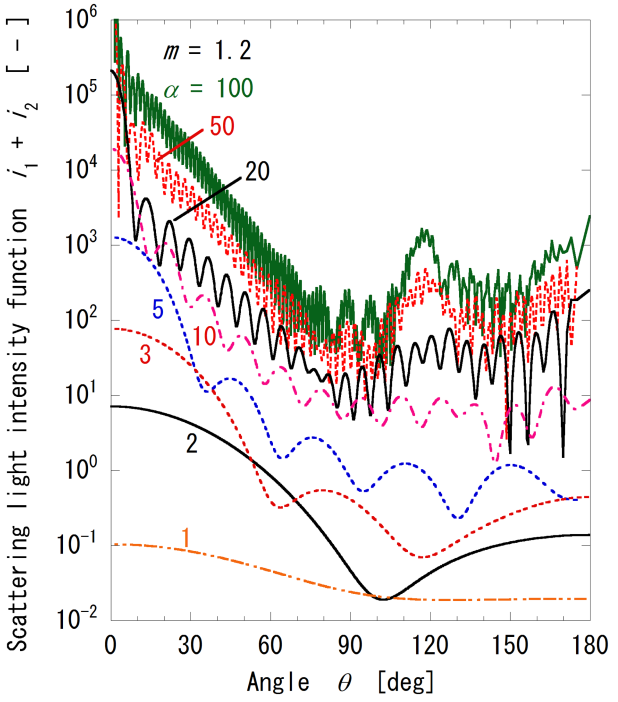


FIGURE 2.1.3 Angular distribution of scattered intensity for uniform sphere with $m = 1.2$.

If a particle is much smaller than the wavelength of light ($m\alpha < 0.5$), the contribution of the nth term rapidly decreases as n increases in Equations (2.1.6 and 2.1.7). When the values of a_n and b_n are adopted to a sum of $n = 1$ and 2, and a value only of $n = 1$, respectively, and the value for higher than α^3 is neglected, the Rayleigh scattering equation is obtained:

$$I = \frac{\pi^4 D_p^6}{8r^2\lambda^4}\left(\frac{m^2-1}{m^2+2}\right)^2 \left(1+\cos^2\theta\right) I_0 \tag{2.1.12}$$

In the Rayleigh scattering regime ($\alpha < 2$), the scattered intensity is proportional to the sixth power of the particle size, as shown as Equation (2.1.12). In the Mie scattering regime ($\alpha = 2$–10), the scattered intensity increases with particle size while fluctuating. In the geometrical optics regime ($\alpha > 10$), the intensity increases as the square of particle size, and the intensity fluctuation is more drastic than in the Mie scattering regime.

When the particle size is much larger than the wavelength ($\alpha > 300$), the light beam is diffracted near the particle, as shown in Figure 2.1.1 or Figure 2.1.5. For a low diffraction

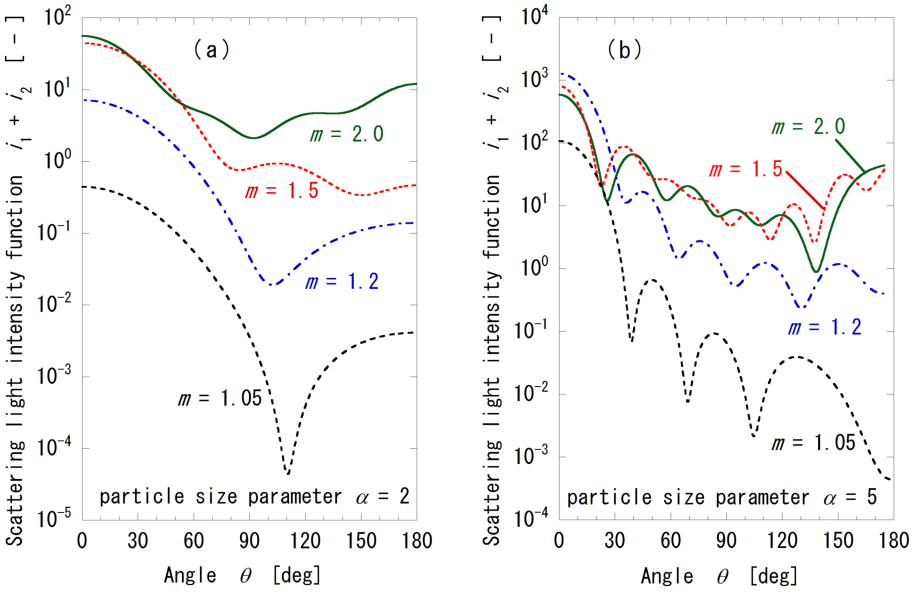


FIGURE 2.1.4 Angular distribution of scattered intensity for uniform sphere with various ratio of the refractive indexes of the absorbing material and the medium. (a) size parameter $\alpha = 2$, (b) $\alpha = 5$.

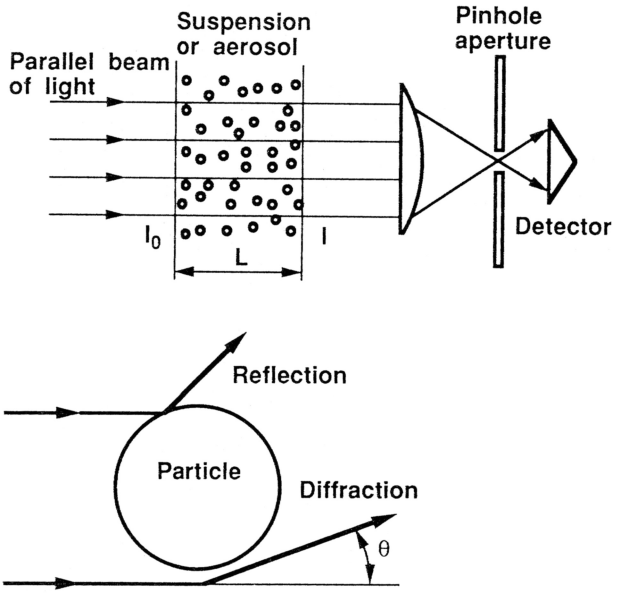


FIGURE 2.1.5 Setup for light-extinction measurements.

angle ($\theta < 10°$), the angular distribution of the intensity of diffracted beam $I(\theta)$ is given by the Fraunhofer formula:

$$I(\theta) = \frac{\pi^4 D_p^6}{4\lambda^4}\left\{\frac{J_1(\alpha \sin\theta)}{a\sin\theta}\right\}^2 I_0 \tag{2.1.13}$$

where $J_1(\alpha \sin \theta)$ is the first-order Bessel function. As the intensity of the Fraunhofer diffraction depends on the particle size and is independent of the refractive index of the particle material, this fact is often useful in particle-sizing applications.

The light scattering technique is nowadays one of the typical particle size analysis methods.[3] However it is difficult to apply to nonuniform and nonspherical particles for the above theory. The analysis for nonuniform[4] and nonspherical particles[5] was made. Mishchenko et al. recently published a book on light scattering by nonspherical particles in which theoretical and numerical techniques are also included.[6]

2.1.3 LIGHT EXTINCTION

Aerosol particles or colloidal particles illuminated by a light beam absorb some light, as well as scatter. Thereby, the intensity of the light beam diminishes, as shown in Figure 2.1.5. According to the Lambert–Beer law, the light extinction can be expressed by

$$I = I_0 \exp(-K L) \tag{2.1.14}$$

where I_0 and I are respectively the intensity of incident light and the intensity at penetrated distance L. K is the turbidity given as

$$K = N Q_{ext}(D_p) \tag{2.1.15}$$

where N is the particle number concentration, and $Q_{ext}(D_p)$ is the extinction cross section of one particle, whose projected area equivalent diameter is D_p. As the extinction cross section of a particle is the sum of its scattering cross section and its absorption cross section, the following relation for monodisperse particles holds:

$$Q_{ext} = Q_{scat} + Q_{abs} \tag{2.1.16}$$

where Q_{scat} and Q_{abs} are respectively the scattering and absorption cross sections. For a spherical particle, Q_{ext} and Q_{scat} can be calculated when Equation (2.1.5) is integrated on all solid angle.[7]

$$Q_{scat} = \frac{\lambda^2}{2\pi}\sum_{n=1}^{\infty}(2n+1)\left(|a_n|^2 + |b_n|^2\right) \tag{2.1.17}$$

$$Q_{ext} = \frac{\lambda^2}{2\pi}\sum_{n=1}^{\infty}(2n+1)\left(Re\{a_n + b_n\}\right) \tag{2.1.18}$$

where $Re\{\}$ means the calculation only of the real part. As Q_{scat}, Q_{abs}, and Q_{ext} have the dimension of area, the nondimensional values are obtained from the division by the projected area of a particle and named the scattering, absorption, and extinction efficiencies, respectively. When the sample of particles has a size distribution, the turbidity can be expressed as follows:

$$K = N_T \int_0^{\infty} Q_{ext}(D_p) q_0(D_p) dD_p \tag{2.1.19}$$

where

N_T is the total particle number concentration,
$q_0(D_p)$ is the density distribution of particles on a number basis.

If the particle number concentration is sufficiently high, the light scattered by each particle illuminates other particles. When such multiscattering occurs, the coefficient Q_{ext} should be corrected.[8]

2.1.4 DYNAMIC LIGHT SCATTERING

Dynamic light scattering has been used for the size measurement of particles between about 3 nm and 5 μm in diameter.[9] When fine particles are illuminated by monochromatic light, a fluctuating scattering intensity occurs due to the Brownian motion of the particles. The fluctuation is correlated to the diffusion coefficient D of the particles.[10]

$$D = \frac{kTC_c}{3\pi\mu D_p} \tag{2.1.20}$$

where

k is Boltzmann's constant,
T is temperature,
C_c is the slip correction factor,
μ is viscosity of the medium.

From this relationship, the particle size D_p can be determined. The advantage of this measurement is that it is independent of the particle refractive index.

Several techniques have been developed for dynamic light scattering. These techniques can be classified in two ways: by the difference in data analysis (photon correlation spectroscopy and frequency analysis method) and by the difference in optical setup (homodyne and heterodyne detection optics). The scattered light from each particle is mixed with either light scattered from the rest of the particles (homodyne) or with light from the incident beam (heterodyne). The detector signal has two components: a constant level, representing the average intensity of the collected light, and a time-varying component, representing the dynamic light scattering effect. The time-dependent component is analyzed by following two methods: time-based correlation function (photon correlation spectroscopy) or frequency-based power spectrum (frequency analysis method).

The normalized intensity autocorrelation function for photon correlation spectroscopy is defined by

$$g^{(2)}(\tau) = \frac{\langle I(t)I(t+\tau)\rangle}{\langle I(t)\rangle^2} \tag{2.1.21}$$

where $I(t)$ and $I(t+\tau)$ are the scattered intensities at time t and $t+\tau$, respectively. The autocorrelation function of the scattered intensity is related to the electric field correlation function, $g_1(\tau)$:

$$g^{(2)}(\tau) = 1 + B\left|g_1(\tau)\right|^2 \tag{2.1.22}$$

where B is an instrumental factor. $g_1(\tau)$ is also expressed as follows:

$$g_1(\tau) = \exp(-\Gamma\tau) \tag{2.1.23}$$

$$\Gamma = Dq^2 \tag{2.1.24}$$

$$q = \frac{4\pi n \sin(\theta/2)}{\lambda_0} \tag{2.1.25}$$

where

n is the refractive index of the dispersion medium,
λ_0 is the wavelength of the laser in vacuum,
θ is the scattering angle.

In the frequency analysis method, the power spectrum for homodyne and heterodyne detection optics are given by

$$p(\omega) = \frac{2\Gamma}{\omega^2 + (2\Gamma)^2} \tag{2.1.26}$$

for homodyne detection optic

$$p(\omega) = \frac{2\Gamma}{\omega^2 + \Gamma^2} \tag{2.1.27}$$

for heterodyne detection optic

When the particle sample has a size distribution, $g_1(\tau)$ and $p(\omega)$ are related to the normalized distribution function of decay rates $G(\Gamma)$, which is a function of particle diameter as shown as Equations (2.1.20 and 2.1.24).

$$g_1(\tau) = \int_0^\infty G(\Gamma)\exp(-\Gamma\tau)\,d\Gamma \tag{2.1.28}$$

$$p(\omega) = \int_0^\infty G(\Gamma)\frac{2\Gamma}{\omega^2 + (2\Gamma)^2}\,d\Gamma \tag{2.1.29}$$

for homodyne detection optic

$$p(\omega) = \int_0^\infty G(\Gamma)\frac{2\Gamma}{\omega^2 + \Gamma^2}\,d\Gamma \tag{2.1.30}$$

for heterodyne detection optic

The average diameter of sample is calculated by

$$\frac{1}{D_p} = \int_0^\infty \frac{1}{x}G(\Gamma)\,d\left(\frac{1}{x}\right) \tag{2.1.31}$$

2.1.5 PHOTOPHORESIS

The mechanism of photophoresis is similar to that of thermophoresis. When a very small particle is illuminated from one side, a temperature gradient is induced in the particle. The difference of strength of the gas molecule impact on the particle causes the particle to move in the direction opposite to the illuminated side. Because photophoresis is a result of an interaction between the particle and the surrounding gas molecules, it cannot occur in the cases of nonabsorbing particles or in a vacuum. The photophoresis force depends on the light intensity and wavelength, the size, shape, and material of the particle, and the gas pressure. Although the evaluation of the force is rather difficult, some analysis has been proposed,[11] and measurement data have been obtained.[12]

REFERENCES

1. Mie, G., *Ann. Phys.*, 25, 377, 1908.
2. Kerker, M., *The Scattering of Light and Other Electromagnetic Radiation.* Academic Press, New York, 1969.
3. Xu, R., *Particle Characterization: Light Scattering Methods.* Kluwer Academic, Dordrecht, 2000.
4. Druger, S. D., Kerker, M., Wang, D. S., Cooke, D. D., *Appl. Opt.*, 18, 3888, 1979.
5. Schuerman, D. W., *Light Scattering by Irregularly Shaped Particles.* Plenum Press, New York, 1980.
6. Mishchenko, M. I., Hovenier, J. W., Travis, L. D., Eds. *Light Scattering by Nonspherical Particles: Theory, Measurements, and Applications.* Academic Press, San Diego, CA, 2000.

7. Hodkinson, J. R., In *Aerosol Science*, Davies, C. N., Ed. Academic Press, New York, 1966, pp. 287–324.
8. Born, M., Wolf. E., *Principles of Optics*, Pergamon Press, Elmsford, NY, 1970.
9. Russel, W. B., Saville, D. A., Schowalter, W. R., *Colloidal Dispersions*, Cambridge University Press, Cambridge, 1989, p. 441.
10. Berne, B., Pecora, R., *Dynamic Light Scattering.* John Wiley and Sons, New York, 1976.
11. Kerker, M., Cooke, D. D., *Opt. Soc. Am.*, 72, 1267, 1982.
12. Lin, H. B., Campillo, A. J. *Appl. Opt.*, 24, 422, 1985.



Taylor & Francis
Taylor & Francis Group
http://taylorandfrancis.com

2.2 Electrification and Electrophoresis

Shuji Matsusaka and Hiroaki Masuda (2.2.1)
Hiroyuki Shinto and Tomonori Fukasawa (2.2.2)

2.2.1 IN GASEOUS STATE

Contact Electrification

When two different metallic materials come into contact, the electrons in the metal with a higher Fermi level move into the other metal, equalizing the Fermi levels of the two materials. Then, the number of electrons in the material with a lower Fermi level increases, resulting in electrification to negative charge. As a matter of course, the other material is electrified to positive charge.

When the contact region acts as an electrical capacitor, the amount of charge stored Δq in the capacitor can be estimated by the following equation.

$$\Delta q = C\, V_c \tag{2.2.1}$$

where

- C is the capacitance, which depends on the state of the contacting surfaces,
- V_c is the contact potential difference.

Assuming the contact surfaces are parallel planes, the capacitance is given by

$$C = \frac{\varepsilon S}{z} \tag{2.2.2}$$

where

- ε is the permittivity of the gas. When the gas is in air, ε is close to the vacuum permittivity ε_0 (8.85×10^{-12} F/m),
- S is the contact area,
- z is the gap between the surfaces.

The contact potential difference V_c is related to the difference in the surface work function ϕ:

$$V_c = V_{1/2} = -\frac{(\phi_1 - \phi_2)}{e} \tag{2.2.3}$$

where

- $V_{1/2}$ is the contact potential difference between material 1 and material 2,
- e is the elemental charge (1.602×10^{-19} C).

Finally, the driving force for the charge transfer between the surfaces is the difference in the work functions of the two surfaces.[1]

The electrification of a nonconductive material is complicated, however, for metal–insulator contacts, the charge transfer can often be explained by a concept similar to that of the metal-to-metal electron transfer. This assumes an apparent or effective work function to be assigned to the insulator. The amount of the transferred charge is determined to equalize the energy levels of the two materials. For insulator–insulator contacts, several modified models have been presented.[2] Some of them are similar to those for insulator–metal contact; however, the movement of electrons in the body is more restricted. In one of the models, it is assumed that the available energy levels of electrons are only on surface, not in bulk, and the available level is called the surface state.[3] When the insulators come into contact, electrons move from the filled surface states of one insulator to the empty surface states of the other. The driving force for the charge transfer between the surfaces is the difference in the effective work functions of the two surfaces. The charge transfer will cease when the Fermi levels of the two materials coincide with each other.

In addition, when the contact bodies are separated, the charges are partially neutralized or discharged through the surrounding medium. This process is called charge relaxation.[4] The maximum charge of a spherical particle is controlled by the discharge from the surface of the particle. The breakdown condition in air is given by an electric field strength of 3 MV/m for particles larger than 200 μm and a surface potential of 300 V for those smaller than 200 μm.[5]

Electrification of a Particle by Impact

Charge transfer between impacted materials proceeds during the very short time of collision. Such high-speed electrification will be represented by[6]:

$$\Delta q = CV_c\left[1 - \exp\left(-\frac{\Delta t}{\tau}\right)\right] \tag{2.2.4}$$

where

- τ is the time constant for electrification,
- Δt is the effective duration of contact.,

Equation (2.2.4) shows that metallic particles ($\tau << \Delta t$) may be highly electrified by impact as long as the back discharge is negligible.[7] For nonconductive particles, τ is given by

$$\tau = \varepsilon\, \rho_d \tag{2.2.5}$$

where ρ_d is the specific resistance of the particle. The charge transferred is given by

$$\Delta q_d = \frac{SV_c}{z\rho_d}\Delta t \tag{2.2.6}$$

Equation (2.2.6) shows that the perfect insulator ($\rho_d \to \infty$) does not acquire charge, which coincides with the experimental results obtained by the use of solid rare gases.[8]

The contact area S depends on the mode of impact. It is nearly proportional to the impact velocity v for inelastic collisions and proportional to $v^{0.8}$ for elastic collisions. In both cases, it is proportional to the square of the particle size.[6]

If the particles collide with the wall several times, they are all electrified and produce a strong electric field. Further, the contact potential difference V_c is affected by both the electric field and the image charge of the particle. The electrification process, including the electric field effect and the image-charge effect, is represented by the following equation:[9,10]

$$\Delta q = q_0 \exp\left(-\frac{N}{N_0}\right) + q_\infty\left[1-\exp\left(-\frac{N}{N_0}\right)\right] \tag{2.2.7}$$

where

- N is the number of collisions of a particle,
- N_0 is the relaxation number of collisions for charge transfer,
- q_0 is the initial charge of the particle,
- q is the final charge attainable in the process.

In gas-solid pipe flow, particle charging depends on other factors, such as the number of particle collisions, the initial charge on the particles, and the state of impact charging. The value of each factor is spread, and therefore, the particles have a distribution after passing through the pipe. The charge distribution on the particles can be estimated with the distribution of the factors.[11]

Electrification of a Particle through Breakage

The electric charge of particles after breakage is represented by a normal distribution with zero mean. Electrification through breakage is caused by the unequal partition of positive or negative charges. The electrification of particles in a crusher is caused by both the contact between different materials (particles and the wall) and breakage. Therefore, the mean value of the charge is no longer zero. Further, smaller particles produced through breakage are apt to take a negative charge because the work function will be higher.[12]

The charge distribution of mist produced through atomization of a water solution is symmetrical. The absolute mean is given by[13]

$$\left|\bar{n}_e\right| = \sqrt{\frac{2}{3}N_i D_p^{1.5}} \tag{2.2.8}$$

where

- $\bar{n}_e$ is the average number of elementary charge,
- N_i is the number density of ions,
- D_p the particle diameter.

Motion of a Charged Particle

When a charged particle is in an electric field, the following force (Coulomb force) will act on it:

$$\mathbf{F} = q\mathbf{E} \tag{2.2.9}$$

where

- $\mathbf{F}$ is the force (N),
- q is the charge (C),
- $\mathbf{E}$ is the strength of the electric field (V/m).

The movement of charged particles produces an electric current, which is affected by a magnetic field, and the force acting on a charged particle is given by

$$\mathbf{F} = q\mathbf{E} + q\mathbf{v}\times\mathbf{B} \tag{2.2.10}$$

where

- $\mathbf{v}$ is the particle velocity (m/s),
- $\mathbf{B}$ is the magnetic flux density (T).

The electrostatic force between the particle and a body with electric charge dq is given by

$$dF = \frac{q}{4\pi\varepsilon r^2}dq \tag{2.2.11}$$

where r is the distance between the particle and the charged body. When the electric charges are distributed on various surrounding bodies, integration of Equation (2.2.11) will give the total force acting on the particle. The velocity and trajectory of a charged particle in a uniform electric field can be obtained by solving an equation of motion, including the Coulomb force term. For example, the terminal velocity v_{et} in an electric field is obtained as

$$v_{et} = \frac{qEC_c}{3\pi\mu D_p} \tag{2.2.12}$$

where

- C_c is Cunningham slip correction factor,
- μ is the viscosity of fluid.

The particle velocity under unit strength of the electric field v/E is called the electric mobility.

Electrically charged particles produce an electric field, which is calculated by Poisson's equation

$$\operatorname{div}\mathbf{E} = \frac{\rho}{\varepsilon} \tag{2.2.13}$$

TABLE 2.2.1 Electric Field Produced by Electrically Charged Particles

	In Cylindrical Tube (E_r [V/m])	Between Parallel Plates (E_x [V/m])	In Spherical Vessel (E_r [V/m])
Inside	$\frac{1}{2}\frac{\rho}{\varepsilon}r$	$\frac{\rho}{\varepsilon}x$	$\frac{1}{3}\frac{\rho}{\varepsilon}r$
Outside	$\frac{1}{2}\frac{\rho}{\varepsilon}\frac{r_0^2}{r}$	$\frac{\rho}{\varepsilon}x_0$	$\frac{1}{3}\frac{\rho}{\varepsilon}\frac{r_0^3}{r^2}$

where ρ is the space-charge density (C/m^3). Table 2.2.1 lists the strength of electric fields for one-dimensional cases. Unipolar charged particles repulse each other and gradually disperse. This phenomenon is called electrostatic dispersion or diffusion. Particle deposition on a wall is enhanced by the electrostatic effect, as estimated by the following Wilson equation,[14] both for a circular tube and a parallel-plate channel: [15]

$$\eta = \frac{t/t_0}{1 + t/t_0} \tag{2.2.14}$$

where

η is the deposition fraction,
t is the residence time,
t_0 is the half-life.

The half-life is given by

$$t_0 = \frac{3\pi\,\mu\,D_p\,\varepsilon}{n_0\,q^2\,C_c} \tag{2.2.15}$$

where

n_0 is the number concentration (m^{-3}),
D_p is the equivalent volume diameter.

A charged particle near the equipment wall will be affected by the image force, which is always attractive. If the particle is assumed to be a point charge, this force is given by

$$F = -\frac{q^2}{16\pi\,\varepsilon\,r^2} \tag{2.2.16}$$

where r is the distance from the wall. For a nonconductive wall of relative permittivity ε_{rw}, the force is given by

$$F = -\frac{q^2}{16\pi\,\varepsilon\,r^2}\frac{\varepsilon_{rw} - 1}{\varepsilon_{rw} + 1} \tag{2.2.17}$$

If point charge assumption does not hold, an infinite set of images should be adopted.[16]

A particle in an electric field attracts other particles, even if the particle is not charged, because the electric field is distorted by the particle. The force acting on a particle in a distorted electric field is given by[17]

$$F = \frac{1}{4}\pi D_p^3 \varepsilon \frac{\varepsilon_{rp} - 1}{\varepsilon_{rp} + 2}\,\mathrm{grad}\,|\mathbf{E}|^2 \tag{2.2.18}$$

where ε_{rp} is the relative permittivity of the particle.

2.2.2 IN LIQUID STATE[18]

The charging mechanism and charge amount of the particles immersed in liquids are the fundamental information to predict and control the stability of particle suspensions and the adhesion of particles onto substrates. In this section, let us consider briefly (i) several charging mechanisms of particles in aqueous solutions, (ii) the electric double layer, which is an ion atmosphere formed around a charged particle, (iii) the zeta potential of a particle, which is a measure of its surface charge density, (iv) electrophoresis, where charged particles migrate under an external electric field, and (v) several theories that link the electrophoretic mobility with the zeta potential. Finally, several methodologies for zeta potential measurements are concisely tabulated with the commercially available instruments. Unless otherwise noted, the chief focus is located on nonconductive particles immersed in aqueous solutions. Suspensions of conductive and semiconductive particles, and non-aqueous suspensions are beyond the scope of the present section and explained elsewhere.[19–21]

2.2.2.1 Surface Charging of Particulate Substances in Aqueous Solutions

When particulate substances are dispersed in aqueous solutions, their surfaces become more or less electrically charged. The following are some examples of charging mechanisms that largely depend on the physicochemical properties of both the particulate substances and their surrounding solutions.

Sparingly Soluble Crystals[19–22]

Silver iodide (AgI) crystal sparingly dissolves in water to generate Ag^+ and I^- ions and their bulk ion concentrations in equilibrium satisfy the solubility product constant of $K_{sp} = [Ag^+][I^-] = 7.5 \times 10^{-17}$ mol^2/L^2 at 25°C. Dissolution of Ag^+ ions from the crystal lattice is more significant than that of I^- ions, resulting in the negatively charged surface of the crystal.

When a readily soluble Ag-containing salt such as $AgNO_3$ is added thereto subsequently, Ag^+ ions enter the crystal lattice of AgI and eventually the sign of the surface charge reverses from negative to positive. Addition of a readily soluble KI salt causes the entry of I^- ions into the crystal lattice and results in another reversal in sign of the surface charge from positive to negative. The bulk ion concentrations at the *point of zero charge* (pzc) are found to be $[Ag^+]_{pzc} = 3.0 \times 10^{-6}$ mol/L and $[I^-]_{pzc} = 2.5 \times 10^{-11}$ mol/L. As for AgI crystals, Ag^+ and I^- ions work as *potential-determining ions*, while NO_3^- and K^+ ions behave as *indifferent (non-potential-determining) ions*. The surface electric potential of the AgI crystal varies with pAg $\equiv -\log[Ag^+]$, as shown schematically by curve (A) in Figure 2.2.1. Other sparingly soluble crystals such as AgCl, AgBr,

and Ag_2S employ the same charging mechanism to have their concentrations of the potential-determining ions at pzc as in Table 2.2.2.

The surface electric potential ψ_0 of the sparingly soluble crystals versus the bulk solution is represented by the Nernst equation:

$$\psi_0 = \frac{kT}{ze} \ln\left(\frac{[M^{z+}]}{[M^{z+}]_{pzc}}\right) \tag{2.2.19}$$

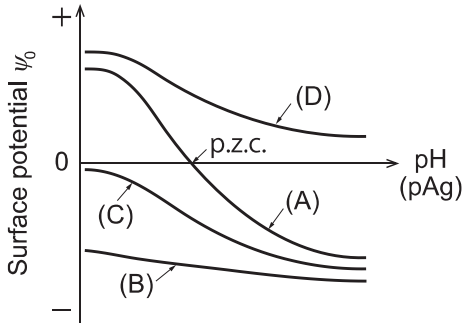


FIGURE 2.2.1 Surface electric potentials of different particles in aqueous solutions as a function of pH or pAg: (A) AgX crystals (X = Cl, Br, and I), oxides, and amphoteric particles; (B) particles bearing strongly acidic groups; (C) particles bearing weakly acidic groups; and (D) particles bearing weakly basic groups. (Modified from Figure 1.8.9 in ref.[18])

where

- k is the Boltzmann constant,
- T is the temperature,
- e is the elementary charge,
- z is the valence of the potential-determining ion, M^{z+}, including its sign (i.e., $z > 0$ for cation and $z < 0$ for anion).

Oxides[19–21]

Oxides such as SiO_2, TiO_2, and Al_2O_3 have highly reactive OH groups on their surfaces, which are called surface hydroxyl groups. The surfaces of the oxides immersed in water are positively charged due to adsorption of H^+ ions (protonation) at low pH, whereas they are negatively charged due to desorption of H^+ ions (deprotonation) at high pH; thus, H^+ ions act as the potential-determining ions. The surface electric potential of the oxides as a function of pH is shown schematically by curve (A) in Figure 2.2.1. The values of pzc for various oxides are given in Table 2.2.2. Metals and nitrides often exhibit oxidized surfaces rather than the neat surface; if this is the case, their oxidized surfaces obey the same charging mechanism as the oxides.

Particles Bearing pH-dependent Dissociable Groups[20,21]

Particles bearing acid- and/or base-dissociable groups exhibit electrically charged surfaces in aqueous solutions through their dissociation, the degree of which depends on the pH value of the solutions. Strongly acidic groups such

TABLE 2.2.2 Points of Zero Charge for Particles in Aqueous Solutions (Modified from Table 1.8.2 in ref.[18])

Material	pH or pAg at pzc	Material	pH or pAg at pzc
Sparingly soluble crystal[19]	$(pAg)_{pzc}$	δ-MnO_2	2.3–3.0
AgCl	4.6	γ-MnO_2	4.8
AgBr	5.4–5.9	NiO	11.3
AgI	5.5–5.6	$Ni(OH)_2$	11.2
Ag_2S	10.2	SiO_2 (Amorphous)	2.0–3.5
	$(pH)_{pzc}$	SnO_2 (Cassiterite)	5.4
$Ca_{10}(OH)_2(PO_4)_6$ (Hydroxyapatite)	8.5	TiO_2 (Anatase)	5.3–6.6
		TiO_2 (Rutile)	5.8
$Ca_{10}F_2(PO_4)_6$ (Fluorapatite)	6.8	ZnO	8.5–9.5
		Clay mineral[24]	$(pH)_{pzc}$
Oxide[19]	$(pH)_{pzc}$	Kaolinite	4.7
α-Al_2O_3	9.1	$(Al_2Si_2O_5(OH)_4)$	
γ-Al_2O_3	8.1–9.1	Talc	7.0
CeO_2	8.1	$(Si_4Mg_3O_{10}(OH)_2)$	
Co_3O_4	11.4	Muscovite	6.6
$Co(OH)_2$	11.4	$(K[(Si_3Al)Al_2O_{10}(OH)_2])$	
α-Fe_2O_3 (Hematite)	8.5–9.3	Phlogopite	8.0
α-FeOOH (Goatite)	7.5–9.3	$(K[(Si_3Al)Mg_3O_{10}(OH)_2])$	
Fe_3O_4	6.8	Edge of clay layer	6–7
La_2O_3	9.6	(SiOH and AlOH groups)[19,20]	

as sulfonyl hydroxide (-SO_3H) are deprotonated almost completely to become negatively charged even in a wide pH range. On the other hand, weakly acidic groups such as carboxyl group (-COOH) and phenolic hydroxyl group (-OH) are deprotonated to become negatively charged, and weakly basic groups such as amino group (-NH_2) are protonated to become positively charged; the degree of these ionization depends on the pH value of the solutions. As shown by curves (B) and (D) in Figure 2.2.1, the surface electric potential of the particles carrying one sort of such pH-dependent dissociable groups exhibits the same sign to take no pzc Carbon blacks and polymer particles (latex) employ this charging mechanism. Amphoteric substances (e.g. proteins) bearing both acidic and basic groups, however, exhibit the positively/negatively charged surfaces at low/high pH to take a pzc at intermediate pH, as shown by the curve (A) in Figure 2.2.1.

Clay Minerals[19–23]

Clay minerals are largely composed of silicates containing aluminum, magnesium, and/or iron. Typical of clay minerals are layered silicates. They have plate-like morphologies and are generally classified into the 1:1 and the 2:1 crystal structures, both of which are laminated with a repeating unit that is about 1 nm thick and formed by bonding two sorts of sheets (i.e. the Si tetrahedral and the Al octahedral sheets). The repeating unit for the 1:1 structure (0.7 nm thick) is a double sheet of the Si tetrahedron and the Al octahedron, while that for the 2:1 structure (1.0 nm thick) is composed of two Si tetrahedral sheets and one Al octahedral sheet intervening between them. The 2:1 structure includes mica, vermiculite, and smectite, which have the negative charges in the flat plane and the positive and negative charges at the edge. The negative charges in the flat plane are termed *permanent charges* caused by *isomorphous substitution*: $Si^{4+} \rightarrow Al^{3+}$ in the Si tetrahedral sheets and $Al^{3+} \rightarrow Fe^{2+}$ or Mg^{2+} in the Al octahedral sheets. The charges at the edge are termed *variable charges* generated by deprotonation and protonation of the surface hydroxyl groups (i.e. -SiOH and -AlOH). On the other hand, kaolin such as kaolinite and halloysite takes the 1:1 structure, which has no permanent charge in the flat plane but variable charges at the edge. The values of pzc for some cray minerals and their edge faces are given in Table 2.2.2.

χ Potential Generated by Interfacial Polarization[19,22]

All the surface charging mechanisms of particles described above are causally attributable to free charges. However, an uncharged particle often exhibits a non-zero value of its surface electric potential in the following way. Polar molecules of solvent or solute are aligned on the particle surface with their dipoles pointing in the same direction due to preferential orientation and/or adsorption. When the dipole alignment is not completely parallel to the surface, the positive partial charges of the molecules on the surface oppose to their negative partial charges, resulting in the formation of a double layer of molecular thickness next to the particle surface. By this mechanism, the particles have the surface electric potential, that is, χ potential. For examples, in a polar solvent such as water and ethanol, solvent molecules are preferentially aligned on the solid surface to form a structured layer (i.e. *solvation layer*) with thickness of a few molecules. Similarly, polar molecules added as one component of mixed solvents preferentially adsorb on the solid surface to form an *adsorption layer*. In this way, a solvation layer and an adsorption layer of the polar molecules are formed on the solid surface to generate the χ potential of the surface.

Charging by Adsorption of Charged Molecules (Secondary Charging)[19–23]

Multivalent ions (e.g. $P_2O_7^{4-}$ and Ca^{2+}), ionic surfactants, charged polymers (including proteins and polysaccharides), and charged impurities have strong affinity for every substance. The driving forces for this affinity include the covalent bonding force, the van der Waals force, the electrostatic force, and the force due to hydrophobic effect. When these charged molecules are adsorbed onto the surface of solids mentioned above, the surface charge is apparently altered and sometimes the sign of the net surface charge reverses. This charging mechanism is called the secondary charging.

2.2.2.2 Electric Double Layer (EDL) around a Charged Spherical Particle[19–23,25–27]

Let us consider the system, where the spherical particles bearing charges are dispersed in aqueous electrolyte solutions containing counter-ions and co-ions; the former have the charges of the opposite sign to the charges of the particle surface and the latter have the charges of the same sign. The counter-ions are not only electrostatically attracted to the charged surface of individual particles, but subject to thermal motion; these opposing effects on the counter-ions determine their spatial distribution around the individual particles, which exhibits a rather diffuse profile of the ion concentration as shown in Figure 2.2.2. The concentration of the co-ions becomes even lower at the point closer to the particle surface because of electrostatic repulsion from the surface. The charged surface of the particle and its surrounding cloud of the counter-ions compose an electric double layer (EDL). From a molecular point of view, some of the co-ions as well as the counter-ions are directly adsorbed on the particle surface and the polar molecules of the solvent are preferentially aligned thereon, resulting in the formation of the structured *Stern layer* with thickness of $\delta < 1$ nm next to the particle surface.[28] The electric potential on the external boundary of this Stern layer versus the bulk electrolyte is referred to as *Stern potential*, ψ_s. The detailed structure of the Stern layer is not understood satisfactorily and remains to be investigated.

The electric potential $\psi(r)$ outside the Stern layer of a spherical particle with radius a is treated by the Poisson–Boltzmann equation, where r is the distance from the center of the particle. Assuming that $|\psi|$ is small enough to satisfy

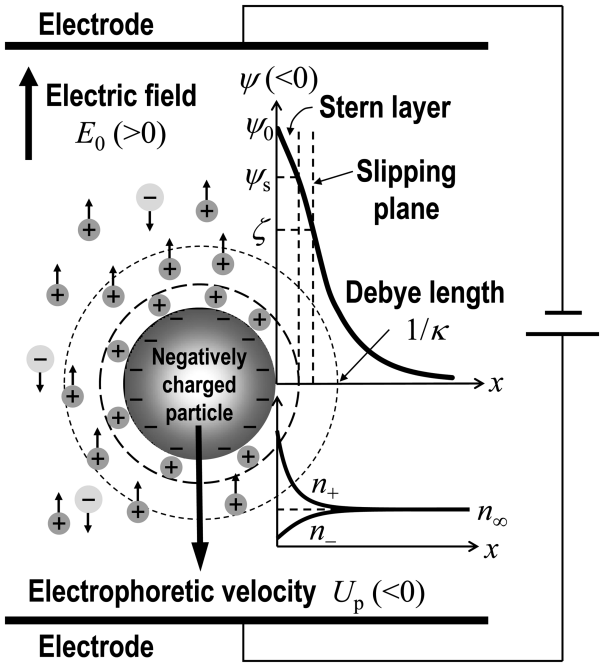


FIGURE 2.2.2 Schematic diagram of electrophoresis of a negatively charged particle and counter- and co-ions under an applied electric field. The profiles of the electric potential and the ion concentrations around the particle are also depicted. (Modified from Figure 1.8.17 in ref.[18])

$ze|\psi| < kT$ (i.e. the Debye–Hückel approximation; $|\psi| < 25.7$ mV for 25°C and $z = 1$) and the electrolyte is symmetrical with valency z, the potential profile $\psi(r)$ is approximated as

$$\psi(r) \approx \psi_s \frac{a}{r} \exp\left[-\kappa\left(r - a\right)\right] \tag{2.2.20}$$

$$\kappa \equiv \sqrt{\frac{2n_\infty z^2 e^2}{\varepsilon_r \varepsilon_0 kT}} \tag{2.2.21}$$

where

n_∞ is the ion concentration of the bulk electrolyte,
ε_r is the relative dielectric constant of the medium,
ε_0 is the dielectric constant of vacuum.

The *Debye length* represented by $1/\kappa$ is a measure of the thickness of the diffuse EDL. In aqueous solutions at 25°C, it is given by

$$\frac{1}{\kappa} = \frac{0.304}{z\sqrt{C}} \quad \text{[nm]} \tag{2.2.22}$$

where C is the molar concentration of the symmetrical electrolyte and has the unit of M ≡ mol/L. The Debye length decreases with increasing z and C. For monovalent electrolytes of $z = 1$, the Debye length is calculated as $1/\kappa \approx 10$, 3, and 1 nm at $C = 0.001$, 0.01, and 0.1 M, respectively.

2.2.2.3 Theories Linking Electrophoretic Mobility of a Particle with Its Zeta Potential[19–22,25–27]

In contrast to the Debye length $1/\kappa$ given by Equation (2.2.21), theoretical estimation of the surface electric potential ψ_0 is impossibly difficult for a wide variety of particles, suggesting that the value of ψ_0 must be experimentally determined. Out of all the experimental methodologies listed in Table 2.2.3, the electrophoretic measurement illustrated in Figure 2.2.2 is the most popular for determining a measure of ψ_0, where the charged particles migrate toward the electrode with the opposite sign under an external electric field. This phenomenon is named electrophoresis.

When a particle undergoes electrophoretic motion, a thin layer of the ions and the solvent molecules next to the particle surface also moves with the particle as if it is fixed on the particle surface. The external boundary of this fixed layer is termed the *slipping plane*. The electric potential thereon is named the electrokinetic potential or the zeta potential symbolized by ζ.[29] Because the slipping plane is considered to be located immediately outside the Stern layer, the magnitude of the zeta potential should be almost equal to or somewhat smaller than that of the Stern potential (i.e. $|\zeta| \approx |\psi_s|$). Thus, the zeta potential of a particle can be correlated with its electrophoretic velocity; several theories for their relationship will be explained below.

Hereafter, let us consider the electrophoretic measurement, where a nonconductive spherical particle (radius a and zeta potential ζ) moves in an aqueous electrolyte solution (relative dielectric constant ε_r, viscosity η, and valency z) of given ion concentration (Debye length $1/\kappa$) under the external electric field of E_0 to reach a constant velocity of U_p. When E_0 is not extremely strong (i.e. $|E_0| < 100$ V/cm), U_p is directly proportional to E_0. Therefore, the electrophoretic mobility of a particle defined by

$$\mu \equiv \frac{U_p}{E_0} \tag{2.2.23}$$

is independent of the magnitude of E_0 in the case of sufficiently weak electric fields. The following are several theories that link the electrophoretic mobility μ with the zeta potential ζ.

When the zeta potential is low in magnitude (i.e. $|\zeta| < 2kT/ze \approx 50$ mV for 25°C and $z = 1$), the electrophoretic mobility is proportional to the zeta potential and analytically represented by the Henry equation:[30]

$$\mu = \frac{2\varepsilon_r \varepsilon_0}{3\eta} \zeta \cdot f(\kappa a) \tag{2.2.24}$$

where $f(\kappa a)$ represents the Henry function displayed by the solid line in Figure 2.2.3 and is mathematically complicated. Alternatively, the approximate expression

$$f(\kappa a) = \frac{3}{2} - \frac{1}{2 + 0.144(\kappa a)^{1.13}} \tag{2.2.25}$$

TABLE 2.2.3 Methodologies of Zeta Potential Measurements for Particles in Solutions (Modified from Table 1.8.3 in ref.[18])

Particle Concentration	Method		Applied External Field	Detection Target	Particle Size Range	Commercially Available Products[a]	References
Dilute	Electrophoresis	Microscopic electrophoresis	DC electric field	Electrophoretic velocity of individual particles (direct observation, image analysis)[b]	> several 100 nm (bright field) > several 10 nm (dark field)	CAD Instruments, ZetaCompact CAD Instruments, ZetaPhoremeter IV Microtec, ZEECOM ZC-3000 Nihon Rufuto, Model 502 Particle Metrix, ZetaView Rank Brothers, Mk II	[19–22,38,39]
		Electrophoretic light scattering (ELS)[c]	DC electric field	Frequency shift of scattered light[d]	Several Å–10 μm (not falling, not rising)	Otsuka Electronics, ELSZ-2000ZS	[19–22, 38–41]
			Rectangular-wave AC electric field	Same as above	Several nm–10 μm (not falling, not rising)	Cordouan Technologies, Wallis ζ Horiba, nano Partica SZ-100-HZ Microtrac, Nanotrac Wave II UZ152[e]	[19–22, 38–40]
				Phase shift of scattered light[f]	Same as above	Anton Paar, Litesizer 500 Malvern, Zetasizer Nano ZSP Particle Sizing Systems, Nicomp ZLS Z3000[g] Wyatt Technology, Möbiuζ	[38–40]
			Sinusoidal-wave AC electric field	Same as above	Same as above	Brookhaven Instruments, NanoBrook Omni	[38–40]
	Resistive pulse sensing		Electric field	Resistive pulses caused by individual particles passing through a single pore	50 nm–10 μm (dependent on pore size of sensor used)	Izon Science, qNano Gold	[42]
Dense	Electroacoustics	Electrokinetic sonic amplitude (ESA)	High-frequency AC electric field	Amplitude of ultrasound caused by vibration of particles	Several nm–several 10 μm	Colloidal Dynamics, AcoustoSizer II Colloidal Dynamics, ZetaProbe analyzer	[19,20,38, 43–45]
		Ultrasonic vibration potential (UVP) Colloid vibration potential (CVP)	Ultrasonic wave	Amplitude of vibration potential caused by vibration of particles and medium	5 nm–100 μm (dependent on density difference between particles and medium)	Dispersion Technology, Model DT-1202 Dispersion Technology, Model DT-310	[19,20,38, 43–45]
	Sedimentation potential		Gravitational or centrifugal field	Electric potential caused by migration of charged particles	——	N/A	[19,21,25,46]
	Streaming potential[h]		See footnote[h]	See footnote[h]	Several nm–several 100 μm	AFG Analytic, CAS touch! BTG, Mütek PCD-05 Particle Metrix, Stabino	[20,21,47]

(*Continued*)

TABLE 2.2.3 (CONTINUED) Methodologies of Zeta Potential Measurements for Particles in Solutions (Modified from Table 1.8.3 in ref.[18])

Particle Concentration	Method	Applied External Field	Detection Target	Particle Size Range	Commercially Available Products[a]	References
Packed bed	Electro-osmosis	DC electric field	Volumetric flow rate of medium caused by ion migration	> several 10 μm[i]	N/A	[19–21,48]
	Streaming potential	Pressure gradient	Electric potential caused by flow of medium containing ions	Same as above	Anton Paar, SurPASS 3 BTG, Mütek SZP-10 CAD Instruments, ZetaCAD HT	[19–21,48]

[a] The listing is based on the best of the authors' knowledge and never means the endorsement to the manufactures listed. The names of manufactures and products listed are trademarks and/or registered trademarks of each manufacture, the symbols of which (™ and ®) are omitted.

[b] Alternatively, the rotary prism method provides only the average value of the electrophoretic velocities of particles.

[c] It uses the laser Doppler velocimetry (LDV) as the basic principle.

[d] Autocorrelation function (ACF) of scattered light intensity is processed through frequency spectrum analysis.

[e] It uses the modulated Brownian motion power spectrum analysis (i.e. the peeling method).

[f] It is named the phase analysis light scattering (PALS) method.

[g] It enables the user to choose LDV or PALS mode for every measurement.

[h] It is a novel method, which relies on a cylindrical PTFE chamber with a vertically reciprocating PTFE piston. The electric double layers of the particles attached onto the chamber wall are distorted by an oscillating flow of the medium induced by the reciprocating piston. The resultant streaming potential between the top and bottom electrodes is proportional to the zeta potential of the attached particles as well as the flow rate.

[i] The particles must be large such that their packed bed has the pores sufficiently larger than $1/\kappa$.

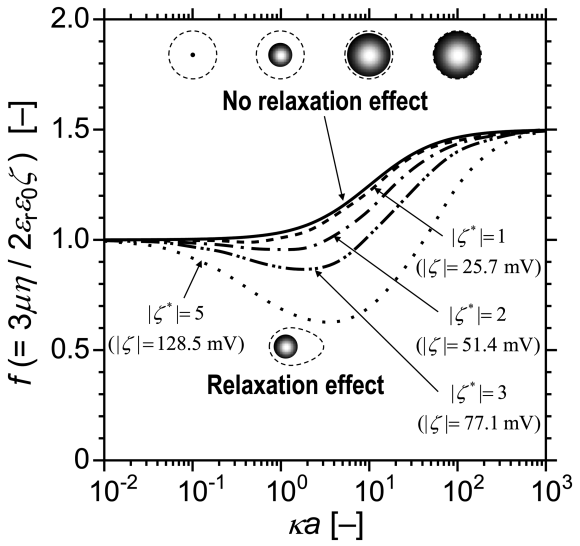


FIGURE 2.2.3 The profiles of the Henry function (solid line, $f(\kappa a)$) and the numerical solutions (dotted lines, $f(\kappa a, \zeta^*, z_\pm, \xi_\pm^*)$ with four different values of ζ by Wiersema et al.[34]) that relate the electrophoretic mobility with the zeta potential of a nonconductive spherical particle of radius a in an aqueous solution of 1:1 symmetrical electrolytes ($\lambda_+ = \lambda_- = 70\ \Omega^{-1}\cdot cm^2\cdot mol^{-1}$) at 25°C. The particles with undistorted/distorted EDL are depicted in the inset. (Modified from Figure 1.8.20 in ref.[18])

is convenient for practical use.[25] The parameter, κa, represents the ratio of the size of a particle (a) to that of its surrounding EDL ($1/\kappa$), as depicted in the inset of Figure 2.2.3. In two limiting cases of κa, the Henry Equation (2.2.24) leads to the Smoluchowski equation

$$\mu = \frac{\varepsilon_r \varepsilon_0}{\eta}\zeta \tag{2.2.26}$$

for $\kappa a >> 1$ (i.e. $f(\kappa a) = 3/2$)[31] and to the H*ü*ckel equation

$$\mu = \frac{2\varepsilon_r \varepsilon_0}{3\eta}\zeta \tag{2.2.27}$$

for $\kappa a << 1$ (i.e. $f(\kappa a) = 1$).[32] Once μ is determined experimentally, ζ can be calculated by Equation (2.2.24) with the known parameters of ε_r, η, κ, and a.

When the zeta potential is higher in magnitude (i.e. $|\zeta| > 2kT/ze \approx 50$ mV for 25°C and $z = 1$) and the EDL around a particle is relatively thick (i.e. $0.1 < \kappa a < 100$), the EDL never follows particle migration and is then distorted. This distortion of the EDL reduces the migration velocity of the particle; it is referred to as the *relaxation effect*, which is ignored in the Henry Equation (2.2.24). A general expression for the electrophoretic mobility taking account of the relaxation effect is given by

$$\mu = \frac{2\varepsilon_r \varepsilon_0}{3\eta}\zeta \cdot f(\kappa a, \zeta^*, z_\pm, \xi_\pm^*) \tag{2.2.28}$$

where $f(\kappa a, \zeta^*, z_\pm, \xi_\pm^*)$ is a function of not only κa but also the additional parameters: $\zeta^* \equiv \zeta/(kT/e)$, the dimensionless zeta potential; $z_\pm$, the valences of the counter- and co-ions; and $\xi_\pm^* \equiv \xi_\pm/(3\eta|z_\pm|^2 e^2/2\varepsilon_r\varepsilon_0 kT)$, the dimensionless drag coefficients of the counter- and co-ions in the solvent.[33,34] It is noted that the molar conductivity at infinite dilution is given by $\lambda_\pm \equiv |z_\pm|e^2 N_A/\xi_\pm$, where N_A denotes the Avogadro constant. Wiersema et al.[34] numerically calculated the electrophoretic mobility as a function of κa under the intermediate values of zeta potential (i.e. $|\zeta| < 5kT/ze \approx 125$ mV for 25°C and $z = 1$); the results of four different values of ζ are drawn by the dotted lines in Figure 2.2.3. O'Brien and White[35] developed a program for numerical calculations of electrophoretic mobility that is applicable in a wide range of κa and ζ. Ohshima et al. reported two approximate analytical solutions for different ranges of the parameters: $\kappa a > 10$ and any ζ;[36] and $\kappa a < 10$ and $|\zeta| < 3kT/ze \approx 75$ mV for 25°C and $z = 1$.[37]

The Smoluchowski Equation (2.2.26) is applicable to the electrophoretic mobility of a particle with arbitrary shape as well, when $\kappa a_{min} >> 1$ (a_{min} is a minimum of characteristic lengths of the particle shape). The effects of particle conductivity and shape are explained elsewhere.[19,21,22,25]

2.2.2.4 Methodologies for Zeta Potential Measurements[18–22]

In order to determine the zeta potential of particles, one has to carry out electrokinetic measurements based on one of four different electrokinetic phenomena (i.e. electrophoresis, sedimentation potential, electro-osmosis, and streaming potential). In recent years, it has become possible to perform the zeta potential measurements quickly and easily for nanometer-sized particles as well as larger particles, because of great advances in measurement principles, analytical procedures, and automation/acceleration of experimental operations/analysis. Several methodologies for zeta potential measurements are classified according to the measured particle concentrations and are summarized in Table 2.2.3.

REFERENCES

1. Harper, W. R., *P. Roy. Soc. A-Math Phy.*, 205, 83–103, 1951.
2. Bailey, A. G., *J. Electrostat.*, 51/52, 82–90, 2001.
3. Cotler P., Castle, G. S. P., Schein, L. B., *J. Electrostat.*, 36, 165–173, 1995.
4. Matsuyama, T., Yamamoto, H., *J. Phys. D Appl. Phys.*, 28, 2418–2423, 1995.
5. Crowley, J. M., *Fundamentals of Applied Electrostatics*, John Wiley & Sons, New York, 1986, pp. 26–30.
6. Masuda, H., Iinoya, K., *AIChE J.*, 24, 950–956, 1978.
7. John, W., Reischl, G., Devor, W., *J. Aerosol Sci.*, 11, 115–138, 1980.
8. Cottrell, G. A., Reed, C., Rose-Innes, A. C., *Inst. Phys. Conf. Ser.*, 48, 249–356, 1979.
9. Masuda, H., Komatsu, T., Iinoya, K., *AIChE J.*, 22, 558–564, 1976.
10. Matsusaka, S., Masuda, H., *Adv. Powder Technol.*, 14, 143–166, 2003.

11. Matsusaka, S., Umemoto, H., Nishitani, M., Masuda, H., *J. Electrostat.*, 55, 81–96, 2002.
12. Gallo, C. F., Lama, W. L., *J. Electrostat.*, 2, 145–150, 1976.
13. Smoluchowski, M., *Phys. Z.*, 13, 1069–1080, 1912.
14. Wilson, I. B., *J. Colloid Sci.*, 2, 271–276, 1947.
15. Masuda, H., Ikumi, S., Ito, T., *KONA*, 3, 17–25, 1985.
16. Smythe, W. R., *Static and Dynamic Electricity*, McGraw-Hill, New York, 1950, pp. 118–122.
17. Pohl, H. A., *Dielectrophoresis*, Cambridge University Press, Cambridge, 1978, chap. 4.
18. Shinto, H., Fukasawa, T., *J. Soc. Powder Technol., Japan*, 54, 673–691, 2018.
19. Lyklema, J., *Fundamentals of Interface and Colloid Science, Vol. II: Solid-Liquid Interfaces*, Academic Press, London, 1995, chaps. 3, 4, A3.
20. Hunter, R. J., *Foundations of Colloid Science*, 2nd edn., Oxford University Press, Oxford, 2001, chaps. 1, 7, 8, 10.
21. Hunter, R. J., *Zeta Potential in Colloid Science*, Academic Press, London, 1981, chaps. 2–4, 6, 7.
22. Berg, J. C., *An Introduction to Interfaces and Colloids: The Bridge to Nanoscience*, World Scientific Publishing, Toh Tuck Link, 2009, chap. 6.
23. Essington, M. E., *Soil and Water Chemistry: An Integrative Approach*, 2nd edn., CRC Press, Boca Raton, FL, 2015, chaps. 2, 8.
24. Sverjensky, D. A., Sahai, N., *Geochim. Cosmochim. Acta*, 60, 3773–3797, 1996.
25. Masliyah, J. H., Bhattacharjee, S., *Electrokinetic and Colloid Transport Phenomena*, Wiley-Interscience, New York, 2006, chaps. 5, 9, 10.
26. Ohshima, H., *Theory of Colloid and Interfacial Electric Phenomena*, Academic Press, London, 2006, chaps. 1, 3.
27. Ohshima, H., *Biophysical Chemistry of Biointerfaces*, Wiley, New York, 2010, chap. 1.
28. Bockris, J. O'M., Devanathan, M. A. V., M*ü*ller, K., *Proc. R. Soc. (London) Ser. A*, 274, 55–79, 1963.
29. Wall, S., *Curr. Opin. Colloid Interface Sci.*, 15, 119–124, 2010.
30. Henry, D. C., *Proc. R. Soc. (London) Ser. A*, 133, 106–129, 1931.
31. von Smoluchowski, M., *Bull. Int. Acad. Sci. Cracovie*, 3, 184–199, 1903.
32. Hückel, E., *Phys. Z.*, 25, 204–210, 1924.
33. Overbeek, J. T. G., *Kolloid-Beih.*, 54, 287–364, 1943.
34. Wiersema, P. H., Loeb, A. L., Overbeek, J. T. G., *J. Colloid Interface Sci.*, 22, 78–99, 1966.
35. O'Brien, R. W., White, L. R., *J. Chem. Soc. Faraday Trans. 2*, 74, 1607–1626, 1978.
36. Ohshima, H., Healy, T. W., White, L. R., *J. Chem. Soc. Faraday Trans. 2*, 79, 1613–1628, 1983.
37. Ohshima, H., *J. Colloid Interface Sci.*, 239, 587–590, 2001.
38. ISO 13099-1, Colloidal systems – Methods for zeta-potential determination - Part 1: Electroacoustic and electrokinetic phenomena, 2012.
39. ISO 13099-2, Colloidal systems – Methods for zeta-potential determination - Part 2: Optical methods, 2012.
40. Xu, R., *Particle Characterization: Light Scattering Methods*, Kluwer Academic Publishers, Dordrecht, 2000, chap. 6.
41. Oka, K., Furusawa, K., in: Ohshima, H., Furusawa, K. (ed.), *Electrical Phenomena at Interfaces: Fundamentals, Measurements, and Applications*, 2nd edn., CRC Press, Boca Raton, FL, 1998, chap. 8.
42. Kozak, D., Anderson, W., Vogel, R., Chen, S., et al., *ACS Nano*, 6, 6990–6997, 2012.
43. ISO 13099-3, Colloidal systems - Methods for zeta-potential determination - Part 3: Acoustic methods, 2014.
44. Dukhin, A. S., Goetz, P. J., *Characterization of Liquids, Dispersions, Emulsions, and Porous Materials Using Ultrasound*, 3rd edn., Elsevier, Amsterdam, 2017.
45. Takeda, S., Tobori, N., Sugawara, H., Furusawa, K., in: Ohshima, H., Furusawa, K. (ed.), *Electrical Phenomena at Interfaces: Fundamentals, Measurements, and Applications*, 2nd edn., CRC Press, Boca Raton, FL, 1998, chap. 13.
46. Ozaki, M. Sasaki, H., in: Ohshima, H., Furusawa, K. (ed.), *Electrical Phenomena at Interfaces: Fundamentals, Measurements, and Applications*, 2nd edn., CRC Press, Boca Raton, FL, 1998, chap. 10.
47. Wäsche, R., Naito, M., Hackley, V. A., *Powder Technol.*, 123, 275–281, 2002.
48. Furusawa, K., Sasaki, H., Nashima, T., in: Ohshima, H., Furusawa, K. (ed.), *Electrical Phenomena at Interfaces: Fundamentals, Measurements, and Applications*, 2nd edn., CRC Press, Boca Raton, FL, 1998, chap. 9.

2.3 Magnetic Properties

Toyohisa Fujita

2.3.1 MAGNETIC FORCE ON A PARTICLE[1]

The magnetic dipole force F_m acting on a paramagnetic particle in vacuum is given by

$$\boldsymbol{F}_m = \nabla \int v\,(\boldsymbol{B}\cdot\boldsymbol{H})\,dV \tag{2.3.1}$$

where

- $\boldsymbol{B}$ is the magnetic polarization of a particle,
- V is the volume of a particle,
- $\boldsymbol{H}$ is the magnetic field strength,

∇ is the operator of the gradient and acting on a scalar φ that can be written as

$$\nabla\varphi = \mathbf{i}\delta\,\varphi/\delta x + \mathbf{j}\delta\,\varphi/\delta y + \mathbf{k}\delta\,\varphi/\delta z \tag{2.3.2}$$

where **i**, **j**, **k** are the unit vectors in the directions x, y, z, respectively. If the particle is sufficiently small it can be reduced to a point dipole moment $\boldsymbol{\mu}_m = \boldsymbol{B}V$. The force on such a point dipole is

$$\boldsymbol{F}^m = (\boldsymbol{\mu}_m \cdot \nabla)\boldsymbol{H} \tag{2.3.3}$$

Permeability of a spherical paramagnetic or diamagnetic particle is given as

$$\mu = (1+\kappa)\,\mu_o \tag{2.3.4}$$

where

- κ is the volume magnetic susceptibility,
- μ_o is the permeability of free space numerically equal to $4\pi \cdot 10^{-7}$ H/m.

The magnetic polarization of the particle is given by

$$\boldsymbol{B} = \mu_o \kappa \boldsymbol{H}/(1+\kappa/3) \tag{2.3.5}$$

Combining Equations (2.3.5 and 2.3.3), the force on a small spherical weakly magnetic particle placed in the external magnetic field can be written as

$$\boldsymbol{F}_m = \left[\mu_o \kappa\, V/(1+\kappa/3)\right](\boldsymbol{H}\nabla)\boldsymbol{H} \tag{2.3.6}$$

or in a simplified form (assuming that $\kappa << 1$),

$$\boldsymbol{F}_m = (1/2)\,\mu_o \kappa V \nabla(\boldsymbol{H}^2) \tag{2.3.7}$$

If a paramagnetic particle (volume magnetic susceptibility: κ_p) is immersed in the fluid (volume magnetic susceptibility: κ_f), the magnetic force per unit volume acting on a particle is given by Equation (2.3.7) (using $\kappa = \kappa_p - \kappa_f$). For practical calculations it is sometimes advantageous to replace the magnetic field strength by the magnetic induction $\boldsymbol{B}$.

Then, Equation (2.3.7) reads as follows:

$$\boldsymbol{F}_m = (\kappa/\mu_o)V\boldsymbol{B}\nabla\boldsymbol{B} \tag{2.3.8}$$

Here $\boldsymbol{B}$ is considered as the external magnetic induction, and $\nabla\boldsymbol{B}$ is the gradient of the magnetic induction. Thus, in the direction of x, the magnetic force $\boldsymbol{F}_{mx}$ can be written by the following equation (where $\boldsymbol{B} = \mu_o\boldsymbol{H}$ and magnetization $\kappa\boldsymbol{H}_x = \boldsymbol{I}_x$),

$$\boldsymbol{F}_{mx} = \mu_o V\boldsymbol{k}(\boldsymbol{H}_x \cdot \delta\boldsymbol{H}_x/\delta x) = \mu_o V\boldsymbol{I}_x \cdot \delta\boldsymbol{H}_x/\delta x \tag{2.3.9}$$

Magnetic force is proportional to the product of the external magnetic field and the field gradient and has the direction of the gradient. In a homogeneous magnetic field, in which $\nabla\boldsymbol{B} = 0$ or $\delta\boldsymbol{H}_x/\delta x = 0$, the force to change the position of a particle is zero.

Along the axis of symmetry, and for values of the external magnetic field $\boldsymbol{H}_{xo}$ lower than the bulk saturation value $\boldsymbol{H}_s$ of the ferromagnetic rod filament, the magnetic field strength is given by the expression

$$\boldsymbol{H}_x = \boldsymbol{H}_{xo}(1 + a^2/r^2) \tag{2.3.10}$$

where a is the rod radius and r is the radius from the center of the rod, as shown in Figure 2.3.1.

For $\boldsymbol{H}_{xo} > \boldsymbol{H}_s$, $\boldsymbol{H}_x$ is given by

$$\boldsymbol{H}_x = \boldsymbol{H}_{xo} + \boldsymbol{H}_s(a^2/r^2) \tag{2.3.11}$$

The magnetic field gradient for $\boldsymbol{H}_{xo} < \boldsymbol{H}_s$ along the x axis of the particle, when the magnetization of the particles is small, is given as

$$d\boldsymbol{H}_x/dx = -2\boldsymbol{H}_{xo}(a^2/r^3) \tag{2.3.12}$$

If the Equations (2.3.10, 2.3.12, and 2.3.6) are combined, the approximate expression for the magnetic force on a point-like spherical weakly magnetic particle is given as

$$\boldsymbol{F}_m = -(8/3)\pi\mu_0 \boldsymbol{k} b^3 \boldsymbol{H}_{xo}(1 + a^2/r^2)\boldsymbol{H}_{xo}(a^2/r^3) \tag{2.3.13}$$

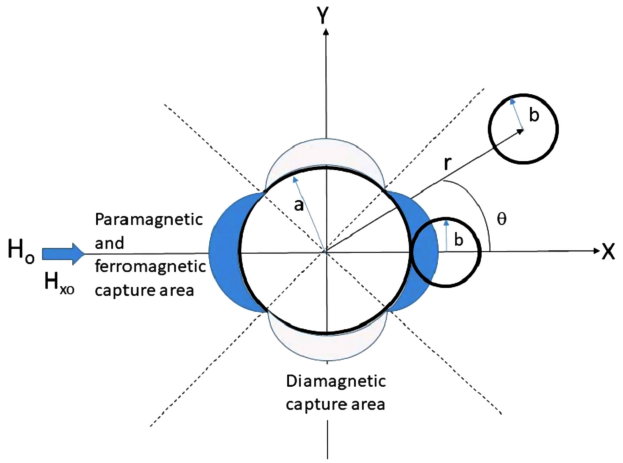


FIGURE 2.3.1 Cross section of spherical particle of radius b and ferromagnetic wire rod of radius a (magnetized uniform magnetic field H_{xo}).

where b is the particle radius. Equation (2.3.13) can be rewritten for a matched system $a=3b$ as

$$\boldsymbol{F}_{\mathrm{m}} = -\left(75/128\right)\pi\mu_0\kappa b^2\boldsymbol{H}_{\mathrm{xo}}{}^2 \tag{2.3.14}$$

On the other hand, the magnetic force of a small particle into the ferromagnetic rod at the distance r and angle θ in Figure 2.3.1 is obtained as follows,[2,3]

$2\mu_0 H_0 > I_s$

$$F_{\mathrm{mr}} = -\frac{(\kappa_{\mathrm{p}} - \kappa f) I_s V_{\mathrm{p}} a^2}{r^3} \left(\frac{I_s a^2}{2\mu_0 r^2} + H_o \cos 2\theta\right) \tag{2.3.15}$$

$$F_{\mathrm{m}\theta} = -\frac{(\kappa_{\mathrm{p}} - \kappa f) I_s V_{\mathrm{p}} a^2 H_0}{r^3} \sin 2\theta \tag{2.3.16}$$

$2\mu_0 H_0 \leqq I_s$

$$F_{\mathrm{mr}} = -\frac{2\mu_0(\kappa_{\mathrm{p}} - \kappa f) H_0^2 V_{\mathrm{p}} a^2}{r^3} \times \left(\frac{a^2}{r^2} + \cos 2\theta\right) \tag{2.3.17}$$

$$F_{\mathrm{m}\theta} = -\frac{2\mu_0(\kappa_{\mathrm{p}} - \kappa f) H_0^2 V_{\mathrm{p}} a^2}{r^3} \sin 2\theta \tag{2.3.18}$$

If the volume magnetic susceptibility $\kappa=\kappa_{\mathrm{p}}-\kappa_{\mathrm{f}}$ is positive under the following condition, the wire can collect the particles in the direction of magnetic field as shown in Figure 2.3.1.

$$\left(\frac{I_s a^2}{2\mu_0 r^2} + H_o \cos 2\theta\right) > 0 \quad \text{in } 2\mu_0 H_0 > I_s$$

$$\text{or} \quad \left(\frac{a^2}{r^2} + \cos 2\theta\right) > 0 \quad \text{in } 2\mu_0 H_0 \leqq I_s \tag{2.3.19}$$

If the volume magnetic susceptibility $\kappa=\kappa_{\mathrm{p}}-\kappa_{\mathrm{f}}$ is negative under the following condition, the wire can collect the particles in the vertical direction of magnetic field as shown in Figure 2.3.1.

$$\left(\frac{I_s a^2}{2\mu_0 r^2} + H_o \cos 2\theta\right) < 0 \quad \text{in } 2\mu_0 H_0 > I_s$$

$$\text{or} \quad \left(\frac{a^2}{r^2} + \cos 2\theta\right) < 0 \quad \text{in } 2\mu_0 H_0 \leqq I_s \tag{2.3.20}$$

Several competing forces act on the particles placed in a magnetic separator. These are the force of gravity, the inertial force, the hydrodynamic drag, and surface and interparticle forces. The force of gravity $\boldsymbol{F}_{\mathrm{g}}$ can be written as

$$\boldsymbol{F}_{\mathrm{g}} = \rho V \boldsymbol{g} \tag{2.3.21}$$

where

ρ is the density of the particle,
$\boldsymbol{g}$ is the acceleration due to gravity.

The hydrodynamic drag $\boldsymbol{F}_{\mathrm{d}}$ on a particle of small radius is given by Stoke's law,

$$\boldsymbol{F}_{\mathrm{d}} = 6\pi\eta b \boldsymbol{v}_{\mathrm{p}} \tag{2.3.22}$$

where

η is the dynamic viscosity of the fluid,
b is the particle radius,
$\boldsymbol{v}_{\mathrm{p}}$ is the relative velocity of the particle with respect to the fluid.

Magnetic particles will be separated from "nonmagnetic" (i.e. more magnetic particles from less magnetic particles), if the following conditions are met:

$$\boldsymbol{F}_{\mathrm{m}}^{\mathrm{mag}} > \sum \boldsymbol{F}_{\mathrm{c}}^{\mathrm{mag}} \quad \text{and} \quad \boldsymbol{F}_{\mathrm{m}}^{\mathrm{nonmag}} < \sum \boldsymbol{F}_{\mathrm{c}}^{\mathrm{nonmag}} \tag{2.3.23}$$

where $\boldsymbol{F}_{\mathrm{c}}$ is a competing force, while $\boldsymbol{F}^{mag}$ and $\boldsymbol{F}^{nonmag}$ are forces acting on magnetic and nonmagnetic particles respectively. Although these conditions are clearly defined, a complication arises because the relative significance of the forces is determined mainly by the particle size. It can be seen from Equation (2.3.8, 2.3.21, and 2.3.22) that, since $\boldsymbol{F}_{\mathrm{m}} \propto b^3$ or b^2, the competing forces have the following dependence on particles size:

$$\boldsymbol{F}_{\mathrm{d}} \propto b^1 \text{ and } \boldsymbol{F}_{\mathrm{g}} \propto b^3 \tag{2.3.24}$$

In dry magnetic separation, where $\boldsymbol{F}_{\mathrm{d}}$ is usually negligible, the particle size does not affect the efficiency of separation significantly because of the same particle size dependence of the magnetic force and of the force of gravity. On the other hand, when the hydrodynamic drag is important, selectivity of the separation will be influenced by particle size distribution.

TABLE 2.3.1 Effect of Particle Size on Separation

Particle Size*	Magnetic Susceptibility*	Magnetic Force*
10	1	10^3
1	10^3	10^3

* Arbitrary Unit.

With decreasing particle size the relative importance of the hydrodynamic drag increases in comparison to the magnetic force.

The nonselective nature of the magnetic force is illustrated in Table 2.3.1. It can be seen that the magnetic force exerted on a coarse weakly magnetic particle is similar to the one exerted on a smaller and more strongly magnetic particle. Both particles will appear in the same product of separation unless the competing forces acting on particles of different sizes are different.

2.3.2 FERROMAGNETIC PROPERTIES OF A SMALL PARTICLE[4]

Ferromagnetic material is an ensemble of small magnetic domains within which the magnetic moment is unidirectional. The boundary between these domains is called the domain wall. When a diameter d of spherical particle contains width d of several domains, the domain wall energy U_w is given by the following formula:

$$U_m = \sigma\left(\pi r^2\right)2r/d \tag{2.3.25}$$

where σ is a wall energy.

On the other hand, as a magnetic static energy, U_m is two times larger than the single domain's one, U_m is given by

$$U_m = \left(\boldsymbol{I}_s^2/6\mu_o\right)\left(4\pi r^3/3\right)\left(d/2r\right) \tag{2.3.26}$$

where $\boldsymbol{I}_s$ is saturation magnetization of ferromagnetic material. U_w in Equation (2.3.25) is proportional to area, while U_m in Equation (2.3.26) is proportional to volume. When the size of a ferromagnetic material decreases and reaches the critical small size, the wall energy becomes larger than the magnetic static energy. At this critical size the magnetic domain cannot be divided. When the size of ferromagnetic particles is reduced sufficiently and reaches the critical small size, the domain wall disappears (i.e. the particles have a single domain structure), and the susceptibility and coercive force of particles vary as shown schematically in Figure 2.3.2. There is a particle size under which particles are super-paramagnetic, and the coercive force of particles is negligibly small by kT where k is Boltzmann constant and T is absolute temperature.

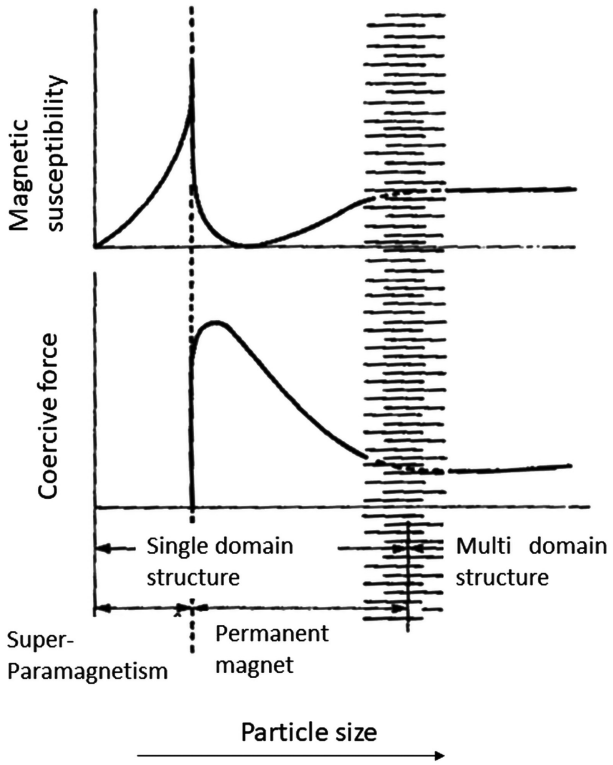


FIGURE 2.3.2 Variation of magnetic properties with particle size[5] (From Mitsui, S., in *Jisei Buturi no Shinpo*, S. Chikazumi, Ed., Agne, Tokyo, 1964, p. 242. With permission.)

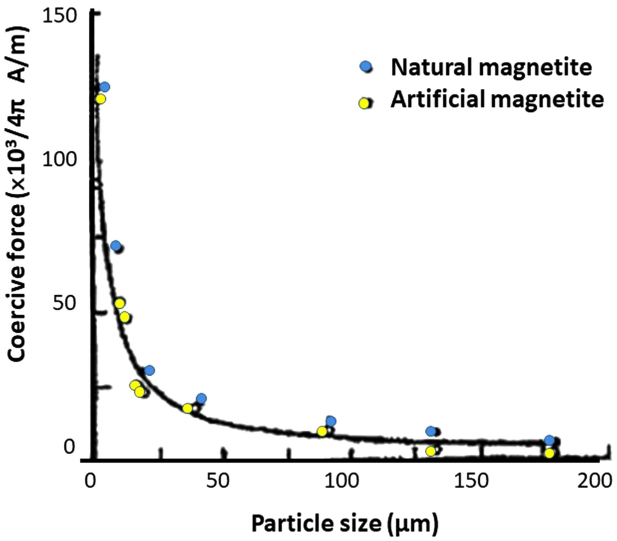


FIGURE 2.3.3 Dependence of coercive force of magnetite on particle size.[6] (From Gottschalk. V H., *Physics* 6, 127, 1935. With permission.)

A typical dependence of the coercive force of magnetite particles on the particle size is shown in Figure 2.3.3. Figure 2.3.4 shows the variation of critical particle size under which

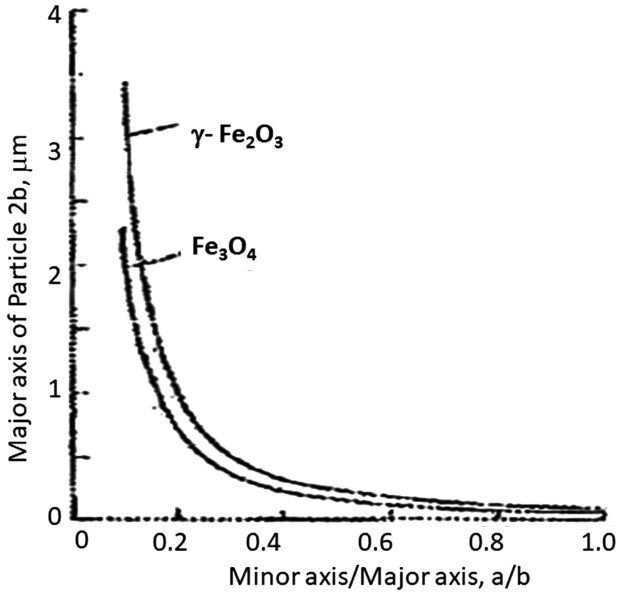


FIGURE 2.3.4 Critical particle size for single domain structure; a and b are the minor and major axes of the particle, respectively.[7] (From Morrish, A. H. and Yu, S. P., *J. Appl. Phys.*, 26, 1049, 1955. With permission.)

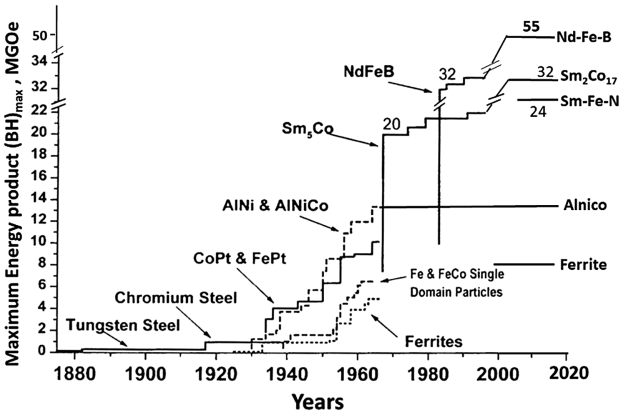


FIGURE 2.3.5 Progress in development of permanent magnetic materials.[9,10]

Fe_3O_4 and γ-Fe_2O_3 particles have a single domain structure with the aspect ratio. Magnetic fluid is one example of an apparent superparamagnetic behavior described by the same Langevin's law,[8] where the Brownian or Neel mechanisms lead.

2.3.3 MAGNETISM OF VARIOUS MATERIALS

The development of permanent magnetic materials and the improvement on their magnetic properties have been particularly studied during the last 30 years. Figure 2.3.5 illustrates the history of improvement in the energy product of permanent magnets.[9] Probably the most significant innovation step was made in the late 1970s when rare-earth magnets became available. Ferromagnetic materials are classified into soft and hard magnetic materials. Hard magnetic materials are used as permanent magnets, which have large coercive force. Typical properties of hard magnetic materials of artificial alloys, ferrites, and bonded in polymer are listed in Tables 2.3.2 and 2.3.3.[4]

There are four kinds of rare earth magnets on the market: $SmCo_5$, Sm_2Co_{17}, $Nd_2Fe_{14}B$, and $Sm_2Fe_{17}N_3$ types. The qualities of those magnets are listed in Table 2.3.4.

On the other hand, properties of soft magnetic materials are listed in Table 2.3.5.[4] Soft iron as well as DC relays, plungers, pole pieces, solenoids, and brakes for intermittent use are used, since the magnetic requirements are low and the cost must also be low. The high permeability, low coercive force, and high saturation magnetization of soft magnetic materials are used in certain applications. In the past, the industry employed ferrites at low power levels; however, nowadays higher power levels of ferrites have been developed.

Relative susceptibility of minerals is listed in Table 2.3.6.[2] Using the magnetization $\kappa H = \mathrm{I}$, permeability μ is given in the following formula:

$$\boldsymbol{B} = (\kappa + \mu_o)\boldsymbol{H} = \mu \boldsymbol{H} \tag{2.3.27}$$

TABLE 2.3.2 Characteristics of Permanent Magnetic Alloys

Alloy	Constituents* (%)	Coercive Force (kA/m)	Residual Magnetic Flux Density (T)	$(BH)_{max}$ (MGOe) [kJ/m^3]	Density (10^3 kg/m^3)
36Co steel	0.7C,36Co	16–20	0.9–1	1.0 [8]	8.2
Alnico 2	12.5Co	38–47	0.7–0.8	1.4–1.6 [11–13]	7.1
Alnico 5	24Co,14Ni	53–50	1.28–1.34	4.5–5.3 [36–42]	7.3
Alnico 5(DG)	24Co,14Ni	51	1.31	5.5 [44]	7.3
New KS steel	27Co,18Ni	76–84	0.55–0.63	1.6–2.1 [13–17]	7.4
Vicalloy 2	52Co,14V	41	1.0	3.5 [28]	—
Alnico 2(S)	2.5Co,17Ni,10Al,6Cu	43	0.69	1.4 [11]	7
Alnico 5(S)	24Co,15Ni,8Al,3Cu	46	1.0	3.5 [28]	6.6
Alnico 9	34Co,15Ni,7Al,5Ti.4Cu	110–140	0.7–1.1	4.5–9 [36–72]	7.3

* Residual constituent is Fe.

TABLE 2.3.3 Characteristics of Ferrite Magnet[10,11]

Magnet	Saturation Polarization (x10kG) (T)	Magnetic Anisotropy Constant (MJ/m^3)	Curie Point (°C)	Maximum Energy Product (BH_{max}) (MGOe) [kJ/m^3]
$BaFe_{12}O_{19}$	0.48	0.325	450	5.8 [46]
$SrFe_{12}O_{19}$	0.48	0.35	462	3.5–4.5[28–36]
$La_{0.3}Sr_{0.7}Zn_{0.3}Fe_{11.7}O_{19}$	0.46			5.2 [41]
$La_{0.3}$ $Sr_{0.7}Co_{0.3}Fe_{11.7}O_{19}$	0.38	0.22	425	
$PbFe_{12}O_{19}$	0.40	0.22	452	
$0.75CoFe_2O_4+0.25Fe_3O_4$	0.34		540	1.3 [10]

TABLE 2.3.4 Characteristics of Rare-Earth Magnets[10,12]

Magnet	Saturation Polarization (x10kG) (T)	Magnetic Anisotropy Constant (MJ/m^3)	Curie Point (°C)	Maximum Energy Product (BH_{max}) (MGOe) [kJ/m^3]	Density (10^3 kg/m^3)
$SmCo_5$	1.14	11–20	727	32.5 [259]	8.3
Sm_2Co_{17}	1.25	3.2	920	39.1 [311]	8.5
$Nd_2Fe_{14}B$	1.60	4.5	313	64.1 [510]	7.5–7.6
$Dy_2Fe_{14}B$	0.71	4.0	325	12.6 [100]	
$Co_2Fe_{14}B$	1.13	2.0	712	31.9 [254]	
$Sm_2Fe_{17}N_3$	1.57	16.2	473	24–30 [190–240]	
$SmFe_9N$	1.70	–	520	13.8 [110]	

TABLE 2.3.5 Characteristics of Soft Magnetic Materials[4]

Name	Composition (%)	Initial Permeability $X10^3\mu_o$ (H/m)	Coercive Force (A/m)	Saturation Magnetization (T)	Curie Point (°C)	Density (10^3 kg/m^3)
Silicon steel	4Si*	0.5	40	1.97	963	7.65
45 Permalloy	45Ni*	3–5	4.8–9.6	1.6		8.17
78 Permalloy	78.5Ni*	30–70	0.8–1.6	1.08	473	8.60
4–79 Permalloy	4Mo,79Ni*	20	4	0.87	733	8.72
Supermalloy	5Mo,79Ni*	70–150	0.4–0.8	0.75–0.81	673	8.77
Mumetal	5Cu,2Cr,77Ni*	20	4	0.65		8.58
Permendur	$50C_O$*	0.8	160	2.45	1253	8.3
Vanadium Permendur	1.8V,49Co*	0.8	64	2.4	1253	8.2
Alperm	16Al*	3	3.2	0.8	673	6.5
Sendast	5Al,10Si*	30	4	1.0	773	7.0
Mn-Zn Ferrite		1–10	16–32	0.32–0.5	120–300	4.9
Ni-Zn Ferrite		0.05–1.5	20–80	0.28–0.41	100–300	5.0

* Residual constituent is Fe.

TABLE 2.3.6 Susceptibility of Minerals

Minerals	Chemical Composition	Specific Susceptibility ($\times 10^{-6}$)
Franklinite	$(Fe,Zn,Mn)O(FeMn)_2O_3$	455–640
Siderite	$FeCO_2$	84.2, 142.6
Zircon	$ZrSiO_4$	–0.17, +0.732
Corundum	Al_2O_3	–0.34
Quartz	SiO_2	–0.461, –0.466
Rutile	TiO_2	1.96, 2.09
Pyrite	FeS_2	0.98
Sphalerite	ZnS	–0.264
Dolomite	$CaMgC_2O_8$	0.787, 1.20
Apatite	$Ca_5Cl(PO_4)_3$	–2.64
Chalcopyrite	$CuFeS_2$	0.85
Spinel	$MgAl_2O_4$	0.62
Galena	PbS	–0.350
Rock salt	NaCl	–0.50
Tourmaline	$H_9Al_2(BOH)_2Si_4O_{19}$	1.12, 0.748
Graphite	C	–2.2, –14.2
Fluorite	CaF_2	–0.285
Aragonite	$CaCO_3$	–0.392, –0.444
Calcite	$CaCO_3$	–0.363, –0.405
Ruby	Al_2O_3	0.47
Topaz	$(AlF)_2SiO_4$	–0.42
Beryl	$Be_3Al_2(SiO_3)_6$	0.826, 0.386
Epidote	$Hca_2(Al, Fe)_3Si_3O_{13}$	23.8, 23.9
Hornblende	$(Ca, Mg, Fe)_8Si_9O_{26}$	24.0, 18.0
Augite	$CaMgSiO_6$	26.6, 22.7
Diopside	$CaMg(SiO_3)_7$	8.8
Columbite	—	33.6–43.2
Monazite	—	18.1
Pitchblende	—	13.0
Gadolinite	—	5.83
Manganite	$Mn_2O_3 \cdot H_2O$	490
Cobaltite	CoAsS	5.8
Feldspar	—	1.6
Limestone	—	6

Here the relative susceptibility means κ/μ_o (SI unit) that is 4 $\pi\rho$ times of susceptibility in CGS units (ρ, g/cm^3).

ACKNOWLEDGMENT

The author gratefully appreciates Dr. Svoboda's useful discussions.

REFERENCES

1. Svoboda, J., *Magnetic Methods for the Treatment of Minerals*, Elsevier, New York, 1987, pp. 3–9.
2. Friedlaender, F.J., Takayasu, M., Nakano T., Neese W.H., *IEEE Trans. Magn.*, 15, 1526, 1979.
3. Svoboda, J., *Magnetic Techniques for the Treatment of Materials*, Kluwer Academic Publishers, Dordrecht, 2004, pp. 181–206.
4. Yashima, S., Fujita, T., *J. Soc. Powder Technol. Jpn.*, 28, 257–266, 1991; Ushiki, K., *Powder Technology Handbook*, 2nd Ed., Macel Dekkar, New York, 1977.
5. Mitsui, S., In *Jisei Buturi no Shinpo*, S. Chikazumi, Ed., Agne, Tokyo, 1964, p. 242.
6. Gottschalk, V. H., *Physics*, 6, 127, 1935.
7. Morrish, A. H., Yu, S. P., *J. Appl. Phys.*, 26, 1049, 1955.
8. Rosensweig, R. E., *Ferohydrodynamics*, Cambridge University Press, London, 1985, pp. 61–62.
9. Svoboda, J., Fujita, T., *Proc. 22 Int. Miner. Process. Congr. (IMPC)*, Cape Town, 2003, pp. 261–269.
10. Iriyama, T., *Magnetics Jpn.*, 8, 293, 2013.
11. Fukunaga, H., *Magnetics Jpn.*, 10, 30, 2015.
12. Taguchi, H., *Magnetics Jpn.*, 9, 69, 2014.

2.4 Diffusion of Particles

Toshiyuki Fujimoto and Kikuo Okuyama (2.4.1)
Shinichi Yuu (2.4.2)

2.4.1 THERMAL DIFFUSION

When a particle is small, Brownian motion is caused by random variations in the incessant bombardment of molecules against the particle. As the result of Brownian motion, aerosol particles appear to diffuse in a manner analogous to the diffusion of gas molecules.

The Brownian motion of a particle of D_p in diameter and m_p in mass is expressed by the equation of motion of a single particle taking account for Stokes' drag:

$$m_p \frac{d\mathbf{v}}{dt} = -\frac{3\pi\mu D_p}{C_C}\mathbf{v} + m_p\mathbf{a}(t) \tag{2.4.1}$$

where

- $\mathbf{v}$ is the velocity of the particle,
- $\mathbf{a}(t)$ is the random acceleration resulting from the thermal motion of the background molecules,
- μ is the viscosity of surrounding fluid,
- C_C is the Cunningham correction factor accounting for noncontinuum effects.

C_C is equal to unity in liquid, and in air it is given by

$$C_C = 1 + 2.514\left(\frac{l}{D_p}\right) + 0.80\left(\frac{l}{D_p}\right)\exp\left[-0.55\left(\frac{D_p}{l}\right)\right] \tag{2.4.2}$$

where l is the mean free path of gas molecules; $l = 6.5 \times 10^{-8}$ m at 25°C under atmospheric pressure.

Figure 2.4.1 shows a particle trajectory in a stationary fluid. In this case, the average square of the particle displacement $\overline{\Delta x^2}$ and the average displacement $\overline{|\Delta x|}$ by Brownian motion in a time interval t are given as follows:

$$\overline{\Delta x^2} = 2Dt, \quad \overline{|\Delta x|} = \sqrt{\frac{4Dt}{\pi}} \tag{2.4.3}$$

In the above equations, D (m²/s) is the Brownian diffusion coefficient of particles of D_p given by

$$D = \frac{C_C kT}{3\pi\mu D_p} \tag{2.4.4}$$

where

- k is the Boltzmann constant (1.38×10^{-23} J/K),
- T is the temperature (K).

Figure 2.4.2 shows the Brownian diffusion coefficient of particles in air and water at 20°C.

For the agglomerate particles, the Brownian diffusion coefficient can be expressed by replacing the solid particle diameter by the collision diameter, D_c, of agglomerate in the Fuchs interpolation expression for Brownian coagulation in the free molecule and continuum regimes[1,2]

$$D = \frac{kT}{3\pi\mu D_c}\left(\frac{5 + 4Kn + 6Kn^2 + 18Kn^3}{5 - Kn + (8+\pi)Kn^2}\right) \tag{2.4.5}$$

where Kn (=$2l/D_c$) is the Knudsen number of the agglomerate. The collision diameter of an agglomerate is proposed as[2,3]

$$D_c = d_p\left(\frac{v}{v_p}\right)^{1/D_f} = d_p\left(n_p\right)^{1/D_f} \tag{2.4.6}$$

where

- d_p and v_p are the diameter and the volume of the primary particle, respectively,
- n_p is the number of primary particles in an agglomerate,
- D_f is the mass fractal dimension.

The number concentration of particles of a uniform size undergoing Brownian diffusion in a flow with gas velocity $\mathbf{u}$ can be determined by solving the following equation of convective diffusion of particles with an allowance for external forces:

$$\frac{\partial n}{\partial t} + \nabla\cdot\mathbf{u}n = D\nabla^2 n - \nabla\cdot\mathbf{v}n, \quad \mathbf{v} = \frac{\tau\sum\mathbf{F}}{m_p} \tag{2.4.7}$$

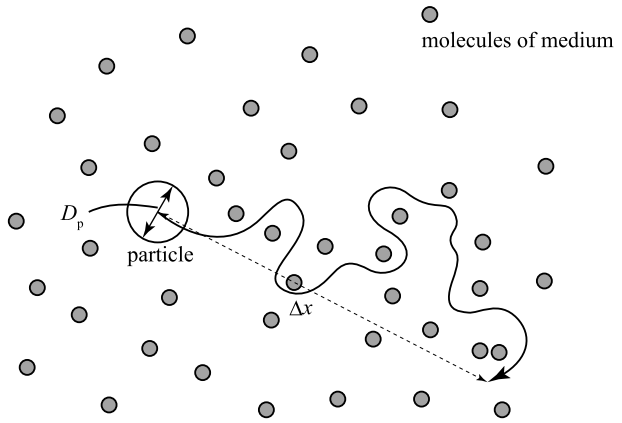


FIGURE 2.4.1 Particle movement by Brownian motion.

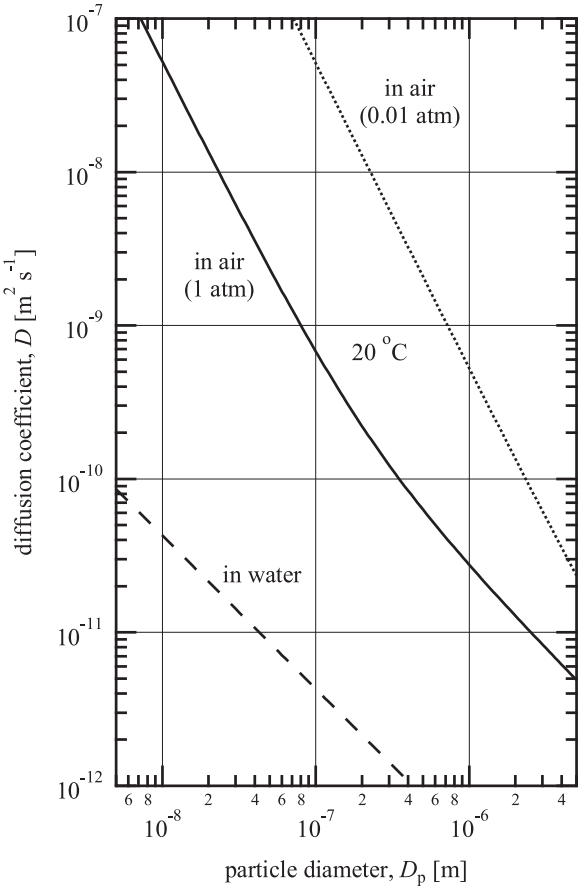


FIGURE 2.4.2 Diffusion coefficient of particle in air and water.

where

- n is the particle number concentration,
- $\mathbf{v}$ is the particle velocity caused solely by total external forces $\Sigma\mathbf{F}$,
- $\mathbf{u}$ is the velocity of the surrounding gas or liquid,
- τ is the relaxation time of the particle ($\rho_p C_C D_p^2/18\,\mu$, ρ_p = particle density, μ = viscosity of fluid).

If particles are polydispersed with a number distribution function $n(D_p, t)$ at time t, the corresponding diffusion equation can be given by substituting $n(D_p, t)$ into n in Equation (2.4.7).[4]

The local deposition rate of particles by Brownian diffusion onto a unit surface area, the deposition flux $\mathbf{j}$ (number of deposited particles per unit time and surface area), is given by

$$\mathbf{j} = -D\nabla n + \mathbf{v}n + \mathbf{u}n \tag{2.4.8}$$

If the flow is turbulent, the value of the deposition flux depends on the strength of the flow and the Brownian diffusion coefficient.

Table 2.4.1 indicates the representative solutions for steady-state particle deposition in laminar flow. The solutions in cases (b) and (c) are applicable to size analysis of small aerosol particles based on Brownian diffusion. Figure 2.4.3 shows the change in number concentration of aerosols in laminar flow through a horizontal cylindrical pipe as a function of the dimensionless parameter μ ($Dx/[u_{xav}R^2]$; u_{xav} = average velocity of fluid, x = pipe length, R = pipe radius).[9] n_0 and n are the cup-mixing particle number concentrations at inlet and outlet, respectively. The value of σ ($u_t R/D$; u_t = gravitational settling velocity) indicates the relative effect of gravitational sedimentation to the Brownian diffusion. Symbols in Figure 2.4.3 show the numerical results of simultaneous diffusion and gravitational sedimentation by Taulbee[9]. Neglecting the gravitational sedimentation ($\sigma = 0$) the results agree well with the analytical solution of Brownian diffusion only indicated by a solid line (case [b] in Table 2.4.1). With increasing σ, the effect of gravitational sedimentation increases. In the case of $\sigma = 50$, numerical results of Taulbee (closed circles) agrees with the analytical solution of gravitational sedimentation without any Brownian diffusion (dashed line)[10]:

$$\frac{\bar{n}}{n_0} = 1 - \frac{2}{\pi}\left(2\alpha\beta - \alpha^{1/3}\beta + \sin^{-1}\alpha^{1/3}\right) \tag{2.4.9}$$

where $\alpha = (3/8)\sigma\mu$ and $\beta = \sqrt{1-\alpha^{2/3}}$.

When small particles are enclosed in a chamber and its number concentration is uniform except in the vicinity of the chamber walls, the change in the number concentration of particles with time is given by

$$n = n_0 \exp(-\beta t) \tag{2.4.10}$$

where

- n_0 is the initial particle number concentration,
- β is the deposition rate coefficient,
- t is the elapsed time.

In the case of a cylindrical chamber having an inner surface area S and volume V_T, β corresponds to $DS/\delta V_T$, and the thickness δ of the concentration boundary layer can be given as $2.884D^{-1/3}$ for natural convection flow.[11]

If the flow is turbulent, β becomes a function of the strength of the flow field and the Brownian diffusion coefficient.[11,12] The transport rate of particles suspended in turbulent flow onto a wall surface over which the fluid stream is flowing as shown in Figure 2.4.4 can be described by

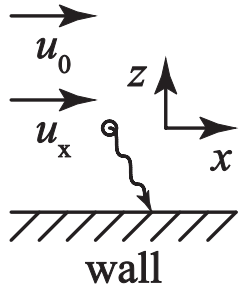
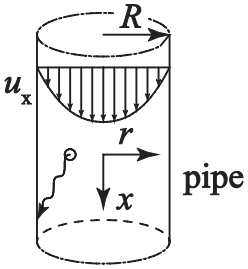
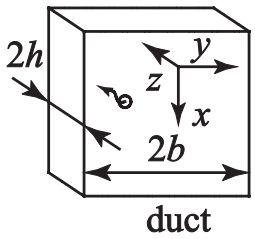
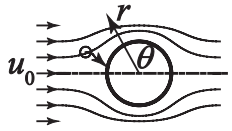
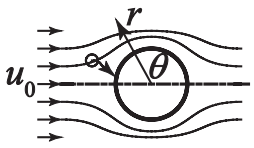
$$N = (D + D_E)\frac{dn}{dy} - mu_t \cos\theta \tag{2.4.11}$$

where

- D and D_E are the Brownian and turbulent diffusion coefficients, respectively,
- u_t is the gravitational settling velocity,
- y is the distance from the surface,
- θ is the angle from the direction of y to the direction of the gravity.

By solving Equation (2.4.11) analytically, Crump and Seinfeld[12] derived an expression for the deposition velocity $V(\theta)$ ([deposition flux]/[particle number concentration above

TABLE 2.4.1 Particle Diffusion at Steady State in a Laminar Flow

Situation	Basic Equation	B. C.	Solution	Reference
(a) Wall 	$u_x \frac{\partial n}{\partial x} + u_z \frac{\partial n}{\partial z} = D \frac{\partial^2 n}{\partial z^2}$	$n(x,0) = 0$, $n(x,\infty) = n_0$	$n(x,z) = \frac{(0.22\mathrm{Sc})^{1/3} n_0}{0.89} \times \int_0^{0.5\sqrt{u_0 z^2/\nu x}} \exp(-0.22\mathrm{Sc}y^3) dy$ $j = 0.34 D n_0 \left(\frac{u_0}{\nu x}\right)^{1/2} \mathrm{Sc}^{1/3}$, $\mathrm{Sc} = \nu / D$, $\nu = \eta / \rho$	Levich[5], pp. 87–91 (1962)
(b) Pipe 	$u_x \frac{\partial n}{\partial x} = D\left(\frac{\partial n}{r\partial r} + \frac{\partial^2 n}{\partial r^2}\right)$, $u_x = 2u_{xav}\left(1 - \frac{r^2}{R^2}\right)$	$n(0,r) = n_0$, $n(x,R) = 0$	$\alpha \geq 0.0312$ $\frac{n}{n_0} = 0.819e^{-3.657\alpha} + 0.0975e^{-22.3\alpha} + 0.0325e^{-57\alpha} + \ldots$ $\alpha < 0.0312$ $\frac{n}{n_0} = 1 - 2.56\alpha^{2/3} + 1.2\alpha + 0.177\alpha^{4/3} + \ldots$ $\alpha = Dx / u_{xav} R^2$	Gormely and Kennedy (1948)[6]
(c) Duct 	$u_x \frac{\partial n}{\partial x} = D \frac{\partial^2 n}{\partial z^2}$, $u_x = \frac{3u_{xav}}{2h^2}\left(h^2 - z^2\right)$ $2h << 2b << \text{length}$	$n(0,z) = n_0$, $n(x,\pm h) = 0$,	$\frac{n}{n_0} = 0.9149e^{-7.54\mu} + 0.05925e^{-89.3\mu} + 0.02587e^{-607\mu} + \ldots$ $\mu = Dx / 4h^2 u_{xav}$	De Marcus and Thomas (1952)[7]
(d) Cylinder 	$u_r \frac{\partial n}{\partial r} + u_\theta \frac{\partial n}{r\partial \theta}$ $= D\left(\frac{\partial^2 n}{\partial r^2} + \frac{\partial n}{r\partial r} + \frac{\partial^2 n}{r^2 \partial \theta^2}\right)$	$n(R,\theta) = 0$, $n(\infty,\theta) = n_0$ $\mathrm{Re} < 1$ $D_p / R \approx 0$	$\eta_D = \frac{2DR\int_0^\pi \frac{\partial n}{\partial r}_{r=R} d\theta}{2u_0 R n_0}$ $= 2.9k^{-1/3}\mathrm{Pe}^{-2/3} + 0.62\mathrm{Pe}^{-1}$ η_D: target efficiency, $\mathrm{Pe} = 2u_0 R / D$ Parallel cylinders: $k = -\frac{1}{2}\ln\alpha - \frac{3}{4} + \alpha - \frac{\alpha^2}{4}$ α: packing fraction isolated cylinders: $k = 2 - \ln \mathrm{Re}$	Stechkina and Fuchs (1966)[8]
(e) Sphere 	$u_r \frac{\partial n}{\partial r} + u_\theta \frac{\partial n}{r\partial \theta}$ $= D\left[\frac{1}{r^2}\frac{\partial}{\partial r}\left(r^2 \frac{\partial n}{\partial r}\right) + \frac{1}{r^2 \sin\theta} \times \frac{\partial}{\partial \theta}\left(\sin\theta \frac{\partial n}{\partial \theta}\right)\right]$	$n(R,\theta) = 0$, $n(\infty,\theta) = n_0$ $\mathrm{Re} < 1$ $D_p / R \approx 0$	$\eta_D = \frac{2\pi DR^2 \int_0^\pi \frac{\partial n}{\partial r}_{r=R} \sin\theta d\theta}{\pi R^2 u_0 n_0}$ $= 4.04\mathrm{Pe}^{-2/3}$ η_D: target efficiency, $\mathrm{Pe} = 2u_0 R / D$	Levich, pp.80–87 (1962)[5]

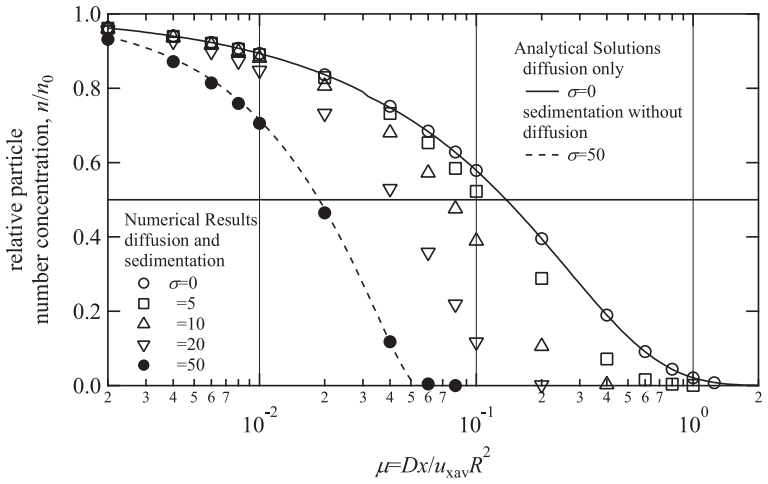


FIGURE 2.4.3 Decrease in number concentration of aerosol due to Brownian diffusion and gravitational settling in a horizontal pipe flow.

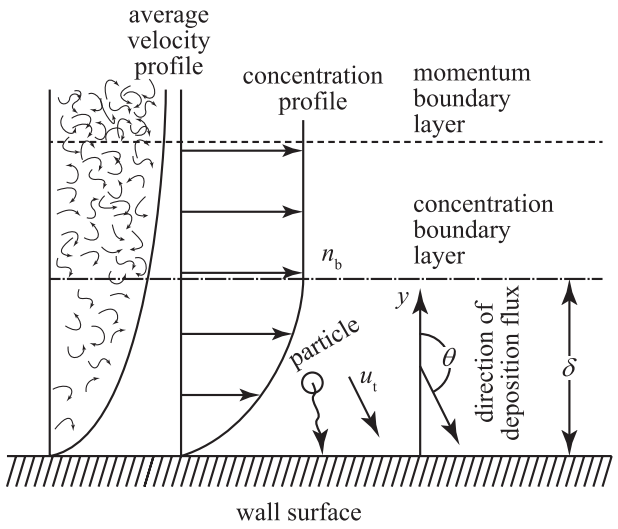


FIGURE 2.4.4 Schematic diagram of particle deposition onto an inclined flat surface.

the surface]) for a wall with the angle θ approximating the turbulent diffusion coefficient D_E to $K_e y^m$ as follows:

$$V(\theta) = u_t \cos\theta \left[\exp\left(\frac{\pi u_t \cos\theta}{m \sin(\pi/m) \sqrt[m]{K_e D^{m-1}}} \right) - 1 \right]^{-1} \quad (2.4.12)$$

In the turbulent diffusion coefficient D_E, K_e is considered to be proportional to the velocity gradient of fluid as $k|du/dx|$, where k is a constant depending on the flow condition of fluid. For stirred turbulent flow field, $k=0.4$ and $m=2.7$ could explain the experimental values reasonably. When the surface area of walls of the chamber with the angle θ is $S(\theta)$, the deposition rate coefficient β can be related to the deposition velocity $V(\theta)$ as

$$\beta = \left(\sum_{\theta=0}^{2\pi} V(\theta) S(\theta) \right) V_T^{-1} \quad (2.4.13)$$

where V_T is a total volume of the chamber.

When external forces such as electrostatic force have influence on particle transport, the deposition velocity can be predicted by considering the particle velocity induced by the forces in Equation (2.4.12).[13] In such a case, $u_t \cos\theta$ in Equation (2.4.12) is replaced by $u_t \cos\theta + v_{ext,}$ where v_{ext} is the component of this velocity in the direction normal to the wall. Deposition velocity is also influenced by wall roughness. Because the concentration boundary layer of gas-borne particles is generally much thinner than the momentum boundary layer, even a wall with very small roughness that does not affect the momentum boundary layer (i.e. a hydraulically smooth wall) can enhance particle deposition rate if the height of the roughness is comparable to the thickness of the concentration boundary layer.[14]

2.4.2 TURBULENT DIFFUSION

Turbulent diffusion is defined as the transportation of physical properties such as mass, heat, and momentum by the turbulent random motion of a fluid. Because knowledge of statistical functions describing turbulent motions is limited compared with that of molecular motions, any solution of turbulent transport problems is incomplete and only approximate.

In comparing turbulent mass flux with the corresponding flux caused by molecular motion, it is usually assumed that the turbulent mass flux is similar in description to molecular diffusion; that is, the flux is directly proportional to the concentration gradient (gradient transport). Although the solution based on the gradient transport cannot be correct in all details, the phenomenological theory (the gradient transport theory) is most useful for practical engineering problems. The present section is devoted to a description of the turbulent diffusion, particularly the particle turbulent diffusion based on the gradient transport.

The treatment of transport phenomena in the various flow fields and these applications are omitted in this section, and fundamental descriptions about the turbulent diffusion (i.e. turbulent diffusion equation, turbulence properties, and diffusion coefficient) are presented.

Turbulent Diffusion Equation

The law of conservation of particle mass gives

$$\frac{\partial n}{\partial t}+\nabla\cdot n\mathbf{v}=D\nabla^2 n+\Gamma \tag{2.4.14}$$

where

n, $\mathbf{v}$, D, and Γ are particle concentration, particle velocity vector, Brownian diffusion coefficient, and source, respectively,

∇ is the nabla operator.

The instantaneous values can be written as

$$n=\bar{n}+n',\qquad \mathbf{v}=\bar{\mathbf{v}}+\mathbf{v}' \tag{2.4.15}$$

where the overbar and prime denote the average and the fluctuating values, respectively. Some rearrangement, after substituting Equation (2.4.15) into Equation (2.4.14) gives

$$\frac{\partial \bar{n}}{\partial t}+\nabla\cdot\bar{n}\bar{\mathbf{v}}+\nabla\cdot\overline{n'\mathbf{v}'}=D\nabla^2\bar{n}+\Gamma \tag{2.4.16}$$

The first term on the left-hand side represents change with time, the second is a convection term, and the third is a turbulent transport term. The first term on the right-hand side represents mass flux due to Brownian motion and the second is a source or reaction term. Only the third term on the left-hand side has turbulence fluctuating values. If the turbulent transport term $\overline{n'\mathbf{v}'}$ is expressed by the time-averaged particle concentration $\bar{n}$, Equation (2.4.16) can be solved because then the only unknown in Equation (2.4.16) is $\bar{n}$. The introduction of the gradient transport, which shows an analogy to the Brownian diffusion, gives

$$\overline{n'v_i'}=-\varepsilon_p\frac{\partial \bar{n}}{\partial x_i} \tag{2.4.17}$$

where ε_p is the particle turbulence diffusion coefficient. If the diffusion coefficient is a tensor of the second order, the relation between $\overline{n\mathbf{v}'}$ and $\delta\bar{n}/\delta x_j$ should be

$$\overline{n'v_i'}=-\varepsilon_{pij}\frac{\partial \bar{n}}{\partial x_j} \tag{2.4.18}$$

In this section the summation convention with respect to repeated indices is used. Substitution of Equation (2.4.18) into Equation (2.4.16) gives

$$\frac{\partial \bar{n}}{\partial t}+\nabla\cdot\bar{n}\bar{\mathbf{v}}=\frac{\partial}{\partial x_i}\left(\varepsilon_{pij}\frac{\partial \bar{n}}{\partial x_j}\right)+D\nabla^2\bar{n}+\Gamma \tag{2.4.19}$$

Equation (2.4.19) is a general form of a particle diffusion equation. If we consider the transport by the turbulent motions without molecular diffusion and source, Equation (2.4.19) reduces to

$$\frac{\partial \bar{n}}{\partial t}+\nabla\cdot\bar{n}\bar{\mathbf{v}}=\frac{\partial}{\partial x_i}\left(\varepsilon_{pij}\frac{\partial \bar{n}}{\partial x_j}\right) \tag{2.4.20}$$

When the time-averaged particle velocity $\mathbf{v}$ and the turbulent diffusion tensor ε_{pij} are known, Equation (2.4.20) can be solved and the solution with the boundary conditions gives a particle concentration distribution. If the time-averaged particle velocity is equal to that of fluid (i.e. the particle inertia is negligibly small), substitution of the fluid continuity equation into Equation (2.4.20) gives

$$\frac{\partial \bar{n}}{\partial t}+\bar{\mathbf{v}}\cdot\nabla\bar{n}=\frac{\partial}{\partial x_i}\left(\varepsilon_{pij}\frac{\partial \bar{n}}{\partial x_j}\right) \tag{2.4.21}$$

where the fluid is assumed to be incompressible.

Turbulent Diffusion Coefficient

The basic problem now is to derive an expression for ε_{pij}. Batchelor showed that when the probability distribution of the displacement of particles has a Gaussian form, the diffusion tensor can be interpreted as[15]

$$\varepsilon_{ij}+\varepsilon_{ji}=\frac{d}{dt}\overline{\left(X_i-\bar{X}_i\right)\left(X_j-\bar{X}_j\right)} \tag{2.4.22}$$

where X_i and X_j are i and j components of the Lagrangian position of the particle. When $i=j=2$, Equation (2.4.22) reduces to

$$\varepsilon_{22}=\frac{1}{2}\frac{d}{dt}\overline{\left(X_2-\bar{X}_2\right)^2} \tag{2.4.23}$$

The mean square value $\overline{\left(X_2-\bar{X}_2\right)^2}$ of the Lagrangian displacement can be obtained by

$$\begin{aligned}\overline{\left(X_2-\bar{X}_2\right)^2}&=2\int_0^t\int_0^{t'}v_2'(t')v_2'(t'-\tau)d\tau\,dt'\\&=2\overline{v_2'^2}\int_0^t(t-\tau)R_L(\tau)d\tau\end{aligned} \tag{1.24}$$

The Lagrangian correlation coefficient $R_L(\tau)$ is defined as

$$R_L(\tau)=\frac{\overline{v_2'(t)v_2'(t+\tau)}}{\left[\overline{v_2'(t)^2}\,\overline{v_2'(t+\tau)^2}\right]^{1/2}} \tag{2.4.25}$$

Now consider some simple cases. The Lagrangian correlation $R_L(\tau)$ is nearly equal to unity for a very small t (i.e. for a very

short time diffusion). Substitution of $R_L(\tau) = 1$ into Equation (2.4.24) gives

$$\overline{\left(X_2 - \bar{X}_2\right)^2} = \overline{v_2'^2}\, t^2 \tag{2.4.26}$$

Substituting Equation (2.4.26) into Equation (2.4.23), we obtain

$$\varepsilon_{22} = \overline{v_2'^2}\, t \tag{2.4.27}$$

Hence, the diffusivity for very short time diffusion depends linearly on the time and the mean square value of fluctuating velocity (i.e. turbulent intensity).

On the other hand, we now consider a long diffusion time. When diffusion time t is much longer than the time t_0 for which $R_L(t_0) \approx 0$, Equation (2.4.24) is reduced to

$$\begin{aligned} 2\overline{v_2'^2}\int_0^t (t-\tau) R_L(\tau)\, d\tau &= 2\overline{v_2'^2} t \int_0^{t_0} R_L(\tau)\, d\tau \\ &= 2\overline{v_2'^2}\int_0^{\infty} R_L(\tau)\, d\tau \\ &= 2\overline{v_2'^2}\, t\, T_L \end{aligned} \tag{2.4.28}$$

where T_L defined as $T_L = \int_0^{\infty} R_L(\tau)\, d\tau$ is the Lagrangian integral time scale. Substitution of Equation (2.4.28) into Equation (2.4.23) gives

$$\varepsilon_{22} = \overline{v_2'^2}\, T_L \tag{2.4.29}$$

Hence, the diffusivity for a long diffusion time is proportional to the integral time scale and the turbulent intensity.

Solid particle, mist, and small bubble cannot follow the fluid motion completely due to their inertia. Hinze derived the relation between ε_p and ε_f as follows:[16]

$$\frac{\varepsilon_p}{\varepsilon_f} = 1 + \frac{1 - B^2}{A^2 T_{fL}^2 - 1} \frac{\exp(-At) - \exp(-t/T_{fL})}{1 - \exp(-t/T_{fL})} \tag{2.4.30}$$

Equation (2.4.30) shows that $\varepsilon_p \approx \varepsilon_f$ for a long diffusion time. This is reasonable for homogeneous turbulence, even though for a long diffusion time ε_p is not equal to ε_f in an inhomogeneous turbulence in which the turbulence characteristics change spatially. The assumption that the same fluid will surround the particle as it moves (no overshooting) causes an unreasonable result. However, it is difficult to take the effect of the overshooting rigorously into account. Hence, the Lagrangian turbulent trajectories of particles and the turbulent diffusivity are calculated by a simple model.

Yuu et al.,[17] Brown and Hutchinson,[18] and Gosman and Ioannides[19] present the models. The model of Yuu is explained here.[17] The particle moves, surrounded by an eddy that has a lifetime T_L defined as

$$T_L = \int_0^{\infty} R_L(\tau)\, d\tau \tag{2.4.31}$$

where

$R_L(\tau)$ is the Lagrangian time correlation coefficient,
T_L is the averaged longest time during which a fluid particle persists in moving in a given direction.

In the model, R_L is 1 when the diffusion time $t \le T_L$, and R_L becomes zero when $t > T_L$. In other words, an independent eddy surrounds the particle and affects the particle motion during the next T_L. The fluid fluctuating velocity is obtained by using a normal random function in which the average value is zero and the variance is equal to the fluid intensity. Substituting the fluid fluctuating velocity into the equation of particle motion, one can calculate the Lagrangian particle trajectory. Similarly, the particle trajectory during the next T_L is calculated, and the process is repeated until the diffusion time passes.

Since the early work by Taylor,[20] the relation between the turbulent diffusivity and Lagrangian displacements has been studied by many investigators to obtain values for the turbulent flux of transferable quantities. Most of them, however, did not completely consider the effect of inhomogeneity of the turbulence field nor the effect of mean velocity distribution in an inhomogeneous turbulent flow. The ensemble average of the Eulerian fluctuating velocities at the Lagrangian positions is not zero in an inhomogeneous turbulent flow. For example, Batchelor's description (Equation 2.4.22) of the turbulent diffusivity for homogeneous turbulence would not be strictly applied to real turbulent flows, as these usually have mean velocity distributions.

Yuu derived the relation (Equation 2.4.32) between turbulent diffusivities and the Lagrangian displacement of particles in a flow field with a mean velocity distribution based on the gradient transport:[21]

$$\begin{aligned} \langle \varepsilon_{ij} \rangle = \frac{1}{2}\frac{\partial}{\partial t}\left\langle \left(x_i - \langle x_i \rangle\right)\left(x_j - \langle x_j \rangle\right)\right\rangle \\ + \left\{ \langle x_i \rangle \langle \bar{u}_j \rangle - \langle x_i \bar{u}_j \rangle \right\} \end{aligned} \tag{2.4.32}$$

in which $\langle\ \rangle$ indicates an ensemble averaged values.

Many researchers, for example Zaichik et al., developed the Eulerian model of particle diffusion called the diffusion inertia model based on a kinetic equation for the probability density function of particle velocity distribution.[22] This model was coupled with Reynolds-averaged Navier Stokes equations in the frame of one way coupling. The results of the model represent the experimental data well. Shotorban and Balachandar[23] and Zaichik, Simonin, and Alipchenkov[24] also developed the Eulerian models of particle diffusion in coupling with Direct Numerical Simulation and Large Eddy Simulation methods for calculating the carrier turbulent

fluids. The merit of the Eulerian diffusion models is that the particle motion is expressed in terms of the carrier fluid.

REFERENCES

1. Seinfeld, J. H., Pandis, S. N., *Atmospheric Chemistry and Physics from Air Pollution to Climate Change*, John Wiley & Sons, New York, 1998, pp. 656–664.
2. Kruis, F. E., Kusters, K. A., Pratsinis, S. E., *Aerosol Sci. Technol.* 19, 514–526, 1993.
3. Matsoukas, T., Friedlander, S. K., *J. Colloid Interface Sci.* 146, 495–506, 1991.
4. Fujimoto, T., Okuyama, K., Yamada, S., Adachi, M., *J. Appl. Phys.*, 85, 4196–4206, 1999.
5. Levich, V. G., *Physicochemical Hydrodynamics*, Prentice-Hall, Englewood Cliffs, NJ, 1962.
6. Gormely, P. G., Kennedy, M., *Proc. Roy. Irish Acad. A* 52, 163–169, 1948.
7. De Marcus, W., Thomas, J., U.S. Atomic Energy Commission Report ORNL-1413, 1952.
8. Stechkina, I., Fuchs, N. A., *Ann. Occup. Hyg.*, 9, 59–64, 1966.
9. Taulbee, D. B., *J. Aerosol Sci.*, 9, 17–23, 1978.
10. Fuchs, N. A., *The Mechanics of Aerosols*, Pergamon Press, London, 1964, pp. 110–112.
11. Okuyama, K., Kousaka, Y., Yamamoto, S., Hosokawa, T., *J. Colloid Interface Sci.*, 110, 214–223, 1986.
12. Crump, J. G., Seinfeld, J. H. *J. Aerosol Sci.* 12, 405–415, 1981.
13. Shimada, M., Okuyama, K., *J. Colloid Interface Sci.*, 154, 255–263, 1992.
14. Shimada, M., Okuyama, K., Kousaka, Y., Seinfeld, J. H., *J. Colloid Interface Sci.*, 125, 198–211, 1988.
15. Batchelor, G. K., *Aust. J. Sci. Res.,* A2, 437–451, 1949.
16. Hinze, J. O., *Turbulence*, 2nd Ed., McGraw-Hill, New York, 1975.
17. Yuu, S., Yasukouchi, N., Hirosawa, Y., Jotaki, T., *AIChE J.*, 24, 509–519, 1978.
18. Brown, D. J., Hutchinson, P., *J. Fluids Eng.*, 101, 265–269, 1979.
19. Gosman, A. D., Ioannides, E., *AIAA Paper* 81-0323, 1981.
20. Taylor, G. I., *Proc. London Math. Soc. Ser. 2*, 20, 196–215, 1921.
21. Yuu, S. *Phys. Fluids*, 28, 466–472, 1985.
22. Zaichik, L. I., Pershukov, V. A., Kozelev, M. V., Vinberg, A. A., *Exp. Therm. Fluid Sci.* 15, 291–310, 1997.
23. Shotorban, B., Balachandar, S., *Phys. Fluids*, 18, 65–75, 2006.
24. Zaichik, L. I., Simonin, O., Alipchenkov, V. M., *J. Turbul.*, 10, 4–8, 2009.



Taylor & Francis
Taylor & Francis Group
http://taylorandfrancis.com

2.5 Particle Motion in Fluid

Shinichi Yuu

2.5.1 INTRODUCTION

Motion of particles in fluid is divided into two classes, i.e. rectilinear or curvilinear motion and random Brownian motion. For particles with diameters larger than about 0.5 μm, inertia or external force acting on the particles and the fluid resistance dominate the motion of particles. In such case, tracing the motion of single particles is applied to picture the motion of whole dispersed system of particles in fluid.

Motion of single particles can be further divided into three classes according to the extent of particle-fluid interaction. The simplest case is one in which the particles have the same density as the fluid at a low particle concentration so that the particles exactly follow the motion of fluid. The second case is such that the particle concentration is fairly low and the fluid induces the relative motion of particles but the particle motion does not affect the motion of fluid. The third case is such that the particle motion and fluid motion interact with each other by exchanging momentum. In this section, motions of single particles in the second case without particle-particle interaction is described.

2.5.2 MOTION OF A SINGLE PARTICLE

Resistance Force on a Spherical Particle

Particle motion relative to a fluid is dominated by resistance forces acting on the particle and external forces, such as gravitational, centrifugal, and electrostatic forces. Therefore, we should first know the resistance force on a particle for the description of particle motion.

Because the resistance force F_D depends on the particle diameter D_p, the fluid velocity u, the fluid density ρ, and the fluid viscosity μ, F_D would be written as

$$F_D = kD_p^a u^b \rho^c \mu^e \tag{2.5.1}$$

Dimensional analysis of Equation (2.5.1) gives

$$F_D = kD_p^2 u^2 \rho \left(\frac{D_p u \rho}{\mu} \right)^{-e} \tag{2.5.2}$$

Substituting the cross-sectional area of spherical particle, $A_c = \left(\pi D_p^2\right)/4$, into Equation (2.5.2) gives

$$F_D = \frac{1}{2}\rho u^2 A_c k' \left(\frac{D_p u \rho}{\mu} \right)^{-e} = \frac{1}{2}\rho u^2 A_c C_D \tag{2.5.3}$$

where $C_D = k'\left(D_p u\rho/\mu\right)^{-e}$ is a resistance coefficient. Equation (2.5.3) shows that C_D depends on only the particle Reynolds number $\mathrm{Re}_p = D_p u\rho/\mu$, that is,

$$C_D = f(\mathrm{Re}_p) = k'\mathrm{Re}_p^{-e} \tag{2.5.4}$$

where k and are constants. $k = 3\pi$ and for the Stokes region given by Equations (2.5.5 and 2.5.6). Experimental results indicate that the exponent e in Equation (2.5.4) also depends only on Re_p. In other words, the value of e is changed by the fluid moving conditions: it depends on whether the fluid flow is viscous, transitional, or turbulent. As the particle size in powder technology is usually small, in most cases the particle Reynolds numbers are less than unity. When $\mathrm{Re}_p < 1$ ($\mathrm{Re}_p < 2$, from the engineering point of view), the fluid flow is dominated by the viscous force. Then, the Navier–Stokes equation of fluid motion reduces to the linear equation, which is the creeping motion equation, by neglecting the inertia terms. Stokes solved firstly the creeping motion equation and obtained the fluid velocity and stress distributions around a spherical particle settling in a uniform flow.[1] He further obtained the resistance force acting on a spherical particle in a uniform viscous flow by integrating the stress distribution over the spherical surface of the particle. The resistance force is

$$F_D = 3\pi\mu D_p u \tag{2.5.5}$$

Equation (2.5.5) is the well-known Stokes resistance law. Substitution of Equation (2.5.5) into Equation (2.5.3) gives the resistance coefficient C_D for the Stokes law:

$$C_D = \frac{24}{\mathrm{Re}_p} \tag{2.5.6}$$

As mentioned earlier, the Stokes law applies to the creeping flow only. As the inertia effect on flow surrounding a particle increases with increasing Re_p, the Stokes law cannot apply to the flow field at $\mathrm{Re}_p > 2$. Resistance forces for flow fields at $\mathrm{Re}_p > 2$ are given by the following experimental formulas:
$2 \leqq \mathrm{Re}_p < 500$, (Allen's region)

$$F_D = \frac{5}{4}\pi\sqrt{\mu\rho}\left(D_p u\right)^{1.5} \tag{2.5.7}$$

$$C_D = \frac{10}{\sqrt{\mathrm{Re}_p}}$$

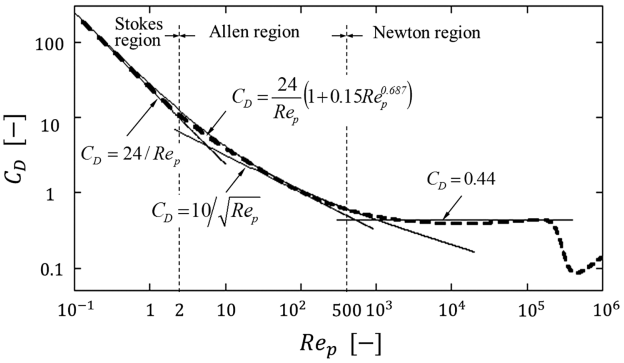


FIGURE 2.5.1 Resistance coefficient versus particle Reynolds number.

$500 \leqq \mathrm{Re}_p < 10^5$, (Newton's region)

$$F_D = 0.055\pi\rho(D_p u)^2 \tag{2.5.8}$$

$$C_D \cong 0.44$$

Figure 2.5.1 shows the relation of resistance coefficients and particle Reynolds numbers.

Recently, the Schiller-Naumann experimental formula has become more popular[2]:

$$0 < \mathrm{Re}_p \leqq 800$$

$$C_D = \frac{24}{\mathrm{Re}_p}\left(1+0.15\,\mathrm{Re}_p^{0.687}\right) \tag{2.5.9}$$

When the particle diameter is comparable to or less than the mean free path of molecules, the effect of their slip around the particle should be considered. Then, F_D is given by

$$F_D = \frac{3\pi\mu u D_p}{C_c} \tag{2.5.10}$$

where C_c is the slip correction factor. Kennard formulized the slip correction factor,[3] using Millikan's experimental data[4]:

$$C_c = 1+\left[2.46+0.82\exp\left(-\frac{0.44D_p}{l}\right)\right]\frac{l}{D_p} \tag{2.5.11}$$

Neglecting the exponential term in Equation (2.5.11) gives the following approximate equation for a particle suspended in air of normal conditions:

$$C_c = 1+\frac{0.165}{D_p} \tag{2.5.12}$$

where the unit of D_p in μm.

Equation of Particle Motion

Tchen[5] derived the Lagrange equation of motion for a particle suspended in an unsteady velocity field by extending the Basset–Buossinesq–Oseen equation.[6]

$$\begin{aligned}\frac{\pi}{6}D_p^3\rho_p\frac{d\mathbf{v}}{dt} &= 3\pi\mu D_p(\mathbf{u}-\mathbf{v})\\ &+\frac{\pi}{6}D_p^3\rho\frac{d\mathbf{u}}{dt}+\frac{\pi}{12}D_p^3\rho\left(\frac{d\mathbf{u}}{dt}-\frac{d\mathbf{v}}{dt}\right)\\ &+\frac{3}{2}D_p^2\sqrt{\pi\rho\mu}\int_{t_0}^{t}\frac{d\mathbf{u}/dt'-d\mathbf{v}/dt'}{\sqrt{t-t'}}\,dt'+\mathbf{F}_e\end{aligned} \tag{2.5.13}$$

The term on the left-hand side of Equation (2.5.13) is the force required to accelerate the particle. The first term on the right-hand side of Equation (2.5.13) is the Stokes resistance force. The second term is the force due to the pressure gradient of the fluid surrounding the particle. The third term is the force to accelerate the virtual added mass of the particle relative to the fluid. The fourth term is the Basset term describing the effect of the deviation in flow pattern from steady state, and $\mathbf{F}_e$ is the external force.

The condition $\left|(\mathbf{u}-\mathbf{v})/\mathbf{u}\right| << 1$ reduces Equation (2.5.13) to

$$\begin{aligned}&\frac{d\mathbf{v}}{dt}+A(\mathbf{v}-\mathbf{u})-B\frac{d\mathbf{u}}{dt}\\ &-C\int_{t_0}^{t}\frac{d\mathbf{u}/dt-d\mathbf{v}/dt}{\sqrt{t-t'}}\,dt'-\frac{6\mathbf{F}_e}{\pi D_p^3\rho_p}=0\end{aligned} \tag{2.5.14}$$

where A, B and C are given by

$$A=\frac{36}{(2\rho_p+\rho)D_p^2},\quad B=\frac{3\rho}{2\rho_p+\rho},\quad C=\frac{18}{(2\rho_p+\rho)D_p}\sqrt{\frac{\rho\mu}{\pi}}$$

As $\rho_p >> \rho$ and $\mu << 1$ in an airflow, B and C in Equation (2.5.14) are much smaller than A. Therefore, the third and fourth terms on the left-hand side of Equation (2.5.14) can be neglected in an air flow.

When the resistance force is expressed with the resistance coefficient C_D, the equation of particle motion is

$$m\frac{d\mathbf{v}}{dt}=-\frac{C_d A_c\rho}{2C_c}|\mathbf{v}-\mathbf{u}|(\mathbf{v}-\mathbf{u})+m\left(1-\frac{\rho}{\rho_p}\right)\mathbf{g} \tag{2.5.15}$$

where the third and fourth terms in Equation (2.5.14) are neglected, and the particle mass $m=(\pi/6)D_p^3\rho_p$ and the cross-sectional area $A_c=(\pi/4)D_p^2$ for the spherical particle. Two-dimensional normalized equations of Equation (2.5.15) are

$$\frac{C_c\rho_p\mathbf{u}_0D_p^2}{18\mu D}\frac{24}{C_D\,\mathrm{Re}_p}\frac{d^2\bar{x}}{d\bar{t}^2}+|\bar{\mathbf{v}}-\bar{\mathbf{u}}|\left(\frac{d\bar{x}}{d\bar{t}}-\bar{\mathbf{u}}_x\right)=0$$

$$\frac{C_c \rho_p u_0 D_p^2}{18\mu D}\frac{24}{C_D \mathrm{Re}_p}\frac{d^2\bar{y}}{d\bar{t}^2}+|\bar{\mathbf{v}}-\bar{\mathbf{u}}|\left(\frac{d\bar{y}}{d\bar{t}}-\bar{u}_y\right)$$

$$-\frac{24C_c}{C_D \mathrm{Re}_p}\frac{\rho_p D_p^2}{18\mu u_0}\left(1-\frac{\rho}{\rho_p}\right)g=0 \qquad (2.5.16)$$

where

$$\bar{x}=\frac{x}{D},\quad \bar{y}=\frac{y}{D},\quad \bar{t}=\frac{u_0 t}{D},\quad \bar{u}_x=\frac{u_x}{u_0},\quad \bar{u}_y=\frac{u_y}{u_0} \qquad (2.5.17)$$

$C_D = 24\mu/\left(D_p|\bar{\mathbf{v}}-\bar{\mathbf{u}}|u_0\rho\right)$ for the Stokes law reduces Equation (2.5.16) to the following equations:

$$\psi\frac{d^2\bar{x}}{d\bar{t}^2}+\frac{d\bar{x}}{d\bar{t}}-\bar{u}_x=0,\quad \psi\frac{d^2\bar{y}}{d\bar{t}^2}+\frac{d\bar{y}}{d\bar{t}}-\bar{u}_y-G=0 \qquad (2.5.18)$$

where ψ and G are the inertia parameter and normalized settling velocity, respectively, defined as

$$\psi=\frac{C_c \rho_p D_p^2 u_0}{18\mu D},\quad G=\frac{C_c(\rho_p-\rho)D_p^2 g}{18\mu u_0} \qquad (2.5.19)$$

The solution of Equation (2.5.18) based on the initial conditions gives the particle trajectory in the airflow with the velocity distribution (u_x, u_y).

2.5.3 PARTICLE MOTION IN SHEAR FLOW

A lift force (lateral force) produced on a particle due to the local velocity gradient of fluid flow and the rotation of a particle, when a particle moves in a shear flow. Saffman theoretically derived the lift force for a spherical particle at a low Reynolds number[7]:

$$F_L=1.62uD_p^2\left(\rho\mu\frac{du}{dy}\right)^{1/2} \qquad (2.5.20)$$

where u is the local relative velocity between the particle and the fluid. The lift force is exerted on the particle in the direction of increasing the fluid velocity. In the shear flow, the particle rotates due to the viscous force. At a steady state, the following equation gives the angular velocity:

$$\omega=\frac{1}{2}\frac{du}{dy} \qquad (2.5.21)$$

The lift force occurs even in uniform flow when the particle is rotating. At a low Reynolds number, the lift force due to the rotation of particle is given by:

$$F_L=\frac{\pi}{8}uD_p^3\rho\omega \qquad (2.5.22)$$

Rubinow and Keller derived the above expression.[8]

In general, particles are not spherical in shape. Even a small deviation of particle shape from sphere causes a large lift force. Since the lift force always acts on particles in the direction perpendicular to the fluid flow, it makes the concentration of particles non-uniform in the direction perpendicular to the fluid flow.

Recently Mao and Alexeev presented the motion of spheroid particles in a simple shear flow at a low and moderate Reynolds number using a lattice Boltzmann method.[9] Particles of sufficiently large Stokes number rotate with constant angular velocities. If the Reynolds number becomes larger than a critical value, the angular velocity decreases to zero and the particle stops rotating. If both of major and minor axes are not initially in the shear plane, the particle rotates three-dimensionally. Prolate spheroids drift towards the shear plane, on the other hand oblate spheroids drift towards the velocity axis with a rolling motion for small Reynolds number. The drift for prolate spheroids with aspect ratio of 2 changes from tumbling to rolling if the Reynolds number is about 60. If the Reynolds number is less than about 20, the superposition is available to calculate the combined effect of fluid and particle inertias on the motions of spheroids. Yeo and Maxey simulated dynamics of concentrated suspensions in a Couette flow to determine the wall effects.[10] Suspensions are divided into three regions. In the wall region a structured particle layering is dominant, in the core region the field of the suspension is quasi-homogeneous and in the buffer region the characteristics of the particle layer and the shear structure exist.

REFERENCES

1. Stokes, G.G. *Trans. Cambridge Philos. Soc.*, 8, 287–318, 1845.
2. Schiller, L., Naumann, A., *Z. Ver. Dtsch. Ing.*, 77, 318–321, 1933.
3. Kennard, E.H., *Kinetic Theory of Gases*, McGraw-Hill, New York, 1938.
4. Millikan, R.A., *Phys. Rev.*, 22, 1–18, 1923.
5. Tchen, C.M., *Mean value and correlation problems connected with the motion of small particles suspended in a turbulent fluid*. PhD Dissertation, Delft, Martinus Nijhoff, 1947.
6. Basset, A.B., *Philos. Trans. R. Soc.*, 179, 43–71, 1888.
7. Saffman, P.G., *J. Fluid Mech.*, 22, 385–403, 1965.
8. Rubinow, S., Keller, J.B., *J. Fluid Mech.*, 11, 447–457, 1961.
9. Mao, W., Alexeev, A., *J. Fluid Mech.*, 749, 145–166, 2014.
10. Yeo, K., Maxey, M., *J. Fluid Mech.*, 649, 205–231, 2010.



Taylor & Francis
Taylor & Francis Group
http://taylorandfrancis.com

2.6 Particle Sedimentation

Shinichi Yuu

2.6.1 INTRODUCTION

Sedimentation is the most important phenomenon not only in measuring fundamental characteristics of particles but also in understanding mechanisms of unit operations such as dust and mist collection, classification, and pneumatic transport. In this chapter, we describe the resistance force on a spherical particle moving through a fluid, the Lagrangian Equation of a particle motion, and the sedimentation velocities of particles in various situations. Particles moving through a viscous fluid interact with each other, thus, interactions between two or more spherical particles falling through a viscous liquid are also discussed.

2.6.2 TERMINAL SETTLING VELOCITY

Substituting fluid velocity $u = 0$ into Equation (2.5.15) in Chapter 2.5 gives the equation of particle motion in a quiescent fluid:

$$\frac{dv}{dt} = -\frac{3}{4}\frac{C_D v^2 \rho}{\rho_p D_p} + \frac{(\rho_p - \rho)g}{\rho_p} \tag{2.6.1}$$

When the first term (the hydrodynamic resistance force) on the right-hand side of Equation (2.6.1) is counterbalanced by the second term (the gravitational force), the spherical particle settling under the gravity attains a uniform velocity. It is called the terminal settling velocity.

Substituting $dv/dt = 0$ and Equations (2.5.6), (2.5.7), or (2.5.8) in Chapter 2.5 into Equation (2.6.1) gives the equation of terminal settling velocity for each region:

$$v_t = \frac{(\rho_p - \rho)D_p^2 g}{18\mu}, \qquad \mathrm{Re}_p \leqq 2 \tag{2.6.2}$$

$$v_t = \left(\frac{4(\rho_p - \rho)^2 g^2}{225\mu\rho}\right)^{1/3} D_p, \quad 2 < \mathrm{Re}_p \leqq 500 \tag{2.6.3}$$

$$v_t = \left(\frac{3g(\rho_p - \rho)D_p}{\rho}\right)^{1/2}, \quad 500 < \mathrm{Re}_p \leqq 10^5 \tag{2.6.4}$$

Resistance Force Acting on a Spherical Particle Settling Relative to Cylindrical and Plane Walls

Lorentz derived the theoretical equation of the resistance force acting on a spherical particle settling near a wall, as shown in Figure 2.6.1[1]:

$$F_D = 3\pi\mu D_p v\left[1 + \frac{9}{16}\left(\frac{D_p}{2H}\right) + \cdots\right], \quad \mathrm{Re}_p << 1 \tag{2.6.5}$$

Faxen derived theoretically the following equation, which describes the torque acting on a particle settling near a wall[2]:

$$T = 2\pi\mu D_p^2 v\left[\frac{3}{32}\left(\frac{D_p}{2H}\right)^4 - \frac{9}{256}\left(\frac{D_p}{2H}\right)^5 + \cdots\right], \quad \mathrm{Re}_p << 1 \tag{2.6.6}$$

Both F_D and T increase with increasing $D_p/2H$. This means that the settling and rotational velocities decrease with increasing $D_p/2H$.

Fayon and Happel presented the following equation, which represents the resistance force for flows of higher Reynolds number than the creeping flow[3]:

$$F_D = 3\pi\mu D_p v\left[\frac{1}{1 - 2.104(D_p/2R_0) + 2.088(D_p/2R_0)^8} + \left(\frac{C_A}{C_S} - 1\right)\right], \qquad \mathrm{Re}_p < 100 \tag{2.6.7}$$

where

C_A is a real resistance coefficient of a spherical particle settling in an unbounded fluid,

C_S is the Stokes resistance coefficient (i.e. $C_S = 24/\mathrm{Re}_p$).

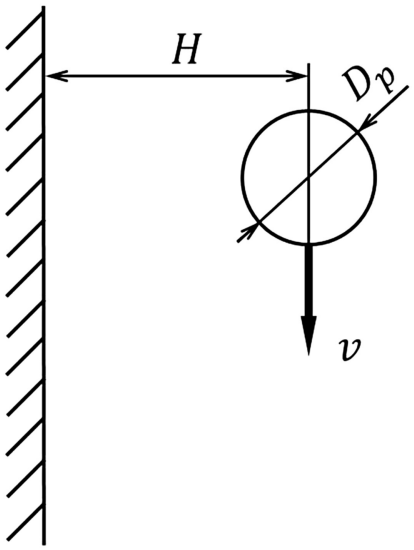


FIGURE 2.6.1 Spherical particle settling near a wall.

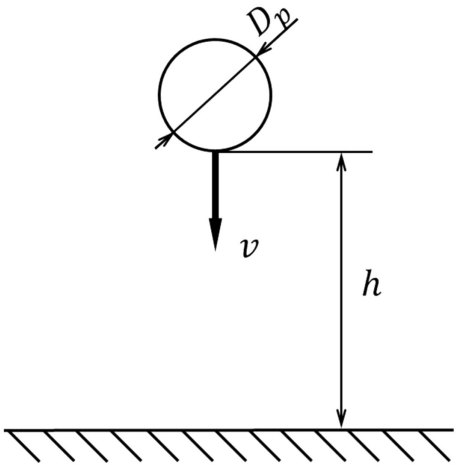


FIGURE 2.6.2 Spherical particle settling toward a plane surface of infinite extent.

Therefore, $(C_A/C_S - 1)$ represents a deviation from Stokes' law.

Brenner obtained the solution of the creeping motion equation for the steady motion of a spherical particle toward or away from a plane surface of infinite extent, as shown in Figure 2.6.2.[4] His equation of the resistance force is

$$F_D = 3\pi\mu D_p v\beta \tag{2.6.8}$$

$$\beta = \frac{4}{3}\sinh\alpha\sum_{n=1}^{\infty}\frac{n(n+1)}{(2n-1)(2n+3)} \times\left(\frac{2\sinh(2n+1)\alpha+(2n+1)\sinh^2\alpha}{4\sinh^2\left(n+\frac{1}{2}\right)\alpha-(2n+1)^2\sinh^2\alpha}-1\right) \tag{2.6.9}$$

where $\alpha = \cosh^{-1}(2h/D_p)$. The approximate equation of Equation (2.6.9) presented by Honig et al. is[5]

$$\beta = \frac{6\bar{h}^{-2}+13\bar{h}+2}{6\bar{h}^{-2}+4\bar{h}}, \qquad \bar{h} = \frac{2\bar{h}}{D_p} \tag{2.6.10}$$

Equations (2.6.8)–(2.6.10) show that in a continuum, the resistance force of a spherical particle moving toward a plane surface (or another particle) increases with decreasing separation distance between them and finally becomes infinite just before touching. However, there are effects of discontinuity in discontinuous media. The atmospheric air in the minimum separation between a particle and a plane surface or two particles whose diameters are less than several tens of microns creates the discontinuum. Therefore, a fine particle collides with another particle or a plane surface more easily. Umekage and Yuu measured resistance forces of a 6.3 mm foam styrene ball under reduced air pressure by using a high-speed camera.[6] At 10 Pa, the mean free path of air is 670 μm and the Knudsen number of a 6.3 mm foam styrene ball is equivalent to that of

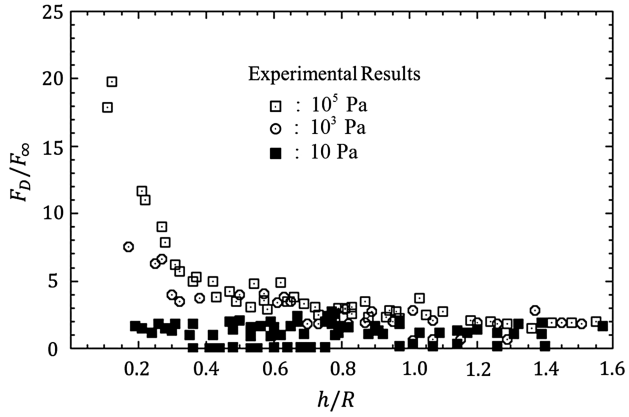


FIGURE 2.6.3 Resistance force acting on a 6.3 mm foam styrene ball near a plane surface under reduced pressure.

a 0.6 μm particle in atmospheric air. The experimental data in Figure 2.6.3 show that the increment of the resistance force acting on a 6.3 mm foam styrene ball near a plane surface under reduced pressure decreases with decreasing air pressure. Therefore, it is concluded that the resistance force of a fine particle moving toward a plane surface or another particle in the air is much less than that acting in a continuum.

Settling Velocity of a Non-Spherical Particle

The dynamic shape factor K defined by Equation (2.6.11) is used to estimate the difference between the settling velocities of non-spherical and spherical particles:

$$K = \frac{\text{Transport velocity of equispherical particle}}{\text{Transport velocity of nonspherical particle}} \tag{2.6.11}$$

where the transport velocity usually corresponds to the settling velocity. The Stokes resistance law reduces Equation (2.6.11) to

$$K = \frac{\text{Equispherical diameter}}{\text{Stokes diameter of nonspherical particle}} \tag{2.6.12}$$

Stöber presented the equations of K for ellipsoids[7]:

$$K_1 = \frac{(8/3)(q^2-1)q^{-1/3}}{\left[(2q^2-3)/\sqrt{q^2-1}\right]\ln\left(q+\sqrt{q^2-1}\right)+q} \quad \text{for } q>1 \tag{2.6.13}$$

$$K_{11} = \frac{(4/3)(q^2-1)q^{-1/3}}{\left[(2q^2-1)/\sqrt{q^2-1}\right]\ln\left(q+\sqrt{q^2-1}\right)-q} \quad \text{for } q>1 \tag{2.6.14}$$

$$K_1 = \frac{(8/3)(q^2-1)q^{-1/3}}{\left[(2q^2-3)/\sqrt{1-q^2}\right]\cos^{-1}q-q} \quad \text{for } q<1 \tag{2.6.15}$$

$$K_{11} = \frac{(4/3)(q^2-1)q^{-1/3}}{\left[(2q^2-1)/\sqrt{q^2-1}\right]\cos^{-1}q-q} \quad \text{for } q<1 \tag{2.6.16}$$

where q = polar diameter of ellipsoid/equator diameter of ellipsoid and, K_1 and K_{11} are dynamic shape factors of nonspherical particles whose settling directions are perpendicular and horizontal to the polar axis, respectively. Stöber measured the settling velocities of polystyrene latex aggregates and obtained the following experimental formulas for dynamic shape factors of aggregate particles:

$$K \approx 1.233 \quad \text{for massive aggregates} \tag{2.6.17}$$

$$K \approx 0.862 n^{1/3} \quad \text{for chainlike aggregates} \tag{2.6.18}$$

where n is the number of single particles composing the aggregate.

2.6.3 SETTLING OF TWO SPHERICAL PARTICLES

The exact solution of Stokes' equation for the motion of a viscous fluid around two spherical particles settling with equal small constant velocities along their line of centers was presented by Stimson and Jeffery.[8] The resistance force for one of two equal spherical particles is

$$F_D = 3\pi\mu v D_p \beta \tag{2.6.19}$$

$$\beta = \frac{4}{3}\sinh\alpha \sum_{n=1}^{\infty} \frac{n(n+1)}{(2n-1)(2n+3)} \times \left(1 - \frac{4\sinh^2\left(n+\frac{1}{2}\right)\alpha - 2(n+1)^2\sinh^2\alpha}{2\sinh(2n+1)\alpha + (2n+1)\sinh 2\alpha} \right)$$

where

$$\alpha = \ln\left\{ \frac{l_0}{D_p} + \left[\left(\frac{l_0}{D_p} \right)^2 - 1 \right]^{1/2} \right\} \tag{2.6.20}$$

When the distance between the centers of two spherical particles l_0 is $1.54\,D_p$, β is 0.7025, that is, the interaction of two particles gives about a 30% reduction in resistance.

Wakiya gave the solutions of the Stokes equation for the motion of two spherical particles of radii a and b moving in an arbitrary direction[9]. The drag forces and angular velocity are given as follows, where subscripts indicate the corresponding particles and directions

$$F_{ax} = 6\pi\mu a \left\{ v_{ax} \left[1 + \frac{9}{4}\frac{ab}{l_0^2} + \frac{3}{4}\left(-2\frac{a^3b}{l_0^4} + \frac{27}{4}\frac{a^2b^2}{l_0^4} + 3\frac{ab^3}{l_0^4} \right) + \cdots \right] - v_{bx} \left[\frac{3}{2}\frac{b}{l_0} - \frac{1}{2}\left(\frac{a^2b}{l_0^3} - \frac{27}{4}\frac{ab^2}{l_0^3} + \frac{b^3}{l_0^3} \right) + \frac{9}{4}\left(\frac{a^3b^2}{l_0^5} + \frac{27}{8}\frac{a^2b^3}{l_0^5} + \frac{ab^4}{l_0^5} \right) + \cdots \right] \right\} \tag{2.6.21}$$

$$F_{ay} = 6\pi\mu a \left\{ v_{ay} \left[1 + \frac{9}{16}\frac{ab}{l_0^2} + \frac{3}{8}\left(\frac{a^3b}{l_0^4} + \frac{27}{32}\frac{a^2b^2}{l_0^4} + \frac{ab^3}{l_0^4} \right) + \cdots \right] - v_{by} \left[\frac{3}{4}\frac{b}{l_0} + \frac{1}{4}\left(\frac{a^2b}{l_0^3} - \frac{27}{16}\frac{ab^2}{l_0^3} + \frac{b^3}{l_0^3} \right) + \frac{27}{64}\left(\frac{a^3b^2}{l_0^5} + \frac{9}{16}\frac{a^2b^3}{l_0^5} + \frac{ab^4}{l_0^5} \right) + \cdots \right] \right\} \tag{2.6.22}$$

$$\omega_a = \frac{3}{4}\frac{bx_0}{l_0^3} \left\{ v_{ay} \left[1 + \frac{9}{16}\frac{ab}{l_0^2} + \frac{3}{8}\left(\frac{a^3b}{l_0^4} + \frac{27}{32}\frac{a^2b^2}{l_0^4} + \frac{ab^3}{l_0^4} \right) + \cdots \right] - v_{by} \left[\frac{3}{4}\frac{a}{l_0} + \frac{1}{4}\left(\frac{a^3}{l_0^3} + \frac{27}{16}\frac{a^2b}{l_0^3} \right) + \cdots \right] \right\} \tag{2.6.23}$$

where $|x_0| = l_0$.

2.6.4 RATE OF SEDIMENTATION IN CONCENTRATED SUSPENSION

The rate of sedimentation of the particles in a suspension which are well distributed throughout the fluid in a vessel is slower than the velocity given by the Stokes resistance law. Steinour considered that the resistance force on a particle in suspension can be represented by the Stokes resistance law with a correction term that is a function of the concentration of particles only, as follows[10]:

$$F_D = \frac{3\pi\mu D_p v}{\phi(\varepsilon)} \tag{2.6.24}$$

where

ε is the function of the volume occupied by liquid which is analogous to the porosity in powder bed.

When $\varepsilon = 1$ at infinite dilution, $\phi(\varepsilon)$ is equal to unity. The force balance between F_D and the gravitational force of the particle given by $\frac{1}{6}\pi(\rho_p - \rho_m) D_p^3 g$ provides the terminal relative velocity:

$$v = \frac{\pi(\rho_p - \rho) D_p^2 \varepsilon \phi(\varepsilon)}{18\mu} = v_t \varepsilon \phi(\varepsilon) \tag{2.6.25},$$

where the density difference between the particle and suspension is

$$\rho_p - \rho_m = \rho_p - \left[(1-\varepsilon)\rho_p + \varepsilon\rho \right] = (\rho_p - \rho)\varepsilon \tag{2.6.26}.$$

The measured rate of sedimentation v_c is not a relative velocity between a particle and a fluid in suspension but a settling velocity of the particle relative to a fixed cross section.

The continuity condition states that the volume of settling particles is equal to the ascending fluid volume, that is, $(1-\varepsilon)v_c = \varepsilon(v - v_c)$. Hence,

$$v_c = \varepsilon v \tag{2.6.27}$$

Substituting Equation (2.6.25) into Equation (2.6.27) gives

$$v_c = v_t \varepsilon^2 \phi(\varepsilon) \tag{2.6.28}$$

Steinour (1944) measured the rate of sedimentation for tapioca particles and glass beads and obtained the experimental formula of $\phi(\varepsilon)$:

$$\phi(\varepsilon) = 10^{-1.82(1-\varepsilon)} \text{ for } \varepsilon > 0.6 \tag{2.6.29}$$

Recently Wang, Li, and Zhou presented the calculated results of settling velocity of many coarse particles using accelerated Stokesian dynamics in which the adjustable parameter is avoided and far field force acting on the particle is opted as dependent variables to express particle – particle hydrodynamic interaction.[11] They also investigated more realistic random suspension sedimentation using the Mont Carlo method. Their method would be capable of predicting the sedimentation motions of particle suspension in natural and industrial phenomena. Abade and Cichocki also presented the sedimentation of a non-Brownian suspension of hard spheres using Stokesian dynamics.[12] Many body hydrodynamic interactions among particles were evaluated by the precise multipole method. Their simulation results represented short range particle correlations in good agreement with the statistical description of sedimentation of suspension by Cichoki and Sadlej.[13]

NOTATION

C_D: Resistance coefficient
D_p: Particle diameter (μm)
F_D: Resistance force (N)
g: Gravitational acceleration (m/s^2)
H: Distance between particle center and vertical wall (m)
h: Minimum distance between particle surface and bottom wall (m)
K: Dynamic shape factor
Re_p: Particle Reynolds number
t: Time (s)
u, v: Fluid and particle velocity (m/s)
v_t: Terminal settling velocity of single particle (m/s)
ε: Fraction of volume occupied by liquid
ρ, ρ_p: Fluid and particle density (kg/m^3)

REFERENCES

1. Lorentz, H.A., *Abhand. Theor. Phys. Leipzig*, 1, 23–42, 1907.
2. Faxen, H., *Ann. Phys. IV, Folge*, 68, 89–98, 1922.
3. Fayon, A.M., Happel, J., *AIChE J.*, 6, 55–63, 1960.
4. Brenner, H., *Chem. Eng. Sci.*, 16, 242–248, 1961.
5. Honig, E.P., Roebersen, G.J., Wiersema, P.H., *J. Colloid Interface Sci.*, 36, 97–103, 1971.
6. Umekage, T., Yuu, S., *Trans. JSME, Ser. B.*, 59, 1559–1565, 1993.
7. Stöber, W., *Fine Particles*, Ed. B. Y. H. Liu, Academic Press., New York, 1976, pp. 351–398.
8. Stimson, M., Jeffery, G.B., *Proc. R. Soc. London*, A111, 110–122, 1926.
9. Wakiya, S., *Niigata Univ. Kogakubu Kenkyu Hokoku*, 6, 155–160, 1957.
10. Steinour, H.H., *Ind. Eng. Chem.*, 36, 618–626, 1944.
11. Wang, L., Li, J., Zhou, J., *Acta. Mech. Sin.*, 25, 303–310, 2009.
12. Abade, G. C., Cichocki, B., *J. Phy., Conf. Series*, 392, 1–9, 2012.
13. Cichocki, B., Sadlej, K., *Europhys. Lett.*, 72, 936–942, 2005.

2.7 Adhesive Force of Single Particle

Kuniaki Gotoh (2.7.1)
Naoyuki Ishida (2.7.2)
Shuji Matsusaka (2.7.3)

2.7.1 IN GASEOUS STATE

The adhesive force between particles or a particle and a solid surface plays an important role in powder-handling processes such as dry dispersion, transportation and classification of particles. The van der Waals force, the electrostatic force and the liquid bridge are the main source of the adhesive force in the gaseous state.

Van der Waals Force

The van der Waals force is a short-range electromagnetic force interacting between two molecules (or atoms). However, the force also acts between macroscopic two bodies such as particle-particle and particle-wall.

The van der Waals force can be determined by London-van der Waals theory (microscopic theory) or Lifshitz-van der Waals theory (macroscopic theory).[1,2] In the London-van der Waals theory, the so-called dispersion force acts between two symmetrical and electrically neutral molecules (or atoms). The potential energy is approximated by

$$E_A = -\beta_{11}/r^6 \tag{2.7.1}$$

where

r is the distance between center points of two molecules (or atoms),

β_{11} is a constant which depends on the molecular (or atom) characteristics.

Hamaker[3] assumed that the interaction between molecules is expressed by the London-van der Waals potential energy (Equation 2.7.1) and the interaction between two macro-bodies can be calculated by the integration of all interaction of molecules that exist in the bodies. Therefore, the fundamental equation for the calculation of van der Waals potential energy is

$$E = -\int_{v1}\int_{v2} \frac{q_1^2\beta_{11}}{r^6}\,dv_1 dv_2 \tag{2.7.2}$$

where

q_1 is the number of molecules per unit volume in the body,

v_1 and v_2 are the volumes of bodies 1 and 2, respectively.

Representative expressions of van der Waals potential energy based on the above equation are summarized in Table 2.7.1.[4–7] In the table, the equations in which the retardation effect is taken into consideration are also listed.[8,9] The retardation effect should be taken into account when the distance between surfaces of two bodies is beyond 100 nm (=$\lambda/2\pi$, λ: the wave length of light). The van der Waals force can be obtained through the differentiation of the potential energy, $-dE/dr$, and are also summarized in Table 2.7.1.

The constant A in these equations is called the Hamaker constant, which is given by

$$A = \pi^2 q_1^2/\beta_{11} \tag{2.7.3}$$

The Hamaker constant can be related to the Lifshitz-van der Waals constant $\nu\varpi$,[10,11] and the Hamaker constant between two different materials in air can be approximately expressed by[12]

$$A_{12} = \sqrt{A_{11}A_{22}} \tag{2.7.4}$$

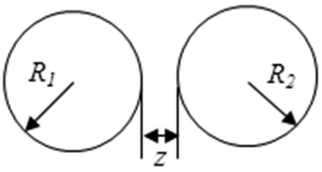
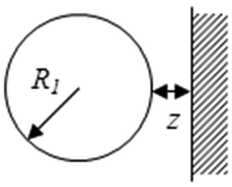
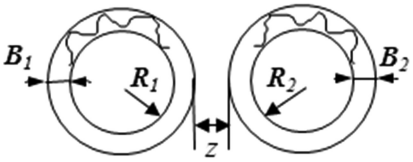
where A_{11} and A_{22} are the Hamaker constants for material 1 and material 2, respectively, in a free space. In the presence of a third material between the two bodies, the Hamaker constant is given by

$$A_{132} = \left(\sqrt{A_{11}} - \sqrt{A_{33}}\right)\left(\sqrt{A_{22}} - \sqrt{A_{33}}\right) \tag{2.7.5}$$

where A_{33} is the Hamaker constant of the third material. The values of the Hamaker's constants in air for carbon hydrate, oxides or halides and metals are $(4\sim10)\times10^{-20}$ J, $(6\sim15)\times10^{-20}$ J and $(15\sim50)\times10^{-20}$ J, respectively.[13] The gap distance z between attached bodies in Table 2.7.1 is determined by the balance of van der Waals force and Born's repulsion force,[2] and usually taken as 0.4 nm in air.

If the particle and/or wall are soft, the elastic deformation occurs at the contact point. In the JKR theory,[14] the van der Waals force for the soft material can be expressed by a linear function of the particle diameter as well as for the hard material. According to Dahneke,[15] the van der Waals force for a soft and large particle can be approximated by a quadratic function of the particle diameter. Derjaguin et al.[16] proposed an equation (DMT theory) that is a linear function of the particle diameter. The value calculated by the DMT theory is 4/3 times the value by the JKR theory. Tabor[17] and Muller et al.[18,19] studied the difference between the JKR theory and the DMT theory, showing that the JKR theory and the DMT theory are the special case of their model. Tsai et al.[20] proposed a new model with introducing a new adhesive parameter that is similar

TABLE 2.7.1 Representative Expression of van der Waals Potential Energy and van der Waals Force between Attached Bodies with the Gap *z*

	Van Der Waals Potential Energy (*E*)	Van Der Waals Force (*F*)	
	Without retardation effect: $-\frac{AR_1R_2}{6(R_1+R_2)z}=E_{sphere},\ z<<R_1$	$-\frac{AR_1R_2}{6(R_1+R_2)z^2}=F_{sphere}$	(1)
	With retardation effect: $-\frac{AR_1R_2}{6(R_1+R_2)z}\left[1-\frac{zb}{\lambda}\ln\left(1+\frac{\lambda}{zb}\right)\right]$	$-\frac{AR_1R_2}{6(R_1+R_2)}\left[\frac{R}{z^2}-\frac{b}{\lambda}\left(\frac{b}{zb+\lambda}-\frac{1}{z}\right)\right]$	(2)
	Without retardation effect: $-\frac{AR}{6z},\ z<<R_1$	$-\frac{AR}{6z^2}$	(3)
	With retardation effect: $-\frac{AR}{6z}\left[1-\frac{zb}{\lambda}\ln\left(1+\frac{\lambda}{zb}\right)\right]$	$-\frac{A}{6}\left[\frac{R}{z^2}-\frac{b}{\lambda}\left(\frac{b}{zb+\lambda}-\frac{1}{z}\right)\right]$	(4)
	Without retardation effect: $\frac{z}{z+0.5(B_1+B_2)}E_{\text{sphere}}$	$-\frac{z(B_1+B_2)}{\left[z+0.5(B_1+B_2)\right]^2}E_{sphere}+\frac{z}{z+0.5(B_1+B_2)}F_{sphere}$	(5)

to the model of Muller et al. In their model, when particle deformation is negligible, the van der Waals force is proportional to the diameter and the value is 0.4 times that calculated by the JKR theory, and the force is proportional to the 4/3 power of the diameter when the deformation is large enough.

Electrostatic Force

The electrostatic force in the gas phase arises from (1) the particle-charge interaction, (2) the image-charge effect and (3) the electrostatic contact potential difference. Between charged two particles, the coulombic force F_{ec} acts, and the force is approximately calculated by the following equation:

$$F_{ec}=\frac{1}{4\pi\varepsilon_0}\frac{q_1q_2}{r^2} \tag{2.7.6}$$

where

q_1 and q_2 are the charge of the particle,
r is the distance between centers of the particles,
ε_0 is a dielectric constant of the medium.

If two particles are in contact and the gap between particle surfaces is extremely smaller than the diameter x, Equation (2.7.6) can be expressed as follows;

$$F_{ec}=\frac{\pi\sigma_1\sigma_2}{\varepsilon_0}x^2 \tag{2.7.7}$$

where σ_1 and σ_2 are the surface charge densities of particles.

The image force F_{ei} acts between a charged particle and a neutral surface.

$$F_{ec}=\frac{1}{4\pi\varepsilon_0}\frac{\varepsilon-\varepsilon_0}{\varepsilon+\varepsilon_0}\frac{q^2}{(2r)^2} \tag{2.7.8}$$

where

q is the particle charge,
ε is the dielectric constant of the wall material.

When two different materials are brought into contact, both of them are electrified because of the contact potential difference. The induced electrostatic force F_{ed} between a particle and a wall is estimated by the following equation through adopting Dahneke's deformation equation[15] as a first approximation:

$$F_{ed}=\frac{1}{2}\pi\varepsilon_0\frac{V_c^2}{z^2}\left\{\frac{Akx^2}{32z^2}\left(1+\frac{A^2k^2x}{108z^7}\right)\right\} \tag{2.7.9}$$

where $k=\left(1-\nu_1^2\right)/E_1+\left(1-\nu_2^2\right)/E_2$, E_1 and E_2 are Young's modulus and ν_1 and ν_2 are Poisson ratio for the particle and the wall, respectively.

Liquid Bridge Force

When the relative humidity of atmosphere is relatively high (>65%[21]), the liquid bridge is formed at the contact point of

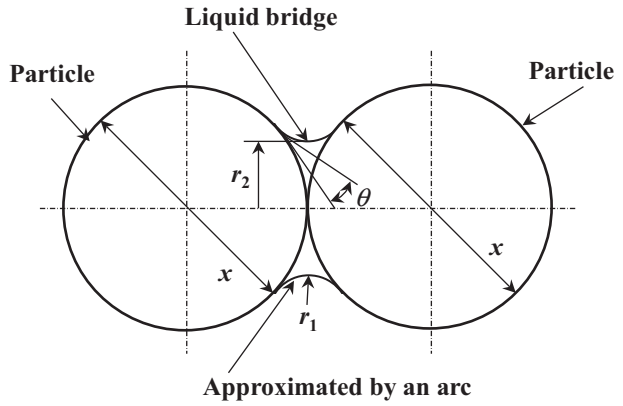


FIGURE 2.7.1 Liquid bridge formed between two particles.

two particles as shown in Figure 2.7.1. For the completely wettable surface of particles, the adhesive force caused by a liquid bridge arises as the sum of the capillary force and the force caused by the surface tension of the liquid as follows:

$$F_L = \pi r_2^2 P_L + 2\pi\sigma r_2 \tag{2.7.10}$$

where

r_2 is a radius of liquid bridge as shown in Figure 2.7.1,
σ is the surface tension of liquid,
P_L is the capillary pressure inside the liquid bridge.

If the cross section of the liquid bridge can be approximated by a circular arc, the capillary pressure P_L is expressed by

$$P_L = \sigma\left(\frac{1}{r_1} - \frac{1}{r_2}\right) \tag{2.7.11}$$

Then, the liquid bridge force can be calculated by

$$F_L = \pi r_2^2 \sigma\left(\frac{1}{r_1} - \frac{1}{r_2}\right) + 2\pi\sigma r_2 \tag{2.7.12}$$

If it is assumed that the r_1 is extremely smaller than both r_2 and particle diameter x, the liquid bridge force for contacting spheres of the same size can be approximated by the following equation[21]:

$$F_L \cong \pi\sigma x \tag{2.7.13}$$

For a spherical particle on a plane wall, F_L is expressed by

$$F_L \cong 2\pi\sigma x \tag{2.7.14}$$

For non-wetting surface, the right-hand sides of Equations (2.7.13) and (2.7.14) must be multiplied by cos θ, where θ is a contact angle between the liquid and the surface.

On the other hand, r_1 and r_2 can be correlated with a vapor pressure P_d at the vicinity of the surface by the Kelvin's equation as follows[22]:

$$\frac{P_d}{P_{s0}} = \exp\left\{-\frac{M\sigma\cos\theta}{RT\rho_L}\left(\frac{1}{r_1} - \frac{1}{r_2}\right)\right\} \tag{2.7.15}$$

where

P_{s0} is the saturation vapor pressure,
M is the molecular weight,
R is the gas constant,
T is the temperature,
ρ_L is the density of liquid,
θ is the contact angle.

If the liquid contains a solute, vapor pressure P_d decreases with the increase in the number of solute molecules. The pressure can be expressed by[22,23]:

$$\frac{P_d}{P_{s0}} = (1-\gamma)P_{kcl} \tag{2.7.16}$$

where $\gamma = in_s / (n_w + in_s)$. P_{kcl} (=P_d in Equation 2.7.15) is the vapor pressure without solute, i is the van't Hoff factor, and n_s and n_w are the number of the solute and the solvent molecules, respectively.

Comparison of Adhesive Force

Adhesive forces calculated by above equations are shown in Figure 2.7.2. The liquid bridge force (Equation 2.7.14) is the dominating adhesive force, as long as the liquid bridge is

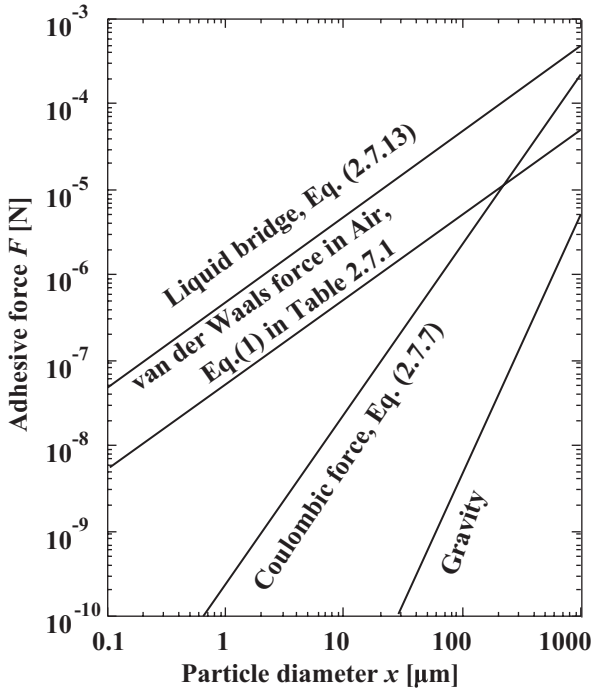


FIGURE 2.7.2 Comparison of adhesive forces under the following conditions; $A = 10^{-19}$ J (in air), $z = 0.4$ nm, $\rho_p = 103$ kg/m^3, g = 9.8 m/s^2, $\sigma_1 = \sigma_2 = 26.5$ μmC/m^2, $\varepsilon_0 = 8.85\text{x}10^{-12}$ F/m.

formed. Without the liquid bridge, the van der Waals force (Equation 1 in Table 2.7.1) dominates. For a charged particle such as toner particles,[25] the coulombic force becomes important. When the surface charge density σ is assumed to be 26.5 $\mu C/m^2$, which is the maximum value decided by the electric field limit for discharging, the coulombic force (Equation 2.7.7) dominates for the particles over 200 μm in diameter. For the particles smaller than 200 μm, the coulombic force may be smaller than the van der Waals force because the maximum surface charge density is determined by the voltage limit rather than the field limit.[26]

In the above discussion, the effects of the atmospheric conditions are not taken into account. The humidity of the atmosphere changes the shape of liquid bridge which alters the adhesive force.[24,27] The humidity also changes the adsorbed water layer thickness,[28] and it also affects the adhesive force.[29,30] The effect of the humidity strongly depends on the roughness of a surface.[31] The adhesive force will also be affected by temperature.[32,33]

2.7.2 IN LIQUID STATE

One of the specific properties of solid surfaces immersed in liquid is that the active adsorption of solutes on solid-liquid interfaces. Since adhesion forces strongly depend on the property of the outermost layers on the surfaces, the adhesion between the particles in liquids are significantly affected by the microstructures of such adsorbed layers on the particle surfaces.

The contribution of numerous studies using atomic force microscopy (AFM) has revealed, as described in Chapter 1.7, the important mechanisms of the adhesion phenomena in liquids. Even in the simplest case of charged surfaces in electrolyte solutions, it is well known that layers of hydrated ions and water molecules form on the solid–liquid interface on the surfaces.[34] Such layers, though their thickness is less than several nanometers, have critical effects on the adhesion forces between the surfaces. The microscopic measurements of adhesive forces between charged surfaces using an atomic force microscope revealed that the strength of adhesive force depends greatly on the structure and property of the adsorbed layers. Vakarelski et al. have extensively studied the adhesive forces between silica surfaces in various electrolyte solutions.[35,36] They found that the adhesive force increased with the hydration enthalpy of the cations in the order of $Li^+ \sim Na^+ > K^+ > Cs^+$. The increasing electrolyte concentration decreased the adhesion force. They also found that the dynamics aspect of the contact between the surfaces is important for the adhesion forces: at a high electrolyte concentration (1 M), the adhesion force strongly depended on the contact time of the surfaces in LiCl solution, whereas the adhesion force in CsCl solution was almost constant and independent of the contact time. These results are schematically depicted in Figure 2.7.3. In solutions with high-hydration enthalpy cations (Li^+ and Na^+), the highly hydrated cations form a thick but weak adsorbed layer, which can be easily destroyed by the surfaces. The resulting close contact between the surfaces brings about a strong adhesion. On the other hand, in solutions with low-hydration enthalpy cations (K^+ and Cs^+), the weakly hydrated cations form a thin but strong adsorbed layer, which is hardly broken by the contact of the surfaces. The gap between the surfaces at contact results in the significant reduction of the adhesive force.

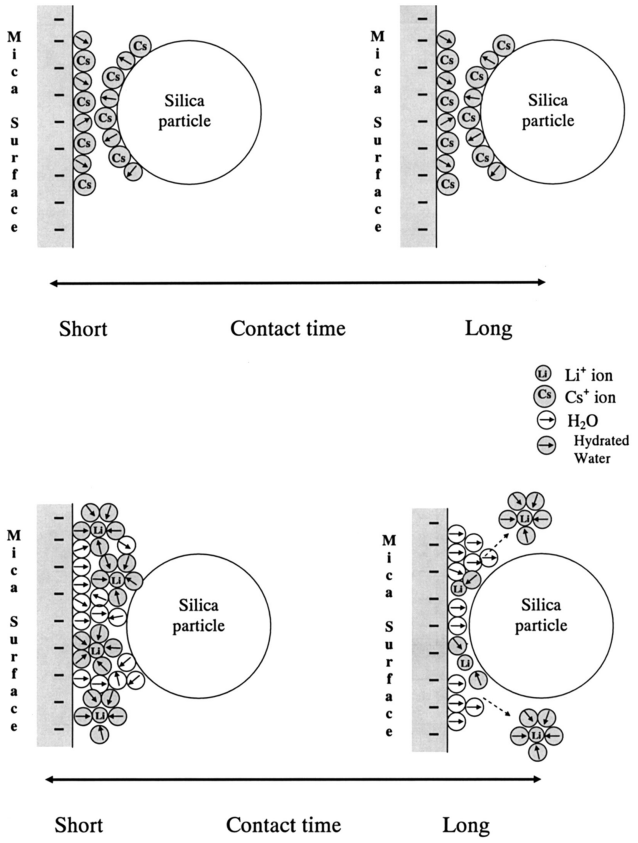


FIGURE 2.7.3 Proposed mechanism for the difference of adhesion force between a silica and a mica in LiCl and CsCl solutions.

The phenomena equivalent to a liquid bridge in air also exists in the liquid phase with several variations, as shown in Figure 2.7.4. The formation of a meniscus between the surfaces due to the phase separation of liquid components, which is common in various systems, induces a strong adhesive force. It is now well known that between hydrophobic surfaces in aqueous solutions, a gas bridge forms by the coalescence of nanosized bubbles attached on the surfaces and causes a strong adhesion,[37] as is explained in detail in section 1.7.3. Moreover, between silica surfaces immersed in cyclohexane, trace amounts of water[38] and ethanol[39] were found to give rise to a strong adhesion force, as mentioned in section 1.7.3. In these cases, capillary condensation and the bridging of water or ethanol, which has higher affinity with silica surfaces than cyclohexane does, causes the adhesion. Wennerström et al.[40] observed that the adhesion force between mica surfaces in an aqueous solution of dextran became stronger upon the addition of a small amount of poly(ethylene oxide) (PEO) in the solution. In this case, the increase in adhesion force can be attributed to the capillary condensation of PEO between the surfaces, which is caused by the incompatibility of dextran and PEO.

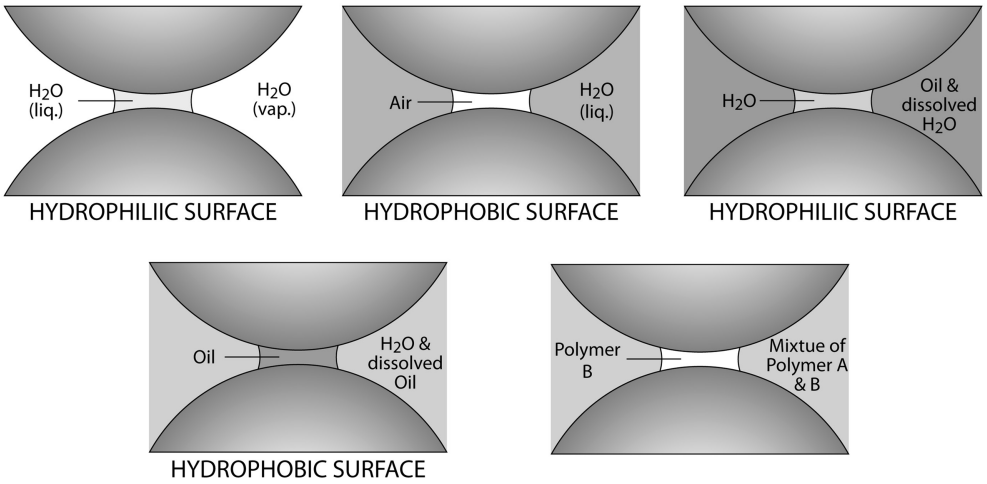


FIGURE 2.7.4 Schematic representation of different cases of capillary bridging in gas and liquid phase. (Adapted with permission from Wennerström et al., *Langmuir*, 14, 5664–5666, 1998. Copyright (1998) American Chemical Society.)

2.7.3 MEASUREMENT OF ADHESIVE FORCE

When a solid particle comes into contact with a wall or another particle, interaction forces act between the surfaces. The forces depend on the physical and chemical properties, particle shape, roughness, electrostatic charge and interaction media. In addition, the forces vary according to the distance between the surfaces. The term "adhesive force" is defined as the maximum attractive interaction force during which the particle is removed in the normal direction, thus, it is called the "pull-off force." In this section, basic techniques for the measurement of adhesive force are summarized, and the analysis based on the force balance and moment balance is explained. Furthermore, atomic force microscopy, which has become a powerful tool for the measurement of a force–distance curve, is described.

Methods of Measurement

The techniques for the measurement of adhesive force can be classified into several categories.[41–43] The principles of the techniques are schematically shown in Figure 2.7.5. They are applicable to the measurement of particle–particle interactions as well as particle–wall interactions.

Gravity method (pendulum type): A vertical plate is brought close to a freely hanging particle until contact is made, and subsequently shifted in a direction perpendicular to the contact area. The gravity component that tends to separate the particle increases with the inclination angle of the plate. From the force balance, the adhesive force F_a can be calculated using the following equation:

$$F_a = M_p g \sin\alpha \tag{2.7.17}$$

where

M_p is the mass of the particle,
g is the gravitational acceleration,
α is the inclination angle.

To separate the particle, the gravity component must be larger than the adhesive force. Therefore, this method is used for comparatively large particles on the order of 1 mm in diameter.

Spring balance method: In this method, the separation force is supplied by a spring. Since the spring force can be made larger than the gravitational force, this method is applicable for micro-sized particles. There are several types of springs, including helical and cantilever springs. The cantilever spring of an atomic force microscope[44] has also been used. Replacing the tip of a cantilever with a spherical particle (i.e. the colloidal probe technique) has accelerated the study of particle–wall interactions.[45–48]

Centrifuge method[49–51]: This method is widely used for the measurement of the adhesive forces of micron-sized particles. The advantages of this technique are its high sensitivity and statistical accuracy. As the adhesive forces of many particles on a surface can be measured in a single experiment, the adhesive force distribution is obtained in addition. The centrifugal force F_{cen} is calculated using the following equation:

$$F_{cen} = M_p \alpha_{cen} \tag{2.7.18}$$

where

α_{cen} is the centrifugal acceleration (= $l\omega^2$), in which l is the distance of the object from the axis,
ω is the angular velocity.

To prevent the effect of aerodynamic drag caused by the rotation, the object should be in a closed box or under vacuum. If the particles are sensitive to temperature changes, the frictional heat generated by rotation should be removed.

Vibration method[52]: The apparatus used to realize this method is rather small and simple since there is no mechanical

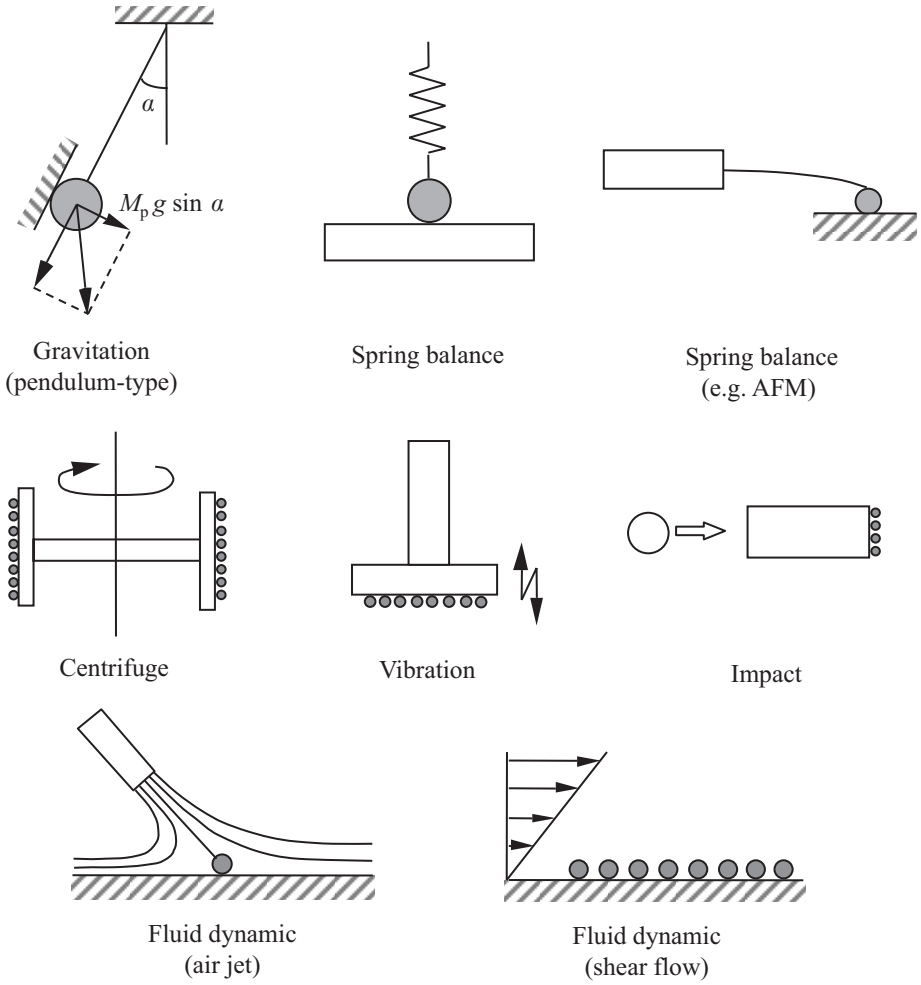


FIGURE 2.7.5 Principles of adhesive force measurements.

rotation unit required. The separation force can be estimated in a similar way to the centrifugal force:

$$F_{vib} = M_p \alpha_{vib} \tag{2.7.19}$$

where

α_{vib} is the vibration acceleration (= $y\omega_f^2$), where y is the amplitude,

ω_f is the angular frequency.

If the vibration waveform is not sinusoidal or contains noise, the maximum acceleration must be measured. To separate fine particles, high vibration acceleration is needed. Since such vibration raises the temperature of the vibrating plate, a cooling system is required.

Impact method[53]: In this method, particles are attached on one side of a wall, and an impact is applied to the reverse side. The impact force does not act directly on the particles, but rather the wall pushes the particles forward. This method is very simple, and the separation force can be calculated from the product of the particle mass and the effective acceleration. However, since the accurate determination of the acceleration is not so easy, this method is often used for qualitative evaluation of the adhesive force.

Fluid dynamic method[54–58]: Particles can be removed by an air jet or a shear flow. This method is suitable for the evaluation of particle adhesion to a wall in a particle–fluid system. The adhesive strength distribution can also be obtained from the relationship between the particle reentrainment efficiency and the fluid dynamic separation force. To analyze the effect of electrostatic force, an external electric field can be applied.[59]

Analysis of Forces Exerted on a Single Particle

Adhesive force is significantly affected by the contact states such as deformation and multiple-point contact, which also depend on the viscoelasticity, geometry and surface roughness. Figure 2.7.6 illustrates several contact states between a particle and a wall. In addition to the contact states, the points of application and directions associated with the force are important in determining the adhesive force.

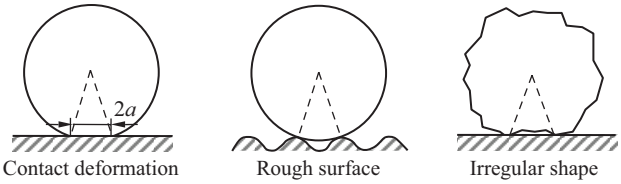


FIGURE 2.7.6 Contact states between a particle and a wall.

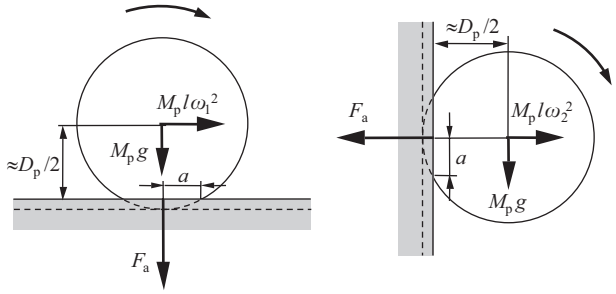


FIGURE 2.7.7 Particle-wall contacts in a centrifugal field.

Figure 2.7.7 shows two cases of particle–wall contacts in a centrifugal field. The moment balance for the particle adhering to a horizontal wall is expressed as[51]

$$\left(F_a + M_p\, g\right)a \approx M_p l\omega_1^2 \frac{D_p}{2} \tag{2.7.20}$$

where a is the distance from the application point to the fulcrum. The adhesive force F_a becomes

$$F_a \approx M_p\left(l\omega_1^2 \frac{D_p}{2a} - g\right) \tag{2.7.21}$$

When the particle adheres to a vertical wall, the adhesive force F_a can be expressed as

$$F_a \approx M_p\left(l\omega_2^2 + g\frac{D_p}{2a}\right) \tag{2.7.22}$$

If $l\omega_2^2 >> gD_p/(2a), F_a$ is simply equal to $M_p l\omega_2^2$. When the gravitational component cannot be neglected, the value of a is important for the estimation of the adhesive force. However, from Equations (2.7.21) and (2.7.22), the term $D_p/(2a)$ can be eliminated, and the adhesive force is calculated using the following equation:

$$F_a = M_p \frac{(l\,\omega_1\,\omega_2)^2 + g^2}{l\,\omega_1^2 - g} \tag{2.7.23}$$

Furthermore, the value of a can be obtained by the expression:

$$a \approx \frac{D_p}{2}\frac{l\,\omega_1^2 - g}{l\,\omega_2^2 + g} \tag{2.7.24}$$

REFERENCES

1. Israerlachvili, J.N., *Intermolecular and Surface Forces with Applications to Colloidal and Biological System*, Academic Press, London, Orlando, San Diego, New York, Toronto, Montreal, Sydney, Tokyo, 1985.
2. Krupp, H., *Adv. Colloid Interface Sci.*, 1, 111–239, 1967.
3. Hamaker, H.C., *Physica*, 4, 1058–1072, 1937.
4. Vold, M.J., *J. Colloid Sci.*, 16, 1–12, 1961.
5. Vincent, B., *J. Colloid Interface Sci.*, 42, 270–285, 1973.
6. Czarnecki, J., Dabros, T., *J. Colloid Interface Sci.*, 78, 25–30, 1980.
7. Göner, P., Pich, J., *J.Aerosol Sci.*, 20, 735–747, 1989.
8. Gregory, J., *J. Colloid Interface Sci.*, 83, 138–145, 1981.
9. Clayfield, E.J., Lumb, E.C., Markley, P.H., *J. Colloid Interface Sci.*, 37, 382–389, 1971.
10. Lifshitz, E.M., *Soviet Phys-JETP*, 2, 73–83, 1956.
11. Langbein, D., *Phys. Rev. B*, 2, 3371–3383, 1970.
12. Israerlachvili, J.N., *Proc. Royal Soc. Ser. A*, 331, 35–55, 1972.
13. Visser, J., *Adv. Colloid Interface Sci.*, 3, 331–363, 1970.
14. Johnson, K.L., Kendall, K., Roberts, A.D., *Proc. Royal Soc. Ser. A*, 324, 301–313, 1971.
15. Dahneke, B., *J. Colloid Interface Sci.*, 40, 1–13, 1972.
16. Derjaguin, B.V., Muller, V.M., Toporov, Y.P., *J. Colloid Interface Sci.*, 53, 314–326, 1975.
17. Tabor, D., *J. Colloid Interface Sci.*, 58, 2–13, 1977.
18. Muller, V.M., Yushchenko, V.S., Derjaguin, B.V., *J. Colloid Interface Sci.*, 77, 91–101, 1980.
19. Muller, V.M., Yushchenko, V.S., Derjaguin, B.V., *J. Colloid Interface Sci.*, 92, 92–101, 1983.
20. Tsai, C.J., Pui, D.Y.H., Liu, B.Y.H., *Aerosol Sci. Technol.*, 15, 239–255, 1991.
21. Zimon, A.D., *Adhesion of Dust and Powder (Second Edition)*, Consultant Bureau, New York, 1982, p. 69, p. 114.
22. Carman, P.C., *J. Phys. Chem.*, 57, 56–64, 1953.
23. Endo, Y., Kousaka, Y., Nishie, Y., *Kagaku Kogaku Ronbunshu*, 18, 950–955, 1992.
24. Endo, Y., Kousaka, Y., Nishie, Y., *Kagaku Kogaku Ronbunshu*,, 19, 55–61, 1993.
25. Lee, M.H., Ayala, J., *J. Imaging Technol.*, 11, 279–284, 1985.
26. Masuda, H., Matsusaka, S., *J. Soc. Powder Technol. Japan*, 30, 713–716, 1993.
27. Chikazawa, M., Nakajima, W., Kanazawa, T., *J. Res. Assoc. Powder Technology, Japan*, 14, 18–25, 1977.
28. Chikazawa, M., Yamaguchi, T., Kanazawa, T., *Proc. Int. Symp. Powder Technol. '81*, Hemisphere Pub. Corp., pp. 202–207, 1981.
29. Danjo, K., Otsuka, A., *Chem. Pharm. Bull.*, 26, 2705–2709, 1978.
30. Gotoh, K., Takebe, S., Masuda, H., Banba, Y., *Kagaku Kogaku Ronbunshu*, 20, 205–212, 1994.
31. Gotoh, K., Takebe, S., Masuda, H., *Kagaku Kogaku Ronbunshu*, 20, 685–692, 1994.
32. Nishino, M., Arakawa, M., Suito, E., *Zairyo*, 1, 535–540, 1969.
33. Otsuka, A., Iida, K., Danjo, K., Sunada, H., *Chem. Pharm. Bull.*, 31, 4483–4488, 1983.
34. Pashley, R.M., *J. Colloid Interface Sci.*, 83, 531–546, 1981.
35. Vakarelski, I.U., Ishimura, K., Higashitani, K., *J. Colloid Interface Sci.*, 227, 111–118, 2000.
36. Vakarelski, I.U., Higashitani, K., *J. Colloid Interface Sci.*, 242, 110–120, 2001.
37. Ishida, N., Sakamoto, M., Miyahara, M., Higashitani, K., *Langmuir*, 16, 5681–5687, 2000.

38. Kanda, Y., Nishimura, T., Higashitani, K., *J. Soc. Powder Tech. Japan*, 38, 316–322, 2001.
39. Mizukami, M., Moteki, M., Kurihara, K., *J. Am. Chem. Soc.*, 124, 12889–12897, 2002.
40. Wennerström, H., Thuresson, K., Linse, P., Freyssingeas E., *Langmuir*, 14, 5664–5666, 1998.
41. Krupp, H., *Adv. Colloid Interface Sci.*, 1, 79–110, 1967.
42. Zimon, A.D., *Adhesion of Dust and Powder*, 2nd Ed., Consultants Bureau, New York, 1982, pp. 69–91.
43. Israelachvili, J. N., *Intermolecular and Surface Forces*, 2nd Ed., Academic Press, London, 1991, pp. 165–175.
44. Binnig, G., Quate, C. F., Gerber, Ch., *Phys. Rev. Lett.*, 56, 930–933, 1986.
45. Ducker, W.A., Senden, T.J., Pashley, R.M., *Nature*, 353, 239–241, 1991.
46. Claesson, P.M., Ederth, T., Bergeron, V., Rutland, M.W., *Adv. Colloid Interface Sci.*, 67, 119–183, 1996.
47. Cappella, B., Dietler, G., *Surf. Sci. Rep.*, 34, 1–104, 1999.
48. Kappl, M., Butt, H.-J., *Part. Part. Syst. Char.*, 19, 129–143, 2002.
49. Asakawa, S., Jimbo, G., *J. Soc. Mater. Sci., Japan*, 16, 358–363, 1967.
50. Emi, H., Endo, S., Kanaoka, C., Kawai, S., *Kagaku Kogaku Ronbunshu*, 3, 580–585, 1977.
51. Matsusaka, S., Koumura, M., Masuda, H., *Kagaku Kogaku Ronbunshu*, 23, 561–568, 1997.
52. Mullins, M.E., Michaels, L.P., Menon, V., Locke, B., et al., *Aerosol Sci. Technol.*, 17, 105–118, 1992.
53. Otsuka, A., Iida, K., Danjo, K., Sunada, H., *Chem. Pharm. Bull.*, 31, 4483–4488, 1983.
54. Visser, J., *J. Colloid Interface Sci.*, 34, 26–31, 1970.
55. Masuda, H., Gotoh, K., Fukada, H., Banba, Y., *Adv. Powder Technol.*, 5, 205–217, 1994.
56. Masuda, H., Matsusaka, S., Imamura, K., *KONA*, 12, 133–143, 1994.
57. Jiang Y., Matsusaka, S., Masuda, H., Yokoyama, T., *Adv. Powder Technol.*, 17, 413–424, 2006.
58. Jiang Y., Matsusaka, S., Masuda, H., Qian, Y., *Powder Technol.*, 186 199–205, 2008.
59. Matsusaka, S., Wei, D., Yasuda, M., Sasabe, S., *Adv. Powder Technol.*, 26, 149–155, 2015.

2.8 Particle Deposition and Reentrainment

Manabu Shimada (2.8.1)
Shuji Matsusaka and Hiroaki Masuda (2.8.2)

Particle deposition is a phenomenon in which particles that are suspended in a fluid are transported to a wall and make permanent or temporary contact with the surface of the wall. Particle deposition is an important phenomenon in many fields including fouling of channel walls exposed to dusty gas, microcontamination problems in advanced material processing, dry deposition of particulate matter in an atmospheric environment, development and efficiency of gas filtration devices, designed positioning and accumulation of particles for the fabrication of functional devices, and inhalation of airborne particulate matter into human lungs. Particle reentrainment refers to the resuspension of particles that had been deposited on a surface. In general, it is difficult to reentrain small primary particles from a wall. However, aggregate particles are readily reentrained from a particle deposition layer. The aggregate reentrainment affects various engineering applications such as powder dispersion, particle size classification, dust collection, particle synthesis, and aerosol sampling.

2.8.1 PARTICLE DEPOSITION

It is necessary to obtain a better understanding of mechanisms that govern the transport process of particles to predict and evaluate particle deposition phenomena. Important mechanisms include transport by fluid flow, transport by Brownian diffusion and turbulent eddies, and motion induced by inertial forces and external forces such as gravitational sedimentation, electrostatic migration, thermophoresis, diffusiophoresis, and photophoresis.

Fundamental Concepts

The transport of particles in a fluid was examined by either the Eulerian method or the Lagrangian method. In the Eulerian method, the particle phase is treated as a continuum or "fluid." The conservation equations for the particle phase are arranged in a form similar to that for gas or liquid and solved to obtain the spatial and temporal distribution of particle concentration. Thus, the particle deposition essentially corresponds to the particle phase flux to a wall, and therefore, it is derived from the concentration distribution. The trajectories of individual particles are tracked in the Lagrangian method. The trajectories are calculated from the equations that describe the particle motion. After obtaining a considerable number of trajectories, the position and rate of particles arriving on the walls provide the quantitative information on the deposition.

The Eulerian method is typically applied to submicron-sized or smaller particles dominated by fluid flow motion, Brownian diffusive motion, and migration by external forces. This method uses the following convection-diffusion equation to describe the spatial and temporal changes in particle number concentration per unit fluid volume, n, as follows:

$$\frac{dn}{dt} = \nabla \cdot \left\{ \rho_f D \nabla \left(n/\rho_f \right) - \left(\mathbf{u} + \mathbf{v} \right) n \right\} + Q \qquad (2.8.1)$$

where

- t denotes the time,
- ρ_f denotes the fluid density,
- D denotes the Brownian diffusion coefficient,
- $\mathbf{u}$ denotes the fluid velocity,
- $\mathbf{v}$ denotes the particle velocity induced by the sum of external forces ($\Sigma\mathbf{F}$) and equals $B\Sigma\mathbf{F}$ (mobility $B = C_C/\left(3\pi\mu D_p\right)$; C_C denotes the Cunningham correction factor; μ denotes the fluid viscosity; D_p denotes the particle diameter,
- Q denotes the rate of generation or consumption of particles.

It is also necessary to solve the energy equation to incorporate the temperature dependence of ρ_f and D into Equation (2.8.1) when deposition in a nonisothermal system is considered. Chapters 2.2, 2.3, 2.5, and 2.6 demonstrate the expressions of particle velocity $\mathbf{v}$ induced by various external forces $\mathbf{F}$. To obtain the rate of deposition, Equation (2.8.1) is solved with appropriate boundary conditions that correspond to the state of the particles on the surface. In strict terms, a particle that apparently arrived at a surface in the gas phase is separated from the surface by a very short distance. However, submicron- or nano-particles, wherein Equation (2.8.1) holds, can be regarded as being held at the surface immediately and permanently once the surface is reached. The separation between a particle and surface is considerably smaller than the particle diameter, and thus, the particle concentration n is typically set to zero at a distance corresponding to half the particle diameter from the surface. The number of particles deposited per unit surface area and time, deposition flux j, is calculated as follows:

$$j = -D \left. \frac{dn}{dz} \right|_{z=D_p/2} \qquad (2.8.2)$$

where z denotes the distance from the surface. Additionally, j is generally proportional to the particle concentration sufficiently far from the surface n_0, and thus, $v_d = j/n_0$ denotes the deposition flux per unit particle concentration and is denoted as the deposition velocity.

In the Lagrangian method, the motion of each individual particle is essentially described by Newton's second law of motion as follows:

$$m_p \frac{d\mathbf{v}}{dt} = \Sigma\mathbf{F}_f + \Sigma\mathbf{F}_e + \mathbf{F}_B + \Sigma\mathbf{F}_p \tag{2.8.3}$$

where

- m_p denotes the mass of the particle,
- $\Sigma\mathbf{F}_f$ denotes the sum of the forces exerted by the fluid surrounding the particle,
- $\Sigma\mathbf{F}_e$ denotes the sum of the external forces imposed on the particle (gravitational force, electrostatic force, etc.),
- $\mathbf{F}_B$ denotes the force that induces Brownian motion,
- $\Sigma\mathbf{F}_p$ denotes the sum of the forces related to the interaction between the particles.

Furthermore, $\mathbf{F}_f$ represents the drag, pressure gradient, virtual mass, Basset, Saffman, and Magnus forces. The detailed explanation and expression of for these forces are described in refs. 1 and 2, and $\mathbf{F}_B$ is discussed in ref. 3. After placing a particle at its initial position in the computational domain, Equation (2.8.3) is repeatedly integrated over Δt until the particle leaves the domain or arrives on any walls. A particle is considered deposited when the distance between the particle center and the nearest wall is lesser than the particle radius, in the absence of particle rebound on the walls.

In both the Eulerian and Lagrangian methods, the velocity of the fluid, $\mathbf{u}$, that surrounds the particles is generally determined by the equations that govern the flow of continuum fluid (the equation of continuity and the Navier–Stokes equations). Analytical or approximate solutions of $\mathbf{u}$ that are typically available for flow in simple configurations are also employed. When the particle concentration is low, it is generally assumed that the existence of particles in the fluid does not influence the fluid motion at all while the fluid flow definitely affects the motion of the particles. This assumption eases the computational effort and is referred to as the "one-way coupling" of fluid and particle motions. However, the momentum and friction of the particles in the fluid will cause a significant change in the fluid motion if the particle concentration is high. In such a case, the motions of the particles and fluid are successively and repeatedly calculated to obtain the converged results for the motions ("two-way coupling").

Eulerian Method

The calculation of fluid motion that uses the equation of continuity and the Navier–Stokes equations corresponds to the Eulerian method. A method in which the fluid velocity $\mathbf{u}$ that is obtained from this *Eulerian* fluid calculation is substituted into the equation for *Eulerian* particle concentration calculation (Equation 2.8.1) is typically termed the Eulerian–Eulerian method. This method is also termed the two-fluid model as the *fluid* motion calculation is followed by an analysis of Equation (2.8.1) that treats the particle phase as a *fluid* as previously mentioned.

Analytical or approximate solutions were obtained for a few systems that are geometrically simple and interesting from an industrial viewpoint. For example, the fraction, f_d, of particles deposited from laminar flow in a pipe to the pipe wall is obtained as follows:

$$f_d = 1 - \left(0.819e^{-14.63\delta} + 0.0976e^{-89.22\delta} + 0.0325e^{-228\delta} + 0.0509e^{-125.9\delta^{2/3}}\right) \tag{2.8.4}$$

where δ denotes the diffusion parameter and equals $DL/\left(4UR^2\right)$ (L, pipe length; U, average axial velocity; R, pipe radius).[4] Additionally, f_d for a deposition dominated by thermophoresis in a long pipe is given for both laminar and turbulent flows as follows:

$$f_d = 1 - \left(\frac{T_w}{T_0}\right)^{\Pr K} \tag{2.8.5}$$

where

- T_w and T_0 denote the temperatures of the pipe wall and fluid at the pipe inlet, respectively,
- Pr denotes Prandtl number,
- K denotes thermophoretic coefficient.[5]

The deposition velocity is approximated as

$$v_d = \frac{1.08D}{d_d}\left(\frac{\rho_f u_0 d_d}{\mu}\right)^{1/2}\left(\frac{\mu}{\rho_f D}\right)^{1/3} - \frac{2D}{D_p}\mathrm{Ex} \tag{2.8.6}$$

for particles suspended in a laminar flow that impinge against a disc with diameter d_d and simultaneously experience a uniform external force in a direction normal to the wall.[6] Furthermore, u_0 and Ex in the above equation denote the flow velocity and a parameter that indicates the magnitude of the external force, respectively. Ex equals $EqC_C/(6\pi\mu D)$ (E denotes the electric field strength, q denotes the particle charge) for the Coulomb force in an electrostatic field, and $\left(\rho_p - \rho_f\right)D_p{}^3 g C_C/(36\mu D)$ (ρ_p denotes the density of the particle, g denotes the acceleration of gravity) for the gravitational force. Figure 2.8.1 shows examples of v_d calculated from this equation for particles suspended above a horizontally oriented disc. Examples of analytical or approximated solutions of v_d for several other systems are found in Chapter 2.4 and in extant studies.[7] Although systems in which such analytical or approximated solutions are directly applicable are limited, these solutions are often useful to approximately estimate deposition when the actual systems are simplified. However, if a detailed distribution of the deposition

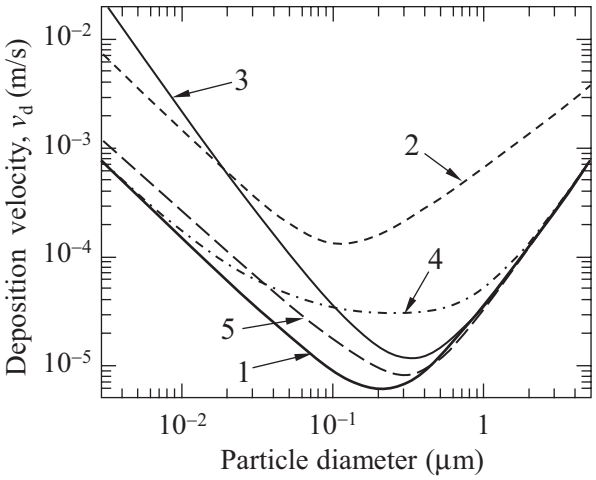


FIGURE 2.8.1 Deposition velocity of airborne particles on the upper surface of a horizontally oriented disc with a diameter of 125 mm; (1) for particles in downward flow at a speed of 0.3 m/s; (2) same conditions as (1) except that pressure is reduced to 1.01 kPa; (3) same conditions as (1) except that each particle possesses a unit elementary charge and that uniform electric field of 1 V/m exists; (4) same conditions as (1) except that uniform temperature gradient of 1 K/mm exists; (5) for particles suspended in turbulent flow at a certain intensity.

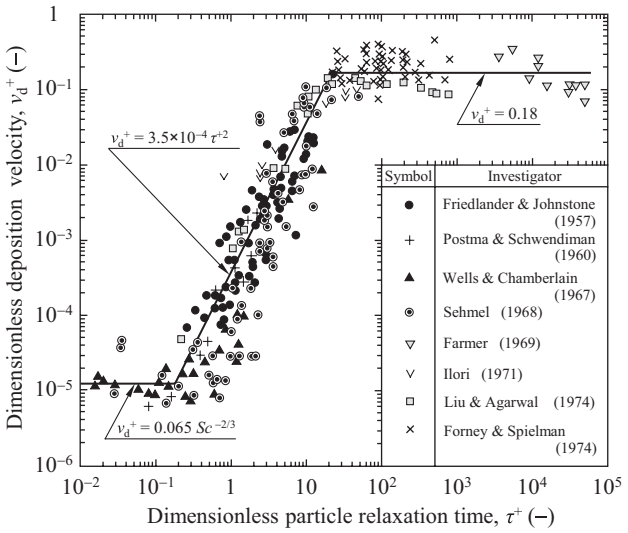


FIGURE 2.8.2 Summary of experimental deposition data in a vertical turbulent flow system. [From Papavergos, P. G. and Hedley, A. B., *Chem. Eng. Res. Des.* 62, 275–295, 1984. With permission.]

velocity is required, then it is necessary to perform a rigorous Eulerian–Eulerian calculation. For example, the distributions of electric potential and temperature were analyzed in detail when nonuniform electrostatic or thermophoretic forces influenced the deposition.[8,9]

The transport of particles suspended in a turbulent flow field is enhanced by turbulent eddies in the fluid. Figure 2.8.2 shows the representative experimental results for turbulent deposition in a circular pipe.[10] The ordinate and abscissa of the figure correspond to the dimensionless deposition velocity v_d^+ (= v_d/u^*, u^*, friction velocity) and the dimensionless relaxation time of particles τ^+ (= $\rho_f\rho_p D_p^2 u^{*2} C_C \big/ \left(18\mu^2\right)$), respectively. Turbulent deposition is approximately divided into the following three regimes based on the magnitude of τ^+ that indicates the effect of particle inertia. For $\tau^+ < 0.2$, the effect of inertia should be small, and thus, particles follow the fluid motion. When $0.2 < \tau^+ < 20$, the deposition velocity depends strongly on τ^+ as the motion of particles tends to deviate from that of fluid near the wall as a result of the inertial force. The deposition velocity for $\tau^+ > 20$ is only slightly dependent on τ^+ as the inertia-induced motion of particles tends to prevail over the entire region of the fluid. The three empirical equations shown in the figure[10] are practically useful as a rough estimation as v_d^+ is highly correlated to τ^+. In addition to the aforementioned equations, several theoretical or semi-empirical models were proposed to explain the measured results for turbulent flows.[11–17] In a recent notable model based on the Eulerian method, a term representing particle transport by turbophoresis (i.e. transport induced by the interaction of particle inertia and the gradient of turbulent intensity) is added to the convection–diffusion equation of particles (Equation 2.8.1). This model was used to quantitatively analyze particle deposition in turbulent pipe flow enhanced by wall roughness, thermophoresis, and electrostatic forces.[18]

Lagrangian Method

In the Lagrangian method, it is necessary to compute the trajectories of thousands of particles to hundreds of thousands of particles to obtain statistically reliable results. Recent advances in computer performance increase the efficiency of these computations. The computation of fluid flow is also easier owing to the recent progress in commercially available software packages for computational fluid dynamics (CFD). Thus, particle deposition analyses in which fluid flow computation by CFD is followed by particle tracking by the Lagrangian method is increasingly used. The technique is termed Eulerian–Lagrangian or CFD–Lagrangian method. Particle deposition in turbulent flow is typically analyzed using this technique. Reynolds-averaged Navier–Stokes equations (RANS),[19] large eddy simulation (LES),[20] and detached eddy simulation (DES)[21] are used as turbulent flow models. The CFD–Lagrangian is notably applied to predict the deposition of inhalable particles in human lungs. Extant studies presented lung deposition analysis that considered Brownian diffusion[22] and extensive reviews of computation results of lung deposition including comparisons with existing simpler or semi-empirical models.[23,24] A deposition analysis that uses direct numerical simulation (DNS) of turbulent flow is termed the DNS–Lagrangian, and it depicts extremely detailed behavior related to particle transport and deposition.[25]

At a high particle number concentration, contact and collision between particles occur frequently and affect particle motion. The Lagrangian method is termed the discrete element method (DEM) when it considers the aforementioned particle–particle interaction by describing $\mathbf{F}_p$ in Equation (2.8.3). The techniques and computation examples of DEM

in combination with CFD for fluid flow (CFD–DEM) are described in detail in Reference [1] and [26]. Additionally, techniques that consider the interaction between particles and fluid (i.e. the two-way coupling) are discussed for DEM as the existence and motion of high-concentration particles tend to significantly affect fluid motion.

The behavior of non-spherical particles (NSPs), such as cylindrical and ellipsoidal particles, is also typically considered interesting. The forces exerted on NSPs from the fluid, $\mathbf{F}_f$ in Equation (2.8.3), are significantly more complicated than those of spherical particles, and it is also necessary to track the change in the NSP orientation in the fluid flow.[27] Thus, CFD–Lagrangian models for NSPs were developed based on this consideration.[28,29] Studies focus on improving CFD–DEM such that it is capable of handling the contact and collision with respect to NSPs,[2] and examples of investigations are described.[30] The two-way coupling is also investigated for the CFD–DEM of NSPs by computing the detailed force distribution over the entire surface of each individual NSP.

2.8.2 PARTICLE REENTRAINMENT

When particles are deposited on a surface, there are adhesive forces acting on them. However, if aerodynamic or other external forces that are acting on the particles are greater than the adhesive forces, then the particles are reentrained into the surrounding fluid. Particle reentrainment is a different phenomenon from rebound and saltation since the former occurs after the particle maintains a stationary state for a period, while rebound and saltation occur in a state of continuous motion. Particle reentrainment depends on the existing conditions. If the particles are very small, reentrainment does not occur even in turbulent flow. When small particles are deeply immerged within a boundary layer, the aerodynamic forces acting on the particles are too weak to remove them from the surface. The deposited particles then accumulate on the surface forming particle layers. However, the aggregated particles on top of the particle deposition layers experience greater aerodynamic forces and can be readily reentrained.[31,32]

Concept of Reentrainment of Aggregates

The concept of reentrainment of aggregates from a particle deposition layer is illustrated in Figure 2.8.3. Since the surface of the particle layer is not smooth, the particles extruding from the surface experience a relatively large drag and, consequently, the aggregate particles can be reentrained. A simple model for the reentrainment of a spherical aggregate is shown in Figure 2.8.4. When the flow around the aggregate is very slow, a creeping flow, the drag force on a small segment of the aggregate in the shear flow is approximated by[33,34]

$$dR_D(y) = \frac{24\tau_w}{D_{ag}}\left(y - y^*\right)\sqrt{y\left(D_{ag} - y\right)}dy \qquad (2.8.7)$$

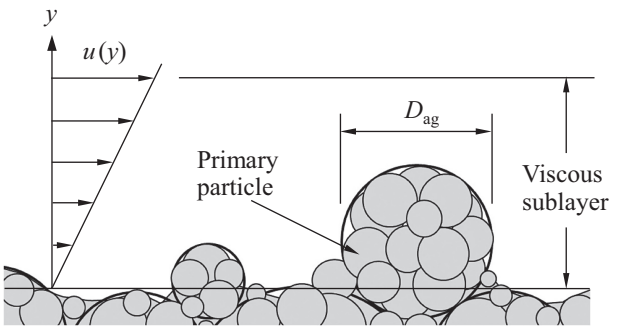


FIGURE 2.8.3 Concept of reentrainment of aggregates from a particle deposition layer in turbulent pipe flow.

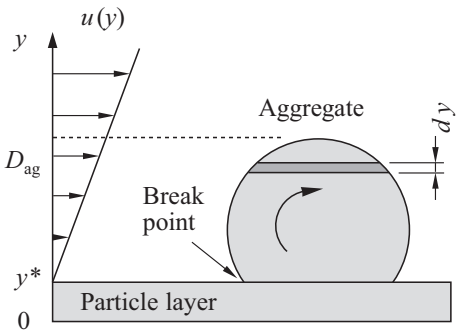


FIGURE 2.8.4 A reentrainment model for an aggregate particle.

where τ_w is the wall shear stress. The moment M on this aggregate is represented by

$$M = \int_{y^*}^{D_{ag}} \left(y - y^*\right) dR_D(y) \qquad (2.8.8)$$

The maximum bending stress σ_b at the break point is given by

$$\sigma_b = \frac{M}{Z} \qquad (2.8.9)$$

where Z is the section modulus:

$$Z = \frac{\pi d^3}{32} = \frac{\pi}{4}\left\{y^*(D_{ag} - y^*)\right\}^{3/2} \qquad (2.8.10)$$

Combining Equations (2.8.7) through (2.8.10), the following equation is obtained:

$$\sigma_b = \frac{96}{\pi}\tau_w f(Y^*) \qquad (2.8.11)$$

where $f(Y^*)$ is represented by

$$f\left(Y^*\right) = \left[Y^*\left(1 - Y^*\right)\right]^{-3/2} \int_{Y^*}^{1} \left(Y - Y^*\right)^2 \sqrt{Y(1-Y)}dY \qquad (2.8.12)$$

where

$$Y^* = \frac{y^*}{D_{ag}} \approx 0.5 \qquad (2.8.13)$$

$$Y = \frac{y}{D_{ag}} \tag{2.8.14}$$

From Equations (2.8.11) through (2.8.14), $\sigma_b = 3\tau_w$ is obtained, indicating that the adhesive strength can be calculated from the wall shear stress.

Particle Reentrainment Efficiency

The adhesive strength distribution is related to the reentrainment efficiency. In general, the distribution function is represented by the following log-normal equation[33]:

$$\gamma(\tau_c) = \frac{1}{\sqrt{2\pi}\ln\sigma_g}\int_0^{\tau_c}\exp\left(\frac{-\left(\ln\tau_c - \ln\tau_{c50}\right)^2}{2\ln^2\sigma_g}\right)d\left(\ln\tau_c\right) \tag{2.8.15}$$

where τ_c is the critical wall shear stress corresponding to reentrainment. For turbulent pipe flow: $3\times10^3 < Re < 10^5$, $\gamma(\tau_c)$ is rewritten as a function of the average velocity $\bar{u}$:

$$\gamma\left(\bar{u}\right) = \frac{1}{\sqrt{2\pi}\ln\sigma_g'}\int_0^{\bar{u}}\frac{1}{\bar{u}}\exp\left(\frac{-\left(\ln\bar{u} - \ln\bar{u}_{50}\right)^2}{2\ln^2\sigma_g'}\right)d\bar{u} \tag{2.8.16}$$

where

$$\sigma_g' = \sigma_g^{4/7} \tag{2.8.17}$$

When aggregate particles are reentrained from the surface of the particle layer, a new particle layer surface is exposed to the flow. The next reentrainment can then occur from the newly exposed surface with the same reentrainment efficiency γ, which results in a hierarchical phenomenon. After renewal of the surface n times, the total reentrainment efficiency $\Gamma(n)$ is represented by

$$\Gamma(n) = \sum_{s=1}^{n}\gamma^s = \frac{\gamma(1-\gamma^n)}{1-\gamma} \tag{2.8.18}$$

The mass of particles reentrained per unit area W/A_p is proportional to $\Gamma(n\to\infty)$:

$$\frac{W}{A_p} = k\Gamma(n\to\infty) = \frac{k\gamma}{1-\gamma} \tag{2.8.19}$$

where k is a constant.

Particle Reentrainment Rate

The particle reentrainment is not instantaneous but, rather, takes place over a period of time. This phenomenon cannot be explained solely by a static concept. It should be considered that the reentrainment has a statistical origin associated with the flow characteristics such as turbulent bursts. Using both the burst generation probability η_B and the adhesive strength distribution (or the reentrainment efficiency γ), the total reentrainment efficiency $\Gamma(m)$ after m fluid fluctuations is represented by

$$\begin{aligned}\Gamma(m) &= \sum_{n=1}^{m}\sum_{s=1}^{n}{}_{n-1}C_{s-1}(1-\eta_B)^{n-s}(\eta_B\gamma)^s \\ &= \frac{\gamma[1-(1-\eta_B+\eta_B\gamma)^m]}{1-\gamma}\end{aligned} \tag{2.8.20}$$

Using the relation $m = t/\Delta t$, where Δt is the interval of the fluctuation, $\Gamma(m)$ is rewritten as a function of the elapsed time t:

$$\Gamma(t) = \frac{\gamma}{1-\gamma}\left[1-\exp\left(\frac{-t}{T_c}\right)\right] \tag{2.8.21}$$

where T_c is a time constant given by

$$T_c = \frac{-\Delta t}{\ln(1-\eta_B+\eta_B\gamma)} \tag{2.8.22}$$

As $0<\eta_B<1$ and $0<\gamma<1$, T_c has a positive value. Additionally, the normalized total reentrainment efficiency $R(t)$ is represented by

$$R(t) = \frac{\Gamma(t)}{\Gamma(t\to\infty)} = 1-\exp\left(\frac{-t}{T_c}\right) \tag{2.8.23}$$

There are actually two types of reentrainment, namely, short-delay and long-delay reentrainment.[35,36] Therefore, the reentrainment flux J is expressed as

$$J = J_S + J_L \tag{2.8.24}$$

When the average fluid velocity increases from $\bar{u}=0$ at a constant acceleration $a = d\bar{u}/dt$, the amount of reentrained particles increases with elapsed time. Taking into account the time delay (see Equation 2.8.23), the reentrainment fluxes $J_S(t)$ and $J_L(t)$ can be calculated by convolution, as follows[33]:

$$J_S(t) = \frac{ak\alpha}{T_S}\int_0^t\frac{1}{(1-\gamma)^2}\frac{d\gamma}{d\bar{u}'}\exp\left(-\frac{t-t'}{T_S}\right)dt' \tag{2.8.25}$$

$$J_L(t) = \frac{(1-a)k\alpha}{T_L}\int_0^t\frac{1}{(1-\gamma)^2}\frac{d\gamma}{d\bar{u}'}\exp\left(-\frac{t-t'}{T_L}\right)dt' \tag{2.8.26}$$

where a is the mass ratio of the short-delay reentrainment to the total reentrainment. Equations (2.8.25) and (2.8.26) can be rewritten as follows:

$$J_S(\bar{u}) = \frac{ak}{T_S}\int_0^{\bar{u}}\frac{1}{(1-\gamma)^2}\frac{d\gamma}{d\bar{u}'}\exp\left(-\frac{\bar{u}-\bar{u}'}{\alpha T_S}\right)d\bar{u}' \tag{2.8.27}$$

$$J_L(\bar{u}) = \frac{(1-a)k}{T_L}\int_0^{\bar{u}}\frac{1}{(1-\gamma)^2}\frac{d\gamma}{d\bar{u}'}\exp\left(-\frac{\bar{u}-\bar{u}'}{\alpha T_L}\right)d\bar{u}' \tag{2.8.28}$$

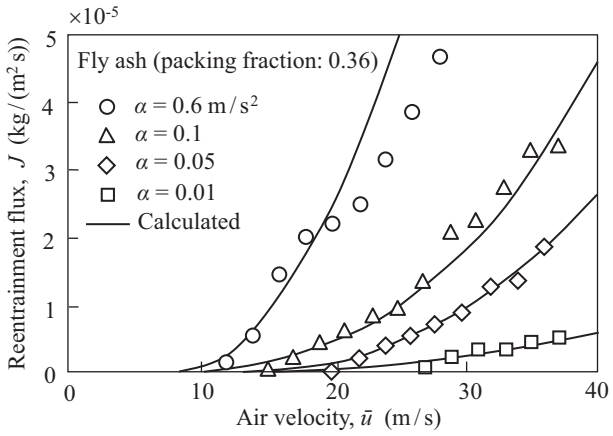


FIGURE 2.8.5 Reentrainment flux of aggregate particles from a particle deposition layer by accelerated air flow (τ_{c50}=4.4 Pa, $\bar{u}_{50}$= 29 m/s, σ_g=2.0, $k=1.7\times10^{-3}$ kg/m^2, a=0.6, T_L=250 s, $T_S=1/\alpha$).

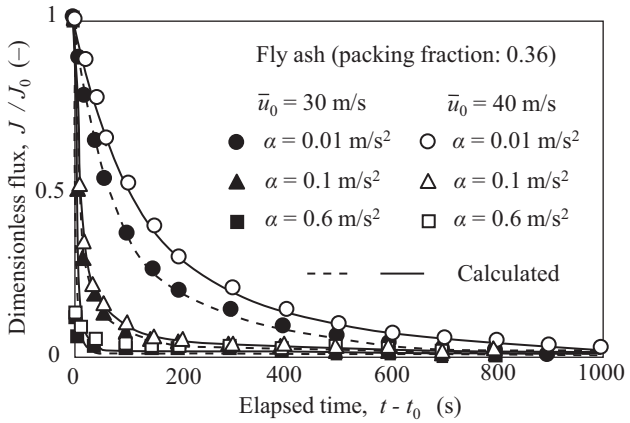


FIGURE 2.8.6 Dimensionless reentrainment in steady-state flow after stopping air acceleration (τ_{c50}=4.4 Pa, $\bar{u}_{50}$=29 m/s, σ_g=2.0, $k=1.7\times10^{-3}$ kg/m^2, a=0.5–0.7, T_L=200–300 s, $T_S=1/\alpha$).

When the fluid velocity increases with a constant acceleration, the reentrainment flux is calculated from Equations (2.8.25) and (2.8.26) or from Equations (2.8.27) and (2.8.28). When the fluid velocity is maintained at $\bar{u}=\bar{u}_0$ after completing the fluid acceleration, the reentrainment flux in the steady-state flow is calculated by substituting zero for $d\gamma/d\overline{u'}$.

Figure 2.8.5 shows the experimental and calculated values for the reentrainment flux in an accelerated airflow (α=0.01, 0.05, 0.1, and 0.6 m/s^2). The reentrainment flux increases with the airflow acceleration as well as with the velocity. Figure 2.8.6 shows the reentrainment flux in steady-state flow after completing the airflow acceleration. The average air velocity is increased at a constant acceleration up to $\bar{u}_0$ = 30 or 40 m/s, and then maintained for 1000 s. The reentrainment flux is normalized by the flux J_0 found at $t=t_0$. The dimensionless flux J/J_0 initially decreases rapidly and then gradually approaches zero. The rate of the decrease is larger for a higher acceleration and the time dependence of the reentrainment in the steadystate flow is still affected by the preceding unsteady-state flow (acceleration effect).

Simultaneous Particle Deposition and Reentrainment

In gas–solids pipe flow, particle deposition and reentrainment often occur simultaneously. The amount of particles deposited on the surface increases with elapsed time. However, the rate of increase gradually decreases asymptotically to a certain value as shown in Figure 2.8.7. This is because the aggregate particles are more readily reentrained as the amount of particles on the wall increases.[31] The variation of the mass of particles per unit area can be expressed as[37]

$$\frac{W}{A}=\left(\frac{W}{A}\right)^{*}\left\{1-\exp\left(-\frac{t}{\tau_0}\right)\right\} \qquad (2.8.29)$$

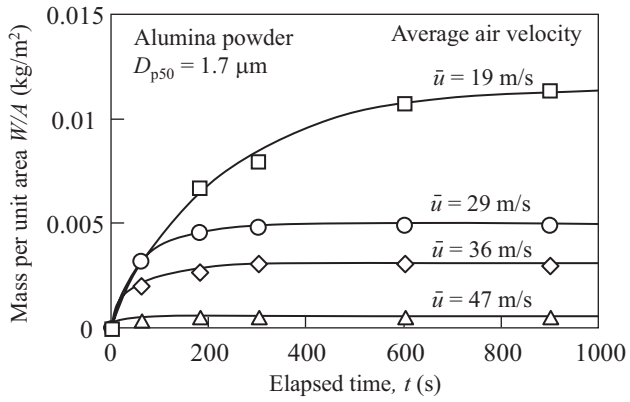


FIGURE 2.8.7 Mass of particles deposited per unit area as a function of time elapsed (horizontal rectangular channel: 3 mm high, 10 mm wide; particle concentration 0.05 kg/m^3).

where $(W/A)^*$ is the equilibrium mass of particles per unit area and τ_0 is a time constant. The calculated lines are shown in addition to the experimental values in Figure 2.8.7. The value of $(W/A)^*$ depends on the adhesion and separation strengths. Figure 2.8.8 shows photographs of typical particle deposition layers formed on a wall.[37] The form of the deposition layer is classified into two categories: a continuous (filmy) deposition layer covering the wall and a striped-pattern deposition layer. The form of the deposition layer depends on the particle diameter and the air velocity as shown in Figure 2.8.9. The submicron-sized particles form only a filmy deposition layer and the micron-sized particles can form either a striped deposition layer or a filmy deposition layer. The formation of the striped deposition layer depends on the inertia of the suspended particles.[38,39] In addition, other factors such as the surface roughness[40–44] and external vibrations[45] should be taken into consideration.

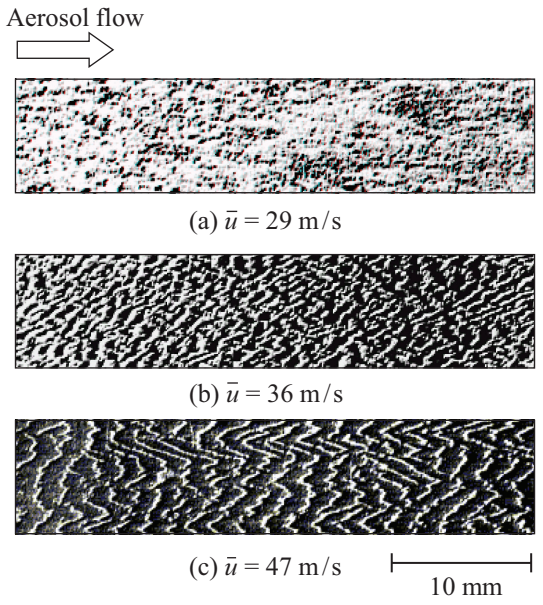


FIGURE 2.8.8 Photographs of particle deposition layers (horizontal rectangular channel 3 mm high, 10 mm wide, alumina powder D_{p50} = 1.7 μm).

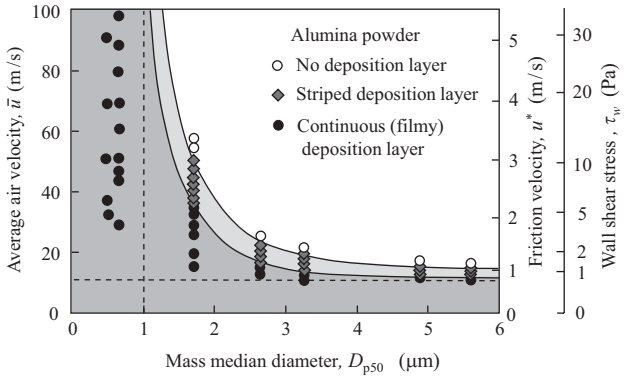


FIGURE 2.8.9 State diagram of particle deposition layer as a function of average air velocity and particle diameter.

REFERENCES

1. Zhu, H. P., Zhou, Z. Y., Yang, R. Y., Yu, A. B., *Chem. Eng. Sci.*, 62, 3378–3396, 2007.
2. Kleinstreuer, C., Feng, Y., *J. Biomech. Eng.*, 135, 021008-1–021008-19, 2013.
3. Li, A., Ahmadi, G., *Aerosol Sci. Technol.*, 16, 209–226, 1992.
4. Ingham, D. B., *J. Aerosol Sci.*, 6, 125–132, 1975.
5. Housiadas, C., Drossinos, Y., *Aerosol Sci. Technol.*, 39, 304–318, 2005.
6. Cooper, D. W., Peters, M. H., Miller, R. J., *Aerosol Sci. Technol.*, 11, 133–143, 1989.
7. Adamczyc, Z., Dabros, T., Czarnecki, J., Van de Ven, T. G. M., *Adv. Colloid Interface Sci.*, 19, 183–252, 1982.
8. Shimada, M., Seto, T., Okuyama, K., *AIChE J.*, 39, 1859–1869, 1993.
9. Tsai, R., Chang, Y. P., Lin, T. Y., *J. Aerosol Sci.*, 29, 811–825, 1998.
10. Papavergos, P. G., Hedley, A. B., *Chem. Eng. Res. Des.*, 62, 275–295, 1984.
11. Friedlander, S. K., Johnstone, H. F., *Ind. Eng. Chem.*, 49, 1151–1156, 1957.
12. Sehmel, G. A., *J. Geophys. Res.*, 75, 1766–1781, 1970.
13. Sehmel, G. A., *J. Aerosol Sci.*, 4, 125–138, 1973.
14. Liu, B. Y. H., Ilori, T. A., *Environ. Sci. Technol.*, 8, 351–356, 1974.
15. Shimada, M., Okuyama, K., Asai, M., *AIChE J.*, 39, 17–26, 1993.
16. Shimada, M., Okuyama, K., Okazaki, S., Asai, T., et al., *Aerosol Sci. Technol.*, 25, 242–255, 1996.
17. Schmidt, F., Gartz, K., Fissan, H., *J. Aerosol Sci.*, 28, 973–984, 1997.
18. Guha, A., *Annu. Rev. Fluid Mech.*, 40, 311–341, 2008.
19. Zhang, Z., Chen, Q., *Atmos. Environ.*, 41, 5236–5248, 2007.
20. Adams, J. F. W., Fairweather, M., Yao, J., *Comput. Chem. Eng.*, 35 893–900, 2011.
21. Lecrivain, G., Barry, L., Hampel, U., *Powder Tech.*, 258, 134–143, 2014.
22. Nowak, N., Kakade, P. P., Annapragada, A. V., *Ann. Biomed. Eng.*, 31, 374–390, 2003.
23. Rostami, A. A., *Inhal. Toxicol.*, 21, 262–290, 2009.
24. Hofmann, W., *J. Aerosol. Sci.*, 42, 693–724, 2011.
25. Soldati, A., Marchioli, C., *Int. J. Multiphase Flow*, 35, 827–839, 2009.
26. Zhu, H. P., Zhou, Z. Y., Yang, R. Y., Yu, A. B., *Chem. Eng. Sci.*, 63, 5728–5770, 2008.
27. Fan, F.-G., Ahmadi, G., *J. Aerosol. Sci.*, 26, 813–840, 1995.
28. Yin, C., Rosendahl, L., Kær, S. K., Sørensen, H., *Chem. Eng. Sci.*, 58, 3489–3498, 2003.
29. Tian, L., Ahmadi, G., Wang, Z., Hopke, P. K., *J. Aerosol Sci.*, 45, 1–18, 2012.
30. Zhong, W., Yu, A., Liu, X., Tong, Z., Zhang, H., *Powder Tech.*, 302, 108–152, 2016.
31. Ikumi, S., Wakayama, H., Masuda, H. *Kagaku Kogaku Ronbunshu*, 12, 589–594, 1986.
32. Matsusaka, S., *Aerosol. Sci. Technol.*, 49, 739–746, 2017.
33. Matsusaka, S., Masuda, H., *Aerosol Sci. Technol.*, 24, 69–84, 1996.
34. Kousaka, Y., Okuyama, K., Endo, Y., *J. Chem. Eng. Jpn.*, 13, 143–147, 1980.
35. Reeks, M. W., Reed, J., Hall, D., *J. Phys. D Appl. Phys.*, 21, 574–589, 1988.
36. Wen, H. Y., Kasper, G., Udischas, R., *J. Aerosol Sci.*, 20, 923–926, 1989.
37. Matsusaka, S., Theerachaisupakij, W., Yoshida, H., Masuda, H., *Powder Technol.*, 118, 130–135, 2001.
38. Matsusaka, S., Adhiwidjaja, I., Nishio, T., Masuda, H., *Adv. Power Technol.*, 9, 207–218, 1998.
39. Theerachaisupakij, W., Matsusaka, S., Akashi, Y., Masuda, H., *J. Aerosol Sci.*, 34, 261–274, 2003.
40. Soltani, M., Ahmadi, G., *J. Adhesion*, 51, 105–123, 1995.
41. Adhiwidjaja, I., Matsusaka, S., Tanaka, H., Masuda, H., *Aerosol Sci. Technol.*, 33, 323–333, 2000.
42. Ziskind, G., Fichman, M., Gutfinger, C., *J. Aerosol Sci.*, 31, 703–719, 2000.
43. Reeks, M. W., Hall, D., *J. Aerosol Sci.*, 32, 1–31, 2001.
44. Jiang, Y., Matsusaka, S., Masuda, H., Qian, Y., *Powder Technol.*, 186 199–205, 2008.
45. Theerachaisupakij, W., Matsusaka, S., Kataoka, M., Masuda, H., *Adv. Powder Technol.*, 13, 287–300, 2002.



Taylor & Francis
Taylor & Francis Group
http://taylorandfrancis.com

2.9 Agglomeration (Coagulation)

Takafumi Seto and Kikuo Okuyama (2.9.1)
Ko Higashitani (2.9.2)

2.9.1 IN GASEOUS STATE

Coagulation of aerosols, which is used to describe the growth process of aerosol particles in contact with each other, causes a continuous change in the size distribution of agglomerates, keeping the total particle volume constant. Among the various coagulation mechanisms which are categorized by the forces of particle interaction, Brownian coagulation (thermal coagulation) is the most familiar and fundamental coagulation process. Others are gradient coagulation, turbulent coagulation, electrostatic coagulation, acoustic coagulation, coagulation due to the velocity difference under gravity or centrifugal force, and so on.

When two particles having diameters D_{pi} and D_{pj} collide, the number of collisions per unit time per unit volume can be written as

$$N = K\left(D_{pi,}\ D_{pj}\right)n_i n_j \tag{2.9.1}$$

where n_i and n_j are the number concentrations of particles i and j, respectively, and $K(D_{pi}, D_{pj})$ is the coagulation rate function or the collision rate between particles of diameters D_{pi} and D_{pj}.

In the special case of the initial stage of coagulation of a monodisperse aerosol having uniform diameter D_p, the decreasing rate of particle number concentration n can be given from Equation (2.9.1) as

$$\frac{dn}{dt} = -0.5K_0 n^2 \tag{2.9.2}$$

where $K_0 = K(D_p, D_p)$. When the coagulation rate function is not a function of time, the decrease in particle number concentration from n_0 to n can be obtained from the integration of Equation (2.9.2) over a time period from zero to t:

$$n = \frac{n_0}{1 + 0.5K_0 n_0 t} \tag{2.9.3}$$

Because the particle volume is kept constant during the coagulation process, the average particle diameter D_p based on particle volume after the period of time t can be given by

$$D_p = D_{p0}\left(1 + 0.5K_0 n_0 t\right)^{1/3} \tag{2.9.4}$$

However, in the case of coagulation of a polydisperse aerosol, the basic equation that describes the time-dependent change in particle number concentration of volume v at time t, $n(v, t)dv$, can be given as

$$\frac{\partial n(v,t)}{\partial t} = \frac{1}{2}\int_0^v K(v', v-v')n(v',t)n(v-v',t)dv' - n(v,t)\int_0^\infty K(v,v')n(v',t)dv' \tag{2.9.5}$$

The first term on the right-hand side represents the rate of formation of particles of volume v due to coagulation, and the second represents the rate of loss of particles of volume v by coagulation with all other particles.

The time-dependent change in number concentration and size distribution of aerosol particles undergoing coagulation can basically be obtained by solving Equation (2.9.5) for a given initial particle size distribution. In the derivation of Equation (2.9.5), however, the following assumptions are made: (1) particles are electrically neutral, and (2) particles are spherical and collide with each other to form another spherical particle whose mass is the same as the combined mass of the two smaller particles. Accordingly, Equation (2.9.5) cannot be applied to evaluate the coagulation of solid particles as particle fusion takes place slowly after the collision. In order to consider the nonspherical effect of agglomerated particles on coagulation, the population balance equation for collision and sintering has recently been derived.[1] Although their model predicted the average primary particles sizes of agglomerates, the effect of agglomerate structure on the collision rate was neglected by using the collision rate of spherical particles having an equivalent volume of the agglomerate.[2]

Brownian Coagulation

For aerosol particles of submicron diameter, Brownian coagulation by Brownian motion of particles is essential for the characterization of the behavior of aerosols. In the general case, the rate function of Brownian coagulation is characterized by the Knudsen number $Kn = 2l/D_p$, where l is the mean path of the background gas.

In the continuum regime, having very small values of Kn, Smoluchowski[3] applied the theory of Brownian diffusion to the statistical problem of the collision of particles thermally agitated in a continuum.

In the diffusion process where a certain particle (radius r_i and diffusion coefficient D_i) among other particles is fixed, the surrounding particles (radius r_j and diffusion coefficient D_j) collide with the fixed particle due to their Brownian motion, as shown in Figure 2.9.1. The number of particle r_j diffusing in unit time is

$$N = 4\pi r_{ij}^2 D_j \left(\frac{\partial n}{\partial r}\right)_{r=r_{ij}} \tag{2.9.6}$$

where $r_{ij}=r_i+r_j$ is the distance between the centers of the two particles at the moment of contact, and n is the concentration of particles r_j at time t as a function of distance r from particle r_i.

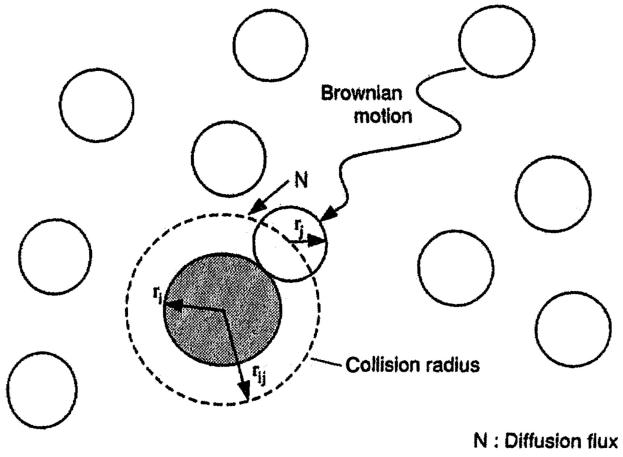


FIGURE 2.9.1 Brownian coagulation by Brownian diffusive deposition.

The value of the concentration gradient $\partial n/\partial r$ can be determined by solving the diffusion equation in spherical coordinates. For submicron particles, this concentration instantaneously shifts to the stationary one by the following equation:

$$n = n_j\left(1-\frac{r_{ij}}{r}\right) \tag{2.9.7}$$

Substitution of this equation to Equation (2.9.6) gives

$$N = 4\pi D_j r_{ij} n_j \tag{2.9.8}$$

Because the central fixed particle is also in Brownian movement, Equation (2.9.8) leads to the next equation by adding the Brownian diffusion coefficient D_i of particle r_i.

$$N = 4\pi(D_i + D_i)(r_i + r_i)n_j \tag{2.9.9}$$

Accordingly, the Brownian coagulation rate function in the continuum regime can be given from its definition as Equation i in Table 2.9.1, which lists the available coagulation function $K_B(D_{pi}, D_{pj})$ for Brownian coagulation.[4,5] Figure 2.9.2 shows the coagulation rate functions of monodispersed particles, $0.5K_B(D_p, D_p)$, as a function of particle diameter in air at ambient conditions. There exists a distinct maxima in the size range from 0.01 to 0.1 μm, depending on particle diameter.[6]

TABLE 2.9.1 Available Expressions for Brownian Coagulation Rate Function

Continuum Regime $Kn < 0.1$	Transition Regime $0.1 \le Kn \le 10$	Free-Molecular Regime $Kn > 10$
$2\pi(D_i + D_j)(D_{pi} + D_{pj})$ ...(i)	$2\pi(D_i + D_j)(D_{pi} + D_{pj})$ $\times\left[\frac{D_{pi}+D_{pj}}{D_{pi}+D_{pj}+2g_{ij}} + \frac{8(D_i+D_j)}{\bar{v}_{ij}(D_{pi}+D_{pj})}\right]^{-1}$ ...(ii)	$\frac{\pi}{4}(D_{pi} + D_{pj})^2 \bar{v}_{ij}$ ...(iii)
k = Boltzmann constant (=1.38×10^{-23} J/K), T = temperature		
$D_i = \frac{kT}{3\pi\mu D_{pi}}$	$D_i = \frac{C_c kT}{3\pi\mu D_{pi}}$	$\bar{v}_{ij} = \left(\bar{v}_i^2 + \bar{v}_j^2\right)^{0.5}$
	$C_c = 1 + Kn\left[1.257 + 0.4\exp\left(\frac{-1.1}{Kn}\right)\right]$	$\bar{v}_i = \left(\frac{8kT}{\pi m_i}\right)^{0.5}$
	$g_{ij} = \left(g_i^2 + g_j^2\right)^{0.5}$	$m_i = \frac{\pi}{6} D_{pi}^3 \rho_p$
	$g_i = \frac{(D_{pi} + l_i)^3 - (D_{pi}^2 + l_i^2)^{1.5}}{3D_{pi}l_i} - D_{pi}$	
	$l_i = \frac{8D_i}{\pi\bar{v}_i}$	

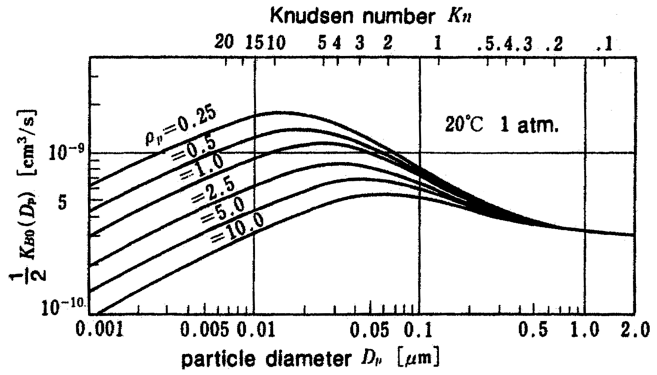


FIGURE 2.9.2 Brownian coagulation rate against particle diameter.

At the present stage, for Brownian coagulation in the transition regime, Fuchs' interpolation formula (Equation ii in Table 2.9.1) is considered to be reasonable due to the better agreement with more rigorous theories. Furthermore, the effect of agglomerate structure on the collision kernel is incorporated by replacing the particle diameter with the collision diameter.[2,7] The collision diameter of agglomerate, $D_{c,i}$ with a primary particle diameter, $d_{p,i}$ and the number of primaries per an agglomerate, $n_{p,i}$ is given by

$$D_{c,i} = d_{p,i}\left(\frac{v_i}{v_{p,i}}\right)^{1/D_f} = d_{p,i}\left(n_{p,i}\right)^{1/D_f} \tag{2.9.10}$$

and

$$d_{p,i} = \frac{6v_i}{a_i} \tag{2.9.11}$$

where $v_{p,i}$ is the volume of a spherical primary particle in agglomerate size i, and D_f is the mass fractal dimension. However, the enhancement of coagulation rate due to the influence of van der Waals or the dispersion force between colliding particles was quantitatively explained by Marlow's theory.[8]

In order to evaluate the change in particle size distribution of aerosols, the following three types of solutions have been obtained: (1) analytical solution, (2) asymptotic solution, and (3) numerical solution. Table 2.9.2 shows representative analytical and approximate solutions. In a series of reports, Friedlander[9] developed the similarity theory for the uniformity in shape of observed size spectra of atmospheric aerosols. The asymptotic size distribution obtained is called the self-preserving distribution function (SPDF). This similarity theory evaluates the size spectra only after a sufficiently long time has passed. Figure 2.9.3 depicts the time-dependent change of particle size distribution obtained numerically solving Equation (2.9.5).[10]

Laminar and Turbulent Coagulation

When aerosol particles are suspended in a laminar shear flow, particles tend to coagulate due to their relative motion, and the coagulation rate function can be given as follows[3]:

$$K_L\left(D_{pi}, D_{pj}\right) = 0.17\eta_L\left(D_{pi} + D_{pj}\right)^3\left|\frac{du}{dx}\right| \tag{2.9.12}$$

where du/dx is the velocity gradient of the flow and η_L is the collision efficiency, which expresses the effect of the aerodynamic interaction between particles.

The collisions between particles suspended in a turbulent flow are generally considered to be caused by the two essentially independent mechanisms. In the first mechanism, particles may collide with each other due to the velocity difference between particles caused by the spatial nonhomogeneity characteristic of turbulent flow. The theoretical rate function by Saffman and Turner[11] is

$$L_{T1}\left(D_{pi}, D_{pj}\right) = 0.16\eta_T\left(D_{pi} + D_{pj}\right)^3\left(\frac{\varepsilon_0}{\nu}\right)^{1/2} \tag{2.9.13}$$

where ε_0 is the energy-dissipation per unit mass of fluid, ν the kinematic viscosity, and η_T the collision efficiency. The second mechanism may be caused by a relative motion of each particle to the local turbulent motion of the fluid, because the inertia of a particle is not the same between unequal-sized particles. Saffman and Turner[11] also obtained the following equation:

$$K_{T2}\left(D_{pi}, D_{pj}\right) = 1.43\eta_T\left(D_{pi} + D_{pj}\right)^2\left|\tau\left(D_{pi}\right) - \tau\left(D_{pj}\right)\right|\left(1 - \frac{\rho_f}{\rho_p}\right)\left(\frac{\varepsilon_0^3}{\nu}\right)^{0.25} \tag{2.9.14}$$

where $\tau(D_p)$ is the particle relaxation time ($=\rho_p C_c D_p^2 / 18\mu$). Figure 2.9.4 shows the turbulent coagulation function. It is seen that the turbulent coagulation plays an important role in the coagulation of aerosol particles larger than a few microns even under the small value of ε_0.[12]

Acoustic Coagulation

In an acoustic field, particles coagulate mainly by the following three mechanisms: (1) orthokinetic coagulation due to relative oscillating motion, (2) coagulation due to hydrodynamic attractive force between particles, and (3) turbulent coagulation due to acoustically induced turbulence in a highly intensive acoustic field. Shaw[13] has published an excellent review on acoustic coagulation.

TABLE 2.9.2 Representative Analytical and Approximate Solutions for Brownian Coagulation

(1) $Kn < 0.01$, initially monodispersed particles[a] $n_k = n_0\left(\frac{t}{\tau_B}\right)^{k-1}\left[\left(1+\frac{t}{\tau_B}\right)^{k+1}\right]^{-1}$ where $\tau_B = \frac{1}{K_{B0}n_0}$, $K_{B0} = 0.5K_B\left(D_p, D_p\right)^a$

(2) $Kn > 10$, initially monodispersed particles[b] $n = 0.1624\alpha^{-6/5}\left(kT\right)^{-3/5}\left(\frac{Mn_0t^6}{\rho_p^4 N_{av}}\right)^{-1/5}$, $d_v = 2.274\alpha^{2/5}\left(\frac{kT}{\rho_p^4}\right)^{1/5}\left(\frac{Mn_0t}{N_{av}}\right)^{2/5}$

(3) $Kn < 0.1$, initially polydispersed particles[c] $\frac{n}{n_0} = \frac{1}{A}, \frac{v_g}{v_{g0}} = A\exp\left(4.5\ln^2\sigma_{g0}\right)\left(2+\frac{\exp\left(9\ln^2\sigma_{g0}\right)-2}{A}\right)^{-1/2}$, $\ln^2\sigma_g = \frac{1}{9}\ln\left(2+\frac{\exp\left(9\ln^2\sigma_{g0}\right)-2}{A}\right)$

where $A = 1+\left\{1+\exp\left(\ln^2\sigma_{g0}\right)\right\}0.5K_{B0}n_0t, K_B(D_p, D_p)$

(4) $Kn > 10$, initially polydispersed particles[d] $\frac{n}{n_0} = \frac{1}{A^{6/5}}, \frac{v_g}{v_{g0}} = E^{9/2}A^{6/5}\left(2+\frac{E^{15/2}-2}{A}\right)^{-3/5}$, $\sigma_g = \exp\left[\frac{2}{15}\ln\left(2+\frac{E^{15/2}-2}{A}\right)^{-1/2}\right]$

where $A = 1+(\frac{5}{8})H\tau, \tau = (6kT/\rho_P)^{1/2}r_{g0}^{1/2}n_0t$, $H = E^{1/8}+2E^{5/8}+E^{25/8}$, $E = \exp(z_0) = \ln^2\sigma_{g0}$

(5) $Kn > 10$, for fractal agglomerates[e] $\frac{n}{n_0} = \left[1+\left(\frac{3D_f-4}{2D_f}\right)H_0bKv_{g0}^{\frac{4-D_f}{2D_f}}n_0t\right]^{\frac{2D_f}{3D_f-4}}$,

$$\frac{v_g}{v_{g0}} = \exp\left(\frac{9}{2}\ln^2\sigma_0\right)\left\{1+\left(\frac{3D_f-4}{2D_f}\right)H_0bKv_{g0}^{\frac{4-D_f}{2D_f}}n_0t\right\}^{\frac{2D_f}{3D_f-4}}\left[2+\frac{\exp\left\{\frac{9(3D_f-4)}{2D_f}\ln^2\sigma_0\right\}-2}{1+\left\{\frac{3D_f-4}{2D_f}\right\}H_0bKv_{g0}^{\frac{4-D_f}{2D_f}}n_0t}\right]^{\frac{-D_f}{3D_f-4}},$$

$$\ln^2\sigma = \frac{2D_f}{9(3D_f-4)}\ln\left[2+\frac{\exp\left\{\frac{9(3D_f-4)}{2D_f}\ln^2\sigma_0\right\}-2}{1+\left\{\frac{3D_f-4}{2D_f}\right\}H_0bKv_{g0}^{\frac{4-D_f}{2D_f}}n_0t}\right]$$

where $H = \exp\left\{\frac{9}{2}\left(\frac{4}{D_f^2}-\frac{2}{D_f}+\frac{1}{4}\right)\ln^2\sigma\right\}+2\exp\left\{\frac{9}{2}\left(\frac{2}{D_f^2}-\frac{1}{D_f}+\frac{1}{4}\right)\ln^2\sigma\right\}+\exp\left\{\frac{9}{2}\left(\frac{4}{D_f^2}+\frac{1}{4}\right)\ln^2\sigma\right\}$,

$$\boldsymbol{K} = \left(\frac{3}{4\pi}\right)^{\frac{2}{D_f}-\frac{1}{2}}\left(\frac{6kT}{\rho_p}\right)^{1/2}r_p^{2-6/D_f}$$

n, particle number concentration (m^{-3}).
r_g, geometric mean radius.
r_p, primary particle radius (m).
n_k, number concentration of particle containing k initial particles.
v_g, geometric mean volume [$= \pi d_{pg}^3/6$, d_{pg}: geometric mean diameter (m)].
σ_g, geometric standard deviation.
k, Boltzmann constant (1.38×10^{-23} J/K).
D_f, mass fractal dimension.
T, absolute temperature (K).
ρ_p, particle density (kg/m^3).
t, time (s).
α, sticking probability between collision.
N_{av}, Avagadro's number.
M, molecular weight 0, initial value.
b, values depend on σ_{g0} and D_f^e.

[a] Friedlander, S. K., Smoke, Dust, and Haze: Fundamentals of Aerosol Dynamics, 2nd Ed., Oxford University Press, New York, 2000, pp. 188–196.
[b] Ulrich, G. D., Combust. Sci. Technol., 4, 47–58, 1971.
[c] Lee, K. W., J. Colloid Interface Sci., 92, 315–325, 1983.
[d] Lee, K. W., Curtis, L. A., and Chen, H., Aerosol Sci. Technol., 12, 457–462, 1990.
[e] Park, S. H. and Lee, K. W., J. Colloid Interface Sci., 246, 85–91, 2002.

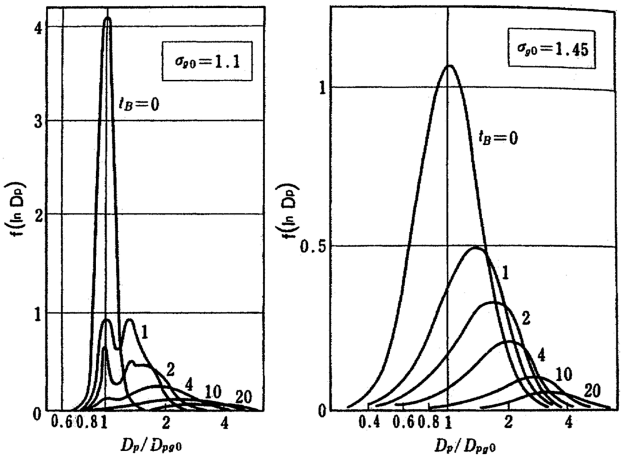


FIGURE 2.9.3 Time-dependent changes in size distribution of particles undergoing Brownian coagulation.

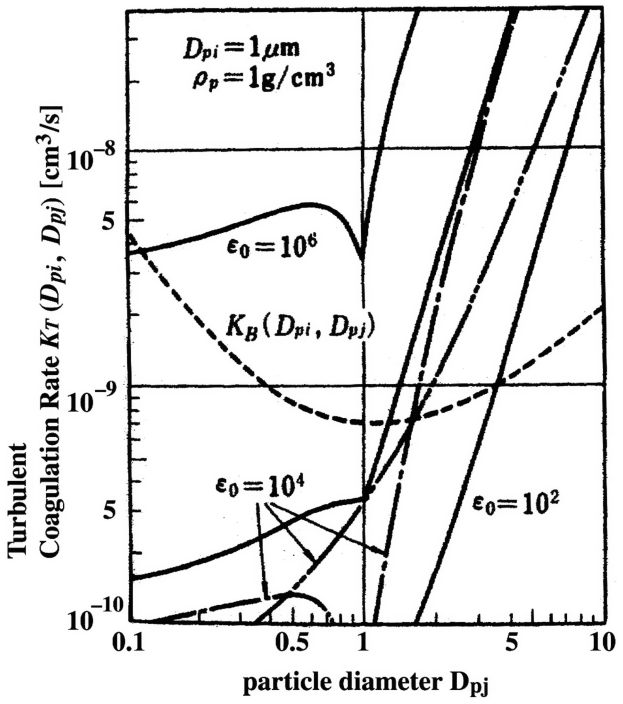


FIGURE 2.9.4 Turbulent coagulation rate against particle diameter. Solid line, Equation (2.9.13) and Equation (2.9.14); dotted–dashed line, Equation (2.9.14); dashed line, Equation (2.9.13).

2.9.2 IN LIQUID STATE

The fundamental behavior of particles in liquids is very similar to that in gases, except that (1) the viscosity and permittivity of the medium are much larger in magnitude, (2) the charge and adsorbed layer on the particle surface influence the particle stability greatly, and (3) the effect of the particle inertia is usually negligible.

The coagulation in liquids proceeds from the collisions between neighboring particles caused by their Brownian motion and/or the flow of the medium. However, every collision does not necessarily result in the coagulation, because the static interactions, such as the electrostatic repulsion, the van der Waals attraction and the hydrodynamic drag force to drain the fluid between the colliding particles, act between particles, when their separation distance is in the order of nanometer, as illustrated in Figure 2.9.5. Hence the macroscopic behavior of particles in liquids is determined by the combination of the kinetic and static interactions between particles. The static interactions have been discussed traditionally in terms of potential energy V rather than force F, which is correlated with V by the relation, $F=-dV/dh$ (h: separation distance between particle surfaces).

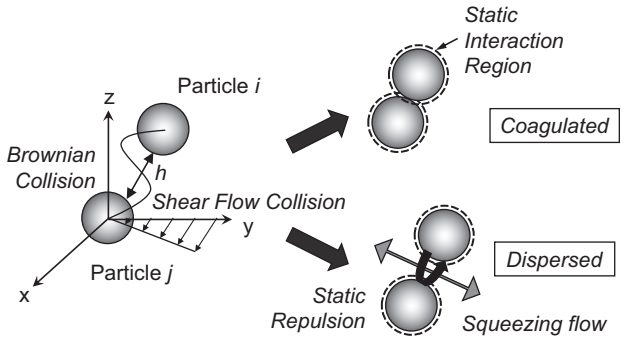


FIGURE 2.9.5 Schematic drawing of the colliding, coagulating, and dispersing behaviors of particle i and j by the Brownian motion and/or the flow of the medium.

2.9.2.1 STATIC INTERACTION AND COAGULATION (DLVO THEORY)

The particles in aqueous solutions are usually charged by various mechanisms at the solid-liquid interface, as described in 2.2.2. Hence, most colloidal particles are electrostatically repulsive with each other. The repulsive potential V_R between particles is originated from the overlapping of the electrostatic potential profiles around particle surfaces described in 2.2.2.2. Because of the mathematical complexity, some assumptions have been introduced to derive the analytical equation of V_R. The following equation is widely used for equal spherical particles of radius a.[14]

$$V_R = \left[64\pi kTan_0\tanh^2\left(\frac{ze\psi_0}{4kT}\right)/\kappa^2\right]e^{-\kappa h} \quad (2.9.15)$$

$$\kappa = \left(2n_0z^2e^2/\varepsilon kT\right)^{0.5} = \left(2\times10^3C_eN_{av}z^2e^2/\varepsilon kT\right)^{0.5} \quad (2.9.16)$$

where ψ_0 is the potential of particle surface; ε, the permittivity of the medium; n_0, the ionic concentration of bulk solution; z, the ionic valency; e, the elementary charge; k, the Boltzmann constant; T, the temperature; C_e, the molar concentration of electrolyte; and N_{av}, the Avogadro number constant. Because the linear superposition and Derjaguin approximations are used in the derivation, Equation (2.9.15) is applicable only

in the region of $\kappa a > 5$. However, this condition is satisfied in most colloidal solutions, because the radius a is usually much larger than the Debye length, $1/\kappa$, which varies from 30.4 to 0.3 nm for 10^{-4} M to 1 M 1:1 electrolyte solutions.

When the potential of particles is small enough to use the Debye-Hückel approximation $\left(ze\psi_0 \ll 4kT\right)$, where the surface charge σ is given by $\sigma = \varepsilon\kappa\psi_0$, the following simple equations are often employed.[15] These equations are known to be usable up to $\psi_0 \lesssim 50\,\mathrm{mV}$ without serious error.

$$V_R = \pm 2\pi\varepsilon a\psi_0^2 \ln\left[1 \pm \exp\left(-\kappa h\right)\right] \quad \kappa a \gtrsim 10 \tag{2.9.17}$$

$$V_R = 2\pi\varepsilon a\psi_0^2 \exp\left(-\kappa h\right) \quad \kappa a \lesssim 5 \tag{2.9.18}$$

where the + and – signs in Equation (2.9.17) indicate the equations for the constant potential and constant charge of particle surface, respectively. Equation (2.9.18) is applicable for both cases.

It is well known that the van der Waals force acts between any particles in the medium. The van der Waals attractive potential between equal spherical particles in solutions, V_A, is given by

$$V_A = -\frac{A}{6}\left[\frac{2a^2}{h^2+4ah} + \frac{2a^2}{\left(h+2a\right)^2} + \ln\left(\frac{h^2+4ah}{\left(h+2a\right)^2}\right)\right] \tag{2.9.19}$$

At $h \ll a$, the equation is simplified to be $V_A = -aA/12h$. A is the Hamaker constant determined only by the properties of the particle and the medium. The values of A are given either theoretically or experimentally, as reported elsewhere.[14,15]

When two particle surfaces are so close that the electron clouds overlap each other, a very strong Born repulsion appears. It is said that the Born potential, V_{Born}, is infinitely large at h~0.4 nm. Then, the total interaction potential, V_T, is given as follows.

$$V_T = V_R + V_A + V_{Born} \tag{2.9.20}$$

A typical potential curve is illustrated in Figure 2.9.6 (a). When the energy given by the Brownian motion or by the fluid flow overcomes the maximum potential energy, particles coagulate at the primary minimum. Otherwise, particles are either dispersed or coagulated loosely at the secondary minimum.

In a given suspension, most parameters in Equation (2.9.20) are fixed, except the values of κ and ψ_0: the value of κ may be changed by the electrolyte concentration C_e, as shown by Equation (2.9.16), and the value of ψ_0 by the solution pH as explained in 2.2.2. Figure 2.9.5(b) and (c) indicates that the maximum value of potential decreases with increasing value of C_e and decreasing value of ψ_0. When the potential peak disappears, every collision results in the coagulation and the dispersion becomes unstable. This electrolyte concentration is called the critical coagulation concentration (*CCC*). The coagulations at $C_e \gtrsim CCC$ and $C_e \lesssim CCC$ are called "rapid" and "slow" coagulations, respectively. The theoretical value

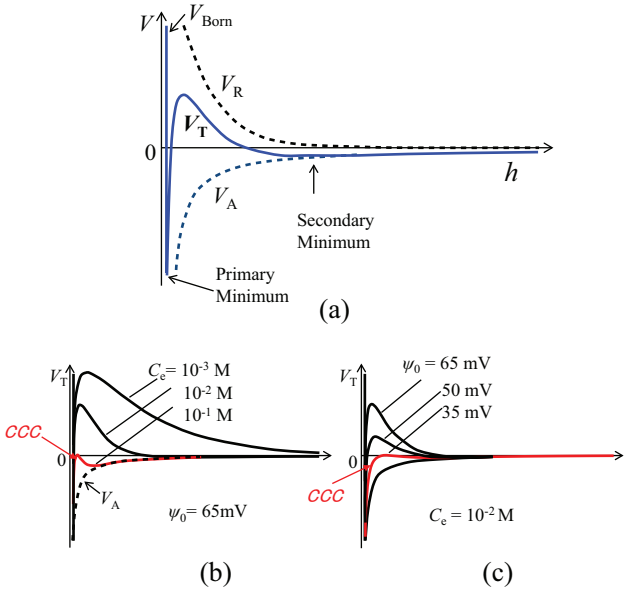


FIGURE 2.9.6 Typical potential curves between charged particles (a), the variation of the potential curves with the electrolyte concentration (b), and the variation of the potential curves with the surface potential (c).

of *CCC* for particles with a relatively high value of ψ_0 in an aqueous solution of 25°C is given by

$$CCC\left(\mathrm{mol\,dm^{-3}}\right) = 87 \times 10^{-40} / z^6 A^2 \tag{2.9.21}$$

where A is in joules. This indicates that *CCC* is extremely sensitive to the value of valency z and, therefore, so is the colloidal stability. This dependence of *CCC* on z has been confirmed experimentally and is known as "Shultze–Hardy rule." When the value of ψ_0 is low, *CCC* is correlated by $CCC\left(\mathrm{mol\,dm^{-3}}\right) \propto \psi_0^4 / z^2$, although this is consistent with Equation (2.9.21), if the feasible equation, $\psi_0 \propto 1/z$, holds.[15]

The stability of dispersions is controllable also by changing the value of ψ_0. The value of ψ_0 is variable with the solution pH in the case of popular particles, such as, oxide particles, and with the concentration of the potential determining ions in the case of the Nernst-type particles, as described in 2.2.2. Note that the dispersions are often regarded as unstable, if $\psi_0 \leq 20$ mV.

Various surfactants and polymers are also employed to control the stability of particles, but these methods are discussed in 4.5.2.

2.9.2.2 Kinetic Interaction and Coagulation Rate

Particles in liquids interact with each other by their Brownian motion and the flow of fluid. As explained above, the stability of particles can be evaluated roughly by the static interactions, but the kinetic interactions must be taken into account to know the degree of stability and the rate of coagulation quantitatively.

Brownian Coagulation and Stability Ratio

The basic theory for the Brownian coagulation of hydrophobic spherical colloids was constructed by Smoluchowski, solving the diffusion equation of colliding particles in the medium.[16] In this theory, the above-mentioned static interactions were not taken into account, but particles were regarded as coagulated when they collided with each other: the coagulation is classified as a rapid coagulation. According to the theory, the rate of collision between particles i and j in a stationary medium, J_{ij}, is given by

$$J_{ij} = \left(\frac{2kT}{3\mu}\right)\left(a_i + a_j\right)\left(\frac{1}{a_i} + \frac{1}{a_j}\right)n_i n_j \qquad (2.9.22)$$

where a_i and n_i are the radius and number concentration of i-fold particle, Then the change of particle concentration is calculated by the following population balance equation:

$$\frac{dn_k}{dt} = \frac{1}{2}\sum_{\substack{i+j=k \\ i=1}}^{i=k-1} J_{ij} - \sum_{i=1}^{\infty} J_{ik} \qquad (2.9.23)$$

At the initial stage of coagulation of monodispersed particles of radius a, the approximation $(a_i+a_j)(1/a_i+1/a_j)\sim 4$ holds. Then, the change of the total particle number concentration, N_t, is obtained by summing up all sizes of particles expressed by Equation (2.9.23), as follows.

$$\frac{dN_t}{dt} = -K_R N_t^2 \qquad (2.9.24)$$

$$\frac{1}{N_t} - \frac{1}{N_0} = \frac{t}{N_0 t_h} \qquad (2.9.25)$$

where K_R ($=4kT/3\mu$) is the rapid coagulation rate, N_0 is the initial total number concentration, and t_h ($=3\mu/4kTN_0$) is the elapsed time when N_t becomes to be $N_0/2$. It is also possible to derive the concentration change of i-fold particles with time, as follows:

$$n_i = \frac{N_0\left(t/t_h\right)^{i-1}}{\left(1+t/t_h\right)^{i+1}} \qquad (2.9.26)$$

Many experimental data of rapid coagulation indicate that this theory overestimates the coagulation rate by about 50%.[17] This problem was solved by modifying the Smoluchowski theory in such a way that the contributions of the van der Waals attraction and the hydrodynamic drag force caused by the squeezing flow between colliding particles were taken into account. The details of these procedures are given elsewhere.[18–21] Then, the modified rate of collision, J_{ij}^M, is written as follows:

$$J_{ij}^M = J_{ij}\left[2a\int_0^{\infty}\beta_{ij}\frac{\exp\left(V_{Tij}/kT\right)}{\left(h+2a\right)^2}dh\right]^{-1} \equiv \alpha_{Bij}J_{ij} \qquad (2.9.27)$$

where the subscripts i and j are equal to 1 at the initial stage of coagulation of mono-dispersed particles, which is eliminated hereafter. β is the coefficient for the effect of the squeezing flow between colliding particles, which is given approximately by $\beta = \left(6h^2+13ah+2a^2\right)/\left(6h^2+4ah\right)$. Because $V_R=0$ in the case of rapid coagulation, the non-dimensional correction factor α_{BR} for the contributions of the van der Waals attraction and the squeezing flow is defined as follows:

$$\alpha_{BR} = \left[2a\int_0^{\infty}\beta\frac{\exp\left(V_A/kT\right)}{\left(h+2a\right)^2}dh\right]^{-1} \qquad (2.9.28)$$

The value of α_{BR}, which depends only on the value of the Hamaker constant A, is calculated by substituting Equation (2.9.19) into Equation (2.9.28), as shown in Figure 2.9.7. Because $A = 10^{-21}\sim10^{-20}$ J for many particles in aqueous solutions,[14] the value of α_{BR} is estimated to be 0.5 ± 0.1, which is consistent with most of experimental data.[22] Then, K_R and t_h are rewritten by $K_R = 4\alpha_{BR}\,kT/3\mu$ and $t_h = 3\mu/4\alpha_{BR}kTN_0$, respectively, and the changes of the total and i-fold particle number concentrations are calculated easily by Equation (2.9.26). This prediction agrees very well with the experimental data measured by using the Coulter counter, as shown in Figure 2.9.8.[17] This implies that the above-mentioned modified Smoluchowski theory is adequate to estimate the rapid coagulation of colloidal particles in solutions.

The above-mentioned modified Smoluchowski theory is certainly available to the coagulation of most of colloids of micron size, but it does not necessarily guarantee the applicability to the coagulation of nanoparticles in solutions, because the effects of the adsorbed layer of water molecules, ions and hydrated ions on the particle surface are not necessarily negligible in the case of nanoparticles. Recently, it was clarified experimentally and theoretically that the rapid coagulation rate reduces by the orders of magnitude with decreasing particle size when the size is comparable with the thickness of the adsorbed layer on the particle surface. The details are reported elsewhere.[23,24]

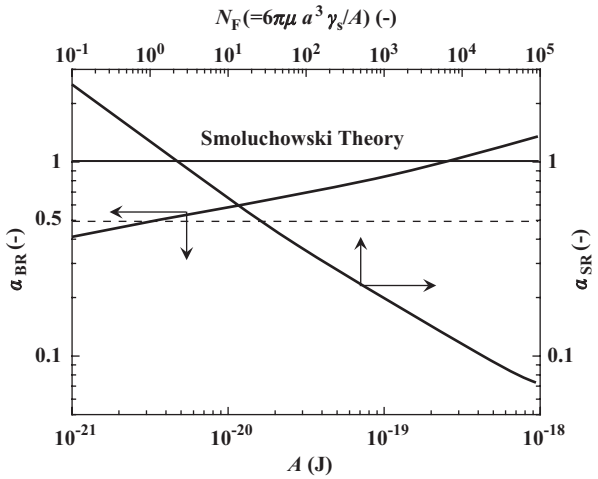


FIGURE 2.9.7 Theoretical dependences of a_{BR} on A and a_{SR} on N_F.

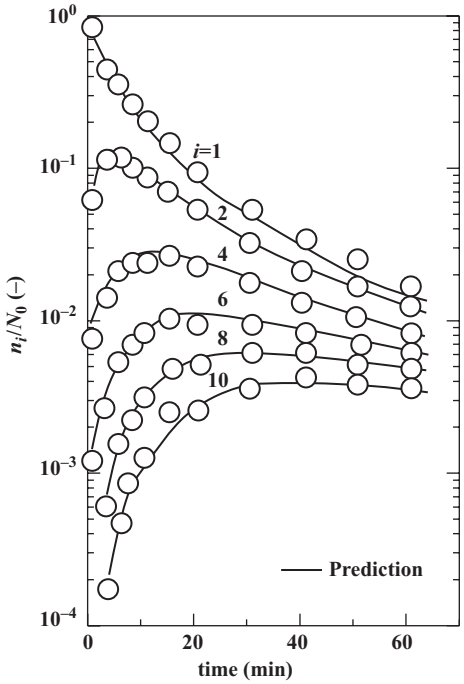


FIGURE 2.9.8 Comparison of the concentration change of 1 to 10-fold particles between the prediction by the modified Smoluchowski theory and the experimental data measured by a Coulter counter.[17] The circle points indicate the average value of three experimental runs, and the lines indicate the corresponding predictions. (Redrawn from the data of Higashitani, and Matsuno, *J. Chem. Eng. Jpn.*, 12, 460, 1979.)

In the case of the slow coagulation ($V_{Rij} \neq 0$), the coagulation rate is not easily predicted. Hence, the stability of suspensions is often evaluated by using the stability ratio W which is a measure of the degree of deviation from the rapid coagulation rate. W is defined as the collision rate of rapid coagulation J_{R0}^M normalized by that of slow coagulation J_{S0}^M at $t=0$, as given by Equation (2.9.29), where the contribution of the squeezing flow is neglected traditionally:

$$W = \frac{J_{R0}^M}{J_{S0}^M} = 2a\int_0^\infty \frac{\exp\left(V_T / kT\right)}{\left(h+2a\right)^2} dh \qquad (2.9.29)$$

where the subscripts R, S, and 0 indicate the rapid and slow coagulation, and $t=0$, respectively. There are various experimental methods to determine the value of J_{R0}^M / J_{S0}^M. The popular method to determine the value of W is to use the following equation by measuring the initial change of the turbidity of suspensions, τ:

$$W = \left(\frac{d\tau}{dt}\right)_{R0} \Big/ \left(\frac{d\tau}{dt}\right)_{S0} \qquad (2.9.30)$$

As known by these definitions of W, the larger the value of W is, the more stable the dispersion is. An example of the comparison of W between the experimental values and theoretical prediction by Equation (2.9.29) is given in Figure 2.9.9. It is

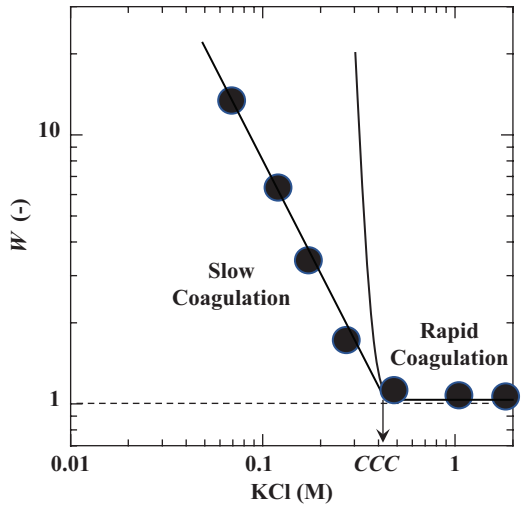


FIGURE 2.9.9 A comparison of W between the experimental values of 0.6 μm latex particle in KCl solution (●) and theoretical prediction by Equation (2.9.29).

clear that the theoretical and experimental values of W agree qualitatively but not quantitatively. This discrepancy is one of the unsolved problems of colloidal phenomena.[19]

Coagulation in Shear Flow

Particles in flow fields collide with each other because of their velocity difference. Their collision results in the coagulation, only if the energy of particles given by the flow field overcomes the maximum energy of their static interaction.

The basic theory of shear coagulation was developed by Smoluchowski, in which particles were assumed to approach along the straight trajectory and collide by the geometrical interception, as shown in Figure 2.9.10.[19,26] This coagulation may be called as the rapid shear coagulation, because no static interactions were not taken into account. Then, the rate of collision J_{ij} is given by the number of particle i across the upstream shaded area per unit time:

$$J_{ij} = \left(4/3\right)\gamma_S \left(a_i + a_j\right)^3 n_i n_j \qquad (2.9.31)$$

where γ_s is the shear rate. Then the total particle number concentration N_t at the initial stage of coagulation is able to be derived as follows:

$$\frac{dN_t}{dt} = -\left(\frac{4\gamma_S \phi}{\pi}\right) N_t \qquad (2.9.32)$$

$$N_t = N_0 \exp\left(-\frac{4\gamma_s \phi}{\pi} t\right) \qquad (2.9.33)$$

where ϕ is the volume fraction of particles. The straight trajectory described above is valid only for particles with large inertia, such as particles in air. In the case of particles in liquids, the effects of the hydrodynamic and van der Waals interactions play the important roles, so that the trajectory becomes much more complicated, as illustrated in Figure 2.9.10.

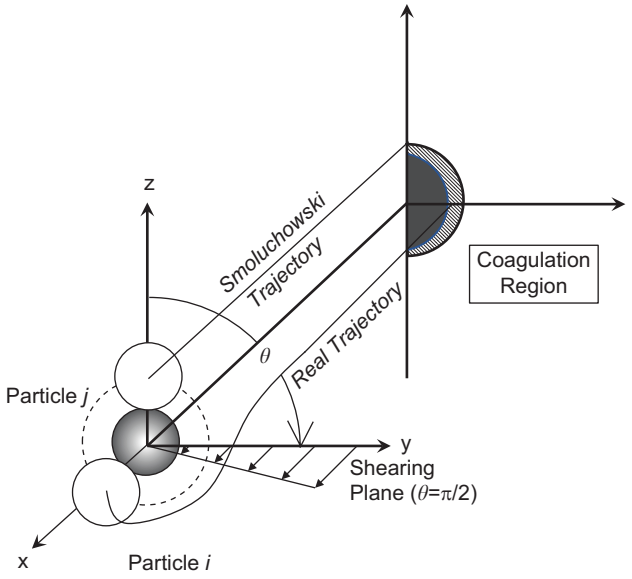


FIGURE 2.9.10 Schematic comparison between the straight trajectory assumed in the Smoluchowski theory and the complicated trajectory estimated by the trajectory analysis.

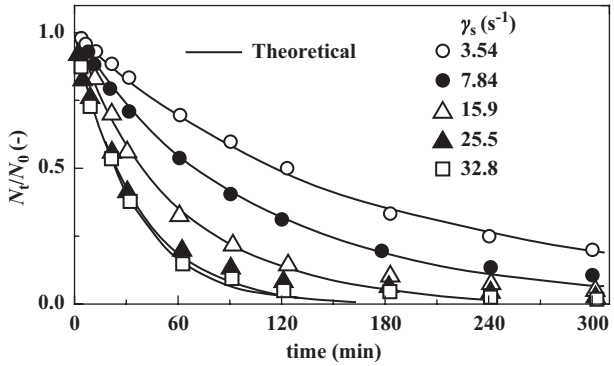


FIGURE 2.9.11 The change of the total number concentration of latex particle of 2.17 μm in diameter with time in various shear flows and the corresponding predictions by Equation (2.9.35) derived from the modified Smoluchowski theory.

The trajectory is obtainable only numerically by using the methodology "trajectory analysis" developed by Batchelor and Green,[18] and the boundary, within which all the particles i collide with the particle j, is determined as shown by a black area in the figure. Then, the correction factor α_{SR} to the Smoluchowski coagulation rate, which is given by the ratio of the black area to the shaded area, is derived as a function of a non-dimensional parameter N_F ($=6\pi\mu a^3\gamma_s/A$) as shown in Figure 2.9.7.[25] Hence γ_s in Equations 2.9.31~2.9.33 should be replaced by $\alpha_{SR}\gamma_s$. Then, the change of N_t is given as follows, assuming that the contributions of the Brownian and shear coagulations are additive:

$$\frac{dN_t}{dt} = -\left(\frac{4\alpha_{BR}kT}{3\mu}\right)N_t^2 - \left(\frac{4\alpha_{SR}\gamma_S\phi}{\pi}\right)N_t \qquad (2.9.34)$$

Because $N_t = N_0$ at $t = 0$, this equation is solved as follows:

$$\ln\left[\left(\frac{N_t + S}{N_t}\right)\left(\frac{N_0}{N_0 + S}\right)\right] = \left(\frac{4\alpha_{SR}\gamma_S\phi}{\pi}\right)t \qquad (2.9.35)$$

where $S = 3\alpha_{SR}\gamma_S\phi\mu / \alpha_{BR}\pi kT$. This is the contribution ratio of the shear rapid coagulation to the Brownian rapid coagulation. The comparison of Equation (2.9.35) is known to agree well with the experimental result, as shown in Figure 2.9.11.[27] This good agreement between the experiment and theoretical prediction implies the adequacy of α_{SR}. As for the concentration change of i-fold particle with time at the initial stage of coagulation, it is able be calculated numerically by the same procedure used to obtain Figure 2.9.8.

In the case of the slow shear coagulation region where the electrostatic repulsive force is not negligible, only the stability map, which depends on the non-dimensional parameters N_F and $N_R (= \varepsilon\psi_0^2 a / A)$, is available. Although this is applicable only under the limited condition, it is important to know qualitatively how the coagulation and stability region depends on various factors within N_F and N_R. The details are given elsewhere.[19]

Coagulation in Turbulent Flow

The basic theory for the rapid coagulation rate in a turbulent flow was constructed by Saffman and Turner.[28] Although the flow field of turbulent is complicated, particles are considered to collide with each other by the shearing flow within the eddies of turbulent. If this is the case, the correction factor, α_{SR}, for the rapid shear coagulation rate should be introduced into the Saffman-Turner equation as follows:

$$J_{ij} = 1.429\alpha_{SR}\left(a_i + a_j\right)^3\left(\frac{\Phi}{\nu}\right)^3 n_i n_j \qquad (2.9.36)$$

where Φ is the energy dissipation per unit mass of fluid and ν is the kinetic viscosity of the medium. The change of the particle size distribution at the initial stage of coagulation is predictable numerically, by substituting Equation (2.9.36) into Equation (2.9.23). It was found that the changes of the total number concentration and i-fold particle concentration with time were well predicted by Equation (2.9.36), as reported elsewhere.[29]

REFERENCES

1. Koch, W., Friedlander, S. K., *J. Colloid Interface Sci.*, 140, 419–427, 1990.
2. Tsantilis, S., Pratsinis, S. E., *AIChE J.*, 46, 407–415, 2000.
3. Smoluchowski, M. W., *Phys. Z.*, 17, 557–571, 1916.
4. Fuchs, N. A., *The Mechanics of Aerosols*, Dover, New York, 1964, pp. 288–302.
5. Sitarski, M., Seinfeld, J. H., *J. Colloid Interface Sci.*, 61, 261–271, 1977.
6. Okuyama, K., Kousaka, Y., Hayashi, K., *J. Colloid Interface Sci.*, 101, 98–109, 1984.

7. Kruis, F. E., Kusters, K. A., Pratsinis, S. E., *Aerosol Sci. Technol*., 19, 514–526, 1993.
8. Marlow, W. H., *J. Chem. Phys*., 73, 6284–6287, 1980.
9. Friedlander, S. K., *Smoke, Dust, and Haze: Fundamentals of Aerosol Dynamics*, 2nd Edition, Oxford University Press, New York, 2000, pp. 210–219.
10. Yoshida, T., Okuyama, K., Kousaka, Y., Kida, Y., *J. Chem. Eng. Jpn*., 8, 317–322, 1975.
11. Saffman, P. G., Turner, J. S., *J. Fluid Mech*., 1, 16–30, 1956.
12. Okuyama, K., Kousaka, Y., Yoshida, T., *J. Aerosol Sci*., 9, 399–410, 1978.
13. Shaw, D. T., *Recent Development in Aerosol Science*, Wiley, New York, 1978.
14. Israelachvili, N. J., *Intermolecular and Surface Force*, 3rd Edition, Academic Press, London, 2011.
15. Hunter, R. J., *Foundations of Colloid Science*, 2nd Edition, Clarendon Press, Oxford, 2009.
16. Kruyt, H. R., *Colloid Science*, Elsevier, Amsterdam, 1952.
17. Higashitani, K., Matsuno, Y., *J. Chem. Eng. Jpn.*, 12, 460, 1979.
18. Batchelor, G. K., Green, J. T., *J. Fluid Mech*., 56, 375, 1972.
19. Russel, W. B., Saville, D. A., Schowalter, W. R., *Colloidal Dispersions*, Cambridge University Press, Cambridge, 1989.
20. Higashitani, K., Tanaka, T., Matsuno, Y., *J. Colloid Interface Sci*., 63, 551, 1978.
21. Masliya, J. H., Bhattacharjee, S., *Electrokinetic and Colloid Transport Phenomena*, John Wiley & Sons, New Jersey, 2006.
22. Higashitani, K., Kondo, M., Hatade, S., *J. Colloid Interface Sci*., 142, 204, 1991.
23. Higashitani, K., Nakamura, K., Shimamura, T., Fukasawa, T., et al., *Langmuir*, 33, 5046–5051, 2017.
24. Higashitani, K., Nakamura, K., Fukasawa, T., Tsuchiya, K., et al., *Langmuir*, 34, 2505–2510, 2018.
25. Higashitani, K., Unpublished work.
26. Higashitani, K., Ogawa, R., Hosokawa, G., Matsuno, Y., *J. Chem. Eng. Jpn*., 15, 299, 1982.
27. Higashitani, K., *Gyoushu Kougaku*, Nikkankogyo Shinbunsha, Tokyo, 1982, p. 53.
28. Saffman, P. G., Turner, J. S., *J. Fluid Mech*., 1, 16, 1956.
29. Higashitani, K., Yamauchi, K., Matsuno, Y., Hosokawa, G., *J. Chem. Eng. Jpn*., 16, 299, 1983.

2.10 Viscosity of Slurry

Yoshiyuki Komoda

2.10.1 INTRODUCTION

Although the origin of the technical term *slurry* is in the thin or flowable mud, the term *slurry* from an industrial aspect covers a wide concept of the dispersion of insoluble solid particles in a liquid, usually water. In some practical applications, the term *paste* or *ink* was used instead of slurry. Suspended solid particles vary in size from very fine colloidal particles to sedimentable coarse particles. Some slurries contain more than two kinds of solid particles, and liquid phase will be the solution of some chemicals in a solvent. Additionally, the particle content is widely changed depending on the purpose of projects. Therefore, the flow characteristics of slurry change widely with the composition. Additionally, the effects of particle size distribution, the shape, and the surface properties of particles on the viscosity of slurry are significant.

The viscosity of slurry usually does not take constant value. In usual cases, viscosity decreases as increasing shear rate or the strength of fluid flow, which is referred as "shear thinning." Recently, the behavior of viscosity increase above critical shear rate is one of the active research fields. In this section, the viscosity behavior of a wide variety of slurries is described, and a brief description of the measuring technique of slurry viscosity is also given.

2.10.2 BASIC FLOW CHARACTERISTICS

The representative flow models for various kinds of slurries are shown in Figure 2.10.1, in terms of the plot of shear stress τ versus shear rate $\dot{\gamma}(= du/dr)$,[1] where u is the fluid velocity and r is the distance perpendicular to the flow direction. These models are used to correlate the data sets of shear rate and shear stress to characterize the flowability of slurry. Figure 2.10.1(a) represents the Newtonian model,

$$\tau = \mu_N \dot{\gamma} \tag{2.10.1}$$

where μ_N is a Newtonian constant viscosity. This behavior usually observed when a small amount of particles are dispersed into a Newtonian fluid. Figure 2.10.1(b) represents the power-law model,

$$\tau = K\dot{\gamma}^n \tag{2.10.2}$$

where K and n are material constants. If n is less than unity, this model represents a pseudoplastic fluid, in which the viscosity decreases with increasing shear rate. On the contrary, if n is greater than unity, the equation represents a dilatant fluid, in which the viscosity increases with increasing shear rate. When n is equal to unity, this model coincides with the Newtonian model. Since the power law model is applicable to any fluids, as far as the shear rate range is sufficiently narrow, the model is frequently used to interpolate the discrete data of viscosity.

Figure 2.10.1(c) indicates the Bingham plastic model,

$$\tau = \tau_y + \mu_B \dot{\gamma} \tag{2.10.3}$$

where μ_B and τ_y are the Bingham plastic viscosity and yield stress, respectively. The Bingham plastic model also represents a pseudoplastic fluid. The Newtonian fluid model is again obtained from Bingham plastic model with zero yield stress. Because the Bingham plastic model is the simplest model to obtain yield stress, it is frequently difficult to correlate the wide range of viscosity date. In such cases, the Herschel–Bulkley model indicated in Figure 2.10.1(d) is an alternative model, which is the combination of the power law model and yielding behavior:

$$\tau = \tau_y + K\dot{\gamma}^n \tag{2.10.4}$$

More complex models have been proposed for non-Newtonian fluids. However, the aforementioned models are simple and widely used for engineering problems.

2.10.3 TIME-DEPENDENT FLOW CHARACTERISTICS

Highly loaded slurries of very fine particles (e.g. plaster, clay, paint pigment, and ceramic powder) show not only the non-Newtonian behavior described above but also time-dependent flow characteristics. Slurries often show the time-dependent decrease of apparent viscosity with increasing shear rate, but the viscosity is recovered when they are settled at rest. This reversible flow characteristic change under constant temperature is called thixotropy. The basic idea of the phenomenological thixotropy model was proposed by Cheng and Evans,[2]

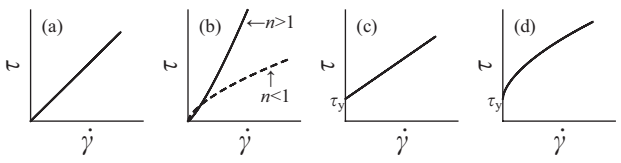


FIGURE 2.10.1 Classification of fluid models: (a) Newtonian model; (b) power-law model; (c) Bingham model; (d) Herschel–Bulkley model.

and thixotropy models proposed so far have been recently reviewed by Mewis and Wagner[3] and Malkin.[4]

Rheological characteristics of certain kinds of suspensions are remarkably and instantaneously changed by applying external electric and magnetic fields. These phenomena are called electrorheological and magnetorheological effects, respectively. The electrorheological fluid is expected to be a new functional fluid for many engineering purposes. The mechanisms and models for the electrorheological behavior can be found elsewhere.[5] The magnetorheological fluid has attracted much attention in industrial applications.[6]

2.10.4 VISCOSITY EQUATIONS FOR SUSPENSIONS OF SPHERICAL PARTICLES OF NARROW PARTICLE SIZE DISTRIBUTION

Superlative reviews on this subject are given by Thomas[7] and Metzner.[8] Figure 2.10.2 shows the increasing trend of apparent viscosity of slurries with the solid concentration in volume. In this figure, the relative viscosity of slurry μ_r (the slurry viscosity normalized by the medium viscosity), increases with the addition of particles. The relative viscosity is a unique function of the volume fraction of solid particle, ϕ, but it has the negligible effect of particle size. The following classic Einstein equation represents accurately the behavior of the suspension only within a vanishingly small range of solid concentration.[9]

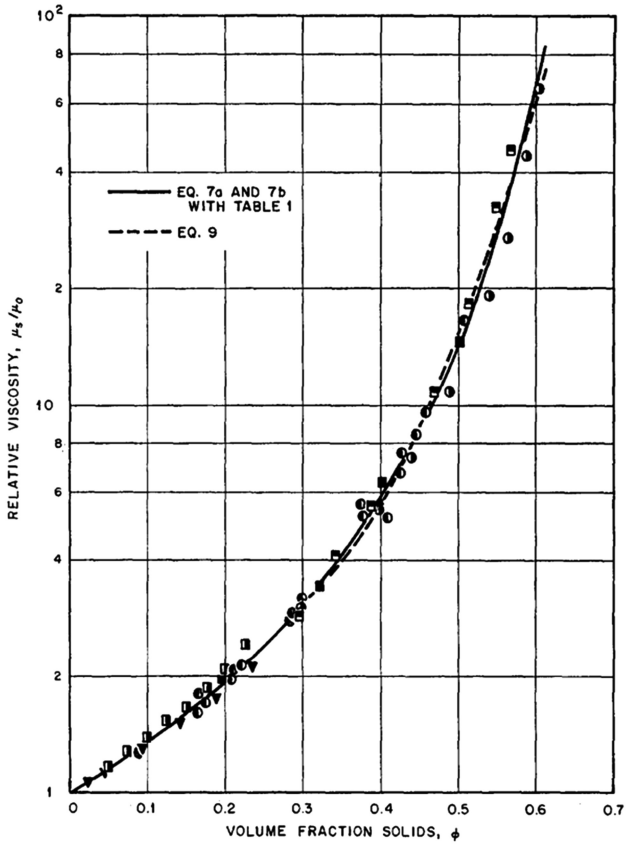


FIGURE 2.10.2 Relative viscosity as a function of particle content for completely dispersed slurries of spheres having narrow size distributions. Particle diameters range from 0.1 to 400 μm. The solid line depicts Equation 2.10.7, and keys for the data are given in the article by Thomas. [From Thomas, D. G., *J. Colloid Sci.*, 20, 267, 1965. With permission.]

$$\mu_r = 1 + 2.5\phi \tag{2.10.5}$$

Guth and Simha[10] proposed the following viscosity equation, which is applicable to a higher solid concentration range. They modified the Einstein equation by taking the effect of interaction between solid particles into account and added the third term which is proportional to the square of solid volume fraction.

$$\tau = \mu_r = 1 + 2.5\phi + 14.1\phi^2 \tag{2.10.6}$$

Thomas recommended the following empirical equation[7]:

$$\mu_r = 1 + 2.5\phi + 10.05\phi^2 + A\exp(B\phi) \tag{2.10.7}$$

with $A = 0.00273$ and $B = 16.6$. This equation gives a prediction similar to the oft-quoted Moony equation[11]:

$$\mu_r = \exp\left(\frac{2.5\phi}{1 - k\phi}\right) \tag{2.10.8}$$

where the parameter k, called as crowding factor, changes depending on the system in the range of $1/k = 0.52$ ($=\pi/6$, densest particle packing) ~ 0.74 (face centered cubic packing). Mooney's equation was partly empirical in terms of particle interaction, but falls into Einstein's equation at the very small solid concentration. The theoretical equations proposed by Krieger-Dougherty[12] contain the intrinsic viscosity $[\eta]$ defined by $\left[(\mu_r - 1)/\phi\right]_{\phi \to 0}$. These equations are also consistent with the Einstein equation with $[\eta] = 2.5$ for a very dilute system.

$$\mu_r = \left(1 - \frac{\phi}{\phi_m}\right)^{-[\eta]\phi_m} \tag{2.10.9}$$

Quemada[13] derived the well-known equation applicable for the wide range of particle concentration up to a percolation transition with the introduction of k_0.

$$\mu_r = \left(1 - \frac{1}{2}k_0\phi\right)^{-2} \tag{2.10.10}$$

where $k_0 = [\eta]$. This equation also coincides with Einstein equation under the same assumption by Krieger-Dougherty. The empirical equation proposed by Kitano et al. has the form similar to the Quemada equation and gives a good prediction for highly loaded slurries.[14]

$$\mu_r = \left(1 - \frac{\phi}{A}\right)^{-2} \tag{2.10.11}$$

The single empirical constant A has a value of 0.680 for slurries of smooth spheres. All the equations mentioned above are applicable only for completely dispersed suspensions.

2.10.5 EFFECT OF PARTICLE SIZE DISTRIBUTION ON SLURRY VISCOSITY

Most systems of interest in practical applications are, of course, more complex in view of particle size than the monodisperse suspensions. If particles with a wide size distribution are employed, the maximum possible packing density of particles, which relates to $1/k$, ϕ_m, k_0, and A in Equations 2.10.8 through 2.10.11, will change considerably. In many cases, this change causes the reduction in slurry viscosity. Chong et al.[15] investigated the effect of bimodal particle size distribution on the slurry viscosity. They showed experimentally that the viscosity of the suspension at $\phi = 0.58$ was reduced to almost 6%, in magnitude, when 25% of the particles in the unimodal suspension are replaced by smaller particles of the size ratio of 0.138. The volume fraction of maximum packing in bimodal systems was investigated experimentally by McGeary.[16] Using the experimental results of McGeary, Lee proposed a prediction method for the maximum packing volume fraction of multimodal suspensions.[17] A linear-mixture packing model to estimate the packing density of particle mixtures was proposed by Yu and Standish.[18] Funk[19] modified the theoretical equation proposed by Andreasen and Andersen[20] to give an optimum size distribution for particles in a limited size range.

In the case of bimodal suspensions composed of colloidal particles, the viscosity of the system shows different behavior as increasing the fraction of smaller particles. Although the viscosity can be reduced below critical fraction of small particles, the drastic viscosity increase is observed above the criteria. This is caused by the significant effect of the interparticle interaction between fine particles.[21–23] They all proposed the model to predict the viscosity of bimodal suspension, which is the simplest case of practical multimodal system. The viscosity reduction is not always observed for any bimodal systems. Lee et al.,[24] demonstrated the mixture of two kinds of Newtonian fluids of alumina and latex particles showed significant shear-thinning behavior due to heteroaggregation of fine latex particles with larger alumina particles. Since bimodal slurries with significantly large size difference are popular in various engineering issues, the rheological behavior of the bimodal slurries of micro and nano-sized particles should be studied.

2.10.6 SHEAR THINNING OR THICKENING BEHAVIOR OF SLURRY

Although the viscosity for slurries of completely dispersed particles is a unique function of solid volume fraction, the apparent viscosity usually decreases with increasing shear rate. The key factor for this discrepancy is the agglomeration of particles. If particles are completely dispersed and no interaction acts between particles, the suspension behaves as a Newtonian. However, if the effect of particle interaction is not negligible or the surface distance between particles becomes sufficiently small, the formation of particle agglomerates increases the apparent volume fraction. As the shear rate increases, particle agglomerates are split into small pieces and the apparent volume fraction is reduced, which attributes to the viscosity decrease. This is the basic mechanism of shear-thinning behavior.

The effect of agglomeration on the non-Newtonian flow characteristics of slurries was discussed by Usui et al.,[25] considering that the stable state of particle agglomeration is determined by the Brownian agglomeration, the shear agglomeration, and the shear break-up. Usui[26] also modified the non-Newtonian viscosity prediction model to apply to the suspensions of nonspherical particles with size distribution by introducing the concept proposed by Lee et al.[17]

On the contrary, the viscosity increase with increasing shear rate is sometimes observed especially for highly loaded slurries of fine colloidal particles. The oobleck composed of starch and water at the volume ratio of 2 is the most popular shear thickening fluid. The transition from the random packing to the body-centered-cubic packing of particles induces the drastic increase of the viscosity of oobleck. However, such a shear thickening mechanism is rarely found in the slurries of industrial applications. Wagner and Mewis proposed the following shear thickening mechanism of highly concentrated dispersion of stably dispersed latex particles.[27] Even in well dispersed particles, the particles are forced to contact each other under highly loaded conditions, which results in their agglomeration. The destruction or ordering of the agglomerated structure of particles along the shear direction results into shear thinning as described above. However, if the particles, which are dispersed sufficiently once, make clusters again under the sufficiently high shear rate, the viscosity increases. When the viscosity increase is gradual, it is called continuous shear thickening. In contrast, the discontinuous shear thickening is observed for highly loaded suspension. This origin was recently proved by Seto et al.: it is caused by the contact friction between particles.[28]

2.10.7 MEASUREMENT OF SLURRY VISCOSITY BY A CAPILLARY VISCOMETER

A capillary viscometer is the simplest and the most frequently used viscometer. The pressurized fluid is forced to flow through a capillary of known diameter D, and the volumetric flow rate Q is measured. The wall shear stress τ_w is calculated by

$$\tau_w = \frac{D\Delta P}{4L} \tag{2.10.12}$$

where ΔP and L are the pressure drop and capillary length, respectively. The relationships between the flow rate and the wall shear stress for the fluid models are given as follows:

Newtonian model (Hagen-Poiseuille equation):

$$Q = \frac{\pi D^3}{32\mu_N}\tau_w \tag{2.10.13}$$

Power-law model:

$$Q = \frac{\pi D^3}{32}\frac{4n}{(3n+1)}\left(\frac{\tau_w}{K}\right)^{1/n} \tag{2.10.14}$$

Bingham model at $\tau_w > \tau_y$ (Buckingham-Reiner Equation):

$$Q = \frac{\pi D^3}{32\mu_B}\left[1 - \frac{4}{3}\left(\frac{\tau_y}{\tau_w}\right) + \frac{1}{3}\left(\frac{\tau_y}{\tau_w}\right)^4\right]\tau_w \tag{2.10.15}$$

Herschel–Bulkley model at $\tau_w > \tau_y$:

$$Q = \frac{\pi D^3}{32}\frac{4n}{(3n+1)}\left(\frac{\tau_w}{K}\right)^{1/n}$$

$$\left(1 - \frac{\tau_y}{\tau_w}\right)\left\{1 - \frac{1}{2n+1}\left(\frac{\tau_y}{\tau_w}\right)\left[1 + \frac{2n}{n+1}\left(\frac{\tau_y}{\tau_w}\right)\left(1 + n\frac{\tau_y}{\tau_w}\right)\right]\right\} \tag{2.10.16}$$

If it is not known what kind of non-Newtonian fluid model is suitable for a given slurry, one cannot use the equations shown above. In this case, the procedure to obtain the relationship between shear rate and viscosity is briefly described here. Firstly, flow rates at various pressure drops are measured. Equation 2.10.17 gives an apparent shear rate, which is corresponding to the wall shear rate for Newtonian case. The slope in the log-log plot of flow rate versus wall shear stress is utilized to calculate actual shear rate at the wall using the Weissenberg-Rabinowitsch equation (Equation 2.10.18).[29] The data sets of shear stress and shear rate at the wall give the relation between the viscosity versus the shear rate.

$$\dot{\gamma}_a = \frac{Q}{2\pi D^3} \tag{2.10.17}$$

$$\dot{\gamma}_w = \frac{\dot{\gamma}_a}{4}\left(3 + \frac{d\ln Q}{d\ln \tau_w}\right) \tag{2.10.18}$$

2.10.8 MEASUREMENT OF SLURRY VISCOSITY BY A ROTATING VISCOMETER

The rotating viscometers are classified into three types: coaxial cylinders, cone and plate, and plate and plate viscometers. The clearance between cone and plate or between plate and plate is generally so narrow that the coaxial rotating cylinder viscometer is preferable for the measurement of slurry viscosity when the size of suspended particles is several micron or smaller. For the case of a coaxial cylinder type (Couette type) viscometer with the rotation of outer cylinder, the relationship between the rotating speed Ω and torque T is given as follows:

Newtonian model:

$$\Omega = \frac{T}{2\mu_N}\frac{1}{2\pi L R_1^2}\left(1 - \left(\frac{R_1}{R_2}\right)^2\right) \tag{2.10.19}$$

where L, R_1, and R_2 are the length of the inner cylinder, and radii of inner and outer cylinders, respectively.

Power-law model:

$$\Omega = \frac{T}{2K^{1/n}}\left(\frac{1}{2\pi L R_1^2}\right)^{1/n}\left(1 - \left(\frac{R_1}{R_2}\right)^{2/n}\right). \tag{2.10.20}$$

Bingham model at $T > 2\pi R_2^2 L\tau_y$:

$$\Omega = \frac{T}{2\mu_B}\frac{1}{2\pi L R_1^2}\left(1 - \left(\frac{R_1}{R_2}\right)^2\right) - \frac{\tau_y}{\mu_B}\ln\left(\frac{R_1}{R_2}\right) \tag{2.10.21}$$

The solutions shown above are all derived assuming sufficiently narrow cylinder gap compared to cylinder radii. The more general description of a Couette viscometer is given elsewhere[29].

REFERENCES

1. Bird, R. B., Stewart, W. E., Lightfoot, E. N., *Transport Phenomena*, Wiley, New York, 1960, p. 10.
2. Cheng, D. C.-H., Evans, F. *Br. J. Appl. Phys*., 16, 1599, 1965.
3. Mewis, J., Wagner, N. J., *Adv. Colloid Interface Sci*., 147, 214–227, 2009.
4. Malkin, A. Y., *J. Non-Newtonian Mech*., 192, 48–65, 2013.
5. Wen, W. J., Huang, X. X., Sheng, P., *Soft Matter*, 4, 200–210, 2008.
6. Park, B. J., Fang, F. F., Choi, H. J., *Soft Matter*, 6, 5246–5253, 2010.
7. Thomas, D. G., *J. Colloid Sci*., 20, 267, 1965.
8. Metzner, A. B., *J. Rheol*., 29, 739, 1985.
9. Einstein, A., Ann. *Phys*., 19, 289, 1906.
10. Guth, E., Simha, R., *Kolloid Z*., 74, 266, 1936.
11. Mooney, M., *J. Colloid Sci*., 6, 162, 1951.
12. Krieger, M., Dougherty, T. J., *Trans. Soc. Rheol*., 3, 137–152, 1959.
13. Quemada, D., *Rheol. Acta*, 16, 82–94, 1977.
14. Kitano, T., Kataoka, T., Shirota, T., *Rheol. Acta*, 20, 207, 1981.
15. Chong, J. S., Christensen, E. B., Baer, A. D., *J. Appl. Polym. Sci*., 15, 2007, 1971.
16. McGreary, R. K., *J. Am. Ceram. Soc*., 44, 513, 1961.
17. Lee, D. I., *J. Paint Technol*., 42, 579, 1970.
18. Yu, A. B., Standish, N., *Ind. Eng. Chem. Res*., 30, 1372, 1991.
19. Funk, J. E., U.S. Patent 4,282,006, 1979.
20. Andreasen, A. H. M., Andersen, J., *Kolloid Z*., 50, 217, 1930.
21. D'Haene, P. and Mewis, J., *Rheol. Acta*, 33, 165–174, 1994.
22. Qin, K. and Zaman, A. A., *J. Colloid Interface Sci*., 266, 461–467, 2003.

23. Daneshfar, Z., Goharpey, F., Nazockdast, H., Foudazi, R., *J. Rheol*., 61, 955–966, 2017.
24. Lee, J., Lee, S. J. Ahn, K. H., Lee, S. J., *Langmuir*, 31, 13639–13646, 2015.
25. Usui, H., Kishimoto, K., Suzuki, H., *Chem. Eng. Sci*., 56, 2979, 2001.
26. Usui, H., *J. Chem. Eng. Jpn*., 35, 815, 2002.
27. Wagner, N. J., Brady, J. F., *Physics Today*, 62, 27–32, 2009.
28. Seto, R., Mari, R., Morris, J. F., Denn, M. M., *Phys. Rev. Lett*., 111, 218301, 2013.
29. Macosko, C. W., *RHEOLOGY Principles, Measurements, and Applications*, VCH, New York, 1994, p. 188, 238.



Taylor & Francis
Taylor & Francis Group
http://taylorandfrancis.com

2.11 Particle Impact Breakage

Mojtaba Ghadiri

In the processing of particulate solids, there are circumstances under which interparticle and particle-wall impacts cause damage to the particles. In some cases, such as comminution, this is desirable, while in other cases it is undesirable, for example, as in the attrition of weak and friable particles in pneumatic conveying. These processes share the same underlying mechanisms, i.e. elasto-plastic deformation followed by the formation and propagation of various types of crack. It is therefore of great interest to identify and quantify the conditions under which particulate solids are damaged. Briefly, any fracture preceded by purely elastic deformation is influenced by the pre-existing flaws, from which cracks emanate. In contrast in the case of elasto-plastic deformation, cracks are initiated by and propagated from the plastic zone, where the stress field and solid state structure influence crack propagation pattern. In the following the impact force and ensuing breakage for various contact deformation modes are addressed.

2.11.1 IMPACT FORCE

The impact of particles causes a transient stress whose magnitude depends on a number of factors such as impact velocity, particle size, material properties, and contact geometry.

Elastic

If the transient stress does not exceed the plastic yield stress, then the impact is treated as elastic. The maximum impact force, F, is commonly obtained by assuming that the relationship between the impact force and displacement is the same as that of a static elastic contact, given by Hertz analysis.[1] For a normal impact between two spheres:

$$F = 1.283\, m^{3/5}\, R^{1/5}\, E^{*2/5}\, V^{6/5} \tag{2.11.1}$$

where

$1/m = 1/m_1 + 1/m_2$

$1/R = 1/R_1 + 1/R_2$

$1/E^* = (1-\nu_1^2)/E_1 + (1-\nu_2^2)/E_2$

- V is the impact velocity
- m is the mass
- R is the radius
- E is Young's modulus
- ν is Poisson's ratio, and subscripts *1* and *2* refer to the two impacting bodies

Particle damage in this case is by brittle failure.

Plastic

The maximum contact force in this case is obtained by first calculating the onset of yield. The contact stress remains at its yield value and if the material does not strain-harden, the maximum force can be estimated from the contact area. The calculation of the contact area is, in turn, based on the impact energy balancing the work of plastic deformation, from which the maximum contact force can be calculated:[2]

$$F = \pi R^2 \left(\frac{4\rho Y}{3}\right)^{1/2} V \tag{2.11.2}$$

where

- ρ is the particle density
- Y is the yield stress
- V is the normal impact velocity

Particle breakdown in this case is by plastic rupture.

Elastic-Plastic

A mathematical treatment of the process has been proposed by Ning and Thornton,[3] where Hertz analysis is used to describe the pre-yield behavior, and a 'coupled' elastic/plastic analysis is used to describe the post-yield behavior. The maximum impact force, F, is given by Ning as:[2]

$$\frac{F}{F_Y} = \sqrt{\frac{6}{5}\left(V/V_Y\right)^2 - \frac{1}{5}} \tag{2.11.3}$$

where F_Y and V_Y are the impact force and velocity at the onset of yield, respectively, given by:

$$F_Y = \pi^3 R^2 Y^3 / \left(6E^{*2}\right) \tag{2.11.4}$$

and

$$V_Y = \left(\frac{\pi}{2E^*}\right)^2 \left(\frac{2}{5\rho}\right)^{1/2} Y^{5/2} \tag{2.11.5}$$

Particle breakage in this case is by fracture, following limited plastic deformation.

Elasto-Plastic and Adhesive

It is commonly assumed that the adhesion effects are not influential during the loading cycle and hence the normal force corresponding to the elasto-plastic case is applicable. However in the unloading cycle the minimum normal force required for detachment is affected by the enlarged area. Following the

approach of Thornton and Ning[4] and considering the specific surface energy remains constant, the minimum force required for detachment may be estimated from the JKR model with the contact area given by the extent of plastic deformation, given by Thornton.[5] Particle breakage in this case is generally considered the same as of elasto-plastic case.

2.11.2 MODE OF BREAKAGE

The current understanding of particle breakage has recently been collated in a special issue of Powder Technology edited by Salman and Hounslow,[6] covering the classic brittle and semi-brittle failure modes. Salman et al.[7] have provided detailed reviews of failure of spheres and discs under both impact and quasi-static loading. Failure of particles is a process which depends on material properties and the mode of loading. The latter is related to the strain rate and contact geometry. Increasing the strain rate from quasi-static to impact can cause a switch in the failure mode from semi-brittle to brittle. The geometric effects are in practice related to particle size and shape, as they affect the size of the contact area. If large particles of a material fail by the brittle mode, it is likely that reducing the size can switch the mode of failure to the semi-brittle failure and ultimately to the ductile failure. Therefore, the determination of critical transition conditions is important and will be addressed in the following sections.

Brittle Failure Mode

This mode of failure is due to the presence of pre-existing internal or surface flaws. In their absence, particles are strong, and can only fail when shear deformations can generate micro-cracks. Surface flaws often produce orange-segmented fragments, and play a major role in damage when the elastic compliance of the particle or the contacting surface is high, producing large tensile hoop stresses.[8] Failure due to internal flaws is dominant when the elastic compliance of the contact is low.[8] It usually produces diametral cracks, splitting the particles into fragments, as the diametrical plane is under the greatest tensile stress.[9] When a very large pre-existing flaw is present elsewhere, a crack initiating from the flaw follows the tensile stress trajectory. A deterministic analysis of particle breakdown in the case of brittle failure requires a knowledge of the size and position of the flaws. In the absence of this information, the empirical determination of the crushing strength of the particles is the only way to characterize the breakdown. The interpretation of data is commonly carried out by statistical analysis, for example by the use of Weibull distribution.[10,11]

Highly localized loading in this mode of failure may lead to the formation of Hertzian cone cracks. Oblique impacts cause tilting of the cone angle, as the tensile stress trajectories are modified by the frictional traction, and this can produce small chips from the particles, which is responsible for the erosive wear of the particles.[12]

Semi-Brittle Failure Mode

This failure mode is identified by *limited* plastic flow, which is responsible for crack initiation. Plastic flow occurs because the impact stress exceeds the onset of yield, whose characteristics are defined by the critical elastic–plastic transition size, as defined by Puttick.[13] The plastic zone produces compressive radial stresses and tensile hoop stresses. The latter type of stress propagates radial and median cracks, initiated from the plastic zone. When the load is removed, the residual tensile stresses, formed by the elastic unloading component, generate sub-surface lateral cracks. Gorham et al.[14] and Chaudhri[15] have investigated the impact breakage of spheres failing in this mode, using polymethyl methacrylate (PMMA) spheres. The most important properties here are the hardness, Young's modulus and toughness (see Chapter 1.5). Qualitatively, 'hard' materials undergo less plastic deformation than 'soft' materials, but can store greater residual stresses depending on the extent of elastic deformation in the hinterland beyond the plastic zone. Therefore, their tendency for generation of lateral cracks is greater than that of soft materials. Impact damage analysis of particles in this mode of failure has been carried out by indentation fracture mechanics.[16] Particle breakdown in the semi-brittle failure mode can be characterized by crack morphology and extension: particle *fragmentation* occurs by the formation of median and radial cracks, and *chipping* occurs by the formation of lateral cracks.

Ductile Failure Mode

Soft materials, such as some polymers, are usually damaged under this failure mode. Ploughing and cutting are the main two mechanisms of material removal.[17] The slip-line field plasticity analysis has widely been used to calculate the deformation pattern.[18] Important factors in the process here are the attack angle, the ratio of Young's modulus to hardness of the surface, the ratio of the hardness values of the two surfaces, and the shear strength of the interface, i.e. the ratio of the shear stress at the interface, and the shear yield stress of the material. In ductile failure, cracking does not readily occur, but instead the plastic rupture operates. The breakdown of particulate solids by this mode of failure has not been widely investigated so far.

2.11.3 ANALYSIS OF BREAKAGE FOR THE BRITTLE FAILURE MODE

Weibull analysis[19] is commonly used to fit experimental observations of breakage in this failure mode, where the probability of breakage, S, is related to the applied stress, σ, using two fitting parameters, z and σ_s, representing a characteristic flaw density and strength, respectively Weichert.[20]

$$S = 1 - \exp\left[-z\left(\frac{\sigma}{\sigma_s}\right)^m\right] \tag{2.11.6}$$

Vogel and Peukert[11] have recently applied the above analysis to the impact breakage of particles by relating the applied stress to the incident kinetic energy W_k:

$$S = 1 - \exp\left[-f_{mat}x\left(W_k - W_{k,min}\right)\right] \quad (2.11.7)$$

where

f_{mat} and $W_{k,min}$ are two fitting parameters similar to those of Equation 2.11.6

x is particle size

In line with the significance of parameters of Equation 2.11.6, Vogel and Peukert[11] suggest f_{mat} and $W_{k,min}$ reflect the material properties and the minimum kinetic energy which causes breakage, respectively. Similar work has also been done by Salman et al.,[21] who related the fraction of unbroken particles to the impact velocity by the use of Weiball analysis.

2.11.4 ANALYSIS OF BREAKAGE FOR THE SEMI-BRITTLE FAILURE MODE

To address the impact breakage of particulate solids on a fundamental basis, fracture mechanics are used to define the conditions for propagation of various types of cracks. i.e. radial and median cracks for the *fragmentation*, and lateral cracks for *chipping*.

2.11.4.1 Chipping

Figure 2.11.1 shows a typical example of chipping. A sequence of images from the impact process has been recorded by a high speed digital video recorder at 27,000 frames per second, where the detachment of a large chip can be seen.[22] The chipping process has been described theoretically by a mechanistic model developed by Ghadiri and Zhang.[16] The formulation of the model is based on the indentation fracture mechanics of lateral cracks. A *fractional loss per impact,* is defined as the ratio of the volume of chips removed from a particle to the volume of the original (*mother*) particle, and it is used as a measure of the breakage propensity break under impact conditions. According to the model, is given by:

$$\xi = a\eta = a\frac{\rho V^2 DH}{K_c^2} \quad (2.11.8)$$

where

η is a dimensionless group describing the *attrition propensity*

ρ is the particle density

V is the impact velocity

D is a linear dimension of the particle

H is the hardness

K_c is the fracture toughness

α is a proportionality factor which depends on particle shape and impact geometry, and is determined experimentally.



FIGURE 2.11.1 High-speed video sequence of impact of porous alumina catalyst carrier beads which broke by chipping when impacted at 16 m s^{-1}, recorded at 27,000 fps by Couroyer et al.[22]



FIGURE 2.11.2 High-speed video sequence of impact of porous alumina catalyst carrier beads which broke by fragmentation when impacted at 20 m s^{-1}, recorded at 27,000 fps by Couroyer et al.[22]

2.11.4.2 Fragmentation

Figure 2.11.2 shows a sequence of digital video images of a particle fragmenting on impact. The recording speed is 27,000 frames per second, as for Figure 2.11.1.[22,23] Fragmentation occurs when the radial or median cracks extend to the full length of the particles. The formation of two large fragments by the propagation of a median crack can be seen in Figure 2.11.2. At higher impact energies, a more extensive cracking takes place, producing a larger number of fragments. However, at present there is no theory which can relate the product size distribution to the impact conditions and material properties in a predictive way. The force for fracture of a sphere of diameter D can be estimated based on indentation fracture. Based on the relationship proposed by Ghadiri and Zhang[16] for crack extension, the fragmentation force is given by:

$$F_{fr} \propto K_c^{4/3} D^{4/3} H^{-1/3} \quad (2.11.9)$$

2.11.4.3 Transition Velocities

The transition velocities from plastic deformation to chipping and from chipping to fragmentation are important features of particle breakage by impact. The dependence of the transition velocities on particle size and material properties has not been widely quantified and it can only be construed by theoretical considerations at this stage.

Plastic Deformation-Chipping Transition

Marshall et al.[24] have shown that there is a critical load to cause lateral fracture, given by:

$$F_{cl} \propto E\left(\frac{K_c}{H}\right)^4 \quad (2.11.10)$$

Hutchings[25] used this criterion to predict the minimum particle size that can cause erosion of surfaces by impact. The same approach can be followed here to define the critical transition velocities for chipping and fragmentation. In the case of a round (or relatively flat) contact between a particle and

target, the critical transition velocity for plastic deformation-chipping is given by:

$$V_{ch} \propto \left(\frac{K_c}{H}\right)^4 \frac{E}{H^{1/2}} \rho^{-1/2} D^{-2} \quad (2.11.11)$$

The above expression indicates that the critical velocity for the onset of chipping is inversely proportional to the square of the particle size.

Chipping-Fragmentation Transition

A similar approach can be followed to specify the threshold conditions for particle fragmentation. Hutchings[25] specified a critical particle size below which no fragmentation occurs, based on the indentation fracture model of Hagan.[26] The critical load for indentation fracture proposed by Hagan[26] is given by:

$$F_{cf} \propto \frac{K_c^4}{H^3} \quad (2.11.12)$$

This equation can be combined with the impact dynamics by making the same assumptions as in the approach used for the chipping case, i.e. the contact deformation under impact follows a quasi-static indentation model. This enables the impact force to be described in terms of the hardness times the impression area, to give a threshold velocity for fragmentation:

$$V_{fr} \propto \left(\frac{K_c}{H}\right)^4 H^{1/2} \rho^{-1/2} D^{-2} \quad (2.11.13)$$

It is interesting to note that the dependence of V on the particle size D is the same as that of chipping.

Limit of Breakdown

Equation 2.11.11 has a lower limit of validity for particle size. This limit is given by an ultimate particle size below which the particles can only be deformed plastically and cannot be fractured at all, irrespective of impact velocity. There are several models for this limit, due to Kendall,[27] Puttick[13] and Hagan.[26] These models are all based on energy requirements for crack nucleation and propagation. The model of Hagan[26] appears to provide a closer agreement with the experimental evidence, and is therefore given below.

$$D_c \cong 30\left(\frac{K_c}{H}\right)^2 \quad (2.11.14)$$

In conclusion, impact damage depends on the mode of failure, which in turn depends on material properties and contact geometry. The rate of breakage and particle transition size and velocities are all affected by the mechanical characteristics such as hardness, toughness and stiffness. Therefore, the determination of these parameters is important for a better understanding of particle breakage (see Chapter 1.5).

2.11.5 ANALYSIS OF BREAKAGE OF AGGLOMERATES

The failure mode of agglomerates can cover macroscopically the three modes described in Section 2. Because of their large degree of freedom arising from many factors which can influence agglomerate strength, such as void fraction, primary particle size, interparticle bond characteristics, and density, the breakage map of agglomerates is not yet fully established. The disintegration of weak agglomerates failing macroscopically in a 'ductile' mode, has been studied by Boerefijn et al.[28] Patterns of failure of large agglomerates of glass ballotini bonded together with a brittle glue have been reported by Subero and Ghadiri[29] and more recently for various dry and wet granules by Salman et al.[6] Extensive description of experimental work addressing agglomerate breakage has been reported by Salman et al.[30,31] Modeling and simulation of particle breakage in the gas phase are covered in Chapter 5.25.4.

REFERENCES

1. Johnson, K.L., *Contact Mechanics*, Cambridge University Press, Cambridge, UK, 1985.
2. Ning, Z., *Elasto-Plastic Impact of Fine Particles and Fragmentation of Small Agglomerates*, PhD Dissertation, Aston University, Birmingham, UK, 1995.
3. Ning, Z., Thornton, C., *Powders & Grains 93*, Thornton, C., Ed., Balkema, Rotterdam, The Netherlands, 1993, pp. 33–35.
4. Thornton, C., Ning, Z., *Powder Technol.*, 99, 154–162, 1998.
5. Thornton, C., *Granular Dynamics, Contact Mechanics and Particle System Simulations*, Springer International Publishing, Cham, Switzerland, 2015.
6. Salman, A.D., Hounslow, M.J., *Powder Technol.*, 143–144, 1, 2004.
7. Salman, A.D., et al., *Powder Technol.*, 143–144, 19–30, 2004.
8. Shipway, P.H., Hutchings, I.M., *Powder Technol.*, 76, 23–30, 1993.
9. Salman, A.D., Gorham, D.A., Verba, A., *Wear*, 186, 92–98, 1995.
10. Van den Born, I.C., *Mechanical Strength of Highly Porous Materials*, PhD Dissertation. University of Groningen, 1992.
11. Vogel, L., Peukert, W., *Powder Technol.*, 129, 101–110, 2003.
12. Lawn, B.R., *Fundamentals of Friction: Macroscopic and Microscopic Processes*, Singer, I.L., Pollock, H.M. Eds., Kluwer Academic Publishers, London, UK, 1991, pp. 137–165.
13. Puttick, K.E., *J. Phys. D Appl. Phys.*, 13, 2249–2262, 1980.
14. Gorham, D.A., Salman, A.D., Pitt, M.J., *Powder Technol.*, 138, 229–238, 2003.
15. Chaudhri, M.M., *Powder Technol.*, 143–144, 31–40, 2004.
16. Ghadiri, M., Zhang, Z., *Chem. Eng. Sci.*, 57, 3659–3669, 2002.
17. Hutchings, I.M., *Powder Technol.*, 76, 3–13, 1993.
18. Childs, T.H.C., *Fundamentals of Friction: Macroscopic and Microscopic Processes*, Singer, I.L., Pollock, H.M. Eds., Kluwer Academic Publishers, London, UK, 1991, pp. 209–226.
19. Weiball, W., *J. Appl. Mech.*, 9, 293–297, 1951.
20. Weichart, R., *Zement -Kalk-Gips*, 45, 1–8, 1992
21. Salman, A.D., et al., *Powder Technol.*, 128, 36–46, 2002.
22. Couroyer, C., et al. *Revue de l'Institut FranÁais du PÈtrole*, 55, 67–85, 2000.

23. Couroyer, C., Attrition of Alumina Catalyst Carrier Beads, PhD Thesis, University of Surrey, 2000.
24. Marshall, D.B., Lawn, B.R., Evans, A.G., *J. Am. Ceram. Soc*., 65, 561–566, 1982.
25. Hutchings, I.M., *Erosion of Ceramic Materials*, Ritter, J.E. Ed., Trans Tech Publications, Zu¨rich, Switzerland, 1992, pp. 75–92.
26. Hagan, J.T., *J. Mater. Sci*., 16, 2909–2911, 1981.
27. Kendall, K., *Nature*, 272, 710–711, 1978.
28. Boerefijin, R., Ning, Z., Ghadiri, M., *Int. J. Pharm*., 172, 199–209, 1998.
29. Subero, J., Ghadiri, M., *Powder Technol*., 120, 232–243, 2001.
30. Salman, A.D., Hounslow, M.J., Seville, J.P.K. Eds., *Handbook of Powder Technology Vol. 11: Granulation*, Elsevier, Oxford, UK, 2006.
31. Salman, A.D., Ghadiri, M., Hounslow, M.J. Eds., *Handbook of Powder Technology Vol. 12*, *Particle Breakage*, Elsevier, Oxford, UK, 2007.



Taylor & Francis
Taylor & Francis Group
http://taylorandfrancis.com

2.12 Sintering

Takafumi Seto and Kikuo Okuyama

Sintering or densification is an irreversible thermodynamic phenomenon to convert unstable packed powder having excess free energy to stable sintered agglomerates. The sintering phenomenon involves the fusion of particles, volume reduction, decrease in porosity, and increase in grain size. In the industrial powder process, sintering is particularly important in controlling the size of nanomaterials, to build up 3D structures by laser sintering and so on.

2.12.1 MECHANISMS OF SOLID-PHASE SINTERING

Sintering kinetics have been studied by many investigators from both experimental and theoretical points of view. Coble[1] divided the sintering process into three successive elementary stages, as shown in Figure 2.12.1. The initial stage corresponds to neck formation and growth, the intermediate stage to the growth of cylindrical vacancies, and the final stage to diffusion and disappearance of the vacancies.

Formation of Necks

Crystalline particles usually contain dislocations at the surface, created while they were produced. These dislocations are moved or recovered at an initial stage of sintering to form a neck at the contact point of particles. The phenomenon usually begins to be observed at the absolute temperature ratio to the melting point $\propto = 0.23$.

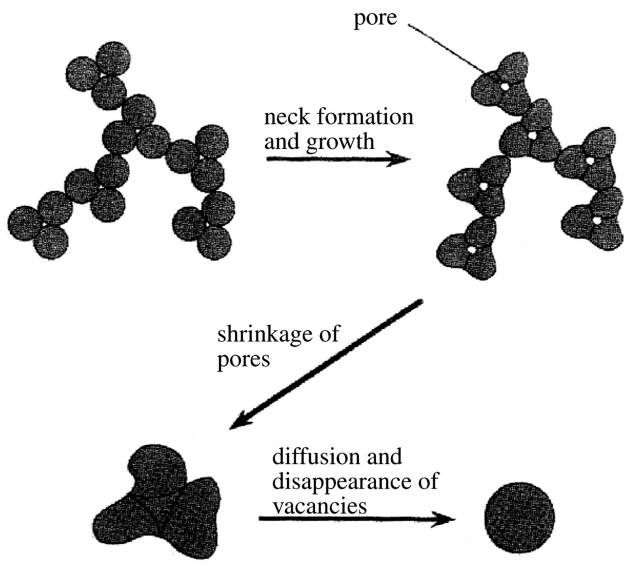


FIGURE 2.12.1 Sintering of multiple primary particles.

Neck Growth

Neck growth is caused by mass transfer such as evaporation–condensation, diffusion, and plastic flow. The principal mass transfer depends on the composition of the material, sintering conditions, and the sintering step.

Evaporation–Condensation

The material evaporates at convex particle points or on the surface of necks with concave curvatures. The process makes round grains.

Diffusion

The equilibrium concentration of atomic or ionic vacancies at the particle surface and necks for crystalline particles varies with the chemical potential at the respective location, which is relatively higher than in the interior of particles. Hence, diffusion occurs from the inside (volumetric diffusion) to the surface (surface diffusion) to the crystalline grain boundary (grain boundary diffusion). Surface diffusion usually occurs at a lower temperature ratio ($\propto = 0.33$ to 0.45) and there is little access of coalesced particles, whereas at a higher temperature ratio ($\propto = 0.42$ to 0.8), volumetric diffusion becomes active and the growth rate of necks is increased due to an increase in the mass transfer rate.

Plastic Flow (Viscous Flow)

Sintering mechanisms of amorphous materials such as glass and resine are usually controlled by plastic flow. Plastic flow also plays a significant role in rapid shrinkage and densification at the initial stage of sintering.

Mechanism of Shrinkage and Bloating of Pores

Shrinkage and bloating of pores at the final stage of sintering are phenomena due to sink or source of mass transfer, and therefore volumetric diffusion and grain boundary diffusion play major roles regardless of mass transfer mechanisms such as evaporation–condensation and surface diffusion.

2.12.2 MODELING OF SINTERING OF AGGLOMERATES

Coblentz et al.[2] proposed sintering rate equations based on several existing sintering models. Ashby[3] presented a sintering diagram to identify the dominant mechanisms of sintering.

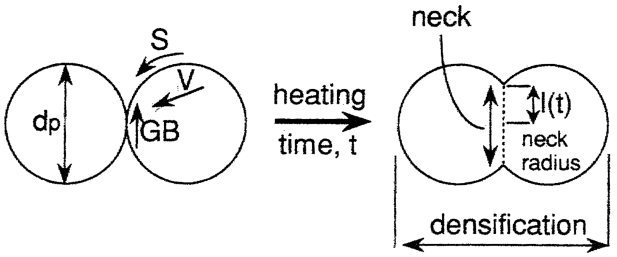


FIGURE 2.12.2 Two-sphere model of initial-stage sintering.

TABLE 2.12.1 Values of Constants in Equation (2.12.1)

m	*n*	Mechanism
1	2	Plastic flow or viscous flow
2	3	Evaporation and condensation
3	5	Volume diffusion
4	6	Grain boundary diffusion
4	7	Surface diffusion

Models describing the sintering of crystalline agglomerates have been presented by numerous researchers. One of the most representative and popular modes uses the ideal geometry illustrated in Figure 2.12.2. The center-to-center approach and the neck growth between two equal spheres are described to evaluate the rate of sintering in the initial stage. Because the neck growth rate depends on the sintering mechanism, it is important to know that what mechanism is dominant.

The change in neck radius l with time t is given as[4]

$$\left(\frac{2l}{d_{p0}}\right)^n = \frac{Kt}{d_p^m} \tag{2.12.1}$$

where

d_p and d_{p0} are the primary particle diameters at $t=t$ and $t=0$, respectively,

K, m, and n are the constants which depend on the physical properties and dominant mass transport mechanisms for sintering, as shown in Table 2.12.1.

When the neck size reaches a certain value, a channel-like vacancy is formed (intermediate stage). In the final stage of sintering, the vacancy grows to be spherical, and sintering rates are expressed in terms of the diffusion of vacancies. There is no kinetic expression that holds over all the stages of sintering. From many scaling factors available to describe the shrinkage due to sintering, the surface area or the density of the sintered body is usually chosen.

Over all the stages of sintering, the reduction rate of surface area due to sintering is approximately given as[5]

$$\frac{da_s}{dt} = -\frac{1}{\tau}(a_s - a_{sc}) \tag{2.12.2}$$

where

a_{sc} is the surface area of the final single sphere after complete fusion,

τ is the rate constant called the sintering time.

Assuming that the sintering of two spheres is complete when the ratio of neck radius l to the primary particle radius $d_p/2$ reaches 0.83, τ is given by

$$\tau = \frac{(2l_f/d_{p0})^n d_p^m}{K} = Ad_p^m \exp\left(\frac{E}{R_g T}\right) \tag{2.12.3}$$

where

l_f is the neck radius at the equilibrium state,

E is the activation energy for self-diffusion,

A is a constant depending on the sintering mechanism.

For example, for grain boundary diffusion[2], A is given by

$$A = \frac{\kappa T(2l_f/d_{p0})^6}{12bD_0\gamma\Omega} \tag{2.12.4}$$

where k, D_0, γ, and Ω are respectively the Boltzmann constant, preexponential factor for the diffusion coefficient, surface tension, and atomic volume. Figure 2.12.3 shows the temperature dependency of τ for ultrafine silver and titania particles as a function of primary particle diameter d_p. τ is a strong function of temperature and changes also with d_p. If τ is constant (i.e. isothermal sintering without grain growth), Equation (2.12.2) indicates that the surface area of the agglomerates decays exponentially. However, τ does not, in general, remain constant because of the increase in the primary particle diameter during sintering. The primary particle diameter d_p is related to the surface area of an agglomerate by

$$d_p = \frac{6V}{a_s} \tag{2.12.5}$$

where V is the volume of the agglomerate that remains constant over the entire sintering process. Equation (2.12.5) states that d_p is inversely proportional to the surface area—thus, that the growth rate of primary particles can be evaluated from the observed decrease in a_s.

2.12.3 SINTERING PROCESS OF NANOPARTICLES

Sintering is an important process to determine the size distribution of nanoparticles synthesized via building-up process. In the building-up processes, however, many phenomena affect particle morphology (e.g. coagulation, condensation, crystallization, and sintering). Sintering is especially important because it influences particle size, shape, and crystal structure. The sintering of silver and titania agglomerates consisting of nanometer primary particles in a heated gas flow was investigated experimentally. The densification of agglomerates accompanying primary particle growth was explained quantitatively by solving the equation of sintering, Equation (2.12.2), under the temperature profile.[6,7] The smaller the

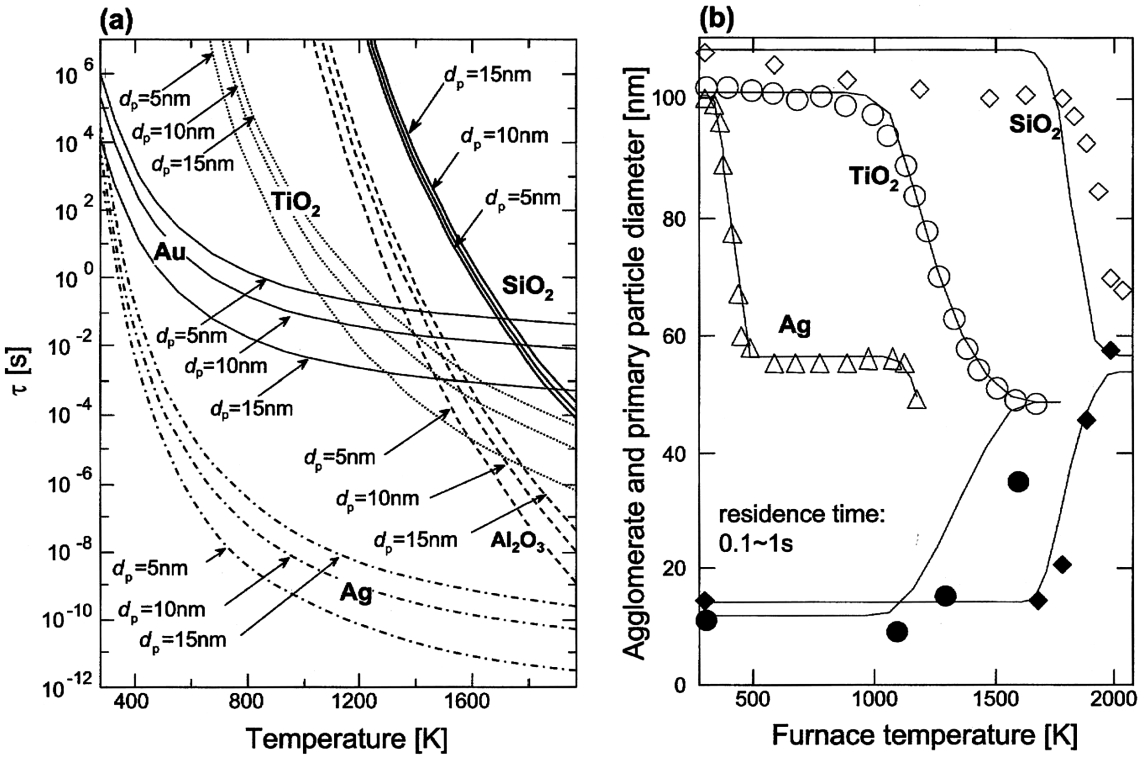


FIGURE 2.12.3 The change in sintering time, τ, with temperature; d_p is the primary particle diameter.

primary particles are, the shorter the time required for sintering. The sintering rate, therefore, slows as primary particles grow in size. This size dependency in sintering rate will be a problem in sintering of nanophase materials from this point of view, as sintering at low temperature without grain growth is necessary to obtain a compact of high density.[7] Such a mechanism has been applied to obtain fully dense nanocrystalline ceramics without grain growth.[8]

2.12.4 SINTERING PROCESS OF PACKED POWDER

Solid-phase sintering of packed powder of a single composition is conducted at a temperature lower than the melting point. Materials having an inexact melting point begin to sinter near the softening temperature, whereas materials having a clear melting point begin to sinter at three fifths of the melting temperature (in kelvin). Bonding between particles takes place at contact points to form necks that grow with time, resulting in shrinkage of the pores and forming isolated spherical voids as shown in Figure 2.12.4. The densification of packed powder due to sintering depends on the density of the compact before sintering and, hence, is evaluated by the densification parameter D:

$$D = \frac{\rho_s - \rho_g}{\rho_t - \rho_g} \tag{2.12.6}$$

where

ρ_s is the density of the sintered body,
ρ_g is the density before sintering,
ρ_t is the net density of the particles.

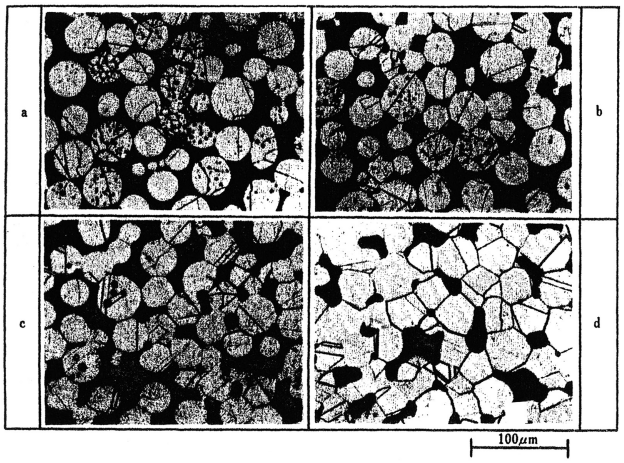


FIGURE 2.12.4 Structures of sintered grounds of spherical copper particles observed by an optical microscope (sintered in hydrogen after being packed with tapping): (a) 1273 K (1000°C), 5 min; (b) 1273 K, 23 min; (c) 1223 K (950°C), 6 h; (d) 1223 K, 20 h.

When solid-phase sintering progresses smoothly, the empirical equation $D = Kt^n$ is widely used as the relationship between sintering time t and densification parameter D. The constant K depends on the temperature, and the exponent n depends on the transfer mechanism of materials and is usually less than unity.

Laser Sintering for 3D printing

Recently, additive manufacturing (AD) and layered manufacturing (LD) have been extensively investigated in relation

with 3D printer technology. In these processes, the 3D model is built by heating the powder bed of the source material (metal, ceramics, or plastic powder) by high intensity laser beam. Laser sintering[9] is an important process to consolidate powder bed into the desired 3D structures. In particular, liquid phase sintering or partial melting is dominant mechanism for laser-based powder consolidation.

Sintering of Multi Component Powder

The sintering process of mixed materials depends primarily on wettability between particles of different types. Mutual solubility and diffusivity are also significant. A binary mixture of *A* and *B* with surface energies γ_A and γ_B, is respectively, and with the interfacial free energy γ_{AB} does not mutually wet if $\gamma_{AB} > \gamma_A = \gamma_B$. Hence, the sintering progresses selectively between particles of the same material. In this case, if a third material reactive to both components is added in small amounts or if the atmosphere is controlled, sintering becomes feasible. Reaction between particles is often applied to sintering (reaction sintering), but the sintered ground is sometimes bloated or broken if the reaction product is of less density.

Mutual diffusion plays a major role in solid-phase sintering. When there is a large difference in the mutual diffusivities, pores remain where particles with larger diffusivity migrate. Grooves and pores are also formed around the neck between particles of different composition.[8] When mass transfer is one-sided, segregation or concentration distribution takes place to form heterogeneous sintering.

REFERENCES

1. Coble, R. L., *J. Appl. Phys.*, 32, 787, 1961.
2. Coblentz, W. S., Dynys, J. M., Cannon, R. M., Brook, R. J., *Mater. Sci. Res.*, 13, 141, 1980.
3. Ashby, M. F., *Acta Metallurgica*, 22, 275, 1974.
4. German, R. M., Munir, Z. A., *J. Ann. Ceram. Soc.*, 71, 225, 1976.
5. Koch, W., Friedlander, K., *J. Colloid Interface Sci.*, 140, 209, 1990.
6. Shimada, M., Seto, T., Okuyama, K., *J. Chem. Eng. Jpn.*, 27, 795, 1994.
7. Seto, T., Shimada, M., Okuyama, K., *Aerosol Sci. Technol.*, 23, 183, 1995.
8. Siegel, R. W., Ramasamy, S., Hahn, H., Zongquan, L., et al., *J. Mater. Res.*, 3, 1367, 1988.
9. Chen, I. W., Wang, X. H., *Nature*, 404, 168 (2000).
10. Kruth, J. P., Levy, G., Klocke, F., Childs, T. H. C., et al., *Annals of the CIRP*, 56, 730, 2007.

2.13 Mechanochemistry

Qiwu Zhang and Fumio Saito

2.13.1 INTRODUCTION

Milling induces mechanochemical effects such as phase transformation and solid state reaction.[1] Some amount of powder is trapped between the two balls when they collide inside a mill pot, and particles deform plastically, and are repeatedly flattened, cold-welded, fractured and rewelded.[2] The force of the impact acts on the powder particles, leading to crystallographic bonds being broken and a new surface is produced. The new surfaces created enable the particles to weld together easily and this leads to an increase in the rate of dissolution of solid material.[3] With continued mechanical deformation, fragments generated by this mechanism may continue to reduce in size, and with the increase in specific surface area of the particle, other profound changes affecting the surface as well as the chemical, physico-chemical and structural properties may also take place.[4] This is manifested by the presence of a variety of crystal defects such as increased number of grain boundaries, dislocations, vacancies and interstitial atoms, stacking faults and deformed and ruptured chemical bonds. The presence of this defect structure enhances the diffusivity of solute elements. Additionally, the slight rise in temperature during milling further aids the diffusion behavior.[5] Consequently, grinding a mixture of two or more solids substances results in microhomogenization of starting components, and sometimes it induces formation synthesis of new fine powders. The following[5] are the typical summarization of mechanochemical phenomena[6]:

1. Formation of dislocations and defects in the crystalline structure.
2. Increase in mechanical activation of solid materials.
3. Promotion in polymorphic transformation, amorphization, crystallization.

Such mechanochemical phenomena are recognized in prolonged milling, especially dry condition, where the strain energy stored in a solid just after reaching at a certain critical level of stable state is released. Some of the releasing styles in the energy stored are the mechanochemical phenomena and agglomeration of fine particles in a fine grinding mill. Accordingly, the solid tends to be a stable state. There are several additives for controlling the degree of activation of solid in its milling. There are many additives recognized for it, and one of them would be water, which could play a big role to control the activation of the solid due to depression of surface energy.[7,8]

2.13.2 PHASE TRANSFORMATION

The polymorphic transformations are the crystallographic structural change from one to other phases, and this does not, of course, involve an alteration of chemical composition. With an increase in milling operation, the polymorphic transformation can take place with increase in mechanical activation. The transformation is accompanied with change in crystallite size and lattice distortion, and the crystallite size decreases and lattice distortion increases with an increasing in grinding time, releasing the stored strain energy. At the same time the lattice distortion decreases while the crystallite size is kept constant. In general, the transformation shifts from unstable to stable forms.

Many reports have been published on polymorphic transformations and alterations in physical properties of the bulk phase: for example, calcite ($CaCO_3$) to aragonite, anatase (TiO_2) to rutile, massicot (PbO) to litharge. Table 2.13.1[9] shows several examples of the available results on the polymorphic transformations induced by the grinding of a solid material.

2.13.3 SOLID STATE REACTION

Gibbs Free Energy Change of Formation in the Reaction

A lot of investigations on mechanochemical reaction have been reported so far, however it seems to be difficult to forward the solid state reactions mechanically by the milling operation due to powder characteristics. That is, the reaction depends on the crystalline structure of both initial and final products as well as the thermodynamic feasibility with Gibbs free energy change of formation (ΔG). The mechanochemical reaction generally takes place when ΔG is of negative value, while no reaction occurs when ΔG is positive.[10]

Synthesis of Complex Oxides, ABO_3 and ABO_4

There have been reports on synthesis of complex oxides, ABO_3, by grinding mixtures of two kinds of oxide, where *A* is divalent metal and *B* is tetravalent metal.[11,12] As for the mixture of calcium oxide (CaO) and titanium oxide (TiO_2), the mechanochemical reaction under ambient temperature can be confirmed by the electron diffraction scattering pattern, high resolution transmission microscopic observation and X-ray diffraction pattern of the milled mixture, as shown in Figure 2.13.1. The reaction equation can be given by Equation 2.13.1.

$$CaO + TiO_2 = CaTiO_3 \qquad (2.13.1)$$

TABLE 2.13.1 Polymorphic Phase Transformation of Materials by Grinding

Co	High Temperature Face-Centered Cubic (fcc)	Low Temperature Hexagonal Close-Packed (hcp), ρ = 8.9 g/cm^3
TiO_2	Tetragonal (anatase), ρ = 3.90 g/cm^3	Tetragonal (rutile), ρ = 4.24 g/cm^3
TiO_2	Orthorhombic (brookite), ρ = 4.10 g/cm^3	Tetragonal (rutile), ρ = 4.24 g/cm^3
ZrO_2	Monoclinic, ρ = 5.74 g/cm^3	Tetragonal, ρ = 5.86 g/cm^3
Dy_2O_3	Cubic (c-type), ρ = 7.81 g/cm^3	Monoclinic (b-type)
Eu_2O_3	Cubic (c-type), ρ = 7.42 g/cm^3	Monoclinic (b-type)
Al_2O_3	Tetragonal (γ-type), ρ = 3.89 g/cm^3	Triclinic (α-type), ρ = 3.97 g/cm^3
Fe_2O_3	Cubic (γ-type), ρ = 5.07 g/cm^3	Hexagonal (α-type), ρ = 5.29 g/cm^3
$MgCl_2$	Octahedral (α-type)	(δ-type)
GeO_2	Tetragonal, ρ = 6.24 g/cm^3	hexagonal, ρ = 4.25 g/cm^3
PbO	Orthorhombic (massicot), ρ = 9.64 g/cm^3	tetragonal (litharge), ρ = 9.35 g/cm^3
PbO_2	Orthorhombic (α-type), ρ = 9.88 g/cm^3	tetragonal (β-type), ρ = 9.63 g/cm^3
SiO_2	Hexagonal, ρ = 2.65 g/cm^3	amorphous, ρ = 2.20 g/cm^3
$CaCO_3$	Rhombohedral (calcite), ρ = 2.72 g/cm^3	orthorhmbic (aragonite), ρ = 2.95 g/cm^3
$CaCO_3$	Hexagonal (Vaterite), ρ = 2.64 g/cm^3	rhombohedral (calcite), ρ = 2.72 g/cm^3
AgI	Hexagonal, ρ = 5.68 g/cm^3	cubic, ρ = 5.68 g/cm^3
ZnS	Hexagonal, ρ = 3.98 g/cm^3	cubic, ρ = 4.0 - 4.1 g/cm^3
Y_2O_3	Cubic, ρ = 5.90 g/cm^3	Monoclinic, ρ = 5.68 g/cm^3
Ga_2O_3	Monoclinic, ρ = 5.90 g/cm^3	hexagonal, ρ = 6.44 g/cm^3

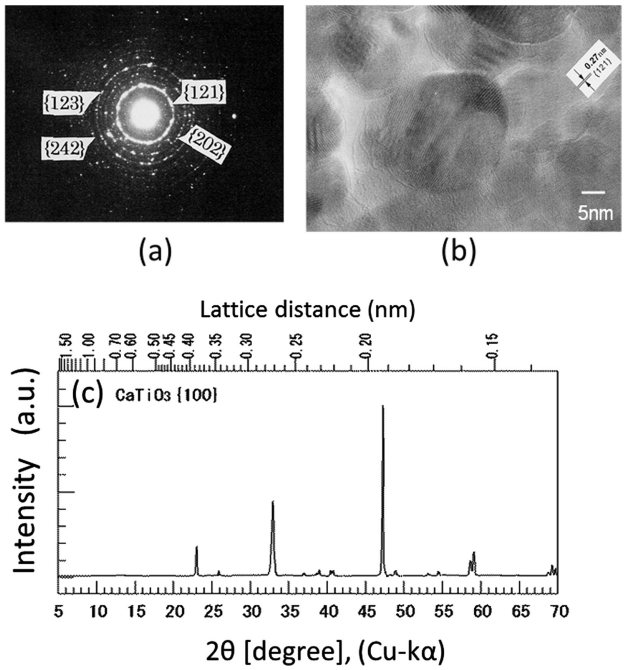


FIGURE 2.13.1 Synthesis of $CaTiO_3$ from a mixture of CaO and TiO_2 milled by a planetary mill for 5 h. (a) Electron diffraction scattering pattern, (b) HR-TEM, (c) XRD pattern of the mixture milled.

Similar reactions can be seen for mixtures of trivalent metal oxides (perovskite group), lanthanum oxide (La_2O_3) and manganese oxide (Mn_2O_3), as given by Equation 2.13.2.[13]

$$La_2O_3 + Mn_2O_3 = 2LaMnO_3 \tag{2.13.2}$$

Complex oxides of manganese (Mn) and other rare earths *R* (=Pr, Nd, Sm) namely $RMnO_3$ have also perovskite-type, and show similar physico-chemical properties to that of lanthanum manganese oxide ($LaMnO_3$). These complex oxides, $RMnO_3$ (R=Pr, Nd, Sm) can be synthesized by milling a mixture of Mn_2O_3 and a trivalent metal oxide, such as Pr_6O_{11}, Nd_2O_3 and Sm_2O_3, as given by Equations 2.13.3 and 2.13.4.

$$3Mn_2O_3 + Pr_6O_{11} = 6PrMnO_3 + O_2 \tag{2.13.3}$$

$$Mn_2O_3 + R_2O_3 \ \left(R = \text{Nd and Sm}\right) = 2RMnO_3 \tag{2.13.4}$$

It is known that trivalent oxides, B_2O_3 (B=Al, Fe, Cr) exhibit different crystal structures, including polymorphic phase transformations under milling. When a trivalent oxide (B_2O_3) with corundum structure, such as α-Al_2O_3, α-Fe_2O_3 or α-Cr_2O_3, is ground with La_2O_3, the starting oxides remain in the ground products.[14,15] This implies that the oxide B_2O_3 with corundum structure does not react with La_2O_3 mechanochemically. On the contrary, when the oxide B_2O_3 with cubic structure, such as Mn_2O_3, In_2O_3, Y_2O_3, γ-Al_2O_3, γ-Fe_2O_3, is ground with La_2O_3, $LaBO_3$ can be synthesized mechanochemically.[16] Trivalent oxides with cubic structure can usually be prepared by heating at lower temperature than ones with corundum structure. The small crystal size of samples prepared by heating at low temperature may be one reason to justify the completion of the corresponding mechanochemical solid state reactions. Figure 2.13.2[16] shows the XRD patterns of the mixtures of α-Ga_2O_3 and La_2O_3, and β-Ga_2O_3 and La_2O_3, each ground by a planetary mill for 2 h. It is found that β-Ga_2O_3 with a monoclinic structure reacts mechanochemically with La_2O_3 to form $LaGaO_3$, while α-Ga_2O_3 does not react easily with La_2O_3, although one small peak attributed to $LaGaO_3$ is seen in the pattern of the mixture of α-Ga_2O_3

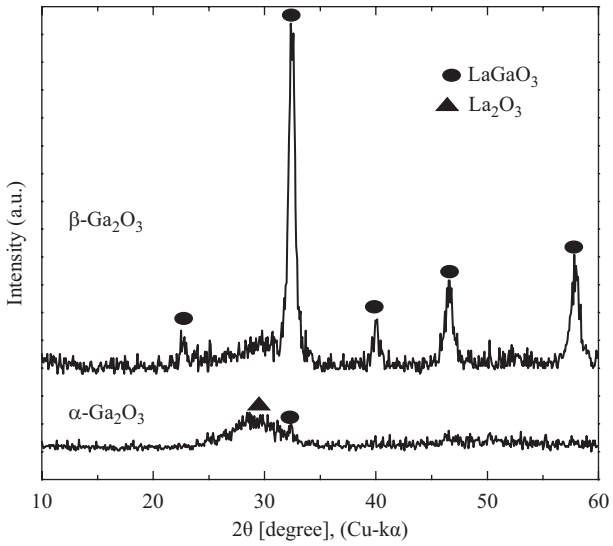


FIGURE 2.13.2 XRD patterns of the mixture s of α- and β- Ga_2O_3 and La_2O_3 ground by a planetary mill for 2 h, respectively.

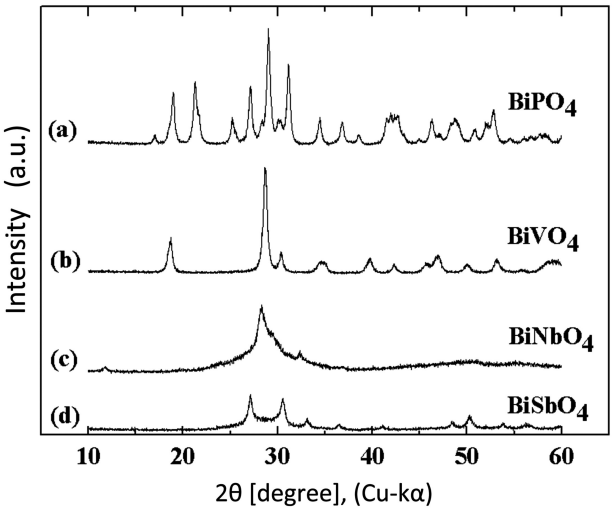


FIGURE 2.13.3 XRD patterns of the mixture of Bi_2O_3 and B_2O_5 (B = P, V, Nb, Sb) milled by a planetary mill for 2 h. (a) Bi_2O_3 - P_2O_5, (b) Bi_2O_3 - V_2O_5, (c) Bi_2O_3 - Nb_2O_5, (d) Bi_2O_3 - Sb_2O_5.

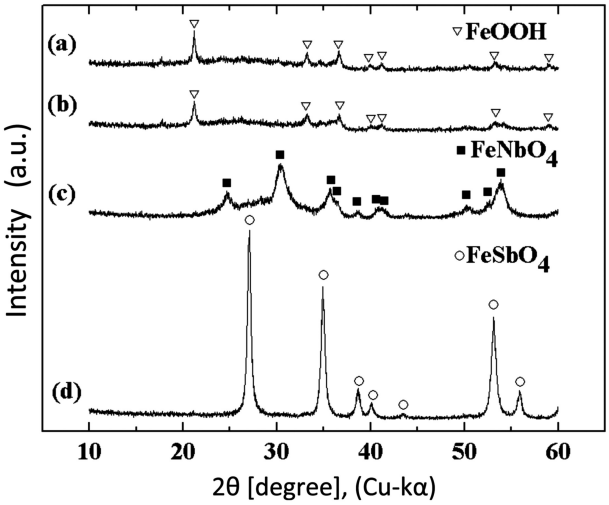


FIGURE 2.13.4 XRD patterns of the mixture of FeOOH and B_2O_5 (B = P, V, Nb, Sb) milled by a planetary mill for 2 h. (a) FeOOH - P_2O_5, (b) FeOOH - V_2O_5, (c) FeOOH - Nb_2O_5, (d) FeOOH - Sb_2O_5.

and La_2O_3. The particle sizes of α-Ga_2O_3 are finer than that of β-Ga_2O_3, however, the reaction in this system does not easily take place. From the result, another reason would be considered for the α-Ga_2O_3 and β-Ga_2O_3 reaction system, and it may be the effect of crystal structure on the reactivity. Further investigation has been attempted and confirmed that the trivalent oxides with cubic structure, such as Mn_2O_3, and amorphous hydrated oxides can react easily with La_2O_3, while other trivalent oxides with corundum structure, such as α-Cr_2O_3, do not show high reactivity with La_2O_3.[17]

When the other oxides, such as γ-Fe_2O_3, β-Ga_2O_3 and C-Y_2O_3, with non-corundum structure are ground individually, polymorphic transformations take place from cubic and monoclinic to hexagonal or similar phases. It is known that changes in density, besides the crystal structure of oxides, by grinding are recognized in the polymorphic transformation of materials. The changes in density and crystal structure suggest that grinding makes the oxide crystal lattice unstable and distorted, varying the relative distance between the atoms. This induces the phase transformation of the oxides from loose to close packing. This is the reason why one of these trivalent oxides, B_2O_3, reacts with La_2O_3 to form LaBO_3. α-Al_2O_3 is normally more stable than γ-alumina (γ-Al_2O_3), so that it does not react easily with other oxide such as La_2O_3, while γ-Al_2O_3 can react mechanochemically with La_2O_3 to form $LaAlO_3$.[14] This can extend to the reaction to form complex oxides (ABO_4) from a mixture of trivalent (A_2O_3) and pentavalent (B_2O_5) oxides, where A denotes Al, Fe, Cr, In, La and Bi, whereas B denotes P, V, Nb and Sb.[18–20] It has been found that the use of starting materials with active crystal structure is a necessary condition but not a sufficient one. The following are summaries of the experimental results: Firstly, two examples are used to show the experimental results. Figure 2.13.3[21] shows XRD patterns of the mixture of Bi_2O_3 and B_2O_5 (B=P, V, Nb, Sb) milled by a planetary mill for 2 h. It has been confirmed that Bi_2O_3 reacts with P_2O_5, V_2O_5, Nb_2O_5 and Sb_2O_5 powders to form $BiPO_4$, $BiVO_4$, $BiNbO_4$ and $BiSbO_4$, respectively, as represented by Equation 2.13.5.

$$Bi_2O_3 + B_2O_5 = BiBO_4 \quad (B = P, V, Nb, Sb) \quad (2.13.5)$$

Other examples are represented by the reactions between FeOOH and one of pentoxides, B_2O_5. The results are shown in Figure 2.13.4,[21] which confirm that $FeSbO_4$ and $FeNbO_4$ are synthesized from the constituent mixtures, however, the starting phase FeOOH still remains unchanged in the mixtures of FeOOH with P_2O_5 or V_2O_5.

Table 2.13.2[21] shows the experimental results on the synthesis of ABO_4-type complex oxides from a mixture of trivalent (A_2O_3) and pentavalent (B_2O_5) oxides, where, A denotes Al, Fe, Cr, In, La and Bi; B denotes P, V, Nb and Sb. The

TABLE 2.13.2 Result on the Mechanochemical Reaction Between A_2O_3 and B_2O_5 to Synthesize ABO_4

Elements *A* and *B*	***B* = P (15), [30.97] *r* = 0.106 nm**	**V (23), [50.94] *r* = 0.122 nm**	**Nb (41), [92.91] *r* = 0.134 nm**	**Sb (51), [121.8] *r* = 0.140 nm**
A = Al (13), [26.98] *r* = 0.118 nm	× (ρ = 2.62 g/cm^3)	× (ρ = 3.34 g/cm^3)	× (ρ = 4.35 g/cm^3)	○ (ρ = 5.83 g/cm^3)
Fe (26), [55.85] *r* = 0.117 nm	× (ρ = 3.06 g/cm^3)	× (ρ = 3.68 g/cm^3)	○ (ρ = 5.40 g/cm^3)	○ (ρ = 5.94 g/cm^3)
Cr (24), [52.0] *r* = 0.118 nm	× (ρ = 3.98 g/cm^3)	○ (ρ = 4.61 g/cm^3)	○ (ρ = 5.33 g/cm^3)	○ (ρ = 6.14 g/cm^3)
In (49), [114.8] *r* = 0.144 nm	○ (ρ = 4.9 4g/cm^3)	○ (ρ = 4.70 g/cm^3)	○ (ρ = 6.29 g/cm^3)	○ (ρ = 6.91 g/cm^3)
La (57), [138.9] *r* = 0.169 nm	○ (ρ = 5.11 g/cm^3)	○ (ρ = 5.08 g/cm^3)	○ (ρ = 5.78 g/cm^3)	○ (ρ = 6.26 g/cm^3)
Bi (83), [209.0] *r* = 0.146 nm	○ (ρ = 6.82 g/cm^3)	○ (ρ = 6.95 g/cm^3)	○ (ρ = 7.47 g/cm^3)	○ (ρ = 8.46 g/cm^3)

O: (8), [16.00], *r* = 0.072 nm.

A = Al, Cr, Fe, In, La, Bi, *B* = P, V, Nb, Sb.

○: successful reaction, ×: unsuccessful reaction.

(-) = atomic number; [-] = atomic weight; *r* (nm): atomic radius; ρ (g/cm^3): density.

successful and unsuccessful reactions are marked by ○ and ×, respectively. It is noted that the successful and unsuccessful reactions are not located randomly, but distributed regularly. This suggests that there is an inherent nature and that the reaction can be regulated by the experimental conditions. The ABO_4 oxides are known to be polymorphic compounds, and no clear relationship between the occurrence of mechanochemical reaction and the crystal structure of the oxide is observed. As shown in Table 2.13.2, the oxides with larger atomic number or ionic radius tend to show higher reactivity. It may not be a coincidence because, for example, other studies on the mechanochemical dechlorination of chlorinated polymers have shown the similar results: That is, an oxide such as lanthanum oxide (La_2O_3) with a larger ionic radius than calcium oxide (CaO) shows its high reactivity against poly-vinyl chloride (PVC) to form La-chloride, in comparison with PVC and CaO system.[22,23] Therefore, the relation between the occurrence of the mechanochemical reaction and the ionic radius of both the starting samples can be qualitatively confirmed. As for both the trioxide and pentoxides (A_2O_3 and B_2O_5), a sample with large atomic radius tends to react with a counterpart to form ABO_4-type oxide, according to Table 2.13.2. When a sample of trioxide or pentoxide is ground with a counterpart, the occurrence of the reaction depends on the radius of the counterpart. Although the oxide with large radius tends to show high reactivity to a counterpart, it is difficult to determine the radius as a criterion for the occurrence of mechanochemical reaction.

A larger cation usually takes more coordination anions around itself. A compound with large-size constituent ions can take a close-packing state. Generally in the ternary oxides $A_xB_yO_z$, with an increase in the ratio of the average radius of *A* and *B* to that of oxygen (O), a close packing of atoms in $A_xB_yO_z$ becomes available, where it is defined as $t=(xr_A+yr_B)/(r_O[x+y])$, and r_A, r_B and r_O denote the radii of *A*, *B* and oxygen (O) ions in $A_xB_yO_z$, respectively. On the other hand, the radius ratio (r_A/r_B), defined as *k*, remains nearly constant due to the small compressibility of cations compared to that of the oxide anion. It indicates that the larger the values of *t*, the closer the packing state of atoms in ABO_4-type oxides. Figure 2.13.5[21] shows the correlation of parameter, k ($=r_A/r_B$) with t ($=[r_A+r_B]/[2r_O]$) for all the ABO_4 oxides shown in Table 2.13.2. The open square mark (□) represents the successful reaction system and the solid square mark (■) indicates the unsuccessful reaction system. Similar to the results shown in Table 2.13.2, the mark distribution is of good regularity rather than random. It can be seen that ABO_4 oxides with larger *t* and *k* tend to be easily formed and those with smaller *t* and *k* are on the contrary. Taking the case of $AlNbO_4$, which is assigned as unsuccessful reaction system, a line between $InPO_4$ and $FeVO_4$ may be drawn and be used as a criterion. A region in the right side from this criterion line suggests a possible successful reaction to form the ABO_4 and a position in the left side to that line show little possibility of the reaction to form the oxides. Taking it as a successful one, it is possible to draw a line used as a criterion. Otherwise it is difficult to draw

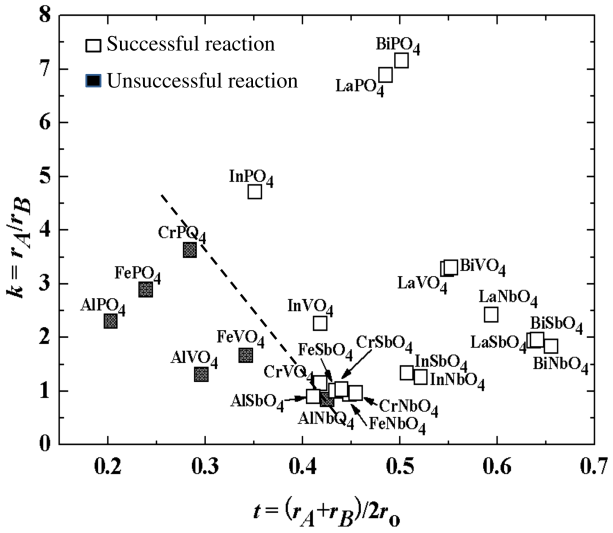


FIGURE 2.13.5 Correlation of k with t for ABO_4 type oxides. Open square □: successful reaction. Solid square ■: unsuccessful reaction.

such a line. Because it is not possible to identify the phase of the ground sample from AlOOH and Nb_2O_5 as a reaction product only with the obtained experimental results, it is not reasonable to draw a line to use as a quantitative assessment. Compared with the simple value of ionic radius of the metal in the starting sample, the application of the integrated parameters, t and k from ionic radius offers a quite reliable approach toward the correlation between the occurrence of mechanochemical reaction and the radii of the compositions in ABO_4 compounds.

Synthesis of Complex Fluoride AMF_3

Besides oxides, a mechanochemical approach can be extended to synthesize complex fluorides. The clear advantage of mechanochemical route lies in the non-thermal effect with mechanical milling operation to form AMF_3 from AF and MF_2 (A = Na, K and NH_4; M = Zn, Ni, Co, Fe, Mn, Ca and Mg), as follow.[24,25] When KF and ZnF_2 at equal molar are milled in air together for different periods of time, the amount of the starting sample (ZnF_2) in the product decreases gradually with an increase in grinding time, while the amount of the new phase, $KZnF_3$, increases accordingly. This suggests that AMF_3 monophase can be synthesized mechanochemically, as given by Equation 2.13.6.

$$AF + MF_2 = AMF_3 \quad (A = \mathrm{K, Na, NH_4}; M = \mathrm{Zn, Ni, Co, Fe, Mn, Ca, Mg}). \tag{2.13.6}$$

Similarly, AMF_4 can be synthesized mechanochemically from a mixture of AF and MF_3 (A = NH_4, K, Na, Li; M: trivalent metal such as rare earth, Pr, Nd, Gd, Ho, Er and Y).[26] As for the case of the milling a mixture of NaF and YF_3, the reaction takes place to form $NaYF_4$, which is composed of a few ten nanometer sized particles agglomerated. Other complex fluorides with alkali can also be synthesized mechanochemically, as shown in Table 2.13.3.[24–26]

TABLE 2.13.3 Mechanochemical Reactions on Complex Fluorides from Mixtures of Alkali and Fluorides

$KF + MF_2 \rightarrow KMF_3$ (M = Mg, Ca, Mn, Fe, Co, Ni, Zn)
$AF + YF_3 \rightarrow AYF_4$ (A = Na, K, NH_4)
$NaF + MF_3 \rightarrow NaMF_4$ (M = Y, Pr, Nd, Gd, Ho, Er)
$3AF + MF_3 \rightarrow A_3MF_6$ (A = Li, Na, K, NH_4; M = Al, Ga)

TABLE 2.13.4 Mechanochemical Reaction to Form Metal Nanoparticles

Reaction
$FeCl_3 + 3Na \rightarrow Fe + 3NaCl$
$CuCl_2 + 2Na \rightarrow Cu + 2NaCl$
$CoCl_2 + 2Na + 1.5NaCl \rightarrow Co + 3.5NaCl$
$NiCl_2 + 2Na + 1.5NaCl \rightarrow Ni + 3.5NaCl$

Synthesis of Well-Dispersed Nanoparticles

One of the methods for producing nanoparticles would be a use of mechanochemical reaction.[27–40] As a matter of fact, several kinds of metals, such as Fe, Cu, Co, Ni, can be synthesized from mixtures of metal chloride and Na, as shown in Table 2.13.4.[36] As for the case of the reaction system of $FeCl_3$ and Na, the reaction product is a mixture of Fe and NaCl. The nanoparticles of metal can be recovered by washing out the soluble compound in the milled mixture with water followed by filtration. The diameters of these fine particles range from 5 to 50, depending on the materials. Similarly, monodispersed fine metal oxides, such as Al_2O_3, ZrO_2, Fe_2O_3, Gd_2O_3, CeO_2, can be synthesized by the milling mixtures of metal chloride and oxide, as shown in Table 2.13.5.[36] These results suggest that complex oxide ($LaCoO_3$) nanoparticles with well dispersion can be synthesized by milling a mixture of $LaCl_3$, $CoCl_2$ and NaOH, followed by heating the product at 600°C and filtration to recover the nanoparticles. In the milling stage, the following reactions are caused.

$$\mathrm{LaCl_3 + 3NaOH = La(OH)_3 + 3NaCl} \tag{2.13.7}$$

$$\mathrm{CoCl_2 + 2NaOH = Co(OH)_2 + 2NaCl} \tag{2.13.8}$$

In the heating, the hydroxides can be transferred into complex oxide, as follows:

$$\mathrm{La(OH)_3 + Co(OH)_2 + O_2 + NaCl = LaCoO_3(s) + NaCl(s) + H_2O(g)} \tag{2.13.9}$$

TABLE 2.13.5 Mechanochemical Reaction to Form Oxide Nanoparticles

Reaction
$2AlCl_3 + 3CaO \rightarrow Al_2O_3 + 3CaCl_2$
$ZrCl_4 + 2CaO \rightarrow ZrO_2 + 2CaCl_2$
$GdCl_3 + 3NaOH \rightarrow 0.5Gd_2O_3 + 3NaCl + 1.5H_2O$
$CeCl_3 + 3NaOH \rightarrow CeO_2 + 3NaCl + H_2O$
$Na_2Cr_2O_7 + S \rightarrow Cr_2O_3 + Na_2SO_4$
$2NbCl_5 + 5Na_2CO_3 \rightarrow Nb_2O_5 + 10NaCl + 5CO_2$
$SnCl_2 + Na_2CO_3 + O_2 \rightarrow SnO_2 + 2NaCl + CO_2$
$2FeCl_3 + 3Ca(OH)_2 \rightarrow Fe_2O_3 + 3CaCl_2 + 3H_2O$
$ZnCl_2 + Na_2CO_3 \rightarrow ZnO + 2NaCl + CO_2$

TABLE 2.13.6 Mechanochemical Reaction to Form Sulfide Nanoparticles

Reaction
$CaS + ZnCl_2 + CaCl_2 \rightarrow ZnS + 2CaCl_2$
$Na_2S + CdCl_2 + 1.5NaCl \rightarrow CdS + 17.6NaCl$

NaCl formed in the milling operation plays a big role in preventing the sintering of the oxide ($LaCoO_3$) particles in the heating operation. The $LaCoO_3$ nanoparticles can be recovered by washing out NaCl with water. Furthermore, fine monodispersed sulphide particles such as ZnS and CdS can be formed by the milling mixtures of metal sulfide and chloride system, as shown in Table 2.13.6.[40]

In addition, oxyfluoride nanoparticles can be produced by the mechanochemical reactions. For example, milling a mixture of La_2O_3 and polytetrafluoroethylene ([PTFE], $[CF_2CF_2]_n$, molecular weight [MW] = 5000–20000, n: polymerization degree) in air, followed by heating gives us the formation of LaOF nanoparticles.[41] In this case, the grinding of the starting mixture causes mechanochemical reaction between the two materials, although a part of La_2O_3 is changed into $La(OH)_3$, due to the hydration of La_2O_3 by its adsorption of moisture from the environment during milling. The amounts of $La(OH)_3$ in the product as well as La_2O_3 are decreased gradually by reacting with PTFE, accordingly, a new phase of LaOF is formed in the milled mixture as the grinding progresses, besides $La(CO_3)F$ and C. The mechanochemical reactions in the system can be given as below:

$$La_2O_3 + (CF_2CF_2) = LaOF + La(CO_3)F + C \quad (2.13.10)$$

$$La(OH)_3 + (CF_2CF_2) = LaOF + La(CO_3)F + H_2O \quad (2.13.11)$$

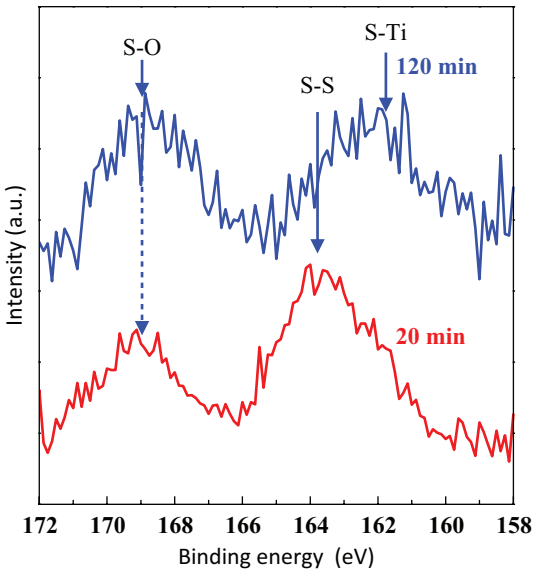


FIGURE 2.13.6 XPS spectra of S-2p of the samples ground for 20 and 120 min.

Heating the milled products at 600°C enables us to eliminate amorphous carbon (C) and decompose $La(CO_3)F$ into LaOF, so that pure LaOF nanoparticles of a few ten nanometer sizes can be obtained as the final product.

2.13.4 MECHANOCHEMICAL DOPING

Another attraction in the mechnaochemical treatment is to dope non-metal elements such as nitrogen, sulphur and fluorine into the surface of a solid such as oxide. Normally, a metal oxide is more stable than the corresponding nitride, sulfide and fluoride, and it is difficult to dope these elements into the oxide in ambient condition. Therefore, high temperature heating is taken to the doping operation. Instead of such operation, milling oxide with urea (CH_4N_2O) or sulfur (S) in air enables us to dope nitrogen (N) or S into the oxide structure.[42,43] In fact, a sulfur-doped TiO_2 sample in rutile structure can be synthesized by milling the mixture of TiO_2 and sulfur (S), and it is confirmed that the bonding force between Ti-S is enhanced by milling the sample for 2 h, as shown in Figure 2.13.6.[42] As a matter of fact, the N- and S-doped products have shown high-photocatalytic reactivity in the decomposition of nitrogen monoxide (NO) under visible-light irradiation over 510 nm in wave length.[42,43] These results indicate that the mechanochemical method allows an easy preparation of rutile phase S- and N-doped TiO_2 with high photocatalytic activity under visible-light illumination. This mechanochemical doing can be applied to the other oxides with different non-metal elements.[44–48]

2.13.5 MECHANICAL SYNTHESIS OF HYDRATED COMPOUNDS

In general, water in the reaction system plays a big role to control the mechanochemical reaction.[7,8] Therefore, water

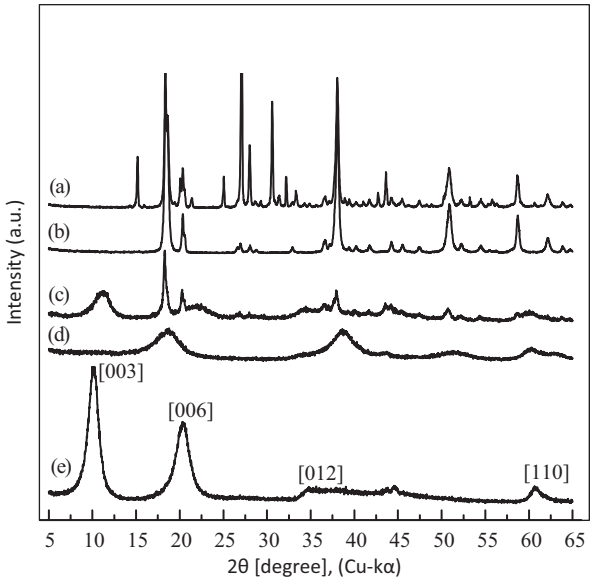


FIGURE 2.13.7 Comparison between the one-step and the two step operations. (a) three starting samples, (b) two starting hydroxides, (c) one-step operation for 3-h, (d) milling the mixture (b) for 1-h, (e) Milling the product (d) with $Mg(NO_3)_2{\cdot}6H_2O$ and water for 2-h.

is a control agent for the mechanochemical reaction.[7,8,49–51] However, in order to synthesize hydrated compound, a water molecule plays a role for the reaction, and leads to synthesize a layered double hydroxide (LDH) in the presence of water.[52] The LDH as a target material is meixnerite ($Mg_6Al_2[OH]_{18}.4H_2O$), and this compound can be synthesized more effectively by a two-step milling than a one step one for a mixture of $Mg(OH)_2$ and $Al(OH)_3$ with water. In the first-step of the two step operation, a mixture of the starting two materials, $Mg(OH)_2$ and $Al(OH)_3$, were mixed at a molar ratio of 3:1 for Mg and Al (Mg:Al = 3:1) without water. Then the second step is to mill the mixture of the product with $Mg(NO_3)_2{\cdot}6H_2O$ and water to synthesize $Mg_6Al_2(OH)_{12}(NO_3){\cdot}4H_2O$. Figure 2.13.7[52] shows a comparison between the one-step and two step operations, where, (a) is the three starting samples, (b) is the two starting hydroxides, (c) is the mixture (a) milled for 3-h in the one-step operation, (d) is the mixture (b) milled for 1-h in the two step operation and (e) is the product (d) with $Mg(NO_3)_2{\cdot}6H_2O$ and water milled for 2-h in the two step operation. It is confirmed in the one-step operation (c) that meixnerite with a small amount of carbonate is synthesized mechanochemically at ambient conditions but a small amount of the starting samples are found to remain in the product. On the contrary, the second-step operation (d) and (e) indicates that most of the starting samples have disappeared, and a new phase of meixnerite compound is formed.

It is important to keep the water addition rate for the formation of hydrated compounds. The reaction mechanism is still unknown, but may be due to local hydrothermal reaction.[8]

2.13.6 DECOMPOSITION OF HALOGENATED POLYMERS

Defluorination of Polytetrafluoroethylene (PTFE)

The grinding stimulates the solid reaction between PTFE ($[CF_2CF_2]_n$, n: polymerization degree) and SrO at room temperature.[53] The grinding PTFE causes the decomposition reaction, to form strontium fluoride (SrF_2) and CO gas, as given by Equation 2.13.12.

$$\left[CF_2CF_2\right]_n + 2n\mathrm{SrO} = 2n\mathrm{SrF_2} + 2n\mathrm{CO} \qquad (2.13.12)$$

The reaction is taken place by the grinding, and it can be recognized from the thermogravimetric analysis of the ground mixture. That is, the rate in weight loss for the mixture ground for 1 hour by a planetary mill (P-7, Fritsch, Germany) is very slow and the loss is about 5% at 1000°C, while the weight loss for an original PTFE is suddenly appeared at about 30% at about 400°C. This indicates that no PTFE exists in the ground sample after the above reaction.

Dechlorination of Polychlorinated Compounds

Recalcitrant polychlorinated compounds, such as DDT, PCBs and dioxins (DXNs) can be reductively dehalogenated by a base metal such as Ca, Mg, Fe and CaO or a hydrogen donor at room temperature, ambient pressure and in a short time using a ball mill as a mechanochemical dehalogenation reactor.[54–58] Comparing with the use of CaO as additive, the rare earth oxides like yttrium oxide (Y_2O_3), lanthanum oxide (La_2O_3), neodymium oxide (Nd_2O_3) and gadolinium oxide (Gd_2O_3) would be very effective for the decomposition of polychlorinated compounds such as monochlorobiphenyl (BP-Cl).[56] In addition, mechanochemical decomposition of a chlorinated compound can be accelerated by inactive agent such as silica or alumina powder in the mixture with reactant such as CaO or metal oxide.[57] All the same, radical is detected in the product after decomposition, so that the degree of the peaks in ESR is a sign of the decomposition state of the chlorinated compounds after mechanochemical treatment.[58] 1,2,3-trichlorobenzene ($C_6H_3Cl_3$) can also be decomposed by its milling with calcium oxide (CaO) in air. The mechanochemical reaction is given by Equation 2.13.13.[59,60]

$$C_6H_3Cl_3 + 3\mathrm{CaO} = 3\mathrm{CaOHCl} + 6C \qquad (2.13.13)$$

Additionally, the other final products detected after grinding are carbon (C) and several minor compounds such as methane, ethane, although the formation of chlorine-containing intermediates such as dichlorobenzene and tetrachlorobenzene can be observed in the early stage of grinding.

As for a polyvinyl chloride material (PVC, $[\text{-}CH_2\text{-}CHCl\text{-}]_n$), it contains a plasticizer such as phthalic ester. Even though, this resin can be mechanochemically decomposed by grinding with metal oxides or hydroxides or carbonates.[61–63] As for the case of the mixture of PVC and La_2O_3 mixed at a constant

molar ratio (PVC:La_2O_3 = 1:2), lanthanum oxy-chloride, LaOCl is formed after 20 minutes grinding, while in the mixture of PVC and CaO the reaction product CaOHCl is not clearly formed by the same milling periods of time. This suggests that La_2O_3 can react with PVC more easily rather than CaO.

Debromination of Hexabromobenzene (HBB)

HBB (C_6Br_6) can also be decomposed by its grinding with CaO in air.[64] In this case, debromination of the HBB sample can occur, and it is accelerated with an increase in both grinding time and molar ratio of CaO addition, as given by Equation 2.13.14.

$$\begin{aligned} &C_6Br_6 + 12CaO + 3nH_2O \\ &= 3CaBr_2nH_2O + (3/2)CaCO_3 \\ &+ (15/2)CaO + (9/2)C \end{aligned} \qquad (2.13.14)$$

One of the products, $CaBr_2$ tends to absorb moisture to form $CaBr_2\ nH_2O$, which is soluble in water. It is found that almost 100% of debromination can be achieved by milling with CaO, and radicals are detected in the ground products, due to rupture in the covalent bonds of C-C and C-Br in HBB.

2.13.7 Material Processing with Mechanical Activation Followed by Chemical or Physical Treatment

Extraction of Useful Components from the Disordered Systems

Acid leaching of the serpentine sample ($Mg_3Si_2O_5[OH]_4$) activated by grinding for various times was conducted at room temperature using HCl and/or H_2SO_4 solutions, respectively.[65] Dry grinding the ore results in the structural change into an amorphous phase. This change is attributed to mainly local disordering around magnesium (Mg) and silicon (Si) in the structure, leading to enhancement of extraction of Mg and Si from the serpentine sample by acid solution. Figure 2.13.8[65] shows yield of both Mg and Si extracted from the sample by H_2SO_4 solution as a function of milling time. More than 90% of Mg and 70% of Si in the sample ground for 4 h can be extracted by the leaching, while no significant extraction is achieved at room temperature in the leaching of the non-activated sample. Similar phenomena can be seen in the milled samples of talc and other mineral.[66,67]

Zeolite Synthesis from Activated Kaolinite

Zeolite-A and X can be synthesized by grinding kaolinite in air, followed by its curing in NaOH solution at 60°C.[68] The kaolinite activated by the grinding enables the release of aluminum (Al) from the structure, due to its disordering around Al, while Si-O and Si-(OH) bonding states are not so damaged. Therefore, the curing operation in NaOH solution facilitates the dissolution of Al, compared with that of Si. As the curing period is long, the molar ratio of (Si/Al) is close to 1.2, which is the same as that in zeolite-X. When the curing time is short, the molar ratio is close to 1.0, corresponding to the ratio in zeolite-A.

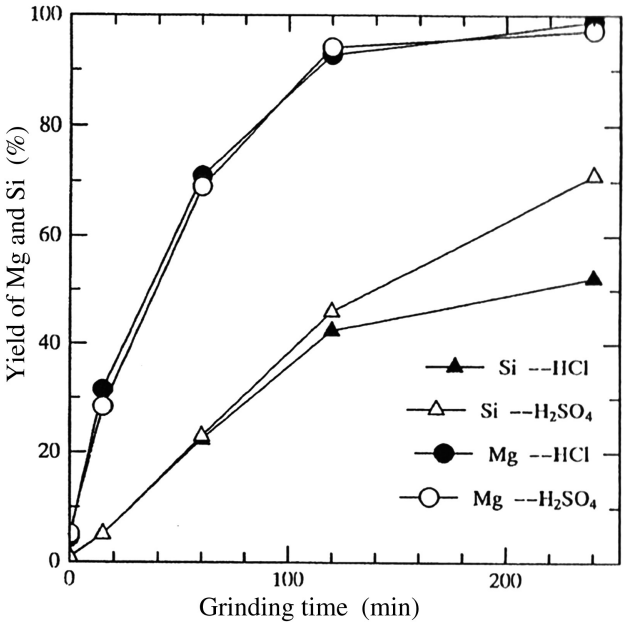


FIGURE 2.13.8 Yield of Mg and Si extracted by acid solutions from the serpentine sample milled for different periods of time.

Formation of $SrCO_3$ and $BaCO_3$ from Celestite and Barite

$SrSO_4$ and $BaSO_4$ can be transferred into their hydroxides by the grinding with NaOH or KOH, as given by Equations 2.13.15 and 2.13.16.[69,70] This is the first step of this process.

$$SrSO_4 + 2NaOH = Sr(OH)_2 + Na_2SO_4 \qquad (2.13.15)$$

$$BaSO_4 + 2KOH = Ba(OH)_2 + K_2SO_4 \qquad (2.13.16)$$

As for the case of celestite processing, $Sr(OH)_2$ formed in the first step tends to easily form $SrCO_3$ due to the reaction with CO_2 in air, and this carbonation is expressed as Equation 2.13.17 (the second step).

$$Sr(OH)_2 + CO_2 = SrCO_3 + H_2O \qquad (2.13.17)$$

After exposing the milled product in air for a while, it is dispersed in water to dissolve Na_2SO_4 and $SrCO_3$ can be selectively separated by filtration (the third step). The yield of $SrCO_3$ depends on the milling periods of time as well as exposing time in air, as shown in Figure 2.13.9.[69] It is important to carry out the milling of the mixture of celestite and NaOH in a dry environment as if it is done in water, no mechanochemical

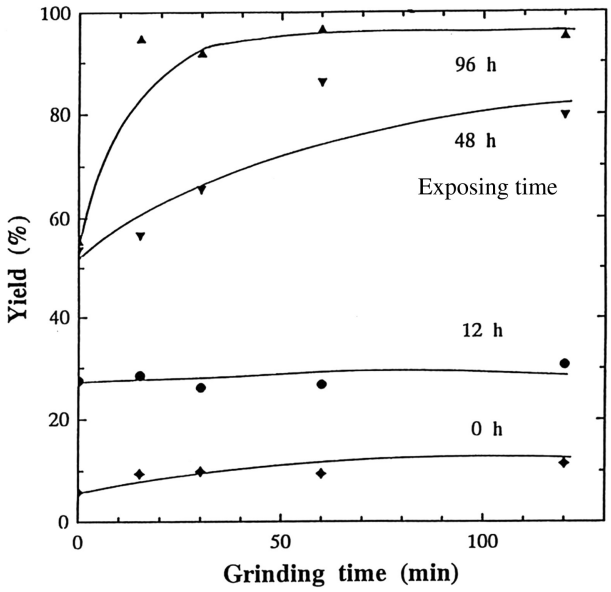


FIGURE 2.13.9 Yield of $SrCO_3$ in the product as a function of grinding time.

reaction takes place, due to the nature of the solubility product between $SrSO_4$ and $Sr(OH)_2$ in water.

Similar phenomena can be seen in the mechanochemical process for producing barium carbonate from barite containing mainly $BaSO_4$.[70] In this case, the process for transferring barite into $BaCO_3$ is composed of three steps: The first step is to produce barium hydroxide and potassium sulfate powders by dry grinding of barite and KOH powders, and $BaCO_3$ can be obtained by exposing the product, as shown in Equation 2.13.18, while K_2SO_4 is unchanged (the second step).

$$Ba(OH)_2 + CO_2 = BaCO_3 + H_2O \qquad (2.13.18)$$

Rinsing the exposed product composed of $BaCO_3$ and K_2SO_4 with K_2CO_3 solution is important to recover $BaCO_3$ at high yield. About 83% of barium in barite is recovered as $BaCO_3$ by this process.

Indium Recovery from the Indium-Tin-Oxide (ITO) Scrap

The ITO scrap is a product discharged from a sandblasting process for scraping the ITO layer deposited on the wall of vacuum vessel, in which ITO is deposited on the surface of electric devises. Thus, the scrap contains a blasting sand (alumina powder) and ITO. The grinding of the scrap causes the crystal structure change of the mixture components, especially ITO into degradation, and the alumina powder acts as an aid for assisting this degradation of ITO. This degradation in crystallinity of ITO in the scrap resulted in easy extraction of indium (In) at high yield even in the room temperature leaching.[71]

Another process for recovering In from ITO has been developed by its grinding with Li_3N under NH_3 or N_2 environment.[72]

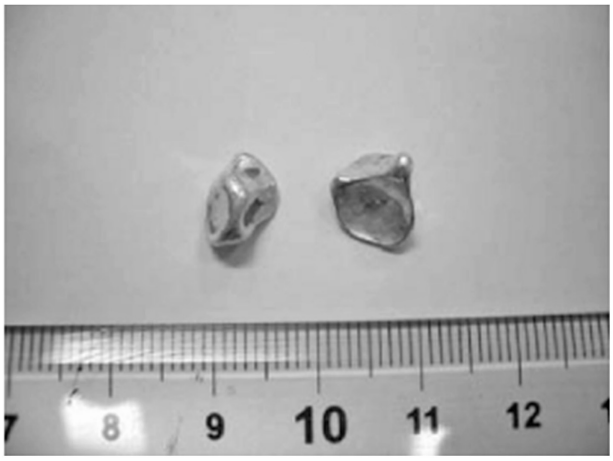


FIGURE 2.13.10 Photo of In-metal pellet obtained after milling a mixture of In_2O_3 and Li_3N (In_2O_3:Li_3N = 1:3) for 2 h under NH_3.

The reactions in the mill are given by Equations 2.13.19 to 2.13.21:

$$In_2O_3 + Li_3N + NH_3 = 2In + 3LiOH + N_2 \qquad (2.13.19)$$

$$In_2O_3 + 2Li_3N + N_2 = 2In + 3Li_2O + 2N_2 \qquad (2.13.20)$$

$$In_2O_3 + 2Li_3N = 2In + 3Li_2O + N_2 \qquad (2.13.21)$$

The milled products (In+LiOH) or (In+Li_2O) were mixed with water and milled again for a short period of time, then LiOH and Li_2O are dissolved into water, while In fine particles are agglomerated into several ingot pellets, as shown in Figure 2.13.10.[72] The purity of In ingot and its recovery data are shown in Table 2.13.7.[72]

Extraction of Rare Earths from Waste Alloy

It is possible to recover metals from alloy-waste (Mm-Ni-Co-Al-Mn system, Mm [Mischmetall]=La-Ce-Pr-Nd system) by its grinding with polyvinyl chloride (PVC). The grinding of the mixture of alloy and PVC causes mechanochemical reaction to form metal chloride, so that the washing with water and

TABLE 2.13.7 Evaluation of Purity and Recovery for Indium with Milling Time from the Data Obtained by ICP Analysis

Milling Time [min]	In Purity [%]	Li Impurity [%]	Total [%]	In Recovery [%]
30	95.73	0.41	96.14	98.12
60	96.76	0.37	97.13	97.25
120	94.21	0.39	94.61	97.11
180	94.25	0.29	94.54	97.39

filtration enables us to remove soluble chloride compounds and recover the rare earths as solutes. The PVC additive plays a significant role as a chlorine source in the reaction. Figure 2.13.11[73] shows the yield of metals extracted from the alloy product as a function of milling periods of time.

Sulfuration of Metal Oxides in Ash

Mechanochemistry on sulfides and sulfide minerals has been intensively investigated by P. Balaz,[74,75] and another effort has been focused on recovery of non-ferrous metal oxides in ash by applying sulfuration followed by flotation.[76] It is well known that non-ferrous metals such as Zn and Pb are easily sulfurized into sulfides such as ZnS and PbS by its grinding with sulfur (S), while these metal oxides are not sulfurized by its grinding with S. However, when iron (Fe) powder, for example, is added to the mixture of metal oxide and S, the metal oxide is changed into sulfide, and Fe powder is transferred to iron oxide (magnetite, Fe_3O_4). There are two kinds of competitive reactions: one is the reaction of S with the metal oxide, and the other is that of S with Fe. As for the Gibbs free energy change of formation (ΔG_{298}) for the Fe and S reaction system, it is −364 kJ/mol. Therefore, the absolute value of ΔG_{298} in the metal and S system should be larger than 364 kJ/mol when the sulfide is formed. As a matter of fact, the mechanochemical reaction for the systems in $|\Delta G_{298}| < 364$ kJ/mol does not proceed, while the reaction systems with $|\Delta G_{298}| > 364$ kJ/mol proceeds further. When Fe powder is absent in these reaction systems, no sulfides are formed mechanochemically by the grinding of the mixtures except PbO which may undergo a different reaction pathway. Fe powder plays a significant role as a reducer against the non-ferrous metal oxides.

As to the flotation of the sulfide samples in ash, using n-amylxanthic acid potassium salt as a collector and $CuSO_4(5H_2O)$ as an activator, the grade of Zn has been raised as high as 17%.

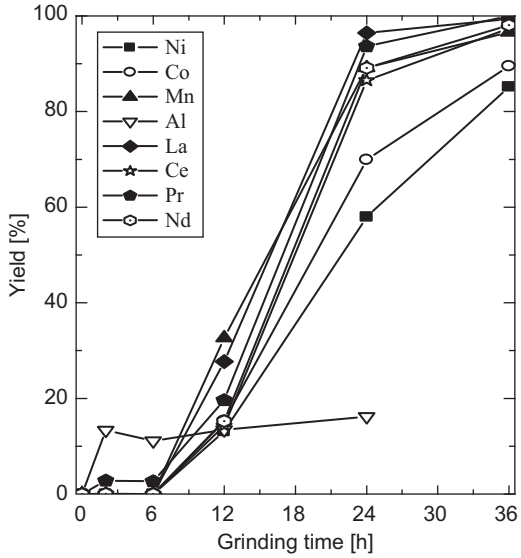


FIGURE 2.13.11 Yield of rare metals in the alloy waste as a function of milling periods of time.

TABLE 2.13.8 Gas Contents Emitted from the Samples

Mixture	T (°c)	H_2 (%)	CH_4 (%)	CO (%)	CO_2 (%)
PE-6Ca(OH)$_2$-Ni(OH)$_2$	450–500	76.1	23.7	0.16	0.01
PVC-6Ca(OH)$_2$-Ni(OH)$_2$	400–500	94.5	4.01	1.15	0.37
PVA-6Ca(OH)$_2$-Ni(OH)$_2$	400–500	98.7	1.0	0.3	0.0
PS-6Ca(OH)$_2$-Ni(OH)$_2$	450–500	95.8	3.1	1.0	0.3

Hydrogen Generation from Plastic and Biomass

A process to generate mainly hydrogen (H_2) from polyethylene $[-CH_2-]_n$ (PE) has been developed by milling with $Ca(OH)_2$ and $Ni(OH)_2$ followed by heating the milled product at 400 to 500°C.[77] Table 2.13.8[77–79] shows the gas contents emitted from the milled samples with $Ca(OH)_2$ and $Ni(OH)_2$. The grinding the mixture plays a significant role to create an activated state among the different compounds in the mixture, leading to easy decomposition of the materials in the heating operation. $Ca(OH)_2$ has a role to capture CO_2 generated during heating, and $Ni(OH)_2$ powder is also an important reagent to emit H_2. Therefore, the exhausted gas does not contain so much, resulting in a high yield in H_2. Similar phenomena can be seen in the milled samples of cellulose based samples such as sewage sludge.[80–84]

REFERENCES

1. Boldyrev, V.V., Tkacova, K., *J. Mater. Synth. Process.*, 8, 121–132, 2000.
2. Benjamin, J.S., *Metall. Trans.*, 1, 2943–2951, 1970.
3. Juhasz, A.Z., Opoczky, L., *Mechanical Activation of Minerals by Grinding: Pulverizing and Morphology of Particles*, Akademiai Kiado, Budapest, 1990, 49–52.
4. Boldyrev, V.V., *Solid State Ionics*, 63–65, 537–543, 1993.
5. Urakaev, F.Kh., Takach, L., Soika, V., Shevchenko, V.S. and Boldyrev, V.V., *Russian J. Phys. Chem.*, 75, 1997–2001, 2001.
6. Kubo, T., *Mechanokemisutori-Gairon* (*Introduction of Mechanochemistry*) (Ver.2), Tokyo-Kagaku Dojin, Tokyo, 1972.
7. Avvakumov, E.G., Devyatkina, E.T., Kosova, N.V., *J. Solid State Chem.*, 113, 379–383, 1994.
8. Boldyrev, V.V., Khabibullin, A.Kh., Kosova, N.V., Avvakumov, E.G., *J. Mater. Synth. Process.*, 4, 377–381, 1996.
9. Lin, I.J., Nadiv, S., *Miner. Sci. Eng.*, 39, 193–209, 1979.
10. Zhang, Q., Kano, J., Saito, F., *Handbook of Powder Technology*, Vol. 12, Eds. Salman, A.D. Ghadiri, M., Hounslow, M.J., Elsevier, Amsterdam, 509–550, 2007.
11. Mi, G., Saito, F., Suzuki, S., Waseda, Y., *Powder Technol.*, 97, 178–182, 1998.
12. Mi, G., Murakami, Y., Shinodo, D., Saito, F., *Powder Technol.*, 104, 75–79, 1999.
13. Zhang, Q., Saito, F., *J. Alloy. Compd.*, 297, 99–103, 2000.
14. Zhang, Q., Saito, F., *J. Am. Ceram. Soc.*, 83, 439–441, 2000.
15. Zhang, Q., Saito, F., *J. Mater. Sci.*, 36, 2287–2290, 2001.
16. Zhang, Q., Lu, J., Wang, J., Saito, F., *J. Mater. Sci.*, 39, 5527–5530, 2004.

17. Zhang, Q., Lu, J., Saito, F., *Powder Technol*., 122, 145–149, 2002.
18. Tojo, T., Zhang, Q., Saito, F., *J. Solid State Chem*., 179, 433–437, 2006.
19. Tojo, T., Zhang, Q., Saito, F., *J. Mater. Sci*., 43, 2962–2966, 2008.
20. Tojo, T., Zhang, Q., Saito, F., *Powder Technol*., 181, 281–284, 2008.
21. Zhang, Q., Tojo, T., Tongamp, W., Saito, F., *Powder Technol*., 195, 40–43, 2009.
22. Zhang, Q., Saito, F., Shimme, K., Masuda, S., *J. Soc. Powder Technol. Jpn*., 36, 468–473, 1999.
23. Tongamp, W., Zhang, Q., Saito, F., *J. Hazard. Mater*., 137, 1226–1230, 2006.
24. Lee, J., Zhang, Q., Saito, F., *Chem. Lett*., 30, 700–701, 2001.
25. Lee, J., Shin, H., Lee, J.C., Chung, H., et al., *Mater. Trans*., 44, 1457–1460, 2003.
26. Lu, J., Zhang, Q., Saito, F., *Chem. Lett*., 31, 1176–1177, 2002.
27. McCormick, P.G., *Mater. Trans. JIM*, 36, 161–169, 1995.
28. McCormick, P.G., *Handbook on the Physics and Chemistry of Rare Earths*, Vol. 24, Eds., Gschneidner, Jr. K.A., Eying, L., North-Holland, 47–82, 1997.
29. Ding, J., Tsuzuki, T., McCormick, P.G., *J. Mater. Sci*., 34, 5293–5298, 1999.
30. Ding, J., Tsuzuki, T., McCormick, P.G., *J. Am. Ceram*., 79, 2956–2958, 1996.
31. Ding, J., Tsuzuki, T., McCormick, P.G., *Nanostr. Mater*., 8, 75–81, 1997.
32. Dodd, A.C., Tsuzuki, T., McCormick, P.G., *Mater. Sci. Eng*., A301, 54–58, 2001.
33. Tsuzuki, T., Harrison, W.T.A., McCormick, P.G., *J. Alloys Comp*., 281, 146–151, 1998.
34. Tsuzuki, T., Pirault, E., McCormick, P.G., *Nanostr. Mater*., 11, 125–131, 1999.
35. Tsuzuki, T., McCormick, P.G., *J. Mater. Sci*., 39, 5143–5146, 2004.
36. McCormick, P.G., Tsuzuki, T., *Proc. NEPTIS-13*, 7–16, 2004.
37. McCormick, P.G., Tsuzuki, T., Robinson, J.S., Ding, J., *Adv. Mater*., 13, 1008–1010, 2001.
38. Tsuzuki, T., McCormick, P.G., *J. Am. Ceram. Soc*., 84, 1453–1458, 2001.
39. Ito, T., Zhang, Q., Saito, F., *Powder Technol*., 143-144, 170–173, 2004.
40. Tsuzuki, T., McCormick, P.G., *Appl. Phys*., A65, 607–609, 1997.
41. Lee, J., Zhang, Q., Saito, F., *J. Alloy. Compd*., 348, 214–219, 2003.
42. Zhang, Q., Wang, J., Yin, S., Sato, T., et al., *J. Am. Ceram. Soc*., 87, 1161–1163, 2004.
43. Yin, S., Yamaki, H., Komatsu, M., Zhang, Q., et al., *J. Mater. Chem*., 13, 2996–3001, 2003.
44. Wang, J., Yin, S., Zhang, Q., Saito, F., et al., *J. Mater. Chem*., 13, 2348–2352, 2003.
45. Wang, J., Yin, S., Komatsu, M., Zhang, Q., et al., *Appl. Catal. B-Environ*., 52, 11–21, 2004.
46. Wang, J., Yin, S., Komatsu, M., Zhang, Q., et al., *Trans. Mater. Res. Soc., Jpn*., 29, 2693–2696, 2004.
47. Kang, I., Zhang, Q., Kano, J., Yin, S., et al., *J. Photochem. Photobiol. A Chem*., 89, 232–238, 2007.
48. Kang, I., Zhang, Q., Yin, S., Sato, T., et al., *Appl. Catal. B Environ*., 80, 81–87, 2008.
49. Kosova, N.V., Khabibullin, A.Kh., Boldyrev, V.V., *Solid State Ionics*, 101–103, 53–58, 1997.
50. Mi, G., Saito, F., Hanada, M., *Powder Technol*., 93, 77–81, 1997.
51. Saito, F., Mi, G., Hanada, M., *Solid State Ionics*, 101–103, 37–43, 1997.
52. Tongamp, W., Zhang, Q., Saito, F., *Powder Technol*., 185, 43–48, 2008.
53. Zhang, Q., Matsumoto, H., Saito, F., *Chem. Lett*., 30, 148–149, 2001.
54. Rowlands, S.A., Hall, A.K., McCormick, P.G., et al., *Nature*, 367, 223, 1994.
55. Loiselle, S., Branca, M., Mulas, G., Cocco, G., *Environ. Sci. Technol*., 31, 261–265, 1997.
56. Tanaka, Y., Zhang, Q., Saito, F., *J. Chem. Eng. Jpn*., 39, 469–474, 2006.
57. Zhang, Q., Saito, F., Ikoma, T., Tero-Kubota, S., *Environ. Sci. Technol*., 35, 4933–4935, 2001.
58. Ikoma, T., Zhang, Q., Saito, F., Akiyama, K., et al., *Bull. Chem. Soc. Jpn*., 74, 2303–2309, 2001.
59. Tanaka, Y., Zhang, Q., Mizukami, K., Saito, F., *Bull. Chem. Soc. Jpn*., 76, 1919–1925, 2003.
60. Tanaka, Y., Zhang, Q., Saito, F., *J. Phys. Chem. B* 107, 11091–11097, 2003.
61. Tongamp, W., Zhang, Q., Saito, F., *J. Hazard. Mater*., 137, 1226–1230, 2006.
62. Inoue, T., Miyazaki, M., Kamitani, M., Kano, J., et al., *Adv. Powder Technol*., 16, 649–658, 2005.
63. Saeki, S., Kano, J., Saito, F., Shimme, K., *J. Mater. Cycles Waste Manag*., 3, 20–23, 2001.
64. Zhang, Q., Matsumoro, H., Saito, F., Baron, M., *Chemosphere*, 48, 787–793, 2002.
65. Zhang, Q., Sugiyama, K., Saito, F., *Hydrometallurgy*, 45, 323–331, 1997.
66. Sanchez, E.C., Sugiyama, K., Saito, F., *MMIJ*, 112, 719–722, 1996.
67. Sanchez, E.C., Saito, F., Horita, H., *MMIJ*, 113, 35–38, 1997.
68. Kim, W., Saito, F., *J. Chem. Eng. Jpn*., 33, 217–222, 2000.
69. Zhang, Q., Saito, F., *Chem. Eng. J*., 66, 79–82, 1997.
70. Zhang, Q., Saito, F., *J. Chem. Eng. Jpn*., 30, 724–727, 1997.
71. Zhang, Q., Aoyagi, T., Nagata, C., Saito, F., *MMIJ*, 115, 185–188, 1999.
72. Kano, J., Kobayashi, E., Tongamp, W., Miyagi, S., *J. Alloy. Compd*., 484, 422–425, 2009.
73. Zhang, Q., Saeki, S., Tanaka, Y., Kano, J., et al., *J. Hazard. Mater*., A139, 438–442, 2007.
74. Balaz, P., Ebert, I., *Hydrometallurgy*, 27, 141–150, 1991.
75. Balaz, P., *Int. J. Miner. Process*., 72, 341–354, 2003.
76. Wang, J., Lu, J., Zhang, Q., Saito, F., *Ind. Eng. Chem. Res*., 42, 5813–5818, 2003.
77. Tongamp, W., Zhang, Q., Saito, F., *Int. J. Hydrogen Energy*, 33, 4097–4103, 2008.
78. Tongamp, W., Zhang, Q., Miyagi, S., Saito, F., *J. Hazard. Mater*., 167,1002–1006, 2009.
79. Tongamp, W., Zhang, Q., Saito, F., *Fuel Process. Technol*., 90, 909–913, 2009.
80. Zhang, Q., Kang, I., Tongamp, W., Saito, F., *Bioresource Technol*., 100, 3731–3733, 2009.
81. Tongamp, W., Zhang, Q., Saito, F., *Fuel Process. Technol*., 91, 272–276, 2010.
82. Zhang, Q., Honda, H., Watanabe, A., Tongamp, W., et al., *High Temp. Mater. Process*., 29, 435–445, 2010.
83. Zhang, Q., Saito, F., *Waste Biomass Valorization*, 1, 41–46, 2010
84. Kumproa, K., Nuntiya, A., Zhang, Q., Kano, J., et al., *Int. J. Hydrogen Energy*, 39, 17554–17562, 2014.



Taylor & Francis
Taylor & Francis Group
http://taylorandfrancis.com

2.14 Ignition and Combustion Reaction

Hisao Makino and Ryoichi Kurose

2.14.1 COMBUSTION PROFILE

Fuel Properties

There are many kinds of solid fuels, including coal, oil sand, oil shale, refuse fuel, and biomass, and coal is the most abundant among these solid fuels. The most common and useful methods for analyzing these solid fuels are the proximate and ultimate analyses.

Proximate analysis is used to quantify the amounts of moisture, volatile matter, fixed carbon, and ash contents. The amounts of moisture and volatile matter contents of a sample of solid fuel are evaluated by measuring the weight losses in air at 107 ± 2°C for 1 h and in an inert gas at 900 ± 20°C for 7 min., respectively. The amount of fixed carbon content is supposed to correspond to the weight loss after further heating in air at 815 ± 10°C for 1 h, and the residual is regarded as ash. Thus, the dried sample consists of combustible matter and ash, and the combustible matter comprises volatile matter, which easily volatilizes to the gas phase, and fixed carbon, which remains in the char even at high temperature.

On the other hand, the major elements such as carbon, hydrogen, oxygen, nitrogen, and sulfur in solid fuels are evaluated using ultimate analysis. In general, ultimate analysis is roughly related to proximate analysis: for example, coals with high fixed carbon content contain much carbon, and coals with high volatile matter content contain much hydrogen (see Table 2.14.1).[1]

Combustion Process of Solid Fuel

Figure 2.14.1[2] shows a schematic of the typical coal combustion processes on pulverized coal, which is one of the most common methods for burning solid fuels. The combustion processes are as follows: (1) moisture in solid fuels is immediately vaporized when solid fuels enter into a high-temperature region in a furnace, (2) evolution of volatile matter (devolatilization) takes place, (3) the volatilized gas is ignited and volatile combustion occurs, (4) char combustion (combustion of fixed carbon) follows the volatile combustion, (5) the combustion is terminated (a piece of the fixed carbon remains in the ash).

2.14.2 DEVOLATILIZATION AND IGNITION

The combustion of solid fuels begins by the ignition of volatilized gas after the evolution of volatile matter takes place in a high-temperature region. Although the devolatilization is believed to finish in about 100 ms, it is very difficult to accurately understand the devolatilization mechanism because

TABLE 2.14.1 Analysis Results of Solid Fuels

		Coal A	Coal B	Refuse Fuel*1	Biomass (Australian Bagasse)
High heating value*2	kcal/kg	7,270	7,030	—	—
Low heating value*2	kcal/kg	9,980	6,750	—	—
		Proximate analysis			
Moisture	wt%	1.1*2	2.4*2	52.7*2	44.0–53.0*2
Ash	wt%	12.2*3	11.6*3	9.5*2	4.0–30.0*3
Volatile matter	wt%	29.1*3	34.1*3	—	75.0–87.0*4
Fixed carbon	wt%	58.7*3	54.3*3	—	—
Fuel ratio	—	2.02	1.59	—	—
		Ultimate analysis			
Carbon	wt%	74.1*3	72.5*3	26.45*2	43.0–52.05*4
Hydrogen	wt%	5.29*3	5.57*3	3.93*2	5.2–6.9*4
Nitrogen	wt%	1.54*3	1.67*3	0.65*2	0.2–0.4*4
Oxygen	wt%	6.5*3	8.4*3	16.21*2	40.8–52.0*4
Total sulfur	wt%	0.34*3	0.32*3	0.08*2	0.02–0.11*4
Combustible sulfur	wt%	0.33*3	0.31*3	—	—

*1 An example of Japanese refuse fuel in Japanese urban areas. Source: Makino, H. and Ito, S., J. Soc. Powder Technol. Japan, 34, 247–254, 1997.
*2 Equilibrium moisture basis.
*3 Dry basis.
*4 Dry ash-free basis.

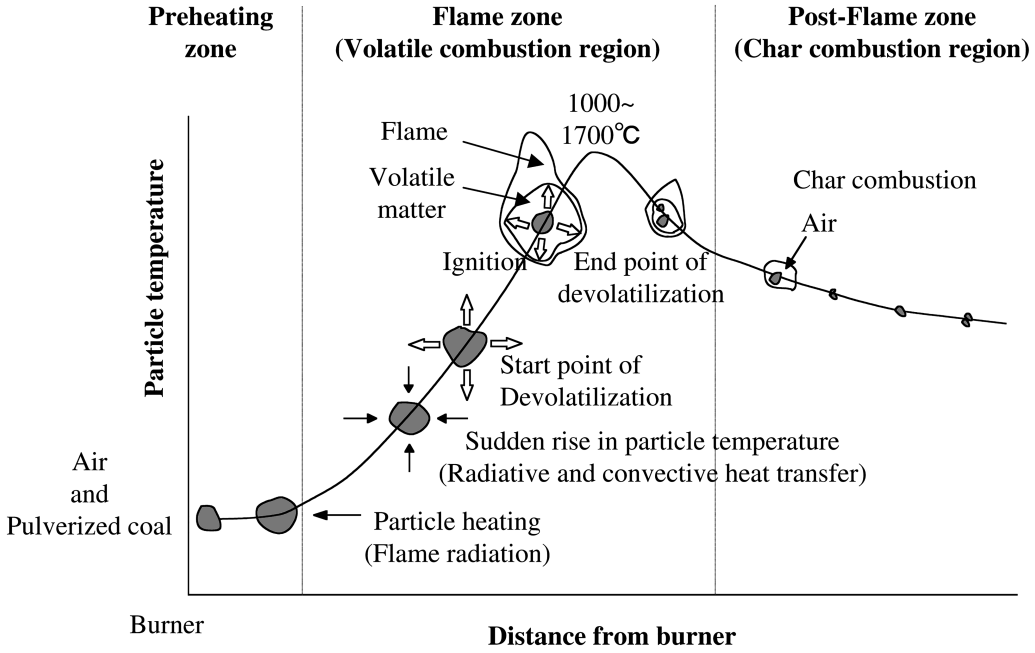


FIGURE 2.14.1 Combustion profile of a coal particle in pulverized coal combustion. (From Tominaga, H., in *Sangyou Nenshou Gijutsu,* The Energy Conservation Center, Japan, 2000, pp. 93–100. With permission.)

devolatilization is an extremely complicated phenomenon. The devolatilization processes are strongly affected by coal properties, temperature, gas compositions, and so on, and these conditions change moment to moment in actual combustion fields. The devolatilization rate of volatile matter is commonly modeled by a single-step Arrhenius reaction scheme,[3] such as

$$\frac{dV}{dt} - K_v(V^* - V) \tag{2.14.1}$$

$$K_v = A_v \exp\left(-\frac{E_v}{RT_p}\right) \tag{2.14.2}$$

where

V^* and V indicate the total volatile matter content in a solid fuel particle and volatilized mass released from the particle
T_p is the particle temperature
R is the universal gas constant

Kinematic parameters of preexponential factor A_v and activation energy E_v in Equation (2.14.2) are determined by various methods.[4–8] Besides, a two-step Arrhenius reaction scheme[9] is also proposed to improve the adaptability. Recently, a tabulated-devolatilization-process (TDP) model[10] is also established to improve the composition of volatile matter.

The definition of ignition temperature has not been explicitly settled yet, since the measurements of ignition temperature of solid fuels with complicated properties are very difficult. Typically, the ignition temperature of brown coals, whose volatile matter content is relatively high, is about 250°C, and that of anthracite, which is a low-volatile coal, is about 500°C. The ignition temperature of bituminous coals, which are generally used in pulverized coal combustion in Japanese coal-fired thermal power plants, is 300–400°C.

For the solid fuels with nonvolatile matter, the ignition temperature is regarded as the temperature at which the heat generated by the combustion on the surface of a solid fuel is beyond the heat loss due to convection and radiation.

2.14.3 GASEOUS COMBUSTION

The combustion of the volatilized gas due to the evolution of volatile matter with combustion air takes place in the gaseous phase. The simple model of gaseous combustion is as follows. The chemical mechanism has two global reactions:

$$C_aH_bO_c + 0.5O_2 \rightarrow \alpha CO + \beta H_2O \tag{2.14.3}$$

$$CO + O_2 \rightarrow CO_2$$

where $C_aH_bO_c$ is the volatilized fuel gas, and a, b, c, α, and β are governed by the coal property. The gaseous combustion provided in Equation (2.14.3) is often calculated using the combination of the kinetics and eddy dissipation models.[11] Regarding the kinetics, the rate of reaction for reactants such as $C_aH_bO_c$ is given as an Arrhenius expression:

$$R_g = A_g \exp\left(-\frac{E_g}{RT_g}\right)\left[\text{Reactant}\right]^d\left[O_2\right]^e \tag{2.14.4}$$

where $[\psi]$ means the mol fractions of chemical species ψ. The values of the preexponential factor A_g, activation energy

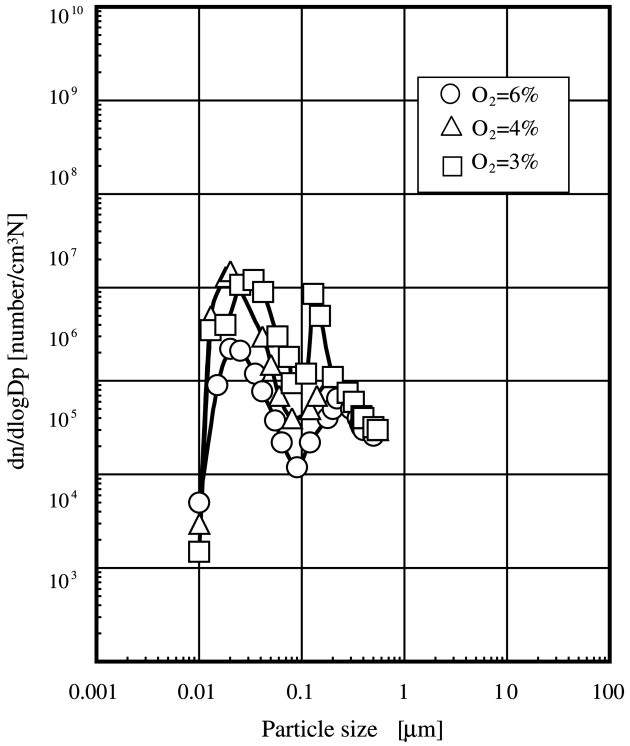


FIGURE 2.14.2 Emission characteristics of fine particles from pulverized coal combustion. (From Makino, H., *J. Aerosol Research Japan,* 4, 206–210, 1989. With permission.)

E_g, and orders d and e are determined experimentally.[12,13] Besides, recently, the rate of reaction, which takes into account the properties of the volatile matter such as transport coefficients, laminar flame speed, and unburned gas temperature, is proposed.[14]

Since the gaseous combustion between volatilized gas and combustion air is strongly affected by the mixing of them, it should be discussed with flow behavior. The reaction rate of volatilized gas is fast, but soot particles are formed under the condition that the mixing of volatilized gases and combustion air is not enough. Figure 2.14.2[15] shows the emission characteristics of fine particles of less than 1 μm against the excess O_2 concentration in the exhaust gas. As the excess O_2 concentration decreases, the concentration of particles of the order of 0.1 μm, which are thought to be soot, increases.

2.14.4 SOLID COMBUSTION

The combustion of fixed carbon, which is often referred to as char, is explained. The char burning rate is calculated using Field et al.'s model[16]:

$$\frac{dC}{dt} = -\left(\frac{K_c K_d}{K_c + K_d}\right) P_g \pi D_p^2 \tag{2.14.5}$$

$$K_d = \frac{5.06\times10^{-7}}{D_p}\left(\frac{T_p + T_g}{2}\right)^{0.75} \tag{2.14.6}$$

$$K_c = A_c \exp\left(-\frac{E_c}{RT_p}\right) \tag{2.14.7}$$

where

C is the char mass

K_c and K_d are the chemical and diffusion rate coefficients, respectively

P_g is the partial pressure of oxygen in the bulk gas

This model is obtained under the assumption that the char burning rate is controlled by both the chemical reaction rate and the diffusion rate of oxygen to the surface of the char particle. The values of the kinematic parameters of the preexponential factor A_c and activation energy E_c in Equation (2.14.7) are determined experimentally.[4] Besides, recently, a char combustion model, which considers the radial distributions of various properties in a particle, is proposed.[17] It is considered that the char burning rate is dominated by the chemical reaction rate at a temperature less than 1000°C, whereas it is dominated by the diffusion rate at higher temperatures.

The remaining particles consist of ash and char. If the particle temperature is higher than the melting points of the particles, the particles become spherical due to the surface tension and solidify again as the particle temperature decreases. The remaining combustible char is exhausted as pure char particles or contained in ash particles.

REFERENCES

1. Makino, H., Ito, S., *J. Soc. Powder Technol. Jpn*., 34, 247–254, 1997.
2. Tominaga, H., *Sangyou Nenshou Gijutsu*, The Energy Conservation Center, Japan, 2000, pp. 93–100.
3. Van Krevelen, D. W., Van Heerden, C., Huntjens, F. J., *Fuel*, 30, 253–258, 1951.
4. Kurose, R., Tsuji, H., Makino, H., *Fuel*, 80, 1457–1465, 2001.
5. Fletcher, T. H., Kerstein, A. R., Pugmire, R. J., Grant, D. M., *Energ. Fuel*., 4, 54–60, 1990.
6. Fletcher, T. H., et al., *Energ. Fuel*., 6, 414–431, 1992.
7. Solomon, P. R., Serio, M. A., Suuberg, E. M., *Prog. Energ. Combust*., 18, 133–220, 1992.
8. Niksa, S., *Combust. Flame*, 100, 384–394, 1995.
9. Kobayashi, H., Howard, J. B., Sarofin, A. F., *Sixteenth Symposium (International) on Combustion*, The Combustion Institute, 1976, pp. 411–425.
10. Hashimoto, N., et al., *Combust. Flame*, 159, 353–366, 2012.
11. Magnussen, B. F., Hjertager, B. W., *Sixteenth Symposium (International) on Combustion*, The Combustion Institute, 1976, pp. 719–729.
12. Borman, G. L., Ragland, K. W., *Combustion Engineering*, McGraw-Hill, 1998, pp. 120–122.
13. Kurose, R., Makino, H., Suzuki, A., *Fuel*, 83, 693–703, 2004.
14. Hara, T., et al., *Combust. Flame*, 162, 4391–4407, 2015.
15. Makino, H., *J. Aerosol Res. Jpn*., 4, 206–210, 1989.
16. Field, M. A., Gill, D. W., Morgan, B. B., Hawksley, P. G. W., *The Combustion of Pulverised Coal*, British Coal Utilisation Research Association, Leatherhead, Surrey, 1967.
17. Umetsu, H., Watanabe, H., Kajitani, S., Umemoto, S., *Combust. Flame*, 161, 2177–2191, 2014.



Taylor & Francis
Taylor & Francis Group
http://taylorandfrancis.com

2.15 Solubility and Dissolution Rate

Hirofumi Takeuchi

2.15.1 SOLUBILITY OF A SOLID

In the characterization of powdered materials, solubility and dissolution rate are important properties. These properties may become critical when a powdered material is used as a solution or when it can work effectively in a molecular form in solution. For example, bioactive components formulated in tablets or granules must dissolve to be absorbed in the gastrointestinal tract. The term "dissolution property" is widely used in these cases in the pharmaceutical sciences.

In chemistry, the material to be dissolved is called a solute, and liquid that dissolves a solute is called the solvent. When a solute is surrounded by a solvent, dissolution starts and will eventually stop. If any solute remains in the solvent at the point, the concentration of the solute is considered the solubility of the material. Solubility is generally intrinsic to the material, although it will vary from solvent to solvent.

The value of solubility is explained thermodynamically. The solubility of a solute B in a solvent A is expressed as follows.

$$-\ln x_B = \frac{\Delta h_B^m}{R}\left(\frac{1}{T}-\frac{1}{T_m}\right)+\ln f_B \qquad (2.15.1)$$

This equation can be derived by dividing the dissolution process into two steps: i) solute B is fused to become a liquid state; and ii) solute B in liquid form is mixed with solvent A. The change in the chemical potential of these steps ($\Delta\mu_B^f$, $\Delta\mu_B^m$) is expressed by the following equations.

$$\Delta\mu_B^f = \Delta h_B^m\left(1-\frac{T}{T_m}\right)\underset{=}{\rangle} 0 \quad \left(T \underset{=}{\rangle} T_m\right) \qquad (2.15.2)$$

$$\Delta\mu_B^m = RT\ln\left(f_B \cdot x_B\right) \qquad (2.15.3)$$

When the dissolution process has reached equilibrium, the increment in chemical potential is zero. Thus the following equation holds:

$$-\Delta\mu_B^f - \Delta\mu_B^m = 0 \qquad (2.15.4)$$

Equation (2.15.1) can be derived by substituting Equations (2.15.2 and 2.15.3) for Equation (2.15.4). When the resultant solution is assumed to be ideal, f_B in Equation (2.15.1) can be approximated to 1, and thus $\ln f_B$ is zero.

This equation can explain some tendencies of solubility to change by changing the dissolving temperature or properties of the solute, such as melting point and heat of fusion. A solute's fusion heat is related to its free energy in a solid state. A single material can contain several crystalline forms, called polymorphs. A metastable crystalline has higher free energy, and thus higher solubility, than a stable crystalline form. The use of polymorphs is one of the usual methods to modify solubility properties.

2.15.2 SOLUBILITY CHANGES AS PROPERTIES OF SOLVENT OR SOLUTE CHANGE

Change in pH of Solvent

As mentioned above, solubility of solute can be changed by changing the type of solute. In aqueous solution, because the ionization of a molecule makes the molecule soluble extensively, the solubility of some types of material can change extensively by changing the pH of the solute.

Weak base or weak acid is this case. As ionization of a weak acid or weak base, HA or B is presented by the acid-base equilibrium constant, K_a, solubility of HA or B can be expressed by the following equations.

$$C_s = [HA]\left(1+\frac{K_a}{[H^+]}\right) \qquad (2.15.5)$$

$$C_s = [B]\left(1+\frac{[H^+]}{K_a}\right) \qquad (2.15.6)$$

As pH = –log $[H^+]$, $pK_a = -\log K_a$, then Equations (2.15.5 and 2.15.6) are expressed as follows.

$$C_s = [HA]\left(1+10^{pH-pKa}\right) \qquad (2.15.7)$$

$$C_s = [B]\left(1+10^{pKa-pH}\right) \qquad (2.15.8)$$

According to these equations, the concentration of HA or B is double that of the unionized HA or B when the pH of the solute is pK_a.

Cosolvents

A solute is frequently more soluble in a mixture of solvents (e.g. water and water-miscible organic solvent) than in one solvent alone (e.g. water). This phenomenon is known as cosolvency, and the mixed solvents are called cosolvents. The solubility of phenobarbital is dramatically higher in

a water–alcohol–glycerin mixture than in water.[1] A linear relationship was found between the logarithm of observed solubility (S_m) of nonpolar nonelectrolyte solutes in a cosolvent–water mixture and the volume fraction of the cosolvent (x), as shown in Equation (2.15.9).[2]

$$\log S_m = S_w + \sigma x \tag{2.15.9}$$

Complex Formation of Solutes

Complex formation of a material with some other molecule sometimes changes an apparatus's solubility. To increase the solubility of a poorly soluble material, D, the addition of a complex forming material, X, leads to an increased apparent concentration by forming complex D-X in the solution. Figure 2.15.1 shows graphically the increase in the concentration of D as the concentration of X increases.

Although the actual solubility of D is constant, as shown in the value of the y-axis, the apparent solubility increases in proportion to the amount of material X. The complex concentration [D-X] is presented by complex formation constant $K_{D\text{-}X}$ as shown in Figure 2.15.1; the higher apparent concentration of D is obtained by the higher $K_{D\text{-}X}$ value.

Particle (Crystal) Sizes of Solutes

Finely divided particles have greater solubility than large particles. Therefore, the smaller particles will dissolve and their masses will re-precipitate on the larger particles. But solubility cannot be simply related to gross particle size, because it depends somewhat on the particle (crystal) face exposed, surface roughness, and surface irregularity. Under ideal conditions, the solubility of a spherical particle is expressed by

$$\log \frac{a_2}{a_1} = \frac{2\sigma_m M}{2.303\rho RT}\left(\frac{1}{r_2} - \frac{1}{r_1}\right) \tag{2.15.10}$$

Assuming that the activity of the solution is proportional to the molar concentration, Equation (2.15.10) can be rewritten as

$$\log \frac{S_2}{S_1} = \frac{2\sigma_m M}{2.303\rho RT}\frac{1}{r_2} \tag{2.15.11}$$

Very fine particles (less than ca. 1 μm in diameter) may affect solubility, which increases with decreasing particle size, as predicted by Equation (2.15.11).

2.15.3 DISSOLUTION RATE ANALYSIS: THEORY AND METHODS

Like solubility, the dissolution rate is also important in considering particle design from a practical point of view, and many researchers have characterized the dissolution rate.

The Noyes–Whitney equation is among the most popular empirical equations. Noyes and Whitney found that the dissolution rate is correlated with the solubility of the material and the surface area faced to a solute, and they proposed the following equation.[3]

$$\frac{dC}{dt} = k \cdot S \cdot (C_s - C) \tag{2.15.12}$$

This equation shows that the dissolution rate is proportional to the surface area faced to the solute. If the concentration of the material dissolved in the solute is low enough to be negligible, the dissolution rate is also proportional to the solubility.

Nernst,[4] as well as Brünner and Tolloczko,[5] assumed a stagnant liquid film, called a diffusion layer, around the particle surface schematically shown in Figure 2.15.2. A theoretical dissolution model was proposed based on this assumption.

In this model, the interface of solute to solvent is covered with the saturated solution of the solute, and the diffusion of a solute molecule from the saturated solution layer to the bulk solution is a rate-limiting step in the dissolution process.

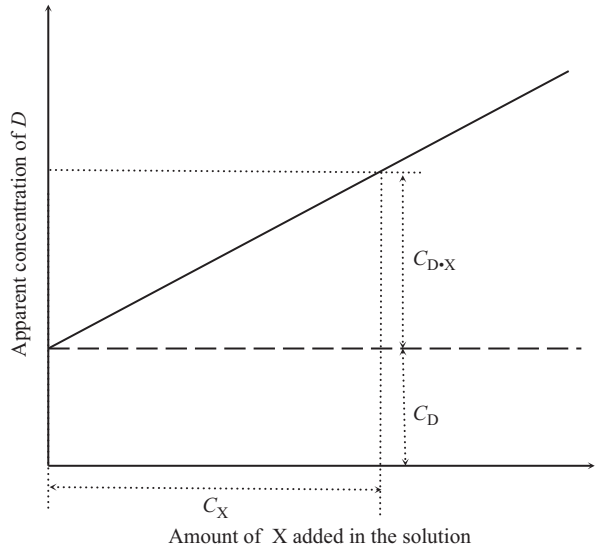


FIGURE 2.15.1 Apparent solubility change by complex formation.

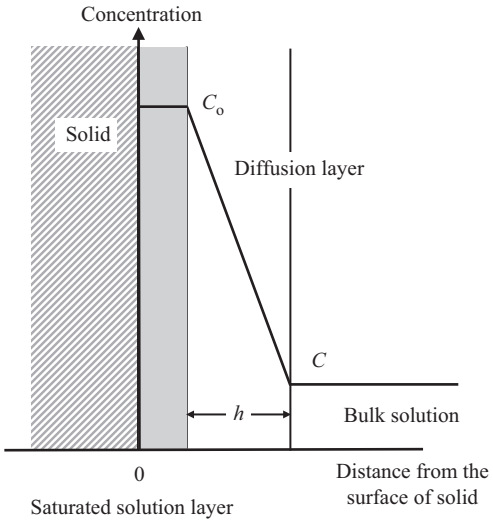


FIGURE 2.15.2 Diffusion layer model for dissolution.

By applying Fick's law to the diffusion process in the model, the flux of solute J is expressed as follows.

$$J = \frac{1}{S} \cdot \frac{dM}{dt} = -D \cdot \frac{dC}{dx} = D \cdot \frac{C_s - C}{h} \qquad (2.15.13)$$

where, M is the amount of solute (M_s).

Thus, the diffusion rate can be expressed as

$$\frac{dM_s}{dt} = S \cdot D \cdot \frac{C_s - C}{h} \qquad (2.15.14)$$

As we measure the concentration of solute in the solvent to analyze the dissolution rate, Equation (2.15.14) is converted to Equation (2.15.15) by changing the mass of solute M to its concentration. The Nernst–Noyes–Whitney equation can be derived as follows:

$$\frac{dC}{dt} = \frac{S \cdot D}{V} \cdot \frac{C_s - C}{h} \qquad (2.15.15)$$

In comparing Equation (2.15.15) with Equation (2.15.12), the apparent dissolution rate constant k in the Noyes–Whitney Equation (2.15.2) can be expressed as

$$k = \frac{D}{V \cdot h} \qquad (2.15.16)$$

When the several factors that affect the dissolution rate of a solute are considered, changes can be well explained by the rate constant k in the Nernst–Noyes–Whitney equation. For example, if the stirring condition is changed from mild to vigorous, the diffusion layer, h, becomes thinner, thus the dissolution rate is accelerated; if the dissolution temperature is increased, the diffusion coefficient increases, as does the solubility of the solute.

The diffusion coefficient, D, is defined by Einstein as,

$$D = \frac{\kappa T}{6\pi\eta\gamma_m} \qquad (2.15.17)$$

This equation means that a decrease in the viscosity of the dissolution medium, in conjunction with an increase in temperature, leads to an increase in the diffusion coefficient.

In the measurement of dissolution rates, the Noyes–Whitney equation is often used because it is simple and well supported theoretically by the Nernst consideration with the diffusion layer model, as mentioned above. The change in the amount of solute in a solvent is measured as its concentration at suitable time intervals. Thus, it is convenient that the equation is expressed as the concentration at the time of measurement. By integrating Equation (2.15.12) under the initial condition, $C = 0$ at $t = 0$, the equation can be expressed as

$$\ln(C_s - C) = -kSt + \ln C_s \qquad (2.15.18)$$

If the surface area of the solute can be kept constant, the dissolution profile based on Equation (2.15.18) may show a straight line in the plot of $\ln(C_s - C)$ against the dissolution time, t, as shown in Figure 2.15.3. However, the effective surface area, S, usually decreases as the dissolution progresses, and thus the plot of $\ln(C_s - C)$ against t gradually deviates below the straight line.

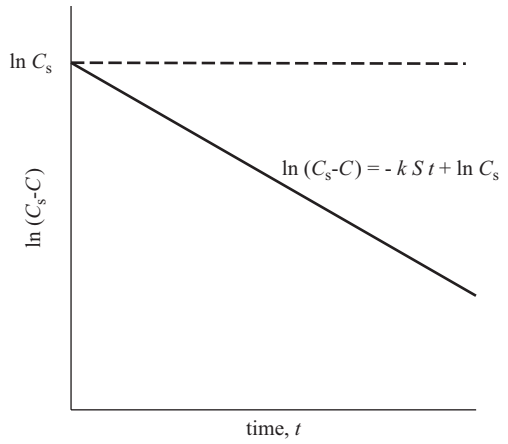


FIGURE 2.15.3 Dissolution profile based on Noyes-Whitney equation.

To establish an experimental condition in which the effective surface area, S, is constant, several techniques, such as the rotation disk method and the stationary disk method, have been reported. In the former method, a typical constant surface area disk is constructed by mounting a tablet on a holder with paraffin wax such that a single surface of the tablet is exposed to the dissolution medium.[6] Wood et al.[7] devised an assembly for compressing the tablet, which can also be used as the tablet holder during dissolution. The apparent dissolution rate can be measured by a simple beaker method.[8]

Hixon and Crowell[9] proposed a dissolution rate equation for the particulate material by considering the decrease in the surface area during the dissolution test. In assuming the surface area of spherical, cubic, or cylindrical monodispersed particles, under the conditions as an isotropic dissolution and sink condition ($C_s >> C$), the following equation can be derived from the Noyes–Whitney equation.

$$W_0^{1/3} - W^{1/3} = \left(\frac{\pi NP}{6}\right)^{1/3} \frac{2DC_s}{\delta P} t \qquad (2.15.19)$$

This is called the Hixon and Crowell equation. As the cube root value of the solute weight loss is proportional to the dissolution time, this equation is alternatively called the cube root law.

To establish a different model than the diffusion layer model, Danckwerts[10] assumed that the surface of a solid particle dispersed in liquid is continuously renewed with fresh liquid by eddy diffusion. According to this model, there is no stagnant liquid film and the solute concentration at the surface of the particle is not C_s, but a lower-limiting concentration, C_i. The solute dissolves into renewed fresh liquid during its stay at the interface. The solvent with the dissolved solute is

continuously replaced by fresh solvent. The model proposed is described by Equation (2.15.20):

$$\frac{dm}{dt} = S\sqrt{\gamma D}(C_s - C) \tag{2.15.20}$$

2.15.4 METHODS TO IMPROVE THE SOLUBILIZATION OF POWDERED MATERIALS

Crystalline Forms Including an Amorphous Form

Polymorphism occurs when different molecular arrangements are present in the solid phase, resulting in two or more crystalline forms. The differences in the crystal energy of polymorphs generally lead to differences in physical properties, such as melting point, solubility, and density, even though the crystals are chemically identical. Crystalline forms can be controlled by changing the type of solvent or temperature in the precipitation process.

As shown in Figure 2.15.1 described in 2.15.1, metastable solid polymorphs having higher thermodynamic activity increase solubility, which may lead to an increased dissolution rate. Thus, in preparing solid pharmaceutical preparations, such as granules or tablets, the crystalline form of an active pharmaceutical ingredient (API) is an important property, especially for drugs that have poor water solubility. So far, many reports have found polymorphs for a number of APIs, such as prednisolone, aspirin, ampicillin, barbital, benzoic acid, sulfathiazole, chloramphenicol, and novobiocin. A comparison of the solubility of polymorphs of chloramphenicol palmitate reveals that the solubility of polymorph B of chloramphenicol palmitate is roughly twice that of polymorph A.[11] Phenylbutazone has five different polymorphic forms. Among them, Form I is thermodynamically the most stable and has the lowest equilibrium solubility.[12] The polymorphism effect of cimetidine with four different crystalline forms (A, B, C, D) having different solubilities on stress ulceration after oral administration in rats was reported.[13]

Regarding the free energy of a solid, that of an amorphous form has greater free energy than metastable crystalline. Thus, higher solubility is expected for a solute in an amorphous form. A list of the solubility ratios of amorphous drugs compared to those of the crystalline form are shown in Table 2.15.1.[14,15]

One of the defects of amorphous forms is their relatively poor stability. Especially, stability during storage for a long term, such as three years, is required for pharmaceutical products containing API. To overcome this problem, a concept of solid dispersion, where API molecules are molecularly dispersed in suitable carriers, has been developed in the design of pharmaceutical dosage forms. The original concept can be found in a paper on the preparation of a eutectic mixture of sulfathiazole and urea, reported by Sekiguchi and Obi.[16] This preparation improved the dissolution of sulfathiazole dispersed in urea as micronized crystals. Coprecipitation of a poorly soluble drug, such as sulfathiazole[17] or griseofulvin,[18] with polyvinyl-pyrrolidone, polyethylene glycol, or urea can increase the dissolution rate. Spray drying is one of the methods of preparing solid dispersion through coprecipitation of a drug and a carrier. Corrigan et al. demonstrated the formation of the amorphous form of thiazide diuretics by spray drying an alcoholic solution of the drug with hydrophilic polymers. Takeuchi et al. reported the preparation of solid dispersion particles of tolbutamide[19] or indomethacin[20] with enteric coating polymers or colloidal silica by use of a spray drying method. The fusion method is an alternative method of preparing solid dispersion systems.

Inclusion Compounds and Complex Formation

Cyclodextrin, which is an oligosaccharide consisting of 6–8 glucose molecules and has a cyclic structure as illustrated in Figure 2.15.4, can form an inclusion compound as a host molecule. Three well-known types of cyclodextrin, α, β, and γ-cyclodextrin, have different cavity sizes depending on the number of glucose molecules constituting the cyclodextrin molecule. As the cavity inside the molecule is hydrophobic, a hydrophobic molecule or hydrophobic parts of a molecule

TABLE 2.15.1 Solubility Ratio for Amorphous to Crystalline Form

Drug (Temp. in °C)	More Soluble Phase/Less Soluble Phase	Solubility Ratio	Ref.
Caffeine (25)	Amorphaous/crystalline	6.5	(14)
Diacetylmorphine (25)	Amorphaous/crystalline	16	(14)
Theophylline (17)	Amorphaous/crystalline	58	(14)
Theobromine (16)	Amorphaous/crystalline	50	(14)
Morphine (20)	Amorphaous/crystalline	268	(14)
Hydrochlorothiazide (37)	Amorphaous/crystalline	1.1	(15)
Bendrofluazide (37)	Amorphaous/crystalline	2.8	(15)
Cyclothiazide (37)	Amorphaous/crystalline	6.2	(15)
Cyclopenthiazide (37)	Amorphaous/crystalline	8.3	(15)
Polythiazide (37)	Amorphaous/crystalline	9.8	(15)

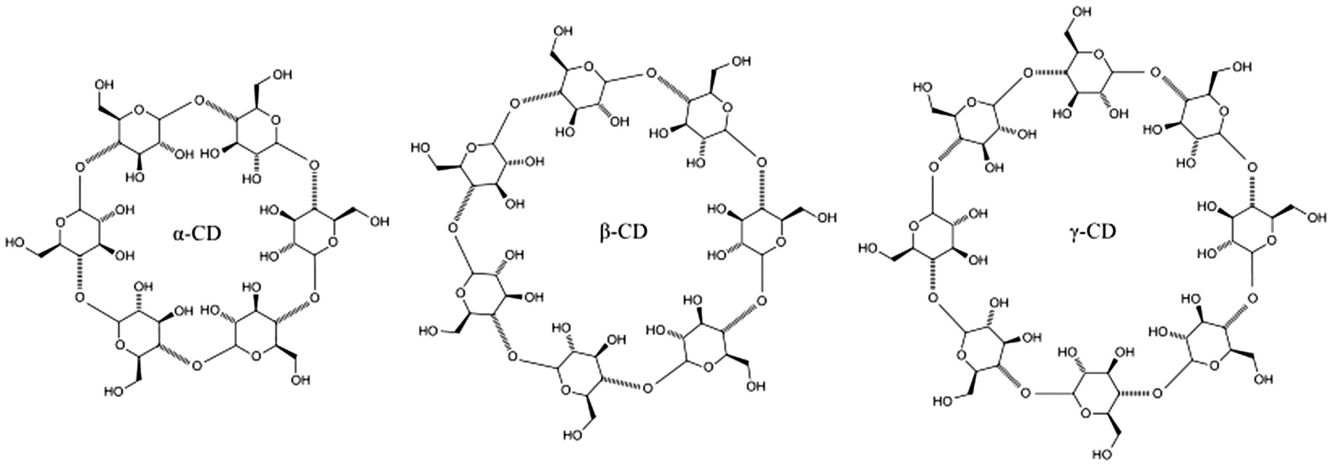


FIGURE 2.15.4 Structure of cyclodextrins (α-,β-,γ-).

tend to be included. As the outer side of cyclodextrin is hydrophilic, the resultant inclusion compounds can have higher solubility than the guest molecule.

Chemical modification of cyclodextrins has been tried in order to develop some useful derivatives such as dimethyl-β-cyclodextrin and hydroxypropyl-β-cyclodextrin. These derivatives have higher solubility than the original β-cyclodextrin. A significant enhancement in drug solubility by using inclusion compounds has been reported by several researchers. Table 2.15.2 lists the solubility of several drugs with poor water solubility in the form of an inclusion compound with hydroxypropyl-β-cyclodextrin.[21]

While cyclodextrins themselves are in crystalline form, their inclusion compounds tend to become amorphous. This property may also help to improve the dissolution properties of inclusion compounds with cyclodextrins.

Complex formation of a solute molecule with a suitable molecule of solubilizing agents can improve its solubilizing property, as mentioned in 2.15.2. In pharmaceutical technology, several combinations of API and solubilizing agents have been used. For example, aminophylline, which was developed to improve the solubilizing property of theophylline, is a combination of theophylline and ethylene diamine. Other combinations are iodine and potassium iodine, caffeine and sodium salicylate, and so on.

Solubilizing with micelles consisting of surface active agents is different from complex formation. However, it is a conventional method of improving the solubilizing property of drugs with poor water solubility. Comprehensive reviews of solubilization in surfactant systems were prepared by Swarbrick[22] and Elworthy et al.[23] Surface active agents are also formulated by simple mixing to improve the dissolution rates of drugs or other materials by increasing wettability on the surface of a particle.

TABLE 2.15.2 Solubility Enhancement through the Use of High Concentrations of HP-β-CD

Solute	%HP-β-CD	Solubility Enhancement
Estriol	50	13,666
Estradiol	40	7,000
Progesterone	40	2,266
Spironolactone	40	1,400
Testosterone	40	1,461
Digoxin	50	971
Dexamethasone	50	240
Chlorthalidone	50	87.5
Diphenylhydantoin	50	57
Furosamide	50	24
Nitroglycerin	40	8.3
Acetamidopen	50	6
Apomorphine	50	5.8
Theophylline	50	1.3

Micronizing of Crystals

Micronization is one of the simplest and most popular methods of improving the solubilizing properties of materials. As described in 2.15.1, an increase in the effective surface area facing a solvent effectively increases the dissolution rate; extremely fine particles less than ca. 1 μm can increase solubility compared with coarse particles of the same material. However, micronized particles tend to aggregate, and as a result their dissolution rates are sometimes slower than before micronization because of the decrease in effective surface area facing the dissolution medium under pharmaceutical dissolution test conditions.

Co-grinding the poorly water soluble drugs with hydrophilic additives is an effective way to increase the dissolution rate of micronized particles of materials having poor water solubility. When ground with microcrystalline cellulose, methylcellulose, chitin, or chitosan using a ball mill, drugs with poor water solubility show significantly increased dissolution rates and solubility.[24] In this process, crystalline drugs become disordered frequently, thereby increasing solubility. Takahata et al.[25] found that co-pulverizing poorly soluble

pharmaceuticals, such as griseofulvin, oxolinic acid, and phenytoin, with a water-soluble additive (e.g. mannitol, sorbitol, glucose, or glycine) was significantly useful to sub-micronize drug particles without changing crystallinities.

To prepare submicron-sized particles, two types of wet processes have been reported. One is the wet milling method with special instruments such as a bead mill or a high-pressure homogenizer.[26] The other is a precipitation method with a high-pressure homogenizer[27,28] or supercritical carbon dioxide.[29] The former method has been applied to prepare commercial products under the trade nameNanoCrystal®. With either method the addition of suitable stabilizing agents such as hydrophilic polymers or sugars is required to maintain very fine particle sizes.[30–32]

NOTATION

A: Surface area of antacid
a: Constant
a_1: Activity of solute in a solution produced with larger particles
a_2: Activity of solute in a solution produced with smaller particles
b: Constant
C: Concentration of solute in solvent
C_s: Solubility of solute
D: Diffusion coefficient of solute
f_B: Fugacity of B
h: Thickness of diffusion layer
Δh_B^m: Molar heat of fusion of B
K_a: Acid-base equilibrium constant
k: Apparent dissolution rate constant
M: Molecular weight
M_s: Amount of solute
m: Dissolved mass
N: Number of particles
R: Gas constant
r_1: Radius of larger particle
r_2: Radius of smaller particle
r_m: Radius of molecule
S: Surface area of solute
S_1: Solubility of larger particle
S_2: Solubility of smaller particle
T: Temperature at the time of dissolution
T_m: Melting point
t: Time
V: Volume of solute
W: Weight of particles at time t
W_o: Initial weight of particles
x: Volume fraction of cosolvent
x_B: Molar concentration (molar faction) of B in solution
γ: Rate of surface renewal
η: Viscosity of medium
κ: Boltzmann constant
ρ: Density of particle
σ: Slope of a plot of log S_m against x
σ_m: Mean interfacial tension

REFERENCES

1. Krause, G. M., Cross, J. M., *J. Am. Pharm. Assoc. Sci. Ed.*, 40, 137–139, 1951.
2. Yalkowsky, S. H., Flynn, G. L., Amidon, G. L., *J. Pharm. Sci.*, 61, 983–984, 1972.
3. Noyes, A., Whitney, W. I., *Z. Phys. Chem.*, 23, 689–692, 1897.
4. Nernst, W., *Z. Phys. Chem.*, 47, 52–55, 1904.
5. Brünner, E., Tolloczko, S. T., *Z. Phys. Chem.*, 47, 56–102, 1904.
6. Nogami, H., Nagai, T., Suzuki, A., *Chem. Pharm. Bull.*, 14, 329–338, 1966.
7. Wood, J. H., Syarto, J. E., Letterman, H., *J. Pharm. Sci.*, 54, 1068, 1965.
8. Levy, G., Hayes, B. A., *New Engl. J. Med.*, 262, 1053–1058, 1960.
9. Hixon, A., Crowell, J., *Ind. Eng. Chem.*, 23, 923–931, 1931.
10. Danckwerts, P. V., *Ind. Eng. Chem.*, 43, 1460–1467, 1951.
11. Aguiar, A. J., Krc, J., Kinkel, A. W., Samyn, J. C., *J. Pharm. Sci.*, 56, 847–853, 1967.
12. Tuladhar, M. D., Carless, J. E., Summers, M. P., *J. Pharm. Pharmacol.*, 35(5), 269–274, 1983.
13. Kokubo, H., et al., *Int. J. Pharm.*, 35, 181–183, 1987.
14. Toffoli, F., et al., *Ann. Chem.*, 63, 1–4, 1973.
15. Corrigan, O. I., Holohan, E. M., Sabra, K. *Int. J. Pharm.*, 18, 195–200, 1984.
16. Sekiguchi, K., Obi, N., *Chem. Pharm. Bull.*, 9, 866–872, 1961.
17. Simonelli, A. P., Mehta, S. C., Higuchi, W. I., *J. Pharm. Sci.*, 58, 538–549, 1969.
18. Chiou, W. L., Riegelman, S., *J. Pharm. Sci.*, 58, 1505–1510, 1969.
19. Takeuchi, H., Handa, T., Kawashima Y., *Chem. Pharm. Bull.*, 35, 3800–3806, 1987.
20. Takeuchi, H., Nagira, S., Yamamoto, H., Kawashima, Y., *Powder Technol.*, 141, 187–195, 2004.
21. Pitha, J., et al., *Int. J. Pharm.*, 29, 73–82, 1986.
22. Swarbrick, J., *J. Pharm. Sci.*, 54, 1229–1237, 1965.
23. Elworthy, P. H., Florence, A. T., Macfarlane, C. B., in *Solubilization by Surface Active Agents*, Chapman & Hall, London, 1968, p. 335.
24. Nakai, Y., *Yakugaku Zasshi*, 105, 801–811, 1985.
25. Takahata, H., Nishioka, Y., Osawa, T., *Funtai to Kogyo (Powder and Industry)*, 24, 53*, 1982.
26. Keck, C. M., Rainer, Muller, R. H., *Eur. J. Pharm. Biopharm.*, 62, 3–16, 2006.
27. Muller, R. H., Perers, K., *Int. J. Pharm.*, 160, 229–237, 1998.
28. Liversidge, E. M., Liversidge, G. G., Cooper, E. R., *Eur. J. Pharm. Sci.*, 18. 113–120, 2003.
29. Langguth, P., et al., *Drug Dev. Ind. Pharm.*, 31, 319–329, 2005.
30. Byrappa, K., Ohara, S., Adschiri, T., *Adv. Drug Deliv. Rev.*, 60, 299–327, 2008.
31. Sigfridsson, K., et al., *Eur. J. Pharm. Biopharm.*, 67, 540–547, 2007.
32. Gao, L., et al., *Drug Dev. Ind. Pharm.*, 33, 1332–1339, 2007.

Part 3

Properties of Powders and Powder Beds



Taylor & Francis
Taylor & Francis Group
http://taylorandfrancis.com

3.1 Specific Surface Area

Takashi Takei

3.1.1 DEFINITION OF SPECIFIC SURFACE AREA

The specific surface area S_W (m^2/kg) of a powder is one of the basic properties of the powder. This value represents the internal and external surface area of total particles contained in a unit mass of powder, which can be measured using various probes, such as gases and liquids. In the case of the adsorption method, adsorptive gas as a probe molecule must be accessible to all of the surfaces in cavities, cracks and micropores. Nowadays, powders used as raw materials and intermediate manufactured goods come to more important materials, and industrial needs concerning particle size, particle shape, purity and uniformity of powders become more severe. For example, fine powders, purity and uniformity are necessary for the manufacturing of precision materials such as electronics and fine ceramics. When the particle size decreases markedly, powdery phenomena depend largely on surface properties. Therefore, characterization of the powder surface becomes significant more and more with a decrease in the diameter of powder particles.

The surface area S of spherical particle type having a diameter of D_i is obtained from

$$S = \pi D_i^2 \tag{3.1.1}$$

The mass W of the particle having the density of ρ is

$$W = \frac{\pi D_i^3 \rho}{6} \tag{3.1.2}$$

If distributions of particle size and shape in a powder sample are known, the surface area of the powder can be calculated. For example, when the particle is spherical and the number of the particles having diameter of D_i is n_i, the specific surface area S_W of the powder is given by

$$S_W = \frac{\sum n_i \pi D_i^2}{\sum n_i \pi D_i^3 \rho / 6} \tag{3.1.3}$$

If the particle size is assumed to be uniform as for the spherical or cubic type, Equation (3.1.3) is reduced to

$$S_w = \frac{6}{D_m \rho} \tag{3.1.4}$$

where D_m represents the particle diameter based on the specific surface area. Therefore, the particle diameter can be estimated from the specific surface area.

3.1.2 ESTIMATION OF SURFACE AREA BY GAS ADSORPTION[1,2]

BET Method

The surface area of powder is generally determined by the gas adsorption method. In this case, it is necessary to obtain the monolayer capacity and cross-sectional area of an adsorbate molecule. To estimate the monolayer capacity V_m, the Brunauer–Emmett–Teller (BET) equation[3] has been applied to experimental adsorption data. The BET equation can be represented by

$$V = \frac{V_m C\left(\frac{P}{P_0}\right)}{\left(1-\frac{P}{P_0}\right)\left(1-\frac{P}{P_0}+C\left(\frac{P}{P_0}\right)\right)} \tag{3.1.5}$$

where V is the adsorbed amount at vapor pressure P. As the saturated vapor pressure at the measurement temperature is P_0, P/P_0 is designated the relative pressure. The constant C value is approximately represented by

$$C \approx \exp\left(\frac{E_1 - E_L}{RT}\right) \tag{3.1.6}$$

where E_1 and E_L are the heat of adsorption of the first adsorbed layer and liquefaction heat of adsorbate, respectively. Therefore, the C value means the interaction between the adsorptive molecules and the solid surface. The shape of the adsorption isotherm in the low relative pressure region depends on the C values (Figure 3.1.1). Above 100 of the C value, the adsorption isotherm shows a sharp "knee" at low pressure ($P/P_0 < 0.1$). The "knee" is rounded below 100.

The experimental formula of the BET equation can be represented by

$$\frac{P}{V(P_0 - P)} = \frac{1}{V_m C} + \frac{C-1}{V_m C}\frac{P}{P_0} \tag{3.1.7}$$

The plot of $P/V(P_0-P)$ against P/P_0 should therefore exhibit a straight line with slope $(C-1)/(V_mC)$ and intercept $1/(V_mC)$. This plot is called the BET plot. The BET plot empirically holds within the relative pressure range 0.05–0.35, however, the linearity should be checked. The slope $(C-1)/(V_mC)$ and intercept values $1/V_mC$, are determined graphically or by linear regression. Therefore, the monolayer capacity V_m can be

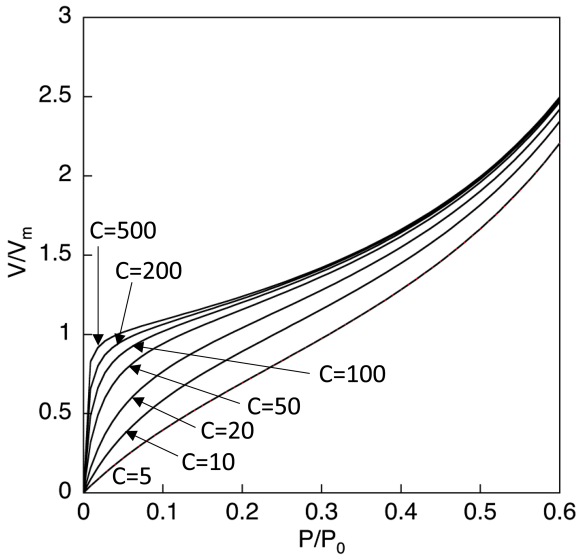


FIGURE 3.1.1 The shapes of the adsorption isotherms based on the BET equation.

derived from the summation between the slope and intercept values, as shown in

$$\frac{1}{V_m} = \frac{1}{V_m C} + \frac{C-1}{V_m C} \tag{3.1.8}$$

The BET equation was proposed about 80 years ago, and has been used as a highly reliable method to determine the specific surface area without a modification of the equation.

To calculate the surface areas of powders, another important value is needed, that is, the cross-sectional area σ of an adsorbate molecule. When the monolayer capacity V_m is given in terms of mlSTP, where STP means the gas volume at standard temperature and pressure (0°C and 1 atm), the surface area S of powder can be obtained from the product of V_m and σ, as follows.

$$S = \frac{V_m \sigma N_A}{22.4 \times 10^3} \tag{3.1.9}$$

where N_A is Avogadro's number. A reasonable estimation of the cross-sectional area of an adsorbate molecule is generally obtained from liquid density ρ of the adsorptive at measurement temperature using Equation (3.1.10) with the following assumptions: (a) shape of an adsorptive molecule is spherical, (b) the liquid structure of the adsorptive is the closest packing structure with 12 nearest neighbors, and (c) the adsorptive molecules are adsorbed on the particle surface with six nearest neighbors in the close-packed hexagonal arrangement:[4]

$$\sigma = 1.091 \left(\frac{M}{\rho N_A} \right)^{2/3} \tag{3.1.10}$$

The factor 1.091 in Equation (3.1.8) is a packing factor deduced from the assumption described above and M is molecular weight of the adsorptive. In the case of nitrogen adsorption at 77 K, the specific surface area (m^2/g) is estimated from the following equation, when the unit of the monolayer capacity V_m represented by mlSTP.

$$S = 4.35 \times V_m \left(\frac{m^2}{g} \right) \tag{3.1.11}$$

TABLE 3.1.1 Cross-Sectional Areas of Molecules Used for the Determination of Surface Area by Gas Adsorption

Gas	Measurement Temperature (°C)	Bulk State*	σ (nm^2)
N2	−183	G	0.170
	−196	L	0.162
Ar	−183	L	0.143
	−196	S	0.138
Kr	−196	S	0.202
Xe	−183	S	0.232

* Phase of bulk state at measurement temperature.
G:gas, L:liquid, S:solid.

The recommended molecular cross-sectional areas of adsorbate gases using the surface area determination are summarized in Table 3.1.1. The nitrogen molecule is generally used as an adsorptive molecule. If the surface area is relatively small (<1 m^2), a krypton[5–7] or xenon[8,9] molecule is used as a probe molecule. In these cases, the accurate pressure measurement of very low pressure (<133 Pa) is required.

Single-Point Method

The BET plots empirically show a linear relationship in the relative pressure range of $0.05 < P/P_0 < 0.35$. The C value in the BET equation is a constant which expresses a magnitude of the interaction between solid surface and adsorptive molecules. When the C value is reasonably high, the intercept value $1/(V_m C)$ becomes zero. Then the BET plots are recognized to be a linear line passing close to the origin. In this case, Equation (3.1.7) is rewritten as

$$\frac{P}{V(P_0 - P)} = \frac{1}{V_m} \frac{P}{P_0} \tag{3.1.12}$$

Equation (3.1.11) is reduced to

$$V_m = V \left(1 - \frac{P}{P_0} \right) \tag{3.1.13}$$

Consequently, the surface area can be determined by measuring only one adsorbed amount at vapor pressure P in the relative pressure range of 0.05–0.35. This method is called "single-point method." This method can be applicable to many inorganic materials exhibiting the large C values for N_2 adsorption, however, in the case of the materials with the small C values, for example, molecular solids (ice, organic polymer, etc.)

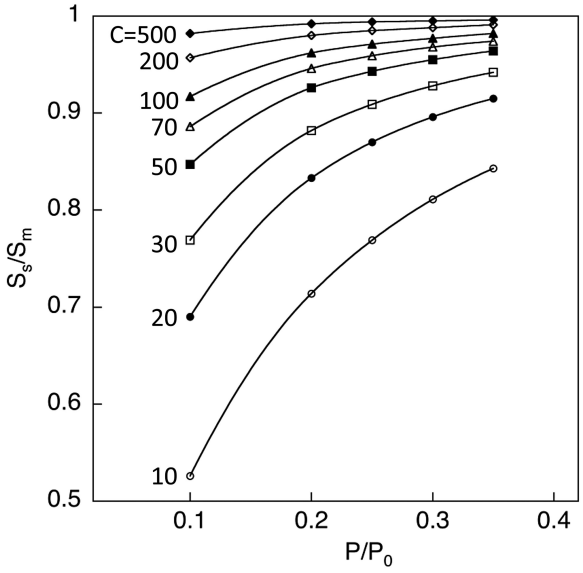


FIGURE 3.1.2 The error of the specific surface areas determined by the single point method (S_s) compared to the BET multipoint method (S_m) in various C values and the employed relative pressures in the calculation by the single point method.

and solids modified by organic functional groups, the careful application of this method should be considered. The error in the single-point method compared to the BET multi-point method shows in Figure 3.1.2. These results suggest that the error is a few percent or less when the C value is 100 or more and the adsorbed amount at high relative pressure (<0.2) is employed. If this method is applied to the materials with the low C value, the adoption of the adsorbed amount at higher relative pressure (=0.35) is recommended.

3.1.3 METHODOLOGY OF GAS ADSORPTION[1,10]

Volumetric Method

This method is the most standard method. A simplified volumetric apparatus is shown in Figure 3.1.3. A dosing volume in an adsorption apparatus must be determined to calculate adsorbed amounts. The volume is obtained by the expanding of noble gases such as He and N_2 from known volume to a volume of an objective part. It is necessary to measure the pressures before and after the expanding of the noble gas. An equilibrium pressure is determined using a pressure transducer, for example, a capacitance manometer.

To obtain an adsorption isotherm, a known amount of adsorptive gas is introduced into a sample tube. The sample adsorbs the adsorptive molecules, and the vapor pressure decreases gradually until equilibrium attains. The introducing pressure and equilibrium pressure must be measured precisely. The adsorbed amount is determined from the difference between the introduced amount and residual amount. The residual amount is evaluated from the same procedure using He gas. In this case, adsorption of He molecules does not occur. Therefore, the adsorbed amount is determined from the difference between the amount of introduced

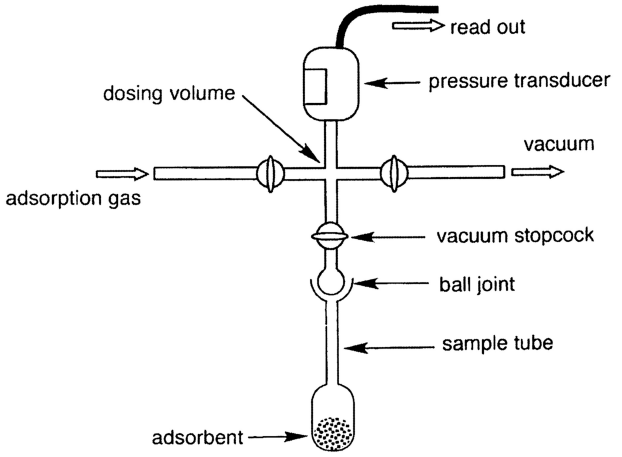


FIGURE 3.1.3 Schematic diagram of a volumetric apparatus.

adsorptive molecules and the amount of He gas introduced into the sample tube, comparing at the same equilibrium pressure. By repeating this procedure, adsorbed amounts at various pressures can be obtained. Generally, estimation of the residual amount of adsorptive molecules is performed using He gas, then a dead volume is determined. The residual amounts of adsorptive molecules at the other vapor pressures are calculated using this dead volume. Usually the adsorptive gas is assumed as an ideal gas in the calculation of the amount of gas. In the special case, the correction of a non-ideal gas and the thermal transpiration effect[11] are required. The dead volume must be measured immediately before or after the adsorption measurement. During the measurement, the surface level of liquid nitrogen in a cooling bath should be maintained constant within 1 mm at least 5 cm above the powder sample.

Nowadays the apparatuses of the automatic analysis of the specific surface area by the gas adsorption is commercially available. So, the researchers can measure the specific surface area easily and efficiently without the knowledge of the principles of the volumetric method. However, the users should carefully determine the following conditions to obtain good data: the sample mass (dependence on surface area), the pretreatment outgassing temperature and time, the kind of adsorptive and the judgement on the equilibrium attainment.

Gravimetric Method

In this method, the adsorbed amount is directly determined by measuring the increase in sample weight. The advantage of this method compared to the volumetric method is that the adsorption measurement of the condensable gas (water, ethanol, etc.) at high relative pressure is easily obtained. Because the condensation of such vapor at high relative pressure on the surface of the apparatus occurs, the amount of gas cannot be preciously estimated from the pressure measurement in the volumetric method.

When a monolayer adsorption is accomplished on a powder surface by nitrogen molecules, the increasing weight is calculated to be 0.287 mg/m^2. If the specific surface area of a

powder is 100 m^2/g, the 1-g powder sample adsorbs 28.7-mg nitrogen molecules. This weight change can sufficiently be measured by an ordinary balance. Initially the quartz spring microbalance was employed, however, it is difficult to get the quartz spring now. Several vacuum electro balance instruments for the gas adsorption measurement are commercially available.[10] In this method, a correction due to buoyancy produced by volumes of sample powder and sample supporter is necessary. In the case of nitrogen adsorption, the buoyancy of a 1-ml volume at a relative pressure of 0.3 and at temperature 77 K is calculated to be 0.0594 mg.

3.1.4 ESTIMATION OF SURFACE AREA BY GAS FLOW (PERMEAMETRY)[12]

The surface area of a powder can be determined by measuring the pressure drop during fluid flow through a packed powder bed. The measuring method is based on the Kozeny–Carman equation[13]

$$S_w = \frac{1}{\rho}\left[\left(\frac{\Delta PtA}{k_k \eta LV}\right)\left(\frac{\varepsilon^3}{(1-\varepsilon)^2}\right)\right]^{1/2} \tag{3.1.14}$$

where

- S_w is the specific surface area of the sample powder
- ΔP is the pressure drop
- t is time
- A is cross-sectional area of the powder bed
- L is length of the powder bed
- ε is the porosity of the powder bed
- ρ is the true density of the sample powder
- k_k is the Kozeny constant which is usually taken as 5
- η is the viscosity coefficient of the fluid
- V is the volume of fluid passed through powder bed during time t

The porosity ε of the powder bed is calculated from the following equation,

$$\varepsilon = 1 - \frac{M}{\rho AL} \tag{3.1.15}$$

where M is the mass of the powder.

Therefore, the specific surface area Sw of the powder bed whose porosity is known can be determined by measuring the flow rate V/t and pressure drop ΔP of fluid. However, in order to use this equation, it is necessary that the stream of permeating fluid has a viscous flow and the Hagen–Poiseuille law can be applied. The surface area thus obtained expresses the external surface area and does not contain internal surfaces in the micro pores and cracks. In this point, the surface area obtained by the permeametry is qualitatively different from that obtained by the gas adsorption.

When air is used as a fluid material, the mean free path λ of gas molecules is calculated to be about $.1 \times 10^{-5}$ cm at 15°C under 1 atm. In this system, it is necessary for the viscous flow that the diameter D of the flow path is about 10 times larger than λ, that is, larger than about 1 μm. The gas flow mechanism changes with a decrease in the particle size of powders from viscous flow to the Knudsen flow which is governed by the rate of molecular diffusion. In the range of $1 << D/\lambda < 10$, both mechanisms coexist, and the following equation[13] holds:

$$\frac{V'L}{\Delta PA} = \frac{P'}{5\eta S_v^2 RT}\frac{\varepsilon^3}{(1-\varepsilon)^2} + \frac{4Z}{3}\frac{v}{S_v}\frac{\varepsilon^2}{(1-\varepsilon)} \tag{3.1.16}$$

$$\rho S_w = S_v \tag{3.1.17}$$

where

- V' is the velocity (mol/s) of fluid gas
- P' is the average pressure in the powder bed
- Z is a constant and is related to the shape of the path
- v is the rate of molecular diffusion
- S_v is the surface area per volume

The first term of the right-hand side is the contribution of viscous flow, and the second term is that of the Knudsen flow. The plots of $V'L/\Delta A$ versus P' should show a linear line. Then, the surface area estimated from a slope of the linear line originates in the viscous flow, and it is assumed to be related with an outer surface area of agglomerate particles. This value depends on the porosity of a powder bed. On the other hand, the surface area calculated from the intercept value is attributed to the Knudsen flow and is considered to represent the total surface area of primary particles. The determination of the Z value is difficult. Derjaguin[14] proposed the Z value to be 0.69 and Kraus et al.[15] reported that the specific surface area estimated by the permeametry using 0.69 agreed with that estimate from the nitrogen adsorption. Arakawa and Suito[16] obtained 0.47 by the comparison between the data of the permeametry and the particle size determined by the electron microscopy. Wasan et al.[17,18] also theoretically and experimentally verified the permeability techniques for fine particles.333 Gas or liquid is used as fluid materials. Apparatuses commercially available are based on air permeametry and many of them are applicable for viscous flow using the Kozeny–Carman equation. Typical apparatuses are shown in Figure 3.1.4.

The surface areas measured by various apparatuses do not agree each other and the differences attain about 20–30% in some cases. Because many flow equations have been proposed and the constants in the flow equations are unstable. In this method, the specific surface area S_w varies with the porosity of the sample bed. In general, S_w increases with a decrease in the porosity and reaches a constant value below a certain porosity. The Kozeny constant k_k in Equation (3.1.14) is taken as 5, however, this value is affected by tortuosity of the flow path, which depends largely on the packing degree of the sample bed.

Although there exist some disagreements among the values measured by different types of apparatuses, the reproducibility of the values measured by a given apparatus is very

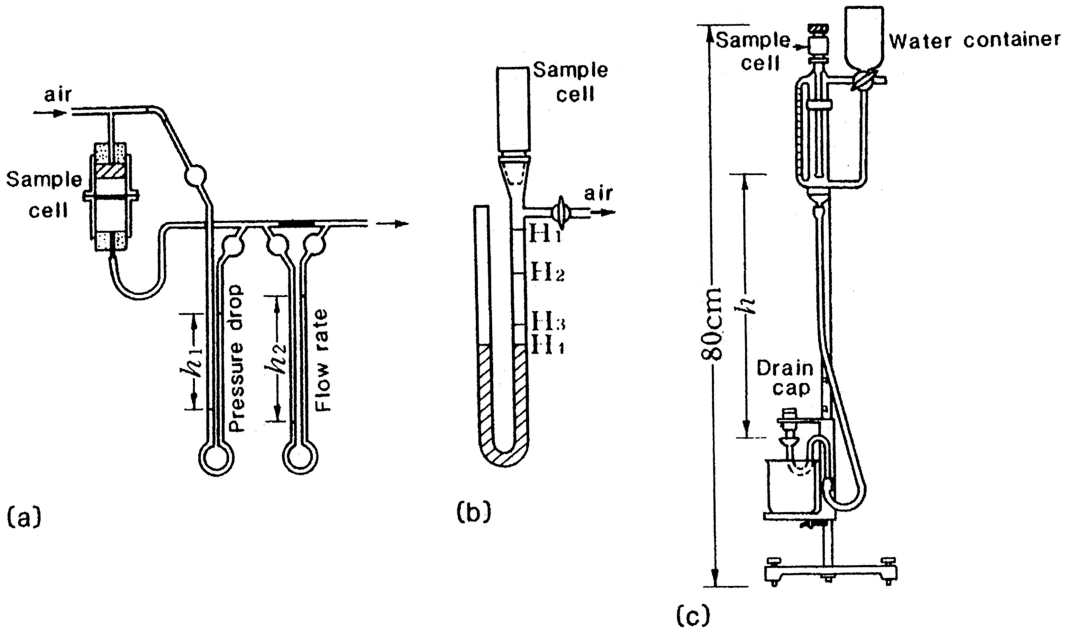


FIGURE 3.1.4 Schematic diagram of some types of permeameter. (a) Lea and Nurse, (b) Blaine, (c) Arakawa-Shimadzu.

high. Furthermore this method has the features of the simple apparatus, facility operation and rapidness of measuring compared with other methods. It is useful for the industrial standard measurement of the quality control in industries such as cement, pigment, pharmacy, food and so on. Real time permeametry[19] is one of the examples taking advantage of characteristics of rapid measurement. The measurement of the external surface area of tablet,[20] pelletized granules[21] and spray dried dairy powders[22] has been reported. Recently *in-situ* monitoring of the surface area of high explosive powder using the metallic sample tube has been developed.[23,24]

REFERENCES

1. Rouqerol, F., et al., *Adsorption by Powders & Porous Solids, Principles, Methodology and Applications*, Second edition, Academic Press, 2014.
2. Thommes, M., et al., *Pure and Appl. Chem.*, 87, 1051–1069, 2015.
3. Brunauer, S., Emmett, P.H., Teller, E., *J. Am. Chem. Soc.*, 60, 309–319, 1938.
4. Emmett, P.H., Brunauer, S., *J. Am. Chem. Soc.*, 59, 1553–1564, 1937.
5. Beebe, R.A., Beckwith, J.B., Honig, J.M., *J. Am. Chem. Soc.*, 67, 1554–1558, 1945.
6. Takei, T., Chikazawa, M., *J. Ceram. Soc. Jpn.*, 106, 353–367, 1987.
7. Yanazawa, H., Ohshika, K., Matsuzawa, T., *Adsorption*, 6, 73–77, 2000.
8. Cannon, W.A., *Nature*, 197, 1000–1001, 1963.
9. Suzuki, I., Oosawa, K., *Rev. Sci. Instrum.*, 68, 4531–4535, 1997.
10. Keller, J.U., Robens, E., *J. Therm. Anal. Calorim.*, 71, 37–45, 2003.
11. Takaishi, T., Sensui, Y., *Trans. Farday Soc.*, 59, 2503–2514, 1963.
12. Allen, T., *Particle Size Measurement Volume 2*, 5th edition, Chapman & Hall, 1997.
13. Carmen, P.C., *Flow of Gases Through Porous Media*, London: Butterworth, 1956.
14. Derjaguin, B., *C R Acad. Sci. U R S S*, 53, 623, 1946.
15. Kraus, G., Ross, J.W., Girifalco, L.A., *J. Phys. Chem.*, 57, 330–333, 1953.
16. Arakawa, M., Suito, E., *Kogyo Kagaku Zasshi*, 63, 556–559, 1960.
17. Wasan, D.T., et al., *Powder Technol.*, 14, 209–228, 1976.
18. Wasan, D.T., et al., *Powder Technol.*, 14, 229–244, 1976.
19. Kaye, B.H., Legault, P.E., *Powder Technol.*, 23, 179–186, 1979.
20. Alderborn, G., Duberg, M., Nyström, C., *Powder Technol.*, 41, 49–56, 1985.
21. Eriksson, M., Nyström, C., Alderborn, G., *Int. J. Pharm*, 99, 197–207, 1993.
22. Börjesson, E., et al., *Powder Technol.*, 298, 9–20, 2016.
23. Edmonds, E., Hazelwood, A., Lilly, T., Mansell, J., *Powder Technol.*, 174, 42–45, 2007.
24. Maiti, A., Han, Y., Zaka, F., Gee, R.H., *Propellants Explos. Pyrotech.*, 40, 419–425, 2015.



Taylor & Francis
Taylor & Francis Group
http://taylorandfrancis.com

3.2 Adsorption Characteristics

Takashi Takei

3.2.1 INTRODUCTION

Adsorption has been defined as the phenomenon that concentration of a component in an interfacial layer of vapor-solid, vapor-liquid, liquid-solid, or liquid-liquid becomes higher or lower than that of the bulk phase. The former case is called a positive adsorption and the latter a negative adsorption. The adsorption phenomenon should be distinguished from the absorption, where adsorbate molecules penetrate interior of a solid. In this section the interactions between vapors and solids, or between liquids and solids, are described. Vapor-solid systems are dealt with in detail.

Generally, adsorption phenomena are classified into two types: physical adsorption and chemical adsorption. In the physical adsorption, attractive forces between individual adsorptive molecules and atoms or ions composing a solid surface originate in a van der Waals force. On the other hand, chemical adsorption takes place only in special cases of vapor-solid and liquid-solid systems where adsorptive molecules are adsorbed by chemical bonds. Chemical adsorption is widely applied to catalytic reactions. In this chapter, physical adsorption is mainly described. Heat of physical adsorption is smaller than that of chemical adsorption, and rate of physical adsorption is faster than that of chemical adsorption. Moreover, physical adsorption and desorption processes are reversible and a relatively large amount of molecules is adsorbed on a solid surface at temperatures below the boiling point of the adsorptive or under high concentration of adsorptive in solution. Namely, multilayer adsorption occurs. On the other hand, in chemical adsorption, chemical bonds must be formed between a solid surface and adsorbed individual molecule so that the multilayer observed in physical adsorption does not occur. Hence the coverage $\theta = V/V_m$ is always lower than unity, where V is the amount of adsorbed molecules and V_m is that for monolayer completion.

The interaction of physical adsorption is considered. If the solid surface is non-polar (e.g. graphite) and the adsorptive molecule is non-polar (e.g. Ar), the interaction is only dispersion force. If the solid surface consists of ions or polar groups (e.g. –OH), they will produce an electric field that induces dipoles in the adsorbed molecules. In this case, the interaction between an induced dipole and a surface electric field appears. Moreover, if the adsorptive molecule possesses a permanent dipole, the interaction between a dipole and a surface electric field occurs. If the adsorptive molecule has a quadrapole (e.g. N_2), the interaction between a quadrapole and a surface electric field is assumed. Another important interaction is a hydrogen-bond interaction. On the other hand, the micropore and mesopore structure enhance adsorption by the micropore filling and capillary condensation phenomena, respectively.

Powder properties, ease of handling, and various problems in powder processes are closely related to their surface properties. Hence inspection of the surface properties of powder is very important. In order to estimate the surface properties such as surface area, pore structure, and surface chemical properties, adsorption techniques are widely used.

3.2.2 ADSORPTION MEASUREMENT

3.2.2.1 Measuring Method

Vapor-Solid System

Measurements of the amount of adsorbed molecules are carried out by gravimetric and volumetric methods which described in Section 3.1.3. The adsorption isotherm which plotted the amount of adsorbed molecules against equilibrium pressure or relative pressure is obtained. The spectroscopic and calorimetric methods are used to evaluate the interaction between adsorbed molecules and solid surfaces.

Liquid-Solid System

An adsorbed amount of molecules or ions is determined from difference in concentration of a component in a solution before and after adsorption. The adsorption isotherm which plotted the amount of adsorbed molecules against equilibrium concentration of a component is obtained. In liquid-solid adsorption systems, a competitive adsorption of a solvent and solute molecule is noted. In the case of a dye adsorption, a dye aggregation should be considered in the experimental concentration of dyes.

3.2.2.2 Importance of Sample Pretreatment

The pretreatment of samples is very important to obtain accurate adsorption characteristics. A clean surface is required for the adsorption measurement. The powder particles are usually handled or reserved under the atmosphere. Therefore, water molecules are mainly adsorbed according to its relative vapor pressure surrounding the powder. To obtain a clean surface of powder particles, elimination of the adsorbed water molecules by heating is necessary. Especially in metal oxides, water molecules are chemically adsorbed and various types of hydroxyl groups are formed on their surfaces. These hydroxyl groups are characteristic for each substance. Since the bonding strength of the surface hydroxyl groups varies with the nature of the metal oxides, the elimination temperatures of the hydroxyl groups are different from each other. So, the heating temperature before the adsorption measurement is important. The contents of the surface hydroxyl groups on several oxides have been reported as a function of the pretreatment

temperature.[1–6] The surface hydroxyl groups have serious effects on the surface properties, such as selective adsorbability, water vapor affinity, catalytic activity, chemical activity, and electric field strength. Moreover, the hydroxyl groups play an important role in the adsorption of polar substances and molecules which can form hydrogen-bond. From these points of view, careful attention should be paid to determine the treatment temperature of sample powders. The surface properties may also be changed by another reason. For example, the release of CO_2 from $CaCO_3$ powder is found at temperatures above 300°C. In the cases of oxides, especially reducing oxide, oxygen defects are produced by high temperature treatment and hence the samples must be kept under oxygen pressure after pretreatment to remove the defects. A decrease in surface area usually occurs in the high-temperature treatment, which stabilizes the surface condition, causing disappearance of active sites and growing stable crystal planes.

3.2.3 THEORY OF ADSORPTION ISOTHERMS

The adsorption phenomenon gives valuable information on the physical and chemical properties of a solid surface and is represented by an adsorption isotherm. In the case of vapor-solid system, the isotherm is usually expressed by the relationship between the adsorbed amount V and equilibrium vapor pressure P of an adsorptive at a fixed temperature T.

$$V = f_T(P) \tag{3.2.1}$$

On the other hand, in the case of liquid-solid system, concentration (C) of adsorptive in a solution is used instead of vapor pressure.

$$V = f_T(C) \tag{3.2.2}$$

The other expressions obtained at a fixed pressure or at a constant amount of adsorbed molecules are given as follows:

$$V = f_P(T) \tag{3.2.3}$$

$$V = f_V(T) \tag{3.2.4}$$

Many equations for the adsorption isotherm are introduced by assuming various adsorption mechanisms. The isotherms of physical adsorption are grouped conveniently into eight classes. The typical classification is proposed by IUPAC.[7] Besides these isotherms, types of isotherm are shown in Figure 3.2.1, which is useful for an understanding of adsorption phenomena.

Henry Equation

The relationship between an adsorbed amount V and an equilibrium pressure P is expressed by

$$V = k_H P \tag{3.2.5}$$

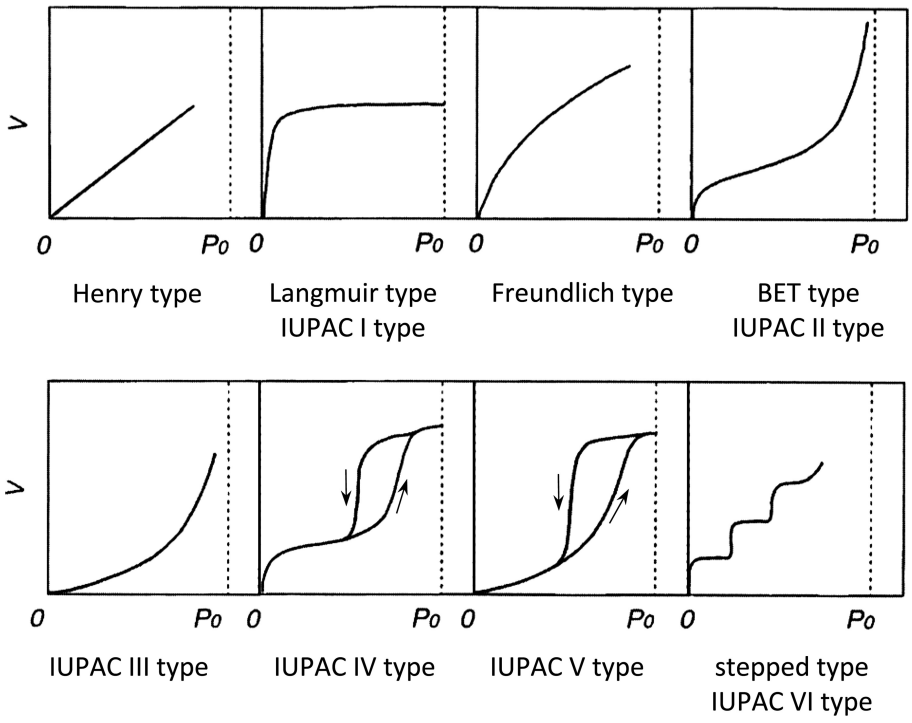


FIGURE 3.2.1 Types of adsorption isotherms. The abscissa is a equilibrium pressure in a gas-sold system. P_0 is a saturated vapor pressure at measurement temperature. In the case of a liquid-solid system, the abscissa is replaced into a equilibrium concentration (C) of solute. IUPAC I and IV type are classified into two types: I(a) and I(b), IV(a) and IV(b)[7].

where k_H is a constant. This equation holds for a small adsorbed amount below 1% of the monolayer capacity. Even in the cases of the other equations, the adsorbed amounts at early stages are represented approximately by the Henry equation.

Langmuir Equation

This equation is introduced from the most basic adsorption model, in which two assumptions are made. The first assumption is that the heat of adsorption is the same for every molecule and that there is no interaction among the adsorbed molecules. The second is that every molecule which collides with a molecule already adsorbed on a site reflects immediately to the vapor phase. Therefore, multilayer adsorption does not occur and the maximum amount of adsorption is obtained at the monolayer completion, where the particle surface is just covered with closely packed molecules adsorbed on the specific adsorption sites. From such adsorption mechanisms, the Langmuir equation is derived as follows.[8] Adsorption velocity is proportional to the number of molecules that strike the bare surface of powder particles. On the other hand, desorption velocity is closely related to the adsorbed amount or the surface coverage θ. In equilibrium, the velocities of adsorption and desorption are equal each other, and hence the following equation is derived:

$$k_{ad}(1-\theta)P = k_{de}\theta \tag{3.2.6}$$

where k_{ad} and k_{de} represent the rate constants of adsorption and desorption, respectively. The value of θ is given by V/V_m, where V_m is monolayer capacity. Hence Equation (3.2.6) is rewritten as follows:

$$V = \frac{V_m(k_{ad}/k_{de})}{1+(k_{ad}/k_{de})} = \frac{AV_mP}{1+AP} \tag{3.2.7}$$

The Langmuir isotherm is typical for chemical adsorption, however it is always observed in the liquid-solid adsorption system (e.g. dye adsorption), and monolayer capacity can be calculated. So the specific surface areas of powder particles: silicate,[9] GO (graphene oxide),[10] soil,[11] etc., are determined from the cross-sectional area of adsorbed molecule by methylene blue adsorption. In the case of physical adsorption of gases, the Langmuir isotherm means the existence of the micropore (d: pore diameter < 2 nm). Nitrogen and argon adsorption on zeolite, ACF (activated carbon fiber), charcoal materials show this type of isotherm. The microporous materials show the strong adsorption force due to the effect of the pore wall. The adsorbate molecules are filled up in the micropore at very low relative pressure. This phenomenon is called micropore filling.

Freundlich Equation

The Freundlich equation is represented by Equation 3.2.8, and widely used in the case of liquid-solid systems:

$$V = k_F C^{1/n} \tag{3.2.8}$$

where k_F is a constant and n is the value in the range 1 to 10. As this equation was obtained experimentally, the physical meaning of k_F and n is not clear.

BET Equation

In order to understand the physical adsorption, the BET equation is most widely used. This equation is derived by expansion of the Langmuir adsorption model to multilayer adsorption under a few assumptions. The isosteric heat of adsorption for molecules other than in the first layer is equal to the liquefaction heat of an adsorptive, interaction among the adsorbed molecules at same layers is not produced, and at saturated vapor pressure the number of adsorbed layers is infinite. From these assumptions, the BET equation is obtained:[12]

$$V = \frac{V_mCX}{(1-X)(1-X+CX)} \tag{3.2.9}$$

where X is the relative vapor pressure P/P_o, C is the value related to the strength of adsorption force, P_o is the saturated vapor pressure at measurement temperature, and V_m is the monolayer capacity. Many elaborate amendments of the BET equation have been attempted, but a more useful and concise equation has not yet been deduced. The BET equation is one of the standard method of estimating the specific surface area of powders. In Chapter 3.1, the principle of the surface determination by gas adsorption is described in detail.

Various adsorption equations are listed in Table 3.2.1, in which expressions convenient for plotting experimental data are also shown.

Other Types of Isotherms

IUPAC III type of isotherm means weak interaction between adsorbed molecule and solid surface. It is typical for water adsorption on hydrophobic surfaces. When the constant C which related to the adsorption interaction in the BET

TABLE 3.2.1
Equations of Adsorption Isotherms

Type of Adsorption Isotherm	Equation	Expression for Plotting Experimental Data
Henry type	$V = k_HP$	$V = k_HP$
Langmuir type	$V = \frac{AV_mP}{1+AP}$	$\frac{P}{V} = \frac{1}{V_mA} + \frac{1}{V_m}P$
Freundlich type	$V = k_FC^{1/n}$	$lnV = lnK_F + \frac{1}{n}lnC$
BET type	$V = \frac{V_mCX}{(1-X)(1-X+CX)}$	$\frac{P}{V(P_0-P)} = \frac{1}{V_mC} + \frac{C-1}{V_mC}\frac{P}{P_0}$

Parameters of equations refer to text.

equation is less than 2, the adsorption isotherm changes to this type from the BET type. IUPAC IV and V type of isotherms show the hysteresis of adsorption and desorption branch. This means the existence of the meso-pore in the solid. The steep increase in the adsorption branch and decrease in the desorption branch are attributed to the capillary condensation and the capillary evaporation in a pore, respectively. Several theories on the origin of the hysteresis have been proposed,[13–16] however, the mechanism is not clear. IUPAC VI type of isotherm is rarely observed and demonstrated in the adsorption on a highly ordered solid surface. The shape of the adsorption isotherm shows the occurrence of two-dimensional condensation. The typical examples are the adsorption of Kr on graphite[17,18] and Kr on alkali halide.[19]

3.2.4 ESTIMATION OF SURFACE PROPERTIES BY ADSORPTION METHOD

Many powder surface properties are determined by adsorption phenomena. Table 3.2.2 shows the relationship between powder surface properties and the estimation methods.

3.2.4.1 Measurement of Adsorption Isotherm

The measurement of adsorption isotherm of water and organic molecules is effective for the evaluation of hydrophilicity and hydrophobicity or lipophilicity. Figure 3.2.2 shows the water vapor adsorption isotherms for the various functional silane-treated silica.[20] The surface hydroxyl groups will exist on the bare surface of the silica. It is clear that hydrophilicity of the surface is controlled by the surface functional groups. It was reported that the adsorption amount of water on the surface of coal depended on the carboxyl group concentration on the surface.[21]

3.2.4.2 Heat of Immersion

When a solid surface is immersed in a liquid which does not dissolve the solid, heat is generated as a result of the interaction between the solid surface and the liquid molecules. This heat is called the heat of immersion. A diagram of the enthalpy changes deduced by immersion and heat of adsorption is shown in Figure 3.2.3. The value h_i represents the heat of immersion of the solid and is equal to the enthalpy change

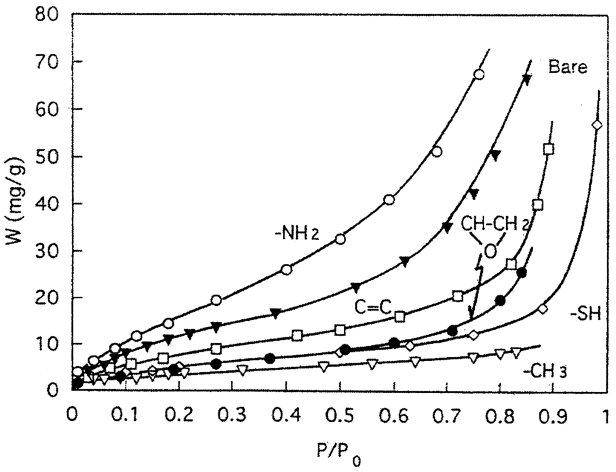


FIGURE 3.2.2 Water vapor adsorption isotherms for the silane-treated silica (Cab-oSil). (From Zettlemoyer and Hsing, *J. Colloid Interface Sci.*, 58, 263-274, 1977. With permission.)

TABLE 3.2.2
Estimation Methods of Surface Properties by Adsorption

Surface Property	Estimation Method
Hydrophilicity, hydrophobicity	Water vapor adsorption Heat of immersion of water
Lipophilicity	Organic vapor adsorption Heat of immersion of organic liquid
Specifying of adsorption site Interaction between adsorbed molecules and solid surface	IR spectroscopy of adsorbed molecule and functional groups on surface Heat of adsorption
Acidity (strength, types, amounts)	Adsorption of acidic molecules Heat of adsorption of acidic molecules IR spectroscopy of pyridine adsorption Temperature programmed desorption of NH_3
Specific surface area	N_2, Ar and Kr adsorption
Dispersity of supported metal particles	H_2 and CO adsorption
Surface fractal dimension	Adsorption of several molecules with different sizes Analysis of isotherm by FHH equation
Pore size distribution	N_2 adsorption-desorption

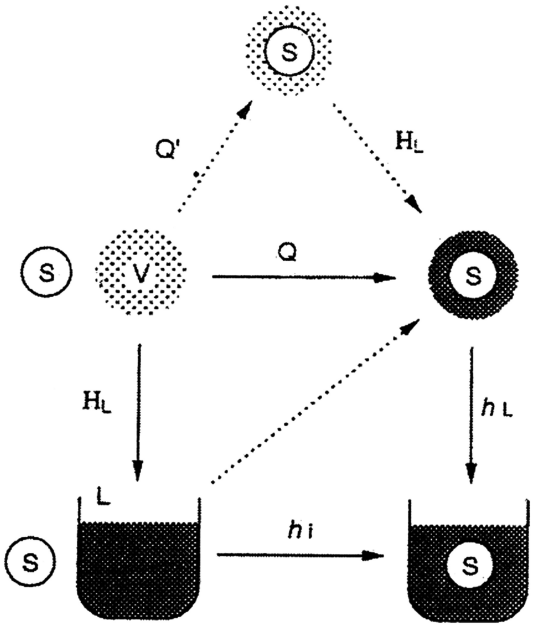


FIGURE 3.2.3 Chemical diagram of heat change. S, solid; L, liquid; h_i, immersion heat; H_L, liquefaction heat of vapor; h_L, enthalpy of liquid surface; Q, adsorption heat; Q', real adsorption heat.

between the solid surface and solid-liquid interface. The Q and Q' values are heat of adsorption and real heat of adsorption, respectively. The symbol H_L is the liquefaction heat of adsorptive gas.

The measurement of the immersion heat is relatively easy, compared with that of the adsorption heat. When water is used as immersion liquid, the heat of immersion represents the degree of hydrophilic or hydrophobic properties of the surface. The change in the immersion heat of a silica powder modified with trimethylsilyl groups for water is shown in Figure 3.2.4.[22] The hydrophilic property of the surface decreases with an increase in the concentration of trimethylsilyl groups. On the other hand, hydrophobicity of organic modified $CaCO_3$ filler has been estimated from the heat of immersion of organic liquid, benzene.[23]

3.2.4.3 IR Spectroscopy

The IR spectroscopy of adsorption is a well-established technique for the determination of adsorption sites. Generally, almost all of surfaces of oxide (SiO_2, TiO_2, α-Fe_2O_3, ZnO, and so on) powders are covered with the various OH groups which are formed by chemical adsorption of H_2O under atmosphere or preparation methods (precipitation of hydroxides and sol-gel method). These groups behave as an effective site of adsorption. The interaction between OH groups and adsorbed molecules has been studied by the IR spectroscopy. These interactions are investigated from changes in OH absorption bands deduced by perturbations of adsorbed molecules. The adsorption of molecules on the surface functional groups causes the shift and decrease of the absorption peaks of surface functional groups. Figure 3.2.5 shows the change in the absorption peak of the surface hydroxyl groups on silica by adsorption of organic molecules.[24] After adsorption, the peak of the surface hydroxyl groups (3747 cm^{-1}) shifted to a lower wavenumber. The peak shift due to benzene adsorption is larger than that due to n-hexane adsorption. The correlation between differential heats (Q_a) of adsorption and peak shift ($\Delta\nu$) of the absorption band of hydroxyl groups on a silica surface was reported.[25] Consequently, the interaction with benzene is larger than that with n-hexane.

Detection of the adsorbed species by IR spectroscopy reveals the kinds of surface adsorption sites. For example, Brönsted and Lewis acid sites can be distinguished by pyridine adsorption on oxide surfaces.[26]

Usually, samples for measuring adsorption infrared spectrum of gases on powder surfaces are prepared by pressing powder samples into self-supporting disks. The sample disks thus obtained are mounted in the cell which can be evacuated and heated in order to control adsorption state. Various cells have been designed by many researchers.[27,28] When it is difficult to prepare a self-supporting disk, a diffuse reflectance spectroscopy (DRS) are used. This technique is just appropriate in this case, because of the easy sample preparation without grinding and pressing samples. However, it should be noted that the spectral shape obtained by the DRS method depends on the particle size of powder samples. When a powder sample is very fine and well dispersed in the liquid, which is transparent for infrared ray, a spectrum of the sample can be obtained in the dispersion in liquid as it is. For example, surface groups on fine silica powders were clearly observed by dispersing the powder samples in carbon tetrachloride.[29]

3.2.4.4 Surface Geometrical Properties

Specific Surface Area

Specific surface area of a powder is one of the fundamental properties of the powders. Nitrogen gas adsorption method, so-called the BET method, is always used as the determination of

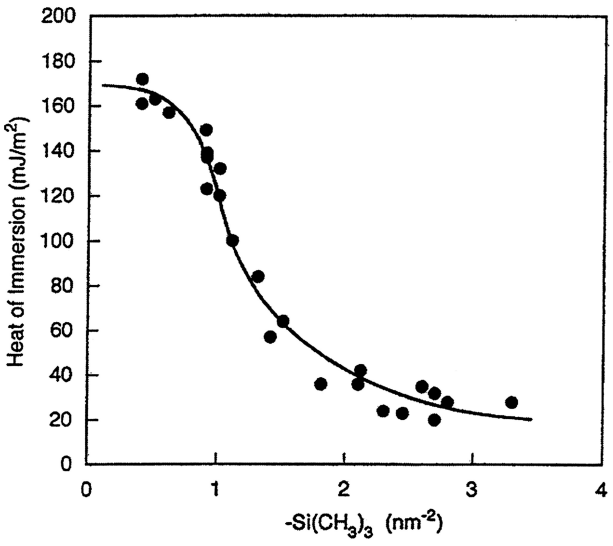


FIGURE 3.2.4 Change in the heat of immersion of water toward the amount of the trimethylsilyl groups on silica surface. (From Tsutsumi and Takahashi, *Colloid Polym. Sci.,* 263, 506–511, 1985. With permission.)

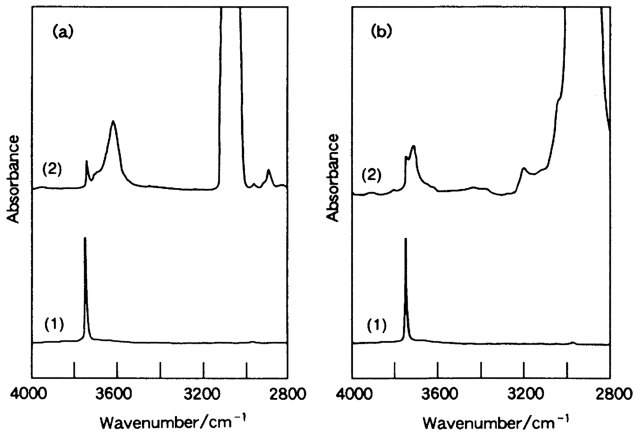


FIGURE 3.2.5 The IR spectra of (a)benzene and (b) n-hexane on silica surface containing the isolated hydroxyl groups; (1) before adsorption and (2) after adsorption. (From Takei, et al., *Thermochim. Acta*, 267, 159–167, 1995. With permission.)

the surface area. The theory of the BET equation and experimental method is explained in Chapter 3.1.

Surface Fractal Dimension

It is difficult to describe geometric irregularities of real particle surfaces. Avnir estimated the geometric structure of the surface using the fractal dimension D.[30,31] There are two ways to evaluate the surface fractal dimension by physical gas adsorption using several gas molecules or a single gas molecule (N_2 or Ar). In the case of the usage of several gas molecules, the fractal dimension of solid surfaces is investigated by measurements of physical adsorption of several gases which have various molecular sizes, and calculated as the following equation:

$$\log n = \left(-\frac{1}{2}D\right)\log\sigma + C \tag{3.2.10}$$

where n is the monolayer capacity of adsorbate molecules on the surface and σ is the effective cross-sectional area of one adsorbate molecule and C is a constant value. The value of D is calculated from the slope of a linear line which is obtained by plotting log n versus log σ. The other way to investigate D is a single gas adsorption method by the application of the Frenkel-Halsey-Hill (FHH) theory of adsorption.[32,33,34] Generally, the D value for the real surfaces ranges from 2 to 3. For typical solid surfaces the values are obtained as follows. For a smooth and regular surface (e.g. graphite) the D value shows nearly 2. However, porous samples which have high specific surface areas and porous structures such as silica gel and charcoal show nearly 3. Table 3.2.3 shows the surface fractal dimensions of various powders by gas adsorption methods.

Pore Size Analysis

The evaluation of the pore size distribution of powders is important. The porous structure is often formed at the interparticle of powders by the aggregation of small particles. Generally, the diameter for a cylindrical pore and the distance between two side walls for a slit-shaped pore are used as representative pore sizes. The pores are classified into three types according to the pore size: micropores for below 2 nm, mesopores for 2–50 nm, and macro pores for above 50 nm. The gas adsorption method using N_2 or Ar is effective for the evaluation of the micropore and mesopore size distribution. The theory and experimental procedures of the pore size analysis are described in Chapter 3.6.

TABLE 3.2.3
Surface Fractal Dimensions (D) of Various Powders by Adsorption Method

Material	D	Method[a]	Reference
Cellulose	2.13–2.50	S	35
Cellulose	2.48–2.99	M	36
Carbon Black	2.25	M	31
W	2.58	S	37
Al_2O_3	2.5–2.6	S	34
TiO_2 Aerogel	2.70–2.82	M	32

[a] M: using multi molecules, S: using a single molecule.

REFERENCES

1. Davydov, V.Y., Kiselev, A.V., Zhuravlev, L.T., *Trans. Faraday Soc.*, 60, 2254–2264, 1964.
2. Morimoto, T., Nagao, M., Tokuda, F., *Bull. Chem. Soc. Jpn.*, 41, 1533–1537, 1968.
3. Morimoto, T., Naono, H., *Bull. Chem. Soc. Jpn.*, 46, 2000–2003, 1973.
4. Naono, H., Kadota, T., Morimoto, T., *Bull. Chem. Soc. Jpn.*, 48, 1123–1126, 1975.
5. Zhuravlev, L.T., *Langmuir*, 3, 316–318, 1987.
6. Morimoto, T., Kishii, J., Okada, O., *Bull. Chem. Soc. Jpn.*, 53, 1918–1921, 1980.
7. Thommes, M., Kaneko, K., Neimark, A.V., Olivier, J.P., et al., *Pure Appl. Chem.*, 87, 1051–1069, 2015.
8. Langmuir, I., *J Am. Chem. Soc.*, 40, 1361–1403, 1918.
9. Hegyesi, N., Vad, R.T., Pukánszky, B., *Appl. Clay Sci.*, 146, 50–55, 2017.
10. Navajas, P.M., Asenjo, N.G., Santamaría, R., Menéndez, R., et al., *Langmuir*, 29, 13443–13448, 2013.
11. Arnepalli, D.N., Shanthakumar, S., Rao, B.H., Singh, D.N., *Geotech. Geol. Eng.*, 26, 121–132, 2008.
12. Brunauer, S., Emmett, P.H., Teller, E., *J. Am. Chem. Soc.*, 60, 309–319, 1938.
13. Michalski, T., Benini, A., Findenegg, G.H., *Langmuir*, 7, 185–190, 1991.
14. Liu, H., Zhang, L., Seaton, N. A., *Langmuir*, 9, 2576–2582, 1993.
15. Rasmussen, C.J., Vishnyakov, A., Thommes, M., Smarshly, B.M., Kleitz, F., Neimark, A.V., *Langmuir*, 26, 10147–10157, 2010.
16. Reichenbach, C., Kalies, G., Enke, D., Klank, D., *Langmuir*, 27, 10699–10704, 2011.
17. Clark, H., *J. Phys. Chem.,* 59, 1068, 1955.
18. Volkmann, U.G., Knorr, K., *Surf. Sci.*, 221, 379, 1989.
19. Takaishi, T., Saito, M., *J. Phys. Chem.*, 71, 453–454, 1967.
20. Zettlemoyer, A.C., Hsing, H.H., *J. Colloid Interface Sci.*, 58, 263–274, 1977.
21. Nishino, J., *Fuel*, 80, 757–764, 2001.
22. Tsutsumi, K., Takahashi, H., *Colloid Polym. Sci.*, 263, 506–511, 1985.
23. Domkam, L., *Colloid Polym. Sci.*, 272, 1190–1202, 1994.
24. Takei, T., Konishi, T., Fuji, M., Watanabe, T., et al., *Thermochim. Acta*, 267, 159–167, 1995.
25. Galkin, G.A., Kiselev, A.V., Lygin, V.I., *Trans. Faraday Soc.*, 60, 431–439, 1964.
26. Parry, E.P., *J. Catal.*, 2, 371–379, 1963.
27. Bell, A.T., *Vib. Spectrosc. Mol. Surf.*, Yates, J.T., Madey, T.E., Eds. Plenum Press, p.116, 1987.
28. Davydov, A., *Mol. Spectrosc. Oxide Catalyst Surf.*, John Wily & Sons, pp.11–15, 2003.
29. Tripp, C.P., Hair, M.L., *Langmuir*, 8, 1961–1967, 1992.
30. Pfeifer, P., Avnir, D., *J. Chem. Phys.*, 79, 3558–3565, 1983.
31. Avnir, D., Farin, D., Pfeifer, P., *J. Chem. Phys.*, 79, 3566–3571, 1983.

32. Meng, F., Schlup, J.R., Fan, L.T., *Chem. Mater.*, 9, 2459–2463, 1997.
33. Sahouli, B., Blacher, S., Brouers, F., *Langmuir*, 13, 4391–4394, 1997.
34. Lee, C.-K., Tsay, C-S., *J. Phys. Chem. B*, 102, 4123–4130, 1998.
35. Strømme, M., Mihranyan, A., Ek, R., Niklasson, G.A., *J. Phys. Chem. B*, 107, 14378–14382, 2003.
36. Burnett, D.J., Heng, J.Y.Y., Thielmann, F., Garcia, A.R., et al., *AAPS Pharm. Sci. Tech.*, 12, 56–61, 2010.
37. Jiqiao, L., Baiyun, H., *Int. J. Refract. Met. Hard Mater.*, 19, 89–99, 2001.



Taylor & Francis
Taylor & Francis Group
http://taylorandfrancis.com

3.3 Moisture Content

Satoru Watano

Water, known as H_2O, covers 70% of our earth and consists 65% of our bodies; it is extremely important in our lives. There are three different forms of water such as solid (ice), liquid (water) and gas (steam). In a particulate system, unique characteristics of water are observed in many cases; surface tension caused by hydrogen bonding of water molecule generates cohesive force. It sometimes causes many troubles such as sticking, consolidation, blocking and caking etc. By contrast, water can be positively used as binders in wet granulation and kneading, as well as solvent and medium in wet systems.

3.3.1 BOUND WATER AND ADHESIVE WATER

Water is achromatic and transparent, and it has three phases (gas, liquid and solid) depending on the temperature and pressure. Due to its unique characteristics, various existing forms are observed.[1,2] In a particulate system, the existing form of water is classified as water in a single particle or water in a particulate (bulk) system as illustrated in Figure 3.3.1.

Generally, water is categorized into two classes; bound water and free water. The bound water, which exists inside crystal, aqueous solution, gel, organism, soil, etc., is stuck to materials by hydrogen bonding. As shown in Figure 3.3.1, the bound water includes combined water, occluded water, adsorption water (hygroscopic water).

The combined water is also called crystal water, which has the following types depending on the structure and the bonding conditions:

1. Constitution water: water exists in compounds as a hydroxyl group.
2. Coordinated water: water forms chelate ion in a chelate complex.
3. Anion water: water is stuck to anions by hydrogen bonding.
4. Lattice water: water exists inside crystal lattice without having direct bonding with neither cations nor anions.
5. Zeolitic water: vacancy of crystal is occupied with water molecules, and the crystal structure does not change due to the dehydration.

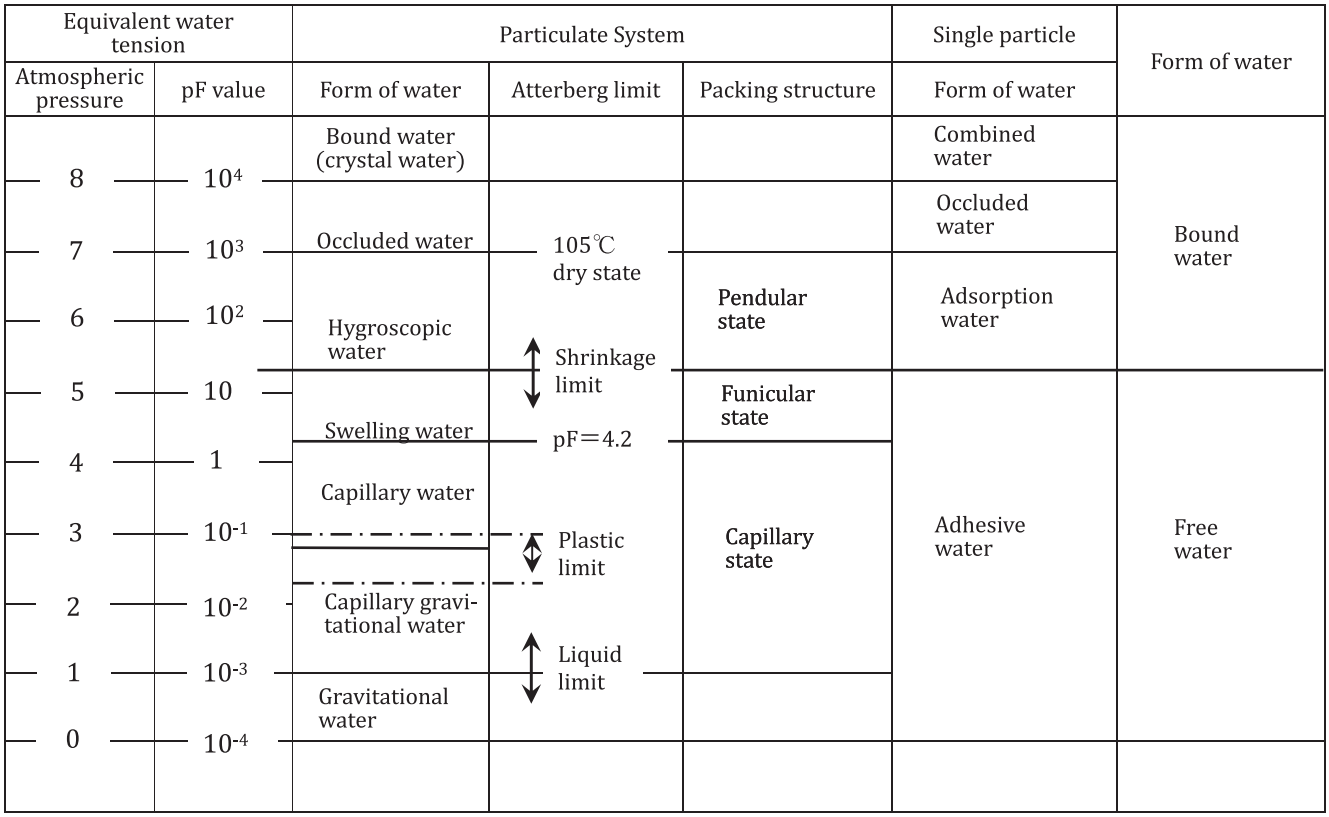


FIGURE 3.3.1 Water existing forms.

The occluded water is captured inside the solid (particle) and it exists as a solid solution or hydrate. The adhesion force of occluded water is smaller than that of combined water (crystal water), although it is still strong enough not to detach from the particle even under the drying over 100°C. In addition, it is not frozen under −100°C.

Adsorption water is entrapped by particles mainly by the hydrogen bonding between free water molecules and water molecules entrapped by particles. The adsorption water can be removed from particles by the drying of 100°C.

Contrary to the bound water, the free water captured by particles with relatively weak bonding strength, and is called adhesive water or swelling water. In a particulate system, damping condition by the free water is categorized into funicular, capillary and slurry states. Especially in a soil particulate system, consistency of soil and the phase dramatically change depending on the water content. In general, the transition point between the different phases is called the Atterberg limit (shrinkage, plastic and liquid limits).[3,4]

Condition of water distribution and bonding strength of water in a particulate system is described as a function of suction potential S(m), which is defined as[5]:

$$S = \left| -\frac{RT}{Mg} \ln\left(\frac{P}{P_0}\right) \right| \tag{3.3.1}$$

where P is the water vapor pressure inside the particulate system, P_o is the vapor pressure on the free surface of pure water, R is the gas constant (=8.315 J/molK), M is the molecular weight of water (=18.02 g/mol) and g is the gravitational acceleration ($=9.81 \times 10^{-3}$ J/gm).

Suction potential is also related to the pF value as:

$$pF = \log S \tag{3.3.2}$$

The relationship between suction potential and the water existing forms is also explained in Figure 3.3.1. For example, boundary between funicular and capillary states can be described by $pF = 4.2$. Also, $pF = 0$ means that particles are completely saturated with water.

Another way of measuring bonding strength of water in a particulate system is to use water removal temperature in heating. Table 3.3.1 indicates the water existing forms in a solid and its removal temperature.

TABLE 3.3.1
Water Existing Forms and Water Removal Temperature

Bonding Strength	Name and Bonding State	Water Removal Temperature (°C)
Weak	Water bound by adhesion or water retained through pores	Dried air at room temperature
	Occluded water	250~300
	Adsorbed water	
	at particle outer surface	100~130
	among submicron channels	~600
Strong	Crystal water	Depending on structure
	Constitution water	Depending on structure
	Zeolitic water	600~1000

3.3.2 METHOD TO DETERMINE MOISTURE CONTENT IN PARTICULATE SYSTEM

The available method for measuring the moisture content is strongly dependent on the water existing form. The simplest way of measuring moisture content of particles is to measure weight loss after drying. Other methods, such as chemical, electric, optical methods, nuclear magnetic resonance (NMR) spectrometer method and method applying radioactive rays are also available. These details are shown in Chapter 6.6, On-Line Measurement of Moisture Content.

Determination methods for water content have been established in various national and international standards, such as JIS and ISO.[6–8]

REFERENCES

1. Gotoh, K., Masuda, H., Higashitani, K., Eds. *Powder Technology Handbook*, *2nd Edn*. Marcel Dekker, New York, 1997, pp. 265–276.
2. Masuda, K., Higashitani, K., Yoshida, H., Eds. *Powdder Technology Handbook, 3rd Edn*. CRC Press, New York, 2006.
3. Smith, K.A., Mullins, C.E., Eds. *Soil and Environmental Analysis: Physical Methods*, Marcel Dekker, New York, 2000.
4. Shimada, J., Kayane, I., Tanaka, T., *Jpn. J. Limnology*, 39, 22–28, 1978.
5. Kawamura, M., Toyama. S., *J. Soc. Powder Technol. Jpn*., 15, 292–297, 1978.
6. JIS K 0068, 2001.
7. ISO 760, Determination of water−Karl Fischer method (General method), 1978.
8. ISO 24557, Determination of moisture content – Air-oven method, 2009.

3.4 Electrical Properties

Ken-ichiro Tanoue and Hiroaki Masuda (3.4.1)
Yasufumi Otsubo (3.4.2)

3.4.1 IN GASEOUS STATE

The specific resistance, dielectric constant, specific charge, and contact potential difference of particles are discussed in this section. These electrical properties are necessary for studying the behavior of electrically charged particles, electrostatic precipitation, electrostatic powder coating, electrostatic powder imaging, and so on.[1]

Specific Resistance

The electric resistance of a powder bed is one of the most important properties, especially in relation to electrostatic precipitation. If the specific resistance ρ_d of particles is lower than 10^2 Ωm, the particles will immediately be neutralized on the dust collecting electrode. Further, they are oppositely charged by the electrode and reentrained by gas flow in the presence of electrostatic repulsion between the particles and the collecting electrode. Then the collection efficiency of the precipitator becomes very poor. On the other hand, if the specific resistance is higher than 10^9 Ωm, back discharge from the collecting electrode will occur, resulting in a decrease in the precipitation efficiency.[1]

The specific resistance can be measured by (a) parallel-plate electrodes, (b) cylindrical electrodes, or (c) needle-plate electrodes, as shown schematically in Figure 3.4.1. After particles are packed or deposited between the electrodes, the applied voltage V and electric current I through the powder bed are measured. Then the specific resistance ρ_d can be calculated from the following equations:[2]

1. Parallel-plate electrodes:

$$\rho_d = \frac{A}{d}\frac{V}{I} \tag{3.4.1}$$

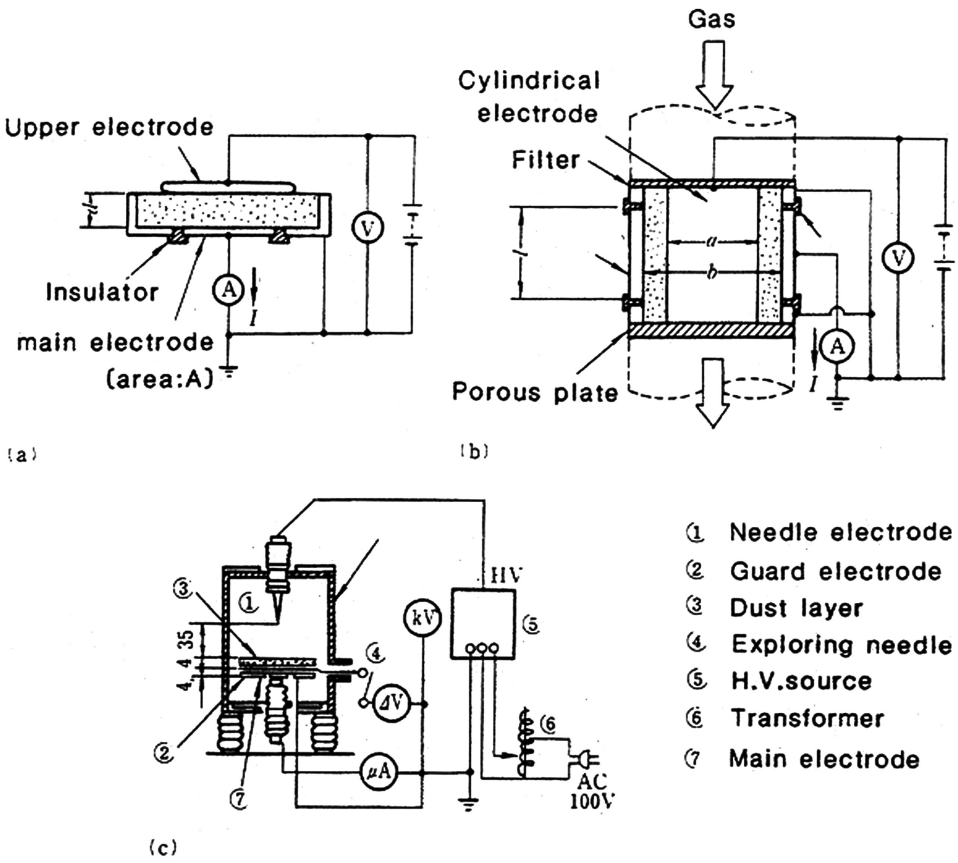


FIGURE 3.4.1 Electrodes for measuring specific resistance. (a) Parallel plate electrodes, (b) Cylindrical electrodes, (c) Needle-plate electrodes.

TABLE 3.4.1 Specific Resistances of Dust and Fumes Collected from Industrial Plans and measured by H. J. White.[4] Unit of Specific Resistance is (Ωm)

	Temperature [°C]				
Material	**21**	**66**	**121**	**177**	**232**
Fly ash A	8×10^{3}	8×10^{3}	8×10^{3}	1×10^{4}	1×10^{4}
Fly ash B	3×10^{6}	5×10^{7}	2×10^{9}	4×10^{9}	1×10^{9}
Fly ash C	2×10^{8}	3×10^{9}	7×10^{10}	5×10^{10}	7×10^{9}
Cement dust lime	8×10^{5}	7×10^{6}	7×10^{8}	3×10^{9}	9×10^{7}
Alumina fume	3×10^{6}	3×10^{9}	2×10^{10}	5×10^{10}	8×10^{8}
Chromium oxide dust	2×10^{6}	4×10^{9}	2×10^{8}	9×10^{8}	3×10^{8}
Scaring machine dust	2×10^{7}	3×10^{9}	1×10^{9}	7×10^{6}	8×10^{5}
Open hearth dust	1×10^{6}	3×10^{7}	3×10^{9}	1×10^{9}	9×10^{6}
Nickel oxide kiln dust	3×10^{8}	8×10^{7}	6×10^{7}	5×10^{6}	1×10^{6}

TABLE 3.4.2 Specific Resistances of Chemical Species at 177°C.[4] Unit of Specific Resistance is (Ωm)

Ferric oxide (Fe_2O_3)	1×10^{9}
Calcium carbonate ($CaCO_3$)	8×10^{9}
Titanium dioxides (TiO_2)	5×10^{7}
Nickelous oxide (NiO)	2×10^{3}
Lead oxide (PbO)	1×10^{9}
Aluminum oxide (Al_2O_3)	1×10^{10}
Calcium sulfate ($CaSO_4\ 2H_2O$)	1×10^{11}
Silica (SiO_2)	3×10^{9}

TABLE 3.4.3 Dependence of Specific Resistances at 177°C on Adding Moisture Content[4]

Adding moisture content (%)	0 (Dry air)	6.6	13.5	20
Specific resistance (Ωm)	2.8×10^{9}	3.3×10^{8}	1.5×10^{8}	1.2×10^{8}

2. Cylindrical electrodes:

$$\rho_d = \frac{2\pi l}{\ln(b/a)}\frac{V}{I} \tag{3.4.2}$$

3. Needle-plate electrodes:

$$\rho_d = \frac{A}{L}\frac{\Delta V}{I} \tag{3.4.3}$$

where V, applied voltage (V); I, electric current (A); A, area of the main electrode (m^2); d, gap between the electrodes (m); l, length of the cylindrical electrode (m); a, outside diameter of the inner cylindrical electrode (m); b, inside diameter of the outer cylindrical electrode (m); ΔV, electrical potential of the exploring needle (V); L, distance between the exploring needle and the plate electrode (m).

The specific resistance usually decreases with the packing density of the powder bed. Therefore, measurements should be carried out after precise setting of the packing density. Needle-plate electrodes are suitable for measurement under the same conditions as in an industrial electrostatic precipitator.[3] The applied voltage should be kept as low as possible to avoid a void discharge. It may take a long time to reach a constant current, especially for high-resistivity powder, because the current is partly absorbed in the powder bed as charge accumulates between particles.

The specific resistance of highly resistive powder is strongly dependent on the ambient temperature, chemical species, and moisture.[4] Table 3.4.1 shows the specific resistance of dusts and fumes. The resistance for most of them has a maximum value at 66°C to 177°C except for fly ash A and Nickel oxide kiln dust. The value of the resistance differs from dusts and fumes due to the chemical components. Table 3.4.2 shows the specific resistance of chemical species at 177°C. The resistance depends strongly on the chemical species. For example, the resistances of Calcium sulfate and Nickelous oxide are 1×10^{11} Ωm and 2×10^{3} Ωm, respectively. Table 3.4.3 shows the dependence of the specific resistance of the cement kiln dust on the moisture content at 260°C. The resistance decreases with the moisture content from 2.8×10^{9} Ωm to 1.2×10^{8} Ωm.

Dielectric Constants

The dielectric constant of particles is necessary to estimate the dielectrophoretic force or the maximum charge attainable by field charging. The dielectrophoretic force is a function of $(\varepsilon_p-\varepsilon)/(\varepsilon_p+2\varepsilon)$, where ε_p is the dielectric constant of the particle and ε is that of the medium. If the medium is air, ε is close to ε_0 ($=8.85\times10^{-12}$ F/m) of vacuum. The ratio $\bar{\varepsilon}_p = \varepsilon_p/\varepsilon_o$ is called the specific dielectric constant. Numerical values of $f(\bar{\varepsilon}_p) = (\bar{\varepsilon}_p - 1)/(\bar{\varepsilon}_p + 2)$ are listed in Table 3.4.4, showing its insensitivity to the specific dielectric constant. The maximum charge acquired by field charging depends on the function $g(\bar{\varepsilon}_p) = 3\bar{\varepsilon}_p/(\bar{\varepsilon}_p + 2)$, whose numerical values are listed in Table 3.4.5.

TABLE 3.4.4 $f(\bar{\varepsilon}_p) = (\bar{\varepsilon}_p - 1)/(\bar{\varepsilon}_p + 2)$

$\bar{\varepsilon}_p$	1	2	5	10	20	50	100	∞
$f(\bar{\varepsilon}_p)$	0	0.250	0.571	0.750	0.864	0.942	0.971	1

TABLE 3.4.5 $g(\bar{\varepsilon}_p) = 3\bar{\varepsilon}_p/(\bar{\varepsilon}_p + 2)$

ε_p	1	2	5	10	20	50	100	∞
$g(\varepsilon_p)$	1	1.50	2.14	2.50	2.73	2.88	2.94	3

The dielectric constant of the powder bed is called the apparent dielectric constant ε_a, which is a function of the packing fraction ϕ of particles as follows:

1. Maxwell model[5,6]

$$\bar{\varepsilon}_a = \frac{\varepsilon_a}{\varepsilon_0} = \frac{3 - 2(1-\phi)(\bar{\varepsilon}_p - 1)}{3 + 2(1-\phi)(\bar{\varepsilon}_p - 1)} \tag{3.4.4a}$$

2. Rayleigh model[7]

$$\frac{\varepsilon_a}{\varepsilon_0} = 1 + 3\phi\left(\frac{(\bar{\varepsilon}_p + 2)}{(\bar{\varepsilon}_p - 1)} - \phi - 1.65\frac{(\bar{\varepsilon}_p - 1)}{\bar{\varepsilon}_p + (4/3)}\phi^{10./13}\right)^{-1} \tag{3.4.4b}$$

3. Böettcher model[6,8,9]

$$\frac{\bar{\varepsilon}_a - 1}{3\bar{\varepsilon}_a} = \frac{\phi(\bar{\varepsilon}_p - 1)}{\bar{\varepsilon}_p + 2}a \tag{3.4.4c}$$

4. Lichtnecker model

$$\bar{\varepsilon}_a = \bar{\varepsilon}_p^{\phi} \tag{3.4.4d}$$

5. Lichtneker–Rother model

$$\bar{\varepsilon}_a^k = \phi\bar{\varepsilon}_p^k + (1-\phi) \tag{3.4.4e}$$

The apparent dielectric constant ε_a can be measured by the parallel-plate or cylindrical electrodes shown in Figure 3.4.1.

$$\bar{\varepsilon}_a = \varepsilon_0\frac{C_1}{C_0} \tag{3.4.5}$$

where C_0 is the electric capacitance of the measuring system without powder and C_1 is the capacitance with powder between the electrodes. The capacitance C_0 is given by the following equations:

1. Parallel-plate electrodes:

$$C_0 = \frac{A}{d}\varepsilon_0 \tag{3.4.6}$$

TABLE 3.4.6 Dielectric Constants of Standard Liquids

Liquid	Specific Dielectric Constant
Cyclohexane	2.023
Benzene	2.284
Chlorobenzene	5.708
Acetone	21.3
Nitrobenzene	35.7

2. Cylindrical electrodes:

$$C_0 = \frac{2\pi l}{\ln(b/a)}\varepsilon_0 \tag{3.4.7}$$

The apparent dielectric constant depends on the packing fraction, temperature, and humidity, as in the case of the specific resistance. The humidity strongly affects the measurement because the specific dielectric constant of water is about 10 times larger (81 at 18°C) than that of particles.

The dielectric constant of a particle ε_p can be measured by use of the standard liquid listed in Table 3.4.6. If the capacitance of a cell filled with the reference liquid does not change by adding particles into the cell, the dielectric constant of the particles is equal to that of the liquid. The dielectric constant of the reference liquid is adjustable by blending it with different liquids.

The following relation is useful in an estimation of the dielectric constant of a multicomponent particle:

$$\frac{1}{(1/\varepsilon)_{av}} \le \varepsilon^* < \varepsilon_{av} \tag{3.4.8}$$

where

$$\varepsilon_{av} = \sum v_i\varepsilon_i \quad \text{and} \quad \left(\frac{1}{\varepsilon}\right)_{av} = \sum\frac{v_i}{\varepsilon_i} \tag{3.4.9a,b}$$

ε_i is the dielectric constant of the i component and v_i is the volume fraction.

Specific Charge

The particle charge q divided by the particle mass m_p is called the specific charge. The specific charge is sometimes approximated by the total charge of powder divided by the mass of the powder. Since the charge on a particle is approximately proportional to its surface area in various electrification processes, the specific charge is almost inversely proportional to the particle size. Therefore, electrostatic phenomena may become predominant for smaller particles. If a fine particle is electrically charged, its motion is usually determined only by the ratio of the electrostatic force and the fluid viscous force. The total charge of powder is measured by an electrically shielded metal vessel, known as the Faraday cage. Powder is put into the Faraday cage and the potential V is measured

by a voltmeter. The charge Q is, then, given by the following equation:

$$Q = CV \tag{3.4.10}$$

where C is the capacitance of the Faraday cage.

The capacitance C is calibrated with a steel ball charged in an electric field supplying sufficient unipolar ions, according to the following equation for the charge of the sphere:

$$q = 3\pi\varepsilon_0 D_P^2 E \tag{3.4.11}$$

where E (V/m) is the electric field strength. Hence the specific charge Q/w is obtainable for known sample mass w.

The specific charge of suspended particles will be obtained through isokinetic sampling. Figure 3.4.2 shows the Faraday cage available for this purpose. The suspended particles are collected on a filter set in the Faraday cage. If the sampling of particles is impossible, a spherical cage made of a steel mesh may be used. The potential at the center of the spherical cage is given by the equation

$$V = \frac{Q}{8\pi\varepsilon_0 R} \tag{3.4.12}$$

where Q is the total charge of particles in the cage.

The specific charge of a particle is obtainable from the particle trajectory in an electric field. Figure 3.4.3 depicts parallel-plate electrodes where charged particles are introduced. The charge q can be obtained from the following equation:

$$q = \frac{3\pi\mu D_p u d}{C_C E x} \tag{3.4.13}$$

where u is the mean air velocity, d is the distance between upper and lower electrodes, C_C is Cunningham's slip correction factor, and x is the position of deposited particle. The electric field strength E is calculated as follows:

$$E = \frac{V}{d + \left(t/\varepsilon_r\right)} \tag{3.4.14}$$

where V is the applied voltage, t is the thickness of the slide glass, and ε_r is the specific dielectric constant of the glass.

The particle will suspend in the space when the electric force qE balances the gravitational force $m_p g$. Hence the specific charge can be obtained from the relation $q/m_p = g/E$. If the particle sediments in a horizontal electric field, it will deposit at a point (x, y) according to the relation $x/y = qE/m_p g$. Hence the distribution of the specific charge will be obtained.[10] The particle motion in a DC electric field superimposed upon an acoustic field or AC electric field can also be utilized in the simultaneous measurement of particle size and charge distributions.[11]

Contact Potential Difference

The contact potential difference of particles is essential for the estimation of the charge polarities and the amount of the charge acquired in various powder handling processes. It relates to the electrostatic powder coating, electrostatic powder imaging,

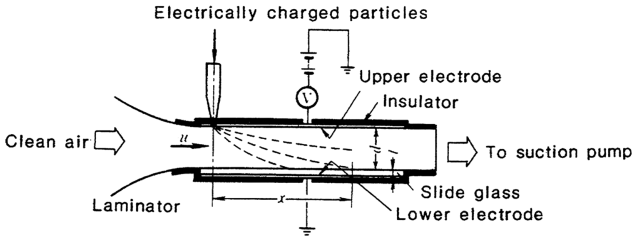


FIGURE 3.4.3 Parallel-plate electrodes for measuring a specific charge of individual particles.

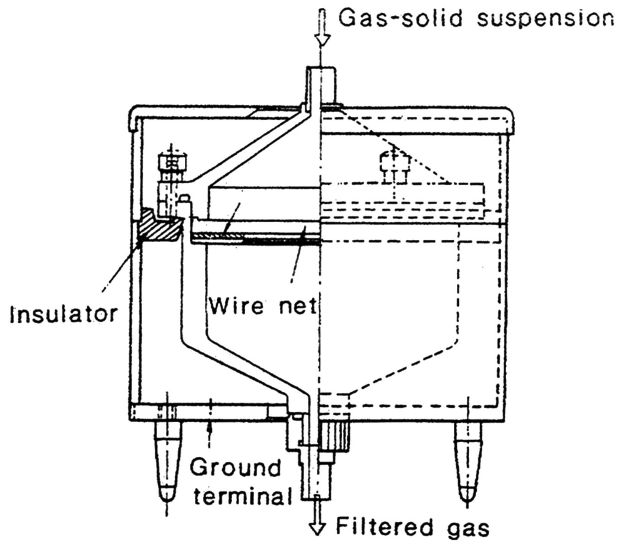


FIGURE 3.4.2 Faraday cage for measuring specific charge of suspended particles.

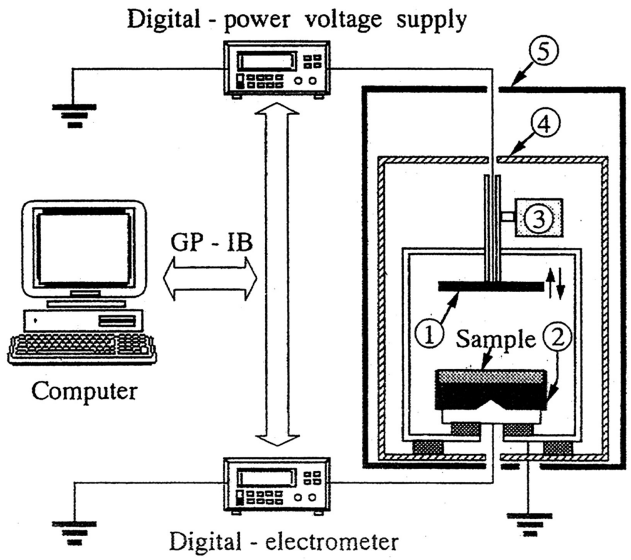


FIGURE 3.4.4 Measuring system for the contact potential difference.

and so on. For pure materials, including metals, there are some reference values available. However, it should be measured for particles, because small amounts of impurities and imperfections and the surface states may change the electrostatic characteristics of the particles.

Figure 3.4.4 shows schematically the measurement apparatus, which is based on the Kelvin method.[12,13] It consists of an upper electrode (1), lower electrode with packed powder layer (2), motor (3), digital-power voltage supply, and a digital electrometer for electric current measurement. The upper electrode moves up and down sinusoidally with a constant frequency. The timing to supply voltage and to detect electric current is controlled by the GP-IB (General Purpose Interface Bus) of a computer. The main device was set in an autodesiccator (5) with an electric shield (4) for noise reduction. The upper electrode is gold plated while the lower electrode is nickel plated so as to have enough strength against forcible contact or friction of the packed powder.

Electric current generated by the cyclic movement of the upper electrode becomes zero, when the applied voltage V to the upper electrode is equal to the apparent contact potential difference. And the contact potential difference is obtained if the charge of the powder layer is fully diminished. The effective work function of the powder is estimated by the equation

$$\phi_P = \phi_{Au} - eV_{P/Au} \tag{3.4.15}$$

where, ϕ_P is the effective work function of the powder, ϕ_{Au} the work function of Au, and $V_{P/Au}$ is the contact potential difference of powder against Au.

3.4.2 IN NONAQUEOUS SOLUTIONS

Particles dispersed in a liquid tend to form flocs(aggregates) due to colloidal forces. In suspensions of conductive particles in nonaqueous solutions, the charge transfer arises from the direct contact of two particles. The electric conductivity of suspensions strongly depends on the floc structures. In high electric fields, the dipole-dipole interactions cause the particle arrangement which leads to changes in physical properties, such as electric conductivity and rheology. The nonlinear effects of electric fields on the physical properties of suspensions will be described in relation to the structural formation of particles.

Electric Conductivity of Flocculated Suspensions

At low particle concentrations, the flocculated suspensions consist of a collection of discrete flocs. As the concentration is increased above some critical level, the flocs cease to be discrete and a three-dimensional network is formed through the system. The infinite network made up of contiguous sequences of conductive particles is required for transport of electric carriers(current) as an overall response.

The distribution of particles in the media and network formation process are often described through percolation theory. Site percolation deals with the distribution of cluster sizes for particles distributed in an infinite lattice composed of sites linked together by bonds. When sites are occupied at random with probability p^S and adjacent occupied sites are connected, there exists a critical probability p_c^S above which unbounded clusters of connected sites occur. Many authors have discussed the critical percolation probability for various lattices. For example, the critical percolation probability p_c^S for a simple cubic lattice has been predicted to be 0.325 by Monte Carlo methods[14] and 0.307 by series methods[15].

In flocculated suspensions, the particle concentration does not directly correspond to p^S, but it can be reasonably adopted that the individual floc has the limiting structure with $p^S = 1.0$. The sedimentation experiments are useful to determine the floc structure, or the limiting structure. Once the limiting floc structure is known, the particle concentration can be converted into the site probability p^S and therefore the critical particle concentration for appearance of drastic increase in electric current can be estimated.

The main task of percolation theory is to predict the transport properties of the percolating network above the critical probability.[16] Scaling argument shows a power law dependence of physical quantity Q on the difference of particle concentration from the critical value C_c[17]

$$Q = k\left(C - C_c\right)^n \tag{3.4.16}$$

where C is the particle concentration, k is a constant, and n is the critical exponent. De Gennes pointed out that the critical exponent is estimated to be 1.8, when the network transmits a scalar quantity. Although k varies with the materials, the concentration dependence of electric conductivity for flocculated suspensions can be explained on the basis of statistical universality.

Column Structures and Conductivity in High Electric Fields

When the dielectric constants of the particles and of the liquid are substantially different, an electric field generates a dipolar field around the particle. The particles attract one another if they are aligned along the field direction, whereas the particles in the plane perpendicular to the field direction repel one another. Since many polarized particles interact in this way, the chains of particles are formed to span the electrode gape even in completely dispersed suspensions without electric fields. As a simplified approach, most existing models assume that the particles all align into chains of single-particle width and equal spacing. Although the ideal single chain model is helpful to understand the basic process of particle arrangement, the chainlike structures are unlikely to be constructed by the separated chains.

The induced structure in electric fields must have the configuration which minimizes the dipolar interaction energy. The force between two particles is attractive if the line of centers is within 55° of the electric field.[18] When placed near a chain, a particle will be repelled by the nearest particles in

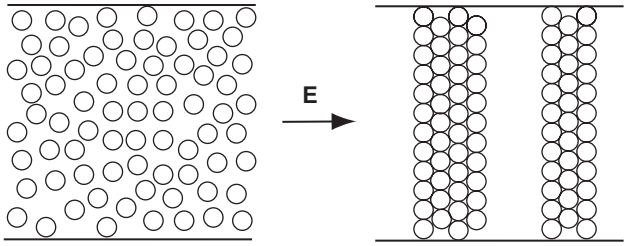


FIGURE 3.4.5 Column formation of particles on the application of electric fields.

the chain. But the particle will be attracted by the chained particles well above and below it. Because many particles are placed near the chain in suspensions, they will be attracted to it and can form a second chain. Consequently, due to long-range interactions, the polarization forces between particles cause the chains to form columns. The structural changes from non-interacting particles to thick columns spanning the electrode gap are schematically shown in Figure 3.4.5. The column may be constructed by three types of chain; fully developed chains connecting the electrodes, chains attached at only one end to an electrode, and drifting chains.

According to the theory on the column structures by Tao and Sun,[19] the dipolar interaction energy per particle strongly depends on the lattice structure. For example, in a simple cubic lattice, a particle in one chain has four particles in other chains as its nearest neighbor and the centers of particles lie in a plane perpendicular to the field vector. Since the forces between neighbor particles are strongly repulsive, the particles hardly construct the simple cubic lattice. In a quiescent state, the most stable structure is a body-centered tetragonal lattice. Therefore, the suspension in electric fields comprises the columns with the body-centered tetragonal lattice. The fully developed columns spanning the electrodes gap can be achieved even in suspensions at a particle concentration of 1 vol%.

Although an electric current is attributed to the particle-medium interface or particle itself, the chains spanning electrode gap are primarily responsible for susceptible current in electrified suspensions. Because the chain formation is promoted at high electric fields and the current density rapidly increases with field strength. In ordinary conditions, the chain formation is induced at electric fields beyond 1 kVmm^{-1}. The local field strength near contact area can reach values as high as 30~100 kVmm^{-1} where partial breakdown of oil is possible. Hence, this mechanism results in non-Ohmic behavior in which the resistance decreases with increasing field strength.

Figure 3.4.6 shows the current density plotted against the field strength for a 40 vol% silica suspension in a quiescent state and under steady shear at a shear rate of 200 s^{-1}.[20] The plots for each shear condition lie on a straight line. In shear fields, the rupture and reformation of columns are constantly repeated. Although the current density is decreased by the application of shear fields, the effect of shear rate is not very strong. The ionic and electronic migration along the columns

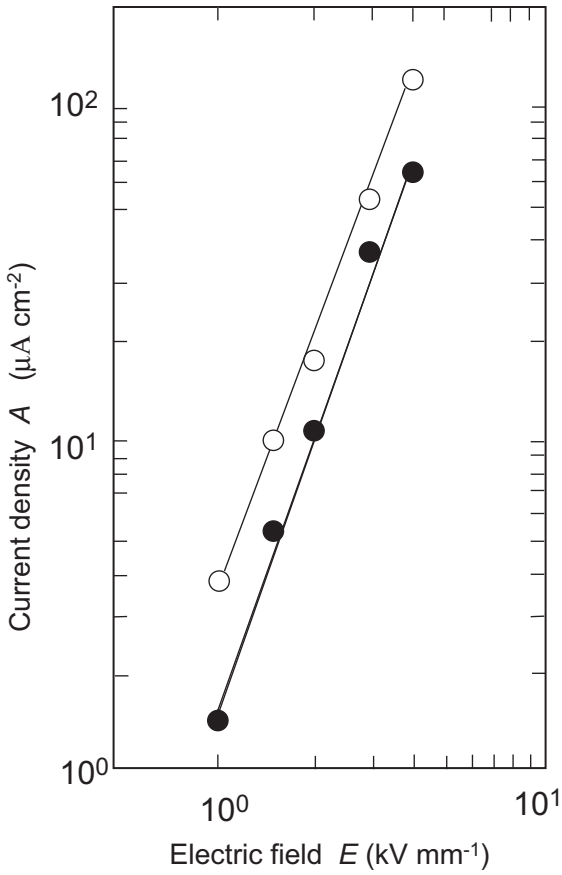


FIGURE 3.4.6 Current density plotted against the field strength for suspension at rest (open circle) and sheared (filled circle) at 200 s^{-1}.

spanning the electrodes is the main origin of current in the static suspensions. But a different mechanism may be couched in the charge transfer of suspensions under shear flow.

If the suspension is completely dispersed to primary particles in electric fields, a charged particle approaches the electrode of opposite charge. When the particle touches the electrode surface, a transfer of charge to the particle occur until the electrode and particle reach the same potential. Then the particle is repelled from the electrode and moves to the other electrode. Since the process is continuously repeated, the oscillatory motion of charged particles leads to the current. Presumably the oscillatory motion of drifting chains between electrodes may contribute to conductivity. Because of combined effects of various mechanisms, the relation between the current density and field strength has not been quantitatively established. However, several authors have reported that the current density A can be expressed by the following equation:

$$A \propto E^n \tag{3.4.17}$$

From the slopes of straight lines in Figure 3.4.6, the n values are determined to be 2.5 for the static suspension and 2.7 for the flowing suspension. The n value has been found to be 2.5~3.0, independent of shear rate.

Rheological and Optical Properties of Electrified Suspensions

In response to electric fields, the suspensions often exhibit a rapid and reversible transition between viscous liquids and rigid solids. This phenomenon is referred to as the electrorheological (ER) effect. The ER fluids are very attractive as effective vehicles in new devices for controlling the motion of liquids through a narrow channel. Possible devices include stop valve, brakes, and dampers.

The columns fully developed between the electrodes can accumulate elastic energy, unless the strain exceed some critical value. The suspensions in electric fields behave as solids at low strains or stresses. The rheological changes of suspensions on the application or removal of electric fields can be characterized as a reversible sol-gel transition. In very high shear fields, the hydrodynamic forces dominate the electric forces. Therefore, the stress linearly increases with shear rate.

Figure 3.4.7 shows the flow curves in electric fields of 0 and 2.0 kVmm^{-1} for suspensions at different particle concentrations.[21] In the absence of electric fields, the shear stress is proportional to shear rate and the flow is Newtonian. The electric fields cause an increase in shear stress over the entire range of shear rates. The stress enhancement is much larger at low shear rates and each flow curve clearly shows a plateau. This implies that the rupture and reformation of column structures are constantly repeated at low shear rates. Since the constant stress is generated in the limit of zero shear rate, the height of plateau is considered to correspond to the yield stress.

The deformation and rupture process of columns is very complicated. On the assumption that the particles all align into chains of single-particle width and equal spacing, Marshall et al. derived a Bingham constitutive equation of ER fluids.[22] In the analysis, all the chains spanning the electrode gap rupture in the center and immediately swing back to reform with the nearest chain on the opposite electrode. Based on the bulk polarization theory, the yield stress σ_0 given by the equation:

$$\sigma_0 \propto \phi \varepsilon_0 \varepsilon_c \beta^2 E^2 \tag{3.4.18}$$

$$\beta = \left(\varepsilon_p - \varepsilon_c\right) / \left(\varepsilon_p + 2\varepsilon_c\right) \tag{3.4.19}$$

where ϕ is the volume concentration of particles, ε_0 is the permittivity of free space, ε_c and ε_c are the dielectric constants of medium and particles, respectively. The theory is successful in correlating the yield stress of suspensions and material functions of components. However, as far as the bulk polarization theory that ignores the surface effects is concerned, the only method for formulating excellent ER fluids is a dielectric mismatch. In actual suspensions, the interparticle forces due to surface polarization play an essential role in the ER effects. For example, the ER behavior of silica suspensions is governed by the amount of surface silanol groups. The surface modification of particles may have great potential to improve the ER performance of suspensions.

In suspensions without electric fields, the particles are randomly and uniformly dispersed by Brownian motion. However, the column structures are developed and the optical anisotropy is induced in electric fields. Figure 3.4.8 shows the effect of field strength on the spectral intensity of transmitted light for an ER suspension containing blue particles at 15 vol%.[23] Without electric fields, the spectrum of transmitted light shows a maximum at a wavelength of 490 nm. As the field strength is raised, the light intensity increases in

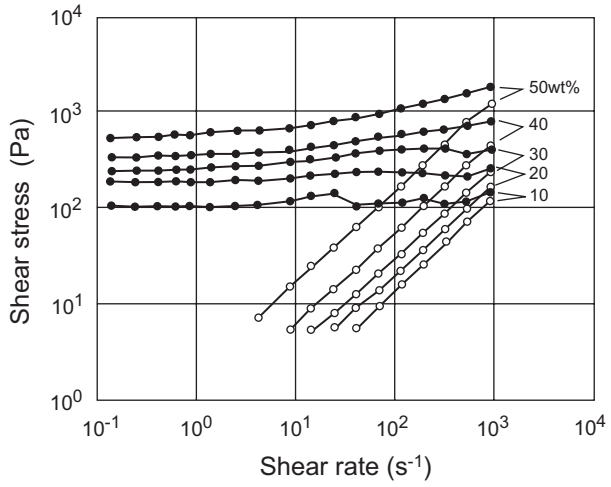


FIGURE 3.4.7 Flow curves in electric fields of 0 (open circle) and 2.0 kVmm^{-1} (filled circle) for suspensions at different particle concentrations.

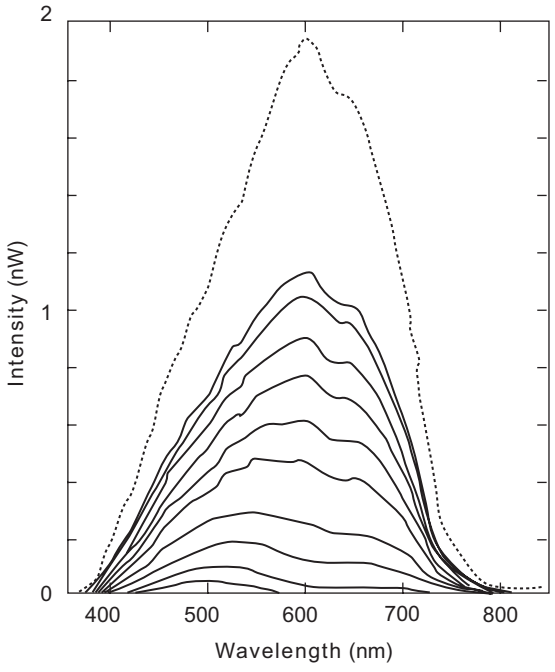


FIGURE 3.4.8 Effect of field strength on the spectral intensity of transmitted light for medium (dotted line) and suspension (solid line) in electric fields of different strength: 0, 0.09, 0.18, 0.27, 0.45, 0.64, 0.91, 1.36, 1.82, and 2.73 kVmm^{-1} from bottom to top.

the entire range and the wavelength at the maximum transmittance shifts toward the red(longer wavelength) side. The wavelength at the peak is 600 nm in high electric fields and this value corresponds to that of incident light which is regarded as colorless. In electric fields, the dilute suspension consists of discrete columns and hence the induced structures are strongly anisotropic. The plane perpendicular to the optical path is occupied by many discrete columns and continuous medium. In ordinary suspensions, the particles are highly absorbing. Because of high optical density, the columns do not transmit light. On the other hand, the vacant area without particles is regarded as transparent. Considering that the irradiation energy is absorbed mainly by the particles and the fraction absorbed by the medium is negligibly small, the cross section of optical path comprises dark (column) and transparent (medium) regions. Because the fraction of vacant area increases with field strength, the transmittance is markedly increased. The light absorption in electric fields is a purely geometrical effect, which depends only on the cross section of columns.

REFERENCES

1. White, H. J., *Industrial Electrostatic Precipitation*, Addison-Wesley, Reading, Mass., 1963, p. 319.
2. Masuda, S., Mizuno, A., *Proc. Inst. Electrostat. Jpn*., 2, 59, 1978.
3. Masuda, S., *Denki Gakkaishi*, 80, 1790, 1960.
4. White H. J., *J. Air Pollut. Control Assoc*., 24, 4, 313, 1974.
5. Maxwell, J. C., *Electricity and Magnetism*, 1, Clarendon, Oxford, 1892.
6. Louge, M., Opie, M., *Powder Technol*., 62, 85, 1990.
7. Rayleigh, W. R., *Philos. Mag. Ser.*, *5*, 34, 481, 1892.
8. Böettcher, C. J. F., *Rec. Trav. Chim*., 64, 47, 1945.
9. Yadav, A. S. Parshad, R., *J. Phys. D Appl. Phys*., 5, 1469, 1972.
10. Masuda, H., Gotoh, K., Orita, N., *J. Aerosol Res. Jpn*., 8, 325–332, 1993.
11. Mazumder, M. K., *KONA*, 11, 105–118, 1993.
12. Thomson, W. (later Lord Kelvin), *Phil. Mag*., 46, 1898.
13. Masuda, H., Itakura, T., Gotoh, K., Takahashi, T., et al., *Adv. Powder Technol*., 6, 295–303, 1995.
14. Frisch, H. L., Sonnenblick, E., Vyssotsky, V. A., Hammersley, J. M., *Phys. Rev*., 124, 1021–1022, 1961.
15. Sykes, M.F., Essam, J. M., *J. Math. Phys*., *5*, 1117–1127, 1964.
16. Stauffer, D., *Introduction to Percolation Theory*, Taylor & Francis, London, 1985.
17. De Gennes, P.G., *Scaling Concepts in Polymer Physics*, Cornell Univ. Press, Ithaca, 1979.
18. Halsey, T. C., *Science*, 258, 761–766, 1992.
19. Tao, R., Sun, J. M., *Phys. Rev. Lett*., 67, 398–401, 1991.
20. Otsubo, Y., Sekine, M., Katayama, S., *J. Rheol*., 36, 479–496, 1992.
21. Otsubo, Y., Edamura, K., *J. Rheol*., 38, 1721–1733, 1994.
22. Marshall, L., Zukoski, C. F., Goodwin, J. W., *J. Chem. Soc. Faraday Trans. 1*., 85, 2785–2795, 1989.
23. Edamura, K., Akashi, K., Otsubo, Y., *J. Imaging Sci. Technol*., 39, 564–569, 1995.

3.5 Packing Properties

Michitaka Suzuki

It is well known that the packing of particulates is one of the most fundamental and important powder-handling processes, and various properties of the particulate assembly are basically determined by the geometrical arrangement of individual particles. Void fraction is a popular and simple expression of macroscopic packing characteristics of a powder bed. In an actual powder system, void fraction ε is defined by

$$\varepsilon = 1 - \frac{\rho_b}{\rho_p} = 1 - \frac{M}{\rho_p V} \tag{3.5.1}$$

where ρ_b, ρ_p, M, and V are apparent density, particle density, and mass and volume of powder bed, respectively. Particle volume fraction or packing fraction defined as $\phi = 1-\varepsilon$ is frequently also used to express the packing structure in place of the void fraction.

In the case of suspension or plastics with filler, the void is filled with a matrix such as liquid or plastics, the volume fraction of matrix can be calculated by

$$\varepsilon = 1 - \frac{M - V\rho_m}{(\rho_p - \rho_m)V} \tag{3.5.2}$$

where ρ_m is the density of matrix. If the value of ρ_m is zero, Equation (3.5.2) is the same as Equation (3.5.1).

In actual powder, the void fraction is changing with the particle size.[1] As shown in Figure 3.5.1, the void fraction shows the constant value ε_c over certain critical particle size x_c, and below this size, the void fraction increases with decrease in the particle size x. This result indicates that particle packing is dominated by gravity in the larger particle size over the critical particle size x_c, and it governs by adhesion force in the smaller particle size under the critical size x_c.

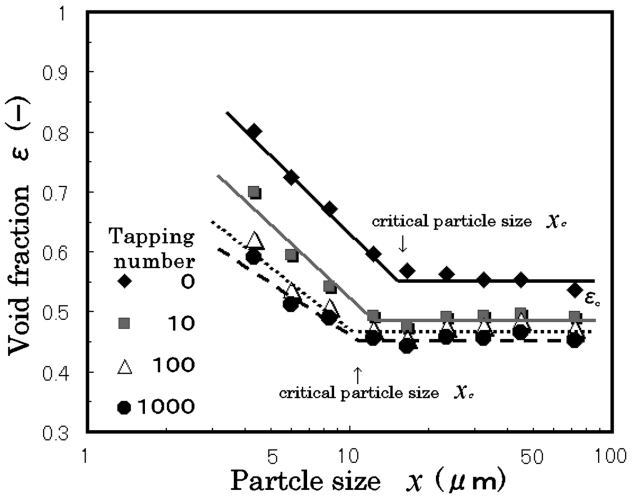


FIGURE 3.5.1 Effect of particle size on void fraction of monosized powder bed.

Based on the experimental packing result, Roller[2] proposed the following empirical equation as a relationship between the void fraction ε and particle size x.

$$\varepsilon = \varepsilon_c \quad (x > x_c) \tag{3.5.2a}$$

$$\varepsilon = \frac{1}{1 + \left(\frac{1}{\varepsilon_c} - 1\right)\left(\frac{x}{x_c}\right)^n} \quad (x < x_c) \tag{3.5.2b}$$

Index n and the critical particle size x_c change with environmental conditions, packing method, and types of powder. Generally n takes the value between 0 and 1.

3.5.1 PACKING OF EQUAL-SIZE SPHERES

Many researchers have investigated the assembly of equal-size spheres because of its simplicity and its convenience in theoretical work. Regular packing is the easiest to use to describe internal structure as a set of unit cells. There are six typical unit cells, as shown in Figure 3.5.2. Graton and Fraser[3] characterized the internal structure of the unit cells, consisting of a few primary spheres in which geometrical features such as the angle and distance between neighboring sphere centers, the void fraction, and the coordination number (or the number of contact points on a particle surface) are obtained. Closest or rhombohedral packing is used frequently as a reference system.

In actual packing of particles the void fraction and coordination number vary widely and continuously, but in regular packings there exist only discrete values: void fraction = 0.2594 (rhombohedral), 0.3119 (tetragonal–sphenoidal), 0.3954 (orthorhombic), and 0.4764 (cubic) and coordination number N_c = 12, 10, 8, and 6, respectively. Heesh and Laves[4] proposed a regular packing of equal-size spheres supported by wire frames as a model structure of particle assembly with high void fraction. But this type of spherical structure scarcely exists in actual particulate assemblies and has fixed values of void fraction and coordination number. Smith et al.[5] proposed a hybrid model obtained by mixing the simple cubic and rhombohedral unit cells, and the model equation (7) in Table 3.5.1 shows the continuous relation between the void fraction ε and the coordination number N_c. Shinohara et al.[6] and Shinohara and Tanaka[7] proposed another hybrid model, which is a random mixture of the simple cubic and rhombohedral unit cells and can explain a wide and continuous change

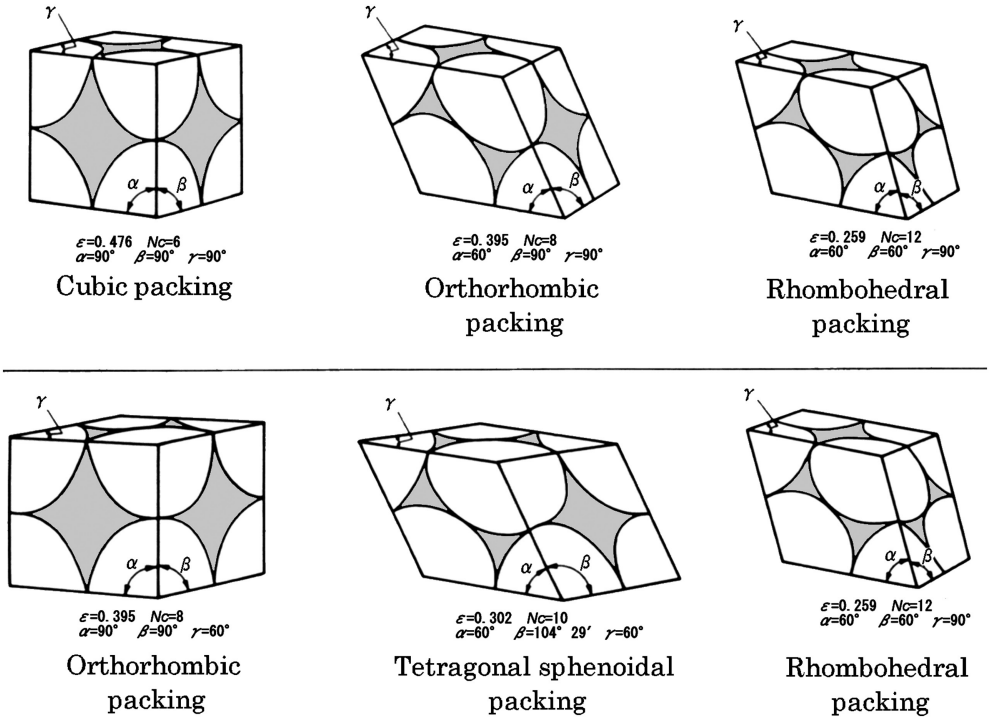


FIGURE 3.5.2 Regular packing structures of equal-size spheres.

TABLE 3.5.1 Expressions of the Relationship between Void Fraction and Average Coordination Number

Expression	Equation No. in Figure 3.5.3
$\bar{N}_c = 3.1/\varepsilon$	(1) Rumpf 1958
$\bar{N}_c = 2e^{2.4(1-\varepsilon)}$	(2) Meissner et al. 1964
$\varepsilon = 1.072 - 0.1193\,\bar{N}_c + 0.0043\,\bar{N}_c^2$	(3) Ridgeway et al. 1967
$\bar{N}_c = 22.47 - 33.39\varepsilon$ $(\varepsilon \le 0.5)$	(4) Haughey and Beveridge 1969
$\bar{N}_c = \left[8\pi/\left(0.727^3 \times 3\right)\right](1-\varepsilon)^2$	(5) Nagao 1978
$\bar{N}_c = 1.61\varepsilon^{-1.48}$ $(\varepsilon \le 0.82)$	(6) Nakagaki and Sunada 1968
$\bar{N}_c = 4.28 \times 10^{-3}\,\varepsilon^{-17.3} + 2.00$ $(0.82 \le \varepsilon)$	
$\bar{N}_c = 26.49 - 10.73/1-\varepsilon)$ $(\varepsilon \le 0.595)$	(7) Smith et al. 1929
$\bar{N}_c = 20.7\,(1-\varepsilon)/\pi - 4.35$ $(0.3 < \varepsilon \le 0.53)$	(8) Gotoh et al. 1978
$\bar{N}_c = 36\,(1-\varepsilon)$ $(0.53 \le \varepsilon)$	
$\bar{N}_c = 2.812(1-\varepsilon)^{-1/3} \Big/ (b/x)^2 \left\{1 + (b/x)^2\right\}$	(9) Suzuki et al. 1980
$b/x = 7.318 \times 10^{-2} + 2.193\varepsilon - 3.357\varepsilon^3 + 3.194\varepsilon^3$	
$\bar{N}_c = (32/13)(7-8\varepsilon)$	(10) Ouchiyama et al. 1980

in the void fraction and the coordination number. These are useful models for close-packing structures with local order. Gotoh[8,9] and Iwata and Homma[10] made similar studies of random packing in terms of the combination of regular packings. Bargiel and Tory[11] investigated the transition from dense random packing and measured the disorder of ultra-dense irregular packing of equal-size spheres.

Many investigations have been made of the coordination number in a random assembly of equal-size spheres; these include studies by Smith et al.,[5] Rumpf,[12] Bernal and Mason,[13] Meissner et al.,[14] Wade,[15] Ridgway and Tarbuck,[16] Arakawa,[17] Haughey and Beveridge,[18] Bernal et al.,[19] and Nagao,[20] and a number of empirical relations have been proposed. Nakagaki and Sunada,[21,22] Bennett,[23] and Tory et al.[24] made computer simulations of three-dimensional random packings from which they obtained the relationship between the average coordination number N_c and the void fraction. Figure 3.5.3 shows a comparison between the results calculated from the equations in Table 3.5.1 and practical experiments and computer experiments. Equation (3.5.1) through Equation (3.5.5) (the dashed curves) expresses the empirical relations, whereas Equation (3.5.6) and Equation (3.5.7) (the dashed curves) are obtained from the random mixture model of regular packings. Gotoh and Finney,[25] Suzuki et al.,[26] and Ouchiyama and Tanaka[27] reported the theoretical relations in Equation (3.5.8) through Equation (3.5.10) (the solid curves). Suzuki and Oshima[28] compared the calculated results obtained by Equation (3.5.1) through Equation (3.5.10) and the four kinds of computer simulated results, showing that Nakagaki et al.'s empirical formula agreed well with three simulation results over a wide range of the void fraction. Some of the above simulation results corresponded well to Suzuki et al.'s and Gotoh's model formula and Nagao's empirical formula in a certain void fraction.

Suzuki et al.[29] investigated the effect of size distribution on the relation between the void fraction and the average

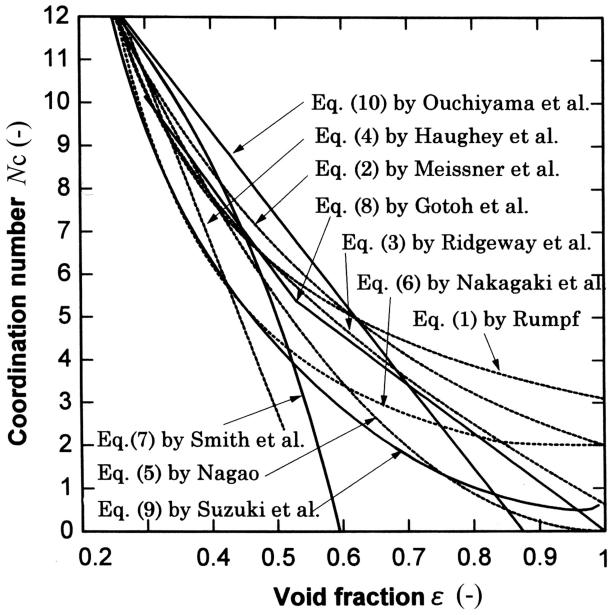


FIGURE 3.5.3 Relationship between void fraction and average coordination number for mono-sized spheres.

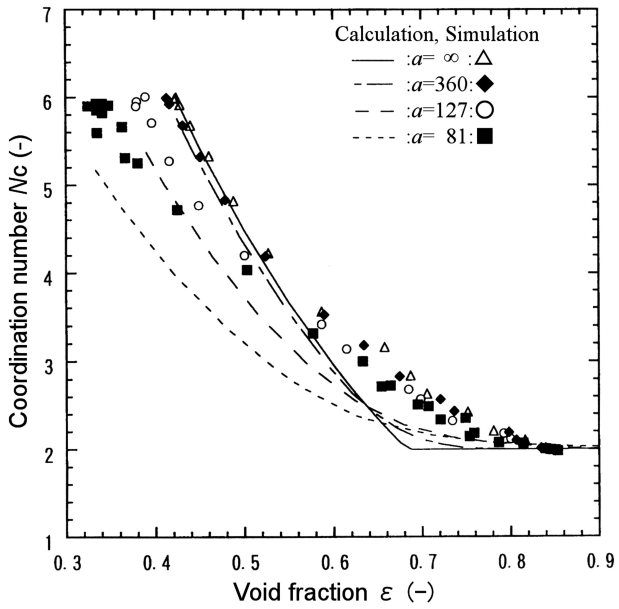


FIGURE 3.5.4 Effect of size distribution on the relation between void fraction and average coordination number for spheres with size distribution.

coordination number using the model calculation and computer simulation results. Figure 3.5.4 shows the relation between the void fraction ε and the average coordination number of the random-packed bed with log-uniform size distribution. Based on the results, the coordination number is not so affected with the size distribution of particles, but the void fraction becomes smaller for wider distribution of particle size. It means that the value of the coordination number, estimated by a conventional equation for equal-size spheres from void fraction data, is overestimated for randomly packed

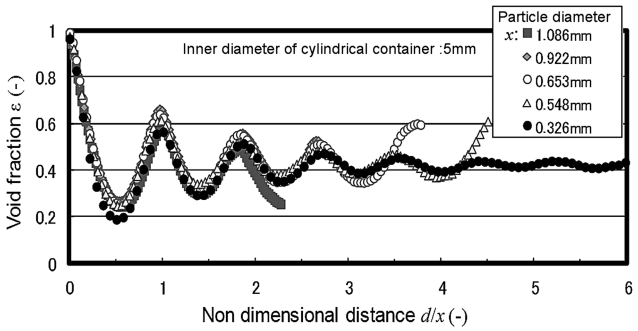


FIGURE 3.5.5 Void fraction distributions near container wall.

beds of multi-component spheres with wider particle size distributions.

Knowledge of the spatial structure of particles in a random assembly is important in dealing with the deformation of a powder bed, the electrostatic and liquid bridge forces between particles, radiative and convective heat transfer in particle systems, and so on. Figure 3.5.5 shows the void fraction distribution closed to the container wall of particle packed bed using X-ray micro focus computer tomography[30]. From this figure, the void fraction is fluctuated with the non-dimensional distance from wall, and the distribution is similar with radial function distribution.

Fractal dimensions of particle beds are also used to describe the particulate assemblies. Witten and Samder[31] and Tohno and Takahashi[32] expressed the particle arrangement in an aerosol agglomerate by the fractal dimension. Kamiya et al.[33] used it to characterize the packing structure of an aggregate in a particle bed. Suzuki and Oshima[34] obtained a fractal dimension of a packed particle system by the scaling method. The fractal dimension enables us quantitatively to distinguish the difference in packing structures that cannot be expressed by the relation between coordination number and void fraction.

3.5.2 PACKING OF MULTI-SIZE PARTICLES

Actual powders have wide distributions in size; hence, a packed bed can be regarded as a mixture of different-size particles. Particle size distribution also effect void fraction. For example, fine particles go into the space between coarse particle packed bed, and closed packed bed can be achieved. Horsfield,[35] White and Walton,[36] and Hudson[37] have discussed the regular packings of multi-sized spheres, in which the interstices of an array of spheres are filled with smaller spheres. The void fractions of the Horsfield's packings are listed in Table 3.5.2. Although the packing densities are expected to be very high theoretically, in practice it is difficult to construct these packings.

Generally speaking, powder has a random structure, and regular packing hardly exists in practice. Experimental data of the void fraction and coordination number in a multi-sized particle bed have been reported by Furnas,[38] Sohn and Moreland,[39] Arakawa and Nishino,[40] and Suzuki and Oshima,[41] Powell,[42] Dinger and Funk,[43] Suzuki and Oshima,[44]

TABLE 3.5.2 Calculated Results of the Horsfield Model for Multi-sized Regular Packing of Spheres

Fraction	X_1/X_2	Relative No. of Spheres	Void
First sphere	1	1	0.2595
Second spheres	0.414	1	0.207
Third spheres	0.225	2	0.190
Fourth spheres	0.177	8	0.158
Fifth spheres	0.116	8	0.149
Filler	Fine	Infinite number	0.039

and Ito et al.[45] devised a computer simulation for random packing of multi-sized spheres and obtained the simulation data.

Many different models have been conceived for the random packing of multi-sized particles, by Furnas,[46] Westman,[47] Tokumitsu,[48] Kawamura et al.,[49] Abe et al.,[50] Ouchiyama and Tanaka, [27,51,52] Suzuki and Oshima,[41] and Suzuki et al.,[53,54] and the void or packing fraction is estimated.

For example, Furnas estimated the void fraction of a binary powder mixture as follows:

$$\varepsilon = 1 - \frac{1-\varepsilon_1}{S_{v1}} \tag{3.5.3a}$$

$$\varepsilon = 1 - \frac{1-\varepsilon_2}{1-S_{v1}\varepsilon_2} \tag{3.5.3b}$$

where ε_1 is the void fraction of a coarse mono-sized powder bed, ε_2 is the void fraction of the fines, respectively, and S_{v1} is the fractional volume of coarse powder 1 in the binary mixture. Equation (3.5.3a) means that the interstices between coarse particles are filled with fine particles, and Equation (3.5.3b) means that the coarse particles are dispersed in the fine powder bed. If the two calculated void fractions are not equal to each other, the higher void fraction should be chosen. The typical results calculated from these equations are shown in Figure 3.5.6 for $\varepsilon_1 = \varepsilon_2 = 0.35$, 0.4, 0.45, and 0.5. The void fraction of the binary mixture becomes much smaller than that of mono-sized powder bed and exhibits the minimum value, because the finer powder fills the interstices of the coarse powder.

Most investigators, except Ouchiyama and Suzuki et al., treated the packing as a continuous medium and did not consider the relation between the void or packing fraction and the coordination number. Furthermore, Ouchiyama and Tanaka's model assumes an equal void fraction for the packing of each size of sphere, but this is not the case in the actual powders. Cross et al.[55] modified the model for expressing the matrix structure of composite materials.

Here Suzuki's model for estimating the void fraction of a packed bed of m different-sized spheres is explained. Figure 3.5.7 shows $m \times m$ basic types of contact between a reference sphere and others. The void fractions about the central spheres are denoted by $\varepsilon_{(1,1)}$, $\varepsilon_{(1,2)}$,……,$\varepsilon_{(m,m)}$, which are defined by

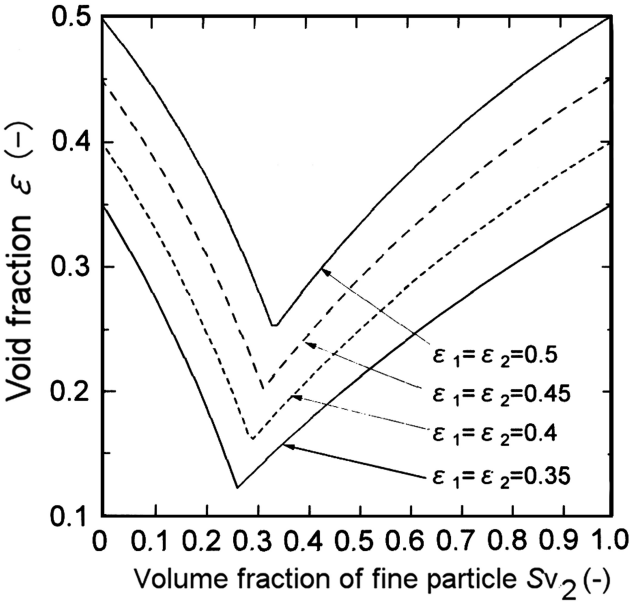


FIGURE 3.5.6 Calculated results from Furnas's equations.

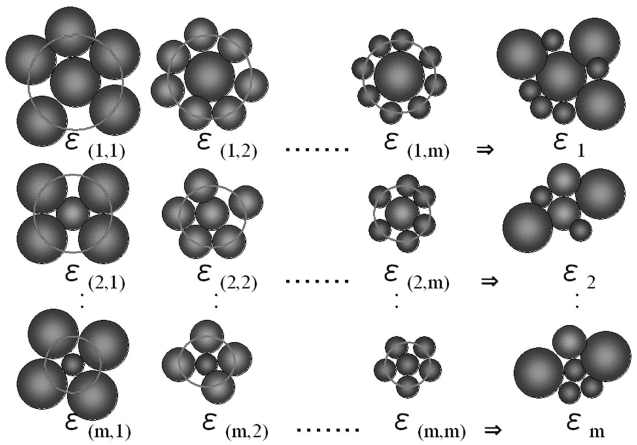


FIGURE 3.5.7 Fundamental combinations of contact in multi-component random mixture of spheres.

Equation (3.5.6) below. The bulk-mean void fraction ε of the bed becomes

$$\varepsilon = \sum_{1}^{m} S_{vj}\,\beta_j\,\varepsilon_j, \qquad \varepsilon_j = \sum_{1}^{m} S_{ak}\varepsilon_{(j,k)} \tag{3.5.4}$$

where S_{vj} is the fractional volume of sphere j, ε_2 is the partial void fraction about sphere j, S_{ak} is the fractional area of sphere k about sphere j, and β_j is a constant that is calculated from the measured void fraction ε of the bed composed of sphere j by putting $S_{ak} = 1$ and $S_{vj} = 1$ in Equation (3.5.4):

$$\beta_j = \frac{\bar{\varepsilon}_j}{\varepsilon_{(j,j)}} \tag{3.5.5}$$

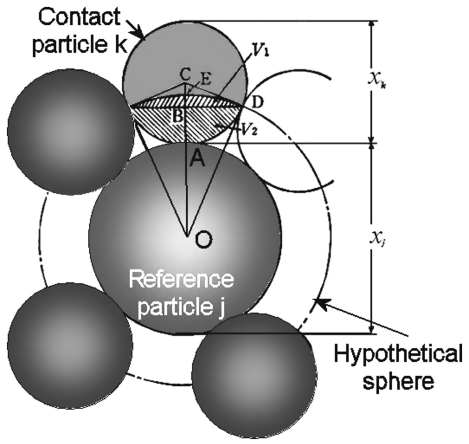


FIGURE 3.5.8 Model of a reference particle j in direct contact with particle k.

The next step is to derive the partial void fraction $\varepsilon_{(j,k)}$. $N_{(j,k)}$ of sphere k of diameter x_k are in direct contract with a reference sphere j of diameter x_j, as shown in Figure 3.5.8. A spherical region of radius $\overline{OD}$ (shown by the dashed curve) is considered, where O is the center of the reference sphere j and D is the contact point of the two adjacent k spheres. The void fraction $\varepsilon_{(j,k)}$ of the spherical region can be determined as follows:

$$\varepsilon_{(j,k)} = \frac{(\pi/6)x_j^3 + N_{(j,k)}(V_1 + V_2)}{V_s} \tag{3.5.6}$$

where V_1 is the partial volume of the spherical region, V_2 is that of the contact particle (see the cross-hatched area in Figure 3.5.8), and V_s is the volume of the spherical region of radius $\overline{OD}$. The coordination number $N_{(j,k)}$ can be calculated from Suzuki and Oshima's model[56] for random packing of different-sized spheres.

A packed bed of two sizes of glass beads is formed for the particle size ratio x_1/x_2 of 2, 2.83, 3.99, and 8.02. Plotted in Figure 3.5.9 are the experiments, and the curves depict the results calculated by Equation (3.5.5).

Figure 3.5.10 shows the relationship between the standard deviation ($\ln \sigma_g$) of log-normal size distribution and the void fraction ε. The void fraction becomes smaller for wider particle size distributions. Figure 3.5.11 shows the relationship between the Fuller constant q of the Gaudin–Schuhmann (Andreasen) size distribution and the void fraction ε. The minimum void fraction is obtainable for the Fuller constant of 0.5–0.8 in this case. This is because the interstices among particles decrease for $q = 0.5$ to 0.8. It was also reported by Kawamura et al.[49] experimentally that the void fraction could become minimum at $q = 0.6$, and Dinger and Funk[57] showed that optimum packing occurs for the distributions with $q = 0.37$. Suzuki and Oshima[50] reported that the q value at minimum void fraction changes with the adhesive property of fine powder and the width of size distribution. Because the calculated results are in good agreement with the experimental

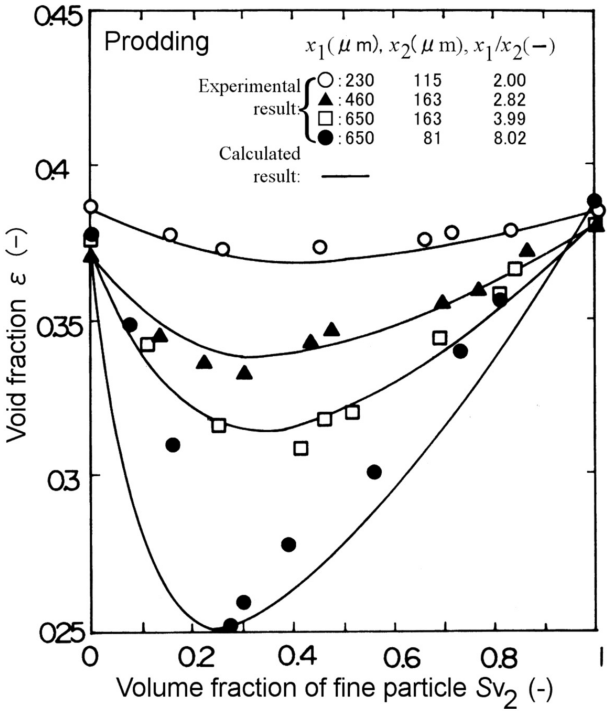


FIGURE 3.5.9 Relationship between fractional volume of fine spheres and void fraction of two-component mixture.

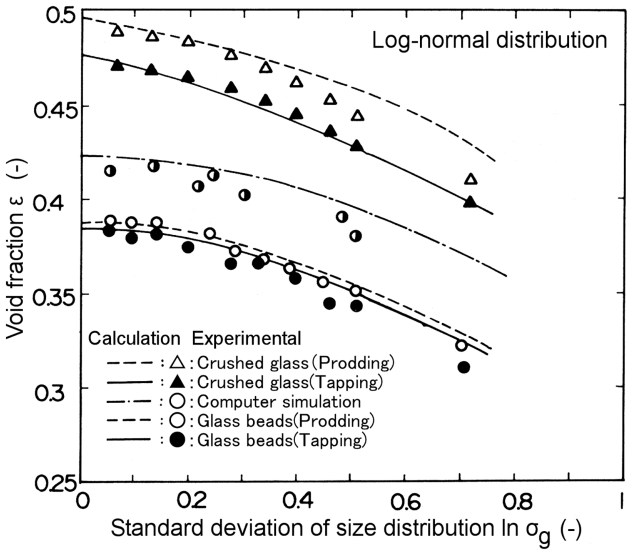


FIGURE 3.5.10 Relationship between standard deviation of log-normal size distribution and void.

and simulation data, the present model may be used in the practical applications.

3.5.3 EFFECT OF PARTICLE SHAPE ON VOID FRACTION

The particle shape especially surface roughness of a particle is affected on particle packing structure. Five kinds of crushed limestone powder were produced by five different

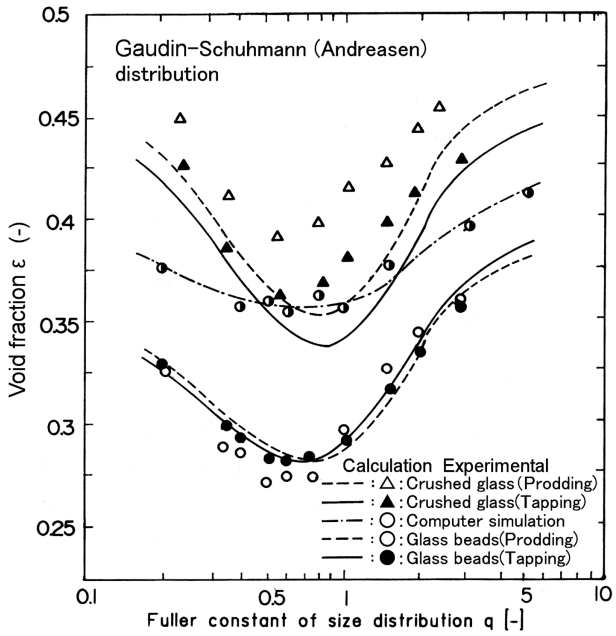


FIGURE 3.5.11 Relationship between Fuller constant of Gaudin–Schumann size distribution and void fraction.

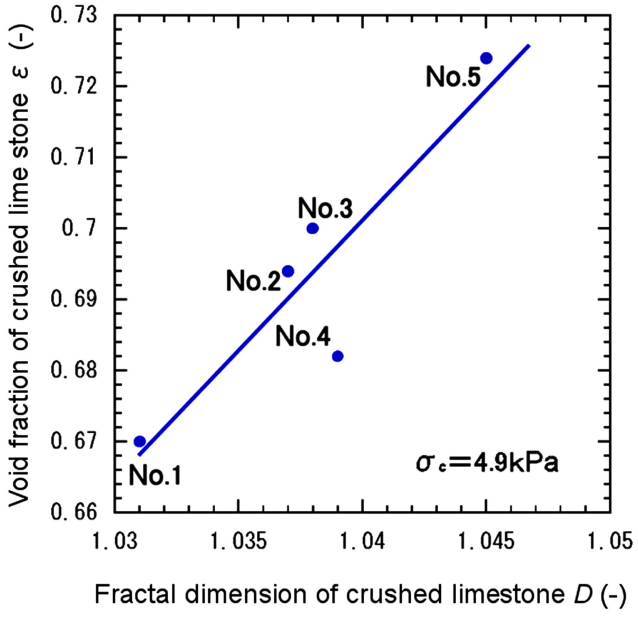


FIGURE 3.5.12 Effect of fractal dimension of particle perimeter on void fraction.

kinds of crusher such as Fluidized jet mill (No.1), ACM pulverizer (No.2), Super micron mill (No.3), Pot mill (No.4), and Media agitating mill (No.5). Figure 3.5.12 shows the relation between Fractal dimension of crushed limestone particle perimeter and the void fraction of the piston compressed powder bed.[58] The void fraction is increased with the increment of Fractal dimension. It means that the surface roughness of the particles increases the friction of the particle surface, resulting in loose packing.

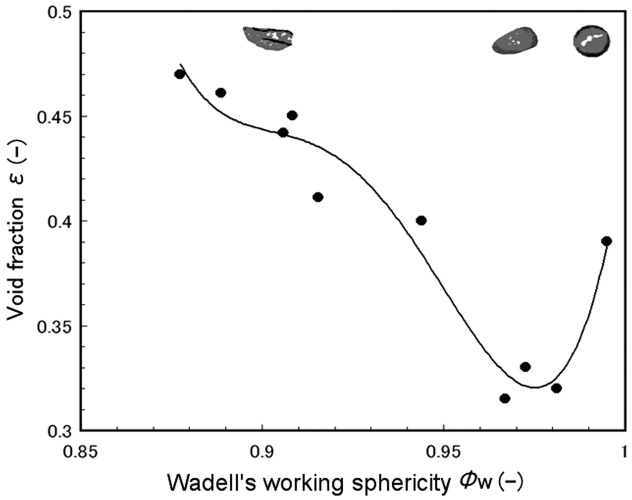


FIGURE 3.5.13 Effect of Wadell's working sphericity on void fraction.

The overall shape of the particle also influences the packing property. Figure 3.5.13 shows the relation between Wadell's working sphericity and the void fraction of packed bed. The Wadell's working sphericity Φ_w of a particle is the ratio of the perimeter of a projected sphere with the same projected area as the given particle to the perimeter of the particle. From the experimental result, the spherical particles are closer packed than the crushed particle, and the void fraction shows a minimum value when the sphericity is around 0.95, and is closest packed. This means that the rugby ball-shaped spheroidal particles are most closely packed. A. Donev et al. reported the same tendency.[59] Based on the micro-focus X-ray computer tomographic image of the packed bed, it was confirmed that the spheroidal particles were oriented by vibration and the closest packing was achieved.

NOTATION

a: slope of logarithmic uniform distribution (-)
b: constant in Equation (h) in Table 3.5.1 (m)
D: Fractal dimension of particle perimeter (-)
d: distance from container wall (m)
M: mass of powder in a packed bed (kg)
m: number of components in a multicomponent mixture
n: index of Roller's Equation (3.5.2b) (-)
$N_{(j,k)}$: coordination number for particle j in direct contact with particle k (-)
N_c: average coordination number in a bed of equal-size spheres (-)
q: Fuller constant of Gaudin–Schumann (Andreasen) distribution (-)
S_{ak}: fractional area of particle k in a multicomponent mixture (-)
S_{v1}: fractional volume of coarse powder in a binary mixture (-)
S_{vk}: fractional volume of particle k in a multicomponent mixture (-)

V: volume of packed bed (m^3)
V_s: volume of a hypothetical sphere in Figure 3.5.7 (m^3)
V_1, V_2: volume of a spherical segment in Figure 3.5.7 (m^3)
x: particle size (m)
x_1, x_2: diameter of coarse particle 1 or fine particle 2 in a binary mixture (m)
x_c: critical particle size of Roller's Equation (3.5.2b) (m)
x_j, x_k: diameter of particle j or k in a multicomponent mixture (m)
β_j: proportionality constant in Equation (3.5.2) (-)
ε: void fraction (-)
ε_1, ε_2: void fraction of coarse mono-sized powder bed or void fraction of fine one (-)
ε_c: void fraction of coarse mono-sized powder over critical particle size (-)
$\varepsilon_{(j,k)}$: partial void fraction around particle j in direct contact with particle k (-)
ε_j: partial void fraction around particle j (-)
ε_j : measured void fraction in uniformly sized particle bed (-)
ρ_b, ρ_m, ρ_p: apparent, matrix and particle density (kg/m^3)
Φ_w: Wadell's working sphericity (-)
σ_g: geometric standard deviation of log-normal distribution(m)

REFERENCES

1. Suzuki, M., Sato, H., Hasegawa, M., Hirota, M., *Powder Technol.*, 118, 53–57, 2001.
2. Roller, P. S., *Ind. Eng. Chem.*, 22, 1206–1208, 1930.
3. Graton, L. C., Fraser, H. J., *J. Geol.*, 43, 785–909, 1935.
4. Heesh, H., Laves, F., *Z. Kristallor*, 85, 433–453, 1933.
5. Smith, W. O., Foote, P. D., Busang, P. F., *Phys. Rev.*, 34, 1271–1274, 1929.
6. Shinohara, K., Kobayashi, H., Gotoh, K., Tanaka, T., *J. Soc. Powder Technol. Jpn.*, 2, 352–356, 1965.
7. Shinohara, K., Tanaka, T., *Kagaku Kogaku*, 32, 88–93, 1968.
8. Gotoh, K., *Nat. Phys. Sci.*, 231, 108–110, 1971.
9. Gotoh, K., *J. Soc. Powder Technol. Jpn.*, 15, 220–226, 1978.
10. Iwata, H., Homma, T., *Powder Technol.*, 10, 79–83, 1974.
11. Bargiel, M., Tory, E. M., *Adv. Powder Technol.*, 12, 533–557, 2001.
12. Rumpf, H., *Chem. Eng. Technol.*, 30, 144–158, 1958.
13. Bernal, D. J., Mason, J., *Nature*, 188, 910–911, 1960.
14. Meissner, H. P., Michael, A. S., Kaiser, R., *Ind. Eng. Chem. Process Des. Dev.*, 3, 202–205, 1964.
15. Wade, W. E., *J. Phys. Chem.*, 69, 322–326, 1965.
16. Ridgway, K., Tarbuck, K. J., *Br. Chem. Eng.*, 12, 384–388, 1967.
17. Arakawa, M., *J. Soc. Mater. Sci. Jpn.*, 16, 319–321, 1967.
18. Haughey, X., Beveridge, G. S. G., *Can. J. Chem. Eng.*, 47, 130–140, 1969.
19. Bernal, D. J., Cherry, I. A., Finney, J. L., Knight, K. R., *J. Phys.*, E3, 388–390, 1970.
20. Nagao, T., *Trans. J.S.M.E.*, 44, 1912, 1978.
21. Nakagaki, M., Sunada, H., *Yakugaku Zasshi*, 83, 73–78, 1963.
22. Nakagaki, M., Sunada, H., *Yakugaku Zasshi*, 88, 705–709, 1968.
23. Bennett, H., *J. Appl. Phys.*, 43, 2727–2734, 1972.
24. Tory, R. M., Church, B. H., Tam, M. K., Ratner, M., *Can. J. Chem. Eng.*, 51, 484–493, 1973.
25. Gotoh, K., Finney, J. L., *Nature*, 252, 202–205, 1974.
26. Suzuki, M., Makino, K., Yamada, M., Iinoya, K., *Int. Chem. Eng.*, 21, 482–488, 1981.
27. Ouchiyama, N., Tanaka, T., *Ind. Eng. Chem. Fundam.*, 19, 555–560, 1980.
28. Suzuki, M., Oshima, T., *KONA Powder Sci. Technol. Jpn.*, 7, 22–28, 1989.
29. Suzuki, M., Kada, H., Hirota, M., *Adv. Powder Technol.*, 10, 353–365, 1999.
30. Suzuki, M., Shinmura, T., Iimura, K., Hirota, M., *Adv. Powder Technol.*, 19, 183–193, 2008
31. Witten, T.A., Samder, L.M., *Phys. Rev. Lett.*, 47, 1400–1403, 1981.
32. Tohno, T., Takahashi, K., *Aerosol Res.*, 2, 117–127, 1987.
33. Kamiya, H., Yagi, E., Jimbo, G., *J. Soc. Powder Technol. Jpn.*, 30, 148–154, 1993.
34. Suzuki, M., Oshima, T., *J. Soc. Powder Technol. Jpn.*, 26, 250–254, 1989.
35. Horsfield, H. T., *J. Soc. Chem. Ind.*, 53, 107–115, 1934.
36. White, H. E., Walton, S. F., *J. Am. Ceram. Soc.*, 20, 155–166, 1937.
37. Hudson, D. R., *J. Appl. Phys.*, 20, 154–162, 1949.
38. Furnas, C. C., *U.S. Bur. Mines Rep. Invest.*, 2894, 1928.
39. Sohn, H. Y., Moreland, C., *Can. J. Chem. Eng.*, 46, 162–167, 1968.
40. Arakawa, M., Nishino, M., *J. Soc. Mater. Sci. Jpn.*, 22, 658–662, 1973.
41. Suzuki, M., Oshima, T., *Powder Technol.*, 43, 147–153, 1985.
42. Powell, M. J., *Powder Technol.*, 25, 45–52, 1980.
43. Dinger, D. R., Funk, J. E., *Interceram.*, 42, 150–152, 1993.
44. Suzuki, M., Oshima, T., *Powder Technol.*, 44, 213–218, 1985.
45. Ito, T., Wanibe, Y., Sakao, H., *J. Jpn. Inst. Met.*, 50, 740, 1986.
46. Furnas, C. C., *Ind. Eng. Chem.*, 23, 1052–1058, 1931.
47. Westman, A. E. R., *J. Am. Ceram. Soc.*, 19, 127–129, 1936.
48. Tokumitsu, Z., *J. Soc. Mater. Sci. Jpn.*, 13, 752–758, 1964.
49. Kawamura, J., Aoki, E., Okuzawa, K., *Kagaku Kogaku*, 35, 777–783, 1971.
50. Abe, E., Hirosue, H., Yokota, A., *J. Soc. Powder Technol. Jpn.*, 15, 458–462, 1978.
51. Ouchiyama, N., Tanaka, T., *Ind. Eng. Chem. Fundam.*, 22, 66–71, 1981.
52. Ouchiyama, N., Tanaka, T., *Ind. Eng. Chem. Fundam.*, 25, 125–129, 1986.
53. Suzuki, M., Yagi, A., Watanabe, T., Oshima, T., *Int. Chem. Eng.*, 26, 491–498, 1986.
54. Suzuki, M., Oshima, T., Ichiba, H., Hasegawa, I., *KONA Powder. Sci. Technol. Jpn.*, 4, 4–12, 1986.
55. Cross, M., Douglas, W. H., Fields, R. P., *Powder Technol.*, 43, 27–36, 1985.
56. Suzuki, M., Oshima, T., *Powder Technol.*, 35, 159–166, 1983.
57. Dinger, D. R., Funk, J. E., *Interceram.*, 43, 87–89, 1994.
58. Suzuki, M., Kobayashi, M., Iimura, K., Hirota, M., *J. Soc. Powder Technol. Jpn.*, 38, 468–472, 2001.
59. Donev, A., Cisse, I., Sachs, D., Variano, E.A., et al., *Science*. 303, 990–993, 2004



Taylor & Francis
Taylor & Francis Group
http://taylorandfrancis.com

3.6 Capillarity of Porous Media

Minoru Miyahara

A macroscopic body composed of fine particles naturally possesses microscopic void spaces with a size several to ten times smaller than the particle diameter. Sometimes particles themselves may have some porosity. Such pore spaces can bring functional characteristics such as adsorptive capacity, selective permeation, and dielectric properties, while in some cases they may stand as a deficit. With increasing demand for functionality, recent powder-based manufacturing has tended to use finer particles of submicron size down to the nanometer range. As a result the characterization of capillarity in the nanometer range becomes more and more important.

In this section, two typical pore-size characterization methods, nitrogen adsorption and mercury porosimetry, are mainly described with their theoretical basis and with attention to be paid especially to the nanometer range. Some other methods are explained briefly.

3.6.1 COMMON PHENOMENON: YOUNG–LAPLACE EFFECT

An important phenomenon that commonly applies to nitrogen adsorption and mercury porosimetry is the so-called Young–Laplace effect. As shown in Figure 3.6.1a, the surface of liquid that wets the wall will form a hemispherical meniscus in a sufficiently thin cylindrical tube to satisfy that the contact angle θ is zero. The Young–Laplace equation describes the pressure difference ΔP brought by the pulling force of surface tension γ, which is given by Equation (3.6.1), including the case of partial wetting shown in in Figure 3.6.1b:

$$\Delta P \equiv P - P' = \frac{2\gamma\cos\theta}{r} \tag{3.6.1}$$

More generally, menisci with arbitrary shape can be described with two principal curvature radii, r_1 and r_2.

$$\Delta P = \gamma\left(\frac{1}{r_1}+\frac{1}{r_2}\right)\cos\theta. \tag{3.6.2}$$

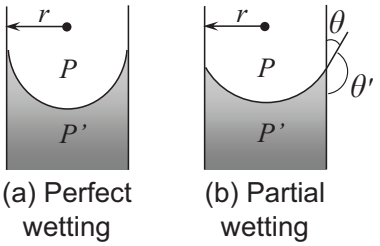


FIGURE 3.6.1 Young–Laplace effect.

For a hemi-cylindrical meniscus formed in a slit space of width W, for example, Equation (3.6.2) will be $\Delta P = 2\gamma\cos\theta/W$ because the two principal radii are $2/W$ and 0. This equation resembles Equation (3.6.1), but note that r is the radius of the space while W denotes the span between walls.

The above stands on macroscopic and classical understandings. In the nanoscale, especially the so-called single-nano length, it fails to express the phenomena because of the hindered characteristics of a liquid surface and the effects of potential energy exerted from pore walls, for instance. With attention paid to the single-nano scale, each method is described in the following.

3.6.2 NITROGEN ADSORPTION METHOD

Pore size distributions, as well as the specific surface area, can be estimated from nitrogen adsorption isotherms at liquid-nitrogen temperature, or the amount adsorbed against relative pressure [= (equilibrium pressure p)/(saturated vapor pressure p_s)]. Measurement is done either by the volumetric method, which detects pressure variation of nitrogen gas introduced in an adsorption system with constant volume, or the gravimetric method, which measures weight variation of a sample contacting with gas of given relative pressure. In the following, the description relating to the measurement refers to the former method unless otherwise specified, since the great majority of commercially available automated apparatuses are based on it.

Principle: Capillary Condensation and the Kelvin Equation

Suppose that liquid nitrogen exists in a cylindrical pore as shown in Figure 3.6.1a. The pressure in liquid phase is lower than that in gas phase by $\Delta P = 2\gamma/r$, which results in a lower free energy than a normal liquid with flat surface by $v\Delta P$, (v being the molar volume of liquid). Then the equilibrium vapor pressure of pore liquid p_g must be smaller than the saturated vapor pressure p_s. Conversely, the vapor with a pressure smaller than p_s can condensate if it goes into a pore, which is termed the capillary condensation.

The equilibrium pressure p_g must satisfy Equation (3.6.3) since the difference of free energy between p_g and p_s equals $v\Delta P$.

$$\ln\frac{p_g}{p_s} = -\frac{2v\gamma}{rRT} \tag{3.6.3}$$

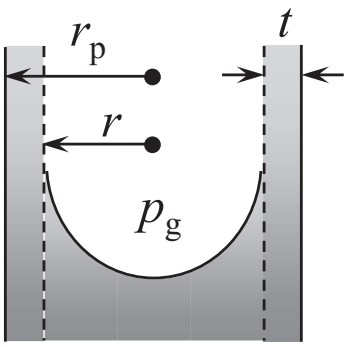


FIGURE 3.6.2 Surface adsorption film and condensation phase.

This is the so-called Kelvin equation, which was derived originally by Lord Kelvin for vapor pressure of a small droplet without the negative sign: the difference apparently comes from the concave geometry. The equation gives the pore radius r from the relative pressure p_g/p_s at which the condensation occurs. The above stands as the principle for estimating pore size distribution from a nitrogen isotherm.

Further to be considered for an adsorption system, however, is the adsorbed film with thickness t on the walls contacting with nitrogen vapor (see Figure 3.6.2). The condensation phase is formed within the core space excluding the films, with the contact angle of zero. The radius for a cylindrical pore is then given by

$$r_p = r + t = \frac{2v\gamma}{RT\ln(p_s/p_g)} + t \tag{3.6.4}$$

and the width of a slit pore will be

$$W = 2r + 2t = \frac{2v\gamma}{RT\ln(p_s/p_g)} + 2t \tag{3.6.5}$$

Many detailed calculation schemes were proposed by, for example, Cranston and Inkley,[1] Dollimore and Heal,[2] and Barell et al (BJH method).[3] Major differences between these methods are the data or the equation for adsorption thickness t, and the schemes of calculation themselves do not produce significant differences if common data for t are used. Therefore, one need not worry which scheme is installed in a commercial apparatus; one should pay more attention to the t-data in the software and consider how precise and how abundant for various materials they are.

Measurable Range of Pore Size

Many automated adsorption apparatuses declare the upper limit of the pore size to be approximately 100 nm, which corresponds to a relative pressure of approximately 0.98. In general, however, the accuracy of the adsorption measurement decreases as the equilibrium pressure approaches the saturated vapor pressure, because the liquid nitrogen temperature will fluctuate following variation in atmospheric pressure. For safety one should understand the upper limit of reliability to be approximately 0.95 of relative pressure, corresponding to a pore size of about 40 nm. Measurement for larger pores should be done with mercury porosimetry.

As for the lower limit, pore size analysis based on the capillary condensation will lose its basis if the size goes down below about 2 nm, because the condensation phenomenon itself (or the first-order phase transition) does not occur in such small space. Many studies conducted in the 1970s to 1990s discussed pore sizes based on the capillary condensation in the range of 1–2 nm for, for example, activated carbons, but nowadays such analysis and discussion cannot be accepted.

Instead, the present understanding of adsorption phenomena in such small pores is the so-called micropore filling, meaning that the gas molecules are gradually filled into the pore space by strongly attractive potential energy exerted by pore walls. Some pore analysis methods based on this mechanism are available in the literature,[4,5] among which the so-called t-plot method[6] and related ones[7,8] are suitable for simple and reliable analysis of micropore size distribution. Refer to the literature for details of these methods.

Further rigorous analysis of micropore size distribution is presently under development by many researchers. Most of the approaches are based on the statistical thermodynamics method, such as molecular simulation and the density functional theory (DFT), which produce so-called local adsorption isotherms for a series of various sizes of micropore, or so-called "kernel." Some commercial nitrogen adsorption apparatuses are equipped with such kernels. An example of the kernel calculated by DFT can be found in literature.[9] The grand canonical Monte Cairo simulation should give more accurate local isotherms than those by DFT, and the kernel determined by this technique[10] is partly equipped in some commercial apparatus and under further development. An experimental nitrogen isotherm is expressed as a convolution integral of the local adsorption isotherms and the pore size distribution function. The latter, including both micropore and mesopore sizes, thus can be determined through minimization of the error between measured and theoretical isotherms. Note that, however, this kind of technique needs further development. Sometimes calculated pore size distribution suffers from an artifact of nonexistent pores, which may result from surface heterogeneity. One has to pay much attention to this kind of artifact, especially if the resultant distribution has bimodal or multimodal distribution.

Kelvin Model's Deficit: Underestimation in Single-Nano Range

The estimation based on the Kelvin model as given by Equations (3.6.4 and 3.6.5) works well for pores larger than 10 nm. It was pointed out since the late 1980s, however, that the model underestimates the pore sizes in the single-nanometer range.[11,12] The research at that time was rather scientific and showed this deficit by complicated statistical thermodynamics techniques or molecular simulations with great computational costs. No method based on simplicity and convenience was

available even in the 1990s, which forced people to use the Kelvin model, though knowing its inaccuracy.

A condensation model with a simple concept and easy calculation had been proposed[13–16] and is explained conceptually below. The important point is that the attractive potential energy from pore walls and the hindered surface tension of a curved interface will enhance or influence the condensation in nanoscale pores. The basic equation is

$$RT \ln \frac{p_g}{p_s} = -\frac{2v\gamma(\rho)}{\rho(r)} + \Delta\phi(r) \tag{3.6.6}$$

in which the free energy for condensation (left-hand side) is compensated not only by the Young–Laplace effect with local curvature dependent surface tension $\gamma(\rho)$, but also by the attractive energy of pore walls relative to the condensing liquid $\Delta\phi$ (r). The latter effect can be determined[15] from adsorption thickness data on nonporous solids that are usually included in the automated adsorption apparatuses. An iterative calculation is needed to determine the relation between pore size and relative pressure because the curvature of the liquid surface depends on location in the pore, but it remains an easy calculation. For further details, see the original papers.

The degree of underestimation by the Kelvin model stays almost constant regardless of the pore size but varies depending on the pore-wall potential energy. Some examples of difference between Kelvin-based prediction and the true pore size are about 1 nm or slightly greater for carbon materials, about 1 nm or less for silica materials, and 0.5–0.7 nm for ordered mesoporous silicates (MCM-41). Thus one should understand that, if the Barrell-Joyner-Halenda (BJH) method[3] gives peak pore size as 3 nm for a silica gel, the true size is about 4 nm or slightly less than that. The model based on Equation (3.6.6) can give the true pore size from the nitrogen isotherm without any additional measurement.

Hysteresis

The capillary condensation phenomenon often suffers from the hysteresis, or an adsorption isotherm takes different paths between adsorption and desorption. The classification of the hysteresis into four types is given by IUPAC, as shown in Figure 3.6.3, recommended in 1985. Recently in 2015 a new classification was proposed, which divides H2 into H2a and H2b, and adds a new H5 type.[17] The new one is, however, so detailed and the old one suffices the purpose of this chapter. (If needed or interested, refer to the literature.) There have been long discussions on "which branch should be used for pore-size determination?." but it is still difficult to obtain a general conclusion.

Neimark and coworkers,[18,19] for example, reported that the adsorption branch for MCM-41, which possesses almost ideally cylindrical pores with open ends, is of spinodal process with higher condensation pressure than thermodynamic equilibrium because the surface adsorption layer has to grow up locally into the central portion of the pore space. A recent study by Hiratsuka et al.[20] further found that the adsorption

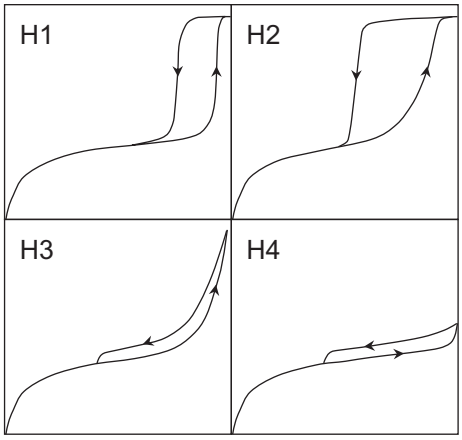


FIGURE 3.6.3 Classification of hysteresis defined by IUPAC.

process is not simply the spinodal, but a kinetic process with certain time constant for making up nuclei of capillary condensation, or the bridging in nanopore. The desorption process, on the other hand, does not suffer from such an energy barrier, resulting in an equilibrium desorption. This mechanism seems to be almost accepted by many researchers lately, while some groups raised questions about it.

By limiting the topic into the structures made up by aggregated particles or a sintered porous body, however, the following understanding can be achieved. The characteristics of this kind of structure would be that there must exist a particles contact point at the end of the pore space, or, their pores are NOT open-ended. Then the contact points and their vicinity are able to provide nuclei for the condensation, and an energy barrier, as is the case for MCM-41, would not stand in the condensation process. Therefore, the condensation process for this kind of materials follows an equilibrium path. Another feature is that pores are connected through narrower spaces between particles, or the pore network is formed with connecting "necks." In this case, the desorption process itself is in equilibrium, but the so-called ink-bottle effect gives hysteresis in which the evaporation of condensate in a pore space is not possible until the pressure goes down to a value corresponding to the size of the neck. The evaporated volume at this hindered process, then, does not provide the pore volume of the pore size corresponding to this pressure. This process exhibits H2-type hysteresis, and the adsorption branch should be used to calculate the size distribution of the pore space. Examples of materials include silica gels and porous polymer gels. Many providers of such materials use desorption branches for showing porous characteristics to users because it gives sharp distribution. One should notice, however, that the peak in the distribution simply gives the neck size, and the real distribution would be broader in most cases.

Another important topic related to hysteresis is the end-closure point of the desorption branch. As seen in clay materials and activated carbons, a hysteresis loop of types H3 and H4 often closes at the relative pressure of 0.40–0.45 for nitrogen. The type H2 may in some cases close at this pressure range if wider mesopores are connected with micropore necks.

As described in detail in the literature,[21] this closure of hysteresis will result from the spinodal evaporation of condensed liquid when exceeding its tensile limit, or cavitation, which is determined not by the pore size but merely by the nature of liquid. This phenomenon should be considered when one uses the desorption branch for characterization.

3.6.3 MERCURY INTRUSION METHOD (MERCURY POROSIMETRY)

An evacuated sample is immersed in mercury, and pressurization of the system cause mercury's intrusion into the pore space. The detection and analysis of the intruded volume against applied pressure gives the pore size distribution. Many automated apparatuses are commercially available.

Principle: Nonwetting Fluid and Washburn Equation

Mercury does not wet almost all of solid surface, which corresponds to the upper portion in Figure 3.6.1b. Also, $P' = 0$ stands because the pore space is evacuated before measurement. Equation (3.6.1) then will be

$$P = \frac{2\gamma \cos\theta}{r} \quad \text{or} \quad D = 2r = -\frac{4\gamma \cos\theta'}{P} \tag{3.6.7}$$

which gives the relation between applied mechanical pressure P and the pore diameter D. θ' is the contact angle for mercury, which is set to be 140° in most cases. The above equation is essentially the same as the Young–Laplace equation, but the equation on the right is called the Washburn equation. Since the intruded volume directly means the volume of pores larger than a size corresponding to the pressure, the differentiation of the volume with respect to the pore size gives the pore-size distribution.

Measurable Range of Pore Size

Many automated porosimetry apparatuses declare the lower limit of the pore size to be 3–4 nm, which corresponds to the applied pressure of about 4000 atm. At this high pressure, the porous framework might be deformed or some other influence may occur. It is also important to point out that the surface of mercury in a single-nanometer range may be different from the surface of bulk liquid, which may result as a hindered contact angle. Much attention, then, should be paid to the reliability of the data in this range, for which the gas adsorption method has far superior accuracy and reliability. The upper limit of mercury porosimetry would be around several hundred microns. The detection of cracks or supermacro pores, which is difficult to measure by gas adsorption, is precisely done by the intrusion method.

Hysteresis

The extrusion process with decreasing pressure generally gives a different path, or hysteresis. Further, it would be almost always the case that a certain amount of mercury remains in the pores even after complete release of the pressure. The extrusion process, therefore, would not be suitable for analysis, and the intrusion branch should be used in general. As clarified by percolation theory, this branch corresponds to the analysis of the desorption branch in gas adsorption, and one should notice that the analysis gives the neck size for aggregated or sintered bodies.

3.6.4 OTHER TECHNIQUES OF INTEREST

Bubble-Point Method

This technique detects perforating pores while the gas adsorption method and mercury porosimetry cannot distinguish these from dead-end pores. Because of this feature the method is often applied to filters, membranes, cloths, or those porous materials whose permeation properties are of importance. Depending on the wettability, the porous material is immersed in freon or water. Pressurized air or nitrogen is then introduced to one side of the material. At a pressure corresponding to maximum size of the perforating pore, the gas starts to permeate. Other than the detection of the maximum pore size, the size distribution can be estimated by applying higher pressures, because smaller pores start to open with increased pressure. Detectable pore size is usually above several tens of nanometers with freon, or a few hundred nanometers with water.

Thermoporometry: Detection of Freezing Point Depression

Based upon the Gibbs–Thomson equation, which assumes that freezing point depression in a pore from bulk temperature is inversely proportional to the pore radius, the size distribution is estimated from calorimetric measurement. It may sometimes be the case that the pore structure under wetted condition varies after drying because of the capillary suction pressure or the de-swelling of base material. The gas adsorption and the mercury porosimetry cannot characterize such porous materials because both methods need evacuation before measurement. The thermoporometry can be used to overcome the above problem: the measurement can be done under wetted condition. However, not much has been clarified for the freezing behavior in confined space. Some studies, for example, clarified that the freezing point may even be higher than the bulk freezing point, depending on the physicochemical nature of the pore walls.[22] The method is thus especially controversial if the single-nano range is concerned, and it is better not to rely on it for the smaller pore sizes.

Small Angle X-Ray Scattering

X-ray scattering with angles smaller than ca. 10° can probe porous characteristics in the single nanometer range. Since X-rays can detect not only open pores but also closed (or isolated) pores, measurements for low-permittivity materials are

often seen as an application. One has to be careful, however, because the resulting space distribution or correlation length does not necessarily relate to the scale of the pores but results from the electron density distribution. Further, an ordered material such as MCM-41 would give clear signals showing its lattice size or the periodicity of the regular pores, but not much sensitivity can be expected for materials with a disordered or random nature.

REFERENCES

1. Cranston, R. W., Inkley, F. A., *Adv. Catal.*, 9, 143, 1957.
2. Dollimore, D., Heal, G. R., *J. Appl. Chem.*, 14, 109, 1964.
3. Barell, E. P., Joyner, L. G., Halenda, P. P., *J. Am. Chem. Soc.*, 73, 373, 1951.
4. Horvath, G., Kawazoe, K., *J. Chem. Eng. Jpn.*, 16, 470, 1983.
5. Saito, A., Foley, H. C., *AIChE J.*, 37, 429, 1991.
6. Lippens, B. C., de Boer, J. H., *J. Catal.*, 4, 319, 1965.
7. Sing, K. S. W., *Surface Area Determination*, Everett, D. H. and Ottewill, R. H., Eds., Butterworths, London, 1970, p. 25.
8. Mikhail, R. S., Brunauer, S., Bodor, E. E., *J. Colloid Interface Sci.*, 26, 45, 1968.
9. Neimark, A. V., Lin, Y., Ravikovitch, P. I., Thommes, M., *Carbon*, 47, 1617, 2009.
10. Miyahara, M. T., Numaguchi, R., Hiratsuka, T., Nakai, K, Tanaka, H., *Adsorption*, 20, 213, 2014.
11. Evans, R., Marconi, U. M. B., Tarazona, P., *J. Chem. Phys.*, 84, 2376, 1986.
12. Miyahara, M., Yoshioka, T., Okazaki, M., *J. Chem. Phys.*, 106, 8124, 1997.
13. Miyahara, M., Yoshioka, T., Okazaki, M., *J. Chem. Eng. Jpn.*, 30, 274, 1997.
14. Miyahara, M., Kanda, H., Yoshioka, T., Okazaki, M., *Langmuir*, 16, 4293, 2000.
15. Miyahara, M., Yoshioka, T., Nakamura, J., Okazaki, M., *J. Chem. Eng. Jpn.*, 33m 103, 2000.
16. Kanda, H., Miyahara, M., Yoshioka, T., Okazaki, M., *Langmuir*, 16, 6622, 2000.
17. Thommes, M., Kaneko, K., Neimark, A. V., Olivier, J. P., et al., *Pure Appl. Chem.*, 87, 1051, 2015.
18. Vishnyakov, A., Neimark, A. V., *J. Phys. Chem. B*, 105, 7009, 2001.
19. Neimark, A. V., Ravikovitch, P., Vishnyakov, A., *Phys. Rev. E*, 65, 031505, 2002.
20. Hiratsuka, T., Tanaka, H., Miyahara, M. T., *ACS Nano*, 11, 269, 2017.
21. Ravikovitch, P., Neimark, A. V., *Langmuir*, 18, 1550, 2002.
22. Miyahara, M., Gubbins, K. E., *J. Chem. Phys.*, 106, 2865, 1997.



Taylor & Francis
Taylor & Francis Group
http://taylorandfrancis.com

3.7 Permeation (Flow through Porous Media)

Chikao Kanaoka

Permeation is the fluid flow through interstices among many discrete particles. Flows of groundwater, crude oil, and natural gas are typical permeations taking place in nature. This type of flow is widely utilized in industrial processes in which both particles and fluid flow play important roles simultaneously, such as a catalytic reaction, filtration, and so on. Thanks to the extensive number of studies on porous media since D'arcy, macroscopic flow characteristics in a porous media can be evaluated fairly well, although the microscopic flow pattern inside the media is complex and not amenable to rigorous solution by the Navier–Stokes equation. In this section, general theories developed to explain resistance to flow through a porous media are described, and the resistances of granular and fibrous packed beds are outlined as typical examples of high and low packing densities, respectively.

3.7.1 RESISTANCE TO FLOW THROUGH A POROUS MEDIA

Porous media is composed of many discrete particles with different shapes and sizes, as shown in Figure 3.7.1a. The packing density of these particles is high and their structure is sophisticated. Porous media can be simplified as an assembly of many tiny channels or uniformly spaced spherical particles of equal size, as shown in Figure 3.7.1b and c.

For the case of the former model, flow resistance can be predicted by analogy with that of a straight circular tube, and for the case of the latter, it can be calculated from the fluid drag acting on individual particles. These two models are usually called "channel" and "drag" models, respectively. Of course, pressure drop can be predicted by either model, but, in general, the former is believed to be suited for a flow-through porous media with high packing density and the latter for one with low packing density.

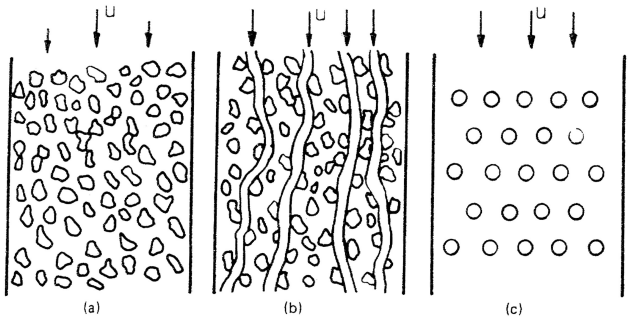


FIGURE 3.7.1 Models of porous media.

Channel Model

Because the porous system is assumed to be a bundle of tiny channels with noncircular cross sections, the pressure drop of the system is identical with that for one of those channels.

When fluid with density ρ and viscosity μ flows through a straight tube with diameter D and length L, the pressure drop ΔP is expressible by the so-called Hagen–Poiseuille equation for laminar flow and by Fanning's equation in general:
Hagen–Poiseuille equation:

$$\Delta P = \frac{32 L \mu u}{D^2} \tag{3.7.1}$$

Fanning's equation:

$$\Delta P = 4 f \frac{L}{D} \frac{\rho u^2}{2} \tag{3.7.2}$$

Here, Fanning's friction factor f is expressed by Equation (3.7.3) in a laminar flow region, which becomes dependent not only on the Reynolds number Re but also on the surface roughness in the turbulent flow region:

$$f = \frac{\mu}{Du\rho} = \frac{16}{\mathrm{Re}} \tag{3.7.3}$$

Equation (3.7.1) through Equation (3.7.3) are applicable to noncircular channels by introducing the hydraulic radius m defined as

$$m = \frac{\text{Cross-sectional area of a channel}}{\text{Wetted periphery}} \tag{3.7.4}$$

The value of m calculated from Equation (3.7.4) equals one-quarter of the tube diameter for circular tubes and about one-quarter of the equivalent diameter for other cross-sectional shapes. The definition above is not applicable, as it is to the porous media; hence, it is modified as follows.

$$m = \frac{\text{Cross-sectional area of a channel} \times \text{tube length}}{\text{Wetted periphery} \times \text{tube length}}$$

$$= \frac{\text{tube volume}}{\text{Wetted area of a tube}}$$

$$= \frac{\text{tube pore volume}}{\text{Total surface area of particles in a porous media}}$$

$$= \frac{\text{prosity}}{\text{Specific surface area based on the volume of porous media}}$$

$$= \frac{\varepsilon}{S_B} = \frac{\varepsilon}{S_v(1-\varepsilon)} \tag{3.7.5}$$

where S_B and S_v are the specific surface areas based on packed layer volume and particle volume, respectively.

According to Carman's tortuousity model,[1] the time required for fluid to travel an equivalent channel is equal to the actual penetration time to pass through the bed. Hence, the following relation is obtained:

$$\frac{L_e}{u_e} = \frac{L}{u/\varepsilon} \tag{3.7.6}$$

Substituting Equation (3.7.5) and Equation (3.7.6) into Equation (3.7.1) gives

$$\Delta P = \frac{32 L_e \mu u_e}{(4m)^2} = \frac{2 L_e \mu S_B^2 (L_e/L)(u/\varepsilon)}{\varepsilon^2}$$

$$= 2\left(\frac{L_e}{L}\right)^2 \frac{S_B^2 L \mu u}{\varepsilon^3} \tag{3.7.7}$$

$$= 2\left(\frac{L_e}{L}\right)^2 \frac{S_v^2 (1-\varepsilon)^2 L \mu u}{\varepsilon^3}$$

As mentioned earlier, the hydraulic radius calculated from Equation (3.7.5) is one fourth of the tube diameter for circular tubes. Hence, four times the hydraulic radius is used in Equation (3.7.7). L_e/L is the ratio of the equivalent channel length to the bed thickness, and it is called the tortuosity. For noncircular channels, the numerical constant in the last two expressions in Equation (3.7.7) differs from 2. Therefore, we write the following expression for the general case of a channel model by replacing the numerical constant 2 by κ_0:

$$\Delta P = \kappa_0 \left(\frac{L_e}{L}\right)^2 \frac{S_B^2 L \mu u}{\varepsilon^3}$$

$$= \kappa_0 \left(\frac{L_e}{L}\right)^2 \frac{S_v^2 (1-\varepsilon)^2 L \mu u}{\varepsilon^3} \tag{3.7.8}$$

Equation (3.7.8) is the expression based on the channel model, and the pressure drop can be evaluated by knowing the values κ_0 and L_e/L. $\kappa = \kappa_0 (L_e/L)^2$ is usually called the Kozeny constant and is dependent on particle shape, packing structure, and so on. κ is about 5 for most cases. Carman obtained the following well-known expression called the Kozeny–Carman equation:

$$\Delta P = 5\frac{S_B^2 L \mu u}{\varepsilon^3} = 5\frac{S_v^2 (1-\varepsilon)^2 L \mu u}{\varepsilon^3} \tag{3.7.9}$$

Because Equation (3.7.9) is derived from the Hagen–Poiseuille equation, Equation (3.7.1), its applicable range is limited to the laminar flow region. In the turbulent flow region, Fanning's equation, Equation (3.7.2), has to be used by modifying the Reynolds number and friction factor as follows:[2]

$$\mathrm{Re} = \frac{m(u/\varepsilon)\rho}{\mu} = \frac{\varepsilon}{S_B}\frac{u}{\varepsilon}\frac{\rho}{\mu} = \frac{u\rho}{\mu S_B} = \frac{u\rho}{\mu S_v(1-\varepsilon)} \tag{3.7.10}$$

$$2f = \frac{\Delta P m}{L\rho(u/\varepsilon)^2} = \frac{\Delta P / S_B}{L\rho(u/\varepsilon)^2}$$

$$= \frac{\Delta P \varepsilon^3}{L\rho u^2 S_B} = \frac{\Delta P \varepsilon^3}{L\rho u^2 S_v(1-\varepsilon)} \tag{3.7.11}$$

Equation 3.7.11 can also be applicable to the laminar flow region. Substituting Equation (3.7.10) and Equation (3.7.11) into Equation (3.7.9), one obtains

$$2f = \frac{\Delta P \varepsilon^3}{L\rho u^2 S_v(1-\varepsilon)} = 5\frac{\mu S_v(1-\varepsilon)}{u\rho} = \frac{5}{\mathrm{Re}} \tag{3.7.12}$$

In Equation (3.7.12) the friction factor is inversely proportional to the Reynolds number. This agrees well with the experiments for $\mathrm{Re} < 2$, as shown in Figure 3.7.2. The friction factor for $\mathrm{Re} > 2$ has to be determined experimentally.[3,4,5]

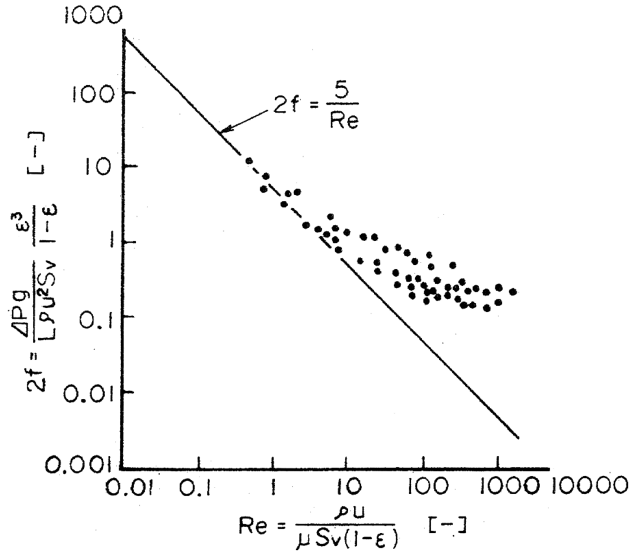


FIGURE 3.7.2 Correlation of experimental friction factor and Reynolds number.

Drag Model

The pressure drop of porous media has to be equal to the fluid drag experienced by particles inside the media:

$$\Delta PA = \sum_{i=1}^{N} R_{mi} \tag{3.7.13}$$

$$R_{mi} = Rf(\varepsilon) \tag{3.7.14}$$

R expresses the fluid drag acting on a single spherical particle in an infinite field and $f(\varepsilon)$ is the correction term due to the change in packing density and is usually referred to as the porosity function. R and N are given by the following equations:

$$R = C_D \frac{\pi D_p^2}{4} \frac{\rho u^2}{2} \tag{3.7.15}$$

$$N = \frac{6AL(1-\varepsilon)}{\pi D_p^3} \tag{3.7.16}$$

where C_D is the drag coefficient of a single sphere.

Substituting Equation (3.7.14) through Equation (3.7.16) into Equation (3.7.13), it becomes

$$\Delta P = \frac{3}{2} C_D (1-\varepsilon) f(\varepsilon) \frac{L}{D_p} \frac{\rho u^2}{2} \tag{3.7.17}$$

By adopting Steinour's[6] expression for $f(\varepsilon)$, which was obtained for hindered settling, Equation (3.7.17) becomes

$$f(\varepsilon) = \frac{25(1-\varepsilon)}{3\varepsilon^3} \tag{3.7.18}$$

$$\Delta P = \frac{25}{2} C_D \frac{(1-\varepsilon)^2}{\varepsilon^3} \frac{L}{D_p} \frac{\rho u^2}{2} \tag{3.7.19}$$

For turbulent flow, the following Burke and Plummer expression[7] obtained from the dimensional analysis is popular:

$$\Delta P = \frac{3.5}{4} \frac{(1-\varepsilon)}{\varepsilon^3} \frac{L}{D_p} \frac{\rho u^2}{2} \tag{3.7.20}$$

One of the most effective expressions for both laminar and turbulent flow regions is the following Ergun's equation (3.7.21), which is a sum of fluid drags proportional to the first and second powers of the fluid velocity:

$$\frac{\Delta P}{L} = 150 \frac{(1-\varepsilon)^2}{\varepsilon^3} \frac{\mu u}{D_p^2} + 1.75 \frac{(1-\varepsilon)}{\varepsilon^3} \frac{\rho u^2}{2} \tag{3.7.21}$$

In the form of a modified friction factor, it becomes

$$2f = \frac{150(1-\varepsilon)}{\mathrm{Re}_p} + 1.75 \tag{3.7.22}$$

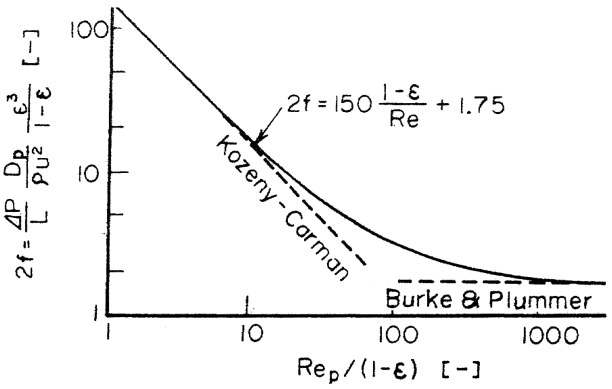


FIGURE 3.7.3 Comparison of Ergun's correlation with others.

where

$$\mathrm{Re}_p = \frac{D_p u \rho}{\mu} \tag{3.7.23}$$

Figure 3.7.3 is the correlation between $2f$, and calculated values from the Kozeny–Carman and the Burke–Plummer equations are also shown. As one can see from the figure, Ergun's expression agrees well with the Kozeny–Carman equation in the laminar flow region[1,8] and with the Burke–Plummer equation in the turbulent flow region.

3.7.2 PRESSURE DROP ACROSS A FIBROUS MAT

A fibrous mat can be considered as a special kind of porous media composed of particles with an extremely large aspect ratio, to which both the channel and drag theories are applicable. The porosity of a fibrous mat is usually higher than 85%; thus, the average interfiber distance becomes larger than several times the fiber diameter. This means that interference effects among neighboring fibers are substantially smaller compared with the ordinary granular packed bed. Hence, most of the equations proposed have been derived based on the drag theory.

According to the drag theory, the pressure drop ΔP across a fibrous mat with cross-sectional area A and thickness L is related to the fluid drag acting on fibers in the mat as follows:

$$\Delta PA = Fl_f AL \tag{3.7.24}$$

where F and l_f denote the fluid drag acting on a fiber with unit length and the total fiber length in a unit mat volume, respectively, and they are defined by the following equations:

$$F = C_D D_f \frac{\rho u_e^2}{2} \tag{3.7.25}$$

$$l_f = \frac{4a}{\pi D_f^2} \tag{3.7.26}$$

Substitution of the preceding two equations into Equation (3.7.24) yields

$$\Delta P = 4C_D \frac{aL}{D_f} \frac{\rho u_e^2}{2} \tag{3.7.27}$$

where

u denotes the average fluid velocity in the mat

C_D is usually given as a function of the Reynolds number based on the approaching velocity u_e

Furthermore, there exist some fibers parallel to the fluid flow. Hence, it would be better in practice to define ΔP by

$$\Delta P = 4C_{De} \frac{a}{\pi(1-a)} \frac{L}{D_f} \frac{\rho u^2}{2} \tag{3.7.28}$$

Table 3.7.1 summarizes the proposed effective drag coefficients C_{De}. In the table, the expression of Langmuir is derived from the channel theory.

NOTATION

A: Cross-sectional area of porous media (m^2)
C_D: Drag coefficient (-)
D: Diameter (m)
D_f: Fiber diameter (m)
D_P: article diameter (m)
F: Fluid drag acting on a fiber with unit length (N/m)
f: Fanning's friction factor (-)
$f(\varepsilon)$: Porosity function (-)
k: Kozeny constant (1/m)
k_o: Numerical constant used in Equation 3.7.8 (1/m)
L: Thickness (m)
L_e: Equivalent channel length (m)
l_f: Total fiber length per unit filter volume (m/m^3)
m: Hydraulic radius (m)
N: Total number of spheres in a porous media (m^{-3})
ΔP: Pressure drop (Pa)
R: Fluid resistance acting on an isolated particle (N)
R_m: Fluid resistance acting on a particle in a porous media

TABLE 3.7.1 Drag Coefficient of Filter

Researchers	Drag Coefficient	Remarks
Kozeny and Carman (1927,1937)[9,11]	$\frac{8\pi k_1}{Re_f}\frac{a}{(1-a)^2}$	Channel model
Langmuir (1942)[10]	$\frac{8\pi B}{Re_f}\frac{1}{2h_K}$	Channel model B = 1.4
Davies (1952)[11]	$\frac{32\pi}{Re_f}a^{0.5}\left(1+56a^2\right)$	Dimensional analysis
Lamb (1932)[12]	$\frac{8\pi}{Re_f}\frac{1}{h_L}$	Perpendicular to the flow, isolated fiber
Iberall (1950)[13]	$\frac{8\pi}{Re_f}$	Parallel to the flow, isolated fiber
Iberall (1950)[13]	$\frac{4.8\pi}{Re_f}\left(\frac{2.4-\ln Re}{h_L}\right)$	Semi-empirical equation
Chen (1955)[14]	$\frac{2}{Re_f}\frac{k_2}{\left\lfloor \ln k_3 a^{-0.5}\right\rfloor}$	$k_2 = 6.1$, $k_3 = 0.64$
Happel (1959)[15]	$\frac{8\pi}{Re_f}\frac{1}{2h_K}$	Tube bank parallel to the flow
Happel (1959)[15]	$\frac{16\pi}{Re_f}\frac{1}{-\ln a+\left(1-a^2\right)/\left(1+a^2\right)}$	Tube bank perpendicular to the flow
Kuwabara (1959)[16]	$\frac{16\pi}{Re_f}\frac{1}{2h_K}$	Tube bank perpendicular to the flow
Kimura and Iinoya (1969)[17]	$\frac{0.6+4.7/\sqrt{Re}+11/Re_f}{1-a}$	Empirical $10^{-3} < Re_f < 10^{-2}$, $3 < D_f < 270\ \mu m$

Lamb's hydrodynamic factor: $h_L = 2 - \ln Re$

Kuwabara's hydrodynamic factor: $h_K = -\frac{1}{2}\ln a + a - a^2/4 - 3/4$

Re: Reynolds number ($Du\rho/\mu$) (-)
Re_f: Reynolds number based on fiber diameter ($D_f u\rho/\mu$) (-)
Re_p: Reynolds number based on particle diameter ($D_p u\rho/\mu$) (-)
S_B: Specific surface of particle based on the bed volume (m^2/m^3)
S_v: Specific surface of particle based on the particle volume (m^2/m^3)
u: Fluid velocity (m/s)
u_e: Effective fluid velocity in a porous media (m/s)
α: Fiber packing density (-)
ε: Porosity (-)
μ: Viscosity (Pa·s)

REFERENCES

1. Carman, P. C., *Trans. Inst. Chem. Eng.*, 15, 150–156, 1937.
2. Blake, F. E., *Trans. Am. Inst. Chem. Eng.*, 14, 415–421, 1922.
3. Chilton, T. H., Colburn, A. D., *Ind. Chem. Eng.*, 23, 913–918, 1931.
4. Brownell, L. E., Katz, D. L., *Chem. Eng. Prog.*, 43, 537–548, 1947.
5. Leva, M., *Fluidization*, McGraw-Hill, New York, 1959.
6. Steinour, H., *Ind. Eng. Chem.*, 36, 618–624, 1944.
7. Burke, S. P., Plummer, W. B., *Ind. Eng. Chem.*, 20, 1196–1200, 1928.
8. Ergun, S., *Chem. Eng. Prog.*, 48, 89–94, 1952.
9. Kozeny, J., Ueber kapillare Leitung des Wassers im Boden, *Sitzungsber. Akad. Wissensch. Wien*, 136, 271–306, 1927.
10. Langmuir, I., *OSRD Rep.* No. 865, 1942.
11. Davies, C. N., *Proc. Inst. Mech. Eng. (London)*, 131, 185–213, 1952.
12. Lamb, H., *Hydrodyamic* 6th ed., Cambridge Univ. Pr., p.614, 1932.
13. Iberall, A. S., *J. Res. Natl. Bur. Stand.*, 45, 85–108, 1950.
14. Chen, C. Y., *Chem. Rev.*, 55, 595–623, 1955.
15. Happel, J., *AIChE J.*, 5, 174–177, 1959.
16. Kuwabara, S., *J. Phys. Soc. Jpn.*, 14, 527–532, 1959.
17. Kimura, N., Iinoya, K., *Kagaku Kogaku*, 33, 1008–1013, 1969.



Taylor & Francis
Taylor & Francis Group
http://taylorandfrancis.com

3.8 Mechanical Properties of a Powder Bed

Michitaka Suzuki

The mechanical properties of powder such as adhesion, cohesion, and flowability have an effect on powder handling and operation. These properties of powder can be measured by a tensile, shear, and compression test of the powder bed. In this section, we discuss how to measure the mechanical properties of a powder bed and how to describe the mechanical strength or flowability of a powder bed based on the powder mechanics.

Various types of shear testers have been devised to measure the powder yield locus (PYL), consolidation yield locus (CYL), and critical state line (CSL), which are projections of the flow surface, consolidation surface, and CSL, respectively, onto the normal stress σ -shear stress τ plane in the Roscoe diagram (see Figure 3.8.8). Several kinds of tensile testers have also been developed to measure the tensile property, which is represented by a curve t_1t_2 in the Roscoe diagram.

3.8.1 SHEARING STRENGTH OF A POWDER BED

Triaxial Compression Test

The schematic diagram of a triaxial compression tester is shown in Figure 3.8.1. A cylindrical specimen is placed into the space surrounded by two pistons and a rubber side membrane, to which vertical and lateral pressures are applied independently. From the pressures at the break point that means the critical stress condition, the Mohr's stress circle with the maximum principal stress σ_1 and the minimum principal stress σ_3 can be obtained, as shown later in Figure 3.8.13. The yield locus is obtainable as an envelope of a family of the Mohr's circles at the critical stress condition. Although the triaxial compression tester is used widely in soil mechanics,[1,2] it is complex in structure and has the disadvantage that the failure surface of test samples becomes irregular. Hence, it is not widely used in the field of powder technology except for a few cases.[3,4] Aoki et al.[5] modified the tensile tester of the split-cell-type, called the Cohe tester (see Chapter 3.8.2), and made a simplified triaxial tester to measure the PYL of loosely packed powders in a low-stress region. Arthur et al.[6] designed a new biaxial tester with flexible membranes stretched to the retaining guides. The tester imposes known uniform principal stresses on a precisely compacted cubical sample powder and measures the resulting strains in a simple and immediate manner.

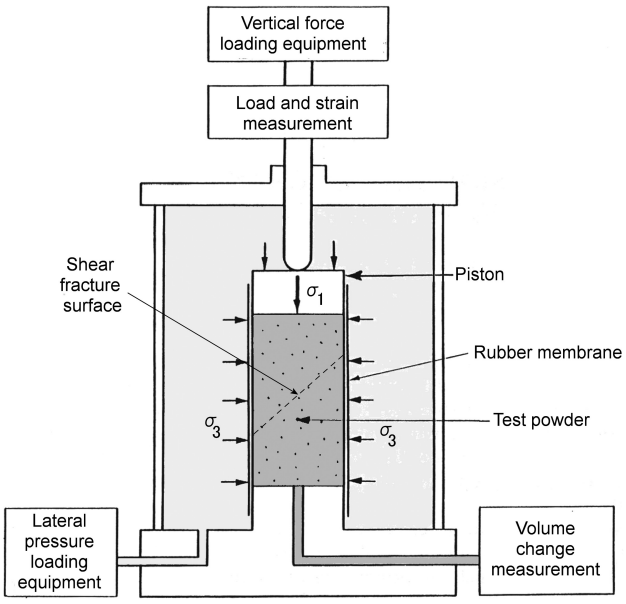


FIGURE 3.8.1 Schematic diagram of triaxial compression tester.

Direct Shear Test

A direct shear tester has a simple structure and the testing procedure is also simple. Hence, it is widely used in powder technology, especially in the field of bulk materials handling. The direct shear tester usually consists of two cells: one cell is placed on the other cell, which is fixed. They are filled with the particulate material under examination, the test sample is consolidated to attain a prescribed packing density, and then under a compression load, a horizontal shear force is applied to the upper cell so as to measure the yield point. The relation between the compression load and shear force at the yield point gives the yield locus for the prescribed packing density. Various types of testers have been proposed for this purpose.

Jenike's Shear Tester

The shear tester developed by Jenike et al.[7] is the most popular and widely used of those designed with a hopper, bin, or silo.[8–13] Jenike's shear tester and test procedure became an international standard.[14] A cross-sectional view of Jenike's shear cell is shown in Figure 3.8.2. A test sample is filled in the cell and consolidated by twisting under normal stress σ_p. Then the ring is sheared under the same normal stress σ_p until 95% of the yield force measured beforehand is attained, and then the normal stress is replaced by a smaller stress, σ ($< \sigma_p$). The cell

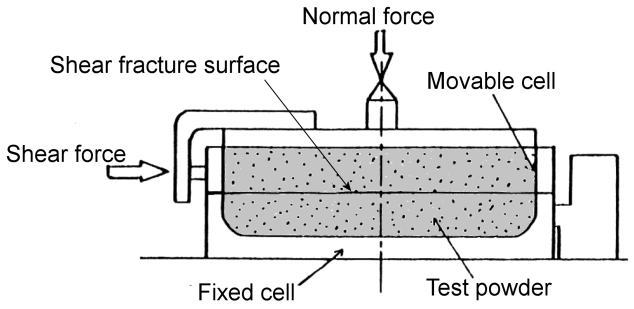


FIGURE 3.8.2 Schematic diagram of Jenike's shear tester.

is sheared again until the specimen reaches yield. In this way, the relationship between σ and τ is obtained. Hirota et al.[15] reported coincidence of the results obtained by the Jenike's shear tester and his parallel-plates-type shear tester using the same procedure. On the Jenike's shear tester, Haaker[16] investigated the effect of the ratio of externally applied load during consolidation and preshearing.

Richmond and Gardner[11] devised shear blades in the cell to avoid the slip of powder on the wall while in shearing. Tsunakawa and Aoki[17,18] modified the Jenike cell to keep a constant volume and obtained the yield locus from a single shear test by recording the normal and shear stresses simultaneously on an X-Y recorder. Shimada, Hatano, and Matsuzaka[19] proposed a new method for evaluating powder flowability using a constant volume shear tester. Kirby[20] subsequently presented a query for their measuring procedure. Terashita et al.[21] measured the normal stress distribution in the cell and noted that the normal stress does not apply accurately on the shear surface because of the wall friction. After correcting the normal stress on the shear surface, they obtained the CSL. Matsumoto et al.[22] modified the direct shear tester to measure the actual normal stress on the shear surface. These types of shear tester have limitations in effective shear surface, and Hirota et al.[23] pointed out that the size of the shear cell affects the measuring results substantially. Hidaka et al.[24] investigated the particle assemblies in the shearing process by computer simulation based on the distinct element method, and discussed the acoustic emission from the shear flow of granular materials.

Annular Ring Shear Tester

Annular ring or torsion shear testers are used for cylindrical powder beds. The major advantages of this type are that the area of the shear surface does not change during the test, there is no limitation in the amount of angular displacement, and the shear characteristics after the yield can also be measured. Walker[25] made the annular shear tester shown in Figure 3.8.3. Suzuki et al.,[26] Gotoh et al.,[27] and Yamada et al.[28] used a similar type of the shear testers. Scarlett and Todd[29] designed a split annular ring shear cell to achieve a simple flow profile of powder, but its structure was complicated. Impeller-type powder rheometer is the one kinds of annular ring shear tester. Hare et al.[30] investigate the impeller-type powder rheometer

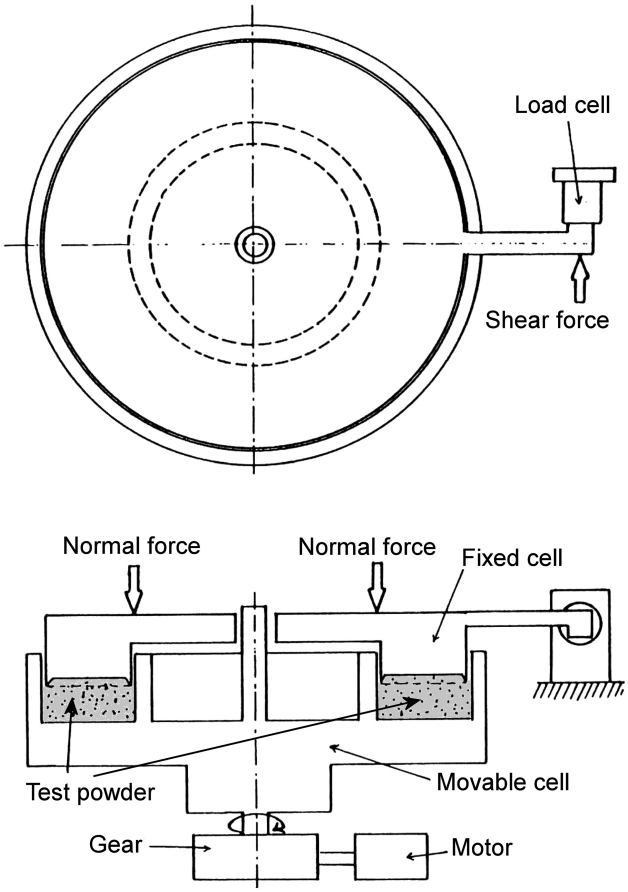


FIGURE 3.8.3 Schematic diagram of annular ring shear tester.

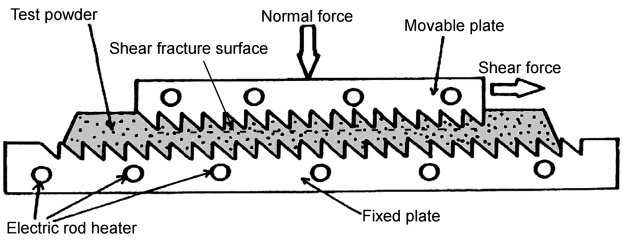


FIGURE 3.8.4 Parallel-plate shear tester for high temperature shear tests.

and discussed the mechanism of the powder rheometer using DEM simulation.

Parallel-Plate Shear Tester

Hiestand and Wilcox[31] and Budny[32] devised a parallel-plate tester, and Hirota et al.[33] installed electric rod heaters in the plates, as shown in Figure 3.8.4, in order to measure the shear properties at high temperatures up to 800 K. The test powder is placed between two solid plates, the bottom plate is fixed, and the normal and shear forces are applied to the upper movable plate. No sidewall exists, so that it is unnecessary to consider the wall friction. Small expansion and contraction on the order of 1 μm are detected during the shear process.[34]

Hirota et al.[35,36] also devised tensile and compression testers similar to the parallel plates shear tester.

3.8.2 ADHESION OF A POWDER BED

The tensile strength of powder bed σ_t can be measured by several kinds of tensile testers, which are classified to two types: one is based on a vertical tensile method and the other a horizontal tensile method.

Horizontal Tensile Method

The tensile force in this method is applied perpendicular to the compression load for consolidation of powder. Ashton et al.[37] developed a split-cell-type tensile tester, which is shown in Figure 3.8.5. Test powder is compacted into the split cell, and half of the cell is fixed on a plate. The other half of the cell is put on ball bearings for movement. The tensile strength of the test powder is measured by a load cell connected to the movable cell. The tensile strength of a loosely packed powder bed can also be measured using this type of tester because the friction of the movable cell is reduced by the ball bearing, but the cleaning of the balls after each test is time-consuming. Schotton and Harb[38] measured the tensile strength of powder using the same kinds of tester on a slanted plate by changing the angle of the plate. Jimbo and Yamazaki[39] developed a modified split-cell-bearing-type tester, which consists of two movable cells. The friction of the tester can be reduced, but the structure of the tester is complicated. Yokoyama et al.[40] devised a frictionless split cell by hanging one half of the cell, like a swing, as shown in Figure 3.8.6, the Cohe tester. This is a tester to measure the tensile strength of a loosely packed powder bed in a high void fraction region.

Vertical Tensile Method

The tensile load can be applied vertically to the compacted powder; it means that the direction of the tensile force is the same as that of the compression force. Shinohara and Tanaka,[41] Arakawa,[42] and Suzuki et al.[25] developed the tensile testers based on this method. Arakawa[42] developed the vertical-type tensile tester from an electric balance, as shown in Figure 3.8.7. He also tried to explain the effect of a particle packing structure on tensile strength of a powder bed by a two-dimensional particle model experiment. Hirota et al.[36] developed a parallel-plate-type shear and tensile tester to obtain the yield loci under the normal stress ranging from positive to negative (including the adhesion force) and measured the PYL in the tensile region, but the operation of the tester was not so easy.

The tensile strength measured by the vertical tensile method is usually larger than that measured by the horizontal tensile method, because the direction of compression force at preconsolidation is the same as the direction of tensile force in the vertical method and is perpendicular to the tensile force in the horizontal method. The relation between the tensile strengths by these methods is not clear yet.

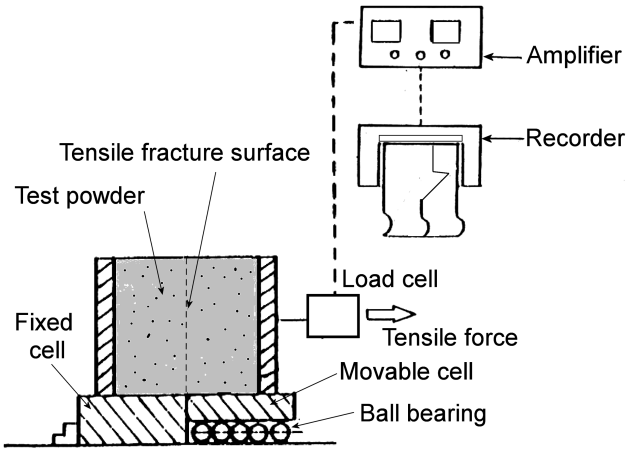


FIGURE 3.8.5 Horizontal tensile tester.

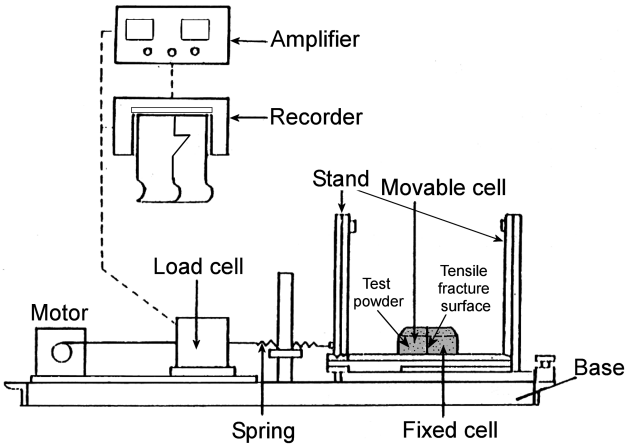


FIGURE 3.8.6 Swing-type horizontal tensile tester called the Cohe tester.

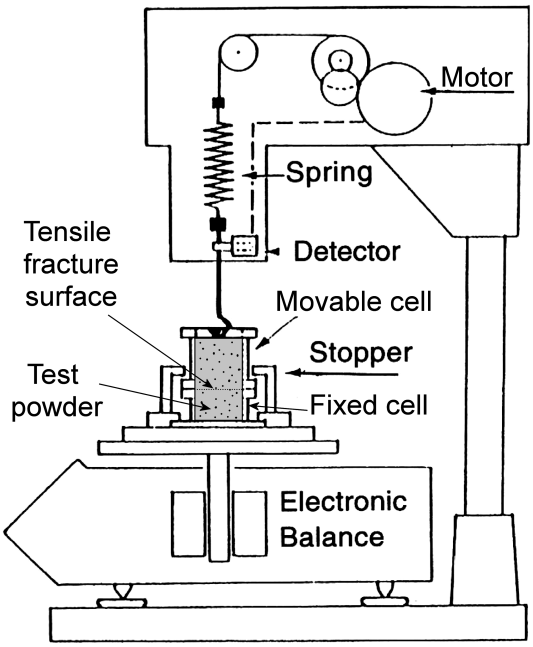


FIGURE 3.8.7 Vertical tensile tester.

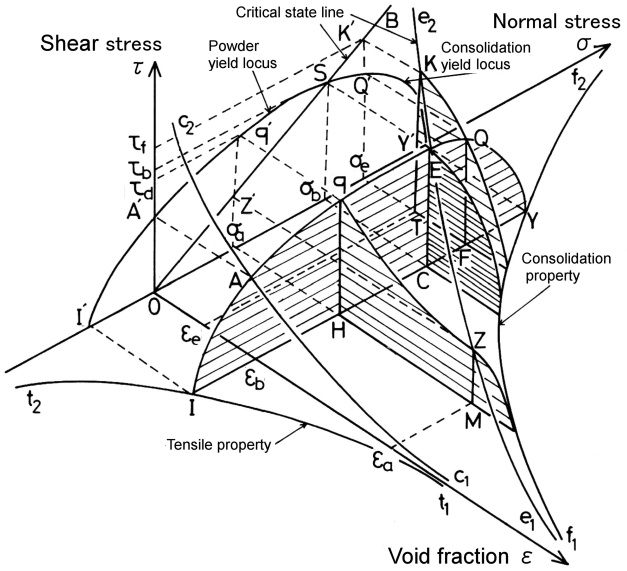


FIGURE 3.8.8 Roscoe's condition diagram of powder.

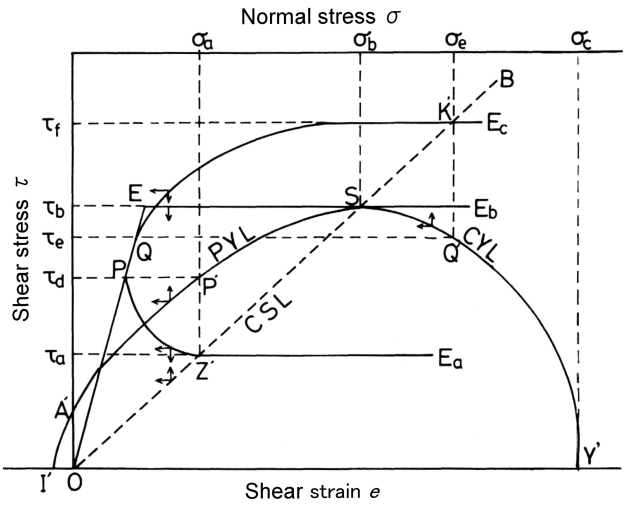


FIGURE 3.8.9 Conceptual diagram of shearing process.

3.8.3 YIELDING CHARACTERISTICS OF A POWDER BED

Figure 3.8.8 shows the concept of the Roscoe diagram or Cambridge model proposed by Roscoe et al.,[43,44] which expresses the yielding characteristics of a powder bed in relation to shear, tensile, and compression strengths (see section 3.8.1). The coordinates of the diagram are the shear stress τ, the normal stress σ, and the void fraction ε of the powder bed. The curve t_1t_2 on the plane $\tau=0$, called the tensile property, depicts the relationship between tensile strength and void fraction. The curve f_1f_2 on the plane $\tau=0$, called the compressive property or consolidation line, is the relation between compression strength and void fraction. Only the region between these two curves is possible.

In the three-dimensional diagram, two failure surfaces, called the flow surface and the consolidation surface, exist between these two curves. The intersection of them is the curve e_1e_2 in Figure 3.8.8, which is called the CSL. The flow surface between curves t_1t_2 and e_1e_2 corresponds to the plastic flow with expansion, and the projection of the flow surface onto the σ-τ plane is called the powder yield locus, or simply the yield locus. The consolidation surface between curves f_1f_2 and e_1e_2 corresponds to plastic deformation with contraction, whose projection onto a σ-τ plane is called the CYL. The elastic condition corresponds to the region below the surface in Figure 3.8.9, while the region above the surface is actually impossible.

Consider the shear process of a powder bed with the void fraction ε_b in the three-dimensional diagram. At the normal stress σ_b, the shear stress increases from point C to point E in Figure 3.8.9, where the steady flow occurs. In this case the stress versus strain curve passes over the line OPES in Figure 3.8.10. A set of τ and σ on the CSL can be obtained from τ_b and σ_b of point E in Figure 3.8.9.

When $\sigma=\sigma_a$ ($\sigma_a>\sigma_b$), τ increases from point H to point P in Figure 3.8.9, where yielding starts with expansion, and then it decreases gradually along PZ with increasing void fraction from ε_b to ε_e until the powder bed begins to flow steadily at point Z. A set of τ and σ on the PYL can be obtained from τ_d and σ_a of point P in Figure 3.8.9.

When $\sigma=\sigma_e$ ($\sigma_e>\sigma_b$), τ increases from point F to Q in Figure 3.8.9, where the yielding starts with contraction, and then it increases gradually along QK with decreasing void fraction from ε_b to ε_e until the powder bed starts to flow steadily at point K. A set of τ and σ on the CYL can be obtained from τ_e and σ_e of point Q in Figure 3.8.9. As a result, the yield locus, which is the relation between τ and σ at the yield point of the powder bed, can be depicted by the curve I′A′P′SQ′, which is the projection of the curve IAPEQ in Figure 3.8.9 onto the σ-τ plane. Point Y expresses the preconsolidation state at the starting point of yielding.

The yield locus at the state of steady flow leads the curve OZ'SK'B, which is the projection of the curve e_1ZEKe_2 in Figure 3.8.9 onto the σ-τ plane and equals the CSL proposed by Schwedes.[45] The void fraction ε decreases with increasing σ, and τ and σ are specified for a given value of ε.

If the Roscoe diagram is obtained for a powder bed, the static mechanics of the bed can be discussed quantitatively.

The examples of the experimental data are shown in Figures 3.8.10 and 3.8.11. These diagrams were obtained from the compression, shear, and tensile testers of parallel-plate-type by use of the three-dimensional computer graphic technique.[46] Figure 3.8.10 is for flyash and Figure 3.8.11 for precipitated calcium carbonate powder. Because the yield locus becomes a straight line on the σ-τ plane, the flyash might be a Coulombic powder, while the upper surface of the yield locus of the calcium carbonate powder looks like a mountain, and it is found to be a cohesive bulk material.

If a powder is a rigid plastic or Coulombic solid, its yield locus can be expressed by

$$\tau = \mu_i\sigma + \tau_c = \sigma\tan\phi_i + \tau_c \tag{3.8.1}$$

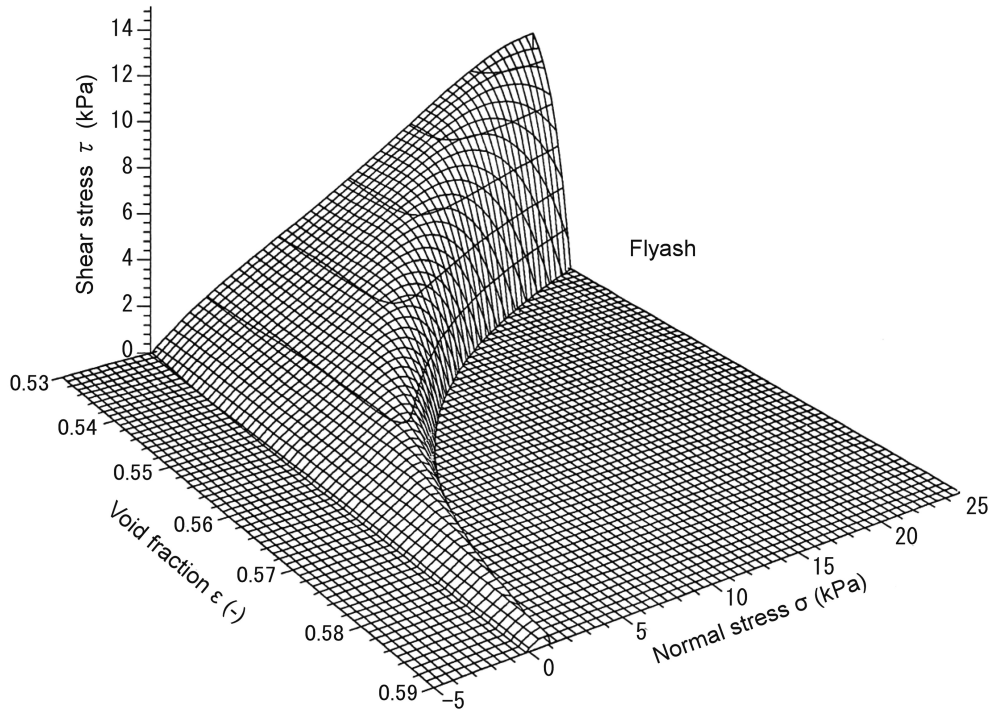


FIGURE 3.8.10 Roscoe diagram based on experimental data of flyash powder.

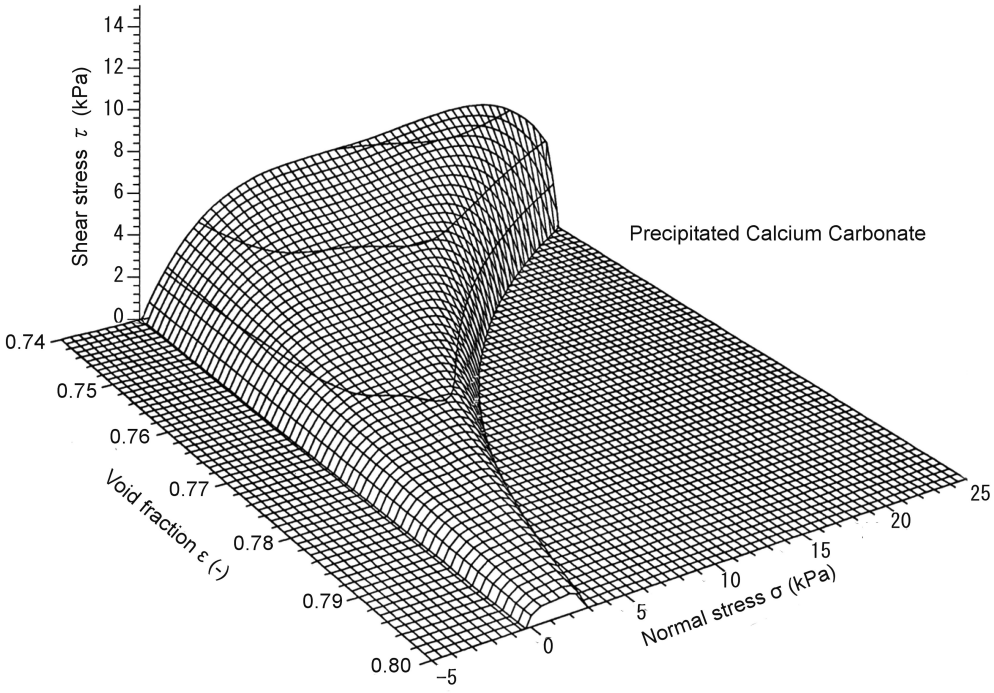


FIGURE 3.8.11 Roscoe diagram based on experimental data of calcium carbonate powder.

where τ and σ are the shear and normal stresses, μ_i the internal friction coefficient, ϕ_i the internal friction angle, and τ_c the cohesion (kPa). Using Equation (3.8.1), the mechanical properties of powder, including the CSL, can be expressed by two parameters, μ_i or ϕ_i and τ_c. The Coulomb equation is applicable in general to cohesionless coarse powders. Because the yield locus is the envelope of a family of yield stress circles (Mohr circles), it should cross the σ axis perpendicularly at point I′, which corresponds to the tensile strength of the powder bed. As one can see from Figure 3.8.12, however, the Coulomb equation does not cross the σ axis at a right angle, a contradiction explained by Jenike et al.,[7] Umeya et al.,[47] and Makino et al.[48]

On the assumption that the particle arrangement is a face-centered cubic and the attractive force between particles is a

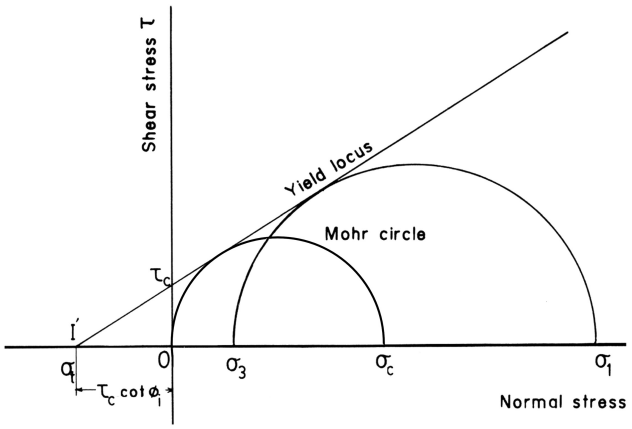


FIGURE 3.8.12 Yield locus of a Coulomb powder.

function of the separation of nearest neighbors with a maximum limit of separation, Ashton et al.[49] derived the following relation:

$$\left(\frac{\tau}{\tau_c}\right)^n = \frac{\sigma}{\sigma_t} + 1 \tag{3.8.2}$$

where σ_t is the tensile strength, τ_c is the cohesion of the powder bed, and n is the shear index. In the case of $n=1$, Equation (3.8.2) reduces to Equation (3.8.1); n is found to be independent of the void fraction and it ranges from about 1 for free-flowing powders up to 2 for very cohesive ones. Umeya et al.[47] derived the same result experimentally.

The values of σ_t and τ_c in Equation (3.8.1) and Equation (3.8.2) vary with the void fraction. Williams and Birks[50] suggested that if a family of yield loci is plotted on the τ/σ_L versus σ/σ_L diagram, where σ_L is the normal stress at the end point of a yield locus, they come to lie on a single PYL curve, which is a straight line on logarithmic scales. Hirota et al.[36] pointed out that it is difficult to measure σ_L; also, Williams's linearization method cannot apply to the CYL. Therefore, they recommended to use a $\tau/(\sigma_c - \sigma_t)$ versus $(\sigma - \sigma_t)/(\sigma_c - \sigma_t)$ diagram in order to express various PYL and CYL curves with a single curve.

The unconfined yield strength σ_c of a powder in Figure 3.8.12 is the stress required to deform or break a powder when it is not confined by a container that means free unstressed surface. The unconfined yield strength σc is found by drawing an unconfined yield stress Mohr circle tangent to the yield locus and passing through the origin ($\sigma=\tau=0$). The uniaxial yield strength σ_c can be obtained geometrically from the intersection point value of the Mohr circle and the normal stress axis. The force used to consolidate the powder packed bed is called the major consolidation stress σ_p.

Flowability of powder is an important factor for powder handing and operation. Jenike defines the flow function F_F as Equation (3.8.3),

$$F_F = \frac{\text{Major Consolidating Strength } \sigma_p}{\text{Unconfined Yield Strength } \sigma_c} \tag{3.8.3}$$

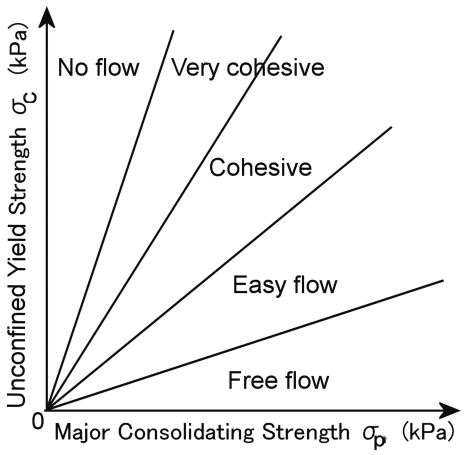


FIGURE 3.8.13 Jenike's classification of powder flowability based on flow index.

TABLE 3.8.1 Jenike's Classification of Powder Flowability Based on Flow Index

Flowability	No flow	Very Cohesive	Cohesive	Easy Flow	Free Flowing
Flow index	<1	<2	<4	<10	>10

Figure 3.8.13 shows flow function on major consolidating strength σ_p versus unconfined yield strength σ_c plane. A flow function F_F line located at the bottom of the graph represents easy flowing material, whereas more difficult flow is represented as the flow function line moves in a counterclockwise direction. The flow index obtained from the inverse of the slope of the flow function line was used by Jenike to classify powder flowability as No flow, Very cohesive, Cohesive, Easy flow, Free flow as shown in Table 3.8.1. The greater the flow index, the better the flowability.

Based on a theoretical model, Rumpf[51] derived the following expression for the tensile strength of randomly packed bed of equal spheres:

$$\sigma_t = \frac{1-\varepsilon}{\pi} N_c \frac{H}{x^2} \tag{3.8.4}$$

where ε is the void fraction, N_c is the average coordination number. H is the cohesion force at a contact point, and x the particle diameter. Molerus[52] supposed that Equation (3.8.3) holds for the relation between the stress and the applied force under the isotropic or hydrostatic pressure, and he analyzed the shear mechanism of a powder bed.

Makino et al.[48] proposed a model for the yield of a powder bed, taking into account a particle arrangement and interparticle force of a Lennard–Jones type. They discussed a yield condition under constant strain, and the PYL and CYL were made obtainable for any void fraction from only four parameters determined by tensile and compression tests. Yamada et al.[27]

subsequently reduced the number of parameters required to estimate the PYL and CYL of a powder bed. But, it is difficult to express the interparticle friction by the Lennard–Jones type of potential.

Nagao[53] proposed a more precise theory of powder mechanics, including equation of stress and moment equilibrium, equation of continuity, a geometric relation, stress–strain relations, and boundary conditions. Based on the fundamental equations, he calculated the stress distribution in compressed powder beds by use of the finite-element method.[54] A principle of similarity in the mechanics of granular materials was also investigated.[55]

Kanatani[56] established a theory of continuum mechanics for the flow of granular materials, which is an application of the theory of polar fluids. He derived theoretically various characteristics of granular materials, such as the critical stress condition, angle of repose, and the effects of coupling stress in the Couette flow between two parallel plates.

Tsubaki and Jimbo[57] reported that Rumpf's equation for tensile strength of a powder bed coincides with Nagao's theory for the stress–strain relation, Molerus's research on the yield of cohesive powders[52] and Kanatani's theory for flow of granular materials. Hence it can be said that Rumpf's equation is applicable not only to the tensile strength but also to the shear and compression strengths of the powder bed.

REFERENCES

1. Newland, P. L., Allely, B. H., *Geotechnique*, 7, 17–34, 1957.
2. Rowe, P. W., *Proc. R. Soc. London A*, 269, 500–527, 1962.
3. Masuda, Y., Sakai, N., *J. Jpn. Soc. Powder and Powder Metall.*, 19, 1–16, 1972.
4. Takagi, F., Sugita, M., *J. Soc. Powder Technol. Jpn.*, 16, 277–282, 1979.
5. Aoki, R., Suganuma, A., Motone, M., *J. Soc. Powder Technol. Jpn.*, 9, 538–542, 1982.
6. Arthur, J. R. F., Dunstan, T., Enstad, G. G., *Int. J. Bulk Solids Storage Silos*, 1, 7–10, 1985.
7. Jenike, A. W., Elsey, P. J., Wolley, R. H., *Am. Soc. Test. Mater. Proc.*, 60, 1168–1190, 1960.
8. Jenike, A. W., *Trans. Inst. Chem. Eng.*, 40, 264–271, 1962.
9. Jenike, A. W., *Trans. Soc. Min. Eng.*, 235, 267–275, 1966.
10. Jenike, A. W., *Powder Technol.*, 11, 89–91, 1975.
11. Richmond, O., Gardner, G. C., *Chem. Eng. Sci.*, 17, 1071–1078, 1962.
12. Williams, J. C., *Chem. Process Eng.*, 46, 173–179, 1965.
13. Eisenhart-Rothe, M., Peschl, I. A. S. Z., *Powder Testing Techniques for Bulk Materials Equipment, in Solid Handling*, McGraw-Hill, New York, 1981.
14. ISO 11697, 1994.
15. Hirota, M., et al., *J. Soc. Powder Technol. Jpn.*, 22, 144–149, 1985.
16. Haaker, G., *Powder Technol.*, 51, 231–236, 1987.
17. Tsunakawa, H., Aoki, R., *J. Soc. Powder Technol. Jpn.*, 11, 263–268, 1974.
18. Tsunakawa, H., Aoki, R., *Powder Technol.*, 33, 249–256, 1982.
19. Shimada Y., Hatano S., Matsusaka S., *J. Soc. Powder Technol. Jpn.*, 54, 90–96, 2017.
20. Kirby, J. M., *Powder Technol.*, 39, 291–292, 1984.
21. Terashita, K., Miyanami, K., Yamamoto, T., Yano, T., *J. Soc. Powder Technol. Jpn.*, 15, 526–534, 1978.
22. Matsumoto, K., et al., *J. Soc. Powder Technol.*, 19, 653–660, 1982.
23. Hirota, M., Oshima, T., Hashimoto, S. *J. Soc. Powder Technol. Jpn.*, 16, 198–206, 1979.
24. Hidaka, J., Kinboshi, T., Miwa, S., *J. Soc. Powder Technol. Jpn.*, 26, 77–84, 1989.
25. Walker, D. M., *Powder Technol.*, 1, 228–236, 1967.
26. Suzuki, M., Makino, K., Iinoya, K., Watanabe, K., *J. Soc. Powder Technol. Jpn.*, 17, 559–564, 1980.
27. Gotoh, A., Kawamura, M., Matsushima, H., Tsunakawa, H., *J. Soc. Powder Technol. Jpn.*, 21, 131–136, 1984.
28. Yamada, M., Kuramitsu, K., Makino, K., *Kagaku Kogaku Ronbunshu*, 12, 408–413, 1986.
29. Scarlett, B., Todd, A. C., *Trans. ASME Ser. B*, 91, 478–488, 1969.
30. Hare C., et al., *Powder Technol.*, 285, 123–127, 2015
31. Hiestand, E. N., Wilcox, C. J., *J. Pharm. Sci.*, 58, 1403–1410, 1969.
32. Budny, T. J., *Powder Technol.*, 23, 197–201, 1979.
33. Hirota, M., Oshima, T., Naitoh, M., *J. Soc. Powder Technol. Jpn.*, 19, 337–342, 1982.
34. Hirota, M., Kobayashi, T., Sano, O., Oshima, T., *J. Soc. Powder Technol. Jpn.*, 21, 137–142, 1984.
35. Hirota, M., Oshima, T., Ishihara, T., Kanazawa, A., *J. Soc. Mater. Sci. Jpn.*, 33, 1125–1129, 1984.
36. Hirota, M., Kobayashi, T., Oshima, T., *J. Soc. Powder Technol. Jpn.*, 22, 271–277, 1985.
37. Ashton, M. D., Farley, R., Valentin, F. H. H., *J. Sci. Instrum.*, 41, 763–765, 1964.
38. Schotton, E., Harb, N., *J. Pharm. Pharmacol.*, 18, 175–178, 1966.
39. Naito, M., Kato N., Jimbo G., Yokoyama T., *J. Soc. Powder Technol. Jpn.*, 23, 500–506, 1986.
40. Yokoyama, T., Fujii, K., Yokoyama, T., *Powder Technol.*, 32, 55–62, 1982.
41. Shinohara, K., Tanaka, T., *J. Chem. Eng. Jpn.*, 8, 46–50, 1975.
42. Arakawa, M., *J. Soc. Mat. Sci. Jpn.*, 29, 881–886, 1980.
43. Roscoe, K. H., Schofield, A. N., Wroth, C. P., *Geotechnique*, 8, 22–53, 1958.
44. Roscoe, K. H., Schofield, A. N., Thurairajah, A., *Geotechnique*, 13, 211–240, 1963.
45. Schwedes, J., *Powder Technol.*, 11, 59–67, 1975.
46. Suzuki, M., Hirota, M., Oshima, T., *J. Soc. Powder Technol. Jpn.*, 24, 311–314, 1987.
47. Umeya, K., Kitamori, N., Araki, Y., Mima, H., *J. Soc. Mater. Sci. Jpn.*, 15, 166–171, 1966.
48. Makino, K., et al., *Int. Chem. Eng.*, 21, 229–235, 1981.
49. Ashton, M. D., Cheng, D. C. H., Farley, R., Valentine, F. H. H., *Rheol. Acta*, 4, 206–218, 1965.
50. Williams, J. C., Birks, A. H., *Powder Technol.*, 1, 199–206, 1967.
51. Rumpf, H., *Chem. Eng. Technol.*, 42, 538–540, 1970.
52. Molerus, O., *Powder Technol.*, 12, 259–275, 1975.
53. Nagao, T., *Trans. Jpn. Soc. Mech. Eng.*, 33, 229–241, 1967.
54. Nagao, T., Katayama, S., *Jpn. Soc. Mech. Eng.*, 46, 355–366, 1980.
55. Nagao, T., *J. Soc. Powder Technol. Jpn.*, 21, 398–405, 1984.
56. Kanatani, K., *J. Soc. Powder Technol. Jpn.*, 16, 445–452, 1979.
57. Tsubaki, J., Jimbo, G., *Powder Technol.*, 37, 219–227, 1984.



Taylor & Francis
Taylor & Francis Group
http://taylorandfrancis.com

3.9 Fluidity of Powder

Toyokazu Yokoyama

3.9.1 DEFINITION OF FLUIDITY

The fluidity of powder is defined intuitively as the ease of flow and relates to the change of mutual position of individual particles forming the powder bed. The fluidity of powder is strongly related to physical properties such as frictional force and cohesive force of the particles. The dynamic behavior of powder seems to be determined basically by interparticle forces and packing structure.

Powder flow in various industrial processes takes place in different ways that can hardly be described in a universal form. Table 3.9.1 classifies the type of powder flow from the practical viewpoint.[1] Based on the source of energy exerted on the particles, powder flow is classified as (1) gravitational flow, (2) mechanically forced flow, (3) vibration flow, (4) compression flow, and (5) fluidized flow, which appear simultaneously in actual processes in most cases.

3.9.2 MEASUREMENT OF FLUIDITY

As the phenomena of powder flow are complicated and involve the combined flow patterns listed in Table 3.9.1, a suitable method of measurement is required for individual cases. Although there are a variety of methods to determine fluidity and related properties, it is difficult to find a general result among them. Therefore, it is essential for measurement to clarify the measuring conditions and powder properties. Furthermore, attention should be paid to the range applicable to the powder-handling processes.

3.9.2.1 Gravitational Flow

The flow from hoppers or through an orifice is often considered to express the fluidity of powder. In this case, the magnitude and uniformity of flow rate, as well as the tendency of choking, are regarded as the criteria of the fluidity. The flow pattern and segregation are also related to the fluidity of powder.

In the field of metallurgy, the time required for a powder sample of 50 g to be discharged by gravitational force from the funnel shown in Figure 3.9.1 is often used as a measure to evaluate fluidity. For cohesive powders, Irani et al.[2] proposed a double-funnel method with larger openings.

Even if the flow rate is high, a flow with a large fluctuation cannot be regarded as a good measure of fluidity. Several reports have been presented on the uniformity of the discharge rate, especially in the pharmaceutical field. Gold et al.,[3] for example, studied the discharge rate and its fluctuation experimentally.

Cohesive powders tend to form a bridge near the outlet of the container. The minimum opening size free of choking corresponds to the critical condition for powder flow and can be a measure of the fluidity. For the Coulomb powders, the critical choking aperture can be obtained from Mohr's stress circle.

The mass-discharge rate is proportional to the product of the height of the surface level and the square root of the orifice diameter in the case of liquid; it is independent of the height of the powder bed and proportional to the orifice diameter to the power of 2.5 to 3 in the case of powders. Numerous experimental equations[4] have been proposed for the flow rate of powder discharged by gravitational force.

Matsusaka et al. investigated the flow of fine powder using a microfeeder with a vibrating capillary tube having a diameter of less than 1.6 mm.[5] Figure 3.9.2 shows the effect of the inner diameter of a capillary tube d on maximum powder flow rate W_{max}. It was confirmed that fine particles of about 10 μm

TABLE 3.9.1 Type of Flow and Fluidity

Type of Flow	Process/Phenomena	Expression of Fluidity
Gravitational flow	Discharge from bin and hopper, chute, sand-glass, tumbling mixer, moving bed, packing	Discharge rate, angle of wall friction, angle of repose, critical discharge opening
Mechanically forced flow	Powder mixing, chain conveyor, screw conveyor, table feeder, ribbon mixer, rotary feeder, extruder	Angle of internal friction, angle of wall friction, mixing resistance
Compression flow	Briquetting, tableting	Compressibility, angle of wall friction, angle of internal friction
Vibration flow	Vibrating feeder, vibrating conveyor, vibrating screen, packing, discharge	Angle of repose, discharge rate, compressibility, bulk density
Fluidized flow	Fluidized bed, pneumatic conveyor, air slide, aerated vibration dryer	Angle of repose, minimum fluidization velocity, aeration resistance, apparent viscosity

Source: Hayakawa, S., Funtai Bussei Sokuteiho, Asakura, Tokyo. 1973, p. 80.

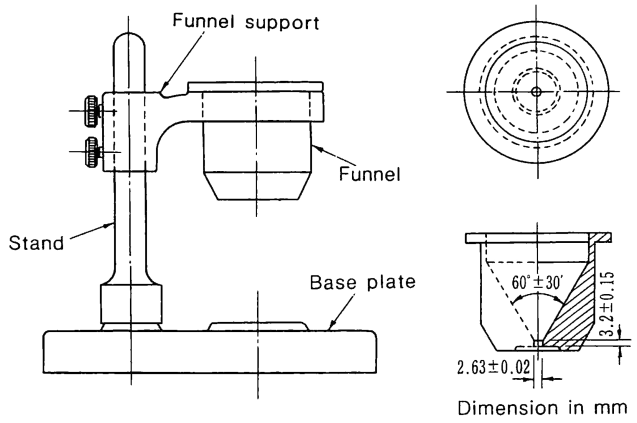


FIGURE 3.9.1 Device for the measurement of fluidity. (From Japanese Industrial Standard Z 2502, 1979.)

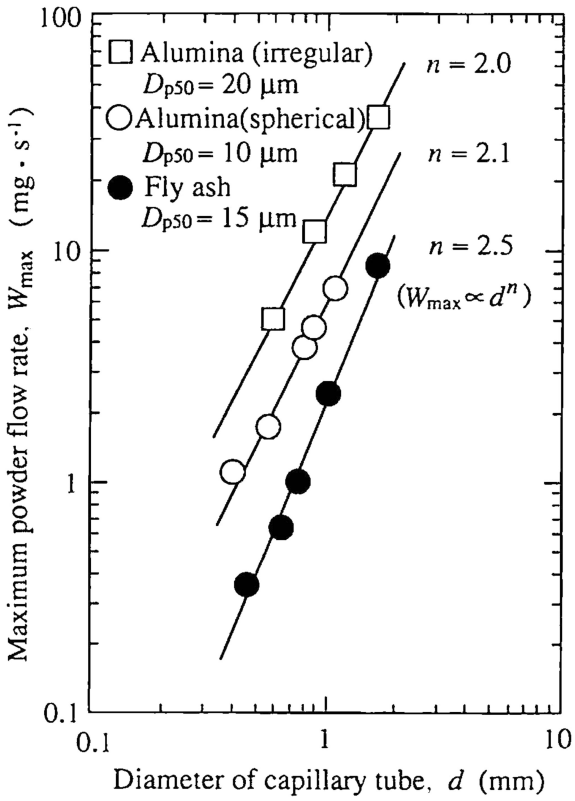


FIGURE 3.9.2 Effect of the inner diameter of a capillary tube d on maximum powder flow rate W_{max}. (From Matsusaka, S., Yamamoto, K., and Masuda, H., Adv. Powder Technol., 7, 141–151, 1996.)

diameter are successfully discharged using a vibrating capillary tube, and that the maximum flow rate is proportional to the 2–2.5th power of the capillary diameter, which is a little low compared with that for the conventional orifice. This flow rate is also regarded as a measure of fluidity of fine powder.

The angle of repose is defined as the angle from the horizontal plane to the free surface of a pile of powder under the critical stress in the gravitational field. There are three

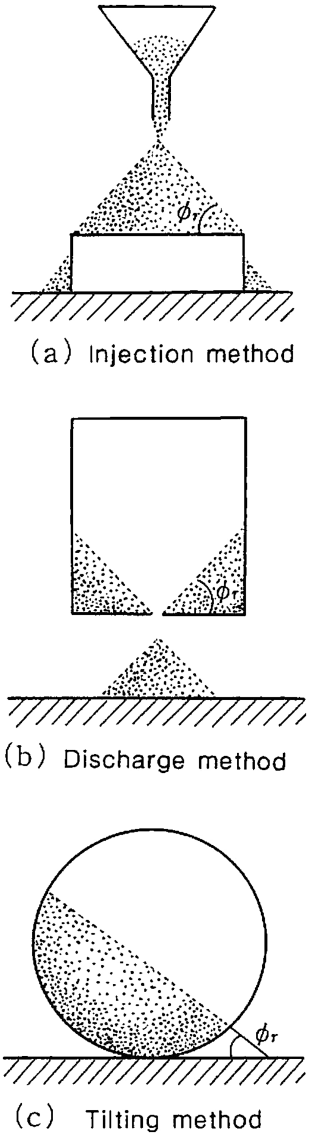


FIGURE 3.9.3 Methods to measure the angle of repose.

principal ways to determine the angle of repose, as shown in Figure 3.9.3. The angle of repose tends to increase in the following order: injection method, discharge method, and tilting method. The major factors influencing the angle of repose are size distribution,[6] surface roughness of the particles, void fraction of the powder bed,[7] and moisture content. In the case of the injection method, the injection rate, falling distance,[8] and size of the conical pile of powder[9] influence the angle of repose.

3.9.2.2 Forced Flow

Mechanically Forced Flow

The powder flow actuated by mechanical force has been studied in relation to torque using various types of rotary viscometers: those of Stomer, Couette, Green, and MacMichael. Iiyama and Aoki[10] obtained an experimental equation to find the torque for the vortex flow of standard silica sands,

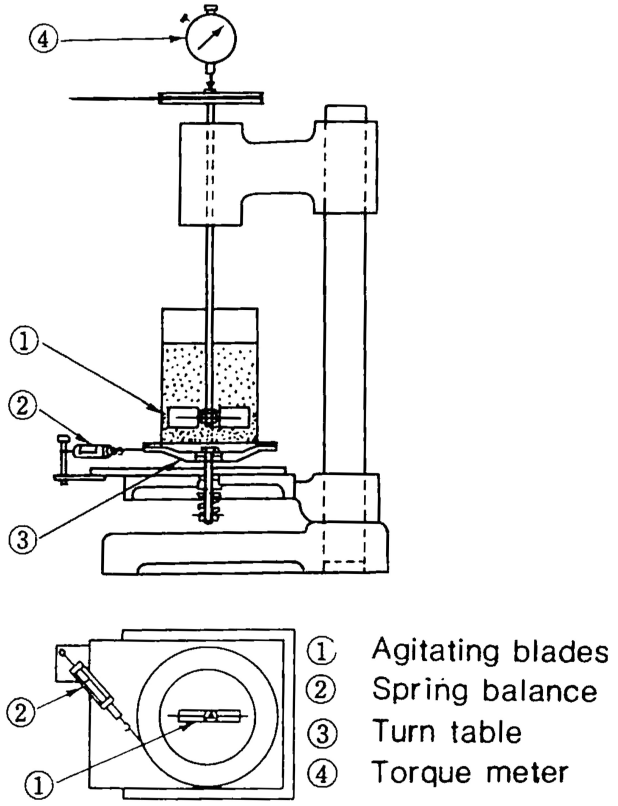


FIGURE 3.9.4 Equipment to determine the mixing resistance. (From Iiyama, E. and Aoki, R., J. Chem. Eng. Jpn., 24, 205–212, 1960.)

in which the apparatus shown in Figure 3.9.4 was used with various-shaped agitating blades.

Compression Flow

In a large vessel such as a huge silo, the value of k in Janssen's equation is used as a measure of the fluidity.[11] A compression test also gives a measure for the fluidity of powder. A number of equations have been proposed for the relationship between the external pressure acting on the powder bed and the change of volume. One typical experimental equation[12] related the apparent volume reduction ratio C to the applied pressure P (Pa):

$$\frac{P}{C} = \frac{1}{ab} + \frac{P}{a} \tag{3.9.1}$$

where a and b are constants, and a is considered to increase with decreasing fluidity of the powder.

Vibration Flow

Vibration changes the packing structure of powder bed and, hence, leads to the change of the fluidity. Miwa[13] proposed the following experimental relation between the mass flow rate through sieves and sieve openings:

$$\frac{W_s}{\rho_a} = kD_s^n D_p^{-2} \tag{3.9.2}$$

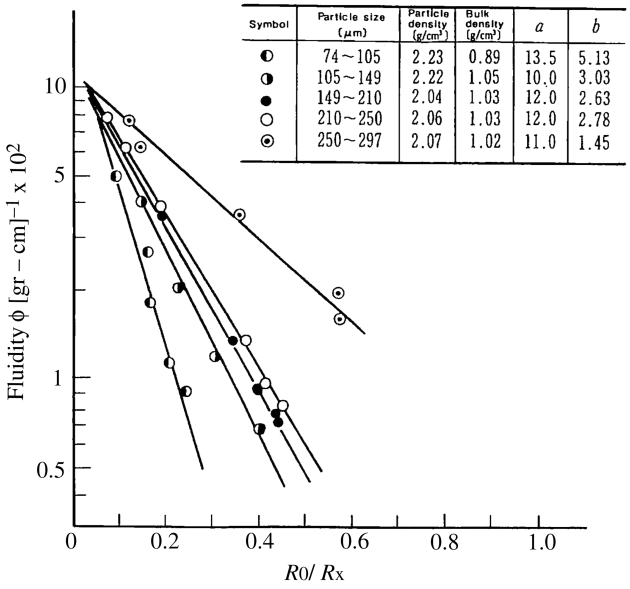


FIGURE 3.9.5 Relationship between R_0/R_x. (From Arakawa, M., J. Soc. Mater. Sci. Jpn., 20, 776–780, 1971.)

where W_s (tons/h) is the mass flow rate, ρ_a (tons/m^3) is the particle specific gravity, D_s (mm) is the sieve opening, D_p (mm) is the particle diameter, and n is a constant (about 2.7). The factor k, called the sieve fluidity index, expresses the ease with which particles pass through sieves and is considered to be a measure of fluidity under dynamic conditions.

Arakawa[14] studied vibration fluidity in relation to the packing structure, paying attention to the vibration in the electric resistance of the electroconductive particles in vibrating motion. Under the condition of gravitational acceleration, the relation between the electric resistance ratio and the fluidity ϕ is shown in Figure 3.9.5 and described by the equation

$$\phi = a\exp\left(-b\frac{R_0}{R_x}\right) \tag{3.9.3}$$

where a and b are constants, R_x and R_0 are electric resistances of the powder beds in flow and in the most densely packed state, respectively.

Sato et al.[15] evaluated the flow characteristics of powders by a vibrating powder tester. A detecting sphere attached to the force transducer is displaced horizontally within the powder bed. The fluidity was discussed in terms of an apparent viscosity obtained from the relationship between the force and displacement velocity.

3.9.2.3 Shear Properties and Fluidity

In powder mechanics, the ultimate balanced condition is estimated from the yield locus obtained by shearing tests. The fluidity defined on the basis of the yield locus indicates the condition where the force balance is about to be lost and is related strongly to the chocking in the pneumatic conveyor or the container outlet.

Jenike[16] defined the yield stress f (kPa) and the maximum compaction stress σ_1 from two Mohr's stress circles coming in contact with the yield locus, and he called the ratio σ_1/f the flow function (FF), which is regarded as a measure of the fluidity. The fluidity increases with the flow function.

The following Warren–Spring equation, proposed by Ashton et al., is widely applied to evaluate the shear stress:

$$\left(\frac{\tau}{C}\right)^n = \frac{\sigma + T}{T} \tag{3.9.4}$$

where C (kPa) is the cohesive stress, T (kPa) is the tensile strength, σ (kPa) is the normal stress, and τ (kPa) is the shear stress. Farley and Valentin[17] took the shear index n as a measure of fluidity and proposed an experimental equation. Stainforth and Berry[18] found a linear relationship between σ_1/f and σ_e/T and defined the gradient as the fluidity, where σ_e (kPa) is the normal stress at the terminal of the yield locus.

One-dimensional yield stress f (kPa) and the bulk density ρ_a (kg/m^3) increase with increasing maximum compaction stress σ_1 (kPa). The ratio f/ρ_a is considered to be another measure of the fluidity:

$$FI = \frac{f}{\rho_a g} \tag{3.9.5}$$

where g is the acceleration due to gravity.

The flow index FI becomes larger as the fluidity decreases. Tsunakawa[19] studied the relationship between FI and the maximum compaction stress σ_1 and obtained the following experimental equation from Figure 3.9.6:

$$FI = a\sigma_1^b \tag{3.9.6}$$

where the coefficient a and index b, which are specific to each powder, increase as the fluidity decreases.

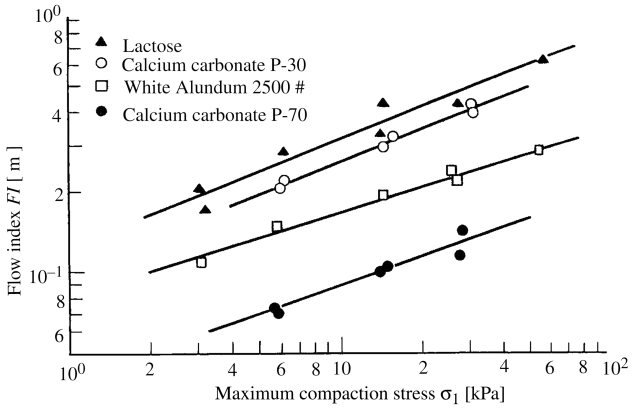


FIGURE 3.9.6 Relationship between the flow index and the maximum compaction stress. (From Tsunakawa, H., J. Soc. Powder Technol. Jpn., 19, 516–521, 1982.)

3.9.2.4 Fluidized Flow

When a powder bed is aerated and agitated, the particles have less opportunity to come in contact with each other, and the powder bed exhibits fluidlike properties. The apparent viscosity of the aerated powder bed measured with a Stomer viscometer[20] decreases with increasing aeration rate. Diekman and Forsythe[21] regarded the time for the apparent viscosity to reach a certain value as a measure of the fluidity.

3.9.2.5 Total Evaluation

In practical powder-handling processes, the various types of powder flow shown in Table 3.9.1 occur simultaneously in most cases. Therefore, it is necessary to evaluate the fluidity from the practical viewpoint for the design of suitable processes.

Carr[22] proposed a method for the evaluation of fluidity by the addition of several indexes from his abundant experience with a variety of powders. This method was not developed on a theoretical basis but is a numerical synthetic evaluation of fluidity from several different factors. A powder tester has been developed to conduct these measurements within one unit.[23]

The flowability is obtained with the powder tester as a sum of the indexes converted from the four properties according to a chart: (1) angle of repose, (2) compressibility, (3) angle of spatula, and (4) cohesiveness (or uniformity). It gives an indication of how to select a means of preventing the formation of powder bridge.

The floodability index is related to the flushing tendency of powder. It is given as a sum of four indexes converted from the flowability index and the following three properties, using another chart: (1) angle of collapse, (2) the difference between angles of repose and collapse, and (3) dispersibility. In general, the compressibility is more reproducible than the angles and correlates well with the flowability index.

Suzuki and Maruko[24] found the relationship between the critical outlet width for the powder discharge and Carr's flowability index experimentally, as shown in Figure 3.9.7. The flowability index has also been investigated in relation to the sieve fluidity index[25] and the coefficient of mixing rate of the horizontal cylindrical mixer.[26]

3.9.3 FACTORS AFFECTING FLUIDITY

The fluidity of powder is influenced by various properties of the particles forming the powder, such as particle size and its distribution, shape and surface roughness of the particles, and other interparticle forces. As a general tendency, finer powders show less flowability. Tsunakawa[27,28] obtained an experimental equation to estimate the flow index of fine powders with the particle true density ρ_s (kg/m^3) and voidage ε from the specific surface diameter D_{sp} (μm) and major consolidation stress σ_1 (kPa) accounting for the mean contact number κ:

$$FI = \kappa\left(g\rho_s\right)^{-1} D_{sp}^{-2\beta} k\left(\frac{\tau\sigma_1^{\beta}}{k\left(1-\varepsilon\right)}\right) \tag{3.9.7}$$

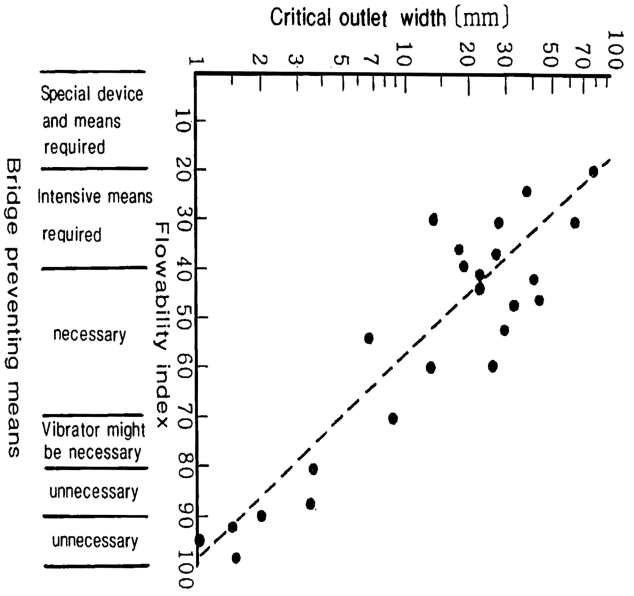


FIGURE 3.9.7 Relationship between the critical discharge opening and the flowability. (From Suzuki, A. and Maruko, O., Funsai (The Micromeritics), 18, 80–88, 1973.)

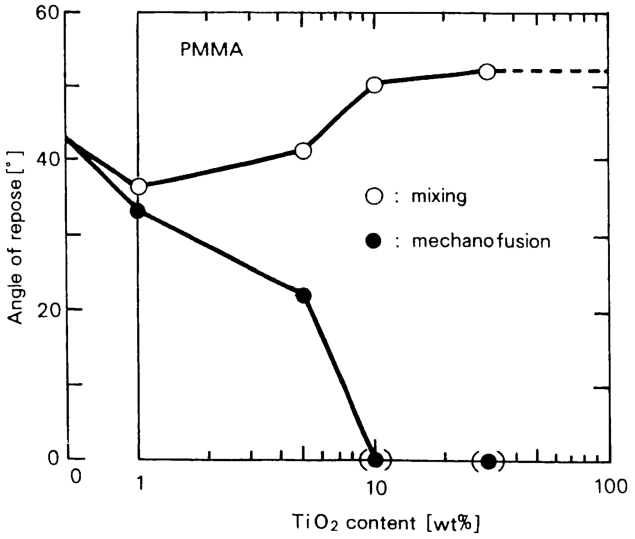


FIGURE 3.9.8 The change in angle of repose of composite powder produced by a mechanical treatment method compared with that by simple mixing. (From Yokoyama, T., Urayama, K., Naito, M., Kato, M., and Yokoyama, T., KONA, 5, 59–68, 1987.)

where κ and β are constants. Additionally, the influence of voidage has been further discussed.

3.9.4 IMPROVEMENT OF FLUIDITY

The fluidity of a powder can be improved by changing its physical properties, such as moisture content and particle size and shape, by means of drying, grinding,[29] classification, and granulation. The fluidity is also improved by altering the dynamic contact of particles, making use of pulsed air pressure. Experimental work on a vibrating two-dimensional hopper[30] and the discharge rate through an orifice by vibration[31] and compressed air have been reported.

A small amount of additive can improve the fluidity of a powder. The mechanism is not yet elucidated clearly but is suggested to be attributable to the additives' properties, alteration of the particle arrangement, and the discharge of electrostatic charge, as confirmed experimentally by Nash et al.[32] and Jimbo.[33] Although the optimum additive fraction varies with the sort of additives, it is effective generally at a low mixing fraction in the range of 0.1–2%. It is well known that an additive has a different magnitude of influence on the fluidity, depending on the type of powder.[34]

Furthermore, it has been pointed out that the mechanical treatment for making composite particles changes the fluidity to a great extent. Figure 3.9.8[35] shows the changes in the angle of repose of polymethylmethacrylate particles (average particle size 5 μm) treated with TiO_2 particles (0.015 μm). It is hardly changed by the simple mixing but decreases drastically by intensive mechanical treatment forming composite particles. It has been also made clear that fluidity shows a maximum value at a certain condition, and excessive treatment deteriorates the fluidity when the surface particles are buried into the core particles.[36] It should also be noted that moisture affects the fluidity of powder considerably.

REFERENCES

1. Hayakawa, S., *Funtai Bussei Sokuteiho*, Asakura, Tokyo, 1973, p. 80.
2. Irani, R. R., Callis, C. F., Liu, J., *Ind. Eng. Chem.*, 51, 1285–1288, 1959.
3. Gold, G., Duvall, R. N., Palermo, B. T., *J. Pharm. Sci.*, 55, 1133–1136, 1966.
4. Miwa, S., *Funryutai Kogaku*, Asakura, Tokyo, 1972, p. 211.
5. Matsusaka, S., Yamamoto, K., Masuda, H., *Adv. Powder Technol.*, 7, 141–151, 1996.
6. Pilpel, N., *Br. Chem. Eng.*, 11, 699–702, 1966.
7. Otsubo, K., *J. Res. Assoc. Powder Technol. Jpn.*, 2, 179–188, 1965.
8. Aoki, R., *J. Res. Assoc. Powder Technol. Jpn.*, 6, 3–8, 1969.
9. Train, D., *J. Pharm. Pharmacol.*, 10 (Suppl.), 127T–135T, 1958.
10. Iiyama, E., Aoki, R., *J. Chem. Eng. Jpn.*, 24, 205–212, 1960.
11. Stepanoff, A. J., *Gravity Flow of Bulk Solids and Transport of Solids in Suspension*, Wiley-Interscience, New York, 1969, p. 26.
12. Kawakita, K., *Funtai to Kogyo*, 9, 59–64, 1977.
13. Miwa, S., *Funsai (The Micromeritics)*, 15, 8–11, 1970.
14. Arakawa, M., *J. Soc. Mater. Sci. Jpn.*, 20, 776–780, 1971.
15. Sato, M., et al., *J. Soc. Powder Technol. Jpn.*, 27, 308–314, 1990.
16. Jenike, A. W., *Utah Unlv. Eng. Exp. Station*, 108, 1961.
17. Farley, R., Valentin, F. H. H., *Powder Technol.*, 1, 344–354, 1967.
18. Stainforth, P. T., Berry, R. E. E., *Powder Technol.*, 8, 243–251, 1973.
19. Tsunakawa, H., *J. Soc. Powder Technol. Jpn.*, 19, 516–521, 1982.

20. Matheson, G. L., Herbst, W. A., Holt, P. H., *Ind. Eng. Chem.*, 41, 1099–1104, 1949.
21. Diekman, R., Forsythe, W. L., Jr., *Ind. Eng. Chem.*, 45, 1174–1177, l953.
22. Carr, R. L., *Chem. Eng.*, 72, 163–168, 1965.
23. Yokoyama, T., Urayama, K., *J. Res. Assoc. Powder Technol. Jpn.*, 6, 264–272, 1969.
24. Suzuki, A., Maruko, O., *Funsai (The Micromeritics)*, 18, 80–88, 1973.
25. Miwa, S., Shimizu, S., *Funsai (The Micromerilics)*, 16, 103–116, 1971.
26. Yano, T., Terashita, K., Yamazaki, T., *Funsai (The Micromeritics)*, 16, 96–102, 1971.
27. Tsunakawa, H., *J. Soc. Powder Technol. Jpn.*, 27, 4–10, 1990.
28. Tsunakawa, H., *J. Soc. Powder Technol. Jpn.*, 30, 318–323, 1993.
29. Oshima, R., et al., *J. Soc. Powder Technol. Jpn.*, 30, 496–501, 1993.
30. Suzuki, A., Tanaka, T., *Powder Technol.*, 6, 301–308, 1972.
31. Yoshida, T., Kousaka, Y., *J. Res. Assoc. Powder Technol. Jpn.*, 6, 194–201, 1969.
32. Nash, J. H., Leiter, G. G., Johnson, A. P., *Ind. Eng. Chem. Prod. Res. Dev.*, 4, 140–145, 1965.
33. Jimbo, G., *Jitsuyo Funryutai Purosesu to Gijutsu*, Kagaku Kogyo, Tokyo, 1977, p. 186.
34. Hayashi, S., *J. Res. Assoc. Powder Technol. Jpn.*, 6, 286–291, 1969.
35. Yokoyama, T., et al., *KONA*, 5, 59–68, 1987.
36. Terashita, K., Umeda, K., Miyanami, K., *J. Soc. Powder Technol.*, 27, 457–462, 1990.

3.10 Blockage in Storage Vessels

Hiroshi Takahashi and Jun Yoshida

Blockage in a storage vessel is one of the serious problems to handle powders or particulate materials smoothly. It causes stoppage or extreme delay of solids flow. Thus, it leads to shortages of production capacity, and degradation of product quality. Also, the increase of the internal pressure by blockage causes damage on vessel walls. Unpredictable discharge rate of solids, nonuniform residence time, and segregation of solids mixtures are also observed because of blockage in storage vessels.

3.10.1 TYPICAL PHENOMENA

The blockage phenomena are roughly classified into the following three kinds. The first is a geometrical interlocking of coarse cohesionless particles at an outlet of the vessel. Statistically, it is said that when the orifice size is smaller than several times the particle diameter, a blockage may occur. In this case frictions between particles and/or a vessel wall are the cause of the blockage and the shape of particle is an important factor. The second is a mechanical stable arch formed inside the bed of cohesive fine powders. Solids pressure and shear strength of powder mass are directly related to this blockage. The dimension and shape of the container and material properties of bulk solids are its main factors.

The third typical blockage is related to caking of bulk solids and/or adhesion to the wall. Caking is caused by chemical or physical bonds. The adhesion is caused by electrostatic or physicochemical attractive force between particles and walls.

The second and third blockages are affected by water contents of the powder, humidity and temperature of the operating atmosphere, period of the resting time, solids pressure exerted, and so on.

From the operational viewpoint, the blockage is sometimes deteriorated by tapping, vibration, and aeration, in case of gravity flow. Usually, hammering and vibration are useful to break a blockage of solids, but they happen to cause compaction and to make stable powder bed in some conditions. Proper intensity and frequency of impact are necessary to break a blockage. Aeration from below the bed may support the arch against discharge, though it is effective to reduce wall friction and caking owing to bed expansion. Therefore, the air pressure and the air flow rate or the aeration period would be relevant.

3.10.2 MECHANISMS AND FLOW CRITERIA

Interlocking of Coarse Particles

Even cohesionless coarse particles are able to form a stable arch at a converging section of the container (see Figure 3.10.1). When the friction force and the reaction force between the particles and the wall support the weight of the solids, the arch formed near the orifice would be stable. According to this arch formation, the critical orifice size compared to the particle diameter depends on particle shape. The following are known as experimental equations. For general granules,[1]

$$\frac{D_s}{d_s} = 1.8 + 0.038\varphi_s^{1.8} \tag{3.10.1}$$

$$\frac{D_c}{d_s} = 2.3 + 0.071\varphi_s^{1.8} \tag{3.10.2}$$

where D_s is the minimum dimensions of a slit of a rectangular container (Figure 3.10.1(a)) and D_c is that of a circular orifice (Figure 3.10.1(b)). Then, d_s is a specific surface diameter of the particle, and φ_s is the shape coefficient based on the specific surface of the particle of circle equivalent diameter; that is, as compared with Equation (3.10.1), experimental results with a two-dimensional hopper indicated more variation in $\varphi_s > 10$, and that the critical dimension was smaller for spheres and cylinders due to easy orientation for discharge around the outlet, but larger for prisms due to plane contact with each other.

Coarse sands and pebbles are typical material for these phenomena. However, it is not difficult to avoid this kind of blockage and recently the numerical experiment can be done to foresee the blockage of coarse particles using the discrete element simulation.[2]

Arching of Fine Powders

Fine powders tend to behave as a continuum due to particle cohesion, and the flow criterion is estimated on the basis of powder mechanics and flow models.

The flow of cohesive powders is disturbed by stable arching or piping. In the case of mass-flow bin, the blockage is formed by self-supporting free arches and the element arch

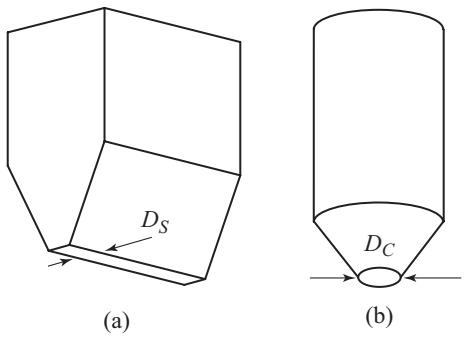


FIGURE 3.10.1 Slit and orifice.

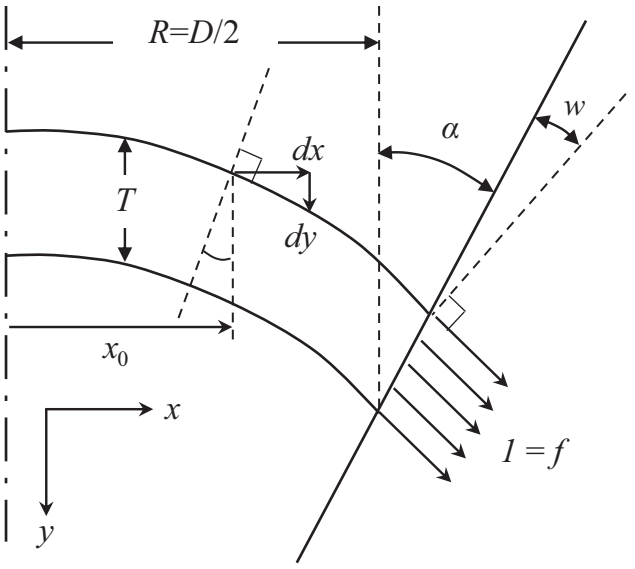


FIGURE 3.10.2 Arch of uniform thickness.

has uniform thickness T, as shown in Figure 3.10.2. The arch is formed along the direction of maximum principal stress. Then, the minimum principal stress equals zero in the perpendicular direction of the arch, because a stress-free surface is assumed. In practice, the material would collapse in the arch due to stress from above, and thus the self-supporting arch would define an upper bound of the critical span for the blockage.

In case of a conical hopper with a smooth wall, Mohr's circle M_R shown in Figure 3.10.3 indicates the stress state of the material in the element arch at the wall. It passes through the origin of τ-σ coordinates and is tangential to the powder yield locus (PYL). Here, the wall yield locus (WYL) is assumed to be linear. PYL and WYL can be determined by shear cell test.[3] φ_w is the angle of material–wall friction. f_c is the unconfined yield strength of the material as a function of the consolidating stress, which can also be determined by shear cell test. The shear stress acting on the wall surface is $\overline{ST}$. The vertical plane makes α as a half of the hopper angle shown in Figure 3.10.2, equivalent to 2α in Figure 3.10.3 from point S to point U along the circle M_R. The shear stress on the vertical plane at the foot of the arch is $\overline{UV}$, which is expressed as

$$\overline{UV} = \frac{f_c}{2}\sin 2\left(\alpha + \varphi_w\right) \tag{3.10.3}$$

Sum of the vertical forces is given as

$$\pi DT\left(\overline{UV}\right) = \frac{\pi D^2}{4} T\rho_b g \tag{3.10.4}$$

Therefore, the limiting diameter D_c for a free arch is obtained as[4]

$$\frac{f_c}{\rho_b g D_c} = \frac{1}{2\sin 2\left(\alpha + \varphi_w\right)} \tag{3.10.5}$$

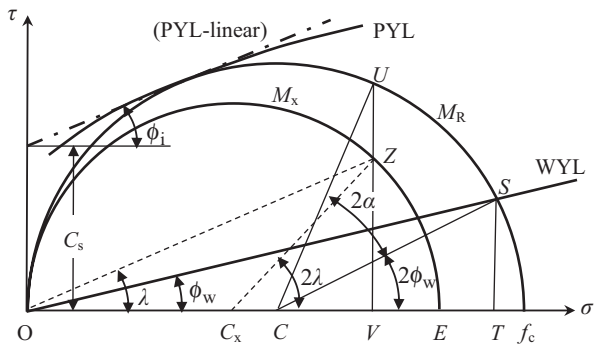


FIGURE 3.10.3 Mohr's circles along free arch.

where ρ_b and g are the bulk density of the material and gravity acceleration, respectively. Thus, the minimum diameter for discharge D_c depends upon f_c, φ_w, and α. In the case of a wedge-shaped hopper, the limiting span for the slit opening S can be derived as a half of D_c, given by Equation (3.10.5). In order to evaluate the critical diameter free from blockage, it is necessary that the strength–stress characteristics of powder, f_c versus σ_s, and the major consolidating stress, σ_1, set up in the arched field are known.

In the case where both PYL and WYL are given by Coulomb-type equations, the limiting diameter is derived by the same consideration as mentioned previously.

$$D_c = \frac{4C_s\left(1+\sin\varphi_i\right)\sin 2\left(\alpha+\beta\right)}{\rho_b g\cos\varphi_i} \tag{3.10.6}$$

$$\beta = \frac{\varphi_w + \sin^{-1}\left(\sin\varphi_w / \sin\varphi_i\right)}{2} \tag{3.10.7}$$

where C_s is the cohesive shear strength of powder and φ_i is the angle of internal friction, defined by PYL: $\tau = \sigma\tan\varphi_i + C_s$. As for WYL, it is assumed that the cohesive tensile strength of powder and that between powder and wall plate are equal (WYL: $\tau = \sigma\tan\varphi_w + C_w$, $C_w = C_s\cot\varphi_i\tan\varphi_w$). The properties C_s, φ_i, and ρ_b are a function of the void fraction, and these values are related to the consolidating stress. Therefore, the limiting diameter usually increases with the hopper apex angle as well as the bed height.

The horizontal normal stress σ_x is assumed to be constant across the arch. Describing Mohr's stress circle at the horizontal distance x from the apex of the arch by M_x in Figure 3.10.3, the vertical plane at x is characterized by the intersection Z of the line $\overline{UV}$ and M_x due to constant $\sigma_x = \overline{OV}$ across the arch. The angle λ between the major principal plane and the vertical plane in Figure 3.10.2 corresponds to the angle $\angle ZC_xE = 2\lambda$ on Mohr's circle M_x. Accordingly, the following relation holds.

$$\frac{dy}{dx} = \tan\lambda = \frac{\overline{ZV}}{\overline{OV}} = \frac{\tau_{xy}}{\sigma_x} \tag{3.10.8}$$

The shear stress τ_{xy} over the vertical plane at x is given by taking the vertical force balance as $\tau_{xy} = \rho_b g x/2$, and the relation

$\sigma_x = (f_c/2)\,(1+\cos 2(\alpha+\varphi_w))$ is derived from Mohr's circle. Hence, the profile of the free arch is parabolic, using Equation (3.10.5).

$$y = \frac{x^2}{D_c}\frac{\sin 2(\alpha+\varphi_w)}{1+\cos 2(\alpha+\varphi_w)} \tag{3.10.9}$$

In the case of a hopper with a rough wall, the value of 45° for $\alpha+\varphi_w$ in Equation (3.10.5) and Equation (3.10.9) is chosen so as to maximize the vertical component of the supporting forces at the foot of the arch, that is, $\overline{UV}$ in Figure 3.10.3.

Critical Size of Outlet

Jenike[3,5,6] proposed the method to determine the critical span of the outlet for flow–no flow criterion. Figure 3.10.4 illustrates the profiles of the stresses along the wall that are required for the design calculation, where σ_f is the major principal stress set up in a passive stress field during flow, and f_c is the unconfined yield strength representing the strength of the self-supporting arch. As the powder fills the bin, it becomes consolidated under the major consolidating stress (i.e. the major principal stress in the active stress field σ_s). σ_s, including the memory effect which is measured in practical hoppers, is also shown as a broken line in Figure 3.10.4. For each value of the major consolidating stress σ_s, there is a corresponding unconfined yield stress f_c. Wherever σ_f exceeds f_c, the powder does not have sufficient strength to support an arch. Therefore, the minimum size of the outlet to judge the blockage from arching is determined by the condition

$$\sigma_f = f_c \tag{3.10.10}$$

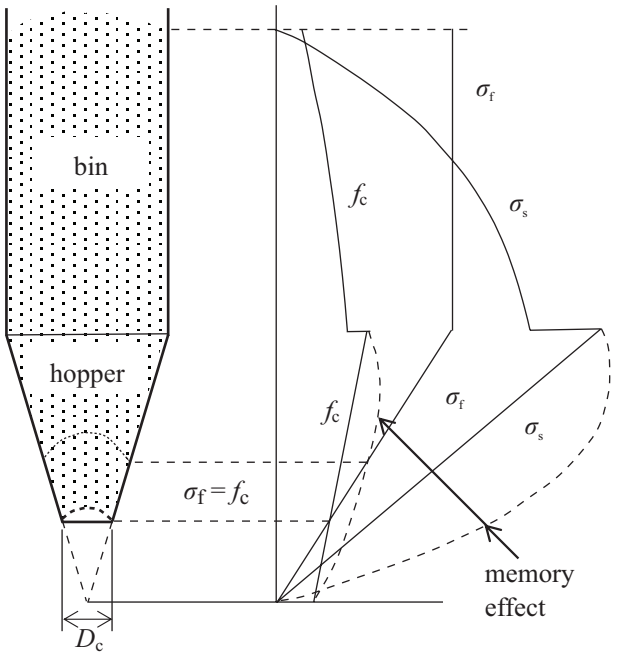


FIGURE 3.10.4 Determination of critical size of outlet.

The condition that ensures steady gravity flow is $\sigma_f > f_c$, and blockage with a stable arch is $\sigma_f \le f_c$. Jenike defined flow function (*FF*) and flow factor (*ff*) as

$$FF = \frac{\sigma_s}{f_c} \tag{3.10.11}$$

$$ff = \frac{\sigma_s}{\sigma_f} \tag{3.10.12}$$

FF depends on the powder properties and is determined by shear cell tests as a function of major consolidating stress σ_s. *ff* represents the stress condition set up in a hopper indicating the flowability from the hopper. The critical diameter D_c is evaluated by

$$\frac{\sigma_f}{\rho_b g D_c} = \frac{1}{H(\alpha)} \tag{3.10.13}$$

$H(\alpha)$ is a function of the geometry of the opening given in Figure 3.10.5, which is derived from the refined arch analysis.[3,5,7]

In the case of a slit aperture of length L longer than three times the width B, D_c represents B. *ff* is also given in graphical form as a function of effective angle of internal friction δ, φ_w, and α, as shown in Figure 3.10.6. Reading the value of *ff* from Figure 3.10.6 with a given set of δ, φ_w, and α, we can draw a straight line, $\sigma_f = (1/ff)\,\sigma_s$, on $\sigma_f - \sigma_s$ rectangular coordinates. The critical value of σ_f defined by Equation (3.10.10) is obtained from the intersection of the above-mentioned *ff* straight line and the *FF* curve by plotting f_c against σ_s, which is obtained by shear tests. The critical span D_c is then calculated from Equation (3.10.13). The assumption of constant *ff* in the hopper means that the profiles of σ_f and σ_s are similar, as shown in Figure 3.10.4. However, if the profile of σ_s is given as a broken line, i.e. considering the memory effect, the value of ff would not be constant. Then, the critical span evaluated would be different from that of the above method.[8]

In funnel flow the solids flow down through a channel formed within the material. According to Jenike's method,[5,6] a lower bound of the critical diameter, D_f, for no-piping is estimated by

$$D_f = \frac{G(\varphi_t)}{\rho_b g}\sigma_f \tag{3.10.14}$$

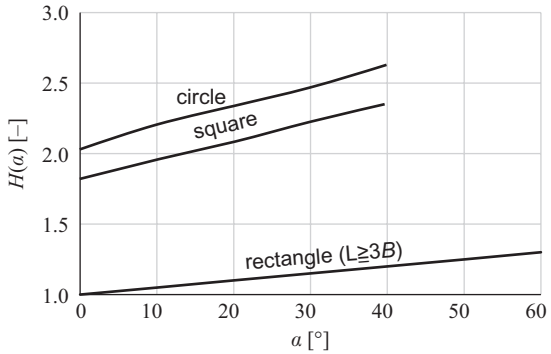


FIGURE 3.10.5 $H(\alpha)$ versus α for conical and pyramidal hoppers.

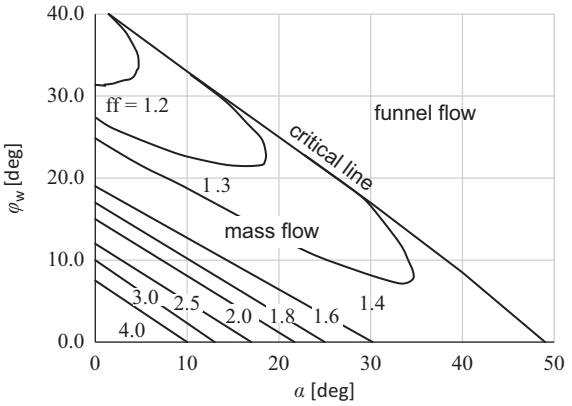


FIGURE 3.10.6 ff as φ_w versus α for conical hoppers (δ=50°).

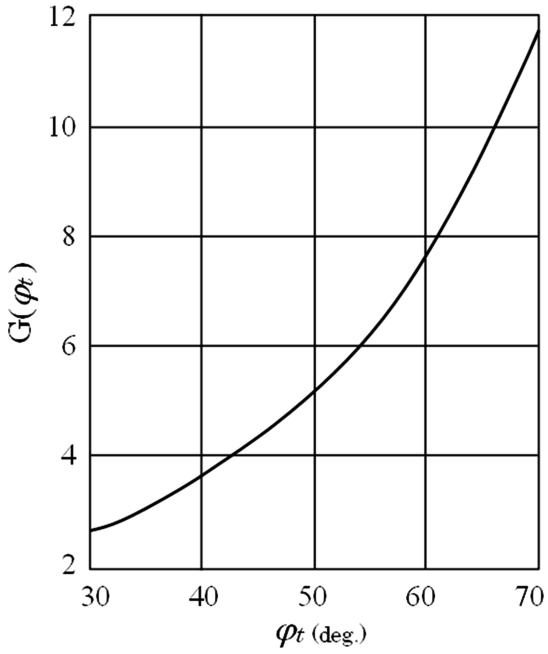


FIGURE 3.10.7 Function $G(\varphi_t)$.[7]

where φ_t is a static angle of internal friction. The function $G(\varphi_t)$ and a flow factor ff_p (= σ_s/σ_f) for no-piping are reproduced in Figure 3.10.7 and Figure 3.10.8[7]. The value of σ_f in Equation (3.10.14) is obtained by drawing the ff_p line on the *FF* graph and finding the intersection, which enables D_f to be predicted. Nevertheless, piping flow would appear in practice, when the powder head descends lower than a critical level.

3.10.3 EXPERIMENTAL STUDY

The experiments have been performed to show the critical condition of the blockage. The examples of coarse particles and fine powders are introduced.

Two-Dimensional Model of Coarse Particles

As for the coarse particles, Sakaguchi et al.[9] reported two-dimensional model tests using acrylic and aluminum bars in order to clarify the mechanism of the blockage. Their results indicate that the particle flow from the hopper is not symmetry and the discharge takes place from the left and right side of the orifice alternately (see Figure 3.10.9). Then, the blockage is formed at the timing of the alternation. They also reported the experimental results were corresponding to the results of the discrete element simulation.

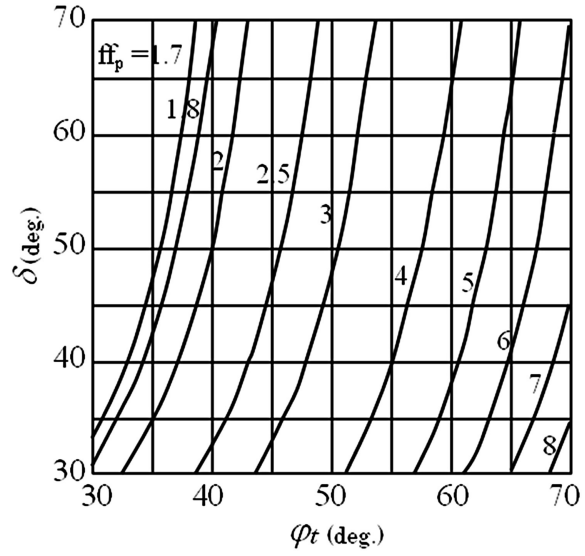


FIGURE 3.10.8 Flow factor for no piping, ff_p^7.

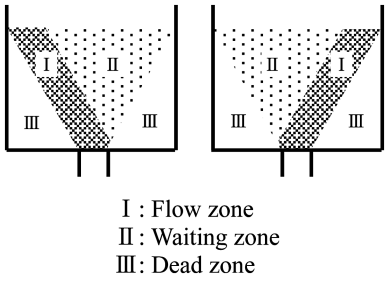


FIGURE 3.10.9 Repeated asymmetric flow.

Centrifugal Experiment of a Miniature Silo

In case of fine powders, Tsunakwa[10] reported the experimental results of the centrifugal miniature silo to explain the critical outlet size proposed by Jenike.[4] The centrifugal experiment is often used in the geotechnical engineering and is efficient to simulate a large-scale structure by a miniature model. Tsunakawa's miniature model silo is 40 mm in diameter and the length of a bin is 40–100 mm (see Figure 3.10.10). The conditions of the experiments are parametrically changed with centrifugal forces, depths of a powder layer, and sizes of an outlet. The rotation frequencies are from 884 to 2000 rpm and the equivalent size of a silo diameter is 5.5–34.0 m. Figure 3.10.11 shows a good agreement

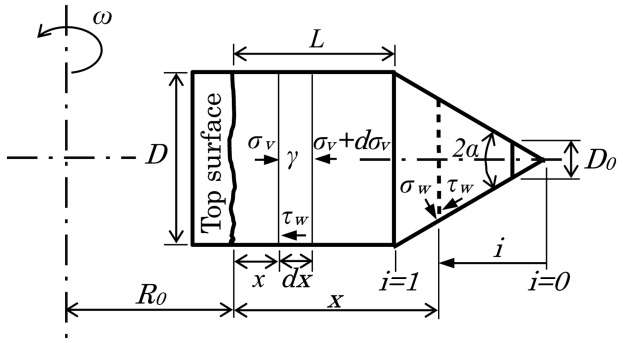


FIGURE 3.10.10 Stresses exerted on powder in a silo under centrifugal force.

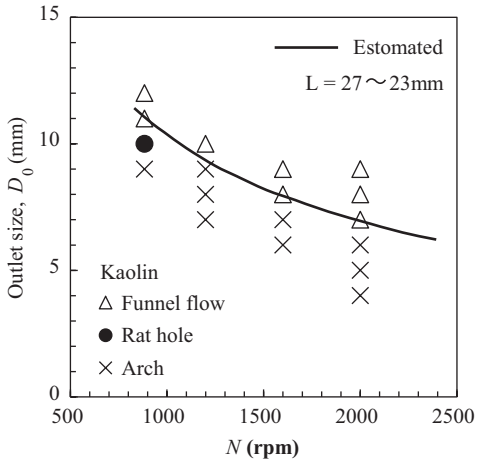


FIGURE 3.10.11 Stresses exerted on powder in a silo under centrifugal force.

between the estimated line using Jenike's method and the experimental results.

3.10.4 METHODS OF PREVENTING BLOCKAGE

The mechanisms mentioned in 3.10.2 are considered to develop the methods to prevent the blockage or to promote the smooth flow in powder bed. Some methods are usually adopted for the hoppers of the practical silos. In order to break the blockage caused by arch action or rat hole, the devices of pounding or air blasting are equipped near the orifice for the powders whose don't have a smooth flow. Some of these methods are introduced in this chapter.

Flow-Promoting Device

In designing storage vessels, a bigger outlet is the most effective, and other contrivances are also useful, such as a steeper wall for the hopper portion, smooth surfaces with smaller wall friction, avoidance of acute corners, and proper inserts.

To make a flow smooth, flow-promoting devices are facilitated near the orifice of a bin or a hopper. They are often used

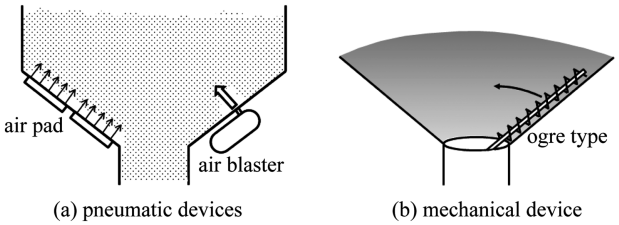


FIGURE 3.10.12 Examples of flow-promoting devices.

in order to prevent blockage and their methods are categorized as follows:

a. pneumatic
b. mechanical
c. vibratory
d. insert

As a pneumatic device, air injections or air pads promote the flow by the effect of floating and stirring. A typical mechanical device is a plow or an ogre rotating on the bottom of the bin and it sweeps the material into the outlet (see Figure 3.10.12). For the powders which don't flow smoothly, sometimes a vibrating hopper is facilitated under the bin in order to confirm steady flow. These devices are used to avoid the arch formation and to realize the smooth flow. Usually, these devices are effective to prevent blockage, but sometimes they accelerate the compaction of the material. In that case, the blockage tends to happen more easily and then the material is stiffer than usual.

To control the flow in a hopper, several kinds of inner structures are attached to a bin and/or a hopper. These structures are called 'insert' and promote the regular flow. The objectives of the insert are not only to realize smooth flow, but also to reduce the wall pressure during the discharge. If an effective insert can be designed, the blockage can be avoided.

Arch Breaker

When the flow of the material from the outlet is stopped by blockage caused by arch action or caking, the arch or the cake block should be broken. Mechanical operations and devices are helpful and these devices are called 'arch breaker' in general. To break an arch, arch breakers with fluidization and air jets, eccentric vibrating motors, hammering, agitating breakers with screws, chain conveyors and so forth are equipped or are used near the outlet.

These devices are usually effective for their purpose, but sometimes they cannot work because of the strength of the arch. Also, sudden change of the pressure distribution may cause trouble on the wall of a hopper or a bin. Therefore, including flow-promoting devices, one should be careful to use such devices smoothly without problems.

REFERENCES

1. Langmaid, R. N., Rose, H. E., *J. Inst. Fuel,* 30, 166, 1957.
2. Cundall, P.A., Strack, O. D. L., *Geotechnique*, 29, 47, 1979.

3. Jenike, A. W., *Bull. Utah Eng. Exp. Station,* 108, 52, 1961.
4. Walker, D. M., *Chem. Eng. Sci.,* 20, 975, 1966.
5. Jenike, A. W., *Bull. Utah Eng. Exp. Station,* 123, 53, 1964.
6. Jenike, A. W., *Powder Technol.,* 1, 237, 1967/1968.
7. Arnold, P. C., McLean, A. G., Roberts, A. W., in *Bulk Solids,* TUNRA Bulk Solids Handling Research Associates, Australia, 1980, pp. 3E11–3E30.
8. Tsunakawa, H., *J. Soc. Powder Technol. Jpn.,* 18, 405, 1981.
9. Sakaguchi, H., Ozaki, E., *J. Soc. Powder Technol. Jpn.,* 30, 183, 1993.
10. Tsunakawa, H., *J. Soc. Powder Technol. Jpn.,* 38, 857, 2001.

3.11 Segregation of Particles

Kuniaki Gotoh

3.11.1 SEGREGATION PHENOMENA AND ITS FACTORS

When a powder flows, a local inhomogeneity of powder component (=particles) due to particle properties such as particle size and particle density is observed frequently. The phenomenon is called segregation. For example, segregation is induced by a powder flow in the formation of a deposition layer[1] or in the particle layer collapse[2], these happen in an operation such as a loading into a container or discharged from a hopper of powder mixture when the powder contains particles having different diameters or densities (Figure 3.11.1-a). In a powder flow in rotating cylindrical vessel, segregation[3] due to a position of cross section in the cylindrical vessel (Figure 3.11.1-b) is induced. In addition, zonal segregation in the axial direction[4] (Figure 3.11.1-c) is also induced in the rotating cylindrical vessel. Besides them, segregation also occurs due to fluidization of powder by vibrations[5], tapping[6] of the powder or granular container and fluidization[7] by the fluid ascending in the powder layer.

When a powder has the differences of the physical properties of particles and powder characteristics, segregation occurs. Therefore, the differences are the factors of the segregation phenomena. The segregation phenomena are classified for each factors as follows.

Particle size difference: size segregation
Density difference: density segregation
Shape difference: shape segregation
Repulsive force difference: resilience segregation

In addition, it has been reported that the dynamic falling angle difference[8], which is a secondary characteristic value dependent on particle size, particle shape, etc., becomes a segregation factor.

Even if the factors causing segregation which is the differences in properties and characteristics of particles are the same, the segregation tendency may be different. For example, in the case of supplying a powder from a hopper into a cylindrical container[1], a deposited layer having almost constant thickness is formed from the outer edge of the bottom of the container at the initial stage of the supplying (Figure 3.11.2-a). In this initial stage, segregation in which large particles are gathered in the center is observed. By continuing the supply, a conical deposition layer with an angle of repose is then formed on the deposited layer with the constant thickness. In this conical sedimentary layer (Figure 3.11.2-b) segregation is observed in which large particles gather at the outer edge of the cone. This example shows that not only the difference in properties and characteristics of particles (Factor I) but also the powder flow state in the apparatus (Factor II) are the factors causing segregation.

Segregation is the phenomenon in which the homogeneity of compositions in a powder becomes heterogeneous. Therefore, it is considered to be the cause of trouble in many cases in powder processes. However, if we actively use the heterogeneity of compositions, it is possible to separate particles depending on their particle properties or powder characteristics. The separation of particles using density segregation in a fluidized bed[9] and shape separation operation[10,11] using shape segregation have been reported.

3.11.2 MECHANISM OF SEGREGATION

The behaviors of the target component in a container and/or device can be predicted by computer simulation using the Discrete Element Method, etc. and the examples of segregation phenomena using the simulation have been reported[12,13]. Recently, by the simulation considering interparticle adhesion such as van der Waals force, the influence of particle adhesion on segregation phenomena has also been studied [14,15]. However, in order to comprehend and

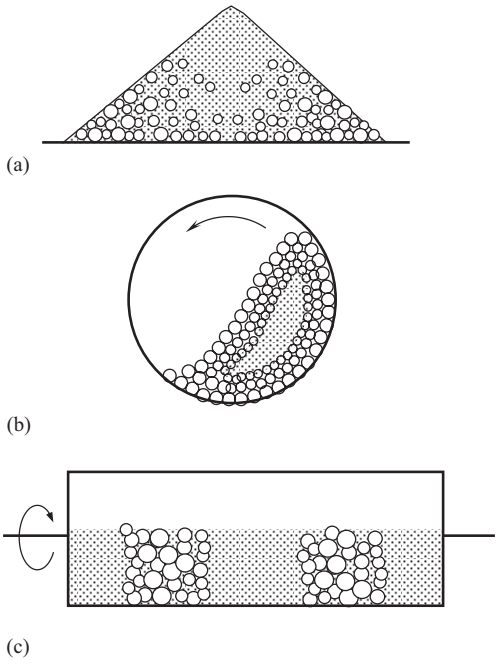
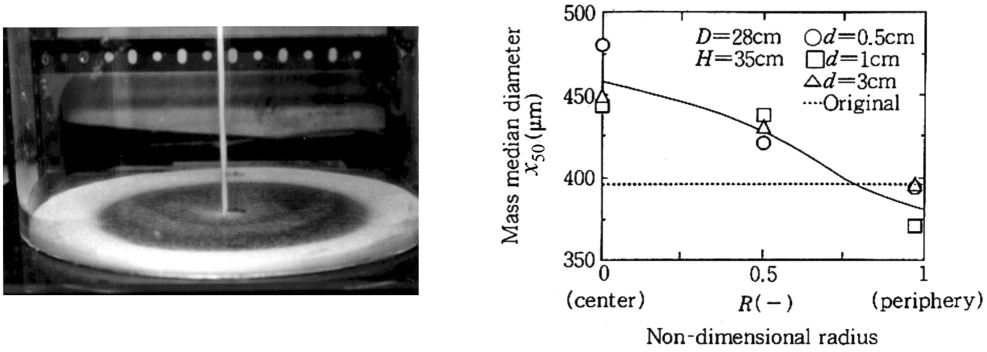
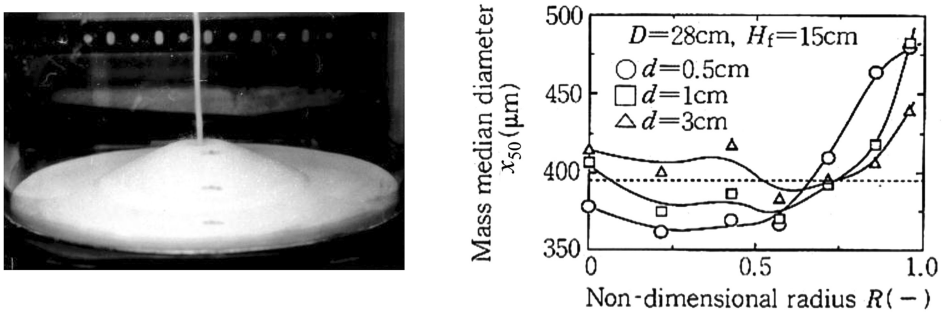


FIGURE 3.11.1 Example of segregation phenomenon accompanying particle fluidization. (a) Segregation of accumulation process, (b) Segregation in cross section direction of rotating cylinder, (c) Separated band segregation in the direction of the rotating cylinder axis.



a) Process of forming a layer from the outer edge of the container



b) Process of forming a deposition layer with repose angle

FIGURE 3.11.2 Example of Segregation Phenomenon with Supply.[1]

understand the phenomenon, a model equation expressing the basic mechanism of the segregation phenomenon is also important.

As described above, "Factor I" of particle segregation includes particle differences, density differences and so on. Here, by defining particles having lower flowability components constituting the mixed powder as segregation components, uniform handling in a model representing segregation mechanism becomes possible. In addition, "Factor II" is roughly divided into "surface segregation," "In-layer segregation" and the combination of them. The surface segregation occurs when the powder moves on the surface of deposited powder layer as seen in the case of filling and supplying particles. The in-layer segregation occurs inside of the layer when the deposited layer moves as seen in the case of discharge from the container. In the following, the basic mechanism of segregation is classified for surface segregation and interlayer segregation, limited to the gravitational field.

3.11.3 SURFACE SEGREGATION

3.11.3.1 Single Particle Motion Model

Flight Effect[16]

When a single particle is injected into a fluid with the horizontal velocity v_h, by applying Stokes' law for the fluid resistance the flight distance L in a fluid is expressed by the following equation.

$$L = \frac{v_h \rho_p x^2}{18\mu} \tag{3.11.1}$$

Here

ρ_p is the particle density
x is the particle diameter
μ is the fluid viscosity

As can be seen from this equation, particles with large particle diameters and large densities move to the far side. This model is applicable to grain size segregation when particles are flying in a gas, such as filling in a container, but not to density segregation in a powder layer.

Rotational Effect[17]

Consider a case where a single particle falls on an inclined plate with an inclination angle θ, as shown in Figure 3.11.3-a. When the particles slide on the horizontal plane after dropping the height H, the moving distance L of the particles due to this sliding motion is expressed by the following equation.

$$L = H\cos^2\theta \frac{1 - f_s / \tan\theta}{f_s} \tag{3.11.2}$$

Where f_s is the sliding friction coefficient. As shown by this equation, since the moving distance L depends only on the sliding friction coefficient during sliding motion, segregation due to the difference in friction coefficient, which is one of the

particle characteristics, can be explained, but segregation by particle size or density cannot be explained.

On the other hand, when the particles rotate on the horizontal plane after dropping the height H, if the rotational friction coefficient is f_r, the moving distance L of the particles due to the rotating motion is expressed by the following equation.

$$L = \frac{xH}{2}\cos^2\theta\frac{1-2f_r/(x\tan\theta)}{f_r} \tag{3.11.3}$$

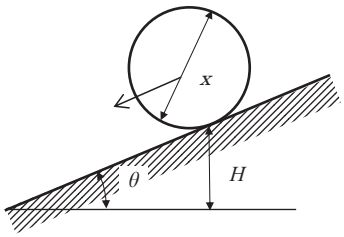
In the case of rotating motion, the moving distance L becomes larger as the particle size x is larger, and it is possible to explain the grain size segregation.

Stumbling Effect[17,18]

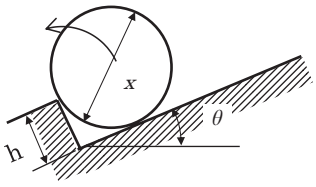
Consider a case where the slope of the particle deposition layer modeled in Figure 3.11.3-a is not a flat surface and there is an obstacle caused by the deposited particles (Figure 3.11.3-b). Assuming that the height of the obstacle is h, the rotational angular velocity ω induced by the particle collision with the obstacle is expressed by the following equation.

$$\omega = \frac{\sqrt{2g\left[x/2-\sin\theta\sqrt{(x/2)^2-(x/2-h)^2}-\cos\theta(x/2-h)\right]\left((x/2)^2-j^2\right)}}{x/2(x/2-h)+j^2} \tag{3.11.4}$$

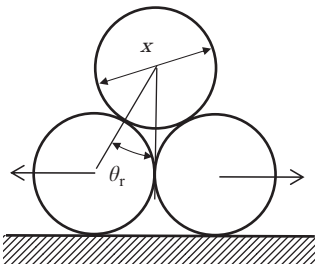
Here, g represents the gravitational acceleration and j represents the rotational radius of the inertia moment, respectively.



(a) Rotation effect



(b) Stumbling effect



(c) Push-off effect

FIGURE 3.11.3 Model analysis of surface segregation.

As described by this equation, large particles have a large rotational angular velocity ω at the time of a collision and can flow down to a long distance.

Push-off Effect

Let us consider the case where a particle rides on a center of two spherical particles laying side by side and push those two particles apart. When the two particles move apart by sliding, the critical sliding friction coefficient f_c is expressed by the following equation[19].

$$f_c = \frac{\tan\theta_r}{1+2\sqrt{\left[\left(\frac{x_t}{x_b}\right)^2\left(\frac{\rho_{pt}}{\rho_{pb}}\right)\right]}} \tag{3.11.5}$$

Here, θ_r is the angle formed by the radius passing through the contacting point and the perpendicular direction. The subscriptions t and b represent the upper and lower grains, respectively. If the friction coefficient between the lower particle and the wall surface is equal to or greater than the critical friction coefficient f_c expressed by the above equation, the lower particle does not move and the upper particle cannot push apart two particles. From the equation, the critical sliding friction coefficient f_c becomes larger as the particle size x_t is larger and the density ρ_{pt} is larger, so that the coefficient of friction between the lower particles and the wall surface must be large in order to prevent the particles from moving. In other words, the larger the particle diameter and the higher the density make the upper particles easy to push down the lower two particles and sink. This is consistent with the trend of density segregation.

With regard to the push-off effect, there is a possibility that particles with a large diameter or large density will settle by creating a space in the particle layer due to its own weight. And the probability that the large particles pass between particles in the lower layer can be defined. A model in which the product of the settling possibility and the passing probability is defined as the segregation factor s has also been proposed[20].

$$s = \frac{\rho_{rc}}{x_{rc}}\left\{\frac{1+V_c(x_{rc}-1)}{1+V_c(\rho_{rc}-1)}\right\} \times \left\{\frac{1-\varepsilon_f\left[-\frac{1-\varepsilon_f}{\varepsilon_f}\left\{\left(1+\frac{1}{1+V_c(x_{rc}-1)}\right)^2\right\}-1\right]}{1-\varepsilon_f\exp\left(-3\frac{1-\varepsilon_f}{\varepsilon_f}\right)}\right\} \tag{3.11.6}$$

Here, x_{rc} and ρ_{rc} represent the particle diameter ratio and density ratio of large and small particles, respectively. And ε_f denotes the porosity of the fine particles, and V_c denotes the deposition rate of the large particles. When the value of the segregation factor s is unity, it means that the large

particle and the small particle are in a mixed state. When the factor s is larger than unity, the large particle sinks in the layer, while when the factor is less than unity, it shows that it floats above the layer.

3.11.3.2 Motion Model of Particle Group

Sieving Effect[18]

When multicomponent powder with different particle sizes flows over an inclined stationary powder layer, it is considered that the gaps between the large particles in the layer act as sieve nets and small particles fall from the flowing powder, then the particles reach the stationary powder layer. For this segregation process, a model applying the formula of particle size distribution change on the sieve is proposed.

$$\log\left(\frac{X_{\mathrm{ol(n)}}}{X_{\mathrm{ol(n-1)}}}\right)=\log\left(\frac{X_{\mathrm{f(n)}}}{X_{\mathrm{f(n-1)}}}\right)-\left(\alpha_{(\mathrm{n})}-\alpha_{(\mathrm{n-1})}\right)l \tag{3.11.7}$$

Here

- l represents the flow length on the stationary powder layer
- $X_{(\mathrm{n})}$ represents the residual rate of the n-th step in the standard sieve
- α is a constant depending on the particle size distribution and the flow condition
- o indicates a sample taken on the deposition surface and "f" indicates that it is a feed material.

Sieve Layer Effect[21]

As shown in Figure 3.11.4, when multicomponent particles flow over an inclined stationary powder layer, the segregation component passes through the flowing layer, reaches the stationary layer surface and then the segregation components will flow down by dragging to the upper flowing layer. This segregation process was modeled by the material balance in each layer where the falling layer is divided into the upper residual region r, the intermediate segregation region rs and the lower separation region s. In addition, the stationary layer sp in the bottom layer is also taken into consideration. These are expressed by the following expressions, respectively.

$$\frac{\partial h_{\mathrm{r}}}{\partial t}=-\frac{\partial\left(h_{\mathrm{r}}v_{\mathrm{r}}\right)}{\partial x}+\frac{Q_{\mathrm{p}}\cos\theta}{\left(1-\varepsilon_{\mathrm{r}}\right)}\frac{1-M_{\mathrm{i}}}{M_{\mathrm{i}}} \tag{3.11.8}$$

$$\frac{\partial h_{\mathrm{rs}}}{\partial t}=-\frac{\partial\left(h_{\mathrm{rs}}v_{\mathrm{r}}\right)}{\partial x}+\frac{Q_{\mathrm{p}}\cos\theta}{M_{\mathrm{i}}\left(1-\varepsilon_{\mathrm{rs}}\right)} \tag{3.11.9}$$

$$\frac{\partial h_{\mathrm{s}}}{\partial t}=-\frac{\partial\left(h_{\mathrm{s}}v_{\mathrm{r}}\right)}{\partial x}+\frac{Q_{\mathrm{p}}-P_{\mathrm{p}}}{\left(1-\varepsilon_{\mathrm{s}}\right)}\cos\theta \tag{3.11.10}$$

$$\frac{\partial h_{\mathrm{sp}}}{\partial t}=-\frac{P_{\mathrm{p}}\cos\theta}{\left(1-\varepsilon_{\mathrm{s}}\right)} \tag{3.11.11}$$

Here, M_{i} is the initial mixing ratio, Q_{p} is the separation rate per unit area of the segregation component and P_{p} is the filling rate, respectively. In addition, ε represents the porosity. From these equations, segregation with different particle physical properties can be handled uniformly, and distribution of segregated components can be obtained.

3.11.4 INTERLAYER SEGREGATION

Diffusion Effect[22]

This model is also known as "percolation effect". In this model, the phenomenon that small particles collect around the particle supply point due to particle size segregation is considered as a diffusion process in which small particles diffuse in the gaps between large particles. Assuming that the apparent diffusion coefficient of small particles is D_{r} and the total

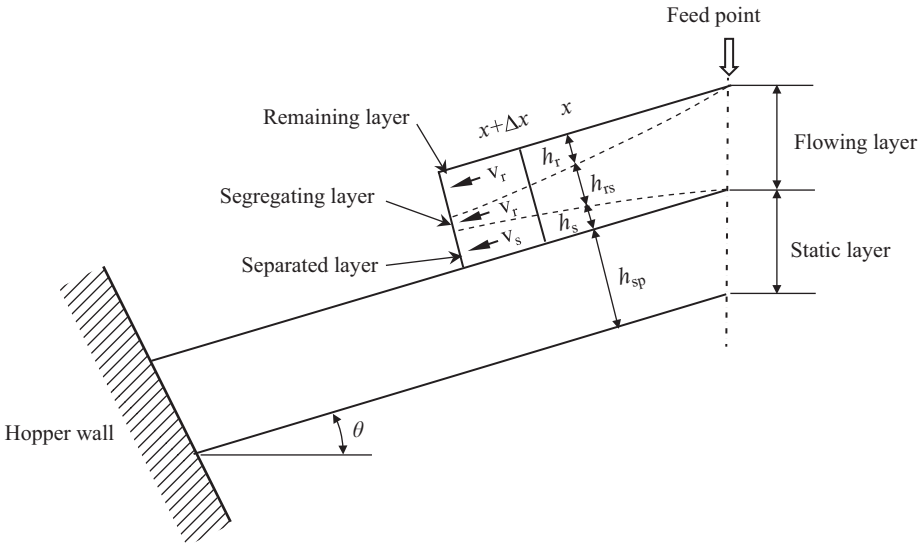


FIGURE 3.11.4 Sieve layer model.[21]

number of small particles is N_0, the number N of small particles per unit cross-sectional area in the direction of radius r_d at time t is expressed by the following equation.

$$\frac{r_d^2}{4D_r t} = \ln\frac{N_0}{N_0 - N} \tag{3.11.12}$$

Permeation Effect[23]

It is assumed that the gap ε_f of the particles with diameter x_f is an assembly of hoppers with an outlet diameter D_0 and that component particles with the diameter x_s segregate by penetrating this hopper. The permeation amount Q_s per unit cross-sectional area is given by the following equation.

$$Q_s = \frac{c_1(1-\varepsilon_f)}{\pi x_f^2/6} c_2 (D_0 - x_s)^n \tag{3.11.13}$$

Here, c_1, c_2, and n are constants.

3.11.5 METHOD TO PREVENT SEGREGATION

It is impossible to prevent segregation completely when powder or granular mixture with different properties and/or characteristics is flowed in the powder or the granule operation. However, it is possible to reduce the segregation by an appropriate way based on the segregation mechanism. First of all, a change of the physical properties and characteristics of particle properties and/or characteristics is necessary for the reduction of the segregation. Next, it is required to design and select devices and/or processes so that segregation is minimized. In addition, operate with optimum operating conditions for segregation reduction is needed.

Since it is impossible to make the physical properties and characteristics of all particles exactly the same within the mixed powder obtained by the mixing of heterogeneous particles, it is effective to reduce the difference in physical properties and characteristics toward the following directions.

- In a system where particle size segregation occurs, grain size is adjusted by crushing coarse particles or granulating fine particles.
- In the system where density segregation occurs, the diameter of large density particles is small, and the diameter of small density particles is made large.
- Before operation, granulate the mixed particles to obtain granules of the same density and single particle size. In this granulation, if mixing and granulation are made by one process, each granulated particle may become a high-quality mixture having all components of the mixed powder, almost avoiding segregation such as particle size, density, shape.

When mixed powder obtained by the mixing of heterogeneous particles or particle group having particle distribution is moved in an operation device, segregation must occur. Therefore, do not move as much as possible is one way for the reduction of segregation, that is, the improvement of equipment to reduce the flow distance is effective to prevent segregation. When the flow distance becomes long, it is effective to make the velocity distribution of the particles uniform. It is also effective to combine suitable mixing operations after segregation occurs. Specifically, for example, the following improvements are conceivable.

- When supplying into a container, use a small container or insert the partition plate in the container so that the flowing distance becomes short.
- When gravity flow occurs in a container, install suitable inserts and partition plates in the container to make the particle velocity distribution uniform during flow.
- When particles are supplied to a hopper and particle size segregation in the radial direction occurs on the surface of the conical sediment layer, the mass flow hopper should be used because components separated at the time of filling are discharged almost at the same time, so apparently uniform mixture is discharged from the hopper.
- Segregation of particles to up and down sides of powder layer caused by belt conveyor, chute, etc. can be reduced by utilizing particle bouncing by placing a vertical plate behind the outflow end.

Not only in the improvement of the apparatus but also in the decision of operating conditions, not to move as much as possible is effective for the reduction of segregation. For example, the following countermeasures can be considered.

- Reduce the number of operations to move particles.
- When transporting, pack the particles tightly in the container to avoid vibration.
- When moving the powder, supply it uniformly in the horizontal direction and do not make an inclined surface on the deposited layer.
- Shorten the free-falling distance of particles, reduce entrainment and collision or repulsion of particles after falling.

REFERENCES

1. Gotoh, K., Maki, T., Masuda H., *J. Soc. Powder Technol. Japan,* 31, 842–849, 1994.
2. Standish, N., *Powder Technol.*, 45, 43–56, 1985.
3. Sugimoto M., Yamamoto K., *J. Soc. Mater. Sci. Japan*, 25, 684–689, 1976.
4. Nakagawa, M., *Chem. Eng. Sci.*, 49, 2540–2544, 1994.
5. Williams, J.C., Shields, G., *Powder Technol.*, 1, 134–142, 1967.
6. Yubita K., Gotoh K., Masuda, H., *J. Soc. Powder Technol. Japan*, 32, 89–96, 1995.

7. Dahl, S.R., Hrenya, C.M., *Chem. Eng. Sci.*, 60, 6658–6673, 2005.
8. Sugimoto M., Yamamoto K., *J. Soc. Mater. Sci. Japan*, 26, 844–849, 1977.
9. Tanaka, Z., Song, X., *Adv. Powder Technol.*, 7, 29–40, 1996.
10. Koyanaka S., Endoh S., Iwata H., *J. Soc. Powder Technol. Japan*, 32, 385–391, 1995.
11. Yamamoto K., Tamao Y., Sugimoto M., *J. Soc. Powder Technol. Japan*, 32, 612–616, 1995.
12. Renzo, A.D., Di Maio, F.P., Girimonte, R., Formisani, B., *Powder Technol.*, 184, 214–223, 2008.
13. Moysey, P.A., Baird, M.H.I., *Powder Technol.*, 196, 298–308, 2009.
14. Yang, S.C., *Chem. Eng. Sci.*, 61, 6180–6188, 2006.
15. Figueroa, I., Li, H., McCarthy, J., *Powder Technol.*, 195, 203–212, 2009.
16. Williams, J.C., *Powder Technol.*, 15, 245–251, 1976.
17. Matthee, H., *Powder Technol.*, 1, 265–271, 1967/1968.
18. Miwa, S., *Funryutai Kogaku*, Asakura Publishing Co., Tokyo., 1972, pp. 221–230.
19. Tanaka, T., *Ind. Eng. Chem. Process Des. Develop.*, 10, 332–340, 1971.
20. Alonso, M., Satoh, M., Miyanami, K. *Powder Technol.*, 68, 145–152, 1991.
21. Shinohara, K., Glodman, B., *Chem. Eng. Sci.*, 57, 277–285, 2002.
22. Bridgwater, J. Sharpe, N.W., Stocker, D.C., *Trans. Inst. Chem. Eng.*, 47, T114–T119, 1969.
23. Shinohara, K., Shoji, K., Tanaka, T., *Ind. Eng. Chem. Process Des. Dev.*, 9, 164–180, 1970.

3.12 Vibrational and Acoustic Characteristics

Jusuke Hidaka

In many treatments of powder in industrial processes, mechanical vibration and sonic energy have been used to increase the efficiency of the operation, and to enhance the transport rates in various industrial operations such as emulsification, size reduction, classification, mixing, drying, and agglomeration.

Furthermore, acoustic noise from powder industrial processes has been used for instrumentation of the state variables in the powder industrial processes. Sound, generally, is radiated by the vibration of a surface, the rapid dilation of fluid medium, and the formation of fluctuating eddies in a fluid. In the instrumentation of a particulate system, impact and frictional sound between particles are important to measure the state variables of the processes.

3.12.1 BEHAVIOR OF A PARTICLE ON A VIBRATING PLATE

A plate with an incline of β to the horizontal plane is vibrating with amplitude A, and angular frequency ω in direction AB as shown in Figure 3.12.1.[1]

Then, the x and y components of displacement of the plate are given, respectively, by

$$x = A\sin\omega t\cos(\alpha+\beta),\ y = A\sin\omega t\sin(\alpha+\beta) \tag{3.12.1}$$

and the velocity and acceleration of the plate are described as follows:

$$\begin{aligned} x &= A\omega\cos\omega t\cos(\alpha+\beta)\\ y &= A\omega\cos\omega t\sin(\alpha+\beta)\\ x &= -A\omega^2\sin\omega t\cos(\alpha+\beta)\\ y &= -A\omega^2\sin\omega t\sin(\alpha+\beta) \end{aligned} \tag{3.12.2}$$

The acceleration b of a plate along the direction AB and the component c of the acceleration in gravitational direction are described as follows:

$$\begin{aligned} x^2+y^2 &= b = \pm a\omega^2\sin\omega t\\ c &= b\frac{\sin(\alpha+\beta)}{\cos\beta} \end{aligned} \tag{3.12.3}$$

The maximum value of acceleration of the plate is $r\omega^2$ when $\omega t=\pi/2$, and then

$$c = \pm r\omega^2\frac{\sin(\alpha+\beta)}{\cos\beta} \tag{3.12.4}$$

Using centrifugal effect K ($=r\omega^2/g$), the ratio, K_v, of the component c in the gravitational direction of acceleration of the plate to gravitation acceleration g is given by

$$K_v = K\frac{\sin(\alpha+\beta)}{\cos\beta} \tag{3.12.5}$$

The relation between displacement and acceleration of the vibrating plate is illustrated in Figure 3.12.2.

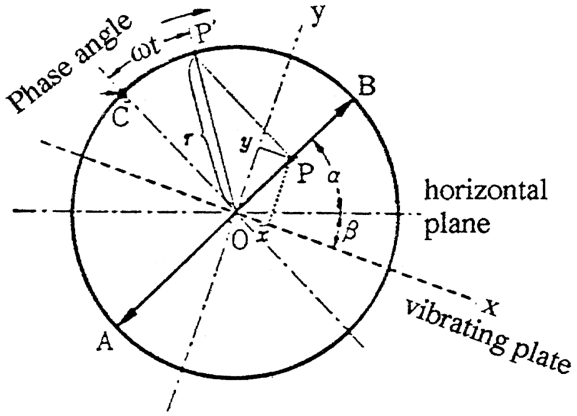


FIGURE 3.12.1 Vibrating plate.

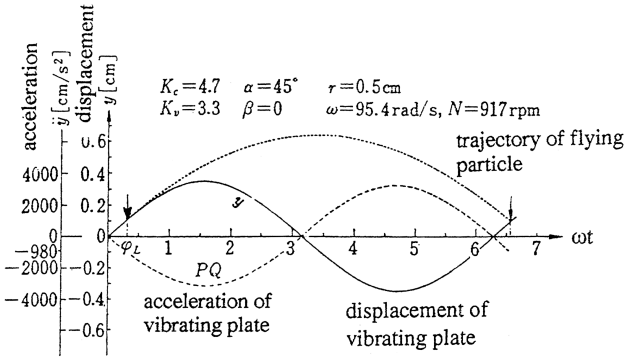


FIGURE 3.12.2 Acceleration, displacement of vibrating plate, and motion of particle on the plate.

For $K_v > 1$, a particle on the vibrating plate leaves the plate with the velocity of the plate at that time. When K_v equals one, the phase angle ϕ_L is given by

$$r\omega^2 \sin\phi_L \frac{\sin(\alpha+\beta)}{\cos\beta} = g$$

$$\sin\varphi_L = \frac{1}{(r\omega 2/g.)\langle \sin(\alpha+\beta)/\cos\beta\rangle} = \frac{1}{K_v} \quad (3.12.6)$$

The particle contacts with the vibrating plate at $0 < \varphi < \varphi_L$ and jumps out of the plate at $\varphi_L < \varphi$. The coordinate (x_L, y_L) of the colliding point between the flying particle and the plate is given by

$$\begin{aligned} x_L &= r\sin\varphi_L \cos(\alpha+\beta) \\ x_L &= r\sin\varphi_L \sin(\alpha+\beta) \end{aligned} \quad (3.12.7)$$

The coordinate (x', y') of the flying particle that jumped out of the vibrating plate at velocity v_L $(=r\,\omega\cos\varphi_L)$ is described as follows

$$x' = x_L + v_L\left(\frac{\cos\alpha}{\cos\beta}\right)$$

$$y' = y_L + v_L \sin(\alpha+\beta)\theta' - (1/2)g\theta'^2\cos\beta \quad (3.12.8)$$

where θ' is the time when the particle jumps out of the plate.

We obtained the time and phase angle at the maximum height of the flying particle as follows:

$$\begin{aligned} \theta'_m &= \frac{v_L \sin(\alpha+\beta)}{g\cos\beta} \\ \varphi_m &= \varphi_L + \frac{v_L \sin(\alpha+\beta)}{g\cos\beta}\omega = \varphi_L + \frac{\cos\varphi_L}{\sin\varphi_L} \end{aligned} \quad (3.12.9)$$

Then, the flying duration of particle is given by $(\varphi_0 - \varphi_L)/\omega$, and during the flying, the particle takes the distance along the vibrating plate as follows:

$$v_L\left(\frac{\cos\alpha}{\cos\beta}\right)\frac{(\varphi_0-\varphi_L)}{\omega} \quad (3.12.10)$$

where φ_0 is the phase angle at colliding point of the flying particle with vibrating plate.

If the phase angle at the colliding time equals φ_L $(=\varphi_0)$, the particle jumps again out of the vibrating plate as soon as the flying particle collides with the plate. The displacement of vibrating particle is shown in Figure 3.12.2.

3.12.2 BEHAVIOR OF A VIBRATING POWDER BED

When a vibration force is applied to a powder bed, the bed can be fluidized and different kinds of flows can be generated in concert with the vibration amplitude and frequency. Vibrating powder beds therefore are widely used in various powder processing operations.

The behavior of vibrating powder beds also depends on the thickness of the powder bed in the vibrating container.[2] For thin powder beds such as those on a sieving medium (less than six particle layers), the surface wave is formed on top of the vibrating bed and it attracts attention from the standpoint of complexity science. For thick beds, different convection patterns are induced in the vibrating bed, depending on the frequency and amplitude of the external vibration. Faraday first discovered the convection phenomenon in vibrating powder beds.[3] He found that when sand is placed on a vibrating membrane, small mounds are formed and slow bulk convection of particles occurs. The convection phenomenon in a vibrating powder bed has attracted considerable attention as it is similar to the Rayleigh Bernard or Marangoni convection observed in fluids. Over the past two decades, the difference in the convection mechanism of powder materials and fluids has been of particular interest for many researchers.

Figure 3.12.3 shows representative flow pattern of the powder bed observed by experimental apparatus as shown in Figure 3.12.4.[4] The particles in the vibrating container

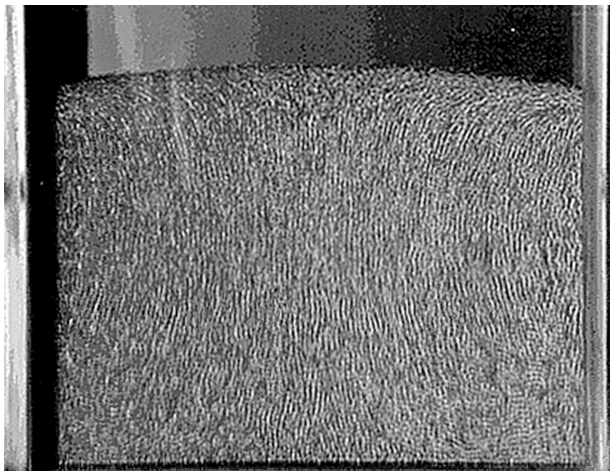


FIGURE 3.12.3 Convection observed in vibrating particle bed.

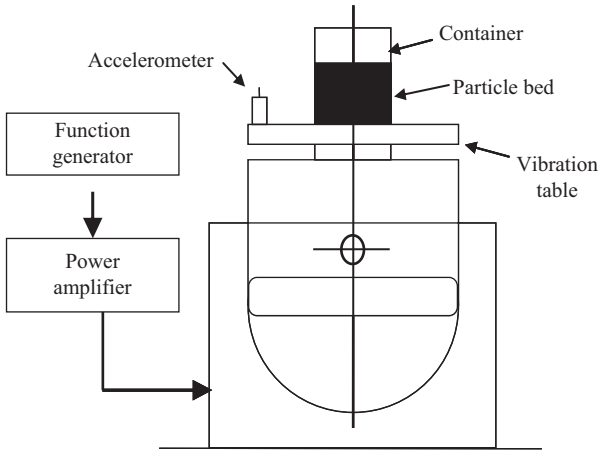


FIGURE 3.12.4 Experimental apparatus.

circulates in two symmetric convection rolls, where the particles moved upward in the central part of the container and downward long the side walls.

The convection behavior of the vibrating powder bed depends on the vibration condition, and Figure 3.12.5 shows experimental results of the relation between the convection behavior and the vibration condition.

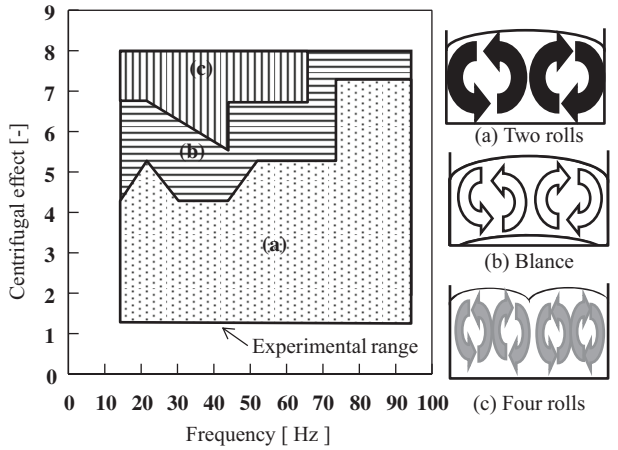


FIGURE 3.12.5 Convection pattern observed in vibrated particle bed (depth of particle bed: 70 mm).

The generation mechanism of convection in the vibrating powder bed was clarified based on the microscopic observation by using computer simulation.[4] Now, let us consider the generation mechanism of two convective rolls as shown in Figure 3.12.6, which is a basic phenomenon in the flow behavior of a vibrating powder bed. The occurrence of this convection is due to the generation of two compressed zones formed in the vibrating powder bed: the triangular and V-shaped compressed zones. The boundary between the compressed and fluidized zones in the bed is called the "slip line" in granular mechanics.

Figure 3.12.6 shows the generation mechanism of two convective rolls by forming two compression zones alternately. Let's start with the phase of vibration in which the vibrating container moves downwards. When the container moves downward in phase (a) of vibration, the particles in the lower part of the container also move downward because the movement of the particles is strongly restricted by the wall friction of the container. Thus the particles pulled down along the wall form V-shaped compressed zone. In the upward movement of the container for the next cycle of vibration [phase (b) of vibration], the particles in the container dilate strongly due to the force from the V-shaped compressed zone of particles formed in the lower part of the container, and then the particles in the container flow towards the center of the container. When the container moves downward for the duration

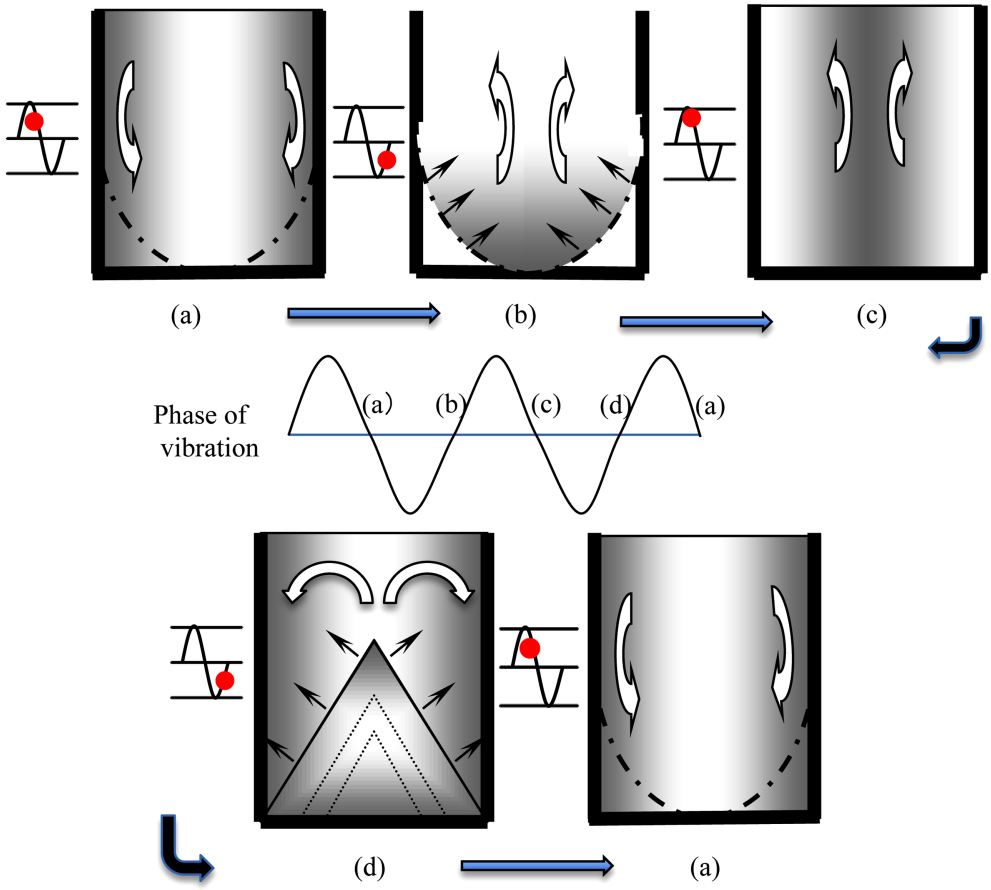


FIGURE 3.12.6 Schematic diagram of generation mechanism of convection in vibrating powder bed.

in which particle concentration in the central zone is higher [phase (c) of vibration], the V-shaped compressed zone does not form unlike in the case of the previous phase (a). This is because the particle concentration near the wall is low and the frictional force acting on the particles in contact with the wall is small. At the next upward motion of the container [phase (d) of vibration], an isosceles triangle-shaped compressed zone is formed at the bottom of the container. The particles in the container are subjected to a very strong force from the isosceles triangle-shaped com pressed zone and then flow toward the wall. The flow behavior of particles at the next downward motion of the container [phase (e) of vibration] is the same as that in phase (a) of vibration, and then the V-shaped compressed zone is formed in the lower part of the container.

In the vibrating powder bed, the V-shaped and isosceles triangle-shaped compressed zones alternately form every two vibration cycles, whereas particle convection in the bed occurs in the form of counter-rotating cells that move particles from the walls to the center of the container.

3.12.3 GENERATING MECHANISM OF IMPACT SOUND BETWEEN TWO PARTICLES

Impact sound from spherical particles stems from the particle surfaces suddenly accelerated by the colliding particles.[5–7] An acceleration waveform acting on two particles colliding elastically can be obtained using Hertz's elastic contact theory described below. When spherical particles 1 and 2, having diameters of a_1 and a_2, respectively, as shown in Figure 3.12.7, collide with each other at relative speed v_0, the following equation holds for the elastic deformation $\xi(t)$ and deformation acceleration $\ddot{\xi}(t)$:

$$\ddot{\xi}_{(t)} = -q_1 q_2 \xi_{(t)}^{3/2} \tag{3.12.11}$$

where

$$q_1 = \frac{m_1 + m_2}{m_1 m_2},\quad q_2 = \frac{4}{3\pi}\left(\frac{1}{\delta_1 + \delta_2}\right)\sqrt{\frac{a_1 a_2}{a_1 + a_2}} \tag{3.12.12}$$

$$\delta_{1,2} = \frac{1 - \nu_{1,2}^2}{\pi E_{1,2}}$$

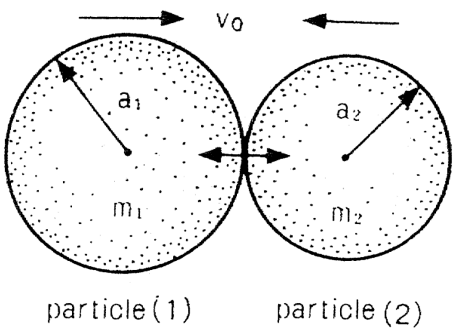


FIGURE 3.12.7 Collision between two elastic particles.

and m_1 and m_2 are the masses of particle 1 and 2, ν_1 and ν_2 are their Poisson's ratios, and E_1 and E_2 are Young's moduli. Elastic deformation $\xi(t)$ can be expressed approximately as

$$\xi_{(t)} = \xi_m \sin\frac{1.068 v_0 t}{\xi_m} \tag{3.12.13}$$

where ξ_m is the maximum deformation of the colliding particles and can be expressed as

$$\xi_m\left[\frac{15\pi v_0^2(\delta_1 + \delta_2)m_1 m_2}{16(m_1 + m_2)}\right]^{\frac{2}{5}}\left(\frac{a_1 + a_2}{a_1 a_2}\right)^{\frac{1}{5}} \tag{3.12.14}$$

Assuming that particle deformation acceleration equals gravity center acceleration, the acceleration waveform [$\alpha_{(t)} = 1/2 \cdot \ddot{\xi}_{(t)}$] of the particle surfaces due to collision can be obtained from Equation (3.12.11) and Equation (3.12.13).

Let us determine the sound pressure waveform (impulse response) radiated by a particle when unit impulse acceleration acts on it. The velocity potential $\phi(r,\theta,t)$ of sound generating when a spherical particle Figure 3.12.8b oscillates reciprocatingly along the z axis at a speed of $U_0 \exp(j\omega t)$ satisfies the following equation:

$$\frac{\partial^2\varphi}{\partial r^2} + \frac{2\partial\varphi}{r\partial r} + \frac{1}{r^2\sin\theta}\frac{\partial}{\partial\theta}\left(\sin\theta\frac{\partial\varphi}{\partial\theta}\right) + k^2\varphi = 0 \tag{3.12.15}$$

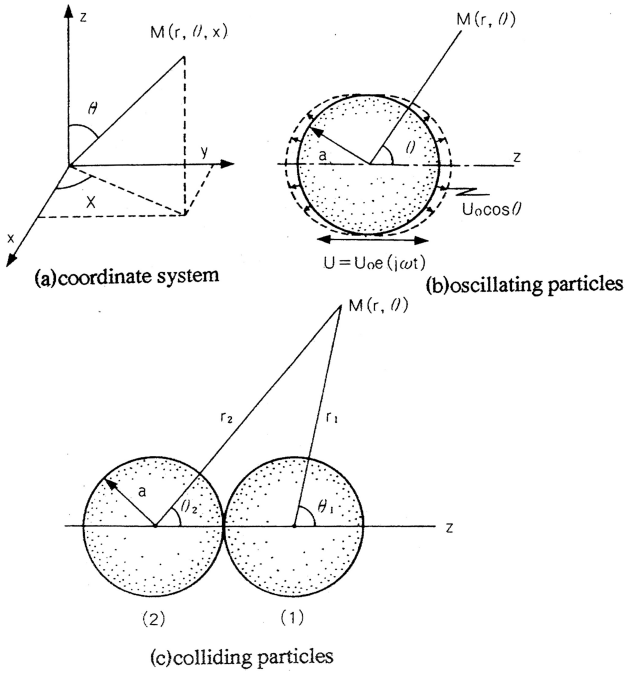


FIGURE 3.12.8 Impact sound emitted from two colliding particles.

where k is the wave number. When one has solved Equation (3.12.15) using the boundary condition that indicates that the speed of the particle surface equals that of the medium, the following velocity potential is obtained:

$$\varphi' = \frac{a^3 U_0}{r^2} \frac{(1+jkr)\cos\theta \cdot e^{j[\cdot\omega t - k(r-a)]}}{\left[2(1+jka) - k^2 a^2\right]} \tag{3.12.16}$$

Based on Equation (3.12.16), we can obtain the sound pressure radiated by the particle subjected to unit impulse acceleration as follows, using the method employed by Koss et al.:

$$P_{\text{imp}} = \frac{\rho_0 C a \cos\theta}{r}\left[\cos\left(\frac{C}{a}t'\right) - \left(1-\frac{a}{r}\right)\sin\left(\frac{C}{a}t'\right)\right]e - \left(\frac{C}{a}t'\right) \tag{3.12.17}$$

where $t' = t - (r - a)/C$ and ρ_0 is medium density, while C is sound speed.

The pressure waveform of sound radiated by a particle when subjected to a given acceleration $\xi(t)$ can generally be expressed as follows:

$$P(r,\theta t) = \int_0^1 P_{\text{imp}}(t-\tau)^* \xi(\tau)\, d\tau \tag{3.12.18}$$

If we approximate the acceleration resulting from Equation (3.12.11) and Equation (3.12.13) by $\xi(t) = 1/2 \cdot \xi_{\text{m}} \sin bt$ for easier calculation, we obtain the following equation from Equation (3.12.17) and Equation (3.12.18) where $b = \pi/T$, and T is the contact time between two colliding particles.

When $0 < t' < T$,

$$\begin{aligned}
P(r_{\text{i}},\theta_{\text{i}}\, t_{\text{i}}) = {} & \frac{\rho_0 a_{\text{m}} a_{\text{i}}^3 \cos\theta_{\text{i}}}{8\left(b^4 + 4l_{\text{i}}^4\right)} \frac{1}{r_{\text{i}}^2}\left\{\left(\frac{2r_{\text{i}}}{a_{\text{i}}} - 1\right)\left[\left(8l_{\text{i}}^3 b - 4l_{\text{i}} b^3\right)\cos bt' + 8l_{\text{i}}^2 b^2 \sin bt_{\text{i}}'\right]\right. \\
& - 4b^4 \sin bt_{\text{i}}' - \left(8l_{\text{i}}^3 b + 4l_{\text{i}} b^3\right)\cos bt_{\text{i}}' \\
& + \left(\frac{2l_{\text{i}}}{a_{\text{i}}} - 1\right)\left[\left(4b^3 l_{\text{i}} - 8bl_{\text{i}}^3\right)\cos l_{\text{i}} t_{\text{i}}' - \left(8bl_{\text{i}}^3 + 4b^3 l_{\text{i}}\right)\sin l_{\text{i}} t_{\text{i}}'\right]\exp\left(-l_{\text{i}} t_{\text{i}}'\right) \\
& + \left[\left(4b^3 l_{\text{i}} - 8bl_{\text{i}}^3\right)\cos l_{\text{i}}\left(t' - \frac{\pi}{2l_{\text{i}}}\right)\right. \\
& \left.\left. - \left(8bl_{\text{i}}^3 + 4b^3 l_{\text{i}}\right)\sin l_{\text{i}}\left(t_{\text{i}}' - \frac{\pi}{2l_{\text{i}}}\right)\right]\exp\left(-l_{\text{i}} t_{\text{i}}'\right)\right\} \\
& + \frac{\rho_0 a_{\text{m}} a_{\text{i}}^3 \cos\theta_{\text{i}}}{2r_{\text{i}}^2}\sin bt_{\text{i}}'
\end{aligned} \tag{3.12.19}$$

When $T < t'$,

$$\begin{aligned}
P(r_{\text{i}},\theta_{\text{i}}\, t_{\text{i}}) = {} & \frac{\rho_0 \alpha_{\text{m}} a_{\text{i}}^3 \cos\theta_{\text{i}}}{8\left(b^4 + 4l_{\text{i}}^4\right)} \frac{1}{r_{\text{i}}^2}\left\{\left(\frac{2r_{\text{i}}}{a_{\text{i}}} - 1\right)\left\{\left[\left(4b^3 l_{\text{i}} - 8bl_{\text{i}}^3\right)\cos l_{\text{i}}\left(t_{\text{i}}' - T\right)\right.\right.\right. \\
& \left. - \left(8bl_{\text{i}}^3 + 4b^3 l_{\text{i}}\right)\sin l_{\text{i}}\left(t_{\text{i}}' - T\right)\right]\exp\left[-l_{\text{i}}\left(t_{\text{i}}' T\right)\right] \\
& + \left[\left(4b^3 l_{\text{i}} - 8bl_{\text{i}}^3\right)\cos l_{\text{i}} t_{\text{i}}' - \left(4b^3 l_{\text{i}} + 8bl_{\text{i}}^3\right)\sin l_{\text{i}} t_{\text{i}}'\right]\exp\left(-l_{\text{i}} t_{\text{i}}'\right)\Big\} \\
& - \left[\left(8bl_{\text{i}}^3 - 4b^3 l_{\text{i}}\right)\cos l_{\text{i}}\left(t_{\text{i}}' - T - \frac{\pi}{2l_{\text{i}}}\right)\right. \\
& \left. + \left(8bl_{\text{i}}^3 - 4b^3 l_{\text{i}}\right)\sin l_{\text{i}}\left(t_{\text{i}}' - T - \frac{\pi}{2l_{\text{i}}}\right)\right]\exp\left[-l_{\text{i}}\left(t_{\text{i}}' - T\right)\right] \\
& - \left[\left(8bl_{\text{i}}^3 - 4b^3 l_{\text{i}}\right)\cos l_{\text{i}}\left(t_{\text{i}}' - \frac{\pi}{2l_{\text{i}}}\right) + \left(8bl_{\text{i}}^3 + 4b^3 l_{\text{i}}\right)\right. \\
& \left.\left.\sin l_{\text{i}}\left(t_{\text{i}}' - \frac{\pi}{2l_{\text{i}}}\right)\right]\exp\left(-l_{\text{i}} t_{\text{i}}'\right)\right\}
\end{aligned} \tag{3.12.20}$$

where the subscript i is an index of the spherical particle, $l_{\text{i}} = C/a_{\text{i}}$. Sound pressure P (r, θ, t) from two colliding particles at the observation point M (r, θ), shown in Figure 3.12.8, must allow for the sum of sound pressure radiated from particles 1 and 2.

$$P(r,\theta,t) = P(r_1,\theta_1,t_1) + P(r_2,\theta_2,t_2) \tag{3.12.21}$$

Figure 3.12.9 shows the comparison of a measured pressure waveform and a calculated one. The relationship between the peak pressure of sound P_{m} and the impact velocity v_0 is shown by the following equation:

$$P_{\text{m}} \propto v_0^{6/5} \tag{3.12.22}$$

The frequency of maximum peak f_{m} in the frequency spectrum of the impact sound is shown experimentally by the following equation as shown in Figure 3.12.10.

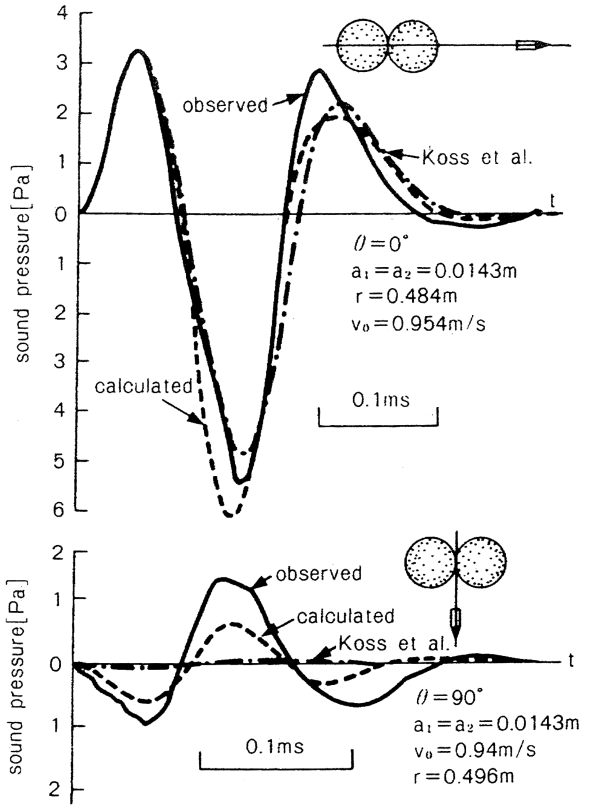
$$f_{\text{m}} \propto D_{\text{p}}^{-1} \tag{3.12.23}$$

where D_{p} is particle diameter ($a = D_{\text{p}}/2$).

Based on these relations, we can measure the state variables of powder industrial processes with the acoustic noise emitted from the processes.

3.12.4 FRICTIONAL SOUND FROM A GRANULAR BED

The sound pressure radiated from the friction between two particles is ordinarily too small to be detected with a microphone, but a granular bed of particles in contact with each other can radiate the frictional sound of which the parameters relate to the frictional properties of the bed.[8,9]



(a) calculated pressure waveforms of impact sound

FIGURE 3.12.9(a) Pressure waveforms and frequency spectra of impact sound.

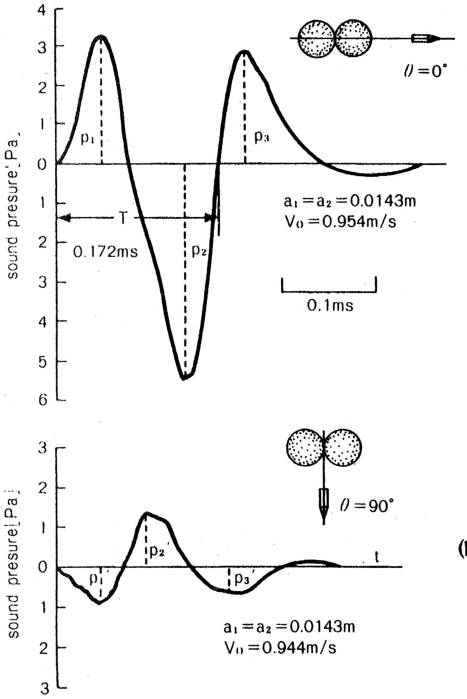
In the flow and deformation of a granular bed, successive intermittent slip lines are formed in the bed, and the periodicity of the intermittent shear yields relates to the frictional properties of the bed. The frictional sound results from the dilation of particles in the vicinity of the slip line. As results of the dilation, the surface of a granular bed vibrates as a piston, and the sound is radiated into space.

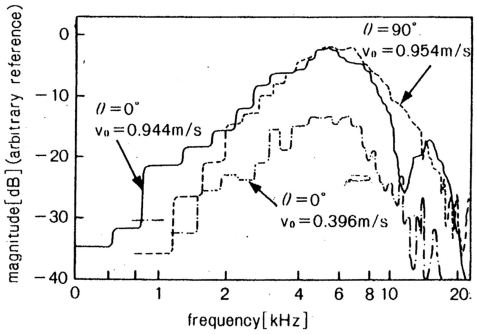
Consider, for the sake of simplicity, a plate penetrating at constant velocity into a dense, infinitely wide bed. In the bed, the successive slip lines as shown in an X-ray radiograph (Figure 3.12.11) are formed, and the intervals, Δh, between the slip lines are shown by the following equation:

$$\Delta h = \frac{B}{2}\left\{\tan\left(\frac{\pi}{4}+\frac{\varphi_s}{2}\right)-\tan\left(\frac{\pi}{4}+\frac{\varphi_e}{2}\right)\right\} \quad (3.12.24)$$

where B is the diameter of the penetrating plate, ϕ_s is the static angle of internal friction, and ϕ_e is the dynamic angle of internal friction. The sound pressure from the surface of the bed can be estimated by the model of sound emission from a piston in an infinite wall. Let the circular piston of radius, a, as shown in Figure 3.12.12, oscillate with a small amplitude and with a velocity given by $U = U_0 \exp(-j\omega t)$. The sound pressure p along the center axis is given by the following equation:

$$P = j^2 \rho C U \sin\frac{kr}{2}\left(\sqrt{1+a^2}-1\right)\exp\left\{\omega t - j\frac{kr}{2}\left(\sqrt{1+a^2}-1\right)\right\} \quad (3.12.25)$$





(b) measured pressure wave forms and frequency spectra of impact sound

FIGURE 3.12.9(b) Pressure waveforms and frequency spectra of impact sound.

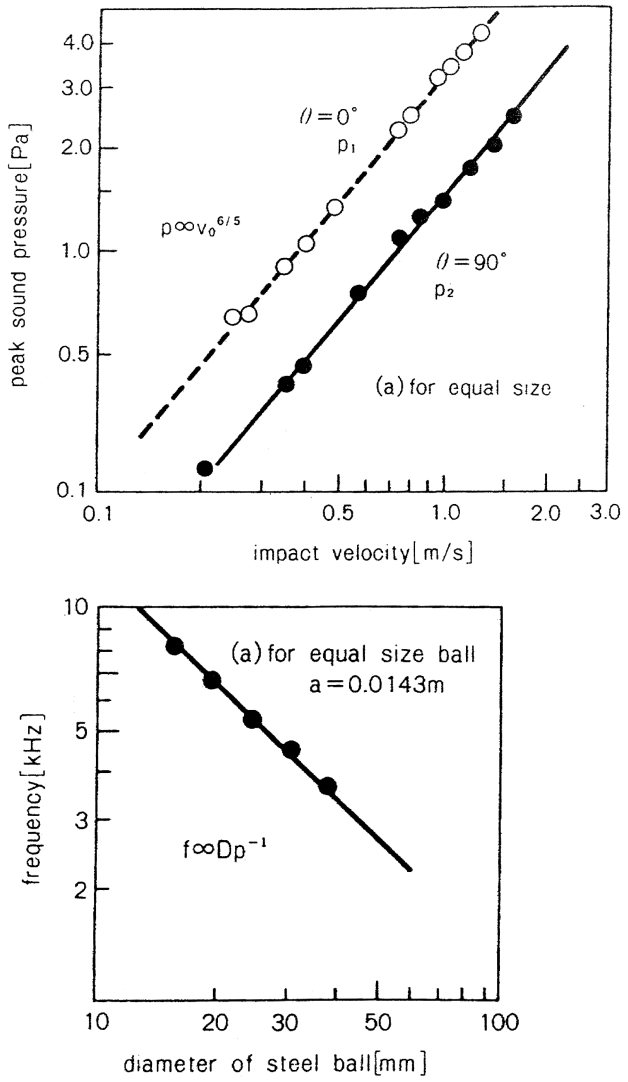


FIGURE 3.12.10 Relationship among peak pressure and frequency of impact sound,

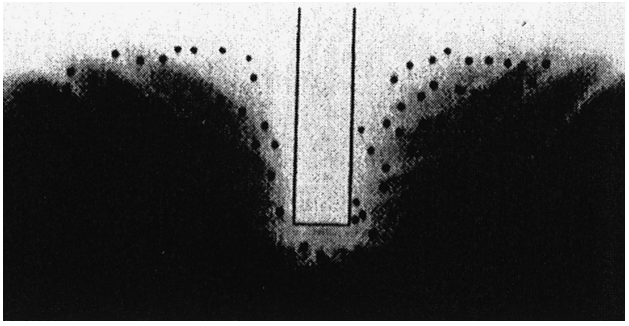


FIGURE 3.12.11 X-ray radiograph of slip lines in a powder bed.

where k is the wave number, $\alpha = a/r$. Thus, the relationship between the peak sound pressure P_m and the radius a is shown as follows:

$$P_m = 2\rho C U_0 \left| \sin \frac{kr}{2} \left(\sqrt{1+a^2} - 1 \right) \right| \tag{3.12.26}$$

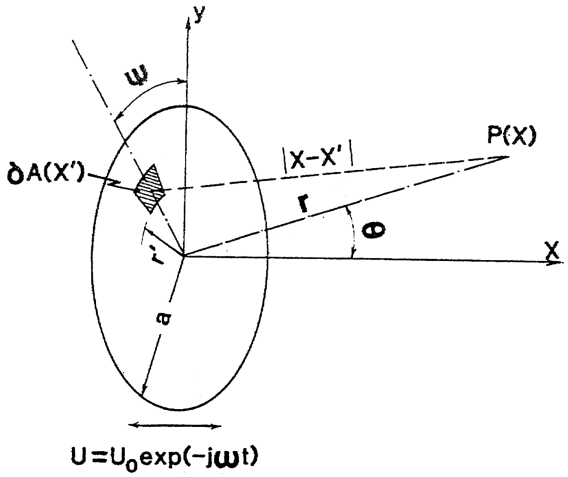


FIGURE 3.12.12 Sound emission by a flat, circular piston in a finite wall.

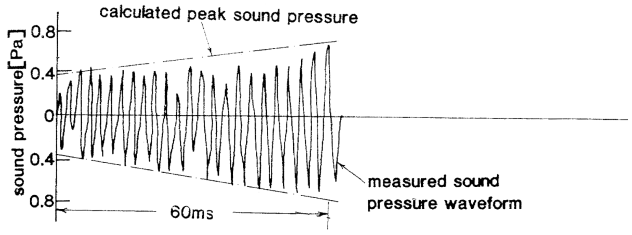


FIGURE 3.12.13 Comparison of the measured sound pressure waveform with the calculated one.

The increase Δa in the radius of the oscillating surface of the bed at each shear yield is given as follows:

$$\Delta a = \frac{\Delta h}{\sin\left(\frac{\pi}{4} - \frac{\varphi_s}{2}\right)} \tag{3.12.27}$$

The amplitude of a vibrating surface is shown by the equation

$$A = \frac{\Delta h}{b}\left(\frac{1}{\lambda_2 - \lambda_1}\right) \tag{3.12.28}$$

where b is the coefficient for describing the average distance between particles in the bed, λ_1 is the linear concentration of particles before rupture, and λ_2 is the linear concentration of particles after rupture.

Figure 3.12.13 is a comparison the measured sound pressure waveform with the calculated one. The frequency of the frictional sound can be estimated by the following equation:

$$f_a = \frac{\omega}{2\pi} = \frac{V_p}{\Delta h} \tag{3.12.29}$$

where V_p is the penetrating speed of the plate into the powder bed. The parameters of this sound closely relate to the frictional properties and the formation of rupture layers in the granular bed.

3.12.5 VIBRATION OF A SMALL PARTICLE IN A SOUND WAVE

The vibration of a small particle in a sound wave is of some importance in a variety of areas, such as in acoustic coagulation of aerosols.[10,11] This motion has been studied by Brandt and Hiedemann.[12]

The amplitude X_m of a fluid medium can be written in terms of angular frequency ω, wavelength λ, maximum amplitude A_m, and the distance from the node of the wave to the specified particle l.

$$X_m = A_m \sin \omega t \sin\left(\frac{2\pi l}{\lambda}\right) \tag{3.12.30}$$

The force acting on the oscillating sphere can be presented by the well-known Stokes' law for drag as follows:

$$R = 3\pi\mu D_p \Delta v = 3\pi\mu D_p \left(\frac{dX_m}{dt} - \frac{dX_p}{dt}\right) \tag{3.12.31}$$

where μ is the coefficient of viscosity of a medium, Δv is the relative velocity between the particle and the fluid, X_p is the amplitude of the particle.

The motion equation of the particle in a sound wave is given by

$$\rho_p \frac{\pi D_p^3}{6} \cdot \frac{d^2 X_p}{dt^2} = 3\pi\mu D_p \left[\omega A \cos \omega t \sin\left(\frac{2\pi l}{\lambda}\right) - \frac{dX_p}{dt}\right] \tag{3.12.32}$$

The solution yields

$$X_p = \frac{A_m \sin(2\pi l/\lambda)\sin(\omega t - \beta)}{\left[1 + \left(\frac{\pi\rho D_p^2 f}{9\mu}\right)^2\right]^{0.5}} \tag{3.12.33}$$

where f is the frequency of the sound wave, and β is the phase difference of the particle and medium in oscillation. The ratio X_p/X_m yields

$$\frac{X_p}{X_m} = \frac{1}{\left[1 + \left(\frac{\pi\rho D_p^2 f}{9\mu}\right)2\right]^{0.5}} \tag{3.12.34}$$

where X_m is the amplitude of the medium. The phase difference β is given by

$$\beta = \tan^{-1}\left(\frac{\pi\rho_p D_p f}{9\mu}\right) \tag{3.12.35}$$

Figure 3.12.14 shows the calculated values of X_p/X_m.

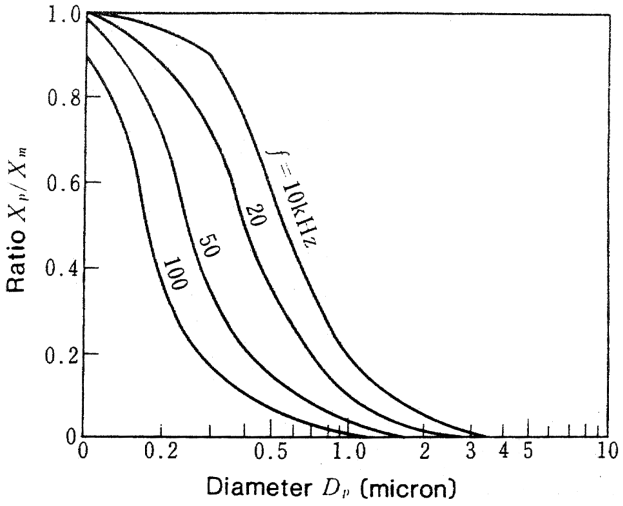


FIGURE 3.12.14 Ratio of the amplitude of a vibrating particle and medium.

3.12.6 ATTENUATION OF SOUND IN A SUSPENSION OF PARTICLES

When a sound wave propagates in a dilute suspension, it is attenuated by the particle-wave interaction, such as the oscillation of the particle and the scattering of the incident wave.[13,14] If a plane sound wave propagates in the suspension, then the decay of sound pressure is given by

$$P = P_0 \exp(-\gamma x) \tag{3.12.36}$$

where P_0 is the sound pressure of incident wave at $x=0$, g is the damping coefficient, and x is the distance along the path. The decay of energy can also be expected to be exponential:

$$E(t) = E_0 \exp(-2\gamma_e t) \tag{3.12.37}$$

where E_0 is the value of E at $t=0$.

If κ is the energy removal rate due to one sphere, the energy dissipation rate per unit volume E is given by

$$E = nk \tag{3.12.38}$$

where n is the number of particles per unit volume. For very small particles, the energy loss rate due to scattering is very small. Therefore the power that must be spent instantaneously to maintain the motion is represented by $\eta_p (v_p - v)$ in terms of the velocity of particle v_p and that of fluid v. Thus, the average energy dissipation rate per unit volume is

$$E = n\eta_p (v_p - v) \tag{3.12.39}$$

For a plane sound wave, the energy per unit volume E_0 equals (1/2) ρv_0^2 where v_0 is the velocity amplitude of the medium. Thus, the coefficient of amplitude attenuation is obtained by Equation (3.12.37)

$$\gamma = \frac{R\left(v_p - v\right)}{\rho C v_0^2} = n \cdot \frac{\mathrm{Re}\left[\tilde{R}\left(\tilde{v}_p - \tilde{v}\right)\right]}{2\rho C v_0^2} \qquad (3.12.40)$$

$$\sqrt{\omega a^2 / 2\lambda} \le 1, \rho_p \rho \le 1$$

For

$$\tilde{R} = 6\pi\mu\left(\tilde{v}_p - \tilde{v}\right), \tilde{v}_p - \tilde{v} = v_0 \frac{j\omega\tau}{1 - j\omega\tau} \qquad (3.12.41)$$

From Equation (3.12.40) and Equation (3.12.41), we obtain

$$\gamma = \frac{3\eta\mu_k na}{C} \frac{\omega^2\tau^2}{1+\omega^2\tau^2} \qquad (3.12.42)$$

where μ_k is the coefficient of kinetic viscosity of the medium. Rewriting Equation (3.12.42) in terms of $\tilde{a} = \gamma C / \omega$ *and* $\psi = (4/3)a^3 n(\rho_p / \rho)$, Equation (3.12.43) is obtained.

$$\tilde{a} = \frac{1}{2}\psi \frac{\omega^2\tau^2}{1+\omega^2\tau^2} \qquad (3.12.43)$$

The above equation shows that the attenuation per wavelength has a maximum at $\omega\tau = 1$. Thus, the sound waves having the frequency of the order of τ^{-1} are damped the most by the attenuation. The frequency for maximum attenuation per wavelength is given by the following equation:

$$f = \frac{1}{4\pi} \frac{9\mu_k}{a^2} \frac{\rho_p}{\rho} \qquad (3.12.44)$$

REFERENCES

1. Miwa, S. *Funryutai kogaku (Japanese)*, Asakura-syoten, Tokyo, 1972.
2. Wassgren, C., Brennen, C., Hunt, M., *J. Appl. Mech*., 63, 712–719, 1996.
3. Faraday, M., *Philoso. Trans. R. Soc. London*, 21, 299–340, 1831.
4. Hamada, K., et al., *J. Chem. Eng. Japan*., 46, 40–50, 2013.
5. Hidaka, J., Shimosaka, A., Miwa, S., *KONA*, 7, 4–14, 1989.
6. Hidaka, J., Shimosaka, A., Ito, H., Miwa, S., *KONA*, 10, 175–183, 1992.
7. Hidaka, J., Shimosaka, A., *Int. J. Mod. Phys.*, 7, 1965–1975, 1993.
8. Hidaka, J., Kirimoto, Y., Miwa, S., Makino, K., *Int. Chem. Eng.*, 27, 514–520, 1987.
9. Hidaka, J., Miwa, S., Makino, M., *Int. Chem. Eng.*, 28, 99–106, 1988.
10. Song L., Koopman, G. H., Hoffman, T. L., *J. Vib. Acoust.*, 116, 208–214, 1994.
11. Hoffman, T. L., Koopman, G. H., *J. Acoust. Soc. Am*., 101, 3421–3429, 1997.
12. Brandt, O., Hiedemann, E., *Trans. Faraday Soc*. 32, 1101–1111, 1936.
13. Temkin, S., *Elements of Acoustics*, John Wiley & Sons, New York, 1981.
14. Richard, S. D., Leighton, T. G., Brown. N. R., *J. Acoust. Soc. Am*. 114, 1841–1850, 2003.



Taylor & Francis
Taylor & Francis Group
http://taylorandfrancis.com

Part 4

Particle Generation and Modification



Taylor & Francis
Taylor & Francis Group
http://taylorandfrancis.com

4.1 Aerosol Particle Generation

Jakub M. Gac and Sotiris E. Pratsinis

Aerosols are suspensions of solid or liquid particles in gases. Smoke, dust, mist, fog, haze and cloud are names that are used frequently for aerosols that can be generated by physical or chemical routes. This chapter will focus on aerosols made by physical routes and the next by chemical ones. Table 4.1.1 summarizes the most common physical routes for generation of aerosol particles with examples of the corresponding typical particle compositions.

Physical routes result in aerosols of liquid or solid particles created either by a) condensation, where vapors convert to droplets or solid particles, or b) atomization or dispersion, where liquids or solids are disintegrated and suspended into a flowing stream.

4.1.1 ATOMIZATION OF FLUIDS

Atomization or nebulization of fluids is by far the dominant way to generate liquid aerosols. Even the common use of the word "aerosol" refers to spraying mists from a pressurized can (e.g. deodorants, insecticides or cooking oil, to name a few). In general, atomization starts with the extrusion of a liquid thread or stream through a nozzle. This results in liquid sheets and ligaments that break-up into droplets either by a) the applied pressure for extrusion (e.g. the above spray can), or b) a gas stream facilitating ligament formation from the gas-liquid interface of the liquid thread. The first is called pressure atomization while the latter two-fluid (air-assist or air-blast) atomization.

Both types are widely used in a broad spectrum of applications for the generation of large volumes of aerosols at high throughput. For example, direct pressure atomizers are used for fuel injection in combustion engines for motor vehicles. A lot of research is dedicated to controlling the average droplet size and size distribution of the fuel. Too large droplets end up splashing to the walls of the engine's combustion chamber leading to premature deterioration of its walls and excess emission of pollutants. Too small droplets lead to soot deposits near the nozzle hindering gradually fuel atomization.

Conditions at which atomization occurs are given by the Weber number which is a measure of the ratio of kinetic energy of surrounding gas to the energy required to form a droplet:

$$\mathrm{We} = \rho V^2 d_p / \sigma$$

where

- V denotes the relative velocity between the liquid and surrounding gas
- σ is the surface tension
- d_p is the droplet diameter
- ρ is the gas density

When the Weber number exceeds a critical value, which is dependent on the geometry of a system (it is typically between 1 to 50),[1] droplets start to form.

As one might sense, there are a lot of atomization techniques. In general, relatively large droplets with rather broad size distributions are generated from micrometers to even a millimeter in diameter. The book by Lefebvre and McDonell[2] gives an excellent treatise on the topic with a wide variety of nozzle designs and spray configurations. They give the following properties of an ideal atomizer: ability to provide good atomization over a wide range of liquid flow rates; rapid response to changes in liquid flow rate; lack or very low flow

TABLE 4.1.1 Aerosol Generation Methods by Physical Routes

Methods	Particles	Material
Liquid atomization (Sec. 4.1.4)		
• Pressure atomizers • Two-fluid atomizers • Nebulizers • Ultrasonic nebulization • Electrospray	Droplets	Dioctyl phthalate (DOP), dioctyl sebacate (DOS)[1], dibutyl phthalate (DBP), mineral oil, solvents (ethanol etc.), fuels (kerozine, gasoline, diesel)
Condensation of vapors (Sec. 4.1.2)		
Seeded liquid evaporation/condensation	Droplets	DOP, DOS, DBP, glycerol
Solid evaporation/condensation	Solid particles	Metals, mineral salts, stearic acid
Gas evaporation method (low pressure)	Nanoparticles	Metals, metal oxides
Inert gas condensation	Nanoparticles	Metals, alloys
Powder resuspension (Sec. 4.1.3)		
Mechanical powder resuspension	Solid particles	Powders, beads, fibers

[1] Also known as Di-Ethyl-Hexyl-Sebacate (DEHS).

instabilities; low power requirements; the ability to scale to provide design flexibility; low cost, light weight, ease of maintenance and ease of removal for servicing; high resistance to damage during production and assembly.

Pressure Atomizers

These atomizers convert pressure (as their name suggests) into kinetic energy of droplets of the resulting aerosol.[3] The main part of every pressure atomizer is a nozzle or injector which ensures local change of pressure that is necessary for the formation of an aerosol. Sprays produced by pressure atomizers are cone-shaped with an opening angle that depends on the properties of the sprayed liquid (viscosity, surface tension) and to a lesser extent on the geometry of the orifice. This angle is typically in the range of 5–15°. However, it can be increased using pressure-swirl atomizers instead of plain-orifice ones.[2] In these atomizers a swirling motion of the liquid is caused. Under the action of centrifugal force, the liquid spreads out in the form of a conical sheet as soon as it leaves the orifice. An example of such a solution is the Delavan solid cone nozzle.[4] The main part of this device is a one-piece cast body with a vane-type core which can be removed. The cylindrical hole inside this core works as a plain-orifice atomizer and provides droplets to the center of conical spray. In other pressure-swirl atomizers a swirling motion of a liquid is caused, instead of solid core, by feeding of a liquid into a swirl chamber through tangential inlet.[2]

Two-Fluid Atomizers

In these devices a gas stream of relatively high velocity strikes or co-flows with a much slower stream of liquid. One can distinguish two basic types of two-fluid atomizers: internal-mixing type and external-mixing type (Figure 4.1.1). The main difference between them is the place of contact between "assisting" air and "atomized" liquid. For internal mixing atomizers this contact takes place inside the nozzle while in external ones – outside the nozzle. The internal-mixing atomizer is suitable for highly viscous liquids. Good atomization can be obtained for relatively low liquid flow rates. In contrast, in external-mixing atomizers a constant spray angle is attained at all liquid flow rates.[2]

A different group of two-fluid atomizers is air-blast atomizers. The main difference between them is the larger amount of air required to achieve good atomization. Furthermore, they produce finer spray droplets than air-assisted atomizers. As a result, air-blast atomizers have found a wide application in combustion systems: finer droplets and higher amount of air results in low soot formation and a minimum of exhaust smoke.[2]

Nebulizers

Nebulizers are atomizers of low throughput that are attractive for the generation of test aerosols (DOP, DOS, DBP, etc., for their low vapor pressure) for instrument development,

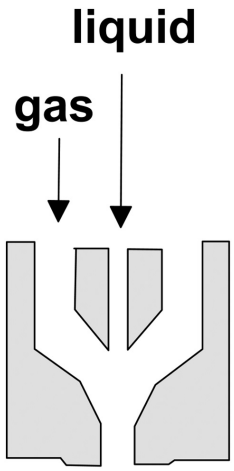


FIGURE 4.1.1A Nozzles of two fluid-atomizers: (a) internal-mixing type,

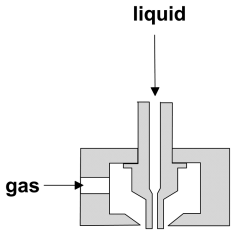


FIGURE 4.1.1B Nozzles of two fluid-atomizers: (b) external-mixing type (Adapted from Lefebvre and McDonell, *Atomization and Sprays*, Taylor & Francis, Boca Raton, 2017.)

inhalation of medical aerosols, bioaerosols, material synthesis etc. Typically, nebulizers operate by blowing compressed air through an orifice or capillary that is partially immersed in the fluid that needs to be aerosolized by aspiration (Figure 4.1.2). The difference in pressure between orifice opening and the free surface of the fluid sucks fluid through the orifice suspending and breaking the fluid into ligaments and eventually droplets by the flowing air over the capillary. From the resulting suspension only the finest droplets are exiting the manifold or chamber containing the orifice to constitute the product aerosol. Larger droplets impact the chamber walls and are recycled into the liquid pool. The aerosol textbook by W. Hinds[5] gives a succinct summary of such nebulizers.

One of the most popular nebulizers, especially for filtration studies, are those containing a Laskin nozzle (Figure 4.1.3). The operating principle of this nozzle is as follows[7]: the nozzle is immersed in the fluid intended for nebulization. Compressed air is fed down the supply pipe to four radial holes. Above these holes there is a ring with four adjacent openings above the air outlets. Because compressed air flows at high velocity from the four radial holes, the liquid is drawn into the air flow and is effectively atomized into the resulting small air bubbles, which then grow as they move to the liquid surface where they break, releasing the atomized droplets into the air above the liquid. Nebulizers based on the Laskin nozzle are commonly applied because of the high reproducibility of size distribution of the generated droplets (e.g. ref. 8).

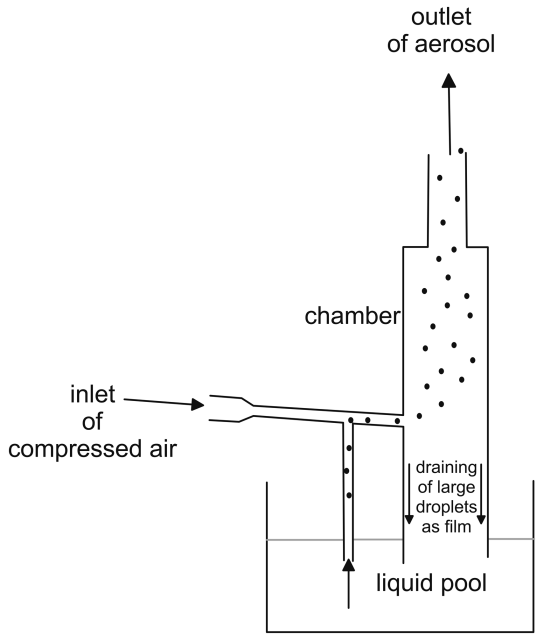


FIGURE 4.1.2 Constant rate nebulizer for dispersion of liquid as fine droplets (adopted from ref.[6]).

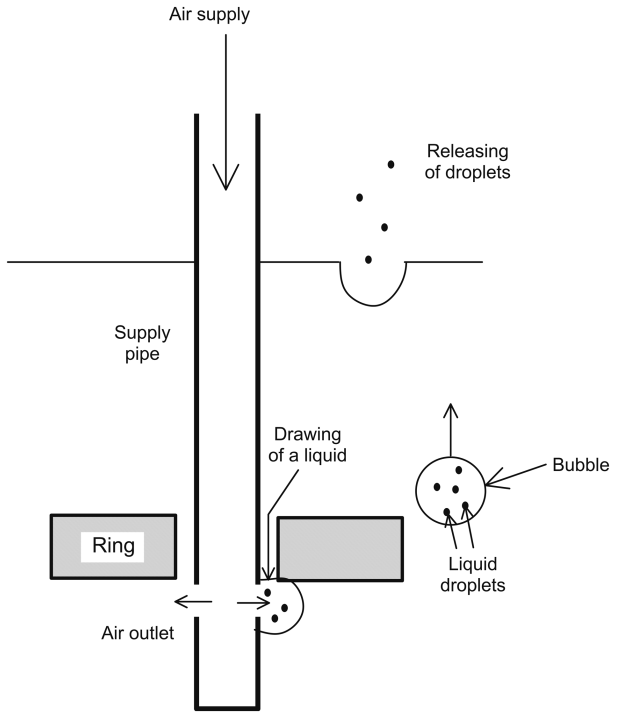


FIGURE 4.1.3 Scheme and principle of operation by the Laskin nozzle.

Ultrasonic Nebulizers

Ultrasonic nebulizers are quite popular and are used widely for humidification of indoor spaces (Figure 4.1.4). They generate aerosols without compressed air. Instead ultrasonic waves are generated by a piezoelectric crystal. During ultrasonication, high shock pressures in the immediate vicinity of an imploded cavity are created within the fluid resulting in jets of liquid by the asymmetrical collapse of adjacent cavities.[9] The resulting droplets form a conical fountain and are carried out by a gentle flow of dispersion air. An empirical expression has been proposed by Mercer[10] for the number median diameter of the produced droplets, d_p:

$$d_p = (\sigma / \rho_L f^2)^{1/3}$$

where σ and ρ_L are the surface tension and density, respectively, of the liquid while f is the excitation frequency. This expression holds best for 0.012–3 MHz.[5]

Typically droplet sizes are 5 to 10 µm for a frequency of 0.1 to 10 MHz.[11] A distinct characteristic of such nebulizers is that most of the ultrasonic energy ends up heating the fluid. While this is hardly an issue for humidification, it is a concern when temperature-sensitive fluids are to be atomized as with bioaerosols, pharmaceutics and thermally sensitive liquid precursors for material synthesis. For example, when ultrasonic nebulizers are used for the generation of multicomponent droplets followed by drying in flames or hot wall reactors for synthesis of mixed ceramics (e.g. superconducting materials), the fluid (e.g. coupling water) must be cooled to assure the steady generation of the desired particle composition.[12]

Electrospray

Electrosprays, contrary to traditional atomizers and nebulizers, generate monodisperse droplets with a relatively small diameter and high concentration but rather low throughput (typically, a few ml/h). Their largest application is mass spectroscopy of biomolecules.[13] A well written treatise on electrosprays is given by Gomez and Deng.[14]

Here the energy needed to create the droplets is provided electrostatically. Typically liquid is fed through a capillary while an electric field is created between the capillary and a coaxial ring just below. At an appropriate voltage, the field distorts the dripping liquid meniscus into the so-called Taylor cone.[15] Taking into account that the surface of this cone is an equipotential surface (otherwise the difference of potential would induce the flow of electric charge and, following that, the deformation of the cone), its semi-vertical angle is equal to 49.3°. If the electric field is higher than a critical value, flow is induced resulting in ejection of liquid from the tip of the cone (jet formation). This jet breaks down into small, highly charged droplets (Figure 4.1.5). The maximal electric charge, q_R, that can be carried by the droplet is determined by the so-called Rayleigh limit:

$$q_R = 2\pi(2\varepsilon_0 \sigma d_p^3)^{1/2}$$

where

ε_0 denotes vacuum permittivity
d_p is a droplet diameter

Hinds gives the maximal electric charge also in terms of absolute (dimensionless) number of charges.[5]

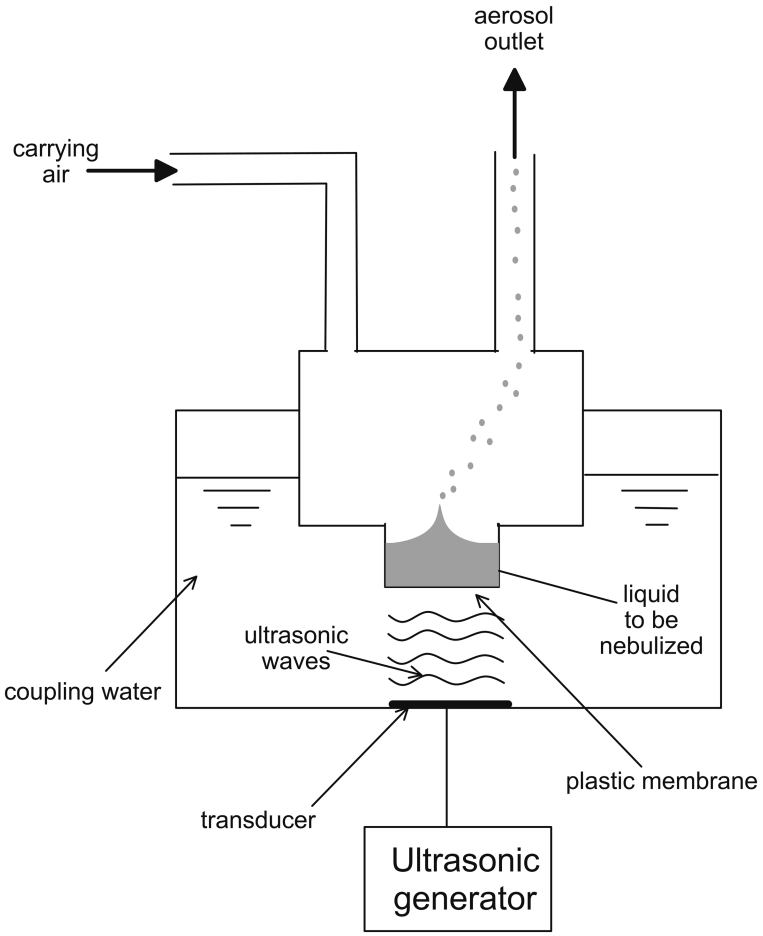


FIGURE 4.1.4 Ultrasonic nebulizer.

If the electric charge on a droplet exceeds this limit, e.g. during droplet evaporation,[16] this droplet becomes unstable and breaks down into smaller droplets or very small satellite droplets detach themselves from the main droplet. Such a cascade of breakups may produce finer and finer droplets. The beauty of electrospray (monodisperse droplets) has attracted a lot of interest in a spectrum of applications for synthesis of nanoparticles and pharmaceutical aerosols[17] but most commonly for instrument validation[18] or film deposition.[19]

Centrifugal Atomizer (Spinning Disk Aerosol Generator)

This device (Figure 4.1.6) disperses a liquid that is supplied to the top surface of a rapidly rotating (spinning) disk into ligaments that break into droplets.[20] The spinning disk may be driven by a motor (more typically) or pneumatically. The droplets may be then dried or solidified to form solid particles. Centrifugal atomization has been successfully applied for processing many kinds of metal powders such as Sn, Pb, Al, Mg, Zn, Ti, Ni, Co and their alloys.[21] The median diameter of droplets, d_p is given by[20,22]:

$$d_p = (6\sigma / \rho_L \eta \omega^2 R)^{1/2}$$

where

- ω is the angular speed
- R is the atomizer disk radius
- η the efficiency of centrifugal atomization (~0.005)

The consumed power used in atomization can be estimated as:

$$P = 6\sigma Q / \eta d_p$$

where Q denotes the melt (liquid) flow rate. Disk diameters are ranging from 2 to 8 cm and the angular velocities from 100 to 10^5 rad/s. Droplets are produced typically at a rate of 10^6 to 10^8 particles/min and dispersed into a gas flow smaller than 1 m^3/min. The standard deviation of the droplet size is often close to one.[21] Sometimes during the formation of droplets leaving the spinning disk, much smaller "satellite droplets" are formed. Some centrifugal atomizers eliminate satellite droplets from the product aerosol by surrounding the disk with a small sheath flow. Only droplets that are large enough to penetrate through the sheath flow are used.

Vibrating Orifice Aerosol Generator (VOAG)

This type of generator is based on the instability of capillary jets that disintegrate into droplets. This disintegration may be

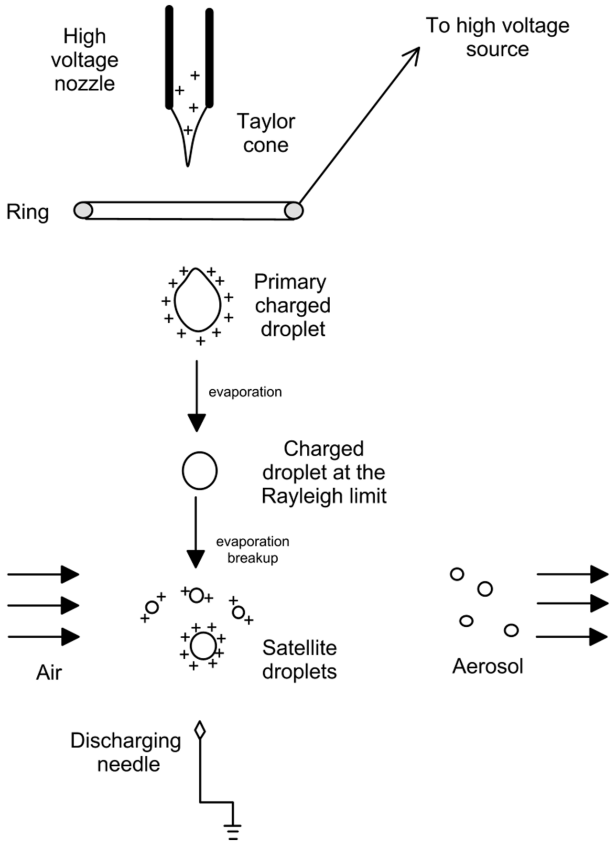


FIGURE 4.1.5 Principle of operation of electrospray atomizers.

caused by the harmonic excitation of a capillary jet resulting in very uniform droplets. The product droplet size depends on the volumetric flow rate of the liquid Q and the excitation frequency, f by[24]:

$$d_p = (6QC / \pi f)^{1/3}$$

where C denotes the volumetric concentration of a nonvolatile compound in the liquid – i.e. solids.

The most common version of the vibrating orifice aerosol generator (VOAG) has been introduced by Berglund and Liu.[25] In the VOAG, a piezoelectric crystal directly vibrates the orifice, thereby generating an acoustic wave which propagates along the capillary jet which is formed by forcing the liquid through the orifice.

One of the most popular devices of this kind was the Vibrating Orifice Aerosol Generator Model 3450 by TSI. This generator operates at a frequency between 1 kHz and 1 MHz and generates droplets with a diameter of up to 200 µm while the geometric standard deviation is below 1.01. The production of this model ended in February 2018. With the VOAG generator it was difficult to obtain droplets smaller than 25 µm in diameter as small orifices were susceptible to clogging. Moreover, using such a small orifice requires the use of relatively high pressure that may also lead to its mechanical damage.

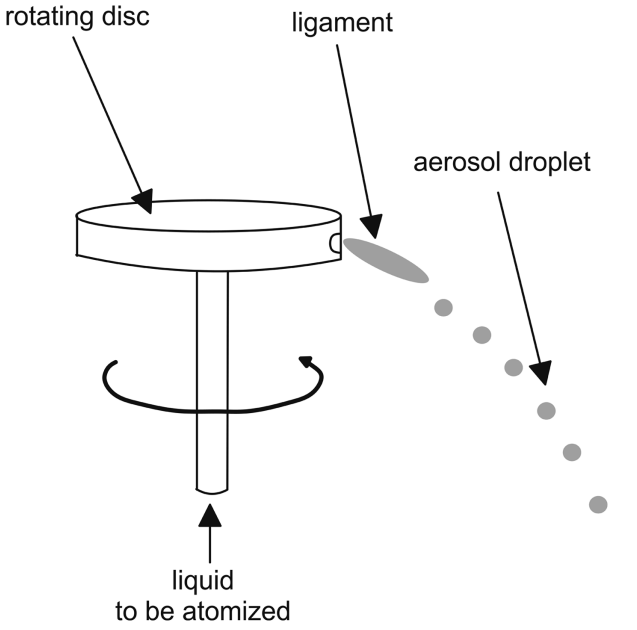


FIGURE 4.1.6 Schematic of the centrifugal atomizer (Adapted from Sungkhaphaitoon et al., *Int. J. Appl. Phys. Math.*, 2, 77–82, 2012.)

Flow-Focusing Monodisperse Aerosol Generator (FMAG)

In this generator the capillary jet is first formed from a nozzle with a relatively large diameter (over 100 µm) and then stretched by flow-focusing air (Figure 4.1.7) through the cylindrical space around the nozzle resulting in the so-called "flow-focusing."[26] The FMAG is also equipped with a piezoelectric crystal which has the same function as in VOAG – vibrations generate acoustic waves inside the jet, leading to its disintegration. The dependence of a generated droplet diameter on liquid flow rate (which is indirectly dependent on flow-focusing air pressure) and excitation frequency is the same as with the VOAG. Compared to VOAG, the FMAG may generate the droplets with a wide range of diameters without exchanging the orifice and with low shear stress inside the jet. The last feature facilitates the application of FMAG to bioaerosol generation. The FMAG is now produced by TSI under the name of Model 1520. This generator allows for the production of droplets with a diameter equal to 0.8–10 µm and geometric standard deviation below 1.1.

4.1.2 CONDENSATION METHODS

Depending on the state of product aerosol one can distinguish two condensation methods. The first and more intuitive is the generation of mist, a suspension of small liquid droplets. The second is fume generation referring to the production of solid particles by vapor cooling.

Generation of Mists

Mists consist of small droplets (with a diameter up to 50 µm) suspended in air or other gases. Formation of mists may be

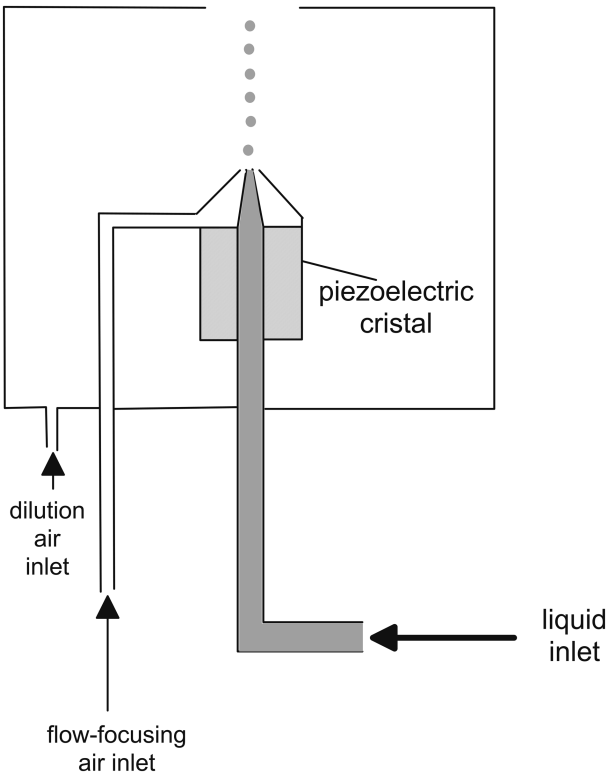


FIGURE 4.1.7 Flow-focusing monodisperse aerosol generator.

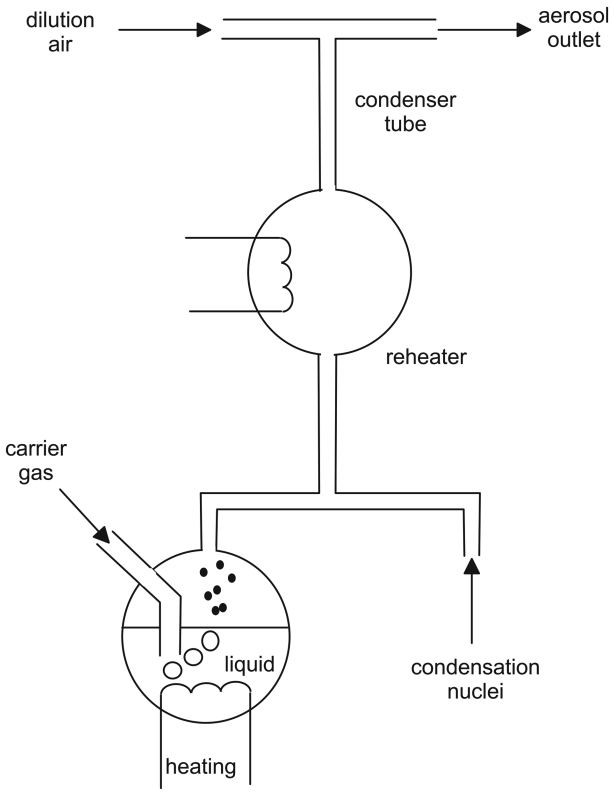


FIGURE 4.1.8 Mist generator developed by Sinclair and LaMer.[27]

accidental as they form when the partial pressure of vapor exceeds its saturation value. So, the main mechanism leading to mist formation is cooling a gas containing a vapor because the saturation vapor pressure drops with decreasing temperature. Formation of mist is promoted almost always by the presence of condensation nuclei – small solid particles of submicron diameter usually. So, mist formation includes the following steps:

- evaporation of a liquid into carrier gas
- mixing of that vapor/gas mixture with condensation nuclei (usually followed by reheating the mixture to avoid uncontrolled condensation)
- chilling the mixture resulting in mist formation.

The goal of this method is the generation of a stable aerosol (i.e. with size distribution constant over the time). The issue of condensation nuclei needs attention. Solid particles which may play the role of condensation nuclei are usually present in the surrounding gas before the start of condensation (e.g. 10^3–10^4 even in clean room air), but their concentration and size distribution may not be constant over time. Thus, in most mist generators the carrier gas is purified from solid particles and solid nuclei are added after liquid evaporation.

One of the most popular devices is the Sinclair-LaMer condensator[27] and its numerous modifications (Figure 4.1.8). It consists of a source of vapor which enables a nearly constant vapor concentration in the carrier gas. The source of vapor is a tank filled with liquid which is heated to a temperature at which evaporation at the desired amount takes place. In some other generators, e.g. that by Rapaport and Weinstock,[28] vapor is obtained by evaporation of atomized liquid droplets. The generated vapor is seeded (i.e. mixed with solid nuclei) for condensation. Usually, these are small particles of metals or mineral salts, responsible also for the formation of mists and clouds in nature. Then, the mixture of vapor and nuclei is homogenized by reheating (e.g. flow through an oven) and enters a condenser tube where condensation of vapor on solid particles takes place.

The mist generation as described above results in droplets with size distribution close to monodisperse one (geometric standard deviation less than 1.2) with average size 0.3–10 μm and total number concentration 10^4–10^6/cm^3. The specific value of the above aerosol characteristics depends on the operational parameters of the generator, mainly carrier gas flow rate, temperature of vapor source, reheater and cooling tube as well as the concentration of condensation nuclei.

Among many modifications of the Sinclair-LaMer condensator it is worth describing the Prodi generator[29] which is used for the generation of solid aerosol particles. In this apparatus, a liquified material fills the thermostated bubbler. Carrying gas (which is usually pure nitrogen) with condensation nuclei is bubbled through the liquid and then the whole mixture goes through a reheater where, except of mixture homogenization, evaporation of small entrained droplets take place. Subsequent slow cooling down of the mixture results in formation of aerosol particles that are nearly monodisperse (geometric standard deviation up to 1.15) with micron-size diameter and spherical in shape. Particle size

and concentration may be influenced mainly by adjusting the bubbler temperature.

Fume Generation

In industrial practice the term "fume" is reserved for aerosols of solid particles made from metals, ceramics or salts. These particles are produced by the evaporation of the desired material followed by the condensation of their vapors. Fume generation takes place by the heating of the material of interest at a high enough temperature for adequate and efficient evaporation. This is done by electrical resistance heaters, infrared ovens, high-frequency induction furnaces as well as devices using thermal plasma or pulsed laser ablation. After evaporation, the cooling of vapor takes place resulting in the desired aerosol by homogeneous nucleation. Contrary to generators described in the previous paragraph, there is no seeding of vapor with condensation nuclei so rather broad size distributions of agglomerates (physically bonded) or aggregates (chemically bonded) of primary particles are obtained. To promote the formation of ultrafine particles with a diameter less than 100 nm, cooled vapor is diluted by cold inert gas.[30]

Inert Gas Condensation

A variety of metal nanoparticles are made for a spectrum of niche applications by the so- called inert gas condensation (IGC) technique[31] that is credited to igniting the field of nanotechnology worldwide originally with the formation of materials with superior mechanical properties due to their nanostructure. Early on Pfund[32] and Burger and van Cittert[33] made Bi and other metal nanoparticles by evaporating the corresponding metals at low pressure. These nanoparticles were formed by homogeneous nucleation, condensation and coagulation and were transported by free convection to a cold surface where they were deposited by thermophoresis. Since these early experiments, direct evaporation of metals from heated crucibles into a gas has been widely studied.[31] By melt evaporation in helium, Yatsuya et al.[34] made Al particles that grew for increased inert gas pressure, evaporation temperature and residence time.

In a heavily cited paper, Granqvist and Buhrman[35] similarly made more than a dozen metal nanoparticle compositions largely in the form of agglomerates. They found that all constituent primary particles made at the low pressures of IGC had a geometric standard deviation of 1.48 +/– 0.12 that is very close to that of the self-preserving size distribution by coagulation in the free-molecule regime, 1.46.[36] Andres et al. proposed the use of forced convention for IGC scale-up that was adopted by Siegel[38] and his spinoff Nanophase that manufactures an array of nanomaterials today. Haas et al.[39] introduced forced convention to classic IGC for the synthesis of pure metal and alloy nanoparticles by directing an inert gas jet above the heated crucible. Detailed fluid mechanics and particle dynamic simulations also showed the dominance of coagulation even at these short residence times of forced convention IGC due to high particle concentrations employed.[40] Today this technology is driven by specialized companies (spinoffs) for niche markets of nanomaterials.

4.1.3 POWDER DISPERSION

Powders can be dispersed into an air flow by a variety of methods. In general, already a simple air flow over a powder bed results in the dispersion of particles and aerosol formation that sometimes is referred as aerosol entrainment. A typical manifestation in nature are the so-called sand-storms and dust-storms that reduce visibility and can ruin fertile lands. In controlled aerosol generation by powder dispersion, the main difficulty is to ensure the stability over time of the resulting aerosol size distribution (mean particle diameter and standard deviation). In many applications like filter testing or inhalers it is important that these parameters not only have a certain value but also that they remain constant over time.

An example of such a device is the Wright dust feeder (Figure 4.1.9). There, powder that has been compacted into a rotating cup is scraped away by a scrapper blade and entrained into a carrier gas flow. A similar arrangement is used in brush generators provided e.g. by PALAS GmbH under the name RGB systems. The filled solid material tank is introduced into the RGB dispersing head, and the powder which is thus uniformly compressed at the filling level, is transferred to a rotating brush with a precisely controlled feed rate.

A great difficulty concerning solid aerosol generation is preventing the formation of agglomerates (which may appear when particles are held together by physical forces, e.g. electrostatic, van der Waals, etc.). Even if we are able to obtain highly monodisperse particles, they may interact by means of attractive forces and form agglomerates consisting of few or more single (primary) particles. This is especially important for inhalers. Here, particles – more or less monodisperse – are

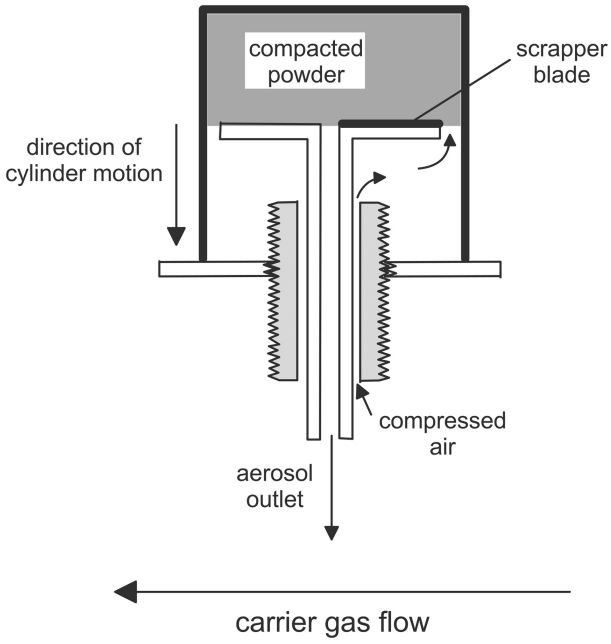


FIGURE 4.1.9 Schematic of the Wright dust feeder.

stored in powder form and are then dispersed by the device. To minimize the risk of agglomerate entrainment, various solutions are used. In most of them the agglomerates are broken up by means of shear stresses (arising from the gradient of gas velocity) and the collisions with other agglomerates and device walls.[41] To break an agglomerate one has to overcome the adhesion forces acting between single particles and/or aggregates. The required shear stress is defined as critical shear stress and is given as[42]:

$$\tau_c = \phi k_n F_{ad} / \pi d_p^2$$

where ϕ denotes the packing density of particle agglomerate, F_{ad} – the adhesion force acting between primary particles with diameter d_p and k_n – the mean particle coordination number in agglomerate (varying from about one for very open or linear agglomerates up to over a dozen for the closest packing density). So, agglomerates will break when the shear stress inside the generator exceeds τ_c. The most popular device elements generating shear flow are eductors, nozzles, Venturi tubes or orifices.[42] In some devices, e.g. inhalers, turbulence promoters are mounted to generate a turbulent flow.[43]

REFERENCES

1. Ashgriz, N., *Handbook of Atomization and Sprays. Theory and Applications*, Springer, New York, 2011.
2. Lefebvre, A. H., McDonell, V. G., *Atomization and Sprays*, Taylor & Francis, Boca Raton, 2017.
3. Merkus, H. G., Meesters, G. M. H. Eds., *Production, Handling and Characterization of Particulate Materials*, Springer, Switzerland 2016.
4. Reed, K. E., Low drift spray nozzle. US Patent 3,934,823, October 12, 1973.
5. Hinds, W. C., *Properties, Behaviour and Measurement of Airborne Particles. Aerosol Technology*, John Wiley and Sons, New York, 1992.
6. Liu, B. Y. H., Lee, K. W., *Am. Ind. Hygiene Assoc.*, 36, 861–865, 1975.
7. Laskin, S., *Submerged Aerosol Unit*, AEC Project Quarterly Report UR-38, University of Rochester, 1948.
8. Gac, J. M., Jackiewicz, A., Werner, Ł., Jakubiak, S., *Sep. Pur. Technol.*, 170, 234–240, 2016.
9. Kusters, K. A., Pratsinis, S. E., Thoma, S. G., Smith, D. M., *Chem. Eng. Sci.*, 48, 4119–4127, 1993.
10. Mercer, T. T., *Arch. Intern. Med.*, 131, 39–50, 1973.
11. Okuyama, K., Kousaka, Y., *Powder Technology Handbook*, 1st Ed., Iinoya, K., Gotoh, K., Higashitani, K., Eds., Marcel Dekker, New York, 1991.
12. Lyons, S. W., et al., *J. Mater. Res.*, 7, 3333–3341, 1992.
13. Fenn, J. B., et al., *Science*, 246, 64–71, 1989.
14. Gomez, A., Deng, W., *Techniques and Applications*, 3rd Ed., Kulkarni, P., Baron, P. A., Willeke, K., Eds., John Wiley & Sons, Inc., Hoboken, New Jersey, 2011.
15. Hartman, R. P. A., et al., *J. Aerosol Sci.*, 31, 65–95, 2000.
16. Wilhelm, O., Madler, L., Pratsinis, S. E., *J. Aerosol Sci.*, 34, 815–836, 2003.
17. Almeria, B., Deng, W. W., Fahmy, T. M., Gomez, A., *J. Colloid Interface Sci.*, 343, 125–133, 2010.
18. Kirsch, A. A., *Colloid J.*, 79, 61–75, 2017.
19. Siefert, W., *Thin Solid Films*, 120, 267–274, 1984.
20. Zhao Y. Y., *Materials & Design*, 27, 745–750, 2006.
21. Dunkley J. J., Aderhold, D., *Proc. Int. Conf. Powder Metal. Particulate Mater.*, Colorado, pp. 26–31, 2006.
22. Gonsrang, S., Plookphol, T., Wisutmethangoon, S., in 4th International Conference on Engineering Technology - ICET 2009, Novi Sad, April 28–30, 2009.
23. Sungkhaphaitoon, P., Plookphol, T., Wisutmethangoon, S., *Int. J. Appl. Phys. Math.*, 2, 77–82, 2012.
24. Mitchell, J. P., Snelling, K. W., Stone, R. L., *J. Aerosol. Sci.*, 18, 231–243, 1987.
25. Berglund, R. N., Liu, B. Y. H., *Environ. Sci. Technol.*, 7, 147–153, 1973.
26. Duan, H., et al., *Aerosol. Sci. Technol.*, 50, 17–25, 2016.
27. Sinclair, D., LaMer, V. K., *Chem. Rev.*, 44, 245–267, 1949.
28. Rapaport, E., Weinstock, S. E., *Experimentia*, 11, 363–364, 1955.
29. Prodi, V., *Assessment of Air-Borne Particles*, Charles C. Thomas Publ., Springfield, IL, 1972, p. 169.
30. Homma, K., *Industrial Health*, 4, 129–137, 1966.
31. Gleiter, H., *Prog. Mater. Sci.*, 33, 223–315, 1989.
32. Pfund, A. H., *Review Sci. Instrum.*, 1, 397–399, 1930.
33. Burger, H. C., van Cittert, P. H., *Zeitschrift Fuer Physik*, 66, 210–217, 1930.
34. Yatsuya, S., Kasukabe, S., Uyeda, R., *Jpn. J. Appl. Phys.*, 12, 1675–1684, 1973.
35. Granqvist, C. G., Buhrman, R. A., *J. Appl. Phys.*, 47, 2200–2219, 1976.
36. Landgrebe, J. D., Pratsinis, S. E., *Ind. Eng. Chem. Res.*, 28, 1474–1481, 1989.
37. Andres, R. P., et al., *J. Mater. Res.*, 4, 704-736, 1989.
38. Siegel, R. W., *Annu. Rev. Mater. Sci.*, 21, 559–578, 1991.
39. Haas, V., Gleiter, H., Birringer, R., *Scripta Metallurgica et Materialia*, 28, 721–724. 1993.
40. Tsantilis, S., Pratsinis, S. E., Haas, V., *J. Aerosol Sci.*, 30, 785–803, 1999.
41. Calvert, G., Ghadiri, M., Tweedie, R., *Adv. Powder Technol.*, 20, 4–16, 2009.
42. Masuda, H., Gotoh, K., *Adv. Powder Technol.*, 6, 305–315, 1995.
43. Gac, J., Sosnowski T. R., Gradoń, L., *J. Aerosol Sci.*, 39, 113–126, 2008.

4.2 Generation of Particles by Reactions

Kakeru Fujiwara and Sotiris E. Pratsinis (4.2.1)
Hisao Suzuki (4.2.2)

4.2.1 GAS-PHASE (AEROSOL) TECHNIQUES

Making particles by gas phase chemical reactions is a fascinating process. It makes some of the most widely used fine particulate commodities (e.g. carbon black, pigmentary titania, optical fibers, filamentary Ni, ferrites, fumed silica, etc.) and sophisticated nanomaterials (e.g. nanosilver, biomedical carbon-coated cobalt particles selling for $200/g). At the same time, this process is responsible for the generation of air pollutants (e.g. soot) with profound effects on human health and environment (climate, visibility). As a result, it attracts keen interest from various scientific fields and many sectors of applications.

In the context of classic particle technology and chemical reaction engineering, the reactors employed for synthesis of these powders are most closely related to lean phase fluidization with pneumatic transport as the solids volume fraction is very low, less than 10^{-3} even at production rates[1] of 25 t/h. The text by Friedlander[2] provides a lucid account of the fundamentals while the book of Kodas and Hampden-Smith[3] details various processes for aerosol synthesis of materials. The history of the industrial development of the above commodities has been summarized[4] and the in-situ (laser) diagnostics for the characterization of such particles have been reviewed.[5] A summary of processes for gas-phase synthesis of materials has been given[6] while the fundamentals for multi-scale design of such processes have been presented quantitatively.[7] Athanassiou et al.[8] have shown how chemical engineering facilitates gas-phase synthesis of nanoparticles. The impact of aerosol processing in heterogeneous catalysis has been brought forward by a review[9] of nearly 500 articles with Koirala et al.[10] highlighting the role of scalable flame aerosol technology in catalyst synthesis and Fujiwara et al.[11] pointing out the significance of strong metal-support interactions in such catalysts. Aerosol particle technology is attractive for the assembly of devices[12] (nanogenerators, battery and fuel cell electrodes) and most notably for highly selective chemoresistive gas sensors for breath analysis.[13]

Here a summary of the fundamental phenomena and main processes for particle synthesis by gas-phase reactions is provided along with references for more detailed coverage of specific aspects.

4.2.1.1 Advantages and Disadvantages

Making particles in the gas phase has distinct advantages[14]:

1. Liquid byproducts are not generated requiring costly cleaning and disposal (e.g. "chloride" vs. "sulfate" process for manufacture of pigmentary TiO_2).
2. Collection of particles from gases is easier and less expensive than from liquids.
3. Fewer unit operations are required than wet-chemistry ones.
4. Ultrapure products can be made (e.g. optical fibers).
5. Materials with unique (e.g. filamentary) morphology can be made.
6. Stable synthesis of metastable phases is possible.
7. Operating in the gas-phase facilitates process design from first principles.
8. Scale-up to tons/h is proven.

There are however certain disadvantages[3,10]:

1. Capital investment is needed even for simple exploration of tiny quantities (hoods, controls, filters, etc.)
2. Safety must be closely observed as particles in gases can easily escape and be inhaled while operating at high temperatures requires close attention.
3. Low-cost precursor availability, preparation and handling is not always trivial.
4. Assuring product composition and uniformity requires thorough process design as on-line monitoring of particle characteristics is practically impossible during their large-scale manufacture.
5. Particles are typically more polydisperse than those made by wet-chemistry processes.

Exploiting the advantages while suppressing or, at least, mitigating the disadvantages, determines success for a particular product and process.

4.2.1.2 Particle Formation

Particles can be made by chemical reactions either in the gas-phase, the so-called gas-to-powder conversion route (Figure 4.2.1), or within suspended aerosol droplets in gases, the so-called droplet-to-powder conversion route. In either case, to initiate and/or sustain the chemical reactions heat is provided by various means (electric, chemical, laser, plasma) that define the actual reactor configuration as discussed below in more detail. The route distinctly affects the product particle characteristics. In gas-to-powder conversion, particles are made by a bottom-up sequence (molecules → clusters → particles) that result in compact or ramified (fractal-like) solid particles. In the droplet-to-powder route a top-down sequence takes place (droplets → particles) resulting in solid, fibrous, porous, hollow or shell-like particles.

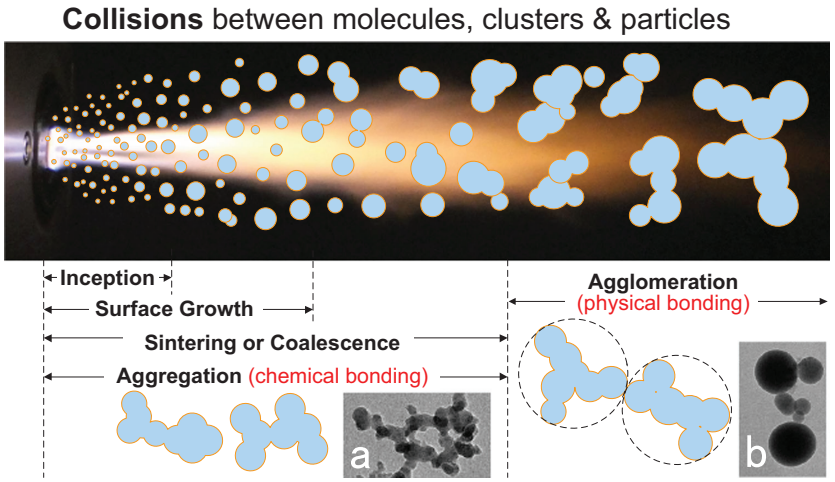


FIGURE 4.2.1 Schematic depiction of particle formation by gas-to-particle conversion delineating the ongoing physical phenomena and particle morphology[7] along with microscopic images of TiO_2 aggregates (a) and agglomerates (b) made by open and enclosed spray flames,[31] respectively.

Sometimes precursors are fed as droplets that fully evaporate so particles are formed solely by gas-to-powder conversion (e.g. carbon black by the so-called "furnace process"). In the development of new products, however, it is not uncommon to form particles by both routes when droplets are fed to a reactor. This is usually quite undesirable and should be avoided by appropriate process design and operation.

Gas-to-Powder Conversion

Figure 4.2.1 shows a schematic of particle formation by gas-to-powder conversion overlaid on a flame. This is typical for manufacture of most of the above commodities and new materials. Usually such particles are formed by gas-phase reactions such as decomposition, oxidation, reduction, nitridation etc. of a precursor (hydrocarbon, $SiCl_4$, $TiCl_4$ or $Ni(CO)_4$ etc.) at high temperatures. Initially numerous chemical species (radicals, oxychlorides, aliphatics, aromatics etc.) are generated leading to creation of a multitude of molecular clusters and/or nuclei that rapidly grow into particles by collisions with each other (coagulation) and chemical reactions with gaseous species (e.g. condensation, surface or epitaxial growth).

At the initial stages of particle formation, small and rather compact particles are created (few nm in diameter). As particles grow larger and/or process temperature drops, their coalescence (sintering or fusion) rate slows down and can become comparable (typically within a factor of 10) to their (ongoing) coagulation rate. Then partially fused or dumbbell-shaped structures (Figure 4.2.1a) are formed as the colliding particles are held together by strong chemical forces (e.g. covalent, ionic bonds). The resulting structures are called aggregates while their constituent particles, primary particles (PPs). When coalescence stops completely and/or gaseous precursors are exhausted, colliding particles (single or aggregated PPs) can be held together by weak physical forces (van der Waals, electrostatic, magnetic etc.) resulting in the so-called agglomerates (Figure 4.2.1b). When the number of constituent PPs follows a power law with the agglomerate radius of gyration (or mobility radius), they are referred as fractal-like particles.

Agglomerates are attractive for suspensions (e.g. paints, slurries) and polymer nanocomposites because they can be broken readily into their constituent smaller aggregates and/or PPs by ultrasonication, high-pressure dispersion etc. On the other hand, aggregates are most attractive for electroceramics (sensors, battery or fuel cell electrodes) as they do not suffer electric losses by contact resistance. They are also attractive for catalysts and lightguides as upon assembly of pellets and preforms, respectively, aggregates form large openings (interparticle pores) that facilitate the transport of fluids to/from the particle surface inside the preform.

Droplet-to-Powder Conversion

Manufacture of micron to submicron sized ceramic particles and most notably ferrites is typically carried out by this route which is similar to spray drying or granulation. In the literature this is referred to as spray pyrolysis or spray roasting or aerosol decomposition. Typically precursor droplets (generated by any of the processes given in the previous chapter) flow through a high temperature chamber to drive the chemical reactions within the droplet components and/or the carrier gas. Particle formation takes place within the droplet as it evaporates. If nucleation and precipitation takes place at the droplet surface, hollow or cenosphere-like particles are formed that can rupture into shell-like fragments. Otherwise solid particles are formed that can have a highly porous surface. A characteristic of this route is that the droplet size affects the size of product particles that tends to be polycrystalline unless high temperatures and long residence times are involved. The textbook of Kodas and Hampden-Smith[3] has provided a thorough account of droplet-to-powder conversion processes.

4.2.1.3 Control of Particle Size Distribution and Morphology

As in every chemical reactor, product characteristics (e.g. size distribution, morphology, crystallinity etc.) are determined by reactant concentrations and reactor residence time (that

depends on the process temperature and velocity profiles). So, their impact on chemical reaction rate, coalescence and coagulation rate determines product particle characteristics. In particle synthesis by gas-to-powder conversion typically high temperatures, steep temperature gradients and high particle concentrations are involved.

Residence Time

As particle growth takes place in high temperatures, the residence time there, the so-called high temperature particle residence time (HTPRT), is of importance.[7] For example, the mean TiO_2 PP diameter (or specific surface area, SSA) is determined when chemical reaction, coalescence and coagulation take place. When only coagulation takes place, agglomerates are formed that can be re-dispersed to their constituent PPs and aggregates (e.g. by ultrasonication or high-pressure dispersion). So, the HTPRT for the primary particle size during gas-phase synthesis of TiO_2 starts with the onset of particle formation and ceases with the end of sintering or coalescence. The start of HTPRT can be defined by the onset of precursor conversion ($TiCl_4$ oxidation) as determined by monitoring the infrared signal of $TiCl_4$. The end of HTPRT can be determined by monitoring when the PP size (or SSA) of TiO_2 stops to change[15] by monitoring it by small angle X-ray spectroscopy or thermophoretic sampling and microscopy (or by nitrogen adsorption). If the goal is to attain a specific crystal size and composition, the HTPRT could be different and typically longer than the above for the PP size. This is a reason, for example, that amorphous fumed SiO_2 reactors (for PP size 5–50 nm) are a few meters long while those of pigmentary rutile TiO_2 (PP diameter 200–250 nm) are much longer (e.g. 100 m).[4]

Controlling the HTPRT controls product particle sizes, morphology and composition. For example, increasing precursor concentration, process temperature and pressure will always increase agglomerate size but PP and aggregate sizes will only increase as long as gas phase reactions and/or coalescence take place also. Suppression of aggregate formation is possible by drastic change of the ratio of characteristic times for particle coagulation to coalescence e.g. by steep cooling rates at constant particle concentration[15] or steep reduction of particle concentration at constant cooling rate.[16] Other process variables (e.g. doping, electric fields) that affect these characteristic times can have similar effects as has been demonstrated in gas-to-powder conversion reactors (flame, hot-wall and plasma).

Size Distribution and Structure

Besides average particle size, particle growth by rapid coagulation facilitates rapid attainment of their self-preserving size distribution (SPSD).[17] This means that particles grow but the shape of their size distribution is intact. For instantly coalescing upon collision spherical particles, the number-based geometric standard deviation, σ_g, is about 1.45.[18] This holds also for the primary particle (PP) size of agglomerates. For example, Granqvist and Buhrman[19] made a dozen metallic particles by inert gas condensation and found the σ_g, of PPs to be 1.48 ∓ 0.12 regardless of composition! In contrast, for aggregates with significant necking between PPs, the σ_g of PPs can become much narrower and nearly monodisperse.[20] Coalescence is faster for smaller particles similar to condensation, red-shifting the small tail of the size distribution and making such powders to exhibit quantum dot behavior.[21]

For agglomerates the σ_g of their SPSD is larger than the above of spherical particles, 2 or 2.3, based on their mobility radius or radius of gyration, respectively, in the free-molecular regime.[22] The SPSD is attained when the average particle size becomes 2–3 times the initial particle size or that reached at the end of new particle formation.[18] The SPSD facilitates enormously the quantitative description of particle growth by coagulation as the total particle concentration, N, can be obtained by assuming a unimodal (e.g. monodisperse) size distribution:

$$dN/dt = -\beta N^2$$

The collision frequency, k, depends on particle size, shape, temperature and pressure and detailed expressions can be found in textbooks.[2] The simplest is for spherical particles in the continuum regime, $\beta = 4k_BT/3\ \mu$, where k_B is the Boltzmann constant, T the temperature in K and μ the gas viscosity. For particles having attained the SPSD, one has to replace 4 by 4.3 in β.

By a mass balance, the average particle size can be determined from N while the entire size distribution can be obtained by scaling to that size the corresponding SPSD for that size regime (continuum or free molecular) and particle shape (sphere or fractal-like). Kruis et al.[23] have developed a monodisperse model for fractal-like particle coagulation-coalescence from the free molecule to continuum regime that has been used for aerosol reactor design for a wide array of ceramic and metallic particle compositions.

The high particle concentrations facilitate also the rapid attainment of the asymptotic, so-called fractal-like structure (fractal dimension, D_f) of agglomerates. When agglomerates are made of monodisperse PPs, the D_f of 1.91 or 1.78 is attained (in the free molecular and continuum regime, respectively) by the time the agglomerate grows to within 2–3 times the PP size (10–15 PPs per agglomerate). As the PPs distribution broadens, it takes longer to attain that D_f. For example, for spherical PPs having their SPSD (e.g. $\sigma_g = 1.45$), attainment of the above D_f requires agglomerates containing 35–50 PPs on the average.[22]

4.2.1.4 Hot-Wall Flow Reactors

In these reactors the required high temperature for driving the chemical reactions for particle formation is provided by external heating of the reactor walls.[3] These reactors and processes come with several names in the literature. For example, when the particle precursor is fed in the vapor form (e.g. by bubbling a carrier gas through its liquid) to the reactor, this process is called high temperature (aerosol) flow reactor, chemical vapor synthesis or condensation (a derivative from chemical vapor

deposition widely used in film deposition). When droplets are fed to the reactor by the generators of the previous chapter and droplets fully evaporate, then the process is called spray pyrolysis or roasting or aerosol decomposition etc.

These reactors are most attractive for basic measurements (e.g. overall sintering[24] or reaction rates) as well as product development[3] due to their well-defined temperature profiles and residence time distributions. Various commodities are made commercially in these reactors: ferrites by spray pyrolysis, lightguide preforms by modified chemical vapor deposition (MCVD), filamentary Ni by $Ni(CO)_4$ decomposition, WC for coating of drilling bits by the carbothermal reduction etc. Typically precursor gases and/or droplets flow into an externally (e.g. electrically) heated tube (the hot-wall reactor) in which particles are formed by chemical reactions. Usually particles are collected downstream by baghouse filters or onto the reactor wall (e.g. lightguide preforms by MCVD). These reactors have been used for the laboratory-scale synthesis of an array of materials like Si for photovoltaic applications and SiC and AlN for structural ceramics in addition to ultrafine alumina, zirconia, silica and titania to name a few. These reactors are used also for the extraction of basic properties for process design as, for example, overall reaction rates leading to particle formation: $SiCl_4$ oxidation for manufacture of optical fibers, and $TiCl_4$ or titanium tetra-iso-propoxide (TTIP) oxidation for particles or films. Such data facilitate the development of quantitative models for particle formation in every aerosol reactor without adjustable parameters as with the deposition efficiency of lightguide preforms made commercially in MCVD reactors[25] and the evolution of spherical titania particle size distribution.[26]

4.2.1.5 Flame Reactors

These reactors are used exclusively in the manufacture of carbon blacks and fumed silica. They are the major processes also for the manufacture of optical fibers, pigmentary and photocatalytic titania as well as other oxides dominating gas-phase synthesis of particles by volume and value. This is due primarily to the relatively low cost of the required energy. Here particle formation takes place usually by exothermic chemical reactions so an external energy source is not needed to sustain the process. Some reactants are preheated by oxidation of light hydrocarbon gases as in manufacture of carbon black and pigmentary TiO_2. When the precursor chemistry does not generate sufficient energy for this task, additional fuel is provided with the precursors to initiate and/or sustain the process.

Despite the broad use of these reactors, their understanding and development has been rather incremental driven by valiant Edisonian research.[4] The complexity of the temperature and velocity profiles in the highly turbulent jets of industrial units (Re ~10^6) along with the ramified structure of the resulting particles have been the main obstacles for systematic understanding of these processes.

Flame reactors are classified according to the state of the particle precursor.[27] Vapor-fed aerosol flame synthesis (VAFS) refers to oxidation or combustion (or hydrolysis) of volatile precursors (e.g. methane, ethylene, $TiCl_4$, TTIP, $SiCl_4$) by oxidant (air, oxygen) and particle formation by gas-to-powder conversion. The availability of volatile precursors at reasonable cost, however, drastically limits VAFS to only few materials.[27]

Non-volatile precursors can be used with liquid-fed aerosol flame synthesis (LAFS) that is employed in the production of carbon black by the widely used furnace process in that industry. Usually a combustible precursor solution is sprayed and ignited to give the particle product by gas-to-powder conversion. Spraying is accomplished typically by solution atomization through air-assist nozzles as described in the last chapter. For a high enthalpy-content organic solution a rather small pilot flame is used to ignite and sustain spray combustion. This is the so-called flame spray pyrolysis process (FSP). For a low enthalpy-content (i.e. aqueous) spray solution of inorganic precursors, an external flame is used as a heat source serving essentially as the hot walls of classic spray pyrolysis. This is the so-called flame-assisted spray pyrolysis (FASP).

Flame-made particles are collected with baghouse filters and cyclones. When flame-made films are desired, particles can be deposited directly on a flat plate, tube, fiber or foam substrate. Such deposition can take place at different substrate temperatures with different particle morphologies affecting film structure and texture. Using masks during deposition allows preparation of films with well-defined patterns for catalytic microsystems and gas sensors.

Recent advances in combustion aerosol characterization and process simulations have improved the understanding of material synthesis by the combustion of liquid precursors at kg/h (e.g. Gröhn et al.[28]). As a result, a wealth of new catalysts, gas sensors and biomaterials have been created[27] from various precursors[29] and most recently reviewed by M*ä*kel*ä* et al.[30] Especially, flame aerosol deposition of noble metal clusters and even, their single atoms on ceramics nanoparticle supports[31] (Figure 4.2.2) opens new frontiers in catalysis and gas sensing as it drastically minimizes the cost of such materials since very small amounts of noble metals are used. In 2017 the German Science Foundation launched the SPP1980 initiative (~6 M Euros) supporting 20 PhDs across Germany for 6 years to advance the fundamentals of FSP.[32]

4.2.1.6 Plasma Reactors

Plasma is a charged or ionized gas that is created by direct (arc) or indirect (inductive) electric discharges using high voltages. Direct are more energy efficient than indirect but can contaminate the product from the erosion of electrodes. This is important for synthesis of nanoparticles having high surface area. Plasmas reach extreme temperatures (e.g. up to 10^4 K) and decompose gases, droplets and even particle feeds down to atoms and radicals. Chemical reaction and/or condensation downstream of the plasma leads to particle formation (e.g. cooling of the plasma plume). Plasma reactors are used widely for deposition of films and hard coatings on commercial scale.[33] Mostly inductively coupled plasma reactors are used on a laboratory-scale for synthesis of an array

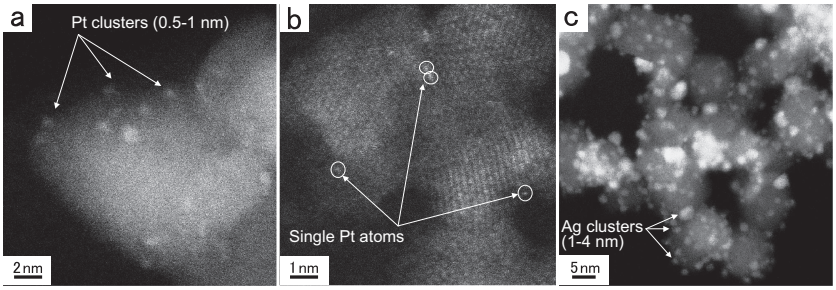


FIGURE 4.2.2 Microscopic images of flame-made (a) Pt subnano-clusters (0.4 wt%), (b) Pt atoms (0.1 wt%) and (c) Ag clusters at very high loading (30 wt%) on TiO_2. Such small clusters (a) and even single atoms (b) are stable during annealing up to 600°C in air taking advantage of strong metal-support interactions.[11]

of nanoparticles with narrow size distributions[33] with many promising applications but have been challenging for the large scale production of powders. Plasma processes for synthesis of various particle compositions and morphologies have been reviewed by Vollath[34] and Phillips et al.[35] These reactors are quite attractive for synthesis of non-oxide particles. Recently plasma reactors have been looked at closely for efficient and environmentally friendly production of carbon black and H_2 by direct conversion of hydrocarbons in the absence of oxidation, reaching 100% yields and significantly reducing CO_2 emissions.[36] This has led to the creation of new carbon black industry (Monolith) which examines them for industrial scale plasma manufacture of carbon black from natural gas.

4.2.1.7 Laser Reactors

Lasers provide the required energy to drive chemical reactions for particle synthesis at precise locations. This is accomplished by absorption of the infrared laser energy by one of the precursors or by an inert photosensitizer (e.g. sulfur hexafluoride). Laser reactors reduce wall deposits and produce high-purity powders with a fairly narrow size distribution because they confine the reaction to a small region where high temperatures and short residence times prevail. As they do not need oxygen to generate the required heat (similar to plasma reactors), they are attractive for the synthesis of metallic and nonoxide powders (e.g. carbide, nitride powders). Early research was done at MIT while significant efforts have been done in TU Delft, especially with process upscaling[37] that has been quite challenging. Focusing on the synthesis of solar silicon, a commercial process was developed by Nanogram, that was acquired by Teijin. The focused energy of lasers has been used also to fuse in-situ agglomerates of flame-made particles.[38] Lasers have been used also to evaporate materials from surfaces e.g. laser ablation. The resulting plume is brought in contact with reactants that can lead to new particle compositions.

4.2.2 LIQUID-PHASE TECHNIQUES

Preparation of powders from liquid phase is usually controlled by the two reaction processes, namely the diffusion-controlled reaction and the rate-limiting reaction. Crystallization by the diffusion-controlled reaction will be described in the next chapter. Therefore, preparation by the rate-limiting reaction is focused in this chapter. Formation or precipitation of particles and/or powders through the liquid phase occurs according to the following three steps: (1) increase in the concentration of the required cations in the solution over the saturation concentration; (2) formation of the new nuclei (embryo); (3) growth of the nuclei over the critical size to stabilize the precipitated particles. Therefore, we can classify the precipitation of powders or particles into two categories depending on the method to increase the concentration of the cations over the saturation concentrations, namely chemical reaction controlled method and physical phenomena controlled method as shown in Figure 4.2.3. As the concentration reaches a certain degree of supersaturation value, nucleation is induced and then the nuclei with a size over the critical size ultimately grow into the particles. Critical size is calculated by the following equation:

$$\Delta G = 4\pi r^3 \Delta G_V / 3 + 4\pi r^2 \gamma$$

where

ΔG_V is the bulk free energy change per unit volume
r is the radius of the particle
γ is the interfacial energy per unit volume.

Nucleation also occurs in the solution homogeneously and/or at the surface of the container inhomogeneously. Therefore, the precipitation reaction is affected by the actual experimental condition.

According to Figure 4.2.3, methods of preparing powders by the supersaturation of the concentration for the required materials could be classified into the techniques listed in Table 4.2.1 where inorganic or organic materials are separated.

Inorganic Powder

Preparation of the inorganic powders from the liquid phase contains two steps: deposition of crystalline or amorphous precursor, usually hydroxide or metal organic compound, and following heat treatment at higher temperatures for the crystallization. Depending on the deposition method of the

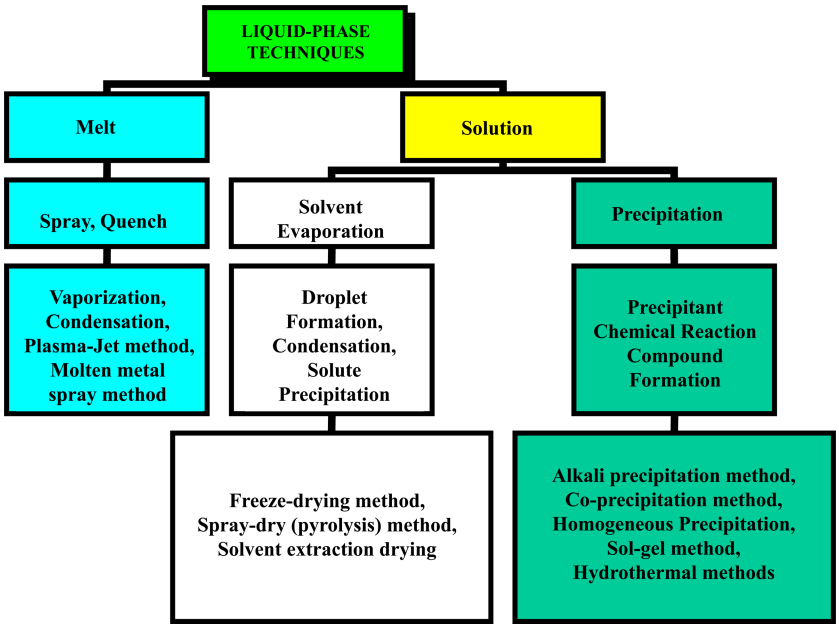


FIGURE 4.2.3 Classification of powder preparation methods from liquid phases.

TABLE 4.2.1 Preparation Methods of Powders from Solution

Inorganic Powder	
Solvent evaporation methods	Freeze drying
	Spray drying (pyrolysis)
Precipitation methods	Addition of precipitating agent
	Formation of compound
	Redox reaction
Sol-gel method	Hydrolysis and poly-condensation of metal alkoxides
Special reaction field	Hydrothermal synthesis
	Supercritical fluid
	Microemulsion
Organic Powder	
Mechanical dispersion methods	Suspension polymerization
Mixing methods	Emulsion polymerization
Interfacial reaction methods	Mini-emulsion polymerization
Capillary methods	Vibration nozzle
	Porous membrane
Phase-separation methods	Soap-free polymerization
	Micro-emulsion polymerization
	Inverse micelle polymerization
	(Nonaqueous) dispersion polymerization
	Coacervation
Other method	Seeding polymerization

precursor, the shape of the resulting particles will be different because the precursor structure depends on the preparation method and conditions. In addition, heating conditions also affect the particle size and shape of the resulting crystalline particles.

Solvent Evaporation Methods

These methods are of physical techniques; that is, the precursor solution is divided into small droplets of liquid, and the powder is formed by the evaporation of the solvent in the liquid droplets to increase the concentration over the supersaturation concentration. These methods are applicable for any multi-component solutions depending on the chemical homogeneity of the precursor solutions. The powders deposited by this process are usually spherical and/or hollow particles, and their size can be controlled by the size of the droplets and solute concentration in the precursor solution. Spray dry and spray pyrolysis methods are the usual way to prepare the spherical dense and hollow particles because the solvent in the small droplets of precursor solution is evaporated very rapidly to reach the supersaturation concentration. These two methods are classified by the operating temperature. If the operating temperature is high enough to crystallize the precursor into crystalline particles, then we call it the spray pyrolysis method. Therefore in these processes, dense and/or hollow particles are deposited depending on the deposition conditions.[39] In spray pyrolysis, a solution is atomized in a reaction tube with carrier gas n at temperatures high enough to decompose the precursor into the final oxide. Roy[40] reported a laboratory-scale process for the production of powders using this method. Usually the high temperature is provided by burning combustible solvents such as alcohol. The metal or oxide powders can be produced directly from a precursor solution by the reduced or complex reactions in hydrogen, inert gases or oxygen gases to fabricate the metal alloys or oxide powders. The homogeneity and the morphology of the resulting powders strongly depend on the structure of the precursor solutions and the spray conditions.

The spray pyrolysis method uses a high temperature to increase the concentration of the solute in the droplets by evaporating the solvent. On the other hand, there is the so called freeze drying method. In the freeze drying method, the solutions are atomized into the refrigerant, and then the sublimated the solvent to produce the dry powders, according to the equilibrium phase diagram. Therefore in this method, we can suppress the coagulation of the resultant powders to increase the specific surface area of the powders because we can deposit the metal salt directly from the solution without forming the liquid during the process by choosing the processing routes.

Precipitation Methods

In the precipitation methods, homogeneous nucleation and growth can occur in the solution, and then the LaMer model[41] is taken as the principle to produce monodispersed particles, in which the nucleation stage should be separated from the growth stage. Sugimoto[42] reviewed the particle formation process to control size and shape based on this model, with many experimental examples, including the process for organic powders. Recently, some studies for particle formation used new analytical techniques, and the results that were found could be explained by the aggregation model rather than the LaMer model.[43] However, monodispersed particles can be basically prepared according to the LaMer model. Uniform and spherical silica particles are often prepared by this technique, as reported by Stöber et al.[44] Precipitation methods are classified into the addition of precipitating agents, hydrolysis and following polycondensation, redox reaction and decomposition of the organic precursor or hydroxide and so on by the reaction type.

Techniques of the addition of precipitating agents are further classified into three categories such as (1) Alkali-precipitation method; simply adding the alkali to the metallic salt solution to form metal hydroxides or hydrous oxides, (2) Coprecipitation method; adding the alkali to the metallic salts solution with more than two metallic ions to precipitate all metallic ions in the solution at the same time by the heterogeneous nucleation mechanism, and (3) Homogeneous precipitation method; adding the urea into the metallic salt solution followed by the heating to decompose the urea into ammonia to increase the pH of the solution homogeneously. The metal hydroxide precipitates from metallic salt solution by adjusting certain pH values. When the simultaneous precipitation occurs at a certain pH value from the mixed solution of metallic ions, almost all metal hydroxides are precipitated in some cases to form a metal hydroxides mixture, because if some metallic ion was precipitated into the particles (solid) at the certain pH, then the other metallic ions with higher pH for the precipitation could be coprecipitated on the surface of the other metallic hydroxide particles in the solution by the heterogeneous nucleation mechanism. This technique is called coprecipitation. However, homogeneity of the metal hydroxides mixture by the coprecipitation method is not atomic level.

In the special case of compound formation, there is a useful precursor compound with a desired composition at molecular revel such as $BaTiO(C_2O_4)_2$ or $CaZrO(C_2O_4)_2$. The homogeneous precipitation technique is a different operation from the above techniques of the addition of precipitating agents, where precipitating agents are produced by a chemical reaction instead of an addition in the solution. For example, urea, thioacetamide or dimethyl oxalate can be used in hydrolysis as a precipitating agent, instead of ammonia, hydrogen sulfide or oxalic acid. Sacks et al.[45] reported the formation of aluminum oxide by homogeneous precipitation followed by the thermal decomposition techniques from the mixture of aluminum sulfate hydrate and urea solutions.

In the redox reaction technique,[46] fine metal particles, such as noble metals and sulfur, are produced by reducing or oxidizing the metal salt or the metal chelate complex solutions. Many kinds of complex or protective colloid agents are frequently employed to moderate the reaction speed and to stabilize the generated particles, so that highly monodispersed particles are obtained. Matijevic also reported that preparation of fine powders of some noble metals and copper, using this technique, was combined with the following technique, called decomposition of the compound.[47] Some organic compounds such as EDTA, triethanol amine, thioacetamide and urea can be used in the technique of decomposition of compound. Haruta et al. obtained molybdenum and cobalt sulfide particles by hydrolysis of thioacetamide promoted with hydrazine in ammonium orthomolybdate and cobalt acetate, respectively.[48]

Sol-Gel Method

In the sol-gel method, metal alkoxides are the common raw materials because metal alkoxides can be hydrolyzed and polycondensed to form metal-oxygen-metal bond, which is very useful as an oxide precursor to crystallize at very low temperatures. The sol-gel method or alkoxide method has the following features[49]: (1) High purity and homogeneity (solution process); (2) Low-temperature synthesis (use of the higher free energy of the resultant gel); (3) Possibility for the metastable or new compounds formation (crystallization from higher energy level); (4) Morphology control by changing the reaction mechanism, such as (a) Nano-particles, (b) Monodispersed, (c) Particles, (d) Bulk, (e) Fiber and (f) Thin films. Basically, there are three types of metal alkoxides depending on the chemical natures such as electron negativity of the metals and the characteristics of the alkoxyl groups as follows: (1) Metal alkoxide which directly form oxide and/or hydrous oxide, for example: $2B(OR)_3 + 3H_2O \rightarrow B_2O_3 + 6ROH$; (2) Metal alkoxide which form hydrous hydroxide, for example: $Al(OR)_3 + H_2O \rightarrow AlO(OH) + 3ROH$, $AlO(OH) + H_2O \rightarrow + Al(OH)_3$; (3) Metal alkoxide which cannot complete the hydrolysis and following polycondensation, for example: $Si(OR)_4 + H_2O \rightarrow SiO_{(4-x-y)/2}(OH)_x(OR)_y + ROH$. If we want to prepare the homogeneous nanoparticles of multicomponents or complex oxides, we have to control the hydrolysis and following polycondensation reactions of the alkoxides to form a homogeneously copolymerized precursor. There are three reaction control methods of alkoxides. The first one is the double alkoxide method.

Metal alkoxides are basically classified into two categories, depending on the electron negativity of the metallic ions, namely, acidic alkoxides and alkalic alkoxides, like metallic salts. Therefore, the reaction between acidic alkoxide and alkalic alkoxide results in the alkoxosalt, like neutralization reaction. In some cases, double alkoxide has same cation ratio with the crystalline oxide such as the case of the spinel [$MgAl_2O_4$; $Mg(OR)_2+2Al(OR)_3 \rightarrow MgAl_2(OR)_8$]. Such double alkoxide could be an idealized precursor of the complex oxide. The second one is the partial hydrolysis method. This method deals with the alkoxide with slow hydrolysis and plycondensation rate such as Si-alkoxide.[50] Si-alkoxide has a higher electron negativity of about 1.8 and shows a very slow hydrolysis rate, meaning the reaction control method of the alkoxide is totally different between silicate and non-silicate. In the silicate system, Si-alkoxide can be partially hydrolyzed to form a Si-O-Si bond in the precursor solution, depending on the hydrolysis conditions. On the other hand in a non-silicate system, it is relatively difficult to use partial the hydrolysis method because hydrolysis and the polycondensation rate of the metal alkoxide with lower electron negativity are very fast if compared with Si-alkoxide. Therefore, we need another method to control the reaction rate of alkali alkoxides. Double alkoxide method is one possibility, however, a more effective method is the chemical modification of the alkoxide. In this method, chelating reagent is added to the precursor solution to increase the steric hindrance of the alkoxide, leading to the reduced functional group in the metal alkoxide molecule for the reaction rate control. Matijevic developed many procedures for uniform metal (hydrous) oxide particles, and some are reviewed in such a system, for example, the formation of iron oxide.[51]

Special Reaction Field

The hydrothermal method is the method for producing crystalline metal (hydrous) oxide particles, thin films and single crystals in an aqueous solution under high temperature and high pressure. In this method, an autoclave is usually used as a reaction vessel and it takes several hours or days to produce fine metal oxide particles. If the temperature and pressure was high enough to reach the supercritical region of the solvent, solvent becomes a supercritical fluid which shows very high solubility, high reaction rate, high density and so on. Recently, Adschiri et al. proposed a new process using supercritical water and showed the synthesis time of AlOOH particles was a few minutes.[52]

The methods of particle formation using supercritical fluids are the rapid expansion of the supercritical solution method[53] and the gas antisolvent recrystallization method reported by Gallagher et al.[54] As the operating temperature is relatively low when carbon dioxide supercritical fluid is used, these methods are now being applied to make the products for the medical and food industries, which is known as the RESS method.

Ultrafine particles, which sometimes have quantum size effects, can be produced by the reaction in pools of water in (water-in-oil) microemulsions. The redox reactions can be used by mixing more than two kinds of microemulsion with the reactant in the water pool, or by adding gas or an aqueous solution into the microemulsion. Nagy et al. prepared uniform and very fine nickel boride and cobalt boride particles for catalysis, and also reviewed the formation of many metal particles.[55] Fendler's review is focused on novel particle formation by the use of a surfactant assembly, such as reversed micelles, microemulsions, vesicles and bilayer liquid membranes.[56]

Organic Powder

Organic polymer particles are produced by chemical reactions among the monomers, which are dissolved or dispersed in a solution. Dispersion methods to make monomer droplets are roughly classified into mechanical dispersion methods and phase-separation methods. The former methods need mechanical energy from agitation or pressure difference, and a dispersing agent, such as a surfactant or polymer, is often used for easy dispersion. On the other hand, the droplets of the monomer can be made spontaneously and quite stable in the latter methods.

Seeding polymerization cannot be classified within the two above methods, because the polymer particles already exist in the system. These polymer particles are used as seeds and grow by polymerization between the surface of the particles and the monomer supplied in the system.[57]

Mechanical Dispersion Methods

Suspension polymerization, emulsion polymerization and mini-emulsion polymerization are included in the mechanical dispersion methods, depending on the droplet size of the monomer. The interfacial reaction technique, which acts at the surface of the dispersed droplets, is also in this category. In this technique, microcapsules can be easily produced, because the chemical reaction rate to make solids decreases rapidly for the high diffusion resistance of the solid film already produced at the interface, and the inner materials cannot be completely converted to solid. Sometimes this technique is applied to inorganic particles, as Nakahara et al. reported of the microcapsule formation of spherical calcium carbonate particles.[58]

Suspension polymerization is one of the methods of polymer formation that uses vigorous agitation of the aqueous solution contained in the dispersing agent and hydrophobic monomer contained in the oil-soluble initiator for polymerization.[59,60] The polymerization occurs in the dispersed small droplets of the monomer. This technique operates easily, but the products have average diameters of 2–10 μm and wide size distributions. Sometimes fine particles or water-soluble polymers can be used as the dispersing agent. In the case of emulsion polymerization, a water-soluble initiator is used with a surfactant, of which concentration is more than the critical micelle concentration. The polymerization is initiated at the surface of the monomer solubilized in micelle, and a fresh

monomer comes from the large-sized organic droplets stabilized by the surfactant.[60] The products are typically 0.5 μm diameter particles with narrow distribution.

In the mini-emulsion polymerization technique, fine oil droplets are made with a small amount of the surfactant, adding to the slightly water-soluble materials like hexadecane or long-chain alcohol.[61] The initiator of both water-soluble types and oil-soluble types can be used. The polymer produced by this technique is 0.1 1 μm in diameter and relatively polydispersed.

Mixing methods essentially lead to particle size distribution. On the other hand, capillary methods are one way to control particle size. The droplets of uniform size are produced by the vibration from the breakup of the liquid jet through a nozzle or a capillary. This vibration is usually created by mechanical systems such as piezoelectric, ultrasonic or pressure difference units. Sometimes an electrostatic spray can be used. Most droplets, however, are dispersed into the gas to make a uniform-size polymer.[62] The porous membrane or tube can be also used to produce the uniform droplets. Omi et al. reported how to make polymer particles of about 8 μm with uniform size by using a porous tube called Shirasu porous glass.[63]

Phase-Separation Methods

The dispersion phase for the reaction can be created spontaneously or by adding a small amount of mechanical energy. Soap-free polymerization is one of the phase-separation methods. In this technique, a very small amount of monomer dissolved in the aqueous solvent becomes the nuclei for the polymer particles. The residue of the initiator for polymerization, which has a charge in the aqueous solution, remains on the surface of the products, and so the stability of the dispersion state of the products is kept due to the repulsion for the surface charge. The particle size of the products is around 1 μm and monodispersed. The greatest advantage of this technique is that the surface of the particles is free of the surfactant.[64]

On the other hand, the micro-emulsion polymerization technique uses a large amount of surfactant with the monomer and the solvent (usually water). The polymerization occurs in a micelle system of high concentration. The particle size of this product is in the range of 5 to 50 nm. Inverse micelle polymerization is the same technique as micro-emulsion polymerization, but a water-soluble monomer is used and produces polymer particles 5–100 nm in diameter in the reversed micelle.[65]

In the dispersion polymerization technique including non-aqueous types, the amphiphilic polymer is used as the dispersing agent with the organic solvent, for example, an alcohol, which is a good solvent for the monomer but is a poor solvent for the polymer. The particle size of the products is from a few micrometers to a few tens of micrometers. They are relatively uniform and can be controlled by the degree of the compatibility between the polymer and the solvent.[66]

The coacervation technique also uses a poor solvent for the deposition of the polymer phase, and it can be controlled by the operated temperature or by the progress of the polymerization. Monodispersed but porous particles, of from a few micrometers to a few tens of micrometers, are produced.[67] The polymer produced by the coacervation has a high surface activity, so that when the other materials are dispersed in the system, the coacervation occurs on the surface of the other materials and polymer membrane covering it. This technique can be applied to make microcapsules.[68]

REFERENCES

1. Wegner, K., Pratsinis, S. E., *Chem. Eng. Sci*., 58, 4581–4589, 2003.
2. Friedlander, S. K., *Smoke, Dust and Haze*, 2nd ed., Oxford University Press, 2000.
3. Kodas, T. T., Hampden-Smith, M. J., *Aerosol Processing of Materials*, John Wiley & Sons, New York, 1999.
4. Pratsinis, S. E., *Aerosol Science and Technology: History and Reviews*, RTI international, Research Triangle Park, NC, 2011, pp. 475–507.
5. Dreier, T., Schulz, C., *Powder Technol*., 287, 226–238, 2016.
6. Swihart, M. T., *Curr. Opin. Colloid In*., 8, 127–133, 2003.
7. Buesser, B., Pratsinis, S. E., *Annu. Rev. Chem. Biomol*., 3, 103–127, 2012.
8. Athanassiou, E. K., Grass, R. N., Stark, W. J., *Aerosol Sci. Technol*., 44, 161–172, 2010.
9. Debecker, D. P., et al., *Chem. Soc. Rev*., 47, 4112–4155, 2018.
10. Koirala, R., Pratsinis, S. E., Baiker, A., *Chem. Soc. Rev*., 45, 3053–3068, 2016.
11. Fujiwara, K., Okuyama, K., Pratsinis, S. E., *Environ. Sci.-Nano*., 4, 2076–2092, 2017.
12. Ostraat, M. L., et al., *J. Electrochem. Soc*., 148, G265–G270, 2001.
13. Righettoni, M., Amann, A., Pratsinis, S. E., *Mater. Today*, 18, 163–171, 2015.
14. Pratsinis, S. E., *AIChE J*., 56, 3028–3035, 2010.
15. Tsantilis, S., Pratsinis, S. E., *Langmuir*, 20, 5933–5939, 2004.
16. Mueller, R., et al., *Powder Technol*., 140, 40–48, 2004.
17. Friedlander, S. K., Wang, C. S., *J. Colloid Interf. Sci*., 22, 126–132, 1966.
18. Landgrebe, J. D., Pratsinis, S. E., *Ind. Eng. Chem. Res*., 28, 1474–1481, 1989.
19. Granqvist, C., Buhrman, R., *J. Appl. Phys*., 47, 2200–2219, 1976.
20. Heine, M. C., Pratsinis, S. E., *J. Aerosol Sci*., 38, 17–38, 2007.
21. Mädler, L., Stark, W. J., Pratsinis, S. E., *J. Appl. Phys*., 92, 6537–6540, 2002.
22. Goudeli, E., Eggersdorfer, M. L., Pratsinis, S. E., *Langmuir*, 32, 9276–9285, 2016.
23. Kruis, F. E., Kusters, K. A., Pratsinis, S. E., Scarlett, B., *Aerosol Sci. Technol*., 19, 514–526, 1993.
24. Seto, T., et al., *Aerosol. Sci. Technol*., 27, 422–438, 1997.
25. Kim, K.-S., Pratsinis, S. E., *Chem. Eng. Sci*., 44, 2475–2482, 1989.
26. Tsantilis, S., Kammler, H. K., Pratsinis, S. E., *Chem. Eng. Sci*., 57, 2139–2156, 2002.
27. Strobel, R., Pratsinis, S. E., *J. Mater. Chem*., 17, 4743–4756, 2007.
28. Gröhn, A. J, et al., *Ind. Eng. Chem. Res*., 53, 10734–10742, 2014.
29. Teoh, W. Y., Amal, R., Mädler, L., *Nanoscale*, 2, 1324–1347, 2010.
30. Mäkelä, J. M., et al., *KONA Powder Part. J*., 34, 141–154, 2017.

31. Fujiwara, K., Pratsinis, S. E., *AIChE J.*, 63, 139–146, 2017.
32. Kelesidis, G. A., Goudeli, E., Pratsinis, S. E., *Proc. Combust. Inst.*, 36, 29–50, 2017.
33. Oehrlein, G. S., Hamaguchi, S., *Plasma Sources Sci. T.*, 27, 023001, 2018.
34. Vollath, D., *J. Nanopart. Res.*, 10, 39–57, 2008.
35. Phillips, J., Luhrs, C. C., Richard, M., *IEEE T. Plasma Sci.*, 37, 726–739, 2009.
36. Fulcheri, L., Schwob, Y., *Int. J. Hydrogen Energ.*, 20, 197–202, 1995.
37. van Erven, J., et al., *KONA Powder Part. J.*, 27, 157–173, 2009.
38. Lee, D., Choi, M., *J. Aerosol Sci.*, 33, 1–16, 2002.
39. Neilson, M. L., et al., Eds., *Ultrafine Particles*, John Wiley & Sons, New York, 1963, p. 181.
40. Roy, D. M., Neurgaonkar, R. R., O'Holleran, T. P., Roy, R., *Am. Ceram. Soc. Bull.*, 56, 1023–1024, 1977.
41. LaMer, V. K., Dinegar, R. H., *J. Am. Chem. Soc.*, 72, 4847, 1950.
42. Sugimoto, T., *Adv. Colloid Interface Sci.*, 28, 65, 1987.
43. Calvert, P., *Nature*, 367, 119, 1994.
44. Stöber, W., Fink, A., Bohn, B., *J. Colloid Interface Sci.*, 26, 62, 1968.
45. Sacks, M. D., Tseng, T. Y., Lee, S. Y., *Am. Ceram. Soc. Bull.*, 63, 301–310, 1984.
46. House, H. O., *Modern Synthetic Reactions*, 2nd ed., W. A. Benjamin, Redwood, CA, 1972.
47. Matijevic, B., *Faraday Discuss.*, 92, 229–239, 1991.
48. Haruta, M., Lamaitre, J., Delannay, F., Delmon, B., *J. Colloid Interface Sci.*, 101, 59, 1984.
49. Suzuki, H., Tomokiya, Y., Suyama, Y., Saito, H., *Ceramic Trans.*, 6, 263–274, 1990.
50. Suzuki, H., Saito, H., Hayashi, H., *Better Ceramics through Chemistry*, 5, 83–88, 1992.
51. Blesa, M. A., Matijevic, B., *Adv. Colloid Interface Sci.*, 29, 173–221, 1989.
52. Adschiri, T. K., Kanazawa, K., Arai, K., *J. Am. Ceram. Soc.*, 75, 1019–1022, 1992.
53. Mohamed, R. S., Halverson, D. S., Debenedetti, D. G., Prud'homme, R. K., *Supercritical Fluids: Science and Technology, ACS Symp. Series*, No. 406, American Chemical Society, Washington, DC, 1989, p. 355.
54. Gallagher, P. M., Coffey, M. P., Krukomis, V. I., Klasutis, N., *Supercritical Fluids: Science and Technology, ACS Symp. Series*, No. 406, American Chemical Society, Washington, DC, 1989, p. 334.
55. Nagy, J. B., et al., In Mittal, K. L., Ed., *Surfactants in Solution*, Vol. 10, Plenum Press, New York, 1989, pp. 1–43.
56. Fendler, J. H., *Chem. Rev.*, 87, 877, 1987.
57. Ugeistad, J., et al., Schmid, R., Berge, A., Ellingson, T., Aune, O., *Science and Technology of Polymer Colloids, Vol. 1, NATO ASI Series B*, No. 67, Kluwer Academic, Dordrecht, 1983.
58. Nakahara, Y., Mizuguchi, M., Miyata, K., *J. Colloid Interface Sci.*, 68, 401–407, 1979.
59. Bishop. R. B., *Practical Polymerization of Polystyrene*, Cahners Publ., Des Plaines, IA, 1971.
60. Blackley, D. C., *Emulsion Polymerization: Theory and Practice*, Applied Science Publ., London, 1970.
61. Barnette, D. T., Schork, F. J., *Chem. Eng. Prog.*, 83(6), 25–30, 1987.
62. Panagiotou, T., Levendis, Y. A., *J. Appl. Polymer Sci.*, 43, 1549–1558, 1991.
63. Omi, S., Katami, K., Iso, M., *J. Appl. Polymer Sci.*, 51, 1, 1994.
64. Ceska, G. W., *J. Appl. Polymer Sci.*, 18, 2493–2499, 1974.
65. Candau, F., Orrewill, R. H., Eds., *Scientific Methods for the Study of Polymeric Colloids and Their Applications, NATO ASI Series C*, No. 303, Kluwer Academic Publ., Dordrecht, 1990.
66. Barrett, K. B. J., Ed., *Dispersion Polymerization in Organic Media*, John Wiley & Sons, New York, 1970.
67. Hou, W. H., Lloyd, T. B., *J. Appl. Polymer Sci.*, 45, 1783–1788, 1992.
68. Nixon, J. R., Ed., *Microencapsulation*, Marcel Dekker, New York, 1976.

4.3 Crystallization

Yoshiyuki Shirakawa

4.3.1 INTRODUCTION

The crystallization operation has been used as a salt production method since a long ago, but also in modern industrial production it plays an important role as the solidification technology mainly of pharmaceuticals and foods.[1] In chemical engineering, crystallization is one of the unit operations for performing chemical separation and purification.[2,3] The crystallization is a bottom-up process for the generation of powder particles. It is possible to create the powder particles of a wide size from centimeter to nanometer by controlling the operation condition of crystallization. Recent increasing demands are the accurate control of particle shape, the crystal polymorphism and the high crystal quality in addition to average particle size. Therefore, further development is desired in crystallization technology.[1]

Crystallization is recognized as a particle production technique in liquid phase. However, it includes particle syntheses in gas and solid phases in a broad sense. In other words, crystallization is used as the engineering term to express the phenomenon of separating a solid phase from a supersaturated state by reducing its concentration and by shifting to a stable equilibrium state. The precipitation occurs through nucleation and growth in microscopic description of the crystallization processes. Incidentally, the crystallization can be classified according to its operation at high pressure, with chemical reaction, etc. In this chapter, the theory of kinetics on nucleation and growth that determines particle morphology are introduced and an application is presented.

4.3.2 SOLID-LIQUID EQUILIBRIUM AND SUPERSATURATED SOLUTION

If a crystallization process is performed under the quasi-static change, all excess solutes above solubility limit can be precipitated. There may be a crystal particle with the equilibrium state and structure in the solution, and then the chemical potential of solute molecule in the solution are equal to that of molecules of precipitated crystal particles. In the actual crystallization processes, precipitation of particles is performed in a non-equilibrium state due to the volume and temperature distribution of crystallizers, and hence a kinetic interpretation is required. In other words, transition from a supersaturated state to a thermodynamically equilibrium state occurs in the crystallization processes. Therefore, since it is a non-equilibrium process, precipitated crystal powder particles are less likely to have the thermodynamically most stable structure, and the particle size distribution and particle shape change depending on the process condition.

Conventional crystallization operations such as a cooling, evaporation and a poor solvent addition method are quite often used in industrial crystallizations. In all methods, crystal particles are precipitated by raising the solution concentration above the solubility limit. However, the crystallizations cannot immediately take place over the limit. When one unsaturated solution is cooled at a rate, excess solute begins to precipitate as the solution concentration becomes much higher than the saturated concentration at temperature T. If the cooling process is continued for a long time, all excess solute precipitates until the saturation concentration is reached as shown in Figure 4.3.1. At this time, the driving force for crystal precipitation is directly related to the magnitude of the chemical potential difference between the molecules of the precipitated particles and of the solute molecules in the solution and depends on how supersaturated the formation state of precipitated crystal particles is. Therefore, in order to control the particle characteristics of precipitated particles, this driving force must be controlled. Then, a supersaturation degree is introduced as a control parameter representing the supersaturated state. The supersaturation degree σ is calculated by using the concentration C of the solution and the saturation solubility C_e

$$\sigma = \frac{C - C_e}{C_e} \tag{4.3.1}$$

The chemical potential difference $\Delta\mu$ between the solute molecules in the supersaturated solution and the precipitated molecules can be expressed as follows, approximately.[4]

$$\Delta\mu = k_B T \ln(1+\sigma) \tag{4.3.2}$$

where

k_B is the Boltzmann constant
T is the temperature

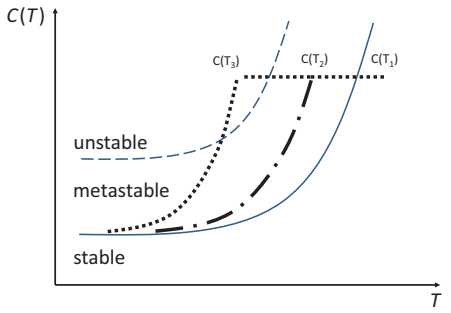


FIGURE 4.3.1 Schematic interpretation for concentration changes of a solution in cooling processes.

In order to grasp the behavior of particle formation in detail, the concentration changes in two cooling processes are shown in Figure 4.3.1. When crystallization is carried out in the cooling process as described above, excess solutes exceeding the solubility limit is precipitated. At that time microscopically, nuclei are formed at first, and then small crystals grow to form the particles. In general, a nucleation is unlikely to occur unless a certain supersaturation state, which has a higher concentration than the saturated state, is reached. In Figure 4.3.1, a curve drawn on the higher concentration side than the solubility curve is called a supersolubility curve, and nucleation occurs at a high concentration past this curve. The nucleation does not occur even when a solution of concentration C (T_1) unsaturated at temperature T_1 is cooled up to T_2, the nucleation occurs at T_3 over the supersolubility curve (depending on the cooling rate). The excess solutes are consumed in the nucleation, the solution concentration decreases, no nucleus is formed in the metastable region between the supersolubility and the solubility curve and the consumption of the solutes is exclusively used for crystal growth. The solution concentration change such as the dot-dash line in Figure 4.3.1 is seen in the case where seed crystals are added in advance. Therefore, addition of seed crystals and their solid particle density in the solution are also operating parameters of the crystallization processes.[4]

4.3.3 NUCLEATION RATE

In order to show the relationship between nucleation and supersaturation degree, consider the homogeneous nucleation rate in solutions.[1–3] Let us suppose that the nucleus is approximately spherical and ignores the heat transfer due to aggregation. Firstly, we have a think of a small aggregate particle of solute molecules called a cluster before forming a nucleus. Assuming that the cluster of radius r is formed in a supersaturated solution, the degree of supersaturation and the free energy change ΔG_v when solid precipitates are related as follows.

$$\Delta G_v = \frac{\Delta \mu}{v} \tag{4.3.3}$$

where v is the volume of one molecule. Therefore, the free energy changes due to the nucleation.

$$\Delta G = 4\pi r^2 \gamma - \frac{4\pi r^3 k_B T}{3v} \ln(1+\sigma) \tag{4.3.4}$$

where γ is the surface energy of the cluster or the nucleus. This free energy changes as shown in Figure 4.3.2. Up to the maximum value of the curves is a cluster formation region where molecule association and dissociation are repeated, and as the solute molecules aggregation of the size exceeding the maximum value becomes larger, the energy decreases and grows as nuclei. ΔG^* is the maximum value at the critical radius and is expressed as the following formula by using supersaturation degree.

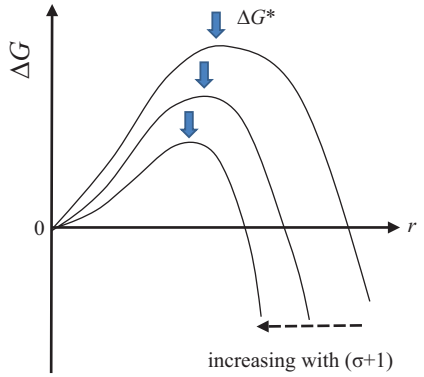


FIGURE 4.3.2 Supersaturation dependence of free energy changes in homogeneous nucleation.

$$\Delta G^* = \frac{16\pi\gamma^3 v^2}{3\left\{k_B T \ln(1+\sigma)\right\}^2} \tag{4.3.5}$$

ΔG^* decreases when increasing the degree of supersaturation, then the energy barrier becomes lower and it is easy to generate the nuclei. This aggregation of the solute molecules includes dehydration in aqueous solutions or desolvation, which is quite different from nucleation and growth in gas phase.

Considering that the nucleation process is like a polymerization reaction, since this ΔG^* corresponds to the activation energy,[5] the nucleus generation rate R_N is calculated using the factor k_N

$$R_N = k_N \exp\left(-\frac{\Delta G^*}{k_B T}\right) \tag{4.3.6}$$

$$k_N = n_0 J_S$$

where

n_0 is the solute molecule density in the solution
J_S is the frequency of incorporation into the cluster per unit time

By substituting Equations 4.3.1 and 4.3.5 into Equation 4.3.6, R_N is described as follows.

$$R_N = n_0 J_S \exp\left\{\frac{-16\pi\gamma^3 v^2}{3\left(k_B T\right)^3 \left(\ln\frac{C}{C_e}\right)^2}\right\} \tag{4.3.7}$$

The nucleation is affected by impurities and the other particles when actually conducting the crystallization operation and is also sensitive to walls of containers. In this way, the phenomenon that the nuclei are generated under the influence of different substances is called heterogeneous nucleation for homogeneous nucleation which occurs in the homogeneous environment mentioned above. Generally, the heterogeneous nucleation rate R_N^{het} becomes larger than the homogeneous nucleation rate

R_N^{hom} under the condition of constant J_s and n_0. This is because the relationship of the energy change between homogeneous nucleation ΔG_{hom} and heterogeneous one ΔG_{het} is

$$\Delta G_{het} < \Delta G_{hom} \tag{4.3.8}$$

The same argument holds for crystal nucleation on substrates in a solution. For example, three-dimensional island nucleation on a substrate and two-dimensional nucleation on a facet plane during crystal growth are also recognized as a heterogeneous nucleation.

4.3.4 CRYSTAL GROWTH RATE

Considering the process of crystal growth in solutions, the solute ions and molecules in the supersaturated solution diffuse to, adsorb to and migrate on the crystal surface and are taken into the step and kink (Figure 4.3.3). This adsorption on the surface takes place with desolvation. Therefore, the growth after the nucleation is a molecular kinetic and transfer process of the solute molecules, then it is a phenomenon handled separately from nuclei generated by fluctuation at the initial stage of the non-equilibrium phase transformation. When considering the crystallization process as a particle generation process, the nucleation is the basis for determining particle number and crystal growth is that for particle size. In both nucleation and crystal growth in supersaturated solution, desolvation is a process requiring the aggregation of the solutes, which is a unique process different from the vapor phase and precipitation from melt. Desolvation in crystallization has a great influence on nucleation and crystal growth.

First, we introduce the Wilson-Frenkel equation that gives the maximum value of crystal growth rate in the molecular dynamics derivation.[6] In this equation, it is assumed that all the solute molecules adsorbed on the crystal surface are instantaneously taken into the crystal, which corresponds to the Hertz-Knudsen equation in the vapor phase growth. Wilson-Frenkel's formula is expressed by a jumping distance

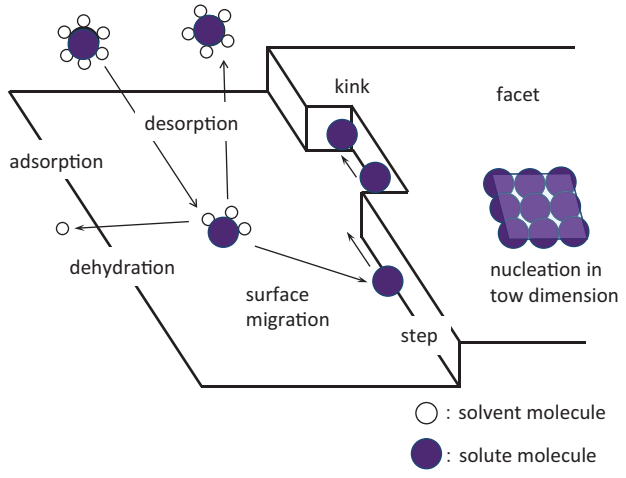


FIGURE 4.3.3 Crystal growth model at the surface with steps and kinks.

a when solute molecules penetrate the solid-liquid interface, and a free energy barrier ΔG_{de} that must be exceeded in the desolvation process when solute molecules attach to the surface, the volume v_C of one molecule of the solute and the frequency f of the solute molecule,

$$R_{max} = \sigma v_c a f C_e \exp\left(\frac{-\Delta G_{de}}{k_B T}\right) \tag{4.3.9}$$

It is understood from this equation that the maximum value of the crystal growth rate is proportional to the supersaturation degree. The actual growth rate is obtained from multiplying R_{max} by a coefficient $\varepsilon\,(0 \le \varepsilon \le 1)$.

Flat surface has no kink and no step that captures solute molecules at the atomic level. The steps and kinks have to be supplied for crystal growth of a surface. By the kinetic and transfer process of solute molecules, the movement of the kink and the advance of the step occurs, and the crystal thickness increases. Such a growth mechanism is called a lateral growth and it occurs in a state where the degree of supersaturation is relatively low. On the other hand, a growth mechanism, in which aggregates of solute molecules adhere to the crystal surface and are immediately taken into the crystal, is called an adhesion growth, occurring in a relatively high concentration region. In this growth, the surface becomes coarser than the lateral growth, and R_{max} seems to be given in this adhesion growth.

4.3.5 CONTROL OF POWDER PROPERTIES IN CRYSTALLIZATION PROCESSES

The control of the particle morphology by using the crystallization process mainly concerns particle size distribution, particle shape and polymorphic control. In considering particle size distribution control, LaMer's model, which represents the temporal change of concentration or supersaturation degree in solutions, is effective.[7,8] As shown in Figure 4.3.4, it is assumed that the supersaturated state is realized by evaporation of the solvent, with the formation of the insoluble compound by reaction and by the concentration rising in cooling operation at the initial stage. Corresponding to the process in Figure 4.3.1, nucleation starts in an unstable region which has a higher supersaturation degree, and the degree decreases for the situation where the consumption speed is higher than the supply. When the supersaturation degree reaches the metastable region, the crystal growth predominates rather than the nucleation, and the growth continues to the saturation concentration. It is possible to determine the residence time, operation temperature program and seed density in the solution for controlling of the supersaturation degree in order to obtain the required number of particles and its size distribution.

A modeling of production volume and particle size distribution of precipitates in a continuous mixing tank crystallizer which recognized Mixed Suspension Mixed Product Removal (MSMPR) has been proposed by Toyokura et al. As the model in producing powder having a particle size distribution $f(l_p)$ by

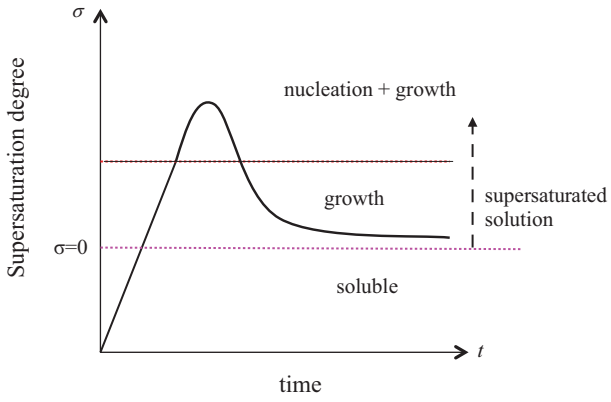


FIGURE 4.3.4 Time course of supersaturation degree with reference to saturated concentration ($\sigma=0$).

production rate P_c[kg/hr] for steady operation in a continuous crystallizer, the following relational expression is shown from the material balance and the number balance in the apparatus.

$$P_c = \rho_c \left(\frac{dl'}{d\theta}\right) a = \rho_c \int_0^{l_{pmax}} k_v f'\left(l_p\right) l_p^3 dl_p \tag{4.3.10}$$

$$a = \int_0^{l_{pmax}} k_a g\left(l\right) l^2 dl \tag{4.3.11}$$

$$V_t = \int_0^{l_{pmax}} k_v g\left(l\right) l^3 dl \tag{4.3.12}$$

where

l	is particle size
k_a and k_v	are surface and volume shape factor
ρ_c	is crystal density
$(1-\varepsilon)$	is suspension density
$g(l)$	is particle size distribution in a crystallizer

$$g\left(l\right) dl = \int_0^{l_{pmax}} f\left(l_p\right) l_p dl_p \tag{4.3.13}$$

$$V' = \frac{V_t}{\left(1-\varepsilon\right)} \tag{4.3.14}$$

Then, the production rate per device volume is

$$\frac{P}{\rho V'} = \left(1-\varepsilon\right)\left(\frac{dl}{d\theta}\right)\frac{\int_0^{l_{pmax}} k_a g\left(l\right) l^2 dl}{\int_0^{l_{pmax}} k_v g\left(l\right) l^3 dl} = \int_0^{l_{pmax}} k_v f\left(l_p\right) l_p^3 dl_p \tag{4.3.15}$$

Using this model, assuming that the particle size distribution in the MSMPR crystallizer is Rosin-Rammler distribution, several cases are shown and investigation of operation conditions and scale up has been made.[9]

The shape of a crystal in the thermal equilibrium state has only one structure and is distinguished from the non-equilibrium state. In the equilibrium structure, it is called an equilibrium form and it consists of crystal planes that minimize the total surface energy by that volume. In the case of liquid, its shape is spherical because the spherical shape has minimum surface area and energy, but in the case of crystal, the surface energy density depends on the orientation of the surface.[10] The relationship between the surface energy density of each surface and the distance from one point in the crystal to that surface is indicated by Wolff's theorem and the equilibrium shape follows this theorem. On the other hand, the crystal structure is called a growth form for the non-equilibrium state, and the growth form is largely influenced by crystallization conditions such as supersaturation degree, pressure and temperature.

In general, the concentration at solid-liquid interfaces is not constant in crystallizations. At corners and ridges in the crystal, the concentration shows a larger value from the average, so that the crystal growth at those parts is promoted (Berg effect). This effect is caused by the energy difference of the points on the crystal. Figure 4.3.5 shows how the crystal shape changes in a supersaturated NaCl aqueous solution due to adding a habit modifier. If multi-valence ions as the habit modifier are added into a NaCl solution including NaCl particles, the multi-valence ions preferentially adhere on the higher energy points and disturb the growth[11] of a crystal plane of the NaCl. As a result, the crystal shape changes in the growth process for decreasing growth rate of the surface adhered by the multi-valence ions.

Crystal polymorphism is the same compound with more than one crystal structures.[12] There are many compounds that are polymorphic irrespective of inorganic and organic materials. For example, the amino acid glycine has α, β and γ polymorphism, and calcium carbonate has three polymorphic forms of calcite, aragonite and vaterite. The reason why attention is paid to polymorphism from an industrial point-of-view is that the physical and chemical properties such as solubility are different in the different crystal structure. Polymorphic control is an important issue because this is closely related to solubility in medicines due to body absorption. In addition, powder with polymorphism may cause consolidation during storage, and it is a matter to be noted in quality control. If there is a compound powder with two polymorphs, the powder has two solubility curves for stable and unstable structures at a certain temperature. According to Ostwald's step rule, when the precipitation from the supersaturated solution including solute molecules with two polymorphs, the primary crystals have the unstable structure. With the precipitation of the unstable crystals, the solution concentration decreases. When the solution has a lower concentration than the saturated one of the unstable structure, the unstable crystals dissolve and the stable ones precipitate. It is solution-mediated phase transition and is especially important for medical screening processes of polymorphs.

4.3.6 SYNTHESIS OF COMPOSITE PARTICLES

Next, as an application using the crystallization method, we will introduce particle composite processes. A composite of

particles with fine interfacial structures can contribute to the development of materials with new functions; therefore, such particles have been recognized as drivers of innovative product development. Several methods are available for producing such composite materials.[13] However, the general crystallization for synthesis of composite particles requires a multi-stage process, which requires time and cost. Then, a method of directly producing the desired composite particles from solutions of multi-component systems is expected, and an example using a micro flow reactor is introduced in this section. In the micro space, the transmission distance of molecules and heat is short so that high-speed heat exchange and fine diffusion are possible.[14] Our group has attempted to develop a new particle shape control and composite technology by crystallization in a limited space including a liquid-liquid interface and microspace.[15,16] In our crystallization process, for example, a solution of sodium chloride and a 2-butanone solution of indomethacin (IMC) are prepared, and the sodium chloride solution continuously suspended in the 2-butanone solution in a microchannel as shown in Figure 4.3.6. When the flow pattern is formed, mutual diffusion occurs at the droplet interface between the solutions and crystals precipitate. When ultrasonic waves are further irradiated for a certain period of time, composite particles with indomethacin attached to the surface of the aggregated particles of sodium chloride are produced, as illustrated in Figure 4.3.7. It is a technique that utilizes the difference in solution physical properties such as precipitation time (induction time) of two kinds of solutes and precipitation speed difference.

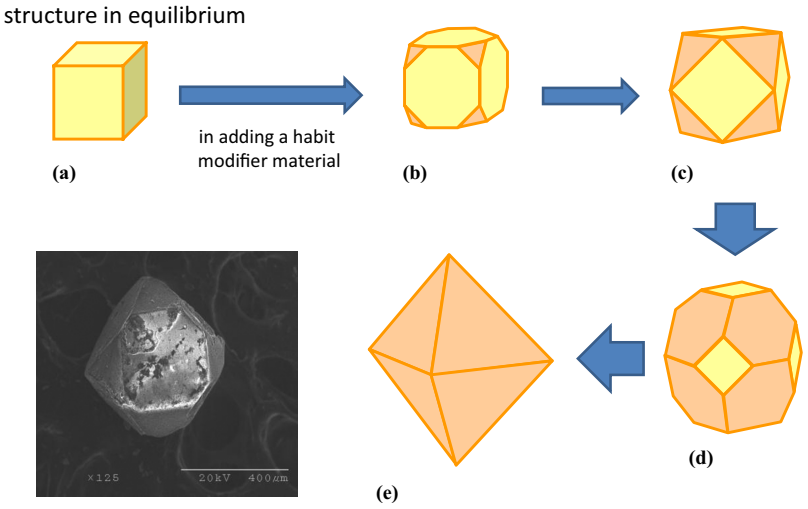


FIGURE 4.3.5 Change of NaCl crystal shape by adding habit modifier. (a) Cubic, (b) Truncated cube, (c) Cubo-octahedron, (d) Truncated-octahedron, (e) Octahedron.

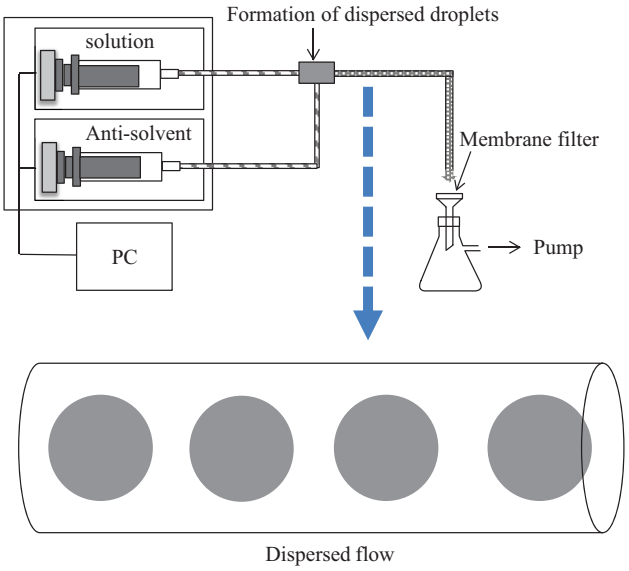


FIGURE 4.3.6 Schematic diagram of microchannel flow dispersed solution droplets.

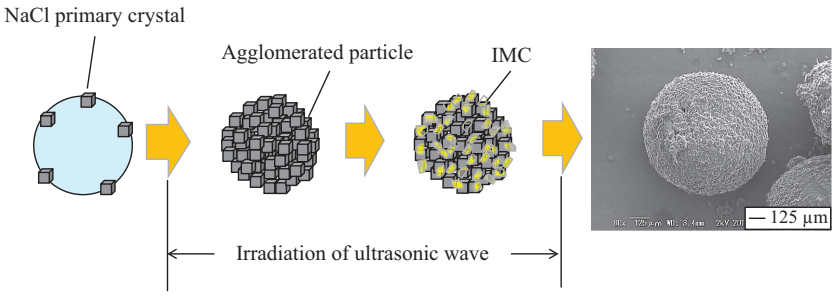


FIGURE 4.3.7 Precipitation model and SEM photograph of the NaCl composite particle in the microchannel.

In this chapter, the particle morphology control using the crystallization process is reviewed, but in practical industrial processes, the powder particle properties are controlled by more sophisticated techniques depending on the purpose. Their details are explained in listed references.

REFERENCES

1. Myerson A. S. Ed., *Handbook of Industrial Crystallization*, 2nd ed., Elsevier, 2002.
2. Mullin J. W., *Crystallization*, 4th ed., Elsevier, 2001.
3. Nyvlt J., Ulrich J., *Admixtures in Crystallization*, VCH, 1995.
4. Mtsuoka M., Abe Y., Uchida H., Takiyama H., *Chem. Eng. Sci*., 56, 2325–2334, 2001.
5. Atkins P., de Paula J., *Physical Chemistry,* 8th ed., Oxford Univ. Press, 2006.
6. Libbrecht K. G., *Annu. Rev. Mater. Res*., 47, 271–295, 2017.
7. LaMer V. K., *Ind. Eng. Chem*., 44, 1270, 1952.
8. Thanh N. T. K., Maclean N., Mahiddine S., *Chem. Rev.*, 114, 7610–7630, 2014.
9. Toyokura K., Sakai H., Seminar on Ind. crystallization in Japan, Czech. Academy of Sci., 1987, p. 87.
10. Phillips R., *Crystals, Defects and Microstructures*, Cambridge Univ. Press, 2001.
11. Kubota N., *Crystal Res. Technol*., 36, 203–208, 1995.
12. Atkins P., de Paula J., *Elements of Physical Chemistry*, 5th ed., Oxford Univ. Press, 2009.
13. Adschiri, T., *Chem. Lett*., 36, 1188–1193, 2007.
14. Gobert S.R.L., Kuhn S., Braeken L., Thomassen L.C.J., *Org. Process Res. Dev*., 21, 531–542, 2017.
15. Gonda K., et al., *Powder Technol.*, 269, 401–408, 2015.
16. Hattori Y., et al., *Chem. Eng. Process*., 97, 233–241, 2015.

4.4 Design and Formation of Composite Particles

Hideki Ichikawa, Tooru Andoh, and Fumihiko Fujii

"Composite particles" can be defined idiomatically as the particles fabricated with two or more components. Usually, they are distinguished from a simple mixture of particulate components such as agglomerates, though such mixtures can be categorized into the composite particles in a broad sense. The composite particles in a narrow sense are referred to as the particles that are fabricated to have a well-designed, established structure and more specifically, sophisticated functions. The major purpose of forming composite particles may be to compensate some disadvantages of one component with another component(s) and/or to give new or specific functionalities to the resulting particles through the composite formation of the components. Traditionally, the composite particles have been produced as "micron-sized particles." Recent advances in nano-technology, however, reveal to us that it is possible to produce even nano-sized composite particles, so-called "nano-composites." This cutting-edge technology is expected to be one of the most fundamental and powerful tools in material sciences. Nowadays, the composite particles can be found in many industrial fields. They are being used not only as raw materials but also as final products, depending on their applications. Thus, the characteristics of the composite particles including sizes, types, materials, structures and formation processes are very comprehensive.

4.4.1 TYPICAL STRUCTURE OF COMPOSITE PARTICLES

The particulate structure plays an important role in the performance of the composite particles. Representative particle structures are shown in Figure 4.4.1. The composite particles can be conventionally classified into two types: monolithic structure and layered-structure. The former is composed of matrix component(s) where some other components are dispersing as a heterogeneous phase(s) in the matrix. This type of the particle structure can be fabricated mainly by kneading, milling, intercalating or including dispersing components with matrix components. The dispersing phases can be distributed one-, two- or three-dimensionally in the inner matrix and/or the dimples located on the matrix surface, depending on the manufacturing processes and the components employed. The layered-structure can be fabricated by the encapsulation of seed particles with other types of components. Encapsulating materials can be deposited on the surface of seed particles in the form of fine particles, films and so on. Using certain apparatuses, especially a spray-coating method using fluid bed processes, a multi-layered structure can be produced.[1] Each layer can be designed to be not only a monolithic structure, but also a random multiphase structure, an ordered multiphase structure, a gradient structure and so on, as shown in Figure 4.4.1. The combination of the different components and layers can produce almost infinite types of composite particle structures, giving rise to a wide variety of functionalities.[1]

4.4.2 PROCESS

There seems to be no particular process for forming composite particles in a traditional sense. In other words, most of the currently available processes for particle production can be potentially applicable for the production of composite particles. Indeed, numerous processes and apparatuses have been proposed in a wide variety of industrial fields. Typical

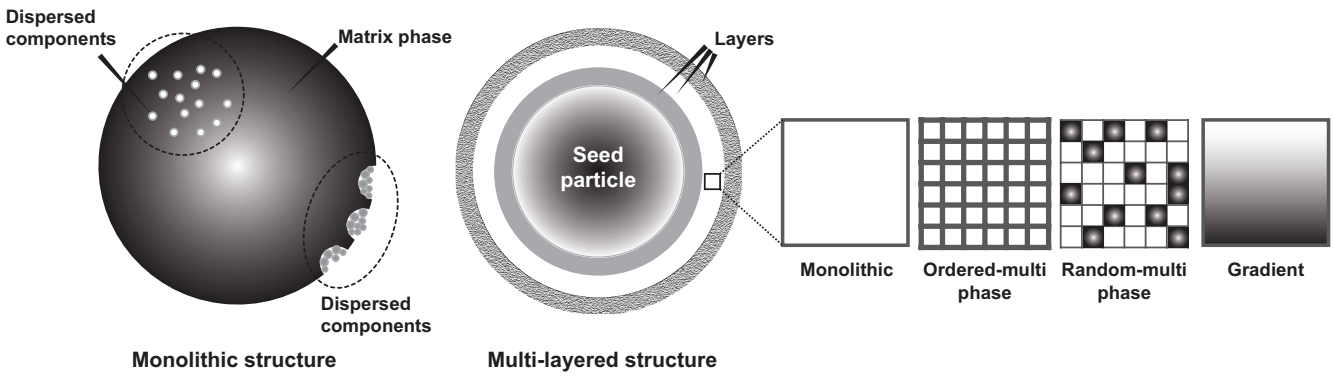


FIGURE 4.4.1 Representative particle structures of composite particles.

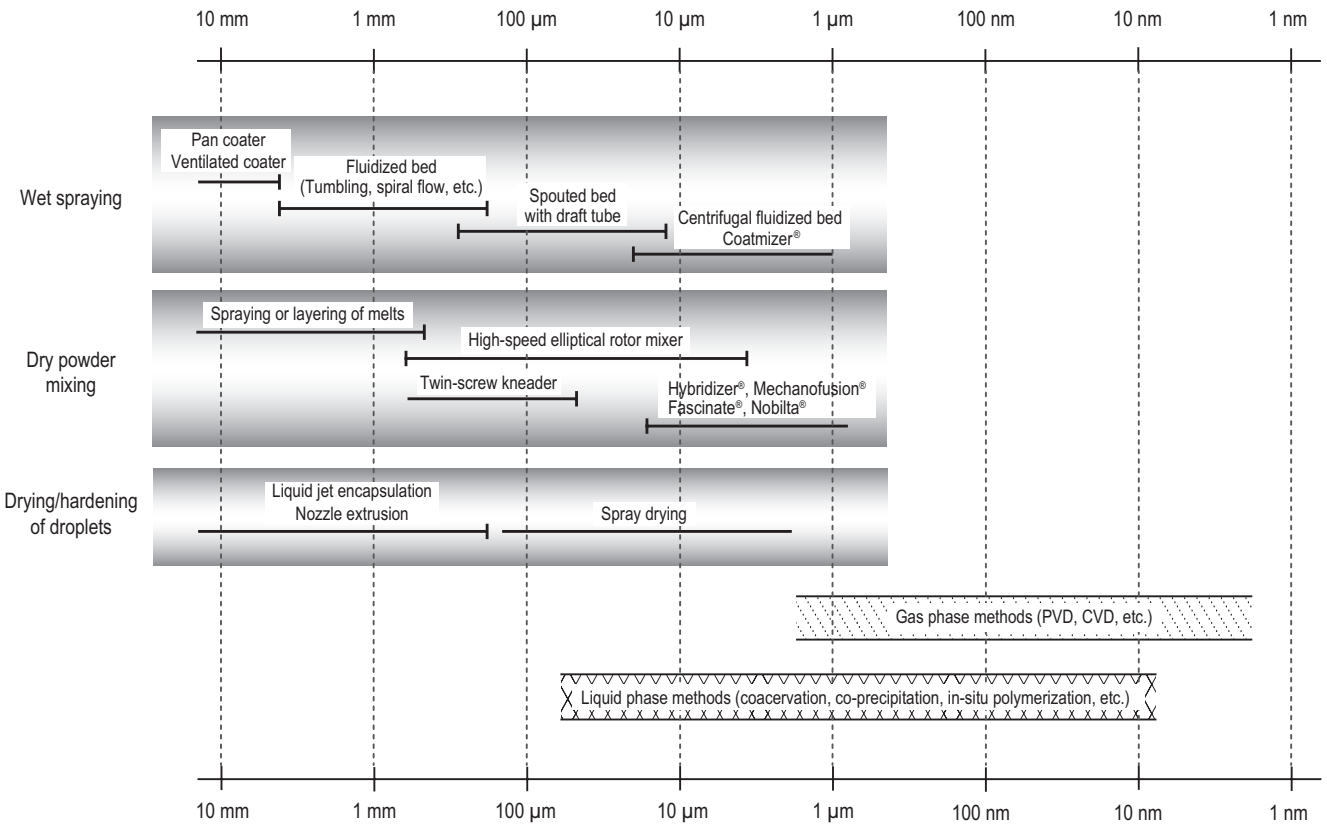


FIGURE 4.4.2 Typical preparation processes of composite particles based on encapsulation.

composite processes with focusing on encapsulation techniques are summarized in Figure 4.4.2.

Deposition/reaction of encapsulating materials on the surface of the solid seed particles is a major way for the composite particles with layered-structure. The composite process through the deposition/reaction takes place either in gas, liquid or solid phase, depending on the phase status of the encapsulating materials. Typical composite processes in the gas phase are chemical vapor deposition (CVD) and physical vapor deposition (PVD). These processes can be employed for the materials that are able to be vaporized. The vaporized materials are deposited on the seed particles in a reactor as a result of chemical reaction or cooling. The deposited layer thus formed is usually very thin (several ten nanometers in thickness).

Several methods can be utilized if the encapsulating materials are in the liquid phase. Spray-coating is a very common process in this context. Fluidized beds equipped with a spraying system are often used for this process, especially in the pharmaceutical field.[1] The liquid-formed materials can be sprayed so as to generate their mists. The resulting mists are deposited and subsequently dried on the seed particles, resulting in a coating layer. Coating of the seed particles can be also carried out in the presence of encapsulating materials in the liquid phase through interfacial deposition/reaction processes such as coacervation, precipitation and in situ polymerization.

The composite processes through the encapsulation of the seed particles with solid materials are getting popular recently.[2,3] Many types of mechanical treatment based on mixing, grinding and fusion of particulate components have been proposed as solvent-free composite processes. Some of them are commercially available as an exclusive apparatus for the production of the composite particles (e.g. Hybridizer®, Mechano-fusion® and Theta-composer®).

There are several ways to fabricate the composite particles with monolithic structure. In addition to some of the aforementioned processes, methods like spray-drying, spray-pyrolysis, co-precipitation and co-grinding are useful for composite process of two or more components. Another class of the composite process is the use of the rapid expansion of supercritical fluid.[4] This modern technique is being investigated for the production of monolithic composite particles as well as the coating of seed particles. Super critical carbon dioxide is often used for this purpose.

4.4.3 MATERIALS

Selection of materials is crucial in design and preparation of composite particles since the possible combinations of the components are almost infinite. In a typical binary system, two homogeneous materials, e.g. metal/metal, inorganics/inorganics and organics/organics can be often used to make composite particles, because the homogeneous materials are likely to have a good affinity in general. The combination of two heterogeneous materials such as metal/inorganics, metal/organics and inorganics/organics is also possible, provided that they are compatible.

The characteristics of materials are involved with the required functionalities of the composite particles. In this regard, several criteria may be given to select the materials. These include shape, dimension, dispersing status, surface properties and physical properties. Much consideration of these characteristics provides us with an efficient way to design and prepare composite particles with the desired functionalities.

4.4.4 EXAMPLES OF PARTICULATE DESIGN AND PREPARATION OF COMPOSITE PARTICLES

In recent years, a wide variety of composite particles have been studied in versatile industrial fields. In fact, the reports on their industrial applications are too many to enumerate. Some of them are already in market as commercially available products. Representative examples of particulate design of composite particles in the life science field, which may be one of the most growing areas in the use of composite particles for the purpose of diagnosis and therapeutics of diseases, are described below.

4.4.4.1 Inorganic Systems

Semiconductor nanocrystals (SNCs), also called quantum dots (QDs), are one of the nano-sized inorganic systems. SNC contains hundreds to thousands of atoms and their sizes are comparable to the exciton Bohr radius. Due to quantum confinement effect, SNCs exhibit novel optical and electric properties that differ from bulk materials.[5] Consequently, SNCs have been applied to the next generation of solar cells, lasers, light emitting diodes, computers and bioimaging probes.

There are two types of SNCs, namely epitaxial and colloidal SNCs.[6] Whereas epitaxial SNCs are grown on substrate by molecular beam epitaxy from vapor phase in dry conditions, colloidal SNCs are synthesized by chemical approaches in wet conditions. In contrast with substrate-bounded epitaxial SNCs, colloidal SNCs are freestanding and therefore are transferred to the post-chemical process, including water solubilization. In this section, typical synthesis procedures of colloidal SNCs, especially for biological application, are described.

Synthesis of SNCs in Visible Region

SNCs typically consist of core and shell structures as shown in the inset of step 5 of Figure 4.4.3. Bare SNCs, namely core-only SNCs, are susceptible to photo-oxidation and have defects on the surface. Core/shell SNCs have high quantum yields in comparison with bare SNCs by covering the surface of the bare SNCs with the shell structure. The quantum yields are detrimentally affected by the lattice mismatch between the core and shell materials.[7] CdSe and CdZnS are one of the popular core and shell materials, respectively. The synthesis procedure of spherical SNCs (CdSe/CdZnS) emitting in the visible region (400–700 nm) is described below as an example

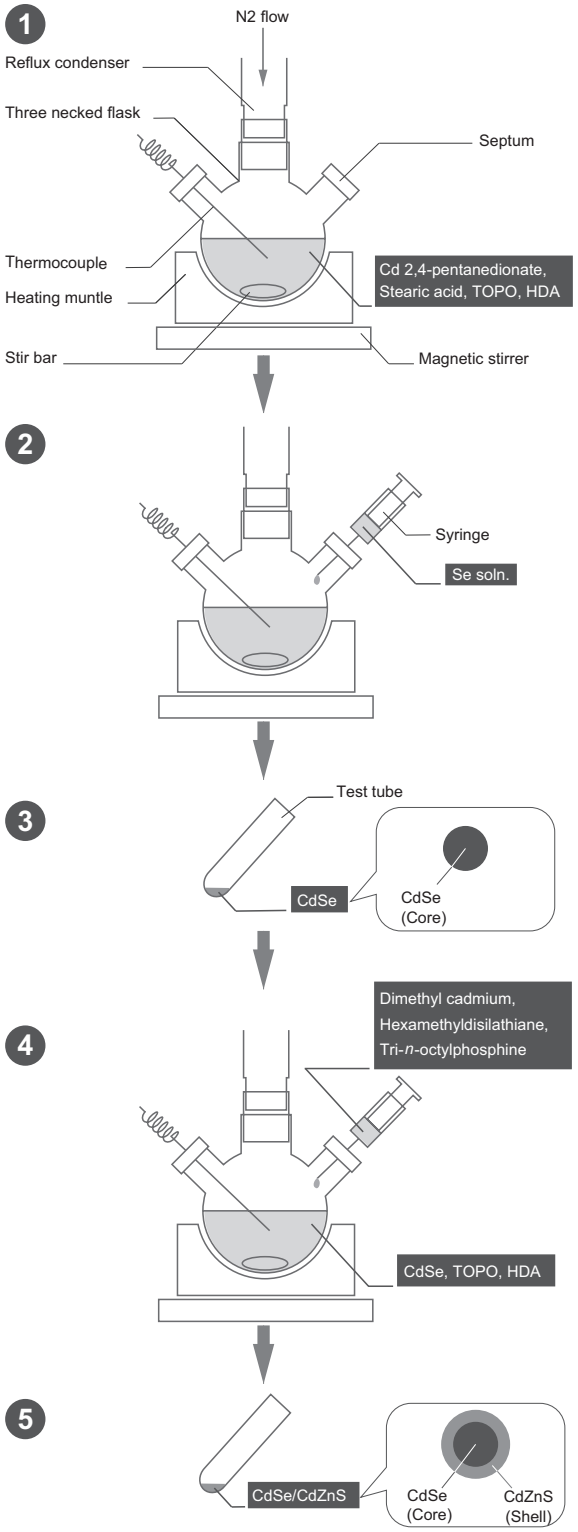


FIGURE 4.4.3 Synthesis of semiconductor nanocrystals (SNCs).

(Figure 4.4.3). The details of the procedure were reported by Tiwari et al.[8]

1. Cadmium 2,4-pentanedionate (0.062 g), stearic acid (0.30 g), tri-*n*-octylphosphine oxide (TOPO, 1.0 g) and hexadecylamine (HDA, 3.0 g) are placed in a

three-necked round bottom flask and degassed at 150°C for 1 hour under N_2 atmosphere with stirring. The flask is equipped with a thermocouple, a reflux condenser and rubber septums.

2. To synthesize core CdSe, the mixture is heated to 300°C and then selenium solution (0.80 mL, 0.10 g in 1 mL tri-butylphosphine) is quickly injected to the mixture using a syringe and cooled to 200°C. When the fluorescence spectrum of the mixture reaches to the purpose one (e.g. 600 nm), the solution is cooled to room temperature.
3. The CdSe are precipitated by the addition of ethanol and separated by centrifugation.
4. The CdSe are re-dispersed in TOPO (1.0 g) and HDA (3.0 g) and then heated to 220°C. To synthesize core/shell CdSe/CdZnS, the mixture of dimethyl cadmium (0.5 mL), diethylzinc (2.0 mL, 1 M hexane solution), hexamethyldisilathiane (0.52 mL) and tri-*n*-octylphosphine (TOP, 7.0 mL) is added dropwise with a syringe to the CdSe solution under stirring. When the fluorescence spectrum of the solution reaches to the purpose one (e.g. 620 nm), the solution is lowered to 100°C and stirred for 1 hour.
5. After the temperature is lowered to 60°C, CdSe/CdZnS are precipitated by addition of excess methanol and separated by centrifugation. The precipitated CdSe/CdZnS are dissolved in tetrahydrofuran (THF) and stored in a dark place.

Synthesis of SNCs in a Near-Infrared Region

The fluorescence of SNCs is originated from the recombination of electron-hole pairs, namely exciton (Figure 4.4.4). The electron in the conduction band and the hole in the valance band are confined in three spatial dimensions of SNC. The band gap between the bottom of the conduction band and the top of the valence band shrinks with an increase in the size of the SNCs (Figure 4.4.4).[9] This shrinkage produces a red shift of both absorbance and emission spectra of SNCs.

Although the choice of CdSe as a core structure produces emission spectra in the visible region, the use of tellurium as an additional composition allows a further shift of the spectrum to the near infrared (NIR) region (Figure 4.4.4). Because NIR light penetrates deeper biological tissue, NIR-SNCs are useful as a contrast agent for *in vivo* fluorescence imaging (see 4.4.4.2).[10] The synthesis procedure of spherical SNCs (CdSeTe/CdS) emitting in a NIR region (700–1,000 nm) as an example was reported by Jin et al. in detail.[11]

Synthesis of Rod-Shaped SNCs

SNCs have various heterostructures, such as rod-shaped nanocrystals (called quantum rods) and tetrapod-shaped nanocrystals. The various SNCs are synthesized by changing the types of capping ligands and crystal structure of core (Table 4.4.1). The heterostructures of SNCs have many interesting photophysical phenomena. For example, the rod-shaped and the tetrapod-shaped nanocrystals exhibit polarized emissions due to large aspect ratio and dual-color emission due to multiexciton, respectively (Figure 4.4.5).[12–13] These phenomena allow for sophisticated fluorescence imaging to investigate the dynamics of biomolecules *in vitro* and in cells (see 4.4.4.2). The synthesis procedure of rod-shaped SNCs (CdSe/CdS) emitting in visible region (400–700 nm) as an example was reported by Deka et al. in detail.[14]

Preparation of Water-Soluble SNCs

The SNCs synthesized in nonpolar organic solvents are water-insoluble (Figure 4.4.6a). For biological applications, the hydrophobic SNCs must be rendered hydrophilic by surface

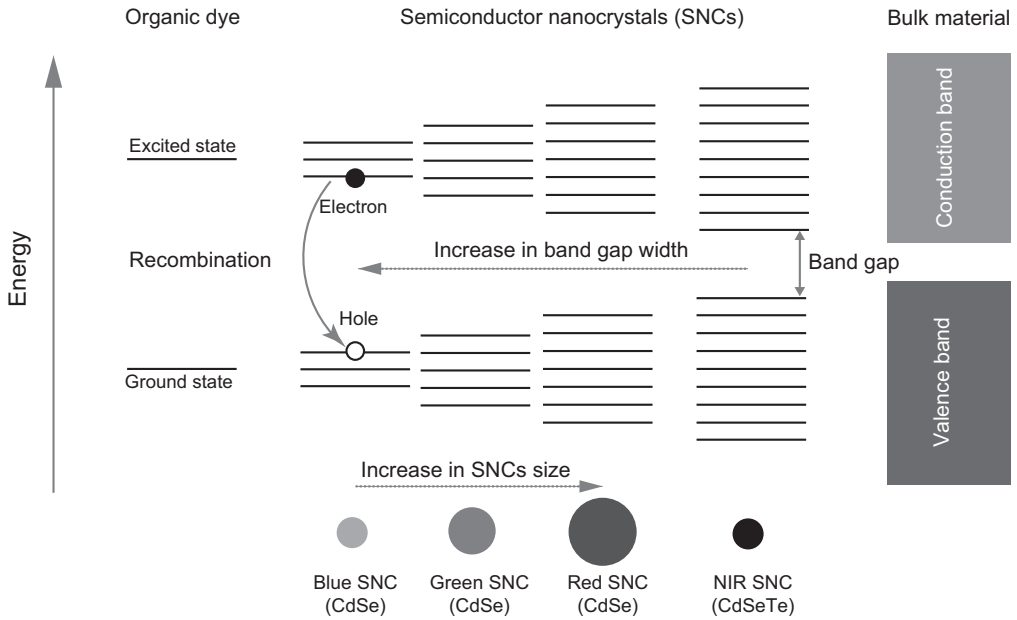


FIGURE 4.4.4 Energy diagram of organic dye, SNCs and bulk material.

TABLE 4.4.1 Comparison of Heterostructured SNCs

	Spherical SNC (Ref. 8)	Rod-shaped SNC (Ref. 14)	Tetrapod-shaped SNC (Ref. 13)
Crystal structure			
(Core)	Wurtzite	Wurtzite	Zinc-blende
Capping ligands			
(Core synthetic step)	TOPO, HAD, Stearic acid	TOPO, ODPA	1-octadecane, oreic acid, oleylamine
(Shell synthetic step)	TOPO, HDA, TOP	TOPO, ODPA, TOP, Hexylphosphonic acid	TOPO, ODPA, TOP, Propylphosphonic acid

TOPO, tri-n-octylphosphine oxide; HDA, hexadecylamine; TOP, tri-n-octylphosphine; ODPA, octadecylphosphonic acid.

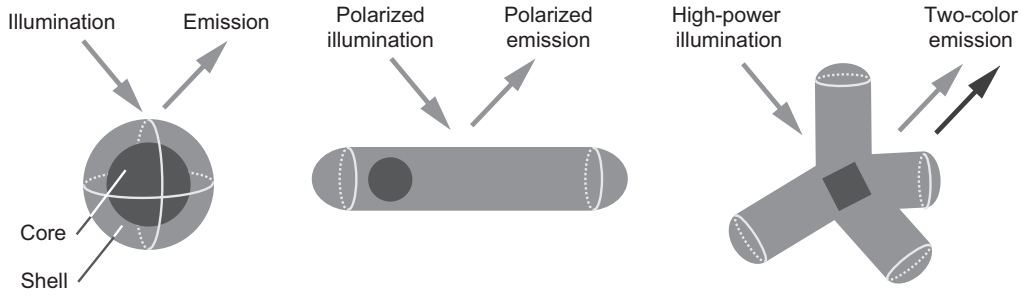


FIGURE 4.4.5 Heterostructured SNCs.

modification. Mainly two different approaches, namely (i) ligand exchange and (ii) encapsulation methods, have been developed for the preparation of water-soluble SNCs.[15]

(i) In the ligand exchange method, the hydrophobic ligands, such as TOPO, TOP and HDA, on the SNCs surface are replaced with amphiphilic ligands (Figure 4.4.6b). One end group of the amphiphilic ligands has a high affinity with the SNCs surface, while the other end group is hydrophilic. Thiolated water-soluble ligands, such as mercaptoacetic acid, mercaptoundecanoic acid, cysteine and glutathione (GSH), are typically used for the preparation of water-soluble SNCs. A drawback of the ligand exchanged SNCs is the relatively poor stability of biological buffers due to desorption of the amphiphilic ligands from the SNCs surface.

(ii) In the encapsulation method, the hydrophobic ligands are retained on the SNCs surface, and then amphiphilic polymers are introduced to the hydrophobic layer through hydrophobic interaction (Figure 4.4.6c). Drawback of the encapsulation method is that the diameter of encapsulated SNCs is much larger than that of the ligand-exchanged SNCs. The polymers, such as oligomeric phosphine, phospholipids and amphiphilic copolymers, are typically used for the preparation of water-soluble SNCs.

The water-soluble SNCs cannot act as bioimaging probes without further modification of the SNCs surface. In order to bind the SNCs to target biomolecules in cells, the water-soluble SNCs must be conjugated to biomolecules, such as peptides, oligonucleotides and proteins, including antibodies. Basic conjugation methods are categorized as electrostatic binding, noncovalent biotin–avidin binding, direct covalent crosslinking.[16] In the direct covalent crosslinking method, the biomolecules are linked to carboxyl and/or amine groups of the water-soluble SNCs using crosslinkers, namely coupling agents (Figure 4.4.6d).

4.4.4.2 Optical Measurement and Imaging

The SNCs have unique optical properties and give various advantages for biological applications over traditional fluorophores, such as organic dyes and fluorescent proteins. Since the absorption cross sections of SNCs are much larger than that of organic dyes, the molar extinction coefficients of SNCs are about 10–50 times larger and fluorescence brightness is much higher than that of organic dyes.[17,18] Although the traditional fluorophores have broad emission spectra, SNCs have narrow emission spectra that can be controlled by changing their core sizes and compositions. Thus, SNCs are suitable for multicolored imaging with no overlap of emission spectra.[19] Since SNCs are highly stable to photobleaching, they are also suitable for continuous tracking studies over a long period of time.[20] Therefore, SNCs have become one of the ideal probes for biological sensing, labeling, *in vivo* fluorescence imaging. In this section, the optical measurement of SNCs and fluorescence imaging using SNCs are described.

Determination of the Size and Concentration of SNCs

The size and concentration of SNCs are typically determined by dynamic light scattering (DLS) and conventional spectroscopic methods, respectively. However, since these methods

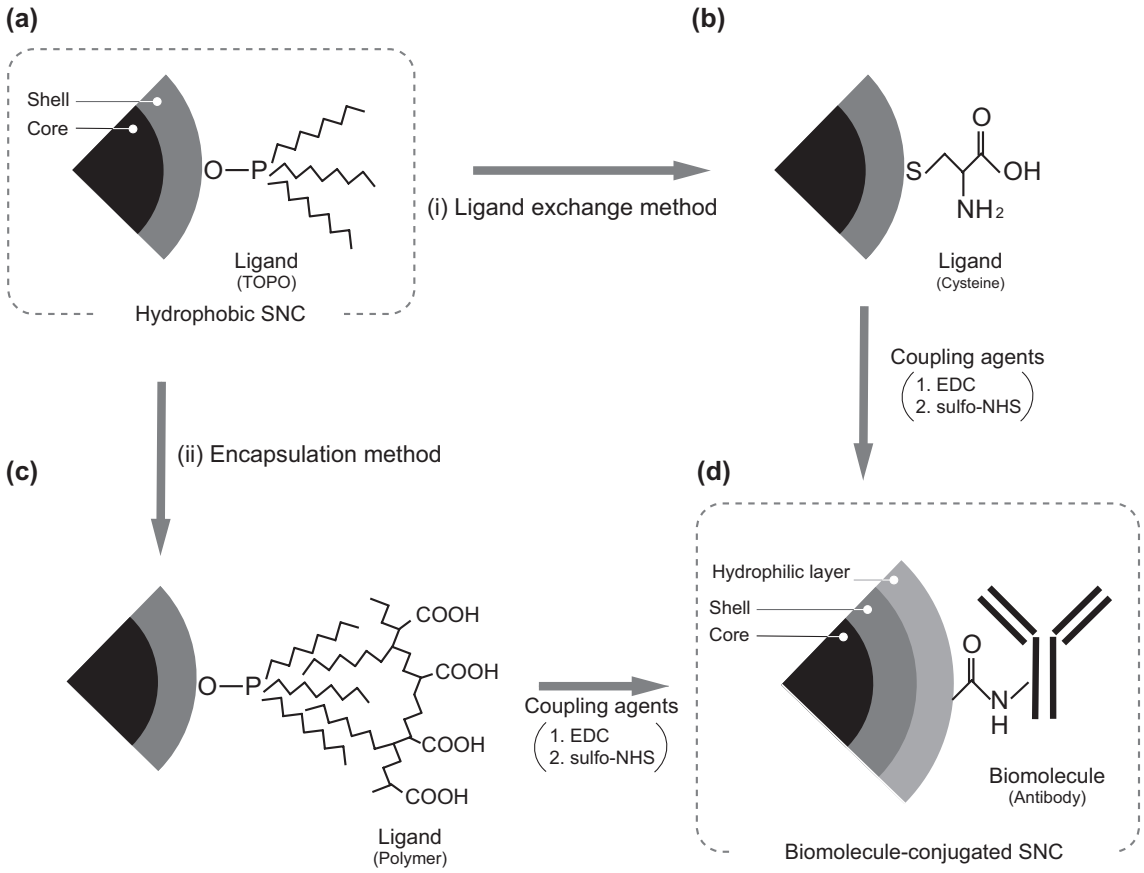


FIGURE 4.4.6 Water solubilization and bioconjugation of SNCs.

required approximately milliliter and micromoler for the measurements, respectively, it is difficult to determine these values of rare biomolecule-conjugated SNCs.

Fluorescence correlation spectroscopy (FCS) overcomes this problem. FCS uses the fluctuations of fluorescence intensity to determine the size and concentration of fluorescent molecules including SNCs. In FCS measurement, the fluorescence signals from the SNCs are detected at very dilute concentrations (~1 pM) in a tiny area (~1 fL) using confocal system (Figure 4.4.7a).[21]

The fluctuations of fluorescence intensity shown in Figure 4.4.7b are analyzed using the auto-correlation functions $G(\tau)$:

$$G(\tau) = \frac{< \delta I(t) \cdot \delta I(t+\tau) >}{< I(t) >^2} + 1 \tag{4.4.1}$$

where I and τ are the fluorescence intensity and the time delay, respectively (Figure 4.4.7c). The symbol < > denotes the ensemble average.

Assuming a one-component diffusion model for SNCs in solution, the acquired $G(\tau)$ is fitted by the following equation:

$$G(t) = \frac{1}{N}\left(1+\frac{\tau}{\tau_d}\right)^{-1}\left(1+\frac{\tau}{s^2\tau_d}\right)^{-1/2} + 1 \tag{4.4.2}$$

where τ_d is the diffusion times of SNCs (Figure 4.4.7c). N is the average number of the SNCs in the tiny area defined by radius w_0 and length $2z_0$ and s is the structure parameter representing the ratio $s = z_0/w_0$.

The value of τ_d is related to the translational diffusion constant D by the following equation:

$$\tau_d = \frac{w_0^2}{4D} \tag{4.4.3}$$

D is related to various physical parameters by the Stokes-Einstein equation as follows:

$$D = \frac{\kappa_B T}{6\pi\eta r} \tag{4.4.4}$$

where

- κ_B is the Boltzman constant
- T is the absolute temperature
- η is the viscosity of the solvent
- r is the hydrodynamic radius of SNCs

The value of N is converted to molecular concentration C by following equation:

$$C = \frac{N}{N_A \times V_{confocal}} \tag{4.4.5}$$

where N_A and $V_{confocal}$ are Avogadro's number and the volume of the tiny confocal area, respectively.

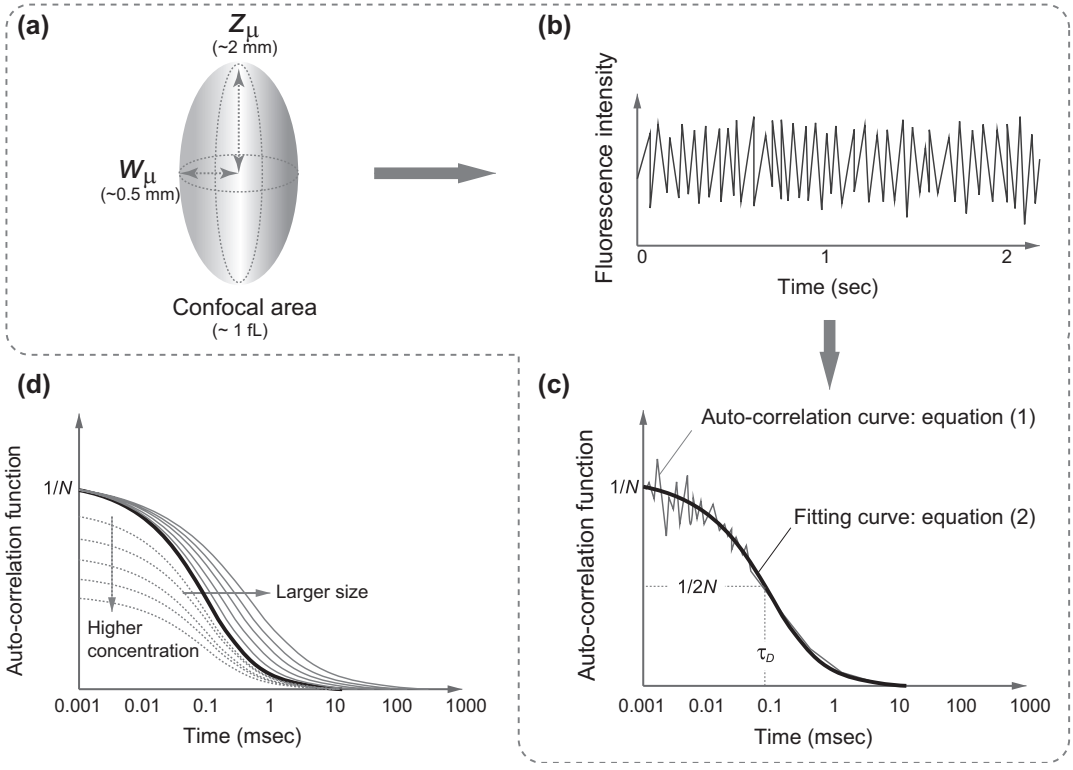


FIGURE 4.4.7 Fluorescence correlation spectroscopy.

If the κ_B, T, η, N_A and $V_{confocal}$ are defined using a standard fluorophore, the hydrodynamic radius r and concentration C of SNCs are determined by FCS analysis (Figure 4.4.7d). Since commercially available confocal microscopes are equipped with FCS, the size and concentration of SNCs can be determined also in living cells.[22]

Orientation Measurement of Biomolecules using SNCs

With the developments in microscopy, single individual fluorophore came to be detectable *in vitro* and also in living cells. The position of fluorophore can be determined by fitting its image with a Gaussian function in excess of optical diffraction limit (named as SPT: single particle tracking). The precision of the position determination depends on the number of emitted photons from the fluorophore. Major drawbacks of traditional fluorophores, such as organic dyes and fluorescent proteins, are their poor brightness and limited observation time due to photobleaching. SNCs overcome this problem due to their strong brightness and resistance to photobleaching. Thus, SNCs are expected to become a standard probe for SPT with nanometer resolution.[23]

In addition to three-dimensional (3D) SPT, the orientation is one of the most important parameters, because the biomolecules in living cells not only moves the X, Y and Z positions but also rotate and interact with partners with particular orientations. Spherical SNCs have isotropic photophysical properties, because their excitons are confined in all dimensions. In contrast, rod-shaped SNCs have anisotropic photophysical properties, namely polarized emissions, because excitons are confined in two dimensions due to their elongated structure. Thus, rod-shaped SNCs can be used to detect molecular orientation by polarized microscopy.

By using rod-shaped SNCs, Ohmachi et al. performed the simultaneous SPT in a 2D position (X and Y) and two types of orientations (θ and ϕ) of a motor protein, Myosin V, walking on an actin filament *in vitro* (Figure 4.4.8a and b).[24] Since a single SNC is bound to the myosin V via two HaloTags at the C terminus, the SNC rotates in synchronization completely with the rotational motion of myosin V. For orientation measurement, the fluorescent signals from the SNCs are divided equally into two beams by a beam splitter. Each beam is further split into two perpendicular polarization components (0° and 90°, 45° and 135°, respectively) by a pair of Wollaston prisms. Angular values of the in-plane and tilt angles (θ and ϕ, respectively) can be obtained by using these fluorescent intensities.

Watanabe et al. performed simultaneous SPT in a 3D position (X, Y, Z) with the orientation (θ) of a scavenger receptor, CD36, labeled with anti-CD36 antibody conjugated SNCs on plasma membrane of an isolated macrophage (Figure 4.4.8c and d).[25] For the 3D measurement, a pair of concave and convex cylindrical lenses is set behind the polarization optics. Two cylindrical lenses generate different optical path lengths along the X- and Y-axes, resulting in a measurable relationship between the Z-position of the fluorophore and the ellipticity of the image. For the orientation measurement, a polarizing beam splitter is set before the cylindrical lens pair to divide the fluorescent image into S- and P- polar channels. The orientation of the receptors can be determined by the ratio of the intensities of the S- and P- polarized images. When the number of photons from a single SNC is about 1,500 per 100 ms and the

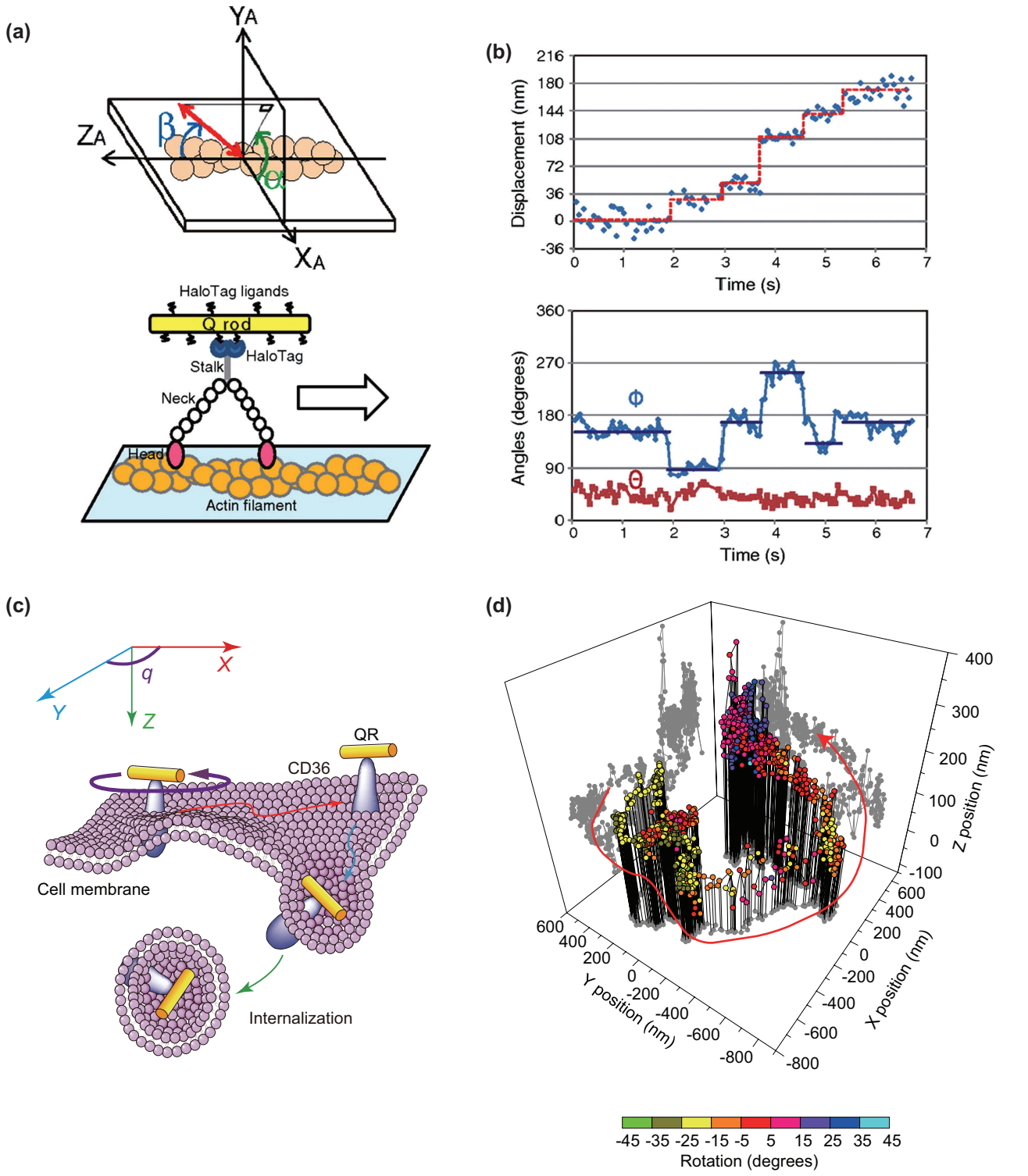


FIGURE 4.4.8 Orientation measurements using rod-shaped SNCs. [(a) and (b) from Ohmachi, M., et al., *Proc. Natl. Acad. Sci. U S A.*, 109, 5294–5298, 2012. With permission. (c) and (d) from Watanabe, T. M., et al., *Biophys, J.*, 105, 555–564, 2013. With permission.]

Z-position was zero, the best calculation precisions for the *X*-, *Y*-, *Z*-positions and angle are 5, 5, 12 nm and <6°, respectively.

In vivo imaging using SNCs

For *in vivo* fluorescence imaging, above NIR region (above 700 nm) has several advantages over the visible regions (400–700 nm): (i) low light absorption, (ii) reduced light scattering and (iii) a rack of autofluorescence.[26] (i) Although the light absorption by water increases from the visible region toward infrared region, the sum of the absorption due to endogenous chromophores, such as hemoglobin and myoglobin, decreases drastically. (ii) The light scattering coefficient,

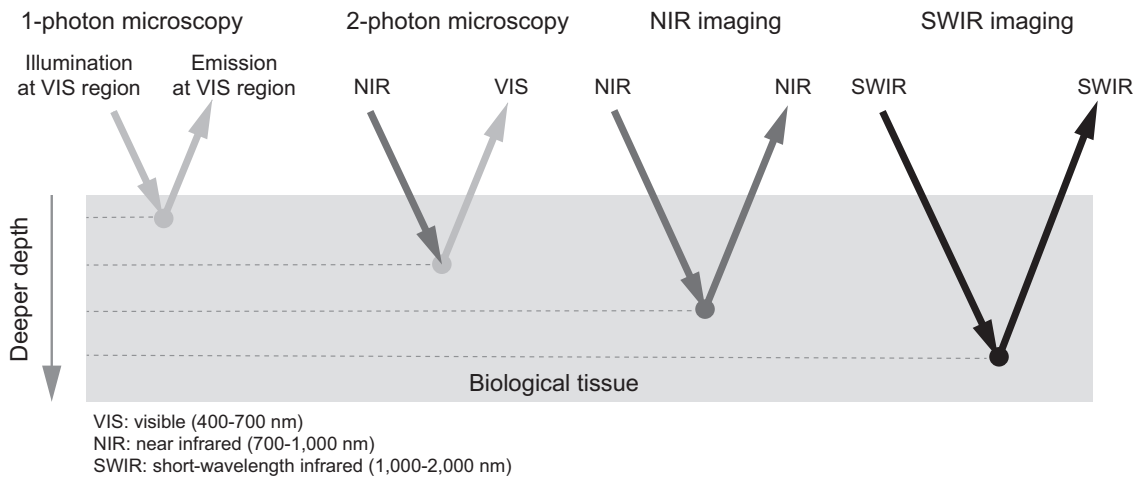


FIGURE 4.4.9 Fluorescence-microscopy and -imaging.

TABLE 4.4.2 Examples of Fluorophores from Visible to SWIR regions

	1- & 2-Photon Microscopy	NIR Imaging	SWIR Imaging
Organic dyes	Alexa 488, Alexa 594, Alexa 647, etc.	Alexa 750, Alexa 790, etc.	–
Fluorescent proteins	GFP, YFP, RFP, etc.	iRFP, miRFP, etc.	–
Semiconductor nanocrystals	CdS, CdSe, etc.	CdSeTe, InP, etc.	InAs, PbSe, etc.

NIR, near infrared; SWIR, short-wavelength infrared; GFP, green fluorescent protein; YFP, yellow FP; RFP, red FP; iRFP, near infrared FP; miRFP, monomeric near infrared FP.

which depends on several physical parameters, including the shapes of cells, the size of organelles, and their refractive index, gradually decreases toward the infrared region. (iii) Although autofluorescence derived from NADH and flavins are detectable in the visible region, there are almost no autofluorescence above NIR region. Thus, light above the NIR region can penetrate deeper tissue, and the fluorophores emitting above NIR region are needed for deeper *in vivo* fluorescence imaging (Figure 4.4.9).

Two-photon microscopy is one fluorescence imaging technique that can visualize fluorescent-labeled biomolecules and cells several hundred microns deep in various organs.[27] In contrast to conventional microscopy, namely one-photon microscopy, the two-photon microscopy equipped pulse laser excites fluorophores by two NIR photons and then detects visible photons from the fluorophores (Figure 4.4.9). The efficiency of two-photon absorption depends on the two-photon absorption cross-section of the fluorophores. The experimental value of the two-photon action cross-section measured for CdSe is several orders of magnitude larger than those of organic dyes and fluorescent proteins.[28] Thus, SNCs are useful for not only conventional microscopy but also the two-photon microscopy.

Short-wavelength infrared region (SWIR; 1,000–2,000 nm) has further advantages over the NIR (700–1,000 nm) regions for *in vivo* fluorescence imaging (Figure 4.4.9).[29] Biocompatible single-walled carbon nanotubes has been applied for deeper *in vivo* fluorescence imaging through the skin. Recently, Bruns et al. synthesized InAs-based SNCs emitting at the SWIR region.[30] The fluorescence quantum yields of the InAs-based SNCs are more than 100 times higher than those of commonly used carbon nanotubes previously applied to biological imaging. Since it is extremely difficult to synthesize organic dyes and fluorescent proteins that emit at SWIR region, SNCs have a bright future especially for *in vivo* fluorescence imaging in the SWIR region (Table 4.4.2).[31,32]

4.4.4.3 Organic Systems

Organic components are often employed as a base material to fabricate composite particles for biomedical uses. Polymers may be a typical organic component that can be utilized for this purpose since these materials can be designed to have biocompatibility and/or biodegradability in general. The polymers can be applied for particulate systems in the range of nano-meter to micro-meter in particle size, according to the purpose of the biomedical uses.

Nanoparticulate Systems

Features and characteristics required for pharmaceutical preparations are diverse. In response to the requirement, design of the particle structure and the material selection is made under the utilization of an optimal preparation process. Several examples of the polymeric nanoparticles with composite structures are illustrated in Figure 4.4.10.

Figures 4.4.10a and b show polymeric nanoparticles with a core-shell structure.[33,34] This type of core-shell nanoparticles

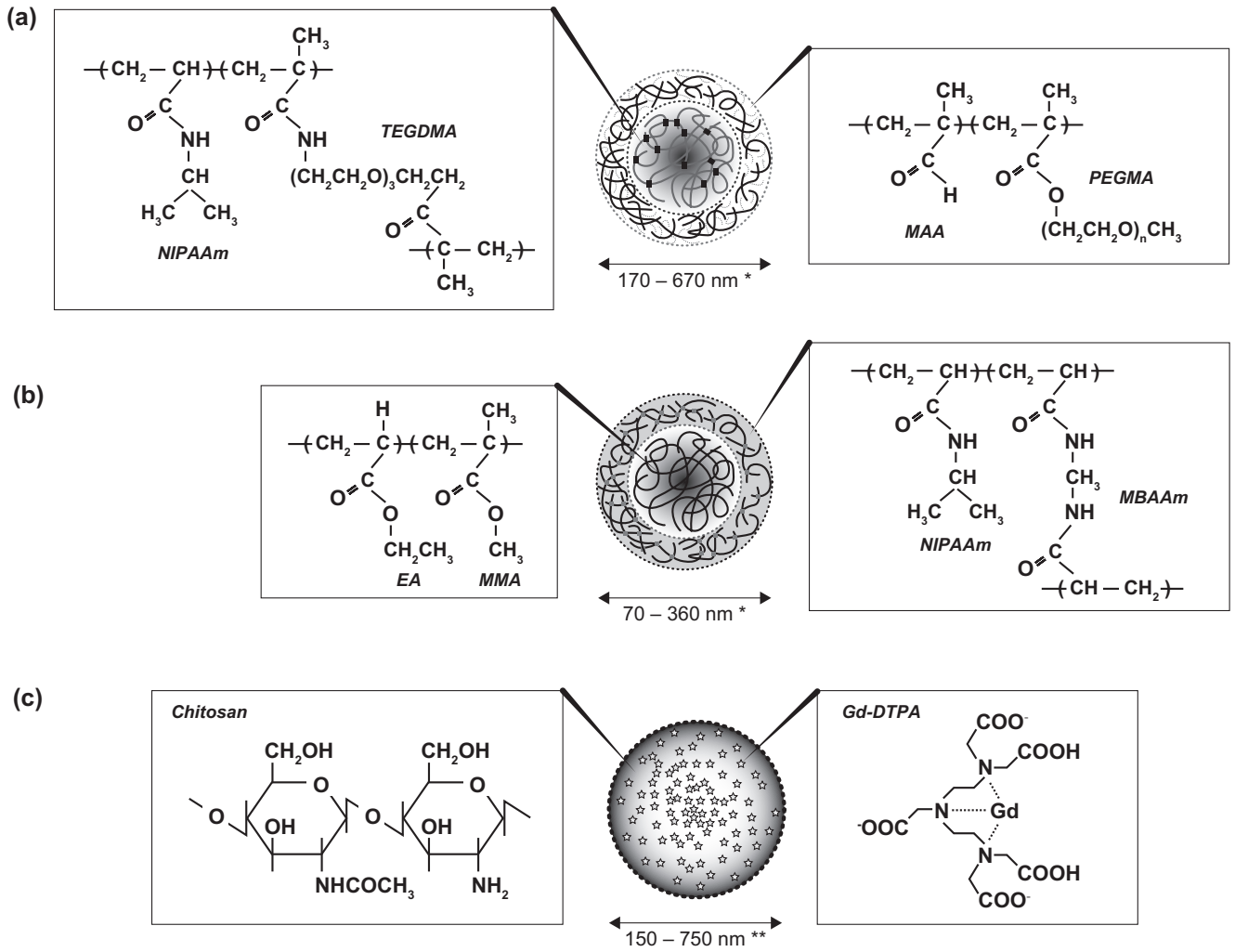


FIGURE 4.4.10 Examples of polymeric composite nanoparticles. *indicates typical particle size changes in response to environmental temperature and/or pH. **indicates the particle size ranges controlled by altering the preparation conditions and/or the grades of polymeric sources. Abbreviations: EA, ethyl acrylate; Gd-DTPA, Gadopentetic acid; MAA, methacrylic acid; MBAAm, methylene bisacrylamide; MMA, methyl methacrylate; NIPAAm, *N*-isopropyl acrylamide; PEGMA, polyethyleneglycol mono-methacrylate; TEGDMA, tetraethyl-eneglycol di-methacrylate.

can be prepared with an emulsion or a dispersion polymerization technique using monomers such as acrylates and methacrylates. The chemical structure of the polymers prepared by these polymerization methods can be determined by the selection of the constituent monomers. Although particle structure of the nanoparticles is also likely to depend on the physicochemical properties of the monomer, the structural control may be possible in some extent by modifying the polymerization procedure. For example, nanoparticles with homogeneous particle structure can be obtained by polymerization in bulk-charge of the monomer mixture, while two-step semi-continuous addition of different types of monomer mixtures can produce those with a core-shell structure. Such core-shell polymeric nanoparticles can be used as a drug carrier for oral delivery of peptide-based drugs (Figure 4.4.10a) and a building block of thermosensitive controlled-release microparticles (Figure 4.4.10b, See also Figure 4.4.11).

Composite nanoparticles containing a low molecular active substance dispersed in the polymeric matrix are a major class of the frequently-employed drug carriers. Many types of polymers including synthetic, semi-synthetic and natural polymers are available as a starting material for fabrication of the composite nanoparticles. Figure 4.4.10c shows chitosan-based nanoparticles containing gadopentetic acid (Gd-DTPA) designed for gadolinium neutron-capture therapy (Gd-NCT).[35–37]

Gd-NCT is a cancer therapy that utilizes γ-rays, X-rays and electrons emitted *in vivo* as a result of the nuclear neutron-capture reaction with administered gadolinium-157.[36] A key factor for success in Gd-NCT at the present stage is a device whereby Gd is delivered efficiently and is retained in a tumor for a sufficient period during thermal-neutron irradiation. Gd-DTPA is traditionally used clinically as an MRI contrast agent. It is reported that Gd-DTPA is rapidly eliminated from systemic circulation and hardly accumulates in tumors because of its high hydrophilicity. Meanwhile, the Gd concentration in tumors required to obtain the minimum tumor inactivation effect was estimated to be as high as about 100 μg Gd-157/g wet tumor.[36]

Chitosan, a polysaccharide, has been widely studied as a material for drug delivery systems due to its bioerodible, biocompatible, bioadhesive and bioactive characteristics. These distinctive features led us to use chitosan as a promising material for design and preparation of Gd-loaded nanoparticulate devices for Gd-NCT. Further, its amino pendants dangling from sugar backbones may be useful for the enrichment of Gd-DTPA into the nanoparticles by a possible ionic interaction between two free-carboxylic groups of Gd-DTPA and the amino groups of chitosan.

The preparation process of chitosan-based nanoparticles containing Gd-DTPA (Gd-nano-CPs) is based on an emulsion-droplet coalescence method.[35,37] Chitosan was dissolved in an aqueous solution of Gd-DTPA. The aqueous solution of Gd-DTPA having very high water solubility as the acidic solvent can act as a good solvent of chitosan in this method. This solution was added to the paraffin liquid containing non-ionic surfactant (Arlacel C) and was stirred using a high-speed homogenizer to form a water-in-oil (w/o) emulsion A. Similarly, a w/o emulsion B consisting of sodium hydroxide solution and paraffin liquid containing Arlacel C was prepared. The emulsions A and B were mixed with stirring to neutralize and solidify chitosan as a result of collision and coalescence between droplets of each emulsion. Interestingly, the content of Gd-DTPA up to 80 wt% can be kept inside the chitosan nanoparticles with the mean particle size of approximately 430 nm.[35] The mechanism of Gd-nano-CP generation is unclear in detail, but it is presumed that the incorporation of Gd resulted from the ionic interaction between two free carboxylic groups in Gd-DTPA molecules and polyamino groups in the chitosan molecules.

A thermal-neutron irradiation study was carried out *in vivo* to confirm its therapeutic potential in Gd-NCT, using B16F10 melanoma-bearing mice. Gd-nano-CP suspension or Gd-DTPA solution as a control was intratumorally injected before thermal-neutron irradiation.[36,37] When the change of tumor volume in mice after the thermal-neutron irradiation was examined, the tumor growth was significantly suppressed in the Gd-nano-CP-administered group with thermal-neutron irradiation while no significant growth-suppression of the tumor was obtained in the cases of no Gd–administered or Gd-DTPA solution–administered group. As is generally recognized, the Gd-DTPA in solution used in ordinary Gd-NCT trials can be eliminated very rapidly from tumor tissue. The enhanced Gd-NCT effects by Gd-nano-CP might result from the high gadolinium quantity retained in tumor tissue.

Microparticulate Systems

Among many classes of surface modification process, the fluidized-bed processes with spraying can most easily produce multilayered particle structures with each layer being monolithic, a random multiphase structure, an ordered multiphase structure, and so on (Figure 4.4.1). Different components and layers can be combined to produce almost infinite types of functional particles. As an example, designs and preparations of thermosensitive controlled-release microparticles are described below.

Controlled-release technology based on externally temperature-activated release can find applications in diverse industrial fields.[34,38,39] In the pharmaceutical area, for example, deviation of the body temperature from the normal temperature (37°C) in the physiological presence of pathogens or pyrogens can be utilized as a useful stimulus that induces the release of therapeutic agents from a thermosensitive controlled-release system. Physically controlled temperature using a heat source such as microwaves from outside the body can also be used for temperature-activated antitumor drug release, combined with local hyperthermic treatment of cancer.

The membranes of the thermosensitive controlled-release microparticles were constructed by a random mixing of ethylcellulose pseudo latex (Aquacoat®) with latex particles having a poly(EA-MMA) core and a poly[*N*-isopropylacrylamide (NIPAAm)] shell (Figure 4.4.11).[34] This is an example where

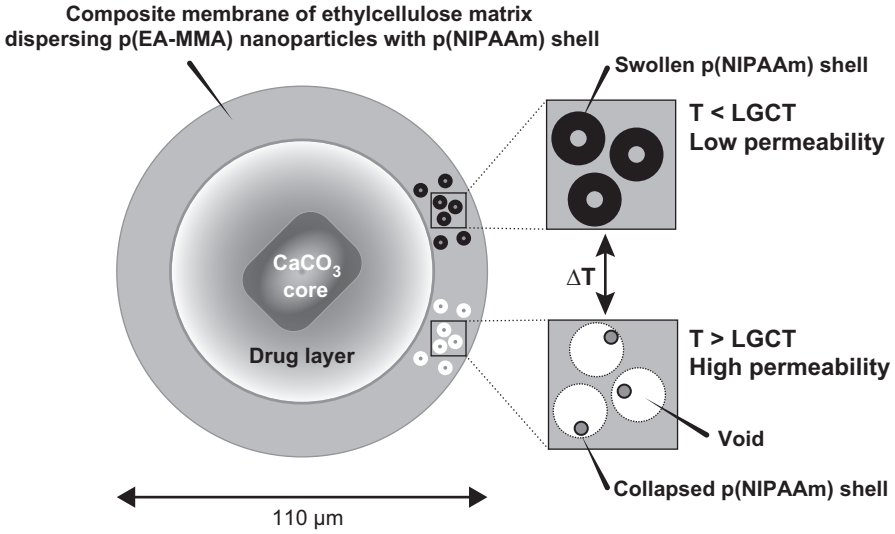


FIGURE 4.4.11 Composite microparticle showing positively thermosensitive drug release.

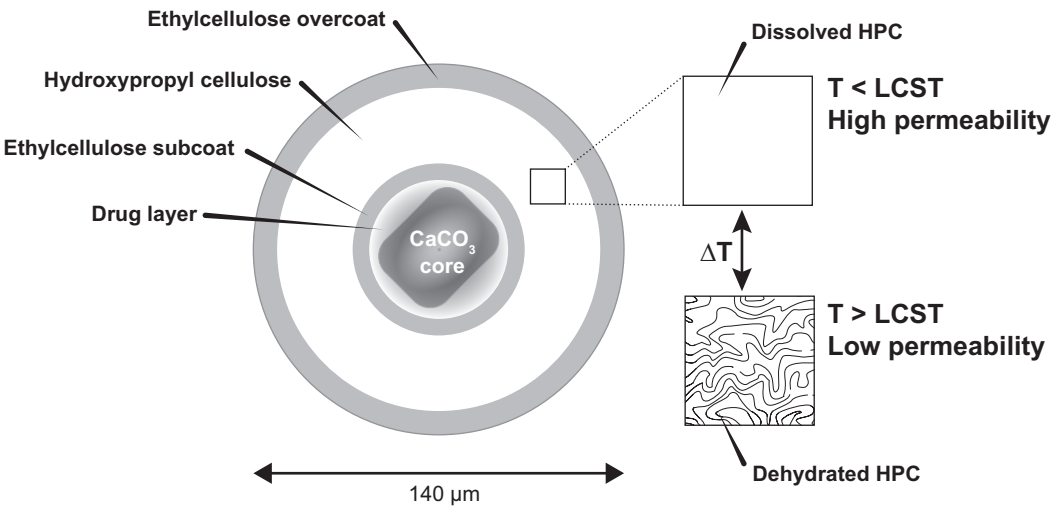


FIGURE 4.4.12 Composite microparticle showing negatively thermosensitive drug release.

the membrane has the random two-phase structure in Figure 4.4.1. The microparticles exhibited a thermosensitive release of the water-soluble drug. The mechanism is explained in Figure 4.4.11. Briefly, a collapse of p(NIPAAm) shell at a temperature higher than a lower gel collapsed temperature (LGCT) generates many voids in the membrane, leading to enhanced permeability of the membrane and thus drug release takes place. In contrast, drug-permeation can be suppressed at temperature lower than LGCT because of no void formation by the swollen p(NIPAAm) shells. When the temperature was changed in a stepwise manner from 30°C to 50°C, the microparticles showed an "on-off" pulsatile release. This on-off response was reversible.

Alternatively, this type of thermosensitive microparticle can be prepared even with already established pharmaceutical ingredients. As is well known, hydroxypropyl cellulose (HPC), the commonly used binder and coating substrate, has a lower critical solution temperature (LCST), around 44°C, and its water solubility drastically changes across the LCST.[39] Negatively thermosensitive drug-release microparticles with an HPC layer were thus designed by utilizing the thermally reversible dissolution/precipitation process resulting from the LCST phenomena (Figure 4.4.12).[39] In this case, particles are constructed with multilayers of monolithic structure (Figure 4.4.1). The release rate from the microparticles with a sandwiched HPC layer was found to be drastically decreased when the temperature came near the LCST: the release rate at 50°C was approximately 10 times lower than that at 30°C.

Unlike many types of milli-sized devices that have been developed so far, the microparticles mentioned here were around 100 μm in diameter (Figures 4.4.11 and 4.4.12). Such small dimensions provided a sharp release rate change in response to temperature change. This may be one of advantages of fine particle coating technology. The above demonstrated flexibility in designing membrane structures also offers considerable advantages over conventional microencapsulation methods.

REFERENCES

1. Jono, K., Ichikawa, H., Miyamoto, M., Fukumori, Y., *Powder Technol.*, 113, 269–277, 2000.
2. Sauer, D., Cerea, M., DiNunzio, J., McGinity, J., *Int. J. Pharm.*, 457, 488–502, 2013.
3. Ichikawa, H., and Fukumori, Y., *Yakuzaigaku*, 67, 288–296, 2007.
4. Debenedetti, P. G., Tom, J. W., Kwauk, X., Yeo, S.-D., *Fluid Phase Equilibr.*, 82, 311–321, 1993.
5. Henglein, A., *Chem. Rev.*, 89, 1861–1873, 1989.
6. Shchukin, V. A., Bimberg, D., *Rev. Mod. Phys.*, 71, 1125–1171, 1999.
7. Smith, A. M., Mohs, A. M., Nie, S., *Nat. Nanotechnol.*, 4, 56–63, 2009.
8. Tiwari, D. K., et al., *Sensors (Basel)*, 9, 9332–9364, 2009.
9. Jasieniak, J., Califano, M., Watkins, S. E., *ACS Nano*, 5, 5888–5902, 2011.
10. Zhao, P., et al., *Wiley Interdiscip. Rev. Nanomed. Nanobiotechnol.*, 10, e1483, 2018.
11. Jin, T., et al., *Int. J. Mol. Sci.*, 9, 2044–2061, 2008.
12. Hu, J., et al., *Science*, 292(5524), 2060–2063, 2001.
13. Mishra, N., et al., *Nat. Commun.*, 8, 15083 , 2017.
14. Deka, S., et al., *J. Am. Chem. Soc.*, 131, 2948–2958, 2009.
15. Michalet, X., et al., *Science*, 307(5709), 538–544, 2005.
16. Xing, Y., et al., *Nat. Protoc.*, 2, 1152–1165, 2007.
17. Bruchez, M. Jr, et al., *Science*, 281(5385), 2013–2016, 1998.
18. Chan, W. C., Nie, S., *Science*, 281(5385), 2016–2018, 1998.
19. Chan, W. C., et al., *Curr. Opin. Biotechnol.*, 13, 40–46, 2002.
20. Alivisatos, P., *Nat. Biotechnol.*, 22, 47–52, 2004.
21. Hess, S. T., Huang, S., Heikal, A. A., Webb, W. W., *Biochemistry*, 41, 697–705, 2002.
22. Dong, C., Irudayaraj, J., *J. Phys. Chem. B.*, 116, 12125–12132, 2012.
23. Chang, Y. P., Pinaud, F., Antelman, J,, Weiss, S., *J. Biophotonics.*, 1, 287–298, 2008.

24. Ohmachi, M., et al., *Proc. Natl. Acad. Sci. U S A.*, 109, 5294–5298, 2012.
25. Watanabe, T. M., et al., *J. Biophys*, 105, 555–564, 2013.
26. Frangioni, J. V., *Curr. Opin. Chem. Biol.*, 7, 626–634, 2003.
27. Helmchen, F., Denk, W., *Nat. Methods*, 2, 932–940, 2005.
28. Larson, D. R., et al., *Science*, 300(5624), 1434–1436, 2003.
29. Smith, A. M., Mancini, M. C., Nie, S., *Nat. Nanotechnol.*, 4, 710–711, 2009.
30. Bruns, O. T., et al., *Nat. Biomed. Eng.*, doi:10.1038/s41551–017-0056, 2017.
31. Resch-Genger, U., et al., *Nat. Methods.*, 5, 763–775, 2008.
32. Chernov, K. G., Redchuk, T. A., Omelina, E. S., Verkhusha, V. V., *Chem. Rev.*, 117, 6423–6446, 2017.
33. Iijima, M., et al., *Langmuir*, 24, 3987–3992, 2008.
34. Ichikawa, H., and Fukumori, Y., *J. Control. Release*, 63, 107–119, 2000.
35. Tokumitsu, H., Ichikawa, H., Fukumori, Y., *Pharm. Res.*, 16, 1830–1835, 1999.
36. Tokumitsu, H., et al., *Cancer Lett.*, 150, 177–182, 2000.
37. Ichikawa, H., et al., *Appl. Radiat. Isotopes*, 88, 109–113, 2014.
38. Ichikawa, H., and Fukumori, Y., *STP Pharma Sci.*, 7, 529–545, 1997.
39. Ichikawa, H., and Fukumori, Y., *Chem. Pharm. Bull.*, 47, 1102–1107, 1999.



Taylor & Francis
Taylor & Francis Group
http://taylorandfrancis.com

4.5 Electrical Charge Control

Takashi Ogi and Kikuo Okuyama (4.5.1.1)
Shuji Matsusaka (4.5.1.2)
Ko Higashitani (4.5.2.1)
Hidehiro Kamiya (4.5.2.2)

4.5.1 IN GASEOUS STATE

4.5.1.1 Charge Control by Gaseous Ions and Electrons

The charging process of particles by gaseous ions depends on two physical mechanisms: field and diffusion charging. When ions drift along electric field lines and impinge on the particle, the charging process is referred to as field charging. Diffusion charging is due to thermal collisions between particles and ions. Photoelectron charging, in which electrons are emitted from particles by UV irradiation, is also used to control the particle charge.

Production Methods

Gaseous ions are produced by three methods of irradiations: UV or other radiations, discharges in gas, and fissions of droplets, as shown in Table 4.5.1. In α-ray (≅5 MeV) and β-ray (≅0.7 MeV) irradiations, high-energy particles collide with air molecules and produce primary positive ions and electrons[1,2]. The primary ions grow metastable positive ions by ion–molecule reactions and ion clustering. The free electrons attach molecules with high electron affinity, such as O_2 or H_2O, and form negative ions. In soft X-ray (≅10 keV) and vacuum UV-ray (≅3~10 eV) irradiations, gas atoms and molecules are excited by multiphoton adsorption and emit electrons[3,4]. These primary positive ions and electrons change to metastable positive and negative ions at atmospheric and low pressures but do not change in vacuum. When UV-rays (≅5 eV) irradiate a metal film, photoelectrons are emitted from the film. Photoelectrons become metastable negative ions by electron attachment and ion clustering at atmospheric and low pressures[5].

Corona discharge is produced in an inequality electric field between a needle electrode and a plate electrode or between a line electrode and a cylinder electrode[6,7]. When energy higher than the ionization potential of gas is given to casual electrons, the accelerated electrons collide with gas molecules and produce pairs of a new electron and a primary positive ion near the needle or the line electrode (discharge electrode). Either the electrons or primary positive ions are drawn toward the plate or cylinder electrode (collection electrode) according to the polarity of the discharge voltage. During the travel from the discharge electrode to the collection electrode, the electrons and primary positive ions change to metastable negative and positive ions, respectively.

When water droplets are broken by a collision with an obstacle, like a waterfall, the space is filled by negative ions[8]. This is called the Lenard effect. In a droplet suspended in air, anions generally form a layer near a surface of the droplet. By the collision of a droplet, many droplets with very small sizes are produced from a surface layer, and a few droplets with relatively large sizes are produced from the body of an original droplet. As a result, the very small droplets have a negative charge and the large droplets have a positive one.

TABLE 4.5.1 Methods for Generation of Ions

Method	Principle	Products	Maximum ion Concentration	Other Applications
Irradiation				
α-ray	Ionization of gas	Bipolar ions	10^7 cm^{-3}	Static charge elimination
β-ray	Ionization of gas	Bipolar ions	10^7 cm^{-3}	Static charge elimination
Soft X-ray	Photoionization of gas	Bipolar ions	10^8 cm^{-3}	Static charge elimination
UV-ray	Photoionization in vacuum	Positive ions and electrons	10^5 cm^{-3}	Static charge elimination
UV-ray	Photoelectron emission from metals	Photoelectrons or negative ions	10^5 cm^{-3}	Contamination control
Discharge				
DC corona	Ionization of gas	Unipolar ions and ozone	10^7 cm^{-3}	Electrostatic precipitator Indoor air cleaner
AC corona	Ionization of gas	Bipolar ions and ozone	10^7 cm^{-3}	Static charge elimination
Fission of droplets				
Collision	Lenard effect	Negative ions and charged droplets	10^4 cm^{-3}	Physical therapy Sterilization
Electrospray	Reyleigh fission	Unipolar ions and charged droplets	10^6 cm^{-3}	Spray pyrolysis Mass spectrometer

The very small droplets with negative charge evaporate and become negative cluster ions consisting of 10~30 water molecules. In electrospray, DC high voltage is applied to the nozzle and droplets have a high unipolar charge. When the repulsive force between charges accumulated on the droplet is stronger than the surface tension, that is Rayleigh limit, and the droplets are broken into very small droplets. Two processes for ion formation are considered. One is that liquid molecules evaporate from the very small droplets and the sizes of the droplets reduce to ions. Another is that ions evaporate directly from the surfaces of droplets.

Formation Process and Reactivity

The primary ions and electrons produced by the high-energy irradiation and the discharge change with time by the following ion–molecule reactions.

$e^- + A \rightarrow A^-$	Electron attachment
$A^+ + B \rightarrow A + B^+$	Charge transfer
$A^- + B \rightarrow A + B^-$	Charge transfer
$A^+B_n + B + M \rightarrow A^+B_{n+1} + M$	Clustering
$A^-B_n + B + M \rightarrow A^-B_{n+1} + M$	Clustering

Ions that have high chemical reactivity, such as O^-, O_2^-, O_3^-, H^+, and N_2O^+, are generated generally in the first stage of growth processes. Furthermore, the ions and electrons often produce radicals and excited molecules by the following recombination reactions:

$AB^+ + e^- \rightarrow A\cdot + B\cdot$	Dissociation recombination
$AB^+ + e^- \rightarrow AB^* + h\nu$	Radiative recombination
$AB^+ + e^- + M \rightarrow A\cdot + B\cdot + M$	Three body recombination
$AB^+ + C^- \rightarrow AC^+ + B\cdot$	Ion–ion recombination

In air, ·O, ·OH, and O_3 are produced by the above process. These radicals and excited molecules induce further chain reactions with other chemical reactants. Effects of the radicals and excited molecules on the particle materials should be considered when the ions are used to control the electrical charge.

Physical Properties

The physical properties of ions depend on the ion–molecule reaction and ion-clustering processes. Table 4.5.2 shows ion properties in air. Electrical mobility was measured by Bricard,[9] and other properties were calculated from them. The positive ions are $H^+(H_2O)_n$ ($n = 5$–8) and negative ions are $O^-(H_2O)_n$, $O_2^-(H_2O)_n$, $OH^-(H_2O)_n$, $NO^-(H_2O)_n$, $CO_3^-(H_2O)_n$, and so forth.[10] The number concentrations N of unipolar and bipolar ions are obtained by

$$N^s = \frac{I}{B_{ei}^s eAE} \quad \text{for unipolar ion} \tag{4.5.1}$$

$$N^+ = N^- = \left(\frac{I_s}{\alpha_i eV}\right)^{1/2} \quad \text{for bipolar ion} \tag{4.5.2}$$

where

- I is the ion current in the electric field of intensity E
- I_s is the saturation ion current
- A is the area of the electrode
- V is the volume of the ion-generation chamber
- B_{ei} is the electrical mobility of ions
- e is the elementary charge (= 1.602×10^{-19} C)
- α_i is the recombination coefficient of a bipolar ion

The superscripts are the polarity of the ion.

Field Charging

Field charging tends to dominate the charging for particles larger than 2 μm in diameter under a strong electric field. The particle charge q can be evaluated from the equation introduced by White:[11]

$$q = \frac{q_\infty (eB_{ei}^s N^s t / 4\varepsilon_0)}{1 + (eB_{ei}^s N^s t / 4\varepsilon_0)} \tag{4.5.3}$$

$$q_\infty = \left(1 + \frac{2(\varepsilon_1 - 1)}{\varepsilon_1 + 2}\right) \frac{\pi\ \varepsilon_0 E D_p^2}{e} \tag{4.5.4}$$

where

- q is the number of elementary charges captured by a particle
- q_∞ is the saturation charge
- D_p is the particle diameter
- t is the charging time
- ε_0 is the dielectric constant of gas (= 8.855×10^{-12} F/m)
- ε_1 is the specific dielectric constant of particles

The average charges q_{av} calculated by Equations (4.5.3) and (4.5.4) at $N^+t = 10^{13}$ s/m^3 are shown in Figure 4.5.1. The particle charge q decreases steeply as the particle size decreases. For

TABLE 4.5.2 Physical Properties of Air Ions

	Property					
Polarity	Electrical Mobility B_{ei} (m^2 s^{-1} V^{-1})	Molecular Weight M_i (kg mol^{-1})	Diffusion Coefficient D_i (m^2 s^{-1})	Mean Thermal Velocity c_i (m s^{-1})	Mean Free Path l_i (m)	Recombination Coefficient α_i (m^2 s^{-1})
Positive ion	1.4×10^{-4}	0.131	3.53×10^{-6}	2.18×10^{2}	1.46×10^{-8}	1.6×10^{-12}
Negative ion	1.9×10^{-4}	0.100	4.80×10^{-6}	2.48×10^{2}	1.94×10^{-8}	1.6×10^{-12}

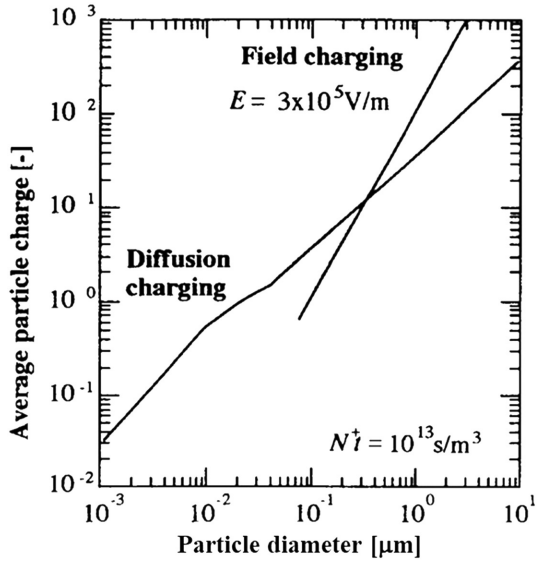


FIGURE 4.5.1 Average particle charge by unipolar ions.

the charging of high-resistivity particles, Equations (4.5.3) and (4.5.4) cannot be applied, and numerical computation is necessary.[12]

Diffusion Charging

Diffusion charging is caused by the kinetic energy of an ion and the electrostatic energy between a particle and an ion in the absence of an external electric field. Charging is classified into bipolar charging, where particles are mixed with both negative and positive ions, and unipolar charging, where they are exposed to either ion. This mechanism dominates the charging in the size range $D_p < 0.2$ μm even in strong electric fields because field charging does not work.

Combination Probability of an Ion with a Particle

In the theoretical estimation for the diffusion charging, a combination probability β of an ion and a particle is necessary because diffusion charging is the coagulation process of ions and particles. The following equation, derived by Fuchs,[13] can be applied to the whole range of particle size:

$$\beta_q^s = \pi c_i^s \xi \lambda^2 \exp\left(-\frac{\phi(\lambda)}{kT}\right) \Bigg/ \left[1 + \exp\left(-\frac{\phi(\lambda)}{kT}\right) \frac{c_i^s \xi \lambda^2}{2D_i^s} \int_\lambda^\infty \frac{\exp[-\phi(\lambda)/kT]}{r^2} dr\right] \tag{4.5.5}$$

where

- λ is the radius of the image sphere ($\cong l_i^s + D_p/2$)
- k is the Boltzmann constant ($=1.380 \times 10^{-23}$ J/K)
- T is the absolute temperature
- D_i is the diffusion coefficient of ion
- c_i is the mean thermal velocity
- l_i is the mean free path of ions
- ξ is the correction coefficient of free molecule collision by the electrostatic force between a particle and an ion

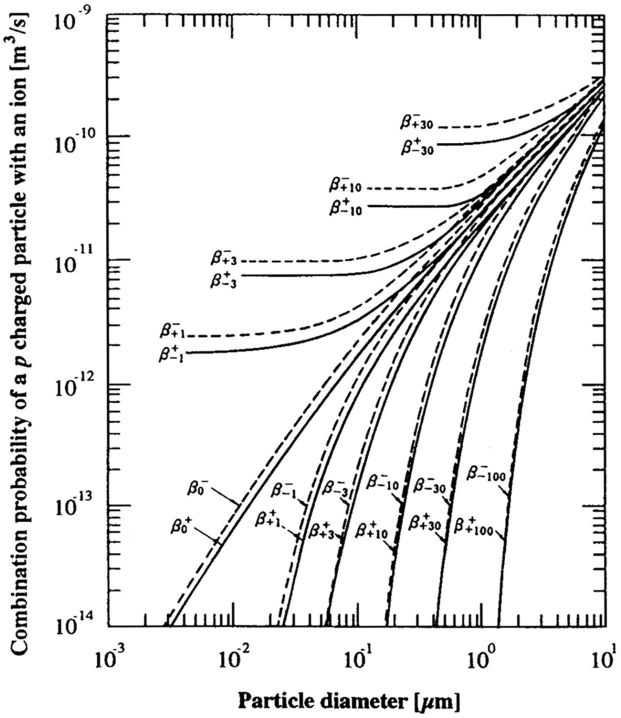


FIGURE 4.5.2 Combination probability of an ion and a particle.

$\phi(\lambda)$ is the electrostatic potential between a particle and an ion given by

$$\phi(\lambda) = \int_r^\infty F_e(r)dr = \frac{qe^2}{4\pi\varepsilon_0 r} - \frac{\varepsilon_1 - 1}{\varepsilon_1 + 1} \frac{e^2}{8\pi\varepsilon_0 r} \frac{D_p^3}{2r^2(4r^2 - D_p^2)} \tag{4.5.6}$$

Figure 4.5.2 shows the calculated results of Equation (4.5.5) using the ion properties listed in Table 4.5.2. The combination probability for a negative ion is larger than that of a positive ion because a negative ion has larger ion properties than a positive ion.

Diffusion Charging by Unipolar Ions

Diffusion charging can be evaluated theoretically by two approaches: deterministic and stochastic, using the combination probability β. In the deterministic approach, the time change in particle charges q is expressed by

$$\frac{dq}{dt} = \beta_q^s N^s \tag{4.5.7}$$

In the stochastic approach, the time-dependent change in charge distribution is expressed by the following birth–death equations:

$$\frac{dn_0}{dt} = -\beta_0^s n_0 N^s \tag{4.5.8}$$

$$\frac{dn_q}{dt} = \left(\beta_{q-1}{}^s n_{q-1} - \beta_q^s n_q\right) N^s, \quad q > 0 \text{ and } s = + \tag{4.5.9}$$

or

$$\frac{dn_q}{dt} = \left(\beta_{q+1}^s n_{q+1} - \beta_q^s n_q\right) N^s, \quad q < 0 \text{ and } s = - \tag{4.5.10}$$

where n is the particle number concentration and the subscripts are the numbers of elementary charges and their polarity. The above equations were solved analytically by Natanson[14] under the initial condition that particles were uncharged:

$$\frac{n_0}{n_T} = \exp\left(-\beta_0^s N^s t\right) \tag{4.5.11}$$

$$\frac{n_q}{n_T} = \left(\prod_{k=0}^{q-1} \beta_k^s N^s\right) \sum_{i=0}^{q} \frac{\exp(-\beta_i^s N^s t)}{\prod_{\substack{i=0 \\ j\neq i}}^{q} \left(\beta_i^s - \beta_j^s\right) N^s}, \quad q > 0 \text{ and } s = + \tag{4.5.12}$$

or

$$\frac{n_q}{n_T} = \left(\prod_{k=0}^{q+1} \beta_k^s N^s\right) \sum_{i=0}^{q} \frac{\exp(-\beta_i^s N^s t)}{\prod_{\substack{i=0 \\ j\neq i}}^{q} \left(\beta_i^s - \beta_j^s\right) N^s}, \quad q < 0 \text{ and } s = - \tag{4.5.13}$$

The average charges q_{av} calculated by Equations (4.5.11) and (4.5.12) at $N^+t = 10^{13}$ s/m^3 are shown in Figure 4.5.1.

A necessary condition to bring uncharged particles to the desired charge distribution is obtained by[15]

$$N^s t = \left(\frac{\ln\left(1 - n_{pT}/n_T\right)}{\beta_0^s}\right) \tag{4.5.14}$$

$$\beta_0^+ = \exp(-33.69 + 1.479 \ln D_p + 0.04214 \ln^2 D_p - 0.01001 \ln^3 D_p) \tag{4.5.15}$$

$$\beta_0^- = \exp(-33.49 + 1.389 \ln D_p + 0.08163 \ln^2 D_p - 0.01448 \ln^3 D_p) \tag{4.5.16}$$

where n_{pT}/n_T is the desired number ratio of total charged particles to total particles. Equations (4.5.15) and (4.5.16) are approximate equations of the theoretical curves shown in Figure 4.5.2. D_p is measured in nanometers in these equations.

A numerical computation is necessary to solve Equations (4.5.5), (4.5.11), and (4.5.12). Although the following equation was derived under incorrect assumptions by White,[11] it is useful for making a rough estimate of the diffusion charging:

$$q = \frac{2\pi\varepsilon_0 D_p kT}{e^2} \ln\left(1 + \frac{D_p c_i^s e^2 N^s t}{8\varepsilon_0 kT}\right) \tag{4.5.17}$$

However, it should be noted that results given by Equation (4.5.17) are about two times higher than strict solutions.

In the range 0.2 μm < D_p < 2 μm, particles are charged by both field and diffusion charging. Liu and Kapadia[16] solved this problem numerically. If errors of 50–100% are allowed, the sum of Equations (4.5.3) and (4.5.17) is available as a simple estimation.

Diffusion Charging by Bipolar Ions (Neutralization)

Bipolar diffusion charging is expressed generally by birth–death equations because the deterministic approach cannot reflect the difference of ion properties:

$$\frac{dn_o}{dt} = \beta_{+1}^- n_{+1} N^- - \beta_0^- n_0 N^- + \beta_{-1}^+ n_{-1} N^+ - \beta_0^+ n_0 N^+ \tag{4.5.18}$$

$$\frac{dn_q}{dt} = \beta_{q+1}^- n_{q+1} N^- - \beta_q^- n_q N^- + \beta_{q-1}^+ n_{q-1} N^+ - \beta_q^+ n_q N^+ \quad |q| > 0 \tag{4.5.19}$$

When the number concentration of bipolar ions is sufficiently high under sufficient charging time, particle charge reaches the equilibrium state. The equilibrium distribution at the steady state is obtained from the above equations.[17]

$$\frac{n_0}{n_T} = \frac{1}{\Sigma} \tag{4.5.20}$$

$$\frac{n_q}{n_T} = \prod_{q=+1}^{+\infty} \left(\beta_{q-1}^+ / \beta_q^-\right) / \Sigma, \quad q \geq +1 \tag{4.5.21}$$

$$\frac{n_q}{n_T} = \prod_{q=-1}^{-\infty} \left(\beta_{q+1}^- / \beta_q^+\right) / \Sigma, \quad q \leq -1 \tag{4.5.22}$$

where

$$\Sigma = \sum_{q=+1}^{+\infty} \left[\prod_{q=+1}^{+\infty} \left(\frac{\beta_{q-1}^+}{\beta_q^-}\right)\right] + \sum_{q=-1}^{-\infty} \left[\prod_{q=-1}^{-\infty} \left(\frac{\beta_{q+1}^-}{\beta_q^+}\right)\right] + 1 \tag{4.5.23}$$

Figure 4.5.3 shows the equilibrium charge distribution in the size range of 0.001 μm ≤ D_p ≤ 10 μm. Fractions of negatively charged particles are higher than those of positively charged particles due to differences in ion properties.

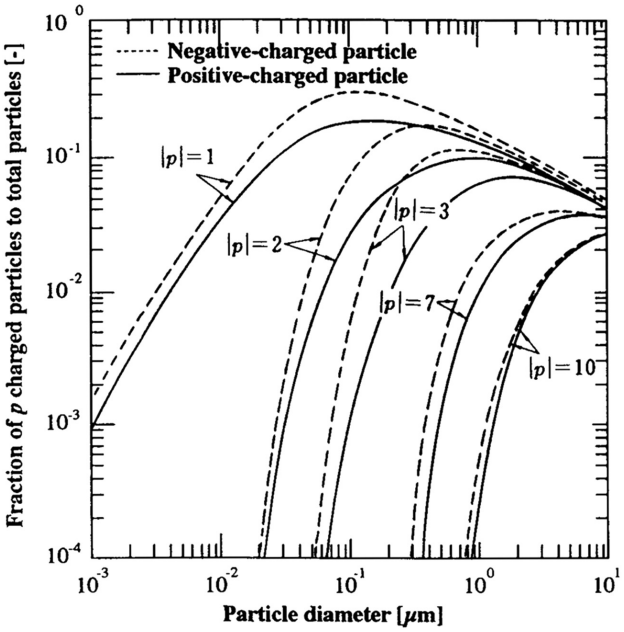


FIGURE 4.5.3 Equilibrium charge distribution by bipolar ions.

In the size range of $D_p \geq 0.5$ μm, strict solutions agree with the Boltzmann charge distribution[18] within 30% error:

$$\frac{n_q}{n_T} = \frac{\exp\left(-q^2e^2/4\pi\ \varepsilon_0 D_P kT\right)}{\sum_{q=-\infty}^{+\infty} \exp\left(-q^2e^2/4\pi\ \varepsilon_0 D_P kT\right)} \tag{4.5.24}$$

The necessary condition for which q_0 charged particles attain the Boltzmann charge distribution is obtained by

$$N^b = -\varepsilon_0 kT \frac{\ln\left(0.1/|q_0|\right)}{D_i e^2} \tag{4.5.25}$$

where N^b is the number concentration of ion pair ($= N^+ = N^-$).

Photoelectron Charging

When a solid is irradiated by UV light, electrons are emitted from the surface. This phenomenon is called a photoelectron emission and is used as a principle of surface analysis by photoelectron spectroscopy. The photoelectron emission is generally explained by the three-step model shown in Figure 4.5.4. Electrons in the solid are first optically excited into states of high energy; then they move to the surface of the solid and escape into the vacuum or gas phase. Therefore, electrons can be emitted from the surface when the photon energy hv is higher than the work function ϕ_w of the solid. Photoelectron emission is also caused by UV irradiation to particles suspended in a gas stream (aerosol). In this case, aerosol particles are charged positively because of the escape of electrons. The potential barrier ϕ_q which must be overcome by an electron to escape from the q charged particle is expressed by[19]

$$\phi_q = \phi_w + \frac{e^2(q+1)}{2\pi\varepsilon_0 D_p} - \frac{5}{8}\frac{e^2}{2\pi\varepsilon_0 D_p} \tag{4.5.26}$$

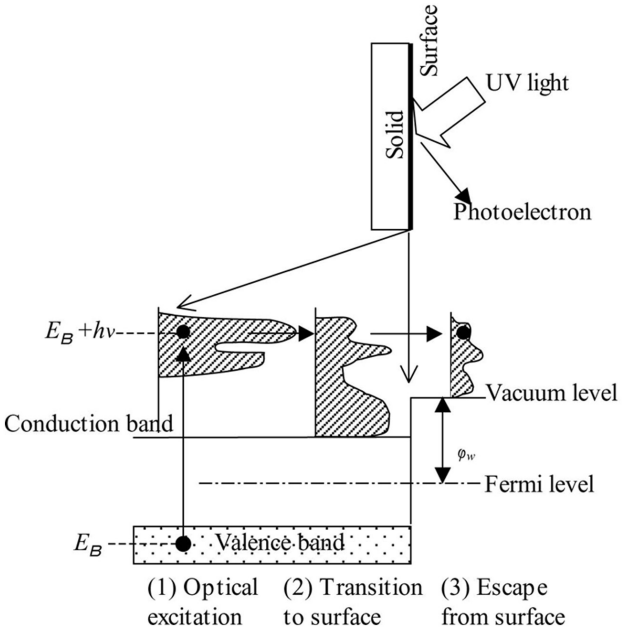


FIGURE 4.5.4 Illustration of three-step model for photoelectron emission from a solid.

When ϕ_q is higher than hv, the particle charges reach to a maximum value q_{max} obtained from Equation (4.5.26).

$$q_{max} = \frac{hv - \phi_w}{e^2} 2\pi\varepsilon_0 D_p + \frac{5}{8} \tag{4.5.27}$$

The probability ζ_q at which an electron is emitted from the q charged particle is obtained by

$$\zeta_q = C\left(hv - \phi_q\right)^m \frac{I\pi D_p^2}{4hv} \tag{4.5.28}$$

where

C and m are material-dependent empirical constants
I is the irradiation intensity

4.5.1.2 Charge Control by Contact Electrification

When two different materials come into contact, charge is transferred according to the contact potential difference, which depends on the work functions of the two materials; thus particle charging can be controlled by changing the wall material. If the work function of the wall is close to that of the particles, particle charging will be suppressed. Furthermore, it is possible to assign opposite polarity to particles by using a different material.

Figure 4.5.5 shows particle charging in dilute gas-solid pipe flow.[20] Alumina particles are charged positively and negatively by contact with stainless steel and brass, respectively. The specific charge of the particles q_m is theoretically derived as a function of the pipe length L, i.e.

$$q_m(L) = q_{m0}\exp\left(-\frac{L}{L_0}\right) + q_{m\infty}\left\{1 - \exp\left(-\frac{L}{L_0}\right)\right\} \tag{4.5.29}$$

where

q_{m0} and $q_{m\infty}$ are the initial and equilibrium specific charges, respectively
L_0 is the characteristic length

These results indicate that particle charging can be controlled by arranging pipes made of different materials.

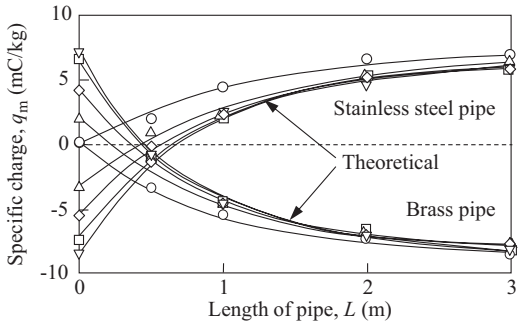


FIGURE 4.5.5 Particle charging in dilute gas-solid pipe flow (alumina particles, count median diameter: 3.3 μm, pipe diameter: 6 mm, air velocity: 40 m/s, mass flow ratio: 5×10^{-4} kg-particle/kg-air).

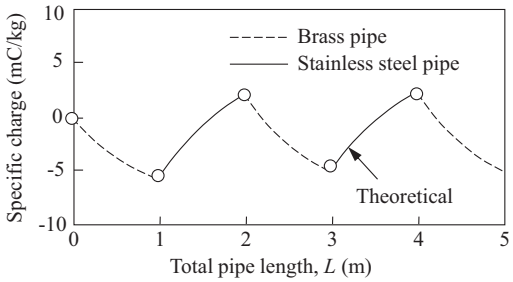


FIGURE 4.5.6 Control of particle charging by a system combining two different pipe materials (alumina particles, count median diameter: 3.3 μm, pipe diameter: 6 mm, air velocity: 40 m/s, mass flow ratio: 5×10^{-4} kg-particle/kg-air).

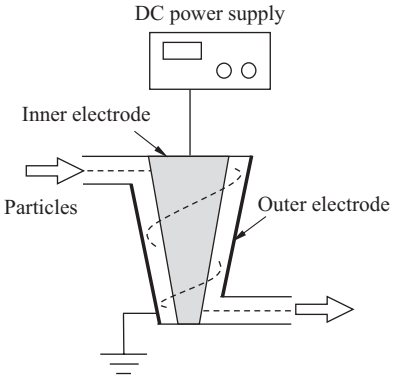


FIGURE 4.5.7 Particle charger for gas-solid flow.

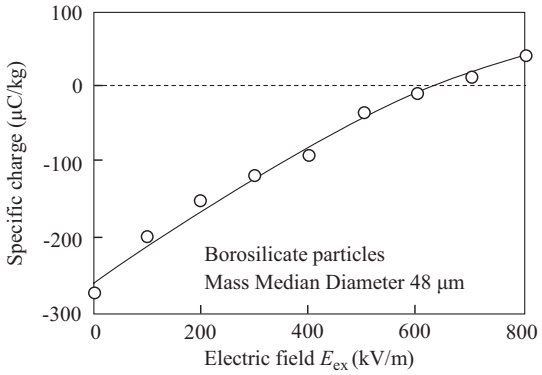


FIGURE 4.5.8 Particle charger control by electrical field in the particle charger (electrodes: stainless steel).

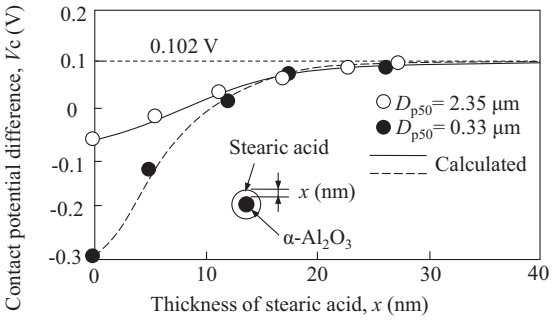


FIGURE 4.5.9 Contact potential difference of coated particles against the reference (Au).

Figure 4.5.6 shows the results obtained by alternately connecting a 1-m brass pipe and 1-m stainless steel pipe.[20] The particle charge values are within a certain range. To more precisely control particle charging, new mixture materials should be developed.

The contact potential difference can also be changed by applying an external electric field. Figure 4.5.7 shows a particle charger with inner and outer electrodes.[21] Particles enter from the top and exit from the bottom of the charger; the broken line illustrates the particle flow path in the particle charger. The conical shape allows for improved particle contact with the outer electrode as the particles flow through the charger. As particles come into contact with the outer electrode, the particles can gain or lose electrons according to the contact potential difference. The charge of the particles leaving the charger depends directly on the charge supplied to the inner electrode.

Figure 4.5.8 shows the results of the particle charge as a function of electric field strength in the particle charger.[21] The polarity of the particle charge is changed from negative to positive. Particle charge control for gas-solid flow is shown here, but this method using an external electric field is also made applicable for the case without air flow by changing the contact mechanism between the particles and the electrode.[22]

Because the charge transfer occurs through the contact area, the surface property is more significant than the bulk property. If the wall is covered with an oxidation layer, or if a layer is removed by particle collision, the surface property will be changed, and thus, the particle charging will fluctuate. To avoid such instabilities, the wall surface is treated chemically or mechanically.

Surface treatments such as surface coating,[23] attaching a charge-control agent,[24] and chemical modification are effective to change the work function of particles. Figure 4.5.9 shows the contact potential difference of alumina particles coated with stearic acid.[23] The value of the contact potential difference varies according to the thickness of the coating layer; however, it is almost constant where the thickness is larger. Therefore, particle charging can be controlled by the thickness of the coating layer.

The amount of charge transferred by elastic collision is proportional to the maximum contact area. When a spherical particle collides with a wall, the maximum contact area S can be approximated by[25]

$$S = 1.36 k_e^{2/5} \rho_p^{2/5} D_p^2 v_i^{4/5} \tag{4.5.30}$$

where

k_e is the elasticity parameter
ρ_p is the density of the sphere
D_p is the particle diameter
v_i is the impact (incident) velocity

If the particle is not spherical, the particle shape should be considered.[26] The elasticity parameter k_e is given by

$$k_e = \frac{1-\nu_1^2}{E_1} + \frac{1-\nu_2^2}{E_2} \tag{4.5.31}$$

where

ν is Poisson's ratio
E is Young's modulus, and subscripts 1 and 2 represent the particle and the wall, respectively

To reduce the charge transferred by impact, it is desirable to choose materials with a larger Young's modulus, that is, to use harder materials. The net contact area depends on the surface state: the net contact area decreases with increasing roughness.[27]

If there is no further electrification, the charge on the surface decreases over time, which is called electric leakage. For conductive particles, the charge tends to leak for a short time. It is more difficult for particles with high electrical resistance to release their charge; however, it is easier if they are mixed with conductive fine particles or fillers, because of the higher conductivity. Hydrophilic surface modification with a surfactant is also effective to release the charge. Charge reduction is prominent at higher humidity;[28] thus, the maximum charge on the particles is lower, even though they are charged repeatedly.

If the wall is made of a nonconductive material, the charge on the wall is also considered. The charge forms an electric field so as to reduce the effective contact potential difference, and also causes electric discharge or dust explosion; therefore, the charge on the wall should be released. One effective method is to induce dielectric breakdown using a thin dielectric wall reinforced with a conductive material, such as metal.[29]

In addition, the external electric field is also effective to control the effective contact potential difference.

4.5.2 IN LIQUID STATE

4.5.2.1 Charge Control in Aqueous Solutions

Particles in solutions bear a surface charge by the various mechanisms described in the section 2.2.2 Then, because of the electroneutrality principle, counterions are attracted toward the particle surface, as illustrated in Figure 4.5.10, and some of them are adsorbed directly on the surface to form the so-called Stern layer. When the counterions excessively adsorb on the surface with specific affinity, the sign reversal of the surface charge may occur. The rest of the ions in the bulk are in thermal motion, balancing the electrical attractive force to form a diffuse double layer. The potential at the particle surface is called the surface potential, ψ_0, and the potential at the outside of the Stern layer is called the Stern potential, ψ_d. Because the structure within the Stern layer is not well known, the Stern potential is often regarded as the surface potential of particles for many engineering purposes. Hence the Stern potential is expressed by ψ_0 in the succeeding subsection unless the specific effect of the Stern layer is discussed.

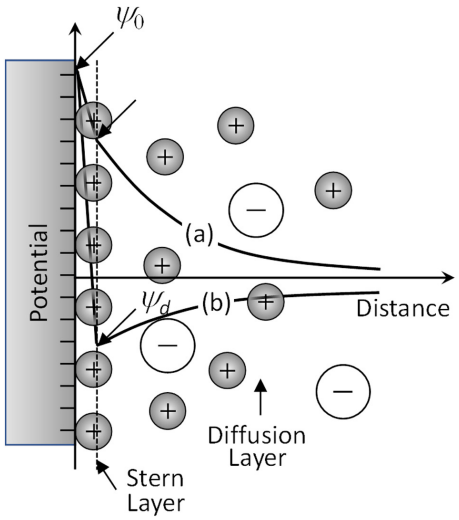


FIGURE 4.5.10 Potentials and ions in the Stern layer and diffuse layer: (a) a certain amount of counter ions are adsorbed on the surface because of their electrostatic attraction; (b) an excessive amount of ion is adsorbed because of their high affinity to the surface.

Potential and Charge in the Diffuse Layer

The Poisson equation holds between the volume density of charge ρ and the potential ψ in the diffuse double layer:[30]

$$\Delta^2\psi = -\frac{\rho}{\varepsilon} \tag{4.5.32}$$

where ε is the permittivity of the medium. The charge density is given by the sum of all the ionic contributions in the unit volume:

$$\rho = \sum n_i z_i e \tag{4.5.33}$$

where n_i and z_i are the number concentration and valency of ions of type i, respectively, and e is the elementary charge. The Boltzmann equation holds at the equilibrium where the electrostatic and chemical potentials of ions balance:

$$n_i = n_{0i} \exp\left(-\frac{z_i e\psi}{kT}\right) \tag{4.5.34}$$

where

n_{0i} is the bulk concentration of ions of type i
k is the Boltzmann constant
T is the temperature

Substitution of Equations (4.5.33) and (4.5.34) into Equation (4.5.32) results in the Poisson– Boltzmann equation:

$$\nabla^2\psi = -\Sigma\left(\frac{n_{0i} z_i e}{\varepsilon}\right)\exp\left(-\frac{z_i e\psi}{kT}\right) \tag{4.5.35}$$

This equation cannot be solved explicitly in general. However, when the Debye–Hückel approximation that ψ is small everywhere [i.e. $ze\psi < kT$ ($\psi < 25.7/z$ mV at 25°C)] holds, and the electrolyte is symmetric with valency $z_+ = -z_- = z$ and concentration $n_{0+} = n_{0-} = n_0$, the equation is simplified and the analytical solution is derived.

When the surface is a flat plate, the potential distribution is given by

$$\psi = \psi_0 \exp(-\kappa x) \tag{4.5.36}$$

$$\kappa = \left(\frac{2n_0 z^2 e^2}{\varepsilon kT}\right)^{0.5} = \left(\frac{2\times 10^3 C_e N_{av} z^2 e^2}{\varepsilon kT}\right)^{0.5} \tag{4.5.37}$$

where

x	is the distance from the plate surface
C_e (M)	is the electrolyte concentration
N_{av}	is the Avogadro constant
κ	is the reciprocal Debye length which is a measure of the ionic concentration of the bulk solution

The charge density of the diffuse layer, σ_d, is given by

$$\sigma_d = -\int_0^\infty \rho dx \tag{4.5.38}$$

Then, Equation (4.5.38) is rewritten as follows:

$$\sigma_d = \varepsilon\left(\frac{d\psi}{dx}\right)_{x=0} = -\left(\frac{4n_0 ze}{\kappa}\right)\sinh\left(\frac{ze\psi_0}{2kT}\right) \tag{4.5.39}$$

When the effect of the Stern layer is regarded as negligible, the surface charge, σ_d, is given by

$$\sigma_0 = -\sigma_d = \left(\frac{4n_0 ze}{\kappa}\right)\sinh\left(\frac{ze\psi_0}{2kT}\right) \tag{4.5.40}$$

This shows the correlation between the surface potential and the charge density of the diffuse layer.

A similar argument can be developed for the potential around a spherical particle of radius a, and the potential in the diffuse layer is given as

$$\psi = \left(\frac{\psi_0 a}{r}\right)\exp[-\kappa(r-a)] \tag{4.5.41}$$

where r is the distance from the center of spherical particle. The total charge of the particle Q is then written as

$$Q = -\int_a^\infty 4\pi r^2 \rho dr = 4\pi\varepsilon a(1+\kappa a)\psi_0 \tag{4.5.42}$$

Charge Control by Electrolytes

In order to control the charge of the particle surface, it is necessary to know not only the charging mechanism but also how the surface charge varies with the surrounding conditions. This is illustrated using a simple model for surface charging.[31]

When the particle surface is charged by the complete dissociation of "strong" functional groups, such as $-OSO_3H \rightarrow -OSO_3^- + H^+$, in an aqueous solution, the surface charge σ_0 depends only on the density of surface dissociation sites, N (= [$-OSO_3^-$]), as shown by Equation (4.5.43), where [] denotes the site density or solution concentration:

$$\sigma_0 = -eN \tag{4.5.43}$$

When the particle surface is charged by the dissociation of "weak" functional groups, such as –COOH, the degree of dissociation is influenced by the property of the aqueous solution. Suppose there is a weak-acid functional group described by –SH. Then it dissociates as

$$-SH \overset{K}{\rightleftarrows} -S^- + Hs^+ \tag{4.5.44}$$

where the equilibrium constant $K = [-S^-][Hs^+]/[-SH]$, [$-S^-$] is the dissociated surface site concentration, and [Hs^+] is the interfacial concentration of protons, which is related to the concentration in the bulk [H^+] by Equation (4.5.34): [H_S^+] = [H^+] $\exp(-e\psi_0/kT)$. Because the density of the surface site, N, is given by $N = [-SH] + [-S^-]$, the surface charge is written as

$$\sigma_0 = -e\left[-s^-\right] = -\frac{eN}{\left\{1+\left[H^+\right]\exp\left(-e\psi_0/\kappa T\right)/K\right\}} \tag{4.5.45}$$

When $K = \infty$, Equation (4.5.45) coincides with Equation (4.5.43). Then the values of σ_0 and ψ_0 will be obtained by solving Equations (4.5.40) and (4.5.45) simultaneously. Hence, it is known that ψ_0 and σ_0 are the functions of N, K, [H^+], and κ. Because the values of N and K are usually fixed in a given solution, it is clear that the surface charge is able to be controlled by [H^+] and κ (i.e. the pH and C_e, respectively) in the bulk solution.

The description of the surface charge of amphoteric materials, such as metal oxides and proteins, is more complicated than that of the monofunctional surface explained above. The dissociation of a metal oxide surface can be written as

$$-SH_{2+}^+ + OH^- \overset{K_1}{\rightleftarrows} -SH + H_2O \overset{K_2}{\rightleftarrows} -S^- + H^+ + H_2O \tag{4.5.46}$$

where K_1 and K_2 are the equilibrium constants. As for metal oxide surfaces, an alternative model, which is called the one-pK model, is used to avoid the usage of the two different equilibrium constants. A generalized one-pK model enables us to evaluate the variation of surface charge of metal oxides with pH, as shown in Figure 4.5.11.[32] The estimated values might not be correct quantitatively, but the qualitative features are well predicted: (1) the positive charge at low pH decreases with pH, the charge at high pH increases negatively with pH, and there is the point of zero charge (p.z.c.) in between; and (2) the absolute value of the surface potential decreases, but

that of the surface charge increases, as the ionic concentration in the bulk increases. It is confirmed that the pH and ionic concentration C_e are the important parameters to control the charge and potential of particle surfaces.

Surface Charge by Specific Adsorption

There are ions that have a certain affinity for the surface that cannot be explained by the simple principles described above. They are called specifically adsorbing ions. When these ions exist, the surface charge or potential in any particular system is not easy to evaluate, although it seems there exists some rule to govern the specific adsorption. It is known experimentally that the adsorption depends on various conditions, such as the pH, the electrolyte concentration, and the type of electrolyte in the solution. The data in Figure 4.5.12 show the electrophoretic mobility of rutile particles as a function of pH in $Ca(NO_3)_2$ solutions and in various nitrate salt solutions of a constant concentration.[32] When no specifically adsorbing ion exists, the mobility must decrease monotonically with pH, as predicted in Figure 4.5.11. The increase of the mobility at high pH in Figure 4.5.12 indicates the existence of specific adsorption. The data in Figure 4.5.12(a) shows that cations adsorb specifically on the negatively charged surface, and the degree of specific adsorption increases with the ionic concentration. Figure 4.5.12(b) shows that the adsorption depends also on the type of electrolyte, and the adsorbing ability can be written as $Ba^{++} > Sr^{++} > Ca^{++} > Mg^{++}$, which coincides with the order given by Hofmeister or lyotropic series.

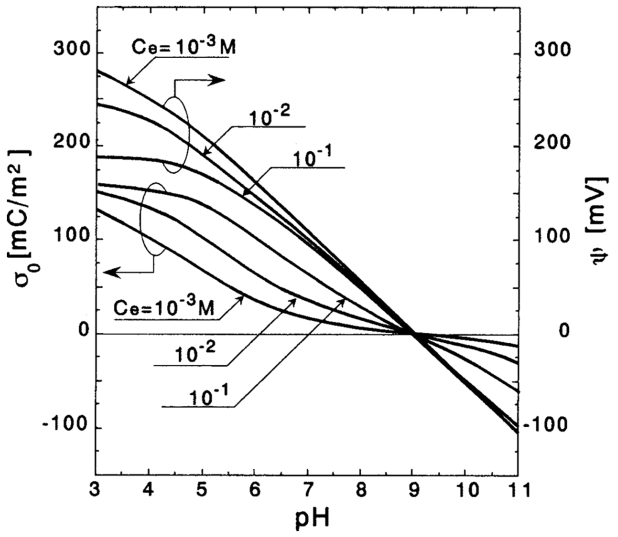


FIGURE 4.5.11 Surface charge and potential predicted using the generalized one-pK model. *Ce* is the electrolyte concentration.[32]

In the recent reports,[33–35] the ionic specificity is considered to be closely related with "kosmotropic (structure-making)" and "chaotropic (structure-breaking)" properties of ions in solutions. The kosmotropic and chaotropic properties are often correlated with the positive and negative values of the Jones-Dole viscosity B coefficient, respectively, and also with the size and Gibbs free energy of hydration of ions. A possible explanation of the higher adsorbing ability of hydrophobic ions is that they tend to be excluded from the bulk solution towards the surface and less energy is needed for them to be dehydrated in their adsorption on the surface.

Charge Control by Surfactants

The surface charge of particles in aqueous solutions is controllable using surfactants. When the alkyl group of a surfactant has a high affinity to the surface, the tail is adsorbed on the surface and the polar head is directed toward the solution, as shown in Figure 4.5.13. Then particles are dispersed and stable because of the interparticle repulsive force caused by the charge of the adsorbed surfactants.

When the bare surface is charged as shown in Figure 4.5.13 and surfactants of the opposite charge are dosed in the solution, the head groups are adsorbed on the surface because of the electrostatic attractive force between them. When the first adsorbed layer is formed completely, the surface becomes hydrophobic, and particles will be unstable because of the

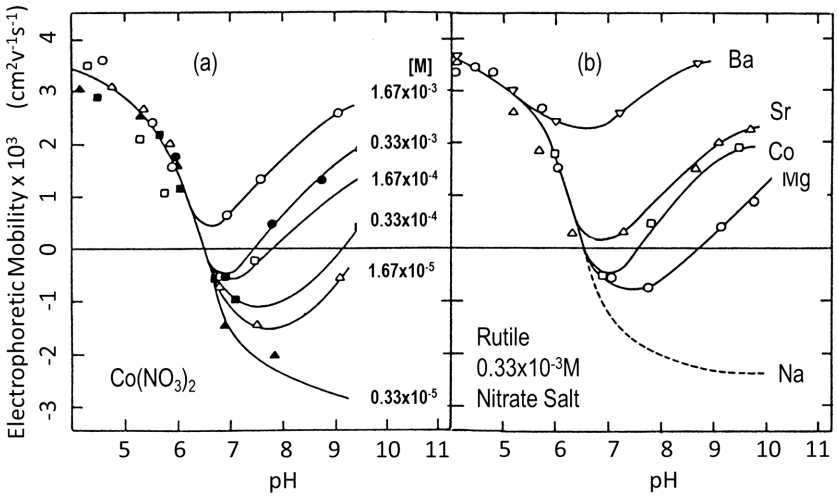


FIGURE 4.5.12 Dependence of electrophoretic mobility on pH for rutile (a) in solutions of various concentrations of $Ca(NO_3)_2$ and (b) in 0.33×10^{-3} M nitrate solutions with various types of cations.[32]

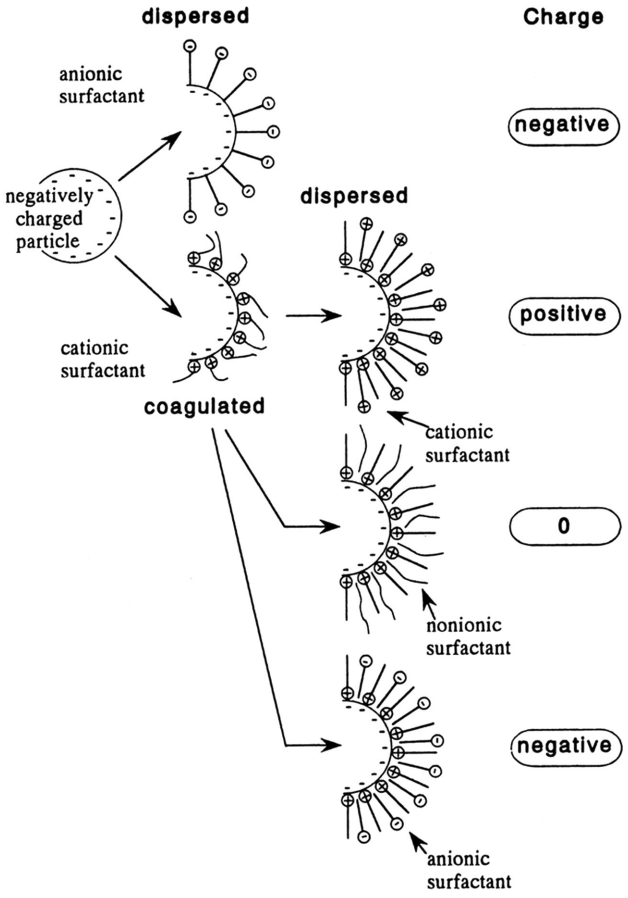


FIGURE 4.5.13 Schematic of the surfactant adsorption, the charge, and the stability of particles.

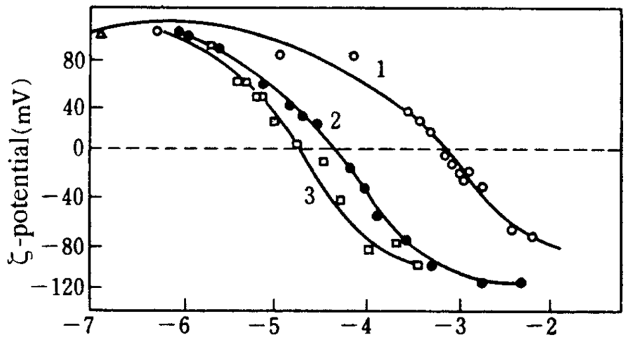


FIGURE 4.5.14 Dependence of the zeta potential of AgI sol on the surfactant concentration: (1) $CH_3(CH_2)_9SO_4Na$; (2) $CH_3(CH_2)_{11}SO_4Na$; (3) $CH_3(CH_2)_{13}SO_4Na$.[36]

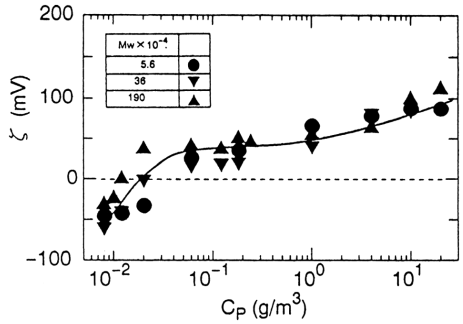


FIGURE 4.5.15 Zeta potential ζ of latex particles versus the concentration of dosed cationic polymers. C_p and Mw are the concentration and molecular weight of dosed polymers, respectively.[37]

hydrophobic attractive force. However, if the surfactant is dosed further, the secondary adsorbed layer will be formed such that the polar heads are directed toward the solution. Then the surface charge is reversed and hydrophilic, and the suspension becomes stable again. An example is given in Figure 4.5.14, showing the change of the zeta potential of AgI sol with the concentration of anionic surfactants.[36] It is important to note that the longer the alkyl group is, the less molar concentration of surfactant is needed to vary the charge of the surface. Because the longer the tail is, the more segregated from water surfactants are, surfactants with the long tail are adsorbed on the surface effectively.

It is possible to control the surface charge in principle, in such a way that the secondary surfactants of different kinds are dosed over the first layer, as schematically illustrated in Figure 4.5.13. In this case, the final surface charge will be given by the charge of the secondary surfactants.

Charge Control by Polymers

Water-soluble polymers are very effective agents to control the surface charge of particles in aqueous solutions. Various polymers, which differ in charge density, hydrophobicity, molecular weight, and so forth, have been synthesized, and even polymers which have several different properties simultaneously are able to be synthesized. Hence, it is possible to prepare a polymer which has a high absorbing ability to the particle surface and the property desired as the adsorbed layer at the same time.

High molecular weight polymers which are opposite to the particle surface in charge are popularly employed to control the charge of particles in solutions. When highly charged polymers are dosed, they adsorb on the particle surface with strong electrostatic attractive force, and the surface charge is altered even by an extremely small dosage. Typical data are presented in Figure 4.5.15, showing the change of the zeta potential of negatively charged polystyrene lattices with the concentration of dosed cationic polymers.[37] The strong coulombic force acts between the polymers and surface, and almost all polymers are adsorbed on the surface unless the amount of dosage is too large. It is interesting to note that the surface charge depends only on the total weight of dosed polymers but does not depend on the molecular weight of the polymer. This is because the charge density of the adsorbed layer is determined by total charge (i.e. the total weight) of adsorbed polymers, as far as the structure of polymer is the same and all the polymers dosed are adsorbed on the surface.

4.5.2.2 Charge Control by Chemical Reaction in Aqueous and Non-Aqueous Solutions

In order to control surface charge in liquid, an important approach is chemical surface treatment and modification.

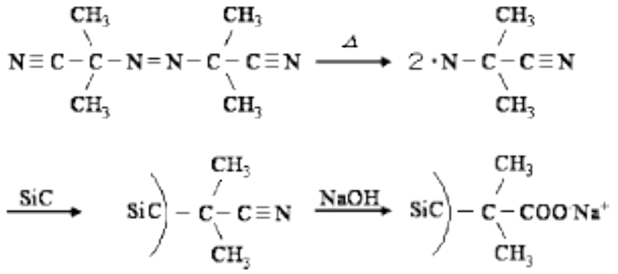


FIGURE 4.5.16 Reaction scheme for surface modification of SiC nanoparticles with AIBN.

The surface properties of carbon, metal carbide particles have generally low wettability and dispersion stability in water and polar organic solvent, because of hydrophobic surface properties. To improve the dispersion stability of hydrophobic particles in aqueous and polar organic solution, various kinds of chemical treatment were applied in the liquid and gas phases. Almost all approaches increase the surface density of hydrophilic functional group, such as OH, COOH and NH_2 etc., and as a result, the absolute value of surface charge in polar solvent.

The most traditional method is surface oxidation by strong acids[38] or photocatalytic reaction by TiO_2 nanoparticles.[39] Other chemical approaches are metal oxide and polymer coating on hydrophobic particle. The main purpose of these approaches is only one molecular-layer oxidation and coating, however, it is very difficult to control the thickness of oxidation and coating on the molecular scale, thick oxidation surface damage reduced the functional properties of particles.

One approach for surface charge control by using the chemical process was the reaction of the unsaturated hydrocarbons on carbon and carbonate particles with radical species generated from azo radical initiators. The scheme for surface modification of SiC nanoparticles with 2,2′-Azo-bisisobutyronitrile (AIBN) is shown in Figure 4.5.16.[40] By using this reaction process, the surface potential in an aqueous solution with various pH was able to control to design surface functional group density, such as -COOH, =NH, and $–NH_2$.

REFERENCES

1. Kousaka, Y., et al., *Aerosol Sci. Technol*., 2, 421–427, 1983.
2. Lui, B. Y. H., Pui, D. Y. H., *J. Aerosol. Sci*., 5, 465–472, 1974.
3. Han, B., Shimada, M., Choi, M., Okuyama, K., *Aerosol. Sci. Technol*., 37, 330–341, 2003.
4. Inaba, H., Ohmi, T., Yoshida, T., Okada, T., *J. Electrostatics*, 33, 15–42, 1994.
5. Shimada, M., et al., *J. Aerosol. Sci*., 28, 649–661, 1997.
6. Akasaki, M., in *Handbook of Electrostatics*, The Institute of Electrostatics, Japan, Ed., Ohm-Sha, Tokyo, 1981, pp. 217–218 (in Japanese).
7. Moore, A. D., in *Electrostatics and Its Applications*, Moore, A. D., Ed., John Wiley, New York, 1973, Chap. 4.
8. Kebarle, P., Tang, L., *Anal. Chem*., 65, A972–A986, 1993.
9. Bricard, J., in *Problems of Atmospheric and Space Electricity*, Coroniti, S. C., Ed., Elsevier, Amsterdam, 1965, pp. 82–117.
10. Mohnen, V. A., in *Electrical Processes in Atmospheres*, Dolezalk, H., Reiter, R., Ed., Steinkopff Verlag, Darmstadt, 1977, pp. 1–16.
11. White, H. J., *AIEE Trans*., 70, 1186–1191, 1951.
12. Masuda, S., Washizu, M., *J Electrostat*., 6, 57–67, 1979.
13. Fuchs, N. A., *Geofis. Pura Appl*., 56, 185–193, 1963.
14. Natanson, G. L., *Sov. Phys*., 5, 538–551, 1960.
15. Adachi, M., Okuyama, K., Kousaka, Y., in *Proceedings of the Second International Conference on Electrostatic Precipitation*, Pittsburgh, Pa. : Air Pollution Control Association, Kyoto, 1984, pp. 698–701.
16. Liu, B. Y. H., Kapadia, A., *J. Aerosol Sci*., 9, 277–242, 1978.
17. Adachi, M., Kousaka, Y., Okuyama, K., *J. Aerosol Sci*., 16, 109–123, 1985.
18. Keefe, D., Nolan, P. J., Rich, T. A., *Proc. R. Ir. Acad*., 60-A, 27–45, 1959.
19. Maisels, A., Jordan, F., Fissan, H., *J. Appl. Phys*., 91, 3377–3383, 2002.
20. Matsusaka, S., Oki, M., Masuda, H., *Adv. Powder Technol*., 18, 229–244, 2007.
21. Bunchatheeravate, P., Curtis, J., Fujii, Y., Matsusaka, S., *AIChE J*., 59, 2308–2316, 2013.
22. Mizutani, M., Yasuda, M., Matsusaka, S., *Adv. Powder Technol*., 26, 454–461, 2015.
23. Yoshida, H., et al., *J. Soc. Powder Technol., Jpn*., 29, 504–510, 1992.
24. Itakura, T., Masuda, H., Ohtsuka, C., Matsusaka, S., *J. Electrostat*., 38, 213–226, 1996.
25. Timoshenko, S. P., Goodier, J. N., *Theory of Elasticity*, 3rd Ed., McGraw-Hill, New York, 1970, pp. 409–422.
26. Masuda, H., Iinoya, K., *AIChE J*., 24, 950–956, 1978.
27. Ema, A., Tanoue, K., Maruyama, H., Masuda, H., *J. Powder Technol. Jpn*., 38, 695–701, 2001.
28. Nomura, T., Taniguchi, N., Masuda, H., *J. Soc. Powder Technol. Jpn*., 36, 168–173, 1999.
29. Matsusaka, S., Nishida, T., Gotoh, Y., Masuda, H., *Adv. Powder Technol*., 14, 127–138, 2003.
30. Hunter, R. J., *Foundations of Colloid Science*, Vol. 1., Clarendon Press, Oxford, 1987.
31. James, R. O., in *Polymer Colloids*, Buscall, R., Corner, T., Stageman, J. R., Eds., Elsevier, London, 1985, p. 69.
32. Koopal, L.K. in *Coagulation and Flocculation*, Dobias, B., Ed., Marcel Dekker, New York, 1993, pp. 122, 127.
33. dos Santos, A.P., Levin, Y., *Phys. Rev. Lett*., 106, 167801, 2011.
34. Peula-Garcı´, J.M., Ortega-Vinuesa, J.L., Bastos-Gonza´lez, D., *J. Phys. Chem. C*, 114, 11133–11139, 2010.
35. Higashitani, K., et al., *Langmuir*, 34, 2505–2510, 2018.
36. Watanabe, A., *Bull. Inst. Chem. Res. Kyoto Univ*., 38, 179, 1960.
37. Higashitani, K., Kage, A., Arao, E., In *Dispersion and Aggregation*, Moudgil, B. M., Somasundaran, P., Eds., Engineering Foundation, New York, 1994, p. 191.
38. Socha, R. P., Laajalehto, K., Nowak, P., *Colloids Surf., A*, 208, 267, 2002.
39. Ishikawa, Y., et al., *J. Am. Chem. Soc*., 125, 6558, 2003.
40. Iijima, M., Kamiya, H., *J. Phys. Chem. C*, 112, 11786–11790, 2008.



Taylor & Francis
Taylor & Francis Group
http://taylorandfrancis.com

4.6 Surface Modification

Makio Naito (4.6.1), (4.6.3)
Hidehiro Kamiya (4.6.2)

4.6.1 PURPOSE OF SURFACE MODIFICATION AND ITS METHODS

Powder has a large specific surface area, which plays an important role in its overall properties. The purpose of surface modification is to change the surface properties of powders, thus leads to higher functions of them. Actually, surface modification is widely applied to change various kinds of powder properties. Mechanical properties, such as powder dispersion and powder flow ability, can be controlled by the surface modification. Interaction between particle surface and its surroundings can also be changed by surface modification. For example, the masking and release of components in particles are controlled by their surface coating.

Many methods have been applied to modify the surfaces of powders. They are mainly classified into two categories, i.e. chemical and physical methods. In this chapter, both methods are introduced.

4.6.2 CHEMICAL METHODS

Overview of chemical treatment on particle surface

Many kinds of chemical methods for particle surface modification have been developed in various application fields. One example for categorization of chemical treatment method is shown in Table 4.6.1. One category for chemical modification on a particle surface is the modified structure, a molecular or nanometer scaled layer structure was generated on particle surface. For the generation of functional structure, the general traditional method is surface chemical treatment on prepared particles, and another method is *in-situ* preparation of a particle with surface modified structure generation. Based on this classification, some examples will be introduced in this chapter. The outline of each process had been described in our reviews.[1,2]

TABLE 4.6.1 An Example of Chemical Method Categorization for Surface Modification on Fine Particles

Modified Process	Interface Structure	
	Molecular Level Structure Formation	Nanometer Scaled Layer, Core/Shell Structure
in-situ preparation	/Hydro-thermal /Super critical fluid	/Polymerization /Crystallization
Surface treatment	/Silane coupling agent /Surfactant and ligand adsorption	/Coating /Composite particle

in-situ Surface Modification for Nanoparticles

Since nanoparticles, which have a size smaller than 100 nm in diameter, have an extremely high tendency of adhesion and aggregation behavior, *in-situ* surface modification which conduct surface modification during the nanoparticle synthesis, has been investigated by many researchers. In this chapter, *in-situ* nanoparticle preparation process with surface modification methods for dispersion control of nanoparticles in liquid will be introduced.

A reverse micelle method[3] is one method in which particle synthesis reaction occurs in the reverse micelle structures. Various kinds of metals, metal oxides,[4] and semiconductors[5] can be synthesized by using this method. Since the particles are synthesized in the reverse micelle structure, the obtained nanoparticles are re-dispersible into organic solvents with low-polarities.

Since this method is not suitable for the mass production of nanoparticles, thermal decomposition method,[6,7] which involves the thermal decomposition of organic metallic compounds in high boiling solvents, are also widely accepted methods to obtain nanoparticles with high crystallinity and sharp size distributions for mass production. In the former two cases, capping agents such as tri-octyl-phosphine oxides (TOPO), oleic acid, and oleyl amines, as shown in Figure 4.6.1, are dissolved in the synthesis solution to prevent the aggregation of Fe_3O_4 nanoparticles. In the case of surfactant-metal uses such as metal oleate, the surfactant acts as the capping agents. It is reported that these thermal decomposition routes have the possibility of particle size tuning on a nanometer scale for various kinds of materials. Since the prepared particles are capped with surfactants, they are typically re-dispersible into low-polar organic solvents.

Based on the aforementioned methods, various nanoparticles including metals, oxides, sulfides, and fluorides that are re-dispersible into many kinds of organic solvents can be synthesized by *in-situ* surface modification techniques. Contrary, a large difficulty lies in carbon related nanoparticles, because the particle synthesis temperature is extremely high. However recently, there are several reports of synthesis of carbon related materials which are dispersible in solvents down to their primary particle size. The first example is the synthesis of carbogenic nanoparticles by the thermal decomposition of various ammonium citrate salts such as octadecyl ammonium citrate salts and 2-(2-amonoethoxy)-ethanol

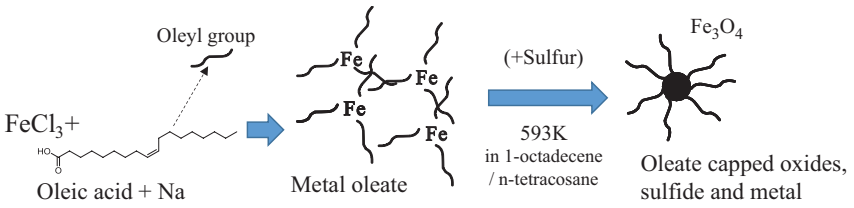


FIGURE 4.6.1 An example of *in-situ* preparation of iron oxide nanoparticles with surface capping by oleyl-group.

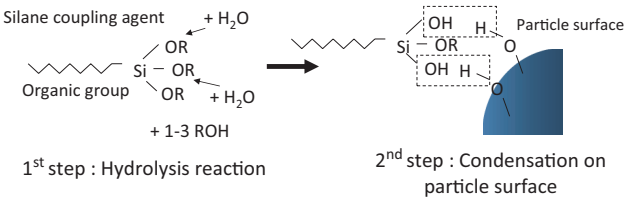


FIGURE 4.6.2 Chemical surface modification process by using silane coupling agent.

salts.[8] It was reported that the citrate groups decompose into carbogenetic nanoparticles while the organic ammonium salts act as a surface modifier. Hydrophilic and hydrophobic carbogeneic nanoparticles about 7 nm were prepared by using octadecyl ammonium salts and 2-(2-amonoethoxy)-ethanol salts, respectively.

The surfactant capped nanoparticles which were synthesized by *in-situ* surface modification procedure can also be further modified in order to tune their surface properties to design dispersion stability in organic solvent. Ligand exchange method,[9,10] which exchanges the capped surfactant, is a typically accepted method and has a large benefit in controlling the particle surface by keeping their dispersion stability in different organic solvents with various polarity. The surface molecular structure can be controlled by exchanging various capping agents.

By applying these methods, various reactive groups can be introduced on the particle surface without formation of strong aggregations. Since the particles are controlled to not aggregate during the entire process, from the particle synthesis to surface modification procedure, it is a useful process to engineer the particle surface for nanotechnology applications.

Molecular Structure Design by Chemical Reaction or Adsorption of Molecules

Surface chemical modification is also a useful technique to improve the stability of nano- and fine particles in various liquid media. As the most traditional modifying method for the oxide particle surface, silane coupling agent, which has 1~3 alkoxy groups and 3~1 organic functional groups as shown in Figure 4.6.2, has been used since the 1960s. The metal-OH group on the particle surface is used as a reaction site. The typical chemical reaction process of the silane coupling agent is shown in Figure 4.6.2. The first step is the hydrolysis of the alkoxy group, and the second step is the condensation being generated by the hydrolysis reaction and the metal-OH on the particle surface. The first purpose of the silane coupling agents was to improve the compatibility of hydrophilic particle surface with hydrophobic polymer surface by introducing various organic functional groups on particle surface after the above reaction process.

Ever since Plueddemann has reported the concept of silane coupling agents,[11] numerous researchers have modified the particle surface to improve the compatibility of particle/polymer surface and to improve the properties of composite materials. The surface modification of nanoparticles by silane coupling agents is also useful to improve the dispersion stability in organic media. The first example is grafting various polymers on the particle surface by using silane coupling agents. Typically, various reactive groups such as amines, epoxides, and vinyls are firstly introduced on the particle surface by silane coupling agents, and then polymers are grafted from or grafted to the particle surface. For examples, the particle surface was modified by aminopropylsilane, and then PEG chains were further grafted to the particle by using epoxy terminated PEG.[12] Various radical polymers such as polyvinylpyrrolidone (PVP) can be grafted on a vinyl functionalized particle surface.[13]

Another example is designing steric silane networks on particle surface by controlling the reaction of silane alkoxides. Chaimberg et al., have reported that the amount of silane coupling agent chemisorbed on oxide supports differs drastically by changing the surface modification procedures.[14] The type of solvents, pH, and amount of adsorbed water on particles largely affected the chemisorbed content of silane coupling agents. Having an impression from this report, we have modified the surface of fumed silica nanoparticles in MEK with slight amount addition of pH controlled water.[15] Compared to the MEK suspension with raw silica nanoparticles, the viscosity was reduced in all cases by the surface modification using silane coupling agents. It appeared that the organic functional groups as well as the pH of the additive water affected the dispersion stability differently.

For the improvement of the dispersion stability of nano- and fine particles in liquid media, one other important surface modification method is the chemical or physical adsorption of surfactants or polymer dispersants or other modifiers to generate an effective repulsive force between particles. In order to control the surface interaction between particles for particle dispersion stability, the optimum molecular structure of the surfactant and dispersant have to select as a function of the combination of particle materials, diameter, and solvent. For the selection of the optimum surfactant and dispersant, one rough guideline is shown in Figure 4.6.3. By the combination

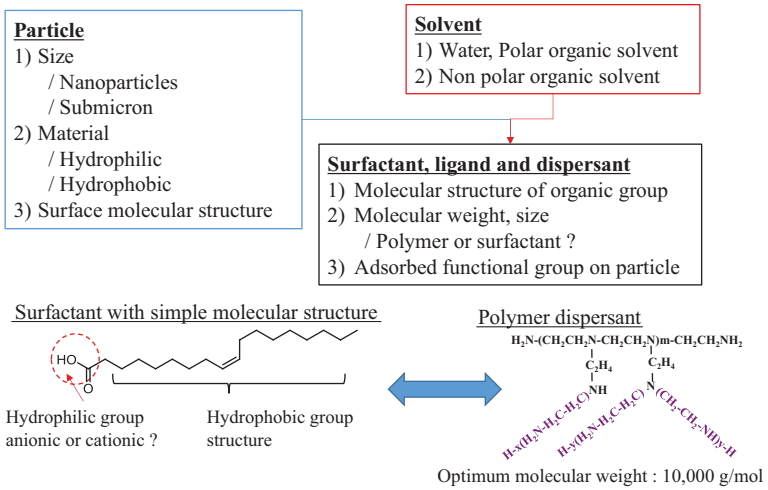


FIGURE 4.6.3 Example for the optimum surfactant and polymer dispersant selection to disperse nano- and fine particles in liquid.

of particle and solvent, the optimum molecular structure of the surfactant and polymer was determined by various previous researches.

For example, the optimum molecular weight of the dispersant for stable dispersion in liquid will decrease with particle diameter. For nanoparticles dispersion, if monolayer molecular surfactants, such as oleyl- group, were covered on the particle surface, nanoparticles were able to disperse in nonpolar organic solvent. On the contrary, for fine particles, of which the primary particle size is larger than 100 nm, the optimum molecular weight is about 10,000 g/mol to prepare a high-concentrated suspension for the fine ceramic preparation process. Since the surface distance between particles attracted by the van der Waals interaction is of the order of several nanometers, it is necessary that the molecular weight of the polymer dispersant must be relatively large to produce an electro-steric repulsive force between particles. However, in the case of dispersion of nanoparticles, mono-molecular surfactants rather than large molecules, such as polymers, are suitable. For example, nonpolar organic solvents, such as toluene, oleic group were useful to disperse nanoparticles sufficiently. However, in the case of a polar solvent, such as methanol, the oleic group is not good for dispersion. By using the special molecular structure ligand with hydrophobic and hydrophilic chain, Iijima et al. discovered that TiO_2 nanoparticles could be successfully dispersed in various organic solvents and polymers.[16] Furthermore, Okada et al. synthesized an anionic and cationic ligand with a simple straight chain of alkyl and PEG as shown in Figure 4.6.4, and the synthesized ligand caped TiO_2[17] and Ag[18] nanoparticles could also be dispersed with various kinds of organic polar and nonpolar solvents. The optimum molecular weight of the synthesized ligand was determined in research for TiO_2 and Ag.

The optimum adsorbed group of surfactant and polymer dispersant depended on the molecular structure and material of particles. Recently, the surface binding strength of the adsorbed group, such as phosphonic acid, carboxylic acid, and catechol in different ligands was investigated on TiO_2

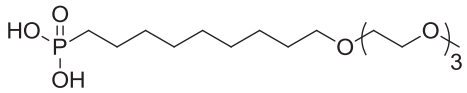


FIGURE 4.6.4 Molecular structure of surfactant for TiO_2 nanoparticles dispersion in various organic solvent.[17]

nanoparticles.[19] Such investigation is useful for the selection of ligand exchange in different organic solvents after *in-situ* preparation.

Surface Layer Structure Formation, Coating, and Composite Particles Design

Since the main purpose of molecular level surface modification by a chemical method is mainly particle dispersion and aggregation behavior control, various kinds of surface coating and thin layer formation technologies on a particle surface have been investigated to develop the particle's functional properties. For example, metal and non-oxide semiconductor nanoparticles have to prevent surface oxidation to keep the functional properties for a long time. Molecular level surface modification is not enough to achieve this purpose. A uniform silica layer coating by using the sol-gel method was the most popular method, and polymer,[20] platinum,[21] and other metal oxide coatings were also applied on core particles as a chemically resistant shell formation. For the resistance of chemical reaction, the surface layer structure needs to have a dense structure without oxygen diffusion. Since sol-gel silica layer has a molecular level porous structure, heat treatment is needed after the sol-gel reaction coating to prepare dense structure. Iron oxide particles with a coated silica layer was reduced to iron by a hydrogen stream at high temperature, silica coated iron crystal particles were obtained by this process as shown in Figure 4.6.5.[22]

Furthermore, a mesoporous silica shell and magnetic nanoparticles core composite particles were prepared[23] and applied to a cascade reactor as a solid catalyst.[24,25]

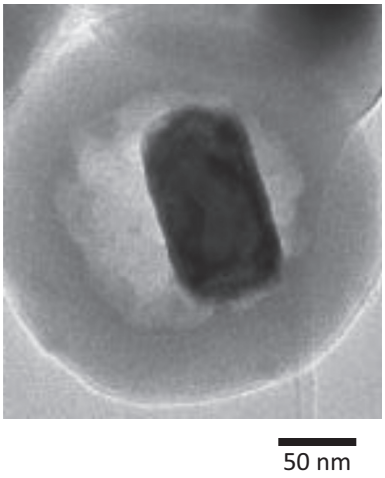


FIGURE 4.6.5 TEM photograph of silica coated iron crystal nanoparticles prepared by sol-gel silica coating and hydrogen reduction process.[22]

4.6.3 PHYSICAL METHODS

Physical methods are based on the bonding between the surface of a core particle and fine particles or cluster deposition on the surface of particles. While the latter makes use of physical vapor deposition (PVD), the former applies particle bonding by mechanical method to modify the particle surface with fine particles[26–28] and is explained in detail here.

A grinding process produces fine particles by employing strong enough mechanical forces on feed materials to fracture them into small pieces. Alternatively, the process can be used to apply an effective force to bond fine particles on the surface of core particles. Table 4.6.2 shows the machines that have been used for particle surface modification.[29] In the table, group I shows the fine grinding machines used for this purpose. It means that most kinds of fine grinding machines can perform the particle surface modification process to bond fine particles onto the surface of core particles. Group II shows a mixing apparatus used for particle surface modification. Intensive mixing is also capable of modifying particle surfaces. Based on these mechanical principles, several advanced machines to achieve particle surface modification have been developed as shown in the right column of Table 4.6.2. Although each advanced machine may be based on a somewhat different working principle, all of them apply mechanical action to powder materials by rotating their rotors or vessels.

Many factors can affect the particle surface modification process. Figure 4.6.6 summarizes the main factors controlling the surface modification by bonding fine particles onto the surface of core particles,[29] which including the condition of starting powder materials and the processing conditions such as mechanical stress, temperature, atmosphere, and charging procedures of starting powder materials into the apparatus.

The properties of powder materials affect the structure and bonding mechanism between core particles and fine particles.

TABLE 4.6.2 Main Machines Used for Particle Surface Modification

	Type	Advanced Machines For Surface Modification
I	Impaction-type Pin mill, disc mill	Hybridization System (Nara Machinery Co.)
	Centrifugal classifying type	KOSMOS (Kawasaki Heavy Industry Co.)
	Frictional grinding mill	Mechanofusion System (Hosokawa Micron Corp.)
	Ball mill tumbling vibration planetary centrifugal fluidizing (CF mill)	
	Agitated ball mill Mixing vessel type	
	Jet mill	
II	Mortar	
	Cylindrical vessel type with rotating disc	Mechanomill (Okada Seiko Co.)
	Elliptical vessel type with high-speed elliptical rotor	Theta-composer (Tokuju Corp.)

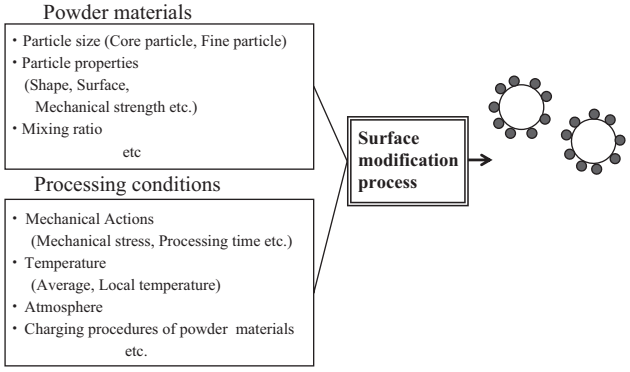


FIGURE 4.6.6 Factors controlling surface modification process.

First, the larger size of the core particle and the finer size of the shell particle should be selected. Their mixing ratio is an important factor to determine the structure of core/shell particles. For example, the weight fraction of fine particles n can be calculated by the following equation[29] as the fine particles are closely distributed to cover the surface of core particle and $d_p >> d_a$,

$$n = \left(1 + \frac{\sqrt{3}}{2\pi} \cdot \frac{\rho_p}{\rho_a} \cdot \frac{d_p}{d_a}\right)^{-1} \tag{4.6.1}$$

where

d_p is the core particle size
d_a is the fine particle size
ρ_p is the true density of core particles
ρ_a is the true density of fine particles.

Equation (4.6.1) is a guideline to determine the fine particle weight fraction. However, the fraction can be selected from a wide range.

As to the bonding mechanism, it depends on the combinations of powder materials. The contact surface between particles where mechanical actions actually occur[30] receives extremely high local temperature and strong mechanical stress. The authors previously reported that the local temperature at the interface between particles during mechanical processing could be ten times higher than the apparent temperature of the processing chamber.[31] Such a high local temperature is expected to cause unique phenomenon such as "micro-welding" or "chemical interaction" between fine particles and core particles. For example, when coating nano-titania particles onto the glass beads, the peak of the binding energy of Ti 2p shifted away from its original position after only 5 min of mechanical processing.[29] It suggested that there was a chemical interaction on their surface during the processing.

From the macroscopic point of view, processing conditions such as mechanical actions can directly affect the particle composite process. As previously mentioned, mechanical actions are given to powder materials by rotating the rotor or vessel of the machine. In case of a core particle coated with fine guest particles, the particle bonding process is proposed as shown on Figure 4.6.7.[29] The rotation speed of the rotor or vessel along with the processing time decides the mechanical action and its recurring number for the powder material. And, the coating process is carried out in the following two steps: First, the surfaces of fine particles and core particles are mechanically activated; consequently, fine particles adhere onto the surfaces of core particles. At this step (I), as fine particles deposit onto the surface of the core particle, the BET specific surface area of composites decreases with the processing time. However, at the second step (II), as the fine particle coating on the surface of core particles are gradually compacted, BET specific surface area reduction levels off with the processing time. It leads to a higher mechanical strength of the surface layer and stronger bonding between the surface layer and core particle. Therefore, by controlling the rotation speed of the machine and its processing time, the apparent density and strength of the surface layer can be altered. However, when the rotation speed exceeds a certain value, the surface layer formed on the core particle is detached after a certain processing time as shown in the dotted line on Figure 4.6.7. In this case, the mechanical stress becomes working as surface grinding for the composite particles when it exceeds a certain level.

During mechanical processing, temperature and atmosphere also affect the particle composite process. Similar to the powder grinding operation, mechanical energy is converted to heat energy; therefore, careful temperature control is needed when heat-sensitive materials are processed. Control can be achieved by cooling the apparatus. Conversely, temperature can also be controlled to make the bonding stronger. Atmosphere is important when processing powder materials in the dry phase. It affects their properties and the particle modification process.

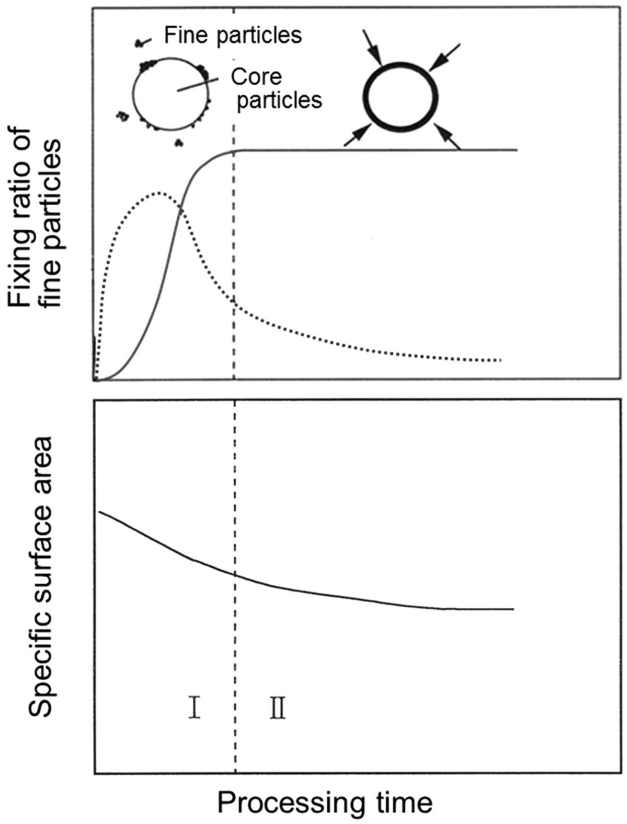


FIGURE 4.6.7 Surface modification process of core particles with fine particles.

Charging procedures of powder materials are the key issues for controlling the structure of composite particles. For example, a uniform surface layer of composite particles was created when a small amount of fine particles were repeatedly added to the processed powder at a certain time interval.[32] Multi-layered composite particles were created by adding different kinds of fine powders at certain time intervals, which have been used for drug delivery.[33]

REFERENCES

1. Iijima, M., Kamiya, H., *KONA*, 27, 119–129, 2009.
2. Kamiya, H., Iijima, M., *Sci. Technol. Adv. Mater.*, 11, 1–7, 2010.
3. Petit, C., Lixon, P., Pileni, M.–P., *J. Phys. Chem.*, 97, 12974–12983, 1993.
4. Park, J., et al., *Angew. Chem. Int. Ed.*, 46, 4630–4660, 2007.
5. Quinlan, F. T., et al., *Langmuir*, 16, 4049–4051, 2000.
6. Murray, C. B., Kagan, C. R., Bawendi, M. G., *Annu. Rev. Mater. Sci.*, 30, 545–610, 2000.
7. Park, J., et al., *Angew. Chem. Int. Edit.*, 44, 2872–2877, 2005.
8. Bourlinos, A. B., et al., *Small*, 4, 455–458, 2008.
9. Hong, R., Fischer, N. O., Emrick, T., Rotello, V. M., *Chem. Mater.*, 17, 4617–4621, 2005.
10. Lü, C., et al., *Adv. Func. Mater.*, 18, 3070–3079, 2008.
11. Ishida H. Koenig J. L., *Polym. Eng. Sci.*, 18, 128–145, 1978.
12. Emoto, K., Alstine, J. M. V., Harris, J. M., *Langmuir*, 14, 2722–2729, 1998.
13. Chainmberg, M., Parnas, R., Cohen, Y., *J. Appl. Polym. Sci.*, 37, 2921–2931, 1989.

14. Chaimberg, M., Cohen, Y., *J. Colloid Interface Sci.*, 134, 576–579, 1990.
15. Iijima, M., Tsukada, M., Kamiya, H., *J. Colloid Interface Sci.*, 305, 315–323, 2007.
16. Iijima, M., et al., *J. Am. Chem. Soc*., 131, 16342–16343, 2009.
17. Okada, Y., Ishikawa, K., Maeta, N., Kamiya, H., *Chem. Euro. J.*, 24, 1853–1858, 2018.
18. Maeta, N., Kamiya, H., Okada, Y., *Langmuir*, 34, 5495–5504, 2018.
19. Zeininger, L., Portilla, L., Halik, M., Hirsch, A., *Chem. Eng. J.*, 22, 13506–13512, 2016.
20. Tang, N. J., et al., *Solid State Commun*., 132, 71–74, 2004.
21. Teng, X., et al., *Nano Lett*., 3, 261–264, 2003.
22. Arias, J. L., et al., *J. Controlled Rel*., 77, 309–321, 2001.
23. Yonemochi, Y., et al., *Adv. Powder Tech.*, 16, 621–637, 2005.
24. Yamada, Y., Yano, K., *Micropor. Mesopor. Mater.*, 93, 190–198, 2006.
25. Yang, Y., et al., *Angew. Chem. Int. Ed*., 51, 9164–9168, 2012.
26. Naito, M., Abe, H., Kondo, A., Yokoyama, T., Huang, C. C., *KONA*, 27, 130–143, 2009.
27. Naito, M., Abe, H., *Ceramic Trans*., 157, 69–76, 2004.
28. Naito, M., Abe, H., Sato, K., *J. Soc. Powder Technol., Japan*, 42, 625–631, 2005.
29. Naito, M., Kondo, A., Yokoyama, T., *ISIJ International*, 33, 915–924, 1993.
30. Dachille, F., Roy, R., *Nature*, 186, 34, 1960.
31. Nogi, K., et al., *J. Jpn Soc. Powder and Powder Metall*., 43, 396–401, 1996.
32. Naito, M., et al., *Kagaku Kogaku Ronbunshu*, 24, 99–103, 1998.
33. Fukumori, Y., Ichikawa, H., Uemura, T., Sato, K., Abe, H., Naito, M., *Proceedings of 8th International Symposium on Agglomeration*, Bangkok, Thailand, 16–18, 31–38. (2005)

Part 5

Powder Handlings and Simulations



Taylor & Francis
Taylor & Francis Group
http://taylorandfrancis.com

5.1 Crushing and Grinding

Fumio Saito

5.1.1 INTRODUCTION

Grinding a solid material is an important operation to reduce its size or to increase the surface area. It has historically been developed in the mineral processing in order to liberate useful substances dispersed inherently in it. With the times, this operation has been extended to other industrial fields such as metals, chemical compounds, foods, pharmaceutical substances and recycling. The purpose of this operation is accordingly for enhancement and improvement of reactivity, mixing degree, flow-ability, formability, shape modification and control in surface property for solids. Recently, there has been a growing demand for fine or ultrafine particles, due to increased expectations of the comminution process. In the meantime, the energy efficiency of comminution is still very low, so that it would be important to improve it more than before. In general, the energy required for comminution of a particle increases with a decrease in feed particle size.[1–4] Fine grinding would bring mechanical activation, leading to their agglomerations and mechanochemical phenomena such as phase transformation and modification of surface property have appeared in fine grinding, especially dry systems. In order to forward the grinding operation with controlling such phenomena, further optimum treatment and operation should be made, so that further research and development works on comminution have been required from the base.[5]

5.1.2 BASIC APPROACH FOR UNDERSTANDING GRINDING PHENOMENA

5.1.2.1 Strength of a Single Particle Compressed by Two Parallel Plates

Comminution of a solid is to break it into several fragments by adding mechanical stress to the solid material. A simple compression of a spherical particle by a parallel plates and its load (P) and deformation Δ curve are shown in Figure 5.1.1.[6] The stress acting to the sphere solid should exceed the strength of the solid, and it is defined by Hiramatsu et al.,[6] as shown in Equation 5.1.1, where, P_{max} (N) is the fracture load and r (m) is a radius of the particle.

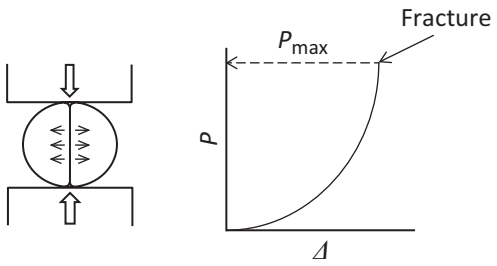


FIGURE 5.1.1 A single particle compressed by parallel plates and a load-deformation curve of this compression test.

$$S = \frac{0.7P_{max}}{\pi r^2} = \frac{2.8P_{max}}{\pi x^2} \tag{5.1.1}$$

Table 5.1.1 shows the average strength of a spherical particle in 2.0 cm diameter (x) measured at 49.0 N/s in loading rate for different kinds of material together with their mechanical properties.[7,8]

5.1.2.2 Fracture Energy Stored in a Particle

In principle, the mechanism of size reduction of solids is based on the fracture energy of a single particle stored during comminution, without consideration of stochastic process. The area surrounded by the load and deformation curve corresponds to the fracture energy E (J), and it can be given by Equation 5.1.2, where P (N) is load, Δ (m) is deformation.

$$E = \int_0^{\Delta_{max}} P d\Delta \tag{5.1.2}$$

In a system composed of an elastic sphere gripped by a pair of rigid parallel plates, the load-deformation curve can be predicted by Hertzian contact theory.[9] According to this theory, the elastic strain energy, E (J), stored into the spherical specimen up to its fracture, can be given by Equation 5.1.3, where Y (Pa) is Young's modulus, ν (-) is Poisson's ratio, V (m^3) is the specimen volume and P (N) is the fracture load. The suffixes 1 and 2 in Equation 5.1.3 are sample and plate material, respectively.

$$E = 0.682\left(\frac{1-\nu_1^2}{Y_1} + \frac{1-\nu_2^2}{Y_2}\right)^{2/3}\left(\frac{\pi}{V}\right)^{1/9} P^{5/3} \tag{5.1.3}$$

Therefore, the specific fracture energy E/M (J/kg) is derived by Equation 5.1.4:

$$\frac{E}{M} = 1.924\rho^{-1}\left(\frac{1-\nu_1^2}{Y_1} + \frac{1-\nu_2^2}{Y_2}\right)^{2/3} S^{5/3} \tag{5.1.4}$$

Considering the fact that $Y_1 \ll Y_2$ ($Y_2 = 5.93 \times 10^2$ GPa), Equation 5.1.4 can be simplified as Equation 5.1.5, where ρ (kg/m^3) is the density of the specimen.

$$\frac{E}{M} \cong 1.924\rho^{-1}\left(\frac{1-\nu_1^2}{Y_1}\right)^{\frac{2}{3}} S^{\frac{5}{3}} \tag{5.1.5}$$

TABLE 5.1.1 Strength, Density, Young's Modulus and Poisson's Ratio of Materials

Sample	Density ρ [kg/m^3]	Sphere Comp. Strength* S [MPa]	Young's Modulus Y [GPa]	Poisson's Ratio ν [–]
Silica glass	2.20×10^3	27.0	73.5	0.16
Borosilicate glass	2.33×10^3	45.1	61.2	0.21
Soda glass	2.52×10^3	31.3	48.0	–
Quartz	2.62×10^3	11.4	87.1	0.16
Feldspar	2.55×10^3	9.75	58.7	0.26
Limestone	2.70×10^3	4.15	68.0	0.32
Marble	2.70×10^3	2.48	53.4	0.30
Gypsum	2.30×10^3	2.42	37.8	0.32
Talc	2.78×10^3	1.05	15.0	0.33
Al	2.70×10^3	–	72.0	–
Cu	8.96×10^3	–	120	–
Polyethylene	9.38×10^2	–	1.10	–
Hard PVC	1.40×10^3	–	2.60	–
Tungsten carbide	15.6×10^3	–	593	0.21

The nominal diameter of specimen compressed is 2.0 cm.
Loading rate is 49.0 N/s.

5.1.2.3 Three Kinds of Effect in Single Particle Crushing

Size Effect on the Strength

According to the Griffith theory,[10] the strength S is increased by decreasing the particle volume due to a decrease in the number of the weakest cracks in it. From a statistical consideration of the flaw distribution, Weibull[11] and Epstein[12] showed that the mean strength of the specimen, S, is proportional to the $(-1/m)$ power of the specimen volume, V (m^3), and this is known as Weibull's equation given by Equation 5.1.6, where S_0 (Pa) is a constant, V (m^3) is the specimen volume and m is Weibull's coefficient of uniformity.

$$S = S_0 V^{-\frac{1}{m}} \tag{5.1.6}$$

Figure 5.1.2 shows the variation of strength of a single particle with its volume for borosilicate glass and limestone measured mostly at 49.0 N/s in loading rate.[13–16] All data plotted for each material are determined by the least squares method, so that it is found that the strength of a particle tends to increase in decreasing in its particle size, although the data are drawn by a straight line for the silica glass while they are drawn by a warped line for limestone. This is called the size effect on the strength, and all other data including the two samples are shown in Table 5.1.2.[13–16] Considering the result on the size effect on the strength, other size effects on the fracture energy (E) and the specific fracture energy (E/M) are derived as follows,[17–19] where $(S_0V_0^{1/m})$ is a constant.

$$E = (0.15)6^{\frac{5}{3m}}\pi^{\frac{5m-5}{3m}}\left(\frac{1-\nu_1^2}{Y_1}\right)^{\frac{2}{3}}\left(S_0V_0^{\frac{1}{m}}\right)^{\frac{5}{3}}x^{\frac{3m-5}{m}} \tag{5.1.7}$$

$$\frac{E}{M} = (0.897)6^{\frac{5}{3m}}\rho^{-1}\pi^{\frac{2m-5}{3m}}\left(\frac{1-\nu_1^2}{Y_1}\right)^{\frac{2}{3}}\left(S_0V_0^{\frac{1}{m}}\right)^{\frac{5}{3}}x^{\frac{-5}{m}} \tag{5.1.8}$$

The value, m can be determined by changing the specimen volume (V), or by a variance or a coefficient of variation (c) of the strength measured at the same specimen volume, given by Equation 5.1.9,[20] where σ is a standard deviation in the strength and S_{av} is its mean value.

$$c = \frac{\sigma}{S_{av}} = \sqrt{\left(\frac{\Gamma\left(1+\frac{2}{m}\right)}{\left[\Gamma\left(1+\frac{1}{m}\right)\right]^2}-1\right)} \tag{5.1.9}$$

Moisture Effect on the Strength

The solid strength (S) in a single particle is influenced by its environmental condition, and is theoretically expressed by Equation 5.1.10,[21] where, C (m) denotes the crack length in the particle, Y (Pa) is Young's modulus, w (J/m^2) and γ (J/m^2) are the surface plastic energy and the surface energy of the crack surface, respectively.

$$S \propto \sqrt{\frac{Y(\gamma+w)}{C}} \tag{5.1.10}$$

As $\gamma \gg w$ for the brittle materials, therefore Equation 5.1.10 can be simplified by Equation 5.1.11.

$$S \propto \sqrt{\frac{Y\gamma}{C}} \tag{5.1.11}$$

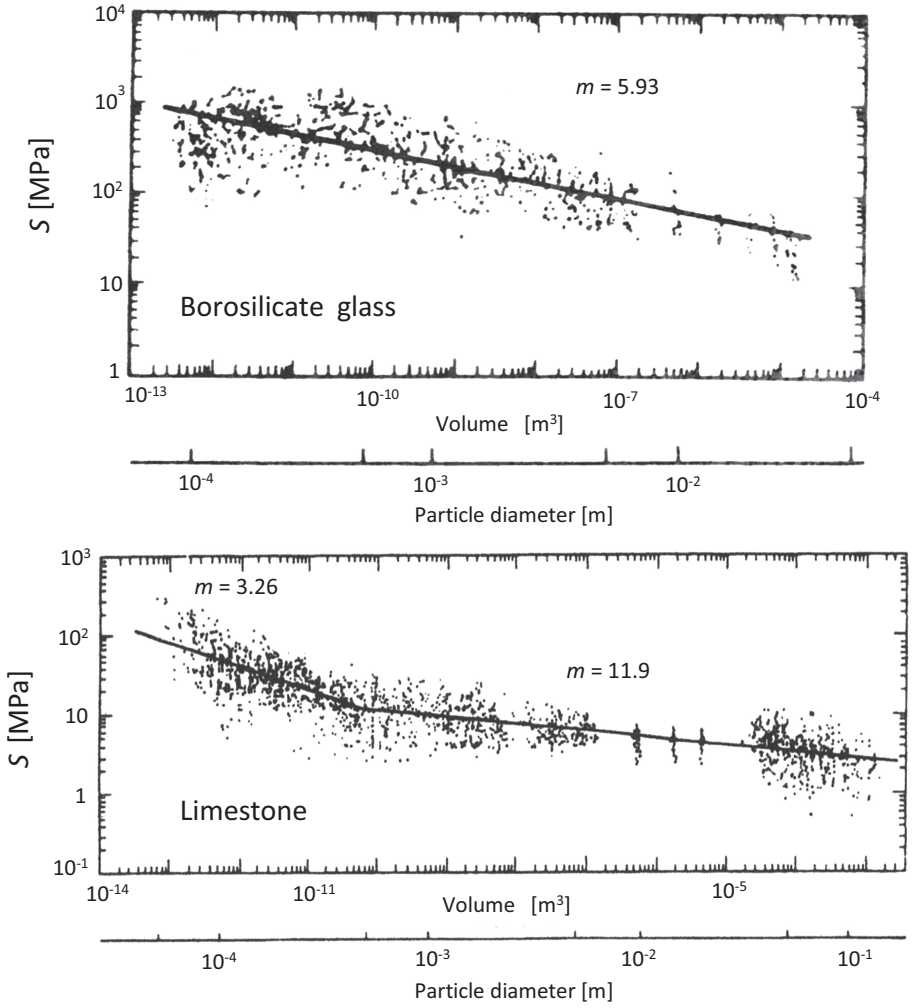


FIGURE 5.1.2 Variation of the strength and volume in single particle crushing test for borosilicate glass and limestone measured at 49.0 N/s in loading rate.

Table 5.1.3 shows the strength of several kinds of spherical sample in 2.0 cm diameter (x) in vacuum, air and water conditions.[22] There is a trend that the strength of a solid in a vacuum is the highest one of the three, the strength in air is the middle one and in water is the lowest value. This is why wet grinding a solid is more effective than dry grinding the solid.

Loading Rate Effect on the Strength

The loading rate, v (N/s), on the strength, S, of a solid is not influenced so much, however, the strength tends to increase with an increase in loading rate (v/v_0). The representative relation between the two is given by Equation 5.1.12,[23] where S_0 and v_0 are a constant and basic loading rate, respectively.

$$S = S_0\left(\frac{v}{v_0}\right)^n \tag{5.1.12}$$

Table 5.1.4 shows the values, S_0, n, standard deviation (S.D.) and loading rate range for various kinds of sample.[24,25] The reason why this trend is achieved can be recognized by the increase in deformation resistance against the applied force as the loading rate is increased. In other words, there is enough time to choose the weakest cracks in the particle when the loading rate is slow, while it is getting hard for the cracks to choose the weakest ones when the loading rate is high. According to the result on the specific surface area of a single particle crushing, it tends to increase remarkably with an increase in the loading rate. Considering the facts on both fracture energy and specific surface area in the single particle crushing, the fracture efficiency defined by the specific surface area to the fracture energy tends to improve when the loading rate becomes high. This basic result may reflect the real grinding phenomena for a material in a mill such as a hammer mill.

5.1.2.4 Minimum Impact Fracturing Velocity of a Single Particle with the Strength

In the impact fracture of a single particle having the mass, M (kg) [$=(1/6)\pi x^3$] colliding against a flat plate, the minimum fracturing velocity, v (m/s) can be given by Equation

TABLE 5.1.2 Parameters in Equation (5.1.6) Measured at Ordinal Loading Rate (49.0 N/s) for Different Kinds of Materials

	$S = S_0 V^{-\frac{1}{m}}$			
Materials	S_0 [Pa]	m [–]	SD [Pa]	Size Range [m]
Silica glass	3.05×10^6	6.16	1.37×10^6	$2.63 \times 10^{-2} \sim 5.60 \times 10^{-4}$
Borosilicate glass	5.56×10^6	5.93	3.82×10^6	$3.29 \times 10^{-2} \sim 8.59 \times 10^{-5}$
Quartz	6.77×10^5	4.56	7.80×10^4	$1.02 \times 10^{-1} \sim 2.52 \times 10^{-2}$
	1.50×10^6	6.49	1.96×10^5	$2.52 \times 10^{-2} \sim 3.00 \times 10^{-3}$
	1.03×10^7	21.3	8.82×10^5	$3.00 \times 10^{-3} \sim 3.00 \times 10^{-4}$
	3.05×10^3	2.57	2.84×10^6	$3.00 \times 10^{-4} \sim 4.04 \times 10^{-5}$
Feldspar	6.71×10^5	5.01	9.80×10^4	$9.33 \times 10^{-2} \sim 3.85 \times 10^{-3}$
	3.25×10^6	10.6	5.88×10^5	$3.85 \times 10^{-3} \sim 5.70 \times 10^{-4}$
	1.67×10^4	3.21	1.18×10^6	$5.70 \times 10^{-4} \sim 4.34 \times 10^{-5}$
Limestone	1.62×10^6	11.9	9.80×10^4	$1.01 \times 10^{-1} \sim 3.80 \times 10^{-4}$
	8.66×10^3	3.26	4.90×10^5	$3.80 \times 10^{-4} \sim 4.54 \times 10^{-5}$
Marble	1.06×10^6	13.2	9.80×10^4	$2.01 \times 10^{-2} \sim 3.68 \times 10^{-3}$
	3.35×10^5	6.38	1.96×10^5	$3.68 \times 10^{-3} \sim 1.96 \times 10^{-4}$
	6.47×10^3	3.20	1.18×10^6	$1.96 \times 10^{-4} \sim 3.28 \times 10^{-5}$
Gypsum	1.58×10^6	24.9	9.80×10^4	$2.01 \times 10^{-2} \sim 3.80 \times 10^{-4}$
	4.84×10^2	2.69	1.08×10^6	$3.80 \times 10^{-4} \sim 4.54 \times 10^{-5}$
Glass[a]	7.68×10^6	9.32	–	$1.10 \times 10^{-3} \sim 1.90 \times 10^{-5}$
Quartz[b]	6.19×10^5	5.86	–	$2.54 \times 10^{-2} \sim 4.40 \times 10^{-5}$
Taconite[b]	$1/16 \times 10^6$	5.78	–	$5.08 \times 10^{-2} \sim 1.04 \times 10^{-4}$
Limestone-1[b]	8.82×10^5	6.21	–	$7.62 \times 10^{-2} \sim 7.40 \times 10^{-5}$
Limestone-2[b]	2.25×10^5	4.78	–	$1.91 \times 10^{-2} \sim 4.17 \times 10^{-4}$

[a] Data by K. Schonert et al.
[b] Data by B.H. Bergstrom et al.

TABLE 5.1.3 Strength of a Single Particle Under Different Water Contents

	S [MPa]*			Strength Ratio			
Sample	**Vacuum (V)**	**Air (A)**	**Water (W)**	**V**	**A**	**W**	**Diameter [cm]**
Silica glass	35.3	27.0	15.2	1.31	1	0.56	2.0
Borosilicate glass	45.2	45.1	33.6	1.0	1	0.75	
Soda glass	43.0	31.5	–	1.37	1	–	
Quartz	–	11.4	10.0	–	1	0.88	
Feldspar	–	9.75	7.02	–	1	0.72	
Limestone	4.91	4.15	3.96	1.18	1	0.96	
Marble	3.10	2.48	2.40	1.25	1	0.97	

Loading rate is 49.0 N/s.

5.1.13, assuming that the kinetic energy of the particle E_K (J) [=(1/2)Mv^2] is perfectly transferred to its fracture energy [E (J)].

$$v = \left[1.79(6)^{\frac{5}{3m}} \rho^{-1} \pi^{\frac{2m-5}{3m}} \left(\frac{1-\nu_1^2}{Y_1} \right)^{\frac{2}{3}} \left(S_0 V_0^{\frac{1}{m}} \right)^{\frac{5}{3}} \right]^{\frac{1}{2}} x^{-\frac{5}{2m}} \tag{5.1.13}$$

Figure 5.1.3 shows variation of v of a particle at fracture with its size, x. It is understood that v becomes high when x is small.[26] As a reference, Table 5.1.5 shows the minimum fracturing velocity (v) of a particle of $x = 100$ μm for different kinds of sample.

On the other hand, when two spherical particles, 1 and 2, collide with each other, S (Pa) generated in the particles is expressed by Equation 5.1.14, where v (m/s) is a relative velocity, M (kg) is the mass of particles, x (m) is the particle size and K is a constant.[27]

TABLE 5.1.4 The Constants, S_0 and n in Equation 5.1.12 for Various Kinds of Sample, Depending on (v/v_0), with Standard Deviation (SD) and Range of Loading Rate

Sample	S_0 [MPa]	n [–]	SD [MPa]	Range of Loading Rate v [N/s]	Number of Specimen N [–]
Silica glass	24.1	0.0156	2.94	$3.26 \sim 5.00 \times 10^6$	200
Borosilicate glass	36.6	0.0152	5.88	$4.90 \sim 4.70 \times 10^6$	200
Soda glass	31.6	0.0132	3.92	$2.42 \sim 8.16 \times 10^6$	500
Quartz	8.72	0.0317	1.27	$1.64 \sim 1.10 \times 10^6$	296
Feldspar	7.45	0.0353	1.86	$0.98 \sim 1.10 \times 10^6$	299
Limestone	2.83	0.0725	0.882	$0.33 \sim 7.85 \times 10^5$	303
Marble	1.70	0.0855	0.588	$0.33 \sim 4.98 \times 10^5$	299
Gypsum	1.53	0.0653	0.490	$0.25 \sim 2.26 \times 10^5$	250
Talc	0.840	0.0581	0.323	$0.16 \sim 6.10 \times 10^4$	250

$v_0 = 0.16$ N/s.

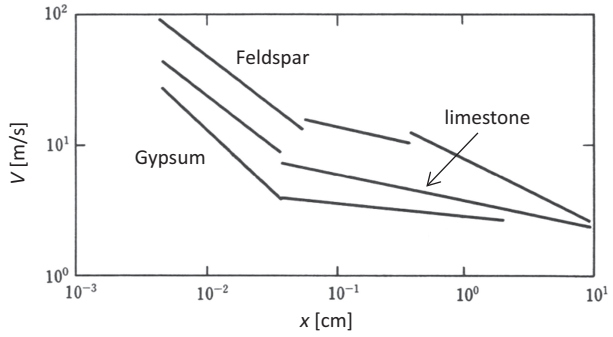


FIGURE 5.1.3 Variation of the velocity of a particle at fracture with particle diameter for different kinds of material.

TABLE 5.1.5 Minimum Fracturing Velocity for Particles of $x = 100$ μm in Diameter

Material	Minimum Fracturing Velocity V [m/s]
Silica glass	114
Borosilicate glass	225
Quartz	66
Feldspar	49
Limestone	23
Marble	22
Gypsum	13

$$S = K\left(\frac{M_1 M_2}{M_1 + M_2}\right)^{\frac{1}{5}} v^{\frac{2}{5}} \left(\frac{2}{x_1} + \frac{2}{x_2}\right)^{\frac{3}{5}} \left(\frac{1-\nu_1^2}{Y_1} + \frac{1-\nu_2^2}{Y_2}\right)^{-\frac{4}{5}} \tag{5.1.14}$$

5.1.2.5 Compression Behavior of a Fine Particle Produced by Grinding

A typical load (P) and deformation Δ curve of a fine particle produced after prolonged grinding is seen in Figure 5.1.4.[28] This

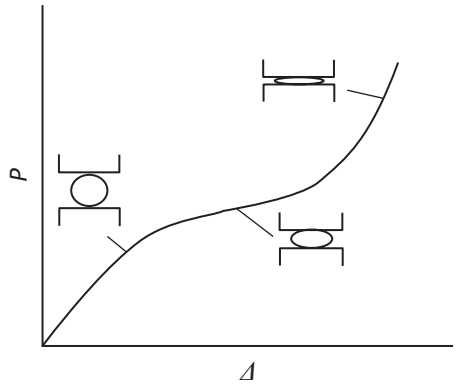


FIGURE 5.1.4 Load-deformation curve of a plastic and/or ductile particle compressed by parallel plates.

curve is clearly different from Figure 5.1.1 for a brittle material, and it seems to behave like a ductile body. Fine particles produced by such prolonged grinding seem to include many micro internal cracks, which may play a role to behave plasticity when stressing even it is a brittle material. Theoretically, the maximum deformation before fracture Δ_f (m) of a brittle particle compressed by parallel plates can be given by Equation 5.1.15, where P_{max} denotes the fracture load and suffices 1 and 2 are particle and compression plate, respectively.[29]

$$\Delta_f = 3^{\frac{2}{3}} \left(\frac{1-\nu_1^2}{Y_1} + \frac{1-\nu_2^2}{Y_2}\right)^{\frac{2}{3}} x^{-\frac{2}{3}} P_{max}^{\frac{2}{3}} \tag{5.1.15}$$

Considering $Y_1 \ll Y_2$, Equation 5.1.16 can be approximately derived, where ε (-) denotes the strain.

$$\frac{S}{\varepsilon^{1.5}} = 0.297 \frac{Y_1}{\left(1-\nu_1^2\right)} \tag{5.1.16}$$

Therefore, when the particle is brittle, ($S/\varepsilon^{1.5}$) (Pa) should be a constant. Whilst it is ductile, the value seems to decrease due to the relatively large value of Poisson's ratio rather than Young's modulus. Figure 5.1.5 shows a variation of ($S/\varepsilon^{1.5}$) for feldspar and coal samples with x.[29] From the data, ($S/\varepsilon^{1.5}$) for

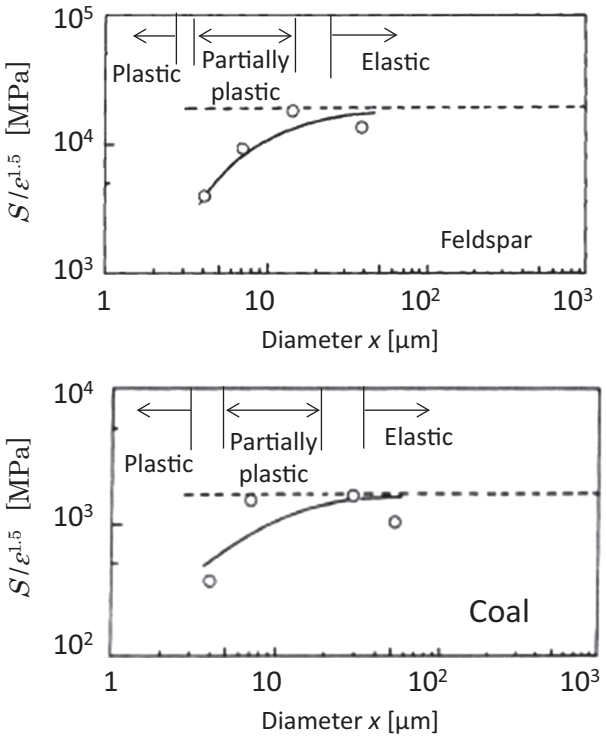


FIGURE 5.1.5 Variation of ($S/\varepsilon^{1.5}$) with d for feldspar.

these brittle materials are changed from the constants to the lower values. This means that these materials tend to behave like plasticity ones when decreasing their particle sizes; one region has a relatively large particle size range where a particle seems to hold the elasticity, the second one has partial plasticity and the third is that a particle behaves plasticity. The two transitional particle sizes from 1) elasticity to partial plasticity and 2) partial plasticity to plasticity are summarized in Table 5.1.6.[29] This is a typical example for the fine particles in 1 to 5 μm diameters prepared by prolonged grinding due to the creation of small and micro internal cracks in the fine ground product, and such cracks may play a significant role to behave like a plastic body when stressing.[30]

5.1.3 COMMINUTION OF MATERIALS

5.1.3.1 Phenomena in Grinding

The grinding of a solid is to reduce its particle size, and this phenomena are triggered by a mill device. During the operation by a mill, a solid receives certain mechanical force by a mill, and the action is not only a compressive force but also other forces like shear, impact and their combined forces. These forces change the shape of a solid as well as its crystal structure. Thus, the grinding has a potential to create following phenomena besides the size reduction of solid:

1. Enhancement of reactivity of solid
2. Improvement of mixing state and flowability
3. Progress of formability
4. Liberation of substances dispersed into a material
5. Shape control of particles
6. Surface treatment and refinement of particles
7. Amorphization, coating and mechanical alloying
8. Appearance and improvement of mechano-chemical effect

TABLE 5.1.6 Transferring Diameters from Elasticity to Partially Plasticity, Partial Plasticity to Plasticity for Different Materials

Materials	Transferring Diameter x [μm]	
	Elasticity to Partial Plasticity	Partial Plasticity to Plasticity
Quartz	10~20	1~2
Feldspar	10~20	2~3
Limestone	20~30	2~3
Marble	20~30	2~3
Gypsum	30~40	4~5
Coal 1	10~20	3~4
Coal 2	20~30	4~5

5.1.3.2 Mean Particle Size and Size Distribution of Ground Product

One of the features of a ground product is to have a wide size distribution of irregular shaped particles. Describing the irregular particles, it is convenient to assume them as spherical particles' size distribution composing of $x^{(1)}$, $x^{(2)}$, $x^{(3)}$ in diameter.

Mean Particle Size of a Ground Product

Mean particle size, x_{av} can be expressed by Equation 5.1.17, where $x^{(1)}$, $x^{(2)}$, $x^{(3)}$ are diameters of fragments in a ground product and n is its number.

$$x_{av} = \frac{x^{(1)} + x^{(2)} + x^{(3)} + x^{(4)} + \cdots \quad x^{(n)}}{n} \tag{5.1.17}$$

As for the diameter for an irregular shaped particle, it is categorized into three types: 1) arithmetical mean diameter such as a three-dimensional mean diameter, 2) equivalent spherical diameter such as Heywood diameter and an equi-volume diameter, 3) statistical diameter such as Martin diameter and Feret diameter.

Size Distribution Equation

The size distribution in the single particle crushing is derived by applying a stochastic theory by Gilvarry,[31] Gaudin and Meloy,[32] or Broadbent and Callcott.[33] These theories are based on the idea that microcracks existed in the solid body are activated with stress and absorb elastic strain energy, so that the cracks develop rapidly and collide into each other to yield a new surface leading to fragments with different sizes. The undersize cumulative fraction $B(\gamma,x)$ produced from a single particle of size $\gamma(>x)$ is called a breakage function and

is written as follows, where c_1, c_2 and c_3 are constants, relating to the probability density function for length, surface and volume of cracks, and j is a constant on the presence of cracks.

1. Gilvarry equation

$$B(\gamma,x)=1-\exp\left[-\left\{\left(\frac{x}{c_1}\right)+\left(\frac{x}{c_2}\right)^2+\left(\frac{x}{c_3}\right)^3\right\}\right] \quad (5.1.18)$$

2. Gaudin-Meloy equation

$$B(\gamma,x)=1-\left[1-\left(\frac{\gamma}{x}\right)\right]^j \quad (5.1.19)$$

3. Broadbent-Callcott equation

$$B(\gamma,x)=\frac{1-\exp(-\gamma/x)}{1-\exp(-1)} \quad (5.1.20)$$

As for the case of size distribution curves of the ground product in a mill, the following equations can be given:

4. Log-normal distribution equation

The distribution can be obtained by plotting a frequency q(ln$x$) against particle size (ln$x$), and its mathematical equation is shown by Equation 5.1.21, where, ln σ_g is arithmetic standard deviation, x_m is median diameter.

$$q(\ln x)=\frac{1}{\ln\sigma_g\sqrt{2\pi}}\exp\left[-\frac{(\ln x-\ln x_m)^2}{2\ln^2\sigma_g}\right] \quad (5.1.21)$$

5. Gaudin-Schumann (G-S) distribution equation[34]

The G-S distribution curve of a ground product is obtained by plotting cumulative weight of undersize particles [$B(\gamma, x)$] against x, and is given by Equation 5.1.22., where, x_0 (normally less than γ) denotes the maximum value in size in the equation and p is a constant.

$$B(\gamma,x)=\left(\frac{x}{x_0}\right)^p \quad (5.1.22)$$

6. Rosin-Rammler (R-R) distribution equation[35]

The R-R distribution can be obtained by plotting cumulative oversized particles, R (γ, x) (-) against x, as given by Equation 5.1.23, where x_e denotes representative particle diameter and q is a constant.

$$R(\gamma,x)=\exp\left(-\left(\frac{x}{x_e}\right)^q\right) \quad (5.1.23)$$

Correlation of Parameters in the Distribution Equations with Specific Surface Area

From Equation 5.1.23, the index, q is given by Equation 5.1.25.

$$\ln R=-\left(\frac{x}{x_e}\right)^q \quad (5.1.24)$$

$$\ln(-\ln R)=q\ln\frac{x}{x_e}$$

$$q=\frac{\ln(-\ln R)}{\ln\left(\frac{x}{x_e}\right)} \quad (5.1.25)$$

Approximating the R-R distribution equation with Tayler's series, Equation 5.1.27 can be derived, as follow:

$$B(\gamma,x)=1-R(\gamma,x) \quad (5.1.26)$$

$$=1-\exp\left(-\frac{x}{x_e}\right)^q$$

$$=\frac{\left(\frac{x}{x_e}\right)^q}{1!}-\frac{\left(\frac{x}{x_e}\right)^{2q}}{2!}+\frac{\left(\frac{x}{x_e}\right)^{3q}}{3!}-\cdots$$

$$\cong\left(\frac{x}{x_e}\right)^q \quad (5.1.27)$$

In the meantime, it is possible to calculate the specific surface area, S_v (m^2/m^3) of the product from the index, q and the representative particle diameter, x_e, in Equation 5.1.27 by the Kieβkalt equation,[36,37] as given by Equation 5.1.28, where, f denotes the shape constant of a specific surface area, and it is 6 for sphere and cubic shape particles.

$$S_v x_e=1.065f\left[\exp\left(\frac{1.795}{q^2}\right)\right] \quad (5.1.28)$$

The relation between S_v (m^2/m^3) and S_w (m^2/kg) is given by Equation 5.1.29.

$$S_w=\frac{S_v}{\rho} \quad (5.1.29)$$

5.1.3.3 Rate Process in Batch Grinding

With respect to batch grinding, the mass in a size interval (x~$x+dx$) during a short time interval (dt) is expressed by Equation 5.1.30, showing that the balance of a discharge amount from this interval and an inflow of ground product from coarse size region, as illustrated in Figure 5.1.6,[38] where $S(\gamma,t)$ is the selection function for particles of size $\gamma(>x)$, t is the grinding time and x_{max} is the maximum size of the product.

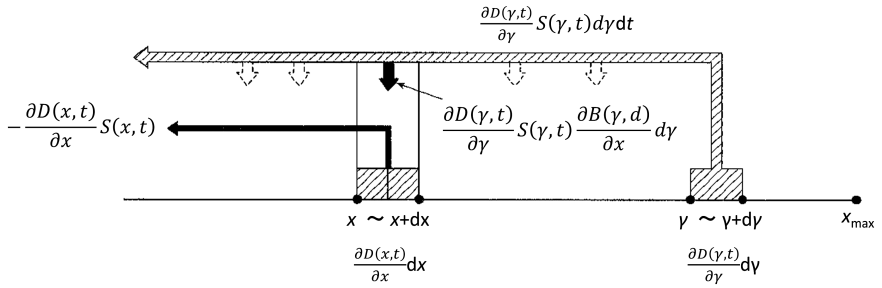


FIGURE 5.1.6 Mass balance of the product in the size range of $x \sim x+dx$ within a short time (dt) during grinding.

$$\frac{\partial^2 D(x,t)}{\partial t \partial x} = -\frac{\partial D(x,t)}{\partial x} S(x,t) + \int_x^{x_{max}} \frac{\partial D(\gamma,t)}{\partial \gamma} S(\gamma,t) \frac{\partial B(\gamma,x)}{\partial x} d\gamma \tag{5.1.30}$$

Thus, the comminution rate of particles is determined by the size distribution after grinding and by the probability that each particle is selected for grinding within a certain time.

Assuming Equation 5.1.31, one analytical approach can give us the empirical relation on the oversize cumulative fraction $R(x,t)$ [$=1-D(x,t)$] as given by Equation 5.1.32 using a grinding rate constant, K,[39,40] where $R(x,0)$ is the initial size distribution and can be regarded as unity if t is long enough.

$$S(x,t) = Kx^n \tag{5.1.31}$$

$$R(x,t) = R(x,0)\exp(-Kx^n t) \tag{5.1.32}$$

Equation 5.1.32 is a rate process on the Rosin–Rammler distribution curve based on the relation between the breakage function and selection function and it is coincidental with another rate process relation determined by Chujo and Alyavdin using a ball mill, shown by Equation 5.1.33.[41,42]

$$R(x,t) = R(x,0)\exp(-Kt) \tag{5.1.33}$$

5.1.3.4 Comminution Energy Laws

Rittinger's Law[43]

This law is based on the assumption that the energy consumed by grinding a solid is proportional to the new surface produced. Thus the comminution energy E is given by Equation 5.1.34, where S_p and S_f are is the specific surface areas, x is particle diameter, C_R and C'_R are constants, suffices f and p are feed and product, respectively.

$$E = C_R(S_p - S_f) = C'_R\left(\frac{1}{x_p} - \frac{1}{x_f}\right) \tag{5.1.34}$$

The value C_R and C'_R are related to the strength (S) of the material, as shown in C_R (or C_R') $= K_R S$.

Kick's Law[44]

Kick's law is assumed as the energy (E) required for comminution is related only to the ratio of the size of the feed particle to the product particle, as given by Equation 5.1.35, where C_K and C_K are constants.

$$E = C'_K \ln\left(\frac{x_f}{x_p}\right) = C'_K \ln\left(\frac{S_p}{S_f}\right) \tag{5.1.35}$$

The values, C_K and C'_K are related to the equation, C_K (or C'_K) $= K_R S$, where S denotes the strength of the material.

Bond's Law[45]

Bond suggests that any comminution process would be an intermediate stage in the breakdown of a particle of infinite size to an infinite number of particles of zero size. Bond's theory states that the total work (E) used in breakage is inversely proportional to the square root of the particle size of the product, and is directly proportional to the length of the crack tips, as well as the square root of the surface area formed, as shown in Equation 5.1.36, where E (kWh/t) is the comminution energy required and F and P are the particle sizes (in micron meter) corresponding to 80% passing size each by the sieve. W_i (kWh/t) denotes Bond's work index, which is recognized as an important parameter for designing a suitable electric motor in a comminution device. Table 5.1.7 shows the work index for different materials with the specific gravity.[45]

$$E = W_i\left(\frac{10}{\sqrt{P}} - \frac{10}{\sqrt{F}}\right) = C'_B\left(\sqrt{S_p} - \sqrt{S_f}\right) \tag{5.1.36}$$

These three energy laws are summarized by Lewis's equation given by Equation 5.1.37,[46] when $n=2$, it shows Rittinger's law and when $n=1$ and 1.5 it gives us Kick's law and Bond's law, respectively.

$$dE = -x^{-n}dx \tag{5.1.37}$$

Tanaka's Theory[47]

Tanaka has proposed the surface limitation theory for the grinding of solids, and gives Equation 5.1.38, where S_w denotes specific surface area at an arbitrary time, where S_∞ (m^2/g) denotes the specific surface area at $t=\infty$ (limitation), K (s^{-1}) is a grinding rate constant.

TABLE 5.1.7 Specific Gravity and Bond's Work Index of Materials Measured in Wet Process

Material	Specific Gravity (—)	Work Index (kW h/Short ton)
Andesite	2.84	18.25
Barite	4.50	4.73
Basalt	2.91	17.10
Bauxite	2.20	8.78
Cement clinker	3.15	13.56
Cement raw material	2.67	10.51
Coke	1.31	15.18
Copper ore	3.02	12.73
Diorite	2.82	20.90
Dolomite	2.74	11.27
Emery	3.48	56.70
Feldspar	2.59	10.80
Ferro-chrome	6.66	7.64
Ferro-manganese	6.32	8.30
Ferro-silicon	4.41	10.01
Flint	2.65	26.16
Fluorspar	3.01	8.91
Gabbro	2.83	18.45
Glass	2.58	12.31
Gneiss	2.71	20.13
Gold ore	2.81	14.93
Granite	2.66	15.05
Graphite	1.75	43.56
Gravel	2.66	16.06
Gypsum rock	2.69	6.73
Iron ore – Hematite	3.55	12.93
Iron ore – Hematite-specular	3.28	13.84
Iron ore – Oolitic	3.52	11.33
Iron ore – Magnetite	3.88	9.97
Iron ore – Taconite	3.54	14.60
Lead ore	3.45	11.73
Lead-zinc ore	3.54	10.57
Limestone	2.65	12.54
Manganese ore	3.53	12.20
Magnesite	3.06	11.13
Molybdenum ore	2.70	12.80
Nickel ore	3.28	13.65
Oilshale	1.84	15.84
Phosphate rock	2.74	9.92
Potash ore	2.40	8.05
Pyrite ore	4.06	8.93
Pyrrhotite ore	4.04	9.57
Quartzite	2.68	9.58
Quartz	2.65	13.57
Rutile ore	2.80	12.68
Shale	2.63	15.87
Silica sand	2.67	14.10
Silicon carbide	2.75	25.87
Slag	2.83	9.39
Slate	2.57	14.30
Sodium silicate	2.10	13.50
Spodumene ore	2.79	10.37
Syenite	2.73	13.13
Tin ore	3.95	10.90
Titanium ore	4.01	12.33
Trap rock	2.87	19.32
Zinc ore	3.64	11.56

1 short ton = 0.9072 ton.

$$S_w = S_\infty\left[1-\exp\left(-Kt\right)\right] \tag{5.1.38}$$

Beyond the time at the maximum value in S_w, then it tends to decrease with an increase in milling time. This suggests that the agglomeration of fine particles starts, and it tends into aggregation state.

5.1.3.5 Crushing Resistance and Grindability

Crushing resistance and grindability of solid materials are evaluated by following indexes:

Hardgrove Index (JIS M 8861,1993)[48]

The hardgrove index (H.G.I.) can be measured by a machine, consisting of a top-rotating ring with eight balls of 1-inch diameter. A load of 284.4 ± 2.0 N is applied on the top-rotating ring, and 50-grams of material sieved between 1.19 and 0.59 mm is ground for the period of 60 revolutions. This index is defined by Equation 5.1.39, where w (g) is the mass of ground product finer than 75 μm.

$$\text{H.G.I.} = 13 + 6.93w \tag{5.1.39}$$

When the index is large, the material means to be easily ground.

Bond's Work Index (JIS M 4002,1976)[45,49]

A standard ball mill for measuring the Bond's work index (W_i) has 12-inch (=305 mm) internal diameter and 12-inch internal width. The steel balls of 285 in total number, as tabulated in Table 5.1.8, are charged in the mill, together with 700 cm^3 in volume of feed material, of which particles size is finer than 3360 μm. The revolution of the mill is kept constant at 70 min^{-1}. This index can be measured by Equation 5.1.40, where P_1 (μm) is the sieve opening, G_{bp} (g/rev) is the ball mill grindability, which is measured as weight of product passing the size of P_1 per one rotation of the mill, P (μm) and F (μm) are 80% product size finer than P_1 and 80% feed size, respectively.

$$W_i = \frac{1.1\times 44.5}{P_1^{0.23}G_{bp}^{0.82}\left(\frac{10}{\sqrt{P}}-\frac{10}{\sqrt{F}}\right)} \tag{5.1.40}$$

TABLE 5.1.8
Composition of Steel Balls in the Measurement of Bond's Work Index

Diameter (mm)	Number of Balls
36.5	43
30.2	67
25.4	10
19.1	71
15.9	94
Sum	285

The mill is rotated a number of times so as to yield a circulating load of 250%, where the circulating load is defined as the component ratio of the oversize to the undersize. The process is continued until the mass of undersize produced per revolution (G_{bp} in Equation 5.1.40) becomes constant. Equation 5.1.40 gives the value at the condition of mill diameter (D_M) = 8 ft (240 cm) in mill diameter operated under wet closed circuit. When the milling conditions are different from them, it needs to modify W_i as below.

1. Dry operation:

$$W_i\left(\frac{4}{3}\right) \tag{5.1.41}$$

2. Different mill diameter (D_M):

$$W_i\left(\frac{8}{D_M}\right)^{0.20} \tag{5.1.42}$$

The data on W_i in Table 5.1.7 are measured by wet process. In fine grinding, when P in Equation 5.1.40 is smaller than 70 μm, the work index, W_i, is multiplied by a factor f_R to account for the increased work input. The factor (f_R) is found from Equation 5.1.43:[45]

3. $P < 70$ μm:

$$f_R = \frac{P + 10.3}{1.145P} \tag{5.1.43}$$

Bond[45] proposed a relationship between W_i, and (H.G.I.), as given by Equation 5.1.44:

$$W_i = \frac{435}{(\text{H.G.I.})^{0.91}} \tag{5.1.44}$$

5.1.3.6 Crushing and Grinding Mills

Various types of crushing and grinding devices have been used industrially for producing fine powder. The working motion of these mills is complex, depending on the mill type, but it is mainly categorized into five types, compression, shear, cut, impact and friction. The mechanism of force transmission or motion mode in grinding media are rotation, reciprocation, vibration, agitation, rolling, and acceleration by the grinding media. In addition, the grinding is operated in dry or wet or both, batch or continuous systems, in association with internal classification or drying and so on. In practice, it is common to classify grinding processes into several stages by the feed or product size. Although these sizes are not clear, they are called coarse, medium, fine, ultrafine and nano-milling. Based on such a concept, typical mill devices with their feed and product sizes can be summarized in Table 5.1.9.

Coarse Grinding

A jaw crusher is one of the typical coarse grinders, and its mill has a fixed jaw and a moving jaw pivoted at the top.[50] The crushing faces themselves are formed either of hard steel or of chilled cast iron and must be carefully fitted because they are brittle; the risk of breakage is reduced by grinding the back surface flat or packing with lead. Since the maximum movement of the jaw is at the bottom, there will be little tendency for the machine to clog though some uncrushed material may fall through and have to be returned to the crusher. Further, the maximum pressure will be exerted on the large material which is introduced at the top. The machine is usually protected so that it is not damaged if lumps of metal inadvertently enter, by making one of the toggle plates in the driving mechanism relatively weak so that if any large stresses are set up, this is the first part to fall. Easy renewal of the damage part is then possible.

A gyratory crusher employs a crushing head, in the form of a truncated cone, mounted on the shaft, the upper end of

TABLE 5.1.9 Feed and Product Sizes of Materials by Coarse, Medium, Fine, Ultrafine and Nano-Milling Devices

		Feed Size Product Size	Representative Mills
Coarse size grinding		1~2 m Below 20 cm	Jaw crusher, Gyratory crusher
Medium size grinding		20~30 cm Below 1 cm	Gyratory crusher, Cone crusher, Rod mill, Ball mill, Pin mill, Hammer mill, Impact mill
Fine size grinding		1~5 cm Below 1 mm	Roller mill, Rod mill, Ball mill, Hammer mill, Pin mill
Ultra-fine grinding	I	1~2 cm Below 1 mm	Roller mill, Rod mill, Hammer mill, Pin mill
	II	1 mm 10~100 μm	Roller mill, Ball mill, Pin mill, Jet mill, Stone mill
	III	10~100 μm 1~10 μm	Agitation mill
Nano-milling		1 μm Nanometer size	Agitation mill

which is held in a flexible bearing, whilst the lower end is driven eccentrically so as to describe a circle.[50] The crushing action takes place round the whole of the cone and, since the maximum movement is at the bottom, the characteristics of the machine are similar to those of the jaw crusher. As the crusher is continuous in action, the fluctuations in the stresses are smaller than in the jaw crushers and the power consumption is lower. It has a large capacity per unit area of grinding surface, particularly if it is used to produce a small size reduction. However, it will not take such a large size of feed as a jaw crusher, but it will give a rather finer and more uniform product. Because the capital cost is high, the crusher is suitable only where large quantities of material are to be handled. The jaw crusher and the gyratory crusher both employ a predominantly compressive force.

Medium Grinding

Roll crushers are of many types, and one of them is a crushing roll.[50] This mill consists of two rolls, one in adjustable bearings, rotate in opposite directions and the clearance(s) between them can be adjusted according to the size of feed and the required size of product. The machine is protected by spring loading against damage from very hard material. Generally, one roll is driven directly and the other by friction with the solids. The crushing rolls which may vary from a few centimeters up to about 1.2 m diameter are suitable for affecting only a small size reduction in a single operation and it is therefore common to employ a number of pair of rolls in series, one above the other. Tires with either smooth or ridged surface are keyed to the rolls. The capacity is usually between one-tenth and one-third of that calculated on the assumption that a continuous ribbon of the material forms between the rolls. Recently, high-pressure roller mills (100–200 MPa) are available to comminute finely brittle materials. The crunch angle (β) is expressed as a function of the roll diameter (D_R (m), the maximum particle diameter x_{max} (m) and the clearance s (m), as given by Equation 5.1.45.

$$\cos\frac{\beta}{2}=\frac{\left(D_R+s\right)}{\left(D_R+x_{max}\right)} \tag{5.1.45}$$

Fine Grinding

Fine grinders produce particles finer than about 10 μm. There are many kinds of machines in this category, and they are roughly classified into two types: 1) ball-media agitation type and 2) hammer impact type.

There are three kinds in the ball-media agitation type mills, and the media such as balls, rods and pebbles transfer the grinding energy to the materials by moving the mill body. Based on the mode of motion of the mill body, they are classified as tumbling ball mills, vibration mills and planetary mills.

A tumbling mill[50] is most widely used in both dry and wet systems, in batch and continuous operations and on small and large scales. The optimum rotational speed is usually set at 65 to 80% of critical speed, N_c (rpm) given by Equation 5.1.46, where D_m (m) and x_B (m) are the mill diameter and ball (medium) diameter, respectively.

$$N_c=\frac{42.3}{\sqrt{D_m-x_B}} \tag{5.1.46}$$

It is desirable to reduce the ball size in correspondence with the smaller size of the feed materials.

A vibration mill[51] is driven by eccentric motors to apply a small but frequent impact or shear to the grinding media. Loose bodies or media contained in a shell caused it to vibrate. In contrast to tumbling mills, the media in vibration mills move only a few millimeters through a complex path, shearing as well as impacting the material between them. The apparent amount of media is 75 to 85% by volume, which is about two times as much as filling mills. One of the advantages of vibration mills compared with tumbling mills is the higher grinding rate in the range of fine particles. But it is unsuitable for heat-sensitive materials.

A planetary mill consists of a revolving base disk and rotating mill pots, shown in Figure 5.1.7.[51] Materials are ground in a large centrifugal field by the force generated during revolution and rotation. The intensity of acceleration can be increased up to 150 G on the scale of gravitational acceleration. It is predicted that the grinding mechanism consists of compressive, abrasive and shear stresses of the balls. Planetary mills are also used in the study of mechanochemistry, mechanical alloying and producing composite particles.

A hammer mill is an impact type of mill, employing a high speed rotating disk, to which a number of hammer bars are

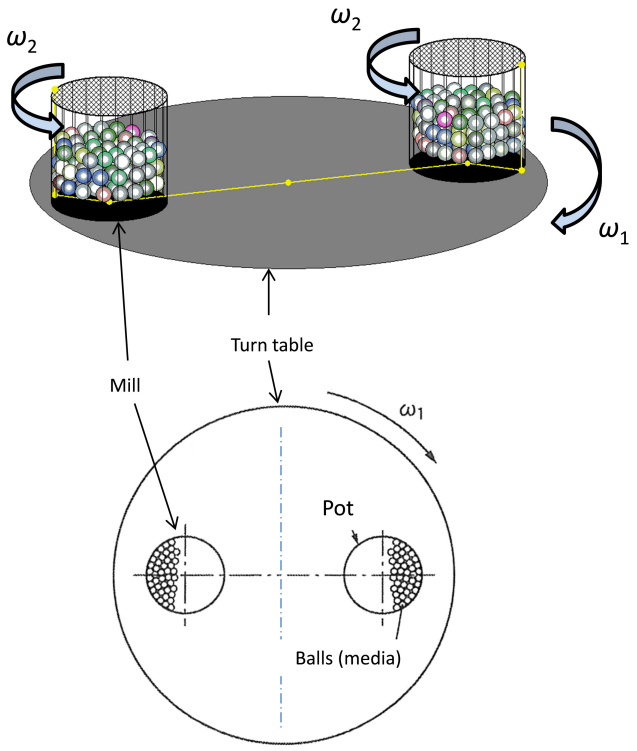


FIGURE 5.1.7 Motion of the turn table and mill pots in a planetary mill.

fixed, and they are swung outwards by centrifugal force.[50,51] The material is fed in, either at the top or at the center, and is thrown out centrifugally and crushed by being beaten between the hammer bars or against plates fixed around the periphery of the cylindrical casing. The material is beaten until it is crushed small enough to fall through the screen which forms the lower portion of the casting. Since the hammer bars are hinged the presence of any hard material does not cause damage to the equipment. The machine is suitable for the crushing of both brittle and fibrous materials, and in the latter case, it is usual to employ a screen with cutting edges. The mill is also suitable for hard materials but since a large amount of fine dust is produced, it is advisable to employ positive pressure lubrication to the bearings in order to prevent the entry of dust. The size of the product is regulated by the opening of the screen and the rotational speed. The tip velocity of the hammer in the mill is normally operated from 15 to 50 m/s, however, it is often driven up to 40 to 100 m/s for high speed type, and in some cases, 120 to 150 m/s for an exceptional type. There are several types of the screen and its openings provided, and for example, the shape of the opening is circle [x_s (mm)], the relation between the mean size (x_m) of the particles passing through this screen and its maximum diameter (x_{max}) is expressed as $x_m = (x_{max}/6) - (x_{max}/8)$. When the relation like $x_m < (x_{max}/6) - (x_{max}/8)$ is measured, then it would be regarded that the mill performance seems to be preferable. There are a number of similar mills, such as pin-type and bar-type with small as well as large scales, rotating in both vertical and horizontal directions.

Ultrafine Grinding

An agitation mill is categorized as an ultrafine grinding device, and it is one of the most efficient mills for micronizing materials and has been actively used for preparation of fine and ultra-fine particles. In this milling, a large number of small grinding media are agitated by impellers, screws or disks in a vessel (chamber). Breakage occurs mainly by collision of the media and the chamber wall. There are two types, one is the horizontal one, and in both types the media (balls, beads or pebbles) are charged in the chamber, in which slurry is flown through the chamber continuously. As shown in Figure 5.1.8 (A) and (B),[52] the disks, pins, or paddles are attached to a shaft to agitate media (balls or beads) and grind particles in a flowing suspension. A tower mill[51] is a large standing mill that has a central shaft with a screw to convey balls upward, and the centrifugal force causes them to collide with the wall.

A fluid-energy mill is widely noted as a jet mill shown in Figure 5.1.9,[51] in which the materials are ground by the collision of a particle with a particle, a wall or a plate of the chamber. The collision energy is generated by a high-speed jet flow. Fluid-energy mills may be classified in terms of the mill action. In one type of mill, the energy is generated by high-velocity streams at a section or whole periphery of a grinding and classification vessel. Typical grinders are Jet-O-Mizer and Spiral Jet-mill, and these fluid-energy mills have no movable mechanical parts, and it has advantages such as dry and continuous operation without a temperature rise, and controlling the particle size by the feed rate of materials and the velocity of jet stream. But the energy efficiency is low, and the power cost is high.

Nano-milling[52]

Nano-milling is employed to produce submicron sized particles or particles less than the submicron size. One of the candidates is a medium agitating type of mills (stirred media mills). As the demand for ultrafine (submicron) particles has increased in many kinds of industries, the research and development for such ultrafine grinding has involved different aspects such as wet grinding, grinding aids and closed-circuit grinding system. In order to achieve ultra-fine grinding, it is necessary to increase the collision probability of the particle and grinding medium, so as to disperse the slurry well. In this media mill, it is better to reduce the diameter of the media, about 50 nm diameter media can be provided and it is possible to separate them from the milled product by sophisticated centrifugal effect in a mill.

5.1.3.7 Improvement of Grinding Efficiency

There have been several methods for improving the grinding efficiency in a sense of practical operation. The first one is the use of grinding aid, the second is to take separation of finer sizes of particles than the target size, and the third is to control the temperature of the materials which exhibit peculiar behavior in lower temperature than its glass transition temperature.

Grinding Aid

A grinding aid is effective for improving the efficiency of grinding. There are several mechanisms, and one is to promote the crack propagation by reducing the surface energy of the solid which is to be ground. Another is to depress the adhesive force of newly formed fine particles. The representative grinding aids with the effective materials are shown in Figure 5.1.10.[53,54]

Classification of Fine Particles

When the undersize product less than the target size is removed out from the grinding zone, the coarse particles remained, and it is ground selectively and effectively by the mill. On the contrary, when the grinding operation is continued without classification of finer powder, then they act to prevent the size reduction of the coarse product, resulting in low grinding efficiency. Therefore, removing fine product is very important to improve the grinding efficiency. To do so, a self-separation type of mill, such as the vertical type of roller mill as shown in Figure 5.1.11,[55] is worked to grind a solid with fine separation particles by air, and another example can be seen in a continuous grinding circuit on an industrial scale, which has a classification device such as cyclone or sieves before the mill charge or after the mill discharge, as shown in Figure 5.1.12.[55]

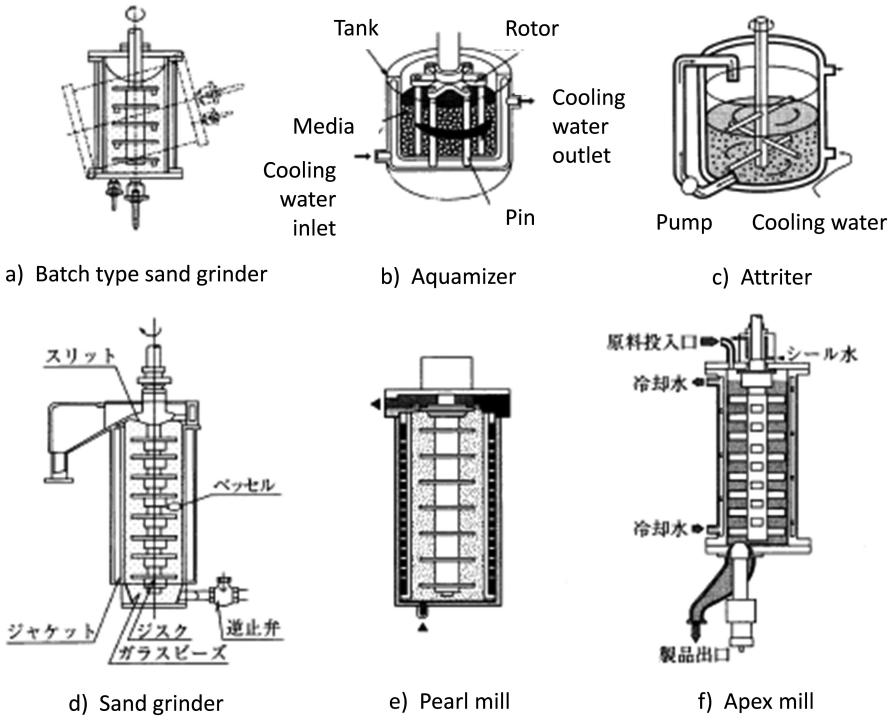


FIGURE 5.1.8 (A) Different types of vertical agitation mill.

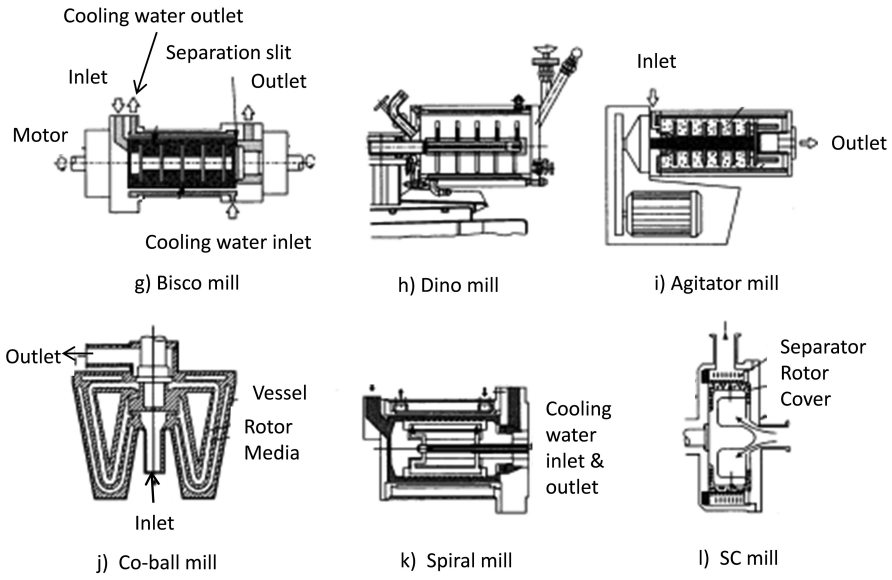


FIGURE 5.1.8 (B) Different types of horizontal agitation mill.

Four Grinding Conditions

It is known to keep the following four grinding conditions in order to improve the efficiency of grinding operation:

1. Mill device has the potential of enough force to grind a solid
2. The force is to fit surely a solid particle resulting in fracture
3. The fragments do not reconnect and agglomerate
4. The slurry in wet milling remains in a stable state

The first condition is the necessary one for a mill, the second one is to increase the probability of fracturing chance for a solid in a mill. The third one is to depress activation of powder during milling and this can be achieved by, for example, adding a grinding aid and operating in wet condition. The last condition is important in wet milling a solid, and this is related to agglomeration and dispersion of fine particles in the liquid phase. The surface electric charge in a solid in a liquid is changed with its pH, and the same surface charge of solid particles tends to agglomerate and aggregate in liquid phase.

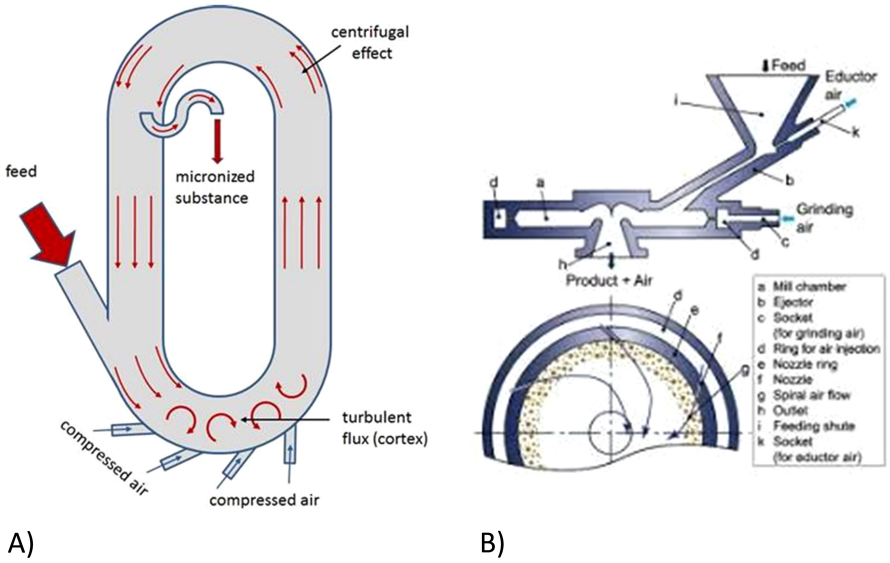


FIGURE 5.1.9 Representative jet mills. (A) Jet-O mizer, (B) Spiral Jet-mill.

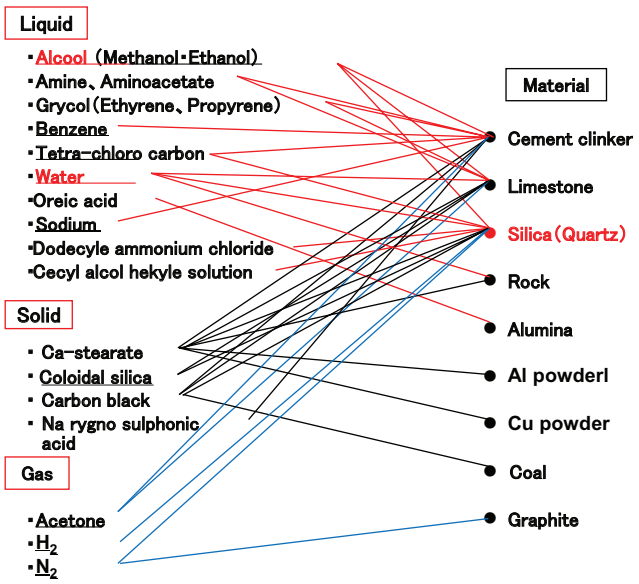


FIGURE 5.1.10 Combination of grinding aids and effective materials.

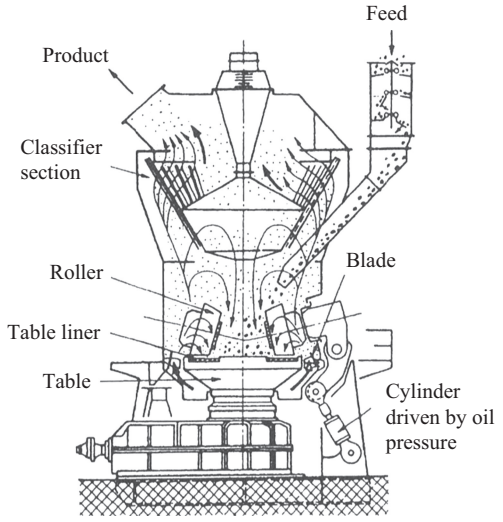


FIGURE 5.1.11 Vertical type of a roller mill.

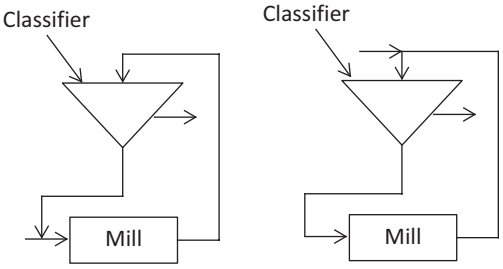


FIGURE 5.1.12 Continuous grinding circuits in an industrial scale, having a classification device such as cyclone or sieve before the mill charge or after the mill discharge.

Figure 5.1.13[56] is a variation of pH in a slurry of alumina particles suspended in water, the δ-potential of alumina and the mean particle size of alumina particles milled by a bead mill as a function of the specific energy of milling. It is known that the δ-potential of alumina shows a plus value in the acid region, while it is close to 0 (zero) at pH = 9 to 10. This means that alumina grinding would be made in the acid region where the zero point charge (ZPC) is far from pH = 9. In fact, when alumina particles are milled in a liquid of pH = 9, they tend to agglomerate and the mean particle size does not decrease at all. In order to avoid such agglomeration of alumina particles in the wet milling, the pH of the liquid should be changed to a lower value such as pH = 5, for example. The mean particle size of alumina is not decreased in the pH = 10 with increasing the specific energy of milling, and it tends to increase with increase in the energy. On the contrary, for the mean size of alumina milled under pH = 5, it tends to decrease smoothly with an increase in the energy. The ZPC of different samples are shown in Table 5.1.10.[57,58]

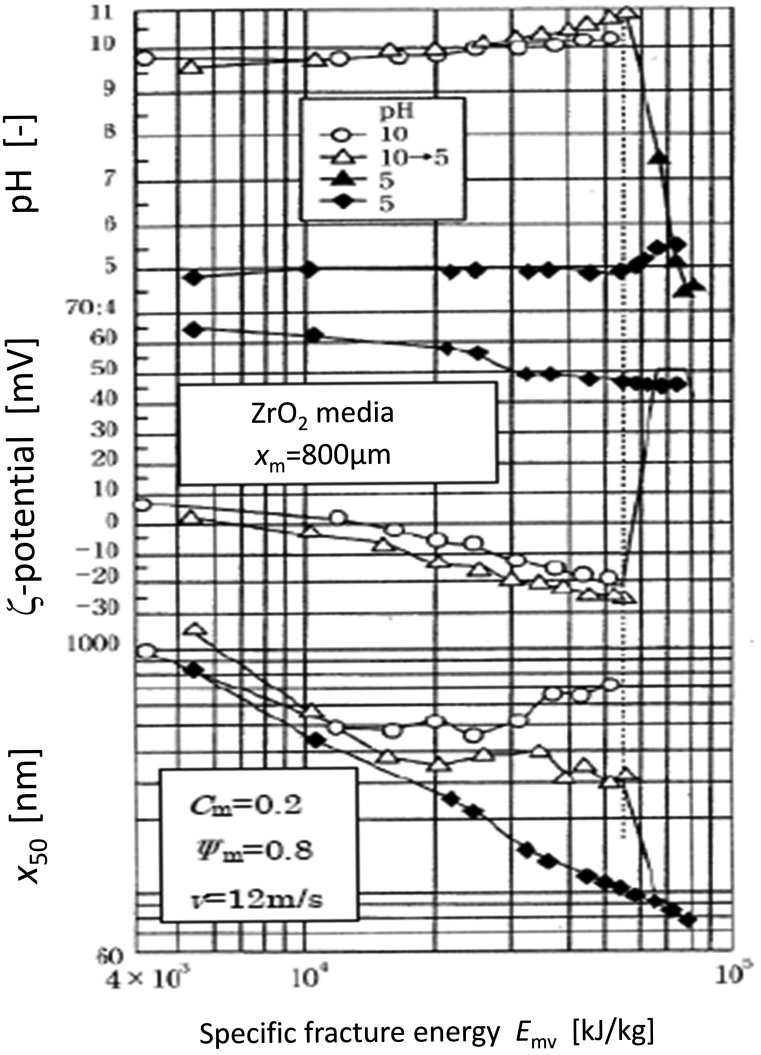


FIGURE 5.1.13 pH, δ-potential and mean particle size of the alumina sample milled by a bead mill as a function of specific energy.

Improvement in Structure of a Mill Chamber

There are several challenging works on improvement of the milling performance from different aspects. These are categorized into two groups: the first group is to optimize the mill structure and design and the second one is to incorporate new concepts, as shown below:

As an example, one has attempted to optimize the inner structure of a horizontal type media mill and gives the data on milling $CaCO_3$ particles by measuring the power. The revision optimizes the ratio of inner diameter D_M to inner length L of the mill body. Table 5.1.11[59] shows the comparison of the mill power of the revised mill ($L/D_M = 0.8$) against those by the ordinary mill ($L/D_M = 1/3$) at the same capacity and the same mean product size. From the data, in spite of the beads filling, the power unit in the revised mill is lower than that in the ordinary mill. They have additional data on the mill power with a specially designed rotor attached in the same media mill, and the results show extremely high performance in the production capacity (kg/h) as well as the power unit (kW h/ton) for the revised mill in comparison with that for the ordinary one. Another example is that the mill performance can be improved by attaching a small piece with ΔV-structure into a stirring disk in a media mill. The criterion of the performance of the mills is the duration time (t) to reach to 80 nm in the mean particle size of the product by its milling. The duration time (t) was 17 min when ΔV-structure was attached in a media mill, while it was 37 min without the ΔV-structure.[59] The data clearly show that the time in the mill with the ΔV-structure piece is extremely shorter than that in the mill without the piece. The energy reduction ratio would be 54%, assuming that the time is proportional to the energy.

As for incorporating of a new concept, a revised separator was attached near the outlet of the media mill, and the particle size in the slurry was measured with time to reach the minimum size. The particle size $(x_{50})_{eq}$ was then 15 nm at $t = 10$ min when a new classifier was used, while it was 150 nm at $t = 60$ min when an ordinary classifier was used.[59] It is found that not only the required time but also the mean minimum size for the mill with the revised classifier are improved more than before. This is due to the separation of beads effectively during the milling by the revised classifier. Another example for taking a new approach with computational fluid dynamic

TABLE 5.1.10 Zero Point Charge (ZPC) (=pH⁰) for Different Materials

Materials	ZPC (pH⁰)
α-Al_2O_3	9.1~9.2
γ-Al_2O_3	7.4~8.6
α-AlOOH	7.4, 9.4
γ-AlOOH	5.5~7.5
α-$Al(OH)_3$	5.0~5.2
γ-$Al(OH)_3$	9.3
CuO	9.5
$Fe(OH)_2$	12.0
α-Fe_2O_3	5.7~6.9
Fe_3O_4	6.5
α-FeO_3	8.3
γ-FeO_3	6.7~8.0
$Mg(OH)_2$	12.4
$Mn(OH)_2$	12.0
NiO	10.3
$Ni(OH)_2$	11.1
SiO_2	1.5~3.7
TiO_2	6.0~6.7
ZnO	9.3~10.3
V_2O_3(水和物)	9.3

TABLE 5.1.11 Power Unit in $CaCO_3$ Milling by a Media Mill of NC Make

	Power Unit (kW h/ton)	
Beads Filling Ratio	L/D = 0.8	L/D = 1/3
Low	235	335
High	220	290

(CFD) simulation in milling devices is to set up a dry and wet milling system. The mill used in this case was a media mill, and its performance was criticized by the power unit of the system and it was compared with that for the wet-wet milling system. The power unit was 1.0 kW h/ton in the dry-wet milling systems, while it was 3.8 kW h/ton in the wet-wet milling one.[59] It is found that the power unit for the combined dry-wet milling system is lower by more than 3 than that for the wet-wet milling system. Similarly, the CFD approach was done to simulate the flow pattern of the air in a jet mill chamber. From the flow pattern, they have attached a small channeling ring in it, and compared the power unit with that for the mill without the ring. The power unit was 6 kW h/ton in the jet-mill with the ring, while it was 12 kW h/ton in the jet-mill without the ring.[59] It is noted that the power for the mill with the ring is half of that for the mill without the ring. The ring plays a significant role to flow smoothly in the chamber so that fine particles would be classified effectively, resulting in low power consumption.

REFERENCES

1. Carry, W.F., Halton, E.M., *Trans. Inst. Chem. Eng.*, 24, 102–108, 1946.
2. Suzuki, S., *J. Powder Technol. Jpn*, 7, 299–306, 1970.
3. Jimbo, G., et al., *FUNSAI*, No.14, 10–17, 1969.
4. Saito, F., Baron, M., Dodds, J., *Morphology Control of Materials and Nanoparticles*, Waseda, Y., Muramatsu, A. Eds., Springer, Berlin, 2003, 3–23.
5. Kanda, Y., Kotake, N., *Handbook of Powder Technology*, (Chap.12), Salman, A.D., Ghadiri, M., Hounslow, M.J. Eds. Elsevier, Amsterdam, 2007, 529–550.
6. Hiramatsu, Y., Oka, T., Kiyama, H., *MMIJ*, 81, 1024–1030, 1965.
7. Yashima, S., Morohashi, S., Awano, O., Kanda, Y., *Kagaku Kogaku*, 34, 210–218, 1970.
8. Sakuma, T., Ino, H., *Zairyo Kagaku Gairon*, Asakura-Shoten, Tokyo, 2000, 127.
9. Timoshenko, S.P., Goodier, J.N., *Theory of Elasticity* (3rd edition), McGraw-Hill Kogakusha Ltd,, Tokyo, 1970, 409–420.
10. Griffith, A.A., *Philos. Trans. R. Soc. London*, A221, 163–198, 1920.
11. Weibull, W., *ASME J. App. Mech.*, Sept., 293–297, 1951.
12. Epstein, B., *J. Appl. Phys.*, 19, 140–147, 1948.
13. Yashima, S., Kanda, Y., Izumi, T., Shinozaki, T., *Kagaku Kogaku*, 36, 1017–1023, 1972.
14. Yashima, S., Saito, F., *J. Soc. Powdor Technol., Jpn*, 16, 714–720, 1979.
15. Schonert, K., Rumpf, H.I., *Europäisches Symposium Zerkleinern*, (Frankfurt A. M.), Verlag-Chemie/VDI-Verlag, 1962, S108–S127.
16. Bergstrom, B.H., Crabtree, D.D., Sollenberger, C.L., *Trans. Soc. Min. Eng., AIME*, 226, 433–441, 1963.
17. Kanda, Y., Yashima, S., Shimoiizaka, J., *MMIJ*, 85, 987–992, 1969.
18. Kanda, Y., Yashima, S., Shimoiizaka, J., *MMIJ*, 86, 435–440, 1970.
19. Kanda, Y., Saito, F., Sano, S., Yashima, S., *Kagaku Kogaku Ronbunshu*, 10, 108–112, 1984.
20. Ueno, G., *Zairyo-Shiken*, 9, 423–427, 1960; *Ibid.*, 9, 428–432, 1960.
21. Orowan, E., *Rept. Progr. Phys.*, 12, 185–232, 1948–1949.
22. Yashima, S., et al., *Kagaku Kogaku*, 37, 630–632, 1973.
23. Kobayashi, R., *MMIJ*, 80, 429–434, 1964.
24. Yashima, S., et al., *Kagaku Kogaku*, 37, 1218–1226, 1973.
25. Yashima, S., Saito, F., Hashimoto, H., *J. Chem. Eng. Jpn*, 20, 257–264, 1987.
26. Yashima, S., Kanda, Y., Sano, S., *Powder Technol.*, 51, 277–282, 1987.
27. Rumpf, H., *Chem. Ing. Tech.*, 31, 323–337, 1959.
28. Saito, F., Hatano, S., *J. Soc. Powder Technol., Jpn*, 54, 234–248, 2017.
29. Sikong, L., Hashimoto, H., Yashima, S., *SENKEN IHO, Tohoku Univ.*, 45, 23–29, 1989.
30. Senna, M., Schonert, K., *Powder Technol.*, 32, 217–221, 1982.
31. Gilvarry, J.J., *J. Appl. Phys*, 32, 391–399, 1961.
32. Gaudin, A.M., Meloy, T.P., *Trans. AIME*, 223, 43–51, 1962.
33. Broadbent, S.R., Callcott, T.G., *J. Inst. Fuel*, 29, 524–528, 1956.
34. Schuhmann, R., *Am. Inst. Min. Met. Eng. Tech.*, No.1189, 1–11, 1940.
35. Rosin, P., Rammler, E., *J. Inst. Fuel*, 7, 29–36, 1933.
36. Kieβkalt, S., Matz, G., *Zeitschrift des VDI*, 93, 58–60, 1951.
37. Miyawaki, I., Fujisaki, K., *FUSEN (Flotation)*, No.32, 37–44, 1967.

38. Toneva, P., Peukert, W., *Handbook of Powder Technology*, Elsevier, Amsterdam, 2007, 873–911.
39. Reid, K.J., *Chem. Eng. Sci.*, 20, 953–963, 1965.
40. Furuya, M., Nakajima, Y., Tanaka, T., *Ind. Eng. Chem. Process Des. Dev.*, 10, 449–456, 1971.
41. Chujo, K., *Kagaku Kogaku to Kagakukikai*, Maruzen, Tokyo, 1949, 1–83.
42. Miwa, S., *Funtaikougaku Tsuron*, Nikkan-Kogyo-Shinbun-Sha, Tokyo, 1981, 151–166.
43. Rittinger, P.R. von, *Lehrbuch der Aufbereitungskunde*, Verlag von Ernst & Korn, Wien, 1867, 19–164.
44. Kick, F.M., *Das Gesetz der propoertionalen widerstande und seine anwendung feli*, Verlag von Arthur Felix, Leipzig, Germany, 1886.
45. Bond, F.C., *Trans. Soc. Min. Eng. AIME*, 193, 484–494, 1952; Bond, F.C., *Brit. Chem. Eng.*, 6, 378–385 & 543–548, 1961.
46. Walker, W.H., Lewis, W.K., MacAdams, W.H., Gilliland, E.R., *Principles of Chem. Eng.*, McGraw-Hill, London, 1937, 255.
47. Tanaka, T., *Kagaku Kogaku*, 18, 160–171, 1954.
48. JIS M8801, *Coal Testing Methods*, 2004.
49. JIS M4002, *Testing Method of Grinding Work Index*, 2000.
50. Coulson, J,M., Richardson, J.F., *Chemical Engineering*, Pergamon Press, Oxford, 1978, 56–85.
51. Kuwahara, Y., *Handbook of Chemical Engineering*, (Chap.16.1.6), SCEJ Ed., Maruzen, Tokyo, 1999, 842–854.
52. Nakayama, T., *Beads Mill Producing Ultra-fine and Nano-particles*, Kogyo-Chosa-Kai, Tokyo, 2010, 76.
53. Saito, F., *Handbook of Chemical Engineering*, (Chap.16.1.1), SCEJ Ed., Maruzen, Tokyo, 1999, 837.
54. Jimbo, G., *Ultrafine Particles–Science and Application*, (Kagaku-Sosetsu), Gakkai-Shuppan-Center, Tokyo, 1985, 100.
55. Ito, M., *Fundamental of Powder Devices and Equipment*, Kogyo-Chosa-Kai, Tokyo, 2005, 23.
56. Mende, S., Stenger, F., Peukert, W., Schwedes, J., *Powder Technol.*, 132, 64–73, 2003.
57. Furusawa, K., *Bunseki*, 5, 247–254, 2004.
58. Enomae, T., *J. Jpn Soc. Colour Mater.*, 86, 67–73, 2013.
59. Igarashi, A., Yamagiwa, A., Inkyo, M., Gunji, S., Kozawa, K., Akiyama, S., Kogawa, J., et al., *Grinding Technology and Eco-Recycle*, (Chap.5), APPIE Ed., NGT, Tokyo, 2010, 437–528.



Taylor & Francis
Taylor & Francis Group
http://taylorandfrancis.com

5.2 Dispersion of Particles

Kuniaki Gotoh (5.2.1)
Ko Higashitani (5.2.2)

5.2.1 IN GASEOUS STATE

In order to disperse an agglomeration of particles in a gaseous state, the external force larger than the adhesive force between primary particles in the agglomeration should be applied to the agglomeration. The dispersion methods can be classified by the applying methods of dispersion forces. Here, we describe the outline of the dispersion methods of agglomerated particles in a gaseous state with particular attention to the external forces that can be utilized for the dispersion force of agglomerates.

5.2.1.1 Dispersion Force

Dispersion Force Induced by Acceleration or Deceleration of Airflow

One of the external forces that can be utilized for the dispersion of agglomerated particles is a fluid resistance induced by the acceleration or deceleration of a fluid. Here, it is assumed that an agglomerated particle can be modeled by a doublet consisting of two primary particles having different sizes, as shown in Figure 5.2.1. When the agglomerated particle is in a uniform flow field, the motion equation of each primary particle can be written as follows,[1,2]

$$m_A \frac{du_p}{dt} = R_{fA} - F_d$$
$$m_B \frac{du_p}{dt} = R_{fB} + F_d \tag{5.2.1}$$

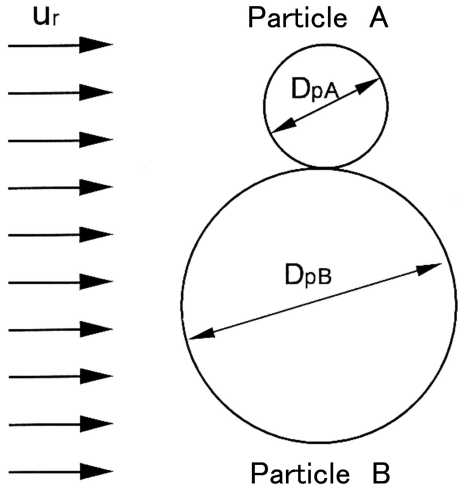


FIGURE 5.2.1 Agglomerated particle in uniform flow.

where:

R_{fA} and R_{fB} are the fluid resistance forces acting on each particle
u_p is particle velocity
F_d is the force acting on each particle to disperse agglomerates
m_A and m_B are the mass of particle A and particle B respectively

These masses can be calculated by the particle diameters x_A, x_B and the particle mass density ρ_{pA}, ρ_{pB}.

$$m_A = \frac{\pi}{6}\rho_{pA}x_A^3$$
$$m_B = \frac{\pi}{6}\rho_{pB}x_B^3 \tag{5.2.2}$$

If the particle's Reynolds number is in the range of Stokes' law, the resistance force R_f can be expressed by

$$R_{fA} = 3\pi\mu u_r x_A$$
$$R_{fB} = 3\pi\mu u_r x_B \tag{5.2.3}$$

where u_r is the relative velocity between particle and fluid. The substitution of Equations (5.2.2 and 5.2.3) into Equation (5.2.1) and the assumption that the mass density of the agglomerated particle is the same as the primary particles (ρ_p=ρ_{pA}=ρ_{pB}) lead to the following equation for the dispersion force F_d.

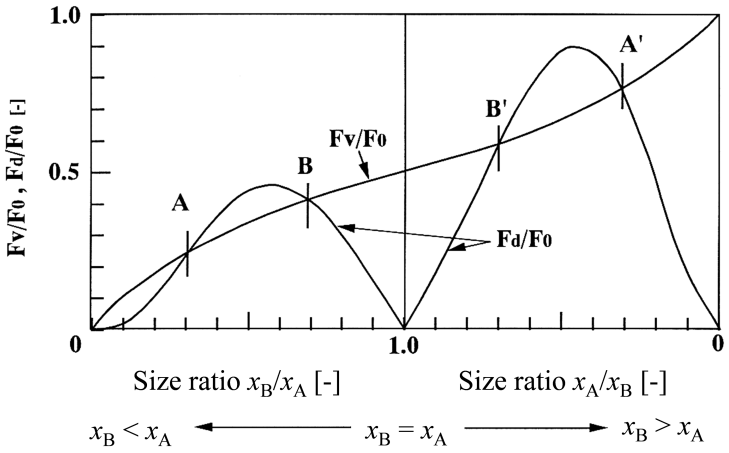
$$F_d = 3\pi\mu u_r x_A x_B \frac{(x_B - x_A)}{(x_A^2 - x_A x_B + x_B^2)} \tag{5.2.4}$$

When the resistance force is beyond Stokes' regime, the resistance force R_f is expressed by the following equation.[2]

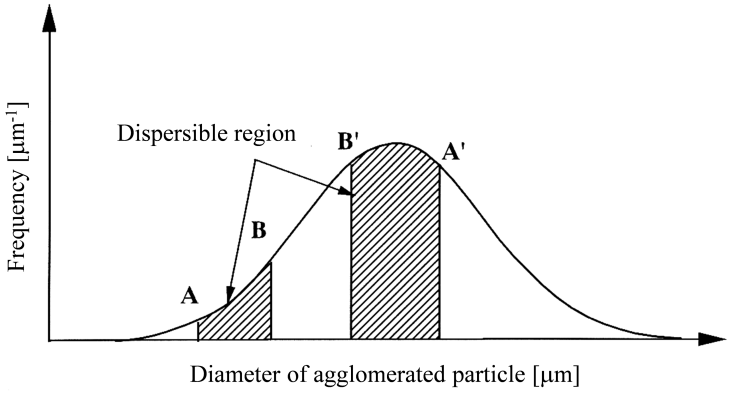
$$R_f = \frac{\pi}{8}x_v^2\rho_f u_r^2\left(0.55 + \frac{4.8}{\sqrt{\mathrm{Re}}}\right) \tag{5.2.5}$$

where:

x_v is equal to x_A/x_B
Re is equal to $x_v\rho_f u_r/\mu$
ρ_f is fluid density



a)



b)

FIGURE 5.2.2 Estimation of dispersible region. (a) Comparison between dispersion force and adhesive force, (b) Dispersible region.

In this case, the dispersion force F_d can be expressed by

$$F_d = \left\{0.119\rho_f u_r^2 x_B^2 x_v^2 \left(\kappa_A - x_v \kappa_B\right) + 2.07\sqrt{\mu\rho_f u_r^3}\, x_B^{3/2} x_v^{3/2} \left(\kappa_A - x_v^{3/2}\kappa_B\right) + 9.05\mu u_r x_B x_v \left(\kappa_A - x_v^2 \kappa_B\right)\right\} / \left(x_v^3 + 1\right) \quad (5.2.6)$$

Above two expressions for the dispersion forces are applicable only for a single agglomerate. The effect of neighbor particles on the dispersion force is also reported.[3]

Figure 5.2.2 shows the calculated result of dispersion force expressed by Equation (5.2.4).[4] In the calculation, the diameter of particle A was kept constant at 1 μm and the diameter of particle B is varied. The difference of diameters is expressed by the ratio of diameters x_B/x_A for the case of $x_B < x_A$ and x_A/x_B for the case of $x_A < x_B$. When the diameter ratio is unity, i.e. the diameter of particle B is the same as that of particle A, the dispersion force induced by the acceleration or deceleration is zero. In addition, when the ratio of the x_A/x_B and x_B/x_A is zero, i.e. the diameter of particle B is quite bigger or smaller than that of A, the dispersion force induced by the acceleration or deceleration is also zero. In other words, the dispersion induced by the acceleration or deceleration of fluid is effective for the agglomeration consisted of primary particles having an adequate size ratio.

Dispersion Force Induced by Shear Flow Field

When an agglomerated particle is placed in a shear flow field with a velocity gradient γ, the dispersion force is induced by the shear flow. Bagster and Tomi [5] studied the force induced by the flow theoretically and reported that the shear stress τ acting on the agglomerated particles has the maximum value in the central plane of the agglomerated particle and the maximum value is expressed by following equation.

$$\tau = 8.5\mu\gamma \quad (5.2.7)$$

On the other hand, when an agglomerated particle consisted of two primary particles, as shown in Figure 5.2.3, is placed in the shear flow field with velocity gradient γ, it can be considered that the bending moment σ_γ is also induced. In the case that the diameter of particle B is quite larger than that of particle A, the bending moment σ_γ is expressed by the following equation.[1]

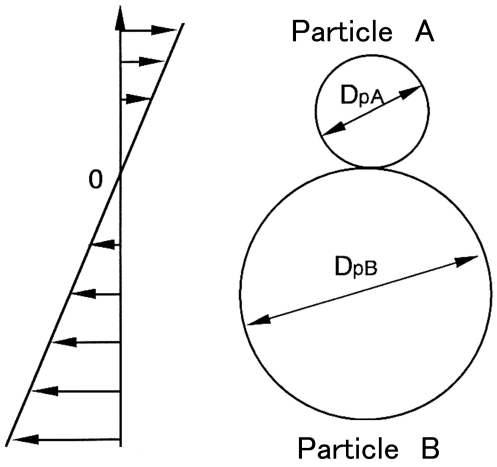


FIGURE 5.2.3 Agglomerated particle in shear flow field.

$$\sigma_\gamma \approx \frac{93\mu\gamma}{\pi c^3} \tag{5.2.8}$$

where c is the ratio of the diameter of circular contact area to the particle diameter. Although the coefficient c depends on the contact configuration, the value is, in general, quite smaller than unity. Thus, the value of the bending moment σ_γ calculated by Equation (5.2.8) is larger than the value of the shear stress τ calculated by Equation (5.2.7). This fact means that the bending moment dominates the dispersion force in the shear flow field.

Impaction Force

When an agglomerated particle of mass m collides to an obstacle with velocity v_i, the impaction force F_i is expressed by the following equation.[1]

$$F_i = mv_i/\Delta t \tag{5.2.9}$$

where Δt is the duration time of the impaction. At the collision, the compression stress σ_i is generated in the central plane of the agglomerate. If the agglomerate is modeled by a single spherical particle of diameter x_{ag}, the compression stress σ_i can be expressed by following equation[1]

$$\sigma_i = \frac{2}{3}\rho_p x_{ag}\left(\frac{v_i}{\Delta t}\right) \tag{5.2.10}$$

When we consider the dispersion of an agglomerate by the impaction against an obstacle, the impaction probability η should be taking into consideration. The probability η is a function of the shape of the obstacle, and either the inertia parameter ψ or the Stokes number S_k, defined by the following equation.

$$\Psi = \frac{\rho_p u D_{pag}}{18\mu D} = \frac{S_k}{2} \tag{5.2.11}$$

where u and D are the representative velocity and length, respectively. The dependence of the impaction probability η on the obstacle shape can be found in the literatures, in which the predictions of collection efficiency of particles on the impactor or filters are discussed. In general, the impaction probability η increases with the inertia parameter ψ. It can be found by Equations (5.2.9–5.2.11) that the impaction force F_i, the compression stress and the inertia parameter increase with the diameter of agglomerated particles. It means that the dispersion by the impaction is effective for large agglomerates, independently of their structure.

The impaction force described above, which is induced by the collision of agglomerates to the other obstacle, has been utilized for industrial dispersers, such as, ball mills and fluidized-bed type dispersers. In these dispersers, not only the impaction force but also the friction and/or the attrition force act as the dispersion force.

Other Dispersion Forces

In the derivation of the dispersion forces described above, the simple flow field and simple particle behavior are assumed. However, the flows in real dispersers are complex and, in many cases, the flow is turbulent. Although the mechanism of dispersion in the turbulent flow is not well known, it was reported that the mass median diameter x_{50} of aerosol passing through the disperser, such as the orifice-type[6] and tube-type dispersers,[7] is proportional to the value of $\varepsilon^{-0.2}$, where ε is the energy dissipation rate calculated from the pressure drop ΔP of the disperser. If the diameter of the agglomerated particles is smaller than the size of micro-scale vortexes in turbulence, the shear stress τ and the bending stress σ_g can be expressed by the flowing equations.[1]

$$\tau \cong 3.1\sqrt{\rho_f \mu \varepsilon}$$
$$\sigma_g \cong \frac{10.8\sqrt{\rho_f \mu \varepsilon}}{c^3} \tag{5.2.12}$$

5.2.1.2 Dispersers in a Gaseous State

Within the disperser, one or several dispersion forces act on agglomerated particles to disperse them. However, the dispersed particles may agglomerate again because of turbulent and Brownian diffusion motions. In the case of dispersion in a liquid state, it is possible to stabilize the particles by preventing the re-agglomeration by means of a surfactant or pH control of the medium liquid. However, in the case of dispersion in gaseous state, there is no effective stabilization method of dispersions. For this reason, many of dry dispersers have the structure in which the particle concentration is promptly lowered to decrease the contact probability between the particles, just after the dispersion force is applied. The structure and the dominant dispersion power of typical dispersers are outlined below.

Orifice

Orifice is a plate with a small hole in a pipe as shown in Figure 5.2.4. It makes converging acceleration and expanding deceleration flows in and out of the orifice, respectively.

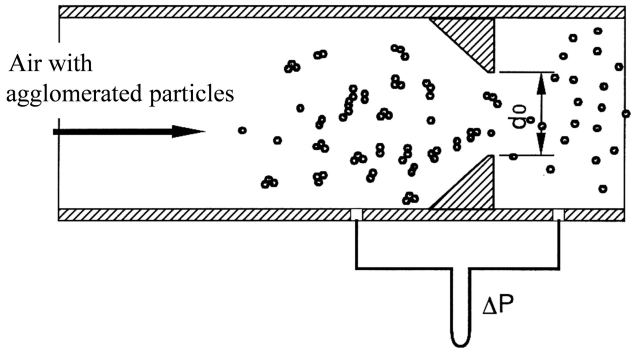


FIGURE 5.2.4 Orifice.

Mass median diameter x_{50} of aerosol particles dispersed by the orifice has the correlation with the energy dissipation rate ε calculated by the pressure drop ΔP at the orifice.[6]

$$x_{50}/x_{50s} = 31.3\varepsilon^{-0.2}$$
$$\varepsilon = 0.4\Delta P\bar{u}/d_0 \tag{5.2.13}$$

where:

x_{50s} is the mass median diameter of primary particles
$\bar{u}$ is the average air velocity
d_0 is the diameter of orifice.

Capillary Tube

When a flow in a capillary tube is a turbulent, the tube can be used as a disperser. Yamamoto et al.[7] reported that x_{50} of aerosol particles dispersed by the capillary tube is correlated with ε, as follows.

$$x_{50} = 15\varepsilon^{-0.2}$$
$$\varepsilon = \Delta P\bar{u}/2.5d \tag{5.2.14}$$

where d is diameter of capillary tube.

Ejector[1, 2]

Schematic cross-sectional view of an ejector is shown in Figure 5.2.5. A pressurized primary air jet generated by a nozzle is introduced into the ejector to induce lower pressure than the atmospheric pressure. This low pressure causes a secondary airflow. When the powder containing agglomerated particles is fed with the secondary airflow, the agglomerated particles are dispersed at the merging point of the primary and the secondary flows by the forces induced by the acceleration and shear flow fields.

Venturi[1,2]

Venturi has a throat that causes the conversing and expanding flows as shown in Figure 5.2.6. In the venture, a low pressure is generalized at the throat, which induces a secondary airflow through the inlet tube. If agglomerated particles are fed with the secondary airflow, the forces induced by the acceleration and shear flow fields can disperse the agglomerated particles.

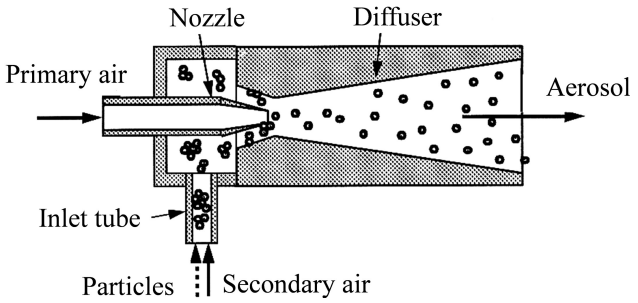


FIGURE 5.2.5 Ejector.

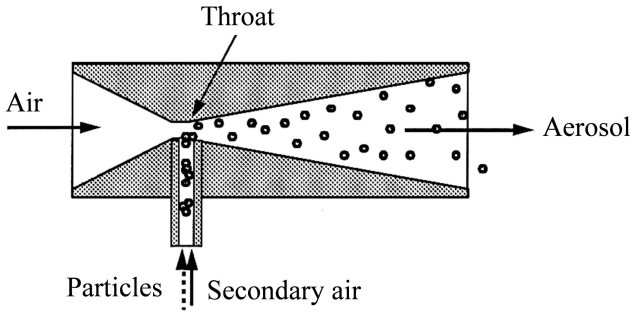


FIGURE 5.2.6 Venturi.

Fluidized bed[8]

In a fluidized bed, a particle suffers mechanical forces, such as the impaction and attrition forces, from the neighbor fluidizing particles. The mechanical forces act as the dispersion forces to the agglomerated particles in the fluidized bed. When the air velocity in the fluidized bed is set at higher velocity than the terminal settling velocity of primary particle fluidized in the bed, the primary particles are entrained to the airflow. Thus, the fluidized bed can be utilized as a disperser.

When particles do not fluidize because of their adhesive force, mixing of large particles, such as glass or metal beads, as the fluidizing medium is effective for dispersion (Figure 5.2.7). The large particles are fluidized easily and generate the impaction and attrition forces that act as the dispersion force to the adhesive particles.

Mixer-Type Disperser[4,8,9]

Mixer-type disperser shown in Figure 5.2.8 is one of the mechanical dispersers with a rotating obstacle. The disperser consists of the impeller rotating at a high speed (from 4000 to 20000, in general), the inlet tube attached to the top of the vessel and the outlet tube are attached tangentially to the vessel. By the rotation of the impeller, a low pressure is generated above the impeller, which causes the suction flow through the inlet tube. The powder containing agglomerated particles is fed through the suction flow. The agglomerated particles are dispersed by the forces induced by acceleration and shear flow and/or the impaction force to the impeller and the vessel wall.

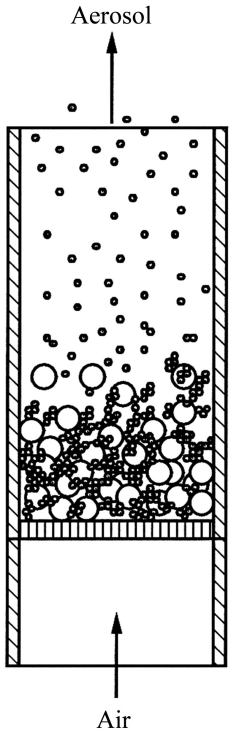


FIGURE 5.2.7 Fluidized bed.

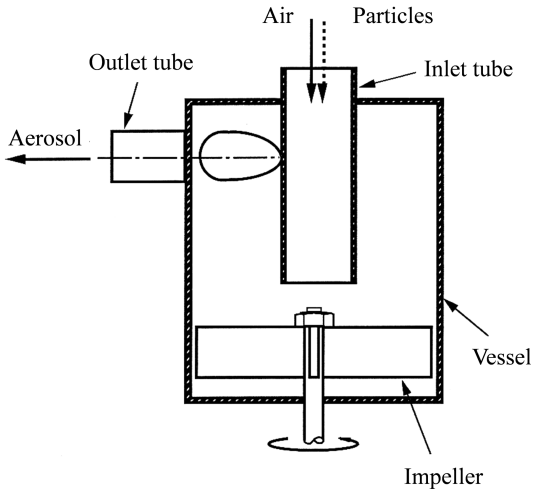


FIGURE 5.2.8 Mixer-type disperser.

5.2.2 DISPERSION IN LIQUIDS

Since particles are essentially unstable in solutions, they are more or less aggregated in many industrial wet processes. These particles must be fully dispersed to make the best use of their functions. Hence, it has been a key technology to disperse coagulated particles (flocs) in solutions, but even the fundamental mechanism of dispersion is poorly understood because of the complexity of the breakup and adhesion mechanisms between particles in liquids. The term "dispersed" state of particles has been used in two different ways. It is often used to imply that particles do not coagulate although they collide into each other as discussed in 2.9.2, but it is also used to describe the state of aggregates fragmented by external forces. The latter is discussed in this section.

Fluid flows, particle collisions, pressure differences and ultrasonic radiations have been employed as the methodologies to disperse aggregates in commercial dispersers. The principles of these devices are drawn schematically in Figure 5.2.9. In the case of fluid flows, coagulated particles will be deflocculated by the difference between the drag forces on the constitutive particles of the different positions within an aggregate. This deflocculation occurs especially in the accelerated flow field, such as the contractile flow into a small gap, as seen in the orifice flow. In the case of particle collisions, flocs are broken by their collision into the solid surface or the other flocs. However, this effect is considered to be small in colloidal solutions, because the particle inertia is small in liquids unless an extremely high power is employed. In the case of large pressure drops of the medium and ultrasonic radiations, the floc breakup has been considered to be caused by the cavitation, vibration and/or turbulence, but the mechanism has not been clarified yet.

Flow and ultrasonic fields have been widely used in the commercial dispersers to deflocculate flocs in suspensions. In this section, the theoretical background and some experimental results of the deflocculations by these fields are discussed. The flow fields of commercial dispersers are usually very complicated, but they can be decomposed into a few fundamental flows: shear, elongational and turbulent flows. In general, the coagulated particles are captured in the primary minimum of the total interparticle potential shown in Figure 5.2.10, as explained in Section 2.9.2 Hence, coagulated particles are deflocculated only if the energy supplied by the external field overcomes the maximum potential peak, as shown by an arrow in the figure.

5.2.2.1 Breakup of Doublets by Shear and Elongational Flows

The deflocculation mechanism of "doublets" is fundamentally important to understand the floc breakup. Suppose a pair of coagulated particle 1 and particle 2 is placed in a flow field as shown in Figure 5.2.11. The relative trajectories between these particles in the shear and elongational flows are able to be calculated numerically by using the trajectory analysis developed by Batchelor and Green.[10] The trajectory depends on the initial position angle θ of the coagulated particle 2 in the case of shear flow, but not in the case of elongational flow. Because the particle 2 in the shearing plane of $\theta=\pi/2$ experiences the strongest separation force from the particle 1, it is reasonable to use the trajectory at $\theta=\pi/2$ as a measure of dispersion in the shear flow. Then, once the value of Ka_{12} (a_{12} is the radius average of particles 1 and 2) defined in 2.9.2, the particle size ratio of the small to large particles, λ, and the gap between the surfaces of coagulated particles, δ, are known, the boundaries between the regions of coagulated and dispersed particles are obtainable as shown in Figure 5.2.12.[11,12] The boundaries

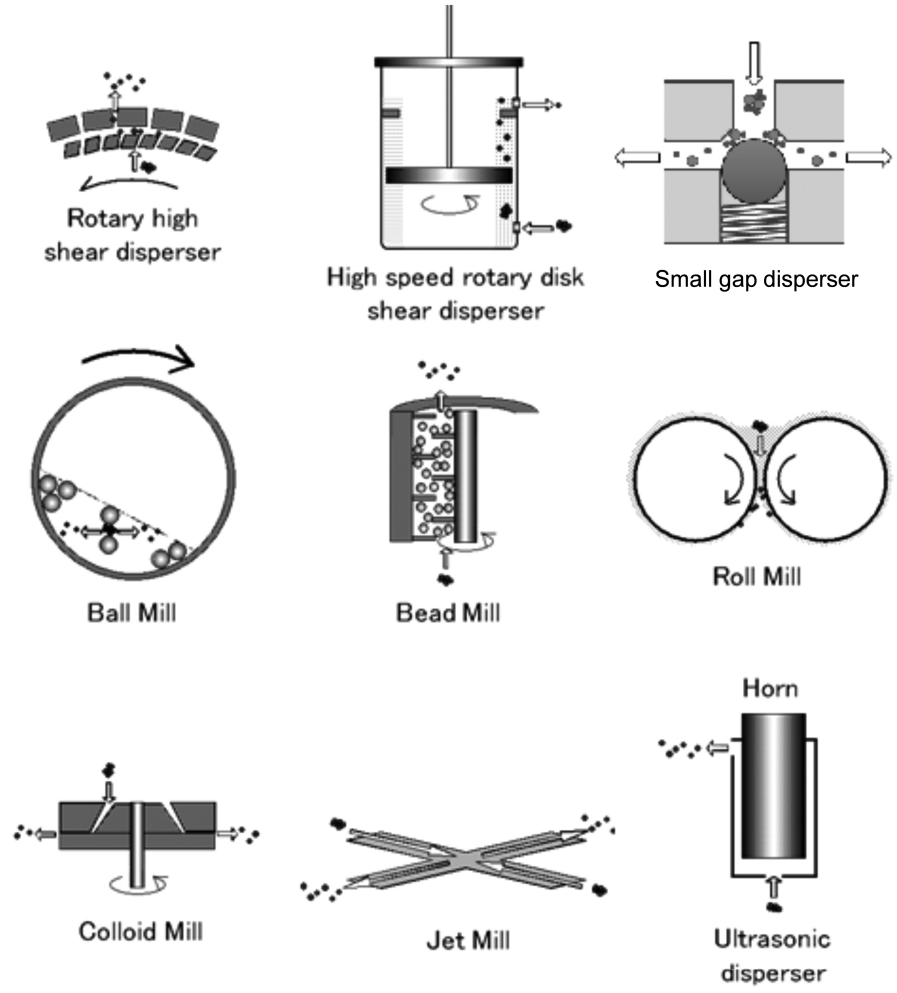


FIGURE 5.2.9 Schematic drawings of the principles of commercial dispersers.

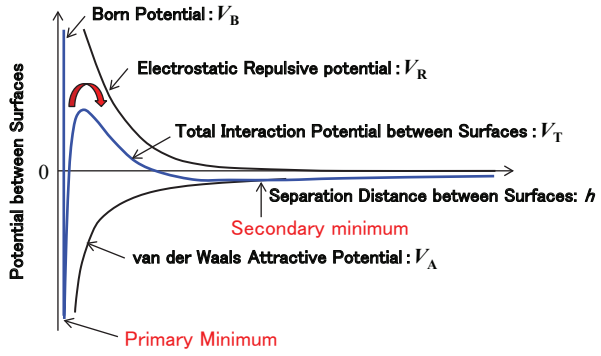


FIGURE 5.2.10 Typical interaction potentials between two surfaces and the peak of the total potential which aggregates must overcome to deflocculate.

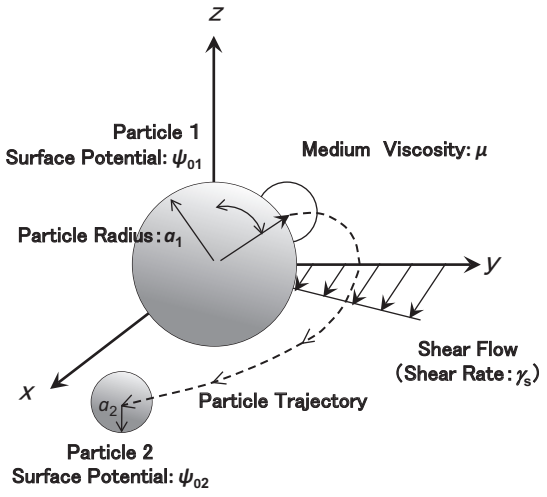


FIGURE 5.2.11 Trajectory of the dispersing particle 2 from the particle 1 by a simple shear flow.

depend on either the shear rate γ_s or the elongational rate γ_e, as well as the dimensionless parameter, $N_R(=\varepsilon\psi_0^2 a_{12}/A)$, where ε is the permittivity of the medium, ψ_0 is the surface potential of particles, and A is the Hamaker constant. The conditions assumed in Figure 5.2.12, such as $Ka_{12}=100$ and $\delta=0.4$ nm, might be far from the real situations. Nevertheless, we can find the following trends from the result: (1) the value of δ/a influences greatly, (2) the elongational flow is more favorable for the dispersion, (3) small particles attached on the large particle are difficult to be removed.

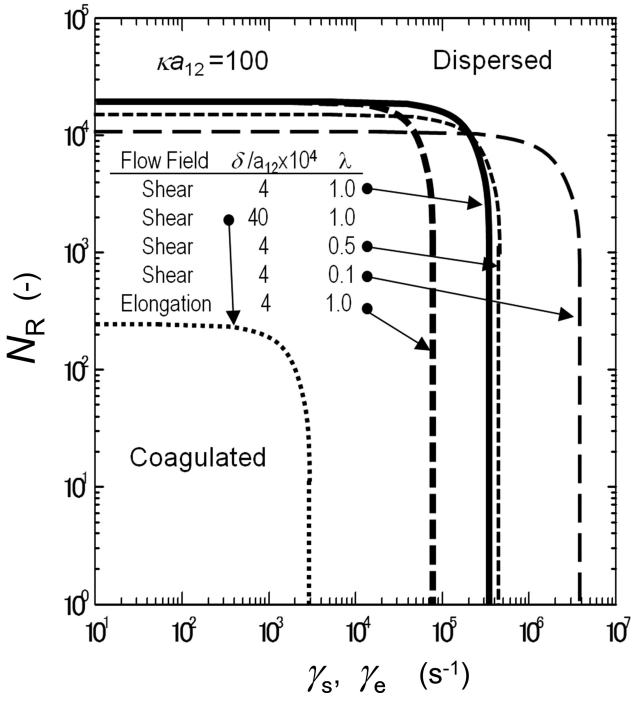


FIGURE 5.2.12 Boundaries between coagulated and dispersed particles estimated by the trajectory analysis for a solution of $\kappa a_{12}=100$.

When the particle size is equal, namely $\lambda=1$, the boundary is given analytically by the following equation.[13]

$$N_F = c\left[\frac{1}{12}\left(\frac{a}{\delta}\right)^2 - \pi\kappa a N_R\right] \tag{5.2.15}$$

where:

N_F is given by $6\mu\pi a^3\gamma/A$
μ is the viscosity of the solution

The deformation rate γ is γ_s and $c=1$ for the shear flow, and $\gamma=\gamma_e$ and $c=0.25$ for the elongational flow.

5.2.2.2 Breakup of Large Aggregates by Shear and Elongational Flows

As for the deflocculation of large aggregates composed of many constitutive particles, a model in which the hydrodynamic effects on the constitutive particles were taken into account and their relative displacements were evaluated by the discrete element method (DEM) was proposed.[14] The details are given in 5.25.5. A fragmentation process of an aggregate in a shear flow simulated by this model is shown in Figure 5.2.13. The average number of particles in a fragment i_{av} is derived by repeating the calculations for various aggregates, as follows.

$$i_{av} \sim \left(\frac{\mu a\gamma\delta^2}{A}\right)^{-n} \propto \varepsilon_{dis}^{-(n/2)} \tag{5.2.16}$$

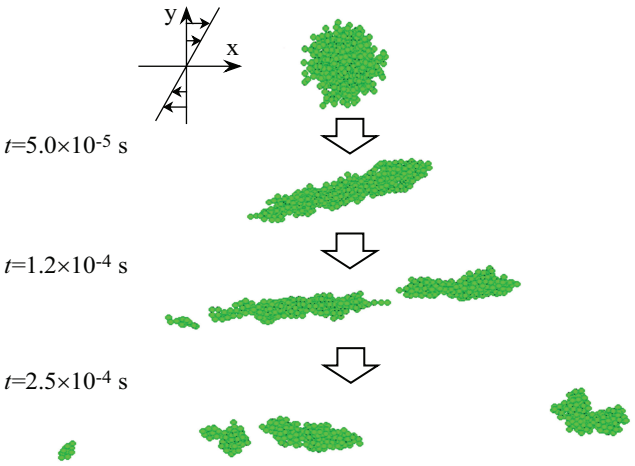


FIGURE 5.2.13 A fragmental process of large coagulated particles in a shear flow simulated by the proposed model.

where ε_{dis} is the dispersion energy of fluid flow. In the case of shear flow ($\gamma=\gamma_s$), the value of n was found to be 0.87, which is consistent with the other data reported elsewhere, $n=0.74\sim0.88$.[15,16] This implies that the proposed simulation model is applicable to the breakup of flocs in the shear flow.

In the case of elongational flow ($\gamma=\gamma_e$), the power n was found to be 1.6. There is no report to examine directly the adequacy of this value, but it was found that the data given by an orifice contractile flow were consistent qualitatively with the prediction by Equation (5.2.16).[17] Hence, we believe that this model is able to estimate at least qualitatively the breakage process of flocs in shear and elongational flows.

5.2.2.3 Breakup of Aggregates by Turbulent Flows

The breakage of aggregates by turbulent flows is usually estimated by the experiments in the stirring tank, because of the difficulty to achieve the uniform turbulent flow experimentally. Hence, the breakage in turbulent flows is correlated with the maximum floc size D_{max} above which flocs are broken by the stirring flow and the energy dissipation of turbulent flow ε_{dis} estimated by the power consumption of the stirrer, as follows.

$$D_{max} \sim \varepsilon_{dis}^{-n} \tag{5.2.17}$$

As for the value of n, a large number of experiments have been carried out, and it is reported that $n=0.15\sim0.75$, but more often $n=0.2\sim0.4$.[18–25]

5.2.2.4 Breakage by Other Fields

The principles of the orifice contractile flow, the flow toward a rotary small gap and the ultrasonic radiation are often used in the commercial dispersers. The characteristics of these flows are described below.

Breakup by Orifice Contractile Flow

The orifice contractile flow can be realized by placing a plate with a small hole (an orifice) in a tube flow. The flow is composed of the elongational flow at the centerline and the high shear flow near the solid wall. In addition, the fluid is contracted accelerating the flow rate abruptly before the orifice, and strong eddies are generated after the orifice. Hence the orifice flow is a very complicated flow, and very few experimental data on the aggregate dispersion are available. According to the data reported so far, the average number of particles in a fragment i_{av} is expressed as follows.

$$i_{av} \sim \left(\mu\gamma_{av}\right)^{-n} \propto \varepsilon_{dis}^{-(n/2)} \tag{5.2.18}$$

where γ_{av} is the average deformation rate at the entrance of the orifice. It was reported that $n=1$ for relatively large aggregates[17,26] and $n=0.22$ for very small aggregates.[27]

Breakup at Small Gap between Cylinder and Rotary Disk[28]

The high shear flow in the small gap between a cylinder and a rotary disk is widely used to disperse aggregates. In this device, aggregates have been considered to be broken by the high shear flow within the gap generated by the high-speed rotor, as illustrated in Figure 5.2.14. However, the flow towards the gap is a complicated flow composed of the rotational, contractile and shear flows. It was found that aggregates are broken by the strong contractile flow before entering the gap, if the gap width d_{gap} is small enough, while they are broken by the high shear flow within the gap if the gap width is large enough. This is very important information in designing the rotary-type devices.

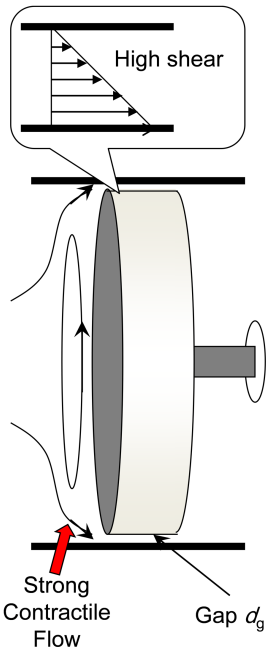


FIGURE 5.2.14 Schematic drawing of rotating disk flow.

Breakup by Ultrasonic Radiation[29]

Ultrasonic dispersers are widely used, but there are very few systematic investigations on the floc breakage by the ultrasonication. Figure 5.2.13 shows the dependence of the maximum number of particles in a fragment i_{max} on the total sonic energy radiated to the suspension of unit volume $E_t(=W_s t_r/V_t)$, where W_s is the power of the sonic generator, t_r is the radiation time and V_t is the volume of suspension. It is clear that all the data are expressed by a single curve independently on various experimental conditions, which implies that the degree of ultrasonic breakage is solely determined by the magnitude of E_t. The dependence of i_{max} on E_t is expressed by the following equation.[29]

$$i_{max} \sim E_t^{-0.53} \tag{5.2.19}$$

As for the needle-shaped nanoparticles, the median diameter D_{50} of fragments broken by ultrasonication was reported to be given as follows.[30]

$$D_{50} \sim E_t^{-0.68} \tag{5.2.20}$$

Ultrasonication is strong enough to break aggregates into single particles if sufficient energy is supplied as shown in Figure 5.2.15, but great care must be taken so that sonic vibration contributes not only to the breakage of aggregates but also to their coagulation.

5.2.2.5 Comparison between Breakages by Flow and Ultrasonic Fields

Figure 5.2.16 shows how the initial size distribution changes with the kind of external field applied. The variation of size

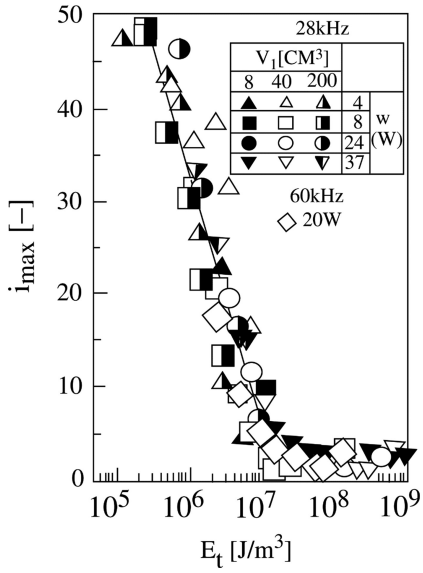


FIGURE 5.2.15 Dependence of the maximum number of particles in a fragment on the total dissipation energy by the ultrasonic radiation under various radiation conditions.

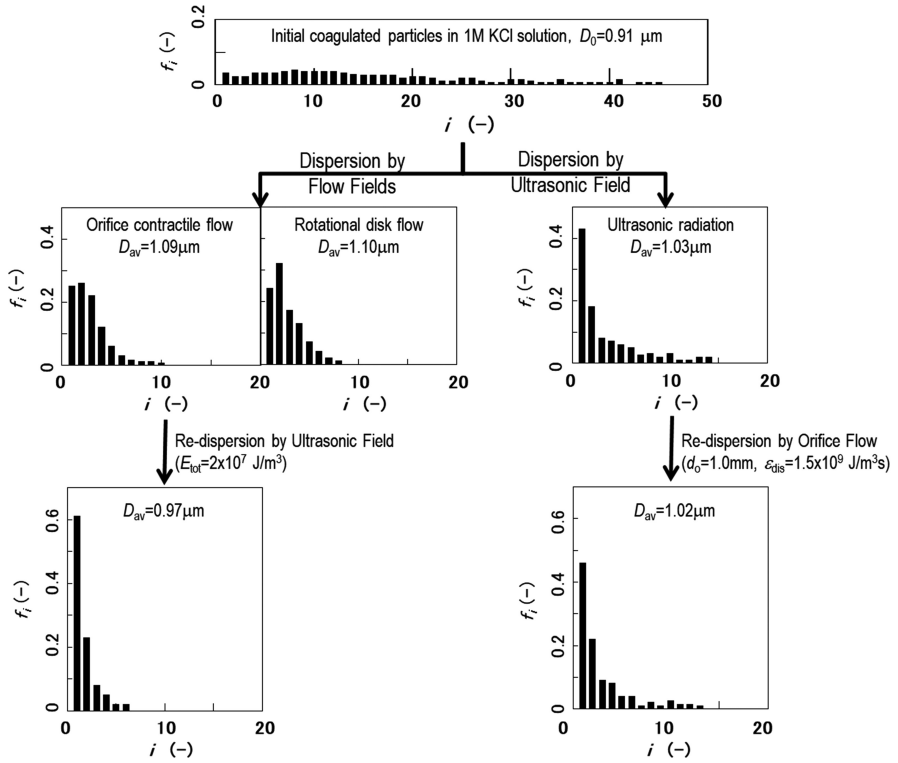


FIGURE 5.2.16 Variations of size distributions of deflocculated particles by different procedures.

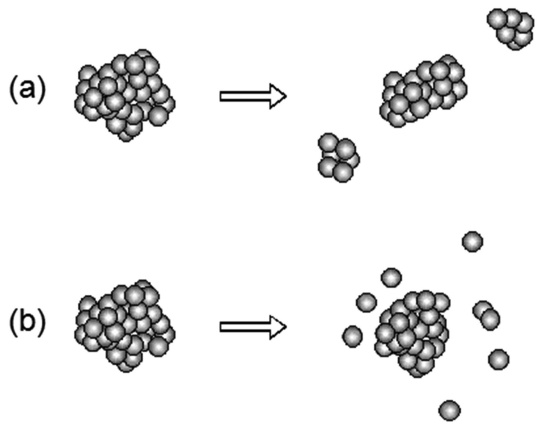


FIGURE 5.2.17 Different breakage process. (a) Splitting, (b) Erosion.

distribution implies that flocs are split into smaller fragments in the case of flow-induced deflocculation,[27,28] while single particles are ripped off one by one from the floc surface in the case of sonic deflocculation, as shown schematically in Figure 5.2.17.[29] The former mechanism is called "splitting" and the latter, "erosion." This difference in deflocculation mechanism suggests that the flow-induced deflocculation with the subsequent sonic deflocculation is the preferable order to deflocculate particles efficiently. This is confirmed by the data shown in Figure 5.2.16.

REFERENCES

1. Kousaka, Y., Okuyama, K., Shimizu, A., Yoshida, T., *J. Chem. Eng. Japan*, 12, 152–159, 1979.
2. Kousaka, Y., Endo, N., Horiuchi, T., Niida, R., *Kagaku Kogaku Ronbunshu*, 18, 233–239, 1992.
3. Yuu, S., Oda, T., *AIChE J.*, 29, 191–198, 1983.
4. Gotoh, K., Takahashi, M., Masuda, H., *J. Soc. Powder Technol., Japan*, 29, 11–17, 1992.
5. Bagster, D.F., Tomi, D., *Chem. Eng. Sci.*, 29, 1773–1783, 1974.
6. Yamamoto, H., Suganuma, A., *Kagaku Kogaku Ronbunshu*, 9, 183–188, 1983.
7. Yamamoto, H., Suganuma, A., Kunii, T., *Kagaku Kogaku Ronbunshu*, 3, 12–18, 1977.
8. Masuda, H., Fushiro, S., Iinoya, K., *J. Res. Assoc. Powder Technol. Japan*, 14, 3–10, 1977.
9. Gotoh, K., Asaoka, H., Masuda, H., *Adv. Powder Technol.*, 5, 323–337, 1994.
10. Batchelor, G. K., Green, J.T., *J. Fluid Mech.*, 56, 375, 1972.
11. Higashitani, K., Tsutsumi, T., Iimura, K., *Proc. of China Japan Symposium on Particology*, Beijing, 1996, pp. 1-16.
12. Higashitani, K., Iimura, K., Vakarelski, I.U., *KONA*, 18, 6, 2000.
13. Russel, W.B., Saville, D.A., Schowalter, W.R., *Colloidal Dispersions*, Cambridge University Press, Cambridge, 1989.
14. Higashitani, K., Iimura, K., Sanda, H., *Chem. Eng. Sci.*, 56, 2927–2938, 2001.
15. Eggersdorfer, M.L., Kadau, D., Herrmann, H.J., Pratsinis, S.E., *J. Colloid Interface Sci.*, 342, 261–268, 2010.
16. Harada, S., Tanaka, R., Nogami, H., Sawada, M., *J. Colloid Interface Sci.*, 301, 123–129, 2006.

17. Soos, M., Ehrl, L., Babler, M.U., Morbidelli, M., *Langmuir*, 26, 10–18, 2010.
18. Muhle, K., *Coagulation and Flocculation*, Marcel Dekker, New York, 1993, p. 355.
19. Tambo, N., Watanabe, Y., *Water Res.*, 13, 421–427, 1979.
20. Tomi, D.T., Bagster, D.F., *Trans. Inst. Chem. Engr.*, 56, 1–18, 1978.
21. Frncois, R.J., *Water Res.*, 21, 1023–1030, 1987.
22. Leentvaar, J., Rebhun, M., *Water Res.*, 17, 895–902, 1983.
23. Glasgow, L.A., Liu, X., *AIChE J.*, 37, 1411–1414, 1991.
24. Bache, D.H., *Chem. Eng. Sci.* 59, 2521–2534, 2004.
25. Babler, M.U., Morbidelli, M., Baldyga, J., *J. Fluid Mech.*, 612, 261–289, 2008.
26. Sonntag, R.C., Russel, W.B., *J. Colloid Interface Sci.*, 115, 390–395, 1987.
27. Higashitani, K., et al., *J. Chem. Eng. Japan*, 25, 502–507, 1992.
28. Higashitani, K., Unpublished work.
29. Higashitani, K., Yoshida, K., Tanise, N., Murata, H., *Colloids Surf. A*, 81, 167–175, 1993.
30. Ding, P., Pacek, A.W., *Powder Technol.*, 187, 1–10, 2008.

5.3 Classification

Hideto Yoshida and Kunihiro Fukui

5.3.1 BASIS OF CLASSIFICATION

Powder separation process is widely used for various industrial fields to enhance particle properties. Depending on particle properties, such as particle size, density and chemical component, a suitable particle classifier is used in real powder handling processes. Generally, the classification includes the wide process of particle separation, but the size separation process is the main part of classification process. Recently, the narrow size distribution of particles is required to improve the performance of products.

Index of Classification Performance

The classification performance is evaluated by use of various index parameters based on the particle separator. Figure 5.3.1 shows the particle material balance of a classifier, where m_0 is the flow rate of feed powder, and m_1 and m_2 indicate the flow rates of classified coarse and fine powders, respectively. The performance of classification is evaluated by collection efficiency E defined by the following equation.

$$E = \frac{m_1}{m_1 + m_2} \tag{5.3.1}$$

In order to evaluate the collection efficiency of each particle in diameter, the partial separation efficiency $\Delta\eta$ defined by Equation (5.3.2) is the important index of classifier.

$$\Delta\eta = \frac{m_1 f_1 \Delta D_p}{m_1 f_1 \Delta D_p + m_2 f_2 \Delta D_p} \tag{5.3.2}$$

where ΔD_p is the particle size interval of each range, and f_1 and f_2 indicate the frequency distribution of coarse and fine particles, respectively. The 50% cut diameter D_{pc} corresponding to the particle size where the efficiency of partial separation is equal to 50% is also the important index to evaluate the separation performance.

$$D_{pc} = D_{p,\Delta\eta=50\%} \tag{5.3.3}$$

The sharpness or accuracy κ of classification defined by the following equation is also the important index of the classifier.

$$\kappa = \frac{D_{p,75}}{D_{p,25}} \tag{5.3.4}$$

where D_{p75} and D_{p25} are the particle diameters corresponding to the partial separation efficiencies of 75% and 25%, respectively. In the case of ideal classification, the value of κ is equal to unity. A relatively good classification is carried out if the value of κ is less than about 1.4.

In order to evaluate the classification performance of a sieve, the Newton efficiency η_N defined by the following equation is used.

$$\eta_N = \frac{m_1 R_1}{m_0 R_0} - \frac{m_1(1 - R_1)}{m_0(1 - R_0)} \tag{5.3.5}$$

where R_0 and R_1 indicate the oversize in the feed and the coarse side, respectively. The Newton efficiency is defined as the subtraction of the collection efficiency of the necessary particles from that of unnecessary particles in the product. In Equation (5.3.5), the coarse side is selected as the product side.

The pressure drop in a classifier is also an important parameter to evaluate separation performance. The collection efficiency and the partial separation efficiency are related by the following equation.

$$E = \int_{D_{p\,min}}^{D_{p\,max}} \Delta\eta\,(D_p)\, f_0\,(D_p)\, dD_p \tag{5.3.6}$$

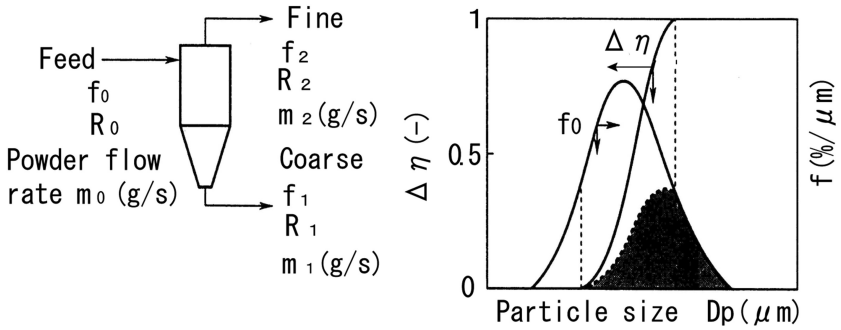


FIGURE 5.3.1 Relation between collated particles and partial separation efficiency.

where $f_0(D_p)$ is the size frequency distribution of feed particles. Hence, the classification performance is evaluated by the use of the collection efficiency, partial separation efficiency, cut size, sharpness index and pressure drop. The cut size control with low pressure drop and high sharpness index is the important factor in the real processes of classification.

5.3.2 DRY CLASSIFICATION

The dry classification is widely used in many industrial processes. Compared to the wet classification, the dry classification does not need drying and slurry treatments. As a result, the dry classification is more widely used, compared to the wet classification. However, to classify particles with a cut size of less than about 3 μm, a suitable particle disperser is necessary before the dry classification apparatus. The theoretical study on the collection efficiency of a cyclone was conducted by Leith and Licht.[1] On the other hand, numerical calculations of fluid flow and particle motions in the cyclone are conducted by Ayers et al.[2], Zhou et al.[3] and Yamamoto et al.[4,5] The rotational-blade-type classifier is generally used to control the cut size. It is difficult to control the cut size in sub-micron range by use of the forced-vortex-type classifier.

Recent experimental results indicate that it is possible to shift the cut size in submicron range by applying the method of local flow control to the free-vortex-type classifier. Recent industrial interests in dry classification are mainly directed toward how to control the cut size accurately in the fine size region. The following are the typical air classifiers used in actual industrial processes.

Gravitational Classifiers

Particles are classified by the difference of their settling velocities or falling positions. Classifiers of horizontal flow, vertical flow and inclined flow are all used in the industrial process. The cut size of these classifiers is generally greater than about 100 μm.

Inertial Classifiers

Particles are classified by the difference in their trajectories. Rectilinear (elbow type), curvilinear (impactor) and inclined (louver) classifiers are commercially available. Figure 5.3.2 shows various inertial classifiers and Figure 5.3.3 shows the louver separator with planes or special blades.[6]

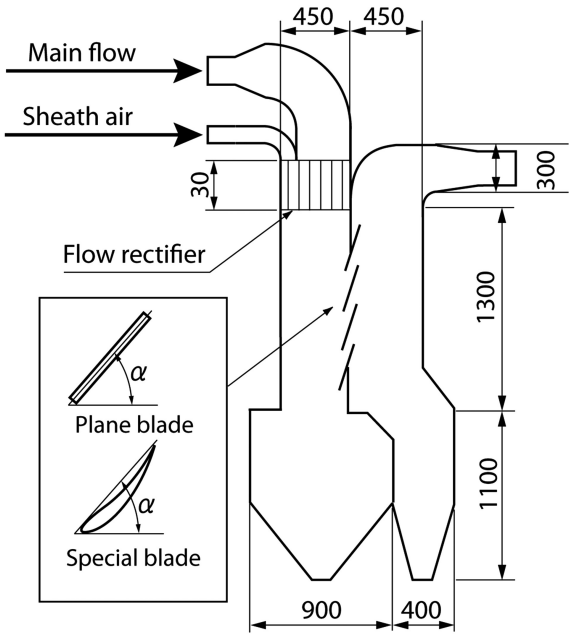


FIGURE 5.3.3 Structure of louver classifier.

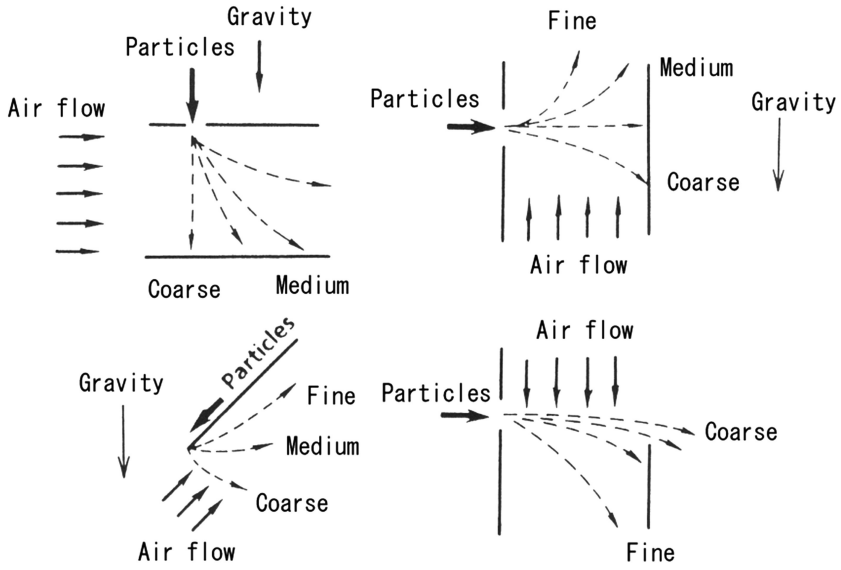


FIGURE 5.3.2 Principle of classification by transverse flow.

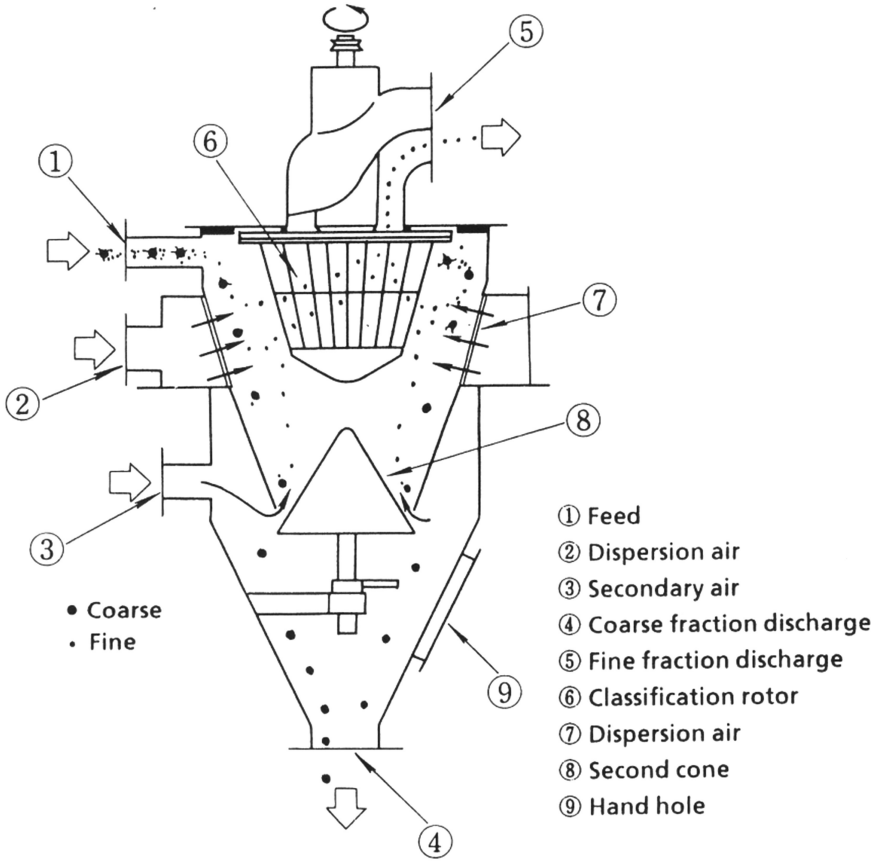


FIGURE 5.3.4 Micron separator. (Courtesy of Hosokawa Micron.)

Centrifugal Classifiers

The centrifugal force is created either by the airflow in cyclone-type classifiers or by the mechanical revolution in air separators. A variety of centrifugal classifiers are available. Typical apparatuses of forced vortex type are Micron separator (Figure 5.3.4) and Turbo classifier (Figure 5.3.5). The characteristics of centrifugal separators are listed in Table 5.3.1. Figure 5.3.6 shows an example of the partial separation efficiency of a special type cyclone with and without blow-down for the sub-micron range.[7]

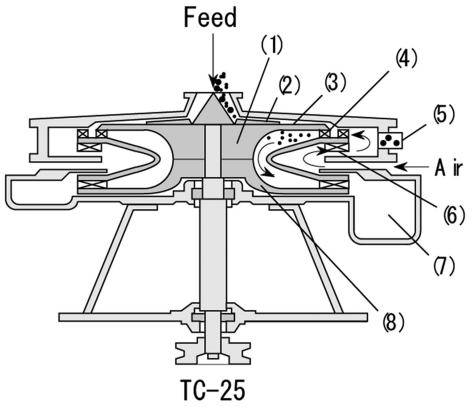


FIGURE 5.3.5 Turbo classifier. (Courtesy of Nisshin Engineering.)

Cut Size Control by Free Vortex Classifier

The inlet movable slide plate shown in Figure 5.3.7 is effective to control the cut size of gas-cyclone. Figure 5.3.8 shows the classification performance for the usage of a movable slide plate and the blow-down method.[8] Both methods are effective to decrease the 50% cut size. An apex cone is set at the upper part of the dust box to decrease the cut size and to increase the collection efficiency. Figure 5.3.9 shows the simulated fluid vectors with and without the apex cone. By using the apex cone, it is possible to decrease the magnitude of the fluid velocity component in the upper part of the dust box. As a result, it is possible to reduce re-entrainment of particles from the dust box to the vortex finder. The cut size of cyclones with the apex cone is smaller than that without the apex cone, as shown in Figure 5.3.10. By use of the apex cone, it is possible to shift the cut size to the region of finer size.[9]

Estimation Method of Cyclone Performance

The design of the cyclone and the individual components to optimize the performance have been investigated, and the

TABLE 5.3.1 Characteristics of Centrifugal Air Classifier

Type of Classifier	Power (kw)	Cut Size (μm)	Capacity (kg/h)	Rotor Speed (rpm)
Micron separator	5–150	150–12,000	200–2,300	0.75–37
Turbo classifier	0.5–150	150–24,000	700–12,000	1.5–70
Turboplex	2–180	40–35,000	120–22,000	1–45

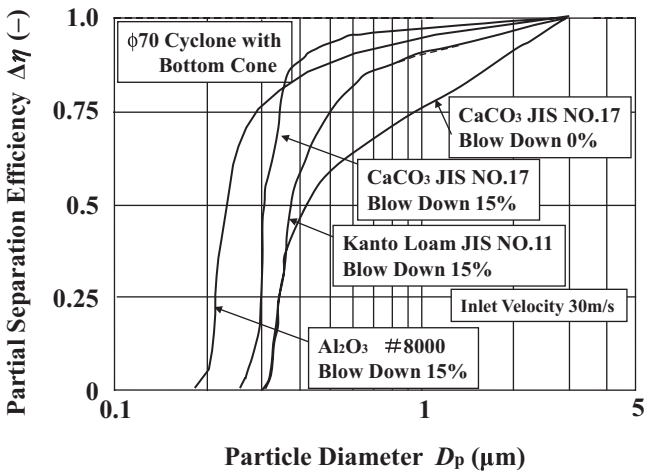


FIGURE 5.3.6 Partial Separation Efficiency of ϕ70 Cyclone Classifier.

sub-micron cut size is achieved, as well as the improvement of separation accuracy.[10–12] Figure 5.3.11 shows the typical flow inlet system of cyclone separators, which can be roughly classified into three types according to the inlet flow into the cyclone: the tangential inlet, the scroll inlet and the axial flow inlet.

The pressure drop of the cyclone mainly contains three losses: the pressure loss at the inlet part, the fluid friction loss caused by the vortex flow in the cyclone and the pressure loss at the vortex finder. The pressure drop of the cyclone is usually approximately proportional to the square of the inlet velocity. When the dust is not loaded, the pressure drop of the cyclone, ΔP_0, can be calculated by the following equation.

$$\Delta P_0 = A\frac{\rho_f u_{in}^{\ 2}}{2} \tag{5.3.7}$$

where u_{in} is the inlet gas velocity, ρ_f is the fluid density and A is a variable parameter which is determined predominantly by the cyclone geometry. It was reported that the value of A is given as follows.[13]

$$A = 16\left(\frac{K_a K_b}{K_e^{\ 2}}\right) \tag{5.3.8}$$

$$A = 11.3\left(\frac{K_a K_b}{K_e^{\ 2}}\right)^2 + 3.33 \tag{5.3.9}$$

where $K_a(=a/D)$, $K_b(=b/D)$ and $K_e(=D_e/D)$ are the ratios of the dimensions defined in Figure 5.3.11 (a) to the cyclone diameter D. These equations mean that the pressure drop depends a little on the cyclone size but also on the dimensional ratios.

The pressure drop of cyclone ΔP decreases with the dust concentration. The following equation was proposed as an empirical formula which provides the dependence of ΔP on the dust concentration C_p.[14]

$$\Delta P = \Delta P_0\left(1 - 0.0086\sqrt{C_p}\right) \tag{5.3.10}$$

where ΔP_0 is the pressure drop at $C_p = 0$. Since the actual air flow in the cyclone involves the complicated secondary flow, such as, the turbulent fluctuation, it is very difficult to estimate the particle motion and the classification performance of the cyclone exactly. However, many models to evaluate the classification performance have been proposed, being based on the simplified and idealized velocities and forces on particles. Some estimation formulae can successfully give the accurate cut size and partial separation efficiency.

Most popular formulae to calculate the 50% cut size $d_{p,50}$ are listed in Table 5.3.2. Lapple's model[15] correlates the number of revolutions of a particle in a cyclone N with the cyclone performance. In the case of Barth's model,[16] the 50% cut size is calculated by two specified tangential velocities defined in the model. Iozia's model[17] also uses the specified maximum tangential velocity u_{tmax}.

The partial separation efficiency $\Delta\eta(D_p)$ of most cyclones can be approximated by the following Equation (5.3.11) with the 50% cut size and the slope exponent β.

$$\Delta\eta\left(D_p\right) = \frac{1}{1 + (D_{p,50}/D_p)^{\beta}} \tag{5.3.11}$$

$$\ln\beta = -0.62 - 0.87\ln\left(D_{p,50}\times 10^3\right) + 5.21\ln\left(K_a K_b\right) + 1.05\left\{\ln\left(K_a K_b\right)\right\}^2 \tag{5.3.12}$$

Equation (5.3.12) is the empirical equation for β reported by Iozia and Leith.[17] The partial separation efficiency curve can be obtained by the 50% cut size calculation in Table 5.3.2 and Equations 5.3.11 and 5.3.12. Other estimation methods of the partial separation efficiency have been also proposed,[18,19] and well-known ones are listed in Table 5.3.3.

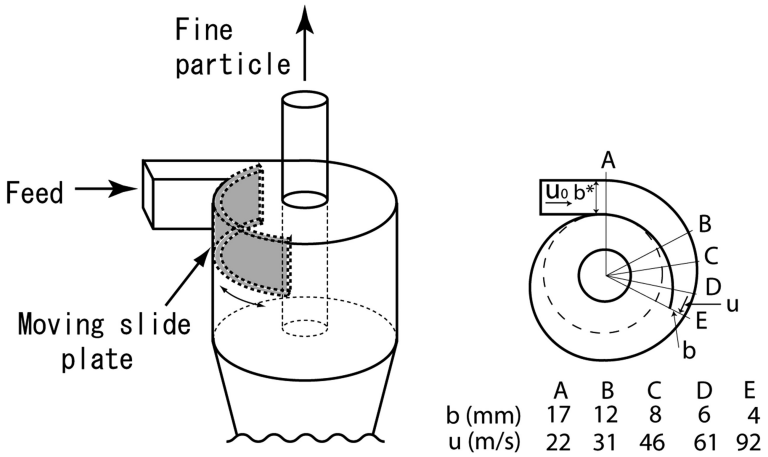


FIGURE 5.3.7 Cyclone with moving slide plate.

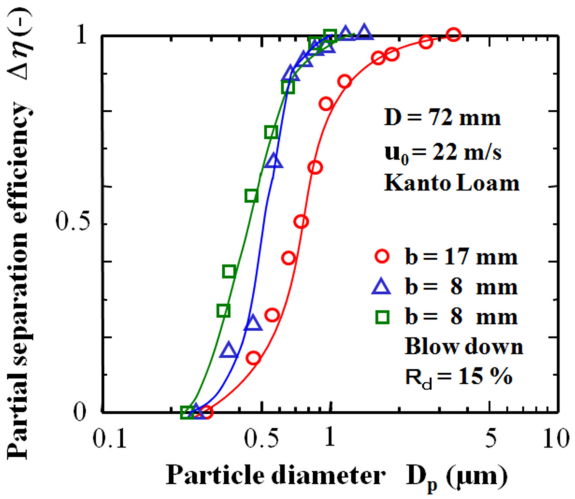


FIGURE 5.3.8 Effect of slide plate and blow down on partial separation efficiency.

Figure 5.3.12 shows the comparison between the partial separation efficiency curves estimated by various models and the real experimental data. Though the estimated results are not in absolute agreement with the experimental data, it is confirmed these models predict the data with satisfactory accuracy from the practical point of view.

As shown in Tables 5.3.2 and 5.3.3, the classification performance of cyclones decreases with increasing cyclone diameter D. The cut size of the cyclone is usually proportional to the square root of the cyclone diameter D, approximately. To treat the large amount of the dust-loaded air flow without reducing the collection efficiency, the multi-cyclone system in which many small size cyclones are contained in parallel is useful. The structure of the multi-cyclone is shown in Figure 5.3.13.

5.3.3 WET CLASSIFICATION

The principle of wet classification is the same as the dry classification. Recently, the wet classification has been used in ceramic production and recycling processes. The following points should be considered in the wet characteristics.

1. Particle dispersion control is easy, compared with dry classification.
2. To separate particles from liquid, the drying or dewatering process is necessary.
3. The viscosity of slurry decreases with increasing temperature, and the sedimentation velocity of particles increases as the slurry temperature increases.

Classification Theory

Figure 5.3.14 shows the two types of classifiers: types of vertical flow and horizontal flow. For the vertical flow type, the collection efficiency E is calculated by the following equations.

$$V_g < u_0 \text{ or } V_g S/Q < 1: \; E = 0 \tag{5.3.13}$$

$$V_g > u_0 \text{ or } V_g S/Q > 1: \; E = 0 \tag{5.3.14}$$

where V_g is the sedimentation velocity of particle, u_0 is the upward velocity of fluid, S is the cross-sectional area and Q is the volume flow rate. An ideal classification may be realized by this type of classification. However, the performance is deteriorated when the fluid turbulence is generated in the classifier.

The collection efficiency for the horizontal type without fluid mixing is as follows:

$$V_g S/Q \le 1 \quad E = V_g S/Q \tag{5.3.15a}$$

$$V_g S/Q > 1 \quad E = 1 \tag{5.3.15b}$$

For the horizontal type with fluid mixing of vertical direction, the collection efficiency is calculated by the following equation.

$$E = 1 - \exp\left(-V_g S/Q\right) \tag{5.3.16}$$

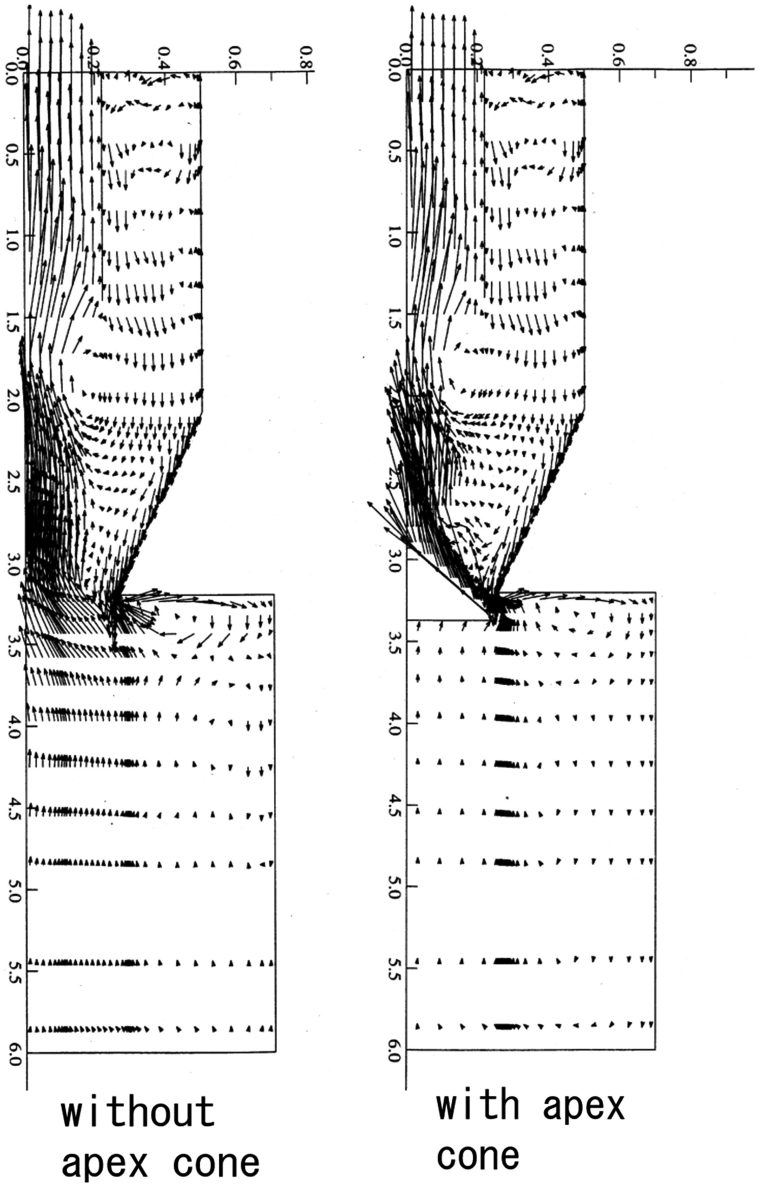


FIGURE 5.3.9 Calculated fluid vectors with and without apex cone.

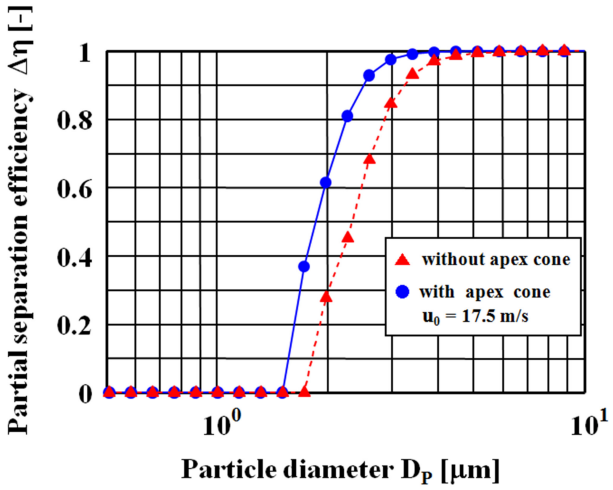


FIGURE 5.3.10 Partial separation efficiency with and without apex cone.

Figure 5.3.15 shows the relation between the collection efficiency E and the parameter ($V_g S/Q$) for three cases. The ideal classification is able to be realized by a vertical flow type, but the classification sharpness decreases in case of the horizontal flow type with fluid mixing.

Sedimentation Velocity

The particle sedimentation velocity in a fluid is important in estimating the separation efficiency. Assuming a steady state, the Stokes sedimentation velocity is as follows:

$$V_s = \frac{(\rho_p - \rho_f) D_p^2 g}{18\mu} \qquad Re_p \le 2 \qquad (5.3.17a)$$

$$Re_p = \frac{D_p V_s \rho}{\mu} \qquad (5.3.17b)$$

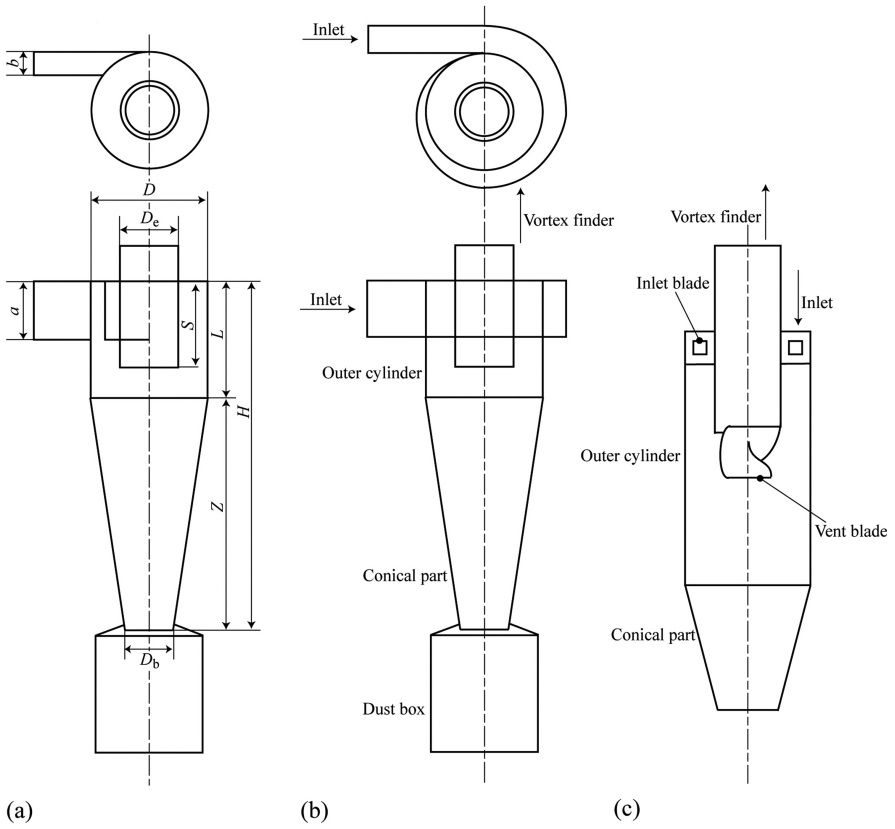


FIGURE 5.3.11 Typical inlet systems for cyclone separator. (a) Tangential inlet, (b) Scroll inlet, (c) axial inlet.

TABLE 5.3.2 Estimation Equations for the 50% Cut Size of Cyclone Separator

Lapple's model	$d_{p,50}=\sqrt{\dfrac{9\mu b}{2\pi N C_c u_{in}(\rho_p-\rho_f)}}, N=\dfrac{H_L+(H_H-H_L)/2}{a}$.
Barth's model	$d_{p,50}=\sqrt{\dfrac{9\mu u_{ti} D_e}{C_c u_{tw}^{\ 2}(\rho_p-\rho_f)}}$.
Iozia's model	$d_{p,50}=\dfrac{1}{u_{t,max}}\sqrt{\dfrac{9\mu a b u_{in}}{\pi z_c(\rho_p-\rho_f)}}$ $u_{t,max}=6.1u_{in}(K_aK_b)^{0.61}K_e^{-0.74}K_H^{-0.33}, d_{cr}=0.47D(K_aK_b)^{-0.25}K_e^{1.4}$ $z_C=H_H-H_S\,(d_{cr}<D_b)$ $z_C=(H_H-H_S)-\left(\dfrac{H_H-H_S}{K_b-1}\right)\left(\dfrac{d_{cr}}{D_b}-1\right)(d_{cr}>D_b)$

TABLE 5.3.3 Estimation Equations for the Partial Separation Efficiency Curve

Clift's model	$\Delta\eta=1-\exp\left[-\dfrac{(\rho_p-\rho_f)}{9\mu}\left(\dfrac{2d_p u_{in}}{D}\right)^2 t_{res}\right]$
Diez's model	$\Delta\eta=1-\left\{K_0-\left(K_1^{\ 2}+K_2\right)^{0.5}\right\}\exp\left[-\dfrac{2\text{À}(2K_S-K_a)}{K_aK_b}St\right]$ $K_0=\dfrac{1}{2}\left\{1+K_2\left(1+\dfrac{K_aK_b}{\text{À}K_1St}\right)\right\}, K_1=\dfrac{1}{2}\left\{1-K_2\left(1+\dfrac{K_aK_b}{\text{À}K_1St}\right)\right\}$ $K_2=K_e^{\ 2\gamma}, K_1=2.3D_e(abD)^{-1/3}$ $\gamma=1-(1-0.67D^{0.14})\left(\dfrac{T}{283}\right)^{0.3}$.

When the particle's Reynolds number, Re_p, is greater than about 2, the sedimentation velocity calculated by the following equations are more accurate.

$$\text{Allen region}\quad Vs=\left(\frac{4(\rho_p-\rho_f)^2 g^2}{225\mu\rho_f}\right)^{1/3} D_p \quad 2\le Re_p\le 500 \tag{5.3.18}$$

$$\text{Newton region}\quad V_s=\left(\frac{3g(\rho_p-\rho_f)D_p}{\rho_f}\right)^{1/2} \quad 500\le Re_p \tag{5.3.19}$$

Particle sedimentation velocities calculated by Equations 5.3.17–5.3.19 are shown in Figure 5.3.16 for various

particle densities. When the particle concentration increases, Equations 5.3.17–5.3.19 should be corrected by using the following equation.

$$V_{sc} = V_s / F(\varepsilon), \quad F(\varepsilon) \geq 1 \tag{5.3.20a}$$

The correction function $F(\varepsilon)$ is experimentally determined.

$$F(\varepsilon) = \varepsilon^{-4.65} \tag{5.3.20b}$$

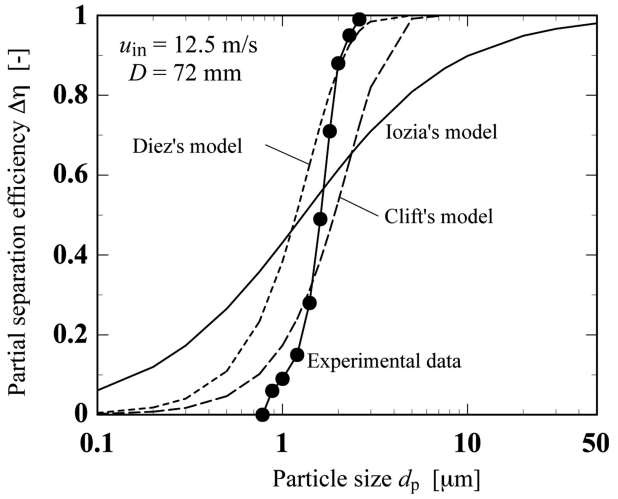


FIGURE 5.3.12 Partial separation efficiency curves estimated by various models.

where ε is the volume fraction of fluid and the value of $F(\varepsilon)$ increases with decreasing ε. The sedimentation velocity calculated by Equation (5.3.20) is referred to as a hindered settling velocity.

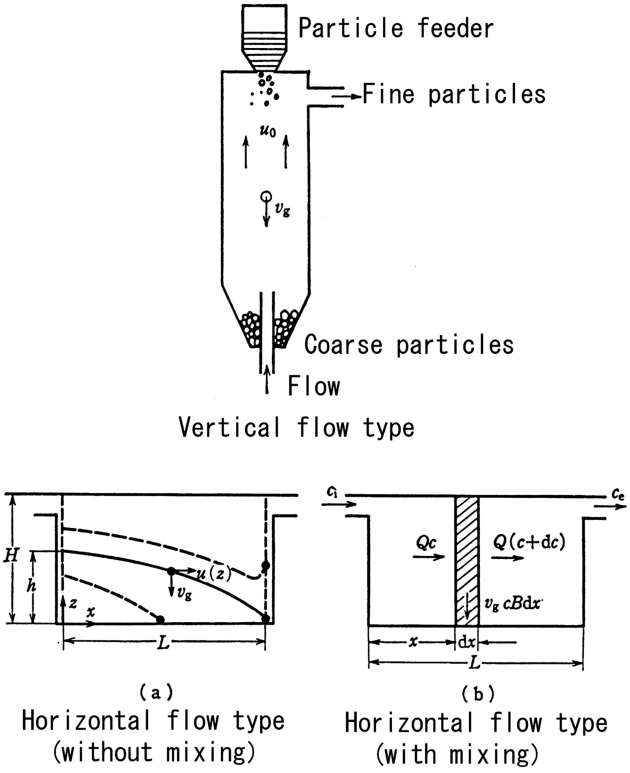


FIGURE 5.3.14 Vertical and horizontal flow type classifier.

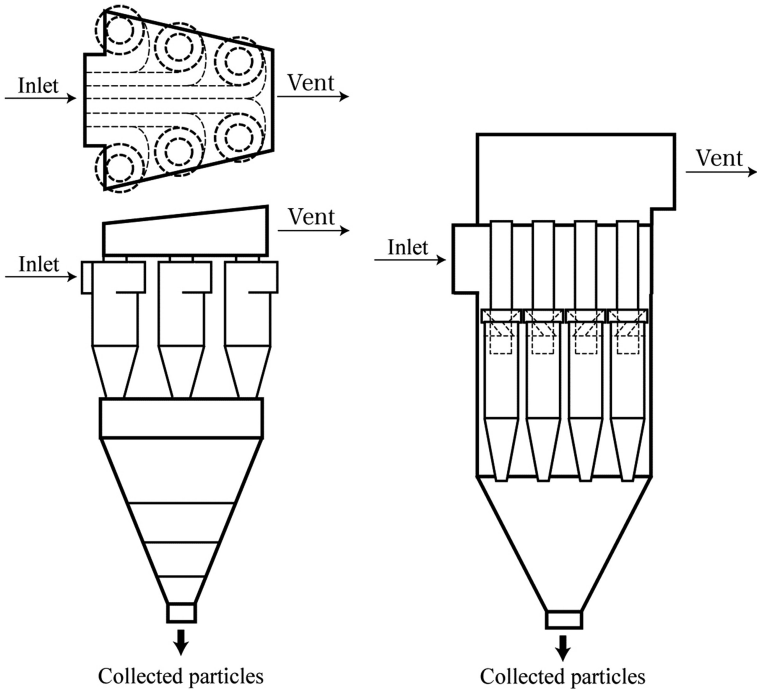


FIGURE 5.3.13 Structure of the multi-cyclone system.

Various Type of Classifier

The apparatus used in wet classification are classified as follows:

1. Horizontal flow type
2. Vertical flow type
3. Hydro-cyclone
4. Centrifugal type with wall or blade rotation

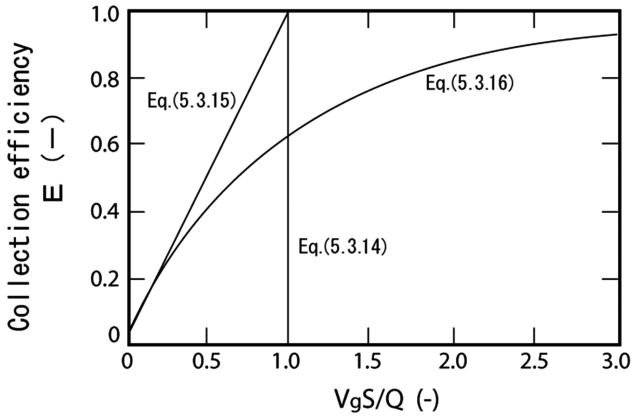


FIGURE 5.3.15 Relation between collection efficiency and parameter (V_gS/Q).

Separators of horizontal flow type are shown in Figure 5.3.17. The coarse particles are collected at the bottom and fine particles are collected at the fluid outlet. Figure 5.3.18 shows a spiral classifier. This type is widely used because of the simple design and good performance. The coarse particles are discharged by the spiral flow, while the fine particles are collected to the overflow part.

Hydro-Cyclone

Hydro-cyclones are widely used in many industrial processes. Experimental studies of the separation efficiency and pressure drop of a hydro-cyclone were reported,[20–22] and several flow controlling methods at the outlet pipe of a hydro-cyclone were proposed.[23,24] On the other hand, a prediction of the flow within a hydro-cyclone was made by using several turbulence

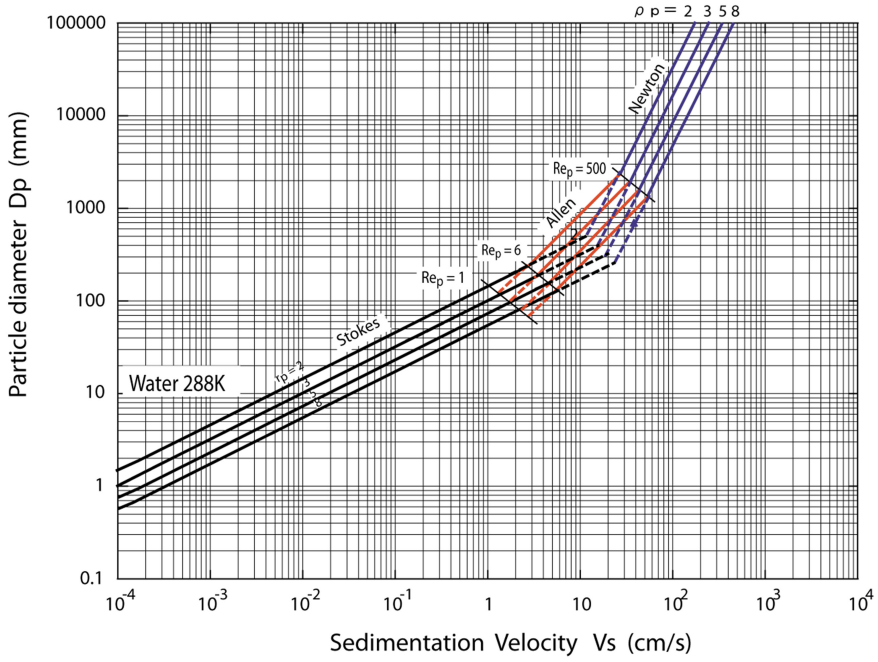


FIGURE 5.3.16 Sedimentation velocity of spherical particle in water (25°C, 1 atm).

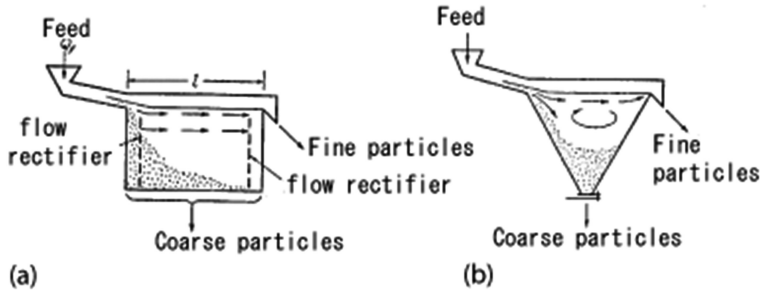


FIGURE 5.3.17 Particle separators of horizontal flow type. (a) Total flow clssifier, (b) Surface flow classifier.

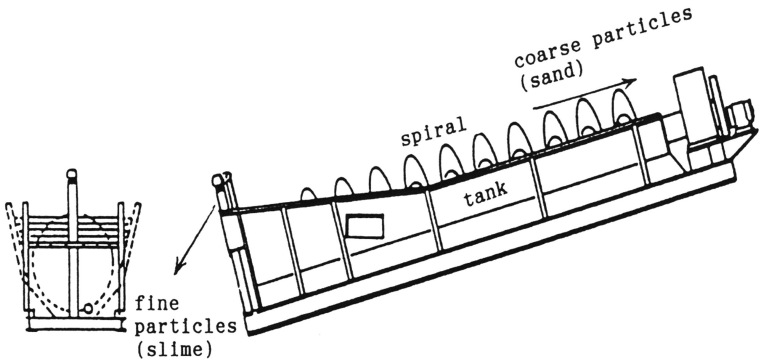


FIGURE 5.3.18 Spiral classifier.

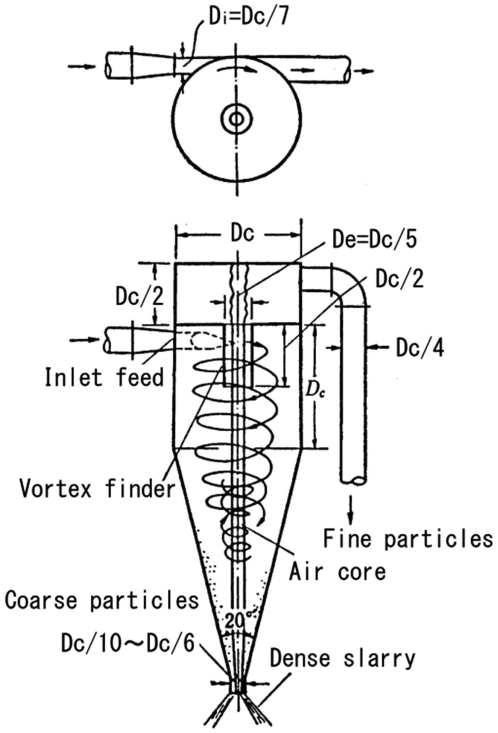


FIGURE 5.3.19 Standard hydro-cyclone and flow pattern.

models.[25] The performance of axial-flow-type hydro-cyclone was studied by Sineath et al.,[26] and the performances of conical and cylindrical hydro-cyclones were examined by Chine et al.[27] The characteristics of hydro-cyclones are summarized as follows:

1. The size of the hydro-cyclone is small compared to other types of wet classifiers.
2. The cut size decreases with increasing inlet velocity or with decreasing cyclone diameter.
3. The pressure drop is about 0.5 to 5 Kg/cm^2, depending on the operating conditions.

Figure 5.3.19 shows the general flow pattern in the standard hydro-cyclone. The coarse and fine particles are collected in the under-flow and overflow sides, respectively. The ratio of inlet volume flow rate to under-flow volume flow rate is referred to as the underflow ratio, R_d. The normal operating conditions for a hydro-cyclone are as follows:

1) Cyclone inlet velocity $u_0 = 2 \sim 10$ m/s
2) Cyclone diameter $D_c = 1 \sim 30$ cm
3) Pressure drop $\Delta P = 0.5 \sim 5$ Kg/cm^2
4) 50% cut size $D_{pc} = 5 \sim 50$ μm
5) Underflow ratio $R_d = 5 \sim 20\%$

Figure 5.3.19 also shows the standard cyclone and the dimension of each part is indicated using the cyclone diameter D_c.[22] The bottom diameter of the conical section is relatively small compared to the gas-cyclone. As the under-flow rate increases, the air core near the axis is observed. To improve the sharpness of classification, the air core region should be eliminated. The typical separation efficiency curve obtained using the standard hydro-cyclone is shown in Figure 5.3.20. The partial separation efficiency approaches to the under-flow ratio R_d as the particle diameter decreases.

To normalize experimental data for different conditions of under-flow ratio, the corrected partial separation efficiency $\Delta\eta_c$ calculated by the following equation is indicated in the Figure 5.3.20.

$$\Delta\eta_c = \frac{\Delta\eta - R_d}{1 - R_d} \tag{5.3.21}$$

The corrected collection efficiency shown in Figure 5.3.20 can be expressed approximately by the following equation.

$$\Delta\eta_c = 1 - \exp\left(- \left(\frac{D_p}{D_{p50}^*} - 0.115 \right)^3 \right) \qquad 0.02 \le \Delta\eta_c \le 0.98 \tag{5.3.22}$$

where D_{p50}^* denotes a 50% cut size under conditions where R_d is zero.

Control of Cut Size

The modified hydro-cyclone shown in Figure 5.3.21 has been developed to improve the cut size control easily.[28,29] The inlet of the hydro-cyclone is attached with a movable guide plate.

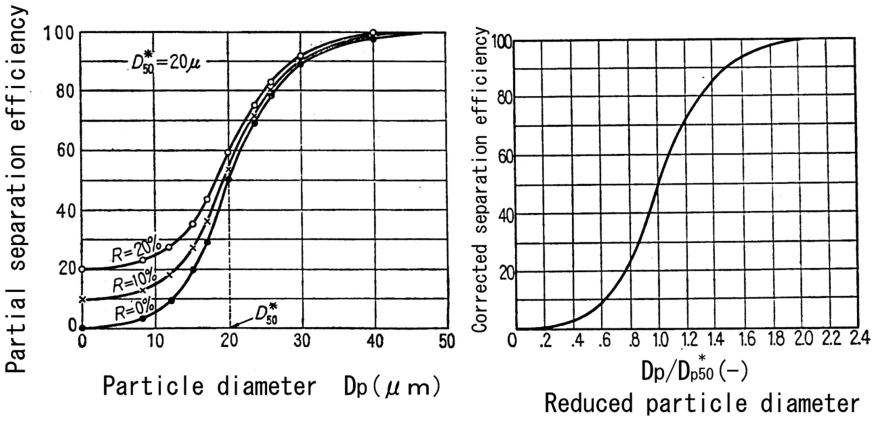


FIGURE 5.3.20 Partial separation efficiency and corrected partial separation efficiency.

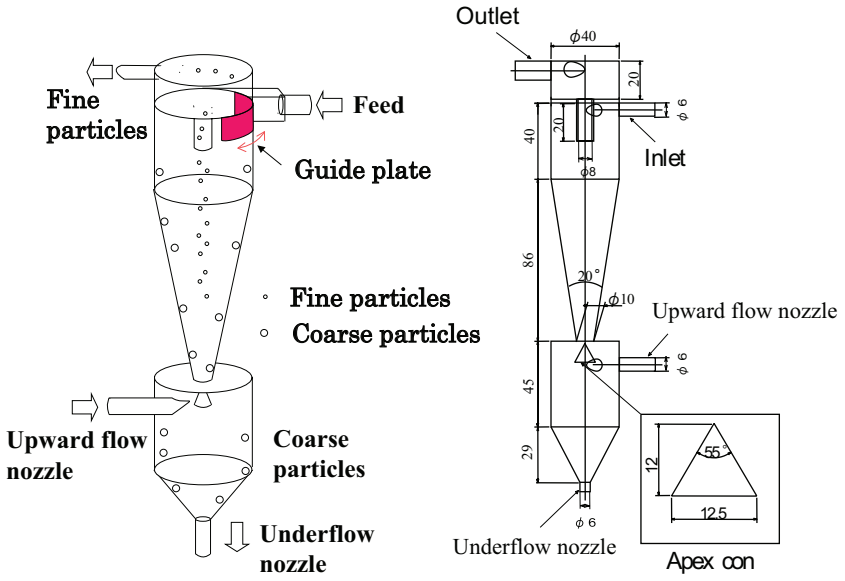
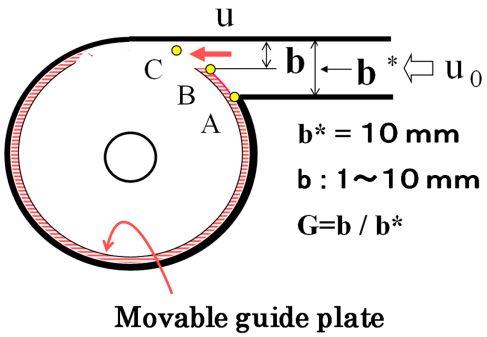


FIGURE 5.3.21 Experimental apparatus of a hydro-cyclone.

The apex cone at the inlet of the under-flow side is also attached. Both the under-flow and upward flow methods are used to increase classification sharpness in fine size. To decrease the 50% cut size, a movable guide plate shown in Figure 5.3.22 is used. Under the condition of constant feed rate, the real inlet velocity u is indicated as u_0/G and increases with decreasing inlet width b. The inlet width ratio G, defined by the following equation, is used as a variable parameter.

$$G = b / b^{*} \tag{5.3.23}$$

where b^{*} is inlet width as shown in Figure 5.3.22. The value of G is equal to one in the standard case. In the case of a small inlet width, small particles are easily collected, because of the increase of the centrifugal force and the small distance of radial sedimentation. Typical experimental results using the guide plate are shown in Figure 5.3.23. The 50% cut size decreases from 10 to 7 μm as the inlet width ratio decreases



G [-]	1.00	0.75	0.50	0.25
u [m/s]	1.4	2.1	2.8	3.5

FIGURE 5.3.22 Cross-section of a cyclone with a guide plate.

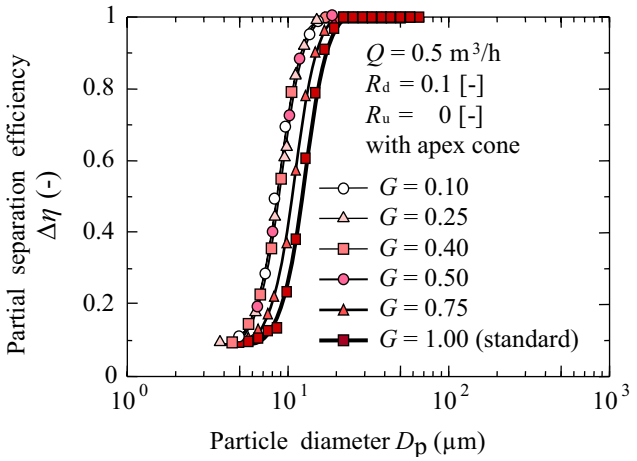


FIGURE 5.3.23 Classification performance using a guide plate and the underflow method.

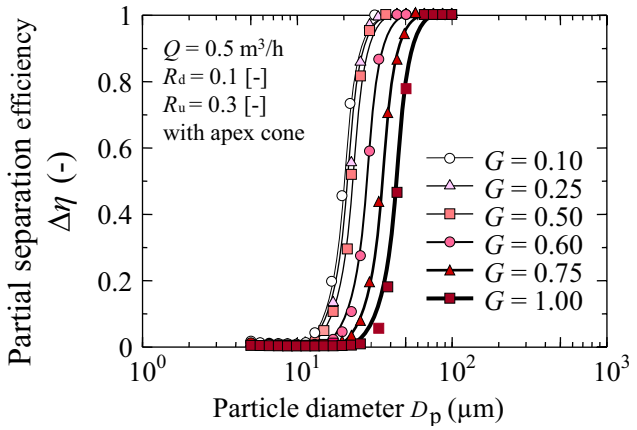


FIGURE 5.3.24 Classification performance using a guide plate, under-flow and upward flow methods.

at a constant inlet flow rate. The partial separation efficiency approaches to 0.1 for the particle diameter less than 5 μm. To increase classification sharpness in the small particle diameter region, the upward flow and under-flow methods were used simultaneously. Some experimental results for the partial separation efficiency are shown in Figure 5.3.24. In this case, the upward flow, under-flow and movable guide plate were used. The upward flow ratio was 30%, the under-flow ratio was 10% and the inlet width ratio was changed from 1 to 0.1. The 50% cut size changes from 35 μm to 10 μm as the inlet width ratio decreases from 1 to 0.1. The partial separation efficiency in this case approaches zero as the particle diameter decreases.

Classification Theory of Centrifugal Type Separator

Figure 5.3.25 shows the centrifugal type separator with wall rotation[30]. The feed slurry is supplied to the bottom part, and coarse and fine particles are classified to collect at the cylindrical wall and upper over-flow side, respectively. The limiting particle trajectory satisfies the following conditions.

$$z = 0 : r = r_c \quad z = L : r = r_2 \tag{5.3.24}$$

where L is the distance of flowing direction from the inlet (z=0) to outlet (z=L), r_c is the radial coordinate of the critical particle trajectory. Integrating the equation of particle motion, the partial separation efficiency can be represented as follows.

$$\Delta\eta = \frac{1}{1-\left(\frac{r_1}{r_2}\right)^2}\left(1-\exp\left(-\frac{2WV_g\omega^2}{gQ}\right)\right) \tag{5.3.25a}$$

where W is the slurry volume in the apparatus and Q is the liquid flow rate defined by the following equation.

$$W = \pi\,(r_2^{\,2} - r_1^{\,2})\,L \tag{5.3.25b}$$

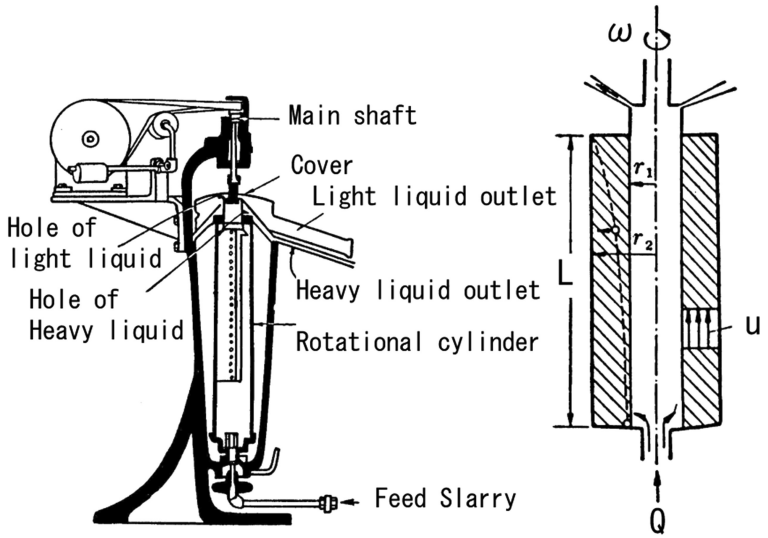


FIGURE 5.3.25 Centrifugal type separator with rotation.

$$Q = u\,\pi\,(r_2^2 - r_1^2) \tag{5.3.25c}$$

where ω is the rotational speed and V_g is the gravitational terminal velocity of the particle. To separate fine particles, it is necessary to increase the length L and the rotational speed ω. The 50% cut size of this type of separator is small compared with the standard hydro-cyclone. However, special care and maintenance are required at the rotor shaft and collection area of coarse particles in the cylindrical wall.

5.3.4 SCREENING

Screening is the separation of solids particles of various sizes into different sizes using a screen surface. The screening surface acts as a multiple go/no-go gauge, and the final product consists of particles of more uniform size than the size of the original material. The purposes of screening are (1) to remove fine particles from a raw material before using grinding equipment, (2) to scalp oversize materials or impurities and (3) to produce or process a commercial-grade product to meet specifications.

Selection of a proper screen surface is very important; opening size, wire or thread diameter, and open area should all be carefully considered. An example of the specifications for test sieves standardized by JIS and ISO is listed in Table 5.3.4. The screening surface may consist of a perforated or punched plate, grizzly bars, wedge-wire sections, woven-wire cloth and nylon, polyester or other bolting cloth. Silk bolting cloth, which was widely used in the past, has largely been replaced by nylon cloth. An electroformed sieve, which has uniform apertures, has also been used for the accurate fractionation of fine powder ranging from 3 to 100 μm.[31,32]

Figure 5.3.26 shows the schematic appearance of typical screening machines such as flat, vibrating and ultrasonic wave screens. Screening machines may be classified into six main categories: grizzlies, revolving screens, vibrating screens, ultrasonic wave screens, sifters and air-assisted screening machines. Grizzlies are used primarily for scalping material of 50 mm and coarser size, while revolving screens or trommel screens are generally used for separations of material more than 1 mm in size. The screening machine consists of a cylindrical frame equipped with a wire cloth or perforated plate. The material to be screened is delivered at the upper end, and the oversize is discharged from the lower end. The screens revolve at a relatively low speed of 15 to 20 rpm. Such screens have largely been replaced by vibrating screens, but they are still used for special purposes, for example, in municipal solid waste separation processes.

Vibrating screens, whose screening surface vibrates perpendicular to the screening surface with a frequency greater than 600 rpm, are available for fine powders as well as coarse powders. There are a large variety of vibrating screens on the market, but basically they can be divided into two main types: mechanically vibrated screens and electrically vibrated screens. The most important factors for the selection of vibrating screens are amplitude and frequency. The centrifugal effect K is defined by the formula[33,34]

$$K = \frac{\left(A/2\right)\omega^2}{g} \tag{5.3.26}$$

where A is the vibration amplitude, $\omega = 2\pi f$, f is the vibration frequency, and g is the acceleration of gravity. If the centrifugal effect is too small, the near-size particles will wedge into the screen openings. This reduces the open area

TABLE 5.3.4 Test Sieves Specifications Defined by ISO and JIS

ISO			JIS
R20/3 [μm]	R20 [μm]	R40/3 [μm]	(Japan)
1000	1000	1000	○
	900		
		850	○
	800		
710	710	710	○
	630		
		600	○
	560		
500	500	500	○
	450		
		425	○
	400		
355	355	355	○
	315		
		300	○
	280		
250	250	250	○
	224		
		212	○
	200		
180	180	180	○
	160		○
		150	○
	140		
125	125	125	○
	112		
		106	○
	100		○
90	90	90	○
	80		○
		75	○
	71		
63	63	63	○
	56		
		53	○
	50		
45	45	45	○
	40		
		38	○
	36		

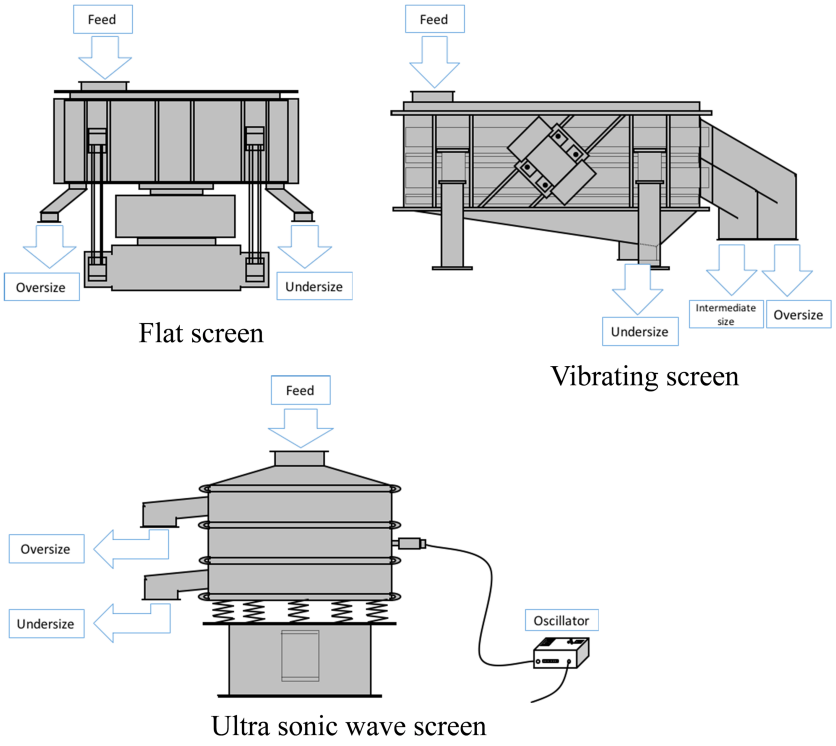


FIGURE 5.3.26 Schematic appearance of typical sieving machines.

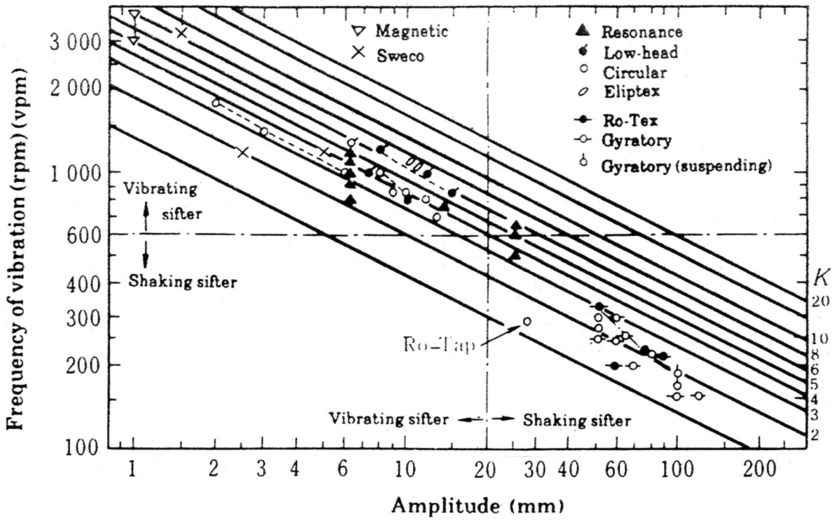


FIGURE 5.3.27 Correlation between the amplitude and frequency for commercially used values of *K*.

available for the passage of other fines and creates probably the single greatest limitation on the capacity of the screen. The proper vibrating action not only keeps the feed materials moving on the screen, but it serves primarily to reduce "blinding" to a minimum. Figure 5.3.27 shows the correlation between the amplitude and frequency for commercially used values of *K*. Sifters are characterized by low-speed (300 to 400 rpm), large-amplitude (smaller than about 50 mm) oscillation in a plane essentially parallel to the screening surface. Sifters are usually used for material of 30 μm to 400 μm or more in size and have many applications in chemical processes.[35] Most gyratory sifters have an auxiliary vibration caused by balls bouncing against the lower surface of the screen cloth. Figure 5.3.28 shows the schematics of a typical screening surface and driving mechanisms of vibrating screens and sifters. The air-assisted screening machine, shown in Figure 5.3.29, has been used for fine powders. The stream of air accelerates the passage of fine particles through the screen and removes the blinding particles in the apertures of screen.

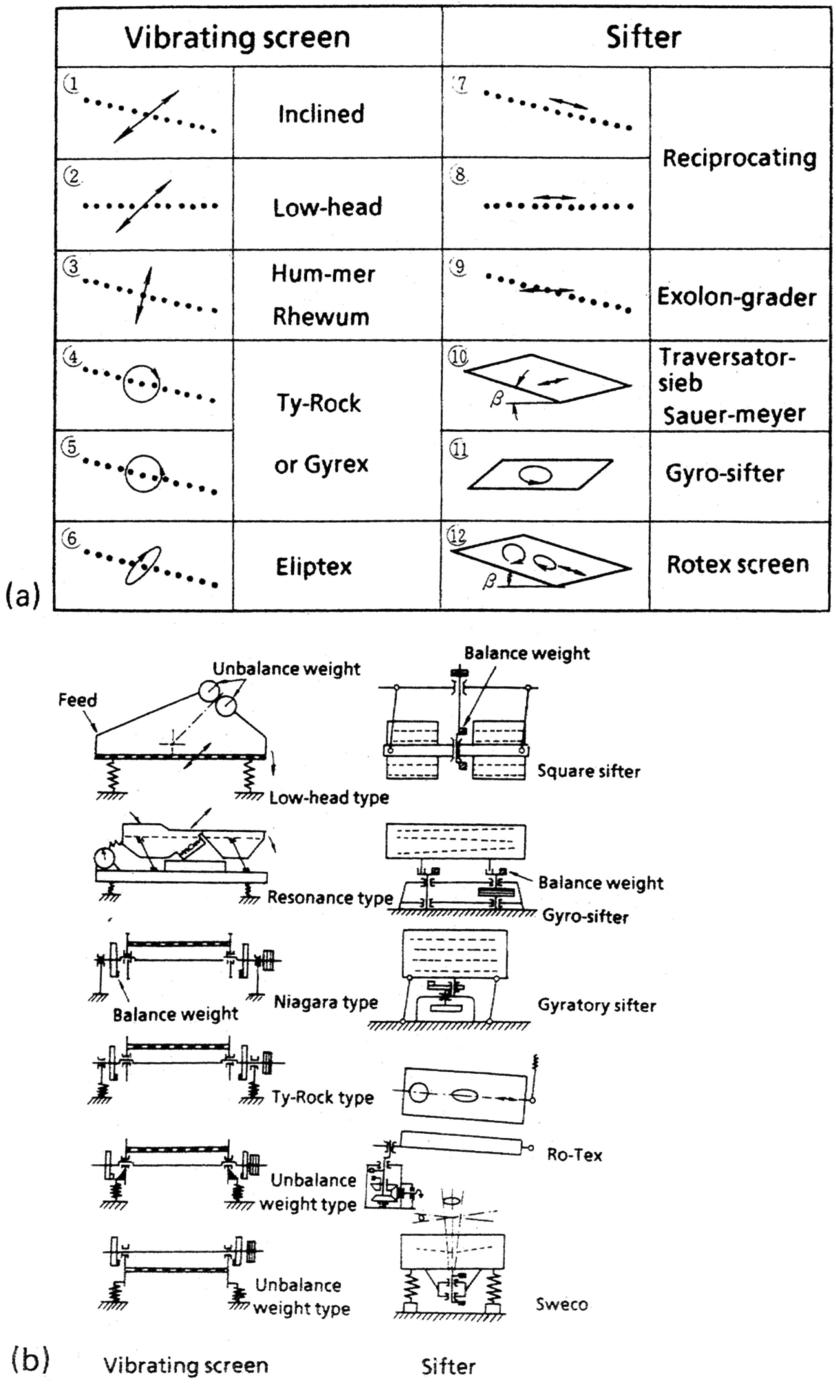


FIGURE 5.3.28 Schematics of a typical (a) screening surface and (b) driving mechanisms of vibrating screens and sifters.

Relation between 50% Separation Size and Screening Length

According to Gaudin's probability theory, the passage probability P of particles of size D_p through an opening of size a in the cloth is given by

$$P = \frac{(a - D_p)^2}{a^2} = \left(1 - \frac{D_p}{a}\right)^2 \tag{5.3.27}$$

Introducing the concept of the number of passage trials i, the oversize fraction of particles after i trails, $\Delta\eta_i$, which is the partial separation efficiency, is expressed by

$$\Delta\eta_i = (1 - P)^i = \left[1 - \left(\frac{a - D_p}{a}\right)^2\right]^i \tag{5.3.28}$$

If i is sufficiently large, Equation (5.3.28) is written approximately as

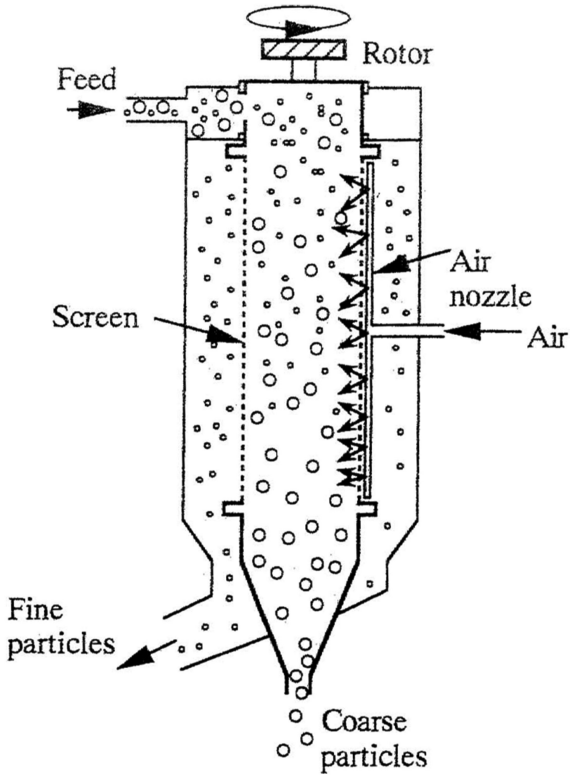


FIGURE 5.3.29 Schematic diagram of air-assisted screening machine.

$$\ln \Delta\eta_i = -i\left(\frac{a - D_p}{a}\right)^2 \tag{5.3.29}$$

Hence the particle size at 50% separation efficiency, D_{p50}, is derived, substituting $\Delta\eta_i = 0.5$ into Equation (5.3.29):

$$D_{p,50} = a - \frac{0.832a}{\sqrt{i}} \tag{5.3.30}$$

In recent years, air flow simulation by the numerical fluid dynamics (CFD) and particle behavior simulation by the discrete element method (DEM) has been widely conducted, and they are used for particle motion and performance evaluation during sieving processing.[36–38]

REFERENCES

1. Leith, D., Licht, W., *AIChE. Symp. Ser.* 126, 196–206, 1972.
2. Ayers, W.H., Boysan, F., *Filtr. Sep.*, 22, 39–43, 1985.
3. Zhou, L.X., Soo, S.L., *Powder Technol.*, 3, 45–53, 1990.
4. Yamamoto, M., Kitamura, O., Arakawa, C., *Trans. Jpn. Soc. Mech. Eng.*, 59, 1959–1964, 1993.
5. Yamamoto, M., Kitamura, O., *Trans. Jpn. Soc. Mech. Eng.*, 60, 4002–4009, 1994.
6. Yoshida, H., et al. *J. Soc. Powder Tech.Jpn.*, 36, 454–461, 1999.
7. Iinoya, K., et al. *KONA*, 11, 223–227, 1993.
8. Yoshida, H., et al. KONA, 12, 178–185, 1994.
9. Yoshida, H., et al. *Kagaku Kogaku Ronbunshu*, 27, 574–580, 2001.
10. Yoshida, H., Ono, K., Fukui, K., *Powder Technol.*, 149, 139–147, 2005.
11. Fukasawa, et al. *Chem. Eng. Technol.*, 39, 484–490, 2016.
12. Huang, et al. *Sep. Purif. Technol.*, 174, 408–416, 2017.
13. Shepherd, C.B., Lapple, C.E., *Ind. Eng. Chem.*, 31, 972–984, 1939.
14. Briggs, L.W., *Trans. Am. Inst. Chem. Eng.*, 42, 511–526, 1946.
15. Lapple, C.E., *Ind. Hyg. Quart.*, 11, 40–47, 1950.
16. Barth, W., *Brennstoff-Warme-Krafn*, 8, 1–9, 1956.
17. Iozia, D.L., Leith, D., *Aerosol Sci. Technol.*, 10, 491–500 1989.
18. Clift, R., Ghadiri, M., Hoffman, A.C., *AIChE J.*, 37, 285–289, 1991.
19. Dietz, P.W., *AIChE J.*, 27, 888–892, 1981.
20. Bradley, D., *J. Ind. Chem. Separation*, 473–485, 1958.
21. Yoshioka, N., Hotta, Y., *Chem.Eng.*, 19, 632–642, 1955
22. Yoshioka, N., *Ekitai-Cyclone*, Nikkan Kogyo, Tokyo, 1962, pp. 38–41.
23. Chu, L.Y., Chen, W.M., Lee, X.Z., *Chem. Eng. Sci.*, 57, 207–212, 2002.
24. Yamamoto, K., Jiao, X., *Trans. Jpn. Soc. Mech. Eng. Ser. B*, 63, 133–138, 1997.
25. Petty, C.A., Parks, S.M., *Filtr. Sep.*, 28, 28–34, 2001.
26. Sineath, H.H., DellaValle, J.M, *Chem. Eng. Prog.*, 55, 59–69, 1959.
27. Chine, B., Ferrara, G., *KONA*, 15, 170–179, 1997.
28. Yoshida, H., et al. *J. Soc. Powder Tech. Japan*, 34, 690–696, 1997.
29. Yoshida, H., et al. *J. Soc. Powder Tech. Japan*, 38, 626–632, 2001.
30. Makino, K., et al. *Kagaku Kougaku Gairon*, Sangyo Tosyo, Japan, 1989, pp. 270–272.
31. Hidaka, J., Miwa, S., *Powder Technol.*, 24, 159–166, 1979.
32. Pierre, B., Jean, C., Albert, L., *Particle Particle Syst.*, 10, 222–225, 1993.
33. Giunta, J., Colijn, H., *Powder Handling Process.*, 5, 45–52, 1993.
34. Modrzewski, R., Wodzinski, P., *Powder Handling Process.*, 10, 167–171, 1998.
35. Sato, Y., Uehara, K., Yasui, A., Sakata, Y., *Trans. Jpn. Soc. Mech. Eng. Part C*, 59, 2688–2693, 1993.
36. Yamane, K., et al. *J. Soc. Powder Technol. Jpn.*, 49, 818–826, 2012.
37. Kruggel-Emden, H., Elskamp, F., *Chem. Eng. Technol.*, 37, 847–856, 2014.
38. Jafari, A., Nezhad, V.S., *Powder Technol.*, 297, 126–143, 2016.

5.4 Storage (Silo)

Jun Yoshida

5.4.1 STORING BULK SOLIDS

A silo is a typical facility for storing powders or granular materials, so to say bulk solids. To store bulk solids on bear grounds or in warehouses is usual when there is not a limitation of the site area. A silo is also necessary when the solids handling should be strictly controlled. To use a silo as a storing facility there are several merits.

1. Granular materials can be collected, distributed, and stored efficiently.
2. Compared with storage on bare grounds or in warehouses, the storing capacity of silos is larger for the same site area.
3. Automatic loading, unloading, and control of storage volume are possible.
4. Operations such as pressurization, heat insulation, moisture proofing, and fumigation can be accomplished.
5. To prevent quality change, decomposition, breakage, and damage of stored materials by insects or rats is easily provided.
6. A silo can be easily incorporated with an industrial production system and has laborsaving advantages.

In spite of these merits, a silo has some problems. One of them is a construction cost. A silo is usually very heavy because of the weight of bulk solids in it. Therefore, its structure, including a foundation, should be stronger than usual buildings. Naturally, the construction cost is expensive. Other problems are related to its handling. Arching, ratholing, and flashing are typical problems of material flow in a silo, especially around a hopper. The blockage of bulk solids is a large problem in running the process and is related to the increase of the internal pressure. Sometimes, dust explosions should be considered for the secure handling of fine powders. These problems may be a cause of the structural failure.

5.4.2 BASIC STRUCTURE AND FUNCTIONS

Structure and Shape

An ordinary silo is mainly composed of a bin, a hopper, and a skirt (see Figure 5.4.1). A bin is usually a cylinder or a block and a hopper is a truncated cone or a wedge shape. A hopper is attached to the bottom of a bin upside down. A volumetric capacity of a silo is those of a bin and a hopper. A skirt is a structure which supports the weight of a bin and a hopper with bulk solids. Since a silo is usually a heavy structure a skirt should be strong enough and be supported by a rigid foundation and a strong ground or a group of piles.

A common silo has a round or rectangular cross section from a horizontal perspective. Cylindrical bins are commonly used because the mechanical stability of the cylindrical bins is superior to the rectangular ones. However, rectangular shapes are suitable from the view point of the effective area usage. Since silos are used to resolve the limitation of a site area, another shape is sometimes adopted, such as polygonal and even a shape of a clover leaf which is applied to the coal silos in a Japanese power plant. In regard to the vertical perspective, a silo was formerly called a shallow bin or a deep bin according to its ratio of height and width, but recently these categories are not commonly used.

A silo is usually made of steel or reinforced concrete (RC). Other materials are aluminum, fiber reinforced plastic, brick, stone, wood, and so on. However, they are used for the specific purposes or as the old fashion silos. One of the purposes is corrosion resistant for bulk solids, which means water proof.

Functions of Silos

A general function of a silo is storage and it should be effective in the system of bulk solids handling. It is said in silos materials should be 'first-in first-out.' A mass flow silo realizes this system, but a funnel flow silo doesn't achieve it (see Section 5.4.4). In order to provide fresh materials, the function of first-in first-out is necessary and a mass flow silo is preferable.

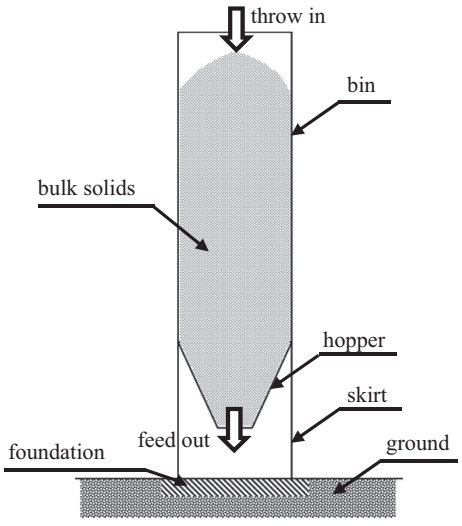


FIGURE 5.4.1 Basic composition of a silo.

Another requirement is constant feeding according to the demand. Usually, a silo is used as a temporary storage so to say a buffer between a provider and a customer. The amount of the products is controlled at a silo. Therefore, constant feeding is an essential function. It is very important to understand the flow in silos in order to achieve this purpose.

To store the materials safely without degradation is also required for an ordinary silo. There are some silos which have additional functions. For example, a blending silo in a cement plant is used to homogenize raw materials and a clinker silo has a role of cooling down.

5.4.3 CLASSIFICATION OF SILOS

Single Bins and Group Bins

For a single bin, a circular cross section is frequently used because of some mechanical and practical advantages. Coal silos 40–50 m in diameter and as high as about 60 m have been constructed in Japan since around the year of 2000, many of which are independent bins. In addition, large single bins such as cement silos and crinker silos have been constructed at the cement plant or at the port of import. They are usually a single bin type.

An example of group bins is a silo for storing grains. When grain silos are planned, sometimes different kinds of grains should be handled. Then, group bins are necessary and each silo is not so large compared to the single silos mentioned previously. Therefore, several to several tens of connected bins are used to utilize the plant efficiently. Their facilities, such as conveyers should be laid out reasonably and appropriately.

Stored Materials

A silo is used for the storage of bulk solids. Typical materials stored in silos are ores, grains, and powders. Coal, iron ore, and limestone are usually stored in the silos. Various grains, such as wheat, rice, corn, and beans are stored at the place of production or at the port of entry. Cement and flour are typical powders stored in silos.

Silos for mineral ores commonly have a problem of wearing. It should be considered when a thickness of the wall is designed. A coal silo is sometimes used at a power plant and has a large capacity. Mass storage of coal has a problem of exothermic reaction. Therefore, the term of storage may be shorter and the cooling facility is sometimes required.

A grain silo is usually located at the port of import. Then, it has a fumigation facility. Another requirement for a grain silo is preservation of quality. The temperature and humidity in a silo must be controlled properly.

When a powder silo is planned, dust explosion should be taken into account. The countermeasure of dust explosion is composed of a blast dispersing port, a duct collection device, an alarm system using thermo censors and so on. If bulk solids create dust in a silo, dust explosion is a common problem for ores or grains.

5.4.4 BEHAVIOR OF BULK SOLIDS IN SILOS

Three Stages

There are three stages to handling bulk solids in a silo. They are "throw-in," "still," and "feed-out." At the stage of "throw-in" bulk solids are usually thrown in from the top of silos and the impact load to the bottom of silos should be considered in the plan and the design. The stage of 'still' means bulk solids don't move in silos after they are thrown in. The static load in this stage is usually used as a basis of the structural design. Also, quality control of bulk solids is very important at this stage, especially for a stock-type silo.

The behavior of bulks solids at the stage of 'feed-out' is the most important when a silo is planned. There are a lot of investigations on this stage. Especially, powder flow in a bin and a hopper is a key issue to design a silo and its facilities.

Flow Behavior of Bulk Solids

As mentioned above, powder flow is a key issue. Flows are roughly categorized into two patterns. The first is called "mass flow" and the other is "funnel flow" as shown in Figure 5.4.2.

"Mass flow" has a flow profile in which all the stored particles are mobilized during discharge. To realize the requirement of 'first-in first-out,' this pattern is suitable because of no residual material after feeding out. Usually, a mass-flow silo is desirable, especially for grains or food powders according to the residual material. Residual materials in silos usually contain some problems, i.e. degradation, corrosion, and so on. However, a mass-flow silo sometimes has a problem of dynamic pressure increase during feeding out. Huge pressure increase causes structural corruption of bins, hoppers, and even skirts. To avoid such a problem, a funnel-flow silo is applied to other kinds of bulk solids in order to reduce the dynamic pressure to the walls.

"Funnel flow" has a flow profile in which a channel of flowing material develops within a confined zone above the outlet and the material adjacent to the wall near the outlet

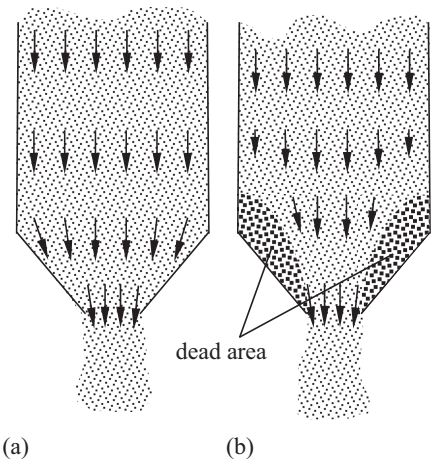


FIGURE 5.4.2 Flow patterns in a silo. (a) mass flow, (b) funnel flow.

remains stationary. The flow channel can intersect the wall of the parallel section or extend to the top surface. In the latter case, the pattern is called "internal flow." Flow patterns depend on the size of a bin and a hopper, the inclination angle of a hopper, and an orifice size. As for a funnel-flow silo, clogging is caused because of arching, caking, or ratholing. When a feed-out system is planned for a funnel-flow silo, flow promoting devices are considered to avoid a trouble of clogging.

To estimate a flow pattern in a silo, some standards provide the charts which show the relationship between material properties and flow profiles. Figure 5.4.3 shows an example of a cylindrical silo and shows a chart of an inclination angle and a wall friction angle of a hopper. As shown in the chart, a higher inclination angle and a lower friction angle tend to show mass flow. However, as shown in the figure, the vague area between mass flow and funnel flow is rather wide and also the difference between ISO11697[1] and the Austrian standard[2] is rather large. In addition to these properties, internal friction angle, cohesive force, and bulk density are related to the flow behavior. Jenike[3–5] proposed the method to estimate the flow profile according to the properties obtained by the experiments and it is quite useful to design the flow pattern of silos. After Cundall et al.[6] proposed the numerical simulation using Discreet Numerical Model, a lot of numerical investigations[7,8] have reported the experimental results. In spite of the rapid progress of computers, it is very difficult to simulate the behavior of powders accurately.

5.4.5 PLANNING SILOS

When a silo is planned, the conditions as follows are considered.

1. Site condition
2. Bulk material condition
3. Silo capacity
4. Silo facilities

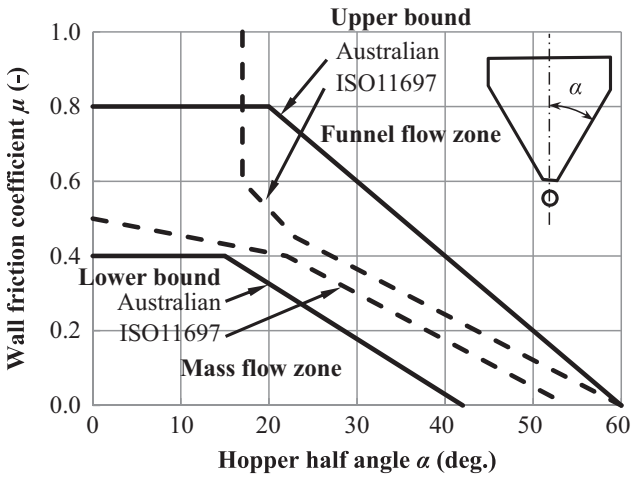


FIGURE 5.4.3 Limit between mass flow and funnel flow for circular hoppers Comparison of ISO11697.

Site condition depends on a location. Among the site conditions there are natural conditions, transportation, industrial environment, and foundation ground. The conditions of stored bulk material are essential and their properties, especially flow properties, should be known before the design.

Planning Silo Capacity

One of the most important elements in planning a silo is to determine its capacity. If a single silo is planned, the capacity is its own, but in the case of group silos, a capacity of each silo and their total amount should be planned. The total capacity is related to supply and demand of bulk materials. To determine the capacity of each silo, a size of each silo and a silo layout at the site are necessary to be fixed.

Effective Capacity of a Single Silo

Silo capacity has two components: total capacity (geometric capacity) and the capacity of loaded stored materials (effective capacity). A geometric capacity, also called water capacity, is used as a standard value for calculating the fumigation gas to be employed in treating imported grains. An effective capacity is the base for calculating the storing weight. In its calculation, the peak of bulk solids pile and the angle of repose should be taken into consideration. If a geometric capacity is represented by V and an effective capacity by V_E, the loss volume V_L becomes:

$$V - V_E = V_L \tag{5.4.1}$$

The loss volume of a cylindrical silo, illustrated in Figure 5.4.4, can be calculated by the following equations.

$$V_L = \frac{4}{3}R^3\left[3F\int_0^{\frac{\pi}{2}}\cos^2 x\sqrt{G}dx\right] + \int_0^{\frac{\pi}{2}}\left[G^{\frac{3}{2}}dx\right]\tan\phi_r = cf_L \cdot R^3 \cdot \tan\phi_r \tag{5.4.2}$$

where

$$F = \left(1 - \frac{a}{R}\right)^2 \tag{5.4.3}$$

$$G = (1 - F) + F\cos^2 x \tag{5.4.4}$$

cf_L is the loss coefficient for the cylindrical silo (see Table 5.4.1), R is the radius of bin, ϕ_r is the angle of heap slope, and a is the location of peak of heap.

For a cylindrical container, the geometrical capacity of silos is calculated as follows:

$$V = A_1 H + \frac{1}{3} h \sqrt{A_1 + A_2 + (A_1 \cdot A_2)} \tag{5.4.5}$$

$$A_1 = \pi R^2, A_2 = \pi r^2 \tag{5.4.6}$$

where:

H is the height of bin
h is the height of hopper
R is the radius of bin
r is the radius of orifice

The effective capacity of a cylindrical silo can be calculated from Equations (5.4.1, 5.4.2, and 5.4.5). Similarly, the calculation of the capacity of a rectangular silo can be made. These calculations of silo capacities are made to decide the size and the facilities of silos.

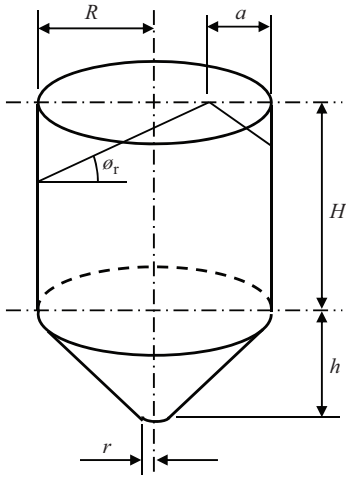


FIGURE 5.4.4 Calculation of effective capacity of cylindrical silo.

Planning Silo Facilities

Feeding is a fundamental element of the silo facilities. Bulk materials move along the transportation line which is composed of a throw-in device, a bin, a hopper, and a feed-out facility. An example of the throw-in device is a bucket elevator which carries bulk solids from the ground level to the silo top. After being thrown in, bulk materials go through a bin and a hopper. As a feed-out facility, an orifice is usually located in the center of a silo and some flow promoting device is attached near the orifice. One of the feed-out devices has a screw auger along the hopper wall. In order to discharge cohesive materials such a kind of device is facilitated. Other methods utilize impact, rotary plow, or air blast. It is essential for the smooth handling of bulk materials to plan these feed-out devices.

Other facilities are measurement devices, coarse sorting devices, fumigation facilities, and explosion-proof systems. The necessity of these facilities depends on the properties of bulk materials and the method of handling. When the silo is planned, it is very important to know the properties of bulk materials and to decide their handling method.

5.4.6 STRUCTURAL DESIGN

A silo is a unique structure which is influenced by the internal load due to bulk solids. In order to design its structure properly, a lot of investigations have been reported about the static and dynamic loads caused by bulk solids and their flow. The standards used for the silo design are proposed according to the results of these investigations. Here, the basis of the structural design is introduced.

Revised version of *Design Recommendation for Storage Tanks and Their Supports*, issued by the Architectural Institute of Japan in 2010 (AIJ2010),[9] is available for the structural design of silos. AIJ2010 includes the earthquake-proofing requirements, which are characteristic for seismic design. There are several standards related to the design load of silos

TABLE 5.4.1 Loss Coefficient for Cylindrical Silo

a/R	cfL	a/R	cfL	a/R	cfL	a/R	cfL
0.00	3.5555	0.26	2.9235	0.52	2.4509	0.78	2.1701
0.02	3.5025	0.28	2.8809	0.54	2.4222	0.80	2.1570
0.04	3.4500	0.30	2.8394	0.56	2.3947	0.82	2.1451
0.06	3.3982	0.32	2.7988	0.58	2.3683	0.84	2.1345
0.08	3.3471	0.34	2.7592	0.60	2.3431	0.86	2.1251
0.10	3.2967	0.36	2.7206	0.62	2.3191	0.88	2.1169
0.12	3.2471	0.38	2.6831	0.64	2.2962	0.90	2.1100
0.14	3.1983	0.40	2.6467	0.66	2.2746	0.92	2.1044
0.16	3.1503	0.42	2.6113	0.68	2.2541	0.94	2.1000
0.18	3.1031	0.44	2.5770	0.70	2.2349	0.96	2.0968
0.20	3.0569	0.46	2.5438	0.72	2.2169	0.98	2.0950
0.22	3.0115	0.48	2.5117	0.74	2.2001	1.00	2.0943
0.24	2.9670	0.50	2.4808	0.76	2.1845		

in other countries. ISO11697[1] mentioned above, ACI313-97[10] of the American Concrete Institute, and AS3774-1996[2] of Australian Standard show the design loads of bulk containers.

In AIJ2010, the following loads should be considered to design a silo structure: (1) dead load, (2) live load, (3) snow load, (4) wind load, (5) earthquake load, and (6) loads appropriate to the containers, as they must consider impact and absorption due to the movement of bulk materials inside the containers.

Calculation of Static Powder Pressure

In the structural design, the static powder pressure is calculated as a basis of bulk loads. The Janssen and Reimbert formulas are employed as silo design standards in various countries. The calculation method of the static powder pressure shown below follows the Janssen's theory which is introduced in ISO11697, AIJ2010, and so on. It is derived from a force balance of the powder stored statically in deep bins, taking into consideration the frictional force generated between the powder and the silo walls (see Figure 5.4.5).

If a silo of cross-sectional area A and circumference L is filled uniformly with a powder of bulk density γ, the vertical pressure P_v (N/m^2) inside the silo on the horizontal plane at the depth x is assumed to be homogeneous. Then, it can be expressed by

$$P_v = \frac{\gamma \cdot r_w}{\mu \cdot \lambda}\left(1 - e^{-\frac{\mu\lambda x}{r_w}}\right) \tag{5.4.7}$$

where r_w is the hydraulic radius (=A/L).

Equation (5.4.7) is called the Janssen formula. According to the assumption, the horizontal pressure P_h is proportional to the vertical pressure P_v and can be expressed as follows, where the proportional constant is denoted by pressure ratio λ and friction force P_f can be obtained by P_h and a wall friction coefficient μ.

$$P_h = \lambda P_v = \frac{\gamma \cdot r_w}{\mu}\left(1 - e^{-\frac{\mu\lambda x}{r_w}}\right) \tag{5.4.8}$$

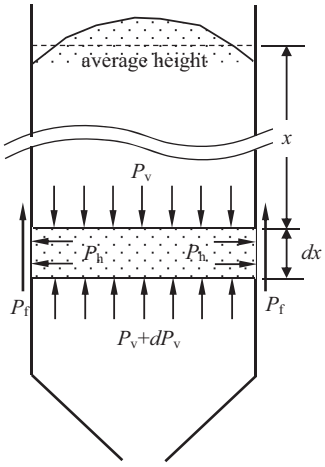


FIGURE 5.4.5 Pressure balance assumed in thin layer in a silo.

$$P_f = mP_h \tag{5.4.9}$$

To determine the λ value, the Rankine's active earth pressure formula gives the relation to the angle of internal friction ϕ:

$$\lambda = \frac{1-\sin\phi}{1+\sin\phi} \tag{5.4.10}$$

To use these formulas in practice, it is necessary to know certain physical properties of the powder. The bulk density γ is generally measured in a laboratory, but has increased due to accumulated consolidation. The angle of internal friction ϕ is usually measured by the shear test. The most difficult measurement is that of the friction angle (coefficient μ) of the powder against the wall. It can be obtained by the shear test which is performed by a similar apparatus used for the shear test of the bulk materials.

Design Loads Due to Bulk Materials

In designing silos, a proper understanding of the behavior of bulk materials inside silos is necessary. However, many unsolved and unanticipated problems still exist. The pressure according to the flow of bulk solids changes in complexity, depending on various properties of the materials stored and the operating conditions of silos.

In AIJ2010 as the design loads, bulk pressures in a silo are defined based on the static pressure of bulk solids to the walls of a bin and a hopper.

1. In order to consider the impact load due to the throw-in of bulk solids, the impact factor C_i is introduced and its lower limit (C_i = 1.5) is shown.
2. The dynamic pressure increase during feeding out is represented by the overpressure factor C_d. It is related to the ratio between height and width of a bin as shown in Figure 5.4.6.
3. Local pressure due to the eccentric flow is introduced as shown in Figure 5.4.7. It depends on the position of an orifice. If an orifice is at the center of a bin, a local pressure coefficient C_L can be assumed to be 0.15. If there is an eccentricity of feeding out, C_L is proportional to the distance between an orifice and the center of a bin.

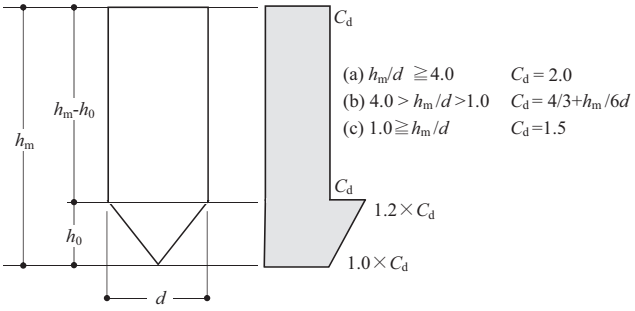


FIGURE 5.4.6 Minimum requirement of overpressure factor.

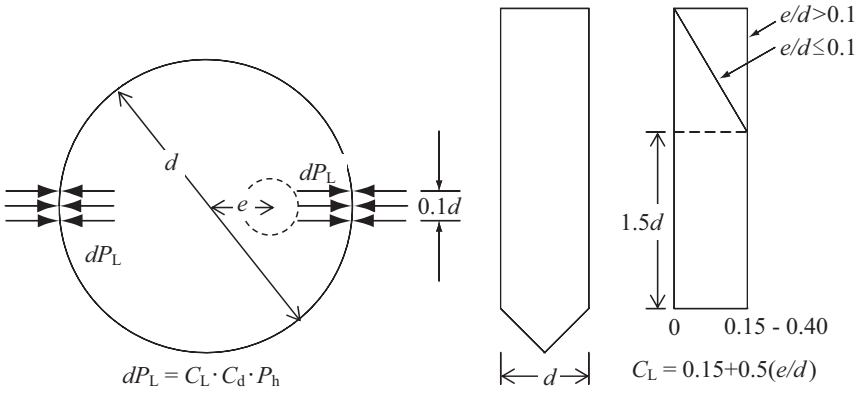


FIGURE 5.4.7 Local pressure dP_L and Local pressure coefficient C_L.

As for seismic load, bulk solids in silos are treated as only a weight for the structural design. From the experience, the weight of the solids can be reduced to 80% of a full volume to calculate the seismic load. Seismic load and wind load are varied due to the area in Japan and the local coefficient is considered.

Structural Design Flow

A silo is structurally designed using the loads mentioned above. In the AIJ2010 standard, a few examples of a structural design are attached in the appendices. Basically, the response forces of the members of the structure such as walls and frames are calculated against each load and they are combined according to the load combination such as that of long-term or of short-term. Then, these forces are compared with the strength of the structural members. If this comparison shows enough safety factor, a silo design is closed. If it doesn't, the structural members are rearranged and the calculation should be repeated (see Figure 5.4.8).

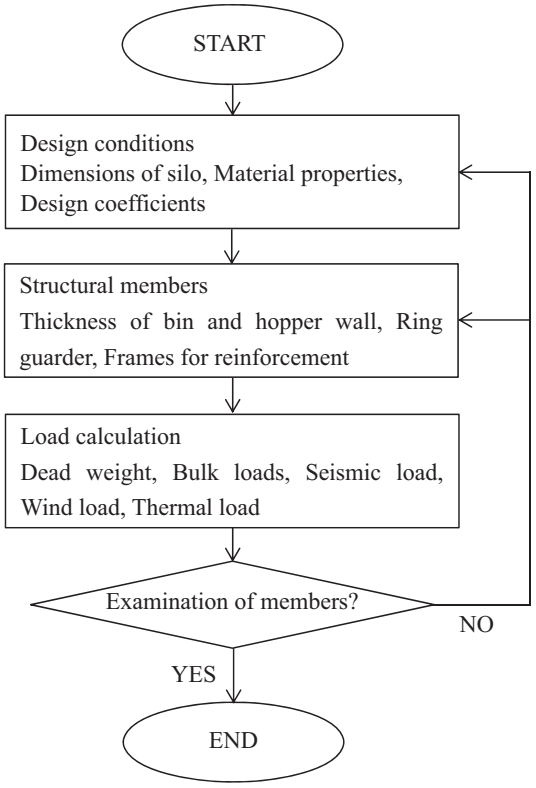


FIGURE 5.4.8 Flow of structural design.

5.4.7 TROUBLE IN SILOS

The examples of the troubles related to a silo are shown here. As mentioned above, there are a lot of unknown factors related to the behavior of bulk solids in a silo. Typical accidents are caused by bulk loads, external loads (i.e. seismic), and thermal loads.

Corruption of Silos Caused by Bulk Loads

As mentioned about a mass flow silo, sometimes dynamic pressures exceed the strength of silo walls and this causes the corruption of a silo.[11] The cause of this corruption is a change of material properties, clogging, or ratholing. In addition to these complex phenomena, aging is a cause of irregularities or faults at the walls. If the structure is healthy, it has enough strength against the usual loads, but if there is deterioration, the strength of the structure will considerably decrease. Therefore, the behavior in silos should be carefully monitored and if there is some problem, reinforcement of the structure, a flow promoting device, or other flow control method should be considered.

Seismic Disaster

Failures of silos due to earthquakes are reported in several countries.[12] Since the silos are a very heavy structure, the seismic load is relatively large compared with the ordinary building. Therefore, in the area where earthquakes often occur, the seismic intensity should be carefully defined and not only the silo structure but the foundations should be designed as earthquake proofing.

Thermal Accidents

Dust explosion is a typical trouble for a silo which contains small particles. The fire proof system and the blast release device must be equipped to ensure that it is explosion proof. However, there are other problems related to thermal troubles. For example, coal heap causes heat spontaneously with time going. So, sometimes a fire occurs in a silo. The Refuse Derived Fuel (RDF) also causes heat and the large fire and explosion in an RDF silo made a huge injury accident in Japan.[13] The cause of the accident was supposed to be clogging of RDF and its chemical reaction. The handling of the materials which causes spontaneous heat is very important.

REFERENCES

1. ISO11697, *Bases for Design of Structures: Loads Due to Bulk Materials*, International Standards Organization, 1995.
2. AS3774, *Loads on Bulk Solids Containers*, Australian Standard, 1996.
3. Jenike, A.W., *Bull. Utah Eng. Exp. Station*, No. 108, Vol. 52, 1961.
4. Jenike, A.W., *Bull. Utah Eng. Exp. Station*, No. 123, Vol. 53, 1964.
5. Jenike, A.W., *Powder Technol.*, 1, 237, 1967/1968.
6. Cundall, P.A., Strack, O.D.L., *Geotechnique*, 29, 47, 1979.
7. Yoshida, J., *Adv. Powder Technol.*, 5, 84, 1994.
8. Potapov, A.V., Campbell, C.S., *Phys. Fluids*, 8, 2884, 1996.
9. Architectural Institute of Japan, *Design Recommendation for Storage Tanks and Their Supports*, Architectural Institute of Japan, 2010.
10. American Concrete Institute, *Standard Practice for Design and Construction of Concrete Silos and Stacking Tubes for Storing Granular Materials* (ACI 313-97), 1997.
11. Carson, J.W., *The 3rd Israeli Conference for Conveying and Handling of Particulate Solids* (https://www.inti.gob.ar/cirsoc/pdf/silos/silo-failures.pdf), 2000.
12. Kawashima, M., et al., *J. Earthquake Eng.*, 14, 816, 2010.
13. National Research Institute of Fire and Disaster, Japan. (http://nrifd.fdma.go.jp/english/research/special_disasters/02/index.html)



Taylor & Francis
Taylor & Francis Group
http://taylorandfrancis.com

5.5 Feeding

Shuji Matsusaka

5.5.1 INTRODUCTION

Powder feeders play an important role in powder-handling processes, such as feeding raw materials or discharging product materials from a storage vessel. The powder load or mass to be treated in the processes depends on the accuracy of the feeders. The product quality depends on the powder load; low-quality products are produced if the load is too high for the process. The feeders should be selected carefully, because some feeders might be unsuited to the process, resulting in failure to feed the material. Further, the dynamic characteristics of the feeders could also affect the accuracy of feeding. If the feeder cannot respond to a rapid change in the manipulating signal, a fluctuation in the flow caused by a disturbance cannot be suppressed, and this could cause a dynamic error in the feeding process.

The static and dynamic characteristics of the feeders will depend on the powder properties such as particle size, shape, internal friction coefficient, and powder flowability. They will also depend on the operating conditions, including temperature, pressure, and moisture content of the powder in the process.

Further, feeders are always used together with feed hoppers, and the design of the feed hoppers might affect the function of the feeders. If the feed hopper is not well designed, the flow mode in the hopper will be an unfavorable one, called funnel flow, which can cause particle bridging, rat holing, and flushing. Failure to feed the material can occur if the selection or maintenance of the feeders is inadequate or the hopper design is improper.

The power supply should be sufficient so that the feeder can operate even under a light overload condition caused by a disturbance. Additional parts, such as a shear pin, are usually incorporated in the feeder design to prevent serious damage. However, if the shear pin is very weak, the feeder will often malfunction. Variations in powder properties or operating conditions are also important factors that can cause feeding failures.

Unstable flow is caused by poor feeder selection or improper hopper design. Unstable flow with bridging or flushing will also be caused by a variation in the powder properties or operating conditions. The wall surface can be coated with an ultrahigh-molecular-weight material to prevent the occurrence of these problems. Suitable vibrators can also be used for this purpose. The addition of a small amount (0.2–5 wt%) of fine particles, such as kaolin, diatomaceous earth, corn starch, silica gel, or magnesium stearate will decrease both the wall and internal frictions of the powders. Granulation, drying, or encapsulation will also decrease the friction, so that the powder flow can be changed from funnel flow mode to mass flow mode.

The following requirements are to be met by the feeders:

1. They must be suitable for the properties of the powder.
2. The operating range must be sufficiently wide.
3. The static characteristics, such as the relationship between powder feed rate and rotational speed of the drive motor, must be stable, and the repeatability of the feed rate must be good.
4. They must have excellent dynamic characteristics.

As mentioned earlier, the powder properties affect the powder flow in the feeder. It is necessary to know the properties such as particle size, particle shape, cohesiveness, frictional property, and abrasive property to select the appropriate feeder. If the feeder is not suitable for the application, the powder feed rate cannot be controlled precisely. Table 5.5.1 presents an empirical rule for the selection of various feeders. The rotary feeder, for example, can be applied to particles between 100 μm and 1 cm in diameter, but it is difficult to use it in the case of particles with diameter less than 100 μm. It can be seen from Table 5.5.1 that there is no feeder suitable for use with adhesive powders; hence, careful attention should be paid to feeder selection in such cases.[1,2] Each type of feeder is described in detail in the next section.

The operating range of a feeder should be wide enough to cover the range of feed rates required in the process, with a margin of 10%, so that the feeder can work well under conditions of unexpected disturbance. Further, the dynamic response should be as fast as possible. The dynamic characteristics of typical feeders are presented in Table 5.5.2.

5.5.2 TYPE OF FEEDERS

Rotary Feeders

A rotary feeder consists of a rotor, a rotor case, and a motor drive. The powder placed in a hopper flows into the rotor space by gravity, and is discharged through the exit after a half revolution. Figure 5.5.1 shows a rotary feeder used in a pneumatic transport line. There are various types of rotary feeders; they are sometimes called rotary valves, rotary dischargers, or vane feeders.

The powder feed rate depends on the rotational speed of the rotor, as depicted in Figure 5.5.2. The volumetric efficiency decreases with increasing rotational speed. The static characteristics depend on the powder properties, depth of

TABLE 5.5.1 Empirical Rule for the Selection of Feeders[a]

	Particle Size[b]					Flowability[c]				Abrasiveness, etc.[d]					
Feeder	**a**	**b**	**c**	**d**	**e**	**f**	**g**	**h**	**i**	**j**	**k**	**l**	**m**	**n**	**o**
Gate valve	D	O	O	O	D	X	O	D	D	D	X	D	O	D	D
Rotary	D	O	O	X	X	O	O	X	X	D	X	X	D	X	X
Table	D	O	O	O	D	D	O	D	D	O	D	X	O	X	D
Belt	D	O	O	O	O	D	O	O	D	O	O	O	O	D	O
Screw	O	O	O	D	X	O	O	D	D	D	X	X	D	D	D
Vibrating	O	O	O	O	X	D	O	O	D	O	X	O	O	X	O

[a] O: applicable; D: difficult; X: cannot be used.
[b] **a**: less than 100 μm; **b**: 100 μm to 1 mm; **c**: 1 mm to 1 cm; **d**: 1 cm to 10 cm; **e**: larger than 10 cm.
[c] **f**: excellent; **g**: moderate; **h**: low; **i**: cohesive.
[d] **j**: abrasive; **k**: fragile; **l**: low bulk density; **m**: high temperature; **n**: slurry; **o**: flaky or fibrous.

TABLE 5.5.2 Characteristics of Feeders as Final Control Means

Feeder	Operating Method	Control Element	Dynamics	Statics
Electromagnetic	Voltage	SCR	Fast	Nonlinear
Screw	rpm[a]	VS motor	Moderate	Linear
Belt	Gate	Servomotor	Dead time	Nonlinear
	Belt speed	VS motor	Moderate	Linear
Table	rpm[a]	VS motor	Fast	Linear[b]
	Scraper	Servomotor	Fast	Nonlinear
Rotary	rpm[a]	VS motor	Moderate	Linear[b]
Gate valve	Gate	Servomotor	Fast	Nonlinear

[a] rpm, nominal speed.
[b] Restricted to low rotational speeds.

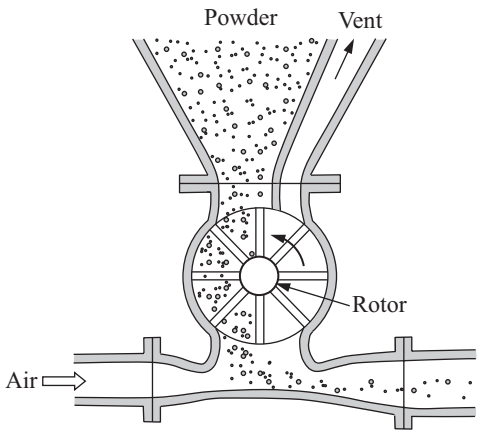


FIGURE 5.5.1 Rotary feeder.

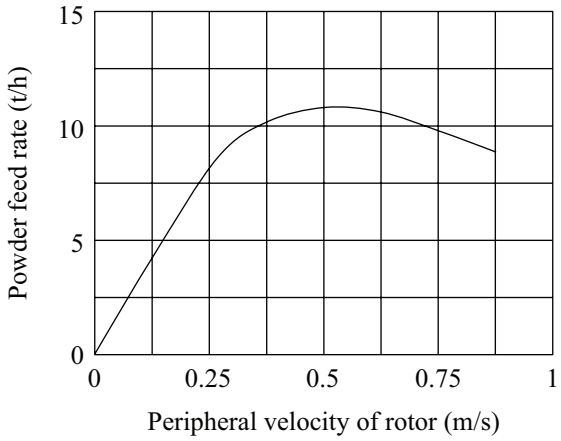


FIGURE 5.5.2 Powder feed rate in a rotary feeder.

rotor space, and inlet area.[3–5] The instantaneous powder feed rate fluctuates periodically because of the rotor configuration. Necessary modifications are incorporated in the rotor (helical rotor) or inlet configuration to suppress the fluctuations. Although a rotary feeder can be used to feed particles against a pressure difference less than 2 atm, the feed rate decreases with increasing pressure difference.[3] The dynamic characteristic of a rotary feeder is represented by a first-order model with time delay.

Screw Feeders

A screw feeder consists of a screw, a U-shaped trough or cylindrical casing, and a motor drive. As the screw rotates, the particles in the hopper are forced to move from the hopper to

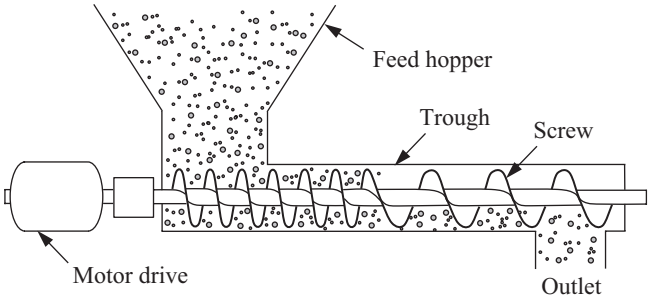


FIGURE 5.5.3 Screw feeder.

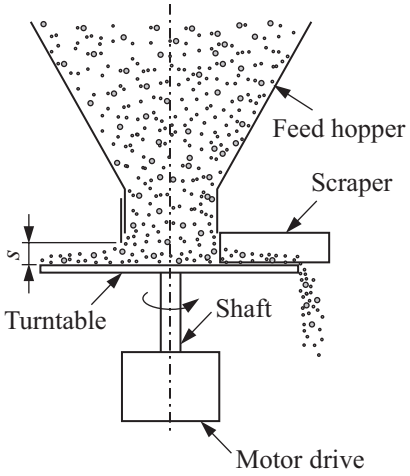


FIGURE 5.5.4 Table feeder.

the outlet of the feeder. Figure 5.5.3 shows a screw feeder with a U-shaped trough. A modified screw (e.g. tapered screw) is used to obtain a uniform flow pattern in the feed hopper.[6,7] Feeding against a pressure difference is possible by modifying the screw configuration. A screw feeder with twin screws is suitable for feeding wet powders. A coil-shaped screw called an auger may also be used instead of a normal screw.

The powder feed rate is proportional to the rotational speed of the screw as long as the powder compressibility is negligible. The instantaneous powder feed rate fluctuates periodically as the screw rotates. The fluctuation can be suppressed by using a smaller screw and higher rotational speed, or by using a coil screw (an auger feeder). The dynamic characteristic of a screw feeder is represented by a second- or third-order model with time delay.[8]

Table Feeders

A table feeder consists of a turntable, a scraper, and a motor drive, as shown schematically in Figure 5.5.4. The powder feed rate can be adjusted by changing either the scraper position or the rotational speed of the turntable. The skirt clearance S in Figure 5.5.4 can also be changed when an extremely wide operational range is required. The powder feed rate is proportional to rotational speed in the practical range of operation, but it is a nonlinear function of the scraper position. For

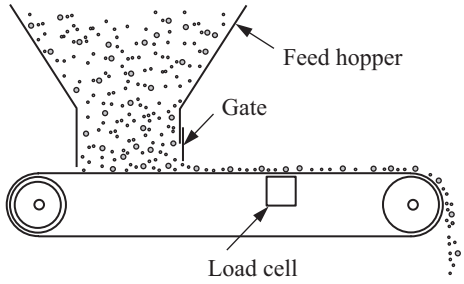


FIGURE 5.5.5 Belt feeder.

controlling the operation of the feeder, the dynamic characteristics are modeled either as a proportional element or as a derivative element.[9,10] The instantaneous feed rate in this type of feeder can be fairly smooth compared with that in a rotary or screw feeder. The flow pattern in the feed hopper is affected by the hopper inclination and scraper position. The disturbance in the flow can be reduced by using more than two scrapers.[11]

For fine powders, a special scraper is used to spread the powder uniformly on the turntable before feeding by normal operation.[12] Further, in some types of table feeders, a rotating shell is used instead of the turntable. A stationary scraper strips off the particles from the gap between the rotating shell and a plate.

Belt Feeders

In a belt feeder, an endless belt extracts the powder from a feed hopper, as shown schematically in Figure 5.5.5. Belt feeders can be easily combined with load cells; thus, they can be used as constant feed weighers or belt scales. The powder feed rate is adjusted by changing the belt speed or gate opening. The relationship between the feed rate and the belt speed is linear, but it is a nonlinear function of the gate opening.[8] Therefore, it is preferable to adjust the flow-rate by changing the belt speed instead of controlling the gate opening. Further, the dead time associated with gate opening causes deterioration of the dynamic response. For fine powders, a deaeration chamber should be attached. This chamber is also effective in preventing the flushing of the powder.

Vibrating Feeders

Vibrating feeders use either electromagnetic or electromechanical drives. Figure 5.5.6 shows an electromagnetic vibrating feeder. The vibrating trough transports the particles smoothly. The vibration frequency is selected near the resonance frequency.[13] The flow pattern in the feed hopper is affected by the type or design of the feeder. For fine powders, an appropriate system is necessary to prevent flushing. The dynamic characteristic is represented by a first-order model with time delay.[14]

Valves and Dampers

Valves and dampers are used in controlling the flow rate of free-flowing particles. The valves used commonly in powder-handling industries are cut gates, slide valves, flap valves,

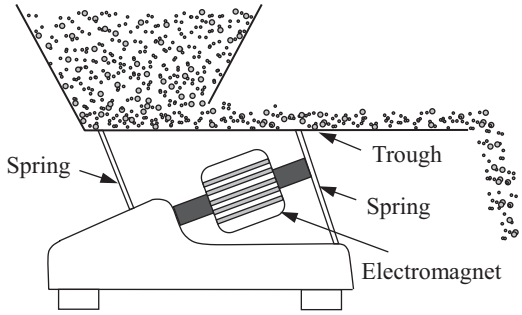


FIGURE 5.5.6 Vibrating feeder (electromagnetic type).

vibrating dampers, inclined chutes, lock hoppers, and sleeve valves. These valves are specially modified to prevent clogging of the particles. In one type of valve, the powder flow rate is controlled by blowing off a heap of particles through air injection.[15] The air is supplied through a special chute called air slide, which is made of porous material. The powder feed rate through the air slide is controlled using a gate and by adjusting the airflow rate.[16]

Micro-Feeder

The demand for submicron and nanoscale particles is increasing because of the need to produce highly functional products. However, with a decrease in particle diameter, adhesiveness increases; hence, handling of the powder becomes more complex for these small particles. This is particularly an issue for particles with diameters less than 10 μm. To reduce the adhesive forces and fluidize the particles, mechanical forces such as vibration must be continuously applied. As an example of the application of the micro-feeder, the micro-feeding of micron-scale particles using a vibrating tube can be cited.[17,18] Even for the micron-sized particles, micro-feeding is possible at a constant rate as small as a few milligrams per second. For fine adhesive powders, ultrasonic vibration is effective in the feeding process.[17] However, feeding of nanoparticles is still difficult with this type of feeder. To solve this problem, a new method was developed. Figure 5.5.7 shows the micro-feeder using a vibration shear flow mechanism.[19] This system consists of a vibrating cylindrical tube and a vibrating bottom plate. The cylinder is held vertically, and the bottom plate is placed below the vibrating tube with a narrow gap. The frequency of vibration is over 300 Hz. The particles in the tube are discharged from the narrow gap. As the fine particles tend to agglomerate owing to adhesiveness, vibration is applied to prevent the agglomerated particles from blocking the narrow gap. Nanoparticles, as well as micron-scale particles, can be continuously discharged using this type of feeder. The mass flow rate of the particles increases with an increase in the gap and/or vibration amplitude. The mass flow rate can be controlled to an accuracy of 1 mg/s.

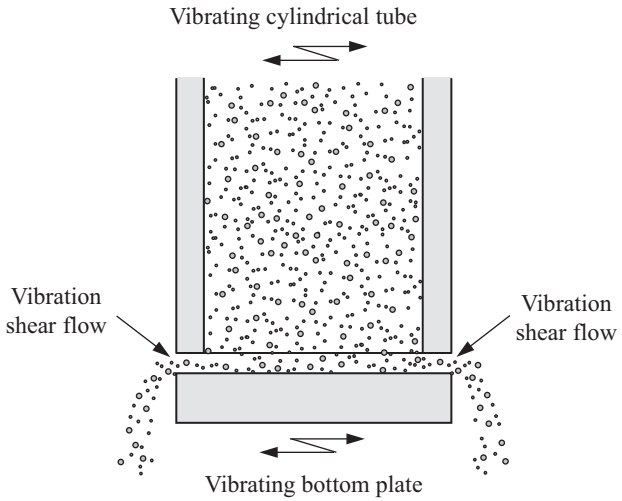


FIGURE 5.5.7 Micro-feeder using a vibration shear flow mechanism.

REFERENCES

1. Aoki, R., Ed., *Funryutai no Choso to Kyokyu Sochi (Feeders and Hoppers in Powder Handling Processes)*, Nikkan Kogyo Shimbun, Tokyo, 1963, Chap. 5.
2. McNaughton, K., Ed., *Solids Handling*, McGraw-Hill, New York, 1981, Sec. 2.
3. Jotaki, T., Tomita, Y., *J. Res. Assoc. Powder Technol. Jpn.*, 7, 534, 1970.
4. Masuda, H., Kameda, T., Iinoya, K., *Kagaku Kogaku*, 35, 917–924, 1971.
5. Finkbeiner, T., *VDI Forschungsh*, 563, 1974.
6. Johnason, J. R., *Chem. Eng.*, 76 (Oct. 13), 75, 1969.
7. Bates, L., *Trans. ASME*, B91, 295, 1969.
8. Masuda, H., Masuda, T., Iinoya, K., *J. Res. Assoc. Powder Technol. Jpn.*, 7, 479–484, 1970.
9. Masuda, H., Masuda, T., Iinoya, K., *Kagaku Kogaku*, 35, 559–565, 1971.
10. Masuda, H., Miura, K., Iinoya, K., *J. Soc. Mater. Sci. Jpn.*, 21, 577–581, 1972.
11. Masuda, H., Han, Z., Kadowaki, T., Kawamura, Y., *KONA Powder Sci. Technol. Jpn.*, 2, 16–23, 1984.
12. Masuda, H., Kurahashi, H., Hirota, M., Iinoya, K., *Kagaku Kogaku Ronbunshu*, 2, 286–290, 1976.
13. Arima, T., *Kagaku Kojo*, 9, 34, 1965.
14. Iinoya, K., Gotoh, K., *Seigyo Kogaku*, 7, 646, 1963.
15. Bendixen, C. L., Lohse, G. E., *Symposium on Solid Handling*, 1969.
16. Mori, Y., Aoki, R., Oya, K., Ishikawa, H., *Kagaku Kogaku*, 19, 16, 1955.
17. Matsusaka, S., Urakawa, M., Masuda, H., *Adv. Powder Technol.*, 6, 283–293, 1995.
18. Matsusaka, S., Yamamoto, K., Masuda, H., *Adv. Powder Technol.*, 7, 141–151, 1996.
19. Matsusaka, S., Yasuda, M., *Chem. Eng. Trans.*, 57, 823–828, 2017.

5.6 Transportation

Yuji Tomita (5.6.1)
Yoshiyuki Komoda (5.6.2)

5.6.1 TRANSPORTATION IN THE GASEOUS STATE

Introduction

The pipeline transportation of powder in the gaseous state is known as pneumatic transport. The advantage of pneumatic transport is the pipeline transport which allows for a flexible route, saves space, is not affected by surroundings, and does not affect the surroundings. In addition, it is easy to automate and maintain the system. The disadvantage is that the power consumption is high. The conveying system comprises a prime mover, an air source, a powder feeder, a conveying pipeline, a gas powder separator, and an air filter.

Figure 5.6.1 shows equipment arrangement for positive pressure systems. The powder is fed into the air flow where the air pressure is higher than the ambient pressure, and discharged at the destination of ambient pressure. Foreign matter cannot enter into the system, because the pressure of the system is higher than the surrounding pressure. Therefore powder may blow out if there is a leak in the system. Since air pressure at the feed point is higher than the ambient pressure, the continuous feeding of powder is difficult without a feeding device. If the required pressure is high, a batch system with blow tanks is adopted.

In the blow tank of top discharge shown in Figure 5.6.2 (a), the powder of relatively low density enters the conveying pipe, compared with the powder to the blow tank of bottom discharge shown in Figure 5.6.2 (b). When fine powder is treated, a fluidization device is installed. Positive systems are advantageous to deliver the powder to several destinations without contamination, and to transport the powder of a large capacity at a long distance, say, up to the distance of 8 km.

If the air source in Figure 5.6.1 is placed after the air filter, it becomes a system of negative pressure. Although the powder is continuously drawn into the pipe inlet at ambient pressure, it is difficult to discharge the powder continuously at the destination where the pressure is lower than the ambient pressure. Powder does not leak out of the pipeline, but there is the possibility that foreign matter may be sucked in if there is a leak. The available transport pressure is less than 100 kPa. Negative systems are generally used to collect powder from several points and transport it to a destination without polluting the environment. There is a combined system with advantages of both the negative and positive pressure systems, as shown in Figure 5.6.3.

The closed system is used for transporting materials like toxic, explosive, and hygroscopic powders by circulating an inert gas such as N_2. Figure 5.6.4 shows a positive closed system, where q_i is the flow rate of leakage gas from the equipment, Q_0 is the delivery gas flow rate from the compressor and Q_{in} is the flow rate of replenishment gas to the system.

Figure 5.6.5 shows the dimensionless power consumption P/gG_sL of various conveyors against gG_sL [kW], which is called a conveying scale. This is based on the questionnaire[1] conducted by the Association of Powder Process Industry and Engineering, Japan (APPIE) on the Japanese industry in 1977, where P is the motor power of the conveying system, G_s is the mass flow rate of powder, L is the transport distance, and g is the gravitational acceleration. It is clear that the value of P/gG_sL decreases when increasing the value of gG_sL, which

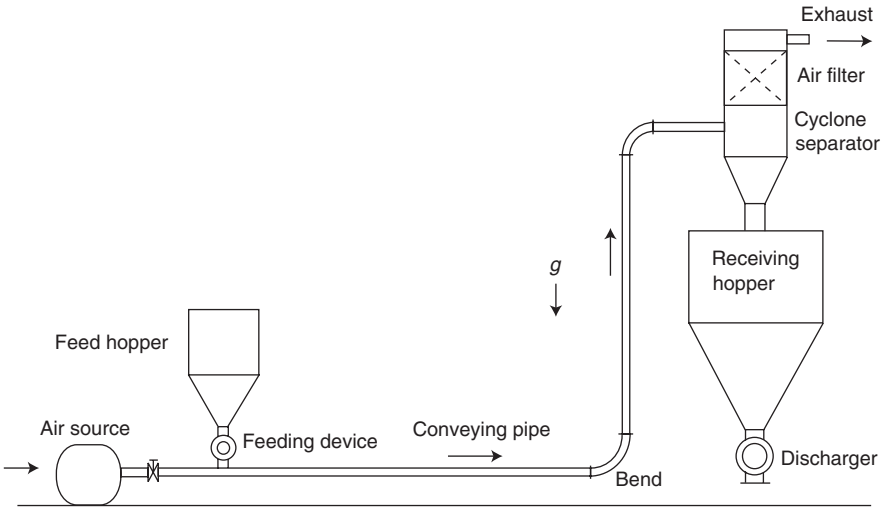


FIGURE 5.6.1 Positive pressure system.

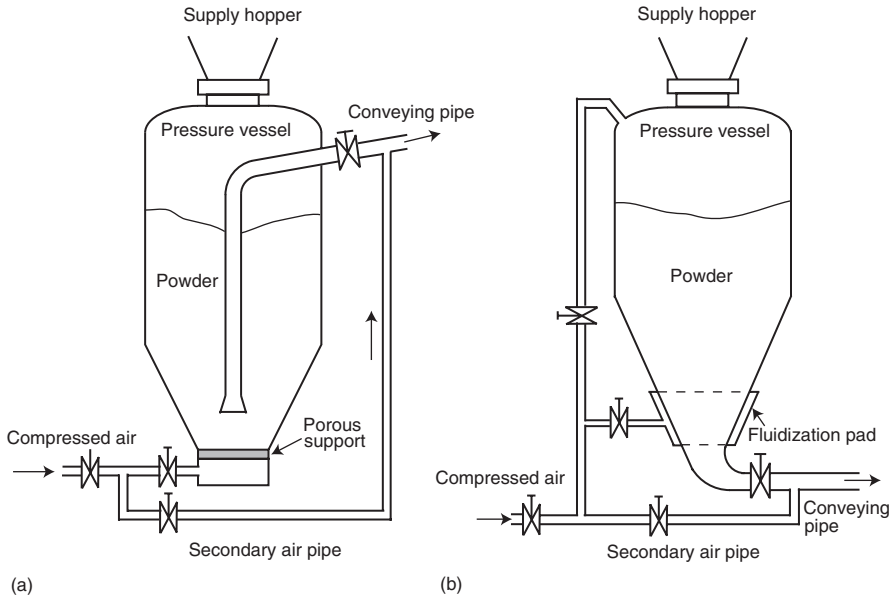


FIGURE 5.6.2 Blow tank, solid conveyors. (a) Top discharge blow tank, (b) Bottom discharge blow tank.

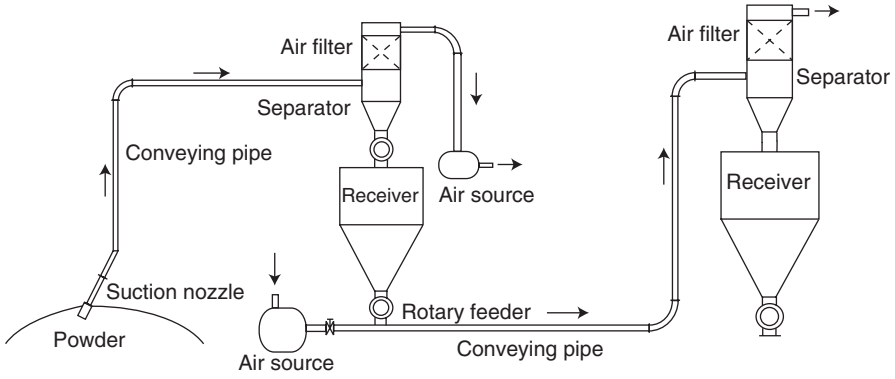


FIGURE 5.6.3 Combined system.

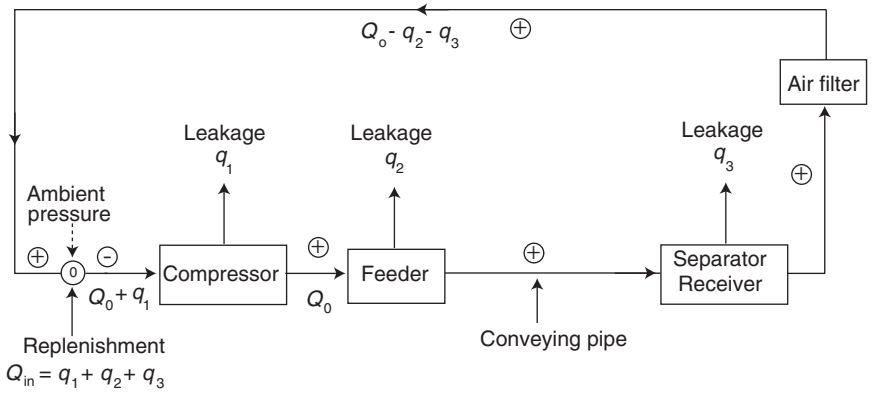


FIGURE 5.6.4 Positive closed systems.

indicates the scale merit. In the case of vertical transport, the lowest power is gG_sL and then it must be $P/gG_sL > 1$, which is confirmed by the data of bucket elevators. P/gG_sL of pneumatic conveyors are approximately ten times that of the mechanical conveyors. The loss of mechanical conveyors is caused by solid friction and is roughly estimated to be μgG_sL, where μ is the friction coefficient. Then, $P/gG_sL \sim \mu$, where the value of μ is typically $0.001 \sim 1.0$. On the other hand, that of pneumatic conveyors is caused by high-speed collision of particles with the pipe wall, and is estimated as $P/gG_sL \sim \lambda_z Fr^2/2$,

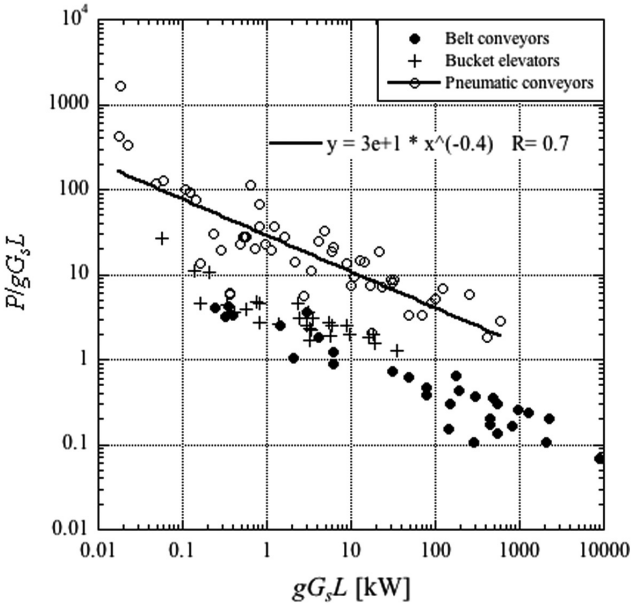


FIGURE 5.6.5 Power consumption.

where λ_z is the additional pressure loss coefficient due to powder, $Fr = U/\sqrt{gd}$ is the Froude number, d is the pipe inside diameter, U is a superficial air velocity defined by

$$U = \frac{4G_a}{\pi d^2 \rho_a} \tag{5.6.1}$$

and G_a is the mass flow rate of gas. For $U = 10$ m·s^{-1}, $d = 100$ mm, and $\lambda_z \sim 0.06$, we have $P/gG_sL \sim 3$.

For the pneumatic conveyors, the following empirical correlation is obtained

$$\frac{P}{gG_sL} = 30\left(gG_sL\right)^{-0.40} \tag{5.6.2}$$

where the unit of P and gG_sL is kW.

Particle Flow Patterns in Pipes

If ρ_a and ρ_s are the densities of gas and solid material, it is $\rho_s/\rho_a \sim 10^3$, which shows that the influence of gravity on the particle flow in pipes is important and the flow pattern of particles depends on the pipeline configuration, such as, horizontal and vertical lines.

Figure 5.6.6 schematically shows a phase diagram in a horizontal pipe with G_s as a parameter for a given pipe diameter d, where $\Delta p/l$ is the pressure drop per unit length and u_g is the terminal settling velocity of particles. Transportation of particles is possible in a region enclosed by three boundary curves, that is, "empty pipe," "fixed bed," and "with settled layer."[2] It is possible to convey a solid by different air velocities for a given G_s, and then there is an optimum air velocity for a given pipe. In design, determination of optimal pipeline parameters including pipe sizes, pipeline configuration, and air source is required when the transport distance and mass flow rate are specified for a given powder.

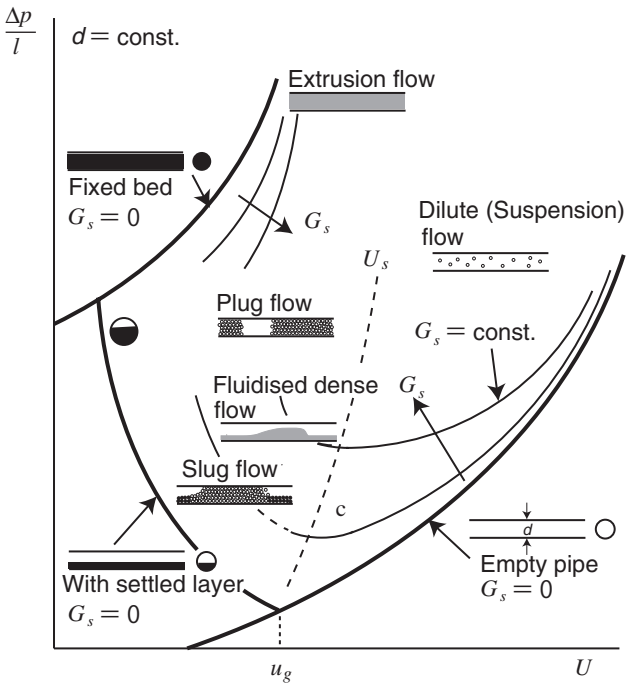


FIGURE 5.6.6 Phase diagram for horizontal flow.

Air velocity at which $\Delta p/l$ becomes minimum for a given G_s is called the saltation velocity U_s.[3] Particles are conveyed in suspension above U_s. Matsumoto et al.[4] give experimental correlations of U_c that particles smaller than U_s start to settle as:

$$m = 5.56\times10^3\left(\frac{D_p}{d}\right)^{1.43}\left(\frac{U_c}{10\sqrt{gd}}\right)^4 \quad \text{for} \quad \frac{D_p}{d} \le 1.39\left(\frac{\rho_s}{\rho_a}\right)^{-0.74}$$

$$m = 0.373\left(\frac{\rho_s}{\rho_a}\right)^{1.06}\left(\frac{u_g}{10\sqrt{gD_p}}\right)^{-3.7}\left(\frac{U_c}{10\sqrt{gd}}\right)^{3.61} \quad \text{for} \quad \frac{D_p}{d} \le 1.39\left(\frac{\rho_s}{\rho_a}\right)^{-0.74} \tag{5.6.3}$$

where:

$m = G_s/G_a$ is the solid loading ratio
D_p is the mean particle size

Low-velocity transport is advantageous to avoid pipeline erosion and particle degradation, and to reduce the power consumption. Below U_s, most particles begin to move along the pipe bottom and various flow patterns are observed depending on the particles. In the case of coarse particles, the flow becomes intermittent and unstable. With further reduction in U, a stable slug flow appears, where a particle settled layer is generated along the pipe, and particles in the settled layer are conveyed by a definite distance at every slug passing. The extrusion flow is observed near the fixed bed curve in a short pipeline, where particles are fully filled throughout the pipeline. In the case of fine particles, the flow pattern changes from the suspension flow to the fluidized, dense phase flow,

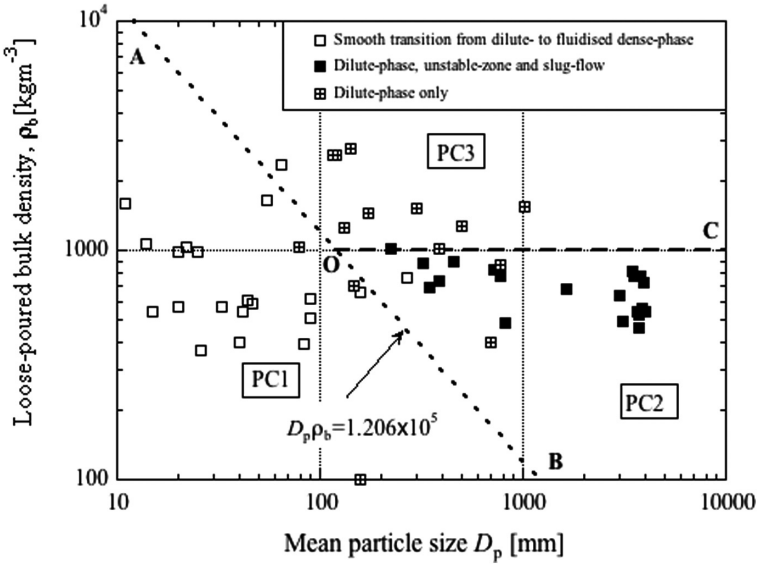


FIGURE 5.6.7 Pan diagram.

where most particles are conveyed in stratified flow or in a dune-like flow. A plug flow without the settled layer is confirmed as well.

Figure 5.6.7 shows Pan diagram[5] in which three kinds of particle flow patterns are classified using median particle size and loose poured bulk density, that is, PC1 particles which can take both dilute and fluidized dense phase flows, PC2 particles which can take dilute and slug flows, and PC3 which can take dilute flow only.

It is difficult to keep the fluidized dense phase flow in a long pipeline which could result in pipeline blockage. To keep this flow along the pipeline without the blockage, a double tube system with inner tube is used as shown in Figure 5.6.8 (a).

A double tube system with outer tube as shown in Figure 5.6.8 (b) is useful for dissolving the pipeline blockage if and when it occurs.

As a special conveying system, there are fluidized gravity conveyors, which are often known with trade names as Airslides, as shown in Figure 5.6.9.

It conveys Geldart A particles by gravity with a small slope at a reasonably low cost. If the supply of fluidized air is stopped, the conveyance ceases quickly.

In the case of vertical upward flow, a similar phase diagram is constructed where the curve of "with settled layer" is replaced "with fluidization curve" between the incipient fluidization and the terminal settling velocity. The vertically upward transportation is possible in a region enclosed by those three curves, and there is a choking velocity $U_{ch} = u_{ch}\varepsilon_{ch}$ corresponding to U_s in horizontal flow. Yang[6] gives the following empirical equations for U_{ch}.

$$G_s = \frac{\pi d^2}{4}\rho_s\left(1-\varepsilon_{ch}\right)\left(u_{ch}-u_g\right),$$

$$\frac{2gd\left(\varepsilon_{ch}^{-4.7}-1\right)}{\left(u_{ch}-u_g\right)^2} = 6.81\times10^5\left(\frac{\rho_a}{\rho_s}\right)^{2.2} \qquad (5.6.4)$$

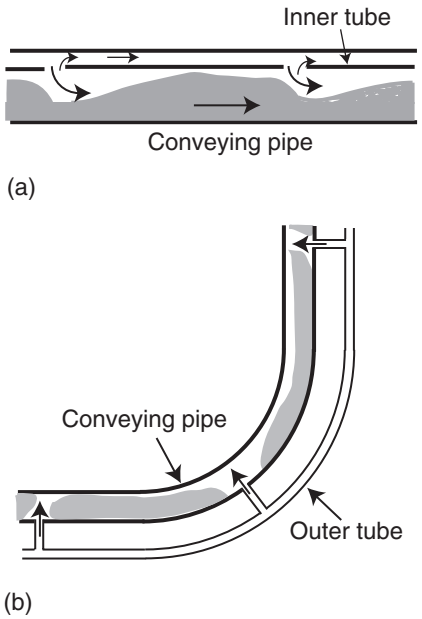


FIGURE 5.6.8 Double tube systems. (a) Inner tube type, (b) Outer tube type.

where ε_{ch}, is the voidage at the point of choking velocity. Above U_{ch} the particles adopt suspension flow. Below U_{ch}, various flow patterns are observed and some of them are similar to those in horizontal flow. If suspension flow is chosen, Equation (5.6.4) is used to check the air velocity in the vertical section.

As a special vertical upward conveying system, there are vertical pneumatic conveyors with fluidized feeder, with trade names such as Airlifts or Pneumatic elevators as shown in Figure 5.6.10. It can convey Geldart A particles continuously in an upward direction in an open system. The available pressure for the conveyance is equal to the powder head in the fluidization tank. The pressure at the top surface of the powder

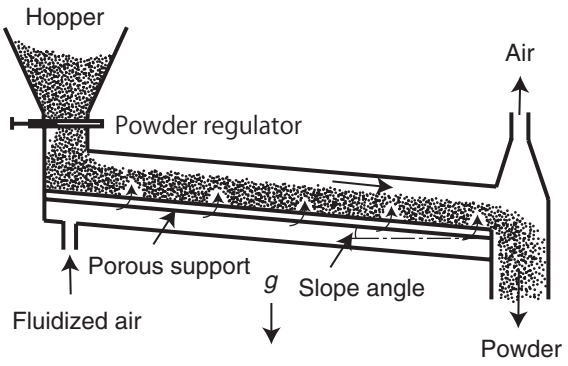


FIGURE 5.6.9 Fluidized gravity conveyors.

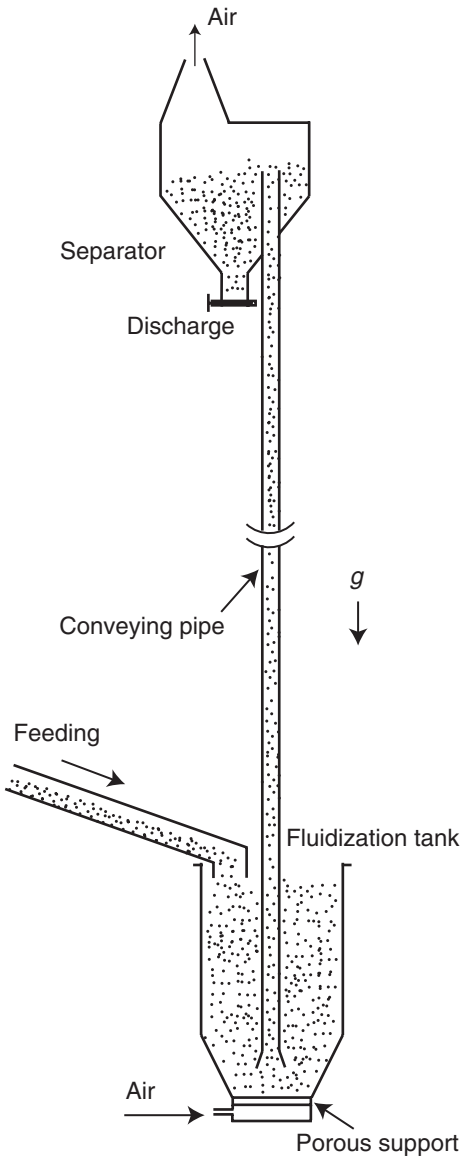


FIGURE 5.6.10 Vertical pneumatic conveyor with fluidized bed feeder.

in the tank is equal to the atmospheric pressure, which means that the pressure in the tank is sealed by the powder head.

Pressure Loss Calculation for Suspension Flow

A working model of gas-solid flow in a pipeline is a steady one-dimensional, two-phase flow approach, and the equation of motion for gas and solid phases are

$$\rho_s c u_s \frac{\mathrm{d}u_s}{\mathrm{d}s} = -\frac{\mathrm{d}}{\mathrm{d}s}(pc) - \frac{4\tau_{ws}}{d} - \rho_s c g \frac{\mathrm{d}z}{\mathrm{d}s} + F \tag{5.6.5}$$

$$\rho_a (1-c) u_a \frac{\mathrm{d}u_a}{\mathrm{d}s} = -\frac{\mathrm{d}}{\mathrm{d}s}\{p(1-c)\} - \frac{4\tau_{wa}}{d} - \rho_a (1-c) g \frac{\mathrm{d}z}{\mathrm{d}s} - F \tag{5.6.6}$$

where c is the solid concentration, u_s and u_a are the solid and gas velocities defined by

$$u_s = \frac{4G_s}{\pi d^2 c \rho_s} \tag{5.6.7}$$

$$u_a = \frac{U}{c} \tag{5.6.8}$$

where:

τ_{ws} and τ_{wa}	are the solid and gas wall shear stresses
p	is the pressure
z	is the vertical height
s	is the coordinates along the pipe axis
F	is the force on the solid by gas

Based on this model, the total pressure drop along the pipeline is given by

$$\begin{aligned}\Delta p = p_e - p_i = {} & \frac{4G_s}{\pi}\int_{u_{si}}^{u_{se}} \frac{du_s}{d^2} + \frac{4G_a}{\pi}\int_{u_{ai}}^{u_{ae}} \frac{du_a}{d^2} \\ & + g\int_{z_i}^{z_e} \{\rho_s c + \rho_a (1-c)\} dz \\ & + 4\int_{s_i}^{s_e} \left(\frac{\tau_{ws} + \tau_{wa}}{d}\right) ds \\ & + \sum_{j=1}^{n} (\Delta p_{sj} + \Delta p_{aj})\end{aligned} \tag{5.6.9}$$

where Δp_{sj} and Δp_{aj} are the local pressure losses by pipeline elements due to solids and gas, subscripts i and e are the pipe inlet and the exit, and the total length of the pipeline L is $s_e - s_i$. To estimate the first term on the right-hand side of Equation (5.6.9), it is necessary to know the information u_s in the pipeline. The following approximation is possible,

$$v \cong U - u_g \tag{5.6.10}$$

There are many types of correlation for the wall shear stresses and the following correlation is recommended,

$$(\lambda_a + m\lambda_z)\frac{\rho_a U^2}{8} = \tau_{wa} + \tau_{ws} \tag{5.6.11}$$

where:

λ_a is the pipe friction coefficient for gas
λ_z is the additional pressure loss coefficient due to solids

A number of measurements on λ_z have been reported for various solids, and Stegmaier's empirical equation[7] for several solids in horizontal flow is useful that is given by

$$\lambda_z = 2.1\frac{\sqrt{Fr_g}}{m^{0.3}Fr^2}\left(\frac{d}{D_p}\right)^{0.1}, Fr_g = \frac{u_g}{\sqrt{gd}} \tag{5.6.12}$$

For a more exact estimation, it is best to use λ_z obtained by own measurements for a given solid. An important local loss is due to 90° bends, Δp_{ab} and Δp_{sb}. E.E.U.A.[8] recommends the following estimation for ignoring the bend configurations

$$\Delta p_{ab} + \Delta p_{sb} = \xi_b \frac{\rho_b U^2}{2} \tag{5.6.13}$$

where:

$\rho_b = \rho_s c + \rho_a(1 - c)$
ξ_b = 1.5, 0.75, and 0.5 for R_b/d = 2, 4, and more than 6, respectively
R_b the radius of bend

Since the gas density changes along the pipeline, it is necessary to consider it in the calculation. For this purpose, the pipeline is divided into small sections,[8] and it is assumed that (1) the gas density is constant in each section, (2) the gas flow is isothermal, and (3) the state equation of gas is given by $\rho_a = p/RT$, where R is the gas constant and T the absolute temperature of gas. If the pressure at either side of the section is known, firstly the total pressure loss in the section is guessed and then the pressure at the other end is calculated as well as the mean pressure in the section. Also, the mean gas density and mean gas velocity U are evaluated, and then the total pressure loss in the section is calculated by Equation (5.6.9), where subscripts i and e mean both sides of the section. If this calculation is close to the first guess, the calculation is stopped. Otherwise, this calculation process is continued using the updated pressure loss until a given convergence level is reached. In the positive pressure system, the pressure at a pipe exit is known, and the calculation can start from the pipe exit toward the pipe inlet, while in the negative pressure system it is *vice versa*. It is important to keep U always larger than the design velocity, in particular, at the pipe inlet where U is minimum. Since the pressure loss is in proportion to U,[2] it is effective to suppress the increase in U by increasing the pipe diameter in a stepwise fashion[8] towards the downstream.

The decrease in the pressure loss results in a decrease in the power consumption P, which is approximately estimated by

$$P = p_0 Q_0 \ln\left(1 + \frac{\Delta p}{p_0}\right) = \frac{G_a RT}{m}\ln\left(1 + \frac{\Delta p}{p_0}\right) \tag{5.6.14}$$

where:

Δp is the total pressure loss along the pipeline
p_0 is the ambient pressure
Q_0 is the volumetric flow rate of free air

Equation (5.6.14) shows that P decreases when m is high and T is low.

Operating Points of Air Sources Working on Pipelines

Figure 5.6.11 shows characteristic curves of a blower and compressor as air sources, and those of conveying pipeline pressure drop, where Δp is the delivery pressure of air sources and the pipeline pressure drop, and Q is the volumetric flow rate of air source and that in the pipeline. Operating points of air source are intersections of the air source and pipeline characteristics. The stable operating point is that at a higher flow rate, that is, point B for blower or C for compressor. The points B′ and C′ are unstable and do not realize as the operating point. It is important for air source characteristics to pass the design point (Q, Δp), which is in the pipeline characteristics, stably and at high efficiency. If this does not happen, it is necessary for air source characteristics to pass the design point, which is possible by changing the revolution of air sources applying an inverter or by inlet valve operation. If a rotary feeder is chosen as the feeding device, air leakage ΔQ from the feeder should be considered, and the air source characteristics should pass a point ($Q + \Delta Q$, Δp) stably. Further, if G_s depends on Q, the feed rate characteristics of the feeder should be also taken into account to realize the operation at the design point.

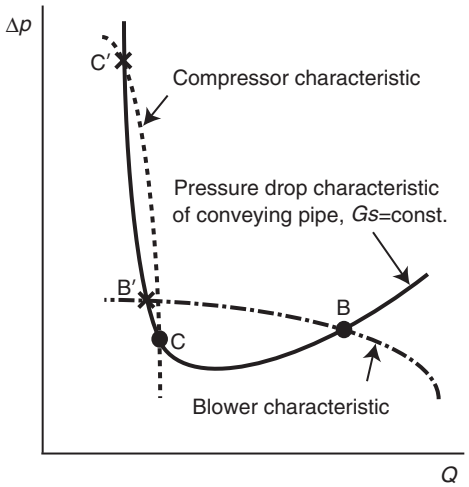


FIGURE 5.6.11 Operating points of air sources.

5.6.2 TRANSPORTATION IN THE LIQUID STATE

Hydrotransport of particulate materials is an acknowledged alternative to conventional forms of transport, such as pneumatic or mechanical conveying. In the mining industries, for example, hydrotransport techniques are now widely adapted to reduce the manpower and operational cost. For long conveying distances and large conveying capacity, the drag reduction of slurry in a pipe flow by additives, such as polymers and surfactants, must be required to reduce the cost, and the reduction mechanism has been extensively studied.[9–12] Recent demands, such as the enlargement of applicable size of particles, the utilization of non-Newtonian fluids as the liquid phase, and the minimization of erosion are important subjects to be overcome in the field of hydrotransport.

Slurry flows are categorized into two groups: Homogeneous or non-settling slurries and Non-homogeneous or settling slurries.

Homogeneous Slurries

The slurry transportation system for a given conveying capacity is usually designed by determining the pipe diameter and estimating the frictional loss. The homogeneous slurries without significant settling and floating particles are usually non-Newtonian fluids, whose characteristics can be tested by using a Couette viscometer. The suitable rheological model should be selected by fitting the data of the shear stress τ versus shear rate $\dot{\gamma}$ to the models described in Chapter 2.10.2, as well as by taking into account the shear rate range of the practical problem.

In the case of laminar flow in the cylindrical tube of inner diameter D $(=2R)$ and length L, the analytical solutions for the relationship between the flow rate Q and the pressure drop ΔP were derived, as follows.[13]

For the power-law fluids expressed by $\tau = m\dot{\gamma}^n$,

$$Q = \left(\frac{\pi R^3}{1/n+3}\right)\left(\frac{\tau_R}{m}\right)^{1/n} \tag{5.6.15}$$

where:

$\tau_R(=\Delta PR/2L)$ is the wall shear stress
m and n are the consistency and power law indices

For the Bingham fluids expressed by $\tau = \eta\dot{\gamma} + \tau_y$,

$$Q = \left(\frac{\pi R^3 \tau_R}{4\eta}\right)\left[1 - \frac{4}{3}\left(\frac{\tau_y}{\tau_R}\right) + \frac{1}{3}\left(\frac{\tau_y}{\tau_R}\right)^4\right] \tag{5.6.16}$$

where:

η is the viscosity
τ_y is the yield stress

In the case of turbulent flows, the prediction methods are proposed by Kemblowski and Kolodziejski for power-law fluids[14] and by Wilson and Thomas for Bingham fluids.[15]

Homogeneous slurries are prepared by matching the density between suspended particles and the medium fluid. Even in case of homogeneous slurries, the local non-uniformity of particle concentration arises from the flow geometry, where the non-uniform distribution of shear rate or rheological properties is induced. This is called "shear-induced migration."[16]

Non-Homogeneous Slurries

Non-homogeneous slurries cause the settling of solid particles. Thus, the velocity field and particle concentration distribution are significantly different between horizontal and vertical tube flows. However, in the long-distance transportation of slurries, the horizontal pipeline flow is mainly concerned. Hence, only the horizontal transportation is discussed in this section.

According to the extensive study by Turian and Yuan,[17] below the critical slurry velocity, v_c, which is called "deposition velocity" or "limit-deposit velocity," most of particles settle down to form the stationary bed on the bottom of the pipe and the liquid phase flows above the bed, as shown schematically in Figure 5.6.12. This is the unwilling flow of slurry transportation. As the slurry velocity increases, particles are entrained by the liquid flow from the moving bed, which is called "saltation flow." At a higher slurry flow, the bed disappears and all the particles flows as a slurry, but lighter particles flow at the upper part and heavier particles flow at the lower part of the tube. This is called "heterogeneous flow." When the slurry velocity is high enough, all the particles of the slurry flows homogeneously. This homogeneous flow is the most appreciable flow for the slurry transportation. Because we can estimate the flow rate Q by measuring the pressure drop ΔP if the friction factor f is known, the following empirical equations defined by $f=(-\Delta P/L)(D/2\rho v^2)$ are proposed for the above-mention flows:[17]

For the flow with a stationary bed (Region 0 in Figure 5.6.12):

$$f = f_w + 0.4036C^{0.7389} f_w^{0.7717} C_D^{-0.4054}\left(\frac{v^2}{Dg(s-1)}\right)^{-1.096} \tag{5.6.17}$$

where:

f_w is the friction factor for the fluid flow without particles
C is the solid volume fraction
C_D $(=(4/3)gd(s-1)/v_\infty^2)$ is the drag coefficient for a free-falling sphere
g is the gravity acceleration
$s(=\rho_s/\rho)$ is the density of solid ρ_s normalized by liquid density ρ
d is the diameter of solid particle
v_∞ is the terminal velocity of particle settling in an unbound fluid
v is the cross-sectional averaged velocity

For the saltation flow (Region 1):

$$f = f_w + 0.9857C^{1.018} f_w^{1.046} C_D^{-0.4213}\left(\frac{v^2}{Dg(s-1)}\right)^{-1.354} \tag{5.6.18}$$

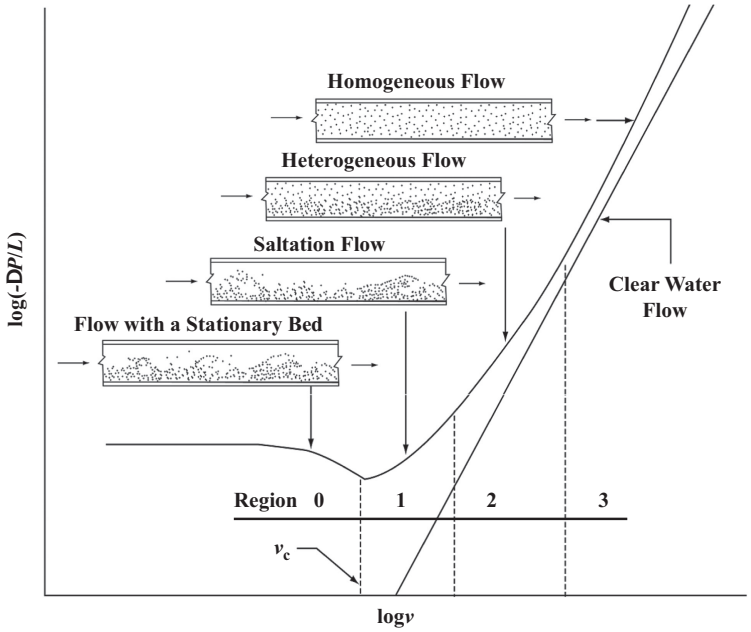


FIGURE 5.6.12 Flow patterns of slurries and pressure drop versus slurry velocity (redrawn figure based on data in the figure of Turian and Yuan, 1977, Flow of slurries in pipelines, *AIChE J.*, 23, 232–243).

For the heterogeneous flow (Region 2):

$$f = f_w + 0.5513C^{0.8687} f_w^{1.200} C_D^{-0.1677} \left(\frac{v^2}{Dg(s-1)} \right)^{-0.6938} \tag{5.6.19}$$

For the homogeneous flow (Region 3):

$$f = f_w + 0.8444C^{0.5024} f_w^{1.428} C_D^{0.1516} \left(\frac{v^2}{Dg(s-1)} \right)^{-0.3531} \tag{5.6.20}$$

As mentioned above, the deposition velocity is the lower limit of the slurry transportation velocity, below which the stable pipeline operation is very difficult. The deposition velocity was discussed by Durand,[18] Oroskar and Turian,[19] and Gillies and Shook.[20]

Gillies et al.[21] have proposed a method to predict the pressure drop in the horizontal slurry pipeline flow based on the two-layer model. The three-layer model has been proposed by Doron and Barnea.[22] Although old models are still used in industrial applications, they sometimes do not give a satisfactory result for the system composed of large pipe diameter, very long pipe lines, and broad particle size distribution. Recently, Delft Head Loss & Limit Deposit Velocity (DHLLDV) Framework, by which the spatial distribution of particle volumetric concentration in a pipe is evaluated, was proposed by Miedema.[23]

REFERENCES

1. Association of Powder Process Industry and Engineering, Japan, *Bulk Handling Technology of Powder*, Tokyo, Nikkan Kogyo Sinbun, 1985.
2. Welschof, G., *VDI-Forsch.-Heft*, 492, 1962.
3. Zenz, F.A., *Ind. Eng. Chem. Fundam.*, 3–1, 65–75, 1964.
4. Matsumoto, S., Kikuta, M., Maeda, S., *J. Chem. Eng. Jpn*, 10–4, 273–279, 1977.
5. Pan, R., *Powder Technol.*, 104, 157–163, 1999.
6. Yang, W.C., *Powder Technol.*, 35, 143–150, 1983.
7. Stegmaier, W., *Fördern Heben*, 28–5/6, 363–366, 1978.
8. Engineering Equipment Users Association, *Pneumatic Handling of Powdered Materials*, London, 1963.
9. Usui, H., Irvine, T.F. Jr., 1980, Drag Reduction in a 90° Triangular Open Channel, *J. Rheol.*, 24, 5, 525–549.
10. Usui, H., Sano, Y., 1983, Turbulence structure of dilute drag-reducing polymer solutions in a rectangular open channel flow, *AIChE J.*, 29, 611–617.
11. Usui, H., Maeguchi, K., Sano, Y., 1988, Drag reduction caused by the injection of polymer thread into a turbulent pipe flow, *Phys. Fluids*, 31, 9, 2518–2523.
12. Usui, H., Saeki, T., 1993, Drag Reduction and Heat Transfer Reduction by Cationic Surfactants, *J. Chem. Eng. Jpn*, 26, 1, 103–106.
13. Skelland, A.H.P., *Non-Newtonian Flow and Heat Transfer*, Wiley, New York, 1967, pp. 82 and 110.
14. Kemblowski, Z., Kolodziejski, J., 1973, Flow Resistances of non-Newtonian Fluids in Transitional and Turbulent Flow, *Int. Chem. Eng.*, 13, 265–279.
15. Wilson, K.C., Thomas, A.D., 1985, A new analysis of the turbulent flow of non-newtonian fluids, *Can. J. Chem. Eng.*, 63, 593–546.
16. Tehrani, M.A., 1996, An experimental study of particle migration in pipe flow of viscoelastic fluids, *J. Rheol.*, 40, 1057–1078.
17. Turian, R.M., Yuan, T.F., 1977, Flow of slurries in pipelines, *AIChE J.*, 23, 232–243.
18. Durand, R., *Proceedings of the Minnesota International Conference on Hydraulic Conveying*, 89, 1953.
19. Oroskar, A.R., Turian, R.M., 1980, The critical velocity in pipeline flow of slurries, *AIChE J.*, 26, 550–558.

20. Gillies, R.G., Shook, C.A., 1991, Deposition velocity correlation for water slurries, *Can. J. Chem. Eng.*, 69, 1225–1227.
21. Gillies, R.G., Shook, C.A., Wilson, K.C., 1991, An improved two layer model for horizontal slurry pipeline flow, *Can. J. Chem. Eng.*, 69, 173–178.
22. Doron, P., Barnea, D., 1993, A three-layer model for solid-liquid flow in horizontal pipes Author links open overlay panel, *Int. J. Multiphase Flow*, 19, 1029–1043.
23. Miedema, S.A., 2015, A head loss model for homogeneous slurry transport for medium sized particles, *J. Hydrol. Hydromech.*, 63, 1–12.



Taylor & Francis
Taylor & Francis Group
http://taylorandfrancis.com

5.7 Fluidization and Fluidized Bed

Xinhua Liu and Shanwei Hu (5.7.1)
Xinhua Liu, Bona Lu, Xizhong Chen and Limin Wang (5.7.2)

5.7.1 OVERVIEW OF FLUIDIZATION

Fluidization is a process where solid granules are transformed into a fluid-like state through suspension in a stream of gas, liquid, or their mixture. Consider a container with an open top and perforated plate at the bottom: solid particles will pack closely at the bottom under the action of gravity, and the total mass of particles is supported by the plate. If a stream of fluid flows upwards through the bed of particles at a low flow rate, the fluid merely percolates through the void spaces between stationary particles, and the particle bed remains in a *fixed* or *packed* state. As the flow rate of the fluid increases to a value at which the drag force of the fluid just counterbalances the effective weight of the particles, *minimum fluidization* is thought to be reached and the corresponding fluid velocity is called the *minimum fluidization velocity* (U_{mf}). As the fluid velocity is increased to near the terminal velocity (U_t) of the particles, the bed expands continuously and the particles are pushed apart to act like a fluid. This state is called *fluidization*.

According to the motion of the particles and fluid as well as the expansion characteristics of the bed, fluidization can be designated as *particulate* or *aggregative*.[1,2] In a liquid–solid system, increasing the liquid velocity from zero to greater than U_{mf} usually results in a smooth, gradual expansion of the particle bed. Such a phenomenon is called particulate fluidization. However, in a gas–solid system, instability arising from vigorous gas bubbling and particle agglomeration intensifies with increasing gas velocity (u) above U_{mf}. Such a bed can be called an aggregative fluidized bed, which is the topic of this chapter.

Pressure Drop across a Particle Bed

The pressure drop (Δp) across a particle bed is commonly used as a rough indication of fluidization quality, especially when visual observations are not available.[3] Figure 5.7.1 exemplifies the variation of Δp with u in a typical gas–solid system. When air flows through a static particle bed at a relatively low u, Δp is approximately proportional to u and can be calculated using the well-known Ergun equation:[4]

$$\Delta p = \left[150 \frac{(1-\varepsilon)^3}{\varepsilon^3} \frac{\mu u}{d_p^2} + 1.75 \frac{(1-\varepsilon)}{\varepsilon^3} \frac{\rho_f u^2}{d_p} \right] H \qquad (5.7.1)$$

where

H and ε are the height and average voidage of the particle bed, respectively
d_p is the particle diameter

As u increases further, Δp usually reaches a maximum value (Δp_{max}) at U_{mf}, which is slightly higher than Δp of the static bed because of the hysteresis effect.[5] Beyond U_{mf}, the bed expands and heterogeneity appears, but Δp remains invariable and equals the weight of particles even as u increases,

$$\Delta p = (\rho_p - \rho_f)(1-\varepsilon) g H \qquad (5.7.2)$$

The Δp values measured while decreasing u of the air gradually are depicted as a solid line in Figure 5.7.1. Under this condition, the particles will settle down to form a loose fixed bed with a voidage at the minimum fluidization state of ε_{mf}. Using this method, U_{mf} can be determined to avoid the influence of the hysteresis effect.

As u is increased until it is greater than U_t, the magnitude of the drag force becomes large enough to facilitate the ceaseless entrainment of particles from the top outlet of the bed. Thus, Δp decreases gradually until all of the particles are blown out of the bed.

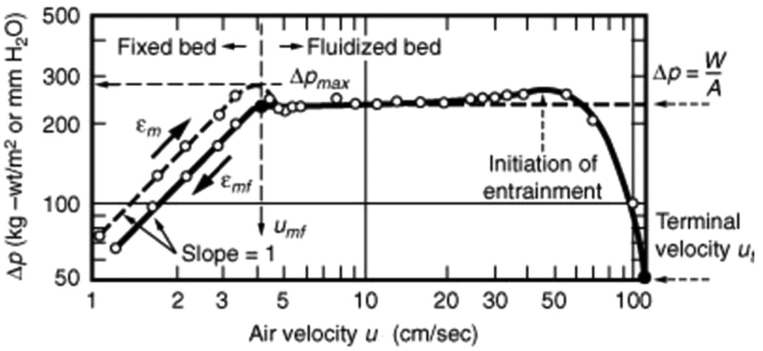


FIGURE 5.7.1 Dependence of pressure drop Δp on gas velocity u.[6]

Local Heterogeneity in Gas–Solid Fluidized Beds

Local heterogeneity in gas–solid fluidized beds is characterized by a two-phase structure consisting of a particle-rich dense phase (emulsion or cluster) and a gas-rich dilute phase (bubble or dilute phase). These interfacial phenomena, gas bubbling and/or particle clustering, can be described by the term "mesoscale structure," which is a relative concept related to a level between the particle and reactor scales. The formation and dynamic evolution of particle clusters and gas bubbles, as nonequilibrium and nonlinear behavior, strongly affect the fluid dynamics as well as the heat and mass transfer in gas–solid fluidized beds.

Particle clusters and gas bubbles can be detected using invasive tools such as optical or electrical fiber probes[7] or noninvasive techniques like high-speed video imaging,[8] phase Doppler velocimetry,[9,10] and particle imaging velocimetry (PIV).[11,12] In general, the voidage of the dilute and dense phases (ε_f and ε_c, respectively) as well as the volume fraction of the dense phase (f) are used to describe the two-phase structure in gas–solid fluidized beds. These parameters can be evaluated by measuring the changes of local resistivity, capacitance, induction, pressure, or optical attenuation in a bed.

The variation of bed density in a fluidized bed measured by an optical probe is plotted in Figure 5.7.2, where $p(\varepsilon)$ and its integral $\int_1^{\varepsilon} p(\varepsilon)d\varepsilon$ are the probability density distribution and probability distribution, respectively. Two peak values appear on the $p(\varepsilon)$ curve, implying mesoscale structures, i.e. dense and dilute phases, coexist in the system. Consequently, the value of $\int_1^{\varepsilon} p(\varepsilon)d\varepsilon$ corresponding to the valley between the two peaks represents the volume fraction of the dilute phase ($1-f$).[13] The drastic fluctuation of the curve indicates that the dilute and dense phases appear alternately in time and space, illustrating the complexity of the mesoscale structures in gas–solid fluidized beds.

Liu et al.[11] investigated the gas–solid interaction in the dense phase by measuring the gas flow penetrating through dynamic particle clusters in a gas–solid fluidized bed. In their experiments, both the gas and solid velocity fields were visualized simultaneously by PIV using fluorescent tracer particles. Based on the calculation of the solids concentration gradient, a general method was proposed to identify particle clusters from solids concentration fields, especially near the bed wall, because the fluctuation of local solids concentration can be filtered efficiently through this treatment of the data. Figure 5.7.3 illustrates the measured particle images and velocity fields as well as the variation of gas penetrating flow with the voidage inside particle clusters. The gas–solid slip velocity inside particle clusters and gas penetrating flow through dynamic particle clusters increase with cluster internal voidage. Thus, the increase of voidage in the identified clustering zone should be taken into account in the mathematical modeling of particle clusters in gas–solid fluidization.

Regime Transition of Gas–Solid Fluidization

In an aggregative fluidization system, as shown in Figure 5.7.4, regimes such as bubbling, turbulent, and fast fluidization are

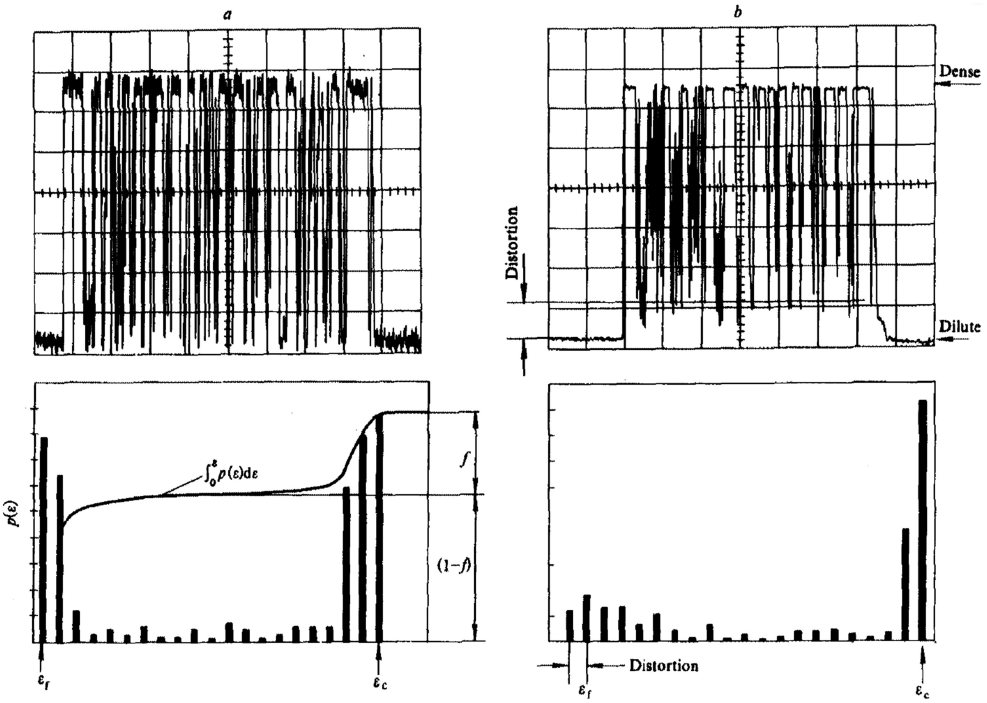


FIGURE 5.7.2 Determination of ε_c, ε_f, and f using an optical probe.[13]

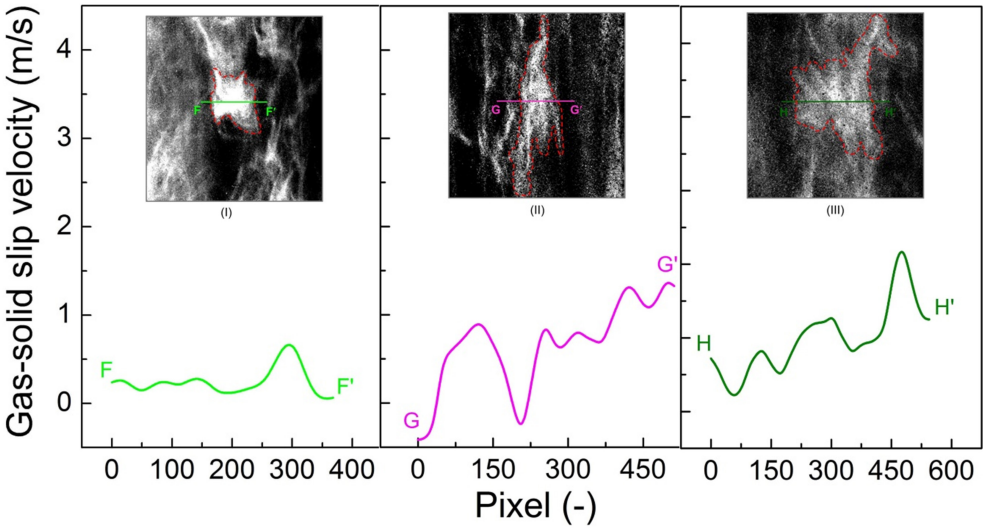


FIGURE 5.7.3 Variation of the measured gas–solid slip velocity along lines FF, GG, and HH'.[11]

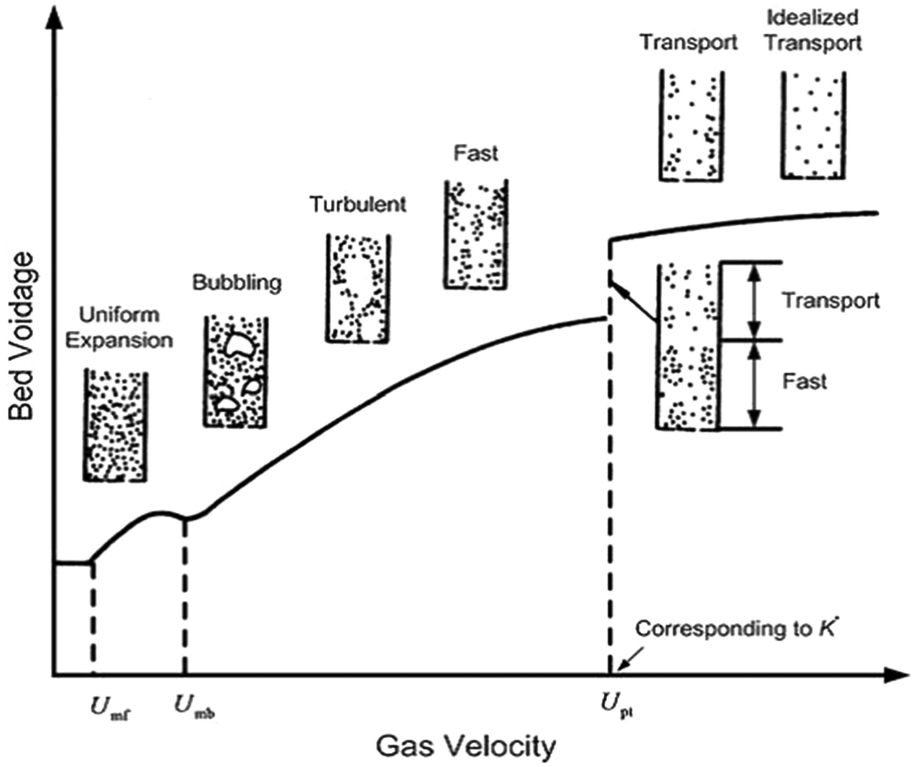


FIGURE 5.7.4 Aggregative particle–fluid two-phase flow.[13]

usually used to describe the configuration of phase combinations dependent on operating parameters.[13]

If a stream of gas passes upwards through a bed of particles at a very low u, the particles in the bed stay quiescent as the gas flows through interstices; that is, in the *fixed bed state*. The transition from a fixed bed to an aggregative fluidization bed is defined by U_{mf}. This regime features the formation of gas bubbles beyond U_{mf} for coarse particles or minimum bubbling velocity (U_{mb}) for fine particles,[14] and thereby is called *bubbling fluidization*. The onset of *turbulent fluidization* is characterized by the maximum amplitude of bed pressure fluctuation.[15] However, the regime transition from bubbling to turbulent fluidization is difficult to determine experimentally because it is generally a gradual process.[16]

If the gas velocity is high enough to alter the shapes of gas bubbles and enable the appearance of a new two-phase structure, that is, particle clusters dispersed as a discontinuous phase in a dilute continuous phase, the system enters the *fast fluidization* regime corresponding to the onset of considerable particle entrainment.[17,18] As u increases further, the

fast fluidization suddenly terminates at a transition velocity (U_{pt}) and the system enters the *dilute transport* regime. The solid circulation rate corresponding to U_{pt} is called the saturation carrying capacity (K^*). Beyond U_{pt}, the system becomes pseudo-homogeneous, with particles behaving discretely.[13]

As described above, when a fluid flows upwards through a bed with a fixed solids inventory (I_m) and suspends the particles with negligible entrainment, this situation is generally called classical fluidization. The concept of fluidization was extended to vertical particle–fluid systems in which both the particles and fluid can move independently either upwards or downwards.[19] For example, in a circulating fluidized bed (CFB), the particles are entrained by the airflow and then circulated back into the bed after separating the gas from the solids.[17] In cocurrent or counter-current downer reactors, the solids move downwards in the direction of gravity in a downward or upward fluid flow, respectively.[19] All these processes are collectively termed *generalized fluidization*.

Overall Heterogeneity in Gas–Solid Fluidization Beds

A typical fluidization system such as CFB riser contains both local mesoscale heterogeneous structures and overall nonuniform distribution of voidage or solids concentration in the axial and radial directions.

Li and Kwauk[20] investigated the axial variation of the cross-sectional average voidage in a CFB riser and found that an S-shaped profile represented the coexistence of a dilute region at the top and dense region at the bottom of the riser. Li et al.[21] experimentally studied the variation of the axial voidage profile with operating conditions such as G_s, U_g, and I_m in a CFB riser with an internal diameter of 90 mm using a scanning transducer valve system. As shown in Figures 5.7.5a and b, the voidage curves for G_s = 14.3 and 24.1 kg/m^2 s are S-shaped, consisting of two different regions with a transition between them. The variation of I_m did not change the voidage at the top or bottom of the riser, but affected the axial position of the inflection point between the top dilute and bottom dense regions. Increasing I_m caused the transition point to move up, while decreasing I_m resulted in the reverse effect. In this situation, the axial S-shaped profile of voidage may disappear and the flow regime will become dense or dilute transport.

A typical radial voidage profile in a gas–solid fluidized bed was observed to consist of a dilute core region occupying about 70% to 85% of the column radius, and a denser annular region near the wall. Local solid velocity in the core region is generally higher and does not change much in comparison with the lower and abruptly decreasing gas u in the annular region.[22] Although the radial voidage distribution in a laboratory-scale CFB riser depends on operating conditions, as illustrated in

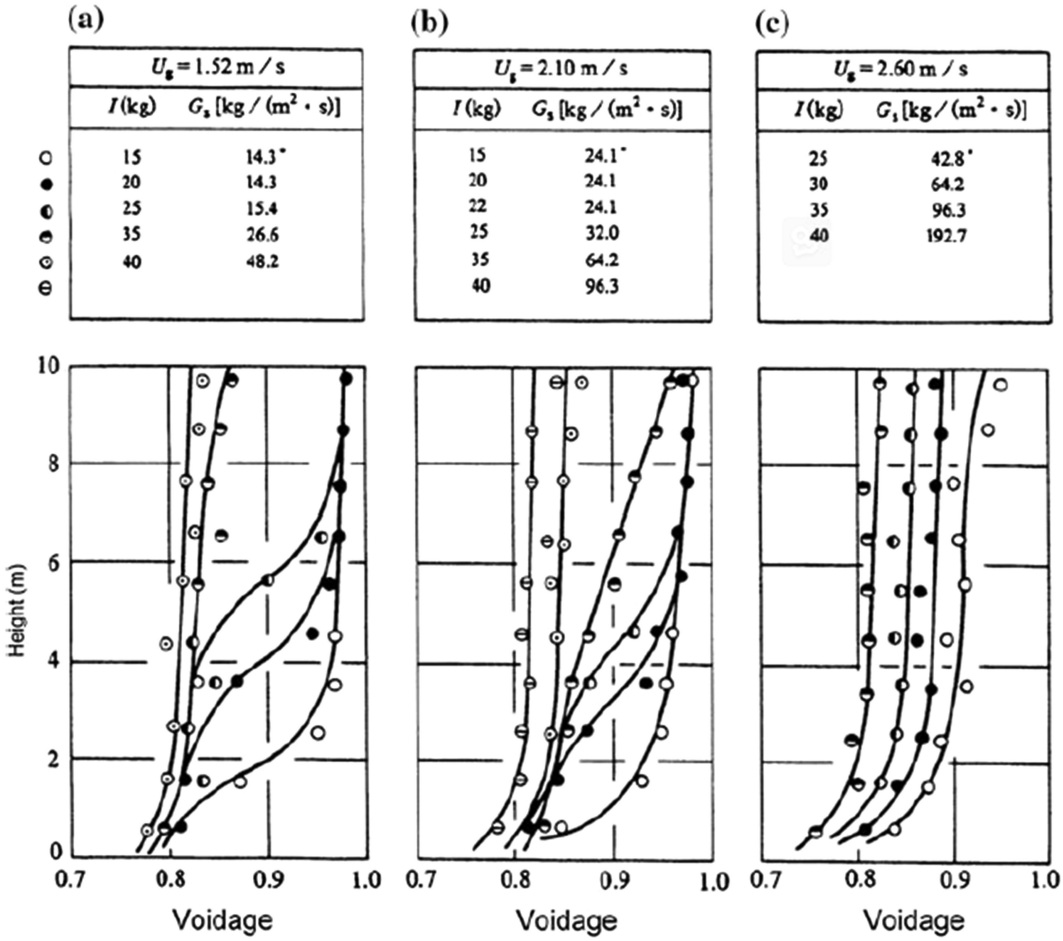


FIGURE 5.7.5 Axial voidage profiles for a fluid catalytic cracking (FCC)/air system.[21]

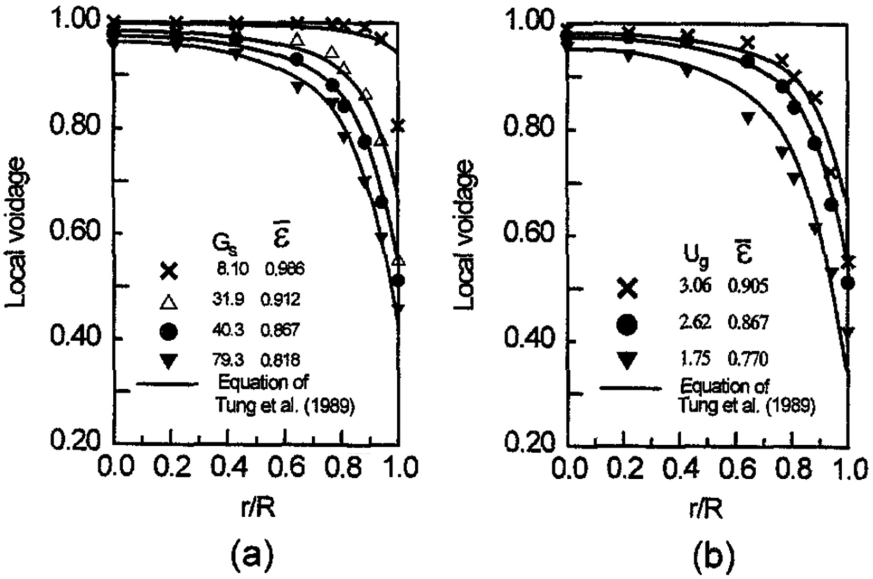


FIGURE 5.7.6 Influence of operating conditions on the radial voidage distribution for an FCC/air system. (a) U_g = 2.62 m/s and (b) G_s = 43 kg/m^2 s.[24]

Figure 5.7.6, the detailed expression was found to be a function of only cross-sectional average voidage, which can be approximated as an exponential function.[23,24]

NOMENCLATURE

d: diameter (m)
f: volume fraction of the dense phase
g: gravity acceleration (m/s^2)
G_s: solids circulation rate or solids flux (kg/m^2 s)
H: height (m)
I_m: solid inventory (kg)
p: pressure (Pa)
$p(\varepsilon)$: probability density distribution
U: superficial velocity (m/s)
ε: voidage
μ: shear viscosity (Pa·s)
ρ: density (kg/m^3)

SUBSCRIPTS

c: dense phase
f: dilute phase
g: gas
max: maximum
mb: minimum bubbling
mf: minimum fluidization
p: particle
t: terminal velocity

5.7.2 COMPUTATIONAL METHODS FOR FLUIDIZATION

Fluidization technology is one of the most important and widely-used technologies in the industry, due to its excellent mass and heat transfer characteristics, continuous powder handling ability and high gas and solids throughput. In recent decades, computer simulation has appeared as an effective tool in studying the hydrodynamics of gas–solid fluidization, and numerous methods have been proposed to explore the nature of gas–solid flow at different spatiotemporal scales. In this chapter we briefly introduce a multiscale method for modeling gas–solid flows, from steady-state modeling for quick engineering design, continuum model for industrial scale reactor simulation, discrete particle method for lab-scale reactor simulation to direct numerical simulation for exploring the underlying mechanics.

5.7.2.1 Steady-State Modeling

Steady-state modeling is usually the first option to realize real-time simulation of industrial processes for quick engineering design. A typical industrial gas–solid system generally consists of many segments with various geometries and sizes. Moreover, the gas–solid flow itself also possesses multiscale complexity because of the variations of temporally and spatially heterogeneous structures with operating conditions. There is still no general theoretical method for full-loop modeling of steady-state hydrodynamics in complex gas–solid reactors, although great efforts have been made. Here we introduce a method developed at the Institute of Process Engineering, Chinese Academy of Sciences.

The energy-minimization multiscale (EMMS) model, which was originally proposed for gas–solid fast fluidization, enables prediction of local heterogeneity, regime transitions, and the choking phenomenon in gas–solid two–phase flow.[13] In the EMMS model, eight parameters are used to describe the state of a system, as shown in Figure 5.7.7, where ε_c, f, U_c, U_{pc}, and d_{cl} describe the dense phase and U_f, U_{pf}, and ε_f explain the dilute one. Six hydrodynamic equations can be formulated to describe the mass and momentum conservation.

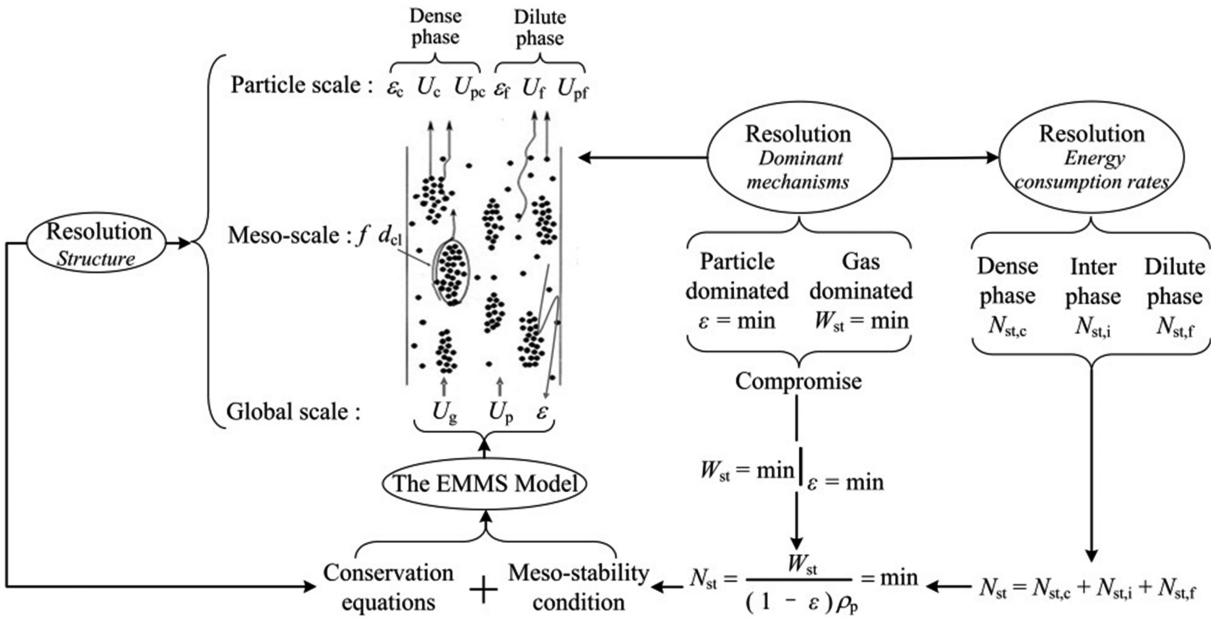


FIGURE 5.7.7 Principle of the EMMS model (Modified from Li and Kwauk, *Particle-Fluid Two-Phase Flow*, Metallurgical Industry Press, Beijing, 1994.)

In cocurrent-up two-phase flow, the fluid tends to choose a flow path with minimal resistance, while the particles tend to arrange themselves with minimal potential energy. They have to compromise in competition, which is characterized by both minimal energy consumption for the gas and minimal voidage for the particles:

$$W_{st} \to \min\big|_{\varepsilon \to \min} \tag{5.7.3}$$

Thus, we can deduce a stability condition for the EMMS model as follows:

$$N_{st} = \frac{W_{st}}{(1-\varepsilon)\rho_p} \to \min \tag{5.7.4}$$

where, N_{st} denotes the mass-specific energy dissipation for suspending and transporting particles. The detailed characteristics of solutions and their theoretical implications were explored by retrieving all roots using a rigorous numerical approach, which enabled the physical mapping of the fluidization regimes.[25]

Unlike in gas–solid fast fluidization, where particle clusters form mesoscale heterogeneous structure, in gas–solid bubbling fluidization, structural heterogeneity originates from the formation of gas bubbles. By analyzing the interaction mechanism between the dense emulsion and dilute bubble phases in gas–solid bubbling fluidization, an EMMS bubbling model was established to realize the hydrodynamic modeling of gas–solid bubbling fluidization without introducing bubble-specific empirical correlations.[16]

As shown in Figure 5.7.8, a gas–solid bubbling fluidization system can be resolved into three subsystems including the dense emulsion phase, dilute bubble phase, and the interphase (gas bubbles with no particles) between them. Such a system can be described by six independent parameters, among which ε_e, U_{ge}, and U_{pe} represent the emulsion phase and f_b, U_b, and d_b describe the bubble phase. Thus, the force balance equations for the emulsion and bubble phases as well as continuity equations for the gas and solids can be established (Figure 5.7.8).

By considering the expansion work of gas bubbles against the normal pressure stress in the emulsion phase, a stability condition can be formulated to close the gas–solid bubbling model, that is

$$N_{st}/N_T = \left(N_{st,e} + N_{st,i} + N_{ex,i}\right)/N_T = \min \tag{5.7.5}$$

where

$N_{st,e}$ and $N_{st,i}$ are the suspension and transporting energy dissipation rates in the emulsion phase and interphases, respectively

$N_{ex,i}$ is the energy dissipation rate resulting from the expansion of gas bubbles

At given U_g and G_s, the EMMS bubbling model can be solved numerically using a two-dimensional optimization method.

In a CFB system, if the riser operates far away from the choking point, the gas–solid flow in the riser exhibits either dilute or dense flow only. At the choking point, a bottom dense flow regime coexists with a top dilute flow regime bridged by a transition zone, forming an S-shaped profile.[20] A stable cross-sectional profile is thought to require the minimization of the cross-sectional suspension and transporting energy dissipation rate, while the minimal global suspension and transporting energy dissipation rate defines the axial heterogeneity in the transition zone. Particle acceleration in both the dilute and dense phases should be taken into consideration

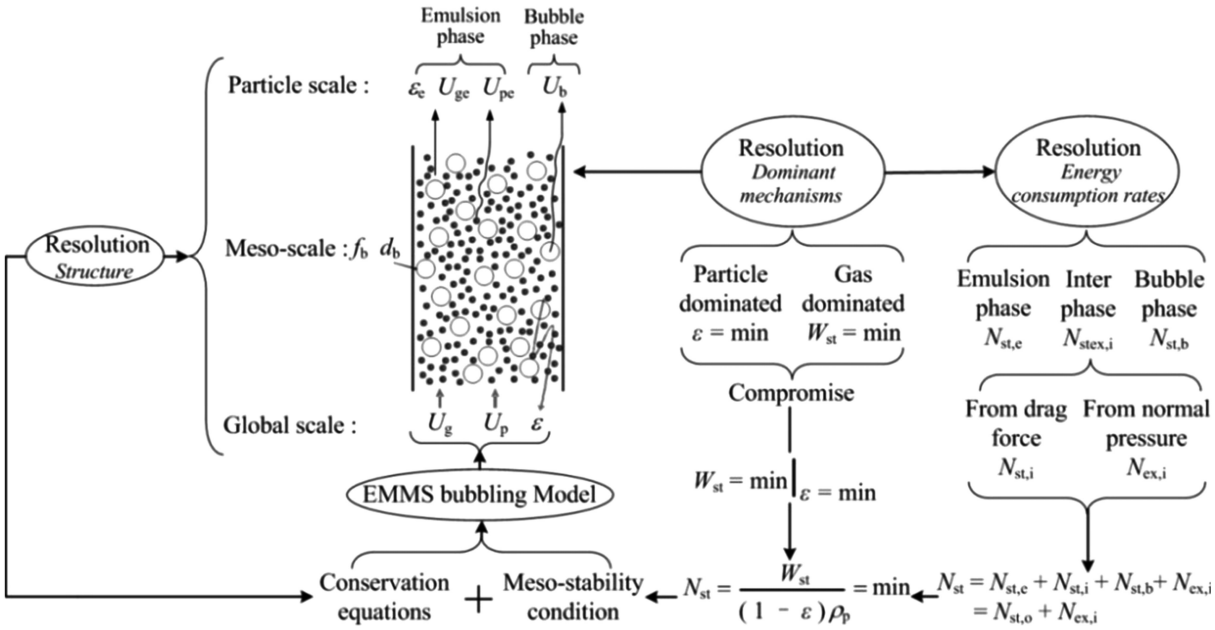


FIGURE 5.7.8 Physical basis of the theoretical EMMS bubbling model.

to account for the dynamical evolution of particle clusters in the transition zone. Considering both force balance and continuity equations at any cross section in the axial direction of the transition zone, Hu et al.[26] established a one-dimensional model for steady-state modeling of the axial heterogeneity in CFB risers by exploring the underlying mechanisms involved in cluster evolution.

Radial heterogeneity in CFB risers generally refers to a dilute core surrounded by a dense annulus next to the wall. Correspondingly, there is high upward gas–solid flow in the core region, but low upward or even downward gas–solid flow in the annular region. The radial heterogeneity in CFB risers can be attributed to the role of the wall in the compromise in competition between dominant mechanisms in gas–solid flow.[27] But the original cluster diameter correlation may predict a smaller value than single particle diameter at a low solids flux or a downward particle velocity near the wall. In fact, particle clusters always evolve over time and space because of the momentum exchange resulting from gas–solid interactions as well as solids mass transfer between the dilute and dense phases. During the evolution of particle clusters, the particles in the dilute phase are generally captured by the cluster due to the interphase velocity difference, while the particles at the cluster surface are likely to shed because of the velocity fluctuation of particles. When a dynamic balance is achieved between the above two opposing processes, the number of particles inside a particle cluster remains constant in theory; that is,

$$\left(u_{pf}-u_{pc}\right)\left(1-\varepsilon_f\right)=4\omega u'_{pc}\left(1-\varepsilon_c\right) \tag{5.7.6}$$

Here, ω is a constant, and u'_{pc} is the velocity fluctuation of particles in the dense phase. The radial EMMS model can thus be upgraded by replacing the cluster diameter correlation with Equation (5.7.6) to avoid the problems associated with the determination of cluster diameter, which can be employed to compute a simplified solution using a function approximation method.[28]

By applying the EMMS model and its extensions to the segments of complex gas–solid systems, an EMMS-based general method was proposed for the full-loop modeling of steady-state hydrodynamics in complex gas–solid reactors such as CFBs.[28,29] Taking a typical gas–solid CFB system as an example, as shown in Figure 5.7.9, full-loop hydrodynamic modeling of this complex system can be performed by the following three steps:

1. The CFB system is first divided into different simple segments according to its configuration and the operating conditions; for instance, riser, exit duct, cyclone, downcomer, and loop seal. The riser does not need to be further divided into various reaction zones as in traditional empirical methods.
2. The superficial gas velocity in each segment is then determined according to its characteristic size and global operating conditions, so as to choose a suitable EMMS model or extension to capture the hydrodynamics in the segment. For example, the axial and radial EMMS models can be used to compute the spatial heterogeneity in the riser, whereas the downcomer and particle seal are approximated as bubbling beds and thereby can be simulated using the EMMS bubbling model.
3. The particle velocity in each segment is finalized by using a trial and error method to generate a full-loop hydrodynamic steady state subject to the global constraints such as the pressure drop and solid mass balance of the whole CFB system.

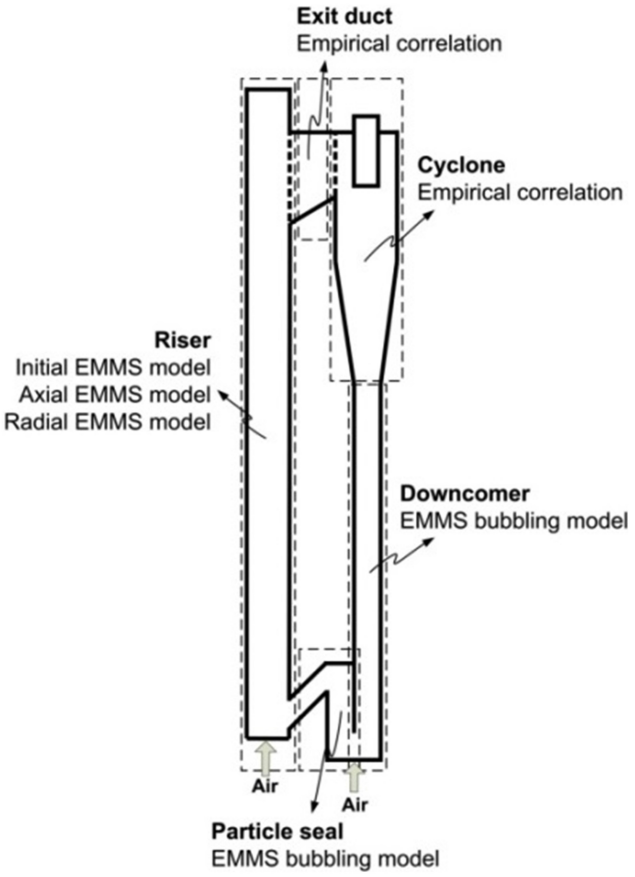


FIGURE 5.7.9 EMMS-based general method for global calculation of a typical CFB system.

It should be noted that the hydrodynamics of the exit duct and cyclone were still computed by empirical correlations. However, this was thought to have no qualitative effect on the full-loop hydrodynamics of the CFB system, because the pressure drop across these segments generally accounts for only a small part of the total driving force in the circulating loop.

5.7.2.2 Continuum Model

The two-fluid model (TFM) or Eulerian-Eulerian method is commonly used for industrial applications. TFM treats gas and solid phases as interpenetrating continua with averaging over the microscopic conservation equations to produce locally averaged quantities.[30] Instantaneous mass, momentum, and energy conservation equations governing two-phase flow at the microscopic level are first derived together with the corresponding interphase jump conditions; averaging techniques are then used to smooth local variables/jump conditions to obtain averaged equations. The equations presented below are from the documentation of commercial software Ansys®Fluent due to the popularity of this CFD solver.

Continuity equation for phase q (q = g, s):

$$\frac{\partial}{\partial t}\left(\varepsilon_{\mathrm{q}}\rho_{\mathrm{q}}\right)+\nabla\cdot\left(\varepsilon_{\mathrm{q}}\rho_{\mathrm{q}}\boldsymbol{u}_{\mathrm{q}}\right)=0 \tag{5.7.7}$$

where ε_q, ρ_q, $\boldsymbol{u}_q$ are the volume fraction, the density and the velocity of phase q, respectively. Momentum balances for gas and solid phases:

$$\frac{\partial}{\partial t}\left(\varepsilon_{\mathrm{g}}\rho_{\mathrm{g}}\boldsymbol{u}_{\mathrm{g}}\right)+\nabla\cdot\left(\varepsilon_{\mathrm{g}}\rho_{g}\boldsymbol{u}_{\mathrm{g}}\boldsymbol{u}_{\mathrm{g}}\right)=-\varepsilon_{\mathrm{g}}\nabla p+\nabla\cdot\boldsymbol{\tau}_{\mathrm{g}}+\varepsilon_{\mathrm{g}}\rho_{\mathrm{g}}\boldsymbol{g}+\boldsymbol{F}_{\mathrm{d}} \tag{5.7.8}$$

$$\frac{\partial}{\partial t}\left(\varepsilon_{\mathrm{s}}\rho_{\mathrm{s}}\boldsymbol{u}_{\mathrm{s}}\right)+\nabla\cdot\left(\varepsilon_{\mathrm{s}}\rho_{\mathrm{s}}\boldsymbol{u}_{\mathrm{s}}\boldsymbol{u}_{\mathrm{s}}\right)=-\varepsilon_{\mathrm{s}}\nabla p-\nabla p_{\mathrm{s}}+\nabla\cdot\boldsymbol{\tau}_{\mathrm{s}}+\varepsilon_{\mathrm{s}}\rho_{\mathrm{s}}\boldsymbol{g}-\boldsymbol{F}_{\mathrm{d}} \tag{5.7.9}$$

where $\boldsymbol{\tau}$ is the stress tensor (q = g, s) using the Newtonian form:

$$\boldsymbol{\tau}_{\mathrm{q}}=\varepsilon_{\mathrm{q}}\mu_{\mathrm{q}}\left[\nabla\boldsymbol{u}_{\mathrm{q}}+\left(\nabla\boldsymbol{u}_{\mathrm{q}}\right)^{\mathrm{T}}\right]+\varepsilon_{\mathrm{q}}\left(\lambda_{\mathrm{q}}-\frac{2}{3}\mu_{\mathrm{q}}\right)\nabla\cdot\boldsymbol{u}_{\mathrm{q}}\boldsymbol{I} \tag{5.7.10}$$

where

μ_q and λ_q	are the shear and bulk viscosity of phase q
p	is the pressure shared by both phases
p_s	is solid pressure

$\boldsymbol{F}_d$ refers to the drag force that is found to play the predominant role in gas–solid fluidization, leaving other interaction forces such as lift force and virtual mass force omitted.

Under this continuum framework, how to close the momentum interaction between gas and solid phases as well as solid phase stress, has become a topic of considerable interest. The kinetic theory of granular flow (KTGF) has been recognized as a reliable way to close the solid phase stress.[31] In KTGF, in addition to the mass and momentum conservation equations, an additional conservation for the granular temperature is needed:[31]

$$\frac{3}{2}\left[\frac{\partial}{\partial t}\left(\varepsilon_{\mathrm{s}}\rho_{\mathrm{s}}\Theta_{\mathrm{s}}\right)+\nabla\cdot\left(\varepsilon_{\mathrm{s}}\rho_{\mathrm{s}}\boldsymbol{u}_{\mathrm{s}}\Theta_{\mathrm{s}}\right)\right]=\left(-p_{\mathrm{s}}\boldsymbol{I}+\tau_{\mathrm{s}}\right):\nabla\boldsymbol{u}_{\mathrm{s}}-\nabla\cdot\boldsymbol{q}-\gamma-3\Theta_{\mathrm{s}}\beta \tag{5.7.11}$$

where Θ_s is the granular temperature. Detailed expressions for granular pressure p_s, solid viscosity μ_s, the flux of fluctuating energy $\boldsymbol{q}$, and collisional energy dissipation γ can be found in ref.[34]

The interphase drag force is another key input in continuum model. One way to express the drag force exerted by the surrounding fluid on a single particle is

$$F_{\mathrm{D}}=\frac{1}{2}C_{\mathrm{D0}}\rho_{\mathrm{g}}A\left|\boldsymbol{u}_{\mathrm{slip}}\right|\boldsymbol{u}_{\mathrm{slip}} \tag{5.7.12}$$

where

A	is an orthographic projection of the particle (frontal area, on a plane perpendicular to the direction of motion)

$\boldsymbol{u}_{slip}$ is the slip velocity
C_{D0} is the drag coefficient for a single particle

The following equations are usually used to express C_{D0}:
For Reynolds number (Re) <0.2,

$$C_{D0} = \frac{24}{\mathrm{Re}} \tag{5.7.13}$$

For Re <5, use the Oseen formula considering the inertial effect

$$C_{D0} = \frac{24}{\mathrm{Re}}\left(1 + \frac{3}{16}\mathrm{Re}\right) \tag{5.7.14}$$

For the range of $0.2 < \mathrm{Re} < 1000$, Schiller & Naumann[32] correlation is often used,

$$C_{D0} = \frac{24}{\mathrm{Re}}\left(1 + 0.15\,\mathrm{Re}^{0.687}\right) \tag{5.7.15}$$

For the inertial regime, $750 < \mathrm{Re} < 3 \times 10^5$,

$$C_{D0} = 0.44 \tag{5.7.16}$$

However, fluidization involves the suspension of an assembly of solid particles. the effective drag coefficient C_D accounts for the influence of surrounding particles is usually expressed as

$$C_D = f \cdot C_{D0} \tag{5.7.17}$$

The surrounding particles may either slow or accelerate the motion of the particle and its influence is denoted by the correction factor *f*. Application of C_D to each control volume in CFD modeling can provide the total drag force for particles per unit control volume and thus the effective drag coefficient for particles in a control volume is denoted by β. In fluid-solid flows, the general form of drag force is:

$$F_D = \frac{3}{4}C_{D0}\frac{(1-\varepsilon_g)\rho_g}{d_p}\left|\boldsymbol{u}_g - \boldsymbol{u}_s\right|\left(\boldsymbol{u}_g - \boldsymbol{u}_s\right)f = \beta\left(\boldsymbol{u}_g - \boldsymbol{u}_s\right) \tag{5.7.18}$$

Extensive research on C_D or β has been conducted, which can be primarily classified into correlations for homogeneous systems and those for heterogeneous systems.

Numerous experimental or empirical correlations for fluidized bed systems have been put forward. These correlations are suitable for relatively homogeneous fluidization, but often fail to predict heterogeneous gas–solid flows, especially when they are used in coarse-grid simulations. Table 5.7.1 lists some widely used experimental/empirical correlations. Noting that many correlations for homogeneous systems derived from direct numerical simulations[33] are available in literature, they are however not included in Table 5.7.1.

TFM simulation of gas–solid fluidization with a drag correlation obtained from homogeneous systems requires a very fine computational cell, which blocks its direct application in industrial-scale systems due to the extremely high computational cost. Therefore, methods have been developed to consider the effects of heterogeneous structures on the gas–solid interphase drag force, such as the EMMS-TFM method that will be introduced[18] and filtered model.[40]

The EMMS model,[13] as introduced in Section 5.7.2.1, was originally proposed to describe the flow structure in a steady-state gas–solid fluidization system. To extend it to account for the non-equilibrium characteristics and therefore to be used in the control volume in TFM, Yang et al.[41] established an EMMS-based drag model by introducing an average acceleration for particles to force balance equations. A heterogeneity index or drag correction factor to quantify the hydrodynamic disparity between homogeneous and heterogeneous fluidization is defined as:

$$H_D = \frac{\beta}{\beta_0} \tag{5.7.19}$$

where the drag coefficient β_0 refers to Wen and Yu model[35] and the resultant β depends on the structural parameters in EMMS model and is formulated as:

$$\beta = \frac{\varepsilon_g^2}{U_{slip}}F_d = \frac{\varepsilon_g^2}{U_{slip}}\left(fF_{dc} + F_{di} + \left(1-f\right)F_{df}\right) \tag{5.7.20}$$

Wang and Li[42] introduced different acceleration terms into the force balance equations of the dense phase, dilute phase, and interphase to extend the EMMS drag model to the sub-grid level, with a two-step scheme for model solution. H_D can be finally expressed as a function of both local voidage ε_g and local superficial slip velocity U_{slip}. The additional dependence on the local slip velocity was critical to lowering the sensitivity of the CFD simulation on grid size,[43] which enables coarse-grid simulations of large-scale reactors. The model and the solution strategy[42,43] have also been extended to establish a bubble-based EMMS drag model for low-velocity gas-fluidized beds without solid entrainment.[44–46]

All those drag force models, as summarized in Table 5.7.2, have been included in the EMMS® software, which have been developed by the EMMS group of Institute of Process Engineering, Chinese Academy of Sciences.

5.7.2.3 Discrete Particle Method

Discrete particle method is another important approach to simulate and understand the fundamental behavior of gas–solid flows. The advantage of the discrete particle method compared with the TFM is that each particle in the discrete phase is tracked and all particle-particle interactions could be resolved. To simulate particle-particle interactions, direct simulation Monte Carlo (DSMC),[47] soft-sphere model,[48] or hard-sphere model[49] are usually used. The soft-sphere model, also known as the discrete element method (DEM), was first proposed by Cundall and Strack.[50] DEM is preferential over the hard-sphere model and DSMC in many cases because

TABLE 5.7.1 Experimental/Empirical Correlations of Drag Coefficient

Authors	Correlations
Richardson & Zaki[34]	$C_D = \dfrac{4d_p(\rho_s - \rho_g)}{3\rho_g U_{slip}^2}, U_{slip} = u_T \varepsilon^n \quad n = \begin{cases} 4.65 & Re_T < 0.2 \\ 4.4Re_T^{-0.03} & 0.2 < Re_T < 1 \\ 4.4Re_T^{-0.1} & 1 < Re_T < 500 \\ 2.4 & Re_T > 500 \end{cases}$
Wen and Yu[35]	$C_D = C_{D0}\varepsilon_g^{-4.7}$
Ergun[36]	$\beta = 150\dfrac{(1-\varepsilon_g)^2\mu_g}{\varepsilon_g d_p^2} + 1.75\dfrac{(1-\varepsilon_g)\rho_g\lvert\boldsymbol{u}_g - \boldsymbol{u}_s\rvert}{d_p}$
Gidaspow[31]	$\beta = \begin{cases} \dfrac{3}{4}C_{D0}\dfrac{\varepsilon_s\varepsilon_g\rho_g\lvert\boldsymbol{u}_g - \boldsymbol{u}_s\rvert}{d_p}\varepsilon_g^{-2.7} & (\varepsilon_g \geq 0.8) \\ 150\dfrac{(1-\varepsilon_g)^2\mu_g}{\varepsilon_g d_p^2} + 1.75\dfrac{(1-\varepsilon_g)\rho_g\lvert\boldsymbol{u}_g - \boldsymbol{u}_s\rvert}{d_p} & (\varepsilon_g < 0.8) \end{cases}$
Nieuwland et al.[37]	$\beta = \dfrac{3}{4}\dfrac{\varepsilon_s\varepsilon_g\rho_g\lvert\boldsymbol{u}_g - \boldsymbol{u}_s\rvert}{d_p}C_{D0}f(\varepsilon_s)$ $f(\varepsilon_s) = \dfrac{1}{0.997 + 443.35\varepsilon_s - 1733.42\varepsilon_s^2}, \ \varepsilon_s < 0.1276$ $f(\varepsilon_s) = \dfrac{1}{29.22}, \ \varepsilon_s \geq 0.1276$
Wang and Li[38]	$\beta = 150\dfrac{\varepsilon_s^2\mu}{\varepsilon_g d_p^2} + 1.75\dfrac{\varepsilon_s\rho_g\lvert\boldsymbol{u}_g - \boldsymbol{u}_s\rvert}{d_p}, \ \varepsilon_g \leq \varepsilon^*$ $\beta = \dfrac{3}{4}\dfrac{\varepsilon_s\varepsilon_g}{d_p}\rho_g\lvert\boldsymbol{u}_g - \boldsymbol{u}_s\rvert C_{D0}\left(0.0232\varepsilon_g^{-12.49}\right), \ \varepsilon_g > \varepsilon^*$ ε^* is the switch voidage where two correlations are equally matched
Syamlal and O'Brien[39]	$\beta = \dfrac{3}{4}\dfrac{\varepsilon_s\varepsilon_g\rho_g}{V_r^2 d_p}\lvert\boldsymbol{u}_g - \boldsymbol{u}_s\rvert\left(0.63 + 4.8\sqrt{\dfrac{V_r}{Re}}\right)^2$ $V_r = \dfrac{1}{2}\left(a - 0.06Re + \sqrt{(0.06Re)^2 + 0.12Re(2b-a) + a^2}\right)$ $a = \varepsilon_g^{4.14}, \ b = \begin{cases} 0.8\varepsilon_g^{1.28} & (\varepsilon_g \leq 0.85) \\ \varepsilon_g^{2.65} & (\varepsilon_g > 0.85) \end{cases}$

TABLE 5.7.2 Frequently Used EMMS-Based Drag Models

Drag Models	Description
EMMS/global[41]	H_D solely depends upon the voidage ε_g. This model is suitable for the fast fluidization with fine particles.
EMMS/matrix[42,43]	The advanced version of EMMS/global. H_D is a binary function of voidage and slip velocity. It is applicable to coarse-grid simulations of fluidized beds with Geldart A, B and D particles.
EMMS/bubbling[45]	H_D solely depends upon the voidage. This model is applicable to bubbling fluidization and turbulent fluidization.
EMMS/bubbling (two-step version)[46]	It is a two-step version of EMMS/bubbling model and applicable to coarse simulations of large bubbling and turbulent fluidized beds.

it can be applied to both dilute and dense phase systems. Therefore, CFD-DEM method is the most popular discrete particle method used in fluidization simulations.

In CFD-DEM method, the governing equations of the motion of the fluid phase can be described by the averaged mass and momentum equations that are the same as Equations 5.7.7 and 5.7.8, the interphase drag force is calculated by,

$$\mathbf{F}_d = \frac{1}{V_c}\sum_{a=1}^{N_p}\frac{\beta V_a}{\varepsilon_s}\left(\mathbf{u}_f - \mathbf{u}_a\right)w\left(\mathbf{x}_a, \mathbf{x}_c\right) \tag{5.7.21}$$

where

V_c is the local volume of a computational cell
N_p is the number of particles in the computational cell
V_a is the volume of the particle a
β is the drag force coefficient

$\mathbf{u}_a$ is velocity of particle a

$w(\mathbf{x}_a, \mathbf{x}_c)$ is the interpolation weight function used to map the properties of particle a to cell c

The governing equations for the movement of a single particle follow Newton's laws,

$$m_a \frac{d\mathbf{u}_a}{dt} = \mathbf{F}_{\text{contact,a}} + \mathbf{F}_{\text{ext,a}} \tag{5.7.22}$$

$$\frac{d\mathbf{r}_a}{dt} = \mathbf{u}_a \tag{5.7.23}$$

$$\mathbf{I}_a \frac{d\boldsymbol{\omega}_a}{dt} = \mathbf{T}_a \tag{5.7.24}$$

Here, m_a is the particle mass, $\mathbf{r}_a$ is the particle coordinate vector, $\mathbf{F}_{\text{contact,a}}$ is the total contact force on the particle, $\mathbf{F}_{\text{ext,a}}$ is the total external force acting on the particle, $\mathbf{I}_a$ is the moment of inertia, and $\mathbf{T}_a$ is the torque of the particle calculated as a function of tangential contact force.

$$\mathbf{T}_a = \sum_{b \in \text{contactlist}} \left(R_a \mathbf{n}_{ab} \times \mathbf{F}_{ab,t} \right) \tag{5.7.25}$$

Note that if other particle-particle forces such as van der Waals forces, electrostatic forces, and liquid bridge forces exist in the system, they could be added to the right-hand side of the force balance equation. This is one of the main advantages of the CFD-DEM method.

The total external force includes the gravitational force and the forces exerted by the surrounding fluid phase including buoyancy force, drag force, lift force, and added mass force. In a typical gas–solid flow system, the lift force and added mass force are usually much smaller than the drag force, so the lift and added mass forces are often neglected. Therefore, we have

$$\mathbf{F}_{\text{ext,a}} = m\mathbf{g} - V_a \nabla p + \mathbf{F}_{\text{d,a}} \tag{5.7.26}$$

The drag force is caused by the fluid-solid friction at the surface of the spheres and can be written as,

$$\mathbf{F}_{\text{d,a}} = \frac{V_a \beta}{1 - \varepsilon_f} \left(\mathbf{u}_f - \mathbf{u}_a \right) \tag{5.7.27}$$

Here, β is the drag coefficient. The total contact force on a particle can be divided into a summation of the normal contact force and tangential contact force:

$$\mathbf{F}_{\text{contact,a}} = \sum_{b \in \text{contactlist}} \left(\mathbf{F}_{ab,n} + \mathbf{F}_{ab,t} \right) \tag{5.7.28}$$

The linear spring, dashpot, and friction slider originally proposed by Cundall and Strack[50] is one of the simplest and most popular contact force models. The normal contact force in this model can be written as a combination of the conservative (spring) force and the dissipative (damping) force and the tangential contact force could be written as a combination of the spring force, damping force, and frictional slider force. The maximum tangential force is limited by the Coulomb-type friction law. The governing equations of linear spring-dashpot-slider model is summarized in Table 5.7.3. A schematic of CFD-DEM simulation of a bubbling fluidized bed is shown in Figure 5.7.10.

TABLE 5.7.3 The Governing Equations of Linear Spring-Dashpot-Slider Model

Variable	Formula
Normal contact force	$\mathbf{F}_{ab,n} = -k_n \delta_n \mathbf{n}_{ab} - \eta_n \mathbf{u}_{ab,n}$
Tangential contact force	$\mathbf{F}_{ab,t} = \begin{cases} -k_t \delta_t - \eta_t \mathbf{u}_{ab,t} & \text{for } \lvert\mathbf{F}_{ab,t}\rvert \le \mu_f \lvert\mathbf{F}_{ab,n}\rvert \\ -\mu_f \lvert\mathbf{F}_{ab,n}\rvert \mathbf{t}_{ab} & \text{for } \lvert\mathbf{F}_{ab,t}\rvert > \mu_f \lvert\mathbf{F}_{ab,n}\rvert \end{cases}$
Normal overlap	$\delta_n = (R_a + R_b) - \lvert\mathbf{r}_b - \mathbf{r}_a\rvert$
Normal unit vector	$\mathbf{n}_{ab} = \frac{\mathbf{r}_b - \mathbf{r}_a}{\lvert\mathbf{r}_b - \mathbf{r}_a\rvert}$
Normal damping coefficient	$\eta_n = \frac{-2\sqrt{m_{ab} k_n} \ln e}{\sqrt{\pi^2 + \ln^2 e}}$
Reduced mass	$m_{ab} = \frac{m_a \cdot m_b}{m_a + m_b}$
Relative velocity	$\mathbf{u}_{ab} = \left(\mathbf{u}_a - \mathbf{u}_b \right) - \left(R_a \boldsymbol{\omega}_a + R_b \boldsymbol{\omega}_b \right) \times \mathbf{n}_{ab}$
Normal relative velocity	$\mathbf{u}_{ab,n} = \left(\mathbf{u}_{ab} \cdot \mathbf{n}_{ab} \right) \mathbf{n}_{ab}$
Tangential relative velocity	$\mathbf{u}_{ab,t} = \mathbf{u}_{ab} - \mathbf{u}_{ab,n}$
Tangential unit vector	$\mathbf{t}_{ab,t} = \frac{\mathbf{u}_{ab,t}}{\lvert\mathbf{u}_{ab,t}\rvert}$
Tangential overlap	$\delta_t = \begin{cases} \int_{t_c}^{t} \mathbf{u}_{ab,t} dt & \text{if } \lvert\mathbf{F}\rvert_t \le \mu_f \lvert\mathbf{F}_n\rvert \\ \mu_f \lvert\mathbf{F}_n\rvert \mathbf{t}_{ab} / k_t & \text{if } \lvert\mathbf{F}\rvert_t > \mu_f \lvert\mathbf{F}_n\rvert \end{cases}$

The common drawback of the CFD-DEM approach is its high computational expense, which limits its applications mostly to laboratory-scale processes and fundamental research. An industrial-scale reactor contains more than a billion particles. The CFD-DEM approach tracks individual particles and their interactions, which makes it formidable for modeling an industrial-scale reactor even using supercomputers.[18] To overcome the limitations, the coarse-grained models have been recently proposed to reduce the computational cost of CFD-DEM method. These models are generally classified into two categories: coarse-grained particle size models and coarse-grained particle contact models.

In coarse-grained particle size models, the concept of parcel or numerical particle is used and the details of interaction between different parcels or numerical particles are calculated using DEM-type techniques. The size of numerical particle is usually set to be several times larger than the physical particle size so that the computational cost significantly decreases.

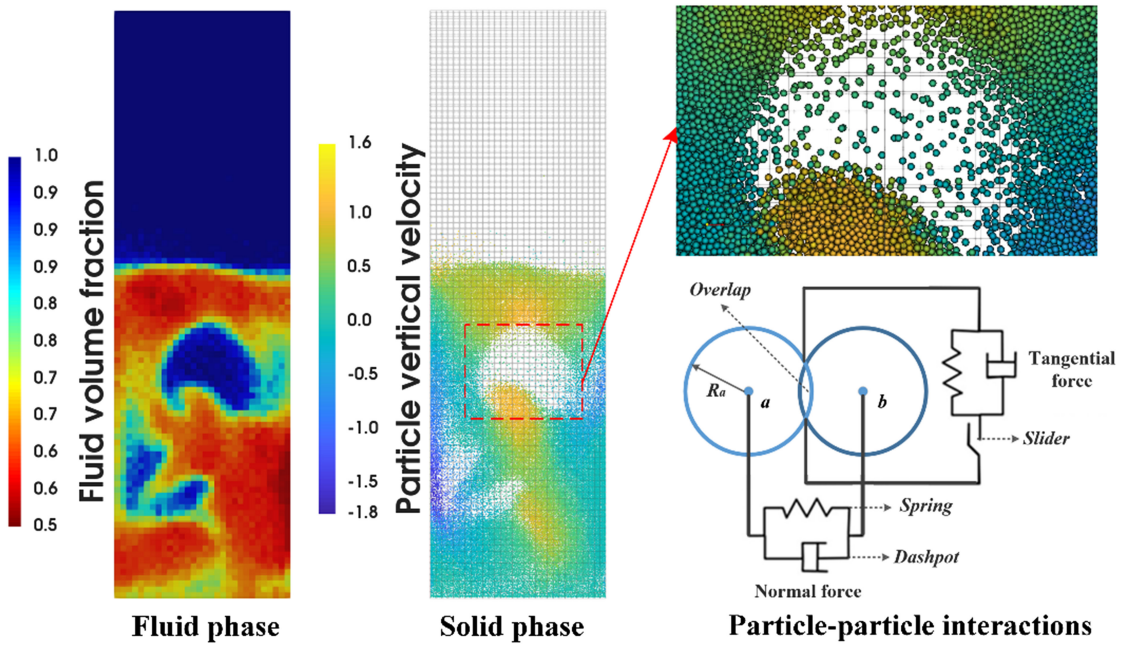


FIGURE 5.7.10 Schematic of CFD-DEM simulation of a bubbling fluidized bed. Left: flow fields of fluid phase are obtained by solving volume-averaged Navier–Stokes equations. Middle: solid phase is tracked explicitly in the Lagrangian reference frame by Newton's second law of motion. Right: Linear spring-dashpot-slider model is used to resolve particle-particle interactions.

However, a similarity condition or scaling law must be applied to ensure the mass, momentum, and energy conservations are consistent between the coarse-graining and original systems. A number of scaling laws are proposed in literatures, such as imaginary sphere model,[51] coarse grain model,[52] similar particle assembly method[53] and its modification,[54] scaled discrete element method,[55] discrete cluster method,[56] principle of similarity method,[57] coarse-grained model with equal energy,[58] EMMS-DPM[59] and coarse-grained time driven hard sphere method.[60]

In coarse-grained particle contact models, researchers used a continuum formula to resolve the interactions between particles instead of directly tracking the collisions between individual particles.[61,62] The general idea is to first map the information of Lagrangian particles to Eulerian grids to calculate the local solid volume fraction and grid-averaged particle velocity. An empirical- or kinetic theory-based granular stress formula could then be calculated based on the local particle information. The gradient of granular stress is mapped back to individual particles to represent the particle-particle interaction forces. Two typical examples of this strategy are the multiphase particle-in-cell (MP-PIC) method (Snider, 2001) and dense discrete phase model (DDPM).[62] The role of granular stress in these models is sometimes more important to avoid excessive overlap between particles rather than to correctly represent the particle contact forces. Because the interactions between particles are not directly resolved, detailed information about particle collisions cannot be obtained using these models. The general accuracy and reliability of these models are correspondingly reduced. However, these models are useful for cases where inter-particle collisions are not very important because they can markedly shorten the computational time.

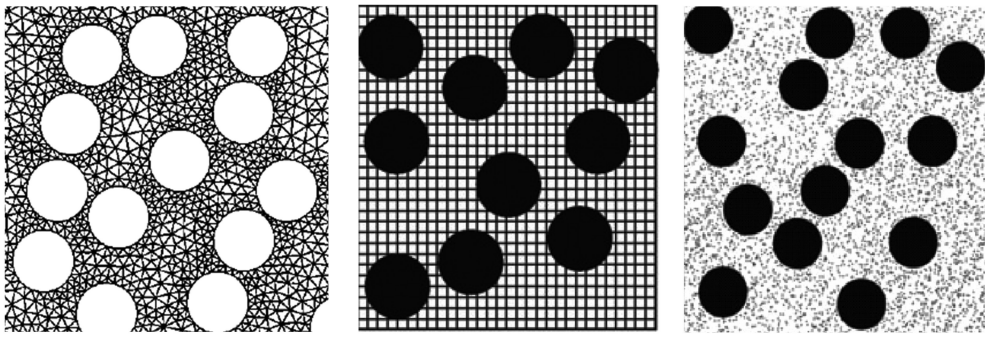
5.7.2.4 Direct Numerical Simulation

To obtain detailed information about the flow behavior, heat and mass transfer, and reactions at particle–fluid interfaces and develop more accurate constitutive correlations of two-phase interactions, the flow field around particles must be described in detail. In addition, the interphase force is strictly determined by the integral of the fluid stress on the particle surface. Therefore, there is an urgent need to develop direct numerical simulation (DNS) methods for modeling gas–solid flow. Similar to the DNS of single-phase turbulence, the governing equations of the fluid phase in particle-resolved DNS are numerically solved without any turbulence model. The computational grid of the flow field in particle-resolved DNS is smaller than both the particle size and Kolmogorov scale. The force acting on the particles is obtained by integrating the viscous force and the pressure on the surface of the particle.

Particle-resolved DNS is regarded as the most accurate computational method available and is thus a powerful tool to describe gas–solid two-phase flow. According to the solution of the fluid phase, the particle-resolved DNS of a particle–fluid system can be divided into three categories: the first is the Navier–Stokes (NS) equation-based DNS method, the second is the lattice-based DNS method, and the third is the particle-based DNS method (Figure 5.7.11).

NS Equation-Based DNS

The governing NS equations for the fluid in the traditional DNS method are usually solved via finite-difference, finite-element, or finite-volume methods on an Eulerian grid. Because the flow field has solid particles in particle-resolved



(a) NS based PR-DNS (b) lattice-based PR-DNS (b) particle-based PR-DNS

FIGURE 5.7.11 Particle-resolved direct numerical simulation (DNS) of particle–fluid systems. (a) NS-based DNS, (b) lattice-based DNS, and (c) particle-based DNS.

DNS, here we should solve the flow field using numerous moving boundaries. Many specific solutions have been developed, including the arbitrary Lagrangian–Eulerian (ALE),[63] front-tracking,[64] front capturing,[65] level set,[66] constrained interpolation profile,[67] and fictitious domain method.[68] These methods have their own characteristics, and their application areas are different. ALE uses an unstructured grid to approximate the surface of the particle with a grid boundary. This method can be very favorable to maintain the particle–fluid interface and can be adapted to different grid sizes. However, grid regeneration and other technologies make the process more complex because of the use of an unstructured grid.

Lattice-Based DNS Method

The lattice Boltzmann method (LBM)[69] is a computational method to resolve governing equations of fluid. Thanks to its unique features drawn from both discrete and continuum methods, the LBM seems to keep a good balance between efficiency, parallelism, and simplicity for the simulation of fluid flow. Therefore, the LBM has been used extensively in the particle-resolved DNS of particle–fluid systems since the pioneering work of Ladd.[70] By adjusting the bounce boundary to ensure the non-slip condition of the motion boundary and calculating the force between the fluid and solid particles from the momentum exchange, Ladd's method successfully simulated a liquid–solid suspension. Noble and Torczynski[71] proposed an IBM method to deal with fluid–solid coupling. Their approach deals with the fluid–solid coupling by adding an additional collision term to the lattice Boltzmann equation, which allows the relatively accurate description of the solid particle boundary, and follows the LBM calculation system, preserving the advantages of locality in the algorithm. Cook et al.[72] used this method to simulate particle–fluid systems by coupling the LBM with the discrete element method (DEM). Wang et al.[73] developed a combined approach of particle and lattice methods, which raised the allowed particle–fluid density ratio from 2.5 to 1500, and successfully reproduced typical fluidization phenomena, demonstrating it was a promising computational strategy to better understand complex behavior in gas–solid fluidization. Subsequently, Xiong et al.[74] implemented GPU parallel computing of this algorithm and conducted the largest scale particle-resolved DNS of gas–solid fluidization to date, with 1,166,400 solid particles for a two-dimensional system and 129,024 particles for a three-dimensional system.

Particle-Based DNS Methods

When particles are considered discretely, the "fluid particles" concept is also used to model the fluid in the grid in a natural manner. The initial slow development of the particle method was because the computational cost of the particle method is usually high. In recent years, with the rapid advance of computational capability, a solid foundation of hardware has enabled a variety of particle methods for modeling fluid-particle flows, such as the pseudo-particle model (PPM),[75] and the macroscale pseudo-particle model (MaPPM).[76] At the same time, traditional molecular dynamics (MD) simulations, as the most common type of simulation, began to be used to simulate fluidization. To describe the flow characteristics on the microscopic level while decrease the computational cost of the simulated two-phase flow, Ge and Li[75] proposed a PPM based on the idea that elaborate description of molecular interactions is not always necessary to faithfully reproduce flow behaviors, even on the microscale. The PPM aims to simplify the interaction between particles while retain the deterministic relationship of adjacent particles. The PPM was established based on MD, but it is more macroscopic than MD, so it can explore the mechanism of fluidization from a microscopic viewpoint and also describe the phenomenon of macroscopic fluidization.

Particle-resolved DNS is a first-principles approach to develop accurate models for gas–solid flow at all levels of statistical closure. In recent years, substantial progress has been made in the particle-resolved DNS of interfacial fluid–particle momentum transport to develop more accurate drag correlations for statistically homogeneous systems, the use of particle-resolved DNS for closures involving chemical reactions and heat and mass transfer as well as the mesoscale structures should be investigated further.

5.7.2.5 Summary

The concept of multiscale simulation, mainly including steady-state modeling, continuum method, discrete particle method and direct numerical simulation, has been firmly established, and they have become an effective toolkit for studying the momentum, heat and mass transfer, as well as chemical reactions in fluidized bed reactors. Different methods resolve gas-solids at different spatiotemporal scales, there is no method suitable for all the problems encountered, therefore, researchers should select a proper method to meet their specific requirements.

REFERENCES

1. Kwauk, M., *Fluidization*, Science Press, Beijing, 1992.
2. Wilhelm, R., Kwauk, M., *Chem. Eng. Prog.*, 44, 201–218, 1948
3. Kunii, D., Levenspiel, O., *Fluidization Engineering*, Elsevier, Butterworth-Heineman, 2013.
4. Ergun, S., *Chem. Eng. Prog.*, 48, 89–94, 1952.
5. Jin, Y., Zhu, J., Wang, Z., Yu, Z., *Fluidization Engineering Principles*, Tsinghua Univ. Pub., Beijing, 2001.
6. Shirai, T., *Fluidized Beds*, Kagaku-Gijutsu-Sha, Kanazawa, 1958.
7. Li, H., Zhu, Q., Liu, H., Zhou, Y., *Powder Technol.*, 84, 241–246, 1995.
8. Bai, D., Jin, Y., Yu, Z., *Fluidization*, 91, 110–115, 1991.
9. Lackermeier, U., et al., *Powder Technol.*, 114, 71–83, 2001.
10. Liu, X., Gao, S. Song, W., Li, J., *Chem. Eng. Sci.*, 61, 7087–7095, 2006.
11. Liu, X., Jiang, Y., Zhang, N., Li, J., *Powder Technol.*, 297, 409–414, 2016.
12. Meng, F., Liu, X., *Powder Technol.*, 224, 404–409, 2012.
13. Li, J., Kwauk, M., *Particle-Fluid Two-Phase Flow*, Metallurgical Industry Press, Beijing, 1994.
14. Lim, K., Zhu, J., Grace, J., *Int. J. Multiph. Flow*, 21, 141–193, 1995.
15. Bi, H., Grace, J., *Int. J. Multiph. Flow*, 21, 1229–1236, 1995.
16. Liu, X., et al., *Ind. Eng. Chem. Res.*, 53, 2800–2810, 2014.
17. Reh, L., *Chem. Eng. Prog.*, 67, 58–63, 1971.
18. Li, J., et al., *From Multiscale Modeling to Meso-Science*, Springer, Berlin, 2013.
19. Kwauk, M., *Scientia Sinica*, 12, 587–612, 1963.
20. Li, Y., Kwauk, M., *Fluidization*, Springer, Boston, 1980, pp. 537–544.
21. Li, J., Tung, Y., Kwauk, M., In: Basu, P., Large, J.F. (Eds.), *Circulating Fluidized Bed Technology II*, Pergamon Press, Oxford, 1988, pp. 193–203.
22. Hartge, E., Rensner, D., Werther, J., In: Basu, P., Large, J.F. (Eds.), *Circulating Fluidized Bed Technology II*, Pergamon Press, Oxford, 1988, pp. 165–180.
23. Tung, Y., Li, J., Kwauk, M., *Fluidization*, 88, 139–145, 1988.
24. Zhang, W., Tung, Y., Johnsson, F., *Chem. Eng. Sci.*, 46, 3045–3052, 1991.
25. Ge W, Li, J., *Chem. Eng. Sci.*, 57, 3993–4004, 2002.
26. Hu, S., Liu, X., Li, J., *Chem. Eng. Sci.*, 96, 165–173, 2013.
27. Li, J., Reh, L., Kwauk, M., In: Basu, P., Horio, M., Hasatani, M. (Eds.), *Circulating Fluidized Bed Technology III*, Pergamon Press, Oxford, 1990, pp. 105–111.
28. Hu, S., et al., *Chem. Eng. J.*, 307, 326–338, 2017.
29. Liu, X., Hu, S., Jiang, Y., Li, J., *Chem. Eng. J.*, 278, 492–503, 2015.
30. Anderson, T.B., Jackson, R., *Ind. Eng. Chem. Fundam.*, 6, 527–539, 1967.
31. Gidaspow, D., *Multiphase Flow and Fluidization*, Academic Press, Boston, 1994.
32. Schiller, L., Naumann, A., *Zeitschrift des Vereines Deutscher Ingenieure*, 77, 318–320, 1933.
33. Deen, N.G., Peters, E.A.J.F., Padding, J.T., Kuipers, J.A.M., *Chem. Eng. Sci.*, 116, 710–724, 2014.
34. Richardson, J.F., Zaki, W.N., *Trans. Inst. Chem. Eng.*, 32, 35–53, 1954.
35. Wen, C.Y., Yu, Y.H., *Chem. Eng. Symp. Series*, 62, 100–111, 1966.
36. Ergun, S., *Chem. Eng. Process.*, 48, 89–94, 1952.
37. Nieuwland, J.J., Huizenga, P., Kuipers, J.A.M., Van Swaaij, W.P.M., *Chem. Eng. Sci.*, 48, 5803–5811, 1994.
38. Wang, W., Li, Y., *Chinese J. Chem. Eng.*, 12, 335–441, 2004.
39. Syamlal, M., O'Brien, T.J., *Int. J. Multiphase Flow*, 14, 473–481, 1988.
40. Igci, Y., Andrews, I.V., Sundaresan, S., Pannala, S., O'Brien, T., *AIChE J.*, 54, 1431–1448, 2008.
41. Yang, N., Wang, W., Ge, W., Li, J., *Chem. Eng. J.*, 96, 71–80, 2003.
42. Wang, W., Li, J., *Chem. Eng. Sci.*, 62, 208–231, 2007.
43. Lu, B., Wang, W., Li, J., *Chem. Eng. Sci.*, 64, 3437–3447, 2009.
44. Shi, Z., Wang, W., Li, J., *Chem. Eng. Sci.*, 66, 5541–5555, 2011.
45. Hong, K., Shi, Z., Wang, W., Li, J., *Chem. Eng. Sci.*, 99, 191–202, 2013.
46. Luo, H,, Lu, B., Zhang, J., Wu, H., Wang, W., *Chem. Eng. J.*, 326, 47-57, 2017.
47. Tanaka, T., *Proc. Int. Conf. Multiphase Flows '91-Tsukuba*, 2, 439, 1991.
48. Tsuji, Y., Kawaguchi, T., Tanaka, T., *Powder Technol.*, 77, 79–87, 1993.
49. Hoomans, B., Kuipers, J., Briels, W., Van Swaaij, W., *Chem. Eng. Sci.*, 51, 99–118, 1996.
50. Cundall, P.A., Strack, O.D., *Geotechnique*, 29, 47–65, 1979.
51. Kazari, M., et al., *Proc. 2nd Int. Conf. Multiphase Flow*, Kyoto, Japan, 1995, pp. FB2.9–FB2.15.
52. Sakai, M., et al., Koshizuka, S., *Int. J. Numer. Methods Fluids*, 64, 1319–1335, 2010.
53. Kuwagi K, Takeda H, Horio M., *Int. Conf. Fluidization Eng. XI*, Ischia, Naples, 2004, pp. 243–250.
54. Benyahia, S., Galvin, J.E., *Ind. Eng. Chem. Res.*, 49, 10588–10605, 2010.
55. Link, J., et al., *Powder Technol.*, 189, 202–217, 2009.
56. Liu, X., Xu, X., Zhang, W., *J. Univ. Sci. Technol. Beijing*, 13, 301–307. 2006.
57. Liu, Z., Suda, T., Tsuji, T., Tanaka, T., *The 14th Int. Conf. Fluidization*, Noordwijkerhout, The Netherlands, 2013.
58. Chu, K., Chen, J., Yu, A., *Miner. Eng.*, 90, 43–54, 2016.
59. Lu, L., et al., *Chem. Eng. Sci.*, 120, 67–87, 2014.
60. Lu, L., Benyahia, S., Li, T., *AIChE J.*, 63, 5320–5334, 2017.
61. Snider, D., *J. Comput. Phys.*, 170, 523–549, 2001.
62. Popoff, B., Braun, M., *Int. Conf. Multiphase Flow*, Leipzig, Germany, 2007.
63. Hu, H.H., Joseph, D.D., Crochet, M.J., *Theor. Comput. Fluid Dynamics*, 3, 285–306, 1992.
64. Glimm, J., Grove, J.W., Li, X.L., Oh, W., Sharp, D.H., *J. Comput. Phys.*, 169, 652–677, 2001.
65. Hirt, C.W., Nichols, B.D., *J. Comput. Phys.*, 39, 201–225, 1981.

66. Osher, S., Sethian, J.A., *J. Comput. Phys*., 79, 12–49, 1988.
67. Takewaki, H., Nishiguchi, A., Yabe, T., *J. Comput. Phys*., 61, 261–268, 1985.
68. Glowinski, R., Pan, T.W., Hesla, T.I., Joseph, D.D., *Int. J. Multiphase Flow*, 25, 755–794, 1999.
69. McNamara, G.R., Zanetti, G., *Phys. Rev. Lett*., 61, 2332–2335, 1988.
70. Ladd, A., *J. Fluid Mech*., 271, 285–309, 1994.
71. Noble, D.R., Torczynski, J.R., *Int. J. Mod. Phys. C*, 9, 1189–1201, 1998.
72. Cook, B., Noble, D., Williams, J., *Eng. Comput*., 21, 151–168, 2004.
73. Wang, L., et al., *Particuology*, 8, 379–382, 2010.
74. Xiong, Q., et al., *Chem. Eng. Sci*., 71, 422–430, 2012.
75. Ge, W., Li, J., *Proc. 5th Int. Conf. Circulating Fluidized Bed*, Science Press, Beijing, 1996, pp. 260–265.
76. Ge, W., Li, J., *Chinese Sci. Bull*., 46, 1503–1507, 2001.



Taylor & Francis
Taylor & Francis Group
http://taylorandfrancis.com

5.8 Mixing

Satoru Watano

5.8.1 INTRODUCTION

Mixing is the most important and frequently used operation in powder handling processes[1–3]. In general, mixing is conducted to combine different kinds of materials into one mass. As listed in Table 5.8.1, the objective of mixing differs depending on the applications. For example, in the pharmaceutical industry, an active ingredient (drug) is mixed with excipients to dilute the concentration while maintaining its uniformity in the unit of dosage form (tablet, capsule or granules). It is also widely used to change the original powder properties by mixing with other materials; mixing of a small amount of additives (silica, talc, magnesium stearate, etc) with bulk powder improves followability and prevents caking, consolidation, clumping and blocking of the original powder. The mixing of fillers with bulk powder increases the functionality of powders, e.g. mechanical strength, electrical conductivity, magnetization, plasticity, antibacterial, UV protection, etc. Several troubles often observed in powder handling process such as segregation, separation, caking, clumping and blocking can be prevented by the mixing operation. In most cases, the mixing is used as a pre-processing of grinding, granulation, tableting, capsulation and molding.

5.8.2 MIXING MECHANISM

Mixing takes place through the exchange of the relative position of each material (powders). Since powders do not have any spontaneous movement, external force should be applied to move the powders. Therefore, the mixing devices can be characterized by the way of applying the external force. The mixing mechanism can be categorized by the movement of materials as follows[1]:

1. Convective mixing: positions of powders are largely exchanged due to the circular flow generated by aeration or movement of mixing vessel or agitation paddle. This mixing mechanism contributes to the macroscopic mixing, resulting in the rapid mixing at the initial stage of the mixing operation.
2. Shearing mixing: exchange of each position takes place in the microscopic level. Slip, separation and collision of powders are taken place due to the velocity distribution inside the bulk powder. Compression and spreading of powders at the clearance between tip of blade and vessel wall also contributes to the shearing mixing.
3. Diffusive mixing: position exchange of neighboring powders is taken place by a random walk generated due to the slight difference in surface conditions, shape, size and velocity difference in the flow direction.

5.8.3 MIXING INDICES AND MIXING RATE

Ideal homogenous mixture is defined as the state that there is no spatial gradient of the objective material concentration in the mixture. The samples taken out at any potion indicate the same concentration, regardless of the sample size. This mixing state and the mixture are referred to as the perfect (ordered) mixing[2] as shown in Figure 5.8.1. In the normal

TABLE 5.8.1 Objective of Mixing

Objective	Operation/Phenomena	Properties	Materials
Achieve Uniformity			
Property change	Improvement	Flowability	Silica, Talc, Magnesium stearate
	Function imparting	Electrical conductivity	Carbon black, Graphite, Carbon fiber, Metal powder, Metal fiber
		Magnetization	Ferrite, Magnetic iron oxide Sm-Co, Nd-Fe-B
		Thermal conductivity	Al_2O_3, AlN, BN, BeO
		Plasticity	Polyester, Phthalate, Phosphate
		Antibacterial	Ag, Catechin, Copper phthalocyanine
		UV protection	TiO_2, ZnO, Iron oxide
Prevention of troubles	Segregation		
	Separation		
	Caking, clumping, blocking		Silica, Talc, Silicon dioxide, Calcium phosphate
Pre-processing	Grinding, granulation, tableting, molding, capsulation		

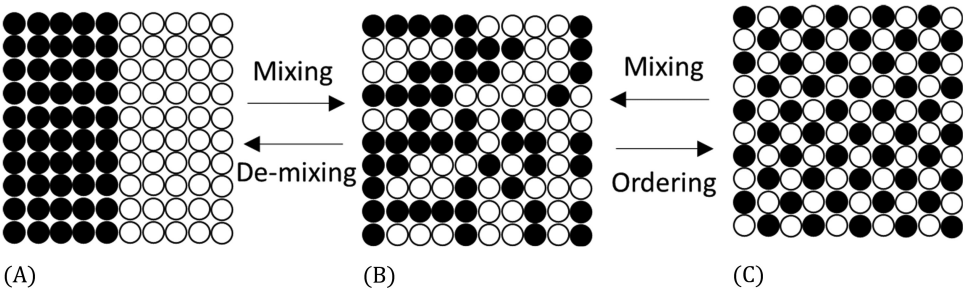


FIGURE 5.8.1 Schematic representation of binary system of black and white particles. (A) Completely un-mixed, (B) Random mixed, (C) Perfect (ordered) mixed.

mixing process, it is impossible to achieve the perfect mixing state. Homogeneous mixture[3] in the normal mixing process is defined as a statistically perfect mixture, meaning that the probability of finding the objective material is all the same in any places in the mixture. This mixture is referred to as a random mixture. In order to understand the degree of mixing, it is important to use a statistical method.

When several samples are randomly taken out from the mixture and concentration of each samples are assumed to be x_i ($i=1,2,3,\cdots N$), the average concentration of the sample is calculated as,

$$\bar{x}_s = \frac{1}{N}\sum_{n=1}^{N} x_i \quad (i=1,2,3\cdots N) \tag{5.8.1}$$

If the sampling is conducted in an appropriate manner, the average concentration of $\bar{x}_s$ is equal to the initial concentration of the objective material of $\bar{x}_c$. The corresponding dispersions of the objective material are defined as follows.

$$\sigma_p^2 = \frac{1}{N}\sum_{n=1}^{N}\left(x_i - \bar{x}_c\right)^2 \tag{5.8.2}$$

$$\sigma_s^2 = \frac{1}{N}\sum_{n=1}^{N}\left(x_i - \bar{x}_s\right)^2 \tag{5.8.3}$$

When the initial concentration of the objective material is known, dispersion of the sample can be calculated by Equation (5.8.2). By contrast, Equation (5.8.3) can be used to calculate the dispersion if the concentration of the objective material is unknown. Most of the actual mixing process, the progress of the mixing can be predicted by calculating the dispersion of σ_s^2 using the data obtained from the sampling. However, it is difficult to make the general and useful mixing indices, since the dispersion might be affected by the size of sample, concentration, operating conditions and evaluation method. Therefore, intensive research has been carried out and more than 40 different indices have been proposed, whereas some examples are listed in Table 5.8.2. In this table, σ_r^2 and σ_o^2 indicate the dispersions of sample in the perfectly mixed and the completely un-mixed conditions, respectively.

$$\sigma_r^2 = \frac{\bar{x}_c\left(1-\bar{x}_c\right)}{n} \tag{5.8.4}$$

$$\sigma_o^2 = \bar{x}_c\left(1-\bar{x}_c\right) \tag{5.8.5}$$

Here, n denotes the number of particles in the sample.

As mentioned previously, mixing progresses by the convective mixing, the shearing mixing and the diffusive mixing. The progress of the mixing can be described schematically by Figure 5.8.2. In the normal mixing devices, the convective mixing takes place at the initial stage of the mixing, where the mass of powder largely moves inside the vessel (macro mixing), followed by the shearing mixing. In these stages, the mixing rate can be expressed as follows;

$$\frac{\sigma}{\sigma_0} = \exp\left(-kt\right) \tag{5.8.6}$$

When the standard deviation σ, which is the square root of dispersion, is plotted in a log scale, the temporal change in the standard deviation can be expressed linearly against the mixing time and the inclination of the mixing curve represents the mixing rate constant of k. After attaining the random mixed condition (σ_r), diffusive mixing takes place (micro mixing). Theoretically, it is impossible to obtain the perfect mixing. However, if the size ratio of large and small particles are approximately more than 10 times and the extremely large energy can be imparted to the powders, the small particles orderly cover the surface of the large particles. If the energy is continued to be imparted, the small particles are embedded beneath the large particle surface or the small particle are fused to form the continuous film. This is the mechanism of the surface modification or the dry particle coating.

5.8.4 EVALUATION OF MIXING CONDITION

In order to evaluate the mixing condition, the degree of mixing of the objective material should be measured. The simplest method to determine the degree of mixing is the measurement of number/mass/volume ratio of the objective material among the mixture using sampling methods during the mixing operation.

Figure 5.8.3 introduces several devices used for the powder sampling. For the sampling of powders located near the surface of powder bed, a spoon sampler, which just scoops the surface powders, is well used. For the sampling of powders at the surface or internal of the mixture, a lance sampler is used.

TABLE 5.8.2 Mixing Index

Author	Mixing Index	M_0 (Completely Un-Mixing Condition)	M_r (Perfect Mixing Condition)	Ref. No.
Fan et al.	$M = 1 - \frac{\sigma}{\sigma_0}$	0	1	(4–7)
Lacey	$M = \frac{\sigma_r}{\sigma}$	$\frac{\sigma_r}{\sigma_0}$	1	(8, 9)
Kramer	$M = \frac{\sigma_0 - \sigma}{\sigma_0 - \sigma_r}$	0	1	(10)
Weidenbaum and Bonilla Ashton and Velentin	$M = \frac{\sigma_0^2 - \sigma^2}{\sigma_0^2 - \sigma_r^2}$	0	1	(11, 12)

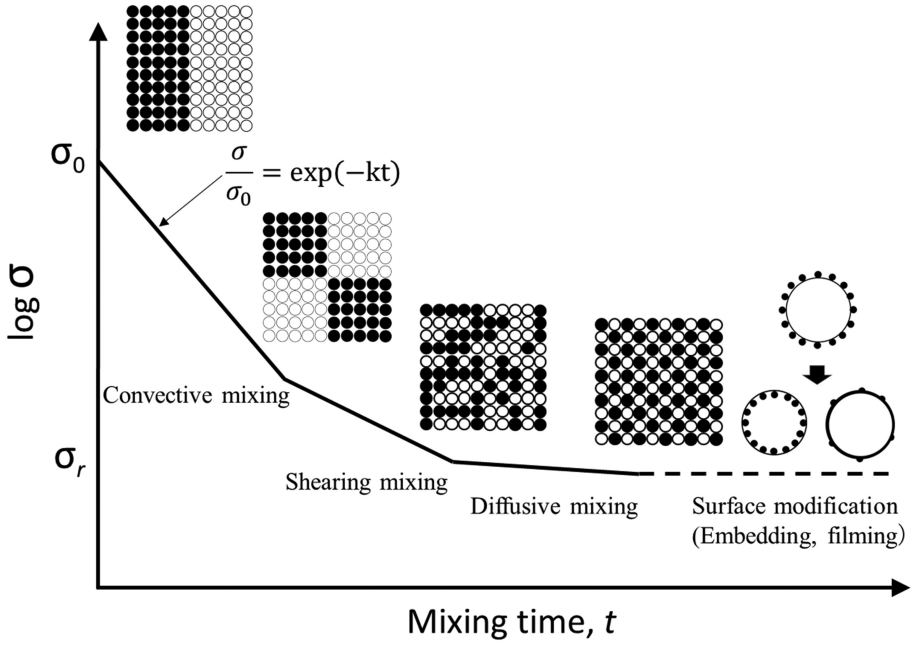


FIGURE 5.8.2 Schematic illustration of mixing process.

A thief, slot and sleeve and trier sampler are also used to take samples from the internal or at the bottom of the mixture. The trier sampler is especially suitable for the cohesive materials. Generally, it is important not to disturb the bulk mixing condition by the sampling procedure and the samples taken out from the mixture should represent the mixing condition of the mixture[12]. Therefore, determination of the appropriate number/mass/volume of the samples and the sample size(amount) are very important. After obtaining the samples, dispersion of the objective material in the mixture can be calculated using Equations (5.8.2 and 5.8.3).

For the evaluation of the mixing condition, different kinds of methods can be used. The methods are summarized in Table 5.8.3. A direct method is the most reliable way to evaluate the mixing condition. If the objective material is different in properties (size, density, shape etc.) from other materials, the objective materials can be separated from the mixture using a sieving, filtering and other separation methods and the number/mass/volume is measured directly. Also, when the properties of mixture vary with the progress of the mixing, the properties are measured for the evaluation. The properties that can be used for the evaluation are many and their examples are electro/electromagnetic, surface and physicochemical properties. Recently, high-performance measurement sensors and devices have been developed, which enable the accurate evaluation of the mixing degree. However, the relationship between the property change and the mixing degree/condition should be investigated previously.

Along with the progress of science and technology, several on-line methods have also been developed to monitor the mixing condition. Satoh et al. developed an optical measurement system to continuously monitor the mixing condition[13,14]. As

Sampling location	Name of Device	Schematic diagram
Surface	Spoon Sampler	
Surface/ Internal	Lance Sampler	
Internal/ Bottom	Thief Sampler	
	Slot Sampler	
	Sleeve Sampler	
	Trier Sampler	

FIGURE 5.8.3 Sampling devices.

TABLE 5.8.3 Mixing Measurement Devices

Category	Principle	Device/Sensor
Direct measurement	Number, mass, volume and density Area occupancy among image Concentration of material Concentration of element	Sieving, filtering Optical/Laser/SEM NIR/UV/HPLC ICP/EDX/ICP/AAS/XPS/ESCA/SIMS
Electro/electromagnetic properties	Electro conductivity Electrical resistivity Volume resistivity Relative permittivity Dielectric constant surface potential	Conductivity meter Resistivity meter Resistivity meter Dielectric spectroscopy Dielectric spectroscopy
Surface properties	Specific surface area Shape Hardness/strength Wettability Lightness/Gloss degree	BET surface area meter Image processing Hardness tester Contact angle meter Colorimeter/gloss meter
Physicochemical properties	Absorption/reflection of X-ray, UV, IR and optical light Crystallinity Thermal properties	X-ray/UV/IR(NIR)/optical light Powder X-ray diffractometer DSC/DTA/TG(TGA)/TMA/DMA
Mechanical properties	Internal friction Adhesion force Hardness/strength Rheology Flowability	Shear tester Spring balance/centrifugal/impact detachment/tensile tester/AFM Hardness(strength)tester Rheometer Flowability tester (angle of repose, etc)

SEM, Scanning electron microscopy; NIR, Near Infrared; UV, Ultraviolet spectroscopy; HPLC, High performance liquid chromatography; EDX, Energy dispersive X-ray spectrometry; ICP, Inductively Coupled Plasma; AAS, Atomic Absorption Spectrometry; XPS, X-ray Photoelectron Spectroscopy; ESCA, Electron Spectroscopy for Chemical Analysis; SIMS, Secondary Ion Mass Spectrometry; UV, Ultra-violet; NIR, Near Infrared; DSC, Differential scanning calorimetry; DTA, Differential thermos analyzer; TG(TGA), Thermo Gravimetry Analyzer; TMA, Thermomechanical analyzer; DMA, Dynamic mechanical analyzer; AFM, Atomic force microscopy.

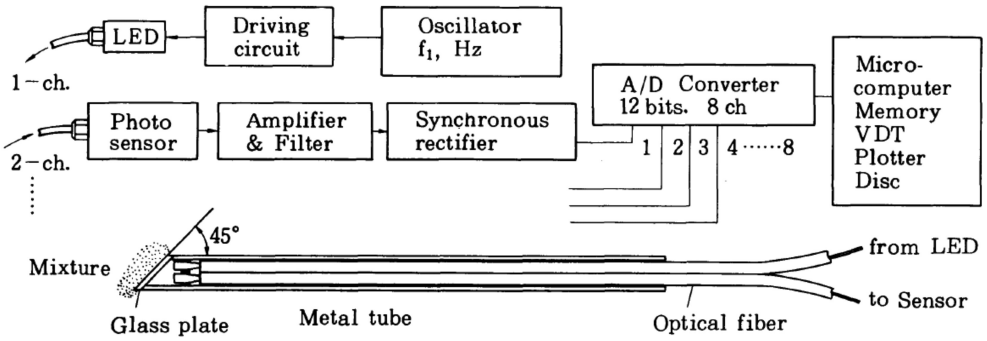


FIGURE 5.8.4 Optical measurement system of mixing degree.

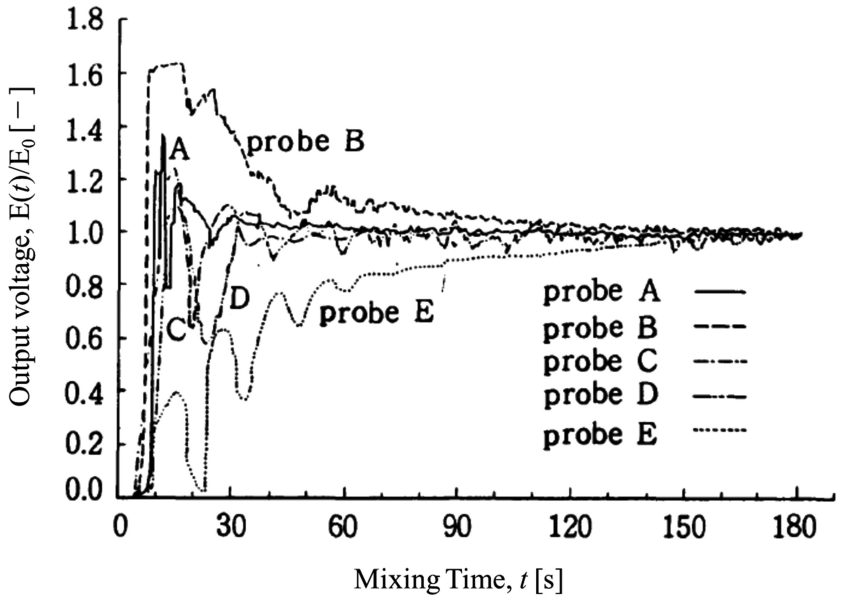


FIGURE 5.8.5 Temporal change in mixing degree by optical measurement system.

shown in Figure 5.8.4, light from a light source was delivered to the mixture through an optical fiber and the reflected light from the mixture was transmitted to a photo-sensor through the optical fiber again and then the change in the intensity of the reflected light was measured continuously. Figure 5.8.5 indicates monitoring of the mixing degree by the optical measurement system. Five probes were installed in the different places of a high shear mixer with a disk-turbine blade at the bottom. The circulating behavior and the time required to reach the terminal mixing degree and the segregation behavior could be monitored.

Recently, precise mixing gathers special interest in the pharmaceutical industries, since the uniformity of each content of active pharmaceutical ingredients (APIs) in the final solid dosage form is strongly required. In most cases, powders are sampled out from the final dosage form such as a tablet and granules and then the content of the API is assayed by using a UV and a HPLC. Although it is important to keep the content of the API within the allowable ranges which is regarded as "Uniformity of Dosage Units," real-time understanding and management of the mixing process hold an important position in the pharmaceutical manufacturing. In this sense, a near infrared (NIR) technology has been attempted for the real-time monitoring of the mixing process[15]. The NIR technology has many advantages as it can measure the content of each material in the mixture simultaneously without contacting to the products. Figure 5.8.6 illustrates the image of a mixer installed on-line NIR system. On a cover plate of a horizontal type high shear mixer, a probe of NIR system is attached directly. Figure 5.8.7 indicates a temporal change in Moving Brock Starboard Deviation (MBSD) of the API among the mixture. Here, the MBSD means the averaged standard deviation of peaks over the full spectrum (all wavelengths). In this figure, it is easily understood that the mixing at the higher rotational speed of the mixer blade indicates the shorter time required to reach the terminal mixing condition and the smaller value of the MBSD.

The mechanism of the mixing has been discussed for a long time. Computer simulation is one of the theoretical approaches to understand the mixing mechanism. Historically, random models[16] have been used, since the mixing takes place by the position exchange of particles and the random models can

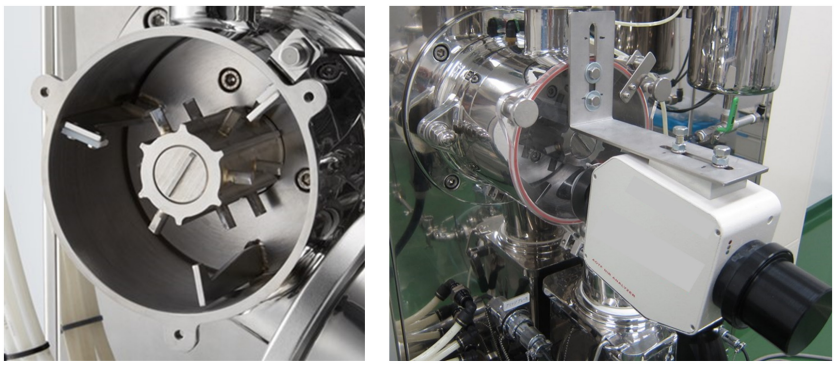


FIGURE 5.8.6 Horizontal high share mixer equipped with NIR sensor.

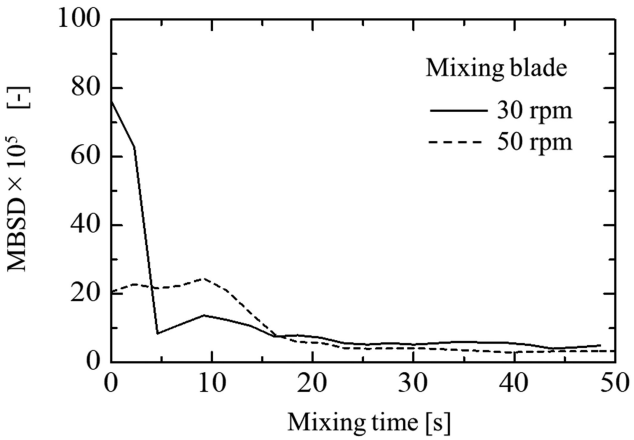


FIGURE 5.8.7 Temporal change in MBSD (Moving Brock Starboard Deviation) of the API among the mixture.

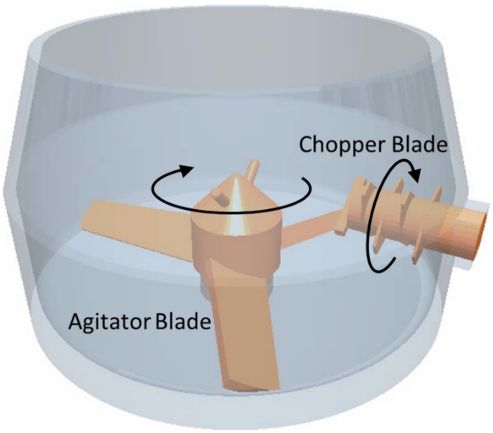


FIGURE 5.8.8 Schematic diagram of high shear mixer used for DEM simulation.

also simulate the position exchange of each particle by using random numbers generated by a computer. However, detailed information regarding the collision, the movement, the circulation and the energy etc. cannot be calculated by the random models. Moreover, it is difficult to design the mixing equipment by using the simulation results.

Recent rapid progress in computer science brings a benefit to the powder technology. Computer simulation especially receives the special benefits. A discrete element method (DEM), a computational fluid dynamics (CFD) and a finite element method (FEM) are the well-known computer simulation methods that can be used in powder handling processes. Especially, the DEM and the CFD models (sometimes they are coupled together) are the most frequently used computer simulation methods recently. In the following, examples of using the DEM for the analysis of the mixing condition are described.

Figure 5.8.8 indicates a schematic diagram of high shear mixer (5L) used for the DEM simulation and Figure 5.8.9 shows snapshots of powder mixing in the high shear mixer using the DEM simulation. In the simulation, spherical particles of 2 mm with non-cohesive force and mono-disperse were used for the simulation. The powder bed during the mixing was divided into 32 sections in the radial direction and 13 sections in the depth directions (total number of divisions were $32 \times 13 = 416$). For the analysis of the mixing condition, two different colors with the same size and other properties were used and then number ratio of each particle among the divided sections were used to calculate the degree of mixing based on the Equation (5.8.7).

$$M = 1 - \frac{\sigma}{\sigma_0} \tag{5.8.7}$$

The degree of mixing was analyzed using three different agitator blades: a blade type with 30 and 15 degrees and a rotating plate without blade. As seen in Figure 5.8.10, the degree of mixing was different, when the agitator blade type varied. The agitator blade with 30 degrees indicates the highest value of the terminal degree of mixing, followed by the values of the agitator blade type with 15 degrees and the disk. The disk type indicates the lowest value of the terminal degree of mixing, implying that the mixing progresses with the movement of the agitator blade and vertically upward movement of particles caused by the rotation of the inclined blade. In this way, the DEM simulation can be used to analyze the mixing condition and behavior of particle segregation due to size, density

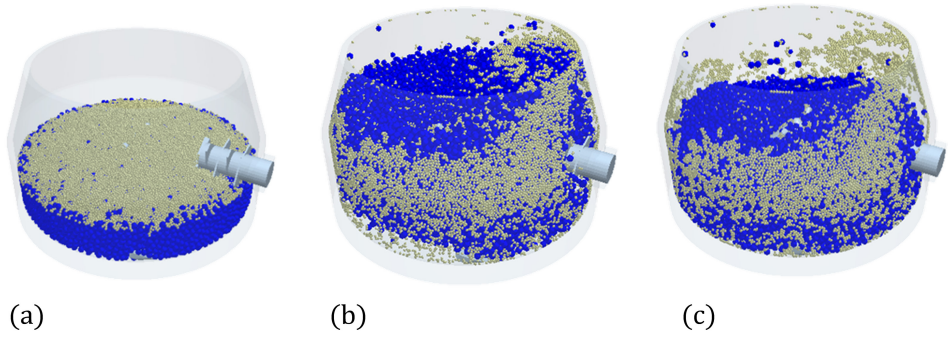


FIGURE 5.8.9 Snapshot of powder mixing in a high shear mixer using DEM simulation. (a) Initial, (b) 0.2 sec, (c) 0.5 sec.

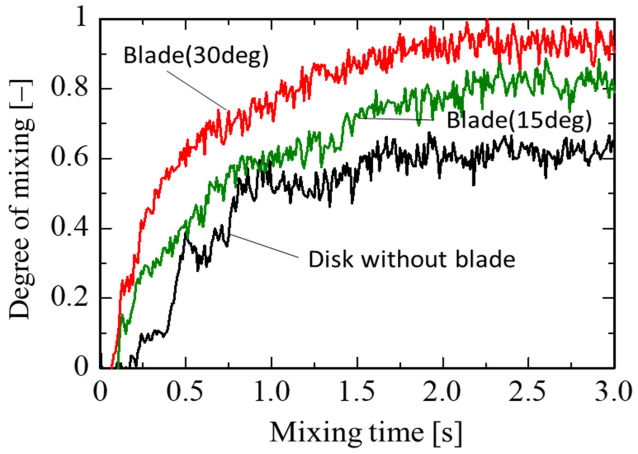


FIGURE 5.8.10 Temporal change in degree of mixing using three different types of agitator blade.

and shape. In addition, it is possible to design the mixing equipment. The simulation can be a promising tool to numerically analyze the mixing process.

5.8.5 CHARACTERIZATION OF MIXING EQUIPMENT

Various types of equipment are used for the mixing and the blending of solid particles. Uniform mixing of particles is required for the equipment and the mixed materials should be stable without any de-mixing and agglomeration during the mixing. However, depending on the properties of particles, the motion and the shear stress imparted during the mixing operation should be considered.

Table 5.8.4 characterizes the mixing equipment based on the vessel, shaft and blade movement and structure. Also, Figure 5.8.11 illustrates schematic images of various types of mixer.

The mixers with movable vessel typically mix powders based on the convective mixing mechanism. These mixers are frequently called tumbling mixers, which consist of horizontal drum, v-cone, double-cone, horizontal cylinder with rocking motion, cubic vessel and inverted cone vessel mixers. The horizontal drum mixer is used for the mild and the gentle mixing of particles. The v-cone and double-cone mixers are often used in the pharmaceutical industry. In these mixers, pharmaceutical granules, tablets and raw materials are mixed by means of free flowing. The convective mixing takes place inside the vessel. Hence, the high shear is not imparted to particles. In the pharmaceutical industry, a small amount of lubricant such as magnesium stearate is mixed into granules before tableting. There is a risk that the strength of a tablet decreases and dissolution speed of API becomes longer due to the excess mixing of the lubricant. In this case, the v-cone and the double-cone mixers are well used. The rocking mixer mixes powders without damage, which utilizes the convective mixing by using the rocking and the rotating actions of the container. Due to the rocking motion, the risk for the segregation becomes much smaller than the other tumbling mixers. The cubic container mixer consists of a cubic container which rotates around the horizontal axis. The powder mixing is promoted by means of the container shape and baffles mounted inside. It is suitable for the gentle mixing of dense powder and granules. The inverted cone mixer uses convective mixing due to the container's inverted motion. Due to the inverted motion, segregation due to the density difference can be prevented. This type of mixer sometimes uses a normal container which can be afterwards used for the storage.

The mixers of which the vessel is fixed is categorized into two types; horizontal and vertical vessels. The horizontal vessel mixer mostly consists of a trough-shaped shell with a semicircular bottom and horizontal longitudinal shaft rotating in a horizontal axis with various types of blades such as screw, ribbon and paddle on the tip of arms mounted on the shaft (single and double shafts are used depending on the application). The clearance between the blades and the semicircular mixer body is quite small so that the amount of the remaining powder becomes minimum. The horizontal vessel mixer can be used in a batch and continuous operations. It is also used for wet granulation and kneading operations.

The vertical vessel mixer with fixed rotating axis is called as a high shear mixer. At the bottom of the vessel, different kinds of blade are mounted on the tip of the axis. The high shear mixer is well used in many industries to mix different kinds of powder materials in a short time. In addition to the bottom blades, some mixers are equipped with a chopper blade rotating at high speed in order to enhance the mixing

TABLE 5.8.4 Characterization of Mixer

Vessel Movement	Vessel Shape	Blade Shaft	Shaft Movement	Common Name	Image
Movable	Horizontal drum	None		Drum mixer	(a)
	V-cone	None		V-cone mixer	(b)
	Double-cone	None		Double-cone mixer	(c)
	Horizontal drum with rocking motion	None		Rocking mixer	(d)
	Cubic drum	None		Cubic drum mixer	(e)
	Inverted drum	None		Inverted drum mixer	(f)
Fixed		Fixed	Screw	Screw mixer	(g)
	Horizontal vessel		Ribbon	Ribbon mixer	(h)
			Paddle	Paddle mixer	(i)
		Fixed		High shear mixer	(j)
	Vertical vessel	Movable	Revolution	Conical mixer	(k)
			Planetary motion	Planetary mixer	(l)

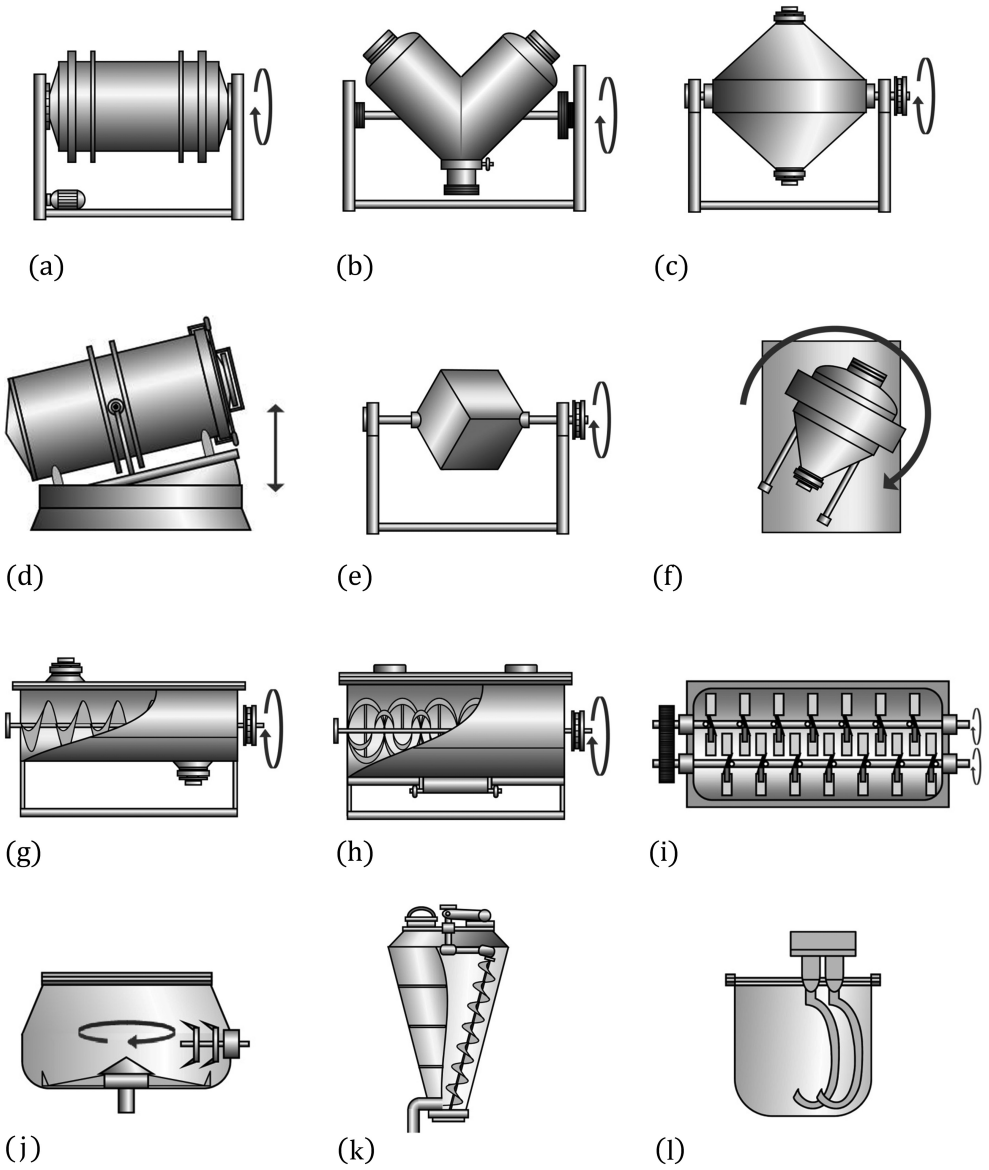


FIGURE 5.8.11 Various types of mixer. (a) Horizontal drum, (b) V-cone, (c) Double cone, (d) Drum with rocking motion, (e) Cubic-container, (f) Inverted cone, (g) Horizontal screw, (h) Horizontal ribbon, (i) Horizontal paddle, (j) High shear, (k) Conical, (l) Planetary.

performance and uniformity and break the agglomerates. Due to the shearing and partial diffusive mixing mechanisms, uniform mixing of a small amount of objective materials into bulk powder is possible. This mixer is used for wet granulation and kneading, as well. Conical vessels with a single movable shaft and vertical cylindrical vessel with a planetary double shaft are used for rapid mixing, wet granulation and kneading. These mixers utilize the convective mixing with the shearing mixing mechanisms.

Besides the above-mentioned mixers, there are airflow and static mixers. The airflow mixer moves and blends powders by the airflow generated mostly from the bottom of the powder bed. Simultaneous operation of the mixing and the drying is also possible. The static mixer does not have any movable part. Typical design of the static mixer is perforated plate and mixer elements in a cylindrical vessel (tube). The energy consumption is very small. In most cases, it is used for the continuous fluid mixing.

For the surface modification of powder, high energy input is necessary. A mixer modified mechanical milling system is sometimes used for this purpose. First of all, guest and host powders (size of the guest powders should be approximately 1/10 smaller than that of the host powders) are put into the mixer and the dispersion and the de-agglomeration of the guest fine powders are taken place to form the ordered mixture, followed by the embedding or the filming of the guest fine powders on the surface of the host powders. This is an example of attaining the perfect mixing shown in Figure 5.8.2.

REFERENCES

1. Masuda, H., Higashitani, K., Yoshida, H., Ed., *Powder Technology Handbook, 3rd Ed*., CRC Press, 2006.
2. Hersey, J.A., *Powder Technol*., 11, 41–44, 1975.
3. Bulslik, D., *Powder Technol*., 7, 111–116, 1973.
4. Fan, L.T., Chen, Y.M., *Powder Technol*., 61, 255–287, 1990.
5. Fan, L.T., Chen, S., Watson, C.A., *Ind. Eng. and Chem*., 62, 53–69, 1970.
6. Fan, L.T., Wang, R.H., *Powder Technol*., 11, 27–32, 1975.
7. Fan, L.T., Chen, S.J., Watson, C.A., *Ind. Eng. Chem. Process Design Develop*., 62, 53–69, 1970.
8. Lacey, P. M. C., *J. Applied Chem*., 4, 257–268, 1954.
9. Lacey, P.M., *Trans. Inst. Chem. Eng*., 21, 53–59, 1943.
10. Kraemer, J., Svensson, J., Melgaard, H., *Drug Dev. Ind. Pharm*., 25, 217–222, 1999.
11. Ashton, M.D., Valentin, F. H. H., *Trans. Inst. Chem. Eng*., 44, 166–188, 1966.
12. Muzzio, F.J., Robinson, P., Wightman, C., Brone, D., *Int. J. Pharm*., 155, 153–178, 1997.
13. Satoh, M., Deguchi, Y., Komura, S., Miyanami, K., *J. Soc. Powder Technol Japan*, 22, 79–84, 1985.
14. Alonso, M., Satoh, M., Miyanami, K., *Powder Technol*., 59, 65–67, 1989.
15. Scheibelhofer, O., et al., *AAPS Pharm. Sci. Tech*., 14, 234–244, 2013.
16. Ottino, J.M., Khakhar, D.V., *Ann. Rev. Fluid Mech*., 32, 55–91, 2000.



Taylor & Francis
Taylor & Francis Group
http://taylorandfrancis.com

5.9 Slurry Conditioning

JunIchiro Tsubaki and Takamasa Mori

5.9.1 SLURRY CHARACTERIZATION

Slurry is usually not a final product but an intermediate one. The slurry is prepared as an intermediate product and then dried to be the final product. Since in the shaping process slurry must have fluidity, the viscosity measurement is very important to characterize the slurry. After shaping, the fluidity is not important because the slurry does not need to deform or flow any more. On this stage, it becomes important to characterize the thickening behavior of the slurry during the drying process.

Dense slurry is able to become a liquid or solid state even though the particle concentration of the slurry is not changed. Because particles in the slurry make an assembling structure depending on the inter-particle force. If the repulsive force is strong enough to prevent the coagulation between particles, every particle suspends individually and the slurry is a Newtonian fluid. Oppositely, if the attractive force is strong enough to coagulate all the particles, the slurry becomes a gel. Thus, the structure of assembled particles plays the dominant role to the slurry behavior. However, the direct observation[1–3] of the structure of assembled particles is capable only in thinner slurry of about 5 vol%, but not in a dense one. The particle assembling structures of dense slurry are usually estimated from the flow or thickening behavior.

Flow Behavior

The flow behavior is evaluated by the deformation of the fluid between two parallel plates with a gap of Δ [m] as shown in Figure 5.9.1.[4] The shear stress τ [Pa] is measured by moving one plate at constant speed of u [m·s^{-1}]. The flow behavior is expressed on the diagram of the shear stress and shear rate shown in Figure 5.9.2.[4] Where the shear rate $\dot{\gamma}$[s^{-1}] is defined by u/Δ. The flow behavior is classified into 5 patterns as shown in Figure 5.9.2. If all the particles in slurry are individually suspended without an assembling structure, this slurry behaves as a Newtonian fluid, and the flow behavior is characterized by viscosity μ [Pa·s]. If particles in slurry make some structures, the flow behavior is deviated from that of Newtonian fluid, depending on the structures. In non-Newtonian fluids, the flow behavior is characterized by apparent viscosity μ_{app} [Pa·s] defined by $\tau/\dot{\gamma}$. The viscosity of Newtonian fluid is constant in spite of the shear rate but the apparent viscosity is depending on the shear rate. Hence, the apparent viscosity should be described as a function of shear rate. The flow behavior can be approximated by the following equation.

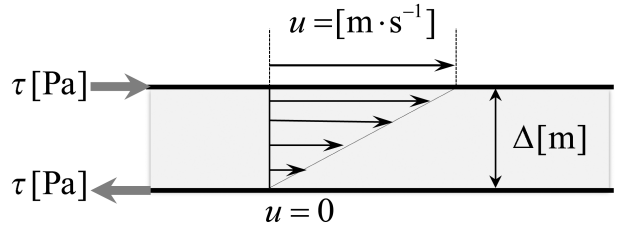


FIGURE 5.9.1 Deformation of a fluid.

$$\tau = \tau_C + k\dot{\gamma}^n \tag{5.9.1}$$

where τ_C [Pa] is the yield shear stress and k [Pa·s^n] and n [–] are experimental constants. If the shear stress acting on slurry is smaller than τ_C, the slurry behaves as a solid.

Various types of viscometers are commercially available, but we have to use the viscometers that can measure the shear stress and the shear rate independently. Such viscometers are a coaxial double cylinder type rotational viscometer and a cone-flat plate type rotational viscometer shown in Figures 5.9.3 and 5.9.4.[5] The shear stress and the shear rate are calculated from the measured torque T [N·m] and rotation speed ω [rad·s^{-1}] by the following equations. In case of a rotational viscometer of coaxial double cylinders:

$$\text{Shear stress:} \quad \tau = \frac{T}{2\pi R_i^2 L} \tag{5.9.2}$$

$$\text{Shear rate:} \quad \dot{\gamma} = \frac{R_i \omega}{R_o - R_i} \tag{5.9.3}$$

where:

R_i, R_o [m] are the radiuses of the inner and outer cylinder
L [m] is the height of the inner cylinder

Considering that the gap of the inner and outer cylinder is parallel, R_o/R_i must be less than 1.1.[6] In case of a rotational viscometer of cone and plate:

$$\text{Shear stress:} \quad \tau = \frac{3T}{2\pi R^3} \tag{5.9.4}$$

$$\text{Shear rate:} \quad \dot{\gamma} = \frac{v}{\Delta} = \frac{r\omega}{r\tan\theta} = \frac{\omega}{\theta} \tag{5.9.5}$$

where:

R [m] is the radius of the cone
θ is the angle between the cone and plate

According to the JIS,[4] θ has to be in the range of 0.3 ~ 3°. The rotational viscometer of a single cylinder and the vibrating viscometer are often used for slurry characterization, in spite of the fact that they are allowed to use only Newtonian

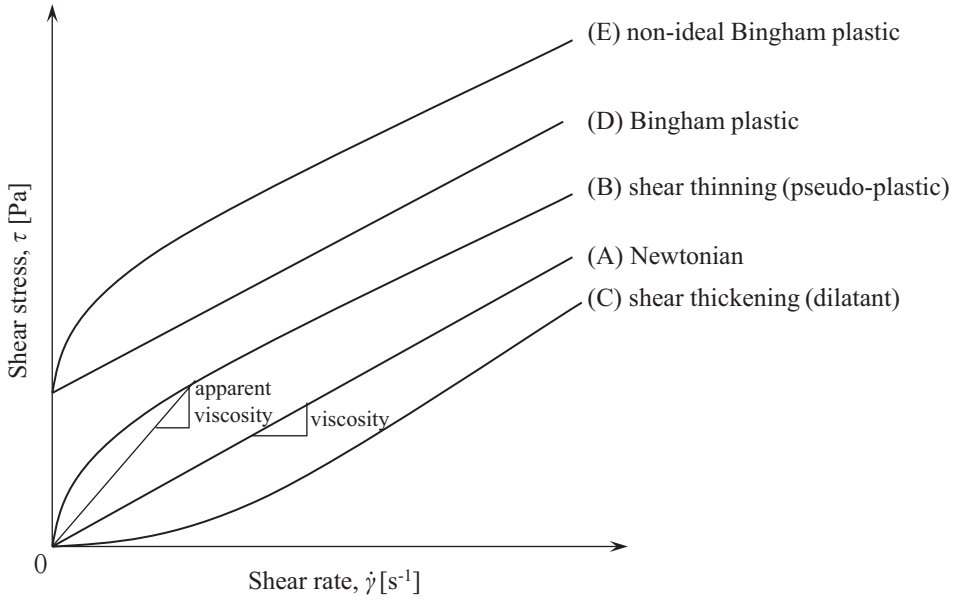


FIGURE 5.9.2 Flow behavior of slurry.

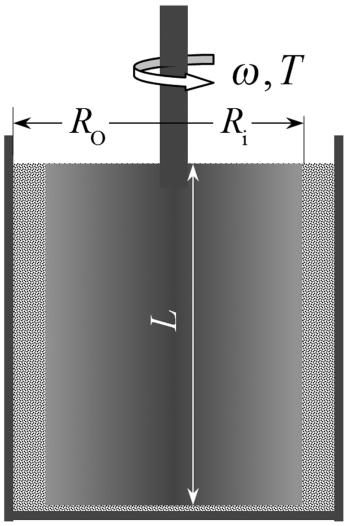


FIGURE 5.9.3 Coaxial double cylinder type rotational viscometer.

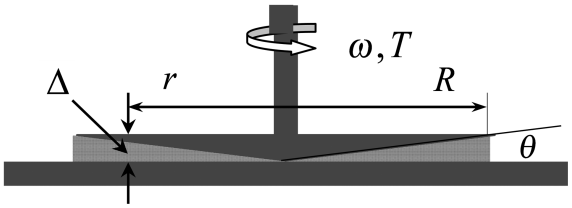


FIGURE 5.9.4 Cone-flat plate type rotational viscometer.

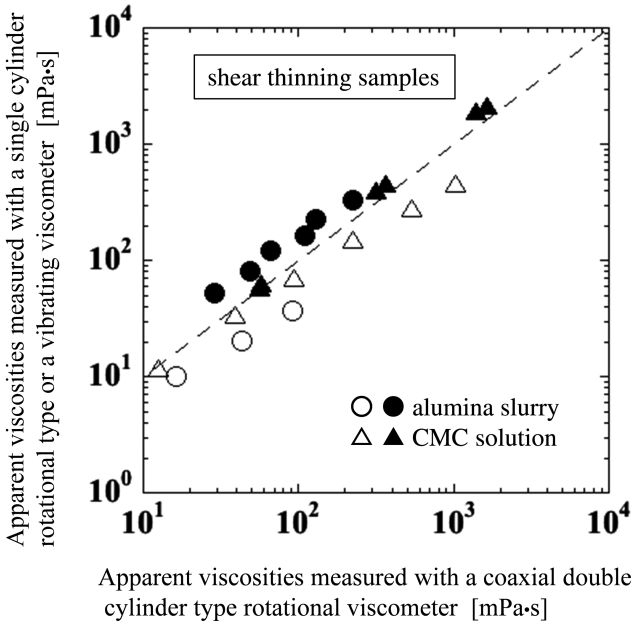


FIGURE 5.9.5 Comparison of different type viscometers (open marks: vibrating, solid marks: single cylinder type).

fluids. Figures 5.9.5 and 5.9.6 are the comparisons of the different types of viscometers.[7] In case of both shear thinning (Figure 5.9.5) and thickening (Figure 5.9.6) slurry, the values of the apparent viscosity measured with a single cylinder rotational type and vibrating viscometer are different from the values of a coaxial double cylinder type rotational viscometer. In case of shear thickening slurry a vibrating viscometer could give the measured values one-tenth of those of a coaxial double cylinder type rotational viscometer as shown in Figure 5.9.6.

Thickening Behavior

A batch-settling test shown in Figure 5.9.7 is the most popular way to evaluate the thickening behavior. In the batch-settling test, the slurry heights are measured against the settling time

like Figure 5.9.8. The batch-settling test is not only the most inexpensive and easiest, and also informative, because we can visibly observe the changing of the slurry state. But this method has a fatal disadvantage that needs a long measuring time. For example, in the case of submicron particles, weeks or months are needed to measure the settling time under the gravity, and several days will be needed even though we use the centrifugal force which is several thousand times larger than the gravitational force. Consequently the settling test is hardly used on the production process in factories.

To shorten the measurement time a new method has been developed,[8–10] which is the settling hydrostatic pressure method shown in Figure 5.9.9.[11] Since a friction on the interface between the particle and fluid supports the mass of a settling particle, the hydrostatic pressure increases as much as the friction. Supposing that slurry has a particle volume concentration of ϕ [–] and the concentration is uniform all over the slurry at the initial stage, the hydrostatic pressure P_{max} [Pa] at depth H [m] is expressed with the following equation.

$$P_{max} = \{(\rho_p - \rho_f)\phi + \rho_f\} gH \tag{5.9.6}$$

where ρ_p, ρ_f [kg·m^{-3}] are particle and fluid density. Until all the particles pass the depth H, the settling hydrostatic pressure P gradually decreases and then becomes P_{min} expressed with the following equation.

$$P_{min} = \rho_f gH \tag{5.9.7}$$

The settling hydrostatic pressure changes into 5 patterns against time as shown in Figure 5.9.10. The descending rate of the settling hydrostatic pressure depends on the assembling structure in slurry. If all the particles are individually settling without coagulation, the variation of P is the smallest as shown by the line (A) in Figure 5.9.10. It increases with the particle coagulation as shown by the line (B). And it sharply descends like the

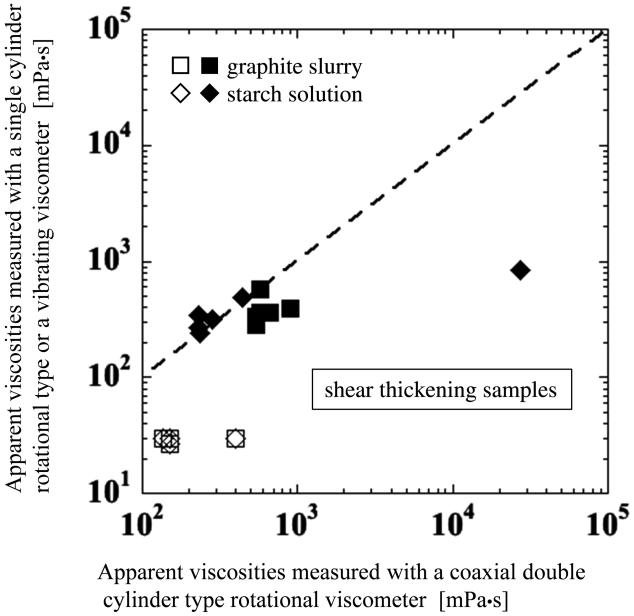


FIGURE 5.9.6 Comparison of different type viscometers (open marks: vibrating; solid marks: single cylinder type).

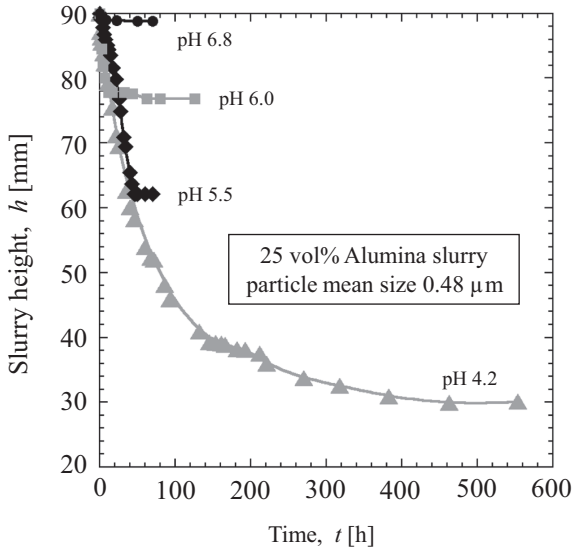


FIGURE 5.9.8 An example of the batch-settling tests.

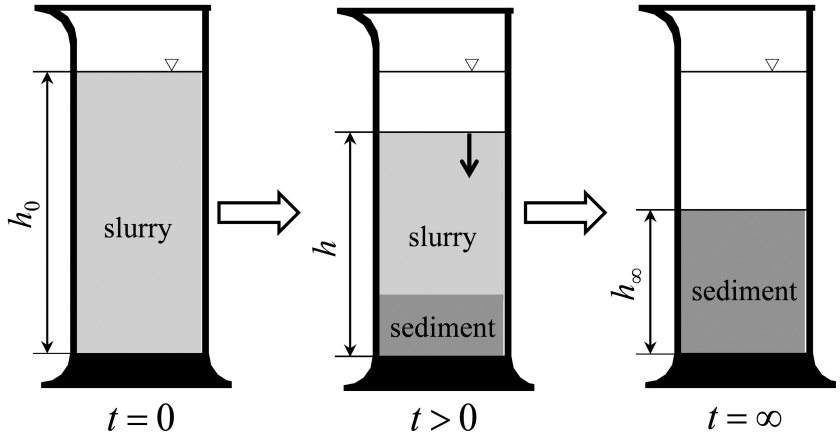


FIGURE 5.9.7 Batch-settling test.

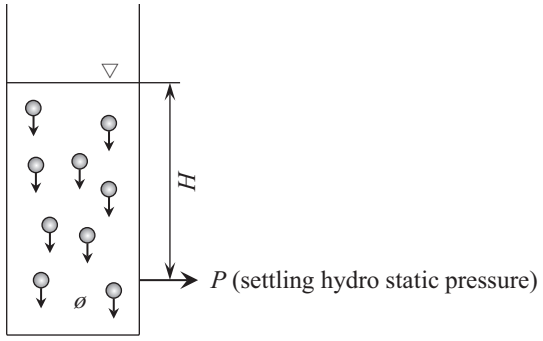


FIGURE 5.9.9 Principle of the settling hydrostatic pressure method.

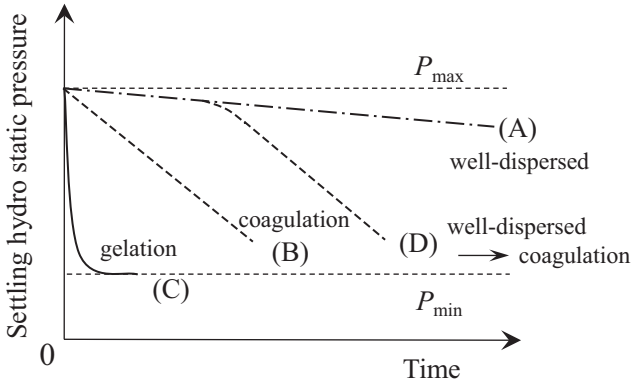


FIGURE 5.9.10 Typical patterns of the settling hydrostatic pressure changing.

curve (C) if all the particles are rapidly coagulated as a gel. When initially well-dispersed particles turn into coagulation on the way, it changes following the polygonal line (D). Figure 5.9.11 is the measured settling hydrostatic pressure of the slurry used in Figure 5.9.8. As is obvious in Figure 5.9.8, the interface between the slurry and the supernatant descend along the same line regardless the slurry condition, so it takes a long time to discern a certain datum from the other data. In Figure 5.9.9, however, the settling hydrostatic pressures individually depend on the slurry condition from the early stage, so the data are easily distinct from the other from the early stage.

A filtration test of slurry by constant pressure is also a useful evaluation method to characterize the thickening behavior.[12–14]

5.9.2 SLURRY PREPARATION

An ideal slurry preparation will be as follows.

1. Hard aggregates are dispersed to primary particles.
2. Particles suspend uniformly in slurry without segregation.
3. Particles repel each other or keep the desired assembling structure in stable state.

First of all, particles and a dispersion medium are mixed, followed by crushing hard aggregates in the mixture with a ball mill or a beads mill. The uniformity of the slurry is increased

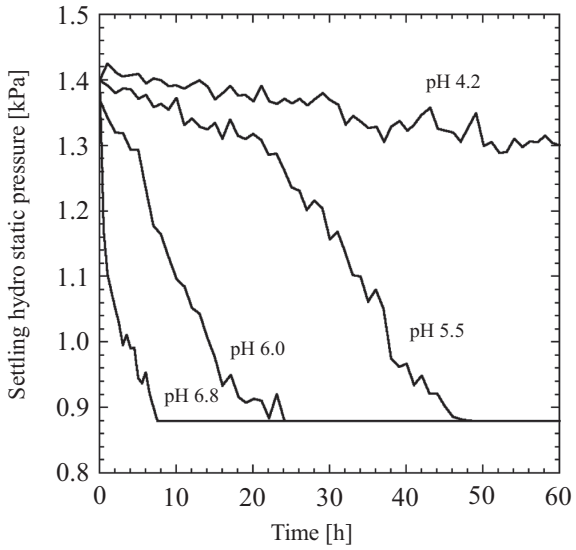


FIGURE 5.9.11 The measured settling hydrostatic pressure of the same slurry as used in Figure 5.9.9.

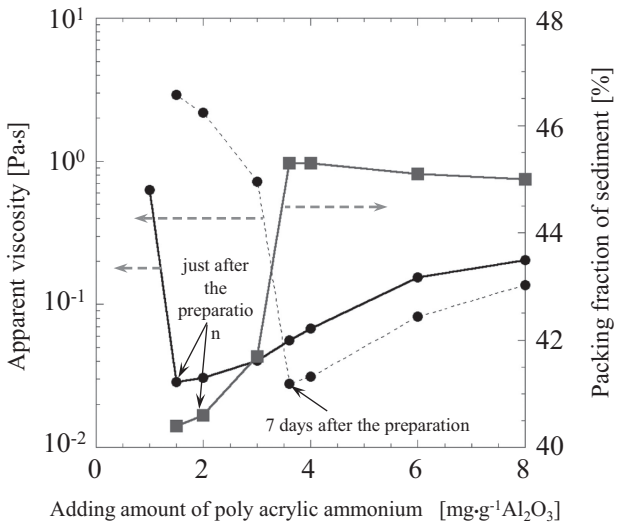


FIGURE 5.9.12 Apparent viscosity and packing fraction of 20 vol% alumina slurry.

with milling time. If the particles do not have any affinity to the dispersion medium, a surfactant or some surfactant-like material is needed to improve wettability of the particles. To prevent particles from coagulation and keep the assembling structure in a stable state, some additives are usually added.

The prepared slurry is usually characterized with an apparent viscosity, because its measurement time is shorter than that of a settling test and hydrostatic pressure, and in many cases they are corresponding with each other. However, when the repulsive force is not enough to prevent particles from coagulation, they are not corresponding as shown in Figure 5.9.12.[15] Figure 5.9.12 shows the apparent viscosity and packing fraction of sediment of 20 vol% aqueous slurry of 0.48 μm alumina particles. The slurry was prepared by changing the adding amount of polyacrylic ammonium. It

is supposed that well dispersed slurry gives densely packed sediment. According to the apparent viscosity measured just after the preparation, the slurry of which adding amount is 1.5 mg $g^{-1}Al_2O_3$ should give the densest sediment, but the densest sediment is given from the slurry of which adding amount is 3.5 mg $g^{-1}Al_2O_3$. It means that the apparent viscosity measured just after the preparation is not corresponding to the packing fraction of the sediment. But if the packing fraction is compared with the apparent viscosity measured 7 days after the preparation, they are corresponding well to each other. The reason why the apparent viscosity measured just after the preparation is not corresponding with the packing fraction can be considered as follows. If the additive amount is not sufficient, here that is less than 3.5 mg $g^{-1}Al_2O_3$, the assembling structure in the slurry changes like the line (D) in Figure 5.9.10. If the changing of the assembling structure has completed in the early stage of the sediment formation, the apparent viscosity measured just after the preparation is not corresponding with packing fraction.

Therefore, we have to pay attention to the long-term changes of the assembling structure to optimize the slurry condition.

REFERENCES

1. Takahashi, M., Oya M., Fuji M., *J. Soc. Powder Technol. Japan*, 40, 410–417, 2003.
2. Asai, K., Naganawa K., Mori T., Tsubaki J., *J. Soc. Powder Technol. Japan*, 48, 518–525, 2011.
3. Asai, K., Naganawa K., Mori T., Tsubaki J., *J. Soc. Powder Technol. Japan*, 49, 177–183, 2012.
4. Tsubaki J., Mori T., Satone H., *Introduction to Slurry Technology*, Maruzen Publishing, Tokyo, 2016, p.98.
5. Tsubaki J., Mori T., Satone H., *Introduction to Slurry Technology*, Maruzen Publishing, Tokyo, 2016, p.115.
6. JIS Z 8803, Methods for viscosity measurement of liquid, 2011.
7. Mori T., Moriyama S., Nakabawa T., Tsubaki J., *J. Soc. Rheolog Japan*, 45, 157–165, 2017.
8. Tsubaki J., Kuno K., Inamine I., Miyazawa M., *J. Soc. Powder Technol. Japan*, 40, 432–437, 2003.
9. Mori T., et al., *J. Soc. Powder Technol. Japan*, 41, 522–528, 2004.
10. Mori T., et al., *Adv. Powder Technol.*, 3, 319–332, 2006.
11. Tsubaki J., Mori T., Satone H., *Introduction to Slurry Technology*, Maruzen Publishing, 2016, p.149.
12. Tsubaki J., Kim H., Mori T., Sugimoto T., *J. Soc. Powder Technol. Japan*, 40, 438–443, 2003.
13. Kim H., Mori T., Tsubaki J., *J. Ceram. Soc., Japan*, 113, 761–767, 2005.
14. Mori T., Kim H., Ato K., Tsubaki J., *J. Ceram. Soc., Japan*, 114, 318–322, 2006.
15. Otsuka H., et al., *J. Eur. Ceram Soc.*, 31, 517–522, 2012.



Taylor & Francis
Taylor & Francis Group
http://taylorandfrancis.com

5.10 Granulation

Kazuo Murase and Isao Sekiguchi

Granulation is one process of particle size enlargement, which agglomerates or compacts fine powders into larger granules to improve powder characteristics for the additional interaction between powders with capillary, viscous and chemical binding forces and promotes the agglomerate growth with the mechanical agitation or compaction. The granulation techniques are adopted to gain the advantages of solids handling, as listed in Table 5.10.1.[1,2]

5.10.1 GROWTH MECHANISMS OF WET GRANULATION

The granule growth mechanisms of wet granulation[1–5] are classified into three steps based on granule rate processes as shown in Figure 5.10.1: (1) wetting of liquid binder over a dry powder and nucleation of primary particles, (2) coalescence or layering of nuclei and granule consolidation by compaction, (3) granule breakage and attrition by agitation.

Wetting and Nucleation

Wetting is the first contact between dry powder and binder liquid in wet granulation. The work of adhesion for an interface per unit interface area (W_{ad}) is described with the works of cohesion for a liquid and a solid, which are required to separate a liquid and a solid.[6,7]

$$W_{ad} = \gamma_{lv} + (\gamma_{sv} - \gamma_{ls}) = \gamma_{lv}(\cos\theta + 1) \qquad (5.10.1)$$

where γ_{lv}, γ_{sv}, γ_{ls} and θ are the liquid-vapor, solid-vapor, liquid-solid surface tension and contact angle. The spreading condition of a liquid over a solid depends on the difference between adhesion and cohesion works. If adhesion works exceed over cohesion works, a liquid distributes around a solid, i.e. high wettability. Two types of nucleation formulation are called as distribution, which identifies with the situation of liquid surrounding over a solid such as a layering and immersion,[3] which describes liquid penetration into a powder bed. Binder characteristics are measured by contact angle meter and surface tensiometer for wettability, Washburn test and capillary rise test for drop penetration rate into a powder bed, flotation test for particle penetration rate into liquid and inverse gas chromatography for the interaction strength of liquid/particle.[8]

Hapgood et al.[9] introduced the dimensionless spray flux (ψ_a) and dimensionless drop penetration time (τ_p) into the nucleation regime map classified by three regions: drop controlled, intermediate and mechanical dispersion regions. ψ_a and τ_p are respectively defined as the ratio of spray flux to solid flux ($\psi_a \equiv 3V/2Ad_d$), which is a measure of binder coverage on the powder surface and the ratio of liquid penetration time to circulation time ($\tau_p \equiv t_p/t_c$). Here, V, A and d_d are spray volumetric flux, spay area and average drop size. In the drop controlled region at lower values of ψ_a and τ_p, the nuclei distribution is controlled by one particle to one drop due to the high wettability. The fast penetration time of the binder results in the narrow nuclei size distribution. In the mechanical dispersion region of higher values of ψ_a and τ_p, the drop coalescence results in the wider size distribution due to viscous poor wettability of the binder, which requires the mechanical dispersion by agitation. The intermediate region demands for the optimal binder spray flux and binder properties, especially viscosity, in order to prevent the trouble shooting such as clumps.

Coalescence & Consolidation

Nuclei coalescence induced by the collision of agglomerates or the device wall causes the granule growth and consolidation by compression, which decreases granule porosity and migrates liquid into an interstice of particles. The extents of coalescence and consolidation of primary agglomerates influence on granule structures, i.e. deformability of granules. The low deformable growth is controlled by the binder liquid dissipating the collision energy in low agitation granulators such as drum, pan and fluidized bed granulators. On the other

TABLE 5.10.1 Purposes of Granulation

Production of particulate materials for easier solid handling or processing.
Reduction of segregating blends and hygroscopic caking for trouble shootings.
Improvement of flow properties and bulk handling for reducing troubles of fine particles such limp formation or entrainment.
Improvement of solubility for hydrophobic materials in food, detergent and pharmaceutic engineering.
Control of compaction for uniform filling and pressing in a die or a mold.
Control of particulate density for packing or feeding without dust losses or hazard.
Control of permeability for a more stable flow of fluids through fixed beds of particulates.
Control of release time and immobilization for chemical ingredients in granular materials such as pharmaceutical or catalytic products.

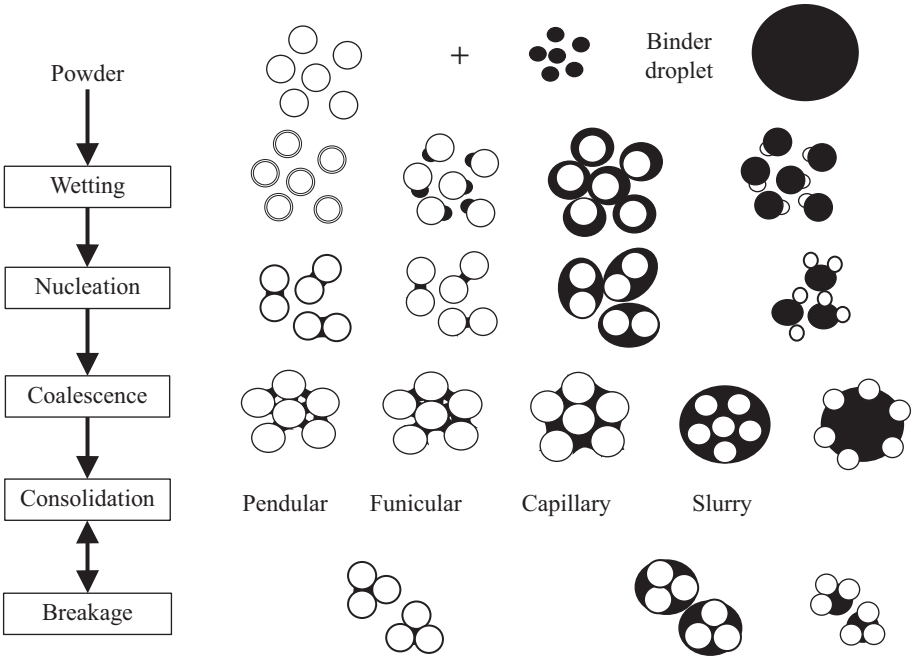


FIGURE 5.10.1 Schematic diagram of granule growth mechanism.

hand, the deformable growth results in the high granule collision, plastic deformation and granule consolidation in high shear types of granulators.

Iveson et al.[10] introduced the maximum granule pore saturation (s_{max}) and Stokes deformation number (St_{def}) into the growth regime map of granulation classified by seven regions: nucleation only, steady and rapid growth, induction growth, dry free flowing powder, slurry and crumb. s_{max} and St_{def} are respectively defined as $w\rho_s(1\text{-}\varepsilon_{min})/\rho_l\varepsilon_{min}$ and $\rho_g U_c^2/2Y_g$, where w, ρ_s, ρ_l, ρ_g, ε_{min}, U_c and Y_g are the mass ratio of liquid to solid, the densities of solid, liquid and granule, the minimum porosity, the representive collision velocity and the dynamic yield stress. The Stokes deformation number is a measure of the ratio of impact kinetic energy to the plastic energy absorbed per unit strain. At the range of relatively low saturation and deformation, the initial wetting and nucleation maintain. In the steady growth mode at the intermediate saturation, the average granule size linearly increases with granulation time, which creates the coarse, weak, narrowly sized distributed and easily deformable granule. In the induction growth mode at the lower deformation, the granule size drastically increases with the rapid coalescence after the liquid binder is squeezed to the surface due to the strong and slow consolidation, which creates the fine, widely size-distributed and lowly deformable granule. The high deformation with high velocity results in crumb states.

Breakage or Attrition

Breakage or attrition results from the external shear force applied by an impeller or chopper blade in high-shear granulator or by granule collisions. Tardos et al.[11] proposed a simple model based on Ennis's model[12] with Stokes deformation number for breakage and attrition (St_{break}), which is defined by $mu_0^2/2V\tau$. Here, m, V, τ and u_0 are the mass and volume of agglomerate, the shear force, the travelling speed. The criterion of breakage and attrition describe $St_{break} > St^*_{break}$, where St^*_{break} is the critical Stokes number determined experimentally.

5.10.2 MECHANICAL PROPERTIES OF WET GRANULES

The states of liquid brides adhered to particles are classified into four cases based on liquid saturation: (1) pendular, (2) funicular, (3) capillary, (4) droplet,[13] as shown in Figure 5.10.1. In the pendular state, each particle is connected by a liquid bridge, which has no overlapped outlines of another bridges. In the capillary state, all the voids in granules are filled with binder liquid, where the capillary suction enhances the interaction of granules. The funicular state is the intermediate between pendular and capillary states. The funicular state is divided into two types in terms of the continuity of liquid and solid phases in granules.[13] In the droplet state, particles are included within a liquid droplet. The categories are divided by water content of Atterberg limits,[14] which are shrinkage, plastic and liquid limit. Monitoring of energy consumption in a kneading machine or in a mixer granulator[15] characterizes the dispersion state of particles and the degree of liquid saturation. During the constant mixing, the capillary force at the pendular state drastically consumes the energy. The continuous profiles of liquid at the funicular state damp the increasing tendency at the capillary state due to the wettability of liquid. The over-wetting suspension above the full saturation decreases the energy due to fluidity of slurry.

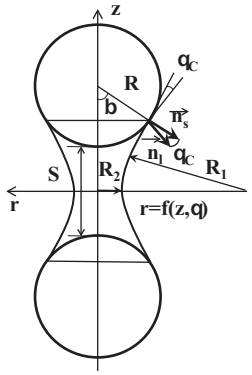


FIGURE 5.10.2 Static liquid bridge adhere to two spheres. R_1, R_2, R, S, β and θ are the principal radius of curvatures, sphere radius, gap between spheres, the half-filling angle and liquid contact angle. $\mathbf{n}_s$ and $\mathbf{n}_l$ are unit normal vectors on sphere and interface at contact line.[16]

Static Strength of Liquid Bridge

The static strength of a pendular liquid bridge adhered to two spherical particles corresponds to the capillary force with an axi-symmetrical liquid binder as shown in Figure 5.10.2,[16] which is composed of a liquid surface tension and the hydrostatic force based on the pressure difference across the interface (ΔP). The capillary forces with the toroidal approximation of a circular liquid surface[17,18] are described by two methods[19] as Gorge method ($F_{C,Gorge}$) at neck part of a bridge and the boundary method ($F_{C,Boundary}$) on the three phase contact line.

$$F_{C,Gorge} = 2\pi R_N \gamma_{lv} + \pi R_N^2 \Delta P \tag{5.10.2a}$$

$$F_{C,Boundary} = 2\pi R \gamma_{lv} \sin\beta \sin(\beta + \theta_C) + \pi R^2 \sin^2\beta \Delta P \tag{5.10.2b}$$

where R_N, R, γ_{lv}, β, θ_C are radius at the narrowest part, particle radius, liquid-vapor surface tension, half-filling angle and contact angle. ΔP is estimated by the Young-Laplace equation.

$$\Delta P = 2H \cdot \gamma_{lv} = \gamma_{lv}\left(\frac{1}{R_1} + \frac{1}{R_2}\right) \tag{5.10.3}$$

where H, R_1 and R_2 are mean curvature of a liquid bridge, principal curvature radius in Figure 5.10.2. The negative ΔP corresponds to the capillary suction, which acts in the attractive direction. The boundary method is recommended for multi-particles configurations due to the asymmetry bridge,[20] which demands for the solution of the Young-Laplace equation. The mean curvature is mathematically evaluated at the curved surface as follows.

$$2H = -\nabla_S \cdot \mathbf{n}_l \tag{5.10.4}$$

where ∇_s and $\mathbf{n}_l$ are a gradient vector and unit normal vector at a curved surface.[21] The solution of Young-Laplace equation is equivalent to the profile at the minimum Gibbs free energy, which is composed of surface tension and gravitational potential energy. The liquid bridge profile at the zero first variation of effective free energy (E) with the constraint of a fixed bridge volume ($\delta E = 0$) corresponds to the outline of the interface at equilibrium. The sign of the second variation ($\delta^2 E$) contributes to the stability analysis. The capillary force depends on the dimensionless Bond number, $Bo=(\rho_l-\rho_v)gR^2/\gamma_{lv}$, which corresponds to the ratio of surface tension to gravity on a liquid bridge.

The strength of wet granules largely depends on liquid saturation regimes, which is measured by the tensile and uniaxial compression test.[22] The relation between isostatic ($\sigma_{Isostatic}$) and uniaxial ($\sigma_{Uniaxialc}$) tensile stresses for a pellet is presented as follows.[23]

$$\sigma_{Isostatic} = \frac{1+\sin\phi}{2\sin\phi}\sigma_{Uniaxial} \tag{5.10.5}$$

where ϕ is the angle of internal friction. Schubert et al.[23] shows tensile strengths depend on liquid states such as pendular, funicular, capillary, droplet states. The tensile strength (σ_t) of wet granular is estimated by Rumpf's model,[24] where a wet granule constitutes of a uniformly equal-sized sphere with liquid bridge and the isostatic stress of liquid bonding force. Note that the model underestimates the tensile strength for fine, wide-size distributed particles. Schubert[23] estimated the pendular and capillary tensile strength of wet granular materials with Rumpf's model as follows.

$$\sigma_{t,Pendular} = \frac{1-\varepsilon}{\varepsilon}\frac{F_{C,Boundary}}{d_p} \tag{5.10.6}$$

$$\sigma_{t,Capillary} = SA\frac{1-\varepsilon}{\varepsilon}\frac{\gamma_{lv}\cos\theta}{d_p} \tag{5.10.7}$$

where ε, d_p, $F_{C,Boundary}$, S and A are the granule porosity, particle diameter, capillary force estimated by boundary method, liquid saturation and a value from 6 to 8. The tensile strength in the funicular state is approximated by a linear combination of tensile strengths at critical pendular and capillary states.[22]

$$\sigma_{t,Funicular} = \sigma_{t,Pendualr}\frac{S_c - S}{S_c - S_f} + \sigma_{t,Capillary}\frac{S - S_f}{S_c - S_f} \tag{5.10.8}$$

where S_c and S_f are saturation at capillary and funicular state.

Dynamic Strength of the Liquid Bridge

The dynamic strength of the liquid bridge depends more on the larger viscous or frictional interaction than capillary force of the static strength and contributes to the granule growth such as coalescence and consolidation. Granule deformability related to the yield strength of a granule depends on liquid saturation,[25] which increases mean granule size and reduces the friction as lubrication and the yield strength due to the dissipation to granule collision.

The strength of a dynamic pendular liquid bridge adhered to two spheres (F_v) is approximated with lubrication theory as follows.[26,27]

$$F_V = \frac{3\pi\mu r_p^2}{2h}\frac{dh}{dt} \tag{5.10.9}$$

where h, r_p and μ are half gap between particles, particle radius and Newtonian viscosity. Viscous force[27] depends on the velocity gradient with in a bridge and act to resist the direction of movement and kinetics of wetting hysteresis.[28]

Iveson et al.[29] shows the relationship between dimensionless peak flow stress of a pellet ($Str^*=\sigma_{peak}d_p/\gamma_{lv}$)) with the dimensionless Capillary number ($C_a=\mu U/\gamma_{lv}$), which is a measure of the ratio of viscous ($\pi\mu U r_p$) to capillary force ($\pi\gamma_{lv}r_p$). Surface tension is dominant for the tensile strength in the Region I at the static state ($C_a < 10^{-4}$), and the strength depends on the binder viscosity, strain rate and particle size in the region II at the dynamic state ($C_a > 10^{-4}$).

Ennis et al.[12] modeled collisions of two spheres of radius (r_p) in the normal direction for coalescence of non-deformable granules, which are coated with a uniform layer of liquid of thickness (h_0) and have surface asperities of height (h_a). Kinematics of particles induces velocities at approach, viscous dissipation and rebound stages, then the relation between the dimensionless viscous Stokes number ($St_v = 8\rho r_p/9\mu$) and the critical Stokes number St_v^* leads to three regimes of granulation condition for coalescence which is determined by the conditions of halt particle velocity at the rebound stage. St_v^* is defined as $(1 + 1/e)\ln(h_0/h_a)$, where e is the restitution coefficient of particles. St_v corresponds to the rationed kinetic energy of particles to the energy dissipated by liquid viscosity through the collision. The ratio of St_v to St^* is classified into three stages: (1) non-inertial regime for $St_v/St^* \longrightarrow 0$, (2) inertial regime for $St_v/St^* \longrightarrow 1$ and (3) coating regime for $St_v/St^* \longrightarrow \infty$.

Liu et al.[30] expanded the Ennis's model to apply for the plastic deformable granules with an elastic modulus (Y_d) and a dynamic yield stress (E^*) in a high shear granulator. The relationship between the dimensionless Stokes deformation number ($St_{def} = mu_0^2/2D_p^3Y_d$) and the dimensionless viscous Stokes number ($St_v = 8mu_0/3\pi\mu D_p^2$) classifies into two coalescence types: In type I, the kinetic energy of the approaching velocity is dissipated by a liquid bridge, and in type II, the kinematic energy of separating velocity is less than the elastic strain energy.

5.10.3 TESTING METHODS FOR EVALUATING THE AGGLOMERATE GRANULATION OF WET POWDERS

Flocculent masses of wet powders prepared by mixing dry powder with liquid binders have a marked tendency for agglomeration with the tumbling, vibrating or agitating motion in granulators.[31] Figure 5.10.3[31] shows a schematic diagram of a tapping-type gyratory agglomerator for evaluation of the generation and growth of agglomerates from the wet powders. This test instrument consists of a shaking pan with a rubber bottom (disk diameter = 200 mm) tapped at the central part through a conic swing of the pendulum. The tapping motion is induced by an eccentric circular motion of the rubber disk and by the subsequent circular swing of the pendulum rod when the lower front of the pendulum strikes the cylindrical obstacles located at the cyclic positions.

Wet powders on the rubber disk accompanied by both the gyratory and the subsequent tapping motion change from a flocculent mass to harder and denser agglomerates in a visible state. The agglomeration behavior of wet powder is subjected to the method of preparing the feed and is often brought into a powdery or pasty state. The quality of the agglomerate at various liquid contents (C_d) can be evaluated by an agglomeration index (I_g), which is defined as the ratio of the liquid binder content for preparing a wet powder to liquid binder content at a plastic limit.

$$I_g = \frac{C_d}{\left[\varepsilon_0/(1-\varepsilon_0)\right](\rho_l/\rho_s)} \tag{5.10.10}$$

where ε_o, ρ_s and ρ_l are the void fraction in a close-packed bed of dry powder after tapping and densities of solid particle

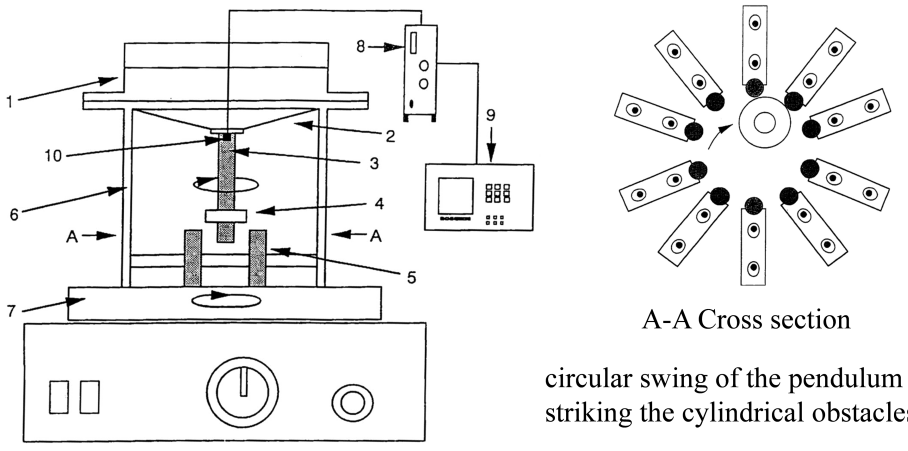


FIGURE 5.10.3 Schematic diagram of a tapping-type gyratory agglomerator: 1. Vessel, 2. Rubber, 3. Pendulum bar, 4. Balance weight, 5. Impact bar, 6. Cylinder, 7. Vibrating disk, 8. Senser amplifier, 9. FFT analyzer, 10. Accelerometer.[31]

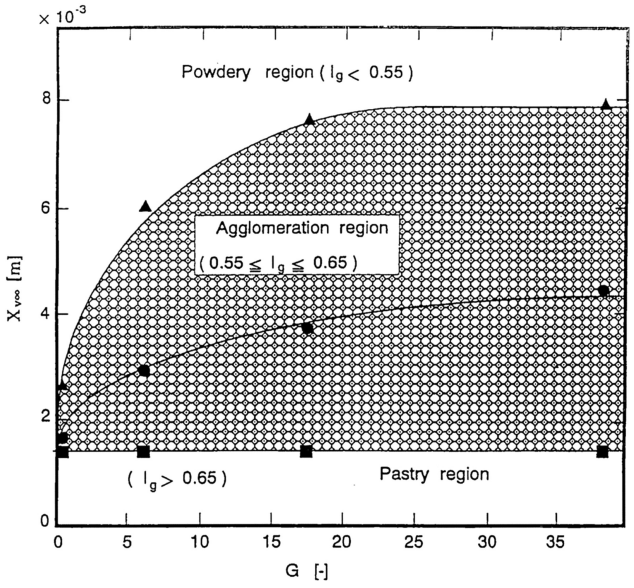


FIGURE 5.10.4 Agglomeration criteria for calcium carbonate powder agglomerated with methanol.[31]

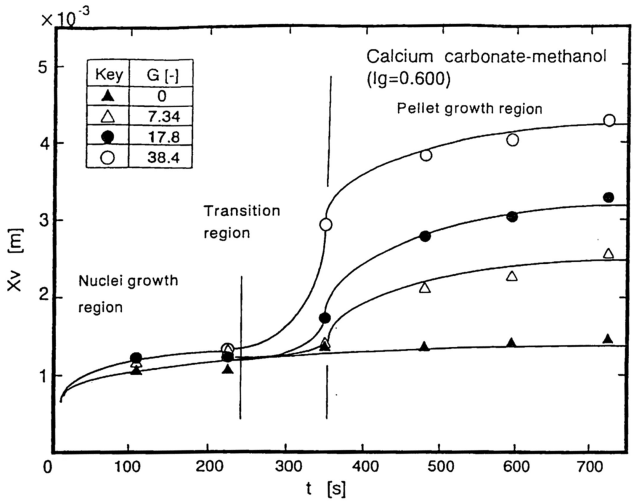


FIGURE 5.10.5 Effect of vibration intensities on the growth rate of agglomerates.[31]

and liquid. In addition, the plastic limit of the wet powder in Equation 5.10.10 can be determined by an agitating torque method in which the torque exhibits a distinct maximum of a liquid binder content corresponding to the plastic limit.[32] The value of I_g for establishing stable agglomerates favorable to a tumbling or agitating granulation generally lies in the range of about 0.50 to 0.75.

Figure 5.10.4[31] shows a relationship between agglomerate diameter ($X_{v\infty}$) and vibration intensity (G) for calcium carbonate (volume mean particle diameter = 10.2 μm, $\varepsilon_o = 0.476$) methanol system. The agglomerate diameter in the Figure 5.10.4 is the final equilibrium value in the agglomerate growth. The growth of equal-sized agglomerates becomes excellent in both ranges $0.55 \leqq I_g \leqq 0.65$ and $0 < G \leqq 38.4$. It is apparent that the agglomerates in such a region become progressively larger in lower values of I_g with increasing vibration intensity. In this region, an important characteristic of agglomerate growth is such that the agglomerates suddenly grow to larger ones in the course of the agglomeration process under sufficient vibration intensity, as shown in Figure 5.10.5.[31] This tendency is remarkable in lower values of I_g because of the combined action of breakage and coalescence. However, smaller agglomerates formed near the critical value of $I_g = 0.65$ experience simple random coalescence in the nuclei region, yielding extremely different agglomerate sizes.

Granulation Due to Granule Growth Modes

A drum granulator in batch operation is important in characterizing the agglomeration behavior of damp powders.

The growth rate of granules in the nuclear growth region is expressed in most cases as follows.[33]

$$\frac{dX_a}{dt} = \frac{k_n}{3} X_a \tag{5.10.11}$$

where X_a and k_n are the arithmetic mean diameter of granules on a mass basis and the time-invariant rate constant of granule growth by coalescence. If a nuclear or smaller agglomerate assembly in the floc-like mass of damp powders has a relatively narrow size distribution, a rate equation of granule growth in the first stage is derived from a random disappearance–coalescence model. The size distribution of a granule originating from a floc-wise mass of damp powders, as mentioned above, is formulated with the aid of statistical mechanics to become.[34]

$$R_m(X) = \exp\left(-BX^3\right) \tag{5.10.12}$$

where $R_m(X)$ is the cumulative mass fraction of granules coarser than diameter (X), and B is a constant. In the case of a wet powder having a relatively narrow-sized floc-like mass prepared by screening or kneading, the granule size data obey Equations 5.10.11 and 5.10.12. The careful preparation of feed material is a prerequisite for a successful granulation in the early stage of tumbling granulation.

The granule growth period in the coalescence region is very short, and the rate of granule growth obtained from the plot of dX_a/dt versus t has a momentary maximum.[35] Formation of large granules in the compaction region is probable because the layering mechanism of fragments onto the growing granules extremely depends on the breakage of granules due to impaction, compaction or abrasion. The rates of granule growth in the above three regions are given by the following proportional connections.[36]

1. Nuclei growth region (nucleation): $dX_a/dt \propto X_a$
2. Transitional growth region (coalescence): $dX_a/dt \propto 1/X_a$
3. Ball growth region (compaction): $dX_a/dt \propto 1/X_a^3$

The point of granulation in a hot fluidized bed with spray is that a liquid binder, suspension, or melt is atomized into the

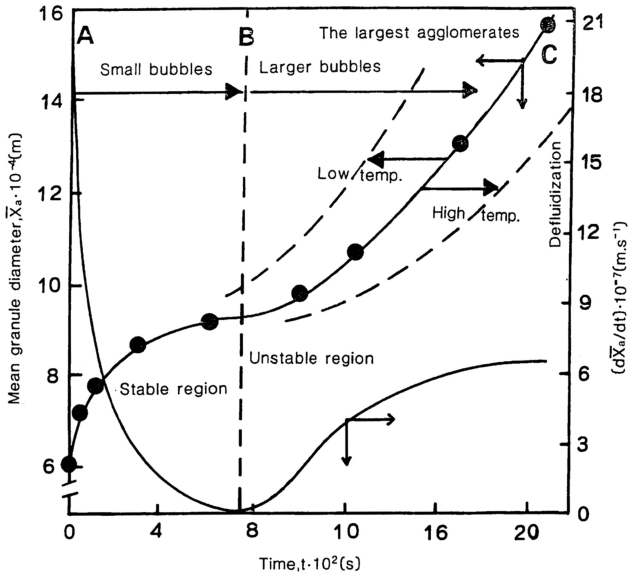


FIGURE 5.10.6 Rate of granule growth in a hot fluidized bed spray granulator.

fluidized bed of the particles to be granulated.[12,37–41] Typical growth of granules formed by a batch fluidized bed spraying system is shown in Figure 5.10.6.[41] The formation of granules at a time interval between A and B is very stable, but the subsequent granulation step forms larger granules or crumbs, so that the fluidized bed becomes extremely bubbly until defluidization occurs. Normal operation of the bed is carried out for the period A to B, in which it is a matter of course that the heat and mass balance must be satisfied. Further treatments of granulation in the granule growth mode, including pan-type granulators, are summarized in Table 5.10.2. Spouted beds developed as the improved type of fluidized bed are often employed to produce granules or coating particles. Spray liquid is introduced as a spray into the conical base of the bed together with the hot spouting gas. This granulation method is usually suitable for the coating or layering particle process due to the rapid evaporation of spray liquid in the spouting gas stream at high temperature.

The seed particle is adapted from Okaniwa et al.[41]; sodium chloride (X_a=0.606 mm), binder, gelatine solution (20.0 wt%). W=6 kg, F_p=0.63 g/s, u=0.703 m/s, air temperature=353K.

Machine-Made Product Modes

The compaction of solid particles or small granules in a confined space can be performed by punch, piston, roll or other means of applying pressure. The degree of consolidation achieved during the compacting press depends mainly on the stress–strain relation[34] and on the physical and chemical properties of solid particles. The compaction mechanism of solid particles is divided into four stages, as follows: (1) increase in the resistance due to the mutual friction of movable particles, (2) breakage of the interlocking among adjacent particles, (3) deformation and fracture of constituent particles and (4) work-hardening of the particle bed. Such behavior seems to occur in the compaction of narrow solid particles. For a wide variety of solid particles, many empirical equations are proposed for the relationship between compacting pressure and void fraction.[54]

Many different machines are used for making the desired compacts. The forming mechanism of a thick disk-shaped compact in a cylindrical die[55] is expressed by

$$\frac{F_U}{F_L} = \exp\left(\frac{4\mu_W kL}{D}\right) \tag{5.10.13}$$

where F_U and F_L are respectively the applied and transmitted forces, k is the ratio of radial to axial stress, μ_w is the coefficient of wall friction and D and L are the diameter and thickness of a compact. The expression is straightforward and simple to use in spite of some drawbacks.

In roll compactions, except briquetting machines, particulate material with or without binders is fed into the compacting zone between two smooth rolls, as shown in Figure 5.10.7,[56] and the compacted sheet can be cut to the desired granule size. The relationship between the void fraction of compacted sheet and the angle of nip (θ_n) is given by

$$\cos\theta_n = 1 + \frac{D_S}{D_B}\left(1 - \frac{1-\varepsilon_P}{1-\varepsilon_n}\right) \tag{5.10.14}$$

where ε_p and ε_n are the void fraction of the compacted sheet and of the material between two rolls at the nip angle (θ_n). The horizontal force (F_H) exerted on the roll-bearing blocks is given by

$$F_H = \frac{\pi D_R B}{360}\int_0^{\theta_n} p\cos\theta d\theta \tag{5.10.15}$$

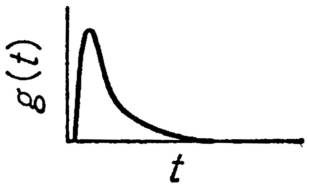
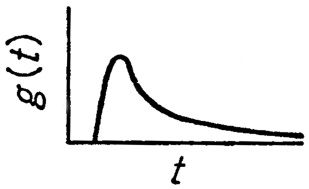
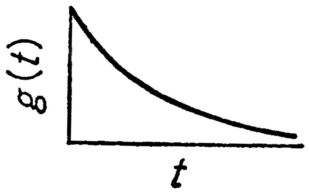
where B is the length of the active roll surface and p is the pressure exerted by the material undergoing compaction on a certain portion of the roll surface. To integrate Equation 5.10.22, it is necessary to measure the compaction pressure distribution and the void fraction along the circumference of the roll.[56] F_H in Equation 5.10.15 is derived from the theory of solids conveyance between two smooth rolls.[57]

In the application of screw-type extruders, the delivery rate of a screw rotating within the barrel should be exactly equal to the flow rate of material through the die. The delivery mechanism of the screw has some difficulties, but there is a theory of the screw conveyance of solids in clay extrusion.[58] On the other hand, in connection with extruding flow characteristics of carbon paste[59] or other solid–liquid mixtures,[60] the pressure P required to extrude the material through a nozzle or multi-hole die is expressed as

$$(V - V_0) = K(P - P_0) \tag{5.10.16}$$

where V is the velocity of piston movement, P_0 and V_0 are the ultimate limit of both P and V and K is a constant related to the fluidity of the material through the dies and related to the structure of a nozzle or multi-hole die. Further useful granulation methods are outlined in the following section.

TABLE 5.10.2 Typical Operating Data for Pan or Drum Granulators and Fluidized Bed Spray Granulators

Granulator Type	Feed Conditions	Operating Conditions	Residence-Time Distribution
PAN	1. Powder and spray droplets 2. Continuous operation 3. I_g=0.50 to 0.75	Rotating speed (N) $N_{optimum}$=(0.40 to 0.75)$N_{critical}$ $N_{critical}=2538(\sin\theta/D)^{1/2}$ θ : Angle of inclined pan θ = 44 to 55 deg. Depth=(0.10 to 0.25)Diameter	[42,43] 
DRUM	1. Damp powders, or powder and spray droplets 2. Batch or continuous operation 3. I_g=0.50 to 0.75	Rotating speed $N_{optimum}$=(0.45 to 0.85)$N_{critical}$ $N_{critical}=2538/D^{1/2}$ θ=0 to 8 deg.	1. Backmixing at a ring dam[44]  2. Ideal pistol flow
FLUIDIZED BED WITH SPRAY	1. Powder and spray droplets 2. Batch or continuous operation	Superficial gas velocity $u_{mf}<u_0<0.5u_t$ u_{mf}: Minimum fluidized velocity u_t: Terminal velocity	Ideal perfect mixing flow 

Granulator Type	Hold-Up (W)	Granule Growth Rate	Size Distribution
PAN	W/F_p $=K(F_p/\rho_s N_d D^3)^{\alpha}(H\alpha_r^{1/2}/D\theta N_d)$[42] F_p: Mass flow rate α_r: Repose angle N_d: Rotating speed of pan	1.$dV/dt=K(V_e-V)$[45] 2.Rate of granule growth due to an elliptical orbit model on the bottom of pan[46] V: Volume of a granule V_e: Ultimate volume of a granule	Larger granules due to size-classifying properties of inclined pan can be separated in part at the discharge rim
DRUM	W/F_P $=K(L\alpha_r^{1/2}/D\theta N_d)$ $\cdot(F_P/\rho_s N_d D)^{\alpha}(H/D)^{\beta}$ [44]	Coalescence growth. $X_a/X_{a,0}=\exp(k_n Z_d/3)$[33] Layering growth $X_a=X_{a,0}+k_s Z_d$	1. Equation 5.10.16[34] 2. Granule size distribution taken both sizes of upper and lower limits into consideration[47,48]
		Granule population balance[49–51]	
FLUIDIZED BED WITH SPRAY	$W/F_P=A_f L_f(1-\varepsilon_f)/F_P$ Expansion ratio (N_v) $N_v=f(u_0/u_t)$	Batch operation $X_a/X_{a,0}=\exp(C_t)$ Continuous operation $X_a/X_{a,0}=1/(1-C_t),(C_t<1)$ Layering rate[52]	Mass balance in a batch or a continuous operation[53]

5.10.4 GRANULATORS

Figure 5.10.8[2] shows the basic designs of various granulators, which are classified into granule growth mechanism mode and mechanical forced granule mode.

Figure 5.10.9[61] shows the schematic diagram of relationship between agglomeration behavior and agitating torque in dense particle-phase granulation systems. The centerline corresponds to dry powder materials with zero liquid saturation. The right regime indicates the phenomena and granulator type for liquid-phase wet materials with increasing liquid saturation, which transits the liquid distribution from pendular to slurry sate by way of funicular and capillary. The left regime corresponds to the system with fluidization by gas including a spray drier.

5.10.4.1 Granule Growth Mechanism Mode

Tumbling Granulation Methods

Typical inclined pan granulators consist of an inclined disk with a rim and a granule size separating ability. Raw materials are fed continuously from above onto the nearly central part of the disk, and larger granules formed are discharged beyond the rim. Binding liquid is sprayed onto incoming

fine particles and smaller granules at a spraying zone on the disk. To form narrow granules, the agglomeration index (I_g) is adjusted in the range of about 0.5 to 0.75. The continuous granulation of damp powders within a slightly inclined rotating cylinder is used in industrial practice. If the equipment is made suitable for an ideal piston flow, experimental data for the batch drum granulator are applicable. The inside wall of the drum is covered with a rugged rubber sheet or wire net and equipped with an adjustable or reciprocating scraper. When the granule product discharged has a wide size distribution, more than two rotating drums are used in a closed-circuit system. A rotating conical drum granulator has a granule size separating ability.[62]

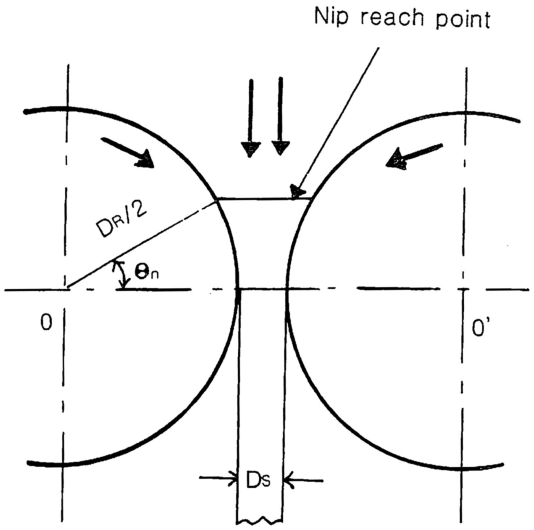


FIGURE 5.10.7 Schematic diagram of a roll compaction. (By Kurtz et al.[56] with permission.)

Fluidized Bed Spray Methods

The fluidized bed spray granulator is composed of a hot gas fluidized bed and a two-fluid spray nozzle. A binding liquid or solution is sprayed onto a bed surface of fluidized particles or is sprayed directly into the bed. The larger spray droplets compared to seed particles generally result in the formation of agglomerates, which are influenced by a wide variation of operating conditions. In relation to granule growth of simultaneous coating and agglomeration in a hot fluidized bed, the size distribution and growth rate of granules under continuous operation can be derived from the material balance of the bed particles.[52,53,63] The general principal in the spouted bed spray granulator is to spray solution,[64–67] melt[68] or slurry[69,70] onto seed particles that circulate in a bed spouted by hot gas. This type of granulator is used to granulate several materials of industrial interest.

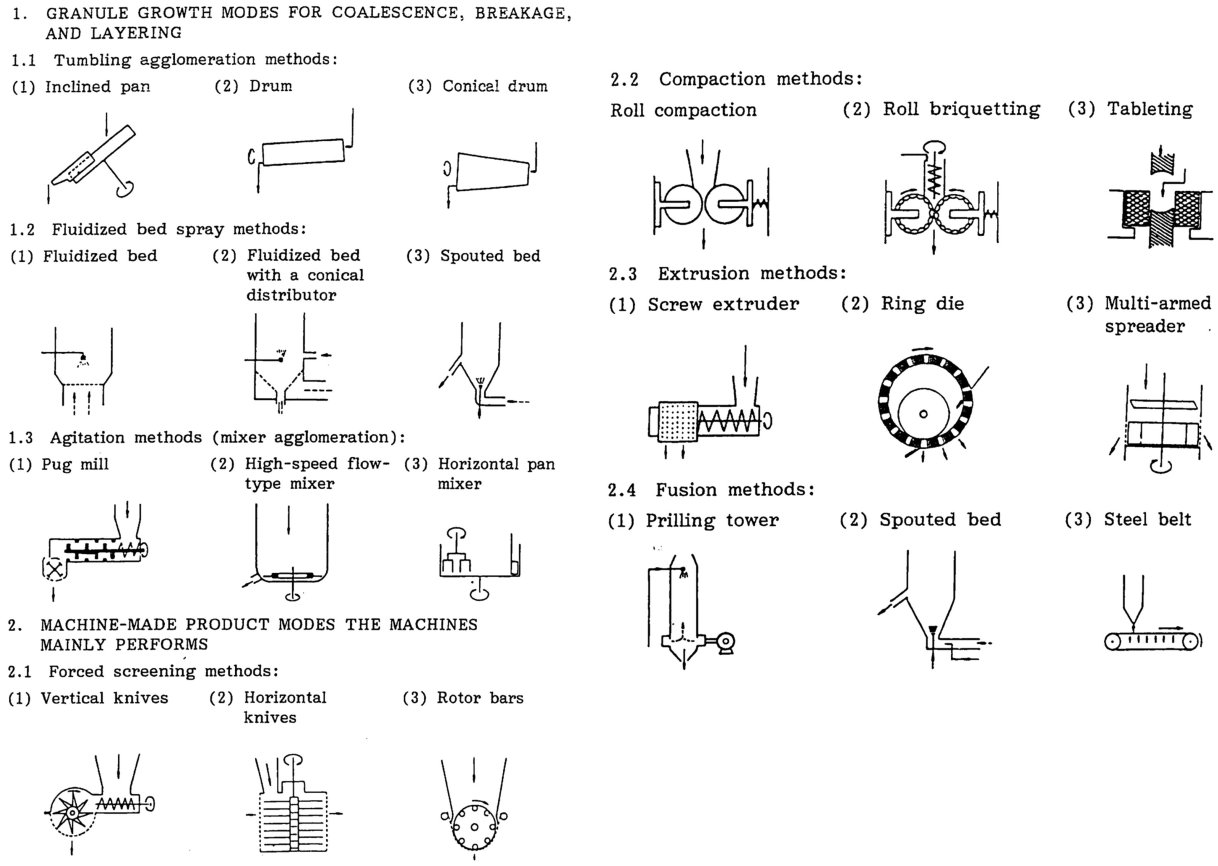


FIGURE 5.10.8 Typical granulation methods and equipment.[2]

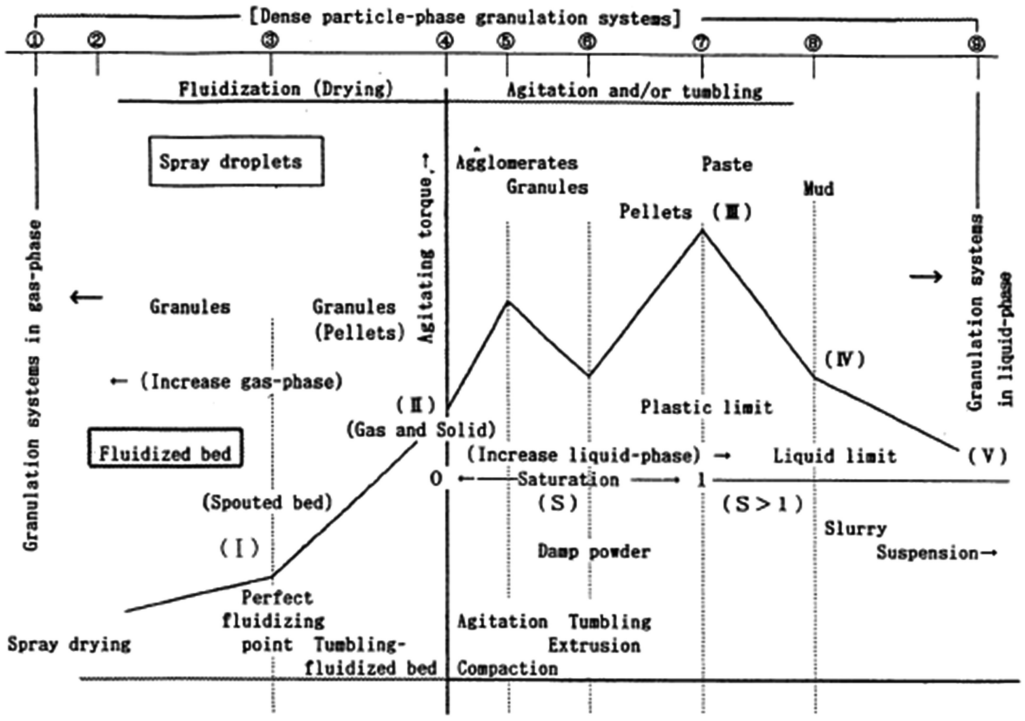


FIGURE 5.10.9 The scheme illustrating relationship between agitating torque and agglomeration behavior with increasing liquid or gas-phase in dense particle-phase granulation systems.[61]

Agitation Methods (Mixer Agglomeration)

The mixing or blending of solid–liquid mixtures not only results in the dispersion of liquid in powders but is also suitable for the formation of small granules or agglomerates. A pugmill is generally used in the pretreatment for further granulating operation, but its application is limited to special fields such as fertilizer formulation or clay preparation. Other mixers by means of pins, pegs or blades are utilized in a similar manner as the above. Granular products tend to show a wide size distribution. The high-speed flow-type mixer is of growing importance in the formation of very small granules and is often used to coat coarse particles with a he-particle layer rather than coalesce with each other. The horizontal pan mixer consists mainly of a rotating mixing pan, a counter-rotating blade and a stationary scraper for cleaning the interior surface of the pan. Dry powders fed into the pan are wetted by adding a liquid binder so that granules are formed depending on the moisture content and the rotational speed of the pan or the blades.

5.10.4.2 Mechanical Forced Granule Modes

Forced Screening Methods

A comminuting granulator consists of rotating vertical knives and a chamber, the lower part of which holds interchangeable screens. The advantages are the disintegration of dry clumps, cakes or larger agglomerates. The tornado mill, a type of screen granulator, is well suited for the disintegration of sticky agglomerates, in which moist material passes through a perforated screen by means of the high-speed rotor with a row of cutting knives. The oscillating granulator is used for processing large granulated materials, and the disintegration mechanism depends on a rubbing action created by a combination of a rotor bar and a wire screen with a suitable aperture.

Compaction Methods

The roll compaction machine consists of two opposing counter-rotating rolls and a feeding arrangement such as gravity feeder or tapered screw feeder. The product, compacted in sheet form, is granulated by a simple disintegrator or mill. The principal feature of a roll briquetting machine is similar to roll compaction, and the feed material is compacted to egg- or pillow-shaped briquettes, according to the pockets on the two rolls. In the formation of a tablet on a single-punch machine granular material or powder is fed from a hopper in a die when the lower punch is at the descent position. The excess filling from the hopper is scraped off by rotating the die table. Subsequently, the upper punch is lowered to press the powder, and then the compacted tablet is ejected when both punches are raised.

Extrusion Methods

The screw-type extruder used in the formation of small pellets like a rod consists of two main parts: a screw and a cylindrical or flat multi-hole die placed at the forward position of the barrel. Moist powder containing a binding liquid is introduced to the barrel through a hopper and kneaded sufficiently to form a plastic mass that is extruded through the multi-hole die. A pellet mill is extensively used in die rolling extrusion machine. In a typical pellet mill, the material fed into the interior of

a large ring-shaped die rolling is pressed by means of one or two smaller press rollers arranged eccentrically inside the die roller. At that time, adjustable knives on the exterior of the die roller cut the extrudates into pellets. Another machine of extruding granulation extrudes plastic or sticky material through a vertical perforated cylinder attached to the top hopper. The extruding force introduced by a multi-armed spreader decreases with the increased resistance of material flow through the holes of a perforated cylinder, so that the preparation of feed material becomes important.

Fusion Methods

The prilling method yields a granular product that is essentially spherical and uniform in size. The principle is that of solidifying droplets of melt in air, water or oil. In air prilling molten material is dispersed by spraying it from the top of the prilling tower, and the falling droplets solidify in the cooling air stream. Other fusion methods include a spouted bed and a steel belt or drum flaker.

REFERENCES

1. Ennis, B.J., Litster, J., *Perry's Chemical Engineers' Handbook*. 8th, ed. Green, D., Perry, R., New York, McGraw-Hill, 2007, pp. 117–145.
2. Association of Powder Process Industry and Engineering, *Zouryuu Handbook*, Tokyo, Ohm-Sha, 1991.
3. Schaefer, T., Mathiesen, C., *Int. J. Pharmaceutics*, 139, 139–148, 1996.
4. Iveson, S.M., Litster, J.D., Hapgood, K., Ennis, B.J., *Powder Technol*., 117, 3–39, 2001.
5. Newitt, D. M., Conway-Jones, J.M., Trans. *Inst. Chem. Eng.*, 36, 422–441, 1958.
6. Dahneke, B.J. *J. Colloid lnterface Sci*., 40, 1–13, 1972.
7. Israelachvili, J.N., *Intermolecular and Surface Forces*, London, Academic Press, 1992.
8. Ennis, B.J. *Handbook of pharmaceutical granulation technology 2nd*. ed. Parikh, D.M., Boca Raton, Taylor & Francis, 2005, pp. 7–78.
9. Hapgood, K.P., et al., *AIChE J*., 49, 350–361, 2003.
10. Iveson, S.M., Litster, J.D., *AIChE J*., 44, 1510–1518, 1998.
11. Tardos, G.I., Irfan-Khan, M., Mort, K.M., *Powder Technol*., 94, 245–258, 1997.
12. Ennis, B.J., Tardos, G.I., Pfeffer, R., *Powder Technol*., 65, 257–272, 1991.
13. Umeya, K., *J. Soc. Rheology Jpn*., 13, 145–166, 1985.
14. Andrade, F.A., Al-Qureshi, H.A., Hotza, D., *Appl. Cray Sci*., 51, 1–7, 2011.
15. Leuenberger, H., Puchkov, M., Krausbauer, E., Betz, G., *Powder Technol*., 189, 141–148, 2009.
16. Murase, K., Mochida, T., H. Sugama, H., *Granular Matter*., 6, 111–119, 2004.
17. Willett, C.D., Johnson, S.A., Adams, M.J., Seville, J.P., *Handbook of Powder Technology 12*, ed. Salman, A.D., Ghadiri, M., Hounslow, M.J., Amsterdam, Elsevier, 2007, pp. 1317–1351.
18. Pierrat, P., Caram, H., *Powder Technol*., 91, 83–93, 1997.
19. Hotta, K., Takeda, K., Iinoya, K., *Powder Technol*., 10, 231–242, 1974.
20. Murase, K., Mochida, T., Sugama, H., *Adv. Powder Technol*., 19, 349–367, 2008.
21. Brown, R.A., Orr, F.M., Scriven, L.E., *J. Colloid Interface Sci*., 73, 76–87, 1980.
22. Pierrat, P., Agrawal, D.K., Caram, H., *Powder Technol*., 99, 220–227, 1998.
23. Schubert, H., *Powder Technol*., 11, 107–119, 1975.; 37, 105–116, 1984.
24. Rumpf, H., *Agglomeration*, ed. Knepper, W. A., New York, John Wiley, 1962, pp. 379–418.
25. Holm, P., Schaefer, T., Kristensen, H.G., *Powder Technol*., 43, 213–223, 1985.
26. Mazzone, D.N., Tardos, G.I., Pfeffer, R., *Powder Technol*., 51, 71–83, 1987.
27. Ennis, B.J., Tardos, G.I., Pfeffer, R., *Chem. Eng. Sci*., 45, 3071–3088, 1990.
28. Willett, C.D., Adams, M.J., Johnson, S.A., Seville, J.P.K., *Powder Technol*., 130, 63–69, 2003.
29. Iveson, S.M., Beathe, J.A., Page, N.W., *Powder Technol*., 127, 149–161, 2002.
30. Liu, L.X., Litster, J.D., Iveson, S.M., Ennis, B.J., *AIChE. J*., 46, 529–539. 2000.
31. Sekiguchi, I., Ohta, Y., *J. Powder Technol. Jpn*., 28, 232–238, 1991.
32. Michaels, A.S., Puzinaskas, V., *Chem. Eng. Prog*., 59, 604–614, 1954.
33. Umeya, K., Sekiguchi, I., *J. Soc. Mater. Sci. Jpn*., 24, 664–668, 1975.
34. Sekiguchi, I., Tohata, H., *Kagaku Kogaku*, 32, 1012–1020, 1968.
35. Kapur, P.C., Fuerstenau, D.M., *Ind. Eng. Chem. Process. Des. Dev*., 8, 56–62, 1966.
36. Ouchiyama, N., Tanaka, T., Ind. *Eng. Chem. Process. Des. Dev*., 13, 383–389, 1974.
37. Kapur, P. C., Fuerstenau, D.M., *Trans. AIME*., 229, 348–355, 1964.
38. Dencs, B., Ormos, Z., *Powder Technol*., 31, 85–91; 93–99, 1982.
39. Smith, P.G., Nienow, A.W., *Chem. Eng. Sci*., 38, 1223–1231; 1233–1240, 1983.
40. Huang, C.C., Kono, H.O., *Powder Technol*., 55, 35–49, 1988.
41. Okaniwa, K., Sekiguchi, I., *Bull. Graduate Studies. Sci. Eng*., Chuo Univ., 14, 159–162, 1984.
42. Ohbayashi, S., *M.Sc. Thesis*, Chuo Univ., 1972.
43. Bhrang, U.N., Johnson, R.T., Myron, T.L., Pelczarski, E.A., *Agglomeration*, ed. Knepper, W.A., New York, John Wiley, 1962, pp. 229–249
44. Sekiguchi, I., Tohata, H., Kiyama, K., *J. Soc. Mater. Sci. Jpn*., 7, 284–289, 1970.
45. Tohata, H., Sekiguchi, I., Abe, J., *J. Soc. Mater. Sci. Jpn*., 3, 497–501, 1966.
46. Macavei, Gh., *British Chem. Eng*., 10, 610–614, 1965.
47. Capes, C.E., Danckwerts, P.V., *Trans. Inst. Chem. Eng*., 43, 116–124; 125–130, 1965.
48. Kapur, P.C., Fuerstenau, D.W., *Ind. Eng. Chem. Process. Des. Dev*., 5, 5–9, 1966.
49. Litster, J., Ennis, B., *The Science and Engineering of Granulation Processes*, Dordrecht, Kluwer Academic Publishers, 2004, pp. 144–170.
50. Kapur, P.C., *Chem. Eng. Sci*., 27, 1863–1869, 1972.
51. Ouchiyama, N., Tanaka, T., Ind. *Eng. Chem. Process. Des. Dev*., 14, 286–289, 1975.
52. Harada, K., Fujita, J., Yoshimura, M., *Kagaku Kogaku*, 31, 790–794, 1967.
53. Harada, K., Fujita, J., Yoshimura, M., *Kagaku Kogaku*, 33, 793–799, 1969; 34, 102–104, 1970.

54. Kawakita, K., Ludde, K.H., *Powder Technol.*, 4, 57–60, 1971.
55. Spencer, R.S., Gilmore, G.D., *J. Appl. Phys*., 21, 527–531, 1950.
56. Kurtz, B.E., Barduhn, A., *Chem. Eng. Prog.*, 56, 67–72, 1960.
57. Murakami, K., *Kobunshi Kagaku*, 17, 571–576, 1960.
58. Parks, J.R., Hill, M.J., *J. Am. Ceram. Soc*., 42, 1–6, 1959.
59. Jimbo, G., et al., *Kagaku Kogaku*, 36, 654–660, 1972.
60. Jimbo, G., Kambe, T., *J. Soc. Powder Technol. Jpn*., 9, 451–457, 1972.
61. Sekiguchi, I., *J. Multiphase Flow Jpn*., 11, 362–369, 1997.
62. Sugimoto, M., Kawakami, T., *Kagaku Kogaku Ronbunshu*, 8, 530–532, 1982.
63. Harada, K., *Kagaku Kogaku*, 36, 1237–1243, 1972.
64. Uemaki, O., Mathur, K.B., *Ind. Eng. Chem. Process. Des. Dev.*, 15, 504–508, 1976.
65. Singiser, R.E., Heiser, A.L., Prillig, E.B., *Chem. Eng. Prog.*, 62, 107–111, 1966.
66. Robinson, T., Waldie, B., *Trans. Inst. Chem. Eng.*, 57, 121–127, 1979.
67. Kurcharski, J., Kmiec, A., *Can. J. Chem. Eng*., 61, 435–439, 1983.
68. Weiss, P.J., Meisen, A., *Can. J. Chem. Eng*., 61, 440–447, 1983.
69. Pavarini, P.J., Coury, J.R., *Powder Technol*., 53, 97–103, 1987.
70. Liu, L.X., Litster, J.D., *Powder Technol.*, 74, 215–2.



Taylor & Francis
Taylor & Francis Group
http://taylorandfrancis.com

5.11 Kneading and Plastic Forming

Minoru Takahashi and Masayoshi Fuji

The term "kneading" is sometimes distinguished from "mixing" to emphasize the compounding of powder with a liquid of high viscosity, or coating of a powder surface with liquid. In industrial applications, kneading is usually combined with the plastic forming processes. In this chapter, the fundamentals of kneading and plastic forming processes are described.

5.11.1 KNEADING

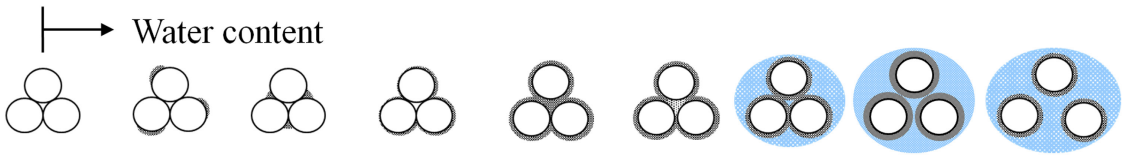
Powder–Gas–Liquid Dispersion System

The packing conditions of powder–gas–liquid mixture systems are ideally classified in Table 5.11.1.[1] The systems are distinguished by the differences in the existence and continuity of each phase. Kneading can be defined as the mixing operation in the mud system. Kneading of either film type or matrix type is employed.[2] Film-type kneading is the thin coating of the surface of each particle with liquid in the funicular state, whereas matrix-type kneading is the coating of the surface of each particle with a large amount of liquid or the dispersing of particles into the liquid in the capillary state.

Critical Powder Volume Concentration

Compounds for plastic forming in a narrow sense should be prepared to a capillary state where the voids among particles are saturated with liquid. The powder concentration corresponding to a capillary state is called a critical powder volume concentration (CPVC). CPVC is highly dependent on the size, size distribution, and shape of particles and can be estimated experimentally from the mixing torque versus liquid content curve using a torque rheometer.[3] With the addition of liquid, torque gradually increases, reaches a maximum, and then decreases sharply, as shown in Figure 5.11.1.[1,4] CPVC is determined by the powder concentration at the maximum torque. The figure also shows that the condition of the powder–gas–liquid system shifts as follows: powder → (powder + granules) → granules → (granules + paste) → paste → slurry.

TABLE 5.11.1 Packing Characteristics of a Powder–Air–Water System Water Content



Particle (Solid phase)	Continuous	Cont	Cont	Discont	Discont	Discont	Discont
Air (Gaseous phase)	Continuous	Cont	Discont	—	—	—	—
Water full (Liquid phase I)	Discontinuous	Cont	Cont	Cont	Cont	Dis-Cont	Discont Cont
Free water (Liquid phase II)				Discont	Cont	Cont	Cont
Stage	Pendular S P	Funicular S. F-1	F-2	Capillar S. C-1	C-2	Slurry S. S-1	S-2
Critical point.	c-1	c-2	c-3	c-4	c-5	c-6	
	P.L. (Plastic Limit)			L. L. (Liquids Limit)			
Rheological System	Power System		Mud System			Slurry System	
Mix	Dry mix	Semi-Dry (or Semi-Wet) mix		Wet mix		Slurry mix	

Source: Umeya, K., J. Soc. Rheol. Jpn., 13, 145–166, 1985.

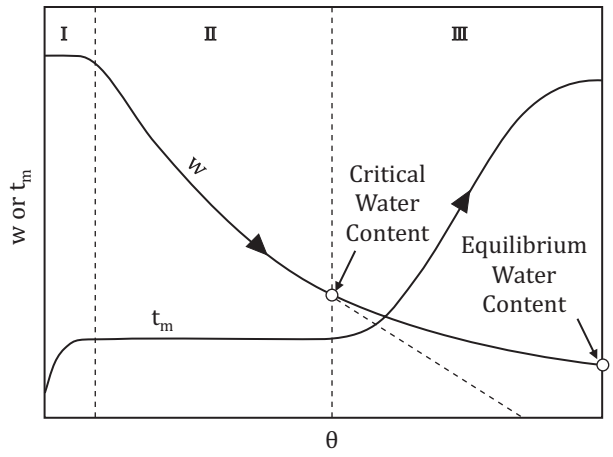


FIGURE 5.11.1 Pelletizing effect in powder–air–water system. (From Umeya, K., *J. Soc. Rheol. Jpn.,* 13, 145–166, 1985. With permission.)

Mechanisms and Machines

Kneading is attained by the mechanisms of convection, shear, and diffusion, as is dry or slurry mixing. However, the convection and shear mechanisms are relatively important in the kneading process, because the mixture systems of a quite high viscosity are dealt. Therefore, kneading machines capable of producing high shear force must be used to coat the particles with liquid. Also, kneading machines with high shear speed will be required to shorten kneading time. Representative kneaders and the applicability are listed in Table 5.11.2.[2] Dispersion of particles into the matrix becomes more critical with decreasing particle size and increasing powder concentration. Special kneading with the assistance of a high temperature or vacuum will be useful to spread the liquid on the particle surface or remove the trapped air. Another route for attaining sufficient dispersion is surface modification of the particles, which improves the wetting between the particles and the organic medium and promotes the penetration of viscous fluid into particle agglomerates.

5.11.2 PLASTIC FORMING

Plastic forming methods among a variety of forming methods include wet pressing, jiggering, extrusion, and injection molding. Plastic bodies prepared by kneading processes are treated in these forming methods.

Wet Pressing

Wet pressing is similar to dry pressing and is often called semidry pressing, or dust pressing. The forming cycle consists of three stages: (a) filling raw powders into the die cavity, (b) compaction, and (c) ejection of the pressed body, as shown in Figure 5.11.2. Usually, the feed material containing 5–10% water is pressed in dies made of steel, cast iron, or tungsten carbide. The packing state of the feed mixture is in the range of funicular I to funicular II in Table 5.11.1. The feed is occasionally prepared by crushing the filtered cake of slurry without the use of a kneader. Compared with the dry feed, the wet feed deforms plastically during compression. Therefore, it is possible to fabricate parts with complex contours by this method. However, dimensional tolerances of wet pressing are only held to ±2%, lower than those of dry pressing.[5] The pressed body after the ejection from the die must be treated carefully because it will deform easily by the force of gravity.

Jiggering

Jiggering is one of the oldest plastic-forming techniques, where a skilled hand-worker can make any hollowware from plastic clay supported on a rotating wheel. Presently, highly automated jiggering systems are used for the industrial fabrication of hollowware.[6] The jiggering process consists of three stages: (1) putting a slice of plastic feed onto a spinning plaster mold, (2) pressing the slice by a hot performance die, and (3) jiggering. A slice of de-aired extrudate is commonly used for feed material. Sticking of the plastic feed to the die is a serious problem. To prevent this, lubrication is produced by heating metal roller tools to generate steam and facilitate release, or a lubricant is sprayed onto a tool to minimize sticking.[5]

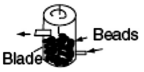
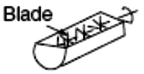
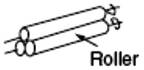
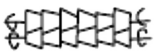
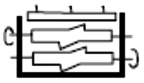
Extrusion

A compound adjusted to a capillary state will show a plastic flow necessary for extrusion. If the powder concentration is too low, a squeezing of liquid from the mixture will occur during extrusion at high pressure. On the other hand, too high of a concentration will bring about the breakage of the extruding machine because of insufficient plasticity. Granulated feed will be fully consolidated in a compression zone of the extruding machine. In the nonclay system, organic additives are added to promote plasticity.

Extrusion is usually carried out by an auger having mixing equipment. In the mixing before extrusion, feed material is shredded and de-aired under vacuum. Major stages of extrusion are (1) feeding, (2) compression in a barrel, (3) flow through a die, and (4) ejection. The exit, with a uniform section, is supported on a suitable surface to prevent distortion and is cut to proper lengths. The very complex parts such as honeycomb structures are fabricated by the use of a specially designed die.[7] Sometimes, the columnar exit can be used as blanks for further machining.

The plastic mixture after compression can be characterized as a Bingham body, which shows two flow modes in a tube: one is laminar flow and the other is plug flow. The laminar flow occurs in the outside portion of the tube, where the shear stress is greater than the yield stress of the body; the laminar flow occurs in the inside portion. The laminar flow causes orientation of particles along its axis if plate-like particles such as clay particles are involved in the body. However, the inside portion has the same random orientation as the original feed.[8] Inevitably, this nonuniform packing structure of the exit results in a differential shrinkage during drying

TABLE 5.11.2 Types and Factors of Kneaders

			Material Factor			Kneader Factor		
Type	Name	Sketch	Particle size [a]	Binder[b] content	Viscosity[c]	Power (kw)	Kneading Force[d]	Kneading Speed[d]
Wheel	Simpson		M–C	FI–C	H	0.75–150	4	2
	Wetpan		M–C	FI–FII	H	5.8–15	4	2
	Counter Flow		M–C	FI–FII	M–H	7.5–11	3	2
	Speed muller		M–C	FI–FII	M–H	15–75	4	4
Ball	Ball mill		F–C	FI–S	L–H	3.7–37	5	1–2
	Sand Grinder		F	S	L–M	0.2–37	5	1–2
Blade	Paddie		M–C	P–FII	M–C	2.2–37	1	3
	Kneader		F–M	FI–C	H	0.25–1500	5	2
	Auger		F	FII–C	H	0.75–19	5	2
	Turbulizer		M–F	P–FI	L	3.7–95	2	5
	Henschal		M–F	P–FI	L	1.8–200	2	5
	Vertical	 e	F–C	FI–C	M–H	0.2–15	2	2
Roll	Roll Mill		F	C–S	H	0.4–200	5	2
	Taper Roll		F	C–S	H	2.2–200	5	2
	Banbury		F	FII–C	H	5.6–1900	5	2
	Continuous	 Roller Screw	F	FII–C	M–H	0.75–300	5	2
Other	Pestle		F–C	P–C	L–H	0.1–2.3	3	2

Source: Hashimoto, K., in Powder Technology Handbook, Iinoya, K., Gotoh, K., and Higashitani, K., Eds., Marcel Dekker, New York, 1990, p. 653.

[a] F, Fine <50 μm; M, middle 50–500 μm; C, course >500 μm.

[b] Refer to Table 5.11.1.

[c] L, Low <10 mPa·s; M, middle 10^2–10^3 mPa·s; H, high >10^4 mPa·s.

[d] Estimated value, 5–1; highest kneading force and speed, *f*.

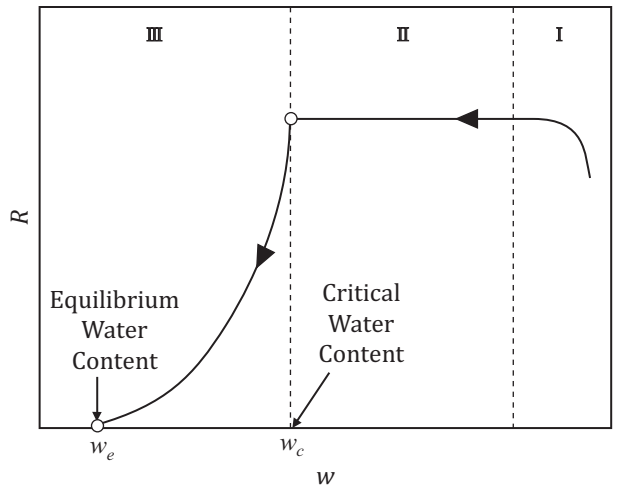


FIGURE 5.11.2 Sequence of wet pressing for a ceramic component.

and sintering. The cracks arising from the differential shrinkage often become serious problems in extrusion forming.

Injection Molding

Raw powders must be mixed with an organic vehicle consisting of a binder, lubricant, plasticizer, and dispersing or wetting agent. Thermoplastic or thermosetting resins are commonly used as the binders. The thermoplastic resins are preferable for the recycling of a large amount of scrap left in the sprue, runner, and gate of a molding die set. High powder concentration in the compound is generally desired in the case of ceramic injection moldings because the organic vehicle should be removed before sintering. However, too high a concentration over the CPVC results in inadequate fluidity of the compound during mixing and molding. A twin screw extruder and a kneader with pressurizing equipment have been verified to be effective for mixing heavily loaded fine fillers and viscous organic systems.[9] It should be noted that thermal or mechanical degradation of thermoplastic resins will sometimes occur during mixing.[10]

The molding processes consist of four stages: (1) preheating of feed materials within an injection machine, (2) injection of the plasticized feed into the cavity, (3) solidification of the cast body by heating and/or cooling, and (4) ejection of the body. Parts accompanied by thermoplastic or thermoset resins can be made by a screw injection machine. The injected body should be free of defects such as weld lines, pores, and cracks.

REFERENCES

1. Umeya, K., *J. Soc. Rheol. Jpn*., 13, 145–166, 1985.
2. Hashimoto, K., *Powder Technology Handbook*, Iinoya, K., Gotoh, K., Higashitani, K., Eds., Marcel Dekker, New York, 1990, p. 653.
3. Markhoff, C. J., Mutsuddy, B. C., Lennon, J. W., *Forming of Ceramics*, Mangels, J. A., Messing, G. L., Eds., American Ceramic Society, Ohio, 1984, pp. 246–250.
4. Michales, A. S., Puzinauskas, V., *Chem. Eng. Prog.*, 50, 604–614, 1954.
5. Reed, R. S., *Introduction to the Principles of Ceramic Processing*. John Wiley, New York, 1988, pp. 355–379.
6. Gould, R. I., Lux, J., *Ceramic Fabrication Processes*, Kingery, W. D., Ed., MIT Press, Cambridge, 1958, pp. 98–107.
7. Richerson, D. W., *Modern Ceramic Engineering*, Marcel Dekker, New York, 1982, pp. 178–216.
8. Norton, F. H., *Fine Ceramics*, McGraw-Hill, New York, 1970, pp. 130–156.
9. Edirisinghe, M. J., Evans, J. R. G., *Mater. Sci. Eng.*, A109, 17–26, 1989.
10. Takahashi, M., Suzuki, S., Nitanda, H., Arai, E., *J. Am. Ceram. Soc*., 71, 1093–1099, 1988.

5.12 Drying

Yuji Tatemoto

5.12.1 FUNDAMENTAL OF DRYING

Drying Process

Drying is a method used to evaporate and remove the liquid, i.e. water, in a wet material. The heat efficiency is important in the drying, because, at least, the latent heat of liquid is needed to remove the liquid. The convective, conductive and radiation heat transfers are used for heating the wet material. In the convective heat transfer, the heat of the gas stream is transported to the wet material. In the conductive heat transfer, the heat of the wall and shelf contacting with the wet material is transported to the material. In the radiation heat transfer, the thermal radiation, such as the infrared radiation, is used for heating.

Figure 5.12.1 shows the typical changes in mass and temperature of wet material in hot-air drying when the temperature, humidity and velocity of the hot air are constant during drying. Figure 5.12.2 shows a plot of the drying rate against the moisture content. Figure 5.12.2 is called as "drying characteristic curve." The dry-basis moisture content w (kg-water/kg-dry material) is more convenient to design a dryer for than the wet-basis water content w' (kg-water/kg-wet material). Three periods are seen during the drying process, i.e. (1) preheating period, (2) constant drying-rate period and (3) falling drying-rate period. During the preheating period, the material temperature increases from the initial temperature to the temperature of the constant drying-rate period, where both the wet-bulb temperature and the drying rate are constant. All the heat supplied to the material is used to evaporate water from the material surface: the surface of material is sufficiently wet during the constant drying-rate period. When the surface of the material is dried, the water within the material starts to evaporate. The heat supplied to the material is partly used to heat the dried part of the material. The dried part becomes the resistance of heat and mass transfers. Therefore, the drying rate decreases with decreasing moisture content. The drying rate is strongly affected by the properties of the material, while the drying rate at the constant drying-rate period is just affected by the operational conditions. The boundary of the moisture content between constant and falling drying-rate periods is called the "critical moisture content." This value changes with operational conditions and properties of material. The moisture content after infinite time drying is called the "equilibrium moisture content."

Drying Rate

The drying rate J [kg-water/(s·m^2)] is expressed by the following equation.

$$J = -\frac{W_s}{A}\left(\frac{dw}{d\theta}\right) \tag{5.12.1}$$

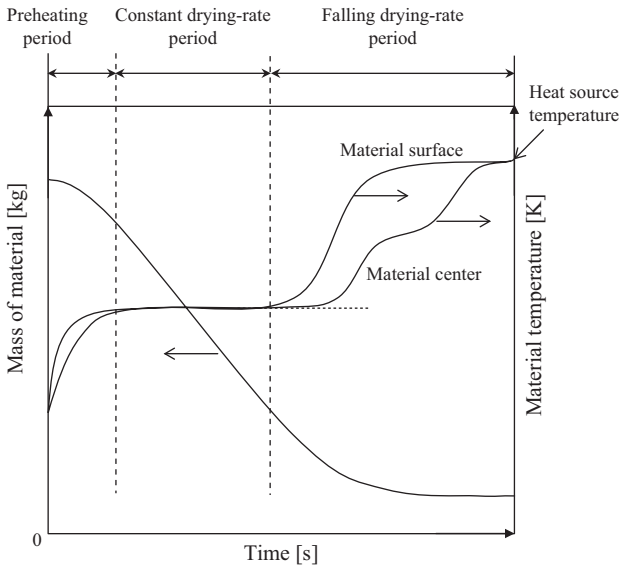


FIGURE 5.12.1 Changes in mass and temperature of material in hot air drying.

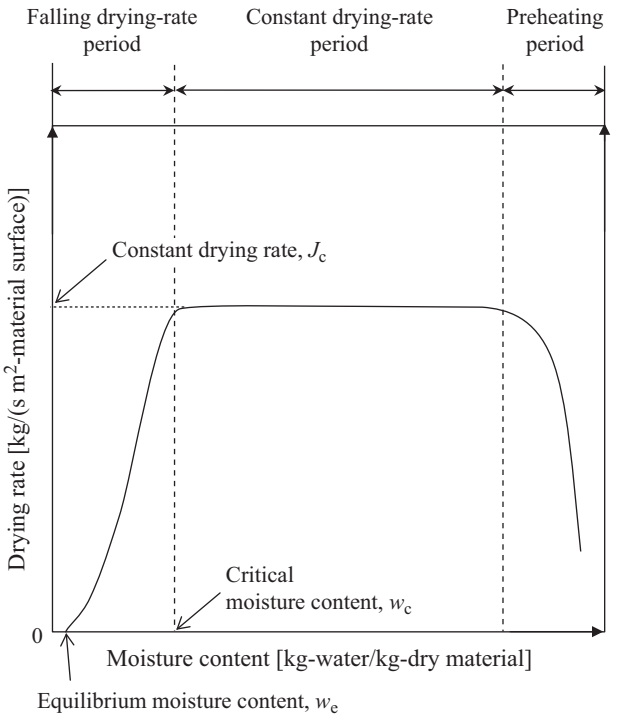


FIGURE 5.12.2 Plot of drying rate against moisture content (drying characteristic curve).

During the constant drying rate period, all the heat supplied to the material is used for the evaporation of water. In the hot-air drying, the constant drying rate J_c can be calculated from the following equation, where the material temperature is equal to the wet-bulb temperature in the hot air.

$$J_c = k_H(H_M - H) = \frac{h_c(T - T_M)}{(\Delta h_v)_M} \tag{5.12.2}$$

The constant drying-rate period is also observed in the other heat transfers: the conductive and radiation heat transfers. The constant drying rate can be estimated by the heat supplied to the material, but the material temperature is generally different from the wet-bulb temperature in case of other heating methods.

In the falling drying-rate period, the drying rate is difficult to predict, because the drying rate is strongly affected by the properties of material, i.e. heat and mass transfers in the material must be estimated to determine the drying rate.[1,2] Figure 5.12.3 shows the drying characteristic curves for various kinds of materials. In the case of Figure 5.12.3 (a), the drying rate in the falling drying-rate period can be approximated from the following equation.

$$J_d = J_c \frac{w - w_e}{w_1 - w_e} \tag{5.12.3}$$

In this case, the drying time in which the moisture content decreases from w_1 to w_2 can be calculated from the following equation, where the initial moisture content w_1 is higher than w_c and the final moisture content w_2 is lower than w_c.

$$\theta = \theta_c + \theta_d = \frac{W_s(w_1 - w_c)}{AJ_c} + \frac{W_s(w_c - w_e)}{AJ_c} \ln \frac{w_c - w_e}{w_2 - w_e} \tag{5.12.4}$$

5.12.2 DRYER SELECTION AND DESIGN

Dryer Selection

Many types of dryers have been developed to dry particulate materials.[3,4] The types of dryers are determined by the state of the material at first, as shown Table 5.12.1. The dryers of continuous type are used when a large amount of material must be dried. Figures 5.12.4 through 5.12.8 show the outlines of continuous dryers: spray dryer,[5] pneumatic conveying dryer, fluidized bed dryer (continuous type),[6] rotary dryer and agitated through dryer.[7] For particulate materials, the dispersion of particles is important to shorten the drying time since the evaporation area increases when the material is dispersed as particles in the dryer.

The spray dryer is widely used to dry solutions, suspensions and slurries. Small droplets are generated from a rotary disk or a nozzle and the droplets contact with the hot air. The dry product comes out to be small powders.

Pneumatic conveying dryer is used to dry sludges, cakes, particles and powders. The drying proceeds while the material is transported with gas stream in the system. The cage mill is often used to disperse the materials like sludges and cakes as the pretreatment before drying.

A fluidized bed dryer is used for particles and powders of relatively low moisture content. Materials are fluidized by the hot air; materials are dispersed in the dryer. The drying time is short because of the extremely large contact area between material and hot air.

A rotary dryer is widely used for particulate materials. Materials are fed into the cylinder rotating continuously and are agitated by the cylinder rotation at the same time. A stirring device is installed to agitate and transport materials smoothly.

Agitation through the dryer is used to dry particulate materials and cakes. Stirrers are equipped to agitate and transport material. The stirrer and dryer wall are heated by a thermal medium, such as steam and warm water, and the heat is supplied on the wet material. Hence, the conductive heat transfer is the main heating mechanism in this dryer.

Dryer Design

To design the dryer, the heat required for the drying of wet material and the dryer capacity should be determined. The required heat can be calculated from the following equation.

$$Q = F_S\left[\left\{\left(C_S + w_1C_L\right)\left(T_M - T_{M1}\right)\right\} + \left(w_1 - w_2\right)(\Delta h_v)_M + \left(C_S + w_2C_L\right)\left(T_{M2} - T_M\right)\right] \tag{5.12.5}$$

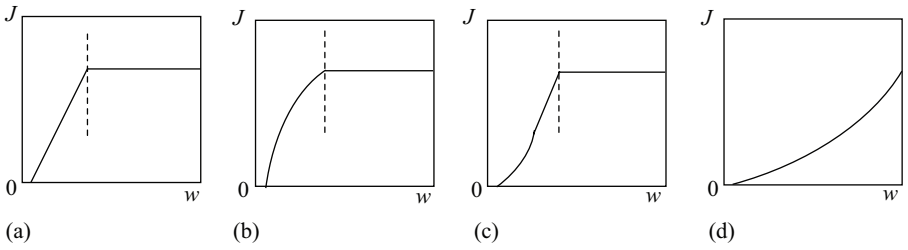


FIGURE 5.12.3 Drying characteristic curves for different materials. (a) Dispersed particulate material, bed of non-hydrophilic material, droplet etc., (b) Bed of non-hydrophilic fine powders, fibrous material etc., (c) Clay, ceramics, wood etc., (d) Gelatin, soap etc.

TABLE 5.12.1 Dryer Selection for Different Types of Materials

State of Material	Moisture Content	Type of Dryer	
		Continuous Type	Batch Type
Solution Slurry	Very high	Spray dryer Powder-particle (medium-particle) fluidized bed dryer Drum dryer	Box type dryer
Sludge Cake	High	Pneumatic conveying (flush) dryer Band dryer Agitated through dryer Agitated rotary dryer Drum dryer	Box type dryer Agitated dryer Rotary dryer
Particles	Low	Pneumatic conveying (flush) dryer Fluidized bed dryer Band dryer Rotary dryer Through-flow vertical dryer Agitated through dryer Agitated rotary dryer (with steam-heated tube)	Fluidized bed dryer Agitated dryer Rotary dryer
Powders	Low	Pneumatic conveying (flush) dryer Fluidized bed dryer Rotary dryer Agitated through dryer Agitated rotary dryer	Fluidized bed dryer Agitated dryer Rotary dryer

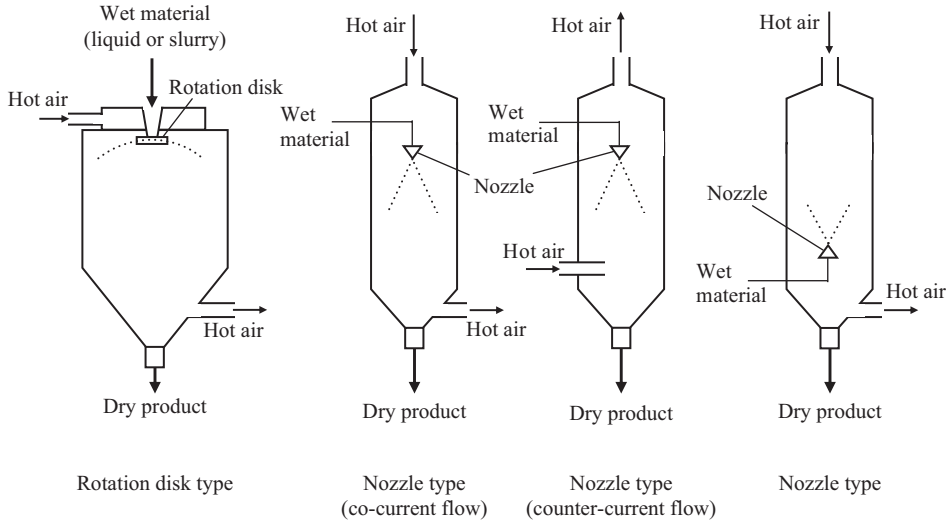


FIGURE 5.12.4 Outline of spray dryer.

where F_s is the feed rate of dry material. For the batch type operation, F_s should be W_s/θ. The first term on the righthand side of Equation (5.12.5) expresses the heat required to raise the temperature T_{M1} of the wet material of moisture content w_1 to T_M. The second term is the latent heat of water to decrease the moisture content from w_1 to w_2. The third term is the heat required to increase the temperature of dry material from T_M to T_{M4}. In many cases, the heat required for the evaporation of water in the second term is much larger than the heats expressed by the other terms. Therefore, the heat required for the drying is approximately estimated just by the second term. The thermal efficiency of the dryer should be considered to determine the heat required for the drying of materials since there is the heat loss from the dryer.

To estimate the dryer capacity, the heat flow into the material must be calculated from the following equations.

Hot air dryer (bath type):

$$Q = haV(T - T_M)_{av} \tag{5.12.6}$$

Hot air dryer (continuous type):

$$Q = haV(T - T_M)_{lm} \tag{5.12.7}$$

Conductive dryer (continuous type):

$$Q = U_K A_K (T_K - T_M)_{lm} \tag{5.12.8}$$

From these equations and Equation (5.12.5), the dryer capacity V or heating area A_K can be roughly estimated. For the typical dryer, the value of ha and U_K are listed in Table 5.12.2.[2]

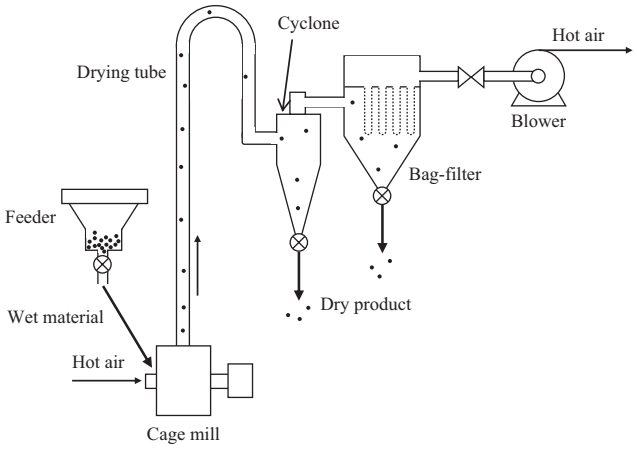


FIGURE 5.12.5 Outline of pneumatic conveying dryer.

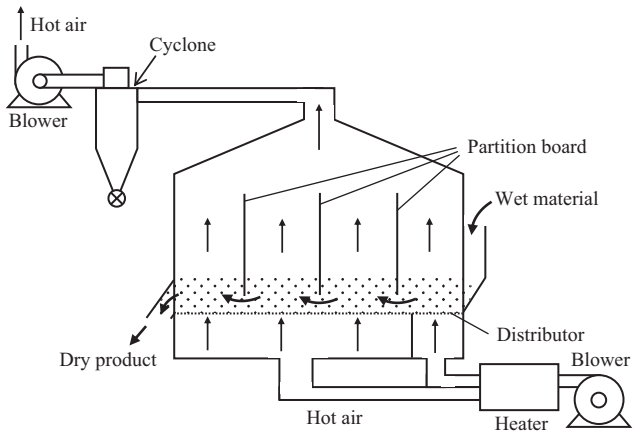


FIGURE 5.12.6 Outline of continuous type fluidized bed dryer.

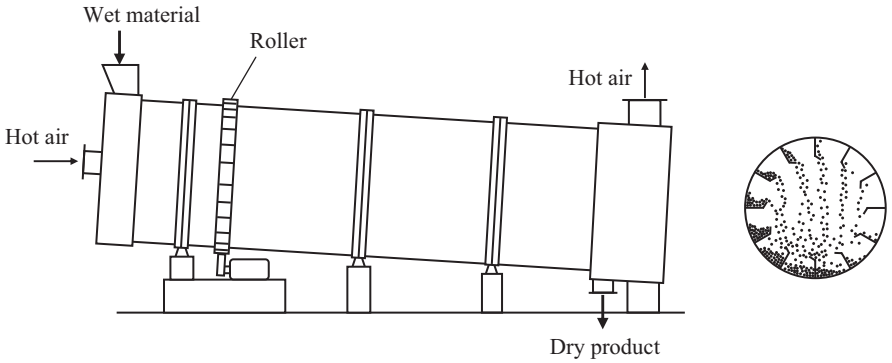


FIGURE 5.12.7 Outline of rotary dryer.

NOTATION

A: Drying area of material [m^2]
A_K: Heating area of material by conduction [m^2]
C_L: Specific heat of water [J/(kg K)]
C_S: Specific heat of dry material [J/(kg K)]
F_S: Feed rate of dry material [kg/s]
H: Absolute humidity [kg-water/kg-dry air]
H_M: Saturated absolute humidity at T_M [kg-water/kg-dry air]
h: Convective heat transfer coefficient [W/(K m^2)]
ha: Volumetric heat transfer coefficient [W/(K m^3)]
k_H: Mass transfer coefficient [kg/(m^2 s ΔH)]
Q: Rate of heat transfer [W]
J: Drying rate [kg-water/(s m^2)]
J_c: Constant drying rate [kg-water/(s m^2)]
J_d: Falling drying rate [kg-water/(s m^2)]
$(\Delta h_v)_M$: Latent heat of water at T_M [J/kg]
T: Temperature of hot air [K]
T_K: Temperature of heat source [K]
T_M: Material temperature [K]
U_K: Overall heat transfer coefficient [W/(K m^2-heating area by conduction)]
V: Volume of dryer [m^3]
W_s: Mass of dry material [kg]
w: Dry-basis moisture content [kg-water/kg-dry material]
w': Wet-basis moisture content [kg-water/kg-wet material]
w_c: Critical moisture content between constant and falling drying rate period [kg-water/kg-dry material]
w_e: Equilibrium moisture content [kg-water/kg-dry material]
θ: Drying time [s]
θ_c: Drying time of constant drying-rate period [s]
θ_d: Drying time of falling drying-rate period [s]

SUBSCRIPT

1: Initial
2: After drying
av: Average
lm: logarithmic mean

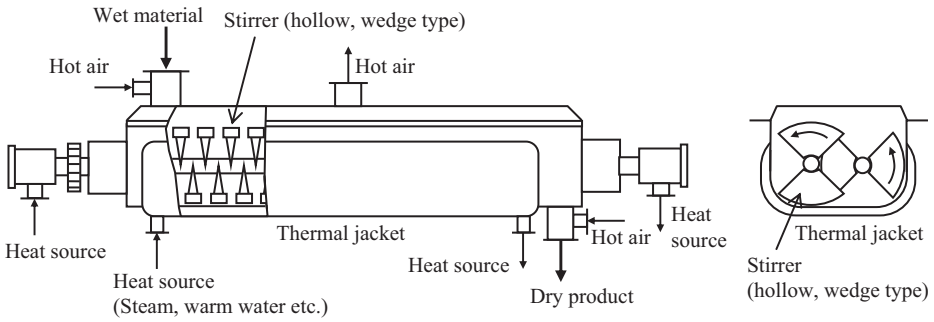


FIGURE 5.12.8 Outline of agitated through dryer.

TABLE 5.12.2 Rough Estimation of Dryer Capacity[2]

(a) Convective-Heating Dryer (Batch Mode)

Type of Dryer	ha [W/(K m³-Dryer Volume)]	Critical Moisture Content [%]	$(T - T_M)$ [K]	Inlet Temperature of Hot Air [°C]
Box (parallel-flow)	200–350 (h=20–35)	>20	30–100[a]	100–150
Box (through-flow)	3500–9000 (granules) 1000–3500 (cake; layer thickness 0.1–0.15 m)	>20	50[a,b]	100–150

(b) Convective-Heating Dryer (Continuous Mode)

Type of Dryer	ha [W/(K m³-dryer Volume)]	Critical Moisture Content [%]	$(T - T_M)_{lm}$ [K]	Inlet Temperature of Hot Air [°C]
Rotary	100–200	2–3	Counter-current 80–150	200–600
			Co-current 100–180	200–350
Rotary (through-flow)	350–1700	2–3	80–100	200–350
Pneumatic conveying	3500–7000	1–2	100–180	400–600
Fluidized bed	2000–7000	2–3	Horizontal (single and multicompartment)	100–600
			50–150	200–350
			Multistate (counter-current) 80–100	
Spray	10 (large particle)-30(fine powder)	30–50	Counter-current 80–90	200–300
			Co-current 70–170	200–450
Through-flow vertical	6000–15000	2–3	Counter-current 100–150	200–300
Tunnel (parallel-flow)	200–350 (h=20–35)	>20	Counter-current 30–60[a,c]	100–200
			Co-current 50–70[a,c]	100–200
Band (parallel-flow)	50–90	>20	Same as tunnel (parallel-flow)[a,c]	100–200
Band (through-flow)	800–2000	>20	40–60[a,b]	100–200

(c) Conductive-Heating Dryer

Type of Dryer	U_k [W/(K m²-area contacting with material)]	Critical Moisture Content [%]	$(T_K - T_M)$ [K]
Agitated cylinder or rotary with steam-heated tubes	70–150[d] (small for very sticky materials)	2–5	50–100[a]

[a] Values for the surface evaporation periods, and maximum drying rates will be obtained.
[b] Mean temperature difference between the hot air passing through the layer and the material temperature during the surface evaporation period.
[c] Mean values at both ends of dryers for case a.
[d] No change in the case of vacuum.

REFERENCES

1. The Society of Chemical Engineers, Japan, *Kagaku Kogaku Binran*, 7th Ed., Maruzen, Tokyo, 2011, pp. 283–331.
2. Toei, R., *Kanso Souchi*, Nikkan Kogyo Shinbun, Tokyo, 1966, pp. 9–11.
3. Mujumdar, A. S., Ed., *Handbook of Industrial Drying*, 4th Ed., CRC press, New York, 2014.
4. Kudra, T., Mujumdar, A. S., *Advanced Drying Technology*, CRC press, New York, 2009.
5. Kubota, N., *Kanso Souchi*, 2th Ed., Energy Conservation Center, Japan, Tokyo, 2004, p. 73.
6. Horio, M., Mori, S., *Fluidization Handbook*, Baifukan, Tokyo, 1999, p. 182.
7. The Association of Powder Process Industry and Engineering, Japan, *Kanso Souchi Manual*, Nikkan Kogyo Shinbun, Tokyo, 1978, p. 48.

5.13 Combustion

Hisao Makino and Kenji Tanno

5.13.1 INTRODUCTION

As shown in Figure 5.13.1,[1] combustion equipment for solid fuels is classified into the fixed-bed type, the fluidized-bed type, and the entrained-bed type, according to slip velocity between gas and particles. The fixed bed uses extremely large solid fuels of more than 10 mm. The actual combustion equipment for particles is mainly the fluidized-bed type and the entrained-bed type.

The bubbling bed, in which the gas velocity is 1–2 m/s, and the circulating bed, in which the gas velocity (4–8 m/s) is faster than that in the bubbling bed, were developed for the fluidized-bed type. In fluidized-bed combustion, the thermal NO_x, which is generated from N_2 and O_2 in the combustion air, becomes lower because the combustion temperature is low.

Pulverized coal combustion is one of the typical entrained-bed combustion materials. In this system, the pulverized coal particles of the order of 40 μm mean diameter are blown from the burner into the furnace to make the flame. Pulverized coal combustion is the most common method, because the combustion efficiency is higher than in the other systems and it is easy to scale up.

In this section, the pulverized coal combustion system is reviewed as an example of combustion of solid fuels.

5.13.2 CONTROL OF THE COMBUSTION PROCESS

In order to utilize the system effectively, it is very important to achieve high combustion efficiency in the operation

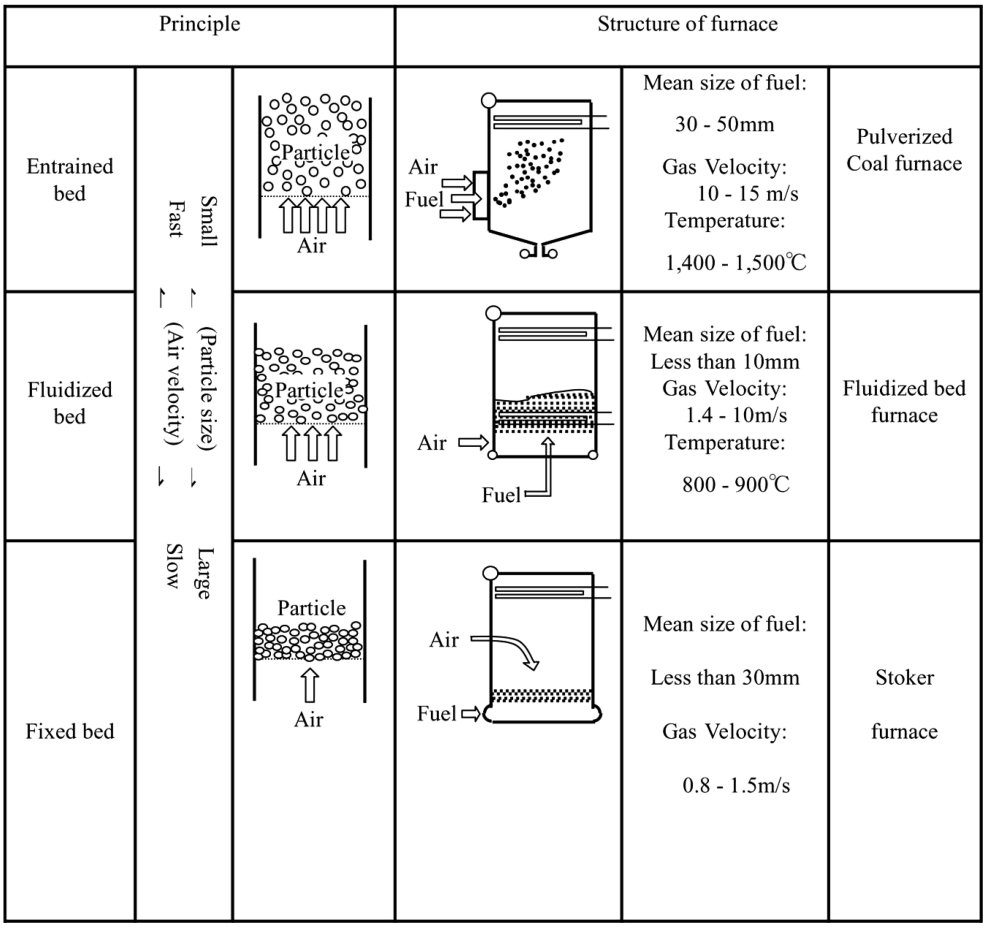


FIGURE 5.13.1 Combustion equipment for solid fuels. (From Miyasaka, T., *Thermal Nucl. Power Jpn.,* 32, 1056–1060, 1981. With permission.)

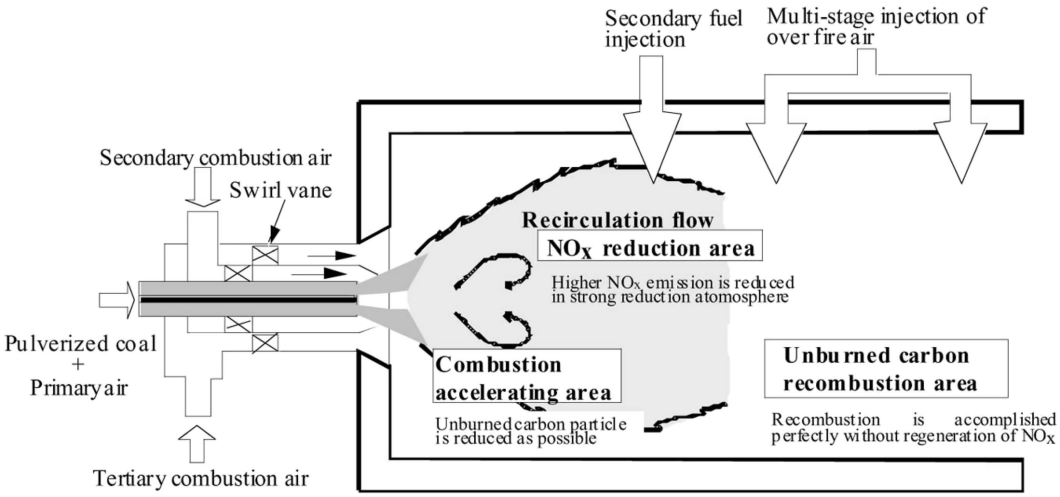


FIGURE 5.13.2 Concept of advanced low NO_x technology. (From Makino, H., Tsuji, H., Kimoto, M., Hoshino, T., Kiga, T., and Otake, Y., in *Ninth Australian Coal Science Conference,* distributed on CD-ROM, 2000. With permission.)

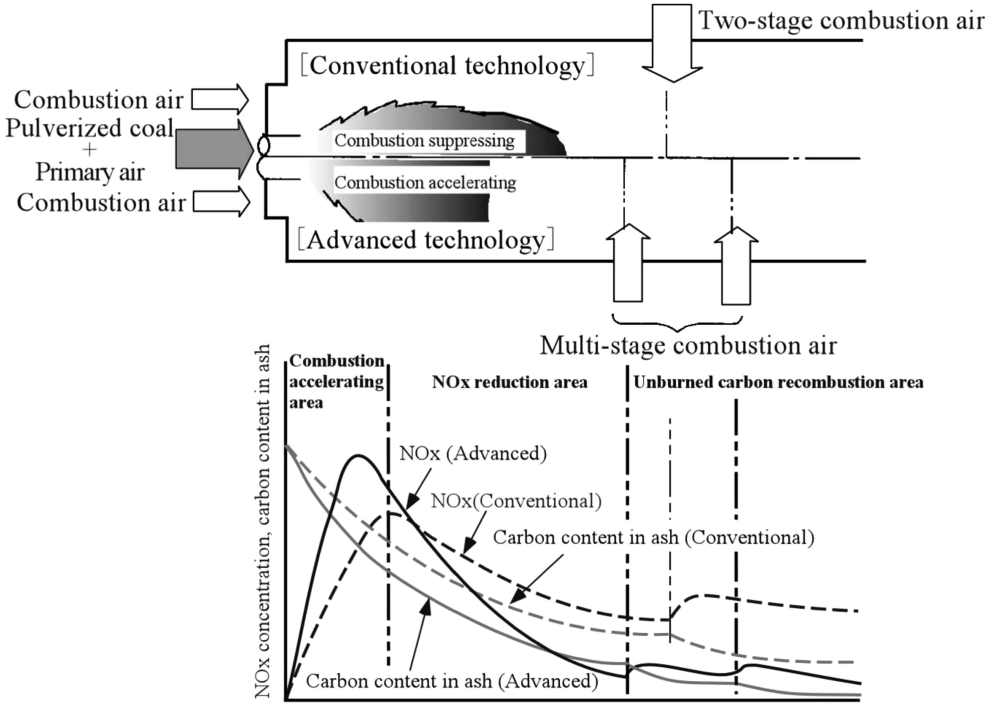


FIGURE 5.13.3 Combustion profiles of conventional technology and advanced technology. (From Makino, H., Kimoto, M., Kiga, T., and Endo, Y., *Thermal Nucl. Power Jpn.,* 48, 64–72, 1997. With permission.)

of combustion systems. In many cases, as the combustion efficiency is increased, concentration of fuel NO_x increases, which is generated from the nitrogen in the coal and the O_2 in the combustion air. It is, therefore, important to develop combustion technology, in which the formation of NO_x is suppressed while improving combustion efficiency. Figure 5.13.2[2] shows the flame structure for this combustion technology. Figure 5.13.3[3] represents combustion profiles of the conventional method and the advanced method for low NO_x combustion. In the conventional method, the combustion reaction near the burner is suppressed. In the advanced method, the combustion reaction at the low air ratio region near the burner is accelerated, and the NO_x reduction region is formed effectively downstream of this combustion acceleration region. It is shown that the NO_x emissions from the advanced method is lower than that from the conventional method.

In order to achieve the further improvement of combustion efficiency and to make the NO_x reduction flame wider, the new technology, in which the coal particles are pulverized into fine particles in the order of 10 μm mean diameter, was developed.

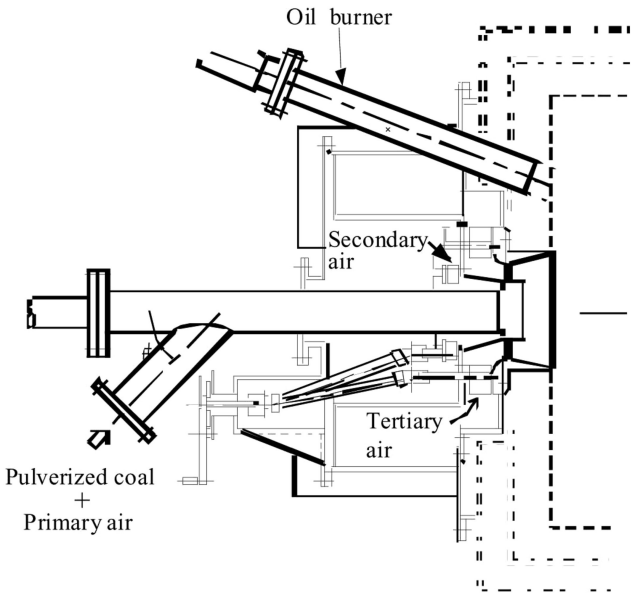


FIGURE 5.13.4 Structure of the advanced low NO_x burner. (From Makino, H., Kimoto, M., *Kagaku Kogaku Ronbunshu,* 20, 747–757, 1994. With permission.)

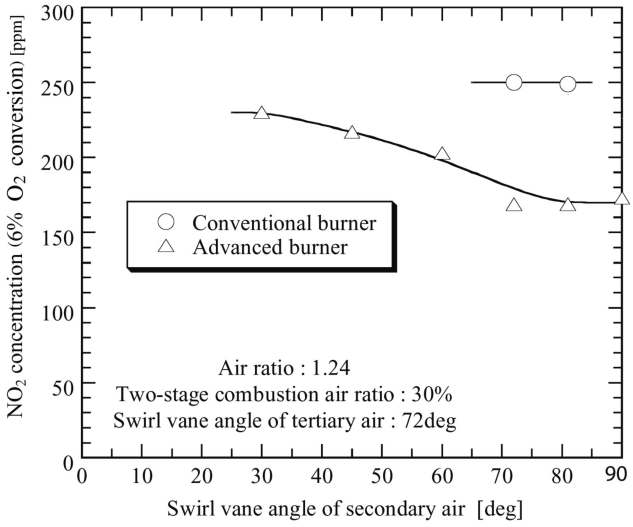


FIGURE 5.13.5 Relationship between the swirl vane angle of the secondary air and NO_x emission. (From Makino, H., Kimoto, M., *Kagaku Kogaku Ronbunshu,* 20, 747–757, 1994. With permission.)

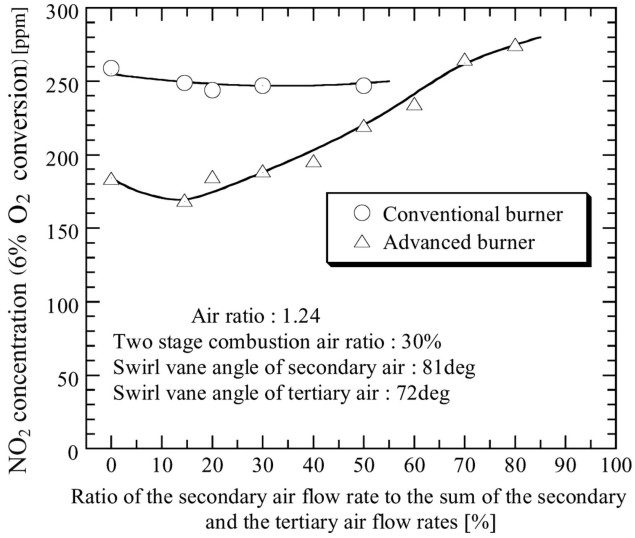


FIGURE 5.13.6 Relationship between NO_x emission and the ratio of the secondary air flow rate to the sum of the secondary and the tertiary air flow rates. (From Makino, H., Kimoto, M., *Kagaku Kogaku Ronbunshu,* 20, 747–757, 1994. With permission.)

5.13.3 COMBUSTION BURNER

Figure 5.13.4[4] shows the structure of the advanced low-NO_x burner for pulverized coal combustion. This burner was developed for the advanced method shown in the previous section. The pulverized coal particles and the primary air are blown into the furnace from the primary air port. The amount of the primary air is about one-fifth of the amount of the total air, which is approximately 1.2 times that of the theoretical air. The secondary air and the tertiary air are provided into the furnace from the outer region of the primary air port. A part of the total air is also provided from the furnace as two-stage combustion air, to suppress the formation of NO_x near the burner. To accelerate the combustion reaction and to make a better NO_x reduction flame, it is necessary that the residence time of the pulverized coal particles near the burner lengthened by the recirculation flow. To achieve this concept, the flow rate and the swirl force of the secondary air and the tertiary air were optimized. Figure 5.13.5[4] shows the relationship between the NO_x emission and the swirl vane angle of the secondary air when using this advanced burner and a conventional burner. For these two burners, NO_x emission changes greatly with the swirl vane angle. NO_x emission from the advanced burner is lower than from that of the conventional burner.

Figure 5.13.6[4] shows the relationship between NO_x emission and the ratio of the secondary air flow rate to the sum of the secondary and the tertiary air flow rates. When decreasing the ratio of the secondary air flow rate, NO_x emission becomes lower.

As the combustion profile of solid fuel is affected by fuel property, the combustion condition is controlled according with fuel property. For example, low carbonized coal includes high content moisture and it becomes fine particles on combustion, so the injection velocity of coal particle from the burner and swirl vane angle of secondary air are reduced for low carbonized coal.

It is well known that the flame stability of conventional burners decreases when lowering the coal feed rate to reduce the load of the furnace, because the coal particle concentration in the primary air decreases at low-load conditions. In order to improve the flame stability at low-load conditions, the new burner was developed.[5,6] In the outer region of the primary air port of this burner, the coal particles are concentrated by the use of the concentrated ring. Figure 5.13.7[6] shows the streamlined concentrated ring, which has been developed for the primary air flow without swirl force. At low-load conditions, the

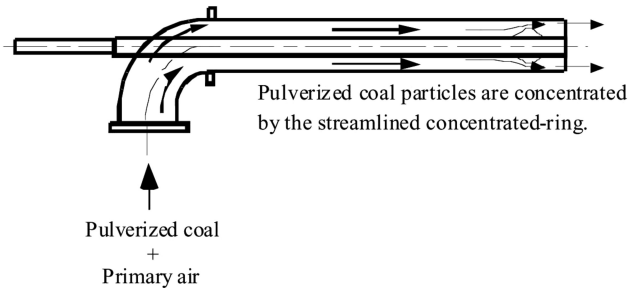


FIGURE 5.13.7 Structure of the streamlined concentrated ring. (From Makino, H., Kimoto, M., and Ikeda, M., *J. Soc. Powder Technol. Jpn.,* 37, 457–463, 2000. With permission.)

ring is moved to the burner exit to improve flame stability. When the load is increased, the ring is moved from the burner exit to unify the whole particle concentration in the burner.

5.13.4 FURNACE AND KILN

Furnace

In the utility boiler, about 10–40 burners are set up in a furnace. Figure 5.13.8 shows the schematic diagram of a pulverized coal-fired thermal power plant. Several burners are arranged in a row, and each burner makes a flame. Two or three rows are arranged in a furnace. The furnace is classified into the front-firing type, the opposed-firing type, and the

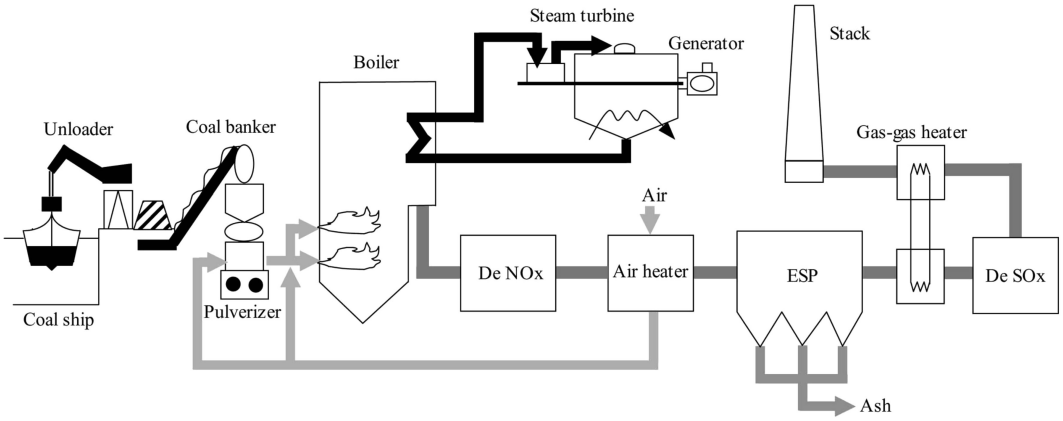


FIGURE 5.13.8 Schematic diagram of a pulverized coal-fired thermal power plant.

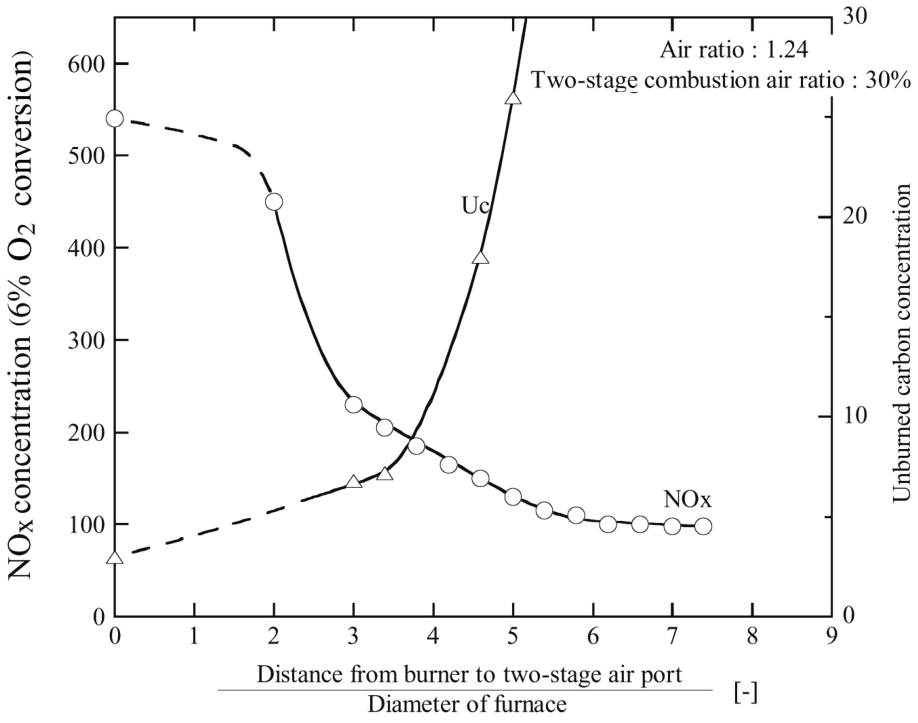


FIGURE 5.13.9 NO_x emission and unburned carbon concentration in fly-ash when altering position of two-stage air port. (From Makino, H., *Nensho Kenkyu,* 111, 55–68, 1998. With permission.)

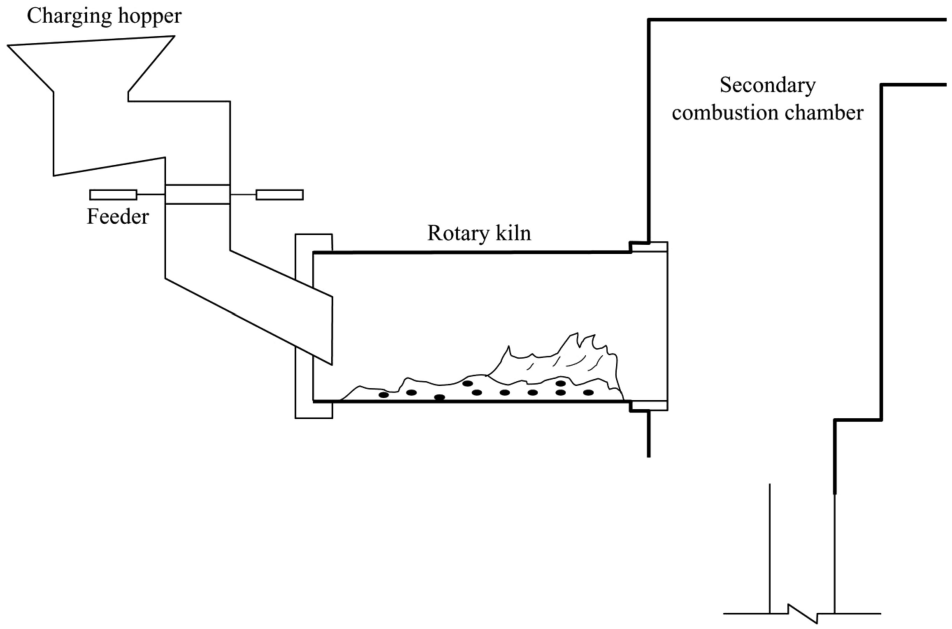


FIGURE 5.13.10 Structure of a rotary kiln. (From Akiyama, H., in *Sangyou Nenshou Gijutsu,* Energy Conservation Center, Japan, 2000, pp. 141–150. With permission.)

corner-firing type. In the front-firing type, burners are set up on one side, and in the opposed-firing type, burners are set up on both sides. Burners are arranged at the four corners of a furnace in the corner-firing type. At the upper part of the burners, two-stage air ports are mounted to inject a part of the combustion air into the furnace. NO_x concentration decreases in the region from the burners to the two-stage air ports, because a reduction atmosphere is formed in this region.

Figure 5.13.9[7] represents NO_x emission and unburned carbon concentration in fly-ash when altering the position of the two-stage air port. By increasing the distance from a burner to the two-stage air port, NO_x emission becomes lower as the reduction atmosphere is expanded. However, unburned carbon concentration in fly-ash increases due to the decrease in combustion efficiency. In the actual furnaces, two-stage air ports are mounted at the optimized position.

Kiln

The kiln is used in the cement, ceramic, and refractory material industry and others. The kiln for the production of cement is the most common among them. The rotary-type kiln, shown in Figure 5.13.10,[8] is mainly used as a cement kiln. Materials such as limestone and clay are supplied from the upper ports into the kiln, and fuels such as heavy oil are fed from the lower ports to heat and burn the materials. The temperature of materials reaches around 1500°C. In some sites, refuse fuels are used instead of fossil fuels. While the kiln type is classified into the wet type and the dry type, the dry type is popular at present.

REFERENCES

1. Miyasaka, T., *Thermal Nucl. Power Jpn.*, 32, 1056–1060, 1981.
2. Makino, H., et al., *Ninth Australian Coal Science Conference*, distributed on CD-ROM, 2000.
3. Makino, H., Kimoto, M., Kiga, T., Endo, Y., *Thermal Nucl. Power Jpn.*, 48, 64–72, 1997.
4. Makino, H., Kimoto, M., *Kagaku Kogaku Ronbunshu*, 20, 747–757, 1994.
5. Makino, H., Kimoto, M., Tsuji, H., *J. Soc. Powder Technol. Jpn.*, 37, 380–388, 2000.
6. Makino, H., Kimoto, M., Ikeda, M., *J. Soc. Powder Technol. Jpn.*, 37, 457–463, 2000.
7. Makino, H., *Nensho Kenkyu*, 111, 55–68, 1998.
8. Akiyama, H., in *Sangyou Nenshou Gijutsu*, Energy Conservation Center, Japan, 2000, pp. 141–150.



Taylor & Francis
Taylor & Francis Group
http://taylorandfrancis.com

5.14 Dust Collection

Chikao Kanaoka

Various types of dust removal equipment are used to recover products from processes or as emissions control equipment for air pollution. They adopt various mechanisms to remove particles, depending on particle and gas conditions. Dust removal equipment can be classified into dry and wet collectors. They are also classified into industrial dust collectors and air filters, depending on inlet dust concentration and the pressure drop. Inlet dust concentration to industrial collectors is usually two or three orders of magnitude higher than that of air filters as shown in Figure 5.14.1.[1] When they are classified according to gas flow and dust collection mechanism, every dust collector belongs to one of the following categories, shown in Figure 5.14.2.

1. Flow-through-type dust collector: This type of collector utilizes the external force perpendicular to the mean gas flow to remove particles outward from the system. Hence the flow does not change with time, and thus removal performance and the pressure drop of the system are stable with time. Gravitational dust collectors, cyclones, and electrostatic precipitators belong to this type.
2. Obstacle-type dust collector: This type of collector captures dust on obstacles in the equipment. When solid particles are collected by a solid obstacle, captured particles remain on the obstacles, and thus it results in the increase in both collection performance and the flow resistance with operation time. This also makes the release of captured particles from the obstacles difficult, so that this type of dust collector is used as a disposable type of collector. Air filters, granular bed filters, louver-type dust collectors, and the venture-scrubber belong to this type.
3. Barrier-type dust collector: This type of collector uses permeable media for gas, not for dust, so that dust is captured and accumulates on the media surface. To maintain the continuous operation of this type of dust collector, accumulated dust has to be removed repeatedly when the pressure drop becomes high. Bag filters and ceramic filters are the typical dust collectors in this type.

Table 5.14.1 summarizes the general features of dust collectors. Among them, the bag filter shows the highest collection performance, but the collector size has to be large, as its filtration velocity is as low as 1 m/min. Furthermore, its highest operating temperature is limited to 250°C because of the poor thermal durability of the filter material.

On the other hand, the electrostatic precipitator can treat gases moving as fast as 1 m/s at a very low pressure drop. However, its collection performance depends on the electrical property of dust particles. Figure 5.14.3 and Figure 5.14.4

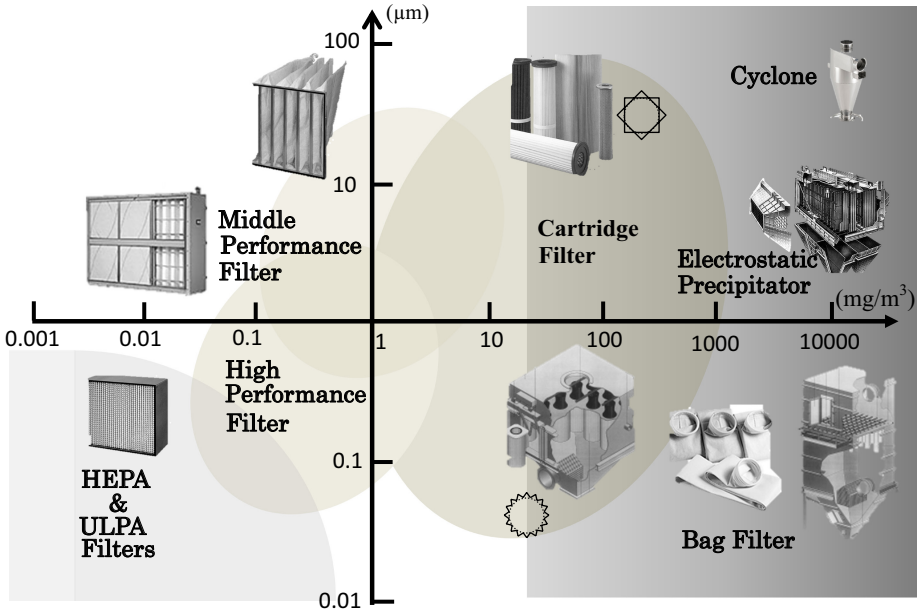
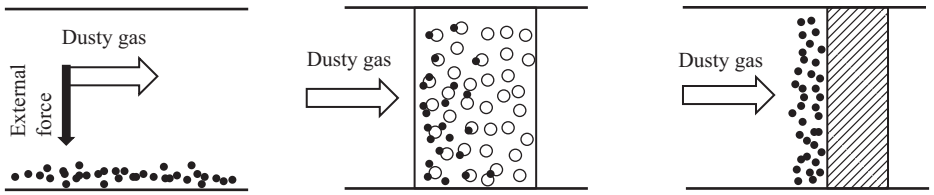


FIGURE 5.14.1 Area map of dry type dust collectors in particle size and concentration space. (Modified from C. Kanaoka, J. Soc., Powder Tech., 54 (2017).)



(a) Flow-through type (b) Obstacle type (c) Barrier type

FIGURE 5.14.2 Classification of dust collectors according to gas flow and collection mechanism.

TABLE 5.14.1 General Features of Dust Collectors

	Type	Removable Particle Size (μm)	Pressure Drop (Pa)	Maximum Temperature (°C)	Inlet Concentration (g/m³)	Initial Capital Cost	Remarks
Flow through type	Gravitational collector	> 20	50–150	1,000	50 >	Low	Pre-dust collector
	Cyclone	> 1	2,000 >	1,000	500 >	Middle	Convenient
	Electrostatic precipitator	> 0.02	300 >	400	20 >	Highest	Not for explosive material
Obstacle type	Scrubber	> 0.2	10,000 >	1,000	100 >	Middle	Require waste water treatment
	Air filter	> 0.01	500 >	100	0.01 >	Low	For building and house
	Air cleaner	> 1	1,000 >	50	1 >	Low	Engine and compressor
	Granular bed	> 1	10,000 >	1,000	50 >	High	Good for hot gas cleaning
Barrier type	Bag filter	> 0.01	2,000 >	250	20 >	High	Not good for condensable material
	Ceramic filter	> 0.01	50,000 >	1,000	50 >	Highest	Good for hot gas cleaning

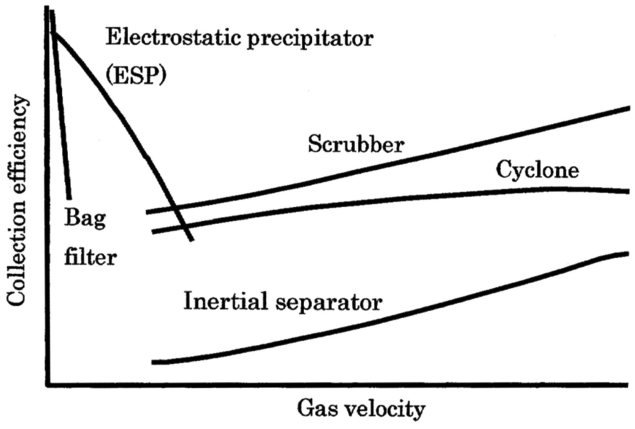


FIGURE 5.14.3 Dependence of collection efficiency on gas velocity.

show, respectively, the collection efficiency of dust collectors in relation to gas velocity and the initial capital cost of the equipment as a function of the handling gas volume. The total annual cost to operate a dust collector is the lowest at an economical gas velocity, which usually differs from the gas velocity at its best performance. Hence, one has to have a criterion for the selection of dust collectors.

5.14.1 FLOW-THROUGH-TYPE DUST COLLECTORS

The collection efficiency of the collector in this type is expressed by $E = vS/Q$, if the air stream does not have turbulence, by $E = 1 - \exp(-vS/Q)$, if the particle concentration in a vertical cross section is assumed to be uniform because of turbulence, and by $E = 1/(1 + Q/vS) - 1$ if complete mixing is assumed in the collector. Here S is the total collection surface, Q is the total gas flow rate, and v is the migration velocity to the wall, and it is determined on the external forces acting on the particle such as gravity, centrifugal force, electrostatic force, and so on.

The separation efficiency of this type is shown in Figure 5.14.5.[2] As one can see from the figure, the existence of turbulence decreases the collection efficiency.

Gravitational Collectors

The gravitational dust collector separates particles by the difference of gravitational settling velocity, which is suited for large particles. In most cases, it is used as a pre-dust collector. Depending on the flow direction of the gas stream, the collectors are classified into single and multi-plate types. In both cases, to improve the gravitational effect, the cross-sectional

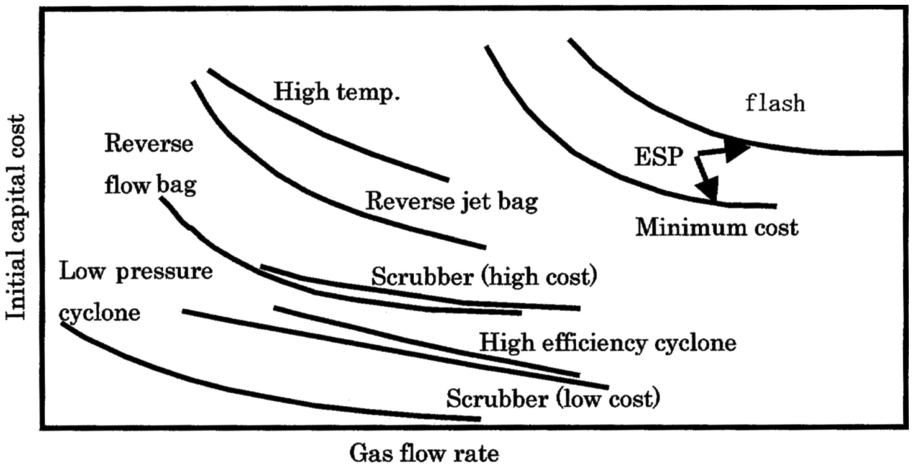


FIGURE 5.14.4 Relation between initial capital cost and flow rate.

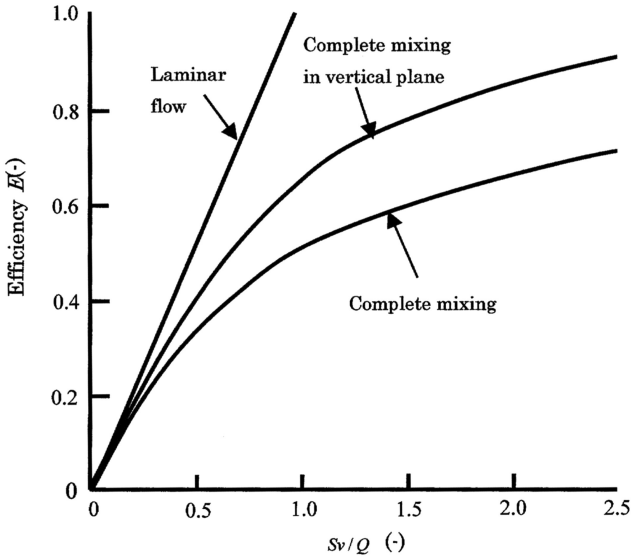


FIGURE 5.14.5 Separation efficiency for flow-through-type dust collector. (Modified from C. Kanaoka, H. Makino, *Hajimete no Shujingijuu,* Nikkan Kogyo Shinbun, Tokyo, 2013.)

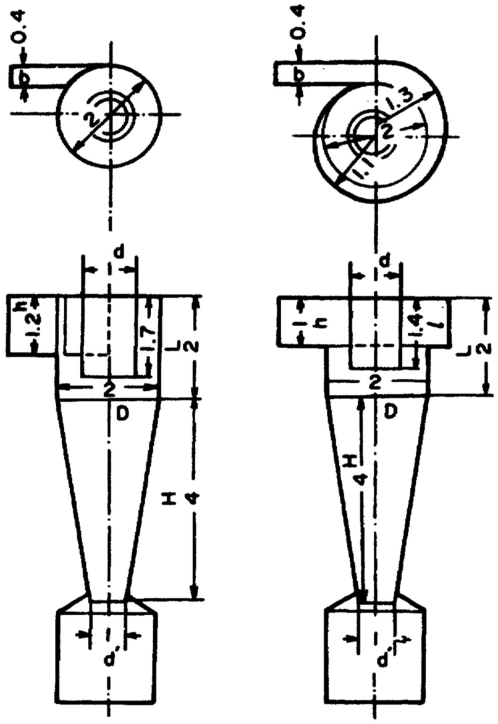


FIGURE 5.14.6 Size of standard tangential cyclone. (From Iinoya, K., *Shujin-Sochi,* Nikkan Kogyo Shinbun, Tokyo, 1965. With permission.)

area of the collector is enlarged to operate at a low gas velocity. A Howard-type separator has many horizontal trays; hence, its separation efficiency is quite high because of the short settling distance. However, discharging separated particles and cleaning the equipment are difficult.

Centrifugal Collectors

This type of dust collector separates particles by the difference in centrifugal force created by the change in flow direction and driving particles to the wall. The cyclone is the most widely used centrifugal dust collector because of its simple structure. It has no moving parts and the initial cost is inexpensive. It can be divided into two types: tangential and axial cyclones, according to the type of gas intake. Although the latter type of cyclone is customarily used in parallel so as to deal with a large volume of gas at a low pressure drop, the collection efficiency is not as high. The pressure drop in a cyclone of similar shape depends on the inlet velocity but not on the size. However, the collection efficiency becomes better with decreasing cyclone size. When the same volume of air is dealt with, both collection efficiency and pressure drop decrease in general at elevated temperatures. When dust loading becomes high, the pressure drop decreases, but the collection efficiency improves somewhat. Blowing some air down into the dustbin improves collection performance because it prevents or minimizes reentrainment of dust from the bin. Figure 5.14.6[3] shows typical cyclone dimensions, and Figure 5.14.7[3] shows the calculated correlation between cut size and cyclone diameter.

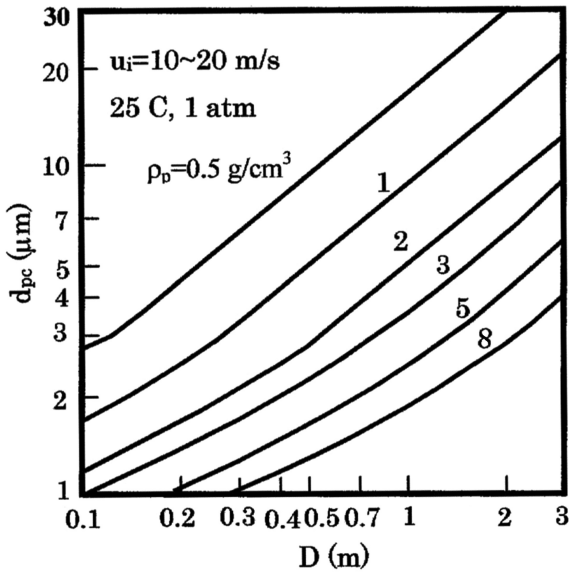


FIGURE 5.14.7 Cut size of standard cyclone. (From Iinoya, K., *Shujin-Sochi,* Nikkan Kogyo Shinbun, Tokyo, 1965. With permission.)

Electrostatic Precipitation

An electrostatic precipitator (ESP) separates particles from the gas stream by utilizing Coulombic forces acting on charged particles. Coulombic forces act directly on particles so that the structure of the ESP is very simple and different from that of other types of collectors. This feature makes it possible to handle a large amount of gas at high temperature and/or at high humidity with a very low pressure drop. An ESP usually consists of particle charging and collection parts. Both charging and collection of particles are accomplished by applying a high voltage between a discharging wire and a plate or cylindrical electrode. Hence, there are two types of ESP: the one-stage type, in which the charging and collection of particles take place simultaneously in one set of discharge and collection electrodes, and the two-stage type, in which charging and collection are carried out separately using two sets of electrodes in series. Figure 5.14.8 shows the structure of the wire and plate-type ESPs.

Approximate collection efficiency of ESPs can be estimated by the following famous Deutsch equation, which is the same equation described before:

$$E = 1 - \exp\left(-\frac{v_e S}{Q}\right) \tag{5.14.1}$$

where

- v_e is the migration velocity of a particle to the collecting electrode
- S is the area of the collecting electrode
- Q is the volumetric gas flow rate

Figure 5.14.9[4] shows the measured collection efficiency of an ESP as a function of particle size. Collection efficiency has a minimum around 0.5 μm because the predominant charging

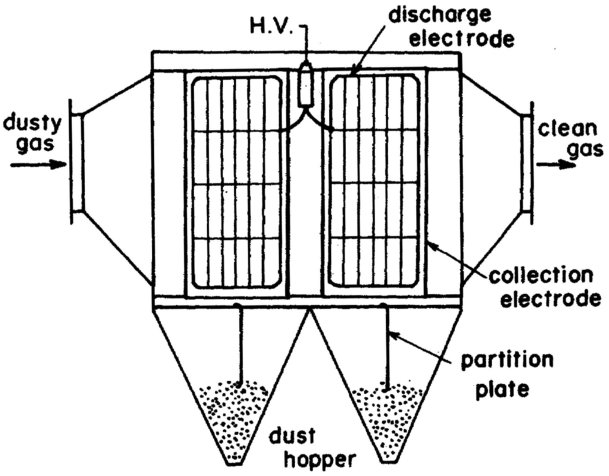


FIGURE 5.14.8 Parallel-plate electrostatic precipitator.

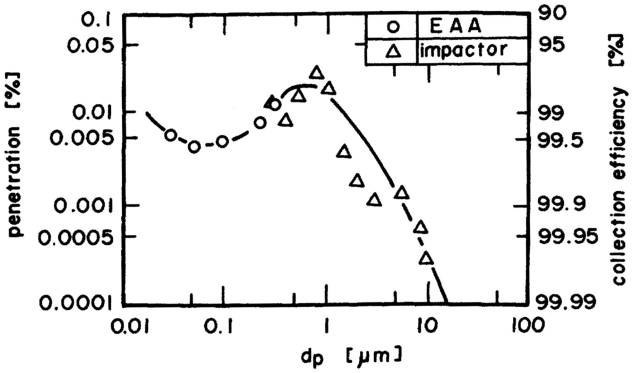


FIGURE 5.14.9 Measured fractional collection efficiency of ESP; measured by EAA (electrical aerosol analyzer) and impactor.

mechanism changes from diffusion to field charging around this size range, and the number of charges by diffusion charging is proportional to particle size but is proportional to the second power of size by field charging, whereas drag force is proportional to particle size. The decreasing trend of collection efficiency below 0.05 μm is also considered to be caused by the increase in the fraction of uncharged particles.

The collection performance of ESPs also depends on the electric resistivity of the particle, ρ:

1. $\rho < 5 \times 10^2$ Ωm: Charges on a particle are released immediately after arriving at the collection electrode so that particles are not retained firmly on the electrode, and thus re-entrainment of particles happens frequently.
2. $5 \times 10^2 < \rho < 5 \times 10^8$ Ωm: Charges on a particle are released at a reasonable rate so that captured particles do not re-entrain but form a stable dust layer on the electrode.
3. 5×10^8 Ωm $< \rho$: Because of the extremely high resistivity of dust, the accumulation rate of charges from a dust layer exceeds their release rate so that an electric field is formed between a thin dust layer and a

collection electrode, and the field strength gets stronger with the accumulation of particles. Finally, back discharge occurs. Furthermore, accumulated dust particles are splashed from the collection electrode when back discharge occurs.

For cases 1 and 3, the collection efficiency of an ESP decreases considerably. Hence, it is very important to control the electrical resistivity in the range between 5×10^2 and 5×10^8 Ωm. Among many factors, humidity and the temperature of the gas are the most influential to the resistivity. Figure 5.14.10[5] shows a measured relationship between the resistivity of fly-ash and gas temperature with humidity as a parameter. The resistivity decreases monotonically against temperature for dry gas, whereas it has a maximum in humid conditions, and it decreases as the water content increases. The appearance of maximum resistivity can be explained as follows. Although the resistivity due to the carriage of charges through a particle, which is referred to as volume resistivity, decreases as the temperature rises, the resistivity due to the carriage on a particle surface, which is referred to as surface resistivity and is thought to be related to the thin water layer absorbed on a particle, decreases as temperature decreases. Accordingly, it is clear that to attain favorable collection performance, an ESP has to be operated at either higher or lower than the temperature giving maximum resistivity. Several methods have been contrived to reduce the resistivity: spraying water, adding a small amount of chemicals to the gas, and so on.

Recently so-called low-low temperature ESP has been developed and popularly used. As mentioned above, the

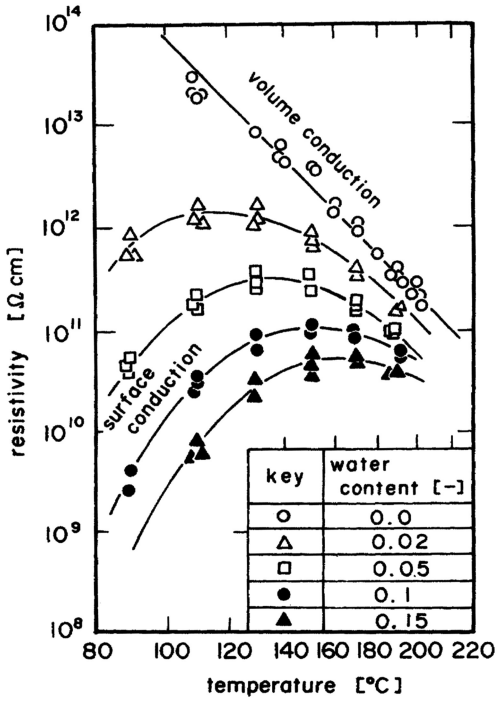


FIGURE 5.14.10 Effect of gas temperature and humidity on electrical resistivity of dust. (Modified from K. M. Sullivan, EPA Report, EPA-600/9/82–005b, 1982.)

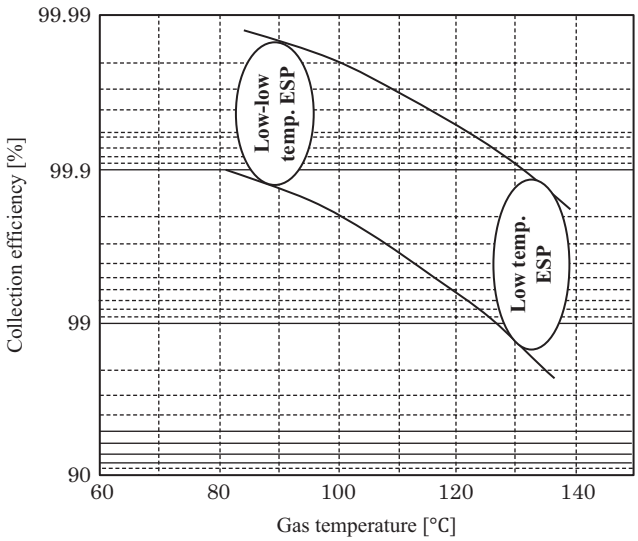


FIGURE 5.14.11 Collection performance of Low-Low temperature ESP [Modified from S. Najima, *Technical Report Sumitomo Heavy Industry*, 146, 2001].

resistivity of particles becomes lower at low temperature and charging performance is also stable. As a result, ESP performance significantly improves by operating at low temperature below acid point of SO_2 as shown in Figure 5.14.11.[6] This type of ESP also makes ESP compact because of low operation temperature so that it has been popularly used recently but very cautious care has to be paid against the corrosion of equipment.

On the higher-temperature side, ESPs have not been used because high temperature can cause problems and can push up the construction cost despite the usefulness of the energy-saving point of view.

Charging particles, especially charging high-resistivity particles, is one of the most important problems to be solved in the field of electrostatic precipitation if high collection performance is to be achieved.

5.14.2 OBSTACLE-TYPE DUST COLLECTORS

Since particles are collected by obstacles in the equipment, collection efficiency for this type of collector is expressed by the following equation:

$$E = 1 - \exp\left(-\frac{A}{v_c}\frac{\alpha}{1-\alpha}\eta L\right) \tag{5.14.2}$$

where

v_c is the volume of one collection obstacle
α is the packing density of the obstacle
L is the thickness of the obstacle
A is the constant determined by the shape of obstacle, that is $4/(\pi D_c)$ for cylindrical collector and $3/(2D_c)$
d_c is the diameter of obstacle.

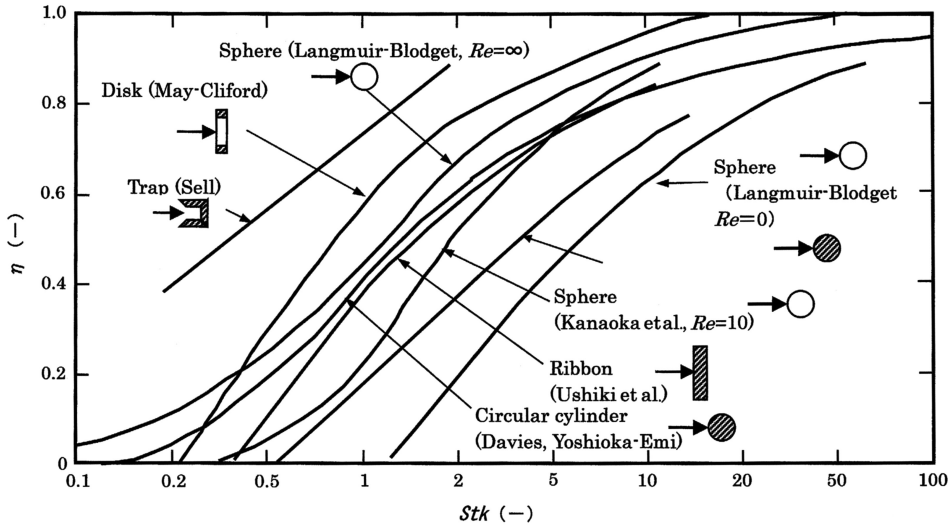


FIGURE 5.14.12 Calculated collection efficiencies of single collection obstacles. (Drawn from references 7–17.)

In the equation, constants other than η are determined from the equipment itself, so that E can be estimated if η is given for a given collector and operation conditions, and thus the collection efficiency of obstacles with different shapes is calculated as shown in Figure 5.14.12.[7–17] In the figure, Stk is the Stokes number defined by

$$Stk = \frac{C_c \rho_p d_p^2 u}{9 \mu D_c} \tag{5.14.3}$$

where

C_c is the Cunningham's slip correction factor
ρ_p is the particle density
d_p is the particle diameter
D_c is the representative length of a collecting body
u is the gas velocity
μ is the gas viscosity.

Inertial Dust Collector

The inertial dust collector separates particles by the difference in motion in a curvilinear flow field between the particle and the gas. Although the collection performance is much better than that of gravitational collectors, it is also used as a pre-dust collector. It is classified into two groups, depending on the method of particle collection: separation of particles by many packed obstacles, and separation by flow channels with different curvatures. Figure 5.14.13 shows some examples of collection bodies and channels.

The collection performance of inertial collectors improves with increasing particle size and gas velocity. Therefore, every inertial collector is designed to intensify the inertial effect by changing the flow direction as often as possible. Figure 5.14.14 shows a louver-type dust collector, which intensifies the inertial effect by a large inversion angle and a small gap between blades. In practical applications of inertial collectors, they are used mainly to separate mist rather than solid particles, as a discharge system for collected particles makes their structure complicated and costly.

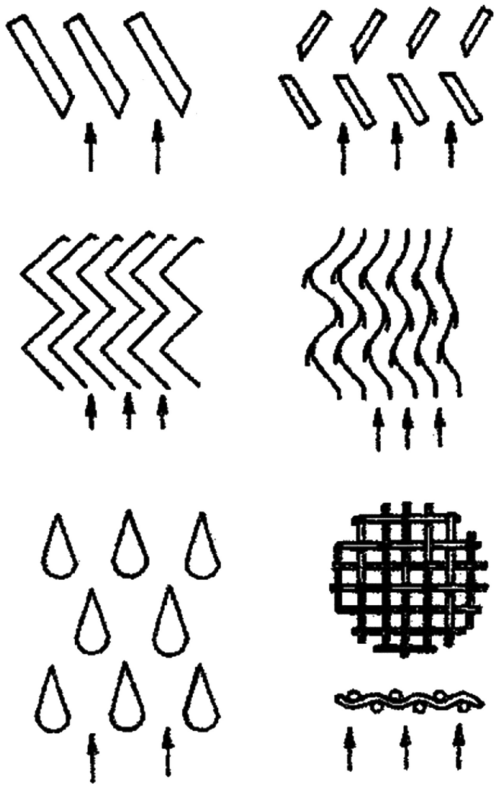


FIGURE 5.14.13 Shapes of packing materials for inertial-type dust collector.

Air Filters

An air filter is one of the most reliable and efficient methods for dust collection, and particles are mainly used at a low dust concentration so that particles are captured inside the filter, and thus this type of particle collection is called a depth filter.

An air filter is mainly used to purify the air in local environments such as hospitals, manufacturing lines, work spaces, and so on. In those environments, the dust concentration is usually lower than 10 mg/m^3 and the particle size is less than several micrometers. Hence, packed filter materials, especially fibrous mats, are used for this purpose. The porosity of a filter mat is generally higher than 85%; hence, particles are captured on individual fibers in the filter. Therefore, the filter efficiency E can be calculated from the single fiber collection efficiency η for a given filtration condition as follows:

$$E = 1 - \exp\left(-\frac{4}{\pi}\frac{\alpha}{1-\alpha}\frac{L}{D_f}\eta\right) \tag{5.14.4}$$

where, D_f, α, and L are the fiber diameter, fiber packing density, and filter thickness, respectively.

Although particles are collected on a fiber by a combination of effects, inertia, Brownian diffusion, interception, and gravity are the major factors in mechanical filtration. Electrostatic force becomes important when either fibers or particles or both are electrically charged, or an external electrical field is applied.

Many theoretical and empirical expressions have been proposed for each collection mechanism. Figure 5.14.15[18] shows a typical single-fiber collection efficiency chart calculated by taking inertia, Brownian diffusion, interception, and gravity into account simultaneously. It is clear from the figure that there exists a particle size or a filtration velocity that gives minimum efficiency, corresponding to the transition region among different mechanisms.

There are two types of air filters: disposable and renewable. For the former type, fiber materials such as glass, metal, and natural and synthetic fibers are packed loosely in a frame or are formed into a mat-like structure. Because captured particles accumulate inside the filter, its pressure drop increases with filtration time, so that a zigzag structure is adopted to increase the filtration area to lengthen its service life. It is finally replaced to avoid an increase in running cost when the pressure drop reaches a certain level. The latter type of

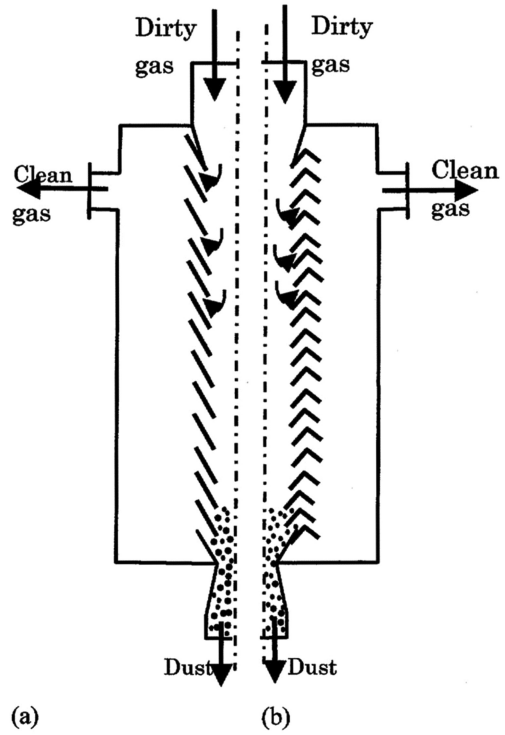


FIGURE 5.14.14 Shape of louver-type dust collector. (a) Flat blade, (b) Curved blade.

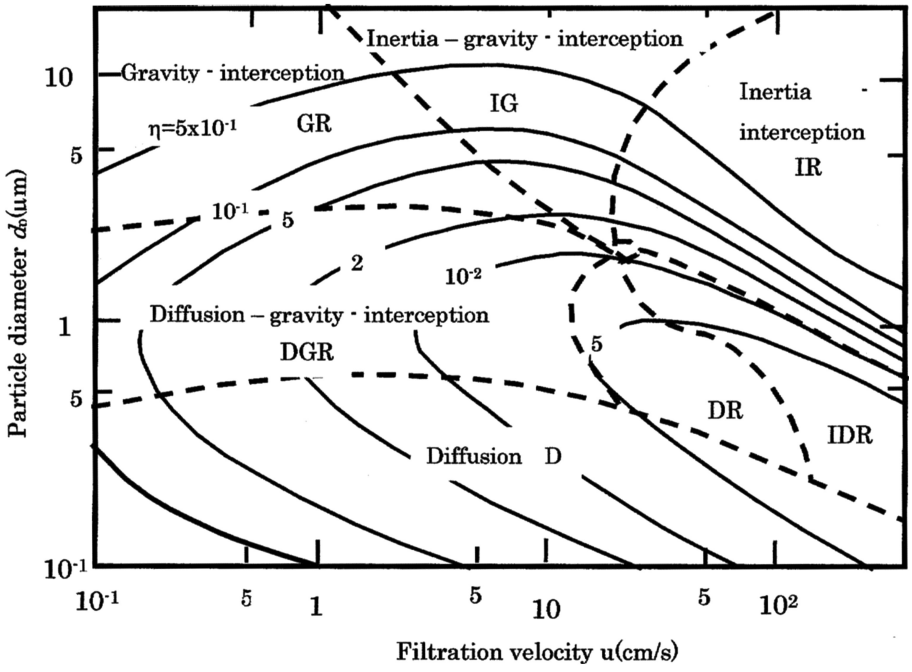


FIGURE 5.14.15 Total single-fiber collection efficiency (D_f = 10 μm, α = 0. 0). (Modified from H. Emi, K. Okuyama, N. Yoshioka, J. Chem. Eng. Jpn., 6, 1973.)

filter renews part or all of a filtering surface periodically, also to avoid the pressure drop increase. High-efficiency particulate air (HEPA) and ultra-low-penetration air (ULPA) filters are types of paper filters composed of very fine fibers, less than 1 μm on average. They are defined as the filters that collect 0.3 μm particles at the efficiency higher than 99.7% and 0.1 μm particles at higher than 99.9997%, with a pressure drop that does not exceed 12.7 mm H_2O at their specified flow rate, usually 2–5 cm/s. For this reason, HEPA and ULPA filters are used to create highly purified environments, which are necessary in the semiconductor industry, the precision machine industry, and so on. Penetration curves of HEPA and ULPA filters are convex against particle size, and the maximum appears around 0.1 μm (i.e. the collection efficiency of the filter is poorest around this particle size at the conventional filtration condition and decreases as filtration velocity increases). Hence, the filter collection performance can be roughly evaluated by measuring the efficiency in this size range.

An electrostatic fibrous filter is another type of air filter that utilizes electrostatic force to remove particles. Electrostatic attractive force becomes effective when at least either fiber or particle is charged, except that both of them are charged in the same polarity. Therefore, several types are designed, depending on the charging state of fiber and particle. In general, an electrostatic fibrous filter is superior in collection performance to a mechanical fibrous filter but is difficult to operate stably. The electric filter is a stable electrostatic fibrous filter because it is composed of permanently charged fibers and is capable of collecting particles at a high efficiency in the initial filtration stage. However, the efficiency decreases with filtration time because of dust loading. Therefore, this drawback has to be eliminated in practical use.

5.14.3 BARRIER-TYPE DUST COLLECTORS

The most pronounced feature of dust collectors in this type is the almost perfect particle collection regardless of size except just after the removal of accumulated particles on the barrier. This is because most of the particle collection is performed by the already captured accumulated particles by a sieving effect. This kind of collection is usually called surface or cake filtration.

Bag Filters

A bag filter is usually made of fabric and in a cylindrical "bag" shape, hence the name "bag" filter. They are popularly called "fabric" filters, also. Although any type of fiber with a different weave can be used as a filter material, synthetic fibers such as polyester, polypropylene, nylon, and glass are often employed because of their strong resistivity to gas and dust. Their lifetime is usually more than two years. However, they cannot be used at a temperature higher than 250°C despite the efforts to develop a high-resistivity fiber. Even the most resistible of glass fibers cannot stand such a high temperature. Because of the small filtration area of each bag (100–300 mm in diameter and length less than 10 m for the cylindrical type and about 1 m × 2 m for the envelope shape), and low filtration velocity (0.5 to 5 m/min), many bags are assembled in a unit, called a bag house, when a large amount of gas must be handled. As mentioned before, collected dust particles accumulate on a fabric surface and thus raise the pressure drop. Hence, the accumulated dust has to be dislodged to maintain continuous operation. Bag filters are categorized into mechanical-shaking, reverse-flow, and pulse-jet types, depending on the method of dislodging dust (i.e. mechanical-shaking and reverse-flow filters have to stop the gas flow during dislodging, thus the bag house of these types is divided into several compartments so that the entire house does not have to be stopped. A schematic drawing is shown in Figure 5.14.16. In the pulse-jet type, a filter can dislodge dust without stopping the house because it injects strong cleaning air for a short time.

A new application of the fabric filter is the simultaneous separation of gas and dust. This technique is mainly applied to remove HCl and SO_x gases from municipal incineration flue gas by injecting lime slurry or $Ca(OH)_2$. Particles upstream in

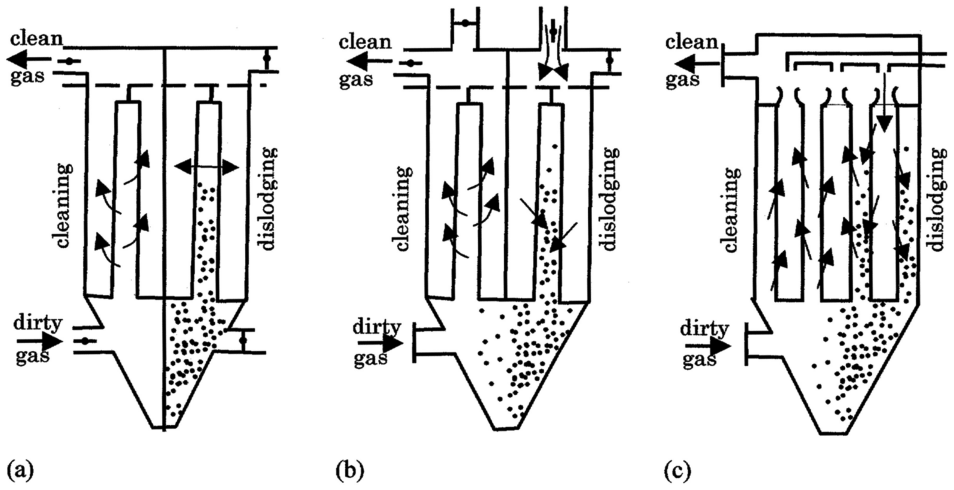


FIGURE 5.14.16 Schematics of bag filters. (a) Mechanical shaking type, (b) Reverse flow type, (c) Pulse-jet type.

the bag filter form solid particles. The resulting solid particles are separated by a filter.

5.14.4 MISCELLANEOUS

Scrubbers are widely used as dust collectors because of their relatively high collection efficiency and low initial cost. The venturi scrubber, especially, operating with a very high pressure drop (about 1000 mm H_2O), shows a collection efficiency as high as that of a bag filter. However, because a large amount of water is consumed and has to be treated afterward, it is not popular nowadays. Acoustic, magnetic, and thermal forces also have the potential to separate particles from a gas stream. However, they have not been put into practical use because of economic drawbacks. Other dust collection methods under development are a ceramic filter, and a granular bed filter for hot-gas cleaning. Although they show about the same performance level as that of a bag filter, there remain problems to be solved, especially durability to thermal shock and service life.

REFERENCES

1. Kanaoka, C., *J. Soc. Powder Technol*., 54, 370–376, 2017.
2. Kanaoka, C., Makino, H., *Hajimete no Shujin Gijutsu*, Nikkan Kogyo Shinbun, Tokyo, 2013, p. 35.
3. Iinoya, K., *Shujin-Sochi*, Nikkan Kogyo Shinbun, Tokyo, 1965.
4. Oglesby Jr., S., Nichols, G., *EPA Report*, EPA-600/8-77-201, 1977.
5. Sullivan, K.M., *EPA Report*, EPA-600/9/82-005b, 1982, pp. 141–148.
6. Najima, S., *Sumitomo Heavy Industry Technical Review*, No.146, pp. 35–38, 2001.
7. Langmuir, I., Blodgett, K.B., *U.S. Army Air Forces Technical Report*, No.5418, 1946.
8. Davies, C.N., *Air Filtration*, Academic Press, London, 1973.
9. Yoshioka, N., Emi, H., Fukushima, M., *Kagaku Kougaku*, 31, 157–163, 1967.
10. Sell, W., *VDI Forsch*., Staubausscheidung an Einfachen Körpern und In Luftfiltern, 347, 1931.
11. Kanaoka, C., Yoshioka, N., Iinoya, K., Emi, H., *Kagaku Kogaku*, 36, 104–108, 1971.
12. May, K.R., Clifford, A., *Ann. Occup. Hyg*., 10, 83–95, 1967.
13. Lewis, W., Brun, R.J., *NACA*, TN3658, 1954.
14. Masliyah, J.H., Duff, A., *J. Aerosol Sci*., 6, 31–43, 1975.
15. Brun, R.J., Dorsch, R.G., *NACA*, TN3147, 1954.
16. Dorsch, R.G., Saper, P.G., Kadow, C.F., *NACA*, TN3587, 1955.
17. Ushiki, K., Kubo, K., Iinoya, K., *Kagaku Kogaku Ronbunshu*, 3, 172–178, 1977.
18. Emi, H., Okuyama, K., Yoshioka, N., *J. Chem. Eng. Jpn*., 6, 349–354, 1973.



Taylor & Francis
Taylor & Francis Group
http://taylorandfrancis.com

5.15 Electrostatic Separation

Ken-ichiro Tanoue and Hiroaki Masuda

Electrostatic separation based on the difference of electric conductivity of particles or their tribo-charging characteristics has been widely utilized for about 100 μm to 3 mm size range. Tribo-electrostatic separator has been also investigated for fine coal preparation of 86 μm in coal and a few micron in minerals.[1]

Electrostatic force, which works on a charged particle, is given by

$$F = qE \tag{5.15.1}$$

where

q is the charge of particle
E is the strength of electric field

Electrostatic separation utilizes this force. Although there are many kinds of methods for particle charging, induced charging, corona charging, and tribocharging are mainly applied in particle separation. Table 5.15.1 shows the relationship between separating materials and charging method.

5.15.1 SEPARATION MECHANISM

Induction Charging

Figure 5.15.1 shows electric conductivity for many kinds of materials.[2] As electric conductivity differs from the materials, the motion of a particle under an electrostatic field changes dramatically, as shown schematically in Figure 5.15.2.[2] If a particle is conductive, the particle contacting the surface under an electrostatic field is charged up as high voltage is applied, and it becomes equipotential with the electrode surface. Then the particle jumps up from the surface because of the electrostatic repulsive force. On the other hand, a particle of insulating material needs a much longer time in order to get an induction charge. So, electrostatic force hardly works on it. The induction charge Q is given by[3]

$$Q = C\Delta V\left[1 - \exp\left(-\frac{\sigma t}{C}\right)\right] \tag{5.15.2}$$

where

C is the capacitance of the particle
ΔV is the voltage difference between electrodes
σ is the electric conductivity of the particle
t is the induction charging time

Corona Charging and Induction Charging

When negative high voltage is applied to a metal of large curvature, ionization of gas occurs around it, and then negative ions are accelerated to the grounded surface. Figure 5.15.3 shows the motion of particles under an electrostatic field. The particles, which are made of high or low electric conductivity, electrify negatively on the grounded surface. As the charge of the particle having high electric conductivity leaks easily to the grounded surface, it is electrified positively by induced electrification. It jumps from the grounded surface by electrostatic repulsive force. On the other hand, the particle with low electric conductivity hardly moves, because the charge of the particle does not leak; therefore, the particle remains on the plate by image force.

Various Factors in Relation to Electrostatic Separation by Corona Charging or Induction Charging

There are three processes in the separation of particles by use of electrostatic force: selective charging of particles, charge transfer between particles and electrode, and dynamic motion of particles near the electrode surface. These processes depend strongly on relative humidity ψ. If moisture adsorbs on the surface of a particle of insulating material, the apparent electric conductivity of the particle may increase. Especially, if ionic concentration in the moisture is high, the electric conductivity may dramatically increase. Generally, the empirical

TABLE 5.15.1 Relationship between Separating Materials and Methods

Separating Material	Charging Method	Apparatus for Electrification
Wasted electric wires	Induction charging	Rotating drum
Farm produce	Corona and induction charging	Sliding belt, rotating drum
Pulverized coal	Tribo-charging	Pipe, fluidized bed, cyclone, pulverizer
Plastics	Tribo-charging	Fluidized bed, vibrating transport
Food	Tribo-charging	Pipe

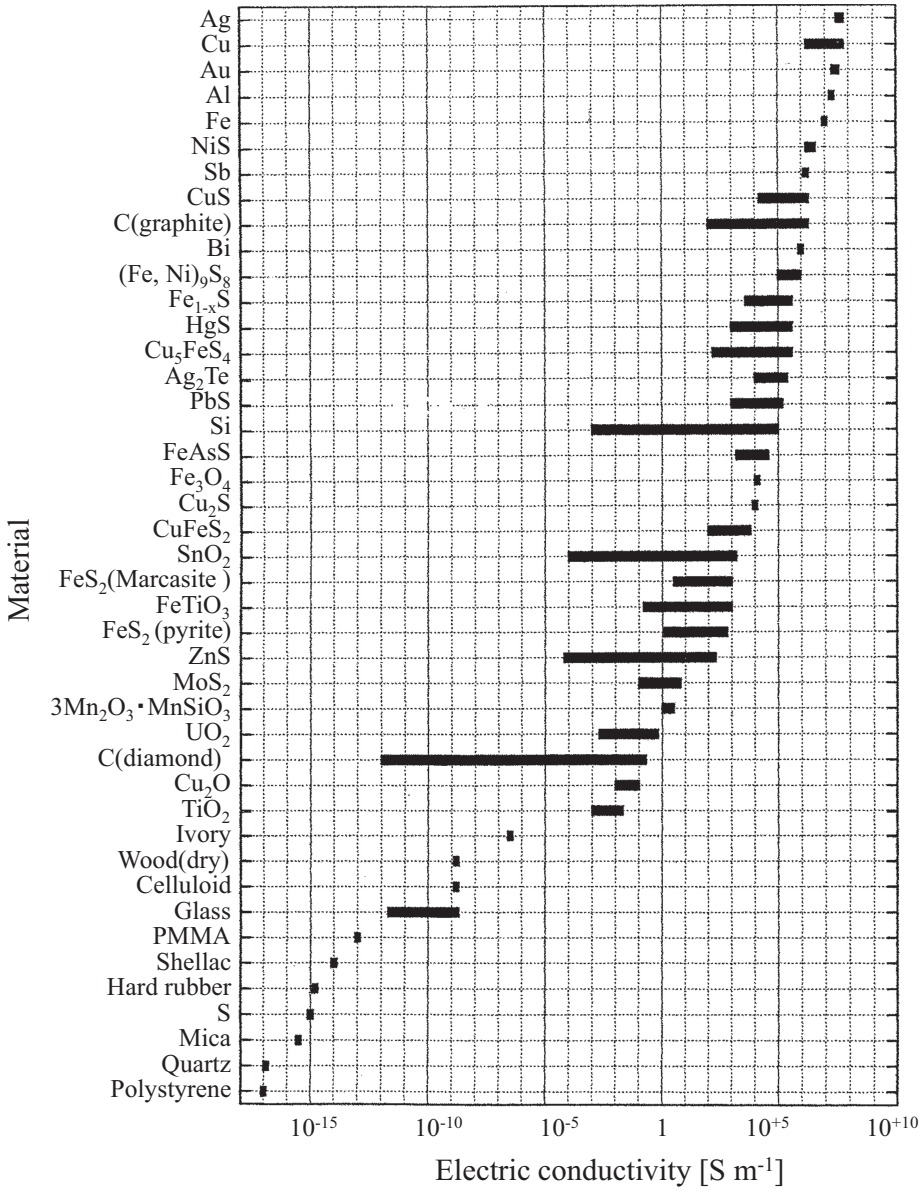


FIGURE 5.15.1 Electric conductivity for various materials.

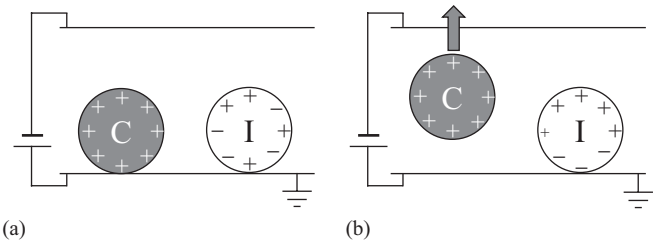


FIGURE 5.15.2 Motion of particles under an electrostatic field. C, particle made of conductive material; I, particle made of insulating material. (a) Induction charging and (b) Particle movement.

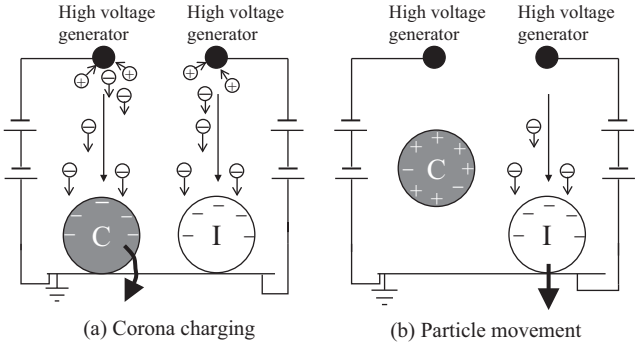


FIGURE 5.15.3 Motion of particles under corona charging. C, particle made of conductive material; I, particle made of insulating material.

relationship between the conductivity and the humidity is given by[4]

$$\log\sigma = -K_1 + K_2\psi \qquad (5.15.3)$$

TABLE 5.15.2 Work Functions for Various Materials in vacuum[5–8]

Metal		Metal Oxides		Polymer Compounds and etc.	
Material	Work Function (eV)	Material	Work Function (eV)	Material	Work Function (eV)
Zn	3.63	BaO	1.1	Polyethylene LDSR[a)]	5.24 ± 0.24
C	5	CaO	1.60 ± 0.2	Polyethylene LDNSR[b)]	6.04 ± 0.47
Al	4.06–4.26	Y_2O_3	2	Polypropylene SR[c)]	5.43 ± 0.16
Cu	4.25	Nd_2O_3	2.3	Polypropylene NSR[d)]	5.49 ± 0.34
Ti	4.33	ThO_2	2.54	Polystyrene	4.22 ± 0.07
Cr	4.5	Sm_2O_3	2.8	Polyvinyl chloride	4.85 ± 0.2
Ag	4.52–4.74	UO_2	3.15	Polycarbonate	3.85 ± 0.82
Si	4.60–4.91	FeO	3.85	Polymethyl methacrylate	4.30 ± 0.29
Fe	4.67–4.81	SiO_2	5	Polytetrafluoroethylene	4.25 ± 0.10
Co	5	Al_2O_3	4.7	Polyethylene Terephthalate	4.25 ± 0.10
Ni	5.04–5.35	MgO	4.7	Niron66	4.08 ± 0.06
Pt	5.12–5.93	ZrO_2	5.8	Pylex7740	4.87 ± 0.21
Au	5.31–5.47	TiO_2	6.21	Quartz	4.87 ± 0.22

a) low density, stress relieved; b) low density, not stress relieved; c) stress relieved; d) not stress relieved.

where K_1 and K_2 are constants specific to the material. The conductivity is the inverse of the specific resistivity. Dependence of the specific resistivity not only on the relative humidity but also on the temperature is discussed in Section III 4.1.

Tribocharging

It is hardly practical to separate special plastics from mixed plastic materials or to separate ash and minerals from coal powder by using a corona charge or an induction charge, because the difference in electric conductivity is usually very small. In these cases, tribocharging is used on the basis of contact potential difference (CPD). The CPD that shows the work function difference between two materials is the most direct physical property in relation to particle electrification. Table 5.15.2 shows the typical work functions[5–8] for many kinds of materials.

It is very important to select suitable materials for tribocharging. Charged particles are introduced into the electrostatic field and then separated according to the polarity of the particles.

In order to increase the purity of foods (wheat, grain, flour, protein, oilseeds, pulses, etc.), the tribocharging electrostatic separators from lab-scale to pilot-scale have been developed.[9] Furthermore, the tribocharging separator with both the fluidized bed and belt-conveyer have been also investigated for the polymer compounds of 2–4.5 mm.[10]

5.15.2 SEPARATION MACHINES

Electrostatic separation has been utilized in industries for refining mineral resources, treatment of pulverized coal, treatment of waste plastics, recycling of electrical appliances, and so on. In this section, some practical separation machines, which have been reported in recent years, are presented.

Refining of Mineral Resources[11–17]

As fewer and fewer high-grade mineral ore deposits are discovered and developed and more become depleted, it becomes increasingly important to develop processes whereby the available low-grade ores may be mined profitably.

The benefaction of mineral ores[15] has been conducted by use of induction and tribocharging, as shown in Figure 5.15.4. The apparatus consists of a horizontal aluminum plate with a vibrator, an inverted metallic roof sloped at a certain degree to the aluminum plate, an alternating voltage power supplier, and collecting bins. Figure 5.15.4a shows that ore particles are supplied on the vibrating aluminum plate, where the particles are charged by a combination of tribocharging and induction charging. They move in the alternating current field. In Figure 5.15.4b, centrifugal force acts on the particles due to their complex circular motion induced by the force field, resulting in an outward movement of the particles. The highest charged particles move the furthest and tend to collect in the lateral bins.

Treatment of Pulverized Coal[1,18–21]

In order to use low-quality coals in a thermal power plant, it is important to remove the ash and mineral contents from pulverized coal. As charcoal contents and ash contents have high conductivity, electrostatic separation has been conducted by use of tribocharging.

Figure 5.15.5 shows the separation machine used to eliminate ash from pulverized coal. The coal is conveyed by high-speed gas flow to the tribocharging section. Charcoal contents

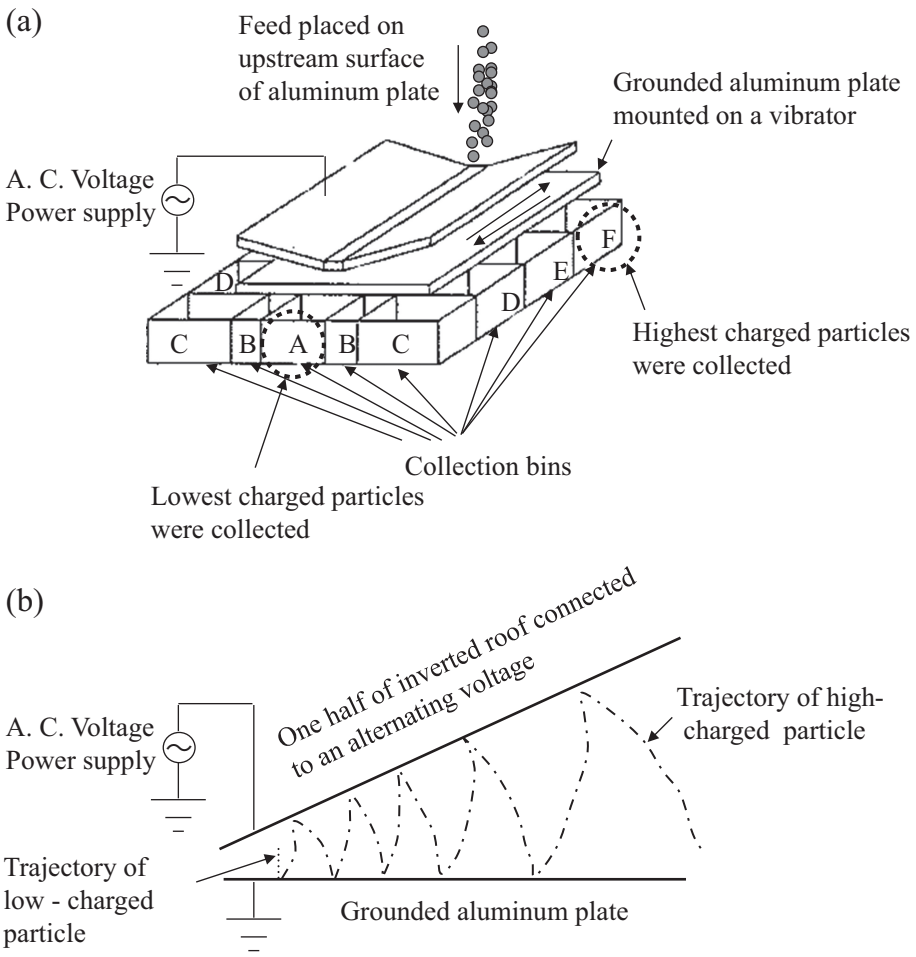


FIGURE 5.15.4 Electrostatic beneficiation apparatus: (a) oblique view of apparatus showing inverted roof and collection bin locations; (b) end view showing trajectories of charged particles.

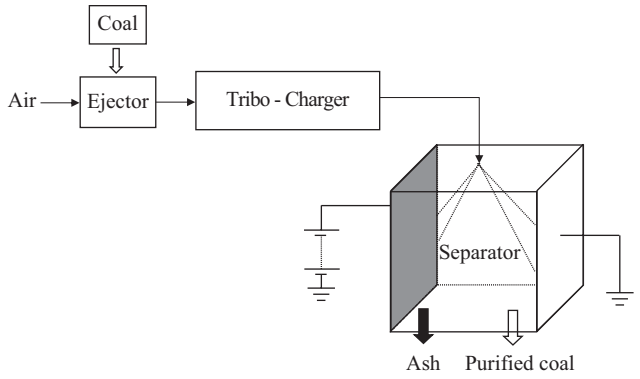


FIGURE 5.15.5 Electrostatic separation machine for purified coal by use of tribocharging.

are electrified positively while the remaining ash was charged negatively. In order to electrify them effectively, a spiral copper pipe is introduced in the charging section.

Separation Technologies Inc.[21] has developed an electrostatic separation machine, as shown in Figure 5.15.6. Two parallel plates are set horizontally. The upper plate has a slit to introduce powdered coal. Positive and negative voltages are applied on the upper and lower plate, respectively. A meshed polymer belt is set between the plates and moved by drive rollers. The particles fed into the plates are tribocharged by the belt. Negatively charged particles with ash approach the upper electrode, while positively charged particles with carbon approach the lower electrode; each move in different directions and then separate.

Treatment of Waste Plastics[22–24]

The development of a process to separate different types of plastics from each other can significantly improve the possibilities to recycle municipal waste. The waste plastics are crushed to pieces and separated into PMMA, ABS, PS, PE, PP, PET, and PVC materials by the use of tribocharging.

Hitachi Zosen Corp.[24] has developed a new electrostatic separation machine for plastics, as shown in Figure 5.15.7. Plastics are fed into a mixer having many pins inside the vessel, where tribocharging of the plastics occurs. The charged plastics are supplied to a grounded rotating drum and are

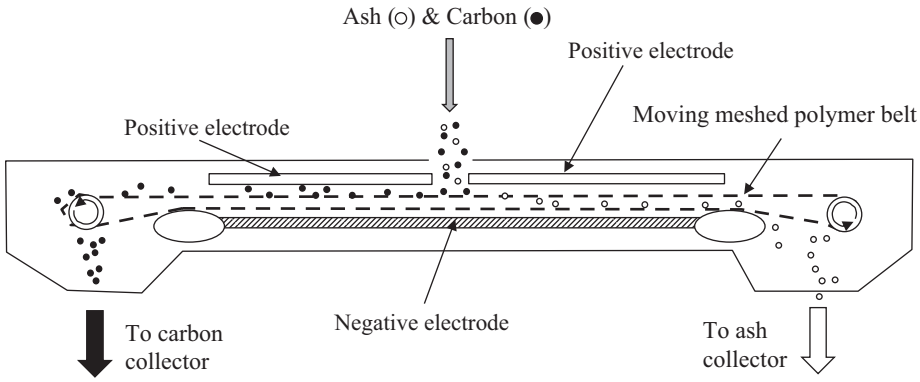


FIGURE 5.15.6 Electrostatic separation system for pulverized coal in Separation Technologies, Inc.[21]

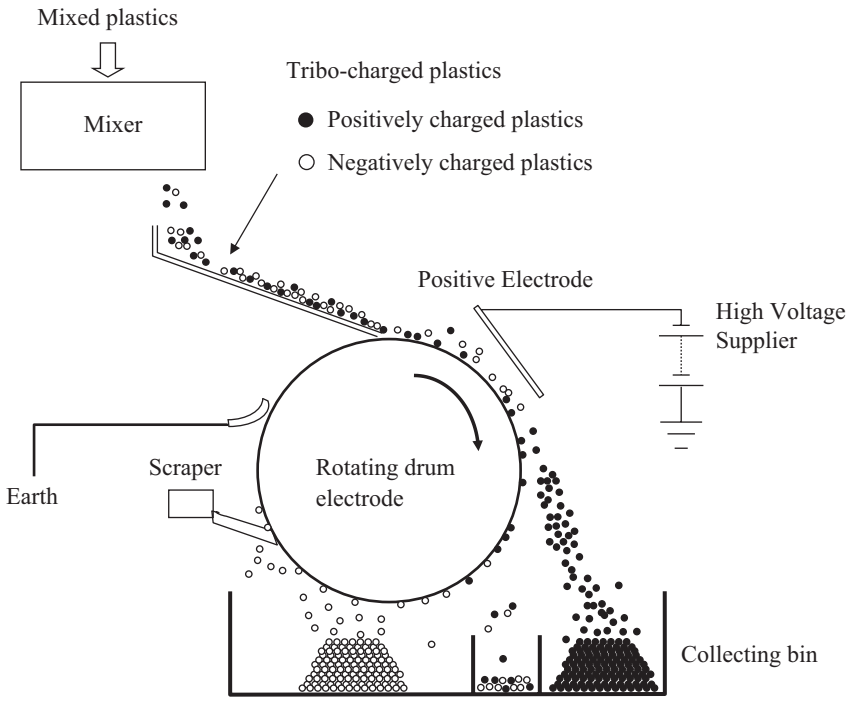


FIGURE 5.15.7 Electrostatic separation machine for waste plastics.

separated under an electrostatic field between the drum and the positive electrode where high voltage is applied.

Treatment of Waste Electrical Wires[25]

It is important to collect the copper and aluminum contents of waste electrical wires for recycling. In this case, waste wires must be stripped of their covering materials and then crushed to the desired size. They are separated by the use of induction charging or induced and corona combined charging.

Recycling of Electrical Appliances[26–29]

Waste electrical appliances are broken down, pulverized, and then sorted out into sizes of a few millimeters. The materials are composed of many kinds of compounds. Furthermore, these compounds are separated by wind force, magnetic force, and eddy-current force and then collected. However, plastics having PVC and metal wires are not separated. Recently, a separation method for metal wires and PVC has been developed by Higashihama recycle center.[26] The area enclosed by the solid line in Figure 5.15.8 shows the developed treatment method. The plastics with metal wires are pulverized again. Most metal wires are collected by use of a dry gravitational separator, while the powdered metal is collected by use of an electrostatic separator due to the induction charge. Finally, an electrostatic separator based on tribocharging is utilized for eliminating the PVC materials. The metal compounds are recycled as an ingredient of copper, while the plastics without PVC are utilized as a reducing agent in a blast furnace. Therefore, the amount of reclamation is reduced by one-fifth to one-tenth of the previous amount.

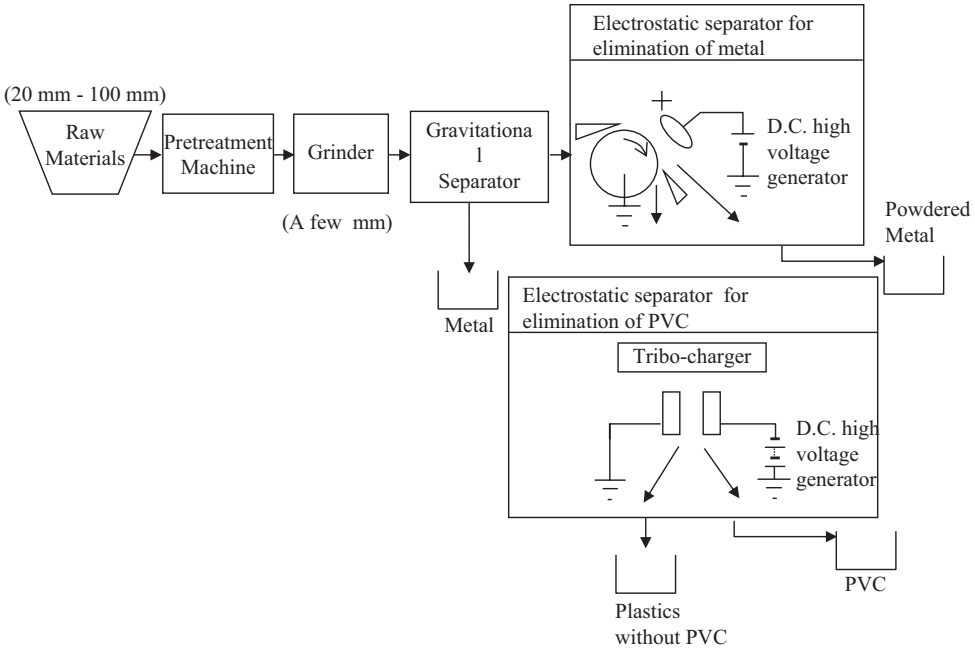


FIGURE 5.15.8 Application of electrostatic separation for treatment of plastics in recycling plant for electrical appliances.

REFERENCES

1. Dwari, R. K., Janumantha, R., *Miner. Eng.*, 22, 119–127, 2009.
2. Kelly, E. G., Spottiswood, D. J., *Miner. Eng.*, 2, 33–46, 1989.
3. Vieweg, H. F., *J. Phys. Chem.*, 30, 865–889, 1926.
4. Kakovsky, I. A., Revnivtzev, V. I., *Fifth International Mineral Processing Congress*, London, pp. 775–786, 1960.
5. *CRC Handbook of Chemistry and Pysics*, 78 edition, CRC Press, New York, 1998.
6. Fomenko, V. S., NTIS, *US Department of commerce report*, No. JPRS-56679, 1972.
7. Greason, W. D., Inclet, I. I., *Proceeding of the 1975 IEEE IAS Annual Meeting*, 432–435, 1975.
8. Davies, D. K, *J. Phys. D: Appl. Phys.*, 2, 1533, 1969.
9. http://steqtech.com/wp-content/uploads/2017/04/Electrostatic-Separation-of-Dry-Granular-Food-Material-R4.pdf
10. Miloudi, M., Dascalescu, L., Li, J. EI-Mossouess, S., Medles, K., *IEEE Trans. Dielectr. Electr. Insul.*, 20, 1510–1515, 2013.
11. Dance, A. D., Morrison, R. D., *Miner. Eng.*, 5, 751–765, 1992.
12. Yongzhi, L., *Proceedings of the First International Conference on Modern Process Mineralogy and Mineral Processing*, Beijing, 1992, pp. 385–390.
13. Okur, E., Onal, G., *Proceedings of the First International Conference in Modern Process Mineralogy and Mineral Processing*, Beijing, 1992, pp. 391–396.
14. Zhou, G., Moon, K., *Can. J. Chem. Eng.*, 72, 78–84, 1994.
15. Celik, M. S., Yasar, E., *Miner. Eng.*, 8, 829–833, 1995.
16. Inculet, D. R., Quigley, R. M., Inculet, I. I., *J. Electrostat.*, 34, 17–25, 1995.
17. Li, T. X., et al., *J. Electrostat.*, 47, 133–142, 1999.
18. Gupa, R., Gidaspow, D., Wasan, D. T., *Powder Technol.*, 75, 79–87, 1993.
19. Thomas, A. L., Rochard, P. K., Robert, H. E., Nicholas, H. H., *DOE-PETC-TR*, 90–11, 23, 1990.
20. Bouchillon, C. W., Steele, W. G., *Part. Sci. Technol.*, 10, 73–89, 1992.
21. Tondu, E., et al., *Miner. Eng.*, 48, 47–50, 1996.
22. Inculet, I. I., Castle, G. S. S., *Air. Inst. Phys. Conf. Ser.*, No. 118, Section 4, Electrostatics'91, Oxford, 1991.
23. Inculet, I. I., Castle, G. S. S., Brown, J. D., *IEEE Trans.*, IAS, 1397–1389, 1994.
24. Maehata, H., et al., *Hitachi Zosen Technical Information*, 59, 222–226, 1998.
25. Dascalescu, L., Iuga, A., Morar, R., *Magn. Electr. Separ.*, 4, 241–255, 1993.
26. Matsumura, T., *Hyomengijyutsu*, 52, 244–249, 2001.
27. Zhou, Y., Qiu, K., *J. Hazard. Mater.* 175, 823–828, 2010.
28. Das, A., Vidyadhar, A., Mehrotra, S. P., *Resour. Conserv. Recycl.*, 53, 464–469, 2009.
29. Chao, G., et al., *Waste Manage.*, 31, 2161–2166, 2011.

5.16 Magnetic Separation

Toyohisa Fujita

Many kinds of forces are used to separate or filter materials of different quality and size. Mineral processing especially includes the separation of solids, recovery of valuable solids from waste materials, and water or air purification. Materials have electric and magnetic properties; therefore, electromagnetic fields are employed to separate solids with different electric and magnetic properties. Consequently, for efficient separation it is important to increase the electromagnetic forces and decrease the interaction forces between different solid particles. Here various magnetic separation methods and unit operations to separate particles by virtue of differences in their magnetic properties are described.

5.16.1 CLASSIFICATION OF MAGNETIC SEPARATORS[1]

The magnetic separation technique is classified as shown in Table 5.16.1. In a narrow sense, magnetic separation is a separation technique whose goal is to concentrate a magnetic material, to remove magnetic impurity, or to extract valuable magnetic materials. This is accomplished by discharging the particles captured by a magnet at a position depending on their magnetic properties. Magnetic filtration is the method to separate magnetic particles by capturing them with a filter. When suspended particles are magnetic, the direct method, in which particles are captured directly on the filter, is employed. When the separation target is nonmagnetic or an ion, the magnetic reagent method,[2] in which the separation target is sprinkled with a magnetic reagent, is employed. This magnetite seed method can also be used in the magnetic separation[3] of various diamagnetic particles using the surface charge difference in water. Separation by electromagnetic induction is known as eddy-current separation. Magnetohydrostatic separation is a method used to separate nonmagnetic particles immersed in a magnetic fluid by adjusting the magnetic buoyant force on particles with a magnetic field gradient.

Magnetic separators are classified in terms of the difference of the separation mechanism (Table 5.16.2). A look at Table 5.16.2 shows that they are classified into static-magnetic-field-type and AC-magnetic-field-type. The first type is further classified into two main types on the basis of intensity, that is, a low-intensity and a high-power type. Moreover, the second type is classified into three further types, that is, a traveling-magnetic-field-type, a vibrating-magnetic-field-type, and an electromagnetic-induction-type. Drum-type, belt-type, and high-gradient-type separators have been extensively employed. The low-intensity type uses less than 0.2 T, the medium-intensity type uses from 0.3 to 1.0 T, while the high-intensity one employs more than 1 T.

The magnetic capture condition is equal to the magnetic field strength multiplied by the gradient of magnetic field strength, and it is given by the following formula:

$$H\nabla H \text{ or } B\nabla B \tag{5.16.1}$$

The magnetic field strength, field gradient, and conditions are listed in Table 5.16.3. A look at Table 5.16.3 shows that the capture condition of a medium-intensity-type separator is about 10 times larger than that of a low-intensity type, while the magnetic capture condition of the high-intensity type is very large (i.e. is more than 10 to 10^4 times higher than that of a medium-intensity-type separator).

TABLE 5.16.1 Magnetic Separation in a Broad Sense[1]

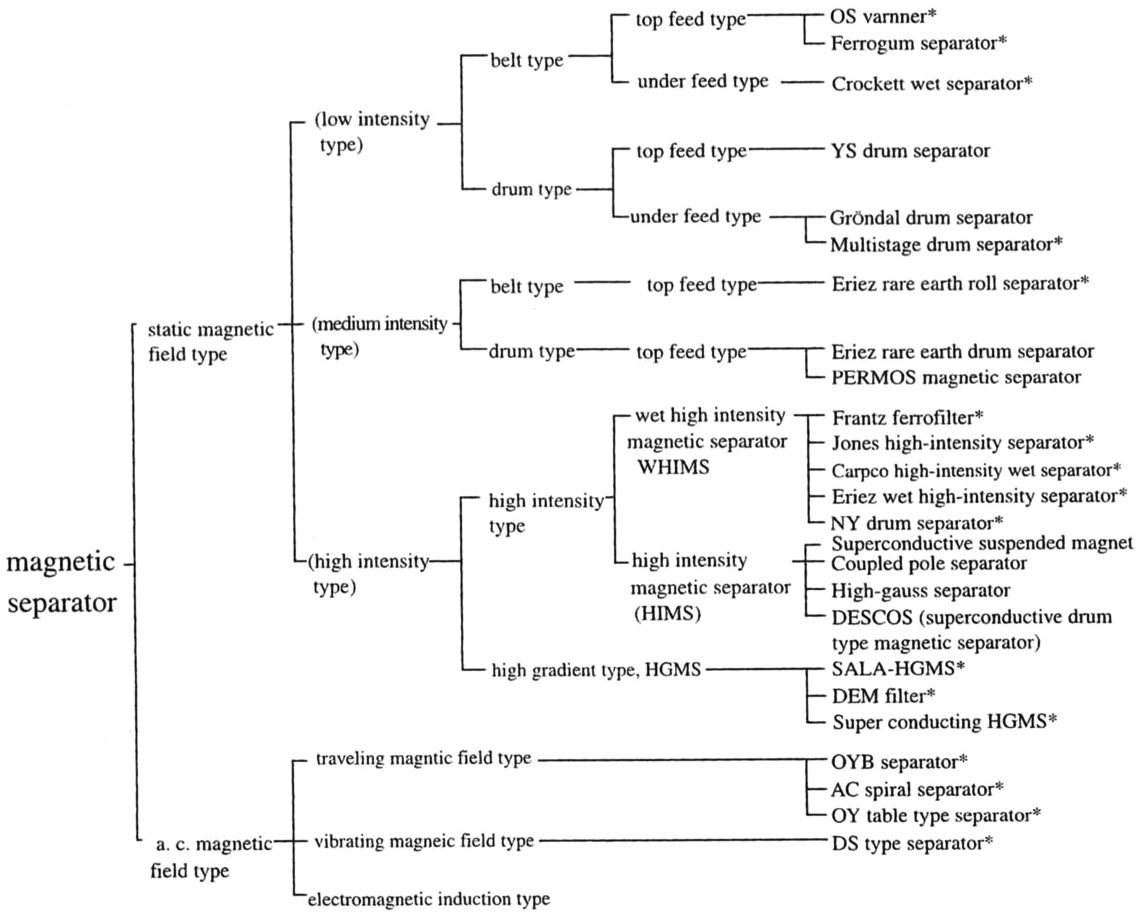
1. Magnetic separation (in a narrow sense)
   Concentration, purification, extraction
2. Magnetic filtration
   a. Direct method
   b. Magnetic reagent method
   Magnetic seed method, ferrite coprecipitation method, iron flocculants method, adsorption method, organic reagent containing iron addition method
3. Separation by electromagnetic induction
   Eddy current separation
4. Magnetohydrostatic separation
   Separation using magnetic fluid

5.16.2 STATIC MAGNETIC FIELD SEPARATORS

Open Gradient Magnetic-Field-Type Magnetic Separation

The main application of low-intensity magnetic separators is either removal of strongly magnetic impurities of tramp iron or concentration of a strongly magnetic valuable component. The Groendal drum wet separator has been widely used for the concentration of different materials. A permanent magnet is used instead of electromagnets, and raw material is fed from the lower part, as shown schematically in Figure 5.16.1.[4] The drum with fixed magnets inside rotates in contact with the floating or suspended particles in compartment a. Then magnetic particles are removed as they are attracted and captured on the drum surface by the magnetic force. Nonmagnetic particles are carried over to the next compartment, b. It was reported that the highest capturing efficiency of particles on

TABLE 5.16.2 Classification of Magnetic Separation[1]



* Matrixes like wire or balls are loaded between magnetic poles.

TABLE 5.16.3 Magnetic Capture Conditions of Various Magnetic Separators

Classification	agnetic separator	H (kA/m)	$\partial H/\partial x$ (MA/m^2)	Magnetic condition $H(\partial H/\partial x)$ (10^{12}A^2/m^3)
Conventional low intensity	Drum separator	40	4	0.16
	Davis tube tester	320	32	10
Medium intensity	Rare earth drum or roll separator	360~720	10~100	3.6~72
High intensity — High intensity	Frantz ferrofilter	800	800	640
	NY type drum separator	1600	440	700
	Jones separator	1600	1600	2560
	DESCOS	2550	10~50	25~130
High intensity — High gradient	Solenoid separator (Kolm-Marston)	1600	16000~160000	25600~256000
	Superconducting HGMS	4000	16000~200000	64000~800000

the drum surface is obtained when the peripheral velocity of the drum is equal to the feeding velocity.

Figure 5.16.2 illustrates a drum separator of the dry type, in which raw material is fed on the top of the rotating drum with a fixed permanent magnet or electromagnet inside. Particles are classified by the balance in magnitude between magnetic and centrifugal forces. In addition, three different kinds of fixed magnets configuration in the separator are also shown. The crisscross and axial types are suitable for cleaning the collected magnetic particles, whereas the radial type is convenient for increasing the recovery of magnetic particles.[5] When rare-earth permanent magnet blocks are used in the drum, they are fixed inside the drum in such a way that different poles are placed alternately. In this case the magnetic flux density on the surface of the drum is 0.7 T at the maximum. This separator is used for the purification of zircon, quartz, feldspar, glass cullet, coal, and so forth.[6] It is effective in separating relatively large particles (from 75 μm to 25 mm).

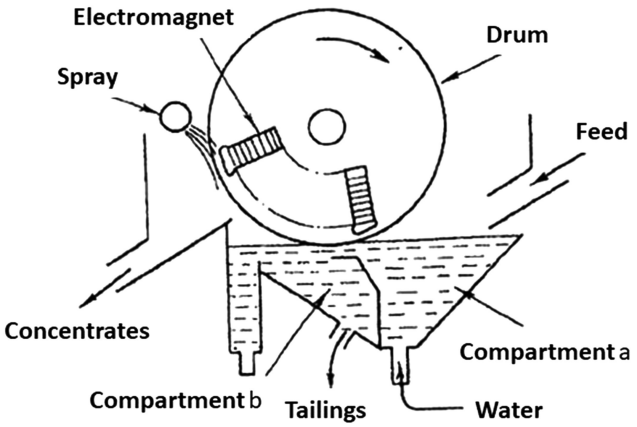


FIGURE 5.16.1 Groendal drum wet magnetic separator. (From Gaudin, A. M., *Principle of Mineral Dressing*, McGraw-Hill, New York, 1939, p. 450. With permission.)

The drum-type magnetic separator with a superconducting magnetic system[7] is shown in Figure 5.16.3. The magnetic flux density on the drum surface is approximately 3 T. The drum, which has an exterior diameter of 1.2 m and an external length of 1.5 m, is made of carbon-reinforced plastics. The drum rotates at a speed of 2–30 rpm. The evaporating helium is led back to the liquefying plant, which is connected to the drum. For example, the magnetizable gangue serpentine could be completely separated from magnesite in the 1–100 mm range size. Also the results of separation of hematite and goethite from refractory crude bauxite (1–10 mm) and the separation of clay from potassium raw salts (1–4 mm) were reported, indicating a very effective process. On the other hand, in China, a suspended superconductive magnet is employed to remove iron impurities from coals. The magnetic flux density is 1.7 T on the surface of the bottom magnet and 1 T at 300 mm from bottom.[8]

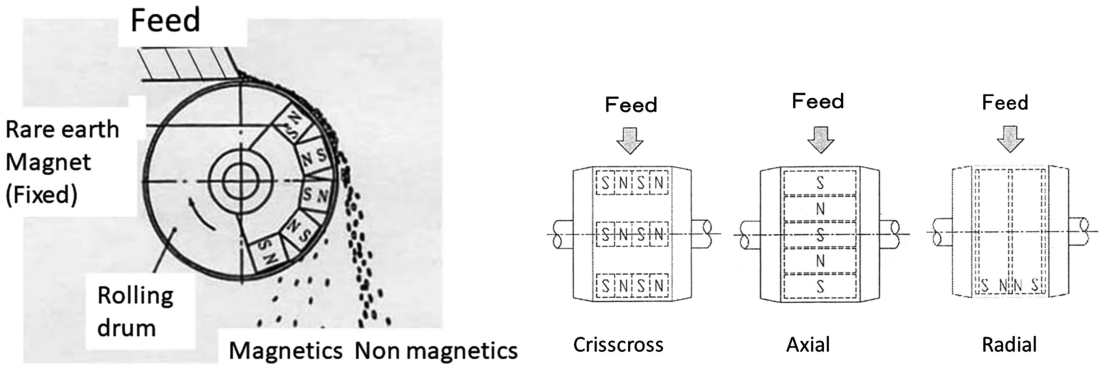


FIGURE 5.16.2 Drum magnetic separator of the dry type and three different kinds of fixed magnets configuration in the separator.[5]

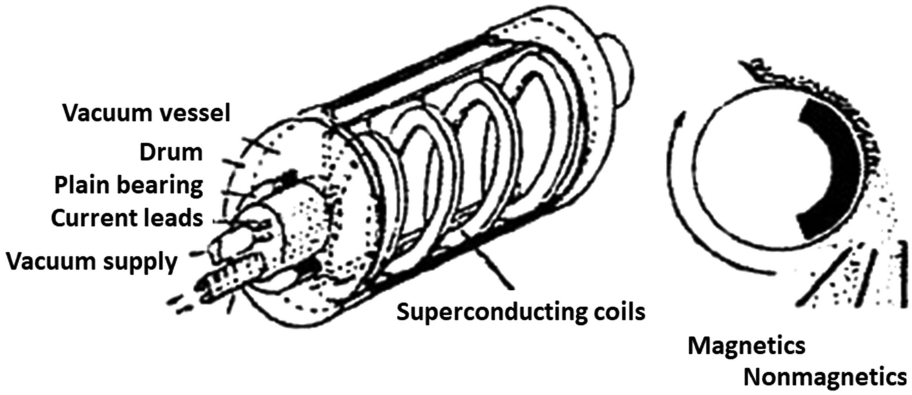


FIGURE 5.16.3 High-intensity drum-type magnetic separator with superconductive magnetic system (DESCOS).

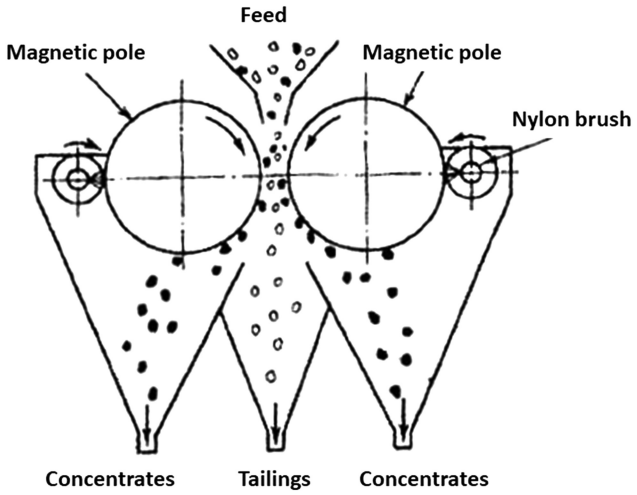


FIGURE 5.16.4 A coupled-pole dry magnetic separator. (Nippon Magnetic Dressing Co., Ltd.)

The coupled-pole dry separator, high-gauss separator, Dings-induced roll separator, and Wetherilll–Rowand separator belong to the High-Intensity Magnetic Separation (HIMS) type. A coupled-pole dry magnetic separator is shown in Figure 5.16.4. It is designed to generate a magnetic flux at the gap between two rotors, creating a high-intensity magnetic field of more than 2 T. This type of separator is used for the concentrated recovery and the purification of material.

Matrix-Loaded-Type Magnetic Separation

When matrixes such as ferromagnetic wire or balls are set between magnetic poles, a high-gradient magnetic field can be produced. The Frantz Ferrofilter separator (Figure 5.16.5), Jones high-intensity wet magnetic separator (Figure 5.16.6), Carpco high-intensity wet magnetic separator (Figure 5.16.7), and New York (NY) drum magnetic separator (Figure 5.16.8) belong to the Wet High Intensity Magnetic Separator (WHIMS) type. The Frantz Ferrofilter separator, which is the oldest model, is equipped with metal screens or grids as the matrix. Magnetic particles are separated as they are captured by the matrix, and placed in the magnetic field during the processing of pulp through the matrix. This type of separator has been employed to remove iron particles from clay. The Jones-type separator, which has a matrix of corrugated iron sheets, has been used to dress hematite ore. Balls, cubes, and twisted rods are employed as the matrix in the Carpco-type separator, while expanded metal or steel wool is used in the Eriz-type separator. The NY drum separator is a Yashima (YS) magnetic separator with many steel balls on the drum surface. Magnetic particles are captured by the high-intensity magnetic field created around the contact points of the balls.

The high-gradient magnetic separator has been known since 1968 when the device was first installed at a Georgia kaolin plant to remove weakly magnetic particles less than 2 μm in size from clay. When the matrices are arranged between the solenoid coil and the slurry, the flow is parallel to the magnetic field direction, and the captured amount is much larger

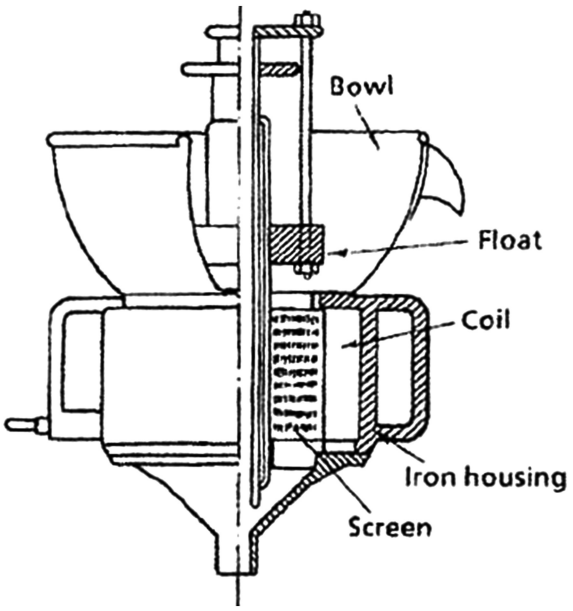


FIGURE 5.16.5 Frantz Ferrofilter (U.S. Patent 20,704,085).

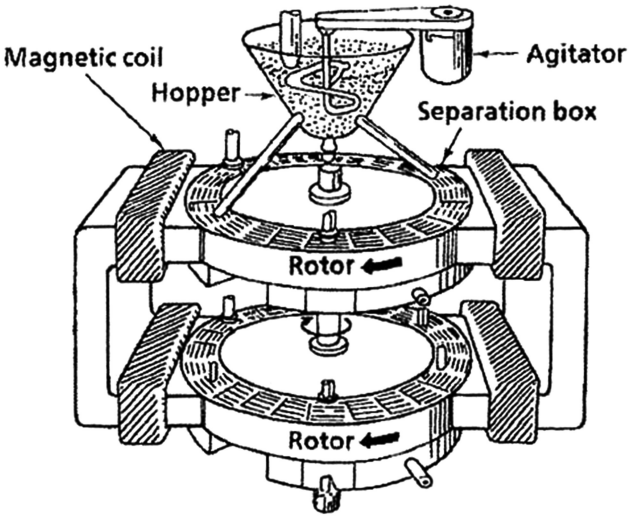


FIGURE 5.16.6 Jones high-intensity wet magnetic separator (U.K. Patents 768,451 and 767,124).

when compared to the device with the matrices between the magnetic poles.[9] The continuous high-gradient magnetic separator (SALA-HGMS)[10] is shown in Figure 5.16.9. Expanded metal or steel wool compose ferromagnetic matrices that are filled in the area under the influence of the magnetic field generated by a solenoid coil with a yoke. Moreover, it is desirable that matrices be corrosion and abrasion resistant. Matrices, filled in the magnetic field, sharply increase the magnetic force, that is, $H\nabla H$ in Equation (5.16.1). The separation box with matrices rotates continuously, with the magnetic flux density in the separator less than 2 T (Figure 5.16.9). This high-gradient magnetic separator has been applied to the separation of iron ores, purification of industrial minerals, separation of rare-earth minerals, water treatment, and so forth. Also, the continuous high-gradient magnetic separation,

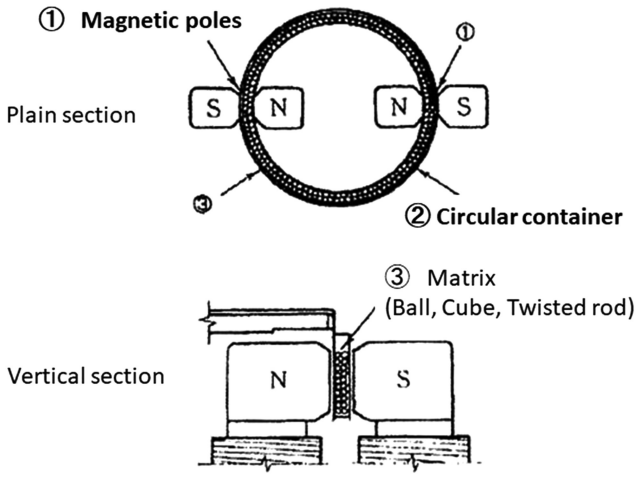


FIGURE 5.16.7 Carpco high-intensity wet magnetic separator.

which uses high-quality permanent magnets (Fe-Nd-B), has been produced to capture magnetic particles while the magnetic flux density between magnetic poles is about 0.4 T. On the other hand, a high-gradient magnetic separator using superconducting magnets has been developed. Compared to the ordinal HGMS, the magnetic force condition is very much larger. Therefore, finer and lower magnetic susceptibility paramagnetic particles can be captured. In addition, the high magnetic flux density enables an increase of the separation capacity as the flow rate also increases. One example is the superconducting high-gradient magnetic separator that is shown in Figure 5.16.10. 5 T of magnetic flux density is generated in the space of 500 mm height and 100 mm diameter, which is filled with steel-wool-type matrices. The superconducting coil is placed in liquid helium and is connected to a liquefying plant of the vaporized helium gas, while recently the cryogen free superconducting magnet is utilized. The

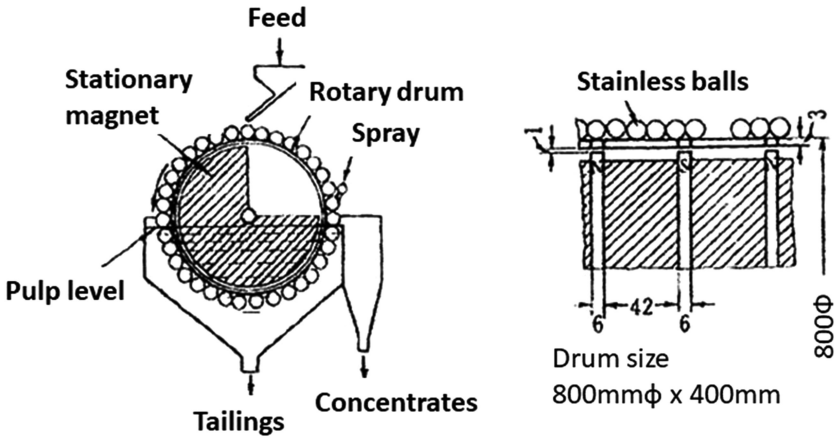


FIGURE 5.16.8 NY drum separator.

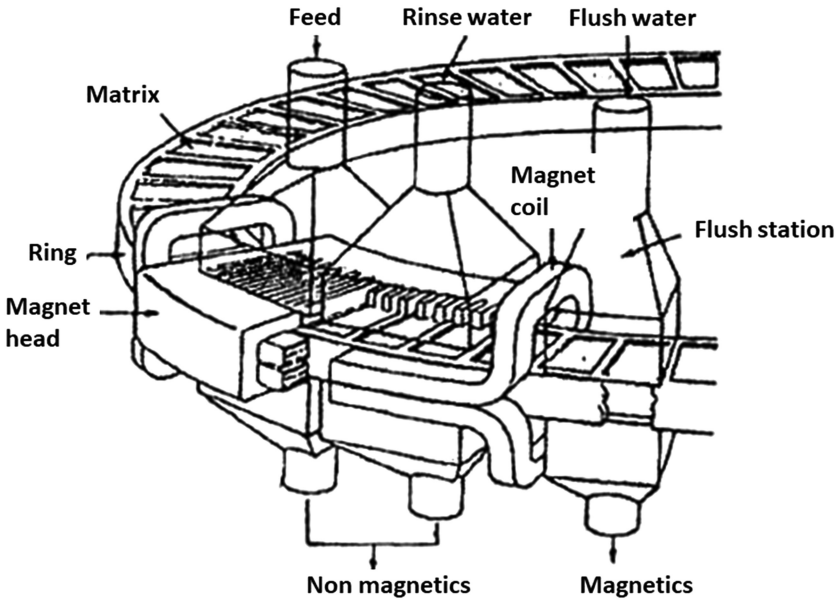


FIGURE 5.16.9 Continuous high-gradient magnetic separator (SALA-HGMS).

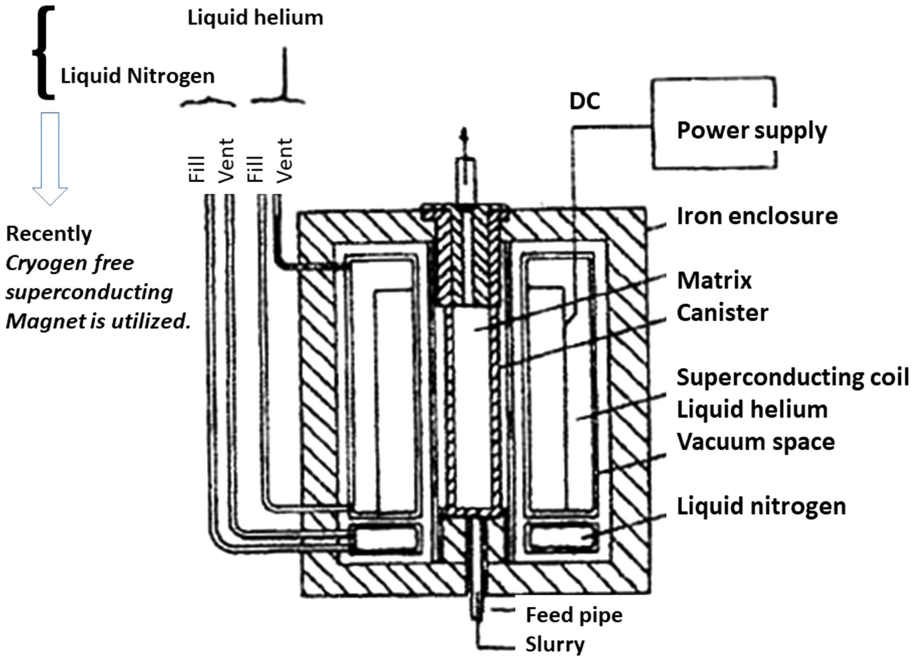


FIGURE 5.16.10 Superconducting high-gradient magnetic separator.

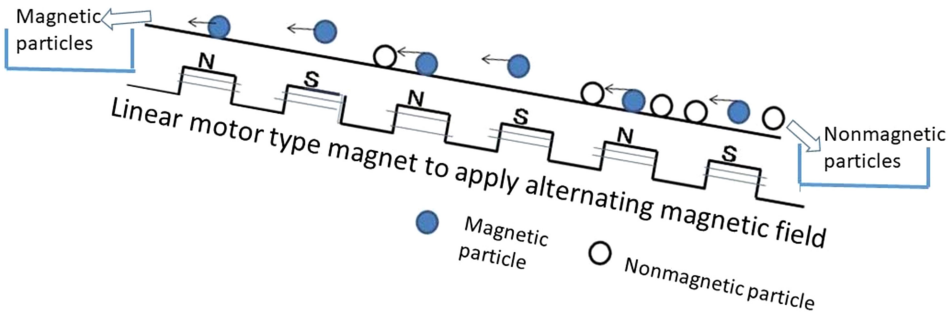


FIGURE 5.16.11 Alternating magnetic field (Linear motor, alternating magnetic field) type magnetic separator.

slurry is fed from the bottom of the canister and discharged from the top. This separator has been employed to remove ferric impurities of micron size from kaolin clay. The 2 T separator using a superconducting magnet can operate on 80–90% of the power required for conventional HGMSs.

The travelling-magnetic-field-type separator listed in Table 5.16.2 is shown in Figure 5.16.11. Linear motor producing alternating magnetic field is convenient to carry magnetic particles to the one direction. If the magnetic particles on the inclined plate move against the gravitational force, nonmagnetic particles drop on the direction of gravitational force. Therefore magnetic particle can be separated from nonmagnetic particles. Both wet and dry types of separations are possible.

5.16.3 APPLICATION OF MAGNETIC SEPARATION

High Gradient Magnetic Separation (HGMS)

The magnetic capture rate of fine paramagnetic particles in water by HGMS is related to the strength of magnetic field and hydrodynamic drag force, which depends on the flow velocity shown in Chapter 3.4. The right figure in Figure 5.16.12 shows the comparison between magnetic capture rate and capture area by magnetic field direction. The capture rate in the flow parallel to magnetic field, which generates by the solenoid coil can capture particles more than the one in the flow perpendicular to magnetic field by counter magnetic poles. However, the mechanical trap of particles in the zero magnetic field is higher in the flow parallel to magnetic field. The left figure in Figure 5.16.12, the other hand, shows the submicron size fine particles magnetic capture rate by HGMS in different magnetic susceptibility. The higher magnetic field generated by superconductive magnet is needed to get the higher magnetic capture rate for low magnetic susceptibility of TiO_2 particles.

The diamagnetic particles can also be captured with HGMS by increasing the magnetic susceptibility of dispersed liquid as described in the Chapter 3.4. The diamagnetic silica (SiO_2) can be captured on the ferromagnetic wire matrix in the perpendicular direction of magnetic field in the paramagnetic aqueous $MnCl_2$ solution as shown in the left of Figure 5.16.13. The capture rate of silica particles depending on their

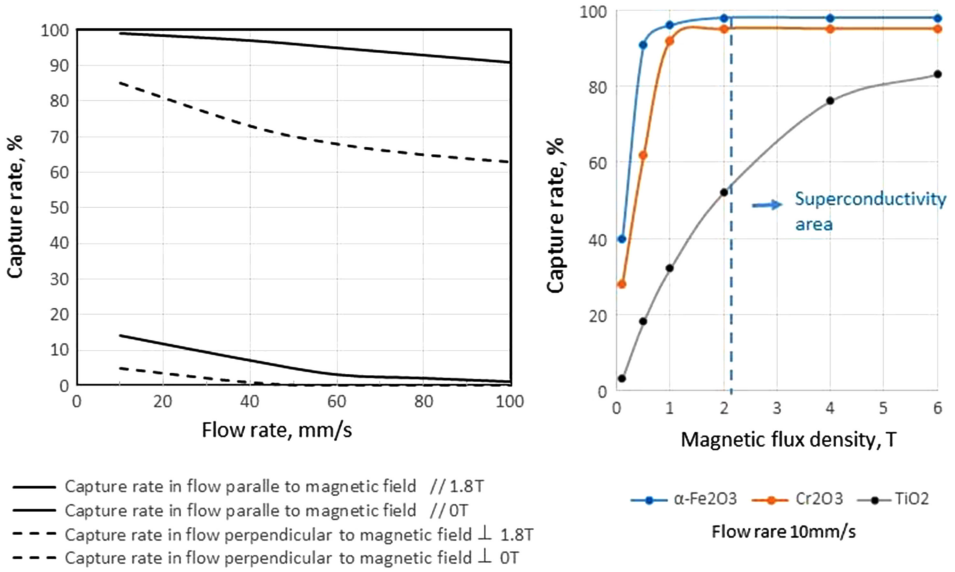


FIGURE 5.16.12 HGMS capture rate of different paramagnetic particles in water. (Left: comparison between magnetic capture rate and capture area by magnetic field direction.[9] Chalcopyrite size 9 μm (1.6×10^{-4} SI). Right: magnetic capture rate of different magnetic susceptibility particles.[11] α-Fe_2O_3 size 0.5 μm (20×10^{-4} SI), Cr_2O_3 size 0.4 μm (11×10^{-4} SI), TiO_2 size 0.3 μm (0.1×10^{-4} SI).)

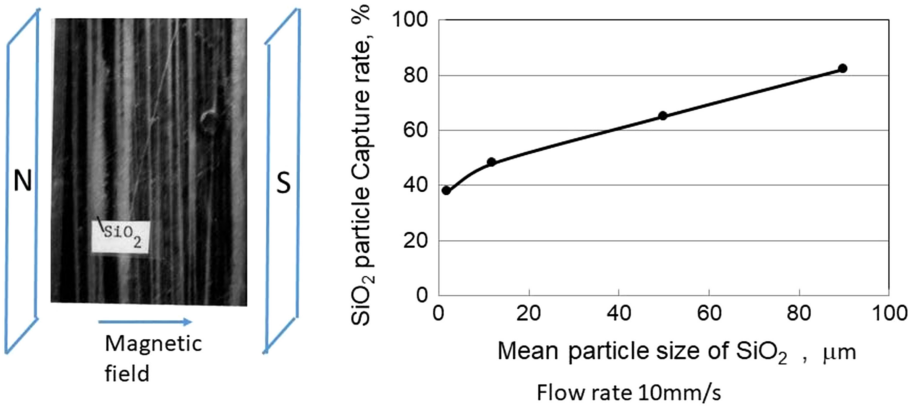


FIGURE 5.16.13 HGMS capture rate of diamagnetic particles in aqueous $MnCl_2$ solution (Density of solution 1.3 g/cm^3 after dissolving $MnCl_2$ in water). (Left: captured SiO_2 particles on the ferromagnetic iron wire. Right: SiO_2 capture rate depending on particle size. SiO_2 (-0.2×10^{-4} SI), magnetic flux density 1.8 T.)

size is shown in the right of this Figure. The larger particles can be collected in higher rate.

The mixture of paramagnetic particles can be separated with HGMS by controlling the magnetic susceptibility of dispersed liquid. If one particle in liquid is $\kappa_p - \kappa_f > 0$ and the other particle in liquid is $\kappa_p - \kappa_f < 0$ as shown in the Chapter 3.4, only the larger magnetic susceptibility particle can be captured and separated from the other. HGMS results of both paramagnetic particles in water and aqueous paramagnetic solution ($FeCl_2$) are shown in Table 5.16.4. In the water both TiO_2 and α-Fe_2O_3 particles can be captured on the matrix in HGMS. If the 1 g/L of $FeCl_2$ aqueous solution is used as a dispersant, only α-Fe_2O_3 particles can be collected magnetically, while TiO_2 particles cannot be captured.

The Carrier Magnetic Separation

Fine particles can coagulate or disperse depending on the zeta-potential of a particle by controlling the pH of water. If the precipitated fine magnetite (about 10 nm size) is added in the suspension, the hetero coagulation with magnetite and other particles occurs depending on the pH of solution. The HGMS of the carrier magnetic separation depending on the pH by using hetero coagulation in water is shown in Figure 5.16.14. Silica particles can be well captured by adding 10% of magnetite from pH 2 to 7 by hetero coagulation. The table in the right-hand side of Figure 5.16.14 lists the isoelectric point of several particles. The addition of fine magnetite as seeds causes the hetero coagulation with suspended particles in the certain pH and the suspended particles can be collected

TABLE 5.16.4 HGMS of Both Paramagnetic Particles in Water and Aqueous Paramagnetic Solution ($FeCl_2$)[11]

			Grade %		Recovery %	
	Product	Mass %	TiO_2	α-Fe_2O_3	TiO_2	α-Fe_2O_3
Water	Magnetics	92.4	43.1	56.9	**91.5**	**93.1**
	Non magnetics	7.6	48.7	51.3	8.5	6.9
$FeCl_2$ (1 g/L)	Magnetics	54.5	25.6	**74.4**	27.9	**81.1**
Solution	Non magnetics	45.5	**79.2**	20.8	**72.1**	18.9

TiO_2 (0.3 μm): α-Fe_2O_3 (0.5 μm) = 50:50 mass%, flow rate 10 mm/s, magnetic flux density 1 T.

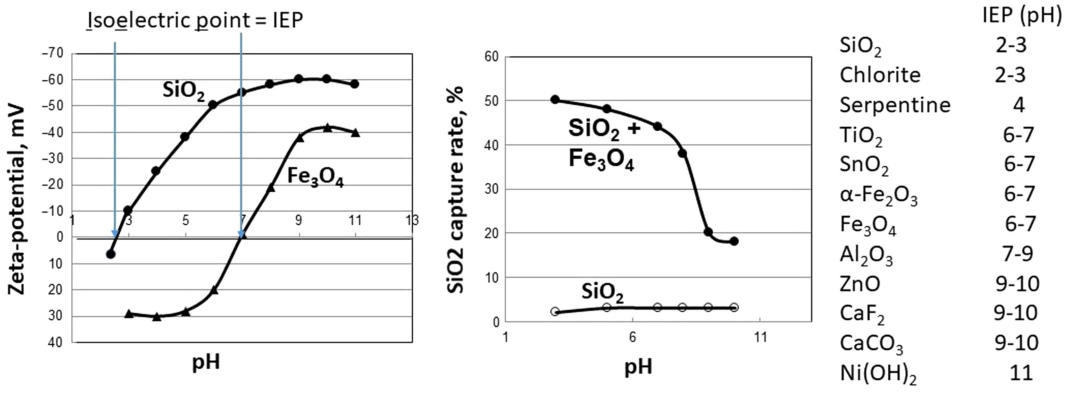


FIGURE 5.16.14 HGMS of carrier magnetic separation depending on pH by using hetero coagulation in water.[5] (Left: zeta-potential of SiO_2 and Fe_3O_4. SiO_2 size 26 μm, Fe_3O_4 10 nm. Middle: HGMS result depending on pH by adding 10% of Fe_3O_4. 10% addition of Fe_3O_4 in SiO_2. Right: isoelectric point of several particles. Magnetic flux density 0.5 T, Flow rate 10 mm/s.)

magnetically. The magnetically collected particles can release the magnetite by changing the pH of suspension. This phenomena is applied to the separation of magnetic minerals,[12] waste water treatment, and bio related area like the separation of protein and DNA,[13] etc.

Heat Treatment and Magnetic Separation

If the particles are heated at different temperatures and atmosphere, the particle structure and magnetic susceptibility change. Some examples are shown as follows. After the laterite is heated at 500°C in an air atmosphere, the magnetite contained in laterite changed to hematite. The nickel grade in magnetic fraction increased by preventing nonmagnetic particles trap by magnetite.[14] Also the low-grade hematite particles ground by a steel ball mill contain iron powder produced from a steel ball. If the ground hematite was heated at 800°C in an air atmosphere, the iron in low-grade hematite changed to hematite. The iron grade in magnetic capture increased several % by HGMS to prevent the trap of nonmagnetic silica etc.[15] The sulfide minerals phase change occurred by heating with a microwave and so on. The chalcopyrite phase boundary changes to the bornite.[16]

The steelmaking slag powder contains the ferrite whose Curie point is 120°C. If the HGMS of slags is performed in 150°C oil, the grade of phosphor contained in calcium silicate has increased to prevent the magnetic trap of ferrite at the temperature more than the Curie point.[17]

TABLE 5.16.5 Application of Magnetic Separation

Conventional utilization
Iron recovery from steel making process, pyrite removal from coal
Iron removal as a filter to remove ferromagnetic particles
↓
High gradient magnetic separator appearance
Mineral processing, waste water treatment, impurity removal from food and clay etc.
↓
Increase of bioresearch
Protein, cell, drug delivery system, biocatalyst separation etc.

Application History of Magnetic Separation

The application history of magnetic separation is listed in Table 5.16.5. The conventional utilization of magnetic separation is to recover iron in the steel plant, remove the iron as an impurity in the factory and remove pyrite from coal in a coal power plant. After HGMS was emphasized in 1970s, HGMS has been utilized in various fields such as mineral processing, waste water treatment, food and clay industries. Recently the magnetic separation research in the biological field has increased to separate protein, cell, catalyst and it is also applied in the drag delivery system.[18–20] For example the magnetic susceptibility of red blood cell is 3.88×10^{-6} SI magnetic susceptibility.[18] The concept of a protein or cell selectively separating by adding magnetite is shown in Figure 5.16.15.

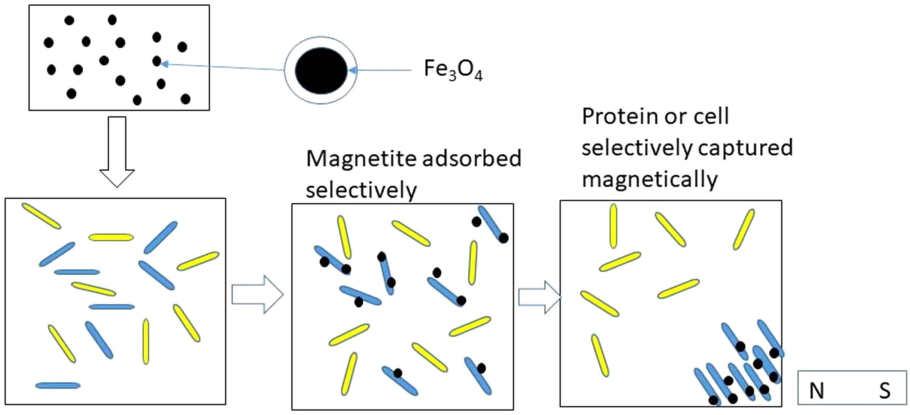


FIGURE 5.16.15 Concept of magnetic separation of protein or cell by adding magnetic particles.

5.16.4 MAGNETOHYDROSTATIC SEPARATION

A colloidal solution of surfactant-coated ferromagnetic particles of 10 nm size, which remains uniform and stable even under a magnetic or centrifugal field, is called a magnetic fluid or ferrofluid. When nonmagnetic materials are immersed in the magnetic fluid under a magnetic field gradient, a magnetic force acts on the nonmagnetic materials toward the direction of low magnetic intensity. If the magnetic field gradient is directed in the gravity direction, the net force on a nonmagnetic material F is given by

$$F = V\left[\left(\rho_p - \rho\right)g - I\nabla H\right] \tag{5.16.2}$$

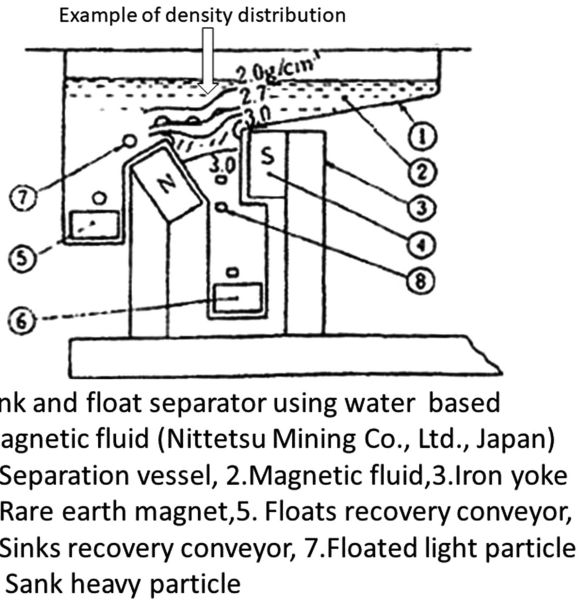
where

V	is the volume of nonmagnetic material immersed in the fluid
ρ_s and ρ	represent the densities of the nonmagnetic material and magnetic fluid, respectively
I	is the average magnetization of magnetic fluid
∇H	is the magnetic field gradient positioned nonmagnetic material
g	is the gravitational acceleration

The nonmagnetic material sinks if $F_G < 0$ and floats if $F_G > 0$ when F_G is the direction of g. This separator enables even a nonmagnetic material of density 20 g/cm^3 to float; thus materials can be separated by adjusting the magnitude of F_G. For example, $I = 0.025$ T and $\nabla H = -8 \times 10^6$ A/m^2 give $F_G/V = 2 \times 10^5$ N/m^3, which is enough to float a nonmagnetic particle of specific gravity of 20.

On the other hand, if the volume magnetic susceptibility $\kappa = \kappa_p - \kappa_f$ is negative as shown in Chapter 3.4.1 by using paramagnetic solution (κ_f) dissolving paramagnetic salts in water, the similar levitation force to the particles of magnetic susceptibility of κ_p in the paramagnetic solution is generated by the magnetic field gradient, though the levitation force is smaller.[21]

For the magnetohydrostatic separator, a full equipped pilot plant for sink–float separation for recovering nonmagnetic metal scraps has been developed. The separator that recovers



Sink and float separator using water based magnetic fluid (Nittetsu Mining Co., Ltd., Japan)
1.Separation vessel, 2.Magnetic fluid,3.Iron yoke
4.Rare earth magnet,5. Floats recovery conveyor,
6.Sinks recovery conveyor, 7.Floated light particle
8. Sank heavy particle

FIGURE 5.16.16 Sink–float separator using magnetic fluid. (Nittetsu Mining Co., Ltd., Japan.)

aluminum as a float product is shown in Figure 5.16.16. The use of rare-earth permanent magnets serves the purpose of reducing capital investment and energy consumption, while the use of water-based magnetic fluid is nontoxic, easy to wash out from the products, and easily reused.[22] Shredded automobile nonferrous metal scraps can be separated effectively; for example, 99.9% recovery of aluminum at a grade of 98% at 500 kg/h capacity can be achieved. The distance between magnetic poles can be regulated to float zinc from a mixture of zinc, copper, and lead. This separator is convenient for recovering particles of 0.5–100 mm size. For industrial operation, De Beers Consolidated Mines Ltd. uses a sink–float separator, which employs a kerosene-based magnetic fluid to separate diamond minerals.[23]

On the other hand, the Mag-sep Corporation (MC) process[24] with a magnet-hydrodyamic separator has been developed to separate finer particles ranging from about 5 μm to 1 mm in size by using a more diluted magnetic fluid of low cost.

The mineral particles are fed through the duct as a slurry in a magnetic fluid. As the slurry and duct are rotated, low- and high-density particles are discharged from the inner and outer cylinders respectively. Large oppositely directed force can be applied to particles as light as 0.3 g/cm^3, leading to rapid and precise separation. Also the rotating type density separator using magnetic fluid was developed to separate fine mineral particles (0.5–0.15 mm) to prevent the nonmagnetic particles arrangement attracting in the magnetic field direction.[25]

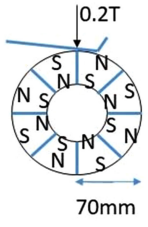
The density separation of metal scraps using magnetic fluid has been used in Germany since 2009. Also the diluted magnetic fluid was used to separate the plastic mixture of polypropylene and polystyrene of different density.

5.16.5 ELECTROMAGNETIC-INDUCTION-TYPE SEPARATION

Eddy-current separation is used for the recovery of nonferrous metals from material mixtures whose magnetic fractions are removed by a magnetic separator. A time-dependent change of a magnetic field exerts repulsive forces on electrically conductive particles, which can be used to separate metallic particles from nonmetallic particles. The conductivity/density of several metals are shown in the left of Figure 5.16.17. The larger eddy current in a metal plate generates a larger magnetic field change per time by electromagnetic induction with a higher electric conductivity and a larger area of metal. The lower density metal can move largely against the gravitational force. If the same magnetic field change per time acts on the metal plate of the same size, the metal of larger conductivity/density can be separated from the metals of smaller conductivity/density. The effect of metal size in several metals (Al, Cu, and Zn) separation by rotating the permanent magnet of a laboratory-scale eddy-current separator is shown on the right of Figure 5.16.17. The larger conductivity/density and larger size of metal plates can recover as the metal recovers by movement. To separate, the lower conductivity and smaller size of metals needs the higher rotation speed of the magnet.[26]

Many eddy-current separators were developed for the recovery of nonferrous metals from shredded car scrap, granulated power cables, municipal solid waste, and so on. The alternating magnetic fields can be generated by the utilization of a linear motor or permanent magnet configurations. Two types of eddy-current separators with permanent magnets are shown in Figure 5.16.18. By using permanent magnets, the generation costs of eddy-current separation can be reduced considerably and the construction of equipment can be less complex. Figure 5.16.18a shows a static separator where particles are moving through a field distribution generated by the configuration of permanent magnets mounted on stable ramps or walls. Figure 5.16.18b shows a dynamic separator where the magnetic field is generated by machinery with moving magnets and the repulsive forces can be enhanced by the motion of the magnetic fields. Two belt drums support the conveyer belt. One drum is driven, and inside the other the magnet system rotates at an appreciably greater speed, for example, 2500 rpm. The repulsive force acting on the particle can become larger as the value of conductivity divided by density increases. Also, the separation condition depends on particle dimensions and shape and the field distribution in the separation area. In particular, recent use of high-quality rare-earth permanent magnets in eddy-current separation has improved the separation efficiency. For example, 3–100 mm sizes of aluminum from a mixture can be separated effectively at 5 m^3/hr.[27]

Metal	Conductivity /Density $10^2 m^2 \Omega^{-1} kg^{-1}$ (293K)
Al	139
Mg	131
Cu	66
Ag	60
Zn	24
Ni	16
Cr	11
W	10
Pb	4



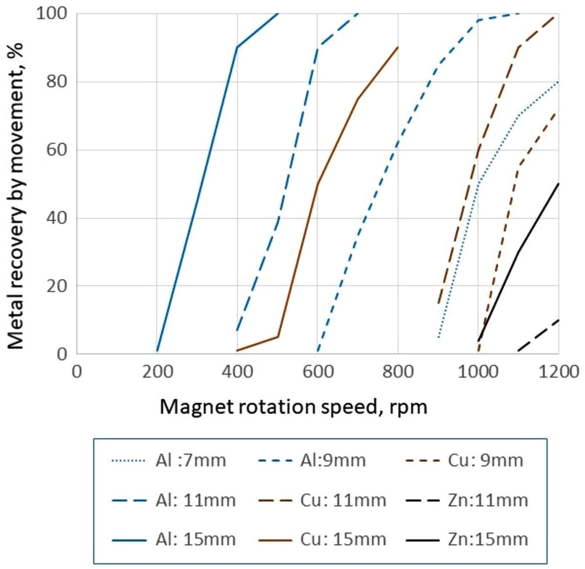


FIGURE 5.16.17 Effect of metal size in several metals' separation by rotating magnet of laboratory scale eddy-current separator.[26] (The magnetic flux density of 0.2 T on the surface of permanent magnet shown in the center rotates.) Each metal square size (7, 9, 11, 15 mm), metal thickness (0.5 mm).

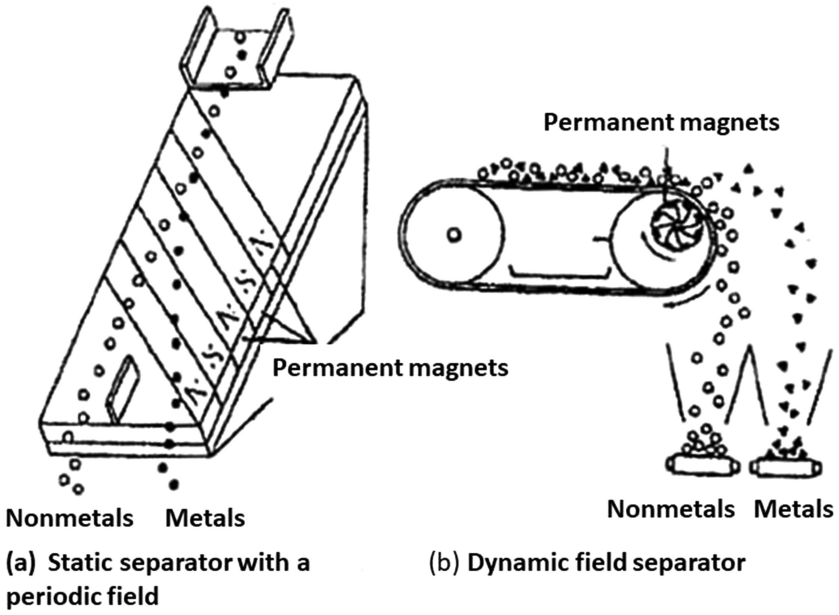


FIGURE 5.16.18 Eddy-current separator.

ACKNOWLEDGMENT

The author gratefully acknowledges Dr. K. Ushiki's work for writing the Chapters 2.3 and 5.16.

REFERENCES

1. Yashima, S., Fujita, T., *J. Soc. Powder Technol. Jpn.*, 28, 318–328, 1991.
2. Fujita, T., Mamiya, M., *J. Mining Metall. Inst. Jpn.*, 103, 35–40, 1987.
3. Fujita, T, Wei, Y., Mamiya, M., *J. Mining Metall. Inst. Jpn.*, 103, 513–518, 1987.
4. Gaudin, A. M., *Principle of Mineral Dressing*, McGraw-Hill, New York, 1939, p. 450.
5. The Resource Processing Society of Japan, *Application of Powder Purification, Hydrometallurgy*, Nakanishi Printing Company, Japan, 2014.
6. Marinescu, M., *IEEE Trans. Magn.*, MAG-25, 2732–2738, 1989.
7. Wasmuth, H. D., *Aufbereitungs-Technik*, 30, 753–760, 1989.
8. Homma, T., *Proc. Fall Annual Meeting MMIJ Ube*, C2–C18, 2003.
9. Kim, Y. S., Fujita, T., Hashimoto, S., Shimoiizaka, J., *Proc. 15th Int. Miner. Process. Congr. (IMPC)*, Cannes, 1, 381–390, 1985.
10. Oberteuffer, J. A., Wechsler, I., *Proc. Fine Part. Process.*, Las Vegas, 1178–1216, 1980.
11. Ito, R., Fujita, T., Tanno, H., Okada, A., *J. MMIJ*, 123, 342–350, 2007.
12. Lian, R., Fujita, T., Numata, Y., *Int. J. Soc. Mater. Eng. Resour.*, 11, 66–76, 1998.
13. Yavuz, C. T. et al., *Chem. Eng. Sci.*, 64, 2510–2521, 2009.
14. Kim, J., et al., *Miner. Eng.*, 23, 282–288, 2010.
15. Jurng, L., Fujita, T., Shimoiizaka, J., *J. Mining Metall. Inst. Jpn.*, 101, 525–530, 1985.
16. Iwazaki, Y., et al., Copper 2016, Kobe, Japan, MP4-1, 229–235, 2016.
17. Fujita, T., Iwasaki, I., *J. Mining Metall. Inst. Jpn.*, 105, 673–678, 1989.
18. Borlido, L., Azevedo, A. M., Roque, A. C. A., Aires-Barros, M. R., *Biotechnol. Adv.*, 31, 1374–1385, 2013.
19. He, J., et al., *J. Pharm. Biomed. Anal.*, 101, 84–101, 2014.
20. Antfolk, M., Laurell, T., *Anal. Chim. Acta*, 965, 9–35, 2017.
21. Zimmels, Y., *IEEE Trans. Magn.*, MAG-13, 959–962, 1977
22. Fujita, T., *Magnetic Fluids and Applications Handbook*, Berkovski, B., Ed., Begell House, New York, 1996, pp. 755–789.
23. Sbovoda, J., *Proc. MINPREX*, Melborne, 297–301, 2000.
24. Walker, M. S., *Proc. 15th Int. Miner. Process. Congr. (IMPC)*, Cannes, 1, 307–316, 1985.
25. Shimoiizaka, T., Nakatsuka, K., Fujita, T., Matakawa, K., *J. Mining Metall. Inst. Jpn.*, 95, 199–203, 1979.
26. Fujita, T., Sotojima, Y., Kuzuno, K., *J. Mining Mater. Process. Inst. Jpn.*, 111, 177–180, 1995.
27. Warlitz, G., *Aluminium*, 65, 1125–1131, 1981.



Taylor & Francis
Taylor & Francis Group
http://taylorandfrancis.com

5.17 Dry Dense Medium Separation

Jun Oshitani

Dense medium separation is a gravity separation based on the floating and sinking of objects in a separation medium. Generally, a wet dense medium separation is utilized in many industries, in which a heavy liquid is used as the separation medium. Since a large amount of water is needed in the conventional wet separation, the wet separation cannot be used in dry or cold areas. Hence the dry dense medium separation is in great demand as the substitute of the wet separation. The specialty of the dry separation is to use a fluidized powder as the separation medium. Here the dry separation by using a gas–solid fluidized bed is described.

5.17.1 BASIS OF SEPARATION

When air is injected into a powder bed from the bottom and the air velocity u_0 is larger than the minimum fluidization velocity u_{mf}, the powder can be fluidized; the gas–solid fluidized bed is formed. It is well known that the gas–solid fluidized bed has liquid-like properties in terms of density and viscosity.[1] When objects are put into the fluidized bed, they float or sink just like in water as shown in Figure 5.17.1. This float-sink feature is utilized in the dry dense medium separation.

Estimation of Fluidized Bed Density[2–4]

The density of a fluidized bed is an important parameter for the dry dense medium separation. The average density can be estimated by dividing the weight of bed powder by the bed volume which is derived from the cross-sectional area and the height of fluidized bed. The density of fluidized bed can be estimated also by putting a sphere of various densities in the fluidized bed and measuring the sphere height staying within the bed. The staying height of the sphere normalized by the bed height is plotted as a function of the sphere density, as shown in Figure 5.17.2. Spheres of low density float, while those of high density sink. Between the float and sink ranges, there exists the range where the staying height of spheres decreases linearly with the sphere density. This range is named "non-float-sink" range. The mean density of a sphere in the non-float-sink range is regarded as the fluidized bed density ρ_{fb}. The width $\Delta\rho_{fb}$ of the non-float-sink range is an important parameter to determine the separation efficiency; the small width implies that the objects are sharply separated.

Control of Fluidized Bed Density[2–4]

There is a great demand to separate many kinds of mixtures of different densities. Hence, it is necessary to control the fluidized bed density in a wide range. One of the methods to control the separation performance is to vary the air velocity. Figure 5.17.3(a) shows the separation performance of spheres at various air velocity ratios u_0/u_{mf}, and Figure 5.17.3(b) shows the values ρ_{fb} and $\Delta\rho_{fb}$ as a function of u_0/u_{mf}. It is clear that the non-float-sink range shifts to the left and ρ_{fb} decreases with increasing u_0/u_{mf}. When the air velocity increases, the fluidized bed expands to increase the bed volume, although the powder weight is constant. As a result, the fluidized bed density decreases when increasing the air velocity, and $\Delta\rho_{fb}$ increases when increasing u_0/u_{mf} from 2.0. This implies that the fluidization of powders becomes intensive and the

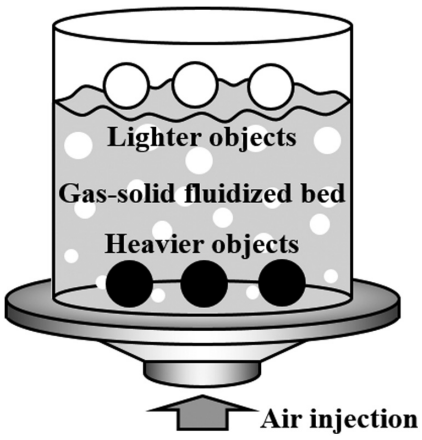


FIGURE 5.17.1 Schematic illustration of the float-sink behavior of objects in the gas–solid fluidized bed.

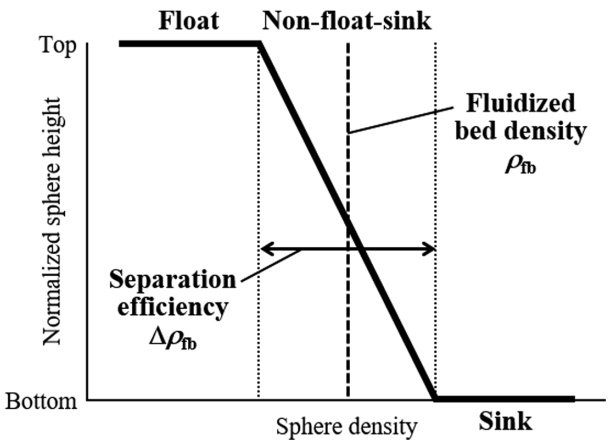


FIGURE 5.17.2 Schematic drawing of floating and sinking characteristics of spheres in fluidized bed.

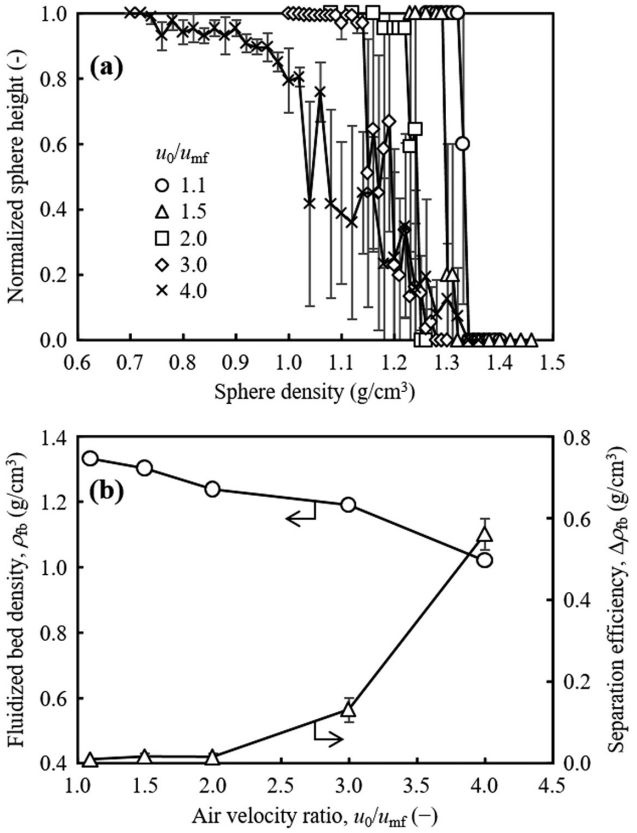


FIGURE 5.17.3 (a) Float-sink characteristics of spheres at various air velocity ratios, (b) the fluidized bed density and separation efficiency as a function of the air velocity ratio (fluidized powder: glass beads of 150–180 μm in diameter).

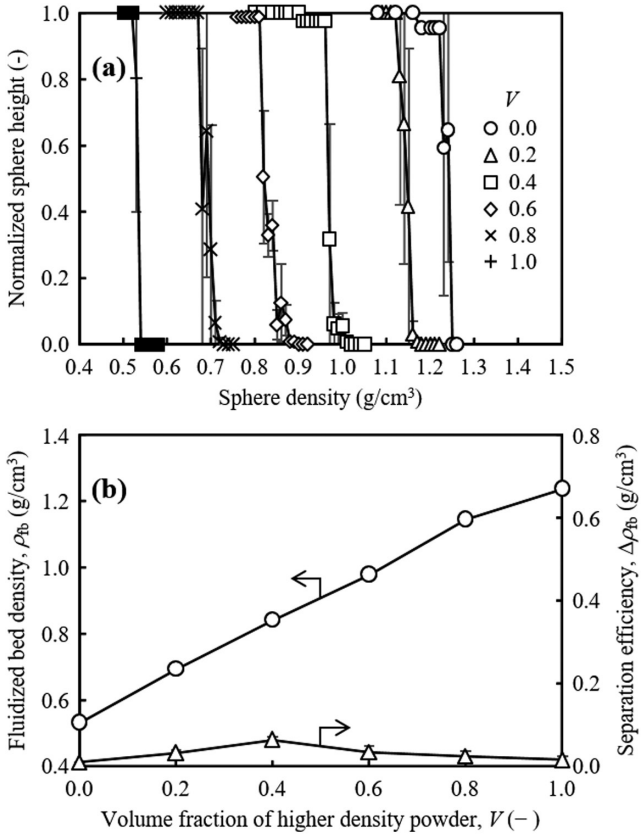


FIGURE 5.17.4 (a) Float-sink characteristics of spheres at various volume fractions of high density powder, and (b) the fluidized bed density and separation efficiency as a function of the volume fraction of high density powder (fluidized powder: mixture of glass beads of 150–180 μm in diameter and polystyrene beads of 355–425 μm in diameter, air velocity ratio $u_0/u_{mf}=2.0$).

float-sink behavior of spheres becomes unstable. Hence, the proper adjustment of air velocity is necessary for effective separation.

A mixture of binary powders of different densities is also used as the fluidizing powder to vary the volume fraction. Figure 5.17.4 (a) shows the float-sink characteristics of spheres at various volume fractions of higher density powder *V*, and Figure 5.17.4 (b) shows the values of ρ_{fb} and $\Delta\rho_{fb}$ as a function of *V*. The non-float-sink range shifts to the right and ρ_{fb} increases with the increasing value of *V*, while the float-sink behavior is stable regardless of the volume fraction and $\Delta\rho_{fb}$ is kept to be almost constant as a small value. It should be noted that, in this case, one has to take care of the density segregation; powder of low density goes upward and powder of high density goes downward during the fluidization. If the density segregation occurs, the separation efficiency may not sufficient enough. It is recommended to use a mixture of powders of low density and large size and those of high density and small size to avoid the density segregation by the size segregation.

Effect of Fluidization Intensity on Separation Efficiency[5]

The float-sink stability of objects can be affected not only by the air velocity as described above, but also by the bed height and the size of fluidized powder. Vertical shaking of the fluidized bed surface, which is a measure of the fluidization intensity, becomes intense by increasing the bed height and the size of the fluidized powder, which results in the unstable float-sink characteristics. The float-sink stability is correlated with the amplitude of the vertical shaking.

Size Effect of Objects on Separation Efficiency[6,7]

Spheres of diameter ≥ 20 mm are able to float or sink, by using the usual fluidized bed. As for the spheres of diameter < 20 mm, the float-sink behavior is unstable, since such small spheres are easily susceptible to the fluidization intensity. However, when the bed height is low, the size of air bubbles is small and the fluidization is gentle. As a result, the float-sink movement of small spheres becomes stable.

Separation of Wet Object Using Hydrophobic Powder[8]

When the wet objects are put into the fluidized bed, the water on the objects is transferred to the fluidizing powder. The powder adhesion due to the wetted surfaces hinders the smooth fluidization, and then wet objects cannot be separated

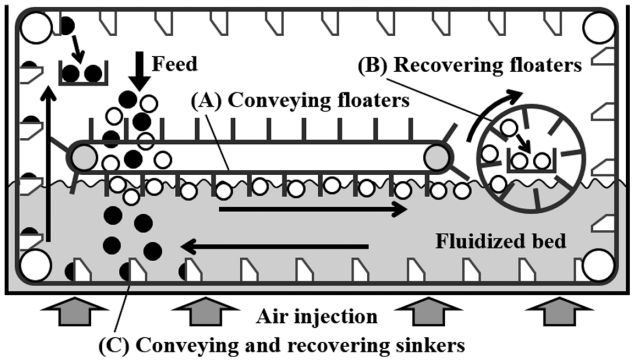


FIGURE 5.17.5 Schematic drawing of feeding and recovering by a continuous separator.

efficiently. However, if the hydrophobic powder is used as the separation medium, even wet objects can be separated because the powder does not get wet. The hydrophobic powder can be prepared by surface modification using silicon or silane coupling agent.

5.17.2 APPLICATION OF SEPARATION

Separation of Ore Particles, Agricultural Products, and Waste Materials

The dry dense medium separation has been applied to various mixtures. Fraser et al. used the dry separation for coal cleaning for the first time in the 1920s.[9] Joy et al. applied the dry separation for ore processing to separate fluorspar, pallasite, and galena in the 1970s.[10] Zaltzman et al. separated agricultural products such as potatoes from mud or pebbles in the 1980's.[11–13] Coal cleaning based on the dry separation has been actively investigated since 2000.[14–21] Iron ore[22,23] and copper ore[24] were also separated. Waste treatment is another application. The dry separation was applied to separate plastics and copper wires in automobile shredder residue,[25] plastics containing chlorine from shredder residue of a home electrical appliance,[26] shredded municipal bulky waste,[27] and mortar and gravel in waste concrete.[28]

Continuous Separator

Floaters and sinkers in the gas–solid fluidized bed have to be continuously recovered for practical use of the dry dense medium separation. Various kinds of separators have been developed.[9–12,14,15,18,19,21,23,26] Figure 5.17.5 shows an example of the continuous separator.[21,23] The mixture is fed at the left side. The floaters are conveyed toward the right side of the fluidized bed by moving fins (device A), and recovered by a rotating basket (device B). The sinkers are conveyed toward the left side at the bottom and recovered by moving small cages (device C).

REFERENCES

1. Kunii, D., Levenspiel, O., *Fluidization Engineering*, 2nd ed., Butterworth-Heinmann, Boston, 1991.
2. Oshitani, J., Kondo, M., Nishi, H., Tanaka, Z., *Adv. Powder Technol.*, 14, 247–258, 2003.
3. Yoshida, M., et al., *KONA*, 26, 227–237, 2008.
4. Oshitani, J., et al., *Miner. Eng.*, 24, 70–76, 2011.
5. Oshitani, J., Ono, K., Ijiri, M., Tanaka, Z., *Adv. Powder Technol.*, 15, 201–213, 2004.
6. Oshitani, J., et al., *Adv. Powder Technol.*, 23, 27–30, 2012.
7. Oshitani, J., et al., *Adv. Powder Technol.*, 23, 120–123, 2012.
8. Yoshida, M., Oshitani, J., Tani, K., Gotoh, K., *Adv. Powder Technol.*, 22, 108–114, 2011.
9. Fraser, T., Yancey, H.F., *Coal Age*, 29, 325–327, 1926.
10. Joy, A. S., Douglas, E., Walsh, T., Whitehead, A., *Filtr. Sep.*, 9, 532–538&544, 1972.
11. Zaltzman, A., Feller, R., Mizrach, A., Schmilovitch, Z., *Trans. ASAE*, 26, 987–990&995, 1983.
12. Zaltzman, A., Schmilovitch, Z., *Trans. ASAE*, 29, 1462–1469, 1986.
13. Zaltzman, A., Verna, B.P., Schmilovitch, Z., *Trans. ASAE*, 30, 823–831, 1987.
14. Tanaka, Z., et al., *Kagaku Kogaku Ronbunshu.*, 26, 327–331, 2000.
15. Luo, Z., Chen, Q., *Int. J. Miner. Process*, 63, 167–175, 2001.
16. Luo, Z., Chen, Q., Yaomin, Z., *Coal Preparation*, 22, 57–64, 2002.
17. Chen, Q.R., Yang, Y.F., *Coal Preparation*, 23, 3–12, 2003.
18. Oshitani, J., Tani, K., Takase, K., Tanaka, Z., *J. Soc. Powder Technol. Jpn.*, 41, 334–341, 2004.
19. Dwari, R.K., Hanumantha Rao, K., *Miner. Process. Extr. Metall. Rev.*, 28, 177–234, 2007.
20. Firdaus, M., O'Shea, J.-P., Oshitani, J., Franks, G.V., *Int. J. Coal Prep. Util.*, 32, 276–289, 2012.
21. Okamoto, R., et al., *J. Soc. Powder Technol. Jpn.*, 50, 640–645, 2013.
22. Oshitani, J., Franks, G.V., Griffin, M., *Adv. Powder Technol.*, 21, 573–577, 2010.
23. Oshitani, J., et al., *Adv. Powder Technol.*, 24, 468–472, 2013.
24. Franks, G.V., Firdaus, M., Oshitani, J., *Int. J. Miner. Process.*, 121, 12–20, 2013.
25. Oshitani, J., Kajiwara, T., Kiyoshima, K., Tanaka, Z., *KONA Powder Part. J.*, 21, 185–194, 2003.
26. Yoshida, M., et al., *Adv. Powder Technol.*, 21, 69–74, 2010.
27. Sekito, T., Matsuto, T., Tanaka, N., *Waste Manage.*, 26, 1422–1429, 2006.
28. Yoshida, M., et al., *J. Soc. Powder Technol. Jpn.*, 43, 260–269, 2006.



Taylor & Francis
Taylor & Francis Group
http://taylorandfrancis.com

5.18 Gravity Thickening

Eiji Iritani

Sedimentation is a separation of solid particles from a suspension under action of a body force, which may be either gravity or centrifugal, on the buoyant mass of the particle. The sedimentation operation is often referred to as either thickening or clarification. If the main purpose of the operation is to concentrate solids into a denser slurry, the operation is generally called thickening, whereas, if the major concern is to produce a relatively clear liquid phase, the operation is usually called clarification. Since both thickening and clarification occur in any sedimentation basin, both functions have to be considered in the thickener design.

5.18.1 PRETREATMENT

The sedimentation rate of fine particles can be artificially increased by the addition of coagulants or flocculants, which causes precipitation of colloidal particles and thus the formation of flocs. For these to be effective, it is often necessary to adjust the pH of the slurry. Coagulants are usually inorganics that neutralize the surface charges on the particles, thereby allowing them to collide and adhere. Common examples include aluminum sulfate, ferric chloride, and ferric sulfate. Flocculants are organic polyelectrolytes or long-chain polymers which cause a physical linkage by bridging and enmeshment, and sometimes by particle-charge interaction. Examples include polyacrylamide and polyacrylate. Performance of coagulants or flocculants proposed for a given case can be determined beforehand in jar tests. The chemicals are combined with the slurry by rapid mixing, then allowed to settle at a lower shear rate consistent with the plant unit. A very useful test for filtration applications is the capillary suction time (CST) test which measures the permeability of a flocculated suspension by using the uniform capillary suction of a filter paper.[1]

5.18.2 IDEAL SETTLING BASIN

A slurry of discrete particles settling in an ideal basin will be considered here. The paths followed by the particles are straight lines determined by the vector sums of the two velocity components, as illustrated in Figure 5.18.1. The horizontal velocity component of the particle, due to the fluid flow across the basin, is equal to v. A particle with settling velocity u_0, starting at the top of the inlet, will reach the bottom at the outlet. Consequently, particles with a settling velocity less than u_0 will be only partially removed. A particle with settling velocity u_s will reach the bottom at the outlet if it enters the settling basin at height h from the bottom. Only particles initially at heights less than h will be removed. Therefore, the fraction η_p of particles with settling velocity u_s that are removed from an ideal basin is given by

$$\eta_p = \frac{h}{H} = \frac{u_s}{u_0} = \frac{u_s}{Q/A} \tag{5.18.1}$$

where

H is the liquid depth
Q is the volumetric flow rate of slurry
A is the surface area of the basin

The analysis of sedimentation in an ideal basin clearly demonstrates that the slurry depth should be as shallow as practical. Gravity settlers that use inclined surfaces in the form of flat plates (lamellae) or tubes have the effect of increasing the settling rate of the particulates.[2] When flat plates or tubes are inclined at a steep angle, the settled sludge slides downward. This induces an upward flow of the clarified effluent, and the solids can be effectively collected at the bottom.

5.18.3 SETTLING CURVE

A typical batch settling curve is illustrated in Figure 5.18.2. The height H of the interface between the settling particles and the clear supernatant liquid is plotted as a function of time t. In zone settling, the slurry settles as a mass with a clear interface between the slurry (zone B) and supernatant (zone A) because of the relatively high solids concentration. In this stage, the slurry moves downward at a uniform velocity, which is dependent on the initial solids concentration. As the settling solids approach the bottom of the basin, they develop a layer with a higher concentration of suspended solids. After the subsiding interface reaches the rising layer of higher concentration, the sedimentation rate of the interface decreases gradually. During this transition zone, the subsidence rate of

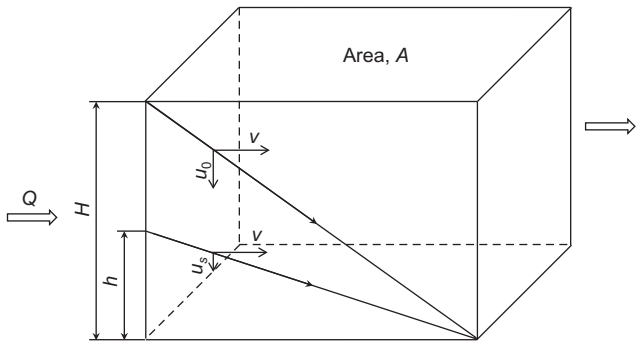


FIGURE 5.18.1 Settling behavior of discrete particles in ideal settling basin.

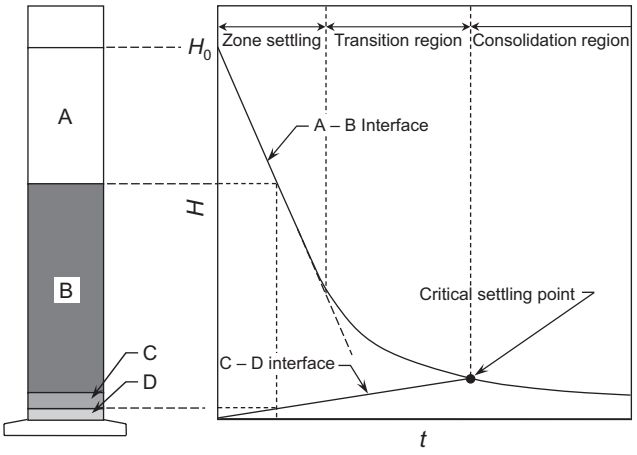


FIGURE 5.18.2 Batch settling curve for settling slurry.

the interface is closely related to the instantaneous concentration at the interface. As the concentration continues to increase at the bottom, a zone D of compacting sediment forms where solids are supported partially by the solids beneath them. The interface continues to subside controlled by the mechanism of consolidation-sedimentation until an equilibrium condition is attained.[3]

The sedimentation rate $(-dH/dt)$ in the consolidation region is given approximately by

$$-\frac{dH}{dt} = k\left(H - H_\infty\right) \tag{5.18.2}$$

where

H_∞ is the final height of the sediment
k is the constant

Integrating Equation (5.18.2), the time taken for the slurry line to fall from a height H_c, corresponding to the critical settling point where the compression zone begins, to a height H can be obtained by

$$\ln\left(H - H_\infty\right) = -kt + \ln\left(H_c - H_\infty\right) \tag{5.18.3}$$

Consequently, when $\ln(H - H)$ is plotted against t, a straight line with slope $-k$ is obtained.

5.18.4 KYNCH THEORY

Kynch[4] analyzed the behavior of concentrated suspensions during batch sedimentation using a continuity approach. The theory is mainly based on the assumption that the settling velocity of solids is a function alone of the local solids concentration. When the settling velocity is u at some horizontal level where the volumetric concentration of particles is C, the volumetric sedimentation rate G per unit area (i.e. the solids flux) is given by

$$G = Cu \tag{5.18.4}$$

Consider a material balance of an elemental layer between a height H above the bottom and a height $H+dH$. Since in a time interval dt the accumulation of particles in the layer is given by the difference in flux, between $G(H+dH)$ into the upper layer and $G(H)$ out through the lower layer, one obtains

$$\frac{\partial C}{\partial t} = \frac{\partial G}{\partial H} = \frac{dG}{dC}\cdot\frac{dC}{dH} \tag{5.18.5}$$

Because the concentration of particles is generally a function of both position and time, one obtains

$$dC = \frac{\partial C}{\partial H}dH + \frac{\partial C}{\partial t}dt \tag{5.18.6}$$

Constant-concentration conditions $(dC=0)$ are therefore defined by

$$\frac{\partial C}{\partial H} = -\frac{\partial C}{\partial t}\left(\frac{dH}{dt}\right)^{-1} \tag{5.18.7}$$

Substituting Equation (5.18.7) into Equation (5.18.5), one obtains

$$-\frac{dG}{dC} = \frac{dH}{dt} = V \tag{5.18.8}$$

Because Equation (5.18.8) refers to a constant concentration, dG/dC must also be constant. Consequently, V (= dH/dt) is constant too for any given concentration and is the propagation velocity of a zone of constant concentration C. While the interface between the clear liquid and the settling solids is moving downwards during sedimentation, layers of constant concentration appear to move upwards at the base of the vessel.

This result is widely employed to obtain the relation between the solids flux and concentration needed for thickener design from a single batch sedimentation test. It is possible to obtain the plot of G vs. C over the concentration range C_0 to C_{max} (concentration at the compression point) from only a single experiment of a slurry with an initial solids concentration C_0. The sedimentation curve has a decreasing negative slope reflecting the increasing concentration of solids at the interface after point B, as illustrated in Figure 5.18.3. Line OP represents the locus of points of some concentration C $(C_0 < C < C_{max})$. It corresponds to the propagation of a wave at the upward velocity V from the bottom of the sediment. When the wave propagates the interface of point P, all the particles in the slurry must have passed through the plane of the wave. Therefore, one obtains

$$C\left(u+V\right)t_1 = C_0H_0 \tag{5.18.9}$$

By drawing a tangent to the settling curve ABPD at point P, the intercept T of the tangent on the H axis is located. Then, ut_1 is equal to QT because $-u$ is the slope of a tangent to the settling curve at point P, and Vt_1 is equal to OQ because V is

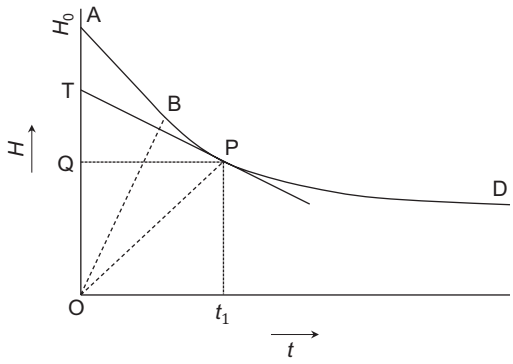


FIGURE 5.18.3 Construction of Kinch theory.

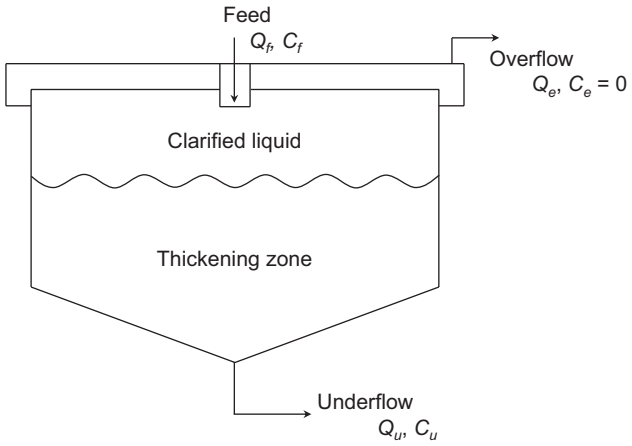


FIGURE 5.18.4 Schematic view of continuous thickener.

the slope of line OP. Consequently, the concentration C corresponding to the line OP is given by

$$C = C_0 \frac{\text{OA}}{\text{OT}} \tag{5.18.10}$$

and the corresponding solids flux is obtained from

$$G = Cu = C_0 \frac{\text{OA}}{\text{OT}} u \tag{5.18.11}$$

By drawing the tangent at a series of points on the curve BPD and measuring the corresponding slope $-u$ and intercept OT, it is possible to calculate the solid flux G for any concentration C ($C_0 < C < C_{max}$).

5.18.5 DESIGN OF CONTINUOUS THICKENER

A thickener is a sedimentation basin that is employed to concentrate a slurry prior to filtration or centrifugation. Normally a larger fraction of the total liquid is removed in thickening than in subsequent operations. In most cases, the particles in a thickener settle collectively in the zone settling regime. As illustrated in Figure 5.18.4, the bottom part of a thickener is filled with a layer of settled solids, which increases in concentration with greater depths. A clarified liquid separates from the thickened liquid at the interface and is taken off at the top. A thickener therefore fulfills the dual function of providing a concentrated underflow and a clear liquid overflow. In designing a thickener, the areas needed for clarification and thickening are therefore examined separately. The larger of the two areas determines the size required to achieve the specified performance.

Clarification Area

The cross-sectional area needed for clarification can be calculated from the initial sedimentation velocity obtained from a batch sedimentation test. The area must be large enough so that the rising velocity of overflow liquid is less than the batch sedimentation velocity. The minimum area required in a thickener for clarification is, therefore, determined by

$$A_c = \frac{Q_e}{u_s} \tag{5.18.12}$$

where

A_c is the surface area needed for clarification
Q_e is the overflow rate of the clear liquid
u_s is the initial sedimentation rate of slurry at the feed concentration

Coe and Clevenger Method

In the thickening region, solids move toward the underflow both by gravity sedimentation and by bulk movement resulting from underflow withdrawal. The total flux G of solids at concentration C_i can, therefore, be given by

$$G = C_i u_i + C_i u_b \tag{5.18.13}$$

where

u_i is the sedimentation velocity at concentration C_i
u_b is the downward velocity of slurry arising from the removal of the underflow

The form of solids flux terms is shown in Figure 5.18.5. The flux of solids by bulk transport is a linear function of solids concentration with slope u_b. The gravity flux of solids goes through a maximum as the concentration increases, as obtained from batch sedimentation tests for various concentrations. For most zone settling slurries, the combination of gravity and bulk flow flux terms produces a total flux curve with a maximum and minimum. The minimum in the total flux curve exists at some limiting concentration between the feed and underflow concentrations and represents the limiting solids-handling capacity of the slurry. The total solids contained in the feed must be less than the solids-transmitting capability of this limiting concentration layer. Since the gravity flux becomes zero at the bottom of the thickener, all solids are taken off by bulk flow only. Consequently, if a horizontal line is drawn tangent to the minimum in the total flux curve, it intersects the bulk flux line at the underflow concentration C_u.

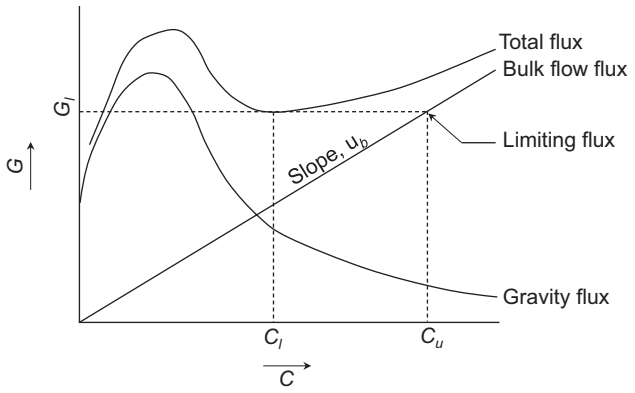


FIGURE 5.18.5 Total solids flux curve in continuous thickener.

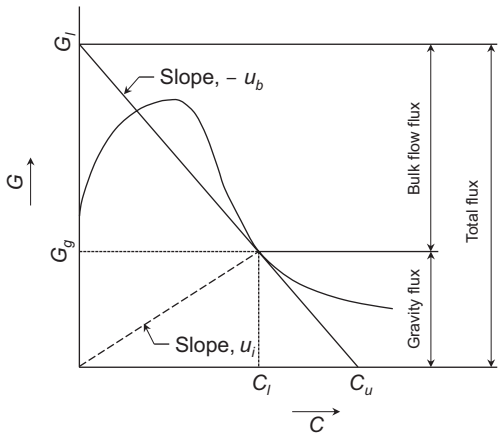


FIGURE 5.18.6 Solids flux in continuous thickener based on batch flux curve.

Assuming that all solids in the feed leave in the underflow, the cross-sectional area required for thickening can be obtained from[5]

$$A = \frac{C_f Q_f}{G_l} = \frac{C_u Q_u}{G_l} \tag{5.18.14}$$

where

C_f is the solids concentration of the influent
Q_f is the flow rate of the influent
G_l is the limiting solids flux at concentration C_l
Q_u is the flow rate of the underflow

An alternative approach employs the batch flux curve directly.[6] The settling velocity u_i by gravity is the slope of line from the origin to any point on the batch flux curve, as illustrated in Figure 5.18.6 (often known as a Kynch flux plot). If this line intersects a tangent to the batch flux curve at the point of tangency, the intersection corresponds to the limiting solids concentration C_l, and gravity flux, G_g. By using Equation (5.18.14), the bulk velocity is given by

$$u_b = \frac{Q_u}{A} = \frac{G_l}{C_u} \tag{5.18.15}$$

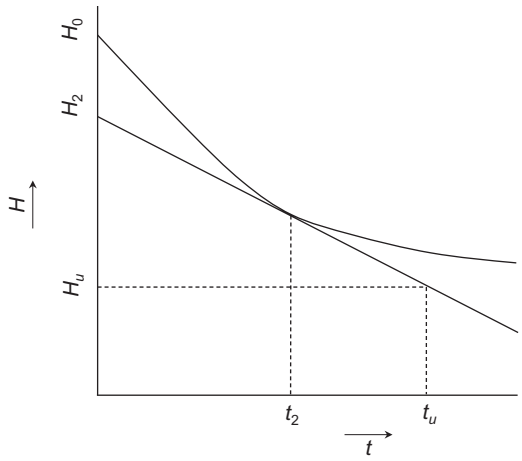


FIGURE 5.18.7 Talmage and Fitch method.

Thus, the bulk downward velocity is the slope of a tangent operating line connecting solids flux G_l on the flux axis to the corresponding underflow solids concentration C_u on the concentration axis. The distance from G_g to G_l is the solids flux by bulk downward transport when solids are removed at concentration C_u. Consequently, the limiting solids-handling capacity G_l in Equation (5.18.15) can be determined for a given underflow concentration C_u.

Talmage and Fitch Method

The procedure of Talmage and Fitch[7] requires data from only a single batch settling curve by using the method of Kynch. On the basis of the material balance, the values of H_2 and H_u shown in Figure 5.18.7 are given by

$$C_0 H_0 = C_2 H_2 = C_u H_u \tag{5.18.16}$$

where C_2 is the concentration at the compression point t_2. An underflow line is drawn parallel to the time axis at $H = H_u$ on a plot of height H vs. sedimentation time t. By drawing a tangent to the settling curve through point H_2 on the H axis, the value of t_u can be determined from the intersection of the tangent and the underflow line. Consequently, the required thickener area A can be found from

$$A = C_f Q_f \left(\frac{t_u}{C_0 H_0} \right) \tag{5.18.17}$$

REFERENCES

1. Gale, R.S., *Filtr. Sep.*, 8, 531–538, 1971.
2. Nakamura, H., Kuroda, K., *Keijo J. Med.*, 8, 256–296, 1937.
3. Iritani, E., Hashimoto, T., Katagiri, N., *Chem. Eng. Sci.*, 64, 4414–4423, 2009.
4. Kynch, G.J., *Trans. Faraday Soc.*, 48, 166–176, 1952.
5. Coe, H.S., Clevenger, G.H. *Trans. Am. Inst. Mining Eng.*, 55, 356–384, 1916.
6. Yoshioka, N., et al., *Kagaku Kogaku*, 21, 66–74, 1957.
7. Talmage, W.P., Fitch, E.B., *Ind. Eng. Chem.*, 47, 38–41, 1955.

5.19 Filtration

Eiji Iritani

Filtration is the operation separating a dispersed phase of solid particles from a fluid by means of a porous filter medium, which permits the passage of the fluid but retains the particles. Filtration is probably one of the oldest unit operations. The old forms of filtration by straining through porous materials were described by the earliest Chinese writers. A gravity filter used in a chemical process industry was described in an Egyptian papyrus which has its origin in about the third century A. D. In recent years, many developments have increased the application of filtration. Filtration steps are required in many important processes and in widely divergent industries. The importance of filtration techniques has been emphasized by the increased need for environmental protection. Recently, membrane filtration of colloids has become increasingly important in widely diversified fields.

The operations are divided into two broad categories: "cake" and "depth" filtration. In cake filtration, particles in a slurry form a deposit as a filter cake on the surface of the supporting porous medium while the fluid passes through it. After an initial period of deposition, the filter cake itself starts to act as the filter medium whilst further particles are deposited. From the viewpoint of a driving force, cake filtration is further divided into pressure, vacuum, gravity, and centrifugal operations. In depth filtration (sometimes called filter medium filtration or clarifying filtration), particles are captured within the complex pore structures of the filter medium, and the cake is not formed on the surface of the medium. In many processes, a stage of depth filtration precedes the cake formation. The first particles can enter the medium, and with very dilute slurries, there can be a time lag before a cake begins to form. Smaller particles enter the medium, whereas larger particles bridge the openings and start the buildup of a surface layer. Depth filtration is generally used to remove small quantities of contaminants. Cake filtration is primarily employed for more concentrated slurries. In practice, cake filtration is employed in industry more often than depth filtration. The following discussion will be concerned with cake filtration.

For purposes of mathematical treatment, cake filtration processes are classified according to the variations of both the pressure and filtrate flow rate with time. The pumping mechanism generally determines the flow characteristics and serves as a basis for division into the following categories: (a) constant-pressure filtration (the actuating mechanism is compressed gas maintained at a constant pressure, or a vacuum pump), (b) constant-rate filtration (positive displacement pumps of various types are employed), and (c) variable-pressure, variable-rate filtration (the use of a centrifugal pump results in the rate varying with the back pressure on the pump). The relation between filtration pressure p and filtration time t for the three types of filtration is illustrated in Figure 5.19.1. The constant-pressure curve is represented by a horizontal line. The pressure increases with time linearly for the constant-rate filtration of an incompressible cake. For a compressible cake formed in constant-rate filtration, the p vs. t curve is concaved upward. Variable-pressure, variable-rate filtration is conducted by using a filter equipped with a centrifugal pump. Depending on the characteristics of the centrifugal pump, widely differing curves might be encountered.

The structure of the cake forms and, consequently, its resistance to liquid flow depend on the properties of the solid particles and the liquid-phase suspension, as well as on the conditions of filtration. The cake structure is first established by such hydrodynamic factors as cake porosity, mean particle size, size distribution, particle specific surface area, and sphericity. It is also strongly influenced by some factors that can be denoted conditionally as physicochemical. The influence of physicochemical factors is closely related to surface phenomena at the solid–liquid boundary. For fine particle suspensions, colloidal forces control the nature of the filter cake. The repulsive electrostatic forces will vary with the surface charge of the suspended particles, which varies with the solution environment. Therefore, the filtration behaviors of the colloids are affected significantly by the solution properties, including pH and electrolyte strength.[1]

5.19.1 BASIS OF CAKE FILTRATION THEORY

Equations of Filtrate Flow through Filter Cake

Basic laws governing the flow of liquids through uniform, incompressible beds serve as a basis in developing formulas

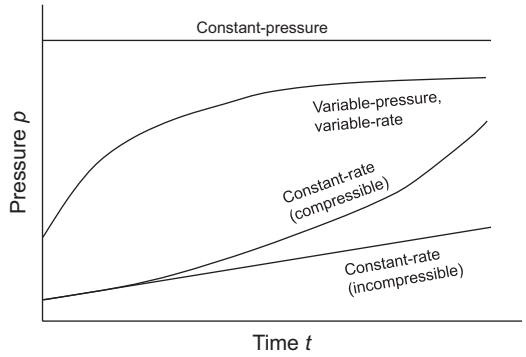


FIGURE 5.19.1 Relation between filtration pressure and time for different operations.

for more complex, non-uniform, compressible filter cakes formed on the filter medium during cake filtration. Darcy's law can be expressed in the form:

$$\frac{dp_L}{dx} = \frac{\mu}{K_p} u \tag{5.19.1}$$

where

p_L is the local hydraulic pressure
x is the distance from the filter medium
μ is the viscosity of liquid
K_p is the permeability
u is the apparent liquid velocity relative to the solids

This velocity is expressed as the volumetric flow rate per unit filter medium area, which is defined by

$$u = q - \frac{\varepsilon}{1-\varepsilon} r = q - er \tag{5.19.2}$$

where

q is the apparent flow rate of liquid
ε is the local porosity
r is the apparent migration rate of solid particles
$e\ (=\varepsilon/(1-\varepsilon))$ is the local void ratio

In filtration, it is customary to use the volume ω of dry solids per unit filter medium area instead of the distance x from the filter medium. Thus, the incremental volume $d\omega$ is given by

$$d\omega = (1-\varepsilon)\, dx \tag{5.19.3}$$

Substituting Equation (5.19.3) into Equation (5.19.1), one obtains

$$\frac{dp_L}{d\omega} = \frac{\mu}{K_p(1-\varepsilon)} u = \mu \rho_s \alpha u \tag{5.19.4}$$

where

ρ_s is the true density of solids
α is the local specific filtration resistance of the cake

Drag Acting on Particles

When suspended solids are deposited during cake filtration, liquid flows through the interstices of the compressible cake in the direction of decreasing hydraulic pressure. The solids forming the cake are compact and relatively dry at the filter medium, whereas the surface layer is in a wet and soupy condition. Thus, the porosity is minimum at the point of contact between the cake and the filter medium where $\omega = 0$ (Figure 5.19.2) and maximum at the cake surface ($\omega = \omega_0$, where ω_0 is the solids volume of the entire cake per unit filter medium area) where the liquid enters. The drag imposed on each particle is communicated to the adjacent particles. As a result, the net solid compressive pressure increases as the filter medium is approached, thereby accounting for the decreasing porosity.

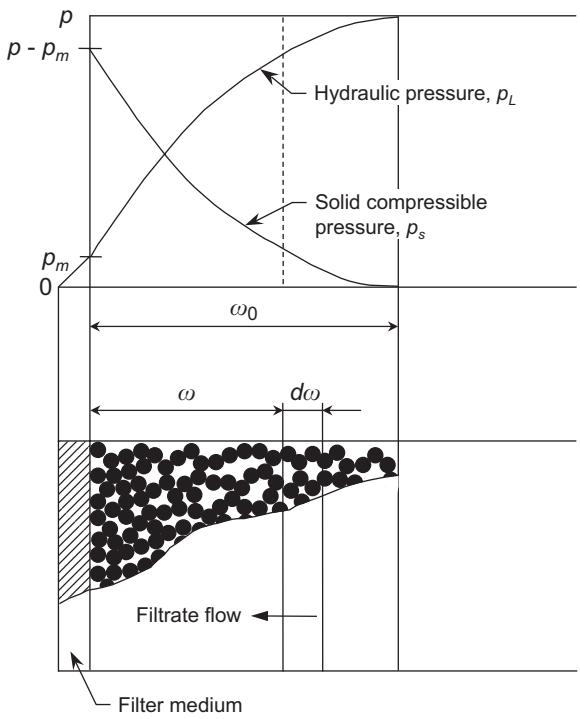


FIGURE 5.19.2 Schematic diagram of compressible filter cake.

Assuming that inertial forces are negligible, the force balance over the increment $d\omega$ can be described by

$$\frac{\partial p_L}{\partial \omega} + \frac{\partial p_s}{\partial \omega} = 0 \tag{5.19.5}$$

or on integration,

$$p_L + p_s = p \tag{5.19.6}$$

where p_s is the local solid compressive pressure. Equations (5.19.5) and (5.19.6) clearly indicate that the solid compressive pressure increases as the hydraulic pressure decreases, as illustrated in Figure 5.19.2.

Cake Porosity and Specific Cake Resistance

It is generally assumed in compressible cake filtration theory that both the local porosity and specific cake resistance are unique functions of the solid compressive pressure. These relations can be determined accurately by use of the compression-permeability cell.[2] Such relations can be also determined directly from the filtration experiments in which a filter is subjected to a sudden reduction in its filtration area.[3] As a fair approximation of compression-permeability cell data for a number of substances, the power functional relations among the porosity, specific cake resistance, and solid compressive pressure can be employed as follows:

$$\begin{aligned} \varepsilon &= \varepsilon_i, \quad p_s \le p_i \\ \varepsilon &= \varepsilon_0 p_s^{-\lambda}, \quad p_s > p_i \end{aligned} \tag{5.19.7}$$

$$\alpha = \alpha_i, \quad p_s \le p_i$$
$$\alpha = \beta_p + \alpha_{0p} p_s^n \approx \alpha_{0p} p_s^n, \quad p_s > p_i \tag{5.19.8}$$

where n is a compressibility coefficient, which is equal to zero for incompressible substances. The local specific cake resistance α is related to the local porosity ε in the form

$$\alpha = \frac{kS_0^2(1-\varepsilon)}{\rho_s \varepsilon^3} \tag{5.19.9}$$

where

S_0 is the effective specific surface area per unit volume of the particles
k is the Kozeny constant which normally takes the value of 5.0

Average Specific Cake Resistance

Combining Equation (5.19.4) with Equation (5.19.5), the basic flow equation can be rewritten as

$$\frac{dp_L}{d\omega} = -\frac{dp_s}{d\omega} = \mu \rho_s \alpha u \tag{5.19.10}$$

Integration of Equation (5.19.10) is carried out between the limits (see Figure 5.19.2) of $\omega = 0$ at the filter medium and $\omega = \omega_0$ at the cake surface. In addition, p_s is taken as $(p - p_m)$ at the filter medium and 0 at the cake surface. The pressure p_m at the exit of the filtrate from the cake is related to the resistance R_m of the filter medium by

$$p_m = \mu u_1 R_m \tag{5.19.11}$$

where u_1 is the filtration rate. Integrating Equation (5.19.10) on the assumption that u is constant $(= u_1)$ throughout the cake, one obtains

$$\frac{dv}{dt} = u_1 = \frac{p}{\mu(\alpha_{av} w + R_m)} \tag{5.19.12}$$

where

v is the filtrate volume per unit filter medium area
$w\ (= \rho_s \omega_0)$ is the solids mass of the entire filter cake per unit filter medium area
α_{av} is the average specific cake resistance defined by

$$\alpha_{av} = \frac{p - p_m}{\int_0^{p - p_m} (1/\alpha)\, dp_s} \tag{5.19.13}$$

The total cake resistance $R_c\ (= \alpha_{av} w)$ changes as the mass of cake grows with time. Many analyses of filtration start with Equation (5.19.12). Recently, the cake filtration theory can be also used to analyze membrane filtration such as ultrafiltration of protein solutions and nanocolloids, and thus it has the potential for analyzing the membrane fouling during ultrafiltration.[4]

The above-mentioned derivation is not rigorous in that it has been assumed that u is constant throughout the cake. Shirato et al.[5] developed a more complex equation, which took the variation of u with distance into account. Equation (5.19.13) is only approximately correct; hence, the average specific cake resistance must be modified for a general expression. This is apparent especially for thick slurries, as

$$\alpha'_{av} = J_s \alpha_{av} \tag{5.19.14}$$

where

α'_{av} is the average specific cake resistance which accounts for the internal flow variations through the filter cake
J_s is the correction factor

The factor J_s depends on both the filtration pressure and the slurry concentration. Although the pressure has relatively little effect, J_s can change remarkably for the concentrated slurry of compressible materials.[5]

Whenever the filtering area varies with the progress of filtration, as in radial flow filtration, Equation (5.19.12) must be modified. In the external two-dimensional filtration onto the cylindrical element, the filtration rate under constant-pressure conditions can be given by

$$\frac{dv}{dt} = \frac{p\left\{(r_o / r_i)^2 - 1\right\}}{2\mu \alpha_{av} w \ln(r_o / r_i)} \tag{5.19.15}$$

where

r_i is the radius of the surface of the filter medium
r_o is the radius of the cake surface.

Material Balance in Filtration

From an overall viewpoint of filtration, a material balance can be written on a unit medium area basis in the form:

$$\frac{w}{s} = mw + \rho v \tag{5.19.16}$$

where

s is the average mass fraction of solids in the slurry
m is the ratio of the mass of wet to mass of dry cake
ρ is the density of the filtrate

This material balance assumes that all feed slurry is filtered to form a cake. Solving for w in Equation (5.19.16), one gets

$$w = \frac{\rho s}{1 - ms} v \tag{5.19.17}$$

Frequently, the quantity m is related to the average cake porosity ε_{av} by

$$m = 1 + \frac{\rho \varepsilon_{av}}{\rho_s (1 - \varepsilon_{av})} \tag{5.19.18}$$

It is important to relate the cake thickness L to the filtrate volume v per unit filter medium area. For the entire cake, Equation (5.19.3) in combination with Equation (5.19.17) yields

$$w = \frac{\rho s}{1 - ms} v = \rho_s (1 - \varepsilon_{av}) L \tag{5.19.19}$$

5.19.2 CONSTANT-PRESSURE AND CONSTANT-RATE FILTRATION

Constant-Pressure Filtration

An accurate solution of Equation (5.19.12) requires numerical techniques. However, on the assumption of constant-pressure filtration that α_{av} is constant throughout the course of filtration and a function of p alone, a simple relation between v and t can be obtained. Combining Equation (5.19.12) with Equation (5.19.17), one obtains

$$\frac{dt}{dv} = \frac{2}{K_v}(v + v_m) \tag{5.19.20}$$

where

v_m is the fictitious filtrate volume per unit filter medium area required to form a filter cake with the resistance equal to the filter medium resistance R_m

K_v is Ruth coefficient of constant-pressure filtration defined by[6]

$$K_v = \frac{2p(1 - ms)}{\mu \alpha_{av} \rho s} \tag{5.19.21}$$

Integrating Equation (5.19.20), one gets

$$(v + v_m)^2 = K_v (t + t_m) \tag{5.19.22}$$

where t_m is the fictitious filtration time corresponding to the filter medium resistance. Equation (5.19.22) yields a parabolic relation between v and t. Constant-pressure filtration has long been the favorite method for obtaining experimental data in the laboratory because of its simplicity. Interpretation of data of constant-pressure filtration test is generally based on Equation (5.19.20). It might appear easier to use Equation (5.19.23) in the form:

$$\frac{t}{v} = \frac{1}{K_v} v + \frac{2}{K_v} v_m \tag{5.19.23}$$

Thus, plotting t/v against v produces a straight line, as illustrated in Figure 5.19.3. Equation (5.19.20) is, in fact, better because it does not require identification of the precise time at which $t = 0$. Plotting the reciprocal filtration rate (dt/dv) against v may lead to a straight line having the slope of $2/K_v$ in accordance with Equation (5.19.20), as shown in Figure 5.19.3. Knowing the value of K_v, it is possible to obtain the value of α_{av} from Equation (5.19.21) and then to construct a logarithmic graph of α_{av} vs. p. The filter medium resistance

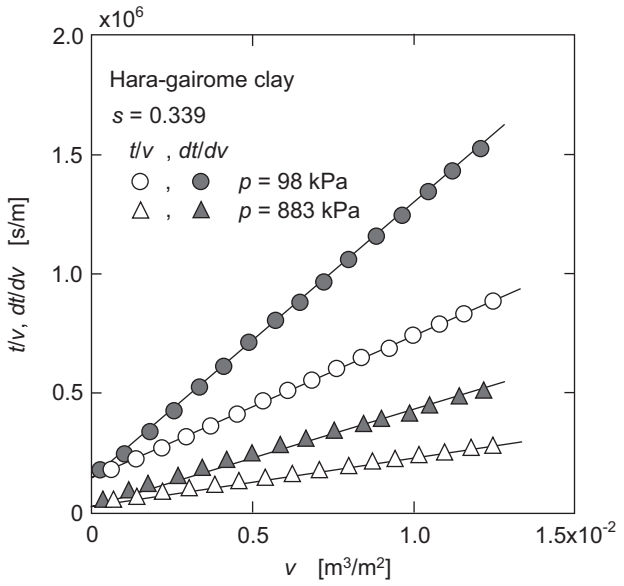


FIGURE 5.19.3 t/v and dt/dv vs. v.

can be calculated from the intercept. Empirically, α_{av} can be represented as a function of p by

$$\alpha_{av} = \alpha_0 (p - p_m)^{n'} \approx \alpha_0 p^{n'} \tag{5.19.24}$$

Constant-Rate Filtration

Substituting Equations (5.19.11) and (5.19.17) into Equation (5.19.12), one obtains

$$u_1 = \frac{1 - ms}{\mu \alpha_{av} \rho s v} (p - p_m) \tag{5.19.25}$$

In constant-rate filtration, the filtrate volume v per unit filter medium area is related to the filtration time t by the simple relation

$$v = u_1 t \tag{5.19.26}$$

Substituting Equation (5.19.26) into Equation (5.19.25) and solving it with respect to the filtration time t, one obtains the relation between p and t at constant-rate filtration as

$$t = \frac{1 - ms}{\mu \alpha_{av} \rho s u_1^2} (p - p_m) \tag{5.19.27}$$

If α_{av} is represented by Equation (5.19.24), Equation (5.19.27) leads to

$$t = \frac{1 - ms}{\mu \alpha_0 \rho s u_1^2} (p - p_m)^{1 - n'} \tag{5.19.28}$$

In constant-rate filtration, the pressure-time relationship is measured. A logarithmic plot of the pressure drop across the filter cake against time yields a straight line. When the cake is incompressible ($n' = 0$), Equation (5.19.28) implies a linear

relationship between filtration time and pressure drop, as illustrated in Figure 5.19.1.

5.19.3 INTERNAL STRUCTURE OF COMPRESSIBLE FILTER CAKE

In filter cakes, the variation of porosity with distance from the cake surface is important from both theoretical and industrial viewpoints. In the development of filtration theory, the porosity plays a fundamental role in its relation to flow rates, pressure, and other parameters involved in the differential equations of flow through compressible filter cake. Porosity variation determines the average porosity and liquid content of the filter cake in commercial operation.

Equation (5.19.10) is integrated over a portion of the cake and then the entire cake, assuming that u is constant ($=u_1$) throughout the cake. Also, it is assumed that the filter medium resistance is negligible. Integrating from ω to ω_0 and 0 to ω_0 yields, respectively

$$\frac{1}{\rho_s}\int_0^{p_s}(1/\alpha)\,dp_s = \mu u_1(\omega_0-\omega) \tag{5.19.29}$$

$$\frac{1}{\rho_s}\int_0^{p}(1/\alpha)\,dp_s = \mu u_1\omega_0 \tag{5.19.30}$$

Equation (5.19.30) provides a relationship among the filtration rate u_1, the solids volume ω_0, and the pressure drop p across the filter cake. Dividing Equation (5.19.29) by Equation (5.19.30), one obtains

$$\frac{\int_0^{p_s}(1/\alpha)\,dp_s}{\int_0^{p}(1/\alpha)\,dp_s} = 1-\frac{\omega}{\omega_0} \tag{5.19.31}$$

To convert ω/ω_0 in Equation (5.19.31) into x/L, the following equation can be employed:

$$\frac{x}{L} = \frac{\int_0^{\omega/\omega_0}\frac{d(\omega/\omega_0)}{(1-\varepsilon)}}{\int_0^{1}\frac{d(\omega/\omega_0)}{(1-\varepsilon)}} \tag{5.19.32}$$

Consequently, Equation (5.19.31) with the aid of Equation (5.19.32) gives the fractional distance through the cake as a function of the upper limit p_s of integration. It indicates that p_s vs. x/L curves are independent of flow and total thickness. In turn, p_L ($=p-p_s$) and ε can be related to x/L through their functional relationships to p_s. Equation (5.19.10) with the aid of Equation (5.19.3) can be used in an analogous manner to relate p_s to the distance through the cake directly by the form:

$$\frac{\int_0^{p_s}\frac{dp_s}{\alpha(1-\varepsilon)}}{\int_0^{p}\frac{dp_s}{\alpha(1-\varepsilon)}} = 1-\frac{x}{L} \tag{5.19.33}$$

Since u_1 varies markedly throughout the cake for highly concentrated slurries, Equations (5.19.31) and (5.19.33) must be modified. The power relation can be used to approximate the porosity vs. solid compressive pressure data as follows:

$$1-\varepsilon = E' p_s^{\lambda'} \tag{5.19.34}$$

Substituting Equations (5.19.34) and (5.19.8) into Equation (5.19.33), the integral in Equation (5.19.33) can be replaced by approximate formulas to yield[7]

$$\left(1-\frac{p_L}{p}\right)^{1-n-\lambda'} = 1-\frac{x}{L} \tag{5.19.35}$$

In Figure 5.19.4, the fractional hydraulic pressure drop is shown as a function of the fractional distance through the cake for different substances.[8] As the compressibility increases, the hydraulic pressure drop becomes larger near the filter medium. In Figure 5.19.5, the porosity is plotted against the fractional distance through the cake.[9] Under constant-pressure

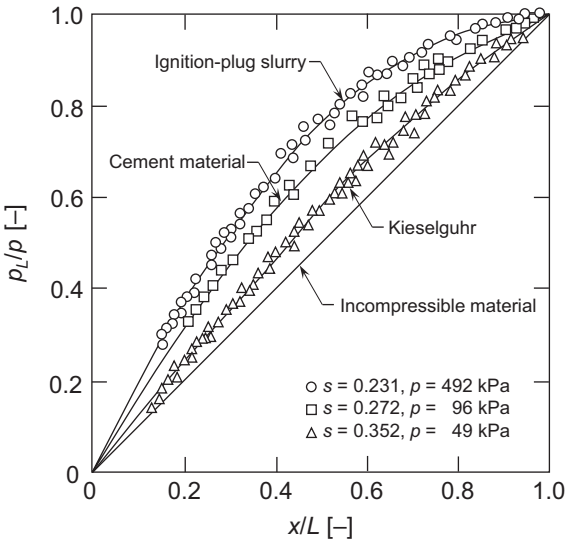


FIGURE 5.19.4 Relation between hydraulic pressure and normalized distance.

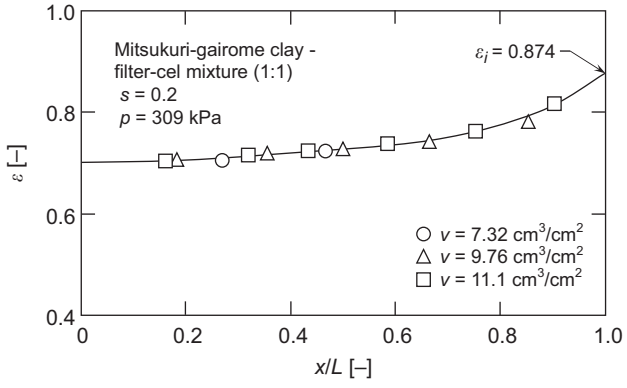


FIGURE 5.19.5 Relation between local porosity and normalized distance.

filtration, the local porosity depends on the normalized distance x/L alone.

5.19.4 FILTRATION OF NON-NEWTONIAN FLUID–SOLID MIXTURES

In filtration of non-Newtonian fluid–solid mixtures, an empirical relation known as a power law is widely used in representing the rheological behavior of the filtrate in the form:

$$\tau = K\dot{\gamma}^N \tag{5.19.36}$$

where

- τ is the shear stress
- K is the fluid consistency index
- $\dot{\gamma}$ is the shear rate
- N is the flow behavior index, which is a measure of the degree of the non-Newtonian behavior of the fluid; the greater the departure from unity of N, the more remarkable is the non-Newtonian behavior of the fluid

On the basis of Equation (5.19.36), the equation for describing the filtration rate of power-law non-Newtonian fluids can be obtained in the form:[10]

$$\left(\frac{1}{u_1}\right)^N = \left(\frac{dt}{dv}\right)^N = \frac{K\gamma_{av}\rho s\left(v+v_m\right)}{p\left(1-ms\right)} \tag{5.19.37}$$

where γ_{av} is the average specific cake resistance for power-law fluids.

In Figure 5.19.6, dt/dv and $(dt/dv)^N$ are plotted against v for constant-pressure filtration. The curve of dt/dv vs. v is concave upward, whereas the plot of $(dt/dv)^N$ vs. v shows a linear relationship in accordance with Equation (5.19.37). From the analysis for the internal structure of filter cake, it is derived that the filter cake formed by non-Newtonian filtration of pseudoplastic fluids ($N < 1$) is denser in structure than that formed by usual Newtonian filtration.

5.19.5 FILTRATION EQUIPMENT

A wide variety of filters are commercially available in many industries. The operating principles and important features of typical filtration equipment are described below.[11,12]

Filter Press

The filter press has been the best known and perhaps the most widely used of all batch pressure filters. The common filter press is the plate-and-frame design, which is held together as a pack in a strongly constructed framework, as illustrated in

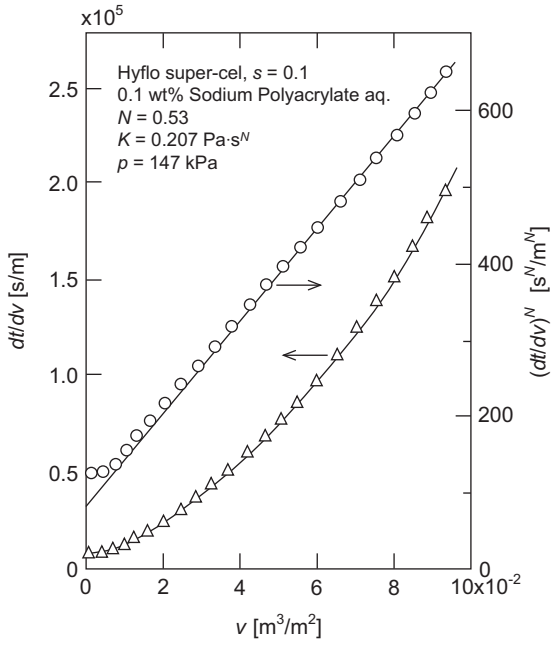


FIGURE 5.19.6 dt/dv and $(dt/dv)^N$ vs. v in non-Newtonian filtration.

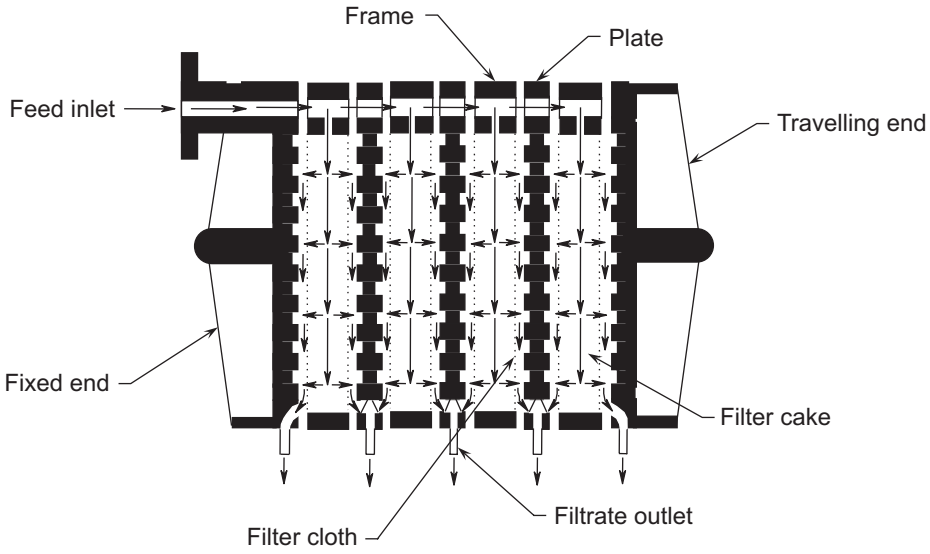


FIGURE 5.19.7 Schematic view of plate-and-frame filter press.

Figure 5.19.7. A varying number of filter chambers are assembled, which consist of medium-covered plates alternating with frames which provide space for the filter cake. The chambers are closed and tightened by a screw or hydraulic ram, which forces the plates and frames together, making a gasket of the filter cloth. The slurry feed is introduced into the chambers under pressure and fills each chamber approximately simultaneously. The liquid passes through the filter medium, which in turn retains the solids. The filtrate is removed at a discharge outlet. The filter cake forms until the frames are full. Completion of the cake formation is judged from the filtering time, decrease in the rate of the feed, or rise in back-pressure.

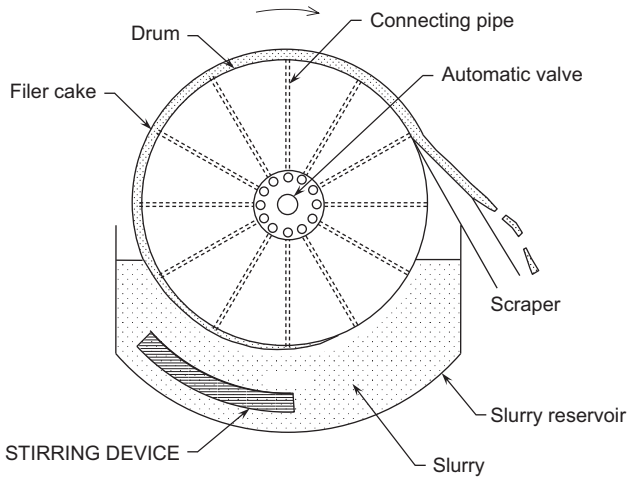


FIGURE 5.19.8 Schematic view of rotary drum filter.

Once the frames are full of cake, filtration is stopped and a wash liquid is applied if the solids are to be recovered. This can be followed by the deliquoring of the filter cake.

Rotary Drum Filter

The rotary drum filter is the most common continuous filter. A standard drum filter consists of three main parts: a drum mounted horizontally with an automatic filter valve; a slurry reservoir with a stirring device; and a scraper for cake discharge, as illustrated in Figure 5.19.8. The cylindrical drum, having a porous wall and covered on the outside with the filter media, rotates about a horizontal axis with a portion immersed in the slurry. The filter operates continuously through stages of cake formation due to filtration, washing, drying with air or steam, and discharge with an air blower. The normal driving force is vacuum, although enclosed pressurized units are sometimes built. The drum is usually subdivided into a number of separate compartments so that the various stages can be performed. The principal advantage of this filter is the continuity of its operation.

Thin-Cake or Dynamic Filter

The thin-cake or dynamic filter has appeared on the market in recent years. Crossflow filtration operates by recirculating the feed flow parallel to the filter medium. The velocity of the feed in recirculation sweeps away particles deposited on the filter medium, thereby limiting the cake thickness. Crossflow filtration is especially effective for membrane filtration of colloids. The continuous pressure filter shown in Figure 5.19.9 is

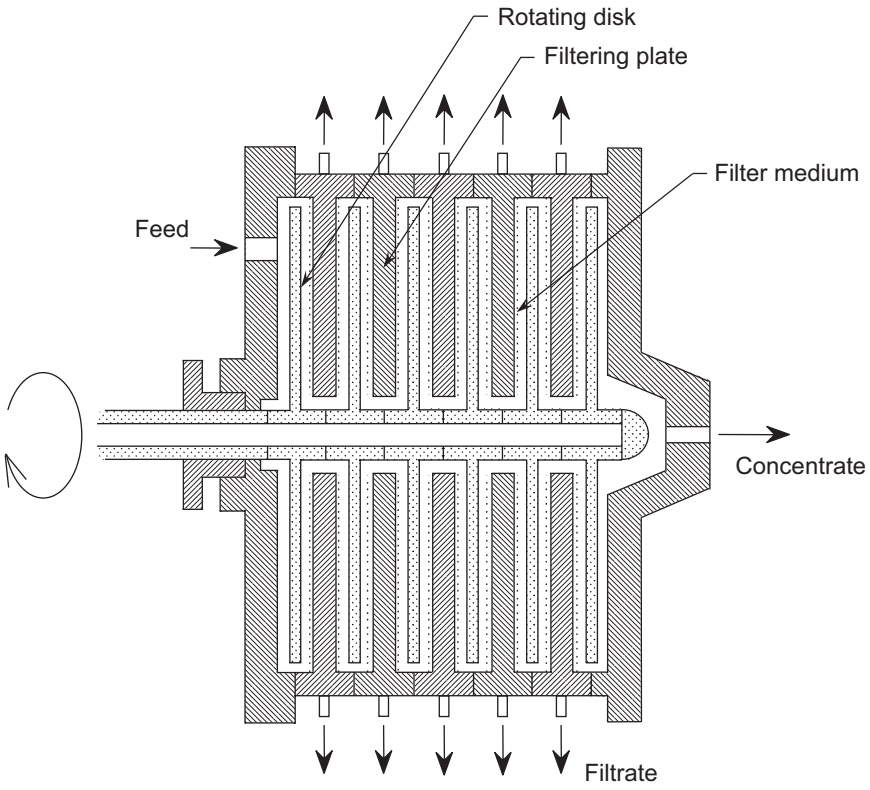


FIGURE 5.19.9 Schematic view of thin-cake filter.

a kind of filter-thickener, consisting of fixed filtering plates alternating with thin rotating disks. The filtering plates are covered with a filter medium on both sides, and the thin disks are rotated at a high speed sufficient to prevent the cake from growing on the filter medium. The feed slurry is dewatered as it flows through the stages, and it emerges continuously from the discharge valve as a concentrate of a paste-like consistency without the danger of filter blocking because the slurry is continuously moving. Little cake formation occurs in the intensive shearing induced by high slurry velocities parallel to the filter medium. As a result, high filtration rates are accomplished. Very thin cake formation allows such a filter to be designed of relatively small size.

REFERENCES

1. Iritani, E., Toyoda, Y., Murase, T., *J. Chem. Eng. Jpn.*, 30, 614–619, 1997.
2. Grace, H.P., *Chem. Eng. Prog.*, 49, 303–318, 1953.
3. Iritani, E., , *AIChE J.*, 61, 4426–4436, 2015.
4. Iritani, E., Hattori, K., Murase, T., *J. Membrane Sci.*, 81, 1–13, 1993.
5. Shirato, M., Sambuichi, M., Kato, H., Aragaki, T., *AIChE J.*, 15, 405–409, 1969.
6. Ruth, B.F., *Ind. Eng. Chem.*, 27, 708–723, 1935.
7. Tiller, F.M., Cooper, H.R., *AIChE J.*, 8, 445–449, 1962.
8. Tiller, F.M., Shirato, M., *AIChE J.*, 10, 61–67, 1964.
9. Shirato, M., Aragaki, T., Ichimura, K., Ootsuji, N., *J. Chem. Eng. Jpn.*, 4, 172–177, 1971.
10. Shirato, M., et al., *J. Chem. Eng. Jpn.*, 10, 54–60, 1977.
11. Cheremisinoff, N.P., *Liquid Filtration*. Woburn, MA, Butterworth-Heinemann, 1998, pp. 88–117.
12. Shirato, M., et al., *Filtration, Principles and Practices*, eds. Matteson M.J., Orr, C. New York, Marcel Dekker, 1987, pp. 309–324.

5.20 Expression

Eiji Iritani

Expression is the operation squeezing the liquid from solid–liquid mixtures by compression under conditions that allow the liquid to pass while the solid particles are retained between the supporting porous media. It is distinguished from filtration in that the pressure is applied by movement of the retaining walls such as pistons, membranes, rollers, or belts rather than by pumping a slurry into a fixed-volume chamber. In filtration, the material is sufficiently fluid to be pumpable, whereas in expression, the material can appear to be either entirely semi-solid or slurry. Operational expressions have become increasingly important in such widely divergent fields as food processing and fermentation industries, wastewater treatments, and chemical process industries, because the energy required to squeeze liquid from cakes is negligible compared to the heat required for thermal drying.

5.20.1 BASIS OF EXPRESSION

Figure 5.20.1 shows the schematic view of the compression-permeability (C-P) cell employed to examine the deliquoring mechanism of the compressed cake during an expression operation. In the experiments, the solid–liquid mixture is introduced into a cylinder, and a constant mechanical load is applied through the piston. The liquid squeezed from the mixture is allowed to drain from both the top and bottom supporting porous media. The variation of the thickness L of the mixture or compressed cake with time t is measured by the dial gauge.

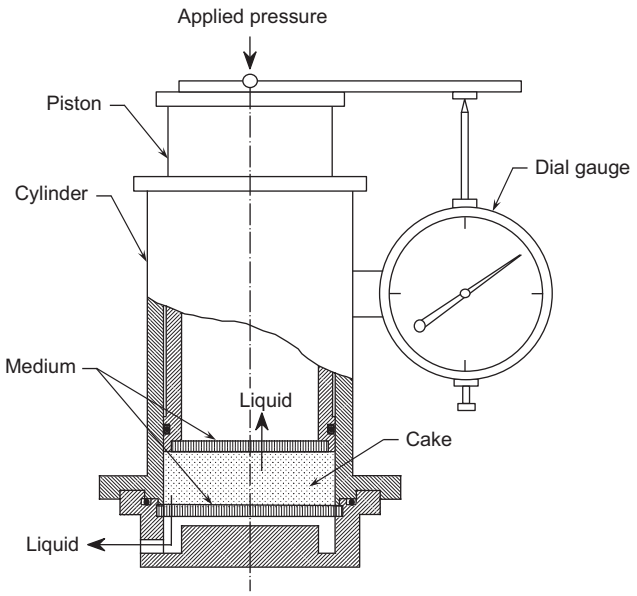


FIGURE 5.20.1 Schematic view of C-P cell.

The expression is made up from two stages comprised of filtration and consolidation according to the flow mechanism within the porous materials. When the original mixture in the cylinder can flow as a slurry, applying a load to the piston causes a sudden, uniform increase of hydraulic pressure in the slurry and the resulting hydraulic pressure is equal to the applied pressure, and consequently deliquoring proceeds on the principle of filtration. Filtration terminates in cake consolidation when the whole slurry forms a filter cake. In the consolidation stage, the bulk volume of the cake is reduced. On the basis of a mass balance, the maximum thickness L_1 of the filter cake can be determined from

$$L_1 = \left(\frac{m-1}{\rho} + \frac{1}{\rho_s} \right) \rho_s \omega_0 \tag{5.20.1}$$

where

- m is the ratio of the mass of wet to mass of dry cake
- ρ is the density of liquid
- ρ_s is the true density of solids
- ω_0 is the net solid volume per unit medium area

The hydraulic pressure distribution through a filter cake during constant-pressure filtration essentially remains unchanged. Deliquoring due to consolidation is distinguished from that due to filtration in that the hydraulic pressure distribution through a compressed cake varies significantly with time. Provided the original concentration of the mixture is larger than a limiting value, deliquoring of the mixture proceeds from the beginning on the principle of consolidation.

5.20.2 MODIFIED TERZAGHI MODEL

Equations for describing the consolidation behaviors are derived from the basic equation of flow through porous media. It is convenient to use a solid particle volume represented by ω divided by the cross-sectional area, where ω is a moving plane which represents the solid volume between the plane and the medium per unit cross-sectional area. The apparent velocity u of the liquid viewed from this moving material can be described by

$$u = \frac{1}{\mu \alpha \rho_s} \cdot \frac{\partial p_L}{\partial \omega} = -\frac{1}{\mu \alpha \rho_s} \cdot \frac{\partial p_s}{\partial \omega} \tag{5.20.2}$$

where

- μ is the viscosity of liquid
- α is the local specific flow resistance
- p_L is the local hydraulic pressure
- p_s is the local solid compressive pressure

The mass balance of liquid in the infinitesimal layer leads to the equation of continuity in the form:

$$\frac{\partial e}{\partial t_c} = \frac{\partial u}{\partial \omega} \tag{5.20.3}$$

where

e ($\varepsilon/[1-\varepsilon]$)	is the local void ratio of the cake
t_c	is the consolidation time
ε	is the local porosity

Combination of Equation (5.20.2) with Equation (5.20.3) leads to

$$\frac{\partial p_s}{\partial t_c} = C_e \left\{ \frac{\partial^2 p_s}{\partial \omega^2} - \frac{1}{a} \cdot \frac{da}{dp_s} \left(\frac{\partial p_s}{\partial \omega} \right)^2 \right\} \tag{5.20.4}$$

where C_e is the modified average consolidation coefficient defined by

$$C_e = \left\{ \mu a \rho_s \left(-\frac{de}{dp_s} \right) \right\}^{-1} \tag{5.20.5}$$

Combining Equation (5.20.2) with Equation (5.20.3) on the assumption that C_e is constant during consolidation, one obtains the well-known form of the diffusion equation

$$\frac{\partial p_s}{\partial t_c} = C_e \frac{\partial^2 p_s}{\partial \omega^2} \tag{5.20.6}$$

This equation is similar to the basic consolidation equation proposed by Terzaghi[1] in the field of soil mechanics with spatial fixed coordinates.

It is necessary to know the initial condition, specifically distributions of the solid compressive pressure (or the hydraulic pressure) in the cake, in order to obtain the solution of Equation (5.20.6). The hydraulic pressure distributions within filter cakes with moderate compressibility can be generally approximated by a sinusoidal curve. Thus, the solution of Equation (5.20.6) for a constant-pressure expression of filter cake leads to[2]

$$U_c = \frac{L_1 - L}{L_1 - L_\infty} = 1 - \exp\left(-\frac{\pi^2 T_c}{4} \right) \tag{5.20.7}$$

where

U_c	is the average consolidation ratio
L_1, L, and L_∞	are the thickness of the cake at $t_c = 0$, t_c, and ∞, respectively

The dimensionless consolidation time T_c in Equation (5.20.7) is defined by

$$T_c = \frac{i^2 C_e t_c}{{\omega_0}^2} \tag{5.20.8}$$

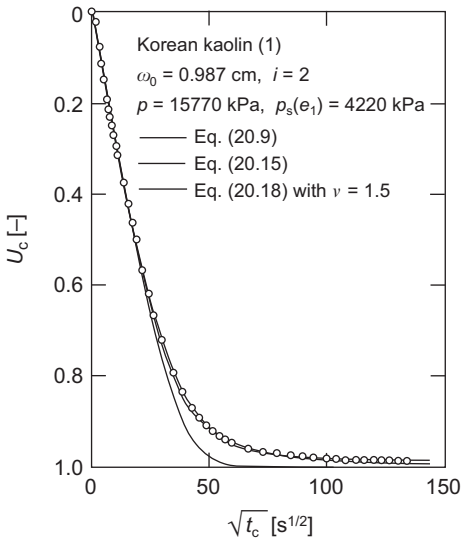


FIGURE 5.20.2 Constant-pressure expression of semi-solid material.

where i is the number of drainage surfaces. This equation clearly indicates that the consolidation time t_c required for attaining a specified value of the degree of consolidation is directly proportional to ω_0^2 and is inversely proportional to i^2. The solution of Equation (5.20.6) for a constant-pressure expression of homogeneous semi-solid materials leads to

$$U_c = 1 - \sum_{N=1}^{\infty} \frac{8}{(2N-1)^2 \pi^2} \exp\left\{ -\frac{(2N-1)^2 \pi^2}{4} T_c \right\} \tag{5.20.9}$$

Figure 5.20.2 compares the experimental data for consolidation of a homogeneous semi-solid of the Korean kaolin[1] with calculations using Equation (5.20.9). The agreement is rather poor, whereas the calculated curve is similar in shape to the experimental one. In addition, although Equation (5.20.4) can be solved numerically by considering variations of C_e, the agreement is still poor.

The practical and important quantity C_e can be determined by the so-called fitting method by consideration of the similarity in shape of the theoretical curve of U_c vs. $\sqrt{t_c}$, and experimental observations. In constant-pressure expression of the filter cake, the time t_{90} for attaining 90% of U_c can be obtained from the experimental data, as illustrated in Figure 5.20.3, and thus the value of C_e is calculated from

$$C_e = \frac{0.933 {\omega_0}^2}{i^2 t_{90}} \tag{5.20.10}$$

The quantity C_e can also be evaluated using the C-P cell data shown in Figure 5.20.4. The specific flow resistance α is plotted against the solid compressive pressure p_s, at the left in the figure, and the void ratio e is plotted against p_s, at the right, for

materials with widely different compressibility. C-P cell data can be represented by

$$a = a_0 + a_1 {p_s}^n \tag{5.20.11}$$

$$e = e_0 - C_c \ln p_s \tag{5.20.12}$$

On the basis of the empirical constitutive Equations (5.20.11) and (5.20.12), the modified average consolidation coefficient C_e can be calculated from

$$C_e = \frac{p_{s.av}}{\mu \rho_s C_c \left(a_0 + a_1 {p_{s.av}}^n\right)} \tag{5.20.13}$$

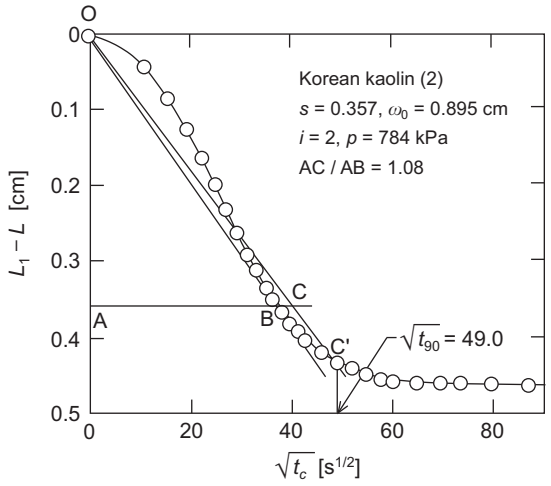


FIGURE 5.20.3 Fitting method for determining C_e from experimental data.

where $p_{s.av}$ is the average solid compressive pressure, which is often approximated by the arithmetic mean value of the initial average solid compressive pressure $p_s(e_{1.av})$ within the cake and the applied pressure p, where $e_{1.av}$ denotes the initial average void ratio. Since this equation essentially affords an estimation of C_e, the consolidation process can be theoretically predicted from calculations based on the C-P cell data.

5.20.3 SECONDARY CONSOLIDATION

Secondary consolidation has to be taken into account in order to obtain more rigorous equations for describing the consolidation behavior. Because the variation of the void ratio e within the cake is caused by both the change in the local solid compressive pressure p_s and the simultaneous creep effect of materials, e is a function of both p_s and the consolidation time t_c. Assuming that the rheological behavior of secondary consolidation is described by the Voigt model illustrated in Figure 5.20.5, the average consolidation ratio U_c is given by

$$U_c = (1-B)\left\{1 - \exp\left(-\frac{\pi^2 T_c}{4}\right)\right\} + B\left\{1 - \exp\left(-\eta t_c\right)\right\} \tag{5.20.14}$$

for constant-pressure expression of filter cakes, and by

$$U_c = (1-B)\left[1 - \sum_{N=1}^{\infty} \frac{8}{(2N-1)^2 \pi^2} \exp\left\{-\frac{(2N-1)^2 \pi^2}{4} T_c\right\}\right] + B\left\{1 - \exp\left(-\eta t_c\right)\right\} \tag{5.20.15}$$

for constant-pressure expression of semi-solid materials[3]

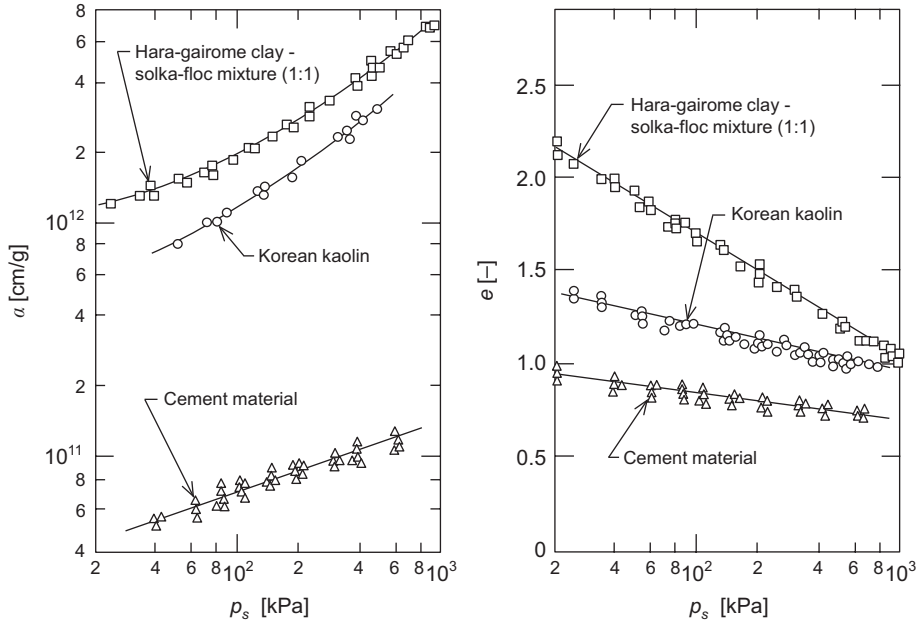


FIGURE 5.20.4 C-P cell data.

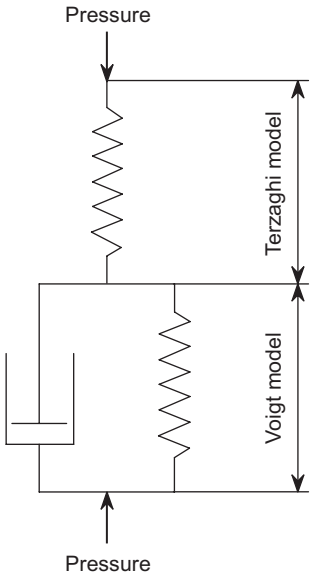


FIGURE 5.20.5 Schematic view of Terzaghi-Voigt combined model.

The quantity B is a constant defined by

$$B = v_{sc.max} / v_{c.max} \tag{5.20.16}$$

where $v_{sc.max}$ and $v_{c.max}$ are the liquid volumes squeezed by the secondary consolidation alone and until final equilibrium, respectively. The quantity η is a rate constant due to creep of the materials. Because $-\pi^2 T_c/4 >> \eta$ for the large values of t_c, Equations (5.20.14) and (5.20.15) become approximately

$$U_c = \frac{L_1 - L}{L_1 - L_\infty} \approx 1 - B\exp\left(-\eta t_c\right) \tag{5.20.17}$$

Consequently, the values of both B and η can be determined from the plot of $\ln(1 - U_c)$ vs. t_c in the later stage of consolidation. In Figure 5.20.2, the prediction based on Equation (5.20.15) is compared with the experimental data, the agreement with the data being relatively good. However, with biological and cellular materials, the consolidation mechanism is much more complicated because the liquid is stored mainly in cells.[4] For instance, consolidation of activated sludge is described by the primary consolidation followed by multistage creep.[5]

5.20.4 SIMPLIFIED ANALYSIS

The solutions based on the modified Terzaghi model give less satisfactory values, especially in the later stage of consolidation. More sophisticated solutions based on the Terzaghi-Voigt combined model coincide very well with the experimental results. However, the solutions might not be useful in normal industrial practice since they include the three empirical constants, C_e, B, and η, which have to be determined based on two graphical plots.

It is clear from Figure 5.20.2 that the relation between U_c and $\sqrt{t_c}$, calculated by Equation (5.20.9), is linear and nearly coincides with experimental data in the early stage of consolidation of semi-solid material under constant-pressure conditions. However, agreement is poor in the later stage, and the theoretical curve approaches the final equilibrium more rapidly than the experimental results. Since U_c is directly proportional to $\sqrt{t_c}$ for small values of t_c and asymptotically approaches unity for large values of t_c, one of the simplest equations, instead of Equation (5.20.9), can be derived as[6]

$$U_c = \frac{L_1 - L}{L_1 - L_\infty} = \left[\frac{4}{\pi}T_c\left\{1 + \left(\frac{4}{\pi}T_c\right)^{\nu}\right\}^{-1/\nu}\right]^{1/2} \tag{5.20.18}$$

where ν is the consolidation behavior index which takes secondary consolidation effects into account. When U_c is plotted against $\sqrt{T_c}$, the maximum percentage of error calculated by Equation (5.20.18) with $V = 2.85$, compared to Equation (5.20.9), is only 0.6. It was previously indicated that Equation (5.20.9) gives less satisfactory values. However, it can be seen from Figure 5.20.2 that Equation (5.20.18) with $V < 2.85$ gives quite satisfactory results, and the effect of secondary consolidation is considered in this range.

5.20.5 EXPRESSION EQUIPMENT

Various types of equipment for expression are available in industry.[7] The automated filter press with a cake compression mechanism was developed in the 1960s in order to reduce the cake moisture content. A lateral, recessed plate and an expression plate with a diaphragm comprises a filter chamber, as shown in Figure 5.20.6. After feed slurry is forced into the chamber under pressure, filtration occurs and the diaphram is pressed against the expression plate. Once the chamber is filled with a filter cake, the diaphram is expanded by pumping compressed air or water into the cavity between the diaphram and the plate. As the diaphram moves toward the opposite

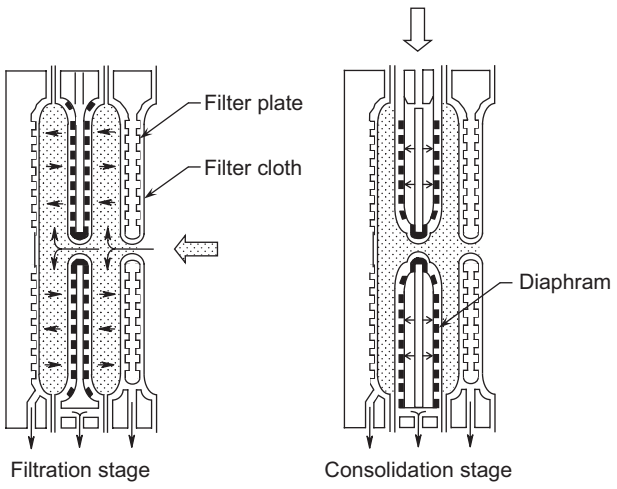


FIGURE 5.20.6 Schematic view of automatic filter press with compression device.

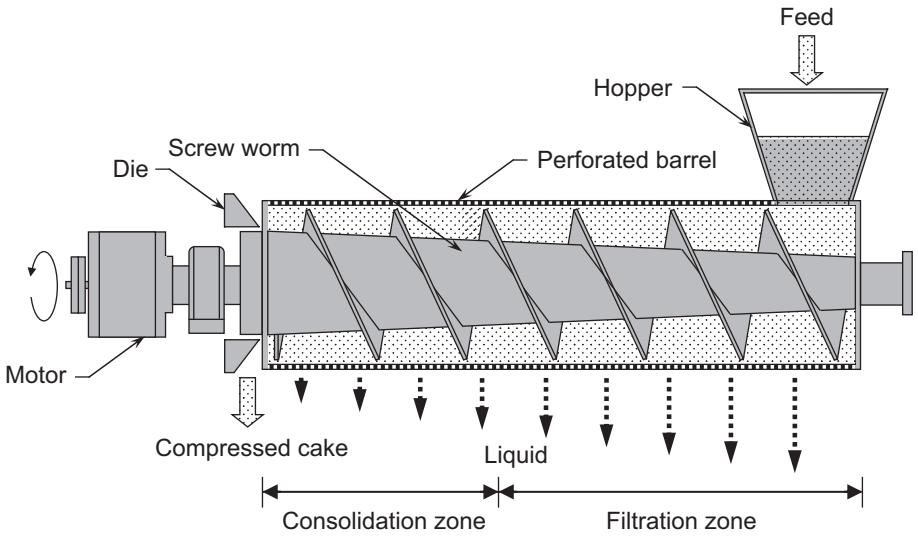


FIGURE 5.20.7 Schematic view of screw press.

plate, deliquoring of the filter cake due to consolidation takes place. On completion of expression, the chamber is automatically opened and then the cake is discharged.

The belt press as an example of continuous expression equipment has a horizontal gravity dewatering zone of belt preceding the pressure dewatering zone. The slurry is sandwiched between the carrying belt and the cover belt at the end of the gravity dewatering zone. From this point to the cake discharge point, the sludge is gradually compressed by compressive and shear forces that are applied through the belt.

In recent years, a screw press, used in the oil milling industry as an expeller, has been widely employed in the chemical industry and sewage sludge treatment. As shown in Figure 5.20.7, materials are fed to a perforated barrel containing a rotating screw worm. Materials trapped between the screw and the inside of the cylindrical barrel pass through a gradually reducing flow area, experiencing an increasing pressure. The compressed cake leaves the unit through an adjustable discharge port.

REFERENCES

1. Terzaghi, K., *Theoretical Soil Mechanics*, New York, John Wiley and Sons, 1948, pp. 265–296.
2. Shirato, M., Murase, T., Kato, H., Fukaya, S., *Kagaku Kogaku*, 31, 1125–1131, 1967.
3. Shirato, M., Murase, T., Tokunaga, A., Yamada, O., *J. Chem. Eng. Jpn.*, 7, 229–231, 1974.
4. Lanoisell, J.L., Vorobyov, E.I., Bouvier, J.M., Piar, G., *AIChE J.*, 42, 2057–2068, 1996.
5. Iritani, E., Katagiri, N., Washizu, T., Hwang, K.J., *Chem. Eng. Sci.*, 112, 1–9, 2014.
6. Shirato, M., et al., *J. Chem. Eng. Jpn.*, 12, 51–55, 1979.
7. Shirato, M., et al., *Filtration, Principles and Practices*, ed. Matteson, M.J., Orr, C., New York, Marcel Dekker, 1987, pp. 371–377.



Taylor & Francis
Taylor & Francis Group
http://taylorandfrancis.com

5.21 Flotation

Wei Sung Ng, George Vincent Franks, Elizaveta Forbes, Luke Andrew Connal and Hiroki Yotsumoto

Froth flotation was developed over a century ago as a viable method for minerals separation, and has since evolved into one of the most important and widely used techniques in the treatment and recovery of valuable minerals. Compared to the prevailing technologies of the day, flotation offered significant improvements in the handling of fine particles at high throughputs, relative to more traditional methods such as gravity separation. Today, flotation is used extensively in the production of copper, gold, silver, zinc, lead, coal, phosphorus, and molybdenite, producing high-grade concentrates prior to further purification with leaching or smelting. In recent years, froth flotation has also been used in the removal of oil from industrial waste, the removal of algae from water, as well as in the removal of hydrophobic impurities in paper recycling.

The basic principle of froth flotation involves the separation of particles based on its surface properties in an aqueous suspension. Following the introduction of bubbles into the system, either pneumatically or mechanically, particles with surfaces displaying hydrophobic properties are able to attach to the bubbles, while hydrophilic particles settle or remain suspended in solution. The hydrophobic particles are then lifted by the buoyancy force of the bubbles to the surface of the pulp to form a froth zone. The result is the recovery of hydrophobic particles into a concentrate product at the top of the cell, separated from the hydrophilic particles which are removed from the bottom of the cell. Flotation is aided by a suite of reagents and selective surface modification agents to ensure that the targeted particles are rendered hydrophobic, while maintaining a hydrophilic surface on the unwanted gangue.

This chapter will begin with the fundamentals of froth flotation, covering both theoretical and practical aspects, followed by a description of the reagents and instruments involved in the process. Subsequently, we will go through an example of typical plant practice, and conclude with a discussion of some of the main challenges in flotation, as well as the technologies that are being developed to tackle these difficulties.

5.21.1 FUNDAMENTALS OF FLOTATION

Froth flotation is a complex physiochemical process involving three separate phases in the form of the particle surface (solid), the surrounding water (liquid), and the froth/bubble (gas).[1–7] The process is performed in flotation cells, which typically feature two distinct regions, the froth zone (the foam on top of the cell) and the pulp zone (the suspension within the cell), as shown in Figure 5.21.1. Attachment of hydrophobic

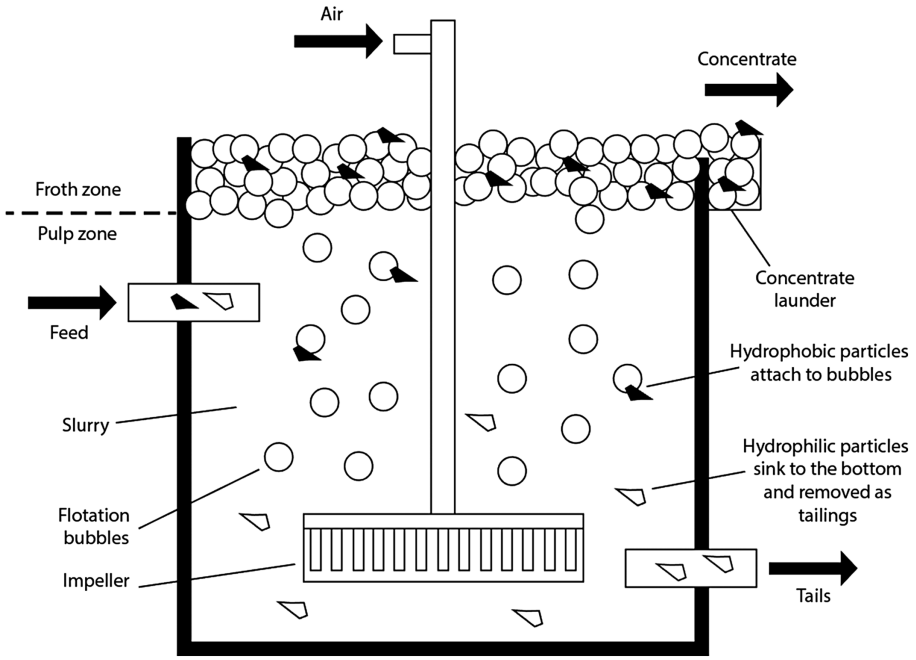


FIGURE 5.21.1 A simplified depiction of a typical flotation cell.

particles to bubbles occurs in the pulp zone, after which the buoyancy force of the bubbles is utilized to lift the attached particles to the froth zone. The froth zone allows any entrained hydrophilic particles to drain into the pulp phase, enhancing the grade of the concentrate product prior to collection into a launder.

Particle–Bubble Attachment

The flotation of a particle to the concentrate begins with the initial attachment to the bubbles. Particle–bubble adhesion hinges on the surface hydrophobicity of the particles – more hydrophobic surfaces have a higher probability of particle–bubble attachment, as opposed to less hydrophobic surfaces. This can be understood theoretically in terms of the Young-Dupre equation for the interfacial forces acting on an air bubble,[2–4,7] as illustrated in Figure 5.21.2. If we consider the equilibrium interfacial tension of a single flat surface and bubble, the equilibrium relationship between the interfacial tensions can be expressed as:

$$\gamma_{S\text{–}G} = \gamma_{S\text{–}L} + \gamma_{L\text{–}G} cos\theta$$

where $\gamma_{S\text{-}G}$, $\gamma_{S\text{-}L}$, and $\gamma_{L\text{-}G}$ represent the interfacial tension between the solid and the gas, the solid and the liquid, and the liquid and the gas phase respectively, while θ is the contact angle of the bubble on the particle surface in the pulp phase. Subsequently, the free energy, or work required for attachment on a unit area, is:

$$\Delta G_{attachment} = \gamma_{L\text{–}G}\left(\cos\theta - 1\right)$$

Hence, a high contact angle between the particle and the bubble, as a result of a low wettability or hydrophobic surface, reduces the free energy of attachment, and facilitates particle–bubble adhesion and the minimization of particle–bubble detachment. For mineral surfaces that are not naturally hydrophobic, the addition of a surfactant called a collector is typically required to alter the surface energies in order to render the surface hydrophobic and enable adhesion to the bubble.

Particle–bubble attachment is influenced by the surface forces between the particle and bubble, which is described by the Derjaguin, Landau, Verwey and Overbeek (DLVO) theory, which is typically used to predict the stability of two particles in close proximity but can be modified to describe the particle–bubble forces.[8,9] Based on the DLVO theory, the energy between the particle and the bubble can be considered as a sum of the attractive and repulsive interactions, and the net potential can be expressed as:

$$V_t = V_e + V_d + V_s$$

where V_t, V_e, V_d, and V_s represent the total, electrostatic, van der Waals, and hydrophobic forces, respectively, acting between the particle and the bubble. In flotation, the electrostatic forces are typically repulsive, while the van der Waals and hydrophobic forces are attractive, as shown in Figure 5.21.3. In the absence of hydrophobic attractive forces, the van der Waals attraction is generally insufficient to overcome the electrostatic repulsion between the particle and the bubble (except at very short distances), due to the negative charge on the bubble. The presence of hydrophobic forces, due to the natural hydrophobicity of the particle or the presence of collectors, facilitates an environment where particle–bubble attachment is energetically favored, as shown in Figure 5.21.3.

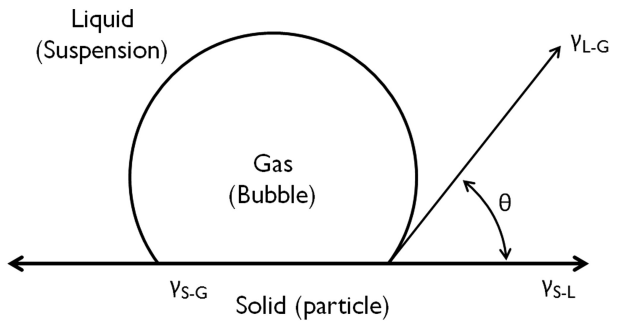


FIGURE 5.21.2 The equilibrium contact angle between an air bubble and a solid surface in a liquid suspension.

Flotation of Particle Attached to a Bubble

Following attachment to a bubble, the buoyancy force of the bubble is utilized to lift and recover the particle to the top of the flotation cell (the froth zone). The buoyancy force needs to be strong enough to counteract the gravitational force of the particle to allow flotation to occur, as shown in Figure 5.21.4. Overall, the net upward force acting on the particle and bubble, F_{up}, can be expressed as:[10,11]

$$F_{up} = F_b + F_c - F_p - F_g$$

where F_b, F_c, F_p, and F_g represent the buoyancy force, capillary force, bubble capillary pressure, and gravitational force respectively. If the net upward force is positive, then the particle can be lifted while attached to the bubble. Otherwise, the bubble and particle are likely to sink, with the particle eventually detaching from the bubble.

Factors Influencing Flotation Performance

While the theoretical aspects of flotation can be explained in terms of contact angles and attractive hydrophobic forces, in practice flotation performance can be influenced by a wide variety of physical and chemical parameters. Flotation performance is often evaluated empirically in terms of the grade and recovery of the targeted mineral. The concentrate grade is strongly influenced by a process called entrainment, which is the unselective recovery of both valuable and gangue particles. Grade is also lowered by the recovery of unliberated gangue material that is physically bound to valuable minerals within composite mineral particles. A trade-off is present between recovery and grade – with an increase in recovery, an increasing amount of progressively lower grade material is recovered

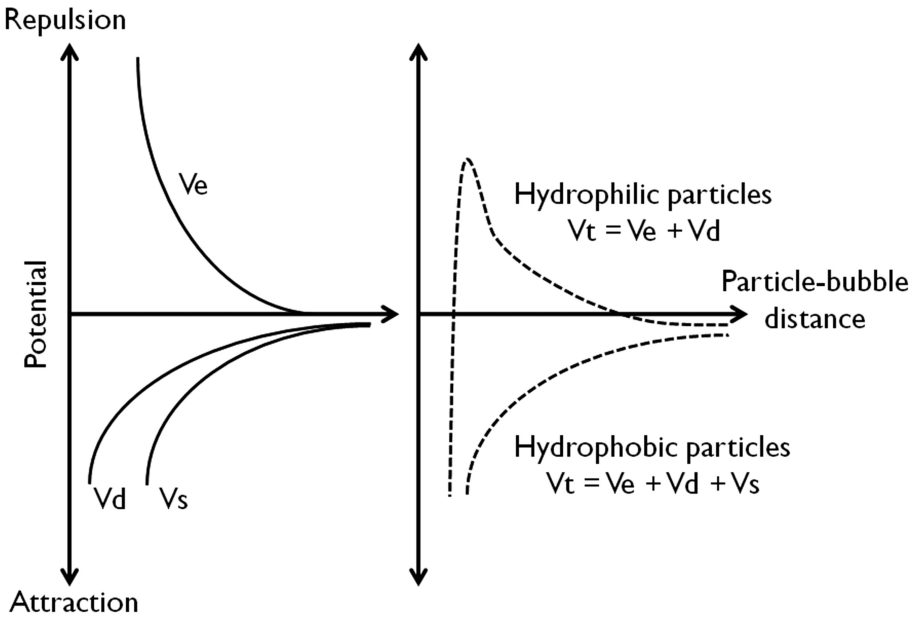


FIGURE 5.21.3 Potential energy curves as a function of surface-to-surface separation distance for particle–bubble attachment under DLVO theory.

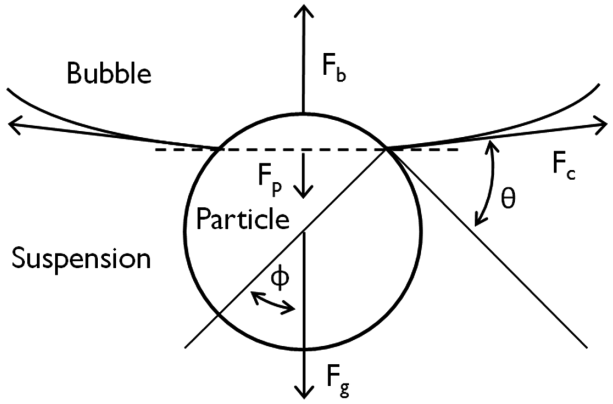


FIGURE 5.21.4 Forces acting on a particle attached onto a bubble.

into the concentrate, which lowers the overall grade of the product. Therefore, fine grinding to particle sizes below 150 μm is typically preferred to improve the liberation of the feed, freeing up the valuable minerals that are locked up as composite particles with the gangue. Flotation recovery can be expressed as:[12]

$$\text{Recovery} = P_C P_A \left(1 - P_D\right)$$

where P_C, P_A, and P_D represent the probability of particle–bubble collision, the probability of particle–bubble attachment, and the probability of particle–bubble detachment respectively. Different terms are used for P_C and P_A, as particle–bubble collision does not always lead to attachment; for adhesion to occur, the attractive forces between the two objects must be able to overcome the repulsive and hydrodynamic forces during the brief period of contact. A brief summary of the main factors that can influence recoveries are as shown in Figure 5.21.5.

Probability of Particle–Bubble Collision

As can be seen in Figure 5.21.5, P_C is mostly affected by mechanical and physical considerations, with the mixing and shearing conditions within the cell varying with the cell type, geometry, and design.[13–15] For example, column cells with taller pulp zones usually feature a higher P_C, as the bubbles remain in the suspension for longer periods of time, while the presence of an impeller in mechanical cells will result in more intense mixing. Another factor is the size of the particles in suspension; for instance, small particles collide more frequently with bubbles, while larger particles have reduced P_C. Fine particles below 20 μm have a higher tendency to be caught in bubble streamlines due to a lack of momentum, resulting in reduced probabilities to contact the bubble for attachment.

Probability of Particle–Bubble Attachment

While the collision of the particle and the bubbles relies on the hydrodynamics of the system, the actual attachment of the particle and bubble is more heavily influenced by the chemistry of the system. The theoretical aspects of particle–bubble adhesion have been described previously with the Young-Dupre equation, and the use of DLVO theory, with the hydrophobic force playing a major role. In practice, attachment depends largely on the collector used, and a higher P_A can be expected with more hydrophobic collectors with longer hydrocarbon chains.[13–15] The selectivity, adsorption density, and surface coverage of the collector dictates the surface area on the particle that is amenable to bubble attachment. The pH and Eh (oxidation/reduction potential) conditions of the pulp can also influence P_A by altering the surface chemistries of the particle.[16] A largely oxidising environment may result in the

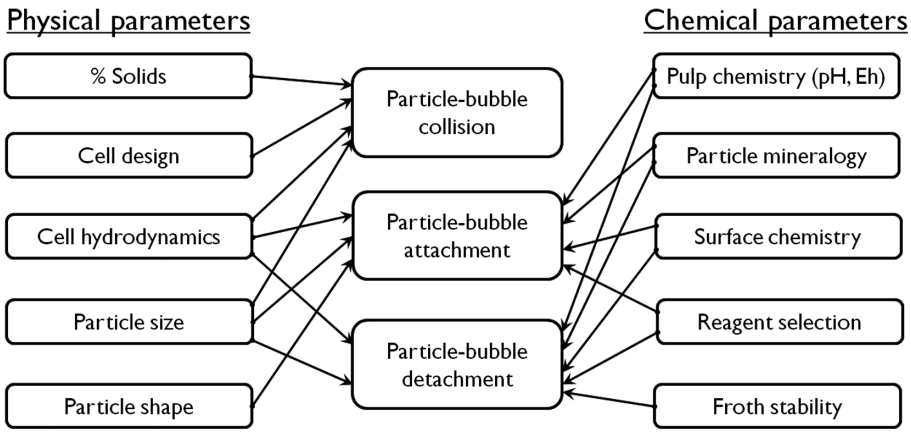


FIGURE 5.21.5 Summary of factors affecting the probabilities of particle–bubble collision, attachment, and detachment.

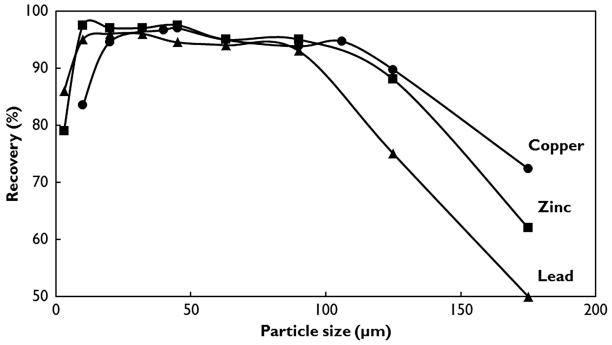


FIGURE 5.21.6 The effect of particle size on recovery. (Data adapted from[19,20].)

presence of hydrophilic oxides and hydroxides on the surface of the desired particles, which would be detrimental to P_A by hampering particle–bubble attachment.[17]

Furthermore, P_A can be affected by the grinding process, which determines the shape and roughness of the flotation feed. For particles of the same size and mineral type, the presence of sharp or jagged edges and rough surface textures can encourage particle–bubble attachment, by reducing surface wettability (and increasing contact angles).[14] Hydrodynamic drainage of the water film between the particle and the bubble also plays an important role in ensuring that collision results in adhesion. Larger particles have more momentum during collision with the bubble, allowing the thin liquid film between the particle and bubble to drain more efficiently, enhancing P_A.

Probability of Particle–Bubble Detachment

After particle–bubble adhesion occurs, the particle needs to remain attached while the buoyancy force of the bubble recovers the particle into the concentrate product. Detachment typically occurs when the net upward force of the particle–bubble moiety, described previously in Figure 5.21.4, is below zero. This can happen if the particle is too large and heavy or if the bubble is too small, and the lifting forces are insufficient to carry the particle to the froth zone.[13–15] High shear forces within the flotation cell may also result in the particle being pulled away from the bubble. Much like P_A, P_D also depends on the pulp and surface chemistries of the system. Conditions that promote strong hydrophobic interactions between the particle and bubble result in lower P_D values, as the particle and bubble are less likely to be separated due to hydrodynamic forces. In the froth zone, the rupturing of bubbles can produce sufficient force to detach and splay the particles.[18] Reagents called frothers are typically added to maintain froth stability, minimizing P_D.

It is important to emphasize that all three factors, P_C, P_A, and P_D, are heavily influenced by particle size, and optimisation of the flotation circuit begins in the grinding circuit. The relationship between particle size and mineral recoveries are as depicted in Figure 5.21.6. Recovery issues with fine particles are typically due to low P_C values, while coarse particles usually suffer from high P_D and low P_C.

5.21.2 MINERALS SEPARATION

A typical flotation system involves a vast number of different minerals in the pulp, each with different properties and surface chemistries. The overall design of a flotation circuit depends on the targeted commodity, which may be contained in one or more mineral types in the ore. The targeted commodity is often a valuable metal or coal that is present in reasonable concentrations, which can be separated from the

non-valuable minerals in a cost-effective manner. A mineral may be considered a product in one circuit, and a gangue in another, depending on the commodity that the circuit is designed to treat. For example, pyrite, which is often associated with copper sulfide minerals, is treated as a gangue in the flotation of copper; however, pyrite may be a desired concentrate product in the flotation of gold, due to the presence of gold in solid solution with the pyrite. Sphalerite would be a desired flotation product in the recovery of zinc, but it is an undesired gangue mineral in the recovery of lead.

The design of flotation circuits is complicated by the varying surfaces properties of the minerals, which can change in the presence of other metal species due to electrochemical and coating interactions. To maintain a high purity concentrate of the desired commodity, flotation reagents are added to ensure that the valuable minerals display hydrophobic properties and the gangue minerals either remain hydrophilic or are rendered hydrophilic. Where the feed contains a high concentration of the desired commodity and a low-to-medium concentrate of gangue minerals, reverse flotation may be employed, whereby the gangue is floated into the froth and removed from the pulp, leaving the valuable minerals in the pulp as a product. An example is the reverse flotation of quartz gangue from iron ore to form a high purity iron product in the pulp stream – the flotation would then be designed to float quartz from the pulp, compared to the direct flotation of iron minerals from the pulp.[21]

5.21.3 FLOTATION REAGENTS

Flotation involves several types of reagents, including surface modification agents such as collectors, activators, and depressants, as well as environmental regulators such as frothers, dispersants, and pH/Eh modification agents, with certain reagents fulfilling multiple roles.[22–24] For example, soluble organic compounds can behave as a frother as well as a collector, while lime, a pH modifier, doubles as a depressant for certain minerals. The types of reagents added will vary from system to system; the chemistry of the reagents added will depend not only on the targeted mineral for the particular reagent, but also on the untargeted minerals. This surface selectivity is important to ensure that the reagent performs the appropriate surface modification only on the targeted particles, and not on other particles.

Collectors

The selection of an appropriate collector is a key consideration in flotation practice, based on the desired product and the type of gangue minerals present in the ore.[25,26] A collector is typically an organic reagent that acts as a selective surfactant, and fulfils two important roles: preferentially adsorbing onto the surface of the desired minerals, and rendering the surface hydrophobic. Collectors typically contain a selective moiety on one end for surface attachment, with the other end being a long hydrocarbon chain, which imparts the hydrophobic behavior. The selectivity of the collector is important to ensure attachment only onto the targeted particles, and not the gangue. For example, cationic collectors such as amines are used for the separation of negatively charged minerals such as quartz from positively charged particles, as the bulk of the collector will be adsorbed onto the quartz due to electrostatic interactions. The use of an insufficiently selective collector can result in concentrate dilution, due to increased gangue recovery. An example is the preference to use thiocarbamates over xanthates in copper flotation in the presence of pyrite gangue, as thiocarbamates are more selective against attachment to pyrite relative to xanthates.

Once adsorbed, the hydrocarbon tail of the collector renders the surface hydrophobic. The increase in contact angles facilitates particle–bubble attachment, allowing particles with a high concentration of the targeted mineral (and hence adsorbed collectors) to be recovered in the product. Small variations in the functional chemistries of the selective moiety, as well as the number and arrangement of carbons in the hydrocarbon chains of the collector, have a significant impact on its efficacy and surface selectivity.[27] Common examples of industrial collectors are as shown in Table 5.21.1.

Depressants

Depressants hamper the flotation of a targeted mineral, by rendering the surface hydrophilic or by blocking collector attachment to the surface. This can be accomplished by selective surface attachment, or by altering the pulp pH or Eh conditions to alter the mineral species present on the surface of the particles. Depressants are typically used to impede the flotation of hydrophobic gangue, as well as gangue minerals with similar chemistries as the targeted flotation mineral, to prevent dilution of the concentrate product. Examples of depressants include cyanide and sodium sulfite for sulfide minerals, and silicates, polysaccharides, starch, tannin, lignite, and xanthan gum for non-sulfide particles.

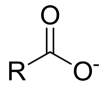
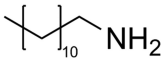
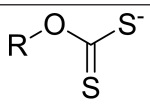
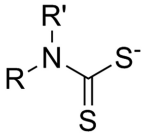
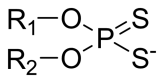
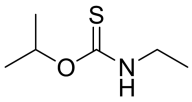
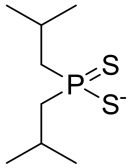
Activators

Activators modify the surfaces of targeted particles to facilitate collector attachment. Unlike collectors, activators do not render the surface of the attached particle hydrophobic, rather, activators provide sites for collector adsorption on surfaces that are inactive. For instance, the adsorption of copper sulfate onto the surface of sphalerite provides an attachment site for xanthate collectors. A common use of activators is to remove the effect of depressants in an earlier flotation stage, to enable the flotation of a previously depressed mineral. Conversely, a sub-class of depressants called deactivators can be used to remove the effect of activators from a prior flotation stage. Examples of common activators include sodium sulfide, copper sulfate, and lead nitrate.

Frothers

Frothers are used to maintain a stable froth zone, improving the carrying capacity of the flotation bubbles and ensuring that the bubbles do not break prior to recovery into the

TABLE 5.21.1 Typical Flotation Collectors

Mineral	Example Collector	Example Chemical Structure	Mechanism
Oxides eg. hematite, phosphates eg. apatite	Anionic collectors: long chain fatty acids and salts of fatty acids (eg. oleic acid/ sodium oleate), petroleum sulfonates		Electrostatic attraction, chemisorption to particle surface; anionic surfactant with cationic oxide surface
Oxides and silicates eg. quartz, mica, feldspar	Cationic collectors: fatty amines, dodecylamine		Electrostatic attraction to particle surface; cationic surfactant with anionic oxide surface
Sulfides eg. chalcopyrite, chalcocite, covellite, sphalerite, galena	Xanthates (eg. Potassium amyl xanthate, sodium ethyl xanthate)		Electron donor-acceptor model; chemisorption to the metal sulfide
	Dithiocarbamates		Electron donor-acceptor model; chemisorption to the metal sulfide
	Thiophosphates		Electron donor-acceptor model; chemisorption to the metal sulfide
	Thionocarbamates		Electron donor-acceptor model; chemisorption to the metal sulfide
	Dithiophosphinates		Electron donor-acceptor model; chemisorption to the metal sulfide
Coal	Kerosene, diesel	Long chain hydrocarbons	Adhesion of insoluble oil droplets to coal enhances surface hydrophobicity

concentrate product. In the absence of frothers, low froth stability can result in the rupturing of bubbles, which produces sufficient force to detach and splay the particles. Examples of frothers include methyl isobutyl carbinol, polyglycols, pine oil, and cresylic acid.

Dispersants

Slimes are ultrafine particles that can coat coarser particles due to electrostatic forces. Slimes' coatings are undesirable, as they can impede collector attachment, and recovery of hydrophilic slimes to the product results in concentrate dilution. When there is an excess of slimes in the flotation feed, dispersants are used to stabilize and disperse the fine particles, preventing the formation of slime coatings. Examples of dispersants include sodium silicate and gum arabic.

pH Modifiers

The charge on the surface of the particles, as well as the chemistry of the collectors and reagents added to the suspension, depend on the pH of the pulp. In order to ensure that the pulp pH remains within the required flotation range, pH modifiers such as nitric acid, sulfuric acid and lime are typically added. Failure to control the pulp pH can hinder recoveries, as the collector is unable to selectively attach onto the targeted surfaces. For instance, xanthate-based collectors generally require alkaline pHs to prevent degradation, while amine-based collectors require acidic pHs to remain protonated. Certain minerals may also be more or less floatable depending on the pH, due to the species present on the surface.

Eh Modifiers

Modification of the pulp potential, or Eh, with Eh modifiers can be important in controlling the oxidative state of the mineral species present on the surface of the particles. For example, the oxidation of sulfides into more hydrophilic oxides or sulfates would not only reduce the floatability of the particles, but will also alter the surface chemistry of the particle for reagent attachment. Example modifiers include peroxide and sodium sulfide.

5.21.4 FLOTATION EQUIPMENT

Flotation cells can be roughly categorized into three main groups: mechanical cells, pneumatic cells, and froth separators.

Mechanical Cells

Mechanical cells are the most widely used flotation instruments, so-called due to the presence of a mechanically driven impeller, as shown in Figure 5.21.7. Air is introduced either through the impeller or through a blower, and the impeller serves to mix the slurry while shearing the inlet air into smaller bubbles. The feed is introduced directly into the pulp phase, where the mechanical agitation encourages particle–bubble attachment. Hydrophobic particles are concentrated in the froth phase at the top of the cells by the bubbles, while hydrophilic particles remain in the pulp phase. The main advantage of mechanical cells is the ability to process high slurry throughputs due to the low residence times resulting from the intensive mixing within the cell. Multiple cells in a bank are also easy to setup through gravity feeding, typically with a "cell-to-cell" arrangement, where a weir or gate is present between adjacent cells. An "open-flow" method is sometimes used, where the tailings are free to flow between the cells. One downside with mechanical cells is the wear on the rotating parts by the abrasive mineral particles, necessitating regular maintenance. Examples of mechanical cells include those produced by Agitair, Aker, Booth, Denver, Dorr-Oliver, Outokompu, Sala, Wedag, and Wemco cells,[28] with varying dimensions, aspect ratios, and impeller types. Recent cell developments have trended towards very large cells to enable high production throughputs, with cell volumes up to 700 m^3 and more.

Pneumatic Cells

In contrast to mechanical cells, pneumatic cells do not utilize mechanical impellers for agitation, requiring less maintenance because wear is reduced. Air is introduced through a blower or plunging jet, and dispersed through baffles or perforated plates to generate bubbles of the correct size. High flow rates of air are typically used to provide sufficient agitation and aeration. The most commonly used type of pneumatic cells is column cells, so-called due to the vertical height of the cell, depicted in Figure 5.21.8. Compared to mechanical cells, column cells operate at reduced footprints, capital costs, and operational costs, and benefit from reduced gangue entrainment due to a tall froth layer and the presence of wash water assisting with the drainage of hydrophilic particles from the froth phase.[29,30] The absence of an impeller and the general reduction in moving parts also translates to less mechanical wear and reduced maintenance requirements. However, banks of column cells have high slurry residence times, and require high pumping costs to feed the tailings from one cell to another.

An improvement on column cells is the Jameson cell, which is able to produce high-grade concentrates of fine particles at substantially smaller footprints.[31] Jameson cells differ from conventional column and pneumatic cells due to their downcomer design, where the air is drawn into the suspension pneumatically during the jetting of the feed slurry in the downcomer, as shown in Figure 5.21.9. This results in high-intensity mixing, and high probabilities of particle–bubble collision and attachment. Thus, shorter slurry residence times are required for Jameson cells, allowing for more compact designs. The bubble residence time is much greater than in column cells, as the downward flow rate of the slurry is only slightly higher than the upward velocity of the bubbles, effectively leading to higher particle–bubble

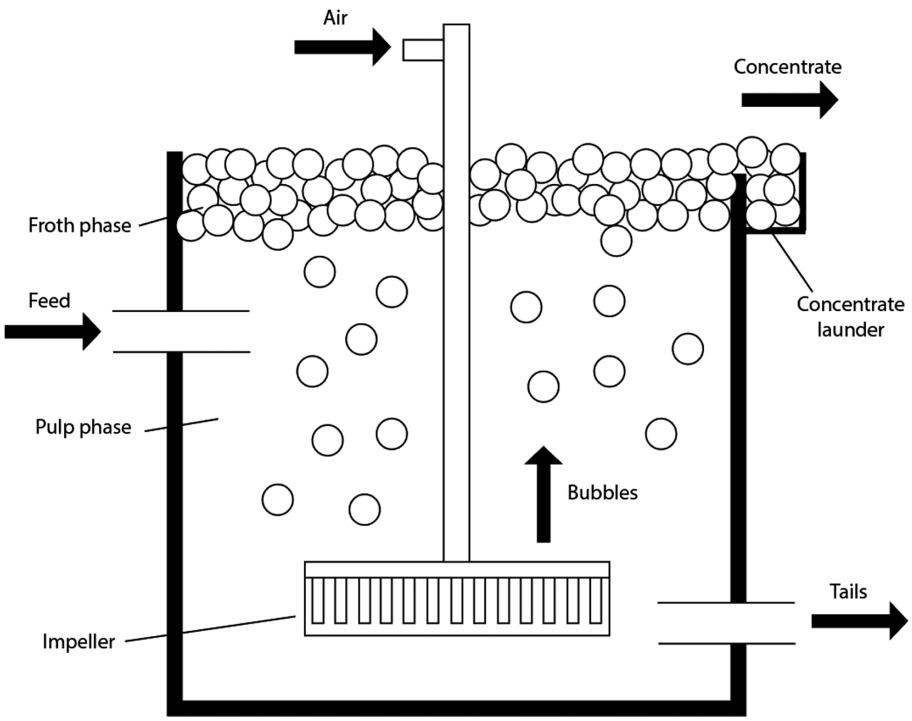


FIGURE 5.21.7 Typical mechanical cell.

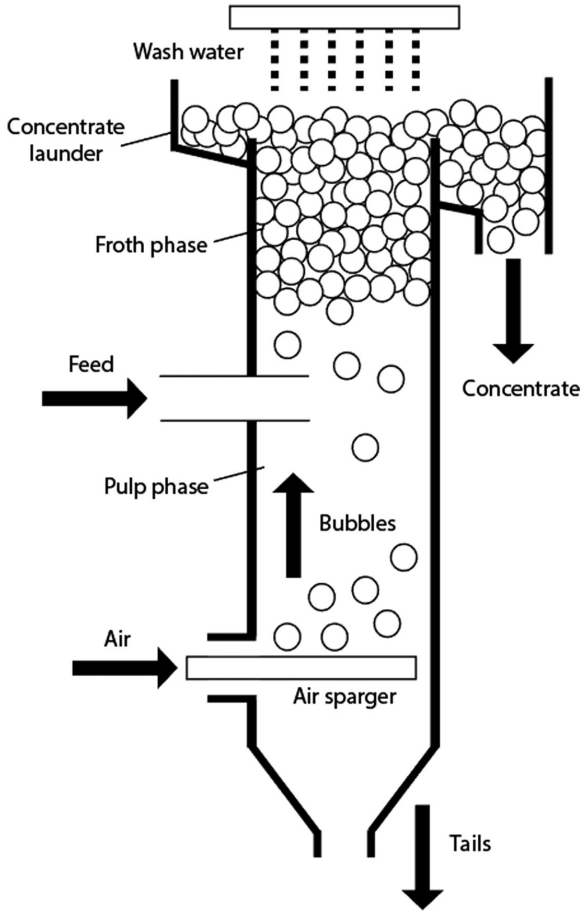


FIGURE 5.21.8 Typical column flotation cell.

contact times. The shearing of the air in the downcomer also produces very fine bubbles, suitable for the flotation of fine particles.

Another pneumatic technique is dissolved air flotation, where the bubbles are generated using a pressure difference. In dissolved air flotation, air is first dissolved into the suspension under elevated pressure.[32] Subsequent exposure of the suspension to atmospheric pressure results in the generation of large quantities of tiny flotation bubbles. While this method may have advantages in the treatment of fine particles due to the presence of fine bubbles, dissolved air flotation cells are more commonly found in water treatment and recycling operations rather than in mineral processing.

Froth Separators

While rarely found in practice, froth separators have been reported to be able to treat coarse particles at significantly higher throughputs compared to mechanical and pneumatic cells.[7] The main difference between froth separators and conventional cells is that the feed is introduced from the top of the froth separator, directly onto the froth phase, rather than into the pulp phase. Hydrophobic particles remain in the froth layer, while hydrophilic particles are drained into the pulp phase and subsequently to the bottom of the cell. In contrast with mechanical and pneumatic cells, an increase in flotation time with froth separators produces cleaner concentrates at lower recoveries, as more particles are drained from the froth.

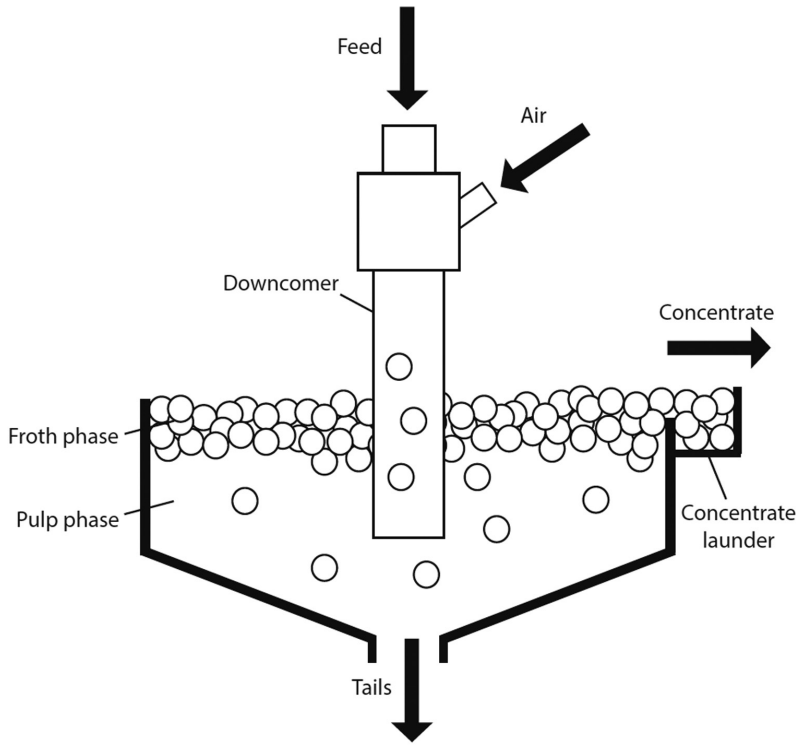


FIGURE 5.21.9 Jameson cell.

5.21.5 PLANT PRACTICE

Circuit Design

Flotation is preceded by the crushing and grinding stages, which reduce the particle size to a suitable range for flotation, typically between 20 to 150 μm. This is an important step for two reasons – to liberate the valuable minerals from the gangue, and to expose the surface of the valuable minerals for reagent attachment. A typical plant involves one or more stages of flotation, depending on the ore mineralogy. In direct flotation, the valuable mineral is concentrated in the product; in reverse flotation, the gangue is floated and removed from the suspension, leaving the valuable minerals in the pulp. Each stage of flotation involves several flotation banks, with each bank consisting of multiple cells in series.

Figure 5.21.10 depicts a typical flotation circuit. Flotation typically begins with a rougher bank, where the aim is to maximize the recovery of valuable minerals, with less regard for grades. The product from the roughers is sent to the cleaner bank, where the aim is to obtain concentrates of the desired grades. Heavy gangue rejection occurs in the cleaners, through reagent addition and pH/Eh modulation. The rougher–cleaner setup allows for significant cost savings on reagents, as the feed to the cleaners, where the bulk of the depressants and pH modifiers are used, represents a smaller flow rate relative to the rougher feed. Subsequently, the concentrate from the cleaners is sent to a leaching or smelting stage. This is often preceded by a thickening or dewatering stage. It is also common for the dried concentrate to be sold or transported for further processing at a different site. The tailings from the cleaners are typically returned to the roughers. The cleaner tailings are generally particles that contain a sufficient area of exposed valuable mineral to be recovered from the roughers, but are not high enough in purity to be collected in the cleaners. Hence, the recycle stream often goes through a regrind stage, which improves mineral liberation.

In contrast to the rougher concentrate, the tailings from each rougher cell are sent down the rougher bank, with the tailings from the last cell being sent to the scavengers. The scavenging stage serves as the final chance at recovering any liberated valuable minerals missed in the roughing and cleaning stages, before the stream is transported to the next stage. The concentrate from the scavengers is typically of medium-grade, and is combined with the cleaner tailings to be recycled to the rougher feed after regrinding. Tailings from the scavenger bank are disposed into the waste thickener, or transported to subsequent stages to recover different minerals.

A single flotation stage is generally sufficient for feed streams containing only a single mineral of interest. Where two or more valuable minerals are present, multi-stage or differential flotation may be used to recover the product in separate circuits, each with its own set of roughers, cleaners and scavengers. Each circuit operates under different conditions, such as pH, Eh, collector type, collector dosages, and possibly different cell types. A depressant may be required in multi-stage flotation, if the different minerals occurring in the same ore deposit display similar surface chemistries in terms of collector attachment. For example, in the multi-stage flotation of chalcopyrite in the first stage and pyrite in the second stage, pyrite is typically depressed in the initial copper flotation stage through pH modulation, as most copper sulfide collectors are also selective towards pyrite. An activator may be added in subsequent flotation stages to refresh the pyrite surfaces for collector attachment. The order in which the minerals are recovered depends on factors such as the natural hydrophobicity of the minerals, depressant efficiency, and the feed grades. To reduce reagent costs and to maximize recovery, minerals that are naturally hydrophobic, less susceptible to depressants, and consist of a larger part of the feed are removed first. Alternatively, flotation may be combined with other mineral processing techniques for the treatment of ore deposits containing multiple minerals of value. For example, magnetic separation may be used for the initial removal of paramagnetic product, followed by a single flotation stage for diamagnetic minerals.

Plant Example

As an example of plant practice involving multi-stage flotation, the flow sheet of the Matsumine mill plant in the Hanaoka mine in Japan is shown in Figure 5.21.11. The mill was closed in 1995 for economic reasons, but a number of technological developments were achieved with respect to complex sulfide ore processing. The treated ore was a complex

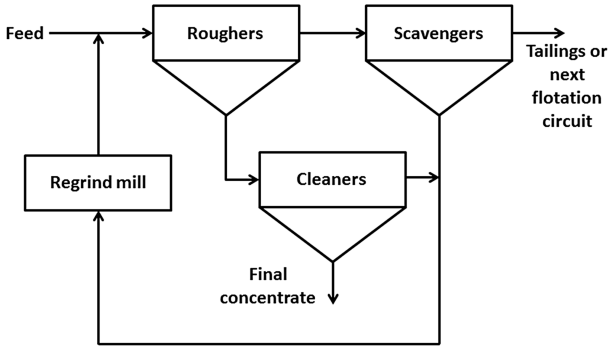


FIGURE 5.21.10 Example circuit arrangement.

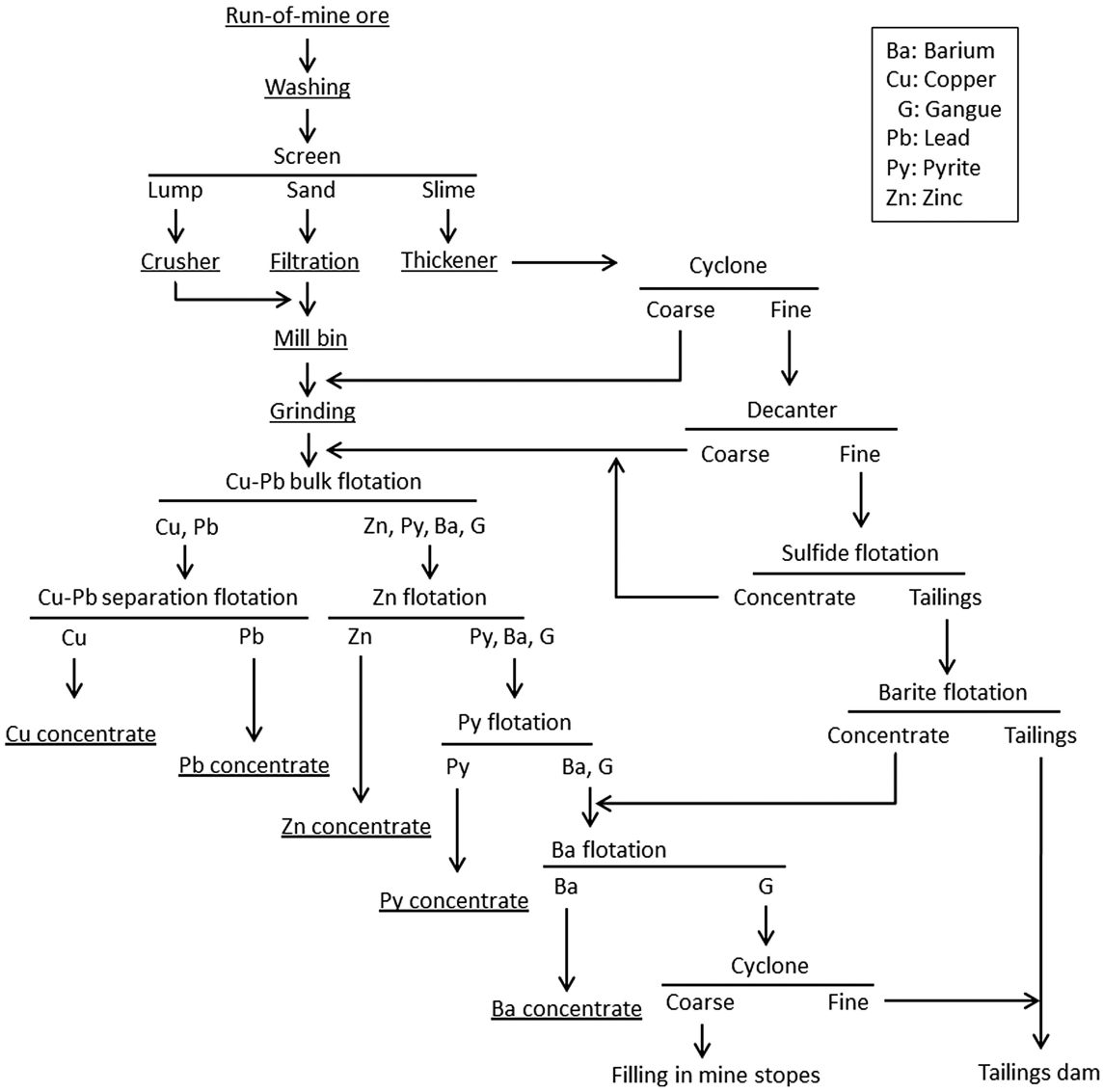


FIGURE 5.21.11 Flowsheet of Matsumine processing plant.

sulfide ore, locally called "Kuroko" (black ore), which was composed of fine-grained minerals. The main sulfide minerals were chalcopyrite, pyrite, galena, and sphalerite, whereas the non-sulfide minerals included barite, gypsum, sericite, chlorite, kaolinite, montmorillonite, and quartz. After the ore was crushed down to less than 100 mm in size at the underground crushing site, the run-of-mine ore was conveyed up to the mill plant. The ore was then washed and screened to 3 size fractions – the lump (>25 mm), the sands, and the slimes. Subsequently, the washed lump ore was transported to the secondary crushing section where the size of the ore was reduced to less than 25 mm. The sand fraction and the product of the secondary crushing section were combined as the feed of the grinding stage. At the grinding section, material was ground down to around 50 μm in size by two-stage grinding, namely the rod–ball mill grinding circuit, to produce the flotation feed.

In the flotation section, the flotation circuit consisted of five sub-circuits to recover the following:

1. Bulk Cu-Pb concentrate in the bulk flotation of copper sulfide minerals and galena using diethyldithiophosphate as a collector after conditioning the flotation feed with sulfur dioxide gas and lime at pH 4 – 5.5.
2. Cu concentrate in the copper mineral flotation by heating the bulk Cu-Pb slurry to about 70°C to depress galena, the tailings being the Pb concentrate.
3. Zn concentrate in the activated sphalerite flotation with copper sulfate as an activator and xanthates as collectors when the bulk flotation tailings were used as the feed.
4. Py concentrate in the flotation of pyrite with xanthate after adjusting the pH of pulp to 3.5.
5. Ba concentrate in the flotation barite with alkyl-sulfonate as a collector at pH 6.0.

Generally, each sub-circuit consisted of rougher, scavenger, and cleaner steps. The slimes obtained at the washing screen stage is thickened in a thickener and then treated through a

specially designed slime-process circuit including cyclones, decanters, and flotation banks. The products of the slime-processing circuit were fed to appropriate sections of the principal concentration circuit, while the tailings were discarded at the dam.

5.21.6 CHALLENGES IN FLOTATION

As with most processes in mining, froth flotation faces the perpetual challenges of energy and water consumption, costs, and environmental impact. Current and future difficulties in flotation can be broadly summarized as follows:

Depletion of High-Grade Deposits

Average grades worldwide have declined substantially over the past few decades due to the gradual depletion of rich ore deposits.[33] This has led to increasing interest in the treatment of low-grade resources, as well as complex ore deposits. However, complex ores are more costly and difficult to treat, as the increase in mineral types and associations usually lead to an increase in flotation stages and reagent consumptions, especially in the presence of multiple species (especially gangue minerals) displaying surface chemistries and properties similar to the targeted particles. Furthermore, low-grade and complex resources require fine grinding to sufficiently liberate the valuable minerals from the gangue, requiring additional energy costs for grinding. In addition, a large portion of the resulting fines are often smaller than 10 μm in size, below the optimal range for flotation recovery.[19,34] The difficulty in treating these particles stems from (a) bubble streamline issues, which impedes particle–bubble contact, (b) slimes coatings, (c) entrainment, and (d) large surface areas, leading to rapid oxidation rates.

Trace Toxic Compounds

Another challenge is the treatment of ore deposits containing trace to moderate amounts of toxic minerals such as arsenic-containing compounds,[35] which result in environmental issues when processed downstream in smelters. Heavy regulatory costs are imposed on saleable concentrates exceeding the trace limit for toxic compounds. These toxic compounds are typically difficult to remove in flotation due to poor liberation, and because they express similar surface properties and collector responsiveness as non-toxic valuable minerals.

Water Quality

The sensitivity of the flotation medium to electrolytes means that clean water is often required for optimal performance, incurring a high cost in the transport of water to remotely located plants. Clean water is especially important in the presence of anionic or cationic collectors, as high salt concentrations can result in screening of the surface charges.[36,37] Furthermore, the solids content required for flotation is typically too low for downstream processes, and the excess water recovered from the dewatering of the flotation outlet streams is often not reused in the flotation circuit due to the presence of multiple reagents. The result is high water consumptions, along with high infrastructure costs for the pumping and storage of clean water. To tackle this issue, there have been several studies on flotation using seawater. While the results indicate that some circuits can tolerate the presence of salt without a significant loss in performance, the recovery is highly ore-dependent, along with corrosion issues with the use of salty water.

5.21.7 EMERGING TECHNOLOGIES

Techniques to tackle the issues mentioned previously typically involve physical means, altering the hydrodynamics within the cell to cope with the ore, as well as chemical methods, developing new reagents better suited to the treatment of complex ores.

Preconditioning in the Grinding Stage

Optimisation of the grinding stage can substantially benefit flotation performance, due to the influence of milling techniques on the size, shape, liberation, and surface roughness of the particles entering the flotation circuit.[38,39] Particles of different aspect ratios and sphericities have been shown to demonstrate differing particle–bubble attachment probabilities, with sharp edges and flat surfaces benefiting adhesion. Partial collector dosage is sometimes conducted in the milling circuit, to facilitate collector adsorption to the freshly exposed particle surfaces. In this instance, milling with fracture and impact grinding may be preferred over erosion-based grinding, as the collector may be physically removed from the particle surface through erosion. Furthermore, electrochemical interactions between the grinding media and the ground feed may result in the production of oxidized species on the surface, and the use of costlier stainless steel media (containing chromium and nickel) can provide improved recoveries over cheaper steel-based materials.

Split Flotation

Due to differences in surface areas and particle hydrodynamics, different reagent dosages and flotation conditions are typically required for the optimal recovery of fines relative to coarse particles. Fine particles, for instance, usually require high shear rates to help with particle–bubble contact. A typical flotation circuit attempts to strike a middle ground in terms of reagent and shear requirements, rather than optimising for either fine or coarse particles. In split flotation, the fine and coarse particles are sized (typically at a cut size between 20 to 50 μm) and treated separately in different circuits that are optimized for the particle size, leading to an overall improvement in grades and recoveries.

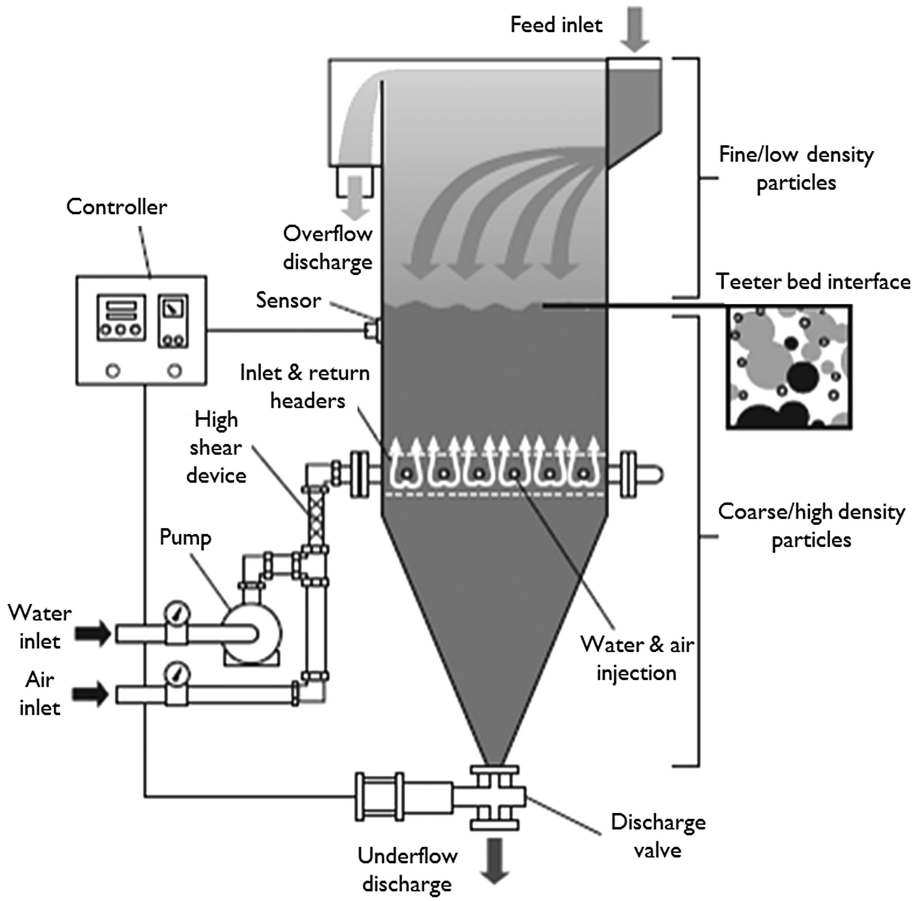


FIGURE 5.21.12 Hydrofloat fluidized bed for the flotation recovery of coarse particles (image provided courtesy of Eriez Flotation).

Coarse Flotation

While flotation has traditionally been used for the treatment of fine particles, the flotation of coarse particles above 300 μm in size has emerged in recent years as a popular topic, due to several advantages. As a preliminary screening stage, coarse flotation is able to remove a large portion of low-grade coarse material prior to further milling to finer sizes, reducing grinding energy and costs due to the lower throughput. Furthermore, the removal of low-grade coarse material increases the average feed grade for subsequent flotation stages. Compared to gravity separation, coarse flotation is able to separate composite particles with similar densities, as the high-grade material is expected to have larger exposed surface areas of the targeted minerals for collector attachment. Coarse flotation also combines well with split flotation methods. One downside of screening with coarse flotation is the possible loss of fine valuable minerals locked up within larger composite particles, if the composites do not contain sufficient exposed surfaces of such minerals for collector attachment. Furthermore, there are limitations with particle buoyancy, where the bubbles are unable to float the heavier coarse particles to the froth layer. This can be circumvented with the utilization of fluidized beds, using the change in bed density to enhance the buoyancy effect. Current strategies for coarse flotation include the Jameson fluidized bed for coarse flotation,[40] and the Eriez Hydrofloat,[41] as shown in Figure 5.21.12.

Flocculation-Flotation

The flocculation-flotation technique aims to alleviate the challenge of recovering fines below 20 μm in size through the flocculation of valuable fines into larger particles within the optimal size range for flotation.[21,42] The flocculation can occur by chemical means, with the use of selective flocculants,[43] multi-functional temperature-responsive flocculant/collectors,[44] and hydrophobic/shear flocculant/collectors,[45,46] or by physical methods, with the use of Proflote[47] (which selectively aggregates paramagnetic minerals) or floc generators.[48] Although this technique can substantially enhance recoveries, one downside is the physical entrapment of unwanted gangue particles within the formed aggregates, resulting in diluted concentrate grades.[49] An additional cleaning stage is likely required to maintain high grades in the final product.

REFERENCES

1. Pryor, E. J., *Mineral Processing*, Springer, Netherlands, 1965, ch. 17, 457–519.
2. Fuerstenau, M. C., Jameson, G. J., Yoon, R. H., *Froth Flotation: A Century of Innovation*, Society for Mining, Metallurgy, and Exploration, Littleton, Colorado, 2007.
3. Fuerstenau, M. C., Han, K. N., *Principles of Mineral Processing*, Society for Mining, Metallurgy, and Exploration, Englewood, CO, 2003.

4. Sutherland, K. L., Wark, I. W., *Principles of Flotation*, Australasian Institute of Mining and Metallurgy, Melbourne, 1955.
5. Hornsby, D., Leja, J., *Surface and Colloid Science*, ed. E. Matijević, Springer, Boston, Massachusetts, 1982, vol. 12, ch. 3, 217–313.
6. Woods, R., *Comprehensive Treatise of Electrochemistry: Electrochemical Processing*, eds. J. O. M. Bockris, B. E. Conway, E. Yeager, R. E. White, Springer US, Boston, Massachusetts, 1981, 571–595.
7. Wills, B. A., Finch, J. A., *Wills' Mineral Processing Technology (Eighth Edition)*, Butterworth-Heinemann, Boston, Massachusetts, 2016, DOI: https://doi.org/10.1016/B978–0-08-097053-0.00012-1, 265–380.
8. Derjaguin, B. V., Dukhin, S. S., *Prog. Surf. Sci.*, 43, 241–266, 1993.
9. Verwey, E. J. W., Overbeek, J. T. G., van Nes, K., *Theory of the Stability of Lyophobic Colloids: The Interaction of Sol Particles Having an Electric Double Layer*, Elsevier Publishing Company, 1948.
10. Omota, F., Dimian, A. C., Bliek, A., *Chem. Eng. Sci.*, 61, 823–834, 2006.
11. Shultze, H. J., *Physio-Chemical Elementary Processes in Flotation*, Elsevier Science, New York, 1984.
12. Laskowski, J., *Miner. Sci. Eng.*, 6, 223–235, 1974.
13. Ralston, J., Fornasiero, D., Hayes, R., *Int. J. Miner. Process.*, 56, 133–164, 1999.
14. Chau, T. T., Bruckard, W. J., Koh, P. T. L., Nguyen, A. V., *Adv. Colloid Interface Sci.*, 150, 106–115, 2009.
15. Yoon, R. H., *Int. J. Miner. Process.*, 58, 129–143, 2000.
16. Kulkarni, R. D., Somasundaran, P., *Colloids Surf.*, 1, 387–405, 1980.
17. Guy, P. J., Trahar, W. J., *Flotation of Sulphide Minerals*, ed. K. S. E. Forssberg, Elsevier, New York, 1985, 63–71.
18. Ata, S., *J. Colloid Interf. Sci.*, 338, 558–565, 2009.
19. Trahar, W. J., Warren, L. J., *Int. J. Miner. Process.*, 3, 101–131, 1976.
20. Batterham, R., Moodie, J. P., Centenary of flotation symposium, Brisbane, Australia, AusIMM, 2005.
21. Bagster, D. F., Gordon, J. H. R., Linkson, P. B., Quan, J. T. B., *6th APCChE congress, 21st Chemeca*, Melbourne, Australia, 1993.
22. Cytec, *Mining Chemicals Handbook: Revised Edition*, Cytec Industries, New Jersey, 2002.
23. Nagaraj, D. R., Farinato, R. S., *Miner. Eng.*, 96–97, 2–14, 2016.
24. Pearse, M. J., *Miner. Eng.*, 18, 139–149, 2005.
25. Crozier, R. D., *Miner. Eng.*, 4, 839–858, 1991.
26. Leja, J., in *Surface Chemistry of Froth Flotation*, Springer US, 1982, ch. 8, 493–547.
27. Quast, K. B., *Miner. Eng.*, 13, 1361–1376, 2000.
28. Young, P., *Mining Magazine*, 146, 1982.
29. Finch, J. A., *Miner. Eng.*, 8, 587–602, 1995.
30. Finch, J. A., Dobby, G. S., *Column Flotation*, Pergamon Press, Oxford, 1990.
31. Harbort, G. J., Jackson, B. R., Manlapig, E. V., *Miner. Eng.*, 7, 319–332, 1994.
32. Rodrigues, R. T., Rubio, J., *Int. J. Miner. Process.*, 82, 1–13, 2007.
33. Mudd, G. M., *48th Annual Conference of Metallurgists*, Ontario, Canada, 2009.
34. Sivamohan, R., *Int. J. Miner. Process.*, 28, 247–288, 1990.
35. Agorhom, E. A., Lem, J. P., Skinner, W., Zanin, M., *Miner. Eng.*, 78, 45–57, 2015.
36. Jeldres, R. I., Forbes, L., Cisternas, L. A., *Miner. Process. Extr. Metall. Rev.*, 37, 369–384, 2016.
37. Wang, B., Peng, Y., *Miner. Eng.*, 66, 13–24, 2014.
38. Crawford, R., Ralston, J., *Int. J. Miner. Process.*, 23, 1–24, 1988.
39. Jameson, G. J., *Miner. Eng.*, 36–38, 132–137, 2012.
40. Jameson, G. J., *New Directions in Flotation Machine Design*, 2010.
41. Fosu, S., Awatey, B., Skinner, W., Zanin, M., *Miner. Eng.*, 77, 137–149, 2015.
42. Forbes, E., *Int. J. Miner. Process.*, 99, 1–10, 2011.
43. Somasundaran, P., Das, K. K., Yu, X., *Curr. Opin. Colloid Interf. Sci.*, 1, 530–534, 1996.
44. Ng, W. S., Sonsie, R., Forbes, E., Franks, G. V., *Miner. Eng.*, 77, 64–71, 2015.
45. Song, S., Lopez-Valdivieso, A., Reyes-Bahena, J. L., Bermejo-Perez, H. I., *Colloids Surf., A*, 181, 159–169, 2001.
46. Akdemir, Ü., *Powder Technol.*, 94, 1–4, 1997.
47. Engelhardt, D., Ellis, K., Lumsden, B., *Centenary of flotation symposium*, Brisbane, Australia, 2005.
48. da Rosa, J. J., Rubio, J., *Miner. Eng.*, 18, 701–707, 2005.
49. Yu, S., Attia, Y. A., in *Interfacial Phenomena in Biotechnology and Materials Processing*, ed. Y. A. Attia, B. M. Moudgil, S. Chander, Elsevier, Amsterdam, 1988, 503–514.



Taylor & Francis
Taylor & Francis Group
http://taylorandfrancis.com

5.22 Electrostatic Powder Coating

Ken-ichiro Tanoue

Electrostatic powder coating has been widely utilized for surface finishing in many industrial applications.[1,2] Recently, the coating has been investigated for use in pharmaceutical manufacturing,[3,4] in drug-eluting stents,[5,6] and in food processing.[7,8] Since the coating process does not use solvents, it is becoming increasingly attractive as a possible new clean air standard for volatile organic compounds. The coating system consists of powder coating guns, powder feeding machine, powder coating booth, and powder collecting machine. It is important to effectively combine the equipment for various objectives.

5.22.1 COATING MACHINES

Different configurations for coating guns have been proposed, and they may use two distinct techniques for powder charging. One is corona-charging and the other is tribocharging. Furthermore, other coating machines have been developed.

Corona-Charging Guns

Figure 5.22.1 shows a corona-charging gun. Powder particles are assembled with air and fed from a nozzle of the gun as a gas–solid two-phase flow. A needle electrode is set in the tip of the nozzle. Negative high voltage is applied on the needle electrode in a range of about –60 kV to –100 kV. At this time, a high electric field is formed between the needle and grounded objects. The powder is exposed to ionized air flow, and corona-charging occurs. With a continued increase in charge collection by particles, electric field strength E will increase until a certain value is reached and this results in a situation where no further transport of ions on the particle is possible. This limiting value of surface charge q, the Pauthenier limit,[9] is expressed mathematically by the following relationship:

$$q = 12\pi\varepsilon_0 \frac{\varepsilon_r}{\varepsilon_r + 2} r_P^2 E \qquad (5.22.1)$$

where

ε_0 is the permittivity of free space, 8.854×10^{-12} Fm^{-1}
ε_r is the relative permittivity of the powder particle
r_p is the radius of the particle
E is the electric field strength

Particles transport toward the objects by coulombic force and drag force, and then deposit. This coating gun has been utilized for almost all powder particles. However, the presence of excess free ions in the booth can lead to an abnormal kind of discharge named back corona or back ionization.[10–12] As a result, it reduces the particle charge and causes a drop in deposition efficiency. New corona guns with an earth ring to collect free ions have been developed to prevent the effect.[13]

Tribocharging Guns

Figure 5.22.2 shows a tribocharging gun. Powder particles are assembled with air flow and they collide with the inner wall of the gun. At this time, tribocharging of particles occurs. As the inner wall of the gun is commonly made of polytetrafluoroethylene, the powder particles are mainly charged positively on a basis of contact potential difference. Then the charged powder particles are ejected from a nozzle of the gun. As a gun of this kind needs no high-voltage generator, the coating system is very simple and has the following merits:

1. Even if we touch the tip of the nozzle, we don't receive an electric shock.
2. As an electric field hardly occurs between guns and objects, the system can uniformly coat objects with some concave parts.
3. There are no free ions in the coating booth. Therefore, the back corona seldom occurs.

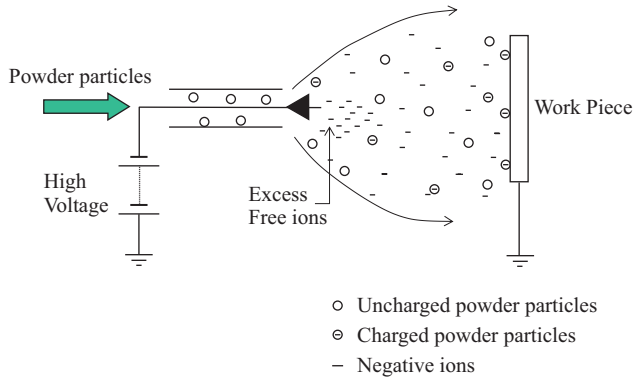


FIGURE 5.22.1 Corona-charging gun.

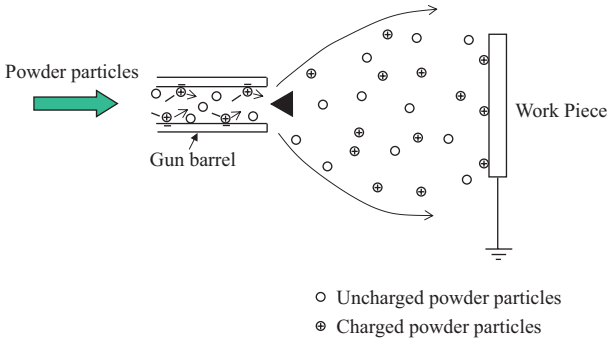


FIGURE 5.22.2 Tribocharging gun.

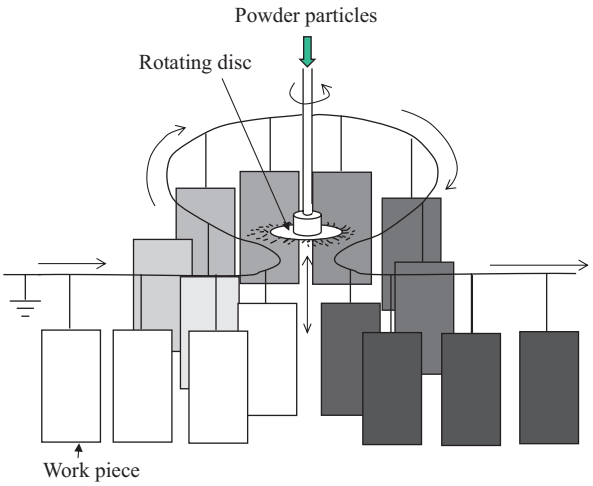


FIGURE 5.22.3 Disk-type coating machine.

However, it is difficult to control the charge freely because the system is influenced strongly by relative humidity and room temperature,[14] contact potential difference[15,16] between particle and inner wall of the gun, particle size,[17] and air velocity[18] in the gun. Furthermore, the tribocharge depends strongly on the tangential impact velocity of the powder particles.[19–20]

Disk-Type Coating Machine (a Kind of Corona-Tribocharging Gun)

Figure 5.22.3 shows the disk-type coating machine. In this coating machine, the disk plate, which is made of resin, is installed at the outlet of the powder. The powder particles transported by the powder feeding machine with air flow are spouted out uniformly from the edge of the disk. Work piece objects are carried by a loop-type conveyor around the disk, as shown in Figure 5.22.3. The coating machine is expected to have six times the ability of the aforementioned guns.

Transfer Efficiency

Transfer efficiency (TE) of electrostatic powder coating is commonly higher than that of traditional coating. TE is given by,

$$\mathrm{TE}[\%] = \frac{\text{Mass of material on the target}}{\text{Mass of material sprayed}} \times 100 \qquad (5.22.2)$$

Ratanatriwong and Barringer investigated the influence of particle size and the kind of particles on TE using corona-charging gun.[21] For nonelectrostatic powder coating, regardless of the kind of powder particles TE increased with particle size and then approached to the constant TE. On the other hand, for electrostatic powder coating, TE was greater than 80% under 160 μm except for Malic acid particles. Mayr and Barringer studied TE of sucrose particles for various electrostatic powder coatings.[22] TE of nonelectrostatic powder coating increased linearly with particle size while TE of electrostatic powder coating increased slightly. Among the electrostatic powder coatings, TE of the corona-charging method was higher than that of tribo charging method.

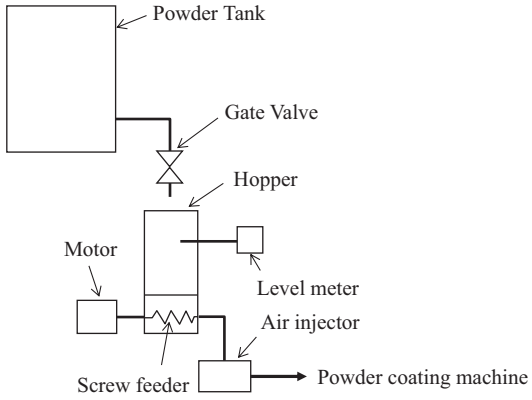


FIGURE 5.22.4 Powder feeding machine with screw feeder.

5.22.2 POWDER FEEDING MACHINE[23]

In order to feed powder particles from a vessel to the gun, a pneumatic conveying system with an air injector is mainly utilized as an easy and low-priced method. However, it is difficult to keep a stable feed of the powder particles using only an air injector. Recently, a few kinds of powder feeders, which are able to supply particles with a constant feed rate, have come onto the market.

Screw Feeder

This type has been mostly applied to the combination with powder coating, as shown in Figure 5.22.4. The apparatus consists of a powder tank, powder-feeding section with screw feeder, and an air injector. The powder particles are fed to the air injector with high accuracy (about ±2%) by controlling the rotational speed of a motor. In this case, the injector has a role that only conveys the powder particles to the coating machine. Therefore, the powder feed rate does not vary even if air flow rate to the air injector is changed. To prevent changing the concentration of the powder in a hopper, the powder tank and the powder feeding section are separated through a control valve. The amount of powder particles is monitored by a level meter and controlled by the gate valve.

Table Feeder

The construction of this apparatus is almost the same as for the screw feeder. The feeder section consists of a turntable, motor, hopper, and air injector. The powder particles on the table are conveyed by air force or a mechanical scraper to the injector. The flow is smoother than in the screw feeder.

5.22.3 POWDER COATING BOOTH

As there are many combinations of powder coating booths and powder collectors, it is necessary to select the booth carefully according to configurations and dimensions of the

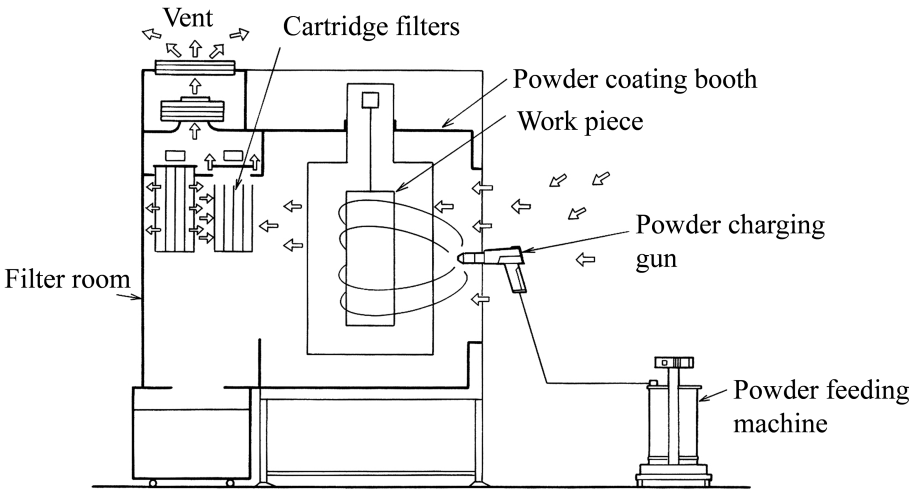


FIGURE 5.22.5 Powder coating booth using cartridge filters.

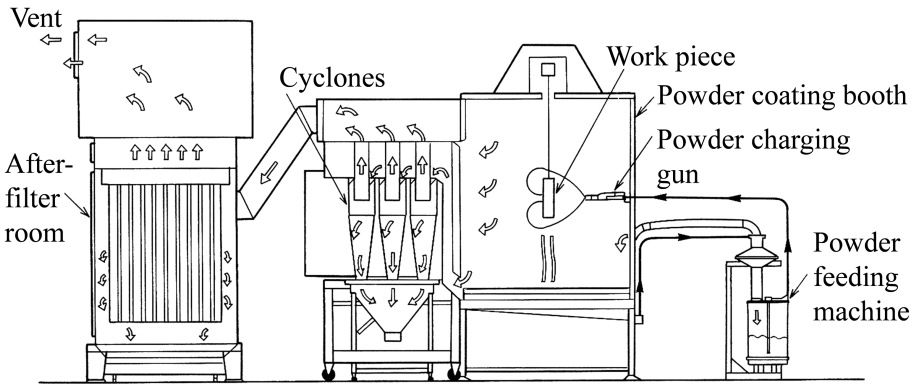


FIGURE 5.22.6 Powder coating booth using multicyclone and after-filters.

objects, ensuring space, change of colors, and protection of the working area. In this section, characteristics of representative coating booths are introduced.

Cartridge Filter Type

In Figure 5.22.5, cartridge filters are set on a wall of the coating booth, and suspended powder particles in the booth are collected directly by suction fan. In order to change colors of powder, it is necessary to prepare the same number of cartridge filters and suction fans as there are colors. Although the coating booth needs no large space, it is difficult to conduct the multicolor powder coating.

Cyclone after Filter Type

In Figure 5.22.6, precipitation of powder particles are conducted in two stages: cyclones and after-filters. First, most of the oversprayed powder particles are collected by the cyclones. At the second stage, small particles passed through the cyclones are collected by after-filters. This coating booth is available for multicolor coating.

5.22.4 NUMERICAL SIMULATION FOR ELECTROSTATIC POWDER COATING[24–30]

Recently numerical calculation for the electrostatic powder coating has been investigated. The equation of motion of a particle is given by

$$m_P \frac{d\boldsymbol{v}}{dt} = -\frac{\pi D_P^2 \rho C_D \,|\boldsymbol{v}-\boldsymbol{u}|\,(\boldsymbol{v}-\boldsymbol{u})}{8C_C} + m_p\boldsymbol{g} + \sum \boldsymbol{F}_E \tag{5.22.3}$$

where

m_p is the mass of particle
$\boldsymbol{v}$ is the particle velocity
$\boldsymbol{u}$ is the air velocity
D_p is the particle diameter
C_D is the drag coefficient
C_c is the Cunningham correction factor
$\boldsymbol{g}$ is the gravity acceleration
$\boldsymbol{F}_E$ is the electro static force

The right-hand terms in the equation show drag force, gravity force, and electrostatic force, respectively. Charged particles are affected by coulombic force ($\boldsymbol{F}_{E,C}=q\boldsymbol{E}$) and other electrostatic forces, which are described in Section 2.2.1.

Air Flow Field

To calculate the aerodynamic forces acting on a particle is complex. The Navier–Stokes equations are used in evaluating fluid flow conditions and normally include three scalar equations for momentum, one for mass conservation, and one for energy conservation. These equations are given by,[31]

$$\rho\frac{D\boldsymbol{u}}{Dt}=-\nabla p-\left[\nabla\cdot\boldsymbol{\tau}\right]+\rho\boldsymbol{g} \tag{5.22.4}$$

$$\frac{D\rho\boldsymbol{u}}{Dt}=0 \tag{5.22.5}$$

$$\rho\frac{D\boldsymbol{e}_f}{Dt}=-\left(\nabla\cdot\boldsymbol{f}_e\right)-\left(\nabla\cdot p\boldsymbol{u}\right)-\left(\nabla\cdot\left[\boldsymbol{\tau}\cdot\boldsymbol{u}\right]\right) \tag{5.22.6}$$

where

ρ is the fluid density
p is the fluid pressure
$\boldsymbol{\tau}$ is the viscous stress tensor
$\boldsymbol{e}_f$ is total fluid energy
$\boldsymbol{f}_e$ is the energy flux

Furthermore, an equation of state is required in order to couple the mass conservation with momentum conservation via fluid density.

$$\rho=\frac{PM}{RT} \tag{5.22.7}$$

where

M is the molecular weight of fluid gas
R is the universal gas constant
T is the fluid temperature

For common electrostatic powder coating, the air flow field can be treated as incompressible. Furthermore, physical properties in the equations are assumed to be constant because the temperature in the coating booth is almost constant. Therefore, the air flow field can be solved using Equation 5.22.3 and Equation 5.22.4.

As the momentum Equation 5.22.3 includes both the pressure field and velocity field, the fields must be solved individually. SIMPLE[32] and SMAC[33] schemes can be utilized as the representative algorithm in order to calculate the Navier–Stokes equations.

Electric Field

The electric field that is generated due to the imposed voltage between the emitting electrode and the grounded plate can be described by a following Laplace equation,

$$\Delta\Phi=0 \tag{5.22.8}$$

where the potential Φ is related to the electric field $\boldsymbol{E}$ according to $\boldsymbol{E}=-\nabla\Phi$. Since a high voltage is applied between the two electrodes, a corona discharge may take place. The presence of a space charge generated by the corona complicates the electric field solution in the computational domain. Such an electric field with a space charge is governed by Poisson's equation:

$$\Delta\Phi=-\frac{\rho_E}{\varepsilon_0} \tag{5.22.9}$$

where

ρ_E is the space charge density
ε_0 is the electrical permittivity of the gas phase

The Laplace and Poisson equations can be solved by the successive overrelaxation method. A numerical technique proposed by Elmoursi[34] is applicable to obtain a self-consistent solution for an ionic space charge field. The Lagrangian particle-tracking model is coupled with the electric field during the iteration. The procedure is described in the following steps:

1. Solve the electric field under Laplace condition ($\rho_E=\phi$). This provides the initial estimation of the electric field.
2. Calculate particle trajectories with discrete phase model using Equation 5.22.3.
3. Determine the charge density distribution due to the charged powder in the ion drift region.
4. Solve the electric field with space charge.
5. Repeat steps 2–4 until the solution of the space charge field is convergent.

This procedure can be utilized for the numerical simulation of the electrostatic powder coating with corona-charging. On the other hand, for tribocharging, the image force works mainly on the charged particles. If many charged particles are deposited on the work piece object, apparent coulombic force decreases with time and then the particles hardly deposit further. Tanoue et al. have investigated the fact experimentally and numerically.[29,35]

REFERENCES

1. Reddy, V., Dawson, S., *Powder Coating Applications*, Society of Manufacturing Engineers Powder Coating Institute, Alexandria, VA, 1990.
2. Boochi, G. J., *Powder Coating*, 4, 14–18, 1993.
3. Leena, K. P., James, W. M., Rovert, O. W., *Int. J. Pharm.*, 505, 289–302, 2016.
4. Quingliang, Y., et al., *Particuology*, 31, 1–7, 2017.
5. Ravi, K. N., et al., *Pharm. Res.*, 27(1), 72–81, 2010.
6. Leena, K. P., et al., *J. Drug Deliv. Sci. Technol.*, 30, 501–510, 2015.
7. Mulhammad, K. K., Maaten, A. I. S., Karin, S., Remko, M. B., *J. Food Eng.*, 111, 1–5, 2012.
8. Teerarat, L., Sheryl, A. B., *J. Electrostat.*, 77, 44–50, 2015.

9. Cross, J. A., *Electrostatic-Principles, Problems and Applications*, Adam Hilger, Bistol, England, 1987.
10. Masuda, S., Mizuno, A., *J. Electrostat.*, 4, 35–52, 1977.
11. Bayley, A. G., *J. Electrostat.*, 45, 85–120, 1998.
12. Mazumder, M. K., Sims, R. A., Biris, A. S., *Chem. Eng. Sci.*, 61, 2192–2211, 2006.
13. Biris, A. S., et al., *Par. Sci. Technol.*, 19, 199–217, 2001.
14. Nomura, T., Taniguchi, N., Masuda, H., *J. Soc. Powder Technol. Jpn.*, 36, 168–173, 1999.
15. Itakura, T., Masuda, H., Ohtsuka, C., Matsusaka, S., *J. Electrostat.*, 38, 213–226, 1996.
16. Tanoue, K., Morita, K., Maruyama, H., Masuda, H., *AIChE J.*, 47, 2419–2424, 2001.
17. Masuda, H., Iinoya, K., *AIChE J.*, 24, 950–956, 1978.
18. Masuda, H., Komatsu, T., Mitsui, N., Iinoya, K., *J. Electrostat.*, 2, 341–350, 1976/1977.
19. Ema, A., Sugiyama, S., Tanoue, K., Masuda, H., *J. Inst. Electrostat. Jpn.*, 26l, 130–136, 2002.
20. Ema, A., Yasuda, D., Tanoue, K., Masuda, H., *Powder Technol.*, 135–136, 2–3, 2003.
21. Ratanatriwong, P., Barringer, S., *J. Electrostat.*, 65, 704–708, 2007.
22. Mayr, M. B., Barringer, S. A., *J. Food Sci.*, 71-Nr4, E171–E177, 2006.
23. Yanagida, K., Morita, T., Takeuchi, M., *J. Electrostat.*, 49, 1–13, 2000.
24. Woolard, D. E., Ramani, K., *J. Electrostatics*, 35, 373–387, 1995.
25. Chen, H., et al., *Part. Sci. Technol.*, 14, 239–254, 1996.
26. Adamiak, K., *J. Electrostat.*, 40, 395–400, 1997.
27. Ye, Q., Steigleder, T., Scheibe, A., Domnick, J., *J. Electrostatics*, 54, 189–205, 2002.
28. Ang, M. L., Lloyd, P. J., *Int. J. Multiphase Flow*, 13, 823–836, 1987.
29. Tanoue, K., Inoue, Y., Masuda, H., *Aerosol Sci. Technol.*, 37, 1–14, 2003.
30. Husam, O., Castle, G. S. P, Adamiak, K., *J. Electrostat.*, 77, 58–68, 2015.
31. Bird, R. B., Stewart, W. E., Lightfoot, E. N., *Transport Phenomena*, 3rd. Ed., John Wiley, New York, 1960, p. 322.
32. Patanker, S. V., *Numerical Heat Transfer and Fluid Flow*, McGraw-Hill, New York, 1980.
33. Amsden, A. A., Harlow, F. H., The SMAC Method: A Numerical Technique for Calculating Incompressible Fluid Flows, Los Alamos Scientific Laboratory Report LA-4370, 1970.
34. Elmoursi, A. A., *IEEE Trans. Ind. Appl.*, 28, 1174–1181, 1992.
35. Tanoue, K., Yamamoto, M., Ema, A., Masuda, H., *Kagaku Kogaku Ronbunsyu*, 28, 196–201, 2002.



Taylor & Francis
Taylor & Francis Group
http://taylorandfrancis.com

5.23 Multipurpose Equipment

Hisao Makino and Hiromi Shirai (5.23.1, 5.23.2)
Junichi Tatami (5.23.3)

5.23.1 FIXED BEDS

5.23.1.1 Principles and Features

A fixed bed is filled with particles, and mass transfer, chemical reactions, and so forth, between particles and a fluid are induced by passing a fluid through the stationary layer of particles. In a fixed bed, particles of size from mm to cm order are used to maintain a low-pressure loss. Fixed beds are used as a catalytic reactor, an adsorber, absorbers, an extractor, and a regenerative heat exchanger. A high yield, high removal efficiency, and high recovery ratio are obtained because a fluid has a long residence time in a fixed bed. However, in an adsorption process, a regenerative heat exchanger process, and so forth, it is necessary to switch between two or more fixed beds to ensure a continuous operation. In the case of an exothermic reaction, effective temperature control is very difficult in a large fixed bed reactor because a fixed bed has low heat conductivity.

The fluid passing through a fixed bed approximates plug flow, however, the velocity of the fluid near the wall of the fixed bed is higher than that at other positions because of the higher porosity of the particle layer near the wall. In particular, in the case of a reactor with a small diameter, it is necessary to pay attention to the flow near the wall.

The scaling up of a fixed bed is relatively easy when the reaction heat and adsorption heat can be neglected. The diameter of the fixed bed is decided so that the fluid velocity is similar to the velocity before scaling up; this is to prevent a large increase in the pressure loss. As the diameter increases, a non-uniform flow tends to form at the fluid inlet. Therefore, the design of the fluid inlet is very important.

5.23.1.2 Types and Configurations

Fixed beds are classified into three types, an adiabatic-type, a self-heat-exchange-type and a heat-exchange-type, as shown in Figure 5.23.1.[1] An adiabatic-type is used in an adsorber, an absorber, an extractor and a regenerative heat exchanger. In the self-heat-exchange-type, a tube is inserted into a fixed bed reactor. Unreacted fluid flows through the tube and is fed into the reactor. Heat is exchanged from the fluid heated by a reaction to the unreacted fluid through the tube, and the reaction heat can be effectively utilized to heat the unreacted fluid. However, this type of fixed bed is only applied in the case of a low reaction heat because the heat transfer capability is low in the case of a gas. In the heat-exchange-type, the temperature of the particles and fluid is controlled using a heat carrier in the case of a strongly exothermic reaction. In this case, a multistage fixed bed reactor and a multi tubular fixed bed reactor are used.

5.23.1.3 Examples of Application

The processes for adsorption separation and for a catalytic reaction are listed as examples of the application of fixed beds.

Pressure Swing Adsorption (PSA) process

PSA is a typical adsorption process using a fixed bed. In PSA, a gas component is adsorbed selectively at a high pressure, and the adsorbed component is desorbed by reducing the pressure of the adsorber. PSA has four operation processes: pressurization, adsorption, decompression, and desorption. These processes are operated cyclically in a multi-adsorber system.

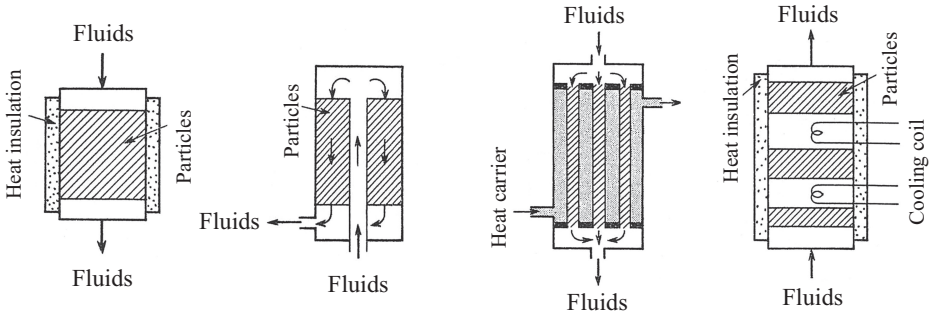


FIGURE 5.23.1 Fixed bed types.

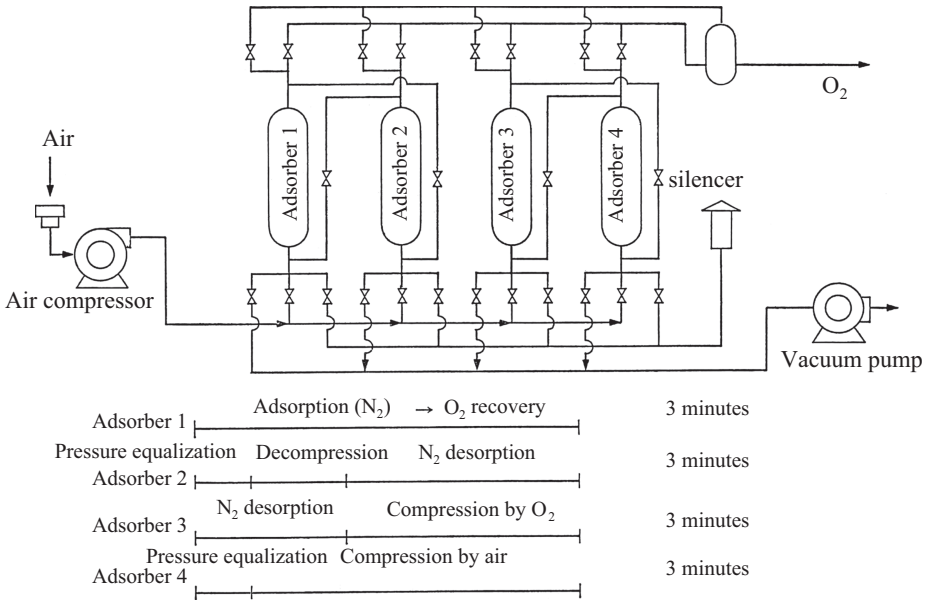


FIGURE 5.23.2 PSA O_2 separation process.

When a product gas component can be adsorbed easily, it is recovered in a desorption process. On the other hand, when a product gas component cannot be adsorbed easily, other gas components are adsorbed, and the product gas component is recovered in an adsorption process. For example, this is applied in the separation of O_2 from air (Figure 5.23.2[2]).

Methanol Synthesis Process

In a fixed bed reactor in which a granulated catalyst (copper-based catalyst, etc.) is packed, methanol (CH_3OH) is synthesized from CO and H_2 in the temperature range from 230°C to 400°C, at pressures from 5 MPa to 40 MPa by the gas phase method.[3] A methanol synthesis reactor is shown in Figure 5.23.3.[4] This reactor is a multistage fixed bed reactor of the indirect-cooling-type because the synthesis is a highly exothermic reaction. In the reactor, cooling tubes are set in the catalyst particle layer. The heat released from this particle layer is removed by the tubes, and the heat is recovered as steam. Various heat-exchange-type fixed bed reactors have been developed.

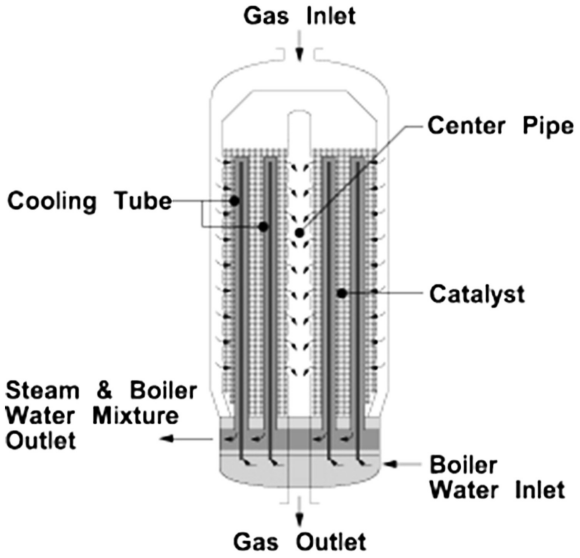


FIGURE 5.23.3 Methanol synthesis reactor (MRF-Z®).

5.23.2 MOVING BEDS

5.23.2.1 Principles and Features

A moving bed is also filled with particles similarly to a fixed bed, and heat and mass transfer, chemical reactions, and so forth, between particles and a fluid are induced by passing a fluid through the moving particle layer. Particles are supplied from the top of the moving bed, move downward by gravity and are discharged from the bottom. In a moving bed, the particle size is similar to that in a fixed bed to maintain a low-pressure loss. The range of roles of a moving bed is wider than that of a fixed bed because continuous operation is possible using a single moving bed. A moving bed is used as a dust collector, a calcination furnace, a gasifier, and a blast furnace, in addition to the uses of a fixed bed. Furthermore, in the broad sense, a stoker furnace and a rotary kiln are classified as moving beds.[5]

In the case of an exothermic reaction, it is difficult to insert a heat exchanger without disturbing the movement of particles in a moving bed. The fluid passing through the moving bed also approximates plug flow, however, the velocity of the fluid near the wall is higher than that at other positions because of the higher porosity of the particle layer near the wall. The flow of particles is also affected by the wall. The velocity of particles near the wall is lower than that at other positions. Similarly to a fixed bed, in the case of a reactor with a small diameter, it is necessary to pay attention to the flow near the wall.

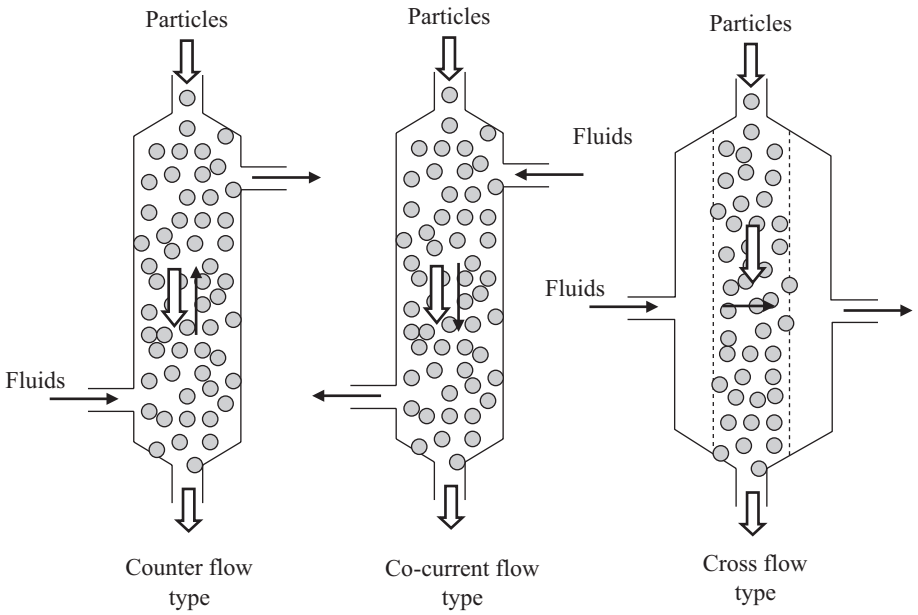


FIGURE 5.23.4 Moving bed types.

5.23.2.2 Types and Configurations

Moving beds are classified into three types as shown in Figure 5.23.4. One is the counter-flow-type, in which a fluid flows upward from the bottom to the top of the moving bed and particles move downward from the top to the bottom. Another is the co-current-flow-type, in which particles move from the top to the bottom and a fluid also flows downward. The third is the cross-flow-type in which particles move from the top to the bottom and a fluid flows horizontally and crosses the current of the particles.

The counter-flow-type is more efficient than the co-current-flow-type for heat and mass transfer and for reactions between a fluid and particles. The co-current-type can be used to prevent the fluidization of particles. The cross-flow-type has a large fluid inlet area and a thin particle layer. Therefore, the pressure loss of the bed can be lower than that of the other types. This type is used for the treatment of large amounts of gas.

5.23.2.3 Examples of Application

The processes for SO_2 removal using activated carbon and a coal gasifier are listed as examples of the application of moving beds.

SO_2 Removal from Flue Gas Using Activated Carbon

A cross-flow-type moving bed is used as a SO_2 removal reactor.[6] As shown in Figure 5.23.5,[7] in the moving bed adsorber, NH_3 is added to a flue gas and SO_2 is adsorbed in the form of ammonium salts ($[NH_4]_2SO_4$ and NH_4HSO_4) on the surface of an activated carbon tablet. The spent activated carbon tablet is discharged from the bottom of the moving bed adsorber. The discharged activated carbon tablet is sent to a moving bed regenerator in which ammonium salts are released and decomposed into SO_2, N_2, and H_2O by heating. The released SO_2-rich gas is recovered as sulfuric acid. The regenerated activated carbon tablet is returned to the moving bed adsorber. This process has already been introduced into a large-scale pulverized coal-fired power station (Figure 5.23.6).

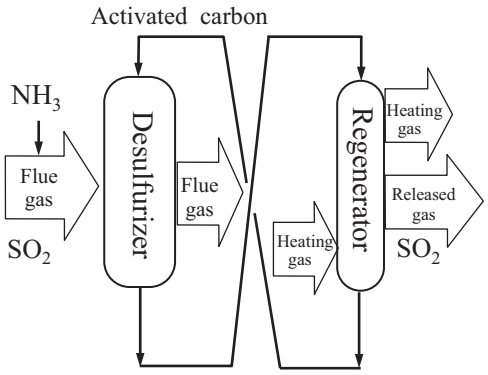


FIGURE 5.23.5 Concept of activated carbon SO_2 removal process.

Coal Gasifier

The gasifier shown in Figure 5.23.7[8] is the moving bed reactor of the counter-flow-type. The size of coal particles supplied from the top of the gasifier is from 3 mm to 30 mm. The gasifying agents used as a fluid are O_2 and steam, which flow from the bottom of the gasifier to the top. They react with coal particles in the temperature range from 750°C to 900°C, at pressures from 2 MPa to 3 MPa, and the generated coal gas is discharged from the top, while coal ash is discharged from the bottom. This gasifier is relatively well known in the world since the generated coal gas was used for the production of a synthetic oil in South Africa.

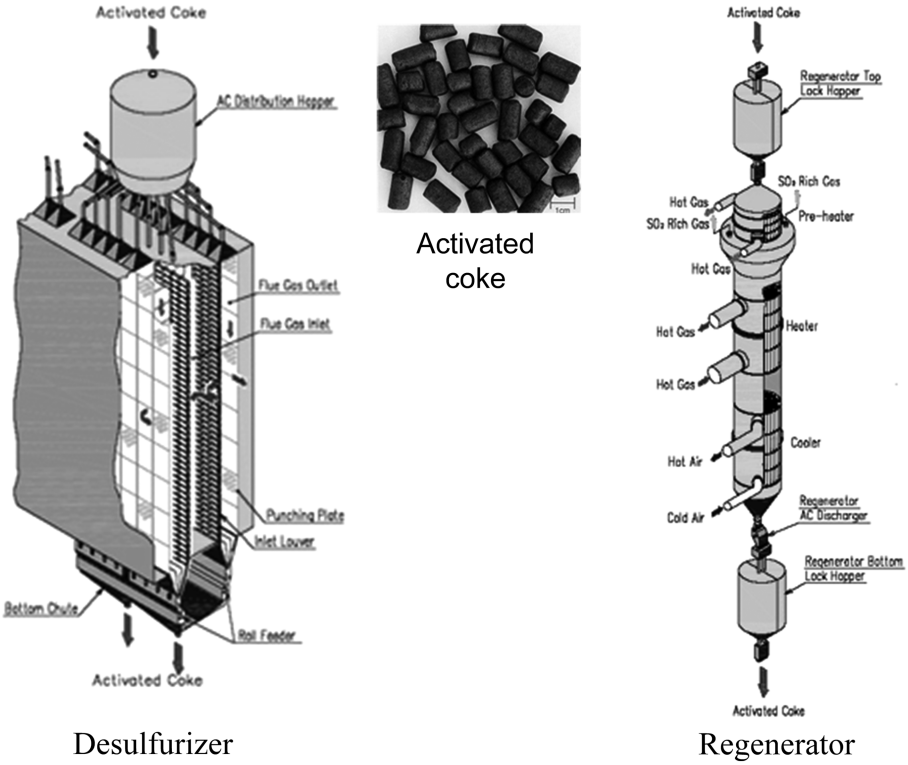


FIGURE 5.23.6 Activated coke desulfurization unit (ReACT) in Isogo thermal power station.

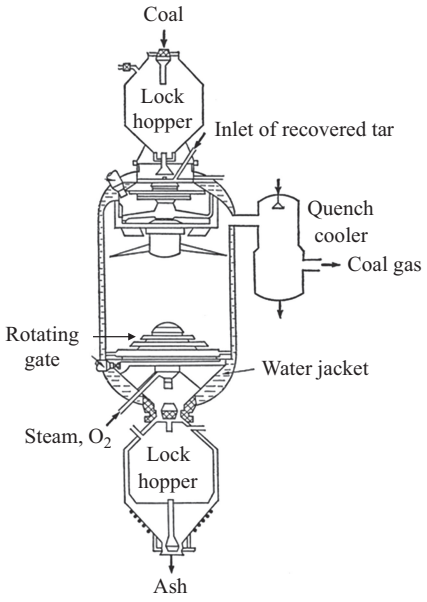


FIGURE 5.23.7 Lurgi gasifier.

5.23.3 ROTARY KILN

The rotary kiln was invented in 1873 by Frederick Ransome. It is one of the devices used to fire materials at high temperature in continuous processes. The products fabricated using the rotary kiln includes cement, refractories, fine ceramic powders, iron ore pellets, and so on. Raw materials are supplied from the upper end of a cylindrical vessel which is slightly inclined, and they gradually move to the lower end and mix by the slope and rotation of the vessel. Attention is currently focused on the rotary kiln because effective and dynamic mixing is needed in order to react to the raw materials rapidly and homogeneously.

Figure 5.23.8 shows the schematic illustration of the rotary kiln for cement production. The geometry of the typical kiln is 4–6 m in diameter, 60–100 m in length, 3–4% in slope, and its rotation speed is 2–4 rpm. The raw materials are fired by heat radiation of the burner flame which is set at the lower end of the kiln. The temperature of the upper end is about 400°C, and maximum temperature of the flame projected from a burner-pipe is about 1450°C. The fuel for the flame is gas, oil, petroleum coke, or coal. The detention time is about 30 min in the cement production. The shell of the kiln is made of steel and the inside is refractory lining to insulate the steel shell from the high temperatures and to protect it from the chemical corrosion by the processed materials.

Continuous and uniform processing during retention is the greatest advantage of the rotary kiln. Many equations have been proposed to estimate the residence time of powders in the rotary kiln. Sullivan proposed the following equation.[9]

$$t = \frac{1.77L\sqrt{\theta}}{pdn} \times f \tag{5.23.1}$$

where

t is time of stay of the material in the kiln [min]
L is length of the kiln [m]
p is slope or pitch of the kiln [°]

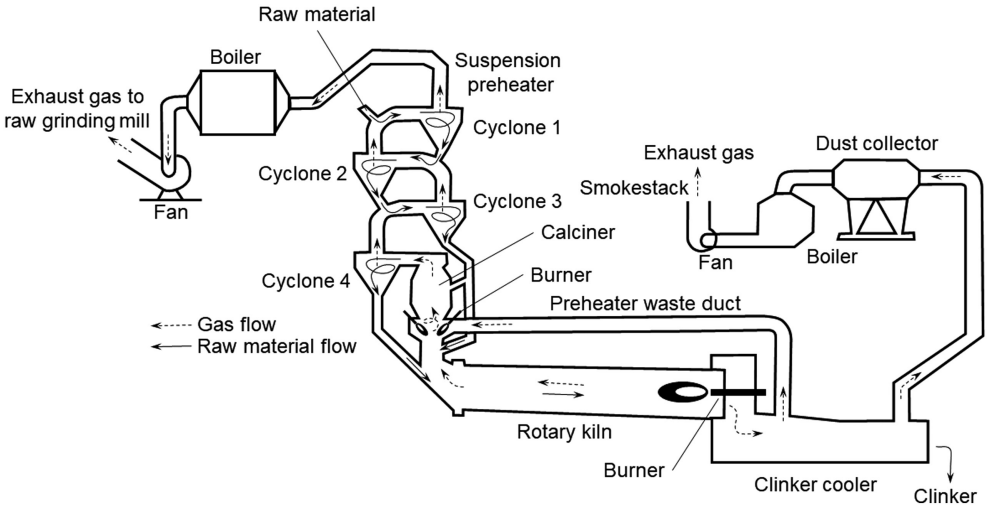


FIGURE 5.23.8 Schematic illustration of the rotary kiln for cement production.

d is diameter of the kiln [m]
n is revolution speed [rpm]
θ is angle of repose of material in the dry condition [°]
f is the correction factor depending on the constriction and obstruction

The value of f is 1 for simple unobstructed rotary kilns, thus this equation is applicable in the case of simply vorticity-based motion of the materials. In other words, it is to be noted that accuracy of the equation should be degraded when adhesive materials or slurry is used.

It is important to estimate the heat balance using a heat transfer model for prediction of the operation condition, optical device design, and saving energy. Simple heat transfer models are classified roughly into two groups taking into account the radiant heat transfer of both a flame and materials and considering a flame as a part of gases. In many cases of the rotary kiln being used for cement production, the model does not distinguish between a flame and flowing gases. These are such simple models that the estimation is carried out easily. Thermal fluid simulation is also developed for detailed analysis of the rotary kiln.

Suspension preheater (SP) is a pre-heating system used in the modern rotary kiln for cement production because of its better heat exchange. The important components of the suspension preheater are cyclones. The raw materials are supplied in the flow of the exhaust gas from the kiln. Furthermore, the new suspension preheater kiln with a precalciner (NSP) is also developed. In the precalciner, calcination of the raw material ($CaCO_3$->$CaO+CO_2$) is carried out. The NSP enables a higher amount of production, lower amount of heat per unit, longer lifetime of the refractories, and lower NO_x emission than the SP.

The rotary kiln has been recently used to produce advanced ceramic powders, which is an indirect-heating-type using ceramics for the retort materials. Use of the ceramic retort enables continuous heat treatment at a high temperature because the ceramics have much better heat and corrosion resistance than the metal retort. Although the ceramic coating by thermal spraying on the metal retort is developed, it has not been widely used yet because the coating is expensive, and it peels off because of thermal expansion mismatch. Sealability is also an important factor to control the atmosphere in the rotary kiln. Therefore, a large ceramic retort is increasingly demanded. In particular, the alumina retort is strongly expected in terms of the balance of strength, heat resistance, and production cost. In recent years, a very large alumina retort was produced by slip casting technique because of advancement of ceramic production technology. The section of the retort has a hexagonal or particular rib structure. Such a ceramic retort will be used extensively by the improvement in surface smoothness and accuracy of dimensions, joining technology for large components, and further development of the options of the internal wall structure such as screw geometry.

REFERENCES

1. Hashimoto, K., *Hannou Kougaku*, Baifukan Tokyo, 1979, pp. 200–204.
2. The Society of Chemical Engineering Japan, Ed., *Kagaku Kougaku Binran*, 5th edition, Maruzen Tokyo, 1995, p. 60.
3. Oyam, S., Ozawa, Y., Fukuzawa, H., *CRIEPI Report*, No.T87110, 1987.
4. http://www.toyo-eng.com/jp/en/products/petrochmical/methanol/, accessed June 8th 2017
5. Shinohara, K., Takahashi, H., Nakamura, M. Eds., *Idou Sou Kougaku*, Hokkaido Daigaku Tosyo Kankoukai Sapporo, 2000.
6. Enami, M., *The Thermal and Nuclear Power*, 55, 1350–1355, 2004.
7. http://www.jpower.co.jp/entech_e/react/index.html, http://www.jpower.co.jp/entech_e/react/regene.html and http://www.jpower.co.jp/entech_e/coke/index.html, accessed June 8th 2017.
8. Kimura, H., Syuuji, F., *Sekitan Kagaku to Kougyo*, Sankyou Syuppan Tokyo, 1984, pp. 60, 404.
9. Sullivan, J. D., Maier, C. G., Ralston, O. C. *Passage of Solid Particulates Through Rotary Cylindrical Kilns*, US-Bureau of Mines, Technical paper, No. 384, 1927.



Taylor & Francis
Taylor & Francis Group
http://taylorandfrancis.com

5.24 Nanoparticle Handling and Formulation

Wolfgang Peukert and Stefan Romeis

5.24.1 INTRODUCTION AND OVERVIEW

The ultimate goal of any process dealing with particles and powders is the formation of products with desired properties: The product properties evolve from multiscale processes which are often organized in form of process chains as shown in the generalized scheme in Figure 5.24.1. Three major steps can be distinguished: particle formation by bottom-up or top-down methods, particle formulation and powder handling, and finally, application. The focus of this chapter is on nanoparticle formulation. The term formulation stands here for all methods which modify and tune the required particle properties for the final application. Property functions of nanoparticle systems are discussed in great detail in Chapter 1.8.

The **process function** (process–structure functions) as defined by Krekel and Polke (1992) relates the process parameters to product properties:[1]

$$\text{Dispersity} = f\left(\text{process parameters}, \text{educt concentrations}\right) \tag{5.24.1}$$

Process parameters include the types of unit operations, their interconnection in the process, the conditions under which the individual unit operations are operated (e.g. temperature, pressure, mass flow rates etc.) and the materials that are processed. Structure–property as well as process–structure functions must be known in order to design optimal process variables and to achieve the desired goal, i.e. to produce well-defined, often multifunctional product properties. Usually, process chains (with or without recirculation loops) are optimized for both the handling and the end-use properties of the particles.

Nanoparticles can be produced by various methods in top-down or bottom-up approaches. These nanoparticles are the building blocks for hierarchical structure formation with many possible applications in science and technology. However, a major hurdle in further developing nanotechnologies is the scale-up from the controlled formation at a small scale in the lab to the relevant industrial scales. The key question is: How to preserve the promising properties of nanoparticles at high throughput and industrial scale along the process chain. Typically, large-scale production leads to wider distributions of the driving forces (supersaturation in bottom-up approaches or stress energy distribution in top-down production) and thus to wider distributions in resulting particle size, shape and application properties. Process economics require high particle concentrations while coagulation scales with the square of the nanoparticle concentration. Therefore, nanoparticles have to be stabilized against coagulation and changes in chemical composition such as oxidation or unwanted surface modifications. All sorts of impurities introduced during particle formation and formulation easily induce structural and electronic defects which deteriorate the desired properties.

To date, systematic studies on nanoparticle formulation and handling are rare because studies on unit operations were mostly performed for larger particles. Scale-up rules exist only in a few cases, e.g. for flame synthesis for the "big three" carbon black, SiO_2 and TiO_2, whereas in other cases the properties of the nanoparticle system often cannot be controlled

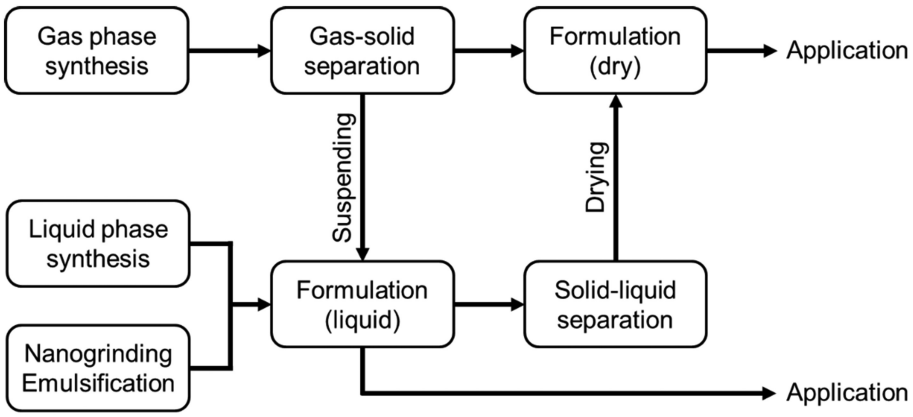


FIGURE 5.24.1 Generalized process scheme for the formation and handling of nanoparticles. Four major pathways exist to form nanoparticles, i.e. gas (i) and liquid phase synthesis (ii), wet grinding of solids (nanogrinding, iii) or liquids (emulsification, iv).

at a larger scale. A prominent example is carbon nanotubes where highly pure, single walled tubes of defined chirality can be made currently only at the lab scale. From larger scale production mostly, bundled multiwall tubes with widely distributed chemical structures are obtained.[2] In the following, we discuss the most important formulation principles and unit operations related to nanoparticle handling.

5.24.2 FORMATION OF NANOPARTICLES

1. Continuous **gas phase synthesis** in flames is the industrially most relevant technique for the production of nanoparticles with carbon black, silica and titania as the most important technical products. In all cases, gaseous precursors react in the flame to form the product particles. Their size, structure and phase composition (in case of titania) is tailored by the time–temperature characteristics of the reactor. In particular, coagulation and sintering are very important for structure formation. Many other methods such as (flame) spray pyrolysis, hot wall reactors or plasma syntheses are employed for special types of nanoparticles. A few examples exist where nanoparticles are directly deposited on substrates, e.g. silica is deposited on preformed substrates during the production of optical fibers. Functional thin films can be produced by direct deposition of nanoparticles from flame (spray) synthesis as highly porous films for sensors.[3,4] Otherwise, the particles are separated by surface filters from the gas phase so that the intermediate product is a powder. For further processing this powder is often transferred to a liquid phase. An important formulation step in the dry state is the coating of cohesive powders with nanoparticles to reduce adhesion and to increase powder flow via reduced van der Waals attraction (see e.g. Sections 1.8.3 and 1.24.6).
2. The most important methods for **liquid phase synthesis** are: Precipitation, sol-gel synthesis (e.g. oxides), hydrothermal (e.g. nanoporous zeolithes) or solvothermal synthesis and hot injection for semiconducting nanoparticles such as quantum dots. Most of these routes employ stirred tank reactors in batch operation. Continuous synthesis is still seldom employed. In all cases, both in the gas and liquid phase, the supersaturation as a thermodynamic driving force must be carefully controlled in order to form nanoparticles. Higher supersaturation leads to a higher nucleation rate and to the formation of smaller nuclei. The interplay between mixing, reaction, nucleation, particle growth and coagulation determines the size, shape and structure of the formed particles and must be carefully tailored for optimal product design. Sintering is an important factor in the gas phase, whereas ripening can play a role in liquid phase synthesis. Nanoparticles must be stabilized against coagulation during synthesis (see Section 5.24.4).
3. **Nanogrinding** in stirred media mills operated in the batch or continuous mode can produce nanoparticles by fracturing crystalline materials such as ceramic oxides in liquids.[5,6] The lower limit to comminution, i.e. the minimal achievable particle size, is directly connected to the activity of defects.[7,8] Particle sizes as small as 10 nm have been achieved, e.g. for alumina and tin oxide (see Section 1.8.5). Mechanical delamination of 2D materials leads to molecularly thin nanosheets of e.g. graphene or boron nitride.[9–12] In all these cases, colloidal stability must be guaranteed by proper formulation. Since mechanical energy input may lead to enhanced solubility of the particles,[13] ripening must be controlled carefully as well. This effect is of major importance for the production of organic nanoparticles for pigments or pharmaceuticals.[14,15]
4. **Emulsification** can lead to liquid nanoparticles and also to solid nanoparticles if the droplets are solidified or used as nanoreactors for solid particle formation.[16–18] Interestingly, scaling laws for grinding and emulsification are very similar, i.e. the mass median particle $x_{50,3}$ scales with the energy per volume E_V: $x_{50,3} \sim E_V^{-b}$ with b between 0.4 and 0.8 for most material systems and unit operations, e.g. stirred media mill, colloid mill, ultrasound (see[19] and literature cited therein). For oil phases with a moderate viscosity and an excellent colloidal stability the smallest droplet sizes are in the range of few 10 nm.[18]

5.24.3 DISPERSION OF NANOPARTICLES

Dispersion of coagulated nanoparticles is always required for nanoparticles produced in the gas phase and also for the phase transfer from one liquid phase to another one. In general, any dispersion device must overcome attractive interactions such as van der Waals forces and solid bridges originating from sintering or ripening.

Dispersion of nanoparticles in the gas phase is only possible via high energy impacts. As nanoparticles follow the streamlines due to their low inertia, dispersion is hardly possible in hammer or jet mills. Impaction can be induced at a reduced pressure and thus only at very low production rates. Therefore, the nanoparticles produced in the gas phase must be transferred to an appropriate liquid phase. Suspending nanoparticles to a liquid requires proper wetting of the nanoparticle surface by the liquid. The same holds true for the phase transfer of nanoparticles from one liquid to another one. Mostly, the particles are separated and dried from the first liquid and then suspended in the second one. The design of direct nanoparticle transfer processes between two immiscible liquids is still at its infancy.[20] Wetting properties of powders in general can be evaluated by contact angle measurements based on the Washburn method whereby a set of different liquids is brought in contact with a bed of the powder and the mass-uptake is measured by a balance.[21] For dispersion, it is helpful to distinguish between soft agglomerates

and hard aggregates: Soft agglomerates are held together by relatively weak adhesion forces whereas hard aggregates are defined by strong solid bridges.[22] Dispersion of soft agglomerates is mostly realized in the liquid phase whereby high-pressure homogenizers, ultraturrax stirrers or ultrasound emitters are often applied in the lab. In the latter case the required high-local shear forces are achieved by dissipating energy from sonotrode tips into a small fluid volume.

At industrial scale, high shear forces are employed by dissolvers in stirred tanks which consist of an agitator disk with tooth-like elements at the circumference. The most efficient dispersion method is stirred media mills which provides the highest energy density and is probably the only dispersion device to break solid bridges, i.e. to disperse hard aggregates efficiently.[23]

The result of a comminution or dispersion process is always determined by the equilibrium between dispersion and agglomeration. From the point of view of dispersing high-efficiency stress energy (energy transferred from the stressing tools inside the mill to the particles) is desirable. For wet grinding the stress energy is given by the kinetic energy of the agitated beads. The maximum stress energy, respectively the kinetic bead energy as estimated from the tip speed of the stirrer, is used for scaling.[24] In case of insufficient colloidal stability, however, too high stressing energies can also promote reagglomeration.[25] The optimal dispersion parameters for perfectly stable systems are determined by the interplay between stress energy and stress number:[23] The product of stress energy and the stress number is proportional to the overall energy input; on the one hand a lower stress energy threshold must be exceeded, on the other hand the stress number must be sufficiently high to disperse the agglomerates. For a given energy input a too high stress energy leads to a low number of stress events and hence an insufficient dispersion. Too low stress energies lead to a high number of stress events which do not supply enough energy to disperse the agglomerates. Furthermore, it is important to note that the critical stress energy scales with the agglomerate size. For the smallest agglomerates very small grinding beads below 100 nm are needed.

For dispersion in highly viscous fluids and polymers kneaders and multi-roller mills are typical options. Thermodynamically stable dispersion of nanoparticles into a polymeric liquid is enhanced for systems where the radius of gyration of the linear polymer is greater than the radius of the nanoparticle. Dispersed nanoparticles swell the linear polymer chains, resulting in a polymer radius of gyration that grows with the nanoparticle volume fraction. This entropically unfavorable process is offset by an enthalpy gain due to an increase in molecular contacts at dispersed nanoparticle surfaces as compared to the surfaces of phase-separated nanoparticles.[26]

Nanoparticle production strongly depends on the ability to stabilize the particles against coagulation. In cases where sintering can be minimized by tailored time–temperature profiles in the reactor, dispersion into single particles can be realized in the liquid phase. In liquid phase-based top-down and bottom-up methods, colloidal stabilization must be faster than the formation kinetics of the particles. Many nanoparticle properties and most of the handling methods strongly depend on proper colloidal stability which will be discussed in the next section.

5.24.4 NANOPARTICLE STABILIZATION

Nanoparticle synthesis, dispersion and formulation are influenced not only by the specific unit operation and the related process parameters (e.g. concentration, residence time, temperature, pressure drop) but most importantly by the stability of the particles. In general, the following aspects of nanoparticle stability can be distinguished:

- Stability against chemical changes. Oxidation is most relevant for non-oxides such as metal nanoparticles (with exception of noble metals, i.e. Au, Ag, Pt), semiconductors (e.g. Si) or ceramic nanoparticles such as carbides or nitrides. Oxidative attack can be reduced by proper surface functionalisation, but not completely avoided in the presence of oxygen in gases or liquids. Therefore gloveboxes with carefully controlled non-oxidative atmosphere in the lab and inert atmosphere at larger scale are a must have. Due to the high surface area of nanoparticles, surface contamination by unwanted adsorbents is an issue which is hard to avoid completely. The characterization of the structural and compositional surface properties of nanoparticles is a major challenge, the control of surface properties is even harder to achieve. This is one of the main reasons why the transfer of nanoparticulate properties to industrial scales is often challenging. In particular, semiconducting nanoparticle systems suffer from uncontrolled defect states.
- Stability against phase transitions and Ostwald ripening. Systems of complex composition and in particular organic molecules can crystallize in various phases or polymorphs. Ostwald's rule of stages states that during crystallization the system moves to equilibrium from an initial high-energy state through small changes in free energy implying that the least stable polymorph forms first. This effect can be particularly strong due to the enhancing influence of curved surfaces via the Kelvin effect. In pharmaceutical materials science, these aspects are highly relevant since any drug substance will be approved only as a well-defined specific polymorph. Stabilization requires the application of tailored surface-active compounds suppressing dissolution and recrystallization.
- Stability against sedimentation. The settling of nanoparticles with hydrodynamic diameters <100 nm is typically small in liquids. However, for long-term stability it is not negligible. Long-term stability can be achieved by tailoring the fluid viscosity, i.e. the addition of polymers can induce a slight Bingham behavior so that the yield stress is able to absorb the

gravitational forces. Coagulation accelerates sedimentation and must be avoided in most applications. In waste water treatment, however, where nanoparticles shall be separated efficiently, flocculation can be induced by flocculation aids in the form of bridging polymers and/or highly valent cations (e.g. Al^{3+} or Fe^{3+}) which quench the electrostatic double layer leading to a reduced electrostatic stability.

- Stability against coagulation. Relative motion of nanoparticles towards each other and attractive forces lead to coagulation. In the gas phase, stabilization is in principle possible by bipolar charging of the aerosol. However, this approach is not feasible in most technical applications due to inefficient and uncontrollable charging at higher concentrations. Therefore, we focus on the following only on colloidal stabilization in suspension.

In principle, there are three different possibilities (see Figure 5.24.2) to induce stability against coagulation in the liquid state: surface charge-induced electrostatic stabilization, steric stabilization by adsorption of macromolecules and electrosteric stabilization by adsorbed charged molecules which is a combination of electrostatic and steric contributions.

i) Electrostatic Interactions

Surfaces in solutions often carry electrostatic charges. Reason for this is a selective adsorption and desorption of specific ions or the adsorption of surfactants with polar groups (see Figure 5.24.3). The ions which determine the surface potential of a crystalline solid particle in solution are called potential determining ions (PDIs). The most important examples are H^+/OH^- for oxides in water.

Oxide surfaces are typically hydroxylated. The surface charge density σ_0 is thus a function of pH due to hydroxylation or dehydroxylation. The point of zero charge (PZC) is the pH at which the surface charge density vanishes. At this point preferred coagulation occurs due attractive van der Waals forces. The isoelectric point (IEP) denotes the point where the net charge vanishes in the statistical mean. PZC and IEP are only identical if there is no specific adsorption of other ions than the potential determining ions. In the presence of specific adsorption, PZC and IEP generally have different values (Figure 5.24.4).[27,28]

Adsorbed molecules and ions (co-ions) are relatively strongly bound only directly at the interface in the so-called Stern layer. Relatively loosely coordinated counter-ions and co-ions arrange themselves in a diffuse double layer (see Figure 5.24.5). The ion concentration in the diffuse layer is strongly dependent on the electrostatic potential which is described in the approach of Gouy and Chapman.[27,28] In brief, the charge density is calculated based on a Boltzmann distribution of the ions in the electric field of the interface. The resulting potential Ψ is given for a flat interface of surface potential Ψ_0 by Equation (5.24.2):

$$\Psi = \Psi_0 e^{-\kappa a} \tag{5.24.2}$$

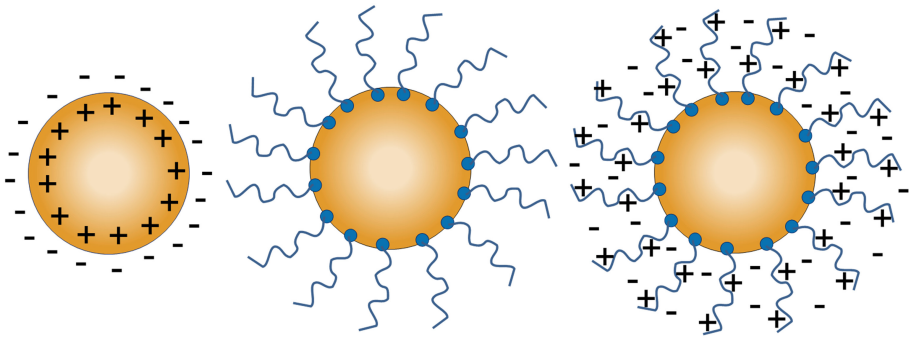


FIGURE 5.24.2 Different possibilities for nanoparticle stabilization, left: electrostatic; middle: steric; right: electrosteric stabilization.

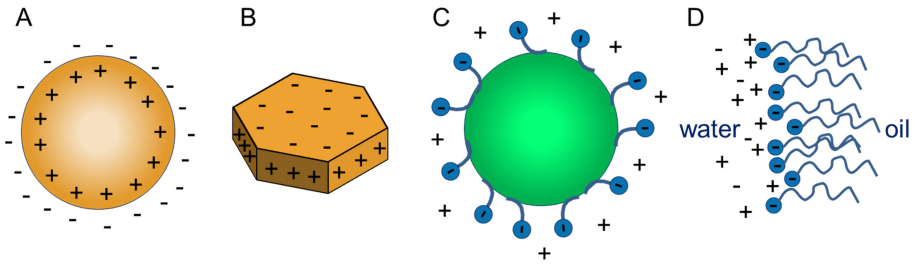


FIGURE 5.24.3 Examples for charged surfaces in solution, (A) homogeneously charged solid particle, (B) clay particle at low pH-value with differently charged surfaces, (C) double layer at a hydrophobic surface due to adsorbed polymers, (D) ionized monolayer at an oil-water interface.

Equation (24.2) shows that the potential decays exponentially with the distance a normal to the surface. The variable κ^{-1} is called Debye length and is a measure for the extension of the double layer.

$$\kappa^2 = \frac{\Sigma_i N_i z_i^2 e^2}{\varepsilon_0 \varepsilon_r k_B T} = \frac{2e^2}{\varepsilon_0 \varepsilon_r k_B T} \cdot I \qquad (5.24.3)$$

I denotes the ionic strength as a function of the valency z_i of anions and cations and their respective number density N_i as given by Equation (5.24.4). The other variables have their usual meaning.

$$I = \frac{1}{2}\Sigma_i N_i z_i^2 \qquad (5.24.4)$$

The Debye length decreases with the concentration of electrolytes c and their valency z_i. The empirical Equation (5.24.5) holds for 1:1 electrolytes in water ($\varepsilon = 78$, $T = 298$ K, c in mol/l):

$$\kappa^{-1} = \frac{3.04 \cdot 10^{-10}}{\sqrt{c}} \qquad (5.24.5)$$

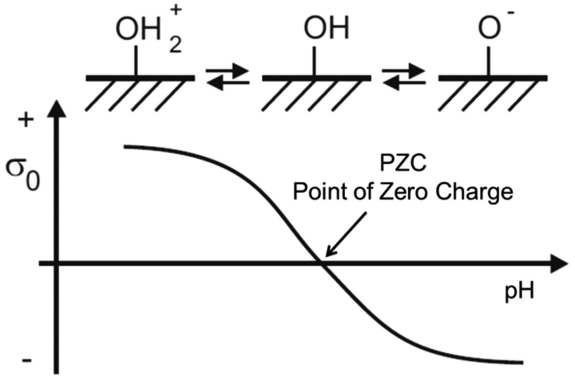


FIGURE 5.24.4 Influence of pH on surface charge.

The surface charge density σ_0 can be approximated from the charge distribution in the solution due to electron neutrality by Equation (5.24.6) (under the assumption of symmetric electrolytes in water for sufficiently small potentials):[27]

$$\sigma_0 = \varepsilon_0 \, \varepsilon_r \kappa \Psi_0 \qquad (5.24.6)$$

The potential distribution around a surface is depicted in Figure 5.24.5. In the Stern layer the ions are steadily adsorbed, while they are mobile in the diffuse layer. The surface charge density can be increased be specific adsorption directly on the surface.

The important ζ-potential denotes the potential at the shear plane and is accessible by electrokinetic measurements, e.g. electrophoreses in cases of dilute systems or electro-acoustic measurements in concentrated suspensions.

ii) Electrostatic Stabilization

The DLVO-theory (after Derjaguin, Landau, Verwey and Overbeek) is based on the sum of attractive van der Waals and repulsive electrostatic interactions. The repulsive forces are based on rejection of like charges and the resulting osmotic pressure due to dilution effects in the solvent between the interacting bodies. The total interaction energy $E_{DLVO}(a)$ as a function of distance a between two spheres of the same radius R is given by Equations (5.24.7) and (24.8):

$$E_{DLVO}(a) = \pi R\left(-\frac{A_{121}}{12\pi a} + 64\frac{N_{i,0} k_B T \Gamma_0^2}{\kappa^2} \cdot e^{-\kappa a}\right) \qquad (5.24.7)$$

$$\Gamma_0 = \frac{e^{\left(ze\Psi_0/2k_BT\right)} - 1}{e^{\left(ze\Psi_0/2k_BT\right)} + 1} = \tanh\left(\frac{ze\Psi_0}{4k_BT}\right) \qquad (5.24.8)$$

The interaction energy is a function of the distance of the two spheres (see Figure 5.24.6). At very short distances the

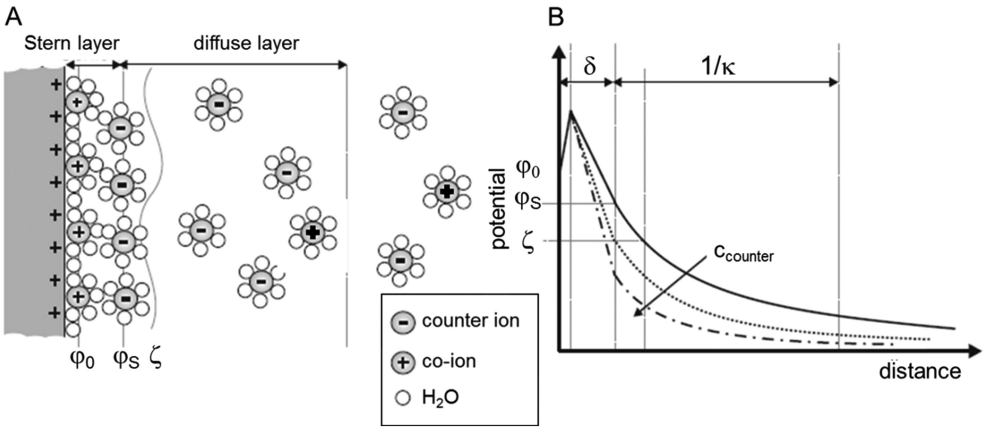


FIGURE 5.24.5 (A) Schematic representation of the arrangement of ions in proximity to a charged surface. Distribution of ions around a flat surface according to the Stern-Graham model. φ_0 denotes the surface potential and ϕ_S is the Stern potential. The ζ potential is located at the shear plane. (B) Corresponding slope of the potential.

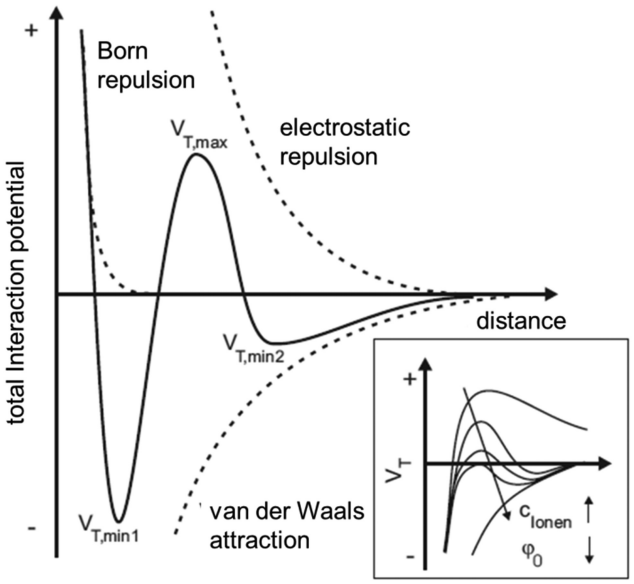


FIGURE 5.24.6 Schematic representation of the individual contributions and total interaction potentials of the DLVO theory.

electron shells of the two bodies are overlapping resulting in the strong Born repulsion which is not included in the equation mentioned above. The graph has – depending on the ionic strength – a primary minimum due to strong van der Waals attractive forces. For efficient stabilization the maximum energy barrier has to be sufficiently high so that the particles are not able to overcome it. By tuning the repulsive interactions ($E_{DLVO\_max} >> k_B T$) the system can be stabilized, i.e. high surface charges and small salt concentrations of low-valent-ions favor electrostatic stabilization. Small van der Waals attractions and sufficiently large electrostatic repulsions lead to stable conditions. The point where the potential maximum is identical to zero ($E_{DLVO,max} = 0$) is called critical coagulation concentration (CCC):

$$CCC \approx 10^5 \frac{\left(\varepsilon_0 \varepsilon_r\right)^3 \left(k_B T\right)^3}{\left(z^6 e^6 A_{121}\right)} \cdot \Gamma_0^4 \qquad (5.24.9)$$

CCC is proportional to z^{-6} (Schulze-Hardy-rule). Ions of higher valence compress the double layer leading to a strong decrease of the repulsive part of the energy profile. This is the reason for the use of the trivalent ions Al^{3+} and Fe^{3+} for the flocculation in waste water treatment processes.

iii) Steric and Electrosteric Stabilization

Steric stabilization occurs when the particle is surrounded by a shell of molecules which effectively screen van der Waals attraction. In the case of ultrafine particles with small van der Waals forces such as quantum dots, for instance, even small molecules such as adsorbed acetate (in case of ZnO) can be sufficient to screen the small van der Waals attraction. In these cases, DLVO theory can be misleading as all interactions are in order of the thermal energy $k_B T$. For these systems, a dimensional analysis where attractive and repulsive interactions were balanced could explain stability.[29] For larger particles, also larger molecules are needed to screen van der Waals attraction sufficiently. In principle, polymers with sufficiently high affinity to the particle surface and good solubility in the solvent are good stabilizers. At this point, it has to be noted that any adsorption process in liquids must be understood in terms of competitive adsorption between two molecules, since at least the solvent molecule must be replaced at the surface. A detailed description of the wide field of polymers at interfaces is given in the literature.[30] The thickness δ of the adsorbed polymer layer on the particle surface can be determined from polymer solution thermodynamics such as regular solution theory or from more advanced molecular simulations. Hildebrand[31] and Hansen[32] parameters can be used to estimate solubility effects. With respect to particle stability, three regimes can be distinguished.

$a > 2\delta$**:** The layers are not in contact with each other. It is possible that van der Waals attraction is acting with the result of a weak secondary minimum in the interaction energy profile (a primary minimum does not occur during steric stabilization).

$\delta < a < 2\delta$**:** The polymer layers interpenetrate.

$a < \delta$**:** The polymer layers interpenetrate and are additionally compressed.

In a good solvent the mixing of the polymers is thermodynamically unfavorable whereas it is preferred in a poor solvent. Under compression the elastic free energy (conformation entropy) of the polymers must be taken into account. The thus derived interactions can be included into extended DLVO approaches.[33–36]

Steric effects can be combined with electrostatic repulsion when charged molecules or polyelectrolytes are bound to the particle surface. Basic requirement for the (electro-) steric stabilization is the adsorption or chemical bonding of the polymers on the particle surface, i.e. at least a part of the polymer molecule must have an adequate affinity to the particle surface. Another part of the polymer should be soluble so that the polymer chains can stretch wide into the solvent in order to enlarge the distance between two particles. Therefore, block copolymers are well suited for stabilization. In most cases the selection of the polymers is empirical according to the following guidelines:

- The ionic group of the polymer should have an opposite charge at the particle at the selected pH.
- Polymers with polar/non-polar groups are effective for a polar/non-polar surfaces and lipophilic or lipophobic surfaces, respectively.
- The longer the hydrophobic chain length the worse the solubility in water and the better the solubility in organic liquids.
- Polar groups (e.g. ethylene oxide) in a hydrophobic chain improve the solubility in water and in organic liquids.
- Aromatic rings within a hydrophobic chain improve the adsorption behavior on polar surfaces.

TABLE 5.24.1 Comparison of Electrostatic and Steric Stabilization

Electrostatic	Steric
Fast (diffusion of ions).	Slow due to diffusion of larger surfactants and polymers.
No contamination.	Possible contamination by polymers.
Relatively easy to control.	Hard to control, complex thermodynamics.
Inline analysis by electroacoustics.	No inline analysis.
Effective only at low ionic strengths and in polar solvents.	Widely independent from ionic strength, solvent and concentration.
Formation of gel-like structures with interacting double layers at higher concentrations.	Good redispersability, no formation of solid bridges.
Formation of (irreversible) solid bridges during drying possible.	Formation of complexes with solutes or micelles possible.

Uncharged or hydrophobic particles can be electrostatically stabilized with polyelectrolytes in polar solvents. On hydrophobic particles in a polar environment preferably the non-polar tails of the polymer will adsorb whereas the polar tails are stretched into the polar solvent resulting in the formation of the double layer, then the DLVO-theory is valid. However, stabilization is enhanced by the formation of a polymer layer. At high ion strength, polyelectrolytes will only stabilize by means of steric stabilization. The advantages and disadvantages of the stabilization methods are summarized in Table 5.24.1. Adsorption kinetics is highly relevant for fast syntheses since stabilization should be always faster than particle formation. Therefore, a combination of the two approaches is an interesting option, i.e. fast short-term stabilization by ion or small molecule adsorption which is then complemented by slower steric stabilization for long-term stability.

5.24.5 FROM SURFACES TO PROPERTIES – THE EFFECT OF SURFACE MODIFICATION

In general, there are four major possibilities to modify the surfaces of particles:

- Chemical functionalization by means of chemisorption or physisorption of ions, molecules (including chemical vapor or atomic layer deposition) or macromolecules (polymers and biopolymers).
- Responsive particle surfaces by adsorption of block copolymers which "respond" to external stimuli and the chemical environment, e.g. polarity, pH or temperature.
- Change of surface structure, i.e. crystallinity and roughness either by coating processes or by tailoring growth processes which lead to a specific surface morphology.
- Process technology, i.e. by generating specific stimuli acting on the particle surfaces, e.g. shear stresses in fluids, mechano-chemical effects in mills and/or time-temperature history (surface diffusion, sintering, rounding).

Accordingly, the chemical and physical properties of the particles can be adapted to specific applications. Chemical functionalization is applied, for instance, for the dispersion of particles in different polar or non-polar matrices, to enhance charge transfer between particles in applications of printable electronics, to control the release of components in life sciences or corrosion protection by design of core–shell systems and capsules or to protect particles from oxidation or other chemical influences.

For the time being, a rigorous modeling and design of particle interactions is only possible for relatively simple model systems. One main bottleneck is the lack of characterization tools for particle surfaces and the related interactions between them. Classical tools of surface science mostly work only in high vacuum and not in liquids. For particles in liquids, several orthogonal techniques may be applied such as ζ-potential measurement, thermogravimetry (surface coverage), NMR, UV-Vis, FTIR, photoluminescence and Raman spectroscopy (chemical information) as well as analytical (ultra-) centrifugation (interactions, core-shell structures).[37] The non-linear optical techniques second harmonic generation (SHG) and sum frequency generation (SFG) are particularly promising methods for the extraction of charge and molecular structure directly from the embedded surface (see e.g.[38–41]).

In general, interactions include "hard" aspects of particles coming directly in contact with each other or with external walls through mechanical forces and "soft" microscopic interactions of dispersed systems induced by molecular effects such as enthalpic electrostatic and van der Waals or entropic hydrophobic forces. The classical picture of molecular interactions and their effect on macroscopic properties is well developed in statistical thermodynamics of phase equilibria. Briefly, molecular interactions determine the potential of the mean force which is directly related to the pair correlation function from which all macroscopic (thermodynamic) properties such as virial coefficients, osmotic pressure and so on can be derived as a function of temperature and pressure. A similar approach adapted and further developed for nanoparticles is missing.

All nanoparticle systems and applications have in common that the interfacial and surface properties of the particles play a central role. The ratio of van der Waals adhesion forces to particle weight scales with particle diameter x^{-2} and is, for instance at 1 µm, in the order of 10^6 (in case of smooth particles in the gas phase). Macroscopic properties can only be tailored by microscopic design of the interfaces. Surface chemistry and physics determine on the one hand the particulate interactions with fluid or solid phases. The types of interactions are van der Waals, electrostatic forces and polarization effects, hydrogen bonds and chemical bonds.[42] On the other hand, particle interactions control particle and structure formation. For formulation of (nano-)particulate systems, we start conceptually at the particle surface which "transports" the respective particle interactions, thus leading to the desired structure. Vice versa, structure formation can only be understood by considering the relevant interactions which are determined by the particle surface. This concept

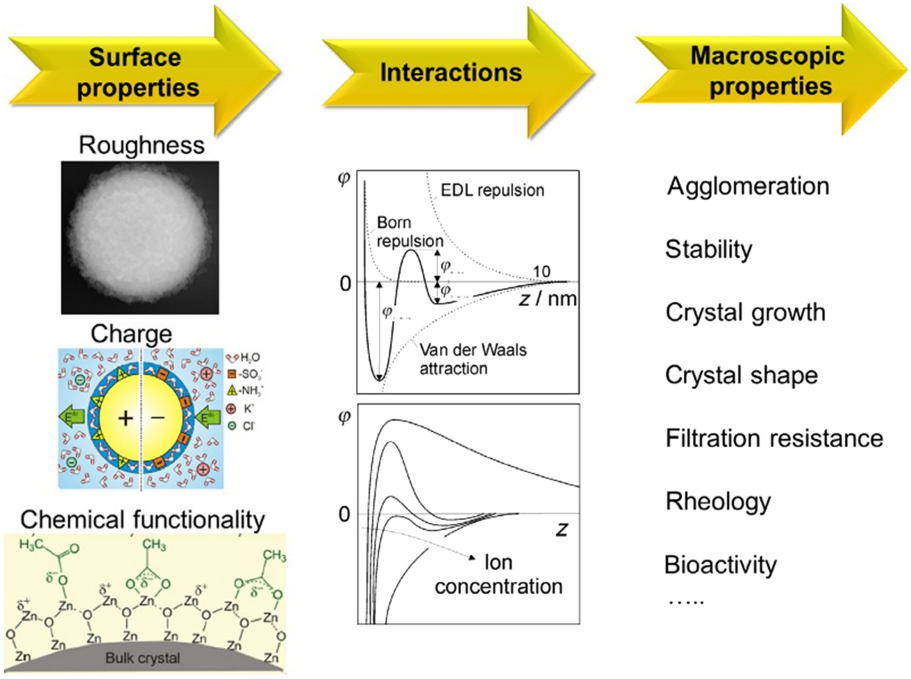


FIGURE 5.24.7 From surface to macroscopic properties – the relevance of particle interactions. (Reprinted from Peukert et al., Adv. Chem. Eng. 46, pp. 1–81. With permission. Copyright 2005 Elsevier.)

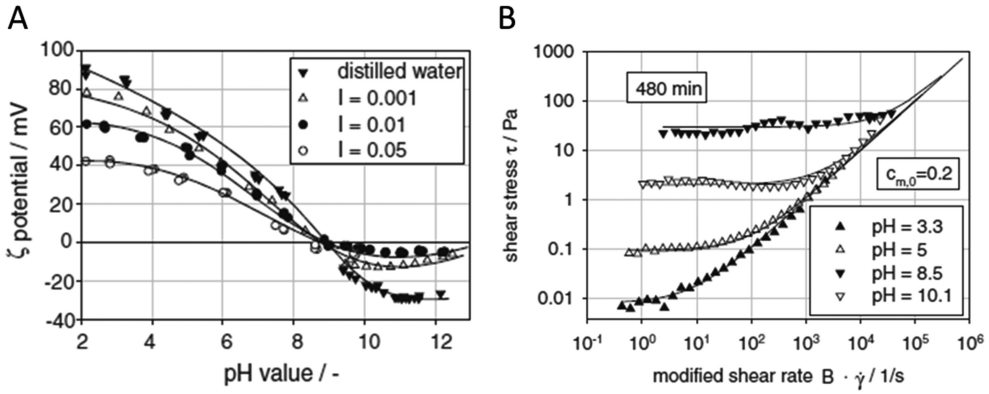


FIGURE 5.24.8 (A) ζ-Potential of an aqueous alumina suspensions (at different ionic strength I) as function of pH at a mass concentration $c_{m,0}$ of 20%. (B) Rheological behavior of the suspensions. The shear rate is modified by a shift B which condenses the flow data in the hydrodynamic regime into one single curve. (Adapted from Stenger et al., Chem. Eng. Technol., 26, pp. 177–183. With permission. Copyright 2003 John Wiley and Sons.)

is illustrated in Figure 5.24.7 for oxide particles in an aqueous solution. Particle interactions can be understood in the view of well-known DLVO-theory as a superposition of van der Waals and electrostatic double layer forces (see Section 5.24.4). This general concept can also be applied to more complicated and less understood types of interactions, e.g. interactions between polymer-modified particles where entropic and structural effects have to be included as well.

This approach is based, however, on some wide-ranging preconditions. In order to bridge the gap between the microscopic molecular nature of a particle surface and the macroscopic properties we need a multi-scale approach covering several orders of magnitude in space and time. By using classical interaction forces, molecular dynamics (MD) and Monte Carlo simulations are nowadays able to describe and even predict mesoscopic phenomena. Thus, we assume the additivity of forces. Macroscopic properties therefore evolve from the interplay of microscopic and mesoscopic effects.[19]

In the following, we briefly describe two examples which support our arguments for two completely differently applications and materials. First, we discuss the influence of the ζ-potential of alumina suspensions which were studied in the context of nanomilling in stirred media mills. The ζ-potential is as a measure of the surface charge of the particles and is here used to tailor the suspension rheology. Figure 5.24.8 shows that the magnitude of the ζ-potential controls

the measured shear stress at low shear rates highlighting the influence of interparticulate interactions. Highly repulsive interactions suppress agglomeration and the suspension shows a low viscosity with just a minor yield stress. At the isoelectric point electrostatic repulsion and the ζ-potential vanish, i.e. the suspension is flocculated. A considerable shear stress is obtained as an integral measure of the attractive forces between the alumina particles. Noteworthy, the change of the surface charge leads to changes of the yield stress by more than four orders of magnitude.[43] Similar trends can be observed for other materials and other unit operations such as solid–liquid separation. For instance, the filtration resistance of a filter cake strongly depends on the surface charge of the particles.

The second example deals with fluid interfaces in protein foams. Protein foams are most relevant in food science and engineering, e.g. in the form of milk foams on a cappuccino. A foam is an aggregate of stabilized gas bubbles. These gas bubbles in turn are stabilized by adsorbed proteins and surfactants at the liquid–gas interface. In the example illustrated in Figure 5.24.9, we present data for β-lactobulin (BLG). BLG is a main component in milk and acts as stabilizer at the gas–liquid interfaces in milk foams. We see the same hierarchy as discussed above: The ζ-potential (A) is a measure of the net surface charge of the proteins. At the isoelectric point (~pH 5), the tendency for protein adsorption at the interface is highest leading to a minimum of surface energy (B). At the interface, the proteins become unstable and agglomerate since the repulsive forces vanish. This leads to a pronounced increase of layer thickness (C) and to a maximum of the elastic modulus of the film (D). At the isoelectric point, the protein foam is most stable and the size of gas bubbles directly after foaming is smallest. Thus, all macroscopic foam properties scale with the surface charge of the proteins.[44,45]

These examples show the influence of surface charge on nanoparticle formulation and handling. Many other possibilities exist to tune surface properties for particle handling and for tailored end-use properties. In the following section we briefly summarize nanoparticle handling in classical unit operations.

5.24.6 NANOPARTICLE HANDLING IN CLASSICAL UNIT OPERATIONS OF POWDER PROCESSING

For most unit operations, systematic studies on the handling of nanoparticles are still rare. Most intensely studied are methods to produce nanoparticles, see Sections 5.24.1 and 5.24.2. Typically, production methods of larger particles are often coupled to a classification step in order to achieve the desired product properties. This is, however, a major challenge for nanoparticles because most known classification methods rely on mass forces (e.g. in rotating wheel classifiers in the gas phase or in centrifuges in liquids) which are too small for submicron particles. Therefore, no technical solutions exist so far although a couple of techniques are known and used for analytical purposes. A promising approach for size classification is size-selective precipitation. This technique is sometimes employed (mostly empirically) in synthesis labs to narrow distributions of colloidal particles in liquids and has only recently been studied from an engineering formulation perspective for the case quantum dots. In brief, careful tuning of the dielectric properties of the fluid induces size-selective agglomeration. The µm-sized flocs can be easily separated by settling or in hydrocyclones at larger scale. The measured grade efficiencies in Figure 5.24.10 for the ZnS quantum dots are surprisingly sharp. In principle, this promising approach is scalable since it involves only scalable process steps, i.e. mixing of fluids and mechanical separation of flocs.[46,47]

Product recovery by solid–liquid separation is either based on mass forces in e.g. centrifuges or on cake filtration. For both cases, flocculation of nanoparticles is a must. The best method to separate nanoparticles from gases at an industrial scale is surface filtration in bag houses; their operation is

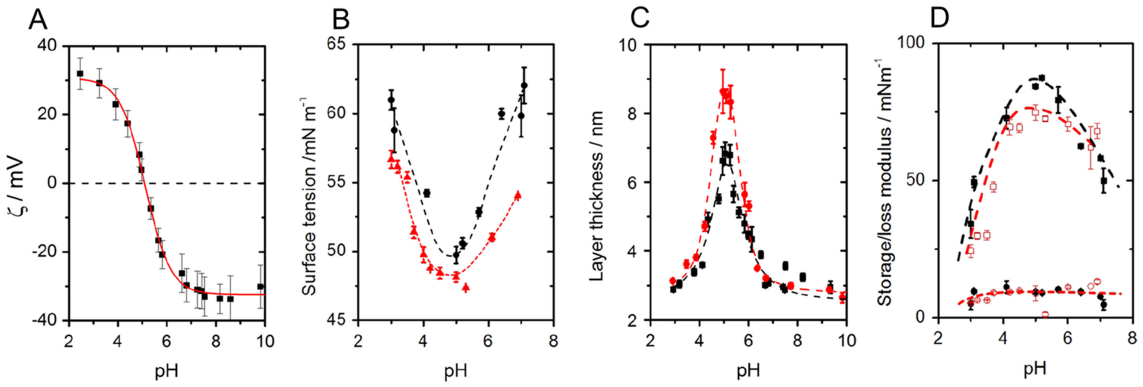


FIGURE 5.24.9 (A) ζ-Potential of a β-lactoglobulin (BLG) aqueous suspension. (B) Surface tension for 10 µM (circles) and 50 µM (upward triangles) BLG aqueous suspension as function of pH value. (C) Thickness of BLG layers adsorbed at the air-water interface as function of the pH value. BLG concentrations were 15 µm (boxes) and 54 µm (circles). (D) Interfacial dilational elasticity E' (boxes) and viscosity E'' (circles) of BLG. Filled symbols correspond to a concentration of 10 µM; open symbols represent 50 µM BLG in water. (Adapted from Engelhardt et al., Langmuir 29, pp. 11646–11655. With permission Copyright 2013 American Chemical Society.)

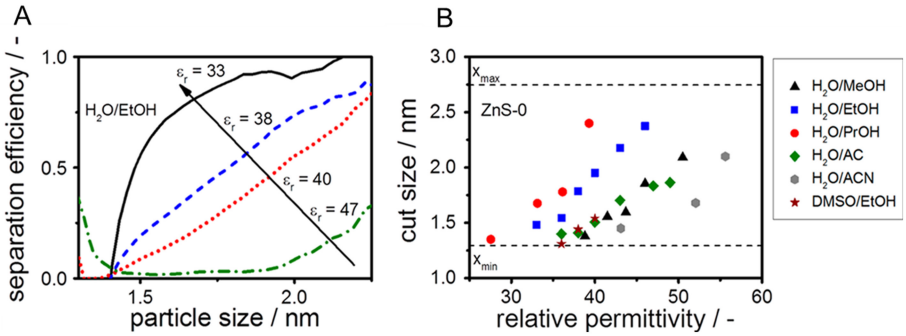


FIGURE 5.24.10 (A) Evolution of the separation efficiency for H_2O/EtOH mixtures with relative permittivities ε_r adjusted between $\varepsilon_r = 47$ and $\varepsilon_r = 33$. (B) Cut sizes for mixtures of water with different solvent mixtures the minimum (x_{min}) and the maximum (x_{max}) particle size of the feed are included by black horizontal lines as guide to the eye. (Adapted from Segets et al., J. Phys. Chem. C 119, pp. 4009–4022. With permission. Copyright 2015 American Chemical Society.)

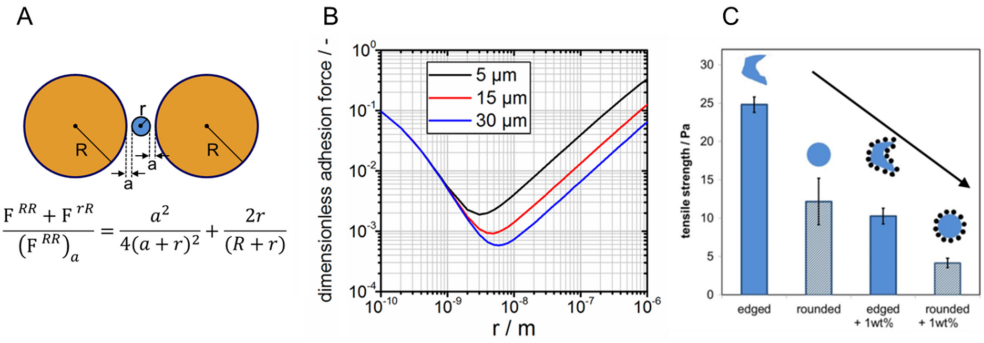


FIGURE 5.24.11 (A) Sketch of the "Sandwich model" according to Zimmermann et al.[55] which describes the adhesion forces keeping an agglomerate comprising two spheres (radius R) separated by a smaller particle (radius r) together. (B) Adhesion force for the agglomerate normalized by the adhesion acting between two bare spheres calculated for the spheres sizes 5 µm, 15 µm and 30 µm. The used contact distance is 0.165 nm. Furthermore, the identical Hamaker constant is assumed for all interactions. (C) Experimental optimization of the flowability and packing density of polystyrene as mimicked by the measured tensile strength of the powders for edged, rounded and coated particles. (Adapted from Schmidt et al., Pow. Technol., 261, pp. 78–86. With permission. Copyright 2003 Elsevier.)

well-understood, even small nanoparticles can be effectively removed in the filter cake with high efficiency.[48]

Nanoparticles in powders typically exist in the form of agglomerates whose sizes and structures determine the overall behavior. This is in line with fluidization studies of Dave and Pfeffer. Upon the fluidizing of different nanoparticle materials, two types of nanoparticle fluidization behavior, agglomerate particulate fluidization (APF) and agglomerate bubbling fluidization (ABF) were observed. Using the Ergun equation, the experimentally measured pressure drop, bed height and the minimum fluidization velocities for APF nanoparticles could be estimated based on characteristic agglomerate size of APF nanoparticles. A classification criterion (see Equation 5.24.9) based on the value of a combination of dimensionless groups (Froude number Fr, Reynolds number Re, relative density and bed height H vs. bead diameter d_t, taken at minimum fluidization (mf) velocity) allows the differentiation between particulate and bubbling fluidization:[49] For $\Pi < 100$ smooth fluidization is observed. For $\Pi > 100$ bubbling fluidization occurs.

$$\Pi = \mathrm{Fr}_{mf}\,\mathrm{Re}_{mf}\,\frac{\rho_a - \rho_g}{\rho_g}\,\frac{H_{mf}}{d_t} \tag{5.24.9}$$

The flow of cohesive powders, their fluidization behavior, their tendency to agglomerate and their packing characteristics can be strongly influenced by coating nanoparticles onto the surfaces of the cohesive microparticles. This effect was studied early in the Karlsruhe group by Sommer, Krupp and Rumpf,[50–52] and is now widely applied in industry, e.g. the adhesion forces of toner particles in electrophotographic printing are tailored this way. Recent applications include powder flow optimization for additive manufacturing and 3D printing. Here, all sorts of powders in the size range of a few 10 µm are treated by selective laser or in the case of conductive metal particles electron beam melting. The mechanical properties of the final parts critically depend on the powder flow and dense packing characteristics in the powder bed which can be tuned by proper adjustment of the powder size, shape and in particular by their surface properties.[53,54] An example is given in Figure 5.24.11.

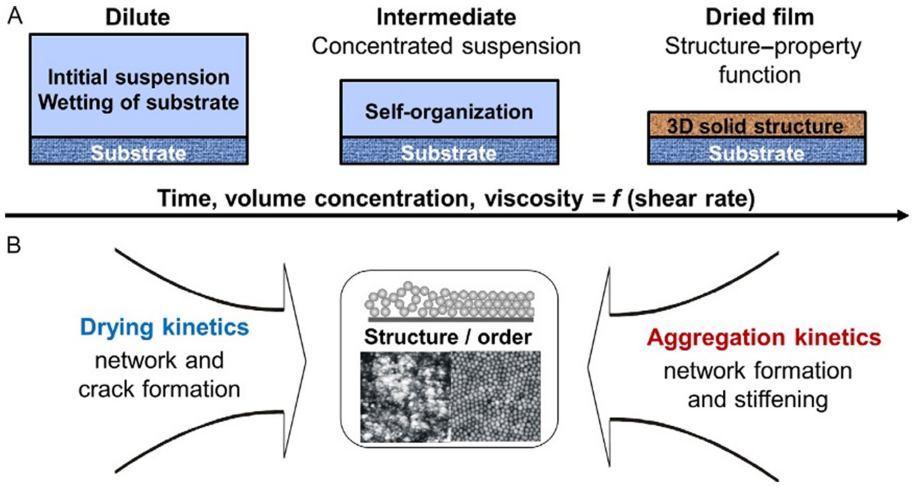


FIGURE 5.24.12 Structure formation in thin films from liquids; (A) temporal evolution of concentrations, interactions and viscosity due to drying; (B) interplay between drying and aggregation kinetics. (Reprinted from Peukert et al., Adv. Chem. Eng. 46, pp. 1–81. With permission. Copyright 2005 Elsevier.)

5.24.7 PROCESSING OF FUNCTIONAL THIN FILMS FROM LIQUIDS

Many modern applications of nanoparticles are related to functional films which can, in principle, be deposited from gases or from liquids. The applications of such films is wide ranging: energy conversion and storage strongly depends on electrode layers in solar cells, electrolysis for water splitting, fuel cells, batteries or supercaps. Printable electronics are highly relevant for the production of cost-effective fabrication in the form of displays, light emitting diodes and field effect transistors. In the chemical industry catalyic films are of utmost importance, whereas biofilms are important for biocatalysis, for pharmaceutical or medical applications, and for food science and technology (e.g. cappuccino, beer). In the following we focus exemplarily on thin films processed from liquids.

A liquid film can be deposited on a solid substrate by a number of methods such as spin, dip or die/slot coating, tape casting, spraying or by various continuous roll-to-roll processes. Further, we may distinguish between reacting (e.g. via sol-gel methods) and non-reacting systems, for instance in the fabrication of ceramic tapes. Structure formation may be induced either at the interface, i.e. at the solid–liquid or the gas–solid interface or in the bulk of the fluid. The interfaces can be understood as templates whereas in the bulk coagulation, processes are monitored. In the liquid phase the interplay between drying and aggregation kinetics controls the structure evolution and the final structure (see Figure 5.24.12). Upon drying, the solvent evaporates and the concentration of the building blocks increases while the interactions between them change simultaneously. Therefore, colloidal stability, aggregation and self-organization are all functions of time, concentration and viscosity. Noteworthy, the latter is a function of the acting shear rates. Drying kinetics trigger coagulation kinetics and thus determine ordering and structure. Highly regular structures may form by pre-formation of liquid crystalline structures or templating at the interfaces.[56] Space-filling films come within reach if particles of distinct shape (e.g. nanorods) are deposited in highly ordered structures.[57] The transient interaction-dependent aggregation leads to network formation whereby stiffening mechanisms determine the strength of the network. At the end of the first drying phase the particles are immobilized and the solvent is only present inside the pores. Upon further drying, the pores are successively emptied whereby drying stresses act on the particle network which induces compression and undesired crack formation. Thus, a major challenge is the formation of crack-free assemblies, both in 2D and 3D. The functional properties of the film are determined by the 3D structure, by percolation effects for charge carrier mobility (e.g. ions in case of a battery or electrons in case of a field effect transistor) and by the arrangement of the building blocks.

The key question is always how to tailor the meso-structure of the film to meet a specific film property by tuning the particles interaction, the fluid dynamics of the coating processes and the drying conditions. A typical process chain leading to opto-electronic devices is depicted in Figure 5.24.13 exemplarily for a field effect transistor (FET) with an active layer of ZnO quantum dots.[58,59] The first step, particle formation by gas or liquid phase synthesis, leads to particles which are further functionalized at their surface to ensure colloidal stabilization and to allow charge-transfer across particle–particle interfaces in the final layer. The surface and electronic properties of the particles are typically characterized by a whole set of techniques including time-resolved measurements of charge carrier transport. The best way of cost-efficient industrial production would be continuous roll-to-roll production followed by controlled drying and densification, e.g. by pulsed lasers. Due to the latter, the layer can be formed even on substrates which only tolerate temperatures below e.g. 200°C. This way, a layer with a 3D morphology and many grain boundaries is

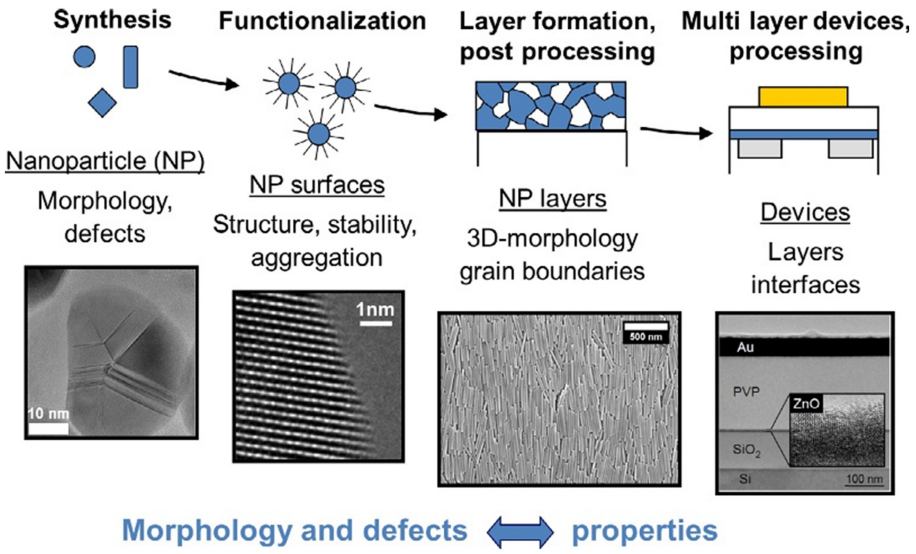


FIGURE 5.24.13 Process chain for printable opto-electronics process chain for printable opto-electronics. (Reprinted from Peukert et al., Adv. Chem. Eng. 46, pp. 1–81. With permission. Copyright 2005 Elsevier.)

formed. A key question is how defect states at the surface or in the bulk influence the properties along the process chain and the quality of the resulting final device.

5.24.8 CONCLUSIONS

Nanoparticle handling and formulation is the key for successful industrial implementation of particle-based nanotechnology. The transfer from lab- to industrial-scale still remains a challenge. Although many applications and a great number of different materials are involved, five common design principles for nanoparticulate products can be identified.[19] In detail these are:

1. Nanoparticle formation by bottom-up or top-down methods.
2. Intermolecular and interparticulate interactions.
3. Structure formation and self-organization by an interplay between transport phenomena and particle interactions.
4. Characterization across all relevant length scales along the process chain.
5. Multiscale modeling, simulation and optimization at the molecular, particle, continuum and process level.

In-depth studies of these common principles will unlock the tremendous potential of particle technology for the design of novel products, their economic and ecological production. These overarching principles can be understood as next generation unit operations in nanoparticle science and technology.

REFERENCES

1. Krekel, J., Polke, R., *Chem-Ing-Tech.*, 64, 528–535, 1992.
2. Baughman, R.H., Zakhidov, A.A., Heer, W.A.de, *Science*, 297, 787–792, 2002.
3. Mädler, L., Roessler, A., Pratsinis, S.E., Sahm, T., et al., *Sensor Actuat. B-Chem.*, 114, 283–295, 2006.
4. Kilian, D., Polster, S., Vogeler, I., Jank, M.P.M., et al., *ACS Appl. Mater. Inter.*, 6, 12245–12251, 2014.
5. Knieke, C., Steinborn, C., Romeis, S., Peukert, W., et al., *Chem. Eng. Technol.*, 33, 1401–1411, 2010.
6. Stenger, F., Mende, S., Schwedes, J., Peukert, W., *Chem. Eng. Sci.*, 60, 4557–4565, 2005.
7. Knieke, C., Sommer, M., Peukert, W., *Powder Technol.*, 195, 25–30, 2009.
8. Knieke, C., Romeis, S., Peukert, W., *AIChE J.*, 57, 1751–1758, 2011.
9. Damm, C., Körner, J., Peukert, W., *J. Nanopart. Res.*, 15, 2013.
10. Damm, C., Nacken, T.J., Peukert, W., *Carbon*, 81, 284–294, 2015.
11. Knieke, C., Berger, A., Voigt, M., Taylor, R.N.K., et al., *Carbon*, 48, 3196–3204, 2010.
12. Nacken, T.J., Damm C., Xing H., Rüger A., et al., *Nano Res.*, 8, 1865–1881, 2015.
13. Romeis, S., Schmidt, J., Peukert, W., Romeis, S., *Int. J. Miner. Process.*, 156, 24–31, 2016.
14. Konnerth, C., Damm, C., Schmidt, J., Peukert, W., *Adv. Powder. Technol.*, 25, 1808–1816, 2014.
15. Bitterlich, A., Laabs C., Busmann E., Grandeury A., et al., *Chem. Eng. Technol.*, 37, 840–846, 2014.
16. McClements, D.J., *Soft Matter*, 8, 1719–1729, 2012.
17. Müller, R., *Eur. J. Pharm. Biopharm.*, 50, 161–177, 2000.
18. Schmidt, J., Damm, C., Romeis, S., Peukert, W., *Chem. Eng. Sci.*, 102, 300–308, 2013.
19. Peukert, W., Segets, D., Pflug, L., Leugering, G. In Li, J., Marin, G.B., eds. *Mesoscale Modeling in Chemical Engineering Part I.* Elsevier, The Netherlands, 2015.
20. Machunsky, S., Grimm, P., Schmid, H.-J., Peuker, U.A., *Colloid. Surface A*, 348, 186–190, 2009.
21. Washburn, E.W., *Phys. Rev.*, 17, 273–283, 1921.
22. Teleki, A., Wengeler, R., Wengeler, L., Nirschl, H., et al., *Powder Technol.*, 181, 292–300, 2008.
23. Schilde, C., Mages-Sauter, C., Kwade, A., Schuchmann, H.P., *Powder Technol.*, 207, 353–361, 2011.

24. Kwade, A., *Powder Technol.*, 105, 14–20, 1999.
25. Reindl, A., Mahajeri, M., Hanft, J., Peukert, W., *Thin Solid Films*, 517, 1624–1629, 2009.
26. Mackay, M.E., Tuteja, A., Duxbury, P.M., Hawker, C.J., et al., *Science*, 311, 1740–1743, 2006.
27. Hunter, R.J., *Foundations of Colloid Science*, Oxford University Press, Oxford, United Kingdom, 2009.
28. Lyklema, J., *Fundamentals of Interface and Colloid Science. Soft Colloids*, Elsevier, The Netherlands, 2005.
29. Segets, D., Marczak, R., Schäfer, S., Paula, C., et al., *ACS Nano*, 5, 4658–4669, 2011.
30. Napper, D.H., *Polymeric Stabilization of Colloidal Dispersions*, Academic Press, 1983.
31. Hildebrand, J., Scott, R., *Solubility of Nonelectrolytes*, Reinhold, New York, 1949.
32. Hansen, C.M., *Hansen Solubility Parameters. A User's Handbook*, CRC Press, Boca Raton, Florida, Taylor & Francis Group, 2007.
33. Vincent, B., Edwards, J., Emmett, S., Jones, A., *Colloid. Surface*, 18, 261–281, 1986.
34. Saunders, S.R., Eden, M.R., Roberts, C.B., *J. Phys. Chem. C*, 115, 4603–4610, 2011.
35. Reindl, A., Peukert, W., *J. Colloid Interface Sci.*, 325, 173–178, 2008.
36. Mori, Y., *KONA*, 32, 102–114, 2015.
37. Lin, W., Walter, J., Burger, A., Maid, H., et al., *Chem. Mater.*, 27, 358–369, 2014.
38. Eisenthal, K.B., *Chem. Rev.*, 96, 1343–1360, 1996.
39. Roke, S., Gonella, G., *Annu. Rev. Phys. Chem.*, 63, 353–378, 2012.
40. Schneider, L., Peukert, W., *Part. Part. Syst. Charact.*, 23, 351–359, 2006.
41. Schürer, B., Wunderlich, S., Sauerbeck, C., Peschel, U., et al., *Phys. Rev. B*, 82, 15, 2010.
42. Israelachvili, J.N., *Intermolecular and Surface Forces*, Elsevier, The Netherlands, 2015.
43. Stenger, F., Peukert, W., *Chem. Eng. Technol.*, 26, 177–183, 2003.
44. Engelhardt, K., Lexis, M., Gochev, G., Konnerth, C., et al., *Langmuir*, 29, 11646–11655, 2013.
45. Engelhardt, K., Rumpel, A., Walter, J., Dombrowski, J., et al., *Langmuir*, 28, 7780–7787, 2012.
46. Segets, D., Komada, S., Butz, B., Spiecker, E., et al., *J. Nanopart. Res.*, 15, 1111, 2013.
47. Segets, D., Lutz, C., Yamamoto, K., Komada, S., et al., *J. Phys. Chem. C*, 119, 4009–4022, 2015.
48. Förster, H., Thajudeen, T., Funk, C., Peukert, W., *Waste Manag.*, 52, 346–352, 2016.
49. Zhu, C., Yu, Q., Dave, R.N., Pfeffer, R., *AIChE J.*, 51, 426–439, 2005.
50. Rumpf, H., Sommer, K., Steier, K., *Chem-Ing-Tech.*, 48, 300–307, 1976.
51. Rumpf, H. In *Particle Technology Series*. Springer, 1975.
52. Rumpf, H., *Chem-Ing-Tech.*, 46, 1–11, 1974.
53. Blümel, C., Sachs, M., Laumer, T., Winzer, B., et al., *Rapid Prototyping J.*, 21, 697–704, 2015.
54. Schmidt, J., Sachs, M., Blümel, C., Winzer, B., et al., *Powder Technol.*, 261, 78–86, 2014.
55. Zimmermann, I., Eber, M., Meyer, K., *Z. Phys. Chem.*, 218, 51–102, 2004.
56. Srikantharajah, R., Gerstner, K., Romeis, S., Peukert, W., *Nanoscale*, 8, 7672–7682, 2016.
57. Srikantharajah, R., Schindler, T., Landwehr, I., Romeis, S., et al., *Nanoscale*, 8, 19882–19893, 2016.
58. Faber, H., Klaumünzer, M., Voigt, M., Galli, D., et al., *Nanoscale*, 897–899, 2011.
59. Faber, H., Burkhardt, M., Jedaa, A., Kälblein, D., et al., *Adv. Mater.*, 21, 3099–3104, 2009.



Taylor & Francis
Taylor & Francis Group
http://taylorandfrancis.com

5.25 Simulation of Powders and Particles in Dry and Wet Phases

Junya Kano and Jusuke Hidaka (5.25.1)
Mikio Sakai (5.25.2)
Yutaka Tsuji (5.25.3)
Mojtaba Ghadiri, Tina Bonakdar and Sadegh Nadimi (5.25.4)
Kenji Iimura and Ko Higashitani (5.25.5)
Ryoichi Yamamoto (5.25.6)

5.25.1 POWDER SIMULATION USING DISCRETE ELEMENT METHOD (DEM)

Powder simulation, or the computer simulation of powder behavior, has played an important role in the understanding of powder phenomena and its use in industry. Recently the performance of computers significantly has been developed, and also computer simulation methods have been advanced. Computer simulation has the following advantages:

1. It can give lots of detailed information on physical quantities that cannot be observed in experiments.
2. It can examine in detail the effects of various parameters on the powder phenomenon.
3. It can examine the effect of configuration of equipment without actuallly manufacturing the equipment.
4. It can give detailed information on large scale instruments under severe condition that are difficult to do experiment.

There are several simulation methods in powder technology, as follows: DEM (Distinct Element Method),[1] FEM (Finite Element Method),[2] DSMC (Direct Simulation Monte Carlo),[3] SPH (Smoothed Particle Hydrodynamics),[4] and automaton,[5] and the method in which these methods are coupled to each other.

DEM (also known as the discrete element method), developed by Candall and Strack, was the first powder dynamics simulation, and has been the most reliable simulation method in the field of powder technology. In DEM simulation, the flow behavior of a powder is simulated by tracking the movement of individual particles based on the following equation for translational and rotational motions of particle i, with mass m_i, and a moment of inertia I_i:

$$m_i \frac{d\boldsymbol{v}_i}{dt} = \sum \boldsymbol{F}_i \tag{5.25.1}$$

$$I_i \frac{d\boldsymbol{\omega}_i}{dt} = \sum \boldsymbol{M}_i \tag{5.25.2}$$

Here, $\boldsymbol{v}_i$ and $\boldsymbol{\omega}_i$ are the translational and angular velocities of particle i respectively, $\sum \boldsymbol{F}_i (= \boldsymbol{F}_i^c + \boldsymbol{F}_i^{nc} + \boldsymbol{F}_i^f + \boldsymbol{F}_i^g)$ is the summed external forces acting on particle i, $\boldsymbol{\omega}_i$ is the torque acting on particle i, $\boldsymbol{F}_i^c$ is the contact force acting on particle i (by adjacent particles or the wall), $\boldsymbol{F}_i^{nc}$ is the noncontact forces by electric or magnetic fields, $\boldsymbol{F}_i^f$ is the particle-fluid interaction force on particle i, and $\boldsymbol{F}_i^g$ is the gravitational force.

By solving Equations (5.25.1) and (5.25.2), the trajectories, velocities, and transient forces of all particles within the powder can be determined. The detailed temporal and spatial information on powder phenomena obtained from this simulation offers us a better fundamental understanding of powder behavior required to design powder processing.

On the other hand, DEM has a fatal flaw, which is that there is a limit to the number of particle elements the simulation can handle, and this number is relatively small. This means that large-scale powder phenomena involving a substantial number of particles cannot be simulated by DEM. The following describes the recent progress, and problems encountered by the authors regarding the use of DEM.

5.25.1.1 Application of DEM Simulation to Powder Phenomena

DEM simulation using particle element reproduces the discrete properties peculiar to powder behavior well, such as the segregation of particles and generation of slip lines in a flowing particles.[6,7] DEM has, therefore, been applied to the understanding of powder phenomena necessary for the design of powder processing such as storage, comminution, granulation, mixing, and classification.

Slow Powder Flow

The mechanisms behind the "slow flow of powders," so often encountered in industrial processes, was clarified using DEM. Powder flows can be classified into two types: rapid flow, and slow flow.[8,9] Slow flow is also called dense powder (granular) flow or frictional powder (granular) flow. While many studies regarding rapid flow have been done,[10] the study regarding dense powder flow was one by Bagnolds only.[11] As such, our understanding of slow flow remained poor.

Dense powders are an assembly of particles transmitting forces by means of friction at the contact point between particles. An analysis of flow behaviors for dense flow powders was conducted using DEM simulation, demonstrating that it has a discontinuous flow peculiar to the powder layer. The mechanism of this discontinuous flow was mechanically clarified using continuum mechanics,[12,13] and the flow's characteristics with respect to the flow of a fluid were explicitly explained. This fundamental understanding of dense powder flow is invaluable for the design of industrial powder equipment.

Comminution

Comminution is one of the important unit operations in size reduction of solid particles to produce fine powder, and it has been carried out in many fields of industries. Grinding operations can be done by using several types of media mills such as tumbling, vibration, planetary, and stirred mills.

DEM simulation for media milling such as tumbling,[14–16] vibration,[17,18] and planetary[19–22] ball mills has been performed. The purpose of the simulation is to predict grinding behavior such as particle size and particle size distribution. Figure 5.25.1 shows the comparison between the DEM simulation and experiment results of particle behavior in the tumbling ball mill when the mill is operated in six typical rotation rates.[23] The particles are colored according to their speed. The particle behaviors in the simulation and experiment are highly consistent when the mill speed is changed. The method to estimate the particle size during grinding has been proposed by the impact energy of media calculated with DEM simulation.[24,25]

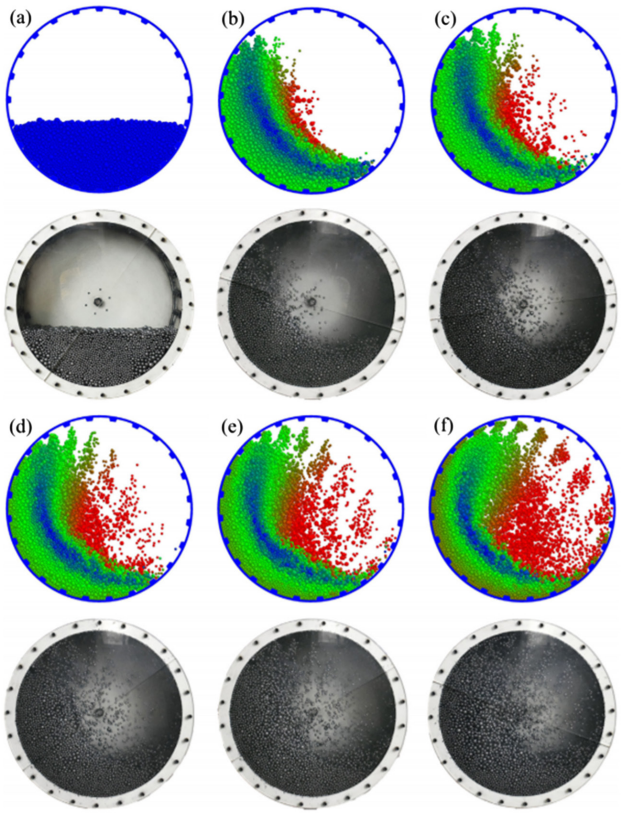


FIGURE 5.25.1 Comparison between the DEM simulation and experiment results of particle behavior when the mill is operated in six typical rotation rates.

The stirred mills are also wildly used in many industrial production processes, such as for electric parts, cosmetics and ink, and media motion in stirred mills simulated by DEM.[26–29] Figure 5.25.2 shows the representative flow patterns in the stirred mill from the experiments and simulations when the flows reach the steady states determined by examining power draw and particle velocity.[30] DEM coupled with CFD(Computational Fluid Dynamics) simulation has been applied to wet milling processing.[31–34]

Direct particle breakage models have been developed on the basis of DEM.[35,36] Figure 5.25.3 shows the particle breakage behavior simulated by DEM.[37] The impact velocity against the wall is 50 m/s. It can be found that cracks are initiated and propagate between the primary particles.

Figure 5.25.4 shows particle flow through and breakage within a jaw crusher itself with frames just before and after a number of breakage events.[38] Figure 5.25.5 shows the shapes of fragments after the compression test in the simulation by Advanced DEM(ADEM).[39] ADEM has been developed for understanding particle breakage.

Granulation

Figure 5.25.6 shows a model of the particulate internal structure of a spray dried granule generated with the DEM based on real structure parameters to obtain the correlation between structural and mechanical properties.[40] Granules' behavior in a continuous drum mixer was simulated by DEM.[41]

Mixing

Powder mixing of particulate materials is one of the crucial operations in chemicals, food, and plastics fields. It is well known that particle size distribution and particle density distribution lead to segregation.[42–44] Figure 5.25.7 shows snap shots of the mixing behavior of alumina and stainless steel particles in the experiment and the DEM simulation at different times.[45] The density of alumina and stainless steel particles are 3600 and 7930 kg/m^3, respectively. The alumina particles with lower density are close to the container wall and in the vicinity of the surface of particle bed. Figure 5.25.8 shows DEM mixing simulation of low and high moisture content powder. The effect of moisture content on mixing are discussed.[46]

Sieving and Filtration

Particle motion regarding sieving has been simulated by DEM.[47,48] Figure 5.25.9 shows the motion of particles on an inclined screening chute using the DEM.[49] Computational experiments have been conducted to examine the undersize particle motion across the material layer and through the apparatus for bimodal mixtures.

The concentration of particulate matter (PM) such as PM2.5 has reached an unprecedented high level. Nowadays fibrous filters have been widely used in air purification in commercial and residential environments because of excellent

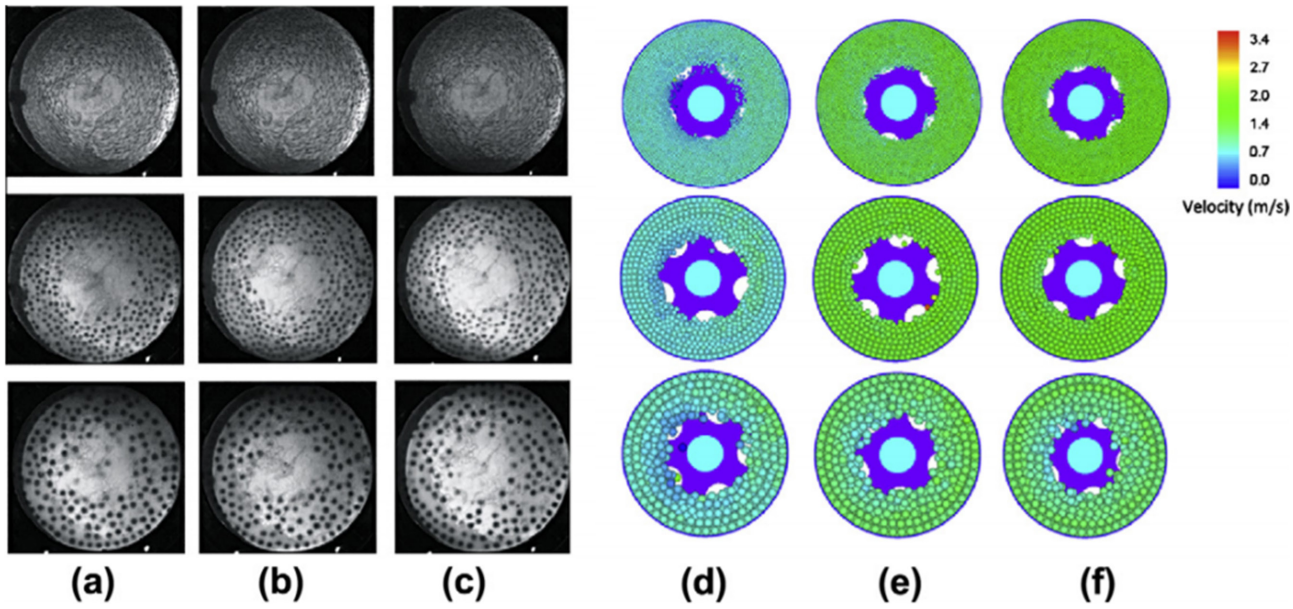


FIGURE 5.25.2 Experimental and simulated flow patterns for 2 mm (top row), 4 mm (middle row), and 6 mm (bottom row) at different disk speeds; (a and d) 800 rpm; (b and e) 1200 rpm; and (c and f) 1400 rpm. The color represents the particle speed.

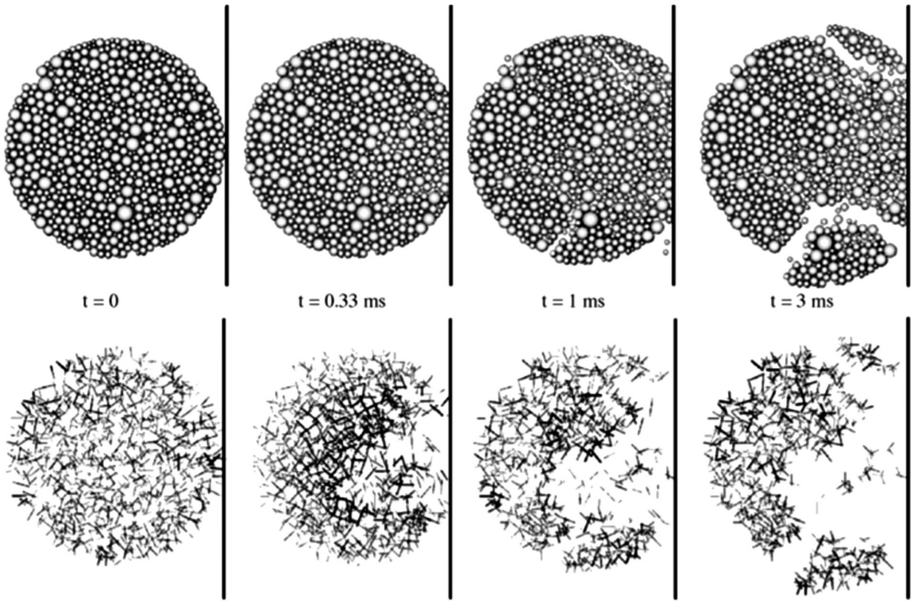


FIGURE 5.25.3 Particle breakage behavior of a single granule simulated by DEM.

filtration efficiency. Figure 5.25.10 shows the particle deposition process on the surface of a fibrous filter with dimensionless time.[50] At the beginning of the filtration, particles mainly collided with fibers and deposited on the surface of fibrous filters. Then, more and more particles were captured by other deposited particles instead of fibrous filters. Other simulations concerning filtration have been done.[51,52]

Ironmaking Process and Others

DEM is also applied to ironmaking processes such as blast furnacing and sintering processes. Understanding the in-furnace state of the blast furnace is important for blast furnace operation in ironmaking processes.[53–58] Figure 5.25.11 shows the distribution of the void fraction in a blast furnace calculated by DEM.[59] The void fraction is one of the important physical property to correlate permeability. The effect of coke rate on the void fraction is discussed.

In ironmaking blast furnaces, hot air is injected laterally from tuyeres, and a void region called a raceway is formed. The raceway plays a crucial role in blast furnaces. Figure 5.25.12 shows the raceway formation process simulated by the DEM-CFD coupled method when gas velocity is 18 m/s.[60] Initially, a small plume-like cavity enlarging towards the vertical direction is generated in front of the tuyere.

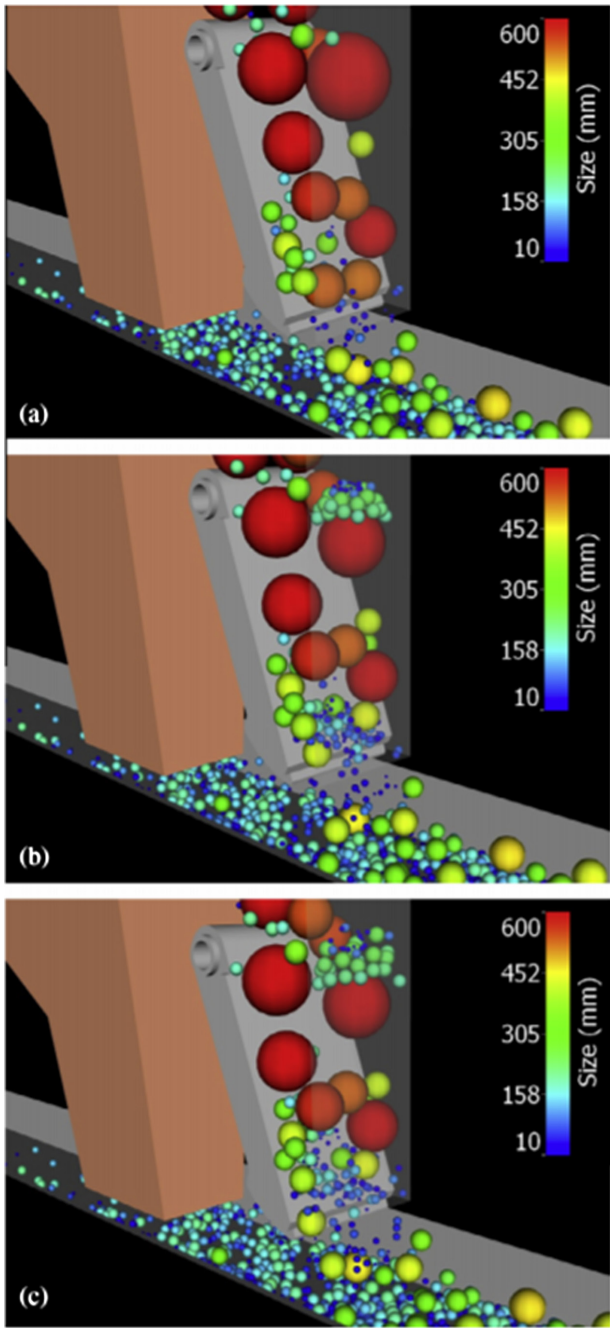


FIGURE 5.25.4 DEM prediction of particle flow through and breakage within a jaw crusher. The particles are colored by size with red being large, green being intermediate, and blue being the smallest. Particles are loaded during the compression phase, (b) intermediately post fracture, and (c) after re-arrangement of the fragments during the opening part of the cycle.

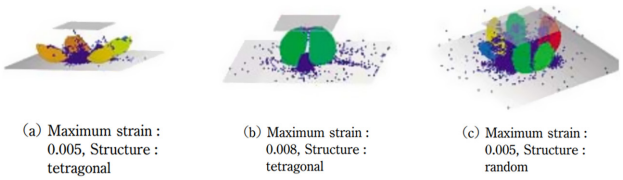


FIGURE 5.25.5 Shapes of fragments in the simulation by advanced DEM.

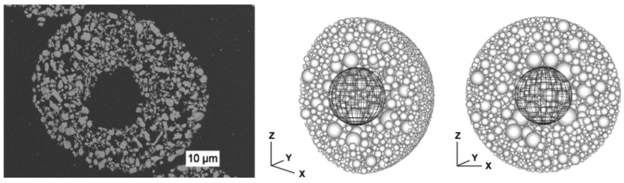


FIGURE 5.25.6 Cross section of real (left) and simulated (middle and right) granule structure.

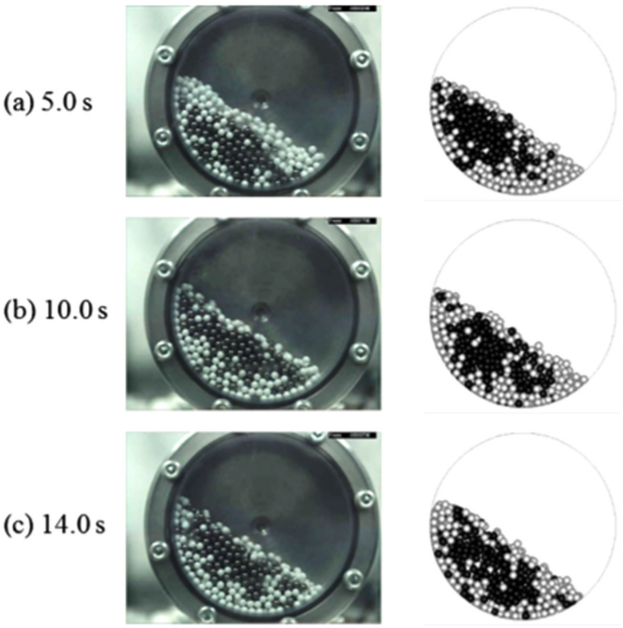


FIGURE 5.25.7 Snap-shots of mixing behavior in the experiment (left) and the DEM (right) at different times: (a) 5.0 s, (b) 10.0 s, and (c) 14.0 s.

5.25.1.2 Problems of DEM Simulation

Powder simulations still have some difficult problems to overcome when it comes to obtaining useful information on the design of large powder systems. The main issues are: (1) the development of large-scale simulations using DEM, (2) the development of a coarse-grained simulation model, (3) the development of a method for representing particle shape, and (4) the development of large-scale simulations method without using DEM.

Development of Large-Scale Simulation Using DEM

DEM simulation traces the movement of individual particle elements, making it difficult to handle a large number of particle elements in the calculation. As such, the acceleration of simulation calculations is necessary to gather useful information for the design of actual powder processing systems. To solve this, improvements in the simulation algorithm, and the application of parallel calculations, have been studied.

Mio tried to accelerate DEM calculation by optimizing the particle detection process,[61] tuning the program,[62] and developing a high-speed DEM code that can calculate more than a million particles by the parallel computing technology using a MPI (Message Passing Interface).[63]

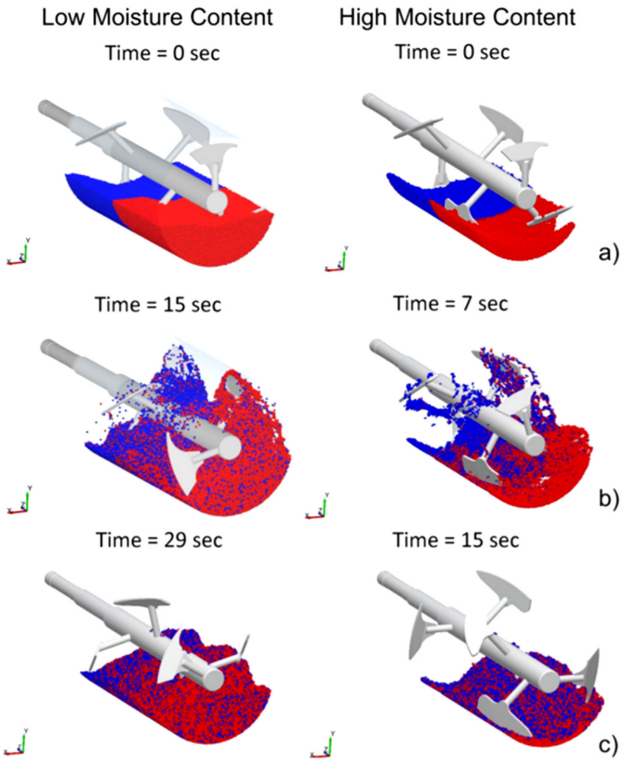


FIGURE 5.25.8 DEM mixing simulation, (a) before mixing, (b) during mixing, and (c) during a stop for sampling.

A DEM simulation calculating a few million particles has been successfully carried out using a super computer. Figure 5.25.13 shows the sedimentation behavior of 1.8 million particles in water, as simulated by the Earth Simulator at Earth Simulation Center in Yokohama, Japan.[64] It was completed using a coupled DEM-direct numerical simulation (DNS) on a highly parallel, vector supercomputer system.

Electronic miniaturization has rapidly advanced, and information gathered by DEM simulation is used directly for the design of production processes related to electronic devices. In these cases, it is important to define DEM parameters that accurately describe the interaction forces between particles, as well as the influences of particle shape.

Except for such few cases, because the direct use of DEM for simulating actual powder phenomena involving huge number of particles continues to be difficult, a coupling of DEM and simulations based on continuum mechanics as a finite element method (FEM) is critical for the future. The idea of a quasi-continuum method in molecular dynamics would also be helpful.[65]

We have proposed the design of hopper–bin system using the continuum dynamics model derived based on the knowledge of dense powder flow obtained by DEM simulation.[66] It would be useful as one of the usages of DEM simulation.

Speed-Up of DEM Simulation Using Coarse-Grained Particle (CGP)

DEM's simulation algorithm is similar to that of the molecular dynamic (MD) simulations known well by computational chemists. MD simulations also require large-scale calculations, since 1 mole of a substance contains 6×10^{23} particles. One approach to MD simulation is the application of the coarse-grained particle (GCP) method, proposed by Rudd and

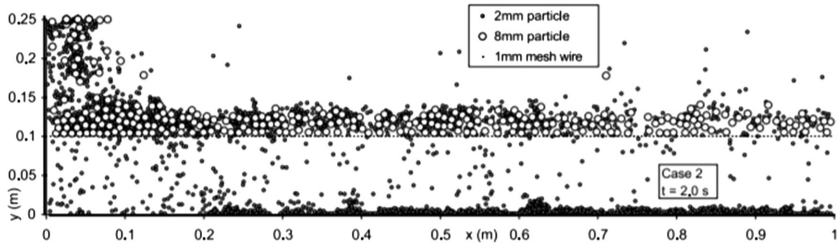


FIGURE 5.25.9 Motion of particles on an inclined screening chute using the DEM.

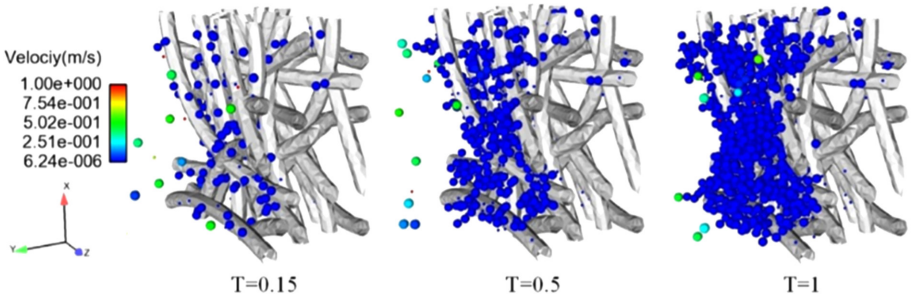


FIGURE 5.25.10 Particle deposition process on the surface of fibrous filter with dimensionless time.

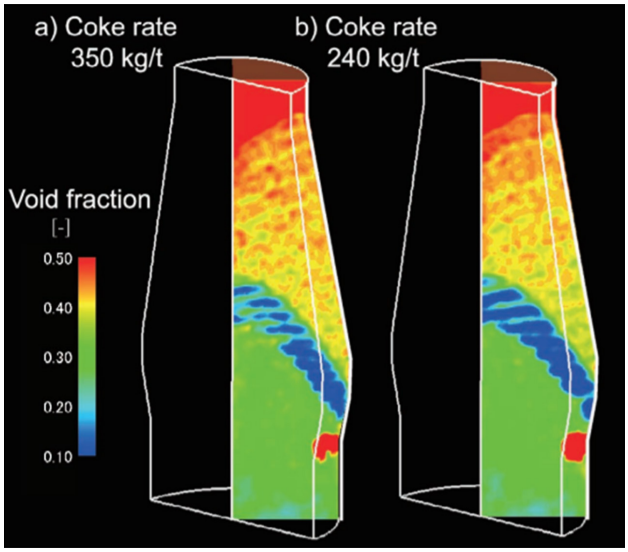


FIGURE 5.25.11 Influence of coke on void fraction in blast furnace.

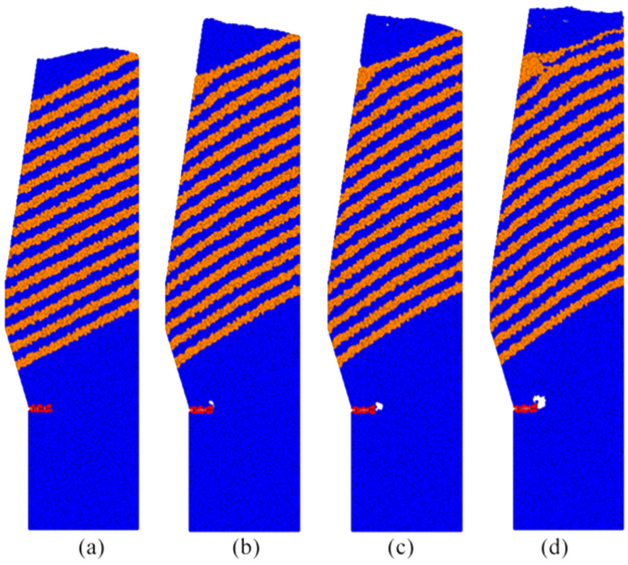


FIGURE 5.25.12 Raceway formation as a function of time. (a) 0 s, (b) 19 s, (c) 29 s, and (d) 54 s.

Broughto,[67] which has been tested successfully and would be useful for DEM.

As stated, DEM simulations represent particle behavior in flow by calculating individual particles trajectories using the Equations (5.25.1) and (5.25.2). By solving these discretized equations, the discrete time Δt is given by $\Delta t \le 2\sqrt{m/k}$, where $m\left(=\rho_p \pi x^3/6\right)$ is the mass of a spherical element particle, ρ_p is the particle density, x is the particle diameter, and k is the spring constant used for expressing interactive forces between particles. To speed up DEM calculations, increasing the discrete time Δt is effective. Δt becomes longer as the diameter of element particles increase: when the element particle's diameter increases about 4–5 times, the discrete time Δt increases approximately 10 times. However, the simulation reliability reduces significantly as particle diameters become larger than those of actual particles.

In CGS, an assembly of actual particles is represented by a single particle, called the coarse-grained particle (CGP), that has the same value as the physical quantity of actual particles. Sakai first proposed using CGP in DEM simulations.[68] If the coarse-grained particles are defined as a spherical particle that is l times larger than the diameter of the actual spherical particles, as shown in Figure 5.25.14, the number of actual particles in the CGP is l^3. Then, the physical quantity of the CGP is given such that the kinetic energy of the CGP equals to that of the actual particles contained in the CGP, as expressed by the following equation:

$$\frac{1}{2}m_{\mathrm{CGM}}\dot{\boldsymbol{x}}_{\mathrm{CGM}}^2+\frac{1}{2}\boldsymbol{I}_{\mathrm{CGM}}\dot{\theta}_{\mathrm{CGM}}^2=\ell^3\left(\frac{1}{2}m_{\mathrm{a}}\dot{\boldsymbol{x}}_{\mathrm{a}}^2+\frac{1}{2}\boldsymbol{I}_{\mathrm{a}}\dot{\theta}_{\mathrm{a}}^2\right) \tag{5.25.3}$$

Here, m is the particle mass, $\boldsymbol{I}$ is the moment of inertia, $\boldsymbol{x}$ is the position vector, and θ is the angular velocity. The subscript CGM denotes the coarse-grained particle and a denotes actual particle. Large-scale simulation for solid–fluid multiphase phenomena, such as a pneumatic conveying and fluidizing bed, has been tried using the coarse-grained particle.[69]

Representation of Particle Shape

Spherical particles are generally used in DEM simulations, and it is preferable from the perspective of speeding up calculations. However, spherical particles are extremely rare in actual powders. The development of a DEM simulation that can express particles with an arbitrary particle shape is needed to increase applicability to actual powders. Approximating an irregularly shaped particle with ellipsoidal particles, or expressing an irregular particle by combining many spherical element particles, has been tried since the outset of DEM research. However, these methods should be avoided in DEM with high calculation loads, except when particles of an extremely needle shape are simulated, or when the formation behavior of a packing bed of irregular particles is examined.

When particle shape affects the behavior of a powder to a considerable extent, the mechanism of the effect of particle shape on the behavior of individual particles differs, depending on powder phenomenon. Let us consider the flow of spherical glass beads versus irregular silica sand. Although both substances are SiO_2, the spherical glass beads are much more flowable than the irregular silica sand. The reason is that spherical particle rotate much more easily in flow than irregular particles. A flowing particle must increase its rotational speed in proportion to the flow velocity of the powder, and then must form an available free space around itself in order for rotation to occur. Spherical particles flow easily because of the free space for rotation around the particles. Powder with an easier rotation of constituent particles has a better flowability. Therefore, in a simulation of flow behavior, the influence of particle shape can be represented by varying the degree of

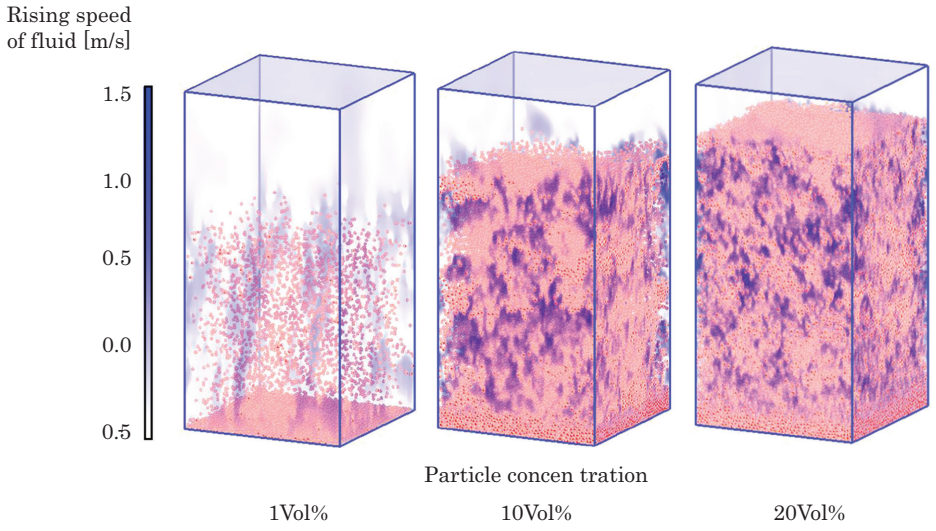


FIGURE 5.25.13 Settling behavior of particles in water (influence of particle concentration).

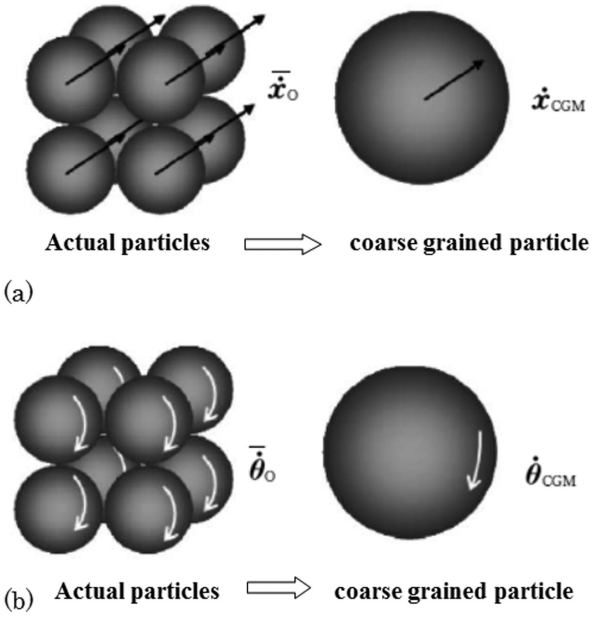


FIGURE 5.25.14 Concept of coarse-grained particle (CGP). (a) Translational and (b) Rotational.

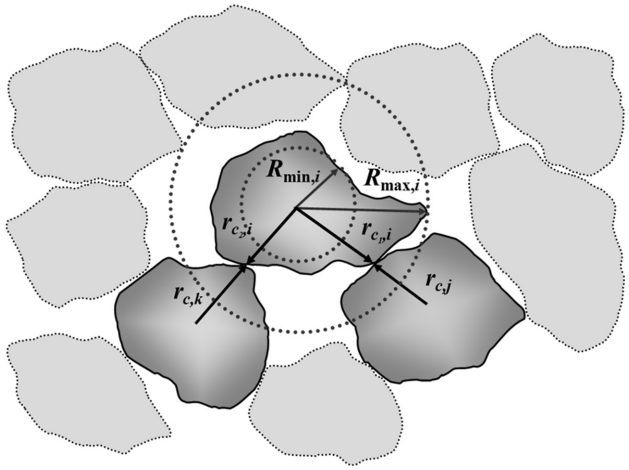


FIGURE 5.25.15 Representation of packing of irregular shaped particles by Spherical particle elements.

ease for rotation of the spherical elements themselves. Particle shape for flowing particles can be expressed using a Fourier descriptor, and thus the rotation of the spherical elements in DEM can be controlled based on the relationship between the Fourier coefficient and the coefficient of rolling friction of flowing particles.[70]

In addition to rotation, vibrating particles collide vigorously with each other. Particle shape also affects their repulsion direction after their collision. As such, the vibration behavior of particles can be simulated using the relationship between the particle shape and the probability distribution of repulsion direction obtained by experiment.[71]

While spherical elements can simulate particles in motion by choosing the appropriate adjustments, DEM simulations on stationary particles packed in a vessel are difficult because the points of contact between irregularly shaped particles differs according to the particle shape. Akashi proposed a solution.[72] For the packing of irregularly shaped particles as shown in Figure 5.25.15, they noticed that the position of contact between specified adjacent particles exists between the inscribed circle and the circumscribed circle of the projected image of the specified particle. Then, the diameter of a spherical element representing an irregularly shaped particle is determined based on the relationship between the degree of circularity of an irregular particle and the diameter of spherical element obtained by experiment. They applied this method to the estimation of the porosity distribution and the particle packing ratio of irregularly shaped coal particles. The results agreed well with experimental data.

It will be difficult to apply the powder simulation to particles of needle or flat shape. The development of the simulation for powders in a stationary state in which the particle shape influences strongly has only just begun.

Other Large-Scale Simulations Without Using DEM

As soon as DEM was introduced to the field of powder technology, developments for large-scale simulation began in the attempt to compensate for the drawbacks. One effective approach would be the application of smoothed particle hydrodynamics (SPH), which is another way to express an assembly of particles using a single particle. SPH is a particle-based Lagrangian method of fluid-flow simulation, and has been applied to the flow of powder discharging from a bin-hopper system.[4]

Another approach would be the application of "cellular automaton."[5] Here, the motion of individual particles within a powder is described by simple automaton rules, without solving the equation of motion of each particle. The automaton simulation developed for powder has been applied to large-scale simulations for the flow of iron ore and coke in blast furnaces, and is expected to function with a high speed.

Materials processing is composed of a series of powder processes. Then, we need to understand the powder processing well to produce desired materials. We have three approaches: experiments, modelings, and computer simulations. In particular, the computer simulation would be the most useful tool to understand the powder phenomena during processing. The computer simulation by DEM or DEM-CFD would be more widely applied to powder processing in the future.

5.25.2 RECENT ADVANCES IN DEM SIMULATIONS FOR INDUSTRIAL APPLICATIONS

Several approaches exist to create a wall boundary in the discrete element method (DEM). In previous DEM simulations, wall boundaries have been modeled by using a combination of simple surface equations or meshes. A combination of surface equations makes it impossible to create geometrically complex walls, such as industrial powder devices. Although arbitrary shaped wall boundaries can be modeled by using meshes, it is difficult to establish the algorithm to describe particle-to-wall interactions. To solve the problem for the wall boundary models, a signed distance function (SDF)-based wall boundary model has been proposed, where the wall boundary is expressed based on a scalar field. Originally, the SDF model has been used in the level set method in computational fluid dynamics.[73] In this section, an overview of the SDF is provided, and then the application of the SDF to powder processes is mentioned.

The SDF makes it possible to detect particle–wall interactions without complicated procedures. Our SDF model[74] considers energy conservation in non-dissipative systems, and hence, the interaction between the particle and the wall can be simulated accurately. In the DEM/SDF, the contact force is derived according to a conservation of elastic energy. The elastic energy is given by:

$$P_{\text{elastic}}^{\text{SDF}} = \frac{1}{2}k\left|\delta_{\text{n}}^{\text{SDF}}\right|^2 = \frac{1}{2}k\left(r-\phi\right)^2 \tag{5.25.4}$$

where ϕ and r are the SDF and minimal distance between the wall and the particle, respectively. The gradient of the energy P gives the elastic force between the particle and the SDF-based wall boundary:

$$\boldsymbol{F}_{\text{elastic}}^{\text{SDF}} = \nabla P_{\text{elastic}}^{\text{SDF}} = -k\boldsymbol{\delta}^{\text{SDF}} \cdot \left|\nabla\phi\right| \tag{5.25.5}$$

Hence, the normal component of the contact force in the DEM is given by:

$$\boldsymbol{F}_{\text{c}_\text{n}}^{\text{SDF}} = -k\boldsymbol{\delta}_{\text{n}}^{\text{SDF}} \cdot \left|\nabla\phi\right| - \eta\boldsymbol{v}_{\text{n}} \tag{5.25.6}$$

which conserves the energy in a non-dissipative systems because of the correction term $|\nabla\phi|$. The DEM/SDF has been applied to several powder processes.[75–80] Here, numerical simulations are addressed for a twin-screw kneader and a powder die-filling system.

At first, the application of the DEM/SDF method to a twin-screw kneader is described according to the previous study.[76] The complex paddle shape and a vessel were created by SDF. Validation tests were performed in a twin-screw kneader to prove the adequacy of the DEM/SDF method. For the validation system, paddles were rotated clockwise, and the paddle rotational velocity was 60 rpm. Figure 5.25.16 shows the SDF for four cross-sectional views of the paddle. The distance and sign are provided in the entire computational domain. 1 mm of glass beads were used in the validation tests. The number of solid particles (400,000) and their mass (0.524 kg) correspond to that in the experiment. Figure 5.25.17 shows the

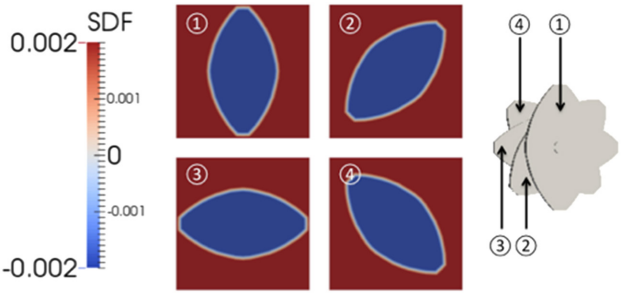


FIGURE 5.25.16 SDF in a twin-screw kneader.

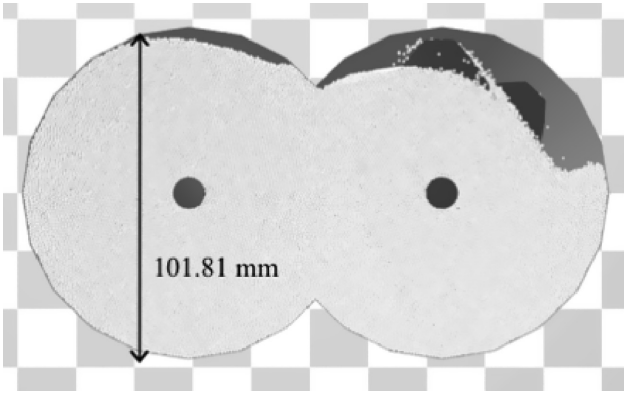


FIGURE 5.25.17 Simulation result in a twin-screw kneader.

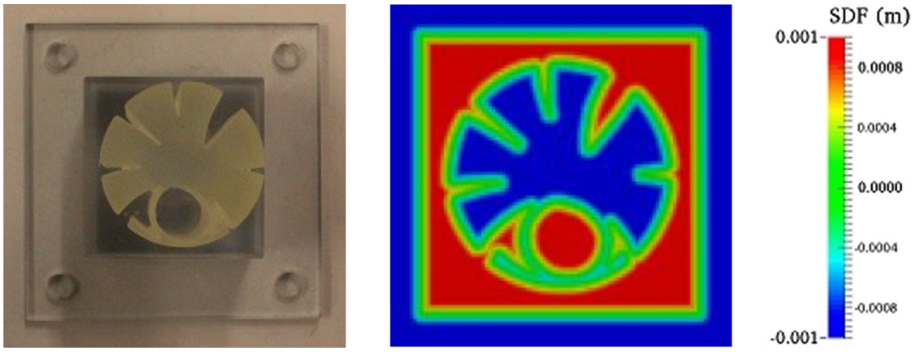


FIGURE 5.25.18 Die shape for a school batch of Univ Tokyo.

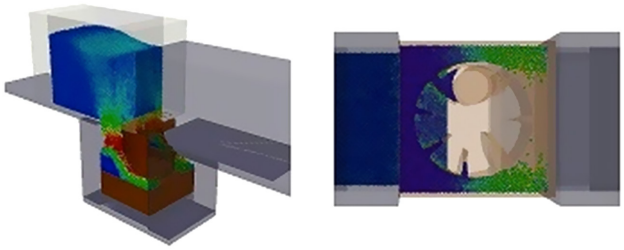


FIGURE 5.25.19 Die-filling simulation (0.15 s).

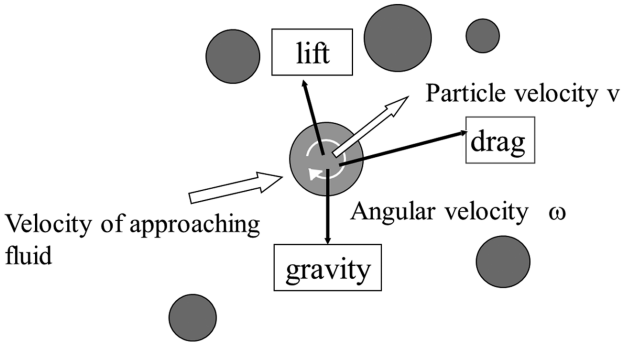


FIGURE 5.25.20 Forces acting on particle in fluid.

validation test results. The quantitative bed height between the simulations and the experiments was compared. The bed heights were estimated to be 101.81 and 101.24 mm in the simulation and experiment, respectively. Thus, the DEM/SDF was shown to simulate granular flow in a twin-screw kneader.

Subsequently, an application of the DEM/SDF method to a die-filling system[77] is described. Validation tests were performed to show the applicability of the DEM/SDF to a die-filling system. A complex shape die, such as the school badge of The University of Tokyo was selected in the validation test as shown in Figure 5.25.18. In this system, solid particles were flown into the die. The die dimensions were 25 mm × 25 mm × 20 mm. The shoe had a cuboid shape and dimensions of 35.5 mm, 30.0 mm, and 25.0 mm, and the shoe moved at 0.052 m/s. The number of computational particles (232000) and the particle size (500 μm) correspond to that in the experiment. Figure 5.25.19 shows the calculation results, where the elapsed time was 0.15 s. The calculation result agreed well with the experimental result in terms of the spatial distribution of particles and the solid particle velocity distribution. Consequently, the adequacy of the calculation result from the DEM/SDF method was proven in the die-filling system.

Thus, the SDF is shown to create a simple arbitrarily shaped wall boundary, and makes the accurate simulation of granular flow in a complex-shaped boundary possible. The author believes that the SDF will become a standard approach for wall boundary modeling in the DEM.

5.25.3 PARTICLE MOTION IN FLUID

In order to calculate the particle motion in fluid, we must consider the particle–fluid interaction. Particle–fluid interaction is sometimes called phase coupling or phase exchange or transport phenomena between phases.[81] There are three kinds of phase coupling, that is, mass coupling, momentum coupling, and energy coupling. All the three couplings must be considered simultaneously when heat and mass transport takes places. These couplings are classified into two kinds; one-way coupling and two-way coupling. In this section, cases without heat and mass transport are described.

The one-way coupling implies that particle motion is affected by fluid motion while fluid motion is not affected by particle motion. If the particle concentration is very low, the one-way coupling is enough. In this case, the fluid motion is given independently on the particle motion. Trajectories of particles in fluid are calculated by integrating the Newtonian equation of motion, taking into account the fluid force and other external forces such as gravity. See Figure 5.25.20. Numerical integration is done step-by-step with an appropriate time step. Concerning the fluid forces, several theoretical and empirical expressions are available which are explained in detail in Chapter 2.5 of this handbook.

In most industrial processes, particle concentrations are not so low that the fluid motion is affected by the presence of particles. Thus, not only forces acting on particles but reaction forces acting on fluid caused by particles must be taken into consideration. This interaction of particle with fluid is called two-way coupling. Fluid motion and particle motion are solved simultaneously in the two-way coupling. The fluid motion is described mathematically by the equation of continuity and the momentum equation. These equations are given

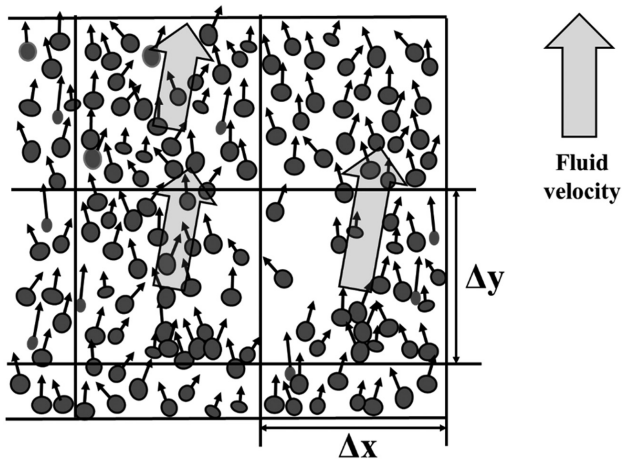


FIGURE 5.25.21 Local averaging approach.

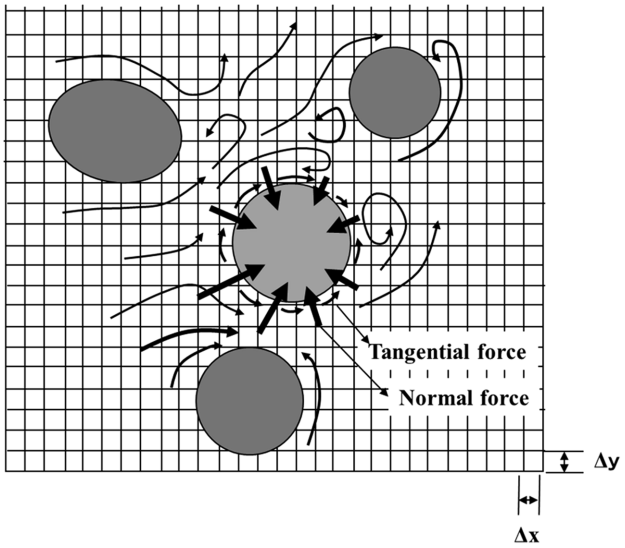


FIGURE 5.25.22 Image of DNS applied to particle–fluid flow.

in the form of partial differential equations and in general solved numerically in such complicated cases as particle–fluid flows.

The method of the numerical analysis of the two-way coupling is classified into two kinds. The first is the local averaging approach which has been developed by Anderson and Jackson.[82] The other is the so-called DNS (Direct Numerical Simulation).

In the local averaging approach, the flow field is divided into cells, as shown in Figure 5.25.21. The size of the cell should be larger than the particle size and smaller than the macroscopic flow scale. Values of fluid motion such as velocity and pressure represent the cell. The effects of particles on the fluid are taken into account through the void fraction of fluid phase and the total drag forces in the cell. The motion of all particles is calculated in the same way as in the one-way coupling by integrating the Newtonian equation of motion using the data of fluid representing cells. The void faction and the total drag force obtained from the results of the particle motion are inserted to equations of fluid of the next step.

To calculate the fluid motion, the equation of fluid motion is discretized based on these cells and the partial deferential equations are converted to multiple simultaneous algebraic equations. Unknown variables are velocities and pressure of the cells. Various numerical schemes and methods have been developed. Tsuji et al.[83] used the SIMPLE method developed by Patankar.[84] Calculated results of fluid are used for the calculation of particle motion at the next step. Most simulations of particle–fluid flows in industrial applications use the local averaging approach.

In DNS (Direct Numerical Simulation), instantaneous flow around each particle is solved based on the Navier–Stokes equation with no auxiliary assumption. The meaning of "Direct" is that this approach uses only rigorous equations and avoids empirical factors. The concept of DNS itself is not new. A numerical analysis of the flow around a single sphere in a uniform flow was one of the examples of early DNS. What is new in DNS is that this approach is applied to the cases where many particles interacting with each other move in the fluid.

Figure 5.25.22 shows an image of DNS in a particle–fluid flow. The flow field is divided into small cells as in the case of other methods of difference solution, but the size of the cell must be small enough compared with the size of the particle to make calculations around the particle as exact as possible. The fluid forces acting on particles are calculated by integrating the local normal and tangential forces on the surface of particles that are the solutions of the basic equations. In DNS, particles behave as moving boundaries. Various numerical techniques, such as finite element method,[85] immersed boundary method,[86] and Lattice Boltzmann method,[87] have been developed and used in DNS of particle–fluid flows.

The DNS is a powerful tool when the interaction with neighboring particles must be dealt with. Such interaction is given empirically in other methods. However, the DNS requires a considerable computation load. As the number of particles increases, DNS is difficult to use in practice. With the increase of computer powder, the number of particles handled by DNS increases steadily but still the case to which DNS is applied is limited.

As the particle concentration becomes higher, particle–particle interaction should be considered in addition to the two-way coupling. Concerning particle–particle interaction, two phenomena are known: collision and contact. If particles are in a dispersed phase, binary collision is dominant. As the particle concentration becomes much higher, particles keep in contact with each other. Particles are subjected to forces from other particles in contact. DEM (Distinct Element Method) has been developed to formulate such contact forces. DEM-CFD is a method of two-way coupling accompanied by the contact force.

The relation between particle motions before and after collision are easily obtained by elemental mechanics if the particle shape is not so complicated and if the coefficient of restitution and friction coefficient are given. The problem in the simulation is how to find collision pairs from many particles in the flow field. There are two methods concerning this problem. The first

is the deterministic method and the other is the stochastic one. In the deterministic method, the collision pairs are sought from trajectories of all particles. The stochastic method is the one making use of the collision probability. The stochastic method is inevitable when the number of particles become enormous. DSMC (Direct Simulation Monte Carlo)[88] was developed in the field of molecular gas dynamics for that purpose, and it has been found to be applicable to dispersed powder flows.[89] In DSMC, calculation is conducted for sample particles, the number of which is much smaller than the actual number.

5.25.4 BREAKAGE OF PARTICLES IN GAS PHASE

Knowledge of particle strength is very important for processes in which particle size reduction takes place deliberately, as in grinding and milling,[90] but also in tableting, dispersion, and powder handling, where particle breakage occurs undesirably and it adversely affects the product quality, dust formation, ability to process, and explosion hazards.[91] Considering the diverse particle structures, ranging from isotropic amorphous continuum (such as glasses), anisotropic crystalline, and a porous monolith to agglomerates of bonded primary particles, simulation of particle breakage poses a great challenge. Development of the field has been most extensive for the case of agglomerate structures. Nevertheless, even in this case the degree of freedom afforded by the primary particles as well as the way the agglomerates are formed add complexity to the breakage pattern, such that the prediction of particle size distribution is still not reliable. Extensive experimental work has been carried out to quantify particle breakage under various conditions (e.g. Salman et al.[92], Zhang and Ghadiri[93], Salman et al.[94], Cheong et al.[95], and Vogel and Peukert[96]). However, characterization of internal stresses of complex structures causing failure is not possible by experimental methods. On the other hand, numerical simulation provides a basis for sensitivity analysis of factors affecting the strength and failure of particles. Here we address agglomerate breakage first and then briefly outline other simulation methods that are more appropriate for the fracture of continuum solids.

Early work addresses the simulation of agglomerate strength and breakage patterns under both impact and quasi-static stressing conditions, assessing the effects of agglomerate morphology, crack morphology, and impact angle.[97–107] In recent years there has been substantial growth in numerical simulation and computational modeling in analyzing the breakage behavior of agglomerates.[108–113] The approaches can generally be divided into two main categories: discrete and continuum mechanics simulations, and are addressed in the following.

5.25.4.1 Discrete Element Method

A recent book by Thornton[114] outlines the principles and applications of DEM. In addition to a large number of codes available in the public domain (e.g. LIGGGHTS, dp3D, MercuryDPM, MFIX, SDEC, GranOO, Yade, Pasimodo, and ESyS-Particle), nowadays there are several commercial proprietary software packages which have been developed and widely used. EDEM (DEM Solutions, Edinburgh, UK), Rocky (ESSS, Florianópolis, Brazil), DigiDEM (Structure Vision Ltd, Leeds, UK), PFC (ITASCA Consulting Group, Inc, USA), ChuteMaven (Hustrulid Technologies Incorporated, USA), RecurDyn/Particles (Function Bay, Inc, Korea), SimPARTIX (Fraunhofer IWM, Germany), DEMpack (CIMNE, Spain), PASSAGE/DEM (Technalysis, Inc, USA), and ELFEN (Rockfield, UK) are examples of these software packages.

The early work[100,115–117] used simple-structured agglomerates, assembly of spherical particles bonded together based on the contact adhesive model of Johnson–Kendall–Roberts (JKR).[118] The effect of structure on agglomerate strength was first simulated by Ning et al.,[98] where three types of agglomerate structures were generated by varying particle size and bond strength and creating an external layer. Both Ning et al.[98] and Subero et al.[100] used the interface energy to calculate the cohesive interparticle forces. Subero et al.[100] generated agglomerates with macroscopic cavities to form different levels of porosity. The impact breakage of the agglomerates was then analyzed by impacting them at different velocities as a function of the porosity. Damage mainly occurred at the impact zone, and a number of particles were detached from the original structure, however some damages, albeit insignificant, were observed in the rest of the agglomerate as well. At high impact velocities, the impacts resulted in higher extents of damage, formation of smaller debris and a larger damage area at the impact zone. The outcome of Subero's work,[119] both experimental and numerical, led to a map for patterns of agglomerate breakage. As an example, the clusters sizes after impact at 8 m/s are shown in Figure 5.25.23 for an agglomerate with a given void fraction.

Moreno et al.[102] and Samimi et al.[107] report on the effect of impact angle on the agglomerate breakage. Based on the outcome of their work, by changing the impact angle, the same agglomerate shows significant spread in the pattern and extent of breakage. Bond properties and agglomerate structure are undoubtedly influential. However the underlying mechanisms

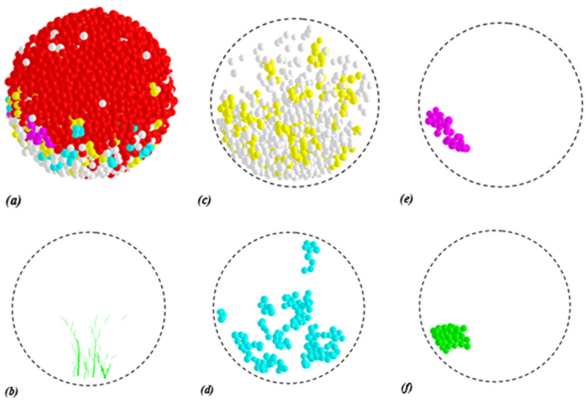


FIGURE 5.25.23 Impact breakage of the agglomerate with a given void fraction void fraction after 8 m/s impact.[120] (a) All the clusters, (b) Load propagation, (c) Clusters with 1 to 3 particles, (d) Clusters with 4 to 10 particles, (e) Clusters with 11 to 30 particles, (f) Clusters with 31 to 100 particles.

are not well understood and there is no predictive model of the effect of tangential loading. The effect of agglomerate structure on the breakage behavior, has been reported by Golchert et al.,[104] using X-ray micro computed tomography (μCT) and DEM simulation. Recently Dosta et al.[105] used a similar approach to analyze the breakage behavior of granules. They formed granules using glass ballotini and PVP binder. The particles and binder position as well as pore distribution were then characterized using μCT. They used the DEM software package MUSEN[121] to analyze the influence of granule microstructure on deformation behavior under compression. Other researchers also analyzed the breakage of the agglomerate by impact.[122–124] Thus, DEM has proved to be a powerful tool for the analysis of the effects of different parameters on the agglomerate strength. A mechanistic analysis based on the DEM results was presented by Kafui and Thornton,[97] who suggested that the extent of damage described by the damage ratio, Δ, (i.e. the number of broken interparticle bonds divided by the total number of bonds present in the agglomerate) is related to the Weber number, *We*:

$$We = \frac{\rho V^2 D}{\Gamma} \tag{5.25.7}$$

where

ρ, D, and Γ are the primary particle density, diameter, and interfacial surface energy
V is the impact velocity

The breakage propensity parameter η given by Equation (2.11.8) from Chapter 2.11 incorporates the Weber number, because K_c can be related to Γ by the use of Linear Elastic Fracture Mechanics. For example, for the case of plane stress:

$$K_c^2 = 2E\Gamma \tag{5.25.8}$$

it then follows that:

$$\eta \propto \frac{\rho V^2 D}{\Gamma} \times \frac{H}{E} \tag{5.25.9}$$

The ratio H/E is attributed to the elastic-plastic deformation characteristics of the agglomerate. When the simulation results are interpreted in the form of fractional loss per impact, Thornton et al.[125] report that at low impact velocities, corresponding to the chipping regime, the fractional loss per impact varies linearly with the Weber number, which is in agreement with the model of Ghadiri and Zhang.[126]

To account for the minimum impact velocity below which no damage occurs, V_0, Thornton et al.[125] proposed a modified version of the Weber number (We'):

$$We' = \frac{\rho D(V - V_0)^2}{\Gamma} \tag{5.25.10}$$

To model agglomerate breakage, Moreno-Atanasio and Ghadiri[103] explored a simple case where the energy required for breakage was linearly related to the incident kinetic energy. Considering the work spent to break a bond, they found that the damage ratio is given by:

$$\Delta \propto \frac{\rho D(V - V_0)^2}{\Gamma} \times \left(\frac{ED}{\Gamma}\right)^{2/3} \tag{5.25.11}$$

Clearly the Weber number and dimensionless group ED/Γ influence the breakage of agglomerates, as demonstrated by the numerical simulations of Moreno-Atanasio and Ghadiri[103] and more recently by Bonakdar and Ghadiri[127] and Loreti et al.,[128] who analyzed the agglomerate failure behavior under impact. In the work of Bonakdar and Ghadiri[127] agglomerates with different levels of porosity (31%, 51%, and 61% by volume) were generated by randomly removing some of the primary particles. The effects of bonding energy, porosity, impact angle, and velocity (0.5, 1, 5, 10, and 20 m/s) were investigated. Analyses of the breakage data were done according to Equation (5.25.11). In contrast to the early work of Moreno-Atanasio and Ghadiri,[103] no unification based on Equation (5.25.11) was observed. This is shown in Figure 5.25.24, where three clear trends, each representing a pattern of breakage prevail. Impacting agglomerates with low level of surface energies (0.5 and 1 J/m^2) results in disintegration. Breakage of agglomerates with intermediate levels of surface energies (1.5 and 2 J/m^2) occurs through fragmentation, whilst agglomerates with high surface energies (3 and 5 J/m^2) fail through chipping. Inspection of simulations for broken contacts in order to reveal broken agglomerates as well as propagated forces within the agglomerates was consistent with the observed patterns.

Loreti et al.[112] also simulated the breakage of auto-adhesive agglomerates impacting at a target wall. A similar case, addressing milling of ribbons, has been analyzed by Hare et al.[111] using the bond model of Brown et al.,[129] described later in this section.

Nguyen et al.[130] analyzed the impact of agglomerates on a spherical surface as relevant to dry powder inhalation technology using DEM as shown in Figure 5.25.25. The levels

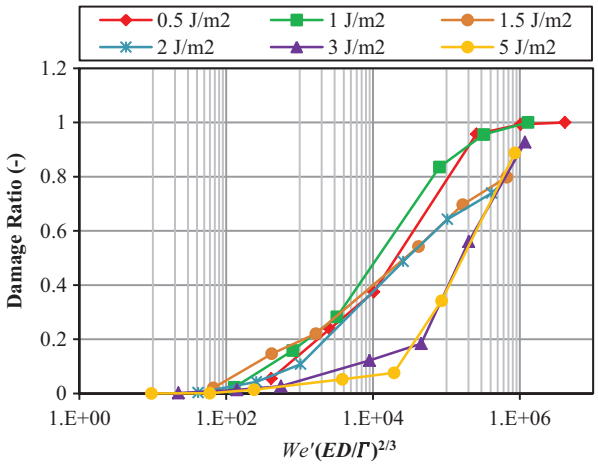


FIGURE 5.25.24 Damage ratio as a function of $\Gamma^{-5/3}$ for agglomerates with different surface energies.[127]

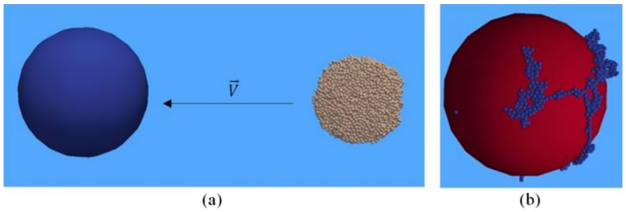


FIGURE 5.25.25 Simulation of inhalation process; (a) before impact, (b) after impact with some fines remained on the carrier particle.

From Ref. [130] with permission from John Wiley and Sons.

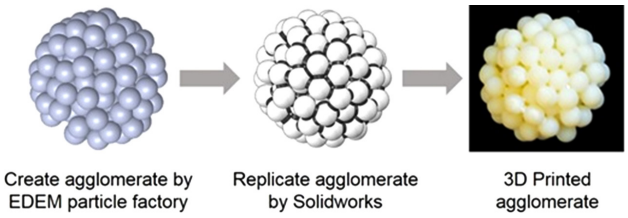


FIGURE 5.25.26 Simulation of 3D printed agglomerates using EDEM and TBBM contact bonding model.[132]

of interfacial surface energy between fines–fines (Γ_{1-1}) and fines–carrier (Γ_{1-2}) were found to be influential in the extent of coverage of the carrier particles. The outcome of the work focused on the coupling effect of adhesion and cohesion on agglomerate impact breakage behavior. The damage ratio was related to the ratio between cohesive to adhesive interfacial surface energies ($\Gamma_{1-1}/\Gamma_{1-2}$). The outcome of the work provided a regime map for preliminary operating conditions in different processes, where breakage matters.

The use of a representative bonding contact model is critical for simulating a realistic predictive breakage pattern. The JKR model is one of the most commonly used bonding models, representative of adhesive bond characteristics. Ning et al.[98] simulated the behavior of weak lactose agglomerates, for which there was a good agreement between the extent of breakage and macroscopic breakage pattern obtained by simulation and experiments. However, the work of Golchert et al.[104] shows that, despite using μCT to create the exact particle positions within the agglomerate, the results obtained from the DEM simulation do not match those of experiments. This implies that the JKR bonding model is not a good representative of the agglomerates generated using binders. A new bonding contact model has been developed by Brown et al.[129] for solid bonds based on Timoshenko beam theory considering bending, shear, and axial behavior of a bond. It is available in the current EDEM code and it has recently been used by Ge et al.[131] to simulate the deformation and failure of bonded agglomerates under quasi-static and dynamic conditions. The agglomerate structure was generated by EDEM for DEM Simulation and replicated by SolidWorks for experiments, where they were prepared by a 3D printing method. Such a method of preparation was chosen to provide precise control over the agglomerate structure. Different material properties

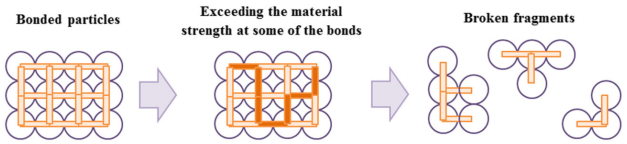


FIGURE 5.25.27 Schematic of the Bonded Particle model.[133]

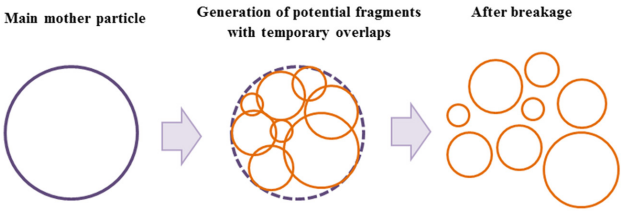


FIGURE 5.25.28 Fragment Spawning (FS) model to simulate particle breakage.[133]

(for both bonds and primary particles), printing orientation and structures were used to replicate agglomerates with different strength and structures in order to assess how predictive the simulations could be, as it is shown in Figure 5.25.26.

Ge et al.[131] reported differences between simulation predictions and experimental results emanating from anisotropic bond deformation and a lack of parity of bond length between experiments and simulations. This is attributed to the effect of printing orientation and the fact that in the TBBM model the bonds are connecting the centers of the particles together rather than their surfaces.

Another approach to simulate the breakage of the particles is the Bonded Particle (BP) model used by Guo and Curtis.[133] An agglomerate is formed by bonding a number of primary particles, as shown in Figure 5.25.27 and previously proposed by Grof et al.[134] and Potyondy and Cundall.[135] Primary particles can be either spheres[134,135] or squares.[136] The bonds used in this model have a simpler form than the TBBM model of Brown et al.[129] They are modeled based on elastic springs with constant shear and normal stiffness values. The breakage occurs when the contact force exceeds the bond strength whereby fracture propagation ensues. The size distribution of the fragments formed as a result of breakage is limited by the number of primary particles in the system. This can be increased to provide a better representation of fragment size distribution at the expense of computational effort.

To overcome this problem, one might use the Fragment Spawning (FS) model, which can in theory give unlimited fragment size fractions.[137–139] The model is schematically shown in Figure 5.25.28. The way the model works depends on the level of the stress in the system. If the stress is less than the breakage strength, the model of fatigue is applied to the system and the structure goes through strength reduction. If on the other hand the stress magnitude is greater than the particle strength, then the particle breaks and progeny particles replace the mother particles according to a pre-defined breakage function of the system.[133] Although using FS model solves the issue with fragment size distribution, the model has its

own drawback, as it is dependent on the empirically obtained breakage function.

Zheng et al.[140] used the BP model to simulate the breakage behavior of six different agglomerates (spherical, cuboidal, regular tetrahedral, regular octahedron, regular dodecahedron, and regular icosahedrons) using spherical primary particles. The agglomerates were impacted at a target wall in a range of velocities (10, 12, 14, and 16 m/s). The parameters required in the bonding model were calibrated using DEM simulation combined with some uniaxial compression experiments using coal samples. The size distribution of the fine particles/fragments after impact was then tracked and compared to that of experiments. A better agreement between simulation and experimental results was achieved for spherical agglomerates when they impacted at higher impact velocities. A complex behavior was observed for impacting non-spherical agglomerates, which produced more debris (fine particles) at the impact zone (near the target wall), while larger fragments produced at the top part of the agglomerates. The wall force and damage ratio were then tracked for different agglomerates, showing the increase in both parameters as the agglomerate sphericity increased. In these simulations the large differences in the strain rate between quasi-static compression and dynamic impact may have played a role in differences between simulation and experimental results.

In a number of cases DEM has been used to estimate the prevailing stresses and strains without taking account of particle breakage, whilst the latter has been quantified empirically, by subjecting a particle assemblage to representative dynamic conditions. Hare et al.[141] analyzed particle attrition in agitated particle beds in this way, for which the experimental work was carried out using a shear cell to quantify the extent of breakage as a function of shear strain and stress. The extent of attrition in the agitated bed was then predicted based on the above data and the simulated strain and stress conditions.

Particle shape is important in influencing particle strength and breakage. Various codes for non-spherical shape have been developed.[142] Examples are work of Rothenburg and Bathurst[143] for elliptical, Cundall[144] on polygonal, Pournin et al.[145] on spherosimplices, Williams and Pentland[146] on superquadric, Potapov and Campbell[147] on bonded assemblies of polygonal and polyhedra particles, and Jia and Williams[148] on bonded voxel assemblies. Favier et al.[149] introduced "clumped spheres" approach, for which a number of touching or overlapping spheres are fixed relative to each other to form the overall particle shape. The accuracy in the shape representation of complex shapes is obtained by increasing the number of spheres, albeit computationally expensive. Implementing the structure with sharp edges is theoretically possible, but it requires a large number of spheres and still it cannot replicate the very sharp edges accurately.[150] Therefore a robust approach is needed when it comes to breakage simulation of crystals or faceted particles; a model with the ability of simulating flat facets as well as sharp edges/corners.

Hart et al.[151] used a system composed of many polyhedral blocks to simulate failure of discontinuous rock mass under a given set of applied loads. The approach has been advanced through the work of Potapov and Campbell,[136] and has led to development of the Rocky software package (ESSS, Florianópolis, Brazil). This method can simulate the fracture of particles composed of polyhedra by failure through their interfaces.

DEM is a rapidly developing tool for predicting the breakage of particles. It is very helpful for obtaining a better understanding of the breakage behavior of materials. For simple structures the predictions are close to those of experiments. For complex structures, there is still a lot of work needed to be done to improve the models and techniques to better describe the physics of fracture. Nevertheless, it provides significant insight into phenomena and processes, where experimental work can either be costly and time consuming (such as plant-scale processes), or impossible (such as stress calculations in the system).

5.25.4.2 Continuum Mechanics Simulation

The approaches outlined in the previous section are useful for the analysis at agglomerate-scale level. However, the approaches based on finite element (FE) for the mesh-based method or smoothed particle hydrodynamics for mesh-free methods are more appropriate for an analysis of the breakage of continuum solids. In this context, the particle assembly mechanics can be simulated in the combined continuum–discrete framework, such as finite–discrete element,[152,153] also termed the multi-particle finite–element method,[154,155] and micro finite–element when it is combined with μCT images for representation of fabric and irregularity.[156]

Considerable research has been carried out in the past on implementing fracture and fragmentation algorithms in a combined finite–discrete element framework, in particular for application in rock blasting.[157] The recent advances in employing continuum fracture mechanics in particle technology can be presented in three categories from lower to higher computational requirements: 1) constitutive models developed in fracture mechanics that accounts for sudden softening in material strength,[157] 2) cohesive element approach which allows physical separation at element–element interface,[158] and 3) numerical technique that enables mesh independent growth of crack.[159]

In a methodology proposed by Bagherzadeh et al.,[160] the conventional DEM simulation has been enhanced by FE simulation to determine particle breakage after each step of DEM analysis. The breakage analysis is performed based on the loading conditions by a full FE stress–strain analysis within the particle and two new particles are generated and replacing the original particle. Two main criteria are required to define the onset of fracture in each particle and breakage line within each particle.

Recently, Nadimi and Fonseca[161] reported the implementation of the elastic–damage constitutive model in a combined finite–discrete element framework. In this model, a grain can crush or crack if it reaches its compressive or tensile strength, respectively. They have conducted a sensitivity analysis of the

parameters used in the theoretical work on the strength of brittle spheres by the Russell and Muir Wood.[162] They investigated the dependency of the normal force-displacement response of an ideal sphere to tensile and compressive strength.

A drawback in the last two case studies is the visualization of breakage and post fracture analysis that can be carried out by either replacing particles with smaller particles or the deletion of elements in fully coupled finite–discrete framework compromising on the particle mass. This can be resolved by inserting zero thickness interface elements between each element, which behave like the cohesive bonds in DEM. Therefore, the fracture can be propagated through the interface of an element. An example of using a cohesive element approach for the modeling of particle breakage is shown in Figure 5.25.29.[158] The initiation and propagation of fractures are explicitly simulated using nonlinear elastic fracture mechanics. The cohesive interface elements are inserted into the FE discretization associated with each particle. Different fracture mechanisms may occur inside the particle and can be represented in this framework. The evolution of a single particle breakage at different stages of loading is shown in Figure 5.25.29(a–d) and the splitting of a round grain is shown in Figure 5.25.29(e). Ma et al.[158] have concluded that the dominant fracture mechanisms are related to grain morphology. It is important to note that these methods are sensitive to mesh size and mesh orientation.

Since development of μCT, there has been a significant improvement in understanding the fracture mechanisms of continuum solids. Ludwig et al.[163] characterized the fracture surfaces of small cracks using a combination of μCT and diffraction contrast tomography. The outcome shows that cracks often propagate on crystallographic planes, although slip planes cause complexity in predicting the crack behavior.[164] Apart from the complex crack path, grain boundaries also affect the crack growth.[165] Figure 5.25.30 shows the three-dimensional visualization of the fracture process of a silica sand under compression observed in μCT.[166] Proudhon et al.[167] studied crack propagation in a crystalline microstructure using a new model, based on propagation through re-meshing. A crack was introduced in the geometry and a damage indicator '*D*' was used to evaluate the growth direction, which is a function of the accumulated plastic activity at the crack tip, as well as normal and shear stresses acting on the glide planes. Reasonably good agreement was obtained with experimental observation. However, this method and other advanced fracture models such as eXtended Finite Element Method (XFEM) have not yet been employed in analyzing particle breakage. It should be noted that the re-meshing and XFEM techniques can technically be implemented into the combined FDEM, but the computational cost will be extremely high when modeling crushable granular materials.

5.25.5 BREAKAGE OF AGGREGATES IN LIQUID PHASE

The breakup of large aggregates of arbitrary shape by the flow field is the fundamentally important problem of particulate science and technology in the liquid phase. Until recently, much attention has not been paid on this problem, mainly because of the hydrodynamic complexity in simulating the behaver of aggregates of irregular shape in the flow field. However, a great advancement of computer performance and simulation methodologies in recent decades made it possible to simulate complicated and large-scale problems. Hence, recently quite a few attempts have been made to simulate the breakup process of aggregates in flow fields as strictly as possible, by using various sophisticated simulation methods described in the preceding and succeeding sections. However, in general, the more strictly we try to simulate the behavior of the breakage of aggregates, the more computational time and cost we need, especially in the case of large aggregates of irregular shape. Hence, a simple, easy, comprehensive, and versatile model is required from the engineering point of view.

In this section, the 3D model for the breakup of large aggregates of arbitrary shape developed for the first time by Higashitani et al.,[168] in which the DEM was coupled with the approximated hydrodynamic approach, is briefly explained. Although some approximations are assumed in this model, the method is straight forward and easy to use without the knowledge of complicated simulation methodology, and the adequacy of simulated results was confirmed by the comparison with experimental data, as well as the other computational results. Hence the model is able to be used to evaluate versatile engineering problems at least qualitatively. A similar strategy with the free draining approximation and the similar

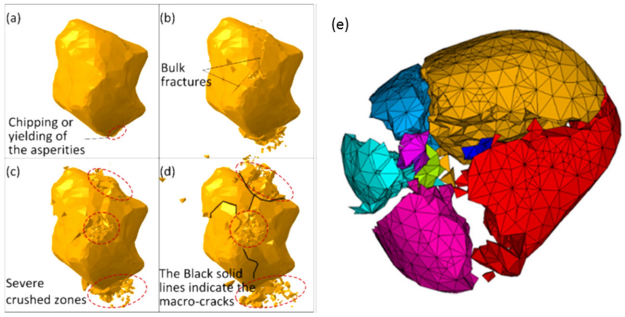


FIGURE 5.25.29 Modeling different types of particle breakage in the combined finite–discrete element framework.

From Ref. [158] with permission from Elsevier.

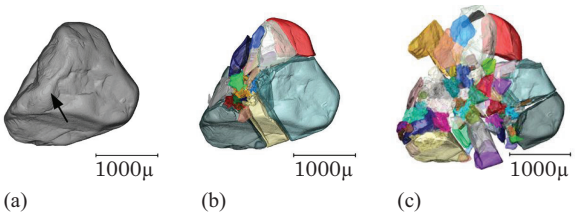


FIGURE 5.25.30 Three-dimensional visualization of fracture process in a silica sand under compression.

From Ref. [166] with permission from ICE Publishing.

concept of effective hydrodynamic force were adopted by Potanin[169] and Fanelli et al.,[170] respectively.

An aggregate in a fluid flow, which is composed of spherical particles of radius a and density ρ_p, deforms and then is fragmented by the hydrodynamic drag force and torque on the surface areas of constitutive particles facing to the flowing fluid. The surface areas were determined as follows: the surface of each particle was fragmented into 2592 sections such that the angle between the grid lines is $\pi/36$, as shown in Figure 5.25.31, and then each section was regarded as facing the fluid flow, if it is placed sufficiently far from the other particles. The local flow field affected by neighboring particles was approximated by using an experimental porosity function around the particle. Then, the force $\boldsymbol{F}_{hi}$ and torque $\boldsymbol{M}_{hi}$ acting on the area S_i of particle i facing to the flowing fluid is able to be calculated by the following equations:

$$\boldsymbol{F}_{hi} = \int_{S_i} \boldsymbol{\tau} \cdot \boldsymbol{n}\big|_{r_i=a}\, dS \tag{5.25.12}$$

$$\boldsymbol{M}_{hi} = \int_{S_i} \boldsymbol{r}_i \times \boldsymbol{\tau} \cdot \boldsymbol{n}\big|_{r_i=a}\, dS \tag{5.25.13}$$

where

- $\boldsymbol{\tau}$ is the stress tensor acting on the particle surface given by the local flow
- $\boldsymbol{r}_i$ is the position vector from the center of particle i
- $\boldsymbol{n}$ is the unit vector normal to the surface

These drag force and torque will be propagated to inside particles through the interparticle mutual interactions $\boldsymbol{F}_{mij}$; the interaction forces given by the DLVO theory for non-contacting particles, and the DEM repulsive force corresponding to their volume exclusion for contacting particles. Then, the equations of motion of constitutive particle i are given as follows.

$$m\frac{d\boldsymbol{u}_{pi}}{dt} = \boldsymbol{F}_{hi} + \sum_j \boldsymbol{F}_{mij} \tag{5.25.14}$$

$$I\frac{d\boldsymbol{\omega}_{pi}}{dt} = \boldsymbol{M}_{hi} + a\sum_j \boldsymbol{F}_{mij} + \boldsymbol{n}_{ij} \tag{5.25.15}$$

where

- m (=(4/3) $\pi a^3\rho_p$) and I (=(8/15) $\pi r a^5\rho_p$) are the mass and moment of inertia of a particle, respectively
- $\boldsymbol{u}_{pi}$ and $\boldsymbol{\omega}_{pi}$ are the velocity and angular velocity of particle i,
- $\boldsymbol{n}_{ij}$ is equal to $\boldsymbol{r}_{ij}/r_{ij}$
- $\boldsymbol{r}_{ij}$ is equal to $(\boldsymbol{x}_i - \boldsymbol{x}_j)$
- $\boldsymbol{x}_i$ is the position vector of the center of particle i

Then, displacements of all the particles from time t to $t+\Delta t$ are estimated by DEM procedure, using Equations (5.25.14) and (5.25.15).[171] Repeating this procedure for a given time period, the time-dependent behavior of the whole aggregate can be simulated. This is the rough skeleton of the present model. The details are given elsewhere.[168]

Figure 5.25.32 shows a series of snapshots of the deformation and breakup of an agglomerate in a simple shear flow of viscosity μ_f and shear rate γ_s. It is found that the aggregate is rotated, elongated into the flow direction, and then split into smaller fragments, but not eroded one by one to single particles from the aggregate surface as in the case of the breakup by ultrasonication,[172] as described in the Section 5.2.2.5.

By repeating the similar computation for shear flows of various intensities, the correlation between the volume-based average number of particles in the final fragments and the shear stress $\mu_f\gamma_s$ can be obtained, as follows:

$$< i >= c\left(\mu_f\gamma_s\right)^{-P} \tag{5.25.16}$$

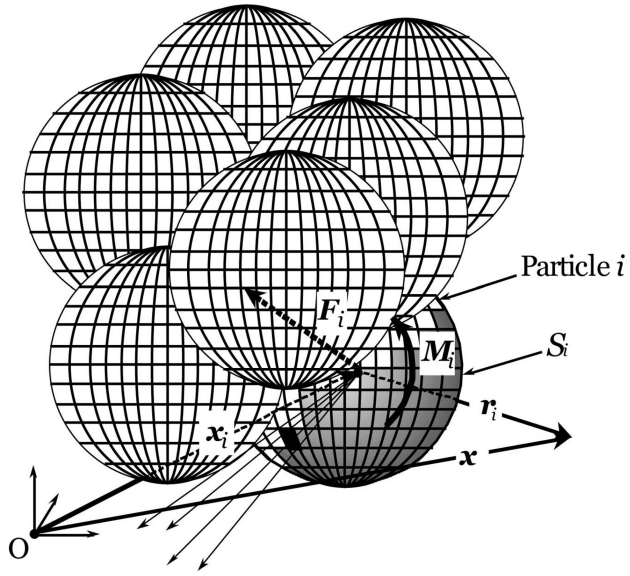


FIGURE 5.25.31 Schematic drawing of the simulation model of an aggregate and the coordinate system. Dark sections on the particle i indicate sections which are regarded as exposed directly to the flow. Lines are drawn to four corners of each section from the particle center in order to check whether the section is exposed to the fluid or not.

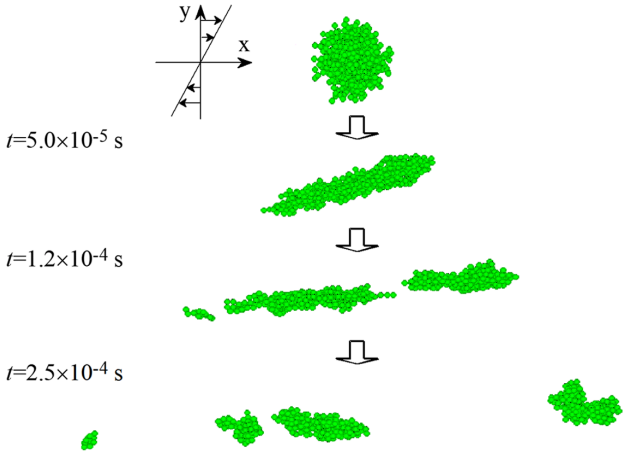


FIGURE 5.25.32 Snapshots of the fragmentation of an aggregate of in a simple shear flow.

where values of c and P are the constants depending on the structure of aggregates. It is found that the value of P for the aggregate of the fractal dimension 2.4 is nearly constant irrespectively of aggregate structures, that is, 0.927 ± 0.054, which is consistent with the experimental value, 0.879, by Sonntag and Russel.[173] On the other hand, the value of c varies with the value of a, the number of particles in an aggregate N, and the gap between constitutive particles δ. However, assuming that the final size of fragments is determined by the balance between the adhesive force between particles and the hydrodynamic drag on particles, and introducing the non-dimensional ratio of the magnitudes of these forces, N_{DA}, defined by the following equation:

$$N_{DA} = 6\pi\mu_f a^2\gamma_s \Big/ \left(\frac{Aa}{12\delta^2}\right) = \frac{72\pi\mu_f a\gamma_s\delta^2}{A} \quad (5.25.17)$$

where A is the Hamaker constant, almost all data of $<i>$ fall around a single line in the graph of log–log scale, irrespectively of the difference of a, N, and δ. This relation is expressed by the following equation:

$$< i >= 27.9 \times N_{DA}^{-0.872} \quad (5.25.18)$$

This equation gives us a good tool to estimate the average size of flocs that exist stably in a given shear flow.

This model is easily applicable to the other problems of aggregates in flows, such as the breakup of aggregates in the elongational flow,[168] in which the prediction agrees well with experimental results by Soos et al.,[174] the deposition and breakage of aggregates colliding to walls[175] or fibers,[176,177] the entrainment of deposited aggregates from the wall by the fluid flow,[178] and so on. An example of the snapshot of entrainment of a deposited aggregate by the shear flow is shown in Figure 5.25.33.[178]

It is interesting to know that the deposited aggregate is firstly peeled off from the wall with rotation and then fragmented by the shear flow under the given condition, although the other entrainment behavior is observed under the other condition.

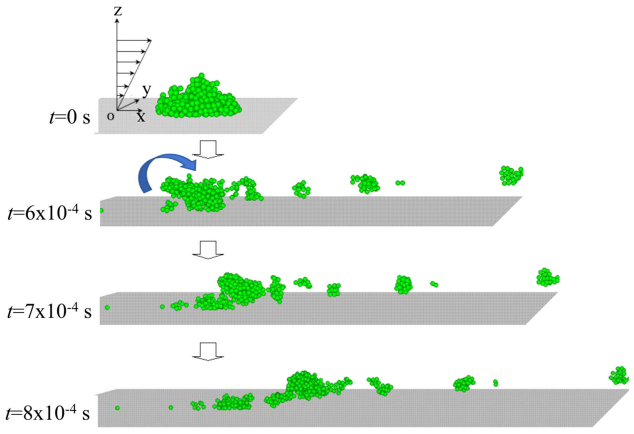


FIGURE 5.25.33 Snapshots of entrainment process of a deposited aggregate from the plate surface in the shear stress of $\mu_f\gamma_s = 267$ Pa.

Recently quite a few attempts to simulate the breakup of aggregates by the fluid flow, mainly the shear flow, have been conducted by sophisticated methods, such as Stokesian Dynamics (SD), the Lattice Boltzmann Method (LBM), and more detailed movements of each constitutive particle are clarified by these simulations.[179–185] As for the overall behaviors of the breakup process of large aggregates, the present model is certainly consistent with these recent models. However, not only these models but also more sophisticated methods will be employed to solve precisely the problems of large aggregates in various flow fields in the future, if the methodologies will be more simplified and the computation time will be shortened.

5.25.6 DIRECT NUMERICAL SIMULATIONS OF COLLOIDAL PARTICLES IN A LIQUID

5.25.6.1 Introduction

Simulation methods for colloidal particle dispersions that do not explicitly solve the motions of fluid, such as Brownian dynamics (BD) and Stokesian dynamics (SD), have been extensively used because of their relatively low computational costs. However, such methods are mostly restricted to neutral particles in simple Newtonian host fluids, and extensions to complex fluids possessing complex internal degrees of freedom such as polymeric fluids or electrolyte solutions have proven extremely difficult. In addition, these approaches are applicable only in the low-Reynolds-number regime ($Re \ll 1$), which is defined in terms of the size of the dispersed particles.

After the introduction of the SD method in the late 1980s, little progress has been reported for more than a decade. This lack of progress suddenly changed around 2000, when developments of direct numerical simulation (DNS) methods that explicitly solve the motions of fluid being coupled with the motions of colloidal particles were started by several researchers worldwide. In this section, we summarize the DNS methods for simulating the motions of colloidal particles in viscous liquids. These methods can simulate systems consisting of arbitrary-shaped particles with or without solute components such as ions; however, for simplicity, here, we describe only the basic formulations and some applications for charged dispersions of spherical colloids in an electrolyte solution composed of water and salt ions.

5.25.6.2 Short Review on Mesoscopic Modeling for Electrokinetics

Understanding the electrokinetics of charged colloids in electrolytes has been a challenging problem in physical chemistry and interface science.[186,187] Theory and numerical simulations both play major roles in revealing the basic aspects of electrokinetic phenomena, including electrophoresis, electroosmotic flow, and electro-acoustics. However, theoretical consideration is often limited to simplified systems.

Interparticle interactions in colloidal dispersions comprise thermodynamic and/or mechanical interactions[186–188] as well as the hydrodynamic interaction (HI).[186,189,190] In electrokinetics, the most typical form of the thermodynamic interactions is the screened Coulombic interactions between charged colloidal particles under the influence of the electric-double-layer (EDL) whose thickness is known as the Debye length. While the thermodynamic and mechanical interactions determine both static and dynamic properties of the dispersions, the hydrodynamic interactions play roles only in dynamic processes such as sedimentation, coagulation, rheology, and electrophoresis of particle dispersions.

Since the screened Coulombic and the hydrodynamic interactions are determined by the distributions of solute ions and the motions of solvent fluids, respectively, resolving the coupled dynamics of solutes, solvents, and colloidal particles is essential for successful simulations of electrokinetics. These coupled dynamics should be more pronounced in nanoparticle suspensions in which the Debye length easily becomes comparable to the sizes of the colloidal particles.

Because the HI in dispersions is essentially long-ranged, studying its role in many body systems using analytical methods alone is extremely difficult. Several theoretical schemes specialized to model the HI between spherical particles in Newtonian solvents have been developed; such schemes include BD using the Oseen tensor or the Rotne–Prager–Yamakawa mobility tensor and the SD method.[6] In these schemes, however, the motions of solvents are not explicitly resolved assuming the quasi steady states where the motions of solvents immediately follow the motions of colloidal particles.

The most straightforward approach to resolving the HI based on the solvent motions is numerically solving the Navier–Stokes equation with the moving boundary conditions to be determined by the motions of colloidal particles using the arbitrary Lagrangian–Eulerian (ALE) method.[192] However, the ALE method requires too much computational cost to simulate many body systems. An alternative technique is to use the Eulerian grid to reduce computational costs. In the distributed Lagrangian multipliers (DLM) method,[193] fluid particle dynamics (FPD),[194] the force coupling method (FCM),[195] and the methods detailed in Ref. [196], the external forces on the particles are distributed within the particle domain and the hydrodynamic forces on the particles are implicitly taken into account.

In the immersed boundary method (IBM)[197] and the smoothed profile method (SPM),[198] the hydrodynamic forces on colloids are explicitly computed and the body force is introduced to impose the rigidity of the particles in the continuum equations. The Lattice Boltzmann method (LBM) is another continuum discretization scheme on an Eulerian grid based on the distribution function.[199] In LBM for suspensions, the rigidity of the particles is embedded in the LBM equations, and the hydrodynamic force is explicitly computed.[200]

Mesoscopic models of HI have been developed also on the sole basis of momentum conservation for virtual particles in the fluid rather than on the basis of the Navier–Stokes equation. Such schemes include the dissipative particle dynamics (DPD)[201] and the stochastic rotation dynamics (SRD),[202] which describe compressible solvent flow and recover long-time hydrodynamics of an incompressible solvent.

All the aforementioned numerical methods for explicitly resolving the solvent motions can, in principle, handle the coupled dynamics of solutes, solvents, and colloidal particles; indeed, some of these schemes have been applied to electrokinetic phenomena. The LBM has been applied to the electrokinetics in Refs. [203–205]. In Refs. [206, 207], the colloids are represented by a network of point-particles and are frictionally coupled to an LBM treatment of the Navier–Stokes equation while the ions are treated as microscopic particles rather than coarse-grained densities. In contrast, many body systems of colloidal particles are successfully simulated using FPD[208,209] and the SPM[210] directly coupled with the usual coarse-grained electrokinetic equations. In the following part, we explain on the basic concept of the SPM as an example of successful simulation methods of electrokinetics. The numerical efficiency and accuracy of the SPM have been proven in Refs. [210–212].

5.25.6.3 Coupled Dynamics of Solute, Solvent, and Colloidal Particles in Electrolyte Solution

Dynamics of Solute and Solvent

We start with the hydrodynamic equations for an electrolyte solution. Consider multi-component ionic solutes in an aqueous solution, and each solute satisfies a law of conservation for the concentration C_α of the αth ionic component:

$$\partial_t C_\alpha + \nabla \cdot C_\alpha \boldsymbol{v}_\alpha + \nabla \cdot \boldsymbol{g}_\alpha = 0 \tag{5.25.19}$$

where

$\boldsymbol{v}_\alpha$ is the velocity of the αth ionic component
$\boldsymbol{g}_\alpha$ is a random current that represents the effect of thermal fluctuations on C_a

Because the inertial time scales of the solute ions are extremely small, $\boldsymbol{v}_a$ can be decomposed into the velocity of the solvent $\boldsymbol{v}$ and the diffusive current arising from the chemical potential gradient $\nabla\mu_\alpha$ as follows:

$$\boldsymbol{v}_\alpha = \boldsymbol{v} - \Gamma_\alpha \nabla \mu_\alpha \tag{5.25.20}$$

where

$\Gamma_\alpha k_B T = D_\alpha$ is the diffusivity of the αth ion
k_B is the Boltzmann constant
T is the absolute temperature

The random current should satisfy the following fluctuation–dissipation relation[213]:

$$\left\langle g_{\alpha,i}(x,t) g_{\beta,j}(x,t') \right\rangle = 2k_B T D_\alpha \delta_{\alpha\beta} \delta_{ij} \delta(x - x) \delta(t - t') \tag{5.25.21}$$

The conservation of momentum implies that the velocity of the solvent follows the equation of continuity with the

incompressible condition and the Navier–Stokes equation with Maxwell stress:

$$\nabla \cdot \boldsymbol{v} = 0 \tag{5.25.22}$$

$$\rho\left(\partial_t + \boldsymbol{v}\cdot\nabla\right)\boldsymbol{v} = -\nabla p + \eta\nabla^2\boldsymbol{v} - \sum_\alpha C_\alpha \nabla\mu_\alpha + \nabla\cdot\boldsymbol{s} \tag{5.25.23}$$

where

- ρ is the total mass density of the fluid
- p is the pressure
- η is the shear viscosity of the fluid

$\boldsymbol{s}$ is a random stress tensor satisfying the fluctuation–dissipation relation[213]:

$$\left\langle s_{ik}(x,t)s_{jl}(x,t')\right\rangle = 2k_B T\eta(\delta_{ij}\delta_{kl} + \delta_{il}\delta_{kj})\delta(x - x)\delta(t - t') \tag{5.25.24}$$

For chemical potential μ_α, we consider the Poisson–Nernst–Planck equation:

$$\mu_\alpha\left(\{C_1,\ldots,C_N\}\right) = k_B T\log C_\alpha + z_\alpha e\left(\Phi - \boldsymbol{E}^{\text{ext}}\cdot\boldsymbol{x}\right) \tag{5.25.25}$$

$$\varepsilon_r\varepsilon_0\nabla^2\Phi = -\rho_e \tag{5.25.26}$$

where

- z_α is the valence of the αth ion
- e is the elementary charge
- Φ is the electrostatic potential due to charged colloids and ions in water
- $\boldsymbol{E}^{\text{ext}}$ is the external electric field
- ε_0 is the permittivity of vacuum
- ε_r is the relative dielectric permittivity (assumed to be uniform)
- ρ_e is the charge density field

This equation describes the Poisson–Boltzmann distribution for ion concentrations at equilibrium as follows:

$$C_\alpha = \bar{C}_\alpha \exp\left[-\frac{z_\alpha e\left(\Phi - \boldsymbol{E}^{\text{ext}}\cdot\boldsymbol{x}\right)}{k_B T}\right] \tag{5.25.27}$$

The bulk concentration of ions $\bar{C}_\alpha$ is related to the Debye length $\kappa^{-1} = \left\{4\pi\lambda_B\sum_\alpha z_\alpha^2\bar{C}_\alpha\right\}^{-1/2}$, where the Bjerrum length is $\lambda_B = e^2/4\pi\varepsilon_r\varepsilon_0 k_B T$, which is approximately 0.72 nm for water at 300 K. This set of equations describes the electrokinetic phenomena of a simple electrolyte solution.

Dynamics of Colloidal Particles

The colloidal dynamics are dependent on the force exerted by the solvent. Consider mono-disperse spherical colloids with radius a, mass M_p, and moment of inertia $\boldsymbol{I}_p$. Momentum conservation between the fluid and the ith colloid implies the following hydrodynamic force and torque:

$$\boldsymbol{F}_i^H = \int(d\boldsymbol{S}_i\cdot\boldsymbol{\sigma}),\ \boldsymbol{N}_i^H = \int\left(\boldsymbol{x} - \boldsymbol{R}_i\right)\times(d\boldsymbol{S}_i\cdot\boldsymbol{\sigma}) \tag{5.25.28}$$

where

- $\boldsymbol{R}_i(t)$ is the center of mass
- $\int d\boldsymbol{S}_i(\ldots)$ indicates the surface integral over the ith colloid
- $\boldsymbol{\sigma}$ is the stress tensor of the fluid

In terms of the electrokinetic equations, the stress is given by

$$\boldsymbol{\sigma} = -p\boldsymbol{I} + \boldsymbol{\sigma}' + \boldsymbol{\sigma}^{st} + \boldsymbol{s} \tag{5.25.29}$$

where

- $\boldsymbol{\sigma}' = \eta\left(\nabla\boldsymbol{v} + (\nabla\boldsymbol{v})^{\mathrm{T}}\right)$ is the dissipative stress
- $\boldsymbol{\sigma}^{st} = \varepsilon\left(\boldsymbol{E}\boldsymbol{E} - \left(|\boldsymbol{E}|^2/2\right)\boldsymbol{I}\right)$ is the Maxwell stress of the total electric field $\boldsymbol{E} = -\nabla\Phi + \boldsymbol{E}^{\text{ext}}$, where $\boldsymbol{I}$ is the unit tensor

The evolution of the colloids follows Newton's equations:

$$\dot{\boldsymbol{R}}_i = \boldsymbol{V}_i \tag{5.25.30}$$

$$M_p\dot{\boldsymbol{V}}_i = \boldsymbol{F}_i^H + \boldsymbol{F}_i^c + \boldsymbol{F}_i^{\text{ext}} \tag{5.25.31}$$

$$\boldsymbol{I}_p\cdot\dot{\boldsymbol{\Omega}}_i = \boldsymbol{N}_i^H + \boldsymbol{N}_i^{\text{ext}} \tag{5.25.32}$$

where

- $\boldsymbol{V}_i(t)$ and $\boldsymbol{\Omega}_i(t)$ are the translational and angular velocities, respectively, of the ith colloid
- $\boldsymbol{F}_i^{\text{ext}}$ and $\boldsymbol{N}_i^{\text{ext}}$ are the external forces and torques, respectively
- $\boldsymbol{F}_i^c$ is the force that arises from the core potential of the particles that prevents the colloids from overlapping

The truncated Lennard–Jones potential, which is often called the Weeks–Chandler–Andersen (WCA) potential, is adopted for $\boldsymbol{F}_i^c$.

Colloid-Solute/Solvent Boundary Conditions

The hydrodynamic equations require relevant boundary conditions at the particle–solvent/solute interface. For the solvent velocity, the non-slip condition is assigned, so $\boldsymbol{v} = \boldsymbol{V}_i + \boldsymbol{\Omega}_i\times\boldsymbol{r}_i$ with $\boldsymbol{r}_i = \boldsymbol{x} - \boldsymbol{R}_i$ for the ith colloidal particle. For the ionic concentrations, the no-penetration condition is enforced as $\boldsymbol{n}\cdot\nabla\mu_\alpha = 0$, where $\boldsymbol{n}$ represents the unit normal to the surface of the colloids. Solving the coupled dynamical equations of colloids, solutes, and solvent is not straightforward because the moving-boundary-conditions to be defined dynamically with the positions and velocities of the colloidal particles.

The usual numerical techniques of partial differential equations require a body-fitted grid at the particle–solvent/

solute interface. The body-fitted grid is necessary not only to explicitly enforce the boundary conditions but also to compute the surface integral of the hydrodynamic force and torque acting on colloids. This approach cannot consider the dynamical evolution of a many-colloid system because the movement of the body-fitted grid requires re-meshing at every discrete time step as the colloids move. The moving-boundary-conditions lead to a huge computational cost, which is the main difficulty in the simulation of many-colloid systems.

By contrast, the SPM provides an efficient scheme for this type of moving-boundary-condition problem and incurs the same level of computational cost as solving a fluid-only problem where no such boundary conditions exist.[211]

5.25.6.4 Computational Method: Smoothed Profile Method

Smoothed Profile for the Particle–Solvent/Solute Boundary

In the SPM, each particle is represented by a smoothed profile that equals unity in the particle domain, zero in the fluid domain, and varies smoothly between zero and unity around the particle–solvent boundary, which is called the interfacial domain. Any function with these properties can be used as a smoothed profile. Several analytic forms are presented in Ref. [198]. One convenient choice for a spherical particle is

$$\phi_i(\boldsymbol{x},t)=\frac{1}{2}\left[\tanh\left(\frac{a-\left|\boldsymbol{x}-\boldsymbol{R}_i(t)\right|}{\xi}\right)+1\right] \tag{5.25.33}$$

where ξ is the thickness of the interfacial domain. An extension of the smoothed profile to general non-spherical particles can be found elsewhere.[212]

The field variables are defined over the entire domain, which comprises the fluid domain and the particle domain. To designate the particle domain, we use a concentration field for the colloids, given by $\phi(\boldsymbol{x},t)=\sum_i \phi_i(\boldsymbol{x},t)$. With the field ϕ, the total velocity field and the concentration fields of the ionic solutes are defined as

$$\boldsymbol{v}=(1-\phi)\boldsymbol{v}_f+\phi\boldsymbol{v}_p \tag{5.25.34}$$

$$C_\alpha=(1-\phi)C_\alpha^* \tag{5.25.35}$$

where $(1-\phi)\boldsymbol{v}_f$ represents the velocity field of the fluid, and

$$\phi\boldsymbol{v}_p(\boldsymbol{x},t)=\sum_i \phi_i(\boldsymbol{x},t)\left[\boldsymbol{V}_i(t)+\boldsymbol{\Omega}_i(t)\times\boldsymbol{r}_i(t)\right] \tag{5.25.36}$$

is the velocity field of the colloids. The auxiliary ionic concentration field C_α^*, which can have a finite value in the particle domain, is introduced; C_a, the physical concentration field, is forced to be zero in the particle domain through multiplication by $(1-\phi)$.

The smoothed profile is used also for the local charge density of the colloids, which becomes $\delta\left(a-\left|\boldsymbol{x}-\boldsymbol{R}_i(t)\right|\right)$ in the sharp interface limit. One convenient choice is to replace $\delta(x)$ with $\left|\nabla\phi(x)\right|$. The charge density field is then represented as

$$\rho_e=(1-\phi)\sum_\alpha z_\alpha eC_\alpha^*+\left|\nabla\phi\right|e\sigma_e \tag{5.25.37}$$

where $\sigma_e=Z/4\pi a^2$ is the surface charge density of the colloids.

Basic Equations for Colloidal Dispersions with Smoothed Profile

The hydrodynamic equations defined on the entire domain are

$$\nabla\cdot\boldsymbol{v}=0 \tag{5.25.38}$$

$$\rho\left(\partial_t+\boldsymbol{v}\cdot\nabla\right)\boldsymbol{v}=-\nabla p+\eta\nabla^2\boldsymbol{v}-\sum_\alpha C_\alpha\nabla\mu_\alpha+\nabla\cdot(1-\phi)\boldsymbol{s}+\phi\boldsymbol{f}_p \tag{5.25.39}$$

$$\partial_t C_\alpha^*=-\nabla\cdot C_\alpha^*\boldsymbol{v}_\alpha^*-\nabla\cdot\boldsymbol{g}_\alpha \tag{5.25.40}$$

$$\boldsymbol{v}_\alpha^*=\boldsymbol{v}+(\boldsymbol{I}-\boldsymbol{nn})(-\Gamma_\alpha\nabla\mu_\alpha) \tag{5.25.41}$$

with μ_α from Equation (5.25.25) and the Poisson Equation (5.25.26) for Φ, where $\boldsymbol{n}=-\nabla\phi/\left|\nabla\phi\right|$ is the unit surface-normal defined on the interfacial domain, and the outer product $\boldsymbol{nn}$ is set to the zero tensor away from the particle diffuse interface. In these equations, the variables to be solved for are $\boldsymbol{v}$ and C_α^* but not $\boldsymbol{v}_f$ and C_α. The boundary conditions at the particle–solvent interface are implicitly considered in the SPM equations. The body force, $\phi\boldsymbol{f}_p$, is introduced to impose the particle velocity field onto the total velocity field. The non-slip condition for v is accounted for by the viscous force, which acts in both the fluid and interfacial domains. The no-penetration condition for the concentration field is directly accounted for by the projection operator $(\boldsymbol{I}-\boldsymbol{nn})$ in the interfacial domain. The expressions for $\phi\boldsymbol{f}_p$, $\boldsymbol{F}_i^H$, and $\boldsymbol{N}_i^H$ should be defined by the momentum conservation law between a particle and the solvent, which is consistently achieved in the time–discretized scheme described in the following subsection.

Temporal Discretization

The time–discretized evolution equations are outlined as follows. To simplify the presentation, we neglect the random currents and focus on an explicit marching algorithm. The implicit marching algorithm can be formulated to enhance the stability, as presented in Ref. [212]. For the initial conditions at the nth discretized time step, the position, velocity, and angular velocity of the colloids, $\left\{\boldsymbol{R}_i^n,\boldsymbol{V}_i^n,\boldsymbol{\Omega}_i^n\right\}(i=1,\ldots,N_p)$, are mapped onto ϕ^n and $\phi^n\boldsymbol{v}_p^n$ and the following conditions are imposed: $\boldsymbol{v}^n=\left(1-\phi^n\right)\boldsymbol{v}_f^n+\phi^n\boldsymbol{v}_p^n$ must satisfy

the incompressibility condition on the entire domain and $\nabla \cdot \boldsymbol{v}^n = 0$, and $C_\alpha^{*,n}$ must satisfy the charge neutrality condition, $\int dx \rho_e^n = 0$. The auxiliary concentrations are determined from Equation (5.25.40) as

$$C_\alpha^{*,n+1} = C_\alpha^{*,n} - \int_{t_n}^{t_n+h} ds \nabla \cdot C_\alpha^* \boldsymbol{v}_\alpha^* \tag{5.25.42}$$

where

h is the time increment
$t_n = nh$ is the nth discretized time

The total velocity field is updated using a fractional step approach. First, the advection and the viscous force are solved:

$$\boldsymbol{v} = \boldsymbol{v}^n + \int_{t_n}^{t_n+h} ds \nabla \cdot \left[\frac{1}{\rho} \left\{ -p\boldsymbol{I} + \eta \left(\nabla \boldsymbol{v} + (\nabla \boldsymbol{v})^{\mathrm{T}} \right) \right\} - \boldsymbol{v}\boldsymbol{v} \right] \tag{5.25.43}$$

$$\boldsymbol{R}_i^{n+1} = \boldsymbol{R}_i^n + \int_{t_n}^{t_n+h} ds \boldsymbol{V}_i \tag{5.25.44}$$

with the incompressibility condition $\nabla \cdot \boldsymbol{v} = 0$. Along with the advection of the total velocity, the particle position is updated using the particle velocity. The electrostatic potential for the updated particle configuration is determined by solving the following Poisson equation:

$$\varepsilon_r \varepsilon_0 \nabla^2 \Phi^{n+1} = -\rho_e^{n+1} \tag{5.25.45}$$

with the charge density field at the $(n+1)$th time. The momentum change as a result of the electrostatic field is solved with

$$\boldsymbol{v}^! = \boldsymbol{v} - h\rho_e^{n+1} \nabla \Phi^{n+1} \tag{5.25.46}$$

At this point, the momentum conservation equations are solved for the total velocity field. The rest of the updating procedure assigns the particle velocity field.

The hydrodynamic force and torque exerted by the solvent on the colloids are derived from momentum conservation. Momentum conservation between the colloids and the fluid dictates that the hydrodynamic force and torque integrated over a time period h are equal to the momentum change over the particle domain during the time interval h:

$$\left[\int_{t_n}^{t_n+h} ds \boldsymbol{F}_i^H(s) \right] = \int dx \rho \phi_i^{n+1} \left(\boldsymbol{v}^! - \boldsymbol{v}_p^n \right) \tag{5.25.47}$$

$$\left[\int_{t_n}^{t_n+h} ds \boldsymbol{N}_i^H(s) \right] = \int dx \left[\boldsymbol{r}_i^{n+1} \times \rho \phi_i^{n+1} \left(\boldsymbol{v}^! - \boldsymbol{v}_p^n \right) \right] \tag{5.25.48}$$

With the above hydrodynamic force/torque and the other forces/torques acting on the colloids, the particle velocity and angular velocity are updated as follows:

$$\boldsymbol{V}_i^{n+1} = \boldsymbol{V}_i^n + M_p^{-1} \left[\int_{t_n}^{t_n+h} ds \boldsymbol{F}_i^H \right] + M_p^{-1} \int_{t_n}^{t_n+h} ds \left(\boldsymbol{F}_i^c + \boldsymbol{F}_i^{\mathrm{ext}} \right) \tag{5.25.49}$$

$$\boldsymbol{\Omega}_i^{n+1} = \boldsymbol{\Omega}_i^n + \boldsymbol{I}_p^{-1} \cdot \left[\int_{t_n}^{t_n+h} ds \boldsymbol{N}_i^H \right] + \boldsymbol{I}_p^{-1} \cdot \int_{t_n}^{t_n+h} ds \boldsymbol{N}_i^{\mathrm{ext}} \tag{5.25.50}$$

The resultant particle velocity field $\phi^{n+1} \boldsymbol{v}_p^{n+1}$ is directly imposed on the total velocity field as

$$\boldsymbol{v}^{n+1} = \boldsymbol{v}^! + \left[\int_{t_n}^{t_n+h} ds \phi \boldsymbol{f}_p \right] \tag{5.25.51}$$

$$\left[\int_{t_n}^{t_n+h} ds \phi \boldsymbol{f}_p \right] = \phi^{n+1} \left(\boldsymbol{v}_p^{n+1} - \boldsymbol{v}^! \right) - \frac{h}{\rho} \nabla p_p \tag{5.25.52}$$

The pressure caused by the rigidity of the particle is determined by the incompressibility condition, $\nabla \cdot \boldsymbol{v}^{n+1} = 0$, which leads to the following Poisson equation for p_p, *viz.*: $\nabla^2 p_p = \frac{\rho}{h} \nabla \cdot \left[\phi^{n+1} \left(\boldsymbol{v}_p^{n+1} - \boldsymbol{v}^! \right) \right]$. Note that, on the left-hand sides of Equations (5.25.47), (5.25.48), and (5.25.52), the integrands $\boldsymbol{F}_i^H$, $\boldsymbol{N}_i^H$, and $\phi \boldsymbol{f}_p$ are not explicitly calculated but their time integrals—specifically, the momentum impulses—are solved. The body force $\phi \boldsymbol{f}_p$ formally introduced in the total momentum Equation (5.25.39) is realized in this time–discretized scheme. Furthermore, the hydrodynamic force and torque are defined as volume integrals rather than surface integrals and are suitable for spatial discretization on a regular grid. The SPM does not require a body-fitted irregular grid, which is the main source of difficulty and inefficiency in modeling many-colloid systems.

5.25.6.5 DNS of Electrophoresis

In this part, to demonstrate the reliability of the SPM,[198,211,206–222] we present results of numerical simulations of electrophoretic motions of charged colloids under an external electric field. We also compare our results with those of classical approximation theories[223–226] with respect to the relationship between the zeta potential and the electrophoretic mobility. Next, comparisons are made for the electrophoretic mobilities of dense dispersions and the simulation results show notable deviations from a mean-field-type theory such as the cell model.[227,228] In addition, electro-hydrodynamic effects are investigated in the absence of external electric fields. The electro-viscous drag on a charged colloid and the lubrication interaction between two approaching charged colloids in an electrolyte solution are computed. Unlike the drag on a neutral colloid, the valence

of the colloid and the thickness of the EDL affect the electroviscous drag and the lubrication interaction.

Numerical Calculations

Simulations were performed in a three-dimensional cubic box with periodic boundary conditions. The linear dimension is $L/\Delta = 64$, where the lattice spacing Δ is chosen as the unit of length and is defined relative to the Bjerrum length as $\Delta = 4\pi\lambda_B$. We use a particle radius of $a = 5$ and a thickness parameter of $\xi = 2$ throughout these simulations. The host fluid contains a 1:1 electrolyte composed of monovalent counterions ($a = +$) and coions ($a = -$). The units of energy and electrostatic potential are k_BT and k_BT/e, respectively. The latter corresponds to 25.7 mV at 300 K. The non-dimensional parameter $m_a = 2\varepsilon k_B T f_a / 3\eta e^2$ is set to $m_+ = m_- = 0.184$, which corresponds to a typical value of KCl solution at 300 K. Our unit of time $\tau = \Delta^2 f_+ / k_BT$ corresponds to 0.44 μsec.

Electrophoretic Mobility and ζ Potential

We first consider a single charged particle moving with drift velocity $V = (-V,0,0)$ in a constant electric field $E^{ext} = (E,0,0)$. The electrophoretic mobility V/E is related to the zeta potential ζ, which is defined as the electrostatic potential on a slipping plane as

$$V / E = f\varepsilon\zeta / \eta \tag{5.25.53}$$

when ζ is small.[186] The Smolchowski equation $f = 1$ is valid in the limit $\kappa a \to \infty$,[223] whereas the Hückel equation $f = 2/3$ is valid in the opposite limit $\kappa a \to 0$.[224] From the Henry equation, an expression $f = f_H(\kappa a)$ is derived that is valid for a general value of κa.[225] These equations indicate that the mobility is proportional to ζ; however, this relation tends to fail for larger ζ, when the relaxation effect via deformations of the EDL becomes notable. O'Brien and White proposed an approximated theory that is also valid for larger ζ values.[226]

We simulated electrophoresis of a single particle in linear response regimes $E \le 0.15$ and compared them with results obtained based on the O'Brien–White theory. A constant, uniform electric field $E = 0.1$ corresponding to 2.85×10^3 V/cm was applied. The terminal value of V was calculated for $50 \le -Z \le 750$ with $\kappa^{-1} = 10$ and $100 \le -Z \le 1000$ with $\kappa^{-1} = 5$. The corresponding salt concentrations were 44 μmol/l for $\kappa^{-1} = 5$ and 11 μmol/l for $\kappa^{-1} = 10$ at 300 K in water.

We chose $\nu = \eta/\rho = 5$, so the particle Reynolds number $Re = aV/\nu$ remains small. In both the O'Brien–White theory and our simulations, the zeta potential is assumed to be the electrostatic potential at the particle surface, $\zeta = \Psi|_{surface}$. Here, the dimensionless zeta potential $y \equiv e\zeta / k_BT$ is introduced. The relationship between the colloidal charge $|Z|e$ and the dimensionless zeta potential y is shown in Figure 5.25.34(a), where our numerical results are plotted along with the analytic solution to the nonlinear Poisson–Boltzmann (PB) equation.[229] We see that our numerical results are consistent with the nonlinear PB theory for $\kappa a = 0.5$ and 1. In Figure 5.25.34(b), the dimensionless mobility $E_m \equiv e\eta V / \varepsilon k_BTE$ is plotted as a function of the dimensionless zeta potential for $\kappa a = 0.5$ and 1. These plots clearly demonstrate that our method reproduced the predictions of the O'Brien–White theory almost perfectly, including the nonlinear regime $y \ge 2$, with an error of only a few percent.

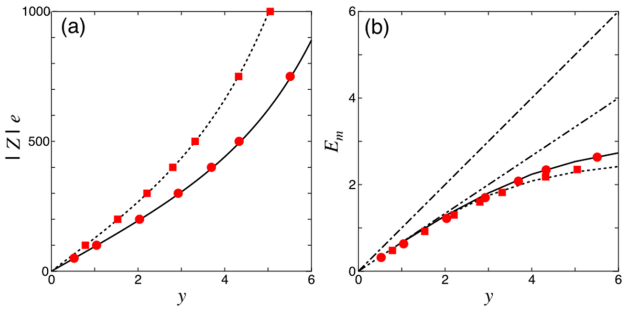


FIGURE 5.25.34 (a) Relationship between the surface charge $|Z|e$ and the dimensionless zeta potential y for $\kappa a = 0.5$ (circles) and $\kappa a = 1$ (squares). Our numerical data are in good agreement with the analytic solution of the nonlinear PB equation for $\kappa a = 0.5$ (solid curve) and $\kappa a = 1$ (dashed curve).[229] (b) The dimensionless mobility E_m of a single particle is plotted as a function of the dimensionless zeta potential y for $\kappa a = 0.51$ (circles) and $\kappa a = 1$ (squares). For comparison, the results of Smolchowski (dot-dashed line), Henry (2 dot-dashed line), and O'Brien–White for $\kappa a = 0.51$ (solid curve) as well as those of O'Brien–White for $\kappa a = 1$ (dashed curve) are shown. Reproduced from Ref. [214] with kind permission from American Physical Society.

Electrophoretic Mobility in Concentrated Dispersions

Because our simulation method is easily applicable to dense dispersions consisting of many particles, we examined the effect of the particle concentration on the electrophoretic mobility. The linearized theory for a single particle (Equation 5.25.53) is still valid for dense dispersions when the external electric field E is small; however, f depends on both κa and φ in this regime. Simulations were conducted with $Z = -100$ and $E = 0.1$ for various particle volume fractions $\varphi \equiv 4\pi a^3 N / 3L^3$ to calculate $f(\kappa a, \varphi) = \eta V / \varepsilon\zeta E$. We used Debye lengths κ^{-1} of 5 and 10, which correspond to $\kappa a = 1$ and 0.5, respectively. Figure 5.25.35 shows typical snapshots of the systems for (a) face-centered cubic (FCC), (b) body-centered cubic (BCC), and (c) random configurations. The horizontal color map represents the charge density for $\kappa a = 1$ on a cross-section perpendicular to the z axis. In the FCC and BCC cases, E was applied perpendicular to both the (1,0,0) and (1,1,1) faces, and we obtained very small differences, within 1%.

The mobility coefficient $f(\kappa a,\varphi)$ for $\kappa a = 1$ and 0.5 is plotted as a function of φ in Figure 5.25.36(a) and (b), respectively. We found that f decreases rapidly with increasing φ. Furthermore, the overall behavior appears to be almost independent of the particle configuration. A theoretical model for the electrophoretic mobility of dense dispersions has been proposed by Levine and Neale using the cell model.[227] They assumed a situation in which a spherical particle with radius

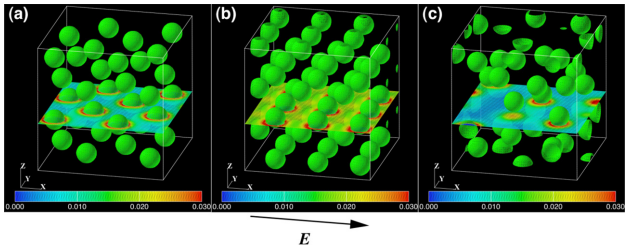


FIGURE 5.25.35 Snapshots of the electrophoresis of dense dispersions with (a) FCC, (b) BCC, and (c) random particle configurations. The color map represents the total ionic charge density $\sum_\alpha ez_\alpha C_\alpha$ in a plane perpendicular to the z axis. The electric field is applied in the $+x$ direction, normal to the (1,0,0) face for the FCC and BCC configurations. Reproduced from Ref. [214] with kind permission from American Physical Society.

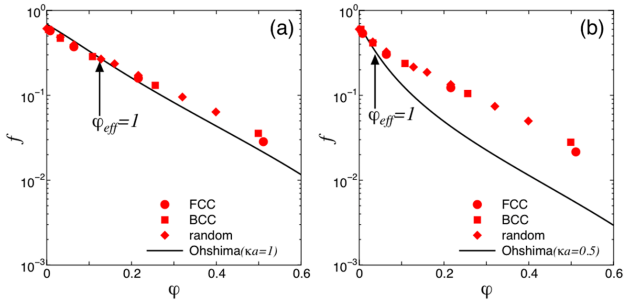


FIGURE 5.25.36 The mobility coefficient $f(\kappa a,\varphi)$ as a function of the volume fraction φ for (a) $\kappa a=1$ and (b) $\kappa a=0.5$. The solid lines represent the approximation theory proposed by Ohshima.[228] The theory is confirmed to be accurate for $\varphi_{\text{eff}}\leq 1$; however, it tends to deviate from our numerical results for $\varphi_{\text{eff}}>1$, where overlapping of the EDLs becomes notable. (Reproduced from Ref. [214] with kind permission from American Physical Society.)

a is located at the center of a spherical container (cell) with radius b and calculated V as a function of κa and $(\varphi)=(a/b)^3$. Ohshima proposed a simpler expression for the mobility coefficient f according to the cell model.[228] Ohshima's prediction is shown in Figure 5.25.36(a) and (b) along with our DNS results. In both (a) and (b), the simulation results tend to become larger than the theoretical values as φ increases. We believe that this deviation arises from the occurrence of overlapping EDLs for larger φ because this effect is neglected in Ohshima's theory. To this end, we estimated an effective radius of ionically dressed colloidal particles $a+\kappa^{-1}$ and defined the effective volume fraction of the dressed colloids, $\varphi_{\text{eff}}\equiv 4\pi(a+\kappa^{-1})^3 N/3L^3=\left(1+(\kappa a)^{-1}\right)^3\varphi$. As clearly shown in Figure 5.25.36(a) and (b), our DNS results agree well with Ohshima's theory for $\varphi_{\text{eff}}\leq 1$ where the effect of overlapping is small. However, for $\varphi_{\text{eff}}>1$, where the overlapping of the EDLs becomes significant, deviations between our DNS results and the theory become notable. Our DNS results are consistent with those of recent studies that also accounted for the effects of the overlapping EDLs.[230–232]

5.25.6.6 Summary

In this chapter, we summarized the basic equations for colloidal particles in an electrolyte solution, and described the difficulties in directly simulating many-colloid systems in traditional numerical schemes. To address this problem, an efficient and accurate numerical scheme, the SPM, was introduced.[198,211,214–222]

The application of the SPM is not limited to electrokinetics of spherical colloids in Newtonian solvents, it can be straightforwardly applied to various systems in more complex and realistic situations. For readers interested in electrokinetics simulations based on the SPM, we introduce a software called KAPSEL which has been developed by the authors and is available for free at http://www-tph.cheme.kyoto-u.ac.jp/kapsel/. Several examples and demo movies are also available at the website.

REFERENCES

1. Cundall, P.A., Strack, O.D.L., *Geotechnique*, 29, 47–65, 1979.
2. Shimosaka, A., Hayashi, K., Shirakawa, K., Hidaka, J., *Kagaku Kougaku Ronbunshu*, 26, 23–30, 2000.
3. Tanaka, T., Yonemura, S., Kiribayashi, K., Tsuji, Y., *Nihon Kikai Gakkai Ronbunshu, B Hen*, 59, 2982–2989, 1993.
4. Shinichi, Y., Umekage, T., Mitsuiki, Y., Koga, F., *Adv. Powder Technol.*, 19, 153–182, 2008.
5. Katsura, N., Shimosaka, A., Shirakawa, Y., Hidaka, J., *ISIJ Int.*, 10, 1396–1405, 2005.
6. Combarros, M., Feise, H.J., Zetzener, H., Kwade, A., *Particuology*, 12, 25–32, 2014.
7. Kano, J., Saito, F., Shimosaka, A., Hidaka, J., *Kagaku Kougaku Ronbunshu*, 23, 687–693, 1997.
8. Savage, S.B., *J. Fluid Mech.*, 377, 1–26, 1998.
9. Zhu, H. Mehrabadi, M.M., Massoud, M., *Comput. Math. Appl.*, 53, 244–259, 2007.
10. Savage, S.B., *Adv. Appl. Mech.*, 24, 289–366, 1984.
11. Bagnold, R.A., *Proc. Roy. Soc.*, A225, 49–63, 1954.
12. Hidaka, J., Kirimoto, Y., Miwa, S., Makino, K., *J. Soc. Powder Technol., Jpn.*, 22, 427–435, 1985.
13. Hidaka, J., Kano, J., Shimosaka, A., *Kagaku Kogaku Ronbunshu*, 20, 397–404, 1994.
14. Mishra, B.K., *Int. J. Miner. Process.*, 71, 73–93, 2003.
15. Mishra, B.K., *Int. J. Miner. Process.*, 71, 95–112, 2003.
16. Kano, J., Chujo, N., Saito, F., *Adv. Powder Technol.*, 8, 39–51, 1997.
17. Kano, J., Miyazaki, M., Saito, F., *Adv. Powder Technol.*, 11, 333–342, 2000.
18. Lee, H., Cho, H., Kwon, J., *Powder Technol.*, 198, 364–372, 2010.
19. Kano, J., Saito, F., *Powder Technol.*, 98, 166–170, 1998.
20. Rosenkranz, S., Breitung-Faes, S., Kwade, A., *Powder Technol.*, 212, 224–230, 2011.
21. Mio, H., Kano, J., Saito, F., *Chem. Eng. Sci.*, 59, 5909–5916, 2004.
22. Ashrafizadeh, H., Ashrafizaadeh, M., *Adv. Powder Technol.*, 23, 708–716, 2012.
23. Bian, X., et al., *Miner. Eng.*, 105, 22–35, 2017.
24. Kano, J., Mio, H., Saito, F., *AIChE J.*, 46, 1694–1697, 2000.
25. Kano, J., Mio, H., Saito, F., Miyazaki, M., *Miner. Eng.*, 14, 1213–1223, 2001.
26. Sinnott, M., Cleary, P.W., Morrison, R., *Miner. Eng.*, 19, 1537–1550, 2006.

27. Cleary, P.W., Sinnott, M., Morrison, R., *Miner. Eng.*, 19, 1551–1572, 2006.
28. Yang, R.Y., Jayasundara, C.T., Yu, A.B., Curry, D., *Miner. Eng.*, 19, 984–994, 2006.
29. Soda, R., Kano, J., Saito, F., *J. Soc. Powder Technol., Jpn.*, 46, 180–186, 2009.
30. Jayasundara, C.T., Yang, R.Y., Yu, A.B., *Miner. Eng.*, 33, 66–71, 2012.
31. Jayasundara, C.T., et al., *Miner. Eng.*, 24, 181–187, 2011.
32. Brosh, T., et al., *Powder Technol.*, 257, 104–112, 2014.
33. Cleary, P.W., Sinnott, M., Morrison, R., *Miner. Eng.*, 19, 1517–1527, 2006.
34. Yamada, Y., Sakai, M., *Powder Technol.*, 239, 105–114, 2013.
35. Kh, A.B., Mirghasemi, A.A., Mohammadi, S., *Powder Technol.*, 205, 15–29, 2011.
36. Wang, J., Yan, H., *Int. J. Numer. Anal. Met.*, 37, 832–854, 2013.
37. Antonyuk, S., et al., *Chem. Eng. Process.*, 45, 838–856, 2006.
38. Cleary, P.W., Sinnott, M.D., *Miner. Eng.*, 74, 178–197, 2015.
39. Ishihara, S., Zhang, Q., Kano, J., *J. Soc. Powder Technol., Jpn.*, 51, 407–414, 2014.
40. Eckhard, S., Fries, M., Antonyuk, S., Heinrich, S., *Adv. Powder Technol.*, 28, 185–196, 2017.
41. Soda, R., et al., *ISIJ Int.*, 49, 645–649, 2009.
42. Kuo, H.P., et al., *Chem. Eng. Sci.*, 57, 3621–3638, 2002.
43. Arratia, P.E., et al., *Powder Technol.*, 164, 50–57, 2006.
44. Hassanpour, A., et al., *Powder Technol.*, 206, 189–194, 2011.
45. Yamamoto, M., Ishihara, S., Kano, J., *Adv. Powder Technol.*, 27, 864–870, 2016.
46. Pantaleev, S., et al., *Powder Technol.*, 311, 287–302, 2017.
47. Wang, G., Tong, X., *Mining Sci. Technol. (China)*, 21, 451–455, 2011.
48. Dong, K.J., Yu, A.B., *Miner. Eng*, 31, 2–9, 2012.
49. Li, J., Webb, C., Pandiella, S.S., Campbell, G.M., *Powder Technol.*, 133, 190–202, 2003.
50. Yue, C., Zhang, Q., Zhai, Z., *J. Aerosol Sci.*, 101, 174–187, 2016.
51. Dong, K.J., et al., *Miner. Eng*, 22, 921–930, 2009.
52. Qian, F., Huang, N., Zhu, X., Lu, J., *Powder Technol.*, 249, 63–70, 2013.
53. Noguchi, T., et al., *ISIJ Int.*, 45, 1426–1431, 2005.
54. Yu, Y., Saxén, H., *ISIJ Int.*, 52, 788–796, 2012.
55. Ueda, S., et al., *ISIJ Int.*, 50, 914–923, 2010.
56. Adema, A.T., Yang, Y., Boom, R., *ISIJ Int.*, 50, 954–961, 2010.
57. Zhou, Z., et al., *ISIJ Int.*, 45, 1828–1837, 2005.
58. Ramos, M.V., Kasai, E., Kano, J., Nakamura, T., *ISIJ Int.*, 40, 448–454, 2000.
59. Kurosawa, H., et al., *ISIJ Int.*, 52, 1010–1017, 2012.
60. Miao, Z., Zhou, Z., Yu, A.B., Shen, Y., *Powder Technol.*, 314, 542–549, 2017.
61. Mio, H., Shimosaka, A., Shirakawa, Y., Hidaka, J., *Adv. Powder Technol.*, 18, 441–453, 2007.
62. Mio, H., Shimosaka, A., Shirakawa, Y., Hidaka, J., *J. Soc. Powder Technol., Jpn.*, 44, 206–211, 2007.
63. Mio, H., et al., *J. Imaging Sci. Technol.*, 53, 010505–010508, 2009.
64. Nishiura, D., Shimosaka, A., Shirakawa, Y., Hidaka, J., *Kagaku Kogaku Ronbunshu*, 32, 331–340, 2006.
65. Feng, B.F., Doi, Y., Kawahara, T., *J. Phy. Soc. Jpn.*, 73, 2100–2111, 2004.
66. Hidaka, J., Kano, J., Shimosaka, A., *Kagaku Kogaku Ronbunshu*, 21, 581–587, 1995.
67. Rudd, R.E., Broughton, J.Q., *Phys. Rev.*, B58, R5883–R5896, 1998.
68. Sakai, M., Koshizuka, S., *Chem. Eng. Sci.*, 64, 553–539, 2009.
69. Sakai, M., Shibata, K., Kawasaki, V.M., Koshizuka, S., *J. Soc. Powder Technol., Jpn.*, 47, 17–25, 2010.
70. Shimosaka, A., et al., *Kagaku Kogaku Ronbunshu*, 36, 86–93, 2010.
71. Yoshida, M., *A study on the design of electrostatic charging characteristic of toner particles in electrographic systems*, Doshisha University Thesis, 2006, pp. 113–139.
72. Akashi, M., et al., *ISIJ Int.*, 48, 1500–1506, 2008.
73. Osher, S., Fedkiw, R., *Level Set Methods and Dynamic Implicit Surfaces*, Berlin: Springer, 2003.
74. Shigeto, Y., Sakai, M., *Chem. Eng. J.*, 231, 464–476, 2013.
75. Sakai, M., *KONA Powder Part. J.*, 33, 169–178, 2016.
76. Sakai, M., et al., *Chem. Eng. J.*, 279, 821–839, 2015.
77. Tsunazawa, Y., Shigeto, Y., Tokoro, C., Sakai, M., *Chem. Eng. Sci.*, 138, 791–809, 2015.
78. Basinskas, G., Sakai, M., *Powder Technol.*, 287, 380–394, 2016.
79. Basinskas, G., Sakai, M., *Powder Technol.*, 301, 815–829, 2016.
80. Sun, X., Sakai, M., Sakai, M.-T., Yamada, Y., *Chem. Eng. J.*, 246, 122–141, 2014.
81. Crowe, C. Schwarzcopf, J.D., Sommerfeld, M., Tsuji, Y., *Multiphase Flows with Droplets and Particles*, 2nd edition, CRC Press, 2012, pp. 29–35.
82. Anderson, T.B., Jackson, R., *Ind. Eng. Chem. Fundam.*, 6, 527–539, 1967.
83. Tsuji, Y., Kawaguchi, T., Tanaka, T., *Powder Technol.*, 77, 79–87, 1993.
84. Patankar, S.D., *Numerical Heat Transfer and Fluid Flow*, Hemisphere Publishing Corporation, 1980.
85. Pan, T.W., et al., *J. Fluid Mech.*, 451, 169–191, 2002.
86. Ikeno, T., Kajishima, T., *J. Comput. Phys.*, 226, 1485–1508, 2007.
87. van der Hoef, M.A.M., van Sint Annaland, M., Deen, N.G., Kuipers, J.A.M., Annu. *Rev. Fluid Mech.*, 40, 47–70, 2008.
88. Nanbu, K., *J. Phys. Soc. Jpn.*, 49, 2042–2049, 1980.
89. Tsuji, Y., Tanaka, T., Yonemura, S., *Powder Technol.*, 95, 254–264, 1998.
90. Salman, A.D., Ghadiri, M., Hounslow, M.J. *Particle Breakage (Handbook of Powder Technology)*, Elsevier Science, 2007.
91. Bonakdar, T., et al., *Powder Technol.*, 304, 1–7, 2016.
92. Salman, A.D., Gorham, D.A., Verba, A., *Wear*, 186–187 (PART 1), 92–98, 1995.
93. Zhang, Z., Ghadiri, M., *Chem. Eng. Sci.*, 57, 3671–3686, 2002.
94. Salman, A.D., Fu, J., Gorham, D.A., Hounslow, M.J., *Powder Technol.*, 130, 359–366, 2003.
95. Cheong, Y.S., Salman, A.D. Hounslow, M.J., *Powder Technol.*, 138, 189–200, 2003.
96. Vogel, L., Peukert, W., *Chem. Eng. Sci.*, 60, 5164–5176, 2005.
97. Kafui, K.D., Thornton, C., *Powders Grains*, 93, 401–406, 1993.
98. Ning, Z., Boerefijn, R., Ghadiri, M., Thornton, C., *Adv. Powder Technol.*, 8, 15–37, 1997.
99. Boerefijn, R., Ning, Z., Ghadiri, M., *Int. J. Pharm.*, 172, 199–209, 1998.
100. Subero, J., Ning, Z., Ghadiri, M., Thornton, C., *Powder Technol.*, 105, 66–73, 1999.
101. Mishra, B.K., Thornton, C., *Int. J. Miner. Process.*, 61, 225–239, 2001.
102. Moreno, R., Ghadiri, M., Antony, S., *Powder Technol.*, 130, 132–137, 2003.
103. Moreno-Atanasio, R., Ghadiri, M., *Chem. Eng. Sci.*, 61, 2476–2481, 2006.
104. Golchert, D., Moreno, R., Ghadiri, M., Litster, J., *Powder Technol.*, 143–144, 84–96, 2004.

105. Dosta, M., et al., *Powder Technol*., 299, 87–97, 2016.
106. Khanal, M., Schubert, W., Tomas, J., *Granul. Matter*, 5, 177–184, 2004.
107. Samimi, A., Moreno, R., Ghadiri, M., *Powder Technol*., 143–144, 97–109, 2004.
108. Tong, Z.B., et al., *Powder Technol*., 240, 19–24, 2013.
109. Kozhar, S., et al., *Adv. Powder Technol*., 26, 767–777, 2015.
110. Yang, J., Wu, C.-Y., Adams, M., *Int. J. Pharm*., 487, 32–38, 2015.
111. Hare, C., et al., *Chem. Eng. Sci.*, 149, 204–214, 2016.
112. Loreti, S., et al., *AIChE J*., 63(9), 3692–3705, 2017.
113. Weber, M., et al., *Comp. Mater. Sci*., 137, 100–106, 2017.
114. Thornton, C., *Granular Dynamics, Contact Mechanics, Particle System Simulations*, Switzerland: Springer International Publishing, 2015.
115. Thornton, C., Randall, W., *Micromechanics of Granular Materials*, Ed. M. Satake and J.T. Jenkins, Amsterdam: Elsevier Science Publishers, 1988.
116. Thornton, C., Yin, K.K., *Powder Technol*., 65, 153–166, 1991.
117. Thornton, C., Ning, Z., *Powder Technol*., 99, 154–162, 1998.
118. Johnson, K.L., Kendall, K., Roberts, A.D., *P. Roy. Soc. A*, 324(1558), 301–313, 1971.
119. Subero, J., Ghadiri, M., *Powder Technol*., 120, 232–243, 2001.
120. Subero, J., *Impact breakage of agglomerates*, PhD Thesis, University of Surrey, UK, 2001.
121. Dosta, M., Dale, S., Antonyuk, S., Heinrich, S., *Ind. Eng. Chem. Res*., 52, 11275–11281, 2013.
122. Schubert, W., Khanal, M., Tomas, J., *Int. J. Miner. Process*., 75, 41–52, 2005.
123. Moreno-Atanasio, R., *Computer simulation of impact behaviour of spherical agglomerates using Distinct Element Method*, PhD Thesis, University of Surrey, Guildford, UK, 2003.
124. Antonyuk, S., et al., *Chem. Eng. Process*., 45, 838–856, 2006.
125. Thornton, C., Yin, K.K., Adams, M.J., *J. Phy. D Appl. Phys*., 29, 424–435, 1996.
126. Ghadiri, M., Zhang, Z., *Chem. Eng. Sci*., 57, 3659–3669, 2002.
127. Bonakdar, T., Ghadiri, M., *EPJ Web Conf*., 140, 15015, 2017.
128. Loreti, S., Wu, C.-Y., Reynolds, G., Seville, J., *AIChE Journal*, 2017.
129. Brown, N.J., Chen, J.-F., Ooi, J.Y., *Granul. Matter*., 16, 299–311, 2014.
130. Nguyen, D., Rasmuson, A., Thalberg, K., Niklasson Björn, I., *AIChE J*., 61, 4059–4068, 2015.
131. Ge, R., Ghadiri, M., Bonakdar, T., Hapgood, K., *Powder Technol*., 306, 103–112, 2017.
132. Ge, R., *Personal communication*, 2018.
133. Guo, Y., Curtis, J.S. *Ann. Rev. Fluid Mech*., 47, 21–46, 2015.
134. Grof, Z., Kohout, M., Stepanek, F., *Chem. Eng. Sci*., 62, 1418–1429, 2007.
135. Potyondy, D.O., Cundall, P.A., *Int. J. Rock Mech., Min. Sci*., 41, 1329–1364, 2004.
136. Potapov, A.V., Campbell, C.S., *Int. J. Modern Phys. C*, 7, 717–729, 1996.
137. Kalman, H., Rodnianski, V., Haim, M., *Granul. Matter*, 11, 253–66, 2009.
138. Brosh, T., Kalman, H., Levy, A.J., *Granul. Matter*, 13, 765–776, 2011.
139. Bruchmuller, J., van Wachem, B.G.M., Gu, S., Luo, K.H., *Powder Technol*., 208, 731–39, 2011.
140. Zheng, K., et al., *Powder Technol*., 286, 582–591, 2015.
141. Hare, C., Ghadiri, M., Dennehy, R., *Chem. Eng. Sci*., 66, 4757–70, 2011.
142. Pasha, M., et al., *Powder Technol. J.*, 296, 29–36, 2016.
143. Rothenburg, L., Bathurst, R.J., *Comput. Geotech*., 11, 315–329, 1991.
144. Cundall, P.A., *Int. J. Rock Mech., Min. Sci. Geomech. Abs*., 25, 107–116, 1988.
145. Pournin, L., et al., *Granul. Matter*, 7, 119–126, 2005.
146. Williams, J.R., Pentland, A.P., *Eng. Comput*., 9, 115–127, 1992.
147. Potapov, A.V., Campbell, C.S., *No. CONF-960730-. AIChE*., 1996.
148. Jia, X., Williams, R.A., *Powder Technol*., 120, 175–186, 2001.
149. Favier, J.F. Abbaspour-Fard, M.H., Kremmer, M., Raji, A.O., *Eng. Comput*., 16, 467–480, 1999.
150. Favier, J.F., Abbaspour-Fard, M.H., Kremmer, M., *J. Eng. Mech*., 127, 971–977, 2001.
151. Hart, R., Cundall, P.A., Lemos, J., *Int. J. Rock Mech., Min. Sci. Geomech*., 25, 117–125, 1988.
152. Ransing, R.S, et al., *Mater. Design*, 21, 263–269, 2000.
153. Munjiza, A., *The Combined Finite-Discrete Element Method*, Chichester, UK: John Wiley & Sons, 2004.
154. Gustafsson, G., Häggblad, H.A., Jonsén, P., *Powder Technol*., 239, 231–238, 2013.
155. Huang, F., An, X., Zhang, Y., Yu, A.B., *Powder Technol*., 314, 39–48, 2017.
156. Nadimi, S., Fonseca, J., *Géotechnique*, 68, 290–302, 2018.
157. Munjiza, A., Andrews, K.R.F., White, J.K., *Int. J. Numer. Method Eng*., 44, 41–57, 1999.
158. Ma, G., et al., *Powder Technol*., 308, 388–397, 2017.
159. Khoei, A.R., *Extended Finite Element Method: Theory and Applications*, John Wiley & Sons, 2014.
160. Bagherzadeh, A., Mirghasemi, A.A., Mohammadi, S., *Powder Technol*., 205, 15–29, 2011.
161. Nadimi, S., Fonseca, J., *8th Int. Conf. Micromech. Granul. Media*, EPJ Web of Conferences 140, 07001, 2017.
162. Russell, A.R., Muir Wood, D., *Int. J. Rock Mech. Min. Sci*., 46, 272–280, 2009.
163. Ludwig, W., et al., *JOM J. Miner. Metals Mater. Soc*., 62, 22–28, 2010.
164. Herbig, M., et al., *Acta Mater*., 59, 590–601, 2011.
165. Schaef, W., et al., *Acta Metall*., 59, 1849–1861, 2011.
166. Zhao, B., et al., *Géotechnique*, 65, 625–641, 2015.
167. Proudhon, H., et al., *Int. J. Fatigue*, 82, 238–246, 2016.
168. Higashitani, K., Iimura, K., Sanda, H., *Chem. Eng. Sci*., 56, 2927–2938, 2001.
169. Potanin, A.A., *J. Colloid Interface Sci*., 157, 399–410, 1993.
170. Fanelli, M., Feke, D.L., Manas-Zloczower, I., *Chem. Eng. Sci*., 61, 473–488, 2006.
171. Cundall, P.A., Strack, O.D.L., *Geotechnique*, 29, 47–65, 1979.
172. Higashitani, K., Yoshida, K., Tanise, N., Murata, H., *Colloids Surf. A*, 81, 167–175, 1993.
173. Sonntag, R.C., Russel, W.B., *J. Colloid Interface Sci*., 113, 399–413, 1986.
174. Soos, M., Ehrl, L., Bäbler, M.U., Morbidelli, M., *Langmuir*, 26, 10–18, 2010.
175. Iimura, K., Nagawa, H., Higashitani, K., *Adv. Powder Technol*., 9, 345–361, 1998.
176. Iimura, K., Suzuki, M., Hirota, M., Higashitani, K., *Adv. Powder Technol*., 20, 210–215, 2009.
177. Iimura, K., et al., *Adv. Powder Technol*., 20, 582–587, 2009.
178. Iimura, K., et al., *Chem. Eng. Sci*., 64, 1455–1461, 2009.
179. Harada, S., Tanaka, R., Nogami, H., Sawada, M., *J. Colloid Interface Sci*., 301, 123–129, 2006.
180. Inamuro, T., Ii, T., *Math. Comput. Simul*., 72, 141–146, 2006.
181. Nishiyama, T., Yasuda, T., Inamuro, T., *Eur. Phys. J. Special Topics*, 171, 145–149, 2009.

182. Vanni, M., Gastaldi, A., *Langmuir*, 27, 12822–12833, 2011.
183. Seto, R., Botet, R., Auernhammer, G.K., Briesen, H., *Eur. Phys. J. E*, 35, No. 128, 2012.
184. Harshe, Y.M., Lattuada, M., *Langmuir*, 28, 283–292, 2012.
185. Harshe, Y.M., Lattuada, M., *J. Phys. Chem. B*, 120, 7244–7252, 2016.
186. Russel, W.B., Saville, D.A., Schowalter, W.R., *Colloidal Dispersions*, Cambridge: Cambridge University Press, 1989.
187. Probstein, R.F., *Physicochemical Hydrodynamics: An Introduction*, 2nd edition, New York: John Wiley & Sons, 2003.
188. Likos, C.N., *Phys. Rep.*, 238, 267–439, 2001.
189. Happel, J., Brenner, H., *Low Reynolds Number Hydrodynamics: With Special Applications to Particulate Media*, 2nd edition, Dordrecht: Martinus Nijhoff, 1983.
190. Kim, S., Karrila, S.J., *Microhydrodynamics: Principles and Selected Applications*, London: Butterworth-Heinemann, 1991.
191. Brady, J.F., Bossis, G., *Annu. Rev. Fluid Mech.*, 20, 111–157, 1988.
192. Hu, H.H., Patankar, N.A., Zhu, M.Y., *J. Comput. Phys.*,169, 427–462, 2001.
193. Glowinski, R., et al., *J. Comput. Phys.*, 169, 363–426, 2001.
194. Tanaka, H., Araki, T., *Phys. Rev. Lett.*, 85, 1338–1341, 2000.
195. Lomholt, S., Maxey, M.R., *J. Comput. Phys.*, 184, 381–405, 2003.
196. Sharma, N., Patankar, N.A., *J. Comput. Phys.*, 205, 439–457, 2005.
197. Peskin, C., *J. Comput. Phys.*, 10, 252–271, 1972.
198. Nakayama, Y., Yamamoto, R., *Phys. Rev. E*, 71, 036707, 2005.
199. Succi, S., *The Lattice Boltzmann Equation for Fluid Dynamics and Beyond*, Oxford: Clarendon Press, 2001.
200. Ladd, A.J.C., Verberg, R., *J. Stat. Phys.*, 104, 1191–1251, 2001.
201. Hoogerbrugge, P.J., Koelman, J.M.V.A., *Europhys. Lett.*, 19, 155–160, 1992.
202. Malevanets, A., Kapral, R., *J. Chem. Phys.*, 110, 8605–8613, 1999.
203. Horbach, J., Frenkel, D., *Phys. Rev. E*, 64, 061507, 2001.
204. Capuani, F. Pagonabarraga, I., Frenkel, D., *J. Chem. Phys.*, 121, 973–986, 2004.
205. Capuani, F., Pagonabarraga, I., Frenkel, D., *J. Chem. Phys.*, 124, 124903, 2006.
206. Lobaskin, V., Dünweg, B., Holm, C., *J. Phys.: Condens. Matter*, 16, S4063–S4073, 2004.
207. Chatterji, A., Horbach, J., *J. Chem. Phys.*, 122, 184903, 2005.
208. Kodama, H. Takeshita, K. Araki, T., Tanaka, H., *J. Phys.: Condens. Matter*, 16, L115–L123, 2004.
209. Araki, T., Tanaka, H., *EPL*, 82, 18004, 2008.
210. Kim, Y.W., Netz, R.R., *Europhys. Lett.*, 72, 837–843, 2005.
211. Nakayama, Y., Kim, K., Yamamoto, R., *Eur. Phys. J. E*, 26, 361–368, 2008.
212. Luo, X., Maxey, M., Karniadakis, G., *J. Comput. Phys.*, 228, 1750–1769, 2009.
213. Landau, L.D., Lifshitz, E.M., *Fluid Mechanics*, London: Pergamon Press, 1959.
214. Kim, K., Nakayama, Y., Yamamoto, R., *Phys. Rev. Lett.*, 96, 208302, 2006.
215. Yamamoto, R., *Phys. Rev. Lett.*, 87, 075502, 2001.
216. Yamamoto, R. Nakayama, Y., Kim, K., *J. Phys.: Condens. Matter*, 16, S1945–S1955, 2004.
217. Kim, K., Yamamoto, R., *Macromol. Theory Simul.*, 14, 278–284, 2005.
218. Yamamoto, R., et al., *J. Phys. Soc. Jpn.*, 77, 084804, 2008.
219. Iwashita, T. Nakayama, Y., Yamamoto, R., *J. Phys. Soc. Jpn.*, 77, 074007, 2008.
220. Iwashita, T. Nakayama, Y., Yamamoto, R., *Prog. Theor. Phys.*, 178, 86–91, 2009.
221. Iwashita, T., Yamamoto, R., *Phys. Rev. E*, 79, 031401, 2009.
222. Iwashita, T., Yamamoto, R., *Phys. Rev. E*, 80, 061402, 2009.
223. von Smoluchowski, M., *Z. Phys. Chem.*, 92, 129, 1918.
224. Hückel, E., *Phys. Z.*, 25, 204, 1924.
225. Henry, D.C., *Proc. R. Soc. London Ser. A*, 133, 106, 1931.
226. O'Brien, R.W., White, L.R., *J. Chem. Soc. Faraday Trans. 2*, 74, 1607, 1978.
227. Levine, S., Neale, G.H., *J. Colloid Interface Sci.*, 47, 520, 1974.
228. Ohshima, H., *J. Colloid Interface Sci.*, 188, 481, 1997.
229. Ohshima, H., Healy, T.W., White, L.R., *J. Colloid Interface Sci.*, 90, 17, 1982.
230. Carrique, F., Arroyo, F.J., Jiménez, M.L., Delgado, Á.V., *J. Phys. Chem. B*, 107, 3199, 2003.
231. Palberg, T., et al., *J. Phys.: Condens. Matter*, 16, S4039, 2004.
232. Lobaskin, V., et al., *Phys. Rev. Lett.*, 98, 176105, 2006.

Part 6

Process Instrumentation



Taylor & Francis
Taylor & Francis Group
http://taylorandfrancis.com

6.1 Powder Sampling

Hiroaki Masuda

6.1.1 SAMPLING EQUIPMENT

When powder is poured into a heap, size segregation will occur: fine particles tend to remain at the center of the heap and coarse ones congregate at the periphery. Even when the powder is slowly transported by a belt conveyor, coarse particles tend to float on the surface of the powder bed. It is known that size segregation occurs more frequently for powders that have a higher flowability. The following are said to be the golden rules of sampling:

1. A powder should be sampled while in motion.
2. The entire stream of powder should be taken out for a long series of short time intervals.

The first rule recommends sampling from flowing powder, such as a discharging flow from a belt conveyor or feeding flow from one storage vessel to another. Even in these cases, size segregation may occur. Therefore, the entire stream of powder should be sampled by traversing the stream, and the sampling should continue for a long series of short time intervals. If the sampling speed v (m/s) is low, the mass of the sampled powder may be too large. The sampled mass w (kg) is calculated from the relation

$$w = \frac{L}{v}\frac{W}{L}b = \frac{Wb}{v} \tag{6.1.1}$$

where

L (m)	is the width of the powder stream
W (kg/s)	the powder flow rate
b (m)	is the width of the sampler's mouth (i.e. sampling width or cutter width)

Samplers obeying the rules above are called full-stream samplers. One of the full-stream samplers, named a cutter sampler, is shown schematically in Figure 6.1.1. There are several types of full-stream samplers, such as car, belt, and rotary. The sampling width (or cutter width) and the sampling speed are adjustable in these samplers. Therefore, it is possible to take out the desired mass of powder according to Equation (6.1.1). Random sampling is also possible by randomly changing the starting time of the sampler.

Other types of samplers are the snap sampler and the slide spoon sampler. These samplers take a small amount of powder out of several positions of a powder stream or powder bed using a specially designed spoon. The mass of the sampled powder, called the increment, is much less than that of the full-stream sampler, and the final sample collected of all increments can be treated easily in a laboratory measurement.

A scoop is used to take a sample from powder loaded on a truck. In this case it is recommended that the sample be dug out from 30 cm below the surface, because the surface region is usually affected by segregation. Sampling positions are determined so as to divide the powder bed into equal areas. Sampling spears can be used to take samples from deep inside the powder bed.

A sampling device of the air-suction type (Figure 6.1.2) is also useful to get vertical samples of the powder bed in which particles are mixed with air at the sampler nose and the resulting gas–solid mixture is sucked into a gas–solid separator such as a cyclone or bag filter.

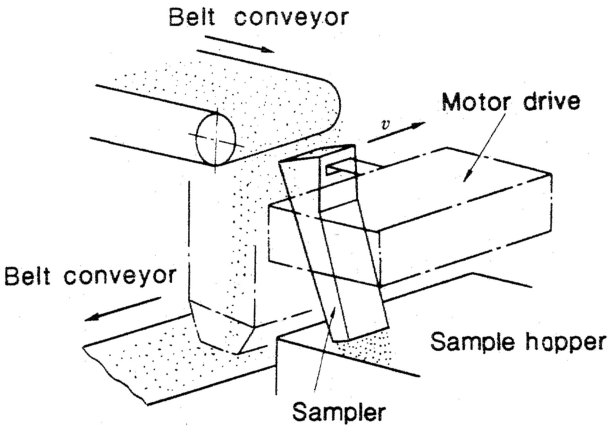


FIGURE 6.1.1 Full-stream sampler (cutter sampler).

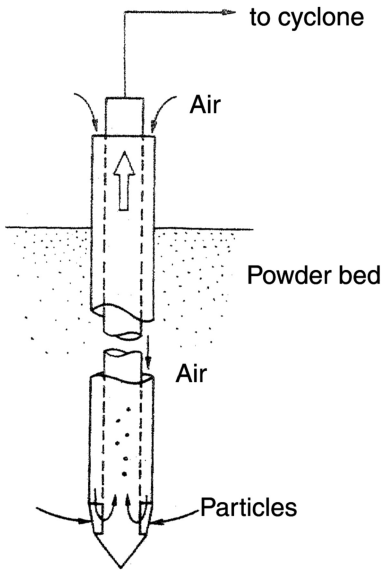


FIGURE 6.1.2 Suction sampler.

When continuous sampling from a storage vessel is necessary, a screw conveyor may be used. A table feeder with multiscrapers developed in the author's laboratory is useful to take small samples during continuous feeding of powder to a process.[1] Particles flowing through the table feeder do not suffer from breakage, whereas a screw conveyor often causes particle breakage. A special constant-volume sampler or slide-valve type of sampler may be adopted in the sampling of powder sliding on an inclined chute. These samplers are inserted into the powder stream very rapidly, so that mechanical parts of the samplers could cause problems. Moreover, if the powder stream is only partly sampled, the effect of size segregation is unavoidable.

The powder assembly of all increments is called the gross sample. The total mass of the gross sample is usually too much to be used as a sample for laboratory measurements of chemical composition, particle size distribution, and so on. It is necessary to reduce the mass of the sample before use in the laboratory. The procedure used to reduce a sample mass is called sample division.

Sample division should be done without segregation. The principles involved here are the same as those already discussed regarding collection of the gross sample. Figure 6.1.3 shows a sample divider called a spinning riffler, which satisfies the golden rules of sampling. This spinning riffler consists of a turntable with many chutes and receivers under the table. The performance of the sample divider depends on the rotational speed of the table. A higher speed (as high as 300 rpm under good condition of feeding) gives a better result.

There is another type of divider which consists of a rotary feeder and several receivers. A sample divider of this type is called a mechanical distributor or sample splitter. Similar but simpler types are an oscillating hopper sample divider and an oscillating paddle sample divider.[2] These two sample dividers are not as effective as the spinning riffler or mechanical distributor in reducing the sample mass.

All of the sample dividers mentioned above has moving parts, which are apt to cause mechanical problems in a dusty atmosphere. On the other hand, a sample divider called a chute riffler or chute splitter has no moving parts. It has a series of two chutes directing right and left, one after another. The number of chutes on the right is equal to that on the left. Powder poured onto a chute riffler is divided by the series of the two chutes. Sample dividing by the chute riffler is affected by particle segregation, although the effect becomes insignificant as the number of chutes is increased. The segregation effect may be diminished by use of a procedure called Carpenter's method.

A chute riffler requires repeated dividing to reduce the sample size (mass). A sample divider called a table sampler or multicone divider can sufficiently reduce the sample size by only one trial. The table sampler has a series of holes and prisms on an inclined table. Powder is fed to the top of the sampler (divider). Prisms placed across the path of the powder stream divide it into many fractions. Some particles fall through the holes and are discarded, while the powder remaining on the table proceeds to the next row of prisms and holes, some powder is removed, and so on. The powder reaching the bottom of the table is the final sample. Sample dividers similar to the table sampler but with no holes are called a 1/16 divider, 1/32 divider, and so on, according to the number of final samples obtained.

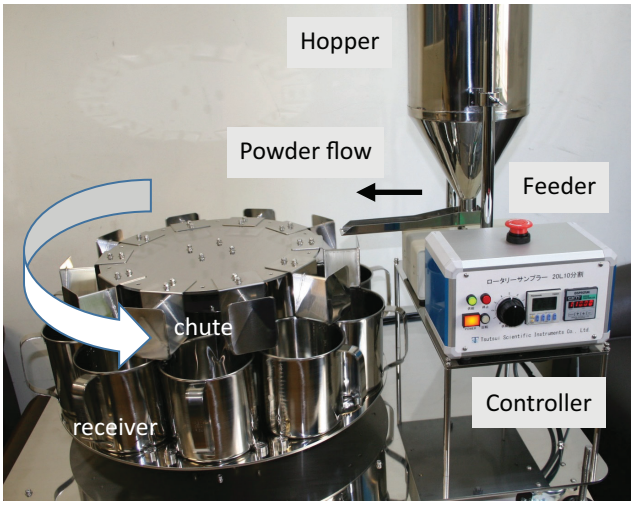


FIGURE 6.1.3 Spinning riffler.

6.1.2 ANALYSIS OF SAMPLING

Various sorts of data can be obtained by analyzing the sampled powder. The mass median diameter (MMD) of the sample, for example, is obtainable from the particle size measurement. The value of the MMD will change for every sample. An entire set of these values is called a population. Let the value x_1 be a first sample extracted from the population with a certain probability. Such a variable (e.g. the MMD) is called a random variable. The random variable x is characterized by a probability density function or frequency distribution $f(x)$. The probability that the sampled value is found in the range $x \sim x + dx$ is given by $f(x)dx$. The following relation is applicable for various types of random variables in natural phenomena and industrial processes:

$$f(x)\,dx = \frac{1}{\sqrt{2\pi\sigma}} \exp\left(-\frac{(x-\mu)^2}{2\sigma^2}\right) dx \qquad (6.1.2)$$

where

μ is the population mean
σ^2 is the population variance

The function $f(x)$ is called the normal distribution or Gaussian distribution

The population mean μ and the population variance σ^2 are unknown parameters in Equation (6.1.2), which should be estimated from the following sample mean $\bar{x}$ and sample variance s^2:

$$\bar{x} = \frac{1}{n}\sum_{j=1}^{m} x_j f_j \qquad (6.1.3)$$

$$s^2 = \frac{1}{n-1}\sum_{j=1}^{m}\left(x_j - \bar{x}\right)^2 f_j \tag{6.1.4a}$$

$$= \frac{1}{n-1}\sum_{j=1}^{m}\left[x_j^2 f_j - \frac{1}{n}\left(\sum_{j=1}^{m} x_j f_j\right)^2\right] \tag{6.1.4b}$$

where

x_j is the representative value of the jth class
f_j is the frequency of x_j ($j = 1$ *to* m)
n is the sample size

$$n = \sum\nolimits_{j=1}^{m} f_j \tag{6.1.4c}$$

The denominator of Equation (6.1.4a) is $(n-1)$ in place of n to make the variance s^2 unbiased.

The confidence interval of the population mean with the confidence level $P(=1-p)$ is given by the following relation:

$$\bar{x} - t(v,p)\frac{s}{\sqrt{n}} < \mu < \bar{x} + t(v,p)\frac{s}{\sqrt{n}} \tag{6.1.5}$$

Some of the numerical values of $t(v,p)$ are listed in Table 6.1.1.[3] The definition of t is

$$t = \frac{\bar{x} - \mu}{s}\sqrt{n} \tag{6.1.6}$$

TABLE 6.1.1 Student's *t* -Distribution *t* (*v*, *p*)

v/*p*	0.25	0.05	0.01
3	1.4226	3.1825	5.8409
4	1.3444	2.7764	4.6041
5	1.3009	2.5706	4.0321
6	1.2733	2.4469	3.7074
7	1.2543	2.3646	3.4995
8	1.2403	2.3060	3.3554
9	1.2297	2.2622	3.2498

This is also a random variable and follows Student's t–distribution with degrees of freedom $v = n-1$. If the population mean is known, one can obtain the bias $d = x - \mu$.

On the other hand, the confidence interval of the population variance with confidence level $P(=1-p)$ is given by

$$\frac{ns^2}{\chi^2\left(v, \frac{1}{2}p\right)} < \sigma^2 < \frac{ns^2}{\chi^2\left(v, 1-\frac{1}{2}p\right)} \tag{6.1.7}$$

The definition of χ^2 is

$$\chi^2 = \frac{ns^2}{\sigma^2} \tag{6.1.8}$$

This is also a random variable obeying the χ^2 distribution. Some of the numerical values of $\chi^2(v,p)$ are listed in Table 6.1.2.[3]

The precision of the sampling is usually represented by 2σ. The standard deviation σ is called the average error and $(2/3)\sigma$ is the probable error. The quantity CV (coefficient of variation) is more often utilized in expressing the precision of the sampling.

$$\mathrm{CV} = \frac{\sigma}{\mu} \times 100(\%) \tag{6.1.9}$$

On the other hand, the accuracy of the sampling is represented by the bias d. Now we will consider, as an example, whether a snap sampling is accurate or not with the confidence level of 95% by assuming that the full-stream sampling is correct. Let the data obtained from the full-stream sampling be denoted by x'_i and that from the snap sampling be denoted by x'_i. The procedure is as follows:

1. Calculate d $i = x_i - x'_i$ for $i = 1,2,...n$.
2. Calculate its variance from Equation (6.1.4).
3. Calculate t from Equation (6.1.6) with $\bar{d} = \bar{x} - \mu$.
4. Find the value of $t(v,0.05)$ from Table 6.1.1.
5. Compare t with $t(v,0.05)$. If $t > t(v,0.05)$, the snap sampling has a significant bias with confidence level of 95%. The bias is given by $\bar{d}$.

TABLE 6.1.2 χ^2 -Distribution χ^2 (*v*, *p*)

v/*p*	0.995	0.975	0.05	0.025	0.01	0.005
1	0.00003927	0.0009821	3.84146	5.02389	6.63490	7.87944
2	0.010025	0.050636	5.99147	7.37776	9.21034	10.5966
3	0.071721	0.215795	7.81473	9.34840	11.3449	12.8381
4	0.206990	0.484419	9.48773	11.1433	13.2767	14.8602
5	0.411740	0.831211	11.0705	12.8325	15.0863	16.7496
6	0.675727	1.237347	12.5916	14.4494	16.8119	18.5476
7	0.989265	1.68987	14.0671	16.0128	18.4753	20.2777
8	1.344419	2.17973	15.5073	17.5346	20.0902	21.9550
9	1.734926	2.70039	16.9190	19.0228	21.6660	23.5893

The next problem is how many particles should be sampled so as to obtain, for example, the particle size distribution by sizing and counting. In case that the log–normal size distribution is applicable, distribution of sample mean particle size can be analytically obtained.[4] Based on the sample mean distribution, the minimum number of particles n^* can be estimated by the following equation:

$$n^* = \frac{\omega}{\delta^2} \tag{6.1.10}$$

where δ is an error admissible in the evaluation of particle size analysis, and ω is a parameter defined by

$$\omega = z_c^2 m^2 s^2 \left(\frac{1}{2} m^2 s^2 + 1 \right) \tag{6.1.11}$$

where z_c is the standardized normal variable for the stated level of confidence which is determined by Table 6.1.3, m is a parameter in the evaluation function $\bar{x}_{m,0}$ given by Equation (6.1.13) below, and s is a standard deviation of log–normal particle size distribution which is given by the natural logarithm of geometric standard deviation s_g as follows.

$$s = \ln s_g \tag{6.1.12}$$

TABLE 6.1.3 Parameter z_c in Equation (6.1.11)

Confidence level (%)	90	95	97.5	99	99.5
	1.64	1.96	2.24	2.57	2.81

The evaluation function $\bar{x}_{m,0}$ is

$$\bar{x}_{m,0} = \bar{x}_{1,0} \exp\left(\frac{1}{2} m s^2 \right) \tag{6.1.13}$$

For particle size measurements, the following evaluation functions are recommended (Table 6.1.4).

TABLE 6.1.4 Recommended Evaluation Functions

Mass median diameter:	$\bar{x}_{6,0} = \bar{x}_{1,0} \exp\left(3s^2\right)$	(6.1.14)
Sauter diameter:	$\bar{x}_{5,0} = \bar{x}_{1,0} \exp\left(\frac{5}{2} s^2\right)$	(6.1.15)
Mean volume diameter:	$\bar{x}_{3,0} = \bar{x}_{1,0} \exp\left(\frac{3}{2} s^2\right)$	(6.1.16)

The minimum number of particles can be estimated if one of these evaluation functions is adopted.[5] The procedure under the mass median diameter as the evaluation function is as follows:

1. Assume the estimation probability (confidence level). If it is assumed as 95%, then Table 6.1.2 gives $u = 1.96$.
2. Comparing Equation (6.1.13) with Equation (6.1.14), the parameter $m = 6$.
3. Calculate the parameter ω by Equation (6.1.11).

$$\omega = 36u^2 s^2 \left(18s^2 + 1\right) = 138.3 s^2 \left(18s^2 + 1\right) \tag{6.1.17}$$

4. Set the admissible error δ. If it is assumed as $\delta = \pm 0.05$ (within ±5% error), Equation (6.1.10) gives

$$n^* = 138.3 s^2 \left(18s^2 + 1\right) / \delta^2 = 55320 s^2 \left(18s^2 + 1\right) \tag{6.1.18}$$

5. Determine the geometric standard deviation s_g of the measured particle size distribution. If s_g for the sample powder is 2.0, for example, then $s = \ln s_g = \ln 2.0 = 0.693$. Therefore, Equation (6.1.18) gives $n^* = 256228$. This is the minimum number of particles which should be sampled so as to obtain the particle size distribution whose mass median diameter is within 5% of the corresponding population value with 95% confidence level.

The above procedure is applicable to other cases such as the analysis of specific surface area, chemical element of particles, and so on, as far as these variables depend on particle size. The evaluation function should be determined appropriately based on the mean particle diameter suitable for each variable.

REFERENCES

1. Masuda, H., Kurahashi, H., Hirota, M., Iinoya, K., Kagaku Kogaku Ronbunshu, 2, 286–290, 1976.
2. Allen, T., in *Particle Size Measurement*, 3rd Ed., Chapman & Hall, London, 1981, chap. 1.
3. Hoel, P. G., *Elementary Statistics*, Wiley, New York, 1966, appendix.
4. Masuda, H., Iinoya, K., *J. Chem. Eng. Jpn.*, 4, 60–66, 1971.
5. Masuda, H., Gotoh, K., *Adv. Powder Technol.*, 10, 159–173, 1999.

6.2 Particle Sampling in Gas Flow

Hideto Yoshida (6.2.1, 6.2.2)
Hisao Makino (6.2.3)

Some problems related to the sampling of particles are reviewed and discussed here. In the particle sampling processes, a so-called sampling loss occurs at the entrance and inner wall of the sampling probe so that the measured value may be incorrect. The subjects to be discussed here are (1) anisokinetic sampling errors, (2) sampling in stationary air, and (3) practical applications of particle sampling.

6.2.1 ANISOKINETIC SAMPLING ERROR

If the sampling velocity u is different from that of the main stream velocity u_o, the particle concentration in the sampling tube becomes different from that in the main stream. This type of discrepancy in particle concentration is referred to as anisokinetic sampling error. Figure 6.2.1 shows a computer simulation of particle trajectories near the sampling probe under anisokinetic sampling conditions. When the sampling velocity u is higher than that of the main stream velocity u_o, the measured concentration C becomes lower than the main stream concentration C_o. Conversely, when $u < u_o$, C becomes greater than C_o.

Table 6.2.1 lists some typical proposed expressions for anisokinetic sampling errors[1,4,5,6]. Figure 6.2.2 shows the relation between the concentration ratio and the velocity ratio. The use of Davies' equation[1] is in good agreement with the numerical results.[2,3] Watson's equation[4] underestimates the sampling error.

Figure 6.2.3 shows the comparison between several empirical or semi-theoretical equations listed in Table 6.2.1[1,5] and the results obtained by the numerical calculations for both potential and viscous flow. The error estimated by a numerical calculation

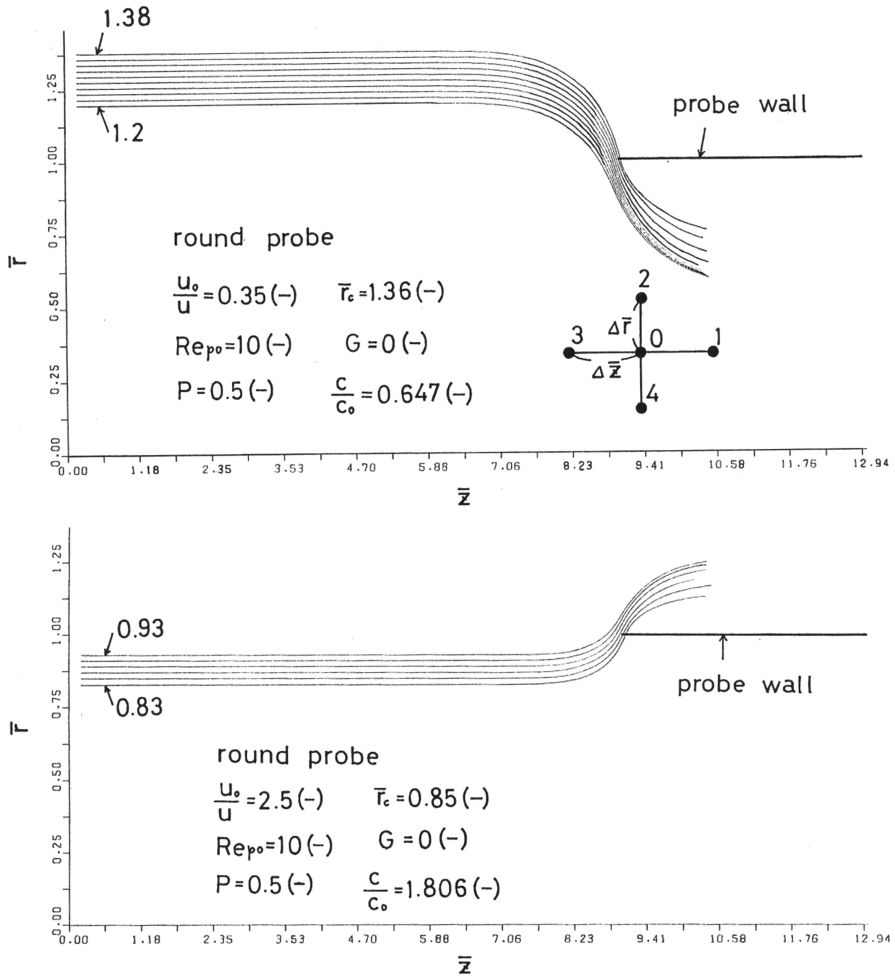


FIGURE 6.2.1 Particle trajectories for anisokinetic sampling conditions.

for potential flow is the highest among them, whereas C/C_o, as estimated by Davies' equation is intermediate between the numerical results of potential flow and viscous flow. From Figure 6.2.2, it can be seen that the concentration ratio C/C_o approaches unity when the velocity ratio u_o/u is less than 0.25. Figure 6.2.4 shows the relation between the concentration ratio and Levin's parameter k for a velocity ratio u_o/u of less than 0.25. The experimental data of Gibson and Ogden[7] and Yoshida et al.[8] are compared with Levin's equation:[9]

$$\frac{C}{C_o} = 1 - 0.8k + 0.08k^2, \quad k = 2P\sqrt{\frac{u_o}{u}} \tag{6.2.1}$$

The experimental data agree well with Levin's equation and with the numerical calculation for point sink flow.

6.2.2 SAMPLING IN STATIONARY AIR

It is impossible to carry out isokinetic sampling in stationary air. Therefore, it is important to estimate the error of anisokinetic sampling. This sampling error has been investigated by Levin,[9] Davies,[1] Kaslow and Emrich,[10] Breslin and Stein,[11] Gibson and Ogden,[7] Yoshida et al.,[8] and Agarwal and Liu.[12] Figure 6.2.5 shows the calculated fluid stream lines near the sampling probe for the case of viscous flow and potential flow. The fluid stream lines for both cases are nearly the same except for the probe inlet.

Figure 6.2.6 shows one of the calculated trajectories for particles in the viscous flow field. Sampling efficiency was also calculated using the point sink approximation. The analytical solution of Levin[9] agrees with the numerical calculations for the point sink flow up to Levin's parameter $k = 0.5$. For larger values of k, some particles orbit about the point sink, as shown in Figure 6.2.7. Experimental data by Yoshida et al.[8] agree well with their theoretical calculations based on the viscous flow. Figure 6.2.8 shows the calculated C/C_o as a function of inertia parameter P and gravitational parameter G. The solid lines represent upward sampling and the dashed lines show downward sampling. The results obtained by Agarwal and Liu[12] and Davies'[1] region of perfect sampling are also shown in Figure 6.2.8. When the probe is facing downwards, the concentration ratio C/C_o is less than unity. However, when the probe is facing upward, the ratio C/C_o can become larger than unity because of the direct settling of larger particles. The effect of gravity is clearly shown in Figure 6.2.9, where the sampling efficiency C_m/C_o is represented by the following equations.

Upward sampling:

$$\frac{C_m}{C_o} = \frac{C}{C_o}\frac{1}{1+G} \tag{6.2.2}$$

Downward sampling:

$$\frac{C_m}{C_o} = \frac{C}{C_o}\frac{1}{1-G} \tag{6.2.3}$$

The maximum value of C_m/C_o is unity, as shown by the particle mass balance. A rapid fall in the efficiency of the downward sampling as the inertia parameter increases is found.

TABLE 6.2.1 Expressions for Anisokinetic Sampling Error

Researchers	Empirical or Semi-Empirical Equation
Watson (1954)	$\frac{u_0}{u}\left[1+F\left(\sqrt{u/u_0}-1\right)\right]^2$, F is a function of P
Badzioch (1959)	$1+\alpha\left(\frac{u_0}{u}-1\right)$, $\alpha=\frac{PD}{2L}\left[1-\exp\left(-\frac{2L}{PD}\right)\right]$, L=6–1.6D
Davies (1968)	$\frac{u_0}{u}\left(\frac{P}{P+0.5}\right)+\left(\frac{0.5}{P+0.5}\right)$
Zenker (1971)	$\frac{u_0}{u}+K\left(1-\frac{u_0}{u}\right)$, $K=\left\{1+\exp\left(1.04+2.06\log\left(P/2\right)\right)\right\}^{-1}$
Belyaev and Levin (1974)	$1+\frac{P\left(1+0.31\sqrt{u/u_0}\right)}{1+P\left(1+0.31\sqrt{u/u_0}\right)}\left(\frac{u_0}{u}-1\right)$, $0.18<\frac{u}{u_0}<6.0$, $0.36<P<4.06$

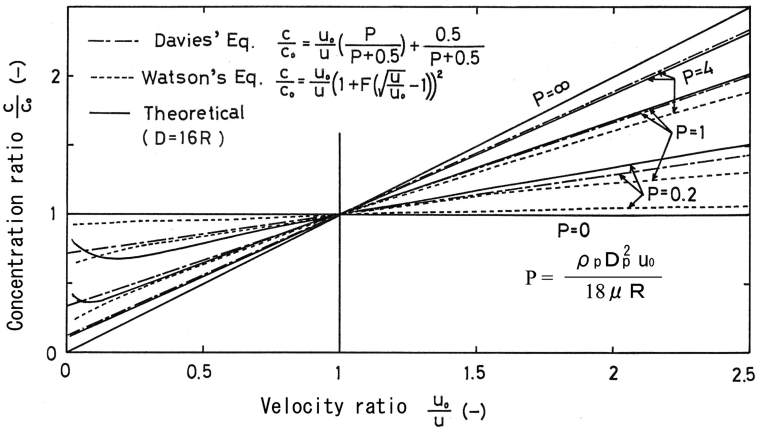


FIGURE 6.2.2 Calculated anisokinetic sampling errors.

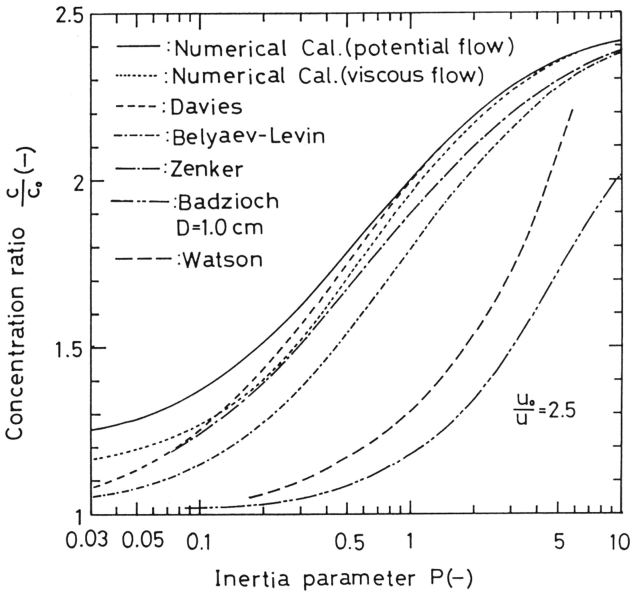


FIGURE 6.2.3 Relationship between concentration ratio and inertia parameter (numerical results compared with other equations).

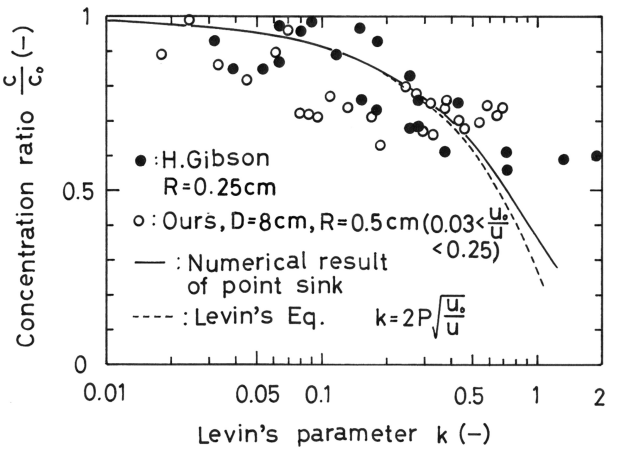


FIGURE 6.2.4 Experimental results of high-speed sampling errors compared with theoretical ones.

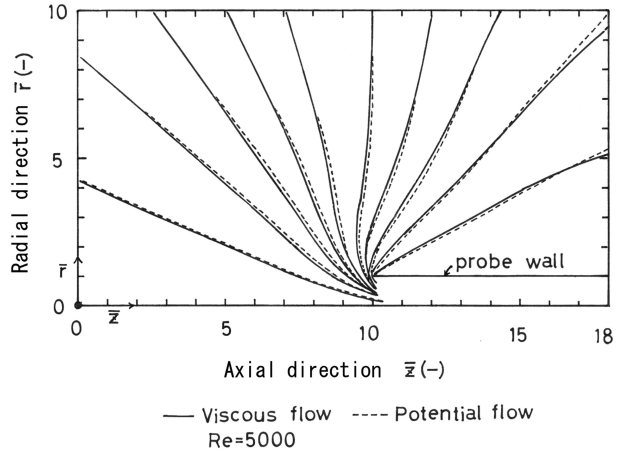


FIGURE 6.2.5 Calculated stream lines near sampling probe.

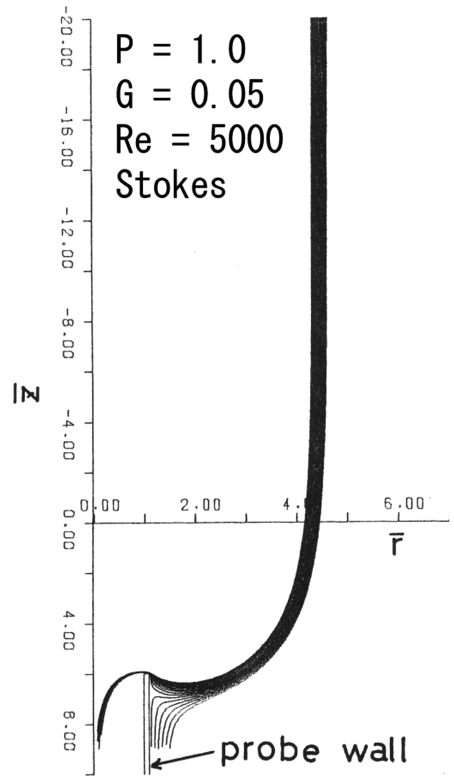


FIGURE 6.2.6 Simulated particle trajectories in stationary air (viscous flow).

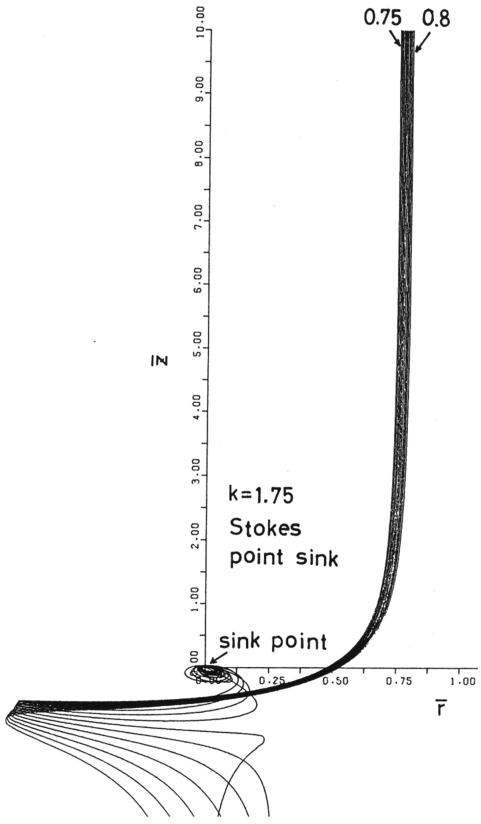


FIGURE 6.2.7 Calculated particle trajectories in stationary air (point sink approximation).

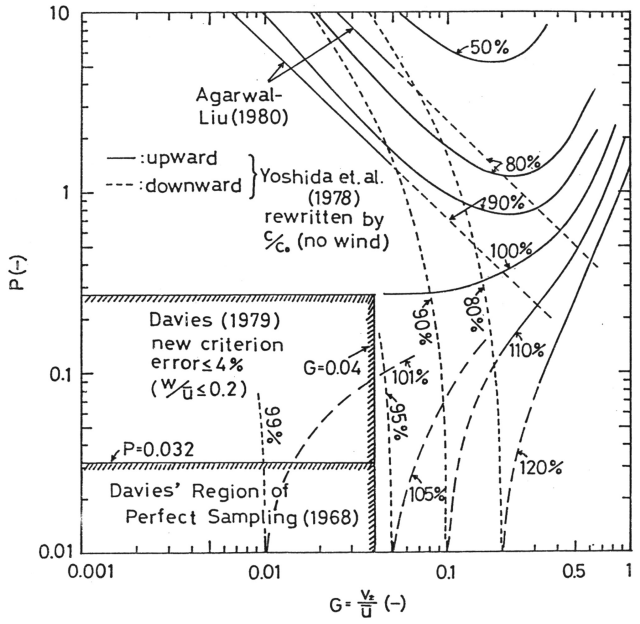


FIGURE 6.2.8 Constant sampling efficiency curves in stationary air.

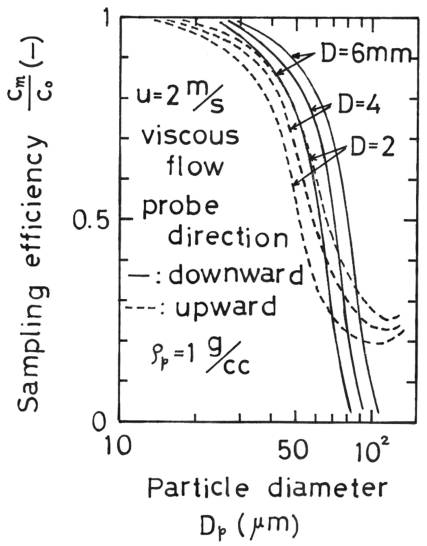


FIGURE 6.2.9 Sampling efficiency curves for downward and upward probe direction.

Particles with a diameter of less than about 10 μm are regarded to be harmful to humans because small particles are easily deposited in the human lung. In Japan, particle concentration measurements with a diameter of less than 10 μm are regulated as a 10 μm cut. The particle deposition efficiency on the lung surface increases sharply for particle diameters less than about 2 μm. The concentration measurement of particles with a diameter less than 2.5 μm is referred to as PM-2.5 sampling. Figure 6.2.10 shows USA regulations regarding a PM-2.5 sampler. In this case, the sampling flow rate and particle density are regulated to 16.7 l/min and 1,000 kg/m^3, respectively.

Particle mass measurement of PM2.5/PM10 by use of a two stage virtual impactor was developed and adopted as the international standard ISO-13271.[13]

6.2.3 PRACTICAL APPLICATIONS OF PARTICLE SAMPLING

Sampling Probe and System Used in Practical Application

Figure 6.2.11 shows the sampling probes which are commonly used for the measurement of dust concentration. They are referred to as static-pressure-balance-type sampling probe and standard-type sampling probe. The inner static pressure must be equal to the outer static pressure for isokinetic sampling in the case of static-pressure-balance-type sampling probe. However, if the inside cross-sectional area of the sampling probe is constant, the sampling velocity is lower than the main flow velocity because of the pressure drop from the nozzle inlet to the static-pressure detecting hole in the sampling probe. Tamori[14] has proposed an advanced static-pressure-balance-type sampling probe, in which the inner diameter expands.

Whitely and Reed[15] investigated the effect of the shape of the sampling probe on measurement of dust concentration. They measured dust concentration using the simplified probe and the standard probe. For the simplified probe, the distance between the probe tip and the bend is short. They concluded that the difference in measured concentration between these two sampling probes is small.

Measured concentration also varies with the angle between the sampling probe and main flow. Watson[4] and Raynor[16] examined the sampling error by changing the angle between the sampling probe and main flow. They found no significant difference at an angle less than ±5. Belyaev and Levin[17] investigated the effect of the thickness of the probe tip and concluded that the sampling error increases when the probe diameter is decreased.

Measuring Method for Particle Size Distribution by Anisokinetic Sampling

The sampling efficiency during anisokinetic sampling is dependent on the particle size when the main flow velocity and the diameter of the sampling probe are fixed. Consequently, it should be noted that the anisokinetic sampling performs the classification of the particles. Particle size distributions can be measured by using this "classification effect" during anisokinetic sampling.[18]

The sampling efficiency of mono-disperse particles has a linear relation with the velocity ratio according to Davies' equation, so that the anisokinetic sampling efficiency can be easily estimated. The slope a of this linear line varies with the particle size, as shown in Figure 6.2.12. In the case of polydisperse particles, the concentration ratio also has a linear relation with the velocity ratio. The slope A of this relation for

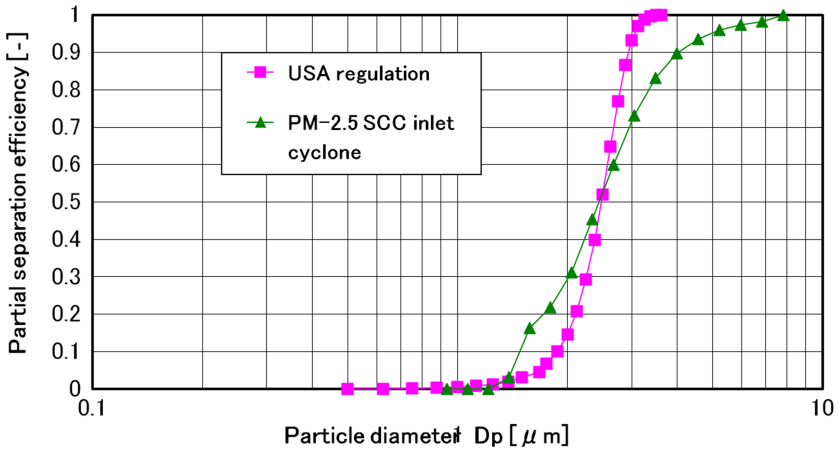


FIGURE 6.2.10 Regulation of PM–2.5 in USA and data of PM-2.5 SCC inlet cyclone.

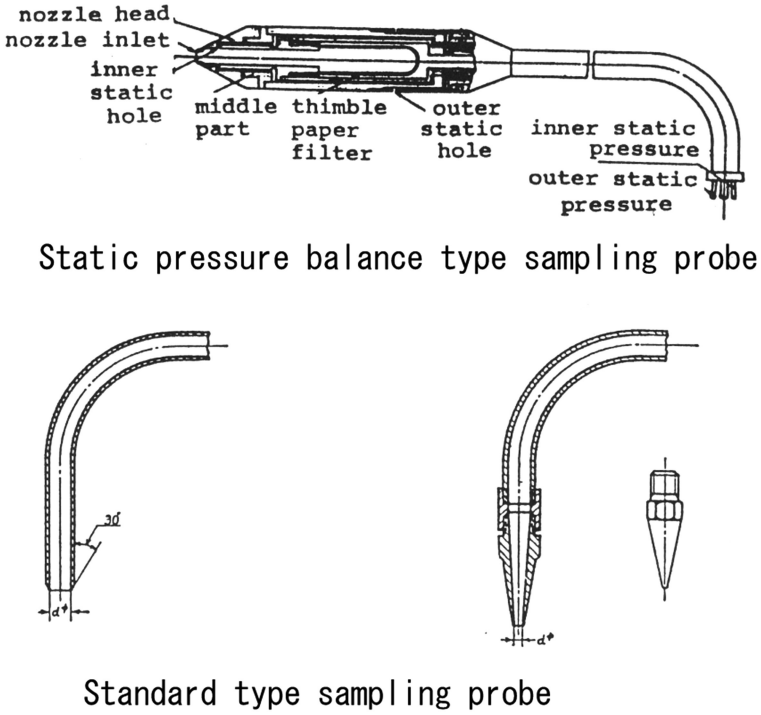


FIGURE 6.2.11 Sampling probes for dust measurement.

polydisperse particles is obtained by integrating the product of the slope a and the particle size distribution function $f(x)$:

$$A = \int_0^\infty af(x)dx = \int_0^\infty \left(\frac{P(x)}{P(x)+0.5} \right) f(x)dx \qquad (6.2.4)$$

Equation (6.2.4) can be used to determine $f(x)$ when the slope A is experimentally obtained, because the inertial parameter can be easily calculated. However, when a large number of variables exist in $f(x)$, a solution of the above equation cannot be obtained. Some assumptions are necessary to calculate the particle size distribution. For example, the particle size distribution function is required. Figure 6.2.13 shows the particle size distribution of fly-ash particles calculated by this method. Fly-ash particles properly follow a log-normal distribution, and the geometric standard deviations of these particles are nearly 2.5, so that the median diameter x_{50} can be calculated. In this figure, the results measured by the Andersen Stack Sampler (A.S.S.), which is one of the most common methods used in the measurement of particle size distribution, are also shown. The full coincidence between the values measured by two different methods is impossible, because the actual particle size distribution does not follow the ideal log-normal distribution. However, the difference in the measured value between this method and a conventional method is very small.

In order to measure complicated particle size distributions, a new method was proposed by Tsuji et al.,[19,20] in which plural sampling probes of different diameters were employed. The

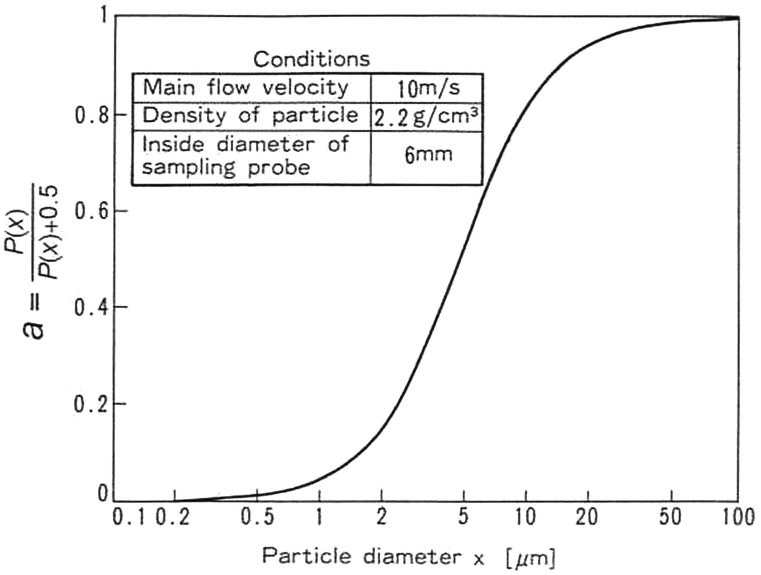


FIGURE 6.2.12 Change of the slope "*a*" in Davies' Eq.

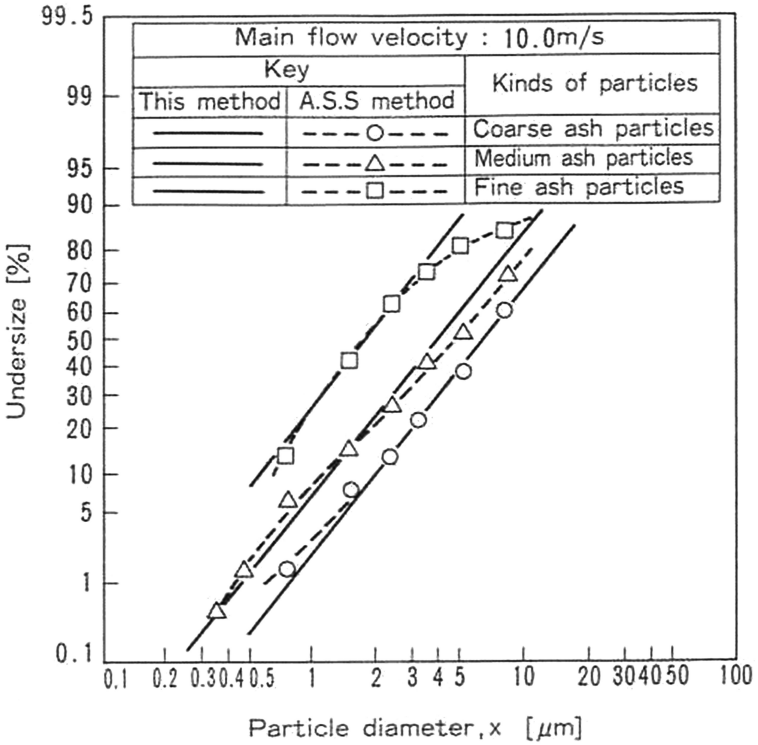


FIGURE 6.2.13 Comparison of size distributions measured by anisokinetic sampling and A.S.S.

inertia parameter can be changed by altering the diameter of the sampling probe. Therefore, it is possible to obtain plural equations such as Equation (6.2.4), which show the relationship between slope A and $f(x)$ when plural sampling probes of different diameters are used. If more than two sampling probes are used, these equations can be solved by the use of Twomey's method.[21] Figure 6.2.14 shows the particle size distributions of fly-ash measured by this method (the three-probe method) and A.S.S. Although there are small differences between the values measured by the two methods, these methods are considered to be roughly in agreement.

Since droplets and melted particles may change their size distributions after sampling and they flow on the plates in A.S.S., the measurement of these particles by the conventional method is very difficult. However, the method mentioned in this section is suitable for these particles, because the result is obtained only from the measurement of particle concentration.

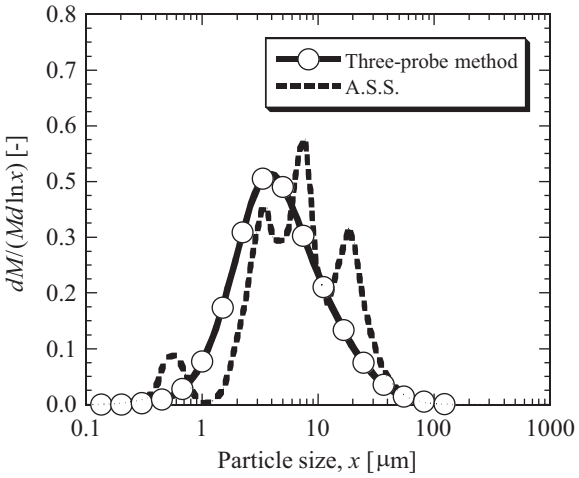


FIGURE 6.2.14 Particle size distribution of fly-ash measured by the three-probe method and A.S.S.

Measuring Method for Particle Size Distribution by Backward Sampling

The method using anisokinetic sampling is able to measure the size distribution of particles whose size is in the order of 10 μm. For fine particles less than several μm, the accuracy of this method becomes lower, because the slope a in Figure 6.2.12 is small and does not vary significantly with particle size. This is due to the reason that the fine particles easily follow the changes of the stream lines near the probe during the anisokinetic sampling because of their small inertia forces. The backward sampling, in which the probe is aligned at 180° to the flow stream, is effective for the classification of fine particles.[22,23] In the backward sampling, the stream line near the sampling probe changes substantially compared to anisokinetic sampling. Large particles cannot follow these stream lines and are not aspirated into the probe. Fine particles, which easily follow the stream line, enter the probe.

Equation (6.2.5) was proposed to express the classification efficiency during the backward sampling.[22,23]

$$\frac{C_i}{C_0} = \exp\left\{-5.09\frac{U_0}{U_i}P(x)\right\} \qquad (6.2.5)$$

As measuring methods of particle size distribution by use of classification effect of backward sampling, the backward sampling method and the combined method of anisokinetic sampling and backward sampling are proposed. The backward sampling method involves classification during backward sampling, and the combined method involves classification during both backward sampling and anisokinetic sampling.

The particle size distributions of fly-ash in a coal combustion exhaust gas measured by the backward sampling method and the combined method are shown in Figure 6.2.15.[24] This fly-ash has a typical size distribution whose peak is at 5 μm. The distributions measured by these two methods nearly agree with the result by A.S.S. This implies that these sampling methods have almost the same accuracy with that of A.S.S.

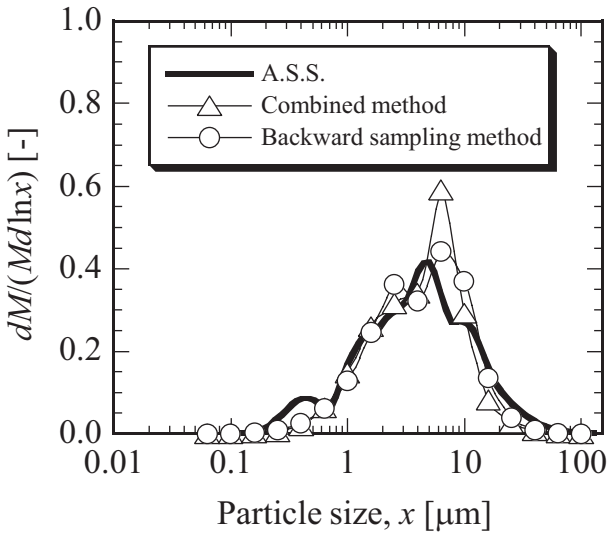


FIGURE 6.2.15 Particle size distribution of fly-ash measured by backward sampling and the combining method.

NOTATION

a:	Slope of linear relation between concentration ratio and velocity ratio for monodisperse particles
A:	Slope of linear relation between concentration ratio and velocity ratio for polydisperse particles
C/C_o:	Particle concentration in a sampling probe and main stream (kg/m^3)
C_m/C_o:	Sampling efficiency in stationary air
D, D_1:	Probe diameter and duct diameter (m)
$f(x)$:	Particle size distribution function (μm^{-1})
G:	Gravitational parameter in duct flow and in stationary air ($=\rho_P x^2 g/18\,\mu u_o = \rho_P x^2 g/18\,\mu u$)
k:	Levin's parameter
P:	Inertia parameter in duct flow and in stationary air ($=\rho_P x^2 u_o/18\,\mu R = \rho_P x^2 u/18\,\mu R$)
R:	Probe radius (m)
Re:	Flow Reynolds Number
Re_{po}:	Free-stream particle Reynolds Number ($=xu_o\rho/\mu$)
$\bar{r}(=r/R)$,:	Dimensionless coordinates
$\bar{r}_c(=r_c/R)$:	Radial coordinate of critical particle trajectory
$u, \bar{u}$:	Sampling velocity of duct flow and in stationary air (m/s)
u_o:	Main flow velocity (m/s)
v_t:	Particle settling velocity (m/s)
u:	Viscosity of fluid (Pa·s)
ρ:	Density of fluid (kg/m^3)
ρ_P:	Particle density (kg/m^3)
x:	Particle diameter (μm)
x_{50}:	Mass median particle diameter (μm)

REFERENCES

1. Davies, C.N., *J. Appl. Phys.*, 1, 921–929, 1968.
2. Yoshida, H., Ohsugi, T., Masuda, H., Yuu, S., et al., *Kagaku Kogaku Ronbunshu*, 2, 336–340, 1976.

3. Masuda, H., Yoshida, H., Iinoya, K., *J. Powder Tech. Japan*, 18, 177–183, 1981.
4. Watson, H.H., *AIHA Quart*, 15, 21–29, 1954.
5. Badzioch, S., *Br. J. Appl. Phys.*, 10, 26–29, 1959.
6. Zenker, P., *Staub Reinhalt. Luft*, 31, 30–38, 1971.
7. Gibson, H., Ogden, T.L., *J. Aerosol. Sci.*, 8, 361–369, 1977.
8. Yoshida, H., Uragami, M., Masuda, H., Iinoya, K., *Kagaku Kogaku Ronbunshu*, 4, 123–128, 1978.
9. Levin, L.M., *Bull. Acad. Sci. USSR Geophys. Ser,* 7, 87–94, 1957.
10. Kaslow, D.E., Emrich, R.J., Technical Report 23, Lehigh University, Bethlehem, Pennsylvania, 1974.
11. Breslin, J.A., Stein, R.L., *Am. Ind. Hyg. Assoc. J.*, 36, 576–586, 1975.
12. Agarwal, J.K., Liu, B.Y.H., *Am. Ind. Hyg. Assoc. J.*, 41, 191–199, 1980.
13. ISO-13271, "Determination of PM2.5/PM10 mass concentration in flue gas," 2012
14. Tamori, Y., *Funtai Kogaku Kenkyu Kaishi*, 11, 3–13, 1974.
15. Whitely, A.B., Reed, L.E., *J. Inst. Fuel*, 32, 316–325, 1959.
16. Raynor, G.S., *Am. Ind. Hyg. Assoc. J.*, 31, 294–299, 1970.
17. Belyaev, S.P., Levin, L.M., *J. Aerosol. Sci.*, 3, 127–136, 1972.
18. Makino, H., Tsuji, H., Kimoto, M., Yoshida, H., et al., *Kagaku Kogaku Ronbunshu*, 21, 896–903, 1995.
19. Tsuji, H., Makino, H., Kimoto, M., Yoshida, H., et al., *J. Aerosol. Sci.*, 26, Suppl. 1, S113–S114, 1995.
20. Tsuji, H., Makino, H., Yoshida, H., Iinoya, K., *J. Aerosol Sci.*, 28, Suppl. 1, S681–S682, 1997.
21. Twomey, S., *J. Comput. Phys.*, 18, 188–200, 1975.
22. Tsuji, H., Makino, H., Yoshida, H., Ogino, F., et al., *Kagaku Kogaku Ronbunshu*, 25, 780–788, 1999.
23. Tsuji, H., Makino, H., Yoshida, H., *Powder Tech.*, 118, 45–52, 2001.
24. Tsuji, H., Makino, H., Yoshida, H., *J. Powder Tech. Japan*, 36, 810–818, 1999.

6.3 Concentration and Flow Rate Measurement

Shuji Matsusaka

6.3.1 PARTICLE CONCENTRATION IN SUSPENSIONS

The concentration of particles suspended in gas or liquid can be expressed in several ways. The various definitions of particle concentration are summarized as follows:

1. Mass flow ratio m (–):

$$m = \frac{W}{Q} \tag{6.3.1}$$

   where W and Q are the mass flow rates of particles and fluid, respectively.
2. Flow concentration c (kg/m^3):

$$c = \frac{W}{Q_v} = \rho_a m \tag{6.3.2}$$

   where Q_v is the volumetric fluid flow rate and ρ_a the density of fluid. If the concentration c is divided by the particle density ρ_p, it becomes dimensionless and is called volumetric concentration.
3. Holdup concentration c_h (kg/m^3):

$$c_h = \frac{dw}{V} = \frac{Wdl}{vV} = \frac{W}{vA} \tag{6.3.3}$$

   where dw is the mass of suspension, V the volume occupied by the suspension, dl the length, v the mean velocity of particles, and A the cross section.

The aforementioned three types of concentration are often called, for simplicity, particle concentration. The holdup concentration c_h is related to the flow concentration c as per the following equation:

$$c_h = \frac{u}{v} c \tag{6.3.4}$$

where u (= Q_v/A) is the velocity of fluid. In gas–solid suspension flow, the particle velocity v is usually smaller than the gas velocity u; thus, the holdup concentration c_h is higher than the flow concentration c. The number concentration is also used instead of the mass or volumetric concentration. The optical particle counter, for example, measures the number concentration.

Table 6.3.1 lists the methods for measurement of relatively high particle concentration in powder-handling processes. A gamma-ray densitometer or density gauge is used especially for the continuous measurement of slurries with high concentration of solids. Figure 6.3.1 shows this instrument, which consists of a radioactive source, radiation detector, amplifier, and analyzer. For the radioactive source, ^{137}Cs (E = 662 keV) and ^{241}Am (E = 60 keV) are usually used. The gamma rays produced by these sources pass through the pipeline and the output is used to get the slurry concentration. The slurry or pulp density can be measured by various methods, including the aforementioned nuclear density meters, hydrometers, balanced flow vessels, differential air bubblers, and ultrasonic density meters.[1–4]

The methods listed in Table 6.3.2 are applicable to fine particles. Table 6.3.3 lists the methods for detecting the mass of fine particles sampled on a filter or in the sensing zone of an instrument.

Electric Capacitance Change

The electric capacitance of a parallel-plate capacitor increases with the increasing of particle concentration in a gas–solid suspension. The measured concentration is the volumetric concentration. As the area of the parallel-plate capacitor is made as small as 1 cm^2, a sensor is used to measure the local concentration of particles in a powder-handling equipment, such as a fluidized bed.[5]

Electrostatic Charging

The electric current generated by particle impact is proportional to the powder flow rate. Therefore, the flow concentration c of a

TABLE 6.3.1 Powder Concentration Meter

Principle	Notes
Electric capacitance increase	Electric condenser, parallel-plate condenser
Gamma-ray attenuation	Gamma-ray densitometer, Lambert–Beer law
Statistical correlation of various noises	Autocorrelation
Microwave resonance	Resonant frequency decrease

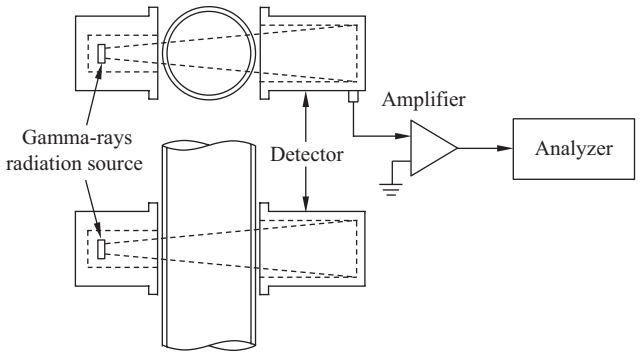


FIGURE 6.3.1 Gamma-ray density gauge.

TABLE 6.3.2 Dust Concentration Meter

Principle	Notes
Photo extinction	Photometer, transmissometer, Lambert–Beer law
Light scattering	Photometer, nephelometer, optical particle counter
Laser radar	Lidar (long-range measurement)
Nucleated condensation	Condensation nuclei counter (ultrafine particles)
Electrostatic charging	Charge transfer by impact

TABLE 6.3.3 Dust Monitor (Sampled Particles)

Principle	Notes
Beta-ray attenuation	Beta gauge, Lambert–Beer law
Light attenuation	Lambert–Beer law
Electrically forced vibration	Mechanical resonance (frequency decrease)
Piezoelectric vibration	Piezobalance[1] (frequency decrease)
Electrostatic charging	Charge measurement after unipolar charging

[1] Trade name.

gas-solid suspension will be obtained if the suspension is sampled with a constant velocity. The particles in the sampled gas impact the sensor target, which is placed in the sampled flow, or impact an inside wall of the sensor tube. Any kind of sensitive materials can be used as the sensor.[6]

Induction Charging

The electroconductive particles will be polarized in an electric field. If the polarized particle makes contact with a target electrode, its negative or positive charge will be neutralized by the opposite charge supplied from the electrode. The particle obtains a net charge after the contact. Therefore, the current required for the charging will be found between the electrodes as a voltage pulse.[7] The number of pulses found per unit time can give the number concentration.

Piezoelectric Effect

A piezoelectric sensor can be employed for the measurement of particle concentration in a flowing suspension. The sensor detects the frequency of impact. At the same time, the particle mass is measured, and thus, it is possible to transform the frequency into the corresponding mass concentration. In this kind of sensor, the impact efficiency should be correctly taken into consideration.[6,8]

Electrically Forced Vibration (Resonance Technique)

This method is based on the electrically forced vibration of the collected particle mass. Suspended particles are sampled isokinetically onto a fibrous filter that is connected to a spring. The sensing element is electrically vibrated. If the frequency of the forced vibration coincides with the natural frequency, resonance will be found. Therefore, if the resonance frequency is detected, the mass m will be calculated. As the particles deposit on the filter, the mass m increases from m to $m + \Delta m$, and the resonance frequency changes. If the frequency shift is measured, the mass of the particles will be obtained.[9] Then, the flow concentration c is calculated by

$$c = \frac{\Delta m}{Q_v \Delta t} \tag{6.3.5}$$

where Δt is the duration of sampling and Q_v is the sampled flow rate.

Quartz Crystal Microbalance

A mass sensor using a quartz oscillator is based on the same principle discussed above. The sensor is called the quartz crystal microbalance (QCM). Suspended fine particles are sampled by use of a suction pump and are collected on the quartz crystal.[10]

The resonance frequency decreases as described above. The frequency shift Δf (Hz) for the quartz crystal with the natural frequency of 5 MHz is given by

$$\Delta f = -5.65 \times 10^6 \frac{\Delta m}{S} \tag{6.3.6}$$

where S is the particle-collection area (m^2). The mass sensitivity (5.65×10^6) is independent of the physical properties of the deposited particles. A frequency shift as small as 0.1 Hz can be measured by using a simple frequency counter. Therefore, Equation (6.3.6) shows that the QCM can detect particles as small as 1.8×10^{-8} kg/m^2 (= 1.8 ng/cm^2).

Attenuation Technique

The energy of waves, such as light (electromagnetic wave), sound, or radioactive rays, will be dissipated through suspended particles or a powder bed because of wave absorption or scattering. If a light beam passes through a uniformly

suspended aerosol layer, the intensity of light will decrease as follows:

$$\frac{I}{I_0} = \exp(-\eta_m C_h L) \tag{6.3.7}$$

where

I_0 is the initial incident intensity of light (i.e. intensity of the transmitted light without particles)
c_h is the holdup concentration
η_m is the mass absorption coefficient
L is the total thickness of the aerosol layer

Equation (6.3.7) implies that the intensity of the light beam decreases exponentially with the thickness of the layer. This fact is known as the Lambert–Beer law. The maximum attenuation will be found for a certain particle size between 0.1 and 2 μm. On the other hand, the mass absorption coefficient for very short wavelengths, such as UV light (0.01–0.4 μm) or X-rays (less than 0.01 μm), is relatively independent of the particle size. For the mass measurement of particles sampled on dust filters, gamma rays used in the density gauge are too strong, and thus, beta rays from ^{14}C, ^{147}Pm (promethium), or ^{63}Ni are used. The concentration meter based on beta rays is applicable to the measurement of higher concentration than the QCM. The mass absorption coefficient η_m is a function of the maximum energy E_{max} of the beta rays, and it is almost independent of the kinds of materials deposited. Therefore, the meter is easily calibrated by using a plastic film, such as a Mylar film.[11]

6.3.2 POWDER FLOW RATE

There are two types of powder flows: bulk solids and suspension flows. The principles of powder flowmeters for bulk solids and suspension flows are listed in Table 6.3.4 and Table 6.3.5, respectively. The weighing method in Table 6.3.4 belongs to direct measurement, but others belong to inferential measurements.

The powder flow rate W (kg/s) in a suspension flow is the product cvA (kg/s) of particle concentration c (kg/m^3), particle velocity v (m/s), and cross-sectional area A (m^2). Therefore, the measurement of the powder flow rate requires a combined measurement of particle concentration and particle velocity. Table 6.3.6 lists the principles of particle velocity measurement. The mean velocity of powder flow across the cross-sectional area should be measured to obtain the powder flow rate from the combined concentration–velocity measurement.

Weighing Method

The weighing method is the most reliable and accurate for measurement of the powder flow rate in a bulk solids flow.[1] The hopper scale (weigh hopper) and the belt scale (belt weigher or conveyor scale) are the typical flowmeters of this kind.

The hopper scale receives powder in the hopper, weighs it, and then discharges it. The frequency of receiving and discharging is 100–400 cycles per hour, which can be changed according to the process requirement. A combination of high speed in the early stage of the feeding and low speed in the final stage allows a short cycle time with high accuracy.[6] A hopper scale, which weighs the hopper scale after the feeding is perfectly stopped, is called the net-weight mode hopper scale. For continuous powder feeding, the hopper scale is operated in the loss-in-weight mode, in which the powder is added before the hopper becomes empty and the discharge flow is kept continuous. The powder adhered on the hopper wall does not cause a weigh error of the hopper scale in this mode.

The belt scale is, however, more suitable than the hopper scale for the continuous feeding of powder, where the flow rate is obtained as a product of the weight of powder on a belt of unit length and the belt speed. When the flow rate is controlled to feed a constant powder mass, the belt scale is called a constant-feed weigher. Belt speed control is preferable to gate opening control in the operation of a constant-feed

TABLE 6.3.4 Powder Flowmeter for Bulk Solids Flow

Principle	Notes
Weighing	Belt scale, hopper scale
Impulsive force	Impact flow meter
Coriolis force	Massometer[1] and others
Back pressure of air jet	Gas purge type of flowmeter
Volume displacement	Turbine type of flowmeter

[1] Trade name.

TABLE 6.3.5 Powder Flowmeter for Suspension Flow

Principle	Notes
Pressure drop	Venturi-type flowmeter, Venturi-orifice flowmeter
Electrostatic charging	Particle electrification by impact
Microwave	Microwave-type flowmeter (microwave resonance)
Statistical phenomena	Correlation-type flowmeter (concentration × velocity)
Heat absorption	Metallic particles

TABLE 6.3.6 Particle Velocity Meter

Principle	Notes
Statistical Phenomena	Correlation technique (electrostatic current, electric capacitance, light extinction)
Spatial filtering	Microwave type, laser velocimeter (lattice window)
Piezoelectric phenomena	Piezocrystal (momentum detector)
Doppler effect Time of flight	Laser Doppler velocimeter. double-beam laser

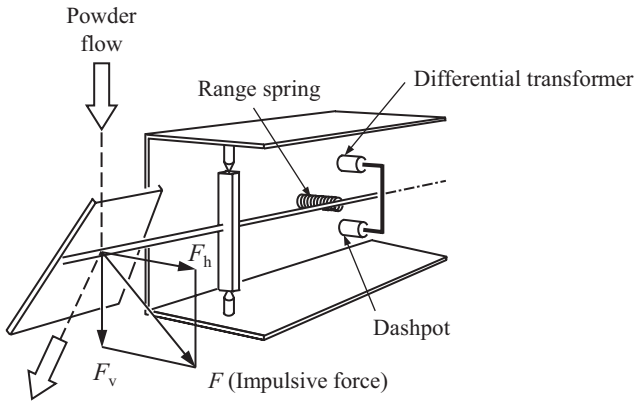


FIGURE 6.3.2 Impact flowmeter.

weigher.[12] A mechanical unit or load cell is used to weigh the powder.

Impulsive Force Flowmeter

The flowmeter shown in Figure 6.3.2, which is based on the impulsive force, is called an impact flowmeter. The powder falls down by gravity and impacts an inclined plate. The force acting on the plate is calculated from the impulse versus momentum relation, and it is expressed by horizontal and vertical components. The impact flowmeter has been able to detect the vertical component since the early stage of its development,[13] and it is the sum of the impulsive force and the weight of the powder adhered to the plate. A recently developed impact flowmeter is able to detect the horizontal component and it is not affected by the adhered powder.[6] The horizontal component of the impulsive force is given by

$$F_h = \frac{1}{2}(e+\mu)K\sin 2\theta\sqrt{2gh}W \tag{6.3.8}$$

where

- e is the coefficient of restitution of particles
- μ is the coefficient of friction
- K is the air-drag coefficient
- h is the free-falling height of the powder
- θ is the inclination of the plate, and W is the powder mass flow rate

The flowmeter is very compact and its dynamic response is very fast. Further, dust intrusion into its mechanical parts is easily shut out. This principle has also been applied to the gas–solid suspension flow.[14] In this case, the gas and particle velocities should be measured by a suitable method. Moreover, the particle inertia must be large enough in order for all particles to impact the detector.

Coriolis Force Flowmeter

When the powder flow is received on a rotating disk and thrown off from the periphery of the disk, the powder suffers from the Coriolis force in the direction counter to the rotation. The resulting total torque T on the rotating axis is given by

$$T = \omega r^2 W \tag{6.3.9}$$

where

- ω is the angular velocity of the table
- r is the table radius
- W is the powder mass flow rate

Equation (6.3.9) contains no calibration constant, which is the most important feature of the Coriolis force flowmeter.

Differential Pressure Method

Mass flowmeters based on the differential pressure or pressure drop are applied mainly to suspension flows. However, the principle is also used in the measurement of bulk powder flows.[15] One feature of the method is that the electric parts of the flowmeter can be isolated from the main process where there might be radioactive rays. When particles are transported by a pneumatic conveyor, the pressure drop along the pipeline usually becomes larger than that of the corresponding airflow alone. The additional pressure drop depends on the mass flow ratio m. In the measurement of a powder flow rate, it is necessary to know the relationship between the mass flow ratio and pressure drop, and besides, in a gas–solid mixture flow, the gas flow rate. The venturi meter[16] and the orifice meter are applicable for this purpose. The powder flow rate W is calculated from

$$W = K\sqrt{\rho}\,\frac{\Delta P - k\Delta P_a}{\sqrt{\Delta P_a}} \tag{6.3.10}$$

where

- ΔP is the pressure drop at the straight pipe section
- ΔP_a is the pressure recovery at the diffuser
- ρ is the air density
- K and k are the calibration constants

The calibration constant k is adjustable to unity if the distance between the pressure taps in the straight pipe section is designed in such a way that the pressure drop for airflow alone is equal to the pressure recovery at the diffuser.

The pressure drop of a venturi nozzle is used in the venturi–orifice flowmeter.[17] A venturi with a long throat is also used to increase the pressure drop and attain higher meter sensitivity.[18] Another version of the flowmeter is composed of a straight pipe with an inserted core to generate an annular flow between them. The particles will be accelerated by the high-speed annular flow, resulting in a pressure drop. The flowmeter is insensitive to upstream disturbances and does not require a long straight inlet section as in the case of the venturi flowmeter.

The aforementioned flowmeters can be used in a gas–solid mixture flow with mass flow ratio m below 10. For a higher mass flow ratio, the relationship between the pressure drop ratio ($\Delta P/\Delta P_a$) and the mass flow ratio m becomes nonlinear.

Electrical Method

The electric currents generated by particle impact can be applied to the measurement of the powder flow rate in gas–solid mixture flow. However, the concentration should be rather small, because the relation between the current and flow rate becomes nonlinear for high concentrations.[19] The sensitivity depends on the material of the detector.[20] If the detector is covered with particles, impact electrification becomes ineffective; therefore, the air velocity should be higher to prevent the particles from adhering. Furthermore, there is a measuring system that uses two detectors, which can measure both the powder flow rate and average electrical charge of particles in an aerosol pipe flow.[21,22]

The electromagnetic flowmeter is based on Faraday's law of electromagnetic induction. Figure 6.3.3 shows an electromagnetic flowmeter, which is truly obstructionless and is widely used for slurry flow measurement. The pipe is made from a nonmagnetic material, such as stainless steel, through which the magnetic field can pass. The inside wall is covered by a nonconductive plastic or ceramic. A pair of electrodes is set on the wall perpendicularly to the magnetic field. The potential difference induced between the electrodes as the slurry moves across the magnetic field is given by

$$V = kBDu \tag{6.3.11}$$

where

- k is the proportional constant (unitless)
- B is the magnetic flux density (T)
- D is the inside diameter of the pipe (m)
- u is the average flow velocity (m/s)

The volumetric flow rate Q_v (m^3/s) is given by

$$Q = \frac{\pi D}{4kB} V \tag{6.3.12}$$

The electromagnetic flowmeter is not affected by variations in density, viscosity, pH, pressure, or temperature. If the concentration is higher than 10%, the proportional constant can become larger because of the increase in magnetic flux density, and recalibration of the flowmeter will be necessary. Moreover, magnetic solids such as magnetite can cause an erroneous reading, and particle deposition on the wall will affect the pickup of potential differences.

There is another method based on electrostatic induction; by monitoring the electrostatic flow noise generated while charged particles are conveyed through a pipeline, the mass flow rate could be calculated.[23]

The piezoelectric method is used only to detect local flow.[24] The sensor is made of a piezoelectric crystal or ceramics. If the dielectric crystal is deformed by an impulsive force, displacement of ions in the crystal takes place (polarization), which induces an electric pulse between the upper and lower surfaces of the crystal. The pulse can be detected if the surfaces are coated with metal and connected to a pulse analyzer. The particle mass should be known to measure the local mass flux or concentration by use of the piezoelectric sensor. A strain gauge can be used as a sensor of the impact force instead of the piezoelectric crystal.[25]

The microwave (i.e. an electromagnetic wave with frequency range of 10^9–10^{12} Hz) method uses a circular tube resonator lined with a dielectric material.[26] If the gas–solid mixture flows through the resonator, the resonance frequency changes; thus, the volumetric concentration c_v can be obtained. On the other hand, there exists a standing wave in the resonator, and it works as a lattice window for the velocity measurement (i.e. spatial filtering). The powder flow rate is obtainable as the product of concentration and velocity.

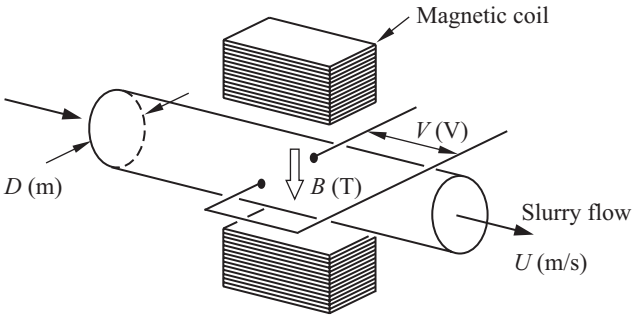


FIGURE 6.3.3 Electromagnetic flowmeter.

Statistical Method

A pair of sensors is set along a conveyor line, the distance L apart. The signals detected by the sensors will fluctuate because of the flow turbulence. The pulsating signals including the electrostatic flow noise can also be used.[27] If the autocorrelation is calculated for various values of the delay-time parameter τ, it takes a maximum at a certain value of $\tau = \tau_0$. τ_0 gives the time interval for the particle cloud to travel between the two sensors. Hence the particle flow velocity v is determined as

$$v = \frac{L}{\tau_0} \tag{6.3.13}$$

The powder flow rate W will be determined as the product of the particle velocity by particle concentration and the cross-sectional area of the flow.[28]

The statistical method does not obstruct the particle flow, and hence, is preferable for process instrumentation. The method can be applied to bulk solids flow in hoppers or chutes by using a sound noise pickup (i.e. a microphone). Fiber optics can be used in the measuring system for particles flowing on a chute or moving in a vessel.

REFERENCES

1. Perry, R. H., Green. D. W., *Perry's Chemical Engineers' Handbook*, 6th Ed., McGraw-Hill, New York, 1984, p. (5) 8–20.
2. Mitchel, J. W., *Coal Preparation*, American Institute of Mining, Metallurgical, and Petroleum Engineers, New York, 1979, p. (19) 42.

3. Wills, B. A., *Mineral Processing Technology*, Pergamon Press, Oxford, 1979, p. 45.
4. Weiss, N. L., Mineral Processing Handbook, American Institute of Mining, Metallurgical, and Petroleum Engineers, New York, 1985, p. (10) 173.
5. Bakker, P. J., Heertjes, P. M., *Br. Chem. Eng.*, 3, 240, 1958.
6. Iinoya, K., Masuda, H., Watanabe, K., *Powder and Bulk Solids Handling Processes*, Marcel Dekker, New York, 1988, pp. 65–130.
7. Keily, D. P., Millen, S. G., *J. Meteorol.*, 17, 349, 1960.
8. Mann, U., Crosby, E. J., *Ind. Eng. Chem. Process Des. Dev.*, 16, 9, 1977.
9. Wang, J. C. F., Kee, B. F., Linkins, D. W., Lynch, E. Q., *Powder Technol.*, 40, 343–351, 1984.
10. Lu, C., Czanderna, A. W., *Application of Piezoelectric Quartz Crystal Microbalances*, Elsevier, New York, 1984.
11. Sem, G. J., Borgos, J. A., *Staub Reinhalt. Luft*, 35, 5, 1975.
12. Grader, J. E., *Control Eng.*, 15 (3), 60, 1968.
13. Iinoya, K., et al., *J. Res. Assoc. Powder Technol. Jpn.*, 3, 424–431, 1966.
14. Barth, W., *Chem. Ing. Technol.*, 29, 599, 1957.
15. Kagami, H., Maeda, M., Yagi, E., *Kagaku Kogaku Ronbunshu*, 1, 327–329, 1975.
16. Masuda, H., Ito, Y., Iinoya, K., *J. Chem. Eng. Jpn.*, 6, 278–282, 1973.
17. Farber, L., *Trans. ASME*, 75, 943, 1953.
18. Iinoya, K., Gotoh, K., *Kagaku Kogaku*, 27, 80, 1963.
19. Masuda, H., Mitsui, N., Iinoya, K., *Kagaku Kogaku Ronbunshu*, 3, 508–509, 1977.
20. Matsusaka, S., Nishida, T., Gotoh, Y., Masuda, H., *Adv. Powder Technol.*, 14, 127–138, 2003.
21. Masuda, H., Matsusaka, S., Nagatani, S., *Adv. Powder Technol.*, 5, 241–254, 1994.
22. Masuda, H., Matsusaka, S., Shimomura, H., *Adv. Powder Technol.*, 9, 169–179, 1998.
23. Gajewski, J. B., *J. Electrostat.*, 37, 261–276, 1996.
24. Heertjes, P. M., Verloop, J., Willems, R., *Powder Technol.*, 4, 38–40, 1970.
25. Raso, G., Tirabasso, G., Donsi, G., *Powder Technol.*, 34, 151–159, 1983.
26. Kobayashi, S., Miyahara, S., *Keisoku Jido Seigyo Gakkai Ronbunshu*, 20, 529, 1984.
27. Matsusaka, S., et al., *Chem. Eng., Sci.*, 63, 1353–1360, 2008.
28. Beck, M. S., Drane, J., Plaskowski, A., Wainwright, N., *Powder Technol.*, 2, 269–277, 1969.

6.4 Level Measurement of Powder Bed

Shuji Matsusaka

6.4.1 LEVEL METERS AND LEVEL SWITCHES

Level meters are classified into two categories: continuous and discrete. Discrete level meters, also known as level switches, are typically used to maintain the powder level between prescribed upper and lower limits by feeding or discharging powder.[1] Table 6.4.1 presents the principles of continuous level meters. Table 6.4.2 presents the principles of various other level switches.

Level meters or level switches should be located in suitable positions as the powder bed surface is not always horizontal. Furthermore, the profile of the surface will gradually change during feeding or discharging. For free-flowing particles, the profile may generally be estimated from the angle of repose. If estimates of the level are difficult to obtain, experiments should be conducted to determine suitable locations for the level meters.

6.4.2 MECHANICAL METHODS

Sounding Level Meters

A sounding level meter mounted at the top of a storage vessel is shown in Figure 6.4.1. A weight connected to a wire is lowered slowly from a wire drum. When the weight reaches the surface of the powder bed, the wire loses tension, and the torque acting on the wire drum decreases. The change of torque is detected mechanically, and the wire is rolled up by reversing the motor rotation. The powder bed level is the length of wire paid out, which is determined from the number of rotations of the drum.

Level meters of this type can measure depths of 50 m, with a resolution of 10 cm. The meter is applicable for high-temperature vessels, such as blast furnaces. The level of solid materials immersed in liquid can also be measured.

Piston Level Switches

Figure 6.4.2 is a schematic diagram of a piston level switch. A shaft with a disk at the end is moved reciprocally by a motor and crank mechanism. If the disk is blocked by particles on the left-hand side of the figure, the spring is compressed by the motor action, and the link takes on a V-shape. The link then activates a microswitch, and the motor is switched off. If the disk is freed from the particles, the spring action returns the link to its original shape, and the motor starts rotating again.

Bearings are isolated by bellows to ensure that dust does not contaminate the mechanical parts. However, adhesion of particles on the disk, bellows, and the shaft can cause problems.

Rotating Blade Level Switches

This level switch has a blade at the end of a shaft, which is rotated slowly (1–3 rpm) by a synchronous motor. Mechanical blockage of the rotating blade by particles is detected by a

TABLE 6.4.1 Powder Level Meter (Continuous Type)

Principle	Notes
Weighing	Load cell
Electric capacitance	–
Electric resistance	–
Sounding	Wire with weight
Attenuation	Radiation, ultrasonic wave
Reflection time (reflectometry)	Ultrasonic wave, electromagnetic pulse, pulsed microwave

TABLE 6.4.2 Powder Level Switch

Principle	Notes
Back pressure increase	Gas purge, gas injection
Elastic deformation (powder pressure)	Diaphragm with mercury switch
Mechanical blockage of motion by powder	Reciprocation, rotation, swinging motion
Electrically forced vibration	Piezoelectric vibration, tuning fork
Attenuation	Microwave, electromagnetic wave

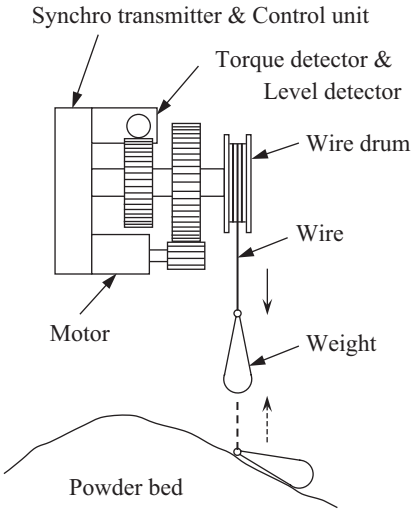


FIGURE 6.4.1 Sounding level meter.

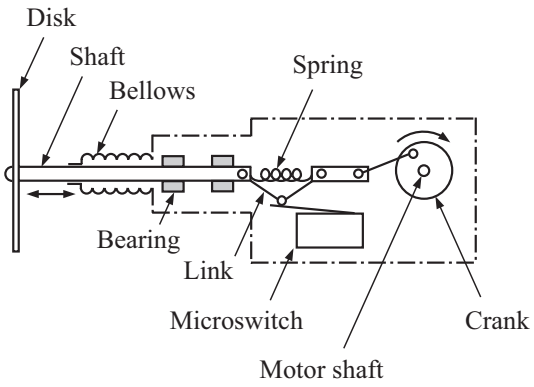


FIGURE 6.4.2 Piston level switch.

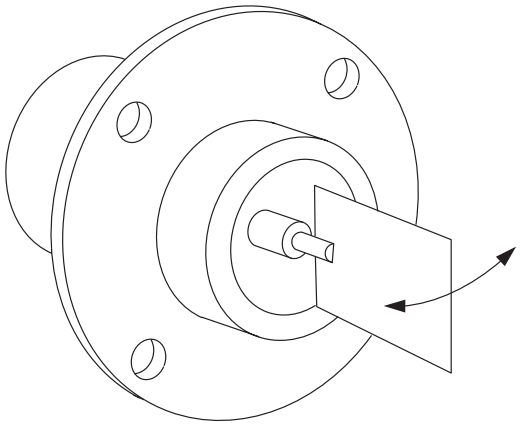


FIGURE 6.4.3 Swing level switch.

spring and two microswitches. If the blade is blocked by particles, the motor housing rotates in the opposite direction and activates a microswitch. The motor then stops, and generates an electrical signal indicating the powder level.

Rotating blade level switches are widely used because of their simplicity. The blade can, however, be broken by a solid powder blockage. If the blade is buried in powder flow, it can be forced to rotate, resulting in an erroneous signal.

Swing Level Switches

Figure 6.4.3 shows a swing level switch. Motor rotation and mechanical connectors swing a blade from side to side. Leaf springs connect the blade shaft and the motor. Mechanical parts are isolated from particles by a diaphragm. If the blade is blocked by particles, the leaf springs bend, and the motor, rather than the blade, is moved along a guide. The motor then activates a microswitch, as in the piston level and the rotating level switches. If the blade is released from the particles, the motor is returned by spring action to its original position.

The blade is set vertically in a storage vessel. Therefore, the drag force caused by powder flow is not as large as in the case of the rotating blade level switches, and the aforementioned erroneous signal, caused by powder flow, can be avoided in swing level switches.

Diaphragm Level Switches

Diaphragm-type level switches have no motors. A diaphragm is connected to a microswitch or a mercury switch. When powder pressure acts on the level switch, the diaphragm deforms elastically and turns the switch on. When the powder level drops, the diaphragm returns to its original position, and the switch is turned off.

This type of level switch has no parts protruding into the storage vessels, as opposed to the level switches mentioned previously. Therefore, diaphragm level switches are not as prone to mechanical damage.

Level Switches Based on Vibration

A weak vibration of a rod or a tuning fork causes deformation of a piezoelectric crystal, which generates an electric output. This output is amplified and supplied to a second piezoelectric crystal as its input. This crystal is electrically excited and, finally, vibrates at its resonant frequency. The resonant frequency decreases when the rod or the tuning fork is constrained by particles, and the level of the powder is detected.

This type of level switch is not affected by the electrical properties of particles (although the vibration is electrically forced, the vibration itself is purely mechanical). The level of powder immersed in liquid can also be detected. However, adhesion of fine particles to the rod or the tuning fork causes the frequency to decrease, resulting in erroneous signals.

6.4.3 ELECTRICAL METHODS

Electric Capacitance Level Meters

Electric capacitance increases with an increase in particles between two electrodes. For continuous measurement of the powder level, a wire electrode is inserted vertically into a storage vessel. The counter electrode is the vessel itself.

Electric capacitance level switches, which have a rod- or bar-type electrode, are also available, and some have an earth electrode at their base. Level switches of this type have no moving parts, and can be easily adapted for high-pressure or high-temperature conditions. It is, however, necessary to adjust their sensitivity at the installation site, as their sensitivity is dependent on the shape of the storage vessel. The sensitivity is also dependent on the dielectric constant of the powder materials. Therefore, readjustment is necessary when the type of powder changes. Fine powder adhering to the electrodes can increase the electric capacitance, and cause erroneous signals.

Electric Resistance Level Meters

Constant voltage is applied between a rod electrode inserted in a storage vessel and the vessel wall. As the specific resistance of particles is lower than that of air, an electric current through the powder layer increases as the powder level increases. The current also depends on the shape of the vessel.

The specific resistance of the powder layer depends on the packing density, types of material, moisture content, and temperature. Therefore, the sensitivity is affected by these variables.

Microwave Level Meters

Microwave level meters can measure distances up to 20 m, with a resolution of 1 cm. When a microwave is transmitted toward a powder bed, part of the wave is reflected by the surface of the powder bed and detected by a sensor on the level meter. The received time of the returned microwave pulse is used to measure the powder level, based on the speed of light.

A single antenna is used for both transmission and detection of the wave. The microwave can pass through plastic, therefore, the powder level in a vessel covered by plastic can also be measured.

Microwave level meters need no mechanical contact with the powder, and are easily installed. Their sensitivity is less affected by suspended dust or water vapor than ultrasonic level meters.

6.4.4 ULTRASONIC WAVE LEVEL METERS

An ultrasonic wave is a sound wave with a frequency higher than 20 kHz, and ultrasonic level meters can measure up to 50 m, with 1–2% accuracy. When an ultrasonic wave is emitted from the level meter to a powder bed, part of the wave is reflected by the surface of the powder bed, and detected by a sensor on the level meter. The received time of a pulsed ultrasonic wave is used to measure the powder level, based on the speed of the wave in air, that is given by

$$u = 331 + 0.6T \tag{6.4.1}$$

where

u is the speed of sound (m/s)
T is the temperature of the air (°C).

Emission and detection of the wave are carried out by a single element, such as a piezoelectric vibrator. The element is excited periodically by a pulsed electric power supply. The surrounding air then vibrates, and an ultrasonic pulse wave is generated. The wave reflected by the powder bed surface is detected by the same element and is transformed into an electric signal.

Ultrasonic level meters require no mechanical contact with the powder, and are easily installed. Their sensitivity is, however, affected by suspended dust or water vapor in storage vessels because of the sound attenuation.

6.4.5 RADIOMETRIC METHOD

Radiation from high-energy gamma-ray sources, such as cesium-137 or cobalt-60, can be used. In most cases, detectors are placed opposite the radiation source to detect a change in the intensity of the transmitted radiation.

A Geiger-type detector is typically used for simple on-off level switches. For continuous level measurements, more stable scintillation counters are preferable. Random decay of radioisotopes can cause short periodic fluctuations in output signals. Therefore, the output signals can be averaged over a certain period of time (that can be selected by varying the time constant of the detector) to avoid errors caused by the fluctuations.

A larger radioisotope source is usually required for larger or thicker-walled vessels. Special windows for sources and detectors, installed in the wall with dead space, will substantially reduce the source size. However, the alignment of the windows is critical. The use of these level meters in empty vessels must be carefully considered to ensure that the operating and maintenance personnel will not receive excessive radiation doses. Human tolerance for safe exposure is approximately 100 mrem/week. A reflectance level switch, instead of an ordinary transmission unit, should be considered for large-scale vessels.[2]

6.4.6 PNEUMATIC AND OTHER METHODS

Pneumatic Method

Pneumatic level switches use air (or gas) nozzles. Air is injected into storage vessels through a nozzle fitted into the side walls. The air flow rate is kept constant by a flow regulator. When the air jet is blocked by the powder bed, the back pressure in the nozzle increases, and is detected by a pressure transducer.

Air must be injected continuously, even if the level measurements are not required, as the nozzles can become blocked by particle intrusion. For adhesive particles, a cavity can form in the powder bed after the particles near the nozzle are blown off. Therefore, no increase in the back pressure is obtained, and the level switch fails to detect the powder bed.

Weighing Method

If the aim of the level measurements is to determine the powder content of a storage vessel, a weighing method is preferable. Load cells are applied to weighing level meters, as in the case of a hopper scale.[1] It should be noted that the weighing will be affected if air or gas flows through the vessel.

Numerical calculations must be carried out, based on the bulk density of powder and the geometrical shape of the vessel, in order to estimate the level of the powder bed when using the weighing method. Powder bridging or rat holing can also cause errors in the estimation.

Optical Method

A high-powered laser is used to obtain the surface profile of a powder bed in a storage vessel. The laser beam scans the surface of the powder bed, and the trajectory of the light on the surface is recorded by a highly sensitive camera, as shown

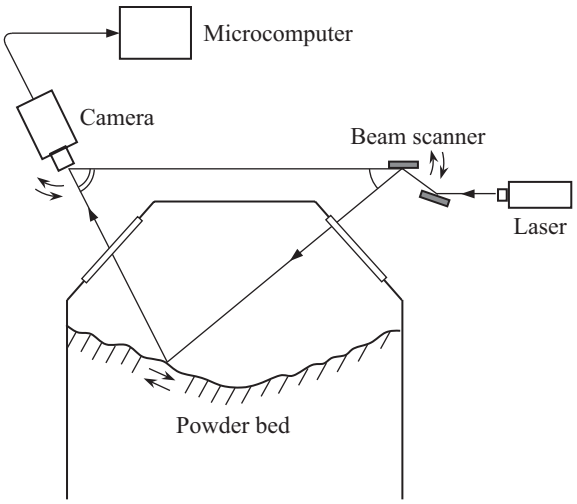


FIGURE 6.4.4 Laser level meter.

in Figure 6.4.4. A microcomputer analyzes the data obtained and determines the level using triangulation.

REFERENCES

1. Iinoya, K., Masuda, H., Watanabe, K., *Powder and Bulk Solids Handling Processes*, Marcel Dekker, New York, 1988, pp. 131–149.
2. Rowe S., Cook, Jr., H. L., *Chem. Eng.*, 76, 159–166, 1969.

6.5 Temperature Measurement of Powder

Koichi Nakaso and Kuniaki Gotoh

Temperature measurement of powder can be classified as either contact or non-contact types. Contact-type devices, such as thermocouples, measure the temperature in the powder bed, whereas those of non-contact type measure the temperature at the surface of the powder.

6.5.1 TEMPERATURE MEASUREMENT BY CONTACT-TYPE THERMOMETERS

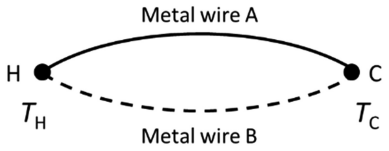
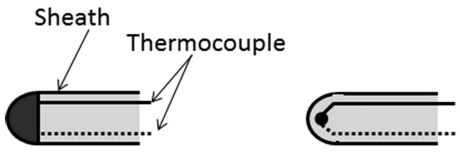
Typical Contact-Type Thermometers

Typical contact-type measurements are performed with thermocouples and thermistors (thermally sensitive resistors). The features of thermocouples and thermistors are summarized in Table 6.5.1. Schematics of typical thermocouples and thermistors are shown in Figure 6.5.1. The measuring portion of a thermocouple is a point, normally at the tip of the sensor. In contrast, the measuring portion of a thermistor has some volume.[1] This implies thermistors are not suitable to make measurements of small objects or narrow areas. Commonly, thermocouples and thermistors are enclosed in metallic sheaths (tubes). As a principle for measurements, the temperature of the measuring portion should reach the same temperature as that of the measured object. If the measurement portion is enclosed in a thick sheath, the time required to measure the temperature precisely increases.

Points of Measurement

As displayed in Figure 6.5.1, thermocouples and thermistors are generally enclosed in metallic sheaths. Because the thermal conductivity of this metallic sheath is generally higher than that of the powder bed, the thermometer does have a measurable influence on the temperature distribution of the measured

TABLE 6.5.1 Features of Typical Contact-Type Thermometers

Type of Thermometer	Thermocouple	Thermistor
Principle	Measures the electromotive force due to the difference between temperatures at two contact points in an electrical circuit composed of two different metal wires (Seebeck effect).  The contact point H (hot junction) is usually welded and used for measurements. Conversely, contact point C (the cold junction) is used for reference.	Converting a measured electrical resistance into the temperature using the temperature dependence of the resistance.
Characteristics	There are three types of the sheath-type thermocouples:  (a) Grounded type (b) Ungrounded type  (c) Exposed type • Response of measurements: Exposed > Grounded > Ungrounded • The ground type thermocouple cannot be used in potentially explosive atmospheres. • The exposed type easily breaks.	• High accuracy • Measurement errors due to Joule heating from the thermistor

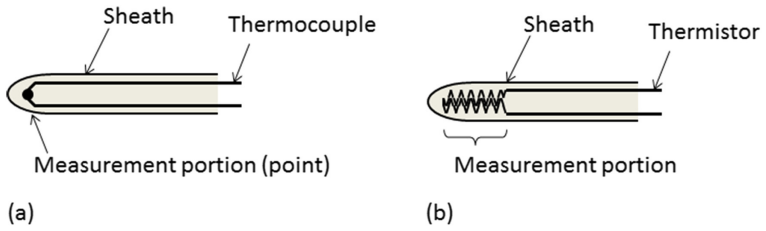


FIGURE 6.5.1 Typical contact-type thermometers. (a) Thermocouple and (b) Thermistor.

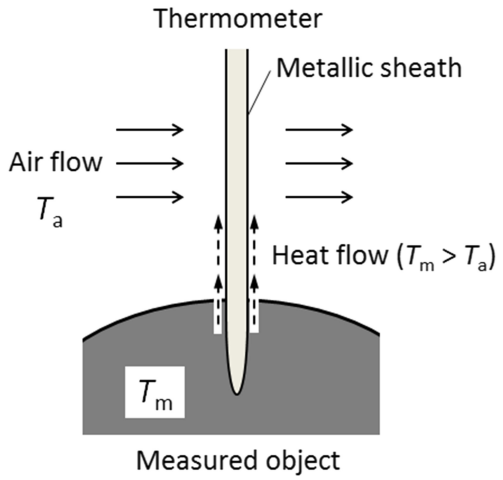


FIGURE 6.5.2 Typical measurement scenario using a contact-type thermometer.

object. A typical example of temperature measurement is shown in Figure 6.5.2. Here, the temperature of the powder is assumed to be higher than that of the ambient air. In this case, heat transfer occurs in the sheath of the sensor. Specifically, heat flows from the inside of the powder bed to the ambient air. When the depth of the thermometer (that is, length of thermometer sunk into the powder bed) is small and the exposed surface of the metallic sheath is large, the temperature around the measurement portion of the thermometer will be lower than the original temperature of the powder bed. This is defined as the "fin effect." Here, fins are typically used to increase the heat transfer rate by extending the heat transfer area. Common examples of this include the radiator in an automobile and the heat sink in a computer. The thermometer may unintentionally work like a fin.

The thermocouple may influence the temperature distribution of the measured object as shown in Figure 6.5.3(a) and (b). To reduce the fin effect, thermometers should be inserted along the isothermal line in the measured object, where the temperature distribution can be estimated by the insertion A in Figure 6.5.3(c). It is also acceptable to insert a portion of the thermometer, including the measuring portion, along this isothermal line as shown by the insertion B in Figure 6.5.3(c). In this case, careful attention should be paid to bending in the sheath thermometer.

Furthermore, the space around the thermometer should be reduced as much as possible to avoid the effect of natural convection heat transfer (Figure 6.5.4). Such convection may result in measurement errors. It should be noted that heat transfer will occur whenever there is a temperature difference.

6.5.2 TEMPERATURE MEASUREMENT BY NON-CONTACT-TYPE THERMOMETERS

Principles of Measurement

All atoms and molecules in an object undergo complex thermal motions unless their absolute temperatures are at zero. Electrons accompanying these atoms and molecules are therefore affected by thermal motion.[2] This results in the emission of thermal radiation energy from objects. The wavelength of thermal radiation energy ranges between 0.3 and 1000 μm. Visible light and infrared rays included within this range are defined as thermal radiation. This thermal radiation can be used for measurements with a non-contact thermometer.[1]

The principle of measurement is based on the thermal radiation of a black body. The intensity of the monochromatic thermal radiation from the black body at absolute temperature T per unit area and unit wavelength, $E_{b\lambda}$, is given by the following equation (Plank's law):

$$E_{b\lambda} = \frac{C_1}{\lambda^5[\exp(C_2/\lambda T) - 1]} \tag{6.5.1}$$

where

λ	is the wavelength of radiation energy
C_1 and C_2	are constants

Accordingly, the thermal radiation energy in the range of λ_1–λ_2 can be obtained by integrating this equation from λ_1 to λ_2. In a radiation thermometer, the temperature is determined by the thermal radiation energy measured by a detector.[3] Because the velocity of thermal radiation is high, the measurement response time of non-contact thermometers is faster than that of contact-type thermometers. The black body absorbs electromagnetic waves of any wavelength. It never reflects or transmits any electromagnetic waves. It should be noted that the black body is an ideal object, whereas practical objects do reflect and transmit some electromagnetic waves. Thus, the radiation ratio ε is defined by the ratio of the ideal overall thermal radiation energy based on a black body $E_b \left(= \int_0^\infty E_{b\lambda} d\lambda \right)$ to the practical one based on the practical object $E \left(= \int_0^\infty E_\lambda d\lambda \right)$.

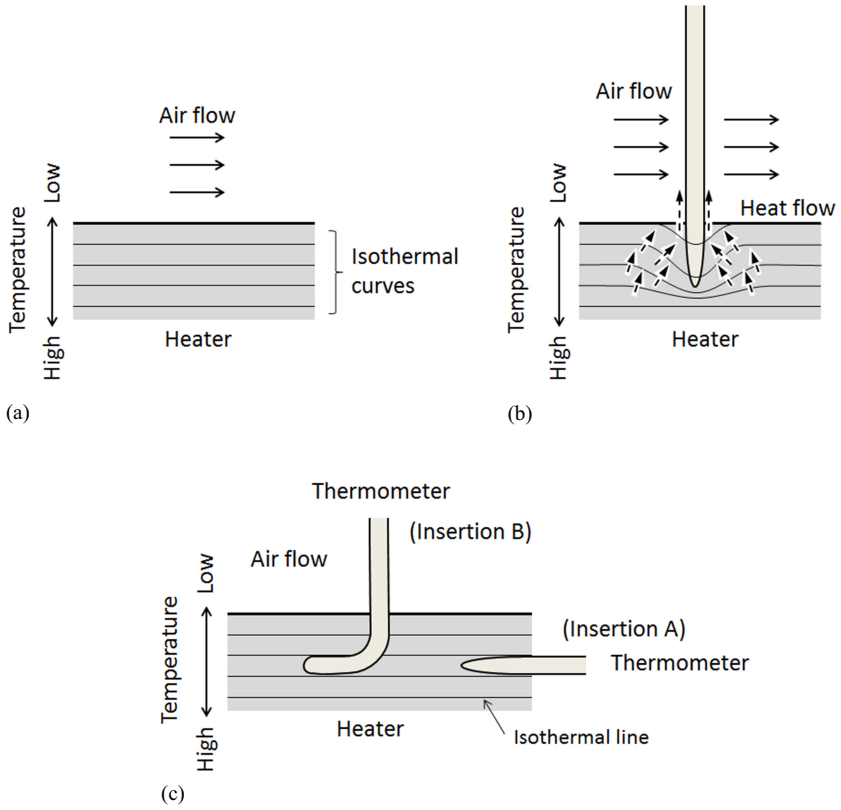


FIGURE 6.5.3 Effect of thermometer on temperature distribution of the measured object. (a) Original temperature distribution (before inserting a thermometer), (b) Temperature distribution afterinserting a thermometer, (c) Recommended methods for inserting a thermometer considering temperature distribution of the measured object.

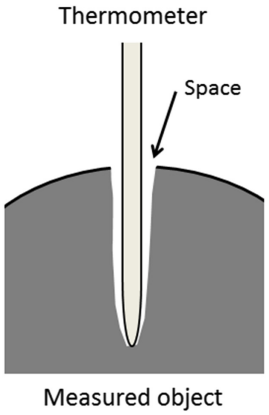


FIGURE 6.5.4 Measurement scenario for the error due to natural convection around the thermometer.

$$\varepsilon = E / E_b \qquad (6.5.2)$$

where $\varepsilon = 1$ for the black body and $\varepsilon = 0$~1 for practical objects. When the temperature is measured using a radiation thermometer, this ε-value should be clarified beforehand and be set as the correction parameter of the radiation thermometer. When the ε-value cannot be obtained from literature, it can be estimated by comparing the temperatures measured using contact-type and non-contact-type thermometers. In this process, temperature measurements must be carried out using both contact and non-contact-type thermometers. The temperature reading of the non-contact-type thermometer can be adjusted by changing the ε-value to reach the same values given by the contact-type thermometer.

Points of Measurement

A radiation thermometer will essentially measure the surface temperature of an object. Thus, it is difficult to measure the internal temperature of objects with this method. In the case of a powder bed, the surface temperature may show discrepancies with the internal temperature because the apparent thermal conductivity of the powder bed is lower than that of the bulk material. Thus, radiation thermometers are best suited to a small amount of powder or thinly layered powder bed. In addition, because the measurement response time is fast, radiation thermometers are suitable for measuring the temperature of particles in particle mixing and granulation processes, such as a pan-type granulator. Because the temperature can be measured without contact with the measured object, no contamination is introduced by temperature measurement. Furthermore, the thermometer does not influence the original temperature distribution or morphology (shape) of the measured object.

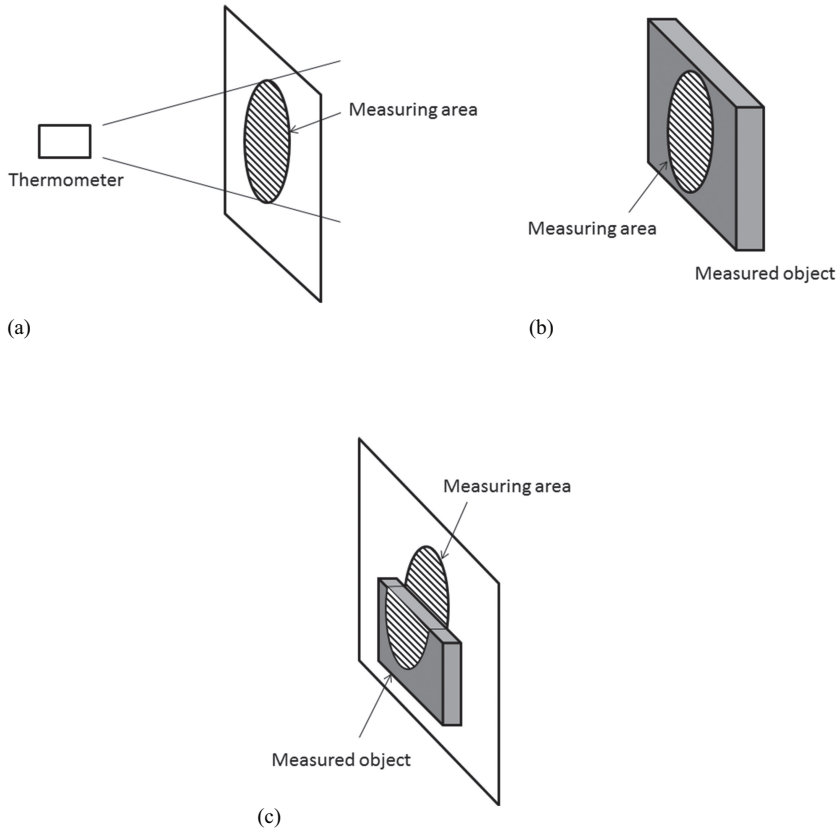


FIGURE 6.5.5 Relation between measuring area and measured object. (a) Measuring area, (b) Appropriate relation between measuring area and measured object, (c) Inappropriate case.

The measuring area for each thermometer is shown in Figure 6.5.5. The measured object should be larger than the measuring area. If this condition is not met, the temperature measurement will include other objects alongside the target object. This would result in measurement errors.[4]

Glass is opaque to infrared rays with wavelengths of above 2–3 μm. Thus, when the thermometer detects the infrared rays within these "opaque" wavelengths, the temperature measured by the thermometer through a glass window is incorrect. In such cases, the material of the window should be selected considering the transmission of infrared rays used for measurement.[4] This implies that thermometers should be selected considering the effect of glass on the transmission of infrared rays.

When the gases between the measured object and detector are H_2, O_2, N_2, and dry air, these gases can be regarded as transparent to thermal radiation. Such gases can be ignored. However, when CO_2, CO, water vapor, NH_3, and hydrocarbon gases are present, they may absorb and emit infrared rays with a wide range of wavelengths. In this case, their influence on temperature measurements should not be neglected. However, if the measured wavelength of the detector differs from the wavelength of the infrared rays absorbed by these gases, the effect of absorption by these gases on the measurement can be ignored. It is therefore essential to know the wavelength measured by the detector.[1]

In addition to reflection, absorption, and transmission, it should be noted that the effect of scattering is sometimes considerable for objects such as powder beds, porous media, particles, and droplets dispersed in gas or liquid phases. Thus, the effect of scattering on measurements must be determined beforehand.[3]

REFERENCES

1. Masanobu Hasatani Ed., *Handbook of Thermal Transport Measurements Technology*, Technosystem, Tokyo, 2011.
2. Shoji, M., *Heat Transfer Textbook*, University of Tokyo Press, Tokyo, 1995.
3. The Japan Society of Mechanical Engineering Ed., *Measurement Technology Series 8, Thermal Measurement Technology*, Asakura Publishing, Tokyo, 1986.
4. Horiba Ltd., *Catalogue of the Radiation Thermometers*, Horiba Ltd., Kyoto, 2014.

6.6 On-Line Measurement of Moisture Content

Satoru Watano

6.6.1 INTRODUCTION

Powder handling processes are mainly categorized into wet and dry processes.[1,2] Among the wet processes, wet agglomeration is well used in many industries to enlarge the original powder size in order to improve the flow and the dispersion/dissolution properties, reduce the dustiness, and to prevent the segregation. In the wet agglomeration, water is used as a binder to promote the adhesion between powders. Thus, the degree of wetting, which is referred to as moisture content, seriously affects the physical properties of the final agglomerates. In the wet coating and kneading processes, the moisture content is also a key parameter to control the properties of the final products. Even in the dry powder handling processes, the moisture content sometimes causes troubles. Generally, powder materials contain moisture to some extent as bound, occluded, adsorption and adhesive water (see Chapter 3.3). In particular, the moisture on the powder surface is very important in the dry powder handling processes. The surface moisture sometimes forms liquid bridge between powders, which causes caking and consolidation. The surface moisture with even a slight amount also changes the friction between powders, which affects the flow behavior. It also causes several problems such as the blocking in the hopper flow and the sticking of powders on the wall of vessel and the transportation pipe. In any cases, monitoring and control of moisture content are necessary in powder handling processes.

6.6.2 ELECTRIC METHODS

Table 6.6.1 lists moisture sensors and their measuring principles.

In powder handling processes, there exist no sensors which can measure moisture content directly. Therefore, moisture content is determined by using the correlation between indirect parameters (absorbance of spectrum, dielectric constant, etc.) and the moisture content that has been previously measured by a weight loss via a drying method.

So far, electrical, optical, radioactive rays and NMR (Nuclear Magnetic Resonance spectrometer) methods have been available for the continuous measurement of the moisture content in powder handling processes. Among them, electric and optical methods have been used in the practical industrial application.

In the following, electric and optical methods are briefly explained for measuring the moisture content of powder materials.

Figure 6.6.1 illustrates a schematic diagram of an electric-resistance-type moisture sensor.

The electric-resistance-type moisture sensor has two types of its construction; in the cell-type sensor, the moisture content is determined by measuring the change of electric resistance due to the increase or decrease of moisture. As seen in Figure 6.6.1(a), powder samples are packed between two electrodes and the apparent specific resistance R is determined by measuring the applied voltage V and the electric current I as

$$R = \frac{VS}{Id} \tag{6.6.1}$$

where S and d indicate the electrode surface area and the distance between two electrodes, respectively. The apparent specific resistance R varies with the moisture content W as

$$\log R = -a \log W + b \tag{6.6.2}$$

where a and b are the constants depending on the shape of electrode, the properties of the powder material and the circumstance conditions, such as humidity and temperature. By using Equation (6.6.2), the moisture content can be calculated. For the electric current, either the direct current (DC) or the alternating current (AC) of high frequency is used.

The needle-type moisture sensor uses the same measuring principle. In this type of sensor, two needle electrodes are penetrated into the powder bed and the electrical resistance between the electrodes is measured.

The electric-resistance-type moisture sensor is widely used, since the electric circuit and the measuring principle are simple, and the time required for the measurement is short. However, it has some demerits: (i) temperature correlation on the electric resistance is required since the electrode generates heat, (ii) the electric resistance is largely influenced by the packing condition, (iii) it cannot be used for a powder bed which moves during the measurement, because the movement affects the powder packing condition as well as the resistance and (iv) the measurement error may occur when the powder sample contains electrolytes.

Figure 6.6.2 shows the schematic illustrations of continuous and static types of dielectric-constant-type moisture sensors.

TABLE 6.6.1 Moisture Sensors and Their Measuring Principle

Methods		Principle of Measurement	Continuous Measurement	Detach/ Detach to Powder	Versatility	Range
Drying method	Normal drying Infrared heating High frequency Induction heating	Weight loss due to drying of wet samples	×	Contact	○	0.1~100%
Chemical method	Distillation method	Distillation and measure water volume	×	Contact	△	0.01~20%
	Karl Fischer (KF) titration method	Titration with KF reagent containing iodine, sulfur dioxide and pyridine in methanol. Infinitesimal moisture content can be determined.	×	Contact	△	0.001~100%
Electric method	Electric resistance method (DC)	Electric resistance change (direct current) due to moisture increase/decrease	○	Contact	△	3~50%
	High frequency	Electric current (high frequency) change due to moisture increase/decrease.	○	Contact	△	0.1~60%
	Dielectric constant (electrostatic capacity)	Electric constant change due to moisture increase/decrease.	○	Contact	△	2~25%
Optical method	Infrared	Absorbance of infrared–ray at absorption band (1.43, 1.94 μm)	○	Detach	○	1~90%
	Microwave	Attenuation of microwave due to water	○	Detach	○	1~90%
Nuclear Magnetic Resonance (NMR) Spectrometer		Dissolve in a solvent and its NMR is measured.	×	Contact	×	0.1~90%
Radioactive rays	Moderation/scattering Attenuation strength	Moderation/scattering of neutron/X-ray Attenuation strength	○	Detach	×	2~80%
Other method	Balanced relative humidity	Calculate moisture content by relative humidity, which is balanced with circumstances	○	Detach	△	1~80%

○: possible/good; ×: impossible/bad; △: not so good.

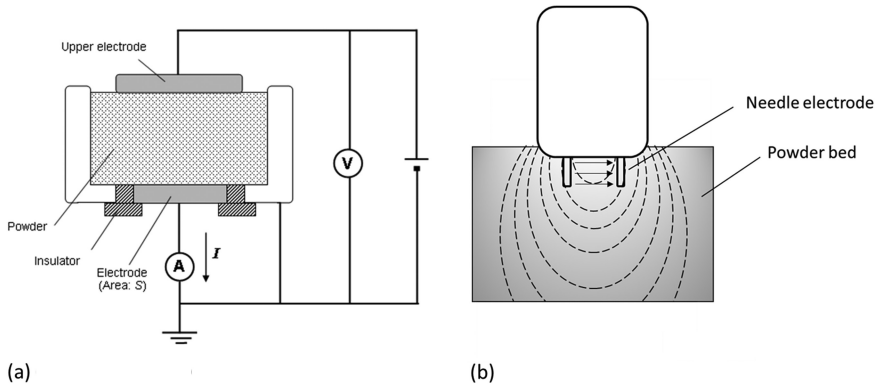


FIGURE 6.6.1 Schematic diagram of electric-resistance-type moisture sensor. (a) Cell Type, (b) Needle Type.

Assuming the simple and ideal structure, in which powder materials are filled inside between two electrodes or inside a cylindrical electrode. The apparent dielectric constant ε_a is obtained as,

$$\varepsilon_a = \varepsilon_0 \frac{C_1}{C_0} \tag{6.6.3}$$

where the electric capacity is C_1 and the one without any powder materials is C_0.

By using the apparent dielectric constant, the moisture content can be calculated, since the apparent dielectric constant ε_a shows approximately the linear relationship to the moisture content as

$$\varepsilon_a = j + kW \tag{6.6.4}$$

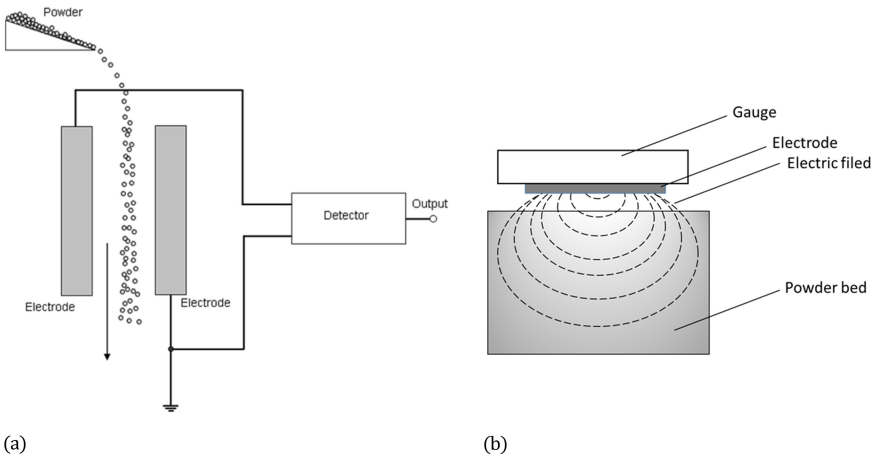


FIGURE 6.6.2 Schematic diagram of dielectric-constant-type moisture sensor. (a) Continuous Type, (b) Static Type.

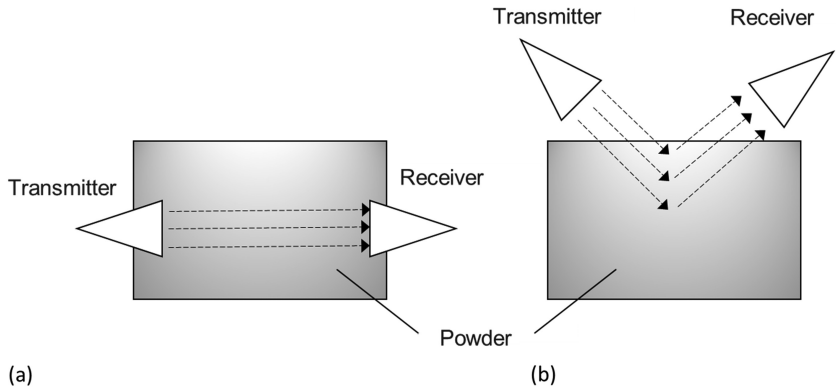


FIGURE 6.6.3 Principle of moisture measurement by microwave. (a) Transparent Type, (b) Reflection Type.

where j and k are the constants. These constants, which vary with powder properties, should be determined by the previous calibration. The dielectric-constant-type moisture sensor has merits that it receives less effect from the temperature and the packing condition than the electric-resistance-type moisture sensor. However, its circuit is complicated and it cannot measure the moisture content of powder materials which contain electrically-conductive materials, such as metal and coal powders.

6.6.3 OPTICAL MOISTURE SENSOR

The microwave and infrared (IR) are available to detect the moisture optically. The microwave moisture sensor is able to measure the moisture content continuously without touching the powder bed. This type of sensor has two measuring methods, the transparent and reflection types (Figure 6.6.3). Figure 6.6.4 indicates the absorbance characteristic of microwaves in the case of flour and cornstarch powders being used.

When the microwave transmits powder material which contains water, water absorbs the microwave and the microwave attenuates. Since the degree of attenuation has almost linear correlation to the moisture content as shown in Figure 6.6.4, the moisture content of powder materials can be determined. However, the microwave moisture sensor has some demerits: the system itself becomes complicated in order to avoid the leakage of microwave. In addition, the measured value may vary to some extent, depending on the leakage/refraction, powder surface condition and temperature.

In general, the optical sensor utilizes the principle that physical values (concentration, distance, etc.) are indirectly detected by using the absorbed/reflected energy of spectra when the spectra are radiated to the object. The so-called "spectra" are categorized into ultraviolet, optical and infrared rays depending on the wavelength, and each sensor uses specific wavelength, which is suitable for the characteristics of the measuring object.

Figure 6.6.5 shows the infrared (IR) absorption characteristics[3,4] in the case of using a powder sample of lactose and cornstarch mixture.

Water absorbs infrared spectra markedly at the wavelengths of 1.43, 1.94 and 3.0 μm, due to the resonance with the atomic vibration between oxygen and hydrogen in water molecule. Since the energy of the IR spectrum is absorbed remarkably at these wavelengths in proportion to the moisture content, the moisture content can be detected by measuring the difference between the irradiated energy and the reflected one. Since a simple method in which only the absorption

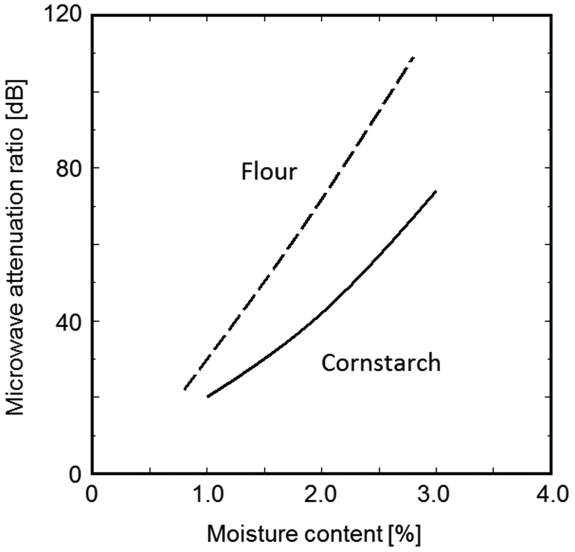


FIGURE 6.6.4 Microwave attenuation characteristics.

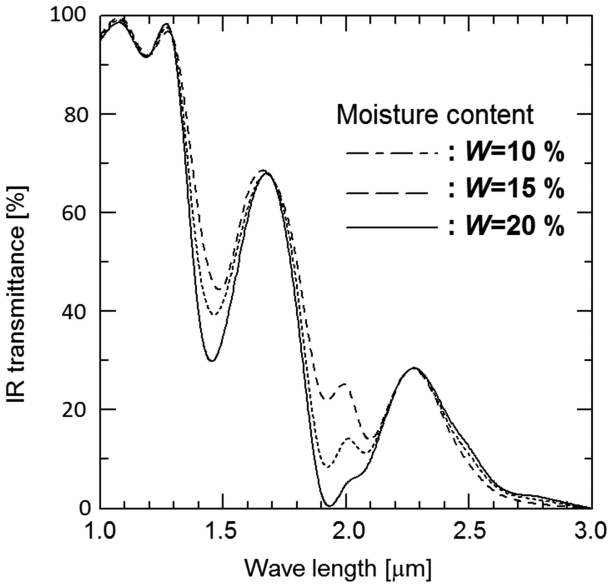


FIGURE 6.6.5 IR absorption characteristics.

spectrum is measured can be easily disturbed by the powder surface conditions and the fluctuation in the beam length, a reference method which calculates the reflected energy ratio of the absorbed spectrum (1.94 μm) and of the bilateral unabsorbed spectrum (reference spectrum of 1.78 and 2.14 μm) has been adopted. This cancels out any disturbance, since the disturbance affects the absorbed and unabsorbed spectra equally.

Details of the IR moisture sensor are illustrated in Figure 6.6.6.

The continuous light from the source is condensed by a condenser, then changed to a chopper beam by passing through a rotating sector with four optical filters composed of the different selective spectra of 1.94 μm for the absorption, the bilateral 1.78 and 2.14 μm for the unabsorbed references

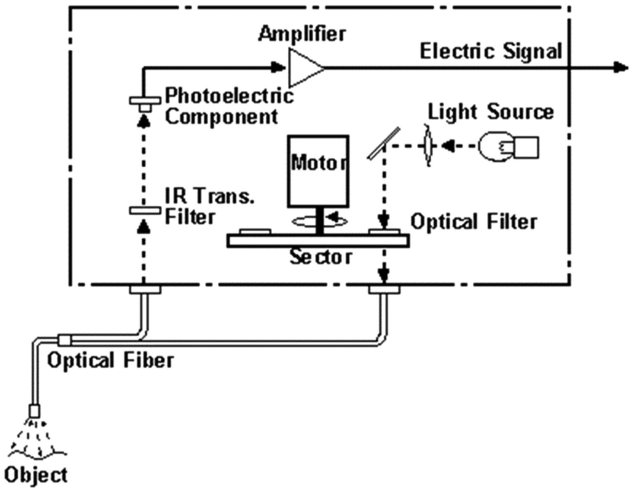


FIGURE 6.6.6 Principle of moisture measurement by IR sensor.

and a visible spectrum. When the spectra are irradiated to the object, the absorption spectrum is absorbed in proportion to the moisture content of the object, while the reference spectra are fully reflected.[4] These spectra are transformed to the electric signals, and the degree of absorptivity, defined as the ratio of absorbed energy to the supplied one of the spectrum, is calculated. Based on the degree of absorptivity, the absorbance X, which is the output from the moisture sensor, is calculated by using the following equation.

$$X = k_0 \cdot \ln\left\{\frac{\left(k_2 \cdot V_2 + V_3\right)/2}{k_1 \cdot V_1}\right\} \tag{6.6.5}$$

where, V_1, V_2 and V_3 show the absorptivities at 1.94, 1.78 and 2.14 μm of the IR spectra after temperature compensation, and k_0, k_1 and k_2 indicate the calibration coefficients, respectively.

Although the infrared moisture sensor is able to measure the moisture content continuously without touching the object and is not influenced by the powder density and the packing condition very much, it measures the moisture content on the surface or just beneath the surface of the objective powder material due to the long wavelength. If there is water distribution between the surface and inside the objective powder material, the relationship between the sensor output (surface moisture content detected by the IR sensor) and the total moisture content measured by a drying method must be determined before measuring the moisture content. This relationship is referred to as the IR absorption characteristics.

Figure 6.6.7 indicates the IR absorption characteristics of organic and inorganic powders; the left side is the IR absorption characteristics when the lactose and cornstarch mixing ratio is varied[3] and the right side is the one measured under different kinds of ion ores.

As seen in Figure 6.6.7, the IR absorption characteristics are different depending on the powder materials.[3] It is because the powder physical properties such as water absorbing potential, powder surface conditions, the IR refraction characteristics and the moisture distribution are different.

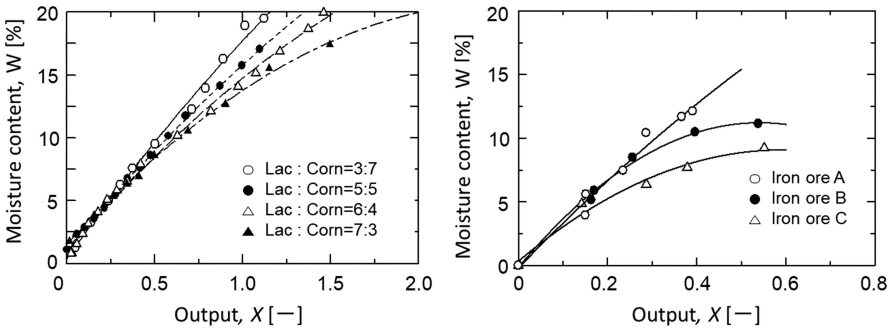


FIGURE 6.6.7 Relationship between moisture content and IR sensor output.

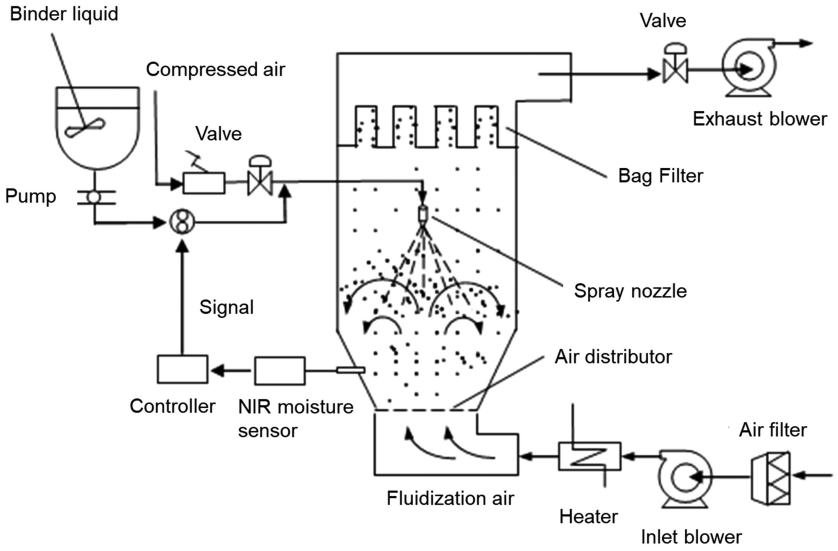


FIGURE 6.6.8 Moisture measurement by IR sensor and moisture feedback control system in fluidized bed granulation.

6.6.4 CONTINUOUS MONITORING AND CONTROL OF MOISTURE CONTENT

Wet granulation is one of the most sensitive operations to the moisture content. Wet granulation is defined as a size enlargement, which adhere/stick powders by using liquid binders to produce granules having the desired size, shape and density. The properties of the final product are influenced by the moisture content significantly.[5–7] Therefore, monitoring of moisture content and its control are required to produce desired product continuously with a high accuracy.

Figures 6.6.8 and 6.6.9 illustrate a system which measures and controls the moisture content by using an IR moisture sensor in a fluidized bed granulation.[4,8,9]

The IR sensor and fluidized bed vessel is connected by optical fibers and heated purge air is blown at the extremity of the sensor (the place where the optical fibers are connected to the vessel wall) to prevent the powder sticking. Based on the measured data, the feed speed of binder liquid is regulated to maintain the pre-determined moisture content value.

Figure 6.6.10 indicates relationship between granule mass median diameter and the moisture content when the pharmaceutical powder mixture composed of lactose, cornstarch and hydroxypropylcellulose (HPC) were granulated by a purified water (binder).[3]

Seen from Figure 6.6.10, the granule mass median diameter has a linear relationship to the moisture content, implying that granule growth can be controlled by measuring and controlling the moisture content.

In the Japanese pharmaceutical industry, automatic manufacturing of drug (granules) is commonly conducted by the fluidized bed granulation with the moisture control. However, the quality of the final products varied due to the atmospheric conditions changing (especially, humidity change), and this was quite a big issue previously, and the scientists and engineers spent much time calculating the binder spraying speed and fluidization air temperature in order to maintain the same dampening speed, since granule growth in the fluidized bed takes place under the balance between dampening by binder spray and drying from the fluidization air. The continuous moisture measurement and feedback control system proposed by Watano et al.,[3,8–10] settled this problem. Nowadays, these systems are commonly used in most of the Japanese pharmaceutical industry.

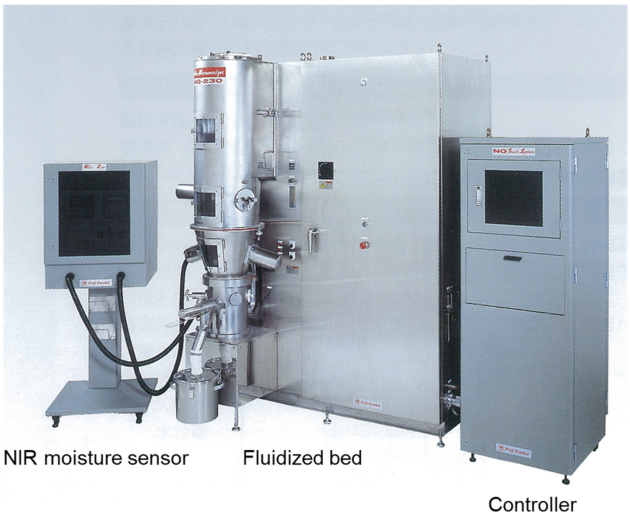


FIGURE 6.6.9 Picture of IR sensor installed to actual fluidized bed.

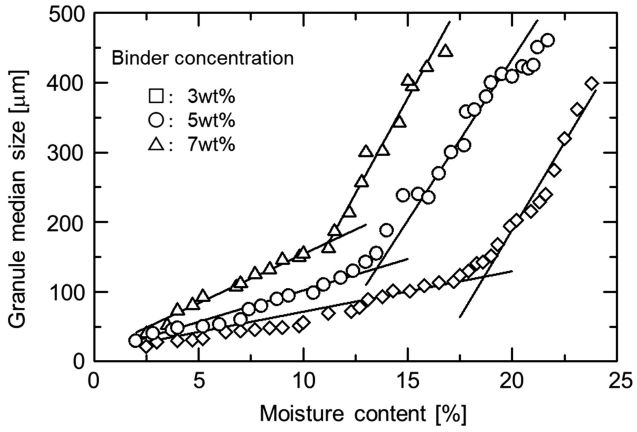


FIGURE 6.6.10 Relationship between granule median size and moisture content in fluidized bed granulation.

REFERENCES

1. Gotoh, K., Masuda, H., Higashitani, K., ed. *Powder Technology Handbook*, 2nd ed. New York, Marcel Dekker, 1997.
2. Society of Powder Technology Japan, ed. *Huntaikogaku Binran*, 2nd ed. Tokyo, The Nikkan Kogyo Shinbun, Ltd., 1998.
3. Watano, S., Takashima, H., Sato, Y., Miyanami, K., et al., *Adv. Powder Technol.*, 7, 279–289, 1996.
4. Watano, S., Sato, Y., Miyanami, K., *J. Chem. Eng. Japan*, 28, 282–287, 1995.
5. Watano, S., Morikawa, T., Miyanami, K., *J. Chem. Eng. Japan*, 28, 171–178, 1995.
6. Watano, S., Morikawa, T., Miyanami, K., *Chem. Pharm. Bull.*, 44, 409–415, 1995.
7. Schaefer, T., Worts, O., *Arch. Pharm. Chem. Sci.*, 6, 1–13, 1978.
8. Watano, S., Yamamoto, A. Miyanami, K., *Chem. Pharm. Bull.*, 42, 133–137, 1994.
9. Watano, S., Takashima, H., Miyanami, K., *J. Chem. Eng. Japan*, 30, 223–229, 1997.
10. Watano, S., Takashima, H., Miyanami, K., Murakami, T., et al., *Chem. Pharm. Bull.*, 42, 1302–1307, 1994.

6.7 Tomography

Richard A. Williams

The use of noninvasive tomographic sensors has become widely used as a laboratory, in-process and industrial scale control tool, since they allow direct observation of the behavior of powders, formulated products and particulate suspensions inside process equipment and pipes. They offer the possibility of acquiring measurements *in situ* enabling observation under process conditions. The methodology can be used for several purposes: product characterization and quality control (agglomerates, tablets, 3d-printed assemblies); process and flow auditing, control and fault detection; and in the development of advanced phenomenological models or to enable verification of complex dynamic computational simulations (e.g. hybrid fluid flow and discrete element models). A simple introduction to the main sensing methods is provided here and illustrated with selected application examples.

6.7.1 INTRODUCTION

Little is known about the behavior of particles during their passage through process equipment. To date, the lack of fundamental particle-scale data has hindered the development of reliable models. Tomographic measurements seek to address the widespread need for the direct analysis of the flow and state of particulate material and the internal characteristics of the process equipment. Such measurement information can also be deployed to assess the structural and even chemical characteristics of the particulate products themselves, from a quality control or audit perspective. Ideally, the measuring instruments for such applications should use robust, noninvasive sensors that can operate in the proximity of aggressive and fast-moving flowing powders and multiphase mixtures.

Tomographic technology typically involves the acquisition of measurement signals from sensors located on the periphery of a process vessel or the pipeline through which material is being transported. This reveals information about the nature and distribution of components within the sensing zone. Most tomographic techniques are concerned with abstracting information to form a cross-sectional image or a user-selected plane or sub-zone. This can, for example, utilize a parallel array of sensors so that their sensing field interrogates a projection of a suitable radiation across the subject. In order to explore the entire cross section, it is necessary to obtain other projections by rotating the subject in the direction normal to the direction of the sensor field or, preferably, to rotate the measurement sensors around the subject. It might not always be possible to adopt such a methodology because it might be impractical to physically rotate the subject, or the sensors, and the time required to rotate the assembly might take too long compared to changes occurring within the subject under investigation. 'Process Tomography' instruments have been devised to overcome these limitations.

The basic components of a simple process tomographic instruments are shown in Figure 6.7.1,[1] embodied in hardware (sensors, signal/data control) and software (signal

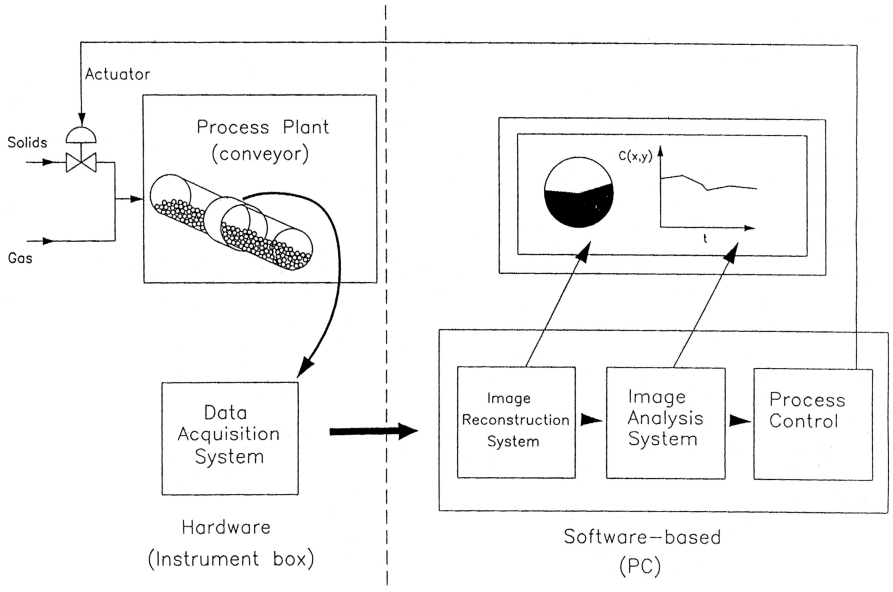


FIGURE 6.7.1 Components of a process tomographic sensing system, showing here an electrical capacitance tomography (ECT) system controlling a pneumatic conveyer.

TABLE 6.7.1 Basic Examples of Sensors for Process Tomography

Principle	Typical Spatial Resolution (Percentage of Diameter of Cross Section)	Practical Realization	Comment
Electromagnetic radiation	1	Optical	Fast, optical access required
		X-ray and gamma ray	Slow, radiation containment
		Positron emission	Labelled particle, not on-line
		Magnetic resonance	Fast, expensive for large vessels
Acoustic	3	Ultrasonic	Sonic speed limitation complex to use
Measurement of electrical properties	10	Capacitive, conductive, inductive	Fast, low cost, suitable for small or large vessels

reconstruction, display and interpretation facilities, generation of output control signals to process hardware). In this figure sensors are mounted around the exterior of the (non-metallic) pneumatic conveying pipe. Data are collected and processed to yield a reconstructed image of the profile of the particulate bed at a given instant of time. The image can be analyzed, for instance, to provide measurements of the local solid concentration $C(x,y)$ at any desired point. The procedure can be repeated by acquiring additional frames with time.

It is, however, necessary to emphasize that obtaining a good-quality computed 'image' property map may only represent the first stage of information input for the powder technologist. Sometimes an image is not even required since measurement data can be fitted directly to a model of the process, as first demonstrated for the flow and particle concentration profiles in a hydrocyclone separator.[2] The ultimate goal is quantitative (numerical) interpretation of an image or, more likely, many hundreds of data sets and/or images corresponding to different spatial and temporal conditions. In most circumstances, a visual diagnosis based on glancing at the images will be insufficient, except perhaps to diagnose gross malfunction occurring in a process. Therefore, in this respect there is a major and fundamental difference between the general philosophy of medical tomography and that of process tomography. However, as in medicine, process tomography can also involve different types of sensing methods (or modalities) and data information can be fused to form different detailed analyses of system properties of enhanced visual imagery. Using digital technologies augmented reality simulations can be created fusing real-time imaging and real-time multi-scale computation, such as in fluidized beds. Outside the medical sector, tomographic methods in science and engineering have has been developed such that modern texts[3] and international congresses on process tomography[4] occur at regular intervals, providing useful opportunities to assess the latest sensors and deployments in particle technology.

6.7.2 SENSOR SELECTION AND SPECIFICATION

The heart of any tomographic technique is the sensor system that is deployed. The basis of any measurement is to *exploit differences in the properties of the process being examined*. A variety of sensing methods can be employed based on measurements of transmission, diffraction or electrical phenomena. Table 6.7.1 shows a selection of the most widely used sensing methods and their principal attributes.

Whereas most devices employ a single type of sensor, there are a number of opportunities for multimode systems using two (or more) different sensing principles. The choice of sensing system will be determined largely by the following:

- The nature of components contained in the pipeline, vessel, reactor or material being examined (principally whether they exist as a solid, liquid, gas or a multiphase mixture, and if so in what proportions).
- The information sought from the process (steady state, dynamic, resolution and sensitivity required) and its intended purpose (laboratory investigation, optimization of existing equipment, process monitoring or control).
- The process environment (ambient operation conditions, safety implications, ease of maintenance, etc.).
- The size of the process equipment and the length scale of the process phenomena being investigated.

High-resolution in-process tomography can be expensive, rather slow, and, in some cases, impose special requirements for safe operation. Nevertheless, such methods can be extremely valuable for detailed laboratory studies.[5] High energy tomographic systems using synchrotron radiation (this requiring highly specialist facilities) can yield very detailed kinetic material chemistry and structural information such as crystal size, position and polymorph mapping.[6] In contrast the easier deployment of bench scale X-ray micro-tomography equipment has made it more commonplace and is used routinely for 3D analysis of material samples and flow tests, described later.

For the particular case of electrical tomography, considered later, the spatial resolution is determined by the nature of the measurement and associated reconstruction method. Imaging frequency (frame rates) from a few up to several hundred frames per second are attainable. Frame rates exceeding 10,000 Hz have been demonstrated.[3] The use of more than

one plane of image sensors, or a sensor array, offers the possibility of three-dimensional imaging. This has led to the adoption of voxel–voxel correlation methods from which velocity information can now be routinely deduced. Related methods such as electrical resistance tomography can be used to image solid concentration profiles in aqueous slurries (e.g. in mixers, separators, etc.) and emulsion reactors.[7,8]

6.7.3 EXAMPLES OF POWDER AND SLURRY PROCESSING APPLICATIONS

Pneumatic Conveying

The transport of dry and damp minerals via hoppers and in conveying lines is of importance, as plant operability is often poor due to the pluggage of conveying lines due to subtle changes in the feedstock (e.g. moisture content, size distribution, particle shape). Electrical capacitance tomography (ECT) can be used to image the dielectric constant inside conveying lines for dilute- and dense-phase processes, and has been in routine laboratory use since about 1999.[9,10] Analyses of the changes in the image with time can be used to identify the prevailing flow regime. For instance, Figure 6.7.2 shows a real-time visualization of powder flow for two conditions in dense phase conveying, from which characteristics such as slug length and velocity can be computed and statistical analysis of void age fluctuation data (Figure 6.7.3).

These methods have been used in a variety of conveying systems and for on-line control.[11–13] For example, in early work on coal conveying estimation of mass flow rate was demonstrated using a simplified fuzzy logic approach, in which each membership function was adapted by means of a genetic algorithm. In this way, the control function did not drift from the ideal due to plant wear or changes in the nature of the transported materials. The genetic algorithm was used to minimize energy consumption.

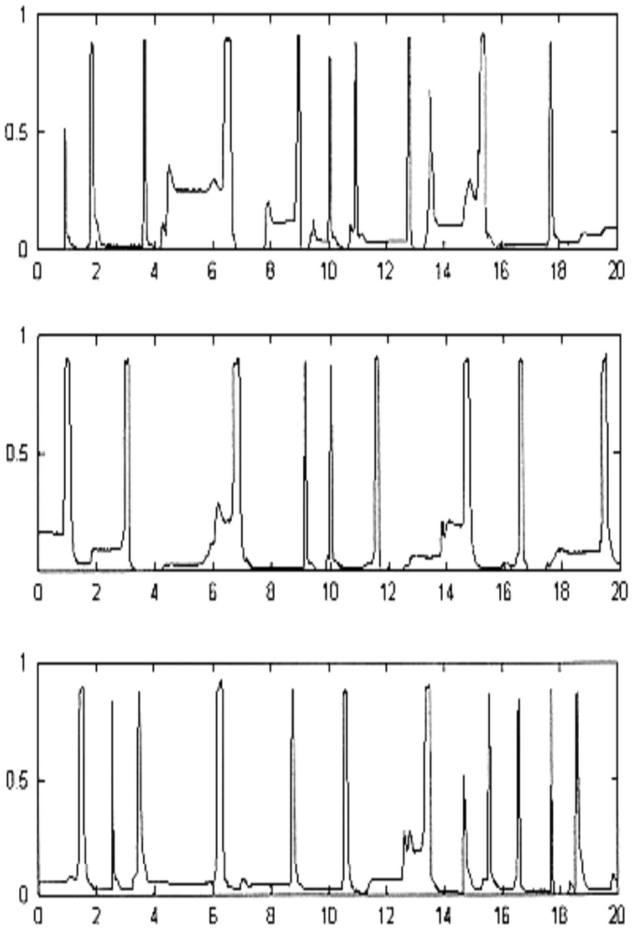


FIGURE 6.7.3 Examples on measurements of fluctuations of the relative volume fraction of solids across at a single plane during dense phase conveying (slugging) with time, for three different dense-phase flows. (From Ostrowski, K. L., Luke, S. P., Bennett, M. A., Williams, R. A., Chem. Eng. J., 3524, 1, 1999. With permission.)[10]

Fluidized Beds

An obvious extension of the measurements described above is the use of ECT to follow the complex dynamic interactions between gas and solids in fluidized bed reactors, dryers and risers.[1,3,5] Figure 6.7.4 shows experimental measurements of the solid volume fraction at the base of a 150 mm diameter bed adjacent to the distributor plate.[14] Images can be acquired for different flow regimes, determined by the superficial gas velocity (u). Detailed time transients can be obtained which allow the bubble size and transit velocity to be estimated. ECT enables the dynamic characteristics of the bed to be assessed and then analyzed, using chaos theory approaches or other statistical methods. The correlation fluctuations in time and space can be deduced either within a plane and between multiple planes spaced up the fluidized bed. These have found widespread application, as reviewed above for a variety of fluidized beds.[3]



FIGURE 6.7.2 Real-time visualization of granular flows in pneumatic conveying using electrical capacitance tomography. (From Ostrowski, K. L., Luke, S. P., Bennett, M. A., Williams, R. A., Powder Technol., 102, 1, 1999. With permission.)[9]

Powder Mixing

For laboratory mixing and scale-up studies, it is possible to label a particle with a positron-emitting tracer and to follow the trajectory of an individual particle in three dimensions using a positron-emission tomography camera.[3,15] The method of positron-emission particle tracking (PEPT) relies on detecting the pairs of back-to-back gamma rays produced by the annihilation of positrons, emitted from a radioactive tracer, with electrons. Typically, the volume that can be probed is

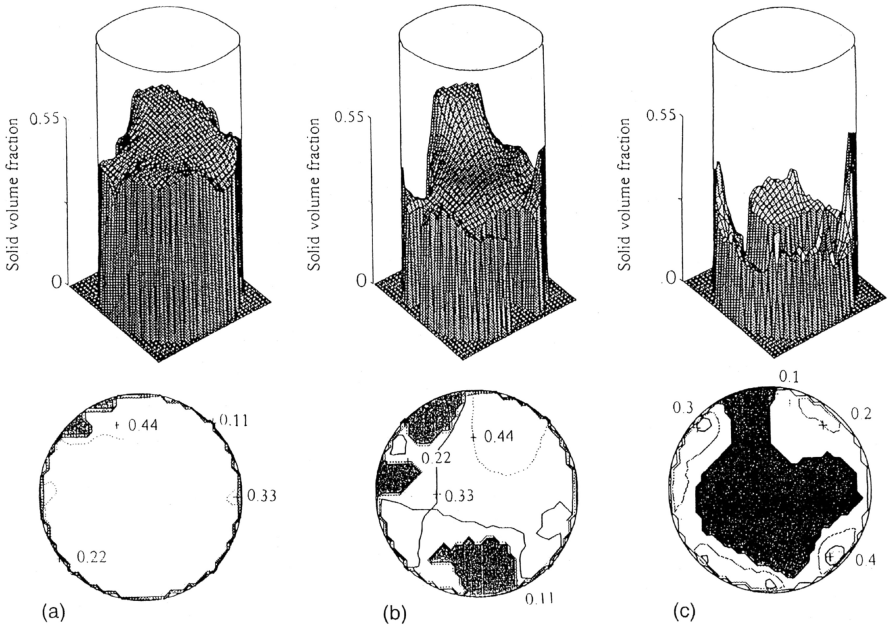


FIGURE 6.7.4 Isometric solid volume fraction plots (upper) and corresponding concentration maps (lower) obtained using real-time ECT in the vicinity of the distributor of a silica–gas fluidized bed for three flow regimes: (a) bubbling fluidization, (b) slugging regime and (c) in the transitional regime from the slugging to turbulent regime.[14]

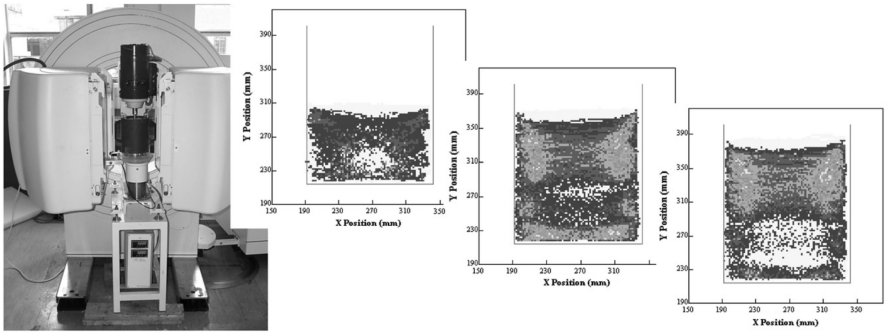


FIGURE 6.7.5 PET studies of a laboratory stirred bead mill (left) showing bead distribution and occupancy changes on increasing stirring speed (200, 600, 800 rpm).[17]

up to $500 \times 500 \times 250\,mm^3$ with a voxel resolution of better than $0.5 \times 1.5 \times 1.5\,mm^3$.[16] Figure 6.7.5 shows a sample result of a two-dimensional slice through a laboratory bead mill), from which detailed information of bead velocities and slip effects can be deduced.[17] Similar methods were also used to follow the size-dependent segregation of particles in a dense suspension; particle motion in granulators, extruders, dryers, conveyors and so forth and for validation of Distinct Element Modeling (DEM) predictions.

Powder and Granule Structure

The use of bench-top X-ray microtomography systems is now commonplace, delivering spatial resolution down to a few microns for three-dimensional scanning of small samples (a few mm^3) over a few hours.[7] These methods can provide detailed information on granule microstructure and packing of assemblies such as granules,[18] as shown in Figure 6.7.6, and structural modifications such as dissolution,[19] drying and for flocculated systems and filter cakes[20,21] and geological materials.[22] The method linked to 3D-visualisaion theatres or personal ocular systems is now common in materials design and specialized areas of additive manufacturing.

Industrial Scale Slurry Hydrotransport Metering

Electrical resistance methods have found industrial application in replacing conventional nucleonic gauges in slurry hydrotransport such as in dredging.[23] Here large diameter (>1 m) pipelines are equipped with highly wear resistant electrodes (Figure 6.7.7) and integrated into the pipe-line. The technique of using high speed data capture[24] has been further developed to estimate monitor slurry velocity and flux in commercial dredgers, as illustrated in (Figure 6.7.8). Such units each monitor the passage of some 50 million tons/annum.

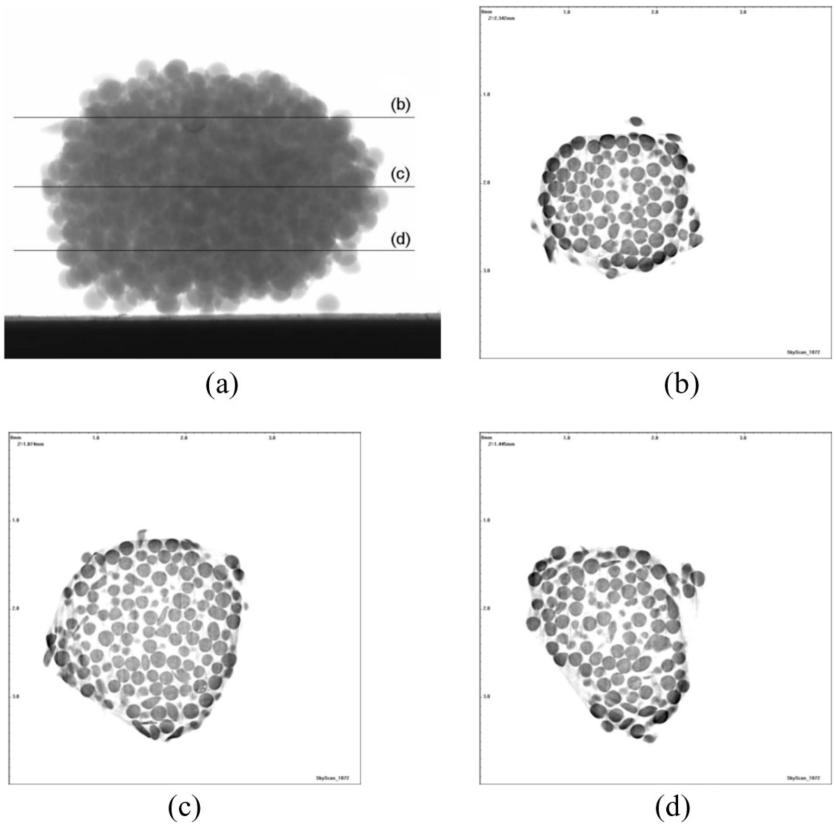


FIGURE 6.7.6 X-ray microtomograms of granules, showing (a) transmission image and (b–d) sections showing particle positions. (After Golchert, D. J., Moreno, R., Ghadiri, M., Litster, J., Williams, R. A., Adv. Powder Technol., 15, 447, 2005. With permission.)[18]

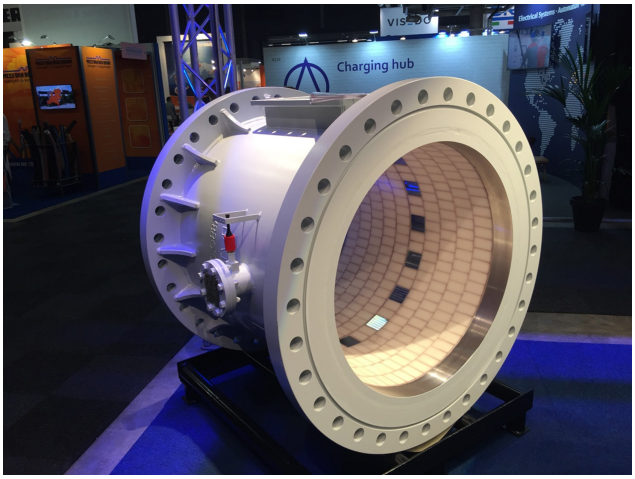


FIGURE 6.7.7 Industrial ceramic and conducting electrical tomography sensor for hydraulic monitoring, showing here 1.2 m diameter pipe section. (Industrial Tomography Systems plc, www.itoms.com. With permission.)



FIGURE 6.7.8 Deployment of industrial hydraulic conveying in commercial dredging, here monitoring solids abstraction rates of order 50 million tons/annum. (Industrial Tomography Systems plc, www.itoms.com. With permission.)[23]

In-Line Rheometry

Electrical resistance methods have been developed to be measure rheological properties of fluids in pipes (Figure 6.7.9).[25,26] Using cross-sectional pixel correlation the radial velocity



FIGURE 6.7.9 Electrical resistance rheometry computes viscosity characteristics from velocity data obtained at 12 locations across the radius from dynamic cross-correlations (from a thermal spike or using particulate fluctuations). The sensor shown is approximately 25 mm inside pipe diameter. (Industrial Tomography Systems plc., www.itoms.com. With permission.)

distribution can be computed and related to the point viscosity. This is perhaps the most advanced digital analytical method using ERT methodologies and it is likely to offer new paradigms in instrumentation for fluids and particulate mixture in the future in high throughput manufacturing and formulation applications.

REFERENCES

1. Williams, R. A., Beck, M. S., Eds., *Process Tomography–Principles, Techniques, and Applications*, Butterworth-Heinemann, Oxford, UK, p. 581, 1995.
2. West, R. M., Jia, X., Williams, R. A., *Chem. Eng. J.*, 77, 1–2, 31, 2000.
3. Wang, M., Ed., *Industrial Tomography: Systems and Application*, Woodhead Publishing, UK, 2015.
4. International Society of Industrial Process Tomography, Manchester, UK, www.isipt.org, 2018.
5. Scott, D. M., Williams, R. A., Eds., *Frontiers in Industrial Process Tomography*, AlChE/Engineering Foundation, New York, 1995.
6. Jacques, S. D. M., et al., *Cryst. Growth Des.*, 5, 395–397, 2005.
7. Williams, R. A., Jia, X., *Adv. Powder Technol.*, 14, 1–16, 2003.
8. Vilar, G., Williams, R. A., Wang, M., Tweedie, R. J., *Chem. Eng. J.*, 141, 58–66, 2008.
9. Ostrowski, K. L., Luke, S. P., Bennett, M. A., Williams, R. A., *Powder Technol.*, 102, 1–13, 1999.
10. Ostrowski, K. L., Luke, S. P., Bennett, M. A., Williams, R. A., *Chem. Eng. J.*, 77, 43–50, 2000.
11. Jaworski, A., Dyakowski, T., *Powder Technol.*, 125, 279–291, 2002.
12. Neuffer, D., et al., *Proc. 1st World Congress on Industrial Process Tomography (Buxton)*, Leeds/Manchester, p. 19, 1999.
13. Romanowski, A., Grudzien, K., Aykroyd, R. G., Williams, R. A., *Part. Part. Syst. Char.*, 23, 3–4, 2006, and 289–296, 2006.
14. Wang, S. J., et al., *Chem. Eng. J.*, 56, 95, 1995.
15. Parker, D. J., et al., *Nucl. Instrum. Methods*, A348, 583, 1994.
16. Parker, D. J., et al., *Nucl. Inst. Meth. Phy. Res. A*, 477, 540, 2002.
17. Conway-Baker, J., et al., *Miner. Eng.*, 15, 53, 2002.
18. Golchert, D. J., et al., *Adv. Powder Technol.*, 15, 447, 2004.
19. Jia, X., Williams, R. A., *Dissol. Technol.*, 13, 2, 11–19, 2006.
20. Selomulya, C., Tran, T. M., Williams, R. A., Amal, R., *AIChE J.*, 52, 10, 3394–3400, 2006.
21. Moreno-Atanasio, R., Williams, R. A., Jia, X., *Particuology*, 8, 81–99, 2010.
22. Menon, M., et al., *J. Hydrol.*, 397, 47–54, 2011.
23. McCormack, D., Primrose, K., Qiu, C., Wei, K., *Proc. World Congress on Dredging (WODCON)*, p. 12, 2016.
24. Wang, M., Wang, Q., Karki, B., *Phil. Trans. R. Soc.* A374, 20150329, 2016.
25. Machin, T. D., *Eng D. Thesis*, University of Birmingham, 2019.
26. Industrial Tomography Systems plc, Manchester, UK, www.itoms.com, 2018.

Part 7

Working Atmospheres-Risks, Hazards and Protection



Taylor & Francis
Taylor & Francis Group
http://taylorandfrancis.com

7.1 Health Effects Due to Particle Matter

Yasuo Morimoto and Toshihiko Myojo

7.1.1 INTRODUCTION

There are many kinds of dusts and other airborne particles in the total environment in which humans work and live. They vary from time to time in number and chemical and physical properties. In the work environment, the health hazards resulting from the exposure to them is of particular importance because they are a common feature and their biological effects are often insidious. In order to prevent or minimize impairment of the health of workers, it is essential to know the concentrations and diameters of harmful substances, their chemical and physical characteristics, and their biological actions. We must be aware not only of the biological effects but also of the mechanisms underlying and controlling their occurrence.

This chapter discusses principles relating to the lung response to exposure to particulate matter in the work environment.

7.1.2 RESPIRATORY SYSTEM

The primary purpose of the respiratory organ is to act as a gas exchange mechanism. Figure 7.1.1 shows a schematic anatomy of the lung. Air inspired through the nose or the mouth enters the larynx and then the trachea, which is divided into two main bronchi. The bronchial tubes repeatedly divide and diminish in diameter with bifurcation, the smallest tubes being called bronchioles. The diameter of the main bronchi and terminal bronchioles are 1.2 cm and 0.5 mm, respectively. These dimensions and numbers have major implications with respect to deposition and clearance of particles entering the lung while entrained in respired air. Terminal bronchioles lead into the respiratory bronchioles and then into the respiratory space which is composed of a number of alveoli. A very thin layer of venous blood is circulated through the pulmonary capillaries, which are arranged in a network over the surface of approximately 300 million air-containing alveoli. The total effective gas exchange surface of the alveoli has been estimated at 100 m^2. The alveolar capillary wall separating the blood from the gas phase is on average 0.55 μm in thickness. During the passage of venous blood over the surface of this barrier, the rapid movement of oxygen from the air into the blood and of carbon dioxide out of the blood into the air phase is carried out by gas diffusion.

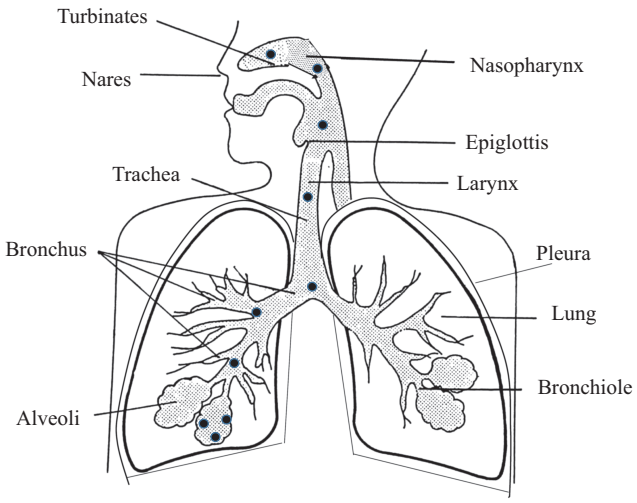


FIGURE 7.1.1 Schematic structure of the respiratory tract.

The trachea and the bronchial tubes are covered with ciliated cells on the epithelium. A carpet of mucus is continuously moved upward by ciliated action, where the mucus is then swallowed or expectorated. This system, known as the mucociliary escalator, is the mechanism whereby particles deposited on the airway surface are removed.

Beyond the terminal bronchioles the surface lining of the airways is no longer ciliated. Each alveolus is lined mainly by type I pneumocytes. Type II pneumocytes apparently secrete surfactant, a material that affects the surface tension of the ultrathin liquid layer on the epithelium. Alveolar macrophages, large free cells 10–50 μm in diameter, are located within the alveolar region. These are large mobile cells that are the principal phagocytic cell. They also are involved in immunologic reactions.

7.1.3 PENETRATION AND DEPOSITION OF PARTICLES IN THE RESPIRATORY TRACT

Particles penetrate into the human body through the respiratory system, causing a local effect on the lungs and other parts of the system and then passing into the blood stream and causing systemic effects. Very soluble substances are easily absorbed from all parts of the respiratory tract. Therefore, the site of deposition is of less importance for systemic effects. For insoluble particles, the site of deposition in the respiratory system is of fundamental importance. It depends on the aerodynamic properties of the particle, its shape, dimensions of the airways, and the pattern of breathing.

Particles vary markedly in shape and density, and both these factors play a role in the behavior of particles in the respiratory tract[1]. For our purposes we consider all particles as being spheres of unit density, with the understanding that there could be some variation between particles with respect to speed of settling, depending on their shape and density. This equivalent spherical diameter of unit density is called the aerodynamic diameter. The dynamics of inhaled particles

in the respiratory tract consider particles in terms of the aerodynamic diameter, to reach a reasonable agreement between theoretical predictions and experimental observations. When considering the deposition of particles, the respiratory system is divided into three regions:

1. Nasal–pharyngea1: This begins at the nose and goes to the level of the larynx or epiglottis.
2. Trancheobronchia1: This next region consists of the trachea and the bronchial tubes down to the terminal bronchioles.
3. Pulmonary: The third region is regarded as the gas exchange space of the lungs.

There are ranges of variability of deposition for a given aerodynamic diameter in each lung compartment. The particles are deposited in the lung by the following four mechanisms:

1. Sedimentation: The deposition is proportional to the particle speed of settling (proportional to aerodynamic diameter squared) and to the time for settling.
2. Internal impaction: The deposition is also proportional to the particle speed of settling and air velocity, especially where the flow line changes direction.
3. Brownian displacement: The deposition of small particles of less than 0.1 μm in size is governed by diffusional force.
4. Interception: The deposition is provided by the geometric dimensions of a particle following an air stream line.

7.1.4 RATE OF DEPOSITED PARTICLES

The rate of the particles deposited in the respiratory tract is dependent on their diameter and solubility and the site of their deposition, following the defense mechanism in the respiratory system for inhaled particles.

Nasal Filtration

Particles larger than 10–15 μm are mainly trapped in the nose by filtration by nasal hairs and in the throat and upper airways by impaction. Ciliated epithelium-covered mucus in the nose contributes to the removal of particles, which are then swallowed. These swallowed particles are significant when dealing with materials that cause systematic intoxication.

Mucociliary Clearance

The trachea and bronchi, down to the terminal bronchioles, are lined with a ciliated epithelium covered by a mucous layer. The cilia are in continuous and synchronized motion, which causes the mucous layer to have a continuous upward movement at a speed usually in the range of 10–30 mm/min. Particles deposited on the ciliated epithelium are moved toward the epiglottis by the mucociliary escalator, and then swallowed into the gastrointestinal tract or expectorated from the organism within a relatively short time.

Coughing and Sneezing

These reactions transport the particles toward the upper respiratory tract. Coughing and sneezing create strong currents of air, which help to clear the airways.

Phagocytosis

The epithelium of the pulmonary spaces is not ciliated. However, insoluble particles deposited in this region are engulfed by alveolar macrophage cells. The engulfed particles move up to the ciliated epithelium and then are removed upward by the mucociliary escalator and out of the respiratory system. They may also remain in the pulmonary space or enter the lymphatic system. Particles containing free crystalline silica are cytotoxic, that is, they destroy the alveolar macrophage cells.

Dissolution

The particles deposited in nonciliated airways are cleared by dissolution.

7.1.5 HEALTH EFFECTS OF INHALED PARTICLES[2]

Some particles cause various biological effects, as follows.

Pneumoconioses

In lung disorders caused by dust (Figure 7.1.2), phagocytosis of dust induces the infiltration of neutrophils and alveolar macrophages, and persistent or progressive inflammation is likely to cause lung injury and lead to irreversible changes, such as fibrosis. In this mechanism, alveolus macrophages englobe dust and produce chemokines such as cytokine induced neutrophil chemoattractant (CINC) and inflammatory cytokines, and inflammatory cells such as neutrophils and macrophages accumulate in the lungs through these chemokines. Persistent inflammation advances the pulmonary injury with free radicals, and finally leads to fibrosis, which is based on abnormal wound repair. There is a long interval known as the latent period between first exposure and development of the disease. Silicosis is the representative disorder among the pneumoconioses. Its risk is linked to the percentage of free crystalline silica of inhaled particles. The typical pathological changes are determined by the cytotoxic, inflammogenic, and fibrogenic capacity of the silica particles. Other pneumoconiosis may be produced by deposition in the distal airways and alveolar spaces of excessive amounts of, for example, asbestos, coal mine dust, beryllium, kaolin, barium, tin, iron oxide, talc, and graphite.

Systemic Poisoning

The inhaled particles migrate internal organs of the body after dissolution or small pieces of particles. Manganese, lead, cadmium, and the other heavy metals are examples of toxic systemic agents occurring in particulate form.

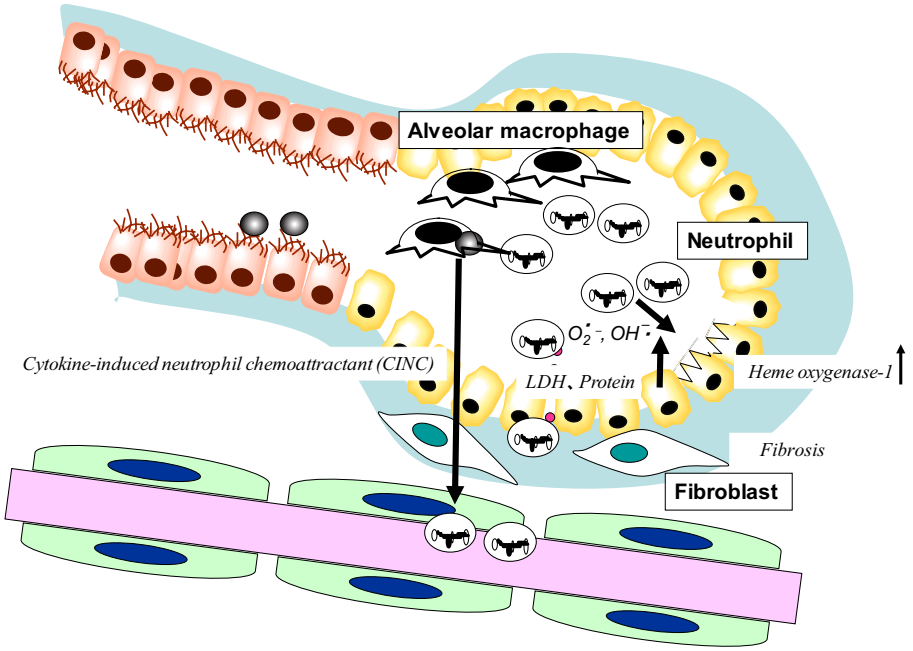


FIGURE 7.1.2 Tentative mechanism of lung disorder induced by dusts.

Cancer

Arsenic, chromate, policyclic aromatic hydrocarbons, nickel, radioactive particles, and asbestos have a carcinogenic potential leading to lung cancer and/or malignant mesothelioma. Soluble carcinogens may be a risk to both lungs and other organs.

Irritation

Exposure to irritant particles may lead to bronchitis, pneumonitis, and pulmonary edema. There are many irritant particles in the work environment, such as fumes of Cd, Be, V, and Zn, pesticides, acid mists, and fluorides.

Allergic Reactions

The deposition and retention of inhaled sensitizing substances may produce allergic reactions or other sensitivity responses. Synthetic organic compounds (amine compound, plastics), many vegetable dusts (bagasse, corn, cotton, flax, flour, straw, tea, tobacco, wood), and metal dusts (nickel, chromium) may produce inhalant allergy, asthma, hay fever, or urticaria.

Metal Fume Fever

This is a condition resulting from exposure to freshly generated metal fumes (zinc oxides, magnesium oxide). The main symptoms include chills, fever, muscle pains, nausea, and weakness. It is an acute condition, of brief duration, and with no after effects.

Infection

Particles containing fungi, viral, or bacterial pathogens may play a role in the transmission of infectious diseases.

7.1.6 THRESHOLD LIMIT VALUE

Regarding chemical substances present in inhaled air as suspensions of particles, the potential hazard depends on particle size as well as mass concentration. The threshold limit value (TLV) refers to the airborne concentration of particles and represents conditions under which it is believed that nearly all workers may be repeatedly exposed day after day without adverse health effects. The TLV is based on available information from industrial experience and from experimental human and animal studies. Health impairments include those that shorten life expectancy, compromise physiological function, impair the capability for resisting other toxic substances or disease processes, or adversely affect reproductive functions or developmental processes.

The size-selective TLV of particles has been recommended for crystalline silica for many years in recognition of the well-established association between silicosis and respirable mass concentration. The size-selective TLV of particles is usually divided into two types:

Inhalable Particles

These materials are hazardous when deposited anywhere in the respiratory tract. The aerodynamic diameter of the inhalable particles is less than 200 μm. The concentration of the inhalable particles is measured as the total dust by an air filter sampler with the inlet air speed of 0.5–0.8 m/s.

Respirable Particles

The materials are hazardous when deposited in the gas exchange region. The particle size having 50 % penetration for the respirable particle is 4 μm. The mass concentration of

TABLE 7.1.1 Occupational Exposure Limits for Dusts[3]

I Respirable crystalline silica: 0.03 mg/m³

II Other dusts

Class	Variety of Dusts	Occupational Exposure Limits (mg/m³)	
		Respirable Dust	Total Dust
Class 1	Activated charcoal, alumina, aluminum, bentonite, diatomite, graphite, kaolinite, pagodite, pyrites, pyrite cinder, talc	0.5	2
Class 2	Dust with less than 3% of crystalline silica, bakelite, carbon black, coal, cork dust, cotton dust, hide powder, iron oxide, grain dust, joss stick material dust, marble, portland cement, titanium dioxide, zinc oxide	1	4
Class 3	Limestone, inorganic and organic dusts other than classes l and 2*	2	8
Asbestos		**Excess lifetime cancer risk**	**Value**
Chrysotile		10^{-3}	0.15 fiber/cc
		10^{-4}	0.015 fiber/cc
Asbestos without chrysotile		10^{-3}	0.03 fiber/cc
		10^{-4}	0.003 fiber/cc

* Exposure to materials with unknown toxicology may induce disorders in the body.

the respirable particles is measured by the air sampler with an elutriator or cyclone.

The Japan Society for Occupational Health has recommended TLVs for airborne particles in the work environment by using the occupational exposure limits as shown in Table 7.1.1[3]. The toxicity of all particles generated in the work environment cannot evaluated. For new particles developed and produced, the nature of the database associating exposure and disease is inconclusive. If a disease is observed in laboratory animals exposed to new particles, this would need to be viewed as a positive indicator of the potential health hazard for humans. Especially, inhalation animal studies are credible because of the similarity of human exposures. The health effects of airborne particles in the work environment should be investigated in order to prevent impairment.

REFERENCES

Task Group on Lung Dynamics, *Health Phys.*, 12, 173–207, 1966.

World Health Organization, *WHO Offset Publication, No. 80*, WHO, Geneva, 1984, p. 75.

Recommendation of Occupational Exposure Limits (2016–2017), *J. Occup. Health*, 58, 489–518, 2016.

7.2 Risks of Nanoparticles

Toshihiko Myojo (7.2.1–7.2.3)
Hidehiro Kamiya (7.2.4)

7.2.1 INTRODUCTION

"Nanomaterials" means materials of which a single unit is between 1 and 100 nm in size, in other words, nanoscale. According to ISO/TS 27687:2008, a single unit is called a *nano-object*, and is defined as a material with one, two or three external dimensions in the size range of nanoscale. Subcategories of the *nano-object* are *nanoplate*, *nanofiber* and *nanoparticle*, based on the nanoscale dimensions. This definition applies to intentionally produced nanomaterials as manufactured nanomaterials, it does not cover other nanoscale particles such as ambient particulate matter. Among the various nanomaterials, carbon black, fumed silica and titanium dioxide are currently mass-produced and used commonly, while the newer carbon nanomaterial fullerene and the fibrous nanomaterials single- and multi-walled carbon nanotubes (SWCNTs and MWCNTs, respectively) are becoming common, with applications and production expanding from the laboratory to industrial levels. Nanomaterials often have unique optical, electronic or mechanical properties, but in addition to offering the intended benefits, they may also have unforeseen environmental, health and social risks. Moreover, during the production and distribution of nanomaterials, laboratory researchers and factory workers may be exposed to nanoparticles before the product package is sealed. For these reasons, the risks of nanomaterials (*nano-risks*) should be elucidated before advancing into the next levels of research and development.

7.2.2 CONCEPT OF RISK ASSESSMENT AND MANAGEMENT OF NANOMATERIALS

The concept of risk assessment for the safety and hazards of assigned chemicals (around 660 species) was introduced into the Industrial Safety and Health Act of Japan. The Guidelines for the Assessment of Risks of Chemical Substances was promulgated in 2016 for the safety and health of workers handling such substances. The concept of risk assessment for the hazards of nanomaterials is shown in Figure 7.2.1. Generally speaking, the risk assessment of nanomaterials involves the search for physical and chemical characterization, potential hazards and the possibility of exposure. Conceptually, risk is a combination of hazard and exposure; that is, a substance with toxicity and a high possibility of exposure is categorized as high risk, whereas chemicals with low toxicity but a high possibility of exposure, or those with high toxicity but a low possibility of exposure, are categorized as medium risk. The scale of the possibility of exposure is the amount of consumption of a substance. By scoring these risks, it is possible to rank the risk of individual substances used in the workplace.

The nanomaterials mentioned above were not assigned as substances requiring risk assessment. The same concept of risk assessment as with chemicals substances could be adopted for nanomaterials, but it is desirable to develop a nanomaterial-specific method of assessment, such as exposure assessment and mitigation techniques. Information about the hazards and the physical and chemical properties of chemicals can be effectively obtained from the Material Safety Data Sheet (SDS), which classifies chemical hazards in accordance with the Globally Harmonized System of Classification and Labeling of Chemicals (GHS) established by the United Nation in 2003. The GHS, which has the purpose of preventing disasters and protecting health and the environment, provides the data of the SDS with pictograms to classify the risks and hazards of chemicals. Table 7.2.1 shows the hazardous part of carbon black in the SDS. As the table shows, hazards are classified into acute toxicity, sensitization, carcinogenicity and mutagenicity.

There is little information about the health hazards of newly developed nanomaterials such as MWCNTs. Titanium dioxides (TiO_2) are well-known as less toxic substances on the micron scale, but nano-scale products have more inflammatory responses. In the research project, "Research and development of nanoparticle characterization method (P06041)," funded by the New Energy and Industrial Technology Development Organization (NEDO), we studied the health hazard of new nanomaterials such as TiO_2, fullerenes, SWCNTs and MWCNTs. The occupational exposure limits

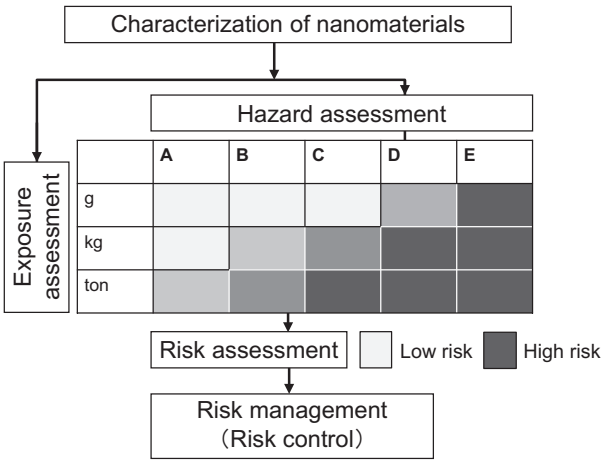


FIGURE 7.2.1 Concept of risk assessment for nanomaterials. In the column, g, kg or ton means handling quantity and A to E means hazard group of specific nanomaterial.

(OELs) proposed by the NEDO project are summarized in Table 7.2.1[1] The National Institute for Occupational Safety and Health in the United States recommended that two exposure limits for TiO_2 should be set as 0.3 mg/m^3 for <100 nm particles and 2.4 mg/m^3 for ≥100 nm particles.[2]

At present, the risk assessment of nanomaterials is not easy because of the lack of hazard information about specific nanomaterials and exposure assessment in the workplace. Even when there is no way to assess the risk of specific nanomaterials, some kind of risk mitigation should be established for workers. It may be useful to incorporate the concept of control banding, as described in the next section.

7.2.3 RISK MANAGEMENT USING CONTROL BANDING OF NANOMATERIALS

Every year, 500–1000 new chemicals are registered on the mandatory list of the already existing tens of thousands of chemicals in Japan, but occupational exposure limits or allowable control levels have yet to be determined for the majority of the chemicals on the list. The concept of control banding, a method to manage the risks of these chemicals, was first proposed by the Control of Substances Hazardous to Health (COSHH) of the United Kingdom to protect the employees of small and medium scale enterprises from exposure to chemicals. COSHH is a law that requires employers to control substances that are hazardous to health. The application of the control banding concept (COSHH essential) was promoted worldwide by the International Labour Organization (ILO).[3] The concept has also been applied to nanomaterials, and the ISO working group on nanomaterials[4] has begun to apply it.

As the word implies, "control bands" mean mitigation measures by engineering control techniques, such as general ventilation, local exhaust ventilation, and enclosure. Even though there are many chemical species used in worksites, there are not so many ways to mitigate the risk of chemicals, including nanomaterials. The process of selection of the mitigation measure based on the risk assessments is now called "control banding," and the process can be conducted with limited information about the target materials. We can evaluate a specific work process or work site by using the concept of control banding and, if necessary, we can improve the work process.

The first step in the process of control banding is to identify the hazard group of the target material(s) on the scale from A (safest) to E (most dangerous, such as carcinogenicity), using the material safety data sheets, which provide detailed information on the physical/chemical, toxicological and ecological properties, as shown in Table 7.2.3. The targeted OELs of the hazard groups are usually set for dusts as follows: A (1–10 mg/m^3), B (0.1–1 mg/m^3), C (0.01–0.1 mg/m^3), D (less than 0.01 mg/m^3) and E (consultation with experts). As applied to carbon black, shown in Table 7.2.1, the hazard group D is assigned by its carcinogenicity (2) and its specific target organ toxicity – repeated exposure (1). The OEL of carbon black recommended by the Japan Society for Occupational Health (2016).[5] however, is "less than 1 mg/m^3," and the hazard group D means a safer side decision than the existing OEL. Other OELs proposed by the NEDO project in Table 7.2.2 also suggest the hazard group C for CNT, but this will be reviewed in future.

The control banding recommended by the ILO classifies the exposure bands based on the combination of handling

TABLE 7.2.1 An Example of Hazard Part of Carbon Black in SDS

CAS: 1333-86-4
Substance Name: Carbon Black
ID: H27-B-047/C-083B_P
Detail (HP URL): http://www.safe.nite.go.jp/english/ghs/15-mhlw-0083e.html

Health Hazard Class	Hazard Category
Acute toxicity (oral)	Not classified
Acute toxicity (dermal)	Classification not possible
Acute toxicity (inhalation: gases)	Not applicable
Acute toxicity (inhalation: vapors)	Not applicable
Acute toxicity (inhalation: dusts and mists)	Classification not possible
Skin corrosion/irritation	Not classified
Serious eye damage/eye irritation	Not classified
Respiratory sensitization	Classification not possible
Skin sensitization	Classification not possible
Germ cell mutagenicity	Classification not possible
Carcinogenicity	Category 2
Reproductive toxicity	Classification not possible
Specific target organ toxicity – single exposure	Classification not possible
Specific target organ toxicity – repeated exposure	Category 1 (respiratory system)
Aspiration hazard	Classification not possible

TABLE 7.2.2 Period-Limited Occupational Exposure Limit[1]

Substance	OEL (mg/m^3)	Manufacturer (Product Name)	Particle Diameter
TiO_2	0.61	Evonik Degussa P25	Primary particle diameter 21 nm Aerosol diameter 1440 nm
C_{60}	0.39	Company F	96 nm
MWCNT	0.08	Company N	Tube diameter 44 nm Aerosol diameter 1250 nm
SWCNT	0.03	Company A	Tube diameter 2.8 nm
Common to CNT	0.03		

TABLE 7.2.3 Hazard Group by Aerosol Exposure

Hazard Group	GHS Hazard Class and Category
Group A	
Acute toxicity (lethality), any route	Class 5
Skin irritancy	Class 2 or 3
Eye irritancy	Class 2
Group B	
Acute toxicity (lethality), any route	Class 4
Acute toxicity (systemic), any route	Class 2
Group C	
Acute toxicity (lethality), any route	Class 3
Acute toxicity (systemic), any route	Class 1
Corrosivity	Subclass 1A, 1B or 1C
Eye irritancy	Class 1
Respiratory system irritancy	
Skin sensitization	
Repeated exposure toxicity, any route	Class 2
Group D	
Acute toxicity (lethality), any route	Class 1 or 2
Carcinogenicity	Class 2
Repeated exposure toxicity, any route	Class 1
Reproductive toxicity	Class 1 or 2
Group E	
Mutagenicity	Class 1 or 2
Carcinogenicity	Class 1
Respiratory sensitization	

quantity (g, kg or ton) and dustiness (pellets, granules or fine powders) for powder form materials. Nanomaterials should also be covered in that way. Then the control measure will be assigned by the hazard band and the exposure band of a specific nanomaterial and a specific work condition, as shown in Figure 7.2.1.

The hierarchy of control measures, a concept of risk management that is widely accepted in the societies of occupational safety and health, consists of an approach to risk reduction, and the elimination of the hazard of or exposure to nanomaterials. In this approach, one should try the following:

1. To eliminate the hazard
2. To substitute a less harmful agent for the hazardous material
3. To change the process
4. To apply engineering controls, such as isolation, local exhaust ventilation or dust suppression techniques
5. To consider administrative controls, such as worker education and training or scheduling
6. To use personal protective equipment (PPE), as a last resort

In the case of nanomaterials, it would be difficult to apply the control measure of elimination or substitution; therefore the first control measure – to change the process – should always be considered first. However, any combination of the above control measures, especially with the inclusion of PPE, will minimize the risk. The selection of respiratory protective devices (respirators) for the handling of nanomaterials should be based on the assigned protection factor (APF) and filter collection efficiencies described in Chapter 7.3. Respirators with an APF of more than 50 and filter collection efficacy of more than 95% are recommended for nanomaterial handling work. We conducted a systematic review on the effectiveness of specific risk mitigation techniques used in the production and handling of nanomaterials and found 41 papers out of 1,131 records in PubMed and other lists (2000–2015) fulfilled our inclusion criteria.[6] For enclosure systems we found a protection factor beyond 100. For other engineering controls, the better controls scored 10–20, but many cases of local exhaust ventilation had a protection factor of less than 10 and some cases even increased exposure. PPE such as N95 or equivalent filtering respirators had a protection factor of approximately 10 tested with nano-sized aerosols.

7.2.4 SPECIFIC RISK AND MEASUREMENT OF PM2.5

Recently, various papers and researches have been reported about PM2.5, which has a size smaller than 2.5 μm in aerodynamic diameter, invades into pulmonary alveoli in the lungs and cause various heart and lung diseases. An example of previous research investigated the effect of PM2.5 on human health, Dockery et al.[7] suggested that fine particle concentration was the most strongly associated with human health risk about average length of life, based on an association between air pollution and mortality in six U.S. cities. In the sixth selected city, the ratio of smoker was almost same as 33–40%. The relationship between mean air pollution level and adjusted mortality-rate ratio estimated from Cox proportional hazards models was shown in Figure 7.2.2. In this figure, if the value of "Rate ratio" is 1.0, the mean age is the same as all American average lengths of life. The maximum value of rate ratio, 1.26 for one city, means the average length of life reduced to about 3 years compared with all U.S. averages. This result suggested that fine particulate air pollution was shown as to have a linear relationship with "Rate ratio" and contributed to excess mortality in certain U.S. cities compared with other air pollutants.

Based on such kinds of various researches, the U.S. environmental standard for the annual average of PM2.5 concentration in ambient air quality was firstly determined at 15 μg/m^3 and then revised from 15 to 12 μg/m^3 in 2012. The same environmental regulation of PM2.5 was also established in the world, for examples, in Japan (2009) and Chinese regulation was also determined in 2012.

For the actual measurement of the mass concentration of PM2.5 in air, working place and flue gas, the required performance of separation method for PM2.5 and 10 had been published on 1995, as ISO 7708 (1995),[8] and the recommended separation efficiency in this ISO was determined as

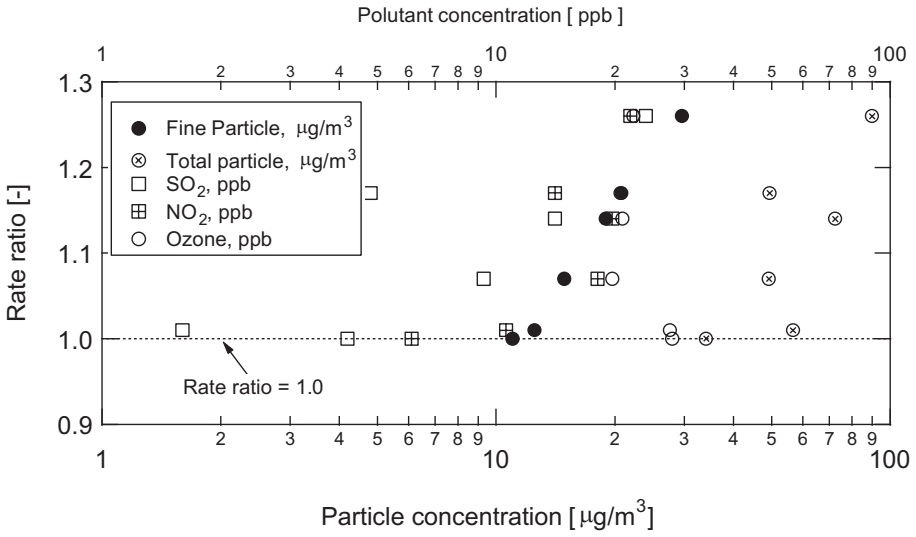


FIGURE 7.2.2 Estimated adjusted mortality-rate ratios and pollution levels in the six cities, USA. Mean values are shown for the measures of air pollution. Original data in Dockery's paper are summarized to one figure.

Figure 7.2.3. If coarse particles were not able to be separated from gas and mixed in fine particles, PM2.5 mass concentration was overestimated from actual concentration. The level of overestimation depended on the size distribution of the particles in gas.

The international standard by three kinds of method for PM2.5 and 10 separation, such as a conventional impactor, virtual impactor and cyclone, were published as PM2.5 and 10 mass concentration in ambient air and flue gas. The principles of separation of the conventional impactor are shown in Figure 7.2.4(a). Conventional impactors have particle collection plates as the impaction surface, on which particles within a certain size interval are collected following inertial size separation. For the measurement in ambient air and working place, the cascade real impactor, which applies grease or other adhesive materials onto the collecting plate of the impactor, was able to separate course particles on impaction plate. However, for in-stack measurements, commercial greases that maintain effective stickiness and constant weight under various flue gas conditions, high temperature and in the presence of reactive components have proven to be unreliable. Since adhesive materials were not able to be used on a collecting plate, some coarse particles rebound on the plate and are entrained in gas and mixed with PM2.5 for the measurement of PM2.5 and 10 in flue gas from stationary sources. In ISO 23210,[11] the limit of permissible deviation by the bounce and re-entrainment of coarse particles larger than 5.0 μm in diameter is about 30% (as shown in Figure 7.2.3) for conventional impactors used filter on collecting plate.

The principle of separation at nozzles for virtual impactor (VIS, Virtual impaction surface) are shown in Figure 7.2.4(b). The particle laden gas enters the particle acceleration nozzles and accelerates, and only a part of the minor gas stream (about 10% of total flow rate) leaving the acceleration nozzles enters

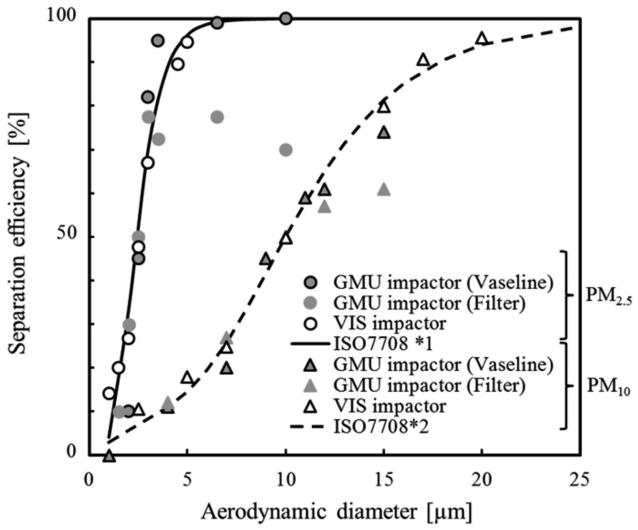


FIGURE 7.2.3 Separation efficiency curve based on ISO 7708 shown with data by conventional impactor (GMU impactor, John et al.[9]) and virtual impactor (VIS impactor, Wada et al.[10]).

the particle collection nozzles. The remaining major part of the flow is redirected and bypasses the particle collection nozzles. Consequently, particles larger than a certain aerodynamic size (cut-off size) are within the minor flow and are received by the particle collection nozzles. Fine particles smaller than this cut-off size stay in the major stream and are directed into the next separation stage. Because of the above separation principle, the VIS impactor showed remarkably good performance for almost same separation efficiency with ISO 7708 and actual PM2.5 and PM10 mass concentrations in flue gas as shown in Figure 7.2.3. Based on this result, a new ISO which used a virtual impactor had been published in 2013.[12]

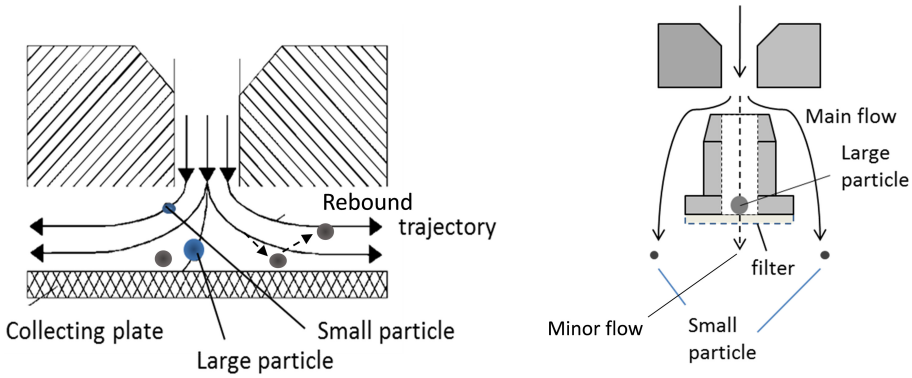


FIGURE 7.2.4 Principle of separation at nozzles for conventional impactor (GMU, a) and virtual impactor (VIS, b).

REFERENCES

1. Nakanishi, J., *Final Report Issued on August 17, 2011*. NEDO Project (P06041) Research and Development of Nanoparticle Characterization Method, 2011. https://www.aist-riss.jp/projects/nedonanorisk/nano_rad2/download/download.cgi?ES_e
2. Department of Health and Human Services, Center for Disease Control and Prevention, National Institute of Occupational Safety and Health. *NIOSH Current Intelligence Bulletin 63*, 2011. https://www.cdc.gov/niosh/docket/archive/pdfs/NIOSH-033/0033-040111-FinalDoc.pdf
3. The International Labour Organization (ILO), *International Chemical Control Toolkit, Draft Guidelines*, 2006. http://www.ilo.org/legacy/english/protection/safework/ctrl_banding/toolkit/icct/resources.htm
4. ISO TS 12901-2, Nanotechnologies-Occupational Risk Management Applied to Engineered Nanomaterials – Part 2: The Use of the Control Banding Approach in Occupational Risk Management, 2011.
5. The Japan Society for Occupational Health, Recommendation of Occupational Exposure Limits (2016-2017) *J. Occup. Health*, 58, 489–518, 2016.
6. Myojo T., Nagata T., Verbeek J., *J. UOEH*, 39, 187–199, 2017.
7. Dockery, D.W., Pope, C.A., et al., *N. Engl. J. Med.*, 329, 1753–1759, 1993.
8. ISO 7708, Air Quality—Particle Size Fraction, Definitions for Health-related Sampling, 1995.
9. John, A.C., et al., *Aerosol Sci. Technol.*, 37, 694–702, 2003.
10. ISO 23210, Stationary Source Emissions—Determination of PM10/PM2.5 Mass Concentration in Flue Gas—Measurement at Low Concentrations by Use of Impactors, 2009.
11. Wada, M., et al., *Aerosol Air Qual. Res.*, 16, 36–45, 2016.
12. ISO 13271, Stationary Source Emissions—Determination of PM10/PM2.5 Mass Concentration in Flue Gas—Measurement at Higher Concent, 2012.



Taylor & Francis
Taylor & Francis Group
http://taylorandfrancis.com

7.3 Respiratory Protective Devices for Particulate Matter

Toshihiko Myojo

7.3.1 INTRODUCTION

Respiratory protective devices (respirators) are used for protecting the respiratory system from the inhalation of contaminants. The use of respirators is generally the last resort of occupational risk management. The first step for management is to improve the working environment, such as to enclose sources of dust-generation, to change methods or processes, or to use local exhaust ventilation systems. Respirators should be used in an environment where the workplace is not safe even though improvements have been made, or where improvements are difficult or impossible.

The respirators introduced in this section are used in work environments only where particulate matters are suspended by any powder handling process, not for potential oxygen deficiency or conditions immediately dangerous to life or health (IDLH).

7.3.2 TYPES OF RESPIRATORS

In principle, respirators are classified into two types: air-purifying respirators and supplied breathable gas respirators. The air-purifying respirator removes contaminants from the ambient air, and the supplied breathable gas respirator provides air from a source other than the surrounding atmosphere. Supplied breathable gas respirators are absolutely necessary in dangerous environments, which should not be entered with air-purifying respirators. Supplied breathable gas respirators are not suitable for work in ordinary worksites because their handling is cumbersome. Both types can be further subclassified by the type of inlet covering and the mode of operation.

7.3.2.1 Air-Purifying Respirators

Air-purifying respirators are further classified into non-powered and powered respirators. Neither type of respirator should be used in atmospheres containing less than 18% oxygen nor in IDLH atmospheres.

Non-Powered Respirators

Air in the atmosphere is introduced into the filter in a manner that corresponds to a worker's breathing. Only tight-fitting coverings are suitable for non-powered respirators, because the pressure in the covering may be negative and contaminants could then enter through the covering during inhalation (see Figure 7.3.1). Non-powered respirators are generally small and are easily maintained. They restrict the wearer's movements the least and may present little physiological strain to the wearer.

Powered Air-Purifying Respirators

The powered air-purifying respirator (PAPR) uses a blower to pass contaminated air through filter element(s) that removes the contaminants and supplies purified air to a respiratory inlet covering. The covering may be a facepiece, helmet, or hood.

Filtration Mechanisms and Lifetime

All particulate respirators use fibrous filter(s) to remove particulate matters (dusts). Particulate filters are of two types: electrostatic filters, such as nonwoven fiber material or resin-impregnated felt, and mechanical filters, such as fine glass fiber filter.

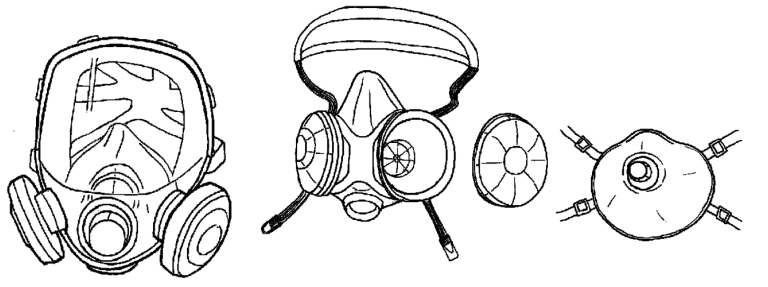


FIGURE 7.3.1 Types of inlet covering of respirators: full facepiece, half mask, and filtering facepiece.

Dust particles are captured by a combination of mechanisms, such as interception, sedimentation, inertial impaction, diffusion, and electrostatic force on the filter fibers. The contribution of each factor to the filtration mechanism depends on the flow rate through the filter and the size of particles.

The airflow resistance of particulate filters increases as the quantity of particles retained in the filter increases. This resistance increases the breathing resistance offered by a non-powered respirator and may reduce the rate of airflow in a powered respirator. A filter element clogged by captured particles may also limit the continuous use time of a respirator.

Electrostatic filters have less airflow resistance and cost less than mechanical filters, and are therefore used as filter elements in disposable respirators (filtering facepiece respirators) or some replicable respirators (elastomeric respirators). Mechanical filters have higher resistance against degradation of filtration performance. The paper-like filters are usually folded to enlarge the filtering area and are packed in cartridges.

Filter Classes of Particulate Respirators

For non-powered air-purifying respirators, the required filtration efficiencies of a particulate filter are defined by the United States NIOSH standards (42 Code of Federal Regulations Part 84),[1] which define the following categories of particulate filters (Table 7.3.1).

The European standard EN 143[2] defines the following classes of particle filters attached to a face mask (Table 7.3.2).

The European standard EN 149[3] defines the following classes of "filtering facepieces"; that is, disposable respirators (Table 7.3.3). The respirators are entirely or substantially constructed of filtering material.

Both European standards test filter penetration with both dry sodium chloride and paraffin oil aerosols, the count median diameters of which range from 0.1 to 0.3 μm; that is, the largest penetrating particle size for fibrous filters.

TABLE 7.3.1 Classes of Particulate Respirators in the United States NIOSH Standards

Oil Resistance	Class	Filter Efficiency Limit (at 85 L/min Air Flow)
Not oil resistant	N95	Filters at least 95% of airborne particles
	N99	Filters at least 99% of airborne particles
	N100	Filters at least 99.97% of airborne particles
Oil resistant	R95	Filters at least 95% of airborne particles
	R99	Filters at least 99% of airborne particles
	R100	Filters at least 99.97% of airborne particles
Oil proof	P95	Filters at least 95% of airborne particles
	P99	Filters at least 99% of airborne particles
	P100	Filters at least 99.97% of airborne particles

TABLE 7.3.2 Classes of Particulate Respirators in the European Standard EN 143

Class	Filter Efficiency Limit (at 95 L/min Air Flow)
P1	Filters at least 80% of airborne particles
P2	Filters at least 94% of airborne particles
P3	Filters at least 99.95% of airborne particles

TABLE 7.3.3 Classes of Particulate Respirators in the European Standard EN 149

Class	Filter Efficiency Limit (at 95 L/min Air Flow)	Inward Leakage
FFP1	Filters at least 80% of airborne particles	<22%
FFP2	Filters at least 94% of airborne particles	<8%
FFP3	Filters at least 99% of airborne particles	<2%

Therefore, certified filters should perform well against aerosol particles that are larger and smaller than the test aerosols.

Figure 7.3.2 summarizes the classes of particulate respirators included in the national standard of Japan. The filtration efficiency is applied only to component parts of the respirator system.

The classes of filter elements for PAPR are also defined in each regulation and are of similar grade as the above or much higher grade.

7.3.2.2 Supplies Breathable Gas Respirators

Airline Respirators

Airline respirators are a type of supplied breathable gas respirator that use compressed air from a stationary source delivered through a hose under pressure. The respiratory inlet covering may be a facepiece, helmet, hood, or complete suit. There are three modes of operation of supplied breathable gas respirators: demand mode, pressure-demand mode, and continuous-flow mode. The demand mode is controlled by a demand valve supplying the breathable gas only when a negative pressure is created inside the facepiece by inhalation. The pressure-demand mode keeps a higher pressure inside the respiratory than that of the ambient atmosphere for the whole breathing cycle. Therefore, a pressure–demand airline respirator provides higher protection for wearers.

The airline respirator may be used for long periods. Its disadvantage is that the air supply tube severely restricts the wearer's mobility.

Self-Contained Breathing Apparatus

The distinguishing feature of a self-contained breathing apparatus (SCBA) is that the wearer need not be connected to a stationary breathing gas source, such as an air compressor, therefore allowing comparatively free movement over an unlimited area. Instead of a stationary breathing gas source,

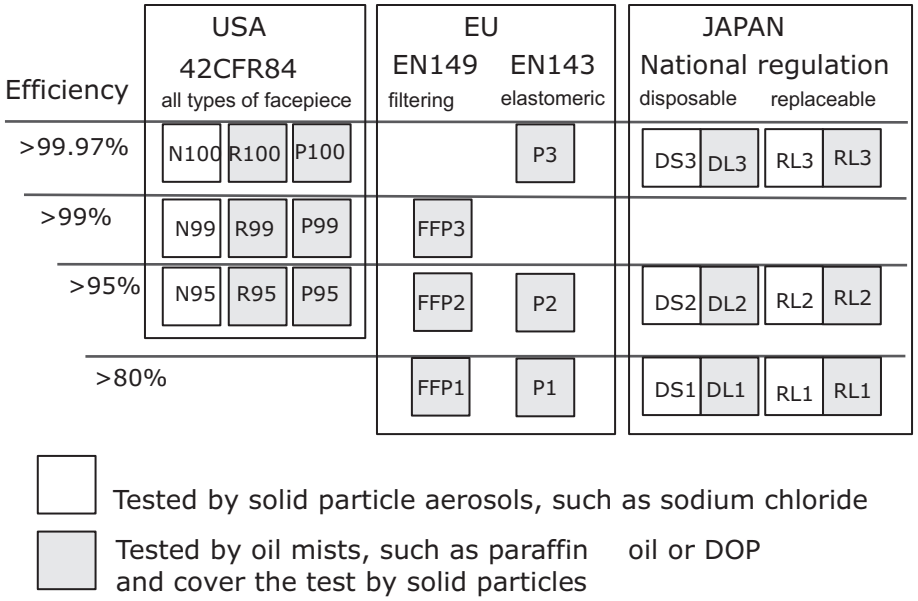


FIGURE 7.3.2 Classes of particulate filters for non-powered respirators. The certified filter elements have been tested by suitable laboratories, but the real performance of respiratory protection by non-powered respirators is affected by the fit between the facepiece and the wearer's face.

the wearer carries enough air or oxygen for up to four hours, depending on the design. This limited service life makes SCBAs unsuitable for routine use for long, continuous periods.

7.3.3 PROTECTION FACTOR

There are several scales of effectiveness of respirators, such as penetration and efficiency. Protection Factor (*PF*) is commonly used to evaluate respirators and is defined as follows:

$$PF = \frac{C_o}{C_{in}} \tag{7.3.1}$$

where

C_o is the concentration of contaminant on the outside of the respirator facepiece

C_{in} is the concentration of contaminant on the inside of the covering

$PF > 1$ means effective and $PF = 1$ means non-effective. When selecting a respirator, the *PF* should be larger than the Hazard Ratio (HR) of the specific contaminants in the work environment. The HR is the estimated/measured airborne concentration of contaminant(s) divided by the occupational exposure limit (OEL) of the contaminant(s).

Assigned protection factor (APF) means the level of respiratory protection that a respirator or class of respirators is expected to provide to wearers, based on previous studies. The APF value can only be applied to a class of respirators when the respirators are properly selected and used with properly selected filters by wearers who received training and fit testing. Table 7.3.4 shows the APF values assigned by the US OSHA (29 CFR 1910.134).[4] Governments or industrial standards provide their own APF values, and respirator users outside of the USA should check the APF values and follow their rules.

TABLE 7.3.4 Assigned Protection Factor by US OSHA (29 CFR 1910.134)

Type of Respirator	Half Mask	Full Facepiece	Helmet/Hood
Air purifying respirators	10	50	–
Powered air purifying respirators	50	1000	25
Airline demand	10	50	–
Airline continuous flow	50	1000	25
Airline pressure demand	50	1000	–

7.3.4 FIT CHECK AND FIT TEST OF RESPIRATORS

Respirators should be tested for their ability to face-seal and ensure protection for the wearer. A fit check should be conducted each time a respirator is worn, following the manufacturer's instructions. It is common to choke the inhalation valve or exhalation valve by hand or a small stopper.

A fit test should be conducted for a wearer of any respirator before using it on the job. If a specific respirator does not fit the face of the wearer and face-seal leakage is detected, that respirator should not be used in the work environment. The fit test method can be qualitative or quantitative. A qualitative fit test relies on the wearer's senses of taste or smell to detect penetration of a test agent, such as saccharin mist or

irritant smoke. The quantitative fit test relies on instruments instead of human sensation. One way to quantitatively determine the quality of fit is to use aerosols to measure the aerosol concentrations inside and outside the respirator, similar to PF. Ambient aerosols are commonly used as tracer aerosols for leakage detection.

7.3.5 SELECTION, USE, AND MAINTENANCE OF RESPIRATORS

Both employees who wear the respirators and their employers who are responsible for the safety and health of the employees should be aware of the following:

Selection:

1. Air-purifying respirators cannot be used if the oxygen concentration in the atmosphere is less than 18%.
2. Respirators should be selected on the basis of hazards to which the worker is exposed.
3. Facepieces should fit the worker's face and the fit should be confirmed by a fit test.

Maintenance:

4. Respirators should be inspected regularly.
5. Deteriorated parts should be replaced.
6. Respirators should be kept clean and disinfected.
7. Respirators should be stored in a clean, dry place.
8. Used filters should be disposed of by a method that does not scatter dust.

Use:

9. Respirators should be worn correctly and their fit should be checked routinely.
10. Workers should be instructed and trained in the proper use of respirators and their limitations.

Actually, any competent person who has knowledge of respirators and is assigned by the employer should instruct workers how to use respirators.

REFERENCES

1. 42 CFR 84 respiratory protective devices; final rules and notice. Federal register 60:110. U.S. Center for Disease Control and Prevention, National Institute for Occupational Safety and Health, 1995.
2. European Standard EN 143: Respiratory protective devices - particle filters - requirements, testing, marking, 2000.
3. European Standard EN 149: Respiratory protective devices - filtering half masks to protect against particles - requirements, testing, marking, 2001.
4. Assigned Protection Factors for the Revised Respiratory Protection Standard. Occupational Safety and Health Administration, U.S. Department of Labor, OSHA 3352-02, 2009.

7.4 Dust Explosion

Ritsu Dobashi and Wei Gao

7.4.1 WHAT IS DUST EXPLOSION?

Combustible particles have potential hazards to cause a dust explosion. Accidental dust explosions often bring serious damages, which spread to wide area in a short moment. Therefore, it is necessary to prevent the accidental dust explosions and mitigate the damages of the dust explosions. In order to take appropriate measures against dust explosions, it is indispensable to understand the phenomena of dust explosions.[1,2] In this section, we would like to explain what the dust explosion is.

Combustible solid materials have potential hazard of fire and explosion. As a mass body, the solid material will burn as a fire (Figure 7.4.1) and will not generate an explosion excluding for the case of explosive materials. The explosive materials can explode as a mass body and such explosive materials are not considered in this section, because they are always handled very carefully in some special manner. If the combustible material becomes powder and is piled on a floor, it will be ignited easily and burn faster, however, an explosion does not occur. When the powder is dispersed into the air to form a combustible particle cloud, it can be ignited and a flame will propagate among the combustible particle cloud. The flame propagation induces the rapid volume generation. That is, a dust explosion happens in this case. Therefore, the dispersion of solid powder into air, which causes the flame propagation, is needed for dust explosions.

The three elements for combustion are "Fuel," "Oxygen," and "Ignition (or Heat)." They are known as "Combustion Triangle" or "Fire Triangle," and are useful for thinking about how a combustion starts and how to prevent fire and gas explosion. As for the dust explosion, "Dust Explosion Pentagon" is used. It consists of "Fuel (Combustible Dust)," "Oxygen," "Ignition," "Dispersion," and "Confinement." "Dispersion," and "Confinement" are added to the combustion triangle. "Dispersion" is needed for dust explosion because it can form a combustible particle cloud as explained in the previous paragraph. If an explosion happens in an open space, the damage will be limited, because the pressure increase is only little. Therefore, "Confinement" is needed for the dust explosion with a certain degree of pressure rise. Also the concentration of particle cloud is not easy to increase in an open space and the confinement assists the concentration to increase easily (Figure 7.4.2).

It is necessary to recognize that the dust explosion is a flame propagation phenomenon among combustible dust suspended in air (combustible particle cloud). Figure 7.4.3[3] shows the photograph of a propagating flame among combustible particle cloud (plastic dust; Stearic acid). A sheet-shaped laser light was exposed perpendicularly to the observed area. In the photograph, a flame is propagating from the center of the photograph (ignition point) to the outside radially. It is seen that the leading flame consists of blue spot flames. Ahead of the zone of blue spot flames, the dark zone is seen, where scattering light from particles are not observed and it means that solid particles are already gasified. By this photograph, it is understood that the flame is propagating in a gas phase where the solid particles become combustible gas. This gas phase consists of the gasified combustible material and air, therefore the concentration of combustible gas is non-uniform. The structure of the leading flame strongly depends on the non-uniformity. In this case, the combustible gas is concentrated near the points where large particles had been gasified, and then discrete flames (the blue spot flames) were formed near these points.

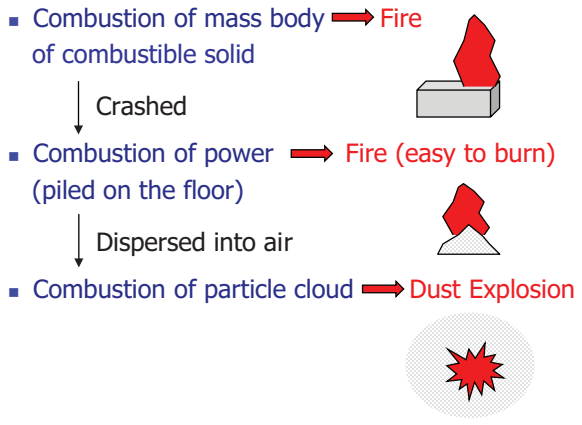


FIGURE 7.4.1 Combustion characters of combustible solid material.

7.4.2 FLAME PROPAGATION MECHANISM IN DUST EXPLOSION

7.4.2.1 Observed Propagation Phenomena

As mentioned in the prior section, a flame is propagating in the gasified phase during a dust explosion. The flame propagating

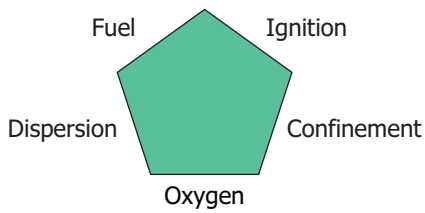


FIGURE 7.4.2 Dust explosion pentagon.

phenomena strongly depend on the condition of the gasified phase. The condition of the gasified phase is determined by the volatility character of the dust (material and size). The photographs of the propagating flame taken during the flame propagations in combustible particle clouds of three kinds of dust materials with different volatility characteristics are shown in Figure 7.4.4.[2]

Case A (left of Figure 7.4.4): The material of the particles is decane (liquid spray). The volatility is high. In this case, the observed flame front is almost smooth and similar to a gas phase premixed flame. It is considered that the rapid gasification and mixing make the gas phase condition similar to premixed gas mixture.

Case B (center of Figure 7.4.4): The material of the particles is stearic acid, and the volatility is not so high and more heat input is needed for the gasification than Case A. In this case, the leading flame consists of many discrete spot flames. The concentration distribution of combustible gas is not uniform as the volatility is not so high. Therefore, the structure of combustion reaction zone (flame) becomes discontinuous.

Case C (right of Figure 7.4.4): The material of the particles are iron, and the volatility is very low. In this case, no gas phase flame is observed. As the combustion temperature is less than the boiling point of iron, the combustion reaction occurs only on the particle surface (in condensed phase). The reaction zones are perfectly discrete. This is a rare case in which the gas phase flame is not formed although a dust explosion occurs. These surface reactions occur consequently at particle to particle, and form the propagation of the combustion reaction. The reaction zone is considered to expand as the propagation of heat wave toward the unreacted region ahead of the reaction region.

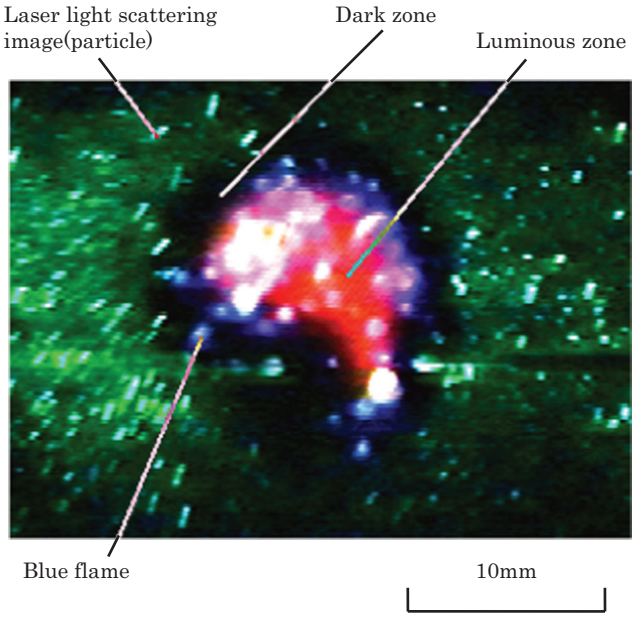


FIGURE 7.4.3 Propagating flame in 1-octadecanol particle cloud.[3]

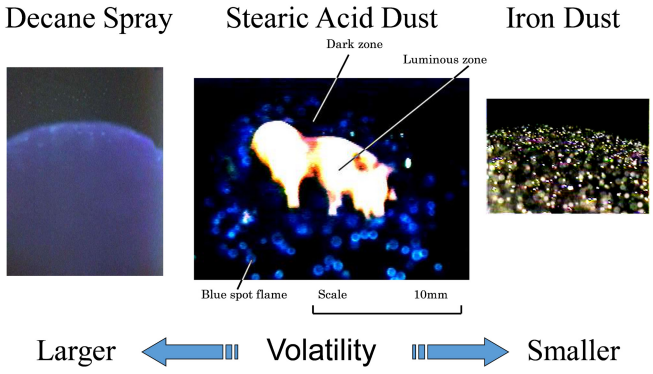


FIGURE 7.4.4 Structures of propagating flames.[2]

To understand more about the flame propagation mechanism, not only the volatility but also the reaction rate are taken into account. The results of a study are introduced here, in which dust explosion experiments were performed with changing the combustible material and particle size systematically.[4]

7.4.2.2 Effects of Particle Thermal Characteristics on Flame Structures

Figure 7.4.5 shows the flame configurations with different materials at same concentration and particle size distributions. For methanol and propanol mist combustion, the flame fronts formed were smooth in shape and blue flames appeared in the flame fronts, which resulted from the sufficient combustion of the fuel. It can be inferred that all of the droplets were pyrolyzed or evaporated before the flame front passed through. The combustion zones seemed connected and continuous in structure, similar to an ordinary gas flame that propagates in homogeneous combustible gas, and the regions retained their surface as they propagated, though propagating velocities differed at each point.

In contrast, the flame propagating through other droplets and particles formed a complicated structure. The flame zones consisted of blue spots of flame at the leading zone and luminous flames behind them. The flame zones seemed to be discrete. The blue spots could represent burning of larger particles or gaseous lumps of materials that resulted from their evaporation. The thickness of the blue spot zone and number of blue spots increased with the decrease of the volatility of the materials. As the particles burned, a small luminous flame appeared that resembled a yellow dot. This phenomenon can be explained as follows: around the particles, local high-concentration regions of fuel existed; when those particles burn without sufficient oxygen, soot particles were formed, and these particles emitted yellow flame. These small luminous flames grew under buoyancy and combined with each other, and in the end formed a whole luminous zone in an irregular shape. This luminous zone was composed of heated soot

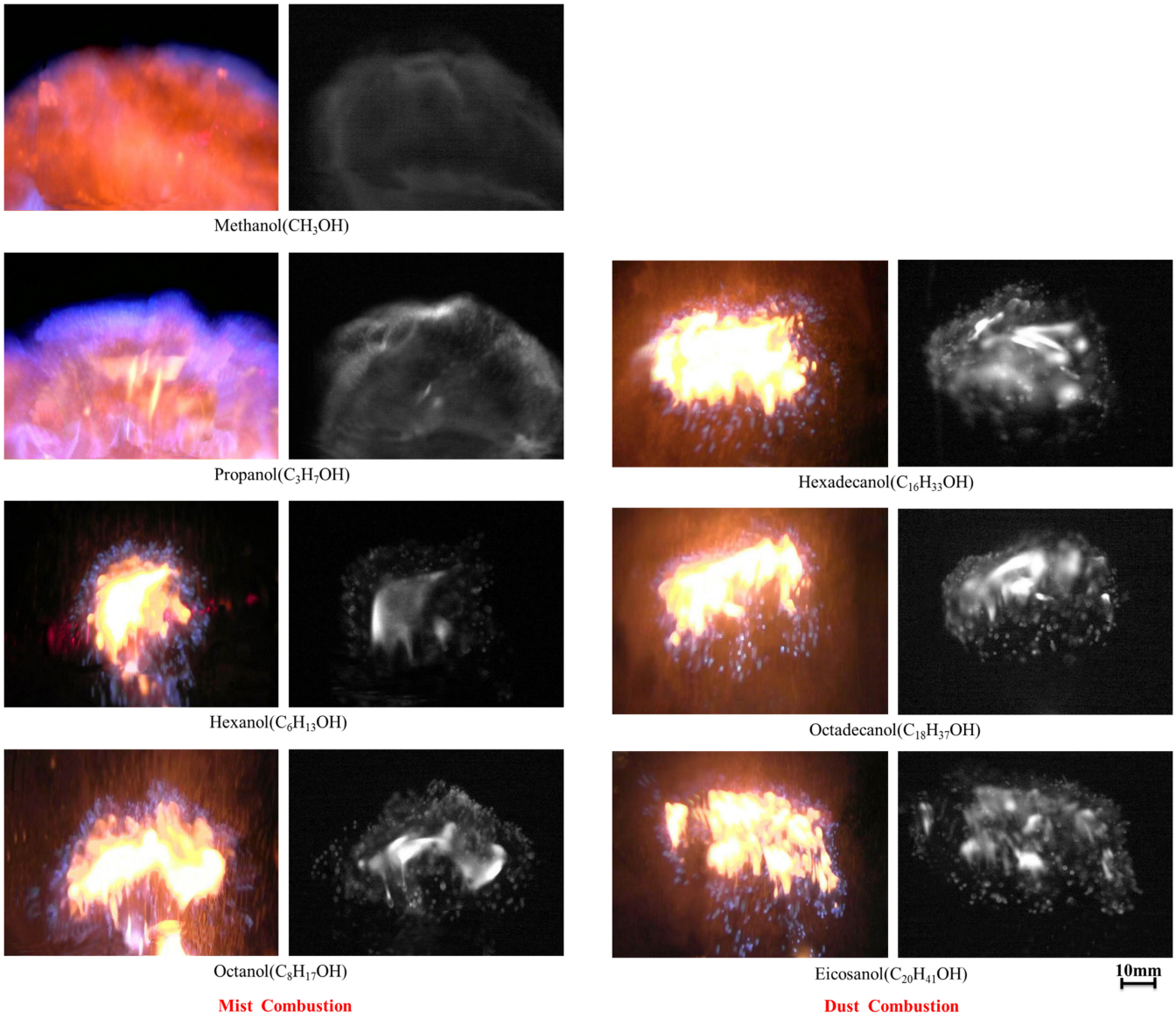


FIGURE 7.4.5 Flame configurations in materials with different particle thermal characteristics (left side is the direct light emission photographs; right side is the CH emission photographs).[4]

particles that were created by the decomposition of gasified fuel ejected from the particle surface. Because the particles were scattered, the gasified fuel concentration was not uniform. This must be the reason for the irregular shape of the luminous zone.

7.4.2.3 Effects of Particle Size Distributions on Flame Structures

Flame propagation processes in octadecanol dust clouds with three different particle size distributions were recorded to reveal the effects of particle size distributions on flame structures. Figure 7.4.6 shows the flame configurations in dust clouds with different particle size distributions. For small particle size, no clear discrete spot flames could be seen on the CH emission photographs. The combustion zone seemed connected and with a continuous structure like the ordinary homogeneous gas explosions, and it kept its surface as it propagated, though propagating velocities differed at each spot. In contrast, for medium particle size, whole flame consisted of discrete, isolated flames at the leading zone and a luminous flame behind them, and it also kept its structure as it propagated. A further increase in diameter resulted mostly in the appearance of isolated flames and the disappearance of luminous flames in the flame propagation process. From the magnified CH emission photographs, it was found that the leading isolated spot flames were supported by the vaporized gas from rather smaller particles, which could quickly vaporize in the preheat zone. But the number of the small particles per volume was small which led to whole flame keeping its discrete structure instead of being united and forming a continuous surface. Hence, the flame firstly propagated towards the small particles nearby, when the small particles were completely pyrolyzed, and the local pre-mixing flame would

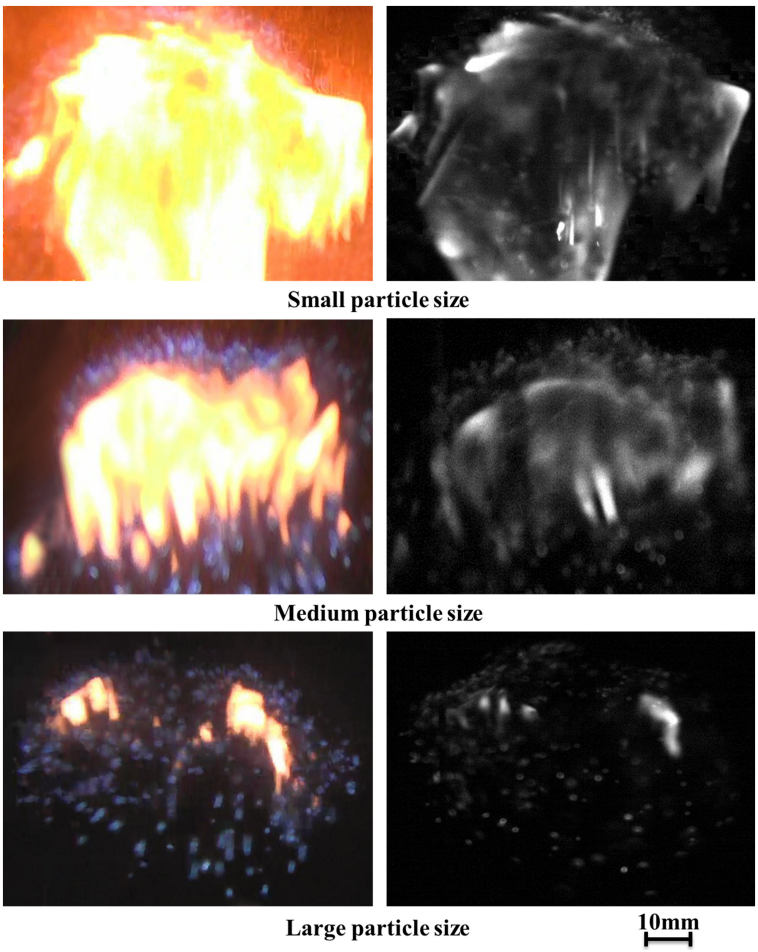


FIGURE 7.4.6 Flame configurations in octadecanol dust clouds with three different particle size distributions (left side is the direct light emission photographs; right side is the CH emission photographs).[4]

continue to heat the larger particles, establishing the local diffusion flame, and then the isolated blue luminous spots. The flame propagation mechanism was locally continuous, obviously unlike the relay ignition mechanism. There must exist a reference diameter, the mass and number densities of particles below this reference diameter are critical for different flame structures.

7.4.2.4 Flame Propagation Mechanism Transition in Dust Explosions

The Damköhler number was introduced to categorize these flame propagation models, which was defined as the ratio of the heating and devolatilization characteristic time (τ_{dv}) to the combustion reaction characteristic time (τ_{cr}):

$$Da = \frac{\text{Heating and devolatilisation characteristic time}}{\text{Combustion reaction characteristic time}} = \frac{C_3^3 \rho_d D_{32}^2 (T_i - T_u) V_f^2 T_u^2}{8 C_1 (\lambda_g / c_{pg})\ \phi \ln(1 + B_s)(\lambda / C\rho_u)(T_f - T_i) T_i^2} \tag{7.4.1}$$

where B_s, the spalding number, is the mass transfer number, which is a complicated function of boiling point, gas temperature, surface temperature, heat of combustion, and the other parameters. For combustion proceeds directly on the surface of the fuel particle, it can be expressed by:

$$B_s = q_{st} \tag{7.4.2}$$

For combustion with oxygen proceeds in vapor phase, it can be expressed by:

$$B_s = \left[q_{st} Q_c + c_p(l)(T_i - T_b)\right] / \left[Q_v + c_p(s)(T_b - T_u)\right] \tag{7.4.3}$$

The parameters used in the Equations (7.4.1–7.4.3) can be divided into two groups, that is the thermal characteristic parameters and particle size parameters. The parameters shown in Table 7.4.1 were determined by the experiments.

It is found that when the Damköhler number was less than 1, homogeneous combustion controlled the flame propagation process; on the contrary, when the Damköhler number was larger than 1, heterogeneous combustion controlled the flame propagation process.

TABLE 7.4.1 Characteristic Parameters

Thermal Characteristics	Particle Size
T_i: Ignition temperature	D_{32}: Sauter mean diameter
T_f: Flame temperature	D_{20}: Surface area mean diameter
T_b: Boiling point	D_{30}: Volume mean diameter
$c_p(l)/c_p(s)$: Constant pressure heat capacity of liquid/solid	C_1: Ratio of mean particle diameters, D_{20}/D_{32}
Q_c: Heat of combustion	C_3: Ratio of mean particle diameters, D_{30}/D_{32}
Q_v: Heat required to generate flammable vapors at room temperature	**Other Parameters**
B_s: Spalding number	ρ_d: Particle density
λ: Thermal conductivity in solid phase	V_f: Flame propagation velocity
C: Specific heat of dust	ρ_u: Density of unburned combustible gas
λ_g: Thermal conductivity in gaseous phase	q_{st}: Fuel/air mass ratio at stoichiometric conditions
c_{pg}: Specific heat in gaseous phase	φ: Equivalence ratio

7.4.3 RISK OF DUST EXPLOSION

7.4.3.1 Risk Analysis and Risk Management of Dust Explosions

Wilson and McCutcheon (2003)[5] define risk as the possibility of injury, loss or environmental injury created by a hazard, with the significance of risk being a function of the probability (or likelihood) of an unwanted incident and the severity of its consequences. Risk therefore arises from a hazard i.e. the potential of a machine, equipment, process, material or physical factor in the working environment to cause harm to people, environment, assets, or production. Risk management is the complete process of understanding risk, risk assessment, and decision making to ensure effective risk controls are in place and implemented. Risk management begins with actively identifying possible hazards leading to the ongoing management of those risks deemed to be acceptable. Meftah Abuswer et al. (2013)[6] focused on QRA of dust explosions with the development of a methodological framework for the management of these risks. This framework is shown in conceptual format in Figure 7.4.7. The QRA framework is based on hazard identification via credible accident scenarios for dust explosions, followed by probabilistic fault-tree analysis and consequence severity analysis. Identification of risk reduction measures in the framework is accomplished in a hierarchical manner by considering inherent safety measures, passive and active engineered devices, and procedural measures.

7.4.3.2 Evaluation of the Occurrence Probability of Dust Explosions

Dust explosion phenomenon is characterized by the sensitivity and severity parameters whose quantitative evaluation and interrelationship are required for designing adequate explosion safety measures.[7] The sensitivity parameters include the minimum ignition temperature (MIT), minimum ignition energy (MIE), minimum explosible concentration (MEC), and limiting oxygen concentration (LOC). There are many evaluation methods and standards to measure the sensitivity parameters. ASTM standards are introduced as an example.

Minimum Ignition Temperature (MIT)

The minimum ignition temperature (MIT) is the lowest temperature of a hot surface that will cause a dust cloud, rather than a dust layer, to ignite and propagate flame. Minimum ignition temperature of dust clouds is usually tested in the "Godbert–Greenwald" furnace, which is schematically shown in Figure 7.4.8.[8] The furnace includes a test chamber, two thermocouples, a dust sample container, an electromagnetic valve, a heater, and a stopstock. The test follows ASTM E1491 standard (Standard test method for minimum autoignition temperature of dust clouds).[9]

A weighed amount of combustible dust is placed in a dust sample container at the top of the temperature-controlled furnace with an open bottom. The dust is dispersed by compressed air downwards past the hot surface of the furnace to see if ignition occurs and flames are produced. If the dust does not ignite, the furnace temperature is increased and the test repeated until ignition of the dust occurs. Once ignition has been established, the mass of the dust sample and injection pressure are varied to find the most vigorous explosive flame discharge. The temperature of the furnace is then reduced incrementally until flame propagation is no longer observed. At this temperature, the dust mass and injection pressure are varied to confirm that no ignition is found over five consecutive tests. The final determination of the minimum ignition temperature must be made by varying the temperature in increments of 25°C or smaller. Usually if the minimum ignition temperature is less than 300°C, the material can be easily ignited. Table 7.4.2 summarizes the minimum ignition temperature of some common dusts.[10]

Minimum Ignition Energy (MIE)

The minimum ignition energy (MIE) of a dust cloud is the lowest energy value of a high-voltage capacitor discharge required to ignite the most readily ignitable dust/air mixture at atmospheric pressure and room temperature. The minimum ignition energy of dust clouds is usually tested in the Hartmann explosion test apparatus, which is schematically shown in Figure 7.4.9.[8] The test apparatus includes a Hartmann tube, two electrodes, a gas driven piston, a micrometer, a sample chamber (the bottom of the Hartmann tube), a dust dispersion nozzle, an inlet valve, a dispersion valve, a gas reservoir, and the supporting case. The test follows ASTM E2019 standard (Standard test method for minimum ignition energy of a dust cloud in air).[11]

Dust is put in the dust container on the bottom of Hartmann tube and can be dispersed to form dust cloud in the Hartmann tube. The capacity in the spark generator is

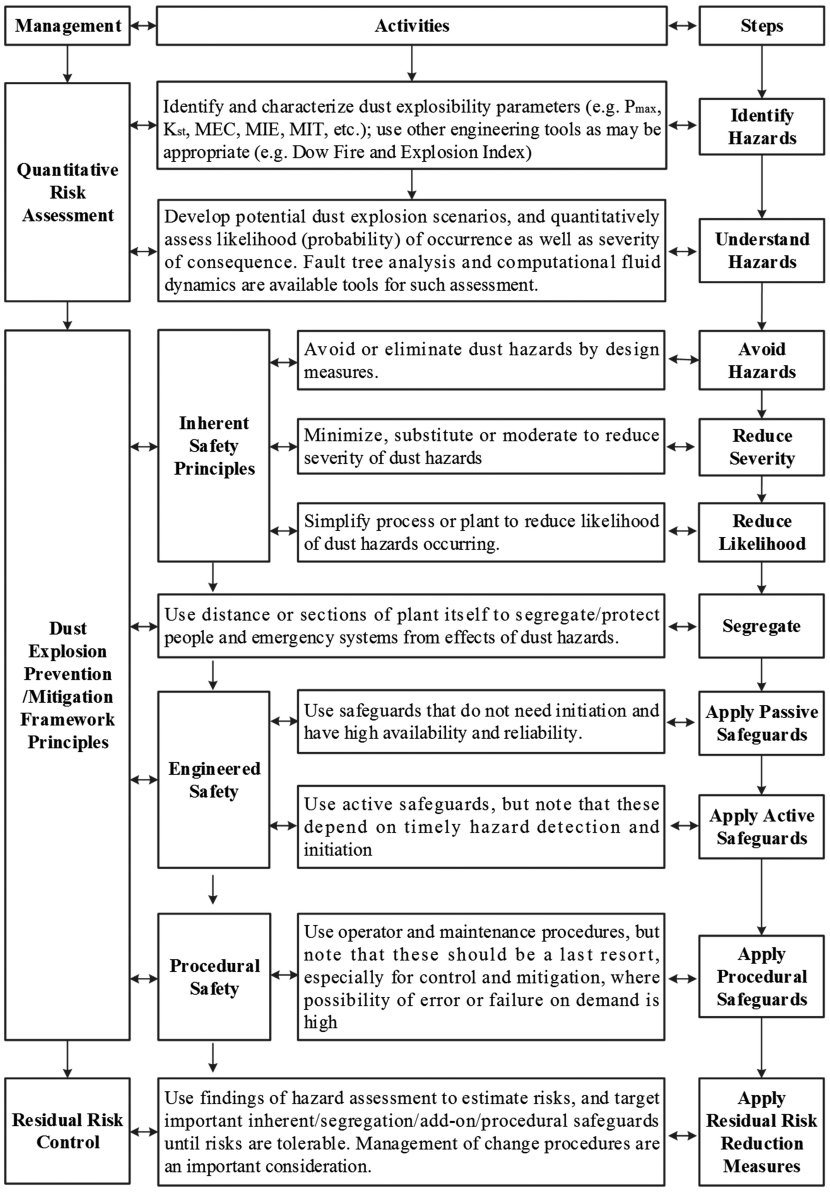


FIGURE 7.4.7 Conceptual risk management framework for dust explosions.[6]

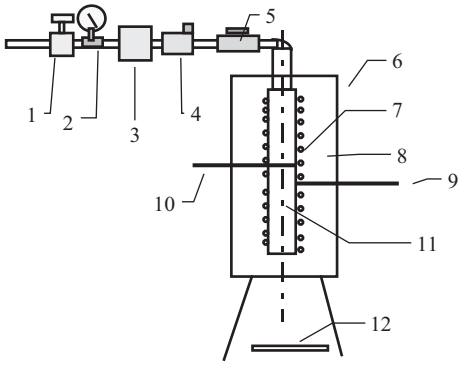


FIGURE 7.4.8 Schematic diagram of the "Godbert–Greenwald" furnace.[8] 1 Stopstock 2 Pressure gauge 3 Pressure vessel 4 Electromagnetic valve 5 Dust sample container 6 Furnace shell 7 Heating 8 Insulation materials 9 10 Thermocouples 11 Quartz furnace tube 12 Mirror.

charged before ignition, and a spark is triggered in given ignition delay by a moving electrode. The energy is just sufficient to ignite the dust under investigation is determined. This ignition energy is then successively reduced with variation of the dust concentration and the ignition delay time (controlling the flow turbulence) in a series of tests until no ignition takes place in at least 10 successive experiments. The minimum ignition energy (MIE) lies between the lowest energy value (E_2) at which ignition occurs and the energy (E_1) at which in at least 10 successive experiments no ignition is observed. The energy range thus determined is called the minimum ignition energy of a combustible dust in admixture with air. However, for purposes of simplification often only the lower limit value (E_1) is specified as the minimum ignition energy (MIE): $E_1 < MIE < E_2$. Table 7.4.3 summarizes the minimum ignition energy of some common dusts.[10]

TABLE 7.4.2 Minimum Ignition Temperature of Some Common Dusts[10]

Dust	Minimum Ignition Temperature (°C)	Dust	Minimum Ignition Temperature (°C)
Magnesium	480	Aluminum	560
Aluminum iron alloy	820	Calcium aluminum alloy	600
Copper silicon alloy	690	Ganister sand	>850
Zinc	510	Titanium	375
Magnesium alloy	560	Ferrosilicon alloy	670
Corn starch	460	Rice starch	530
Wheat starch	520	Fructose	430
Pectinase	510	Potato starch	530
Wheatmeal	470	Soybean meal	500
Milk	450	Lactose	450
Feed	450	Fishbone	530
Blood meal	650	Tobacco	470
Woodmeal	480	Pulp	520
Methyl cellulose	410	Linum Usitatissimum	440
Cotton	560	Resin-oatmeal	470
Rubber	500	Lignite dust	380
Sulphur	280	Hyperoxide	>850
Dyestuff	480	Electrostatic powder coating	480
Toner	530	Naphthalene	660
Lead stearate	600	Emulsifier	430

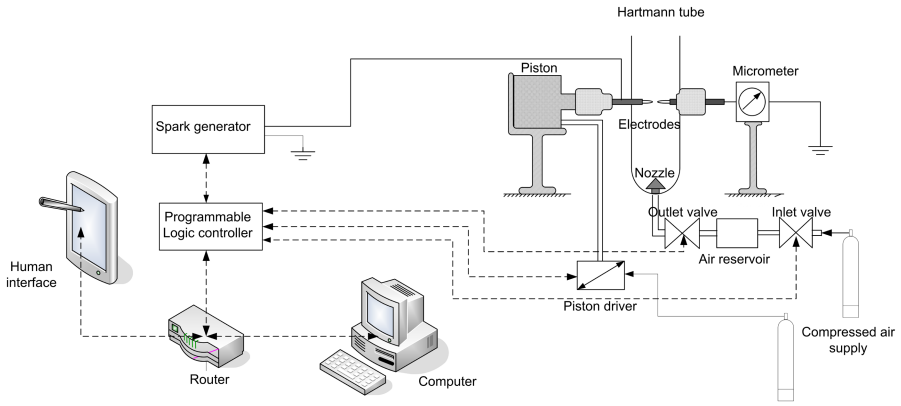


FIGURE 7.4.9 Schematic diagram of the minimum ignition energy test system.[8]

Minimum Explosible Concentration (MEC)

The occurrence of an explosion requires a dust concentration within certain limits. If dust concentration is too low, the heat generation will not be sufficient to support flame propagation; similarly, if it is too high, the quenching effect of the particles will prevent the explosion propagation. The minimum explosible concentration (MEC), also known as the lower explosible limit, is the lowest concentration of dust cloud that allows flame propagation. The minimum explosible concentration of dust clouds is usually tested in the 20 L spherical explosion test apparatus, which is schematically shown in Figure 7.4.10.[8] It is a double-layered stainless steel vessel. Water or other fluid media can be used to maintain the initial temperature of the explosion test. On the vessel wall there are different connections: vacuum, exhaust, fuel inlet, and air inlet. A glass window is used to observe the light of ignition and explosion flames. A fast act valve driven by compressed air is mounted under the bottom of the vessel. A sample vessel of 0.6 L is connected to the fast act valve. The dust sample can be dispersed to the chamber by compressed air through the dispersion nozzle. A pressure sensor is mounted on the vessel wall to record the dynamic pressure during the experiments. The test follows ASTM E1226 standard (Standard test method for minimum explosible concentration of combustible dusts).[12]

The tests are performed with two pyrotechnic igniters of 1 kJ each as ignition source. The explosion pressure and the rate of pressure rise are recorded. The explosion behavior in the 20 liter-sphere is evaluated by means of the corrected explosion pressure. If the corrected explosion pressure exceeds 0.2 bar, an explosion is confirmed to have occurred. Correction of

TABLE 7.4.3 Minimum Ignition Energy of Some Common Dusts[10]

Dust	Minimum Ignition Energy (mJ)	Dust	Minimum Ignition Energy (mJ)
Alfalfa	320	Acrylic alcohol resin	20
Aluminum	10	Aluminum stearate	10
Aspirin	25	Boron	60
Cotton fiber	60	Acetate fiber	10
Bituminous coal	60	Cocoa	100
Corn starch	30	Cork	35
Ferromanganese alloy	80	Asphalt	25
Cereals	30	Iron	20
Magnesium	20	Manganese	80
Phenolic resin	10	Polyethylene	30
Polystyrene	10	Silicon	80
Soybeans	50	Sulfur	15
Titanium	10	Zinc	100
Zirconium	5		

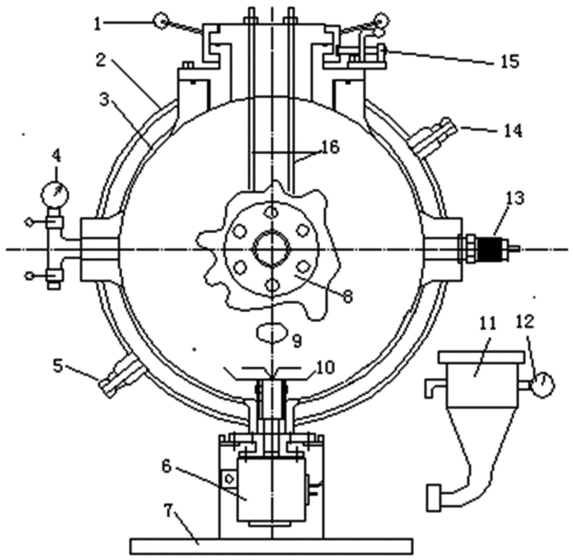


FIGURE 7.4.10 20 L spherical explosion chamber.[8] 1 Handles 2 Outside layer 3 Inside layer 4 Vacuum gauge 5 Inlet of recycling water 6 Dust/air multiphase valve 7 Stand 8 Inspect window 9 Inlet of fuel gas/air 10 Dispersion valve 11 Dust sample vessel 12 Gauge with signal output 13 Pressure sensor 14 Outlet of recycling water 15 Safety interlock.

the measured explosion pressure is necessary to account for the influence of the igniters. Even without an explosive dust in the 20 liter-sphere an important overpressure is recorded, which is caused by the heat liberation from the chemical igniters. The influence of the igniters on the measured explosion pressure diminishes as the pressure effect of the explosion itself becomes larger. A dust which cannot be induced to explode over a wide range of concentrations (normally from 30 g/m^3 to 2000 g/m^3) with an ignition energy of 2 × 1 kJ (pyrotechnic igniters) is classified as not explosible. The test is performed on the sample fraction having a particle size less than 63 μm. Table 7.4.4 summarizes the minimum explosible concentration of some common dusts.[10]

Limiting Oxygen Concentration (LOC)

The limiting oxygen concentration (LOC) is the experimentally determined oxygen concentration which will just not allow an explosion of a dust/air/inert gas mixture. An atmosphere having an oxygen concentration below the limiting oxygen concentration is not capable of supporting combustion and thus cannot support a dust explosion. The limiting oxygen concentration test is used to study explosion prevention or severity reduction involving the use of inert gases and to set oxygen concentration alarms or interlocks in inerted plant and vessels. Limiting oxygen concentration testing can also be measured using the 20 liter-sphere apparatus. The test follows ASTM E2931-13 standard (Standard test method for limiting oxygen (oxidant) concentration of combustible dust clouds).[13] Powder or dust samples of various sizes are dispersed in the vessel and attempts are made to ignite the resulting dust cloud with an energetic ignition source. Trials are repeated for decreasing oxygen concentrations until the LOC is determined. Table 7.4.5 summarizes the limiting oxygen concentration of some common dusts.[10]

7.4.3.3 Evaluation of the Consequence of Dust Explosions

The severity parameters are characterized by maximum explosion pressure (P_{max}) and deflagration index (K_{st}), which are important parameters in dust explosion mitigation including pressure venting, explosion suppression, and isolation. Similarity, ASTM standards are introduced as an example to measure the severity parameters. Maximum explosion pressure (P_{max}) and deflagration index (K_{st}) can also be measured using the 20 liter-sphere apparatus. The test follows ASTM E1226 standard (Standard test method for explosibility of dust clouds).[14] A typical pressure curve is shown in Figure 7.4.11.[15]

The maximum rate of pressure rise depends on the volume. The product of the maximum rate of pressure rise and the third root of the special volume is a constant (Cubic Law) and called deflagration index (K_{st}). The K_{st} value is defined by the following formula:

$$K_{st} = \left(\frac{dp}{dt}\right)_{max} V^{1/3} \tag{7.4.4}$$

The K_{st} value can be used to classify dusts into one of several groups. Table 7.4.6 shows the classification that is generally adopted. Higher St class indicates serious severity.

A fairly comprehensive list of factors influencing the explosibility of dust clouds may look as follows:[16]

- Chemical composition of the dust, including its moisture content

TABLE 7.4.4 Minimum Explosible Concentration of Some Common Dusts[10]

Type	Dust	Minimum Explosible Concentration (g/m³)	Type	Dust	Minimum Explosible Concentration (g/m³)
Metal	Molybdenum	35	Thermoplastics	Acetal	35
	Antimony	420		Alcohol acid	155
	Zinc	500		Ethocel	20
	Zirconium	40		Synthetic rubber	30
	Silicon	160		Acetylcellulose	35
	Titanium	45		Nylon	30
	Iron	120		C cellulose propionate	25
	Vanadium	220		Polyacrylamide	40
	Antaciron	425		Polyacrylonitrile	25
	Magnesium	20		Polytene	20
	Duralium	50		Polyethylene terephthalate pet	40
	Manganese	210		Polyvinyl acetate	40
Thermosetting plastics	Bakelite	30		Polystyrene	20
	Epoxy	20		Polypropylene	20
	Phenol Formamide	25		Polyvinyl alcohol	35
	Phenol furfural	25		Celloidin	30
Plastic primary material	Adipic acid	35	Agricultural products and other materials	Lignin	65
	Casein	45		Rosin	55
	Terephthalic acid	50		Corn and starch	45
	Paraformaldehyde	40		Soybean	40
	Carboxy benzaldehyde	20		Wheat	60
Plastic filler	Cork	35		Peanut shell	85
	Cellulose floc	55		Granulated sugar	19
	Cotton highlights	50		Coal (asphalt)	35
	sawdust	40		Soap	45

TABLE 7.4.5 Limiting Oxygen Concentration of Some Common Dusts[10]

Dust	Limiting Oxygen Concentration (%)
Coal	14% in N_2
Maize starch	9% in N_2
Aluminum	5% in N_2
Sewage sludge	11% in N_2

- Chemical composition, and initial pressure and temperature of the gas phase
- Distributions of particle sizes and shapes in the dust
- Degree of dispersion, or agglomeration, of dust particles
- Distribution of dust concentration in the actual cloud
- Distribution of initial turbulence in the actual cloud
- Possibility of generation of explosion-induced turbulence in the still unburned part of the cloud
- Possibility of flame front distortion by other mechanisms than turbulence
- Possibility of significant radiative heat transfer

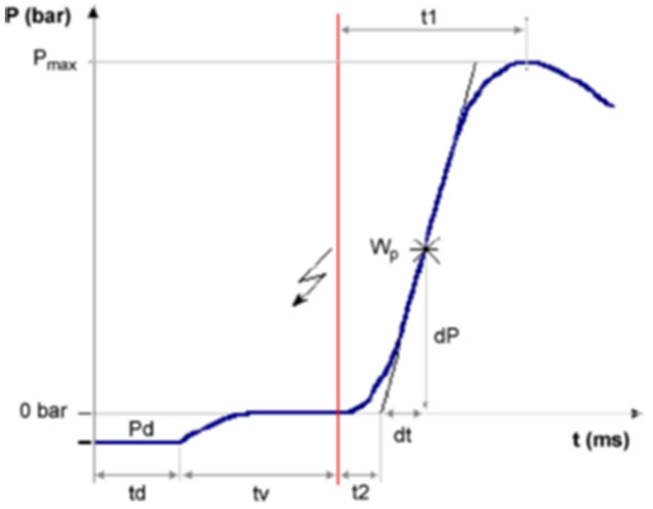


FIGURE 7.4.11 Typical overpressure versus time during a dust explosion.[15] t_1 (combustion time); time between ignition and P_{ex}; t_2 (induction time); time between ignition and intercept with $P=0$ line of the tangent to the inflexion point W_p; P_d, expanding pressure (if any) of the dust reservoir given as the difference between initial pressure before and after dust dispersion; t_v, time between beginning of the dust dispersion and ignition; and $(dP/dt)_{max}$ is the slope of the tangent at W_p.

TABLE 7.4.6 Dust Explosion Classes

K_{st} (bar*m/s)	Dust Explosion Class
0–200	St 1
200–300	St 2
>300	St 3

TABLE 7.4.7 Maximum Explosion Pressure and Deflagration Index of Some Common Dusts[10]

Dust	K_{st} (bar*m/s)	P_{max} (bar)	St Class
Grain	89	9.3	1
Coal	85	6.4	1
Flour	63	9.7	1
Sugar	138	8.5	1
Wood	224	10.3	2
Aluminium	515	11.2	3
Sewage sludge	102	8.1	1
GRP dust	216	7.6	2

Table 7.4.7 summarizes the maximum explosion pressure and deflagration index of some common dusts.[10]

7.4.3.4 Case Examples of Serious Accidents of Dust Explosion

The first reported dust explosion accident is possibly a flour explosion in Turin in 1785. Subsequently, dust explosions were gradually recognized as accidents capable of causing severe damage, stimulating research on the mechanisms of dust explosions and related safety measures to prevent them or to protect plant personnel. Research regarding combustible dusts and dust explosions inevitably affected the operations at worksites. The distribution of accidents along with different time periods is represented in Figure 7.4.12.[17]

During the last five years, the most catastrophic dust explosion occurred in a large industrial plant for polishing various aluminum-alloy parts in Kunshan, China on August 2, 2014. The explosion occurred during manual polishing of the surfaces of aluminum-alloy wheel hubs for the car industry. 75 people lost their lives immediately and another 185 were injured. Subsequently, 71 of the seriously injured also died, which increased the total loss of lives to 146. The direct economic loss of was 351 million yuan. This is probably one of the most serious dust explosion catastrophes known apart from some very major coal dust explosion disasters in coal mines. On the basis of investigations on site after the explosion and subsequent laboratory experiments and data analyses it was concluded that the explosion was most probably initiated by self-ignition of contaminated aluminum-alloy dust in the dust collecting barrel below the external bag filter unit in which the initial primary explosion took place (Figure 7.4.13).[18]



FIGURE 7.4.13 Destroyed process lines in Kunshan dust explosion accident.[18]

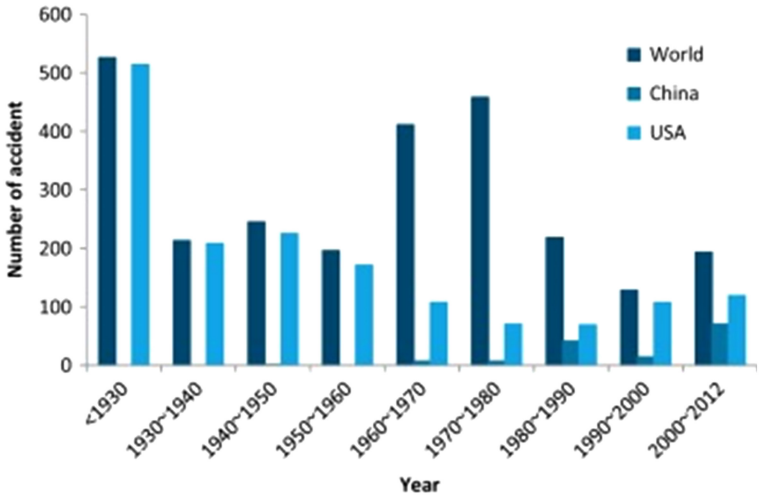


FIGURE 7.4.12 Number of dust explosions in different time periods.[17]

TABLE 7.4.8 Two Groups of Means of Preventing and Mitigating Accidental Dust Explosions[16]

Prevention		
Preventing Explosive Dust Clouds	**Preventing Ignition Sources**	**Mitigation**
Inerting by N_2, CO_2 and other inert gas	Smoldering combustion in dust, dust flames	Explosion isolation
Intrinsic inerting	Open flames	Explosion suppression
Inerting by inert dust	Hot surfaces	Explosion venting
Good housekeeping (dust removal/cleaning)	Electric sparks and arcs, electrostatic discharges	Pressure resistant construction
	Heat from mechanical impact	

TABLE 7.4.9 Relative Merits of Some Commonly Used Inert Gases[19]

Gas	Advantages	Disadvantages
Carbon dioxide	Readily available in compressed form, from proprietary inert gas generators, and in some case as a waste gas from on-site processes. Effective-higher oxygen levels (per cent by volume) are permissible compared with nitrogen. Moderate cost.	Some metal dusts react violently with carbon dioxide (for example, aluminum). Flow of carbon dioxide can generate considerable electrostatic charge.
Nitrogen	Readily available in compressed or cryogenic form, and in some cases as a waste gas from on-site processes. Moderate cost.	Less effective in volume/volume terms than carbon dioxide. Some metal dusts react with nitrogen (for example magnesium) at high temperature.
Rare gases	Unlikely to contaminate products or react with them.	Expensive.
Flue gases	Often readily available as a waste gas from one-site processes or from inert gas generators. Often available at low cost.	Requires additional equipment to cool the gas, remove contaminants, monitor or remove flammable vapors and remove incandescent material. May react with dusts. Storage of flue gas may not be practical, so that adequate quantities may not always be available, for example, during a furnace shutdown.
Water vapor	May be generated by the process.	May not be available during start-up and shut-down. Incompatible with many products. Will condense if temperature falls leading o loss if inert atmosphere.

7.4.4 PREVENTION AND MITIGATION OF ACCIDENTAL DUST

The countermeasures against dust explosion can be pointed out considering "Dust Explosion Pentagon" (Figure 7.4.2). The countermeasures can be divided in two main groups, namely the means for preventing dust explosions and the means for their mitigation. Table 7.4.8 lists the two groups of means of preventing and mitigating accidental dust explosions.[16]

7.4.4.1 Prevention Methods

Prevention methods include preventing the formation of explosive dust clouds and ignition sources. Inerting can be an effective method of the formation of explosive dust clouds. Inerting involves the addition of inert substances to either the dust or the atmosphere to prevent the formation of explosible dust clouds.

Inerting by N_2, CO_2 and Other Inert Gas

Inerting by an inerting gas involved the partial or complete substitution of the air (or any other reactive atmosphere) with which the dust is mixed. Dust explosions can be eliminated if oxygen is excluded completely, or if it is reduced to a concentration (the limiting oxygen concentration) below which flame propagation in the dust cloud, and consequently an explosion cannot occur. Inerting, using an inert gas, is applicable to enclose a plant. A plant that is substantially open to the atmosphere cannot be inerted effectively. Typical inert gases include nitrogen, carbon dioxide, water vapor, and rare gases. Table 7.4.9 shows the relative merits of some commonly used inert gases.[19]

Intrinsic Inerting[16]

In some cases the special protective method called "intrinsic inerting" can be a good solution. This method implies that the required quantity of inert gas is produced in the plant itself, e.g. by controlling combustion in a hot-gas generator and recirculation of the gas. Such hot-gases mainly consist of nitrogen, carbon dioxide, and water vapor. The residual concentration of oxygen is kept at a sufficiently low level to ensure inert conditions. However, normally such combustion gases are not clean enough for being used in connection with food and feed materials, pharmarceuticals, etc.

Inerting by Inert Dust

Explosion dusts are made non-explosible by diluting them with an inert dust such as calcium sulphate, limestone, sodium bicarbonate, common salt, various silicates, or stone dust. Such materials can act as a heat sink or otherwise interfere with flame propagation. In most cases at least 60% diluent dust is required and it is necessary for the diluent dust to be intimately mixed with the explosible dust. Except in coalmines, where it is extensively applied, diluent dust inerting is rarely used because of the large quantities needed and the consequent contamination issue involved.

Good Housekeeping[16]

Considerable quantities of dust can accumulate outside process equipment over a long time due to minor but steady leaks from process equipment. The risk of such leaks is comparatively large if the working pressure inside the process equipment is higher than ambient pressure, whereas running the process at slightly lower than ambient pressure reduces the leaks. Process equipment should be inspected regularly to discover and seal obvious accidental leak points as early as possible. However, often one has to accept a certain unavoidable level of dust leaks from process equipment. It is then important to enforce good housekeeping routines by which accumulations of combustible dust outside process equipment are removed at regular intervals, preferably by explosion-proof vacuum cleaning.

Preventing Ignition Sources

Ignition occurs when the heat generation rate in some volume of the substance exceeds the rate of heat dissipation from the volume and continues to do so as the temperature rises further. According to Scholl (1989)[20] one may distinguish between two categories of ignition sources. Organizational ignition sources, which can be prevented by enforcing adequate working routines, include smoking, open flames, open light (bulbs), welding (gas/electric), cutting (gas/rotating disk), and grinding. Operational ignition sources arise within the process itself and include open flames, hot surfaces, smoldering nests, exothermic decomposition, heat from mechanical impact between solid bodies (metal sparks/hot-spots), and electric sparks/arcs and electrostatic discharges. Among these ignition sources, smoking, hot surfaces, accidental mechanical impacts, and electric sparks and arcs are the most common ignition sources.

Possible methods of preventing smoking in powders with a disposition to self-heat include:[16]

- Control of temperature, moisture, and other relevant powder/dust properties before admitting powder/dust to storage silos
- Adjusting of powder/dust properties to acceptable levels by cooling, drying, etc. before storage, whenever required
- Ensuring that hot solid bodies do not become embedded in the powder/dust mass
- Continuous monitoring of temperature in powder mass at several points by thermometer chains; monitoring of possible development of gaseous decomposition/oxidation products, e.g. CO and methane, for early detection of self-heating

The hot surface temperature of various apparatus can, if the surface is covered by a dust layer, be significant higher that it would normally be without dust, due to thermal insulation by the dust. This both increases the ignition hazard and may cause failure of the apparatus due to increased working temperature. The measures taken to prevent ignition by hot surfaces must cover both layer and cloud ignition. The measures include:[16]

- Removal of all combustible dust before performing hot work; prevention/removal of dust accumulation on hot surfaces
- Isolation or shielding of hot surfaces; use of electrical apparatus approved for use in the presence of the combustible dust of concern; use of equipment with minimal risk of overheating

Although the risk of initiation of dust explosions by accidental single impacts is probably smaller than believed by many in the past, there are special combinations of impacting materials where the ignition hazard is real. It would in any case seem to be good engineering practice to:[16]

- Remove foreign objects from the process stream as early as possible
- Avoid construction and tool materials that can give incendiary metal sparks or thermite flashes
- Inspect process and remove cause of impact immediately in a safe way whenever special noise signals indicating accidental impacts in the process stream are observed

The electrostatic hazard is more complex and it has not always been straightforward to specify clearly defined design guidelines. However, Glor (1988),[21] who has contributed substantially to developing a unified approach, recommends the following measures:

- Use conductive materials or materials of low dielectric strength, including coating, (breakdown voltage across dielectric layer or wall <4 kV) for all plant items that may accumulate very high charge densities (pneumatic transport pipes, dust deflector plates, and walls of large containers that may become charged due to ionization during gravitational compaction of powders). This prevents propagating brush discharges.
- Earth all conductive parts of equipment that may become charged. This prevents capacitive spark discharges from equipment.

- Earth personnel if powder of minimum ignition energies (MIE) <100 mJ are handled. This prevents capacity spark discharges from humans.
- Earth electrically conductive powder (metal, etc.) by using earthed conductive equipment without nonconductive coatings. This prevents capacitive discharges from conductive powder.
- If highly insulating material (resistivity of powder in bulk $>10^{10}$ Ωm) in the form of coarse particles (particle diameter >1 mm) is accumulated in large volumes in silos, containers, hoppers, etc., electrostatic discharges from the material in bulk may occur. These discharges can be hazardous when a fine combustible dust fraction of minimum ignition energy <10–100 mJ is presented simultaneously. So far, no reliable measure is known to avoid this type of discharge in all cases, but an earthed metallic rod introduced into the bulk powder will most probably drain away the charges safely. It is, however, not yet clear whether this measure will always be successful. As a result, the use of dust explosion venting, suppression or inerting should be considered under these circumstances.
- If highly insulating, fine powders (resistivity of powder in bulk $>10^{10}$ Ωm) with a minimum ignition energy <10 mJ as determined with a low-inductance capacitive discharge circuit, is accumulated in large volumes in silos, containers, hoppers, etc., measures of dust explosion mitigation should be considered.

7.4.4.2 Mitigation Methods

Dust Explosion Isolation

Process equipment is, most of the time, connected to other parts of a facility by pipes, such as a dust explosion originating in an enclosure, even vented, will likely propagate through these pipes and reach other equipment or areas. By propagating, the flame front will accelerate and stronger pressure effects will be produced. This means that the resulting explosion in the secondary vessel can be much more violent than the initial event. The objectives of explosion isolation are multiple: firstly, to prevent flame propagation, and therefore ignition of a dust cloud in a secondary enclosure; secondly, to prevent pressure piling and flame jet ignition, i.e. a more severe dust explosion in a secondary enclosure; lastly, to prevent deflagration to detonation transition in pipes (high L/D). Dust explosion isolation can be achieved in two different ways, using either passive or active systems (Table 7.4.10).[22] Basic understanding of flame propagation and pressure build-up in coupled process equipment ("interconnected vessels") is required for specification of performance criteria of various types of active and passive isolation equipment.

Passive systems are activated by the explosion itself and include diverters, float valves, and flap valves. In the case of a flap valve, the pressure generated by the explosion will push a gate and close the pipe, thus avoiding propagation of the flame to the protected area. Passive systems are simpler and typically require less maintenance. Active systems, on the other hand, require tripping by a sensor for activation. Upon triggering, they will close a mechanical valve ahead of the flame front or inject an extinguishing agent in the pipe to stop further flame propagation. Active systems include gate valves, pinch valves, and chemical barriers.

Placement of the device is essential: if an isolation device is placed too far from the ignition, the deflagration can transit into a detonation prior to reaching the device and damage it; if it is placed too close to the ignition, then it may not be entirely closed and able to block the passage of flame when it arrives. The main components that make up the total time for isolation are:

- Time for the pressure growth to exceed the activation pressure of the detector, or for the optical detector to see a flame (T_{ACT})
- Time for the electronics (detector and control panel) to respond (T_{ELEC})
- Time for the mechanical barrier to close, or for the chemical barrier to form (T_{BAR})

$$T_{ISO} = T_{ACT} + T_{ELEC} + T_{BAR} \tag{7.4.5}$$

The time for the flame to travel a certain given distance depends on a number of factors, including the volume (V) of the vessel where the deflagration takes place, the fuel reactivity (K_{St}), the ignition location, the type of protection applied (containment, venting, or suppression), among others. The total time for the isolation process detailed above should always be less than the time for the flame to travel to the barrier's location:

$$T_{ISO} < T_{FLAME} \tag{7.4.6}$$

Dust Explosion Suppression

This active method for dust explosion mitigation is comparatively complex and expensive. It is often used where it is not

TABLE 7.4.10 Dust Explosion Isolation Techniques[22]

Isolation Techniques	Diverter	Float Valve	Flap Valve	Gate Valve	Pinch Valve	Chemical Barrier
Control pressure	×	×	×	×	×	Reduced
Control flame		×	×	×	×	×
Bi-directional barrier	×	×		×	×	×

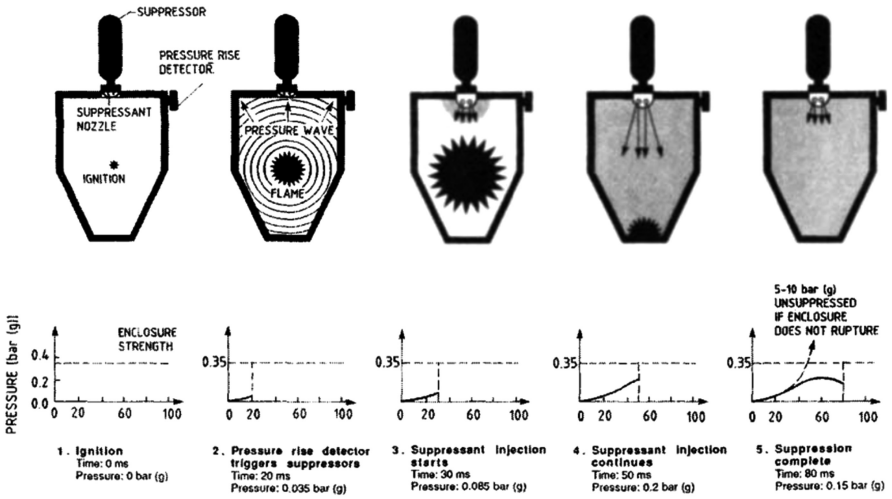


FIGURE 7.4.14 Principles for automatic suppression of accidental dust explosions.[16]

possible to protect by containment or explosion relief venting, and in particular where the pressure and flame of the explosion cannot be vented to a safe location. Dust explosion suppression is particularly important in cases where loss of process containment could cause the emission of toxic dust or other substances harmful to people or the surroundings. Figure 7.4.14 presents the principles for automatic suppression of accidental dust explosions.[16] Following ignition a dust explosion typically takes some 30–100 ms to build up before destructive pressures arise in an enclosure. Dust explosion suppression requires that the incipient explosion is detected soon after ignition, and that sufficient suppressant is discharged into the growing fireball in the enclosure at a fast enough rate to extinguish all flame before a destructive overpressure develops.

A dust explosion suppression system includes the detection system, control system, and injecting suppressant system. The pressure created at an early stage of a dust explosion within an enclosure expands from the flame front at the speed of sound. A low-inertia pressure detection device located at the vessel boundary is well suited to reliably detect the onset of an explosion within milliseconds. Pressure detectors are designed to alarm when a pre-set threshold pressure or a pre-set rate of pressure rise is exceeded in the vessel. The set detection points must be above the process induced pressure fluctuation and be independent of process temperature. The detectors are often programmable so that a detection algorithm can be set up specific to their location and application in the process. More recently, multi-parameter explosion detectors have been developed. These include pressure and infrared (IR) sensors that can be configured and pre-programed to an appropriate algorithm for the specific explosion detection application. It is essential that dust explosion detectors are tolerant of the impact of temperature excursions, vibration and shock, and further that they are resistant to corrosion and moisture ingress. They should also be resistant to abrasion and attrition by the process conditions and provide a hermetic seal between the plant process and the environment.

The active explosion suppression hardware, the explosion detectors and explosion suppressors, plus any explosion isolation hardware such as high-speed gate valves are all connected to a central control and indicating system. Field connection between these components may be radial, or in a loop configuration. The control system of a dust explosion suppression system serves four key purposes:[19]

- It ensures the availability of the system and through interlocks, prevents plant operation unless the explosion suppression system is fully functional
- It activates ALARM closure actions that may be an integral part of the efficacy of the system design, such as blower shut off and isolation valve closure
- It enunciates system status, thus providing information on an ALARM status or a TROUBLE status condition
- It facilitates power back-up such that in any powder outage the process is fully protected through the plant shutdown process

High-rate discharge (HRD) suppressors are the most frequently used dust explosion suppressor type. The HRD suppressor comprises a canister containing a charge of suppressant (liquid, vaporizing liquid, or dry powder) pressurized with nitrogen to a high pressure, usually in the range 20–120 bar. The HRD suppressor has a large diameter valve closure designed to open in a few milliseconds to provide an unimpeded discharge path for the suppressant to be expelled from canister through a discharge nozzle into the plant component. The valve opening time and the mass discharge rate of the suppressant from the HRD suppressor is critical to the effectiveness of the suppression system. The suppressant mass discharge rate dm/dt increases proportionally with the discharge outlet area, A, and the root of the stored pressure, P:

$$\frac{dm}{dt} \propto A \cdot \sqrt{P} \tag{7.4.7}$$

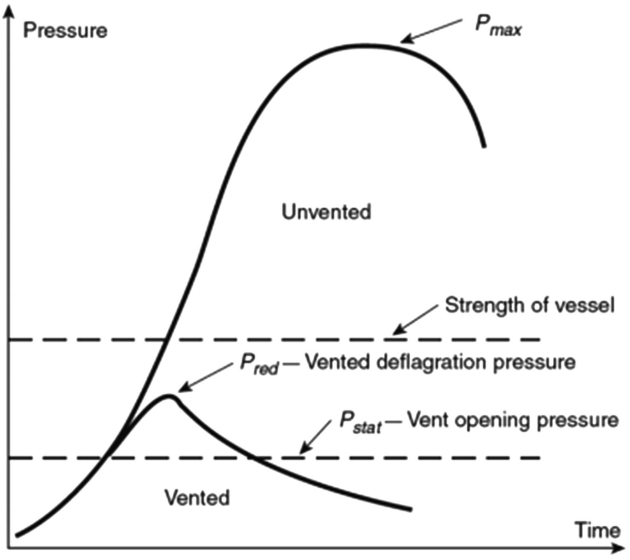


FIGURE 7.4.15 Typical pressure–time history of a vented and unvented dust explosions.[22]

Discharging a spray of liquid or powder suppressant into a growing fireball results in a number of complex effects, which include:

- Quenching–heat abstraction from the combustion zone by energy transfer
- Free radical scavenging–active species in the suppressant compete with chain propagating reactions in the combustion wave
- Wetting–unburned dust particles are rendered non-explosible by absorption of liquid suppressant
- Inerting–concentration of suppressant in suspension in the unburned explosible mixture renders the mixture non-explosible

Dust Explosion Venting

Dust explosion venting is a protective measure that prevents unacceptably high explosion pressures by ensuring that most of the explosion takes place in a safe, open area and not inside a building or dust handling enclosure. Weak areas in the walls of the enclosure are designed to open at an early stage in the explosion. The burning material and products of combustion are released, and the overpressure inside the enclosure is reduced. The residual overpressure from a vented explosion is known as the reduced explosion pressure, P_{red}. Figure 7.4.15 shows the typical pressure-time history of a vented and unvented dust explosions.[22] For the unvented dust explosion, the pressure rises to a maximum value-higher than most plant can withstand. In a vented dust explosion, the maximum pressure is reduced. The value of P_{red} depends on the size and location of the vent, the opening pressure of the vent closure and other factors. The area of the vent is the most important factor that determines the value of P_{red} in a vented dust explosion. Several parameters have an influence on the required area for venting of dust explosions: enclosure volume, length/diameter ratios of enclosure, maximum overpressure P_{red} that the enclosure can withstand, static opening overpressure P_{stat} of vent cover, mass of vent cover, and burning rate of the dust cloud.

For some time it was thought by many that the burning rate of a cloud of dust in air was a constant property of a given dust, which could be determined once and for all, e.g. in the standard 1 m^3 closed vessel test. However, a cloud in air of a given dust can burn with widely different combustion rates, depending on the dust concentration, the turbulence, and the degree of dust dispersion in the actual industrial situation. This means that the required vent depends markedly on the specific industrial situation of dust cloud generation and flame propagation. As a result, a differentiated view on dust explosion venting sizing has gradually evolved, which has been taken into account in the lasted European Union dust explosion venting standard issued by CEN (2002a) and NFPA 68-2013 standard.

Dust explosion venting prevents rupture of the enclosure in which the explosion takes place. However, significant hazards still remain. These include:[16]

- Ejection of flame jets and flame balls from the vent opening
- Emission of blast wave from the vent opening
- Reaction forces on the equipment, caused by the venting process
- Emission of solid objects (vent panels and other possible objects)
- Emission of toxic combustion products

In general, flame ejection will be more hazardous the larger the vent and lower the static opening pressure of the vent cover. This is because with a large vent and a weak cover, efficient venting will start at an early stage of the combustion process inside the enclosure. Then large clouds of unburned explosive mixture may be pushed out through the vent and subsequently ignited when the flame passes through the vent. The resulting secondary fire ball outside the vent opening can present a substantial hazard. If the enclosure is strong, allowing the use of a small vent and a high P_{red}, mainly combustion products are vented, and the flame outside the vent is considerably smaller.

One traditional solution to the flame jet and flame ball problem is the use of a vent duct. This means that a duct of cross-sectional area at least equal to the vent area is mounted between the vent and a place where a flame jet or flame ball will not present any hazard. However, vent ducts will generally increase the flow resistance, and there is also the pressure difference to the atmosphere. Consequently, adding a vent duct increases the maximum explosion pressure in the vented vessel. The pressure increases with increasing duct length, increasing number of sharp bends, and decreasing dust diameter.

Reaction forces from dust explosion venting can significantly increase both the material damage and the extent of the explosion. Process equipment which can tilt ducts can become

torn off, and secondary explosive clouds can be formed and ignited. Whenever a dust explosion vent is installed, it is therefore important to make an assessment of whether the equipment to be vented is able to withstand the reaction forces from explosion venting. The reaction force and its duration can be calculated by:[19]

$$F_r = 1200\,AP_{red} \tag{7.4.8}$$

$$t_F = \frac{0.01\,K_{st}V^{1/3}}{AP_{red}} \tag{7.4.9}$$

REFERENCES

1. Eckhoff, R. K., *Dust Explosions in the Process Industries, Third Edition: Identification, Assessment and Control of Dust Hazards*, Gulf Professional Publishing, 2003.
2. Dobashi, R., *Fire Safety J.*, 91, 21–27, 2017.
3. Chen, J. L., Dobashi, R., Hirano, T., *J. Loss Prevent. Proc.*, 9, 225–229, 1996.
4. Gao, W., et al., *J. Loss Prevent. Proc.*, 36, 186–194, 2015.
5. Wilson, L., McCutcheon, D, *Industrial Safety and Risk Management*, University of Alberta Press, Edmonton, Canada, 2003.
6. Abuswer, M., Amyotte, P., Khan, F., *J. Loss Prevent. Proc.*, 26, 283–289, 2013.
7. Dobashi, R., *J. Phy. Conf. Ser.*, 170, 012029, 2009.
8. Gao, W., et al., *J. Loss Prevent. Proc.*, 26, 186–196, 2013.
9. ASTM E1491, Standard test method for minimum autoignition temperature of dust clouds, *The American Society of Mechanic Engineers*, 2006.
10. Bi, M. S., Yang, G. G., *Gas and Dust Explosion Prevention and Protection*, Chemical Industry Press, Beijing, 2012.
11. ASTM E2019-03, *Am. Soc. Mech. Eng.*, 2007.
12. ASTM E1515, *Am. Soc. Mech. Eng.*, 2012.
13. ASTM E2931-13, *Am. Soc. Mech. Eng.*, 2013.
14. ASTM E1226, *Am. Soc. Mech. Eng.*, 2010.
15. Proust, C., Accorsi, A., Dupont, L., *J. Loss Prevent. Proc.*, 20, 599–606, 2007.
16. Eckhoff, R. K., *Explosion Hazards in the Process Industries*, Gulf Professional Publishing, 2005.
17. Yuan, Z., Khakzad, N., Khan, F., Amyotte, P., *Process Saf. Environ.*, 98, 57–71, 2015.
18. Li, G., Yang, H. X., Yuan, C. M., Eckhoff, R. K., *J. Loss Prevent. Proc.*, 39, 121–130, 2016.
19. Barton, K., *Dust Explosion Prevention and Protection: A Practical Guide*, Gulf Professional Publishing, 2002.
20. Scholl, E. W., *VDI-Berichte*, 701, 477–489, 1989.
21. Glor, M., *Electrostatic Hazards in Powder Handling*, Research Studies Press Ltd., John Wiler & Sons Inc, 1988.
22. Taveau, J., *J. Loss Prevent. Proc.*, 48, 320–330, 2017.

Index

μCT, *see* X-ray micro computed tomography (μCT)
χ potential, 85
3D morphological analysis, 25
3D printing, 153–154

ABF, *see* Agglomerate bubbling fluidization (ABF)
Acidic alkoxides, 276
AC-magnetic-field-type separator, 461
Acoustic coagulation, 131
Acoustic method, 17
Activators, 499–500
Active pharmaceutical ingredients (APIs), 174, 405, 407
Active systems, 629
Additive manufacturing (AD), 153
Additives, 155, 163, 175, 235, 381, 430
ADEM, *see* Advanced DEM (ADEM)
Adhesion of powder bed, 225
  horizontal tensile method, 225
  vertical tensile method, 225
Adhesive force, 113–119
  in gaseous state, 113–116
    comparison, 115–116
    electrostatic force, 114–115
    liquid bridge force, 115
    van der Waals force, 113–114
  in liquid state, 116–117
  measurement, 117–119
    exerted on single particle, 118–119
    methods, 117–118
Adhesive water, 193–194
Adiabatic-type bed, 217
Adsorption characteristics, 185–190
  measuring method, 185–186
    liquid-solid system, 185
    sample pretreatment, 185–186
    vapor-solid system, 185
  overview, 185
  surface properties estimation, 188–190
    adsorption isotherm measurement, 188
    heat of immersion, 188–189
    IR spectroscopy, 189
    pore size analysis, 190
    specific surface area, 189–190
    surface fractal dimension, 190
  theory of adsorption isotherms, 186–188
    BET equation, 187
    Freundlich equation, 187
    Henry equation, 186–187
    IUPAC types, 187–188
    Langmuir equation, 187
Adsorption isotherms, 185
  measurement, 188
  theory, 186–188
    BET equation, 187
    Freundlich equation, 187
    Henry equation, 186–187
    IUPAC types, 187–188
    Langmuir equation, 187
Adsorption layer, 42, 85
Adsorption water, 193, 194
Advanced DEM (ADEM), 536
Aerosol entrainment, 267
Aerosol particle generation, 261–268
  condensation methods, 265–267
    fume generation, 267
    inert gas, 267
    mists generation, 265–267
  fluids atomization, 261–265
    centrifugal atomizer, 264
    electrosprays, 263–264
    FMAG, 265
    nebulizers, 262–263
    pressure atomizers, 262
    two-fluid atomizers, 262
    ultrasonic nebulizers, 263
    VOAG, 264–265
  overview, 261
  powder dispersion, 267–268
Aerosol particle mass (APM) analyzer, 30
AFM, *see* Atomic force microscope (AFM)
After-filters, 511
Agglomerate bubbling fluidization (ABF), 530
Agglomerate particulate fluidization (APF), 530
Agglomerates
  breakage analysis, 148
  sintering modeling, 151–152
Agglomeration, *see* Coagulation
Agitated through dryer, 434
Agitation methods, 425
Agitation mill, 330
AIBN, *see* Azobisisobutyronitrile (AIBN)
AIJ, *see* Architectural Institute of Japan (AIJ)
Air-assisted screening machine, 360
Air-blast atomizers, 262
Air filters, 445, 450–452
Airline respirators, 614
Air-purifying respirators, 613–614
  filter classes of particulate respirators, 614
  filtration mechanisms and lifetime, 613–614
  non-powered, 613
  powered, 613
ALE, *see* Arbitrary Lagrangian–Eulerian (ALE) method
Alkalic alkoxides, 276
Alkali-precipitation method, 275
Alkyl silane reagent method, 46
Allergic reactions, 605
Ammonia, 49, 50
Amorphous form, 174
Analytical ultracentrifugation (AUC), 59
Andreasen pipet method, 14
Angle of collapse, 234
Angle of repose, 232, 234
Angle of spatula, 234
Angular bend function method, 23–24
Anion water, 193
Anisokinetic sampling
  error, 567–568
  particle size distribution and, 570–573
Anisometry, 21
Anisotropy, 33, 65, 201
Annular ring shear tester, 224
APF, *see* Agglomerate particulate fluidization (APF); Assigned protection factor (APF)
APIs, *see* Active pharmaceutical ingredients (APIs)
APM, *see* Aerosol particle mass (APM) analyzer
Apparent dielectric constant, 197
Apparent viscosity, 415
APPIE, *see* Association of Powder Process Industry and Engineering (APPIE)
Aqueous solutions and charge control, 305–308
  non-aqueous, 308–309
  polymers, 308
  potential in diffuse layer, 305–307
  specific adsorption, 307
  surfactants, 307–308
Arbitrary Lagrangian–Eulerian (ALE) method, 396–397, 552
Arch breaker, 241
Architectural Institute of Japan (AIJ), 366
Arrhenius reaction scheme, 168
Artificial neural networks, 25
Ash contents, 167
Assigned protection factor (APF), 609, 615
Association of Powder Process Industry and Engineering (APPIE), 69, 375
Atomic force microscope (AFM), 34, 35, 50, 53, 54–57, 59, 116
  force measurements, 55–57
    in gas and liquid phase, 56–57
    principle of, 55–56
  overview, 53
  principle, 53–54
  surface characterization, 54–55
Attenuation technique, 576–577
Attrition force, 340
AUC, *see* Analytical ultracentrifugation (AUC)
Autocorrelation function, 78
Axial cyclone, 447
Azobisisobutyronitrile (AIBN), 309

Backward sampling method, 573
$BaCO_3$ formation, 162–163
Ball-media agitation type grinders, 329
Barite, 162–163
Barrell-Joyner-Halenda (BJH) method, 213
Barrier-type dust collectors, 445, 452–453
  bag filters, 452–453
Basset–Buossinesq–Oseen equation, 106
Batch grinding, 325–326
Batch-settling test, 413
BD, *see* Brownian dynamics (BD)
Belt feeders, 373
Belt press, 493
Belt scale, 577
Belt-type separator, 461
Benesi method, 49
Berkovitch indenter, 37, 39
BET, *see* Brunauer-Emmett-Teller (BET) equation
Biaxial tester, 223
Bingham constitutive equation, 201
Bingham fluids, 381
Bingham model, 139, 142
Biomass, 164
Bipolar ions and diffusion charging, 301, 302–303

Birth–death equations, 301, 302
BJH, *see* Barrell-Joyner-Halenda (BJH) method
Blockage in storage vessels, 237–241
  experimental study, 240–241
    centrifugal miniature silo, 240–241
    two-dimensional coarse particles, 240
  mechanisms and flow criteria, 237–240
    arching of fine powders, 237–239
    critical size of outlet, 239–240
    interlocking of coarse particles, 237
  overview, 237
  phenomena, 237
  preventing, 241
    arch breaker, 241
    flow-promoting device, 241
Böettcher model, 197
Boltzmann equilibrium charge distribution, 28
Bonded Particle (BP) model, 547, 548
Bond's law, 326
Bond's work index, 327–328
Bound water, 193–194
BP, *see* Bonded Particle (BP) model
Brittle failure mode, 146
  breakage analysis for, 146–147
Brittle fracture, 38
Broadbent-Callcott equation, 325
Brønsted acid site, 50, 189
Brownian coagulation, 129–131
  and stability ratio, 135–136
Brownian diffusion, 9, 97, 98, 101, 129
Brownian displacement, 604
Brownian dynamics (BD), 551
Brownian motion, 29, 97, 101, 133, 134, 201
Brunauer-Emmett-Teller (BET) equation, 18, 179–180, 187, 315
Bubble-point method, 214
Bubbling bed, 439
Bubbling fluidization, 387, 390
Buckingham-Reiner equation, 142
Bulk density, 27, 30
Bulkiness factor, 21–22
Bulk polarization theory, 201
Burke–Plummer equation, 219

CAFM, *see* Conductive AFM (CAFM)
Cake filtration theory, 481–484
  average specific resistance, 483
  drag acting on particles, 482
  equations of filtrate flow, 481–482
  material balance, 483–484
  porosity and specific resistance, 482–483
Calcium oxide (CaO), 158, 161, 162
Cancer, 605
Capillary condensation, 211–212
Capillary state, 418
Capillary suction time (CST), 477
Capillary tube, 340
Capillary viscometer, 141–142
Carbogenetic nanoparticles, 312
Carbon black, 607, 608
Carbon nanotubes, 64
Carman's tortuousity model, 218
Carpco high-intensity wet magnetic separator, 464
Carpenter's method, 564
Carrier magnetic separation, 467–468
Cartridge filter type, 511
Cascade-impactor, 16
Catalytic particles, 65–67
CCD, *see* Charge coupled device (CCD)
Celestite, 162–163
Cellular automaton, 542
Center-to-center approach, 152
Centrifugal atomizer, 264
Centrifugal classifiers, 349
Centrifugal collectors, 447
Centrifugal force, electrostatic and, 29–30
Centrifugal miniature silo, 240–241
Centrifugal particle mass analyzer (CPMA), 30
Centrifugal type separator, 358–359
Centrifuge method, 117
CFB, *see* Circulating fluidized bed (CFB)
CFD, *see* Computational fluid dynamic (CFD) simulation
CFD–DEM method, 124, 393, 394, 395
CFD–Lagrangian method, 123, 124
CGP, *see* Coarse-grained particle (CGP)
Channel model, 217–218
Chaotropic properties, 307
Charge coupled device (CCD), 12, 13
Charge relaxation, 81
Chemical adsorption, 185
Chemical interaction, 315
Chemical methods, 311–313
  in-situ surface modification, 311–312
  molecular structure design, 312–313
  surface layer structure formation, 313
  treatment on particle surface, 311
Chemical reaction methods, 46
Chemical surface relaxation, 42–43
Chemical vapor deposition (CVD), 286
Chevron notch bar (CNB), 37
Chinese Academy of Sciences, 389, 393
Chipping, 147
Chipping-fragmentation transition, 148
Chromatographic method, 15
Chute riffler/splitter, 564
Circulating fluidized bed (CFB), 388, 390–391
Clay minerals, 85
CMOS, *see* Complementary metal oxide semiconductor (CMOS)
CNB, *see* Chevron notch bar (CNB)
Coacervation technique, 277
Coagulants, 477
Coagulation, 60, 129–137, 301, 524
  in gaseous state, 129–133
    acoustic, 131
    Brownian, 129–131
    laminar and turbulent, 131
  in liquid state, 133–137
    kinetic interaction, 134–137
    static interaction, 133–134
Coalescence and consolidation, 417–418
Coal gasifier, 517
Coarse flotation, 505
Coarse-grained particle (CGP), 539–540
Coarse grinding, 328–329
Coaxial double cylinder type rotational viscometer, 411, 412
Co-current-flow-type bed, 517
Coe and Clevenger method, 479–480
Coefficient of variation (CV), 565
Co-grinding, 286
Cohe tester, 223
Collectors, 499
Colloid vibration potential (CVP) effect, 17
Column cells, 501
Column structures and conductivity, 199–200
Combined water, 193
Combustion, 439–443
  burner, 441–442
  control, 439–440
  furnace, 442–443
  kiln, 443
  overview, 439
  reaction, 167–169
    devolatilization and ignition, 167–169
    fuel properties, 167
    solid, 169
    solid fuel, 167
Combustion Triangle, 617
Comminution, 145, 319, 523, 536; *see also* Material comminution
Compaction, 62, 234, 237, 241, 417, 421, 422, 425, 430
Complementary metal oxide semiconductor (CMOS), 12, 13
Complex fluoride synthesis, 159
Complex oxides synthesis, 155–159
Composite particles
  design, 313
  formation, 285–296
    materials, 286–287
    particulate design and preparation, 287–296
    process, 285–286
    structure, 285
  synthesis, 282–284
Compressibility, 234
Compression
  behavior, 323–324
  flow, 233
  strength, 226, 229
Computational fluid dynamic (CFD) simulation, 123, 124, 334, 362, 393, 394, 395, 406, 536
Computational methods for fluidization, 389–397
  continuum model, 392–393
  discrete particle method, 393–396
  DNS, 396–397
    lattice-based method, 397
    NS equation-based, 396–397
    particle-based methods, 397
  steady-state modeling, 389–392
Concavity and robustness, 22
Condensation methods, 265–267
  fume generation, 267
  inert gas, 267
  mist generation, 265–267
Condensation particle/nucleus counter (CPC/CNC), 12, 16, 30, 59
Conductive AFM (CAFM), 55
Conductive dryer, 436
Conductive heat transfer, 433, 434
Cone-flat plate type rotational viscometer, 411
Consolidation yield locus (CYL), 223, 226, 228–229
Constant compliance region, 56
Constant gas volume method, 28
Constant-pressure filtration, 481, 484
Constant-rate filtration, 481, 484–485
Constant volume shear tester, 224
Constitution water, 193
Contact electrification, 81, 303–305
Contact mode, 53, 54
Contact potential difference (CPD), 198–199, 304, 305, 457

Contact-type thermometers
points of measurement, 585–586
typical, 585
Continuous expression equipment, 493
Continuous gas phase synthesis, 522
Continuous high-gradient magnetic separator (SALA-HGMS), 464–465
Continuous level meters, 581
Continuous separator, 475
Continuum mechanics, 229, 548–549
Continuum model, 392–393
Control bands, 608–609
Controlled-release technology, 295
Control of Substances Hazardous to Health (COSHH), 608
Convection-diffusion equation, 121, 123
Convection mechanism, 430
Convective heat transfer, 433
Convective mixing, 401, 402, 407, 409
Conventional crystallization, 279
Coordinated water, 193
Co-precipitation, 275, 286
Core-shell nanoparticles, 293–294
Coriolis force flowmeter, 578
Corner-firing furnace, 443
Corona charging and induction charging, 455, 512
Corona-charging guns, 509
Corona discharge, 299
COSHH, *see* Control of Substances Hazardous to Health (COSHH)
Cosolvents, 171–172
Couette flow, 107, 229
Coughing and sneezing, 604
Coulomb equation, 227
Coulomb force, 82
Counter-flow-type bed, 517
Counting analysis, 10, 11–13
dynamic image analysis method, 12
electro sensing zone method, 13
light extinction method, 12–13
light scattering method, 12
particle tracking method, 13
static image analysis method, 12
time-of-flight method, 13
Coupled-pole dry separator, 464
CPC/CNC, *see* Condensation particle/nucleus counter (CPC/CNC)
CPD, *see* Contact potential difference (CPD)
CPMA, *see* Centrifugal particle mass analyzer (CPMA)
Critical powder volume concentration (CPVC), 429, 432
Critical state line (CSL), 223, 226
Crossflow filtration, 487
Crushing and grinding, 319–334
comminution of materials, 324–334
Bond's law, 326
devices, 328–330
improvement of efficiency, 330–334
Kick's law, 326
mean particle size, 324
parameters correlation in distribution equations, 325
phenomena, 324
rate process in batch grinding, 325–326
resistance and grindability, 327–328
Rittinger's law, 326
size distribution equation, 324–325
Tanaka's theory, 326–327
overview, 319
single particle compression by parallel plates, 319–324
compression behavior, 323–324
fracture energy, 319
impact fracturing velocity, 321–323
loading rate effect, 321
moisture effect, 320–321
size effect, 320
Crystal growth rate, 281
Crystalline forms, 171, 174
Crystallization, 279–284
composite particles synthesis, 282–284
crystal growth rate, 281
nucleation rate, 280–281
overview, 279
powder properties control, 281–282
solid-liquid equilibrium, 279–280
supersaturated solution, 279–280
Crystal polymorphism, 282
Crystal water, *see* Combined water
CSL, *see* Critical state line (CSL)
CST, *see* Capillary suction time (CST)
Cubic container mixer, 407
Cumulants method, 16
Cumulative distribution, 4
Cunningham factor, 60
Curvilinear classifier, 348
Cutter sampler, 563
Cutting-edge technology, 285
$Cu/ZnO/Al_2O_3$ methanol catalysts, 67
CV, *see* Coefficient of variation (CV)
CVD, *see* Chemical vapor deposition (CVD)
CVP, *see* Colloid vibration potential (CVP) effect
Cyclodextrin, 174–175
Cyclone after filter type, 511
Cyclone-type classifiers, 349
CYL, *see* Consolidation yield locus (CYL)
Cylindrical electrodes, 196, 197

Damköhler number, 620
DDPM, *see* Dense discrete phase model (DDPM)
Deactivators, 499
De Beers Consolidated Mines Ltd., 469
Debye-Huckel approximation, 134, 306
Debye length, 86, 525, 552
Decomposition of compound, 275
Deflocculation, 341, 343, 345
Delft Head Loss & Limit Deposit Velocity (DHLLDV) Framework, 382
DEM, *see* Discrete element method (DEM); Distinct element method (DEM)
Dense discrete phase model (DDPM), 396
Density distribution, 4–7
Density functional theory (DFT), 212
Deposition velocity, 381, 382
Depressants, 499
Depth filtration, 481
Derjaguin-Landau-Verwey-Overbeek (DLVO) theory, 56, 133–134, 496, 497, 525, 526, 528, 550
DES, *see* Detached eddy simulation (DES)
Design Recommendation for Storage Tanks and Their Supports, 366
Detached eddy simulation (DES), 123
Deterministic approach, 301
Deutsch equation, 448
Devolatilization, 167–169
DFT, *see* Density functional theory (DFT)
DHLLDV, *see* Delft Head Loss & Limit Deposit Velocity (DHLLDV) Framework
Diaphragm level switches, 582
Dielectric constants, 196–197
Dielectric-constant-type moisture sensors, 589, 591
Dielectrophoresis, 18
Differential mobility analyzer (DMA), 16, 28, 29, 30, 59
Differential pressure method, 578
Diffuse reflectance spectroscopy (DRS), 189
Diffusion, 151
charging, 299, 301
by bipolar ions, 302–303
by unipolar ions, 301–302
coefficient, 60, 130
diameter, 3
effect, 246–247
inertia model, 102
Diffusion-controlled reaction, 273
Diffusive mixing, 401, 402, 409
Dimethyl-β-cyclodextrin, 175
Dings-induced roll separator, 464
Dipolar interaction energy, 199–200
Direct numerical simulation (DNS), 102, 123, 396–397, 539, 544, 551–557
colloidal particles dynamics, 553
colloid-solute/solvent boundary conditions, 553–554
electrophoresis, 555–557
mobility and ζ potential, 556
mobility in concentrated dispersions, 556–557
numerical calculations, 556
lattice-based method, 397
mesoscopic modeling for electrokinetics, 551–552
NS equation-based, 396–397
overview, 551
particle-based methods, 397
smoothed profile method, 554–555
equations for colloidal dispersions, 554
for particle–solvent/solute boundary, 554
temporal discretization, 554–555
solute and solvent dynamics, 552–553
Direct particle breakage models, 536
Direct shear test, 223
Direct Simulation Monte Carlo (DSMC), 393, 545
Discreet Numerical Model, 365
Discrete element method (DEM), 62, 123, 240, 243, 343, 362, 394, 395, 397, 406, 535–557, 545–548
coarse-grained particle (CGP), 539–540
comminution, 536
development of large-scale simulation, 538–539
granulation, 536
for industrial applications, 542–543
ironmaking process, 537
large-scale simulations without, 542
mixing, 536
problems, 538
representation of particle shape, 540–541
sieving and filtration, 536–537
slow powder flow, 535–536
Discrete level meters, *see* Level switches
Discrete particle method, 393–396
Disk-type coating machine, 510
Dispersants, 500

Dispersion interaction, 60
Dispersion polymerization technique, 277
Dispersity, 59–60
Disposable air filter, 451
Dissipative particle dynamics (DPD), 552
Dissolution, 604
  property, 171
  rate analysis, 172–175
Distinct element method (DEM), 544, 598
Distributed Lagrangian multipliers (DLM) method, 552
DLM, *see* Distributed Lagrangian multipliers (DLM) method
DLS, *see* Dynamic light scattering (DLS)
DLVO, *see* Derjaguin-Landau-Verwey-Overbeek (DLVO) theory
DMA, *see* Differential mobility analyzer (DMA)
DMT theory, 113
DNS, *see* Direct numerical simulation (DNS)
DNS–Lagrangian method, 123
D_2O displacement method, 46
Double alkoxide method, 275–276
Double-cone mixer, 407
DPD, *see* Dissipative particle dynamics (DPD)
Drag force shape factor, 24–25
Drag model, 219
Droplet state, 418
Droplet-to-powder conversion, 270
DRS, *see* Diffuse reflectance spectroscopy (DRS)
Drum granulator, 421
Drum-type magnetic separator, 461, 463
Dry classification, 348–351
  centrifugal classifiers, 349
  cut size control, 349
  cyclone performance, 349–351
  gravitational classifiers, 348
  inertial classifiers, 348
Dry collector, 445
Dry dense medium separation, 473–475
  application, 475
    continuous separator, 475
    ore particles, agricultural products, and waste materials, 475
  fluidization intensity effect, 474
  fluidized bed density
    control, 473–474
    estimation, 473
  overview, 473
  size effect of objects, 474
  wet object using hydrophobic powder, 474–475
Drying, 433–436
  and dryer
    design, 434–436
    selection, 434
  process, 433
  rate, 433–434
Dry kiln, 443
Dry operation, 328
DSMC, *see* Direct Simulation Monte Carlo (DSMC)
Ductile failure mode, 146
Dust collectors, 445–453
  barrier-type, 452–453
    bag filters, 452–453
  flow-through-type, 446–449
    centrifugal, 447
    ESP, 448–449
    gravitational, 446–447
  obstacle-type, 449–452
    air filters, 450–452
    inertial, 450
  overview, 445–446
  scrubbers, 453
Dust explosion, 617–632
  definition, 617
  flame propagation mechanism, 617–620
    observed, 617–618
    particle size distributions, 619–620
    particle thermal characteristics, 618–619
    transition, 620
  mitigation methods, 629–632
    isolation, 629
    suppression, 629–631
    venting, 631–632
  prevention methods, 627–629
    good housekeeping, 628
    ignition sources, 628–629
    inerting by inert dust, 628
    inerting by N_2, CO_2 and other inert gas, 627
    intrinsic inerting, 627
  risk, 621–626
    accidents, 626
    analysis and management, 621
    consequence, 624–626
    occurrence probability, 621–624
Dust Explosion Pentagon, 627
Dust removal equipment, 445
Dynamic image analysis method, 12
Dynamic light scattering (DLS), 16–17, 59, 289
Dynamic mode, 53–54, 55
Dynamic separator, 470
Dynamic shape factor, 25

Earth Simulator, 539
ECT, *see* Electrical capacitance tomography (ECT)
Eddy-current separation, 461, 470
EDEM and TBBM contact bonding model, 547
EDL, *see* Electric double layer (EDL)
Effective density, 29
Eh modifiers, 500
Einstein equation, 140
Ejector, 340
Elastic deformation, 33, 36, 37, 145
Elastic impact, 145
Elastic modulus, 33, 35
Elastic-perfectly plastic indentation, 34
Elastic-plastic analysis, 145
Elasto-plastic and adhesion effects, 145–146
Elasto-plastic deformation, 145
Elbow type classifier, *see* Rectilinear classifier
Electrical appliances recycling, 459
Electrical capacitance tomography (ECT), 597
Electrical charge control, 299–309
  in gaseous state, 299–305
    contact electrification, 303–305
    gaseous ions and electrons, 299–303
  in liquid state, 305–309
    aqueous solutions, 305–308
    chemical reaction in aqueous and non-aqueous solutions, 308–309
Electrically forced vibration, 576
Electrical method, 579
  level measurement, 582–583
    electric capacitance level meters, 582
    electric resistance level meters, 582–583
    microwave level meters, 583
  moisture content, 589–591
Electrical mobility classification method, 16
Electrical properties
  in gaseous state, 195–199
    contact potential difference, 198–199
    dielectric constants, 196–197
    specific charge, 197–198
    specific resistance, 195–196
  of nanoparticles, 63–64
  in nonaqueous solutions, 199–202
    column structures and conductivity, 199–200
    conductivity of flocculated suspensions, 199
    rheological and optical properties, 201–202
Electrical resistance methods, 598, 599
Electric capacitance change, 575
Electric capacitance level meters, 582
Electric double layer (EDL), 41, 83, 85–86, 552, 557
Electric filter, 452
Electric leakage, 305
Electric resistance level meters, 582–583
Electric-resistance-type moisture sensor, 589
Electrification and electrophoresis, 81–89
  in gaseous state, 81–83
    charged particle motion, 82–83
    contact electrification, 81
    particle by impact, 81–82
    particle through breakage, 82
  in liquid state, 83–89
    electric double layer (EDL), 85–86
    particle mobility with its zeta potential, 86, 89
    surface charging of particulate substances, 83–85
    zeta potential measurements, 89
Electrokinetic measurements, 89
Electro-kinetic sonic amplitude (ESA) effect, 17
Electromagnetic fields, 461
Electromagnetic flowmeter, 579
Electromagnetic forces, 461
Electromagnetic induction, 579
Electromagnetic-induction-type separator, 461, 470
Electromagnetic radiation, 75
Electromagnetic theory, 75
Electromagnetic waves, 63, 579, 586
Electrometer, 16
Electroneutrality principle, 305
Electronic miniaturization, 539
Electron spin resonance (ESR), 161
Electrophoresis, 83, 555–557
  mobility and ζ potential, 556
  mobility in concentrated dispersions, 556–557
  numerical calculations, 556
Electrophoretic mobility, 60
Electrorheological (ER) effect, 140, 201
Electro sensing zone method, 13
Electrosprays, 263–264
Electrostatic charging, 575–576
Electrostatic energy, 301
Electrostatic filters, 452, 613, 614
Electrostatic force, 82, 100, 113, 114–115, 451, 455
  and centrifugal force, 29–30
  and gravity, 28–29
Electrostatic induction, 579
Electrostatic interactions, 60, 524–525

Electrostatic powder coating, 509–512
  booth, 510–511
    cartridge filter type, 511
    cyclone after filter type, 511
  machines, 509–510
    corona-charging guns, 509
    disk-type coating machine, 510
    transfer efficiency, 510
    tribocharging guns, 509–510
  numerical simulation, 511–512
    air flow field, 512
    electric field, 512
  overview, 509
  powder feeding machine, 510
    screw feeder, 510
    table feeder, 510
Electrostatic precipitator (ESP), 448–449
Electrostatic separation, 455–460
  machines, 457–459
    electrical appliances recycling, 459
    mineral resources refining, 457
    pulverized coal, 457–458
    waste electrical wires, 459
    waste plastics, 458–459
  mechanism, 455–457
    corona and induction charging, 455
    factors in relation to, 455–457
    induction charging, 455
    tribocharging, 457
Electrostatic stabilization, 525–526
Electrosteric stabilization, 526–527
Elongational flows, shear and, 341–343
EMMS, *see* Energy-minimization multiscale (EMMS) model
Emulsification, 522
Emulsion polymerization, 276
Encapsulation, 285, 286
Energy conservation, 392, 395, 512, 542
Energy-minimization multiscale (EMMS) model, 389, 390, 391, 393, 396
Ennis's model, 418
Ensemble analysis, 10, 16–18
  acoustic method, 17
  dynamic light scattering method, 16–17
  induced gradient method, 17–18
  laser diffraction/scattering method, 17
  small angle X-ray scattering method, 17
Entrained-bed combustion, 439
Equal-size spheres packing, 203–205
Equation of continuity, 122, 490
Equation of motion, 15, 82, 97, 379, 511, 542, 543
Equation of particle motion, 106–107
Equation of state, 512
Equivalent area diameter, 3
Equivalent diameter of sphere, 9
ER, *see* Electrorheological (ER) effect
Ergun's equation, 219, 385, 530
Eriz-type separator, 464
ESA, *see* Electro-kinetic sonic amplitude (ESA) effect
ESP, *see* Electrostatic precipitator (ESP)
ESR, *see* Electron spin resonance (ESR)
Eulerian diffusion models, 102, 103
Eulerian-Eulerian method, *see* Two-fluid model (TFM)
Eulerian–Lagrangian method, 123
Eulerian method, 121, 122–123
European standards test filter penetration, 614
Evaporation and condensation, 151
Exothermic reaction, 515, 516
Expression, 489–493
  basis, 489
  equipment, 492–493
  modified Terzaghi model, 489–491
  overview, 489
  secondary consolidation, 491–492
  simplified analysis, 492
EXtended Finite Element Method (XFEM), 549
External-mixing type atomizer, 262
Extinction of incident light, 75
Extrusion, 425–426, 430, 432

Fabric filters, *see* Bag filters
Fanning's equation, 217, 218
Faraday cage, 197, 198
Faraday's law, 579
FASP, *see* Flame-assisted spray pyrolysis (FASP)
Fast fluidization, 387, 390
Fast Fourier transformation (FFT), 16
FCM, *see* Force coupling method (FCM)
FCS, *see* Fluorescence correlation spectroscopy (FCS)
Feed hoppers, 371
"Feed-out" bulk solids, 364
FEM, *see* Finite element method (FEM)
Feret diameter, 3, 20, 22
Ferrofluid, *see* Magnetic fluid
Ferromagnetic material, 93–94
Ferromagnetic nanoparticles, 65
FFF, *see* Field flow fractionation (FFF)
FFT, *see* Fast Fourier transformation (FFT)
FHH, *see* Frenkel-Halsey-Hill (FHH) theory
Fibrous filters, 536–537
Fibrous mat, 219–220
Fick's law, 173
Field charging, 196, 299, 300–301
Field flow fractionation (FFF), 15, 59
Film-type kneading, 429
Filter press, 486–487
Filtrate flow equations, 481–482
Filtration, 481–488
  cake, 481–484
    average specific resistance, 483
    drag acting on particles, 482
    equations of filtrate flow, 481–482
    material balance, 483–484
    porosity and specific resistance, 482–483
  constant-pressure filtration, 484
  constant-rate filtration, 484–485
  equipment, 486–488
    filter press, 486–487
    rotary drum filter, 487
    thin-cake/dynamic filter, 487–488
  internal structure, 485–486
  non-Newtonian fluid–solid mixtures, 486
  overview, 481
Fine grinding, 329–330
Finite–discrete element, 548
Finite element method (FEM), 229, 406, 539, 544, 548
Fire Triangle, *see* Combustion Triangle
Fitting method, 490
Fixed bed, 515–516
  application, 515–516
    methanol synthesis process, 516
    PSA process, 515–516
  combustion, 439
  principles and features, 515
  types and configurations, 515
Fixed carbon content, 167, 169
Flame-assisted spray pyrolysis (FASP), 272
Flame reactors, 272
Flight effect, 244
Flocculants, 477
Flocculated suspensions, 199
Flocculation-flotation technique, 506
Floodability index, 234
Flotation, 495–506
  challenges, 504–505
    depletion of high-grade deposits, 504–505
    trace toxic compounds, 505
    water quality, 505
  emerging technologies, 505–506
    coarse, 505
    flocculation-flotation, 506
    preconditioning in grinding stage, 505
    split, 505
  equipment, 501–503
    froth separators, 502–503
    mechanical cells, 501
    pneumatic cells, 501–502
  fundamentals, 495–498
    factors influencing performance, 496–497
    particle attached to bubble, 496
    particle–bubble attachment, 495–496, 497–498
    particle–bubble collision, 497
    particle–bubble detachment, 498
  minerals separation, 499
  overview, 495
  plant practice, 503–504
    circuit design, 503
    example, 504
  reagents, 499–500
    activators, 499–500
    collectors, 499
    depressants, 499
    dispersants, 500
    Eh modifiers, 500
    frothers, 500
    pH modifiers, 500
Flow behavior, 411–412
Flow-focusing monodisperse aerosol generator (FMAG), 265
Flow-promoting device, 241
Flow through porous media, *see* Permeation
Flow-through-type dust collectors, 445, 446–449
  centrifugal, 447
  ESP, 448–449
  gravitational, 446–447
Fluid dynamic method, 118
Fluid-energy mill, 330
Fluidity, 231–235; *see also* Powder flow
  definition, 231
  factors affecting, 234–235
  improvement, 235
  measurement, 231–234
    fluidized flow, 234
    forced flow, 232–233
    gravitational flow, 231–232
    shear properties, 233–234
    total evaluation, 234
Fluidization and fluidized bed, 385–398
  computational methods, 389–397
    continuum model, 392–393
    discrete particle method, 393–396
    DNS, 396–397
    steady-state modeling, 389–392

overview, 385–389
local heterogeneity, 386
overall heterogeneity, 388–389
pressure drop, 385
regime transition, 386–388
Fluidized bed, 340, 597
combustion, 439
dryer, 434
spray methods, 424
Fluid particle dynamics (FPD), 552
Fluids atomization, 261–265
centrifugal atomizer, 264
electrosprays, 263–264
FMAG, 265
nebulizers, 262–263
pressure atomizers, 262
two-fluid atomizers, 262
ultrasonic nebulizers, 263
VOAG, 264–265
Fluorescence correlation spectroscopy (FCS), 290–291
FM-AFM, *see* Frequency-modulation AFM (FM-AFM)
FMAG, *see* Flow-focusing monodisperse aerosol generator (FMAG)
Focused beam reflectance method, *see* Light extinction method
Force coupling method (FCM), 552
Forced flow, 232–233
compression, 233
mechanically forced, 232–233
vibration, 233
Forced screening methods, 425
Forced-vortex-type classifier, 348, 349
Force measurements, 55–57
in gas and liquid phase, 56–57
principle of, 55–56
Fourier coefficient, 23, 25, 541
Fourier descriptor, 20, 23–24
radial, 23
radius vector method, 24
ZR, 23–24
Fourier transformation, 23–25
FPD, *see* Fluid particle dynamics (FPD)
Fractal dimensions, 24, 205, 208
Fractional loss per impact, 147
Fractionation analysis, 10, 13–16
chromatographic method, 15
electrical mobility classification method, 16
inertial impaction method, 15–16
sedimentation method, 14
sieving method, 13–14
Fracture energy, 38, 319
Fracture toughness, 35, 37–39
Fragmentation, 147, 148, 343, 546, 548
Fragment Spawning (FS) model, 547
Frantz Ferrofilter separator, 464
Fraunhofer and Mie equations, 17
Fraunhofer diffraction, 77
Free vortex classifier, 348, 349
Free water, 193, 194
Freeze drying method, 275
Freezing point depression, 214
Frenkel-Halsey-Hill (FHH) theory, 190
Frequency analysis method, 78
Frequency-based power spectrum, 78
Frequency-modulation AFM (FM-AFM), 54
Freundlich equation, 187
Frictional sound, 253–255
Friction factor, 218, 219
Friction force microscopy, *see* Lateral force microscopy (LFM)
Friedlander's kinetic equation, 61
Front-firing furnace, 442, 443
Frothers, 500
Froth flotation, 495; *see also* Flotation
Froth separators, 502–503
FS, *see* Fragment Spawning (FS) model
Fuel properties, 167
Fullerenes, 607
Full-stream samplers, 563
Fume generation, 267
Funicular state, 418
Funnel flow, 364–365
Furnace process, 270
Fusion methods, 426
Fuzzy logic approach, 597

Gadolinium neutron-capture therapy (Gd-NCT), 294–295
Gadopentetic acid (Gd-DTPA), 294–295
Gas adsorption, 18, 179–181, 214
methodology, 181–182
gravimetric method, 181–182
volumetric method, 181
surface area estimation, 179–181
BET method, 179–180
single-point method, 180–181
Gas chromatography, 46, 49
Gaseous ions and electrons, 299–303
combination probability, 301
diffusion charging, 301
by bipolar ions, 302–303
by unipolar ions, 301–302
field charging, 300–301
formation process and reactivity, 300
photoelectron charging, 303
physical properties, 300
production methods, 299–300
Gas flow and surface area estimation, 182–183
Gas-phase techniques, 269–273
advantages and disadvantages, 269
flame reactors, 272
hot-wall flow reactors, 271–272
laser reactors, 273
particle formation, 269–270
droplet-to-powder conversion, 270
gas-to-powder conversion, 270
particle size distribution and morphology, 270–271
residence time, 271
size and structure, 271
plasma reactors, 272–273
Gas pycnometer, 28
Gas-to-powder conversion, 270
Gaudin-Meloy equation, 325
Gaudin-Schumann (G-S) distribution equation, 325
Gaussian distribution function, *see* Normal distribution
Gd-DTPA, *see* Gadopentetic acid (Gd-DTPA)
Gd-nano-CPs, *see* Nanoparticles containing Gd-DTPA (Gd-nano-CPs)
Gd-NCT, *see* Gadolinium neutron-capture therapy (Gd-NCT)
Geiger-type detector, 583
Gel permeation chromatography (GPC), 15
Generalized fluidization, 388
General Purpose Interface Bus (GP-IB), 199
Genetic algorithm, 597
Geometrical shape descriptors, 20–24
Fourier descriptor, 23–24
fractal dimensions, 24
macroscopic descriptors, 20–21
mesoscopic descriptors, 21–22
Geometric capacity, 365
Geometric diameter, 9
GHS, *see* Globally Harmonized System of Classification and Labeling of Chemicals (GHS)
Gibbs free energy change of formation, 155, 419
Gibbs–Thomson equation, 214
Gilvarry equation, 325
Globally Harmonized System of Classification and Labeling of Chemicals (GHS), 607
"Godbert–Greenwald" furnace, 621
GPC, *see* Gel permeation chromatography (GPC)
GP-IB, *see* General Purpose Interface Bus (GP-IB)
GPU parallel computing, 397
Granulation, 417–426, 536
evaluating agglomerate, 420–423
granule growth modes, 421–422
machine-made product modes, 422–423
granulators, 423–426
agitation methods, 425
compaction methods, 425
extrusion methods, 425–426
fluidized bed spray methods, 424
forced screening methods, 425
fusion methods, 426
tumbling granulation methods, 423–424
growth mechanisms, 417–418
breakage/attrition, 418
coalescence and consolidation, 417–418
wetting and nucleation, 417
mechanical properties, 418–420
dynamic strength, 419–420
static strength, 419
Granulators, 423–426
granule growth mechanism mode, 423–425
agitation methods, 425
fluidized bed spray methods, 424
tumbling granulation methods, 423–424
mechanical forced granule modes, 425–426
compaction methods, 425
extrusion methods, 425–426
forced screening methods, 425
fusion methods, 426
Graphene, 64
Graphical representation, 5
Graphite, 64, 604
Gravimetric method, 181–182
Gravitational classifiers, 348
Gravitational collectors, 446–447
Gravitational flow, 231–232
Gravity, electrostatic force and, 28–29
Gravity filter, 481
Gravity method, 117
Gravity thickening, 477–480
continuous thickener design, 479–480
clarification area, 479
Coe and Clevenger method, 479–480
Talmage and Fitch method, 480
ideal settling basin, 477
Kynch theory, 478–479
overview, 477
pretreatment, 477
settling curve, 477–478

Griffith energy balance, 37
Griffith theory, 320
Grignard reagent method, 46
Grinding process, 314
Grizzlies, 359
Groendal drum wet separator, 461, 463
Guidelines for the Assessment of Risks of Chemical Substances, 607
Guinier diameter, 17
Gyratory crusher, 328–329

Hagen-Poiseuille equation, 141, 182, 217, 218
Halogenated polymers decomposition, 161–162
  HBB debromination, 162
  polychlorinated compounds dechlorination, 161–162
  PTFE defluorination, 161
Hamaker constant, 113, 134, 135
Hammer impact type grinders, 329
Hammer mill, 329–330
Hammett indicators, 48
Hansen solubility parameter (HSP), 51
Hard aggregates, 523
Hardgrove index (H.G.I.), 327
Hard magnetic materials, 94
Hard-sphere model, 393
Harmonic spectrum, 25
Hartmann tube, 621
Hatch's equation, 4, 5
Hausner's surface index, 22
Hazard Ratio (HR), 615
HBB, *see* Hexabromobenzene (HBB) debromination
HDC, *see* Hydrodynamic chromatography (HDC)
Health effects, 603–606
  of inhaled particles, 604–605
    allergic reactions, 605
    cancer, 605
    infection, 605
    irritation, 605
    metal fume fever, 605
    pneumoconioses, 604
    systemic poisoning, 604
  overview, 603
  particles in respiratory tract, 603–604
  rate of deposited particles, 604
    coughing and sneezing, 604
    dissolution, 604
    mucociliary clearance, 604
    nasal filtration, 604
    phagocytosis, 604
  respiratory system, 603
  threshold limit value, 605–606
    inhalable particles, 605
    respirable particles, 605–606
Heat-exchange-type bed, 217
Heat transfer model, 519
Heat treatment and magnetic separation, 468
Henry equation, 86, 186–187
HEPA, *see* High-efficiency particulate air (HEPA) filter
Herschel–Bulkley model, 142
Hertzian contact theory, 319
Hertz-Knudsen equation, 281
Hertz's elastic contact theory, 252
Heterogeneous catalysis, 65
Heterogeneous flow, 381
Heterogeneous nucleation, 275, 280–281
Hexabromobenzene (HBB) debromination, 162
Heywood diameter, *see* Projected area equivalent diameter
H.G.I., *see* Hardgrove index (H.G.I.)
HGMS, *see* High gradient magnetic separation (HGMS)
HI, *see* Hydrodynamic interaction (HI)
High-efficiency particulate air (HEPA) filter, 452
High-gauss separator, 464
High gradient magnetic separation (HGMS), 464, 466–467, 468
High-gradient-type separator, 461
High-Intensity Magnetic Separation (HIMS), 464
High performance liquid chromatography (HPLC), 405
High-power static-magnetic-field-type separator, 461
High-rate discharge (HRD), 630
High-resolution in-process tomography, 593
High-speed flow-type mixer, 425
High-speed video imaging, 386
High temperature particle residence time (HTPRT), 271
Hill's approach, 34
HIMS, *see* High-Intensity Magnetic Separation (HIMS)
Hitachi Zosen Corp., 458
Hixon and Crowell equation, 173
Homodyne and heterodyne detection optics, 78
Homogeneous nucleation, 280–281
Homogeneous precipitation method, 275
Homogeneous slurries, 381
Homogenous mixture, 401–402
Hooke's law, 37
Hopper scale, 577
Horizontal drum mixer, 407
Horizontal flow classifier, 351, 355
Horizontal tensile method, 225
Horizontal vessel mixer, 407
Hot air dryer, 435
Hot injection, 522
Hot-wall flow reactors, 271–272
Howard-type separator, 447
HPC, *see* Hydroxypropyl cellulose (HPC)
HPLC, *see* High performance liquid chromatography (HPLC)
HR, *see* Hazard Ratio (HR)
HRD, *see* High-rate discharge (HRD)
HSP, *see* Hansen solubility parameter (HSP)
HTPRT, *see* High temperature particle residence time (HTPRT)
Hybrid model, 203
Hydrated compounds synthesis, 160–161
Hydration force, 56
Hydro-cyclones, 355–356
Hydrodynamic chromatography (HDC), 15
Hydrodynamic drag force, 57, 133, 135, 136
Hydrodynamic interaction (HI), 15, 112, 552
Hydrogen generation, 164
Hydrolysis, 275, 276
Hydrophilic and hydrophobic carbogeneic nanoparticles, 312
Hydrophilic particles, 495, 499
Hydrophobic attraction, 57
Hydrophobic particles, 309, 495, 499, 502
Hydrostatic pressure method, 413–414
Hydrothermal method, 276
Hydrothermal synthesis, 522
Hydroxypropyl cellulose (HPC), 296
Hydroxypropyl-β-cyclodextrin, 175
Hygroscopic water, *see* Adsorption water
Hysteresis, 213–214

IBM, *see* Immersed boundary method (IBM)
IEP, *see* Isoelectric point (IEP)
IGC, *see* Inert gas condensation (IGC)
Ignition, 167–169
Ignition loss method, 46
ILO, *see* International Labour Organization (ILO)
Image processing, 19, 22, 54
Immersed boundary method (IBM), 397, 544, 552
Impact fracturing velocity, 321–323
Impaction, 15, 339, 340, 522, 604, 610
Impact method, 118
Impactor classifier, *see* Curvilinear classifier
Impeller-type powder rheometer, 224
Impulsive force flowmeter, 578
Inclined classifier, 348
Indentation fracture toughness, 38–40
Indentation hardness, 33–34
  elastic-perfectly plastic indentation, 34
  rigid-perfectly plastic indentation, 33
  work-hardening model, 34
Indifferent ions, *see* Non-potential-determining ions
Indium recovery, 163
Indium-tin-oxide (ITO) scrap, 163
Induced gradient method, 17–18
Induction charging, 455, 576
Industrial dust collector, 445
Industrial Safety and Health Act of Japan, 607
Industrial scale slurry hydrotransport metering, 598
Inert gas condensation (IGC), 267
Inertial classifiers, 348
Inertial dust collector, 450
Inertial impaction method, 15–16
Infection, 605
Infrared (IR) spectroscopy, 46, 47, 50, 189
Injection molding, 432
Ink-bottle effect, 213
In-line rheometry, 599–600
Inorganic powder, 273–274
Inorganic systems, 287–289
  rod-shaped SNCs synthesis, 288
  SNCs synthesis in near-infrared region, 288
  SNCs synthesis in visible region, 287–288
  water-soluble SNCs preparation, 288–289
Insert structure, 241
Institute of Process Engineering, 389, 393
Interception, 136, 451, 604
Interfacial polarization, 85
Interfacial reaction technique, 276
Interlayer segregation, 246–247
  diffusion effect, 246–247
  permeation effect, 247
Internal flow, 365
Internal impaction, 604
Internal-mixing type atomizer, 262
International Labour Organization (ILO), 608
Inverse Hall-Petch effect, 62
Ion-clustering processes, 300
Ion–molecule reaction, 300
IR, *see* Infrared (IR) spectroscopy
IR absorption spectrum, 50
IR moisture sensor, 592, 593
Ironmaking process, 537
Irritation, 605

IR spectra, 591–592
Isoelectric point (IEP), 524
Isosceles triangle-shaped compressed zone, 251–252
ITO, *see* Indium-tin-oxide (ITO) scrap
IUPAC types of isotherm, 187–188

Jameson cells, 501, 502
Japan Society for Occupational Health, 606, 608
Jaw crusher, 328, 329
Jenike's shear tester, 223–224
Jiggering, 430
Johnson–Kendall–Roberts (JKR) model, 113, 146, 547
Jones high-intensity wet magnetic separator, 464

Kanomax USA Inc., 30
Kaolinite, 162
KAPSEL software, 557
Kelvin effect, 61
Kelvin equation, 115, 211–212
Kelvin method, 199
Kelvin model's deficit, 212–213
Kelvin probe force microscopy, 55
Kernel, *see* Micropore
Kick's law, 326
Kinetic interaction and coagulation, 134–137
  Brownian coagulation and stability ratio, 135–136
  in shear flow, 136–137
  in turbulent flow, 137
Kinetic theory of granular flow (KTGF), 392
Kneading, 429–430
  critical powder volume concentration, 429
  mechanisms and machines, 430
  powder–gas–liquid dispersion system, 429
Knudsen diffusion and flow, 60, 182
Kosmotropic properties, 307
Kozeny-Carman equation, 18, 182, 218, 219
Kozeny constant, 182, 218
KTGF, *see* Kinetic theory of granular flow (KTGF)
Kuroko (black ore), 504
Kynch theory, 478–479

$LaCoO_3$ nanoparticles, 159, 160
LAFS, *see* Liquid-fed aerosol flame synthesis (LAFS)
Lagrange equation of motion, 106
Lagrangian correlation coefficient, 101
Lagrangian displacement, 101, 102
Lagrangian method, 121, 122, 123–124
Lagrangian particle-tracking model, 512
LALLS, *see* Low-angle laser light-scattering (LALLS)
Lambert–Beer law, 77, 577
LaMer model, 275, 281
Laminar and turbulent coagulation, 131
Laminar flow, 15, 430
Langevin equation, 60
Langevin law, 93
Langmuir equation, 187
Lanthanum oxide (La_2O_3), 158
Lanthanum oxy-chloride (LaOCl), 162
Laplace equation, 512
Large eddy simulation (LES), 102, 123
Laser diffraction/scattering method, 17
Laser level meter, 583–584
Laser reactors, 273
Laser scattering diameter, 3
Laser sintering, 153–154
Lateral force microscopy (LFM), 54
Lateral growth, 281
Lattice-based DNS method, 397
Lattice Boltzmann method (LBM), 397, 544, 551, 552
Lattice water, 193
Law of conservation of particle mass, 101
Layered double hydroxide (LDH), 161
Layered manufacturing (LD), 153
Layered-structure, 285, 286
LBM, *see* Lattice Boltzmann method (LBM)
LCST, *see* Lower critical solution temperature (LCST)
LD, *see* Layered manufacturing (LD)
LDH, *see* Layered double hydroxide (LDH)
Legendre ellipse of inertia, 20, 22
Lenard effect, 299
LES, *see* Large eddy simulation (LES)
Level measurement, 581–584
  electrical methods, 582–583
    electric capacitance level meters, 582
    electric resistance level meters, 582–583
    microwave level meters, 583
  level meters and level switches, 581
  mechanical methods, 581–582
    diaphragm level switches, 582
    level switches based on vibration, 582
    piston level switches, 581
    rotating blade level switches, 581–582
    sounding level meters, 581
    swing level switches, 582
  optical method, 583–584
  pneumatic method, 583
  radiometric method, 583
  ultrasonic wave level meters, 583
  weighing method, 583
Level switches, 581, 582
Lewis acid site, 50, 189
LFM, *see* Lateral force microscopy (LFM)
LGCT, *see* Lower gel collapsed temperature (LGCT)
Lichtneker–Rother model, 197
Lifshitz theory, 60
Lifshitz-van der Waals theory, 113
Ligand exchange method, 312
Light extinction, 12–13, 77
Light scattering, 75–77
  coefficient, 292
  dynamic, 77–78
  intensity, 9
  method, 12
Limit-deposit velocity, *see* Deposition velocity
Limiting oxygen concentration (LOC), 624
Linear elastic fracture mechanics, 37, 38
Linear-mixture packing model, 141
Liquid bridge, 113, 115, 116, 395, 418, 419–420
Liquid-fed aerosol flame synthesis (LAFS), 272
Liquid phase synthesis, 522
Liquid-phase techniques, 273–277
  inorganic powder, 273–274
  mechanical dispersion methods, 276–277
  organic powder, 276
  phase-separation methods, 277
  precipitation methods, 275
  sol-gel method, 275–276
  solvent evaporation methods, 274–275
  special reaction field, 276
Liquid pycnometer method, 28
Liquid-solid system, 185
Load-crack length, 39
Loading rate effect, 321
LOC, *see* Limiting oxygen concentration (LOC)
Local adsorption isotherms, 212
Log-normal distribution, 4, 5, 11, 207, 325
Log-normal equation, 125
London-van der Waals theory, 113
Louver classifier, *see* Inclined classifier
Louver-type dust collector, 450
Low-angle laser light-scattering (LALLS), 17
Lower critical solution temperature (LCST), 296
Lower gel collapsed temperature (LGCT), 296
Low-inertia pressure detection device, 630
Low-intensity static-magnetic-field-type separator, 461

Macroscale pseudo-particle model (MaPPM), 397
Macroscopic descriptors, 20–21
Macroscopic flow, 217
Magnetic filtration, 461
Magnetic fluid, 469
Magnetic force microscopy (MFM), 55
Magnetic properties
  of nanoparticles, 64–65
  of particles, 91–96
    ferromagnetic properties, 93–94
    magnetic force, 91–93
    magnetism, 94
Magnetic reagent method, 461
Magnetic separation, 461–470
  application, 466–468
    carrier, 467–468
    heat treatment, 468
    HGMS, 466–467
    history, 468
  classification, 461
  electromagnetic-induction-type separation, 470
  magnetohydrostatic separation, 469–470
  static magnetic field, 461–466
    matrix-loaded-type, 464–466
    open gradient magnetic-field-type, 461, 463–464
Magnetism, 94
Magnetohydrostatic separation, 461, 469–470
Magnetorheological effect, 140
Mag-sep Corporation (MC) process, 469
MaPPM, *see* Macroscale pseudo-particle model (MaPPM)
Marlow's theory, 131
Mass conservation, 512
Mass flow, 364
Mass median diameter (MMD), 564
Material comminution, 324–334
  Bond's law, 326
  devices, 328–330
  improvement of efficiency, 330–334
    conditions, 331–332
    fine particles classification, 330
    grinding aid, 330
    mill chamber structure, 333–334
  Kick's law, 326
  mean particle size, 324
  parameters correlation in distribution equations, 325
  phenomena, 324
  rate process in batch grinding, 325–326
  resistance and grindability, 327–328
  Rittinger's law, 326
  size distribution equation, 324–325
  Tanaka's theory, 326–327

Material Safety Data Sheet (SDS), 607
Matrix-loaded-type magnetic separation, 464–466
Matrix-type kneading, 429
Matsumine mill plant, 504
Maximum granule pore saturation, 418
Maxwell equations, 63
Maxwell model, 197
MBP1–10 and 10–100 particles, 69
MBSD, *see* Moving Brock Starboard Deviation (MBSD)
MC, *see* Mag-sep Corporation (MC) process
MCVD, *see* Modified chemical vapor deposition (MCVD)
MD, *see* Molecular dynamics (MD)
MEC, *see* Minimum explosible concentration (MEC)
Mechanical cells, 501
Mechanical conveyors, 376
Mechanical device, 241
Mechanical dispersion methods, 276–277
Mechanical distributor, 564
Mechanical filters, 613, 614
Mechanical forced granule modes, 425–426
  compaction methods, 425
  extrusion methods, 425–426
  forced screening methods, 425
  fusion methods, 426
Mechanically forced flow, 232–233
Mechanical methods, 581–582
  diaphragm level switches, 582
  level switches based on vibration, 582
  piston level switches, 581
  rotating blade level switches, 581–582
  sounding level meters, 581
  swing level switches, 582
Mechanical properties
  of nanoparticles, 62–63
  of powder bed, 223–229
    adhesion, 225
    overview, 223
    shearing strength, 223–225
    yielding characteristics, 226–229
Mechanical-shaking filters, 452
Mechanochemistry, 155–164
  doping, 160
  halogenated polymers decomposition, 161–162
    hexabromobenzene (HBB) debromination, 162
    polychlorinated compounds dechlorination, 161–162
    polytetrafluoroethylene (PTFE) defluorination, 161
  hydrogen generation, 164
  indium recovery, 163
  metal oxides sulfuration, 163–164
  overview, 155
  phase transformation, 155
  rare earths extraction, 163
  solid state reaction, 155–160
    complex fluoride synthesis, 159
    complex oxides synthesis, 155–159
    Gibbs free energy change of formation, 155
    nanoparticles synthesis, 159–160
  $SrCO_3$ and $BaCO_3$ formation, 162–163
  synthesis of hydrated compounds, 160–161
  useful components extraction, 162
  zeolite synthesis, 162
Medium grinding, 329
Mercury intrusion method, 214
  nonwetting fluid and washburn equation, 214
  pore size, 214
Mercury porosimetry, *see* Mercury intrusion method
Mesoscopic descriptors, 20, 21–22
Message Passing Interface (MPI), 539
Metal alkoxides, 275–276
Metal fume fever, 605
Metal oxides sulfuration, 163–164
Metal wires, 459
Methanol synthesis process, 516
MFM, *see* Magnetic force microscopy (MFM)
Micro-emulsion polymerization, 277
Micro-feeder, 374
Micro Materials Ltd, 35
Micronization, 175–176
Micron separator, 349
Micron-sized particles, 285
Microparticulate systems, 295–296
Micropore filling, 187, 212
Microscopic descriptor, 20
Microscopic flow, 217
Microwave level meters, 583
Microwave method, 579
Microwave moisture sensor, 591
Micro-welding, 315
MIE, *see* Minimum ignition energy (MIE)
Mie scattering regime, 76
Mie's theory, 63
Millikan cell, 28
Mineral resources refining, 457
Mini-emulsion polymerization, 276, 277
Minimum explosible concentration (MEC), 623–624
Minimum fluidization, 385
Minimum ignition energy (MIE), 621–622
Minimum ignition temperature (MIT), 621
Mist generation, 265–267
MIT, *see* Minimum ignition temperature (MIT)
Mixed Suspension Mixed Product Removal (MSMPR), 281, 282
Mixer agglomeration, 425
Mixer-type disperser, 340
Mixing, 401–409, 536
  equipment, 407–409
  evaluation of condition, 402–407
  indices and rate, 401–402
  mechanism, 401
  overview, 401
MMD, *see* Mass median diameter (MMD)
Modified chemical vapor deposition (MCVD), 272
Modified radial function, 24
Modified split-cell-bearing-type tester, 225
Modified Terzaghi model, 489–491, 492
MOFs, *see* Molecular Organic Frameworks (MOFs)
Mohr's stress circle, 223, 228, 231, 234, 238–239
Mohs hardness test, 34
Moisture content, 167, 193–194, 235
  adhesive water, 193–194
  bound water, 193–194
  measurement, 589–594
    continuous monitoring and control, 593
    electric methods, 589–591
    optical moisture sensor, 591–592
    overview, 589
  overview, 193
  in particulate system, 194
Molecular dynamics (MD), 397, 528
Molecular Organic Frameworks (MOFs), 60
Molecular simulation, 212
Momentum conservation, 512
Monolithic structure, 285
Monte Carlo method, 112, 199, 212, 528
Moving beds, 516–517
  application, 517
    coal gasifier, 517
    SO_2 removal using activated carbon, 517
  principles and features, 516
  types and configurations, 516
Moving Brock Starboard Deviation (MBSD), 405
MPI, *see* Message Passing Interface (MPI)
MP-PIC, *see* Multiphase particle-in-cell (MP-PIC) method
MSMPR, *see* Mixed Suspension Mixed Product Removal (MSMPR)
Mucociliary clearance, 604
Multi component powder sintering, 154
Multiphase particle-in-cell (MP-PIC) method, 396
Multipurpose equipment, 515–519
  fixed beds, 515–516
    application, 515–516
    principles and features, 515
    types and configurations, 515
  moving beds, 516–517
    application, 517
    principles and features, 516
    types and configurations, 516
  rotary kiln, 518–519
Multi-size particles packing, 205–207
Multistage fixed bed reactor, 516
Multi-walled carbon nanotubes (MWCNTs), 607
MUSEN software, 546
MWCNTs, *see* Multi-walled carbon nanotubes (MWCNTs)

Nano-composites, 285
NanoCrystal®, 176
Nanogrinding, 522
Nano-milling, 330
Nanoparticles, 53, 152–153
  handling and formulation, 521–532
    classical unit operations of powder processing, 529–530
    dispersion, 522–523
    effect of surface modification, 527–529
    formation, 522
    functional thin films processing, 531–532
    overview, 521–522
    stabilization, 523–527
  in-situ surface modification, 311–312
  risks, 607–611
    assessment and management, 607–608
    management using control banding, 608–609
    overview, 607
    PM2.5, 609–610
  sintering process, 152–153
  specific properties, 59–67
    catalytic particles, 65–67
    dispersity, 59–60
    electrical, 63–64
    magnetic, 64–65
    mechanical, 62–63
    optical, 63
    particle interactions, 60–61
    property function, 59–60

thermophysical, 61–62
transport, 60
synthesis, 159–160
Nanoparticles containing Gd-DTPA (Gd-nano-CPs), 295
Nanoparticulate films, 60
Nanoparticulate systems, 293–295
Nano-test device, 34, 35
Nasal filtration, 604
Nasal–pharyngeal region, 604
National Institute for Occupational Safety and Health, 608
Navier-Stokes equation, 105, 122, 217, 512, 544, 552, 553
Navier-Stokes (NS) equation-based DNS, 396–397
n-butylamine, 48–49, 50
Near Infrared (NIR) technology, 405
Nebulization, *see* Fluids atomization
Nebulizers, 262–263
Neck growth, 151, 152
NEDO, *see* New Energy and Industrial Technology Development Organization (NEDO)
Needle-plate electrodes, 196
Needle-type moisture sensor, 589
Negative adsorption, 185
Nernst–Noyes–Whitney equation, 173
Neutralization, 302–303
New Energy and Industrial Technology Development Organization (NEDO), 607, 608
New suspension preheater kiln (NSP), 519
Newton efficiency, 347
Newtonian fluid, 411–412
Newtonian model, 139, 141, 142
Newton's second law of motion, 60, 122
New York (NY) drum magnetic separator, 464
NIR, *see* Near Infrared (NIR) technology
Nitrogen adsorption method, 211–214
capillary condensation and Kelvin equation, 211–212
hysteresis, 213–214
Kelvin model's deficit, 212–213
pore size, 212
Nitrogen gas adsorption method, *see* Brunauer-Emmett-Teller (BET) equation
NMR, *see* Nuclear magnetic resonance (NMR) spectroscopy
Non-aqueous solvents, 57
Non-contact mode, *see* Dynamic mode
Non-contact-type thermometers, 586–588
points of measurement, 587–588
principles, 586–587
Non-DLVO forces, 56
Non-float-sink range, 473
Non-homogeneous slurries, 381–382
Non-Newtonian fluid model, 142
Non-Newtonian fluid–solid mixtures, 486
Non-potential-determining ions, 83
Non-powered air-purifying respirators, 614
Non-powered respirators, 613
Non-settling slurries, *see* Homogeneous slurries
Non-spherical particle (NSP), 124
Nonwetting fluid, 214
Normal distribution, 4
Noyes–Whitney equation, 172, 173
NS equation-based DNS, *see* Navier-Stokes (NS) equation-based DNS
NSP, *see* New suspension preheater kiln (NSP); Non-spherical particle (NSP)
Nuclear magnetic resonance (NMR) spectroscopy, 46
Nucleation rate, 280–281
NY drum magnetic separator, *see* New York (NY) drum magnetic separator

Obstacle-type dust collectors, 445, 449–452
air filters, 450–452
inertial dust collector, 450
Occluded water, 193, 194
Occupational exposure limits (OELs), 607–608, 615
OELs, *see* Occupational exposure limits (OELs)
One-dimensional two-phase flow approach, 379
One-photon microscopy, 293
One-stage ESP, 448
Open-flow method, 501
Open gradient magnetic-field-type magnetic separation, 461, 463–464
Opposed-firing furnace, 442, 443
Optical measurement
and imaging, 289–293
orientation measurement of biomolecules, 291–292
SNCs size and concentration, 289–291
in vivo imaging, 292–293
system, 403, 405
Optical method, 583–584
Optical moisture sensor, 591–592
Optical particle counter, 12
Optical properties
of nanoparticles, 63
of particles, 75–78
definitions, 75
dynamic light scattering, 77–78
light extinction, 77
light scattering, 75–77
photophoresis, 78
Organic powder, 276
Organic systems, 293–296
microparticulate systems, 295–296
nanoparticulate systems, 293–295
Orifice, 13, 339–340
Orifice contractile flow, 343–344
Orifice meter, 578
Oscillating hopper sample divider, 564
Oscillating paddle sample divider, 564
Ostwald ripening, 61, 523
Oxidation, 65, 66, 270, 272, 273, 309, 523, 527

Packed powder
sintering process of, 153–154
laser sintering for 3D printing, 153–154
multi component powder, 154
Packing properties, 203–209
equal-size spheres, 203–205
multi-size particles, 205–207
overview, 203
particle shape effect on void fraction, 207–208
Palladium nanocrystals, 66
PAPR, *see* Powered air-purifying respirator (PAPR)
Parallel computing technology, 522
Parallel-plate electrodes, 195, 197
Parallel-plate shear tester, 224–225
Partial hydrolysis method, 276
Particle-based DNS methods, 397
Particle classification, 347–362
dry, 348–351
centrifugal classifiers, 349
cut size control, 349
cyclone performance, 349–351
gravitational classifiers, 348
inertial classifiers, 348
performance, 347–348
screening, 359–362
50% separation size and length, 361–362
wet, 351–359
centrifugal type separator, 358–359
classification theory, 351–352
cut size control, 356–358
hydro-cyclones, 355–356
sedimentation velocity, 352–354
type, 355
Particle concentration, 575–579
and powder flow rate, 577–579
Coriolis force flowmeter, 578
differential pressure method, 578
electrical method, 579
impulsive force flowmeter, 578
statistical method, 579
weighing method, 577–578
in suspensions, 575–577
attenuation technique, 576–577
electrically forced vibration, 576
electric capacitance change, 575
electrostatic charging, 575–576
induction charging, 576
piezoelectric effect, 576
quartz crystal microbalance, 576
Particle density, 27–30
bulk density, 30
definition, 27
bulk density, 27
true density, 27
measurement method, 27–30
based on balance between electrostatic force and centrifugal force, 29–30
based on balance between electrostatic force and gravity, 28–29
constant gas volume method, 28
piezoelectric microbalance method, 30
pycnometer method using liquid, 27–28
Particle deposition, 121–124
concepts, 121–122
Eulerian method, 122–123
Lagrangian method, 123–124
Particle diffusion, 97–103
thermal, 97–98, 100
turbulent, 100–103
coefficient, 101–103
equation, 101
Particle formation and gas-phase techniques, 269–270
droplet-to-powder conversion, 270
gas-to-powder conversion, 270
Particle group motion model, 246; *see also* Surface segregation
Particle hardness, 33–37
indentation, 33–34
elastic-perfectly plastic indentation, 34
rigid-perfectly plastic indentation, 33
work-hardening model, 34
measurement, 34–37
Particle imaging velocimetry (PIV), 386
Particle impact breakage, 145–148
analysis for brittle failure mode, 146–147
analysis for semi-brittle failure mode, 147–148

chipping, 147
fragmentation, 147
transition velocities, 147
analysis of agglomerates, 148
force, 145–146
elastic, 145
elastic-plastic, 145
elasto-plastic and adhesive, 145–146
plastic, 145
mode, 146
brittle failure, 146
ductile failure, 146
semi-brittle failure, 146
Particle interactions, 60–61
Particle motion in fluid, 105–107
equation, 106–107
overview, 105
resistance force, 105–106
shear flow, 107
Particle reentrainment, 124–127
of aggregates, 124–125
efficiency, 125
rate, 125–126
simultaneous particle deposition and, 126
Particle sampling, 567–573
anisokinetic sampling error, 567–568
practical applications, 570–573
measuring method for particle size distribution, 570–573
probe and system, 570
in stationary air, 568–570
Particles bearing pH-dependent dissociable groups, 84–85
Particles dispersion, 337–345
in gaseous state, 337–340
capillary tube, 340
ejector, 340
fluidized bed, 340
impaction force, 339
induced by airflow acceleration/deceleration, 337–338
induced by shear flow field, 338–339
mixer-type disperser, 340
orifice, 339–340
turbulent flow, 339
Venturi, 340
in liquids, 341–345
aggregates breakup by turbulent flows, 343
breakages by flow *vs.* ultrasonic fields, 344–345
breakup between cylinder and rotary disk, 344
breakup by ultrasonic radiation, 344
doublets breakup, 341–343
large aggregates breakup, 343
orifice contractile flow, 344
Particle sedimentation, 109–112
in concentrated suspension, 111–112
overview, 109
terminal settling velocity, 109–111
of non-spherical particle, 110–111
resistance force acting on spherical particle, 109–110
two spherical particles settling, 111
Particle segregation, 243–247
interlayer, 246–247
diffusion effect, 246–247
permeation effect, 247
mechanism, 243–244
phenomena and its factors, 243
preventing, 247
surface, 244–246
flight effect, 244
push-off effect, 245–246
rotational effect, 244–245
sieve layer effect, 246
sieving effect, 246
stumbling effect, 245
Particles generation by reactions, 269–277
gas-phase techniques, 269–273
advantages and disadvantages, 269
flame reactors, 272
hot-wall flow reactors, 271–272
laser reactors, 273
particle formation, 269–270
particle size distribution and morphology, 270–271
plasma reactors, 272–273
liquid-phase techniques, 273–277
inorganic powder, 273–274
mechanical dispersion methods, 276–277
organic powder, 276
phase-separation methods, 277
precipitation methods, 275
sol-gel method, 275–276
solvent evaporation methods, 274–275
special reaction field, 276
Particle shape characterization, 19–25
dynamic equivalent, 24–25
drag force shape factor, 24–25
dynamic shape factor, 25
geometrical shape descriptors, 20–24
Fourier descriptor, 23–24
fractal dimensions, 24
macroscopic descriptors, 20–21
mesoscopic descriptors, 21–22
overview, 19
representative size, 19–20
Particle shape effect and void fraction, 207–208
Particle size, 3–7, 235
average, 5–6
diameter, 3
distribution, 3–5
graphical representation, 5
log-normal distribution, 4
normal distribution, 4
Rosin-Rammler distribution, 4–5
distribution and morphology, 270–271
residence time, 271
size and structure, 271
distribution effect on slurry viscosity, 141
measurement, 9–18
classification of analysis methods, 10–18
overview, 9
surface area method, 18
X-ray diffraction method, 18
Particle size distribution (PSD), 9, 10–11, 13–15, 16–18, 59, 205, 246
Particle surface properties and analysis, 41–51
characterization, 45–51
classification, 45
surface acidity and basicity, 47–50
surface functional groups, 46–47
wettability, 50–51
structures, 41–42
character, 41
enhanced surface properties, 44–45
influence of element, 43
influence of partially chemical structure, 43–44
relaxation, 41–43
surface acidity and basicity influence on dispersion, 44
Particle toughness, 37–40
indentation fracture, 38–40
Particle tracking method, 13
Particle volume fraction, 203
Particulate design and preparation, 287–296
inorganic systems, 287–289
rod-shaped SNCs synthesis, 288
SNCs synthesis in near-infrared region, 288
SNCs synthesis in visible region, 287–288
water-soluble SNCs preparation, 288–289
optical measurement and imaging, 289–293
orientation measurement of biomolecules, 291–292
SNCs size and concentration, 289–291
in vivo imaging, 292–293
organic systems, 293–296
microparticulate systems, 295–296
nanoparticulate systems, 293–295
Particulate filters, 613
Particulate fluidization, 385
Particulate matter (PM)2.5, 536, 609–610
Particulate system and moisture content, 194
Passive systems, 629
PCS, *see* Photon correlation spectroscopy (PCS)
Pellet mill, 425
Pendular state, 418
PEO, *see* Poly(ethylene oxide) (PEO)
PEPT, *see* Positron-emission particle tracking (PEPT)
Percolation effect, *see* Diffusion effect
Perimeter equivalent diameter, 20
Permanent magnets, 470
Permeability method, 18
Permeametry, 182–183
Permeation, 217–221
flow resistance through porous media, 217–219
channel model, 217–218
drag model, 219
overview, 217
pressure drop across fibrous mat, 219–220
Permeation effect, 247
Personal protective equipment (PPE), 609
PF, *see* Protection factor (PF)
Phagocytosis, 604
Phase Doppler velocimetry, 386
Phase imaging, 54
Phase-separation methods, 277
Phase transformation, 155
Phase transitions, 523
pH modifiers, 500
Photoelectron charging, 303
Photoelectron emission, 303
Photoelectron spectroscopy, 303
Photon correlation spectroscopy (PCS), 16, 78
Photophoresis, 78
Physical adsorption and desorption processes, 185
Physical methods and surface modification, 314–315
Physical surface relaxation, 41–42
Physical vapor deposition (PVD), 286, 314
PIEZOBALANCE Dust Monitor®, 30
Piezoelectric effect, 576
Piezoelectric method, 579
Piezoelectric microbalance method, 30

Piston level switches, 581
PIV, *see* Particle imaging velocimetry (PIV)
Plane strain, 38
Planetary mill, 329
Plank's law, 586
Plasma reactors, 272–273
Plastic deformation, 33, 37, 38, 39, 145, 147, 226, 418
Plastic deformation-chipping transition, 147–148
Plastic flow, 146, 151, 182
Plastic forming process, 430–432
  extrusion, 430, 432
  injection molding, 432
  jiggering, 430
  wet pressing, 430
Plastic rupture, 145
Plug flow, 430
PM2.5, *see* Particulate matter (PM)2.5
PMMA, *see* Polymethyl methacrylate (PMMA)
Pneumatic cells, 501–502
Pneumatic conveying, 597
Pneumatic conveying dryer, 434
Pneumatic conveyors, 376, 378
Pneumatic device, 241
Pneumatic method, 583
Pneumoconioses, 604
Point of zero charge (PZC), 524
Poisson–Boltzmann equation, 85
Poisson equation, 82, 305, 512
Polar coordinate method, 23
Polychlorinated compounds dechlorination, 161–162
Polycondensation reaction, 275, 276
Poly(ethylene oxide) (PEO), 116–117
Polymethyl methacrylate (PMMA), 146
Polymorphic compounds, 158
Polymorphs, 171
Polystyrene latex (PSL), 30
Polytetrafluoroethylene (PTFE), 161
Poly-vinyl chloride (PVC), 158, 161–162, 163, 459
Pore size, 190, 211, 212, 213, 214
Porosity, 27, 182
Porous media capillarity, 211–215
  bubble-point method, 214
  mercury intrusion method, 214
    nonwetting fluid and washburn equation, 214
    pore size, 214
  nitrogen adsorption method, 211–214
    capillary condensation and Kelvin equation, 211–212
    hysteresis, 213–214
    Kelvin model's deficit, 212–213
    pore size, 212
  small angle X-ray scattering, 214–215
  thermoporometry, 214
  Young–Laplace effect, 211
Positive adsorption, 185
Positron-emission particle tracking (PEPT), 597
Potential-determining ions, 83
Powder and granule structure, 598
Powder and slurry processing applications, 597–600
  fluidized beds, 597
  industrial scale slurry hydrotransport metering, 598
  in-line rheometry, 599–600
  pneumatic conveying, 597
  powder and granule structure, 598
  powder mixing, 597–598
Powder dispersion, 267–268
Powdered materials solubilization, 174–176
  crystalline forms and amorphous form, 174
  inclusion compounds and complex formation, 174–175
  micronization, 175–176
Powder feeders, 371–374
  overview, 371
  type, 371–374
    belt feeders, 373
    micro-feeder, 374
    rotary feeders, 371–372
    screw feeders, 372–373
    table feeders, 373
    valves and dampers, 373–374
    vibrating feeders, 373
Powder flow, 577–579; *see also* Fluidity
  Coriolis force flowmeter, 578
  differential pressure method, 578
  electrical method, 579
  impulsive force flowmeter, 578
  statistical method, 579
  weighing method, 577–578
Powder–gas–liquid dispersion system, 429
Powder mixing, 597–598
Powder properties control, 281–282
Powder sampling, 563–566
  analysis, 564–566
  equipment, 563–564
Powder simulation, 535–557
  aggregates breakage in liquid phase, 549–551
  DEM simulations for industrial applications, 542–543
  direct numerical simulations of colloidal particles, 551–557
    colloid-solute/solvent boundary conditions, 553–554
    dynamics of colloidal particles, 553
    dynamics of solute and solvent, 552–553
    electrophoresis, 555–557
    mesoscopic modeling for electrokinetics, 551–552
    overview, 551
    smoothed profile method, 554–555
  particle motion in fluid, 543–545
  particles breakage in gas phase, 545–549
    continuum mechanics simulation, 548–549
    discrete element method, 545–548
  using DEM, 535–557
    coarse-grained particle (CGP), 539–540
    comminution, 536
    development of large-scale simulation, 538–539
    granulation, 536
    ironmaking process, 537
    large-scale simulations without, 542
    mixing, 536
    problems, 538
    representation of particle shape, 540–541
    sieving and filtration, 536–537
    slow powder flow, 535–536
Powder transportation, 375–382
  in gaseous state, 375–380
    operating points of air sources, 380
    overview, 375–377
    particle flow patterns, 377–379
    pressure loss calculation, 379–380
  in liquid state, 381–382
    homogeneous slurries, 381
    non-homogeneous slurries, 381–382
Powder yield locus (PYL), 223, 228–229, 238
Powered air-purifying respirator (PAPR), 613
Power-law fluids, 381
Power-law model, 142
PPE, *see* Personal protective equipment (PPE)
PPM, *see* Pseudo-particle model (PPM)
PPs, *see* Primary particles (PPs)
Precipitation, 176, 275, 522
Pressure atomizers, 262
Pressure swing adsorption (PSA) process, 515–516
Primary particles (PPs), 270, 271
Process function, 521
Prodi generator, 266
Projected area equivalent diameter, 20
Property function, 59–60
Protection factor (PF), 615
Protein foams, 529
PSA, *see* Pressure swing adsorption (PSA) process
PSD, *see* Particle size distribution (PSD)
Pseudo-particle model (PPM), 397
PSL, *see* Polystyrene latex (PSL)
PTFE, *see* Polytetrafluoroethylene (PTFE)
Pugmill, 425
Pull-off force, 117
Pulmonary region, 604
Pulse-jet type filters, 452
Pulverized coal, 439, 441, 457–458
Push-off effect, 245–246
PVC, *see* Poly-vinyl chloride (PVC)
PVD, *see* Physical vapor deposition (PVD)
Pycnometer method, 27–28
PYL, *see* Powder yield locus (PYL)
PZC, *see* Point of zero charge (PZC)

QCM, *see* Quartz crystal microbalance (QCM)
Qualitative descriptors, 19
Quantitative descriptors, 19
Quantum confinement, 64
Quantum dots (QDs), *see* Semiconductor nanocrystals (SNCs)
Quartz crystal microbalance (QCM), 16, 576
Quartz spring microbalance, 182
Quasi-static indentation model, 148

Raceway formation process, 537
Radial Fourier descriptor, 23
Radiation heat transfer, 433, 434
Radiation thermometer, 586–587
Radiometric method, 583
Radius vector method, 24
Random disappearance–coalescence model, 421
Random mixture, 402
RANS, *see* Reynolds-averaged Navier–Stokes equations (RANS)
Ransome, Frederick, 518
Rare earth magnets, 94
Rare earths extraction, 163
Rate-limiting reaction, 273
Rayleigh model, 197
Rayleigh scattering, 17, 76
RDF, *see* Refuse Derived Fuel (RDF)
Rectilinear classifier, 348
Redox reaction technique, 275
Reflection invariance, 19
Refuse Derived Fuel (RDF), 369
Relaxation effect, 89
Renewable air filter, 451–452
"Research and development of nanoparticle characterization method (P06041)," 607

Resistance coefficients and particle Reynolds numbers, 106
Resistance force, 105–106
Resonance technique, 576
Respirators, *see* Respiratory protective devices
Respiratory protective devices, 613–616
  fit check and fit test, 615–616
  overview, 613
  protection factor, 615
  selection, use and, maintenance, 616
  types, 613–615
    air-purifying, 613–614
    supplied breathable gas, 614–615
Reverse-flow filters, 452
Reverse micelle method, 311
Revolving screens, 359
Reynolds-averaged Navier–Stokes equations (RANS), 102, 123
Reynolds numbers, 106, 107, 218
Rigid-perfectly plastic indentation, 33
Rittinger's law, 326
RMS, *see* Root mean square (RMS) roughness
Rod-shaped SNCs, 288
Roll briquetting machine, 425
Roll crushers, 329
Root mean square (RMS) roughness, 54
Rosin-Rammler (R-R) distribution, 4–5, 282, 325, 326
Rotary dischargers, *see* Rotary feeders
Rotary drum filter, 487
Rotary dryer, 434
Rotary feeders, 371–372
Rotary kiln, 443, 518–519
Rotary valves, *see* Rotary feeders
Rotating blade level switches, 581–582
Rotating viscometer, 142
Rotational-blade-type classifier, 348
Rotational effect, 244–245
Rotation invariance, 19
Rumpf, Hans, 59
Rumpf's equation, 229, 419

Saffman-Turner equation, 137
SALA-HGMS, *see* Continuous high-gradient magnetic separator (SALA-HGMS)
Saltation flow, 381
Sauter-diameter, 20
SAXS, *see* Small angle X-ray scattering (SAXS)
Scale invariance, 19
Scanning electron microscopy (SEM), 12, 59
Scanning mobility particle sizer (SMPS), 59
Scanning probe microscopes (SPM), 53
Scanning tunneling microscope (STM), 53
SCBA, *see* Self-contained breathing apparatus (SCBA)
Scherrer equation, 18
Schiller-Naumann experimental formula, 106
Scott Volumeter, 30
Screw conveyor, 564
Screw feeders, 372–373, 510
Screw-type extruders, 422, 425
Scrubbers, 453
SDF, *see* Signed distance function (SDF) model
SDS, *see* Material Safety Data Sheet (SDS)
SEC, *see* Size exclusion chromatography (SEC)
Secondary charging, 85
Secondary consolidation, 491–492
Second Harmonic Generation (SHG), 60
Sedimentation, 523–524, 604
  method, 3, 9, 14
  rate, 477–478
  velocity, 352–354
Seeding polymerization, 276
Seismic disaster, 368
Self-contained breathing apparatus (SCBA), 614–615
Self-heat-exchange-type bed, 217
Self-preserving distribution function (SPDF), 131
Self-preserving size distribution (SPSD), 271
SEM, *see* Scanning electron microscopy (SEM)
Semi-brittle failure mode, 146
  breakage analysis for, 147–148
    chipping, 147
    fragmentation, 147
    transition velocities, 147
Semi-brittle fracture, 38
Semiconductor nanocrystals (SNCs), 64, 287
  orientation measurement of biomolecules, 291–292
  rod-shaped, 288
  size and concentration, 289–291
  synthesis in near-infrared region, 288
  synthesis in visible region, 287–288
  in vivo imaging, 292–293
  water-soluble, 288–289
SENB, *see* Single-edge notch beam (SENB)
Separation Technologies Inc., 458
SEPB, *see* Single-edge pre-cracked beam (SEPB)
Settling slurries, *see* Non-homogeneous slurries
SEVNB, *see* Single-edge V-notched beam (SEVNB)
SFA, *see* Surface force apparatus (SFA)
Shear flow
  coagulation in, 136–137
  particle motion in, 107
Shear-induced migration, 381
Shearing mixing, 401, 402, 409
Shearing strength of powder bed, 223–225
  annular ring shear tester, 224
  direct shear test, 223
  Jenike's shear tester, 223–224
  parallel-plate shear tester, 224–225
  triaxial compression test, 223
Shear properties and fluidity, 233–234
Shear rate, 57, 139, 141–142, 200, 201, 381, 411
Shear stress, 124–125, 139, 141, 142, 146, 201, 223, 224, 226, 234, 238, 268, 407, 411
Shear testers, 223
Shear thinning/thickening, 139, 141
SHG, *see* Second Harmonic Generation (SHG)
Si-alkoxide, 276
Sieve diameter, 3
Sieving and filtration, 536–537
Sieving effect, 246
Sieving method, 13–14
Sifters, 360
Signed distance function (SDF) model, 542
Silane coupling agents, 312
Silicosis, 604
Silos, 363–369
  bulk solids behavior, 364–365
    flow behavior, 364–365
    three stages, 364
  classification, 364
    single bins and group bins, 364
    stored materials, 364
  functions, 363–364
  planning, 365–366
    capacity, 365
    effective capacity of single silo, 365–366
    facilities, 366
  storing bulk solids, 363
  structural design, 366–368
    design loads, 367–368
    flow, 368
    static powder pressure, 367
  structure and shape, 363
  trouble, 368–369
    corruption, 368
    seismic disaster, 368
    thermal accidents, 369
Silver iodide (AgI) crystal, 83
Sinclair-LaMer condensator, 266
Single bins and group bins, 364
Single cylinder rotational type viscometer, 412
Single-edge notch beam (SENB), 37
Single-edge pre-cracked beam (SEPB), 37
Single-edge V-notched beam (SEVNB), 37
Single particle motion model, 244–246; *see also* Surface segregation
Single-point method, 180–181
Single-walled carbon nanotubes (SWCNTs), 607
Sintering, 61–62, 151–154
  modeling of agglomerates, 151–152
  of nanoparticles, 152–153
  of packed powder, 153–154
    laser sintering for 3D printing, 153–154
    multi component powder, 154
  solid-phase, 151
    diffusion, 151
    evaporation–condensation, 151
    formation of necks, 151
    neck growth, 151
    plastic flow, 151
    shrinkage and bloating of pores, 151
Size exclusion chromatography (SEC), 15
Skewness, 23
Slide spoon sampler, 563
Slime coatings, 500
"Slip line," 251, 254
Slipping plane, 86
Slow powder flow, 535–536
Slurry conditioning, 411–415
  characterization, 411–414
    flow behavior, 411–412
    thickening behavior, 413–414
  preparation, 414–415
Slurry viscosity, 139–142
  basic flow characteristics, 139
  equations for spherical particles suspension, 140–141
  measurement by capillary viscometer, 141–142
  measurement by rotating viscometer, 142
  overview, 139
  particle size distribution effect on, 141
  shear thinning/thickening behavior, 141
  time-dependent flow characteristics, 139–140
Small angle X-ray scattering (SAXS), 17
Smoluchowski equation, 89
Smoothed particle hydrodynamics (SPH), 542
Smoothed profile method (SPM), 552, 554–555, 557
  equations for colloidal dispersions, 554
  for particle–solvent/solute boundary, 554
  temporal discretization, 554–555
SMPS, *see* Scanning mobility particle sizer (SMPS)

SNCs, *see* Semiconductor nanocrystals (SNCs)
Sneddon's analysis, 37
Society of Automotive Engineers, 69
Soft agglomerates, 522–522
Soft magnetic materials, 94
Soft-sphere model, *see* Discrete element method (DEM)
Sol-gel method, 275–276
Sol-gel synthesis, 522
Solid combustion, 167, 169
Solid-liquid equilibrium, 279–280
Solid-phase sintering, 151, 153
  diffusion, 151
  evaporation–condensation, 151
  formation of necks, 151
  neck growth, 151
  plastic flow, 151
  shrinkage and bloating of pores, 151
Solid state reaction, 155–160
  complex fluoride synthesis, 159
  complex oxides synthesis, 155–159
  Gibbs free energy change of formation, 155
  nanoparticles synthesis, 159–160
Solubility, 171–172
  change in pH of solvent, 171
  complex formation of solutes, 172
  cosolvents, 171–172
  particle sizes of solutes, 172
  of solid, 171
Solutes, 171
  complex formation, 172
  particle sizes, 172
Solvation layer, 85
Solvent evaporation methods, 274–275
Solvothermal synthesis, 522
Sounding level meters, 581
SP, *see* Suspension preheater (SP)
Space filling factor, 21–22
Sparingly soluble crystals, 83–84
SPDF, *see* Self-preserving distribution function (SPDF)
Specific charge, 197–198
Specific resistance, 195–196
Specific surface area, 179–183, 189–190, 211
  definition, 179
  estimation by gas adsorption, 179–181
    BET method, 179–180
    single-point method, 180–181
  estimation by gas flow, 182–183
  gas adsorption methodology, 181–182
    gravimetric method, 181–182
    volumetric method, 181
  parameters correlation in distribution equations with, 325
SPH, *see* Smoothed particle hydrodynamics (SPH)
Spherical particles
  settling, 111
  viscosity equations for suspension, 140–141
Spinning disk aerosol generator, 264
Spinning riffler, 564
Split-cell-type tensile tester, 225
Split flotation, 505
Splitting and erosion, 345
SPM, *see* Scanning probe microscopes (SPM); Smoothed profile method (SPM)
Spray-coating, 286
Spray dryer, 286, 434
Spray dry method, 274
Spray pyrolysis method, 274–275, 286
Spring balance method, 117
SPSD, *see* Self-preserving size distribution (SPSD)
$SrCO_3$ formation, 162–163
SRD, *see* Stochastic rotation dynamics (SRD)
Standard powders and particles, 69–72
Standard-type sampling probe, 570
Static image analysis method, 12
Static interaction and coagulation, 133–134
Static magnetic field separators, 461–466
  matrix-loaded-type, 464–466
  open gradient magnetic-field-type, 461, 463–464
Static mixer, 409
Static-pressure-balance-type sampling probe, 570
Static separator, 470
Statistical methods, 25, 579
Statistical thermodynamics method, 212
Steady-state modeling, 389–392
Steric and electrosteric stabilization, 526–527
Steric interactions, 60
Stern layer, 85, 86, 305
Stern potential, 85, 86, 305
"Still" bulk solids, 364
Stirred mills, 536
STM, *see* Scanning tunneling microscope (STM)
Stochastic approach, 301
Stochastic Brownian motion, 60
Stochastic rotation dynamics (SRD), 552
Stochastic theory, 324
Stokes deformation number, 418
Stokes' diameter, 3, 9, 14, 25
Stokes-Einstein formula, 13, 16
Stokes' equation, 111
Stokesian drag force, 60
Stokesian Dynamics (SD), 551
Stokes law, 14, 92, 105, 107, 244
Stokes number, 15
Stokes resistance law, 105, 111
Stumbling effect, 245
Superparamagnetism, 65
Supersaturation, 279–280
Supplied breathable gas respirators, 614–615
  airline, 614
  self-contained breathing apparatus, 614–615
Surface acidity and basicity, 47–50
  influence on dispersion, 44
Surface area method, 18
Surface coating, 304, 311
Surface equivalent diameter, 19
Surface force apparatus (SFA), 55, 56
Surface fractal dimension, 190
Surface functional groups, 46–47
Surface hydroxyl groups, 42, 43, 44, 46–47, 84, 85, 185–186, 188
Surface modification, 311–315
  chemical methods, 311–313
    chemical treatment on particle surface, 311
    in-situ surface modification, 311–312
    molecular structure design, 312–313
    surface layer structure formation and coating, 313
  classification, 311
  physical methods, 314–315
Surface relaxation, 41–43
  chemical, 42–43
  physical, 41–42
Surface roughness, 22, 54
Surface segregation, 244–246
  flight effect, 244
  push-off effect, 245–246
  rotational effect, 244–245
  sieve layer effect, 246
  sieving effect, 246
  stumbling effect, 245
Suspension polymerization, 276
Suspension preheater (SP), 519
SWCNTs, *see* Single-walled carbon nanotubes (SWCNTs)
Swelling water, *see* Adhesive water
Swing level switches, 582
Systemic poisoning, 604

Table feeders, 373, 510, 564
Tabulated-devolatilization-process (TDP) model, 168
Talmage and Fitch method, 480
Tanaka's theory, 326–327
Tangential cyclone, 447
Tapping mode, *see* Dynamic mode
Tapping-type gyratory agglomerator, 420
TDP, *see* Tabulated-devolatilization-process (TDP) model
TE, *see* Transfer efficiency (TE)
TEM, *see* Transmission electron microscopy (TEM)
Temperature measurement, 585–588
  by contact-type thermometers, 585–586
    points of measurement, 585–586
    typical, 585
  by non-contact-type thermometers, 586–588
    points of measurement, 587–588
    principles, 586–587
Tensile strength, 225, 226, 229, 238, 419
Tensile testers, 225
Terminal settling velocity, 9, 14
Terzaghi-Voigt combined model, 492
TFM, *see* Two-fluid model (TFM)
Thermal accidents, 369
Thermal diffusion, 97–98, 100
Thermal fluid simulation, 519
Thermal radiation, 586
Thermistors, 585
Thermocouples, 585
Thermophysical properties of nanoparticles, 61–62
  Kelvin effect, 61
  Ostwald ripening, 61
  sintering, 61–62
Thermoporometry, 214
Thermosensitive controlled-release microparticles, 295–296
Thickening, 413–414, 477
Thin-cake/dynamic filter, 487–488
Thixotropy model, 139–140
Three-layer model, 382
Three-point bend test, 37
Threshold limit value (TLV), 605–606
  inhalable particles, 605
  respirable particles, 605–606
"Throw-in" bulk solids, 364
Time-based correlation function, 78
Time-dependent component, 78
Time-dependent flow characteristics, 139–140
Time–discretized evolution equations, 554
Time-of-flight method, 13
Time of transition technique, *see* Light extinction method
Titanium dioxide (TiO_2), 607, 608

Titanium tetra-iso-propoxide (TTIP), 272
TLV, *see* Threshold limit value (TLV)
Tomography, 595–600
  overview, 595–596
  powder and slurry processing applications, 597–600
    fluidized beds, 597
    industrial scale slurry hydrotransport metering, 598
    in-line rheometry, 599–600
    pneumatic conveying, 597
    powder and granule structure, 598
    powder mixing, 597–598
  sensor selection and specification, 596–597
Tornado mill, 425
Torsion shear tester, *see* Annular ring shear tester
Tortuosity, 218
Trace toxic compounds, 505
Trancheobronchial region, 604
Transfer efficiency (TE), 510
Transition velocities, 147
  chipping-fragmentation, 148
  limit of breakdown, 148
  plastic deformation-chipping, 147–148
Transmission electron microscopy (TEM), 12, 59
Transport properties of nanoparticles, 60
Traveling-magnetic-field-type separator, 461, 466
Triaxial compression test, 223
Tribocharging, 457, 509–510, 512
Trommel screens, *see* Revolving screens
True density, 27
TTIP, *see* Titanium tetra-iso-propoxide (TTIP)
Tumbling ball mills, 329, 536
Tumbling granulation methods, 423–424
Tumbling mixers, 407
Turbo classifier, 349
Turbulent diffusion, 100–103
  coefficient, 101–103
  equation, 101
Turbulent flow, 123, 137, 339, 343
Turbulent fluidization, 387
Twin screw extruder, 432
Two-dimensional coarse particles, 240
Two-fluid atomizers, 262
Two-fluid model (TFM), 122, 123, 392, 393
Two-layer model, 382
Two-photon microscopy, 293
Two-stage ESP, 448

ULPA, *see* Ultra-low-penetration air (ULPA) filter
Ultrafine grinding, 330
Ultra-low-penetration air (ULPA) filter, 452
Ultrasonication, 344
Ultrasonic dispersers, 344
Ultrasonic nebulizers, 263
Ultrasonic wave level meters, 583
Ultrasonic waves, 263
Ultrasonic wave screens, 359
Ultraviolet spectroscopy (UV), 405
Under-flow method, 358
Uniaxial compression test, 419
"Uniformity of Dosage Units," 405
Unipolar charging, 301
Unipolar ions and diffusion charging, 301–302
Upward flow method, 358
UV, *see* Ultraviolet spectroscopy (UV)

VAFS, *see* Vapor-fed aerosol flame synthesis (VAFS)
Valves and dampers, 373–374
Van der Waals force, 60–61, 113–114, 115, 134, 135, 136, 185, 243, 527
Vane feeders, *see* Rotary feeders
Vapor-fed aerosol flame synthesis (VAFS), 272
Vapor-solid system, 185
Variable-pressure variable-rate filtration, 481
V-cone mixer, 407
Venturi, 340
Venturi meter, 578
Vertical flow classifier, 351, 355
Vertical tensile method, 225
Vertical vessel mixer, 407
Vibrating feeders, 373
Vibrating hopper, 241
Vibrating-magnetic-field-type separator, 461
Vibrating orifice aerosol generator (VOAG), 264–265
Vibrating screens, 359–360
Vibrating viscometer, 412
Vibrational and acoustic characteristics, 249–257
  frictional sound from granular bed, 253–255
  impact sound between two particles, 252–253
  overview, 249
  small particle vibration in sound wave, 256
  sound attenuation in suspension, 256–257
  vibrating particle behavior, 249–250
  vibrating powder bed behavior, 250–252
Vibration flow, 231, 233
Vibration method, 117
Vibration mill, 329
Virtual impactor, 610
Viscometers, 411
Viscous flow, *see* Plastic flow
VOAG, *see* Vibrating orifice aerosol generator (VOAG)
Void fraction, 203, 205, 206, 207, 208, 226
Volatile matter, 167–169
Volume equivalent diameter, 19, 25
Volumetric method, 181, 211
V-shaped compressed zone, 251–252

Wadell sphericity, 25
Wall yield locus (WYL), 238
Warren–Spring equation, 234
Washburn equation, 214
Waste electrical wires, 459
Waste plastics, 458–459
Water capacity, *see* Geometric capacity
Water quality, 505
Water-soluble polymers, 308
Water-soluble SNCs, 288–289
Weber number, 261, 546
Weibull analysis, 146
Weibull distribution, *see* Rosin-Rammler (R-R) distribution
Weibull's equation, 320
Weighing method, 577–578, 583
Weissenberg-Rabinowitsch equation, 142
Wet classification, 351–359
  centrifugal type separator, 358–359
  classification theory, 351–352
  cut size control, 356–358
  hydro-cyclones, 355–356
  sedimentation velocity, 352–354
  type, 355
Wet collector, 445
Wetherilll–Rowand separator, 464
Wet high intensity magnetic separator (WHIMS), 464
Wet kiln, 443
Wet milling method, 176
Wet pressing, 430
Wettability, 50–51
Wetting and nucleation, 417
WHIMS, *see* Wet high intensity magnetic separator (WHIMS)
Wilson-Frenkel equation, 281
Work-hardening model, 33, 34
Wright dust feeder, 267
WYL, *see* Wall yield locus (WYL)

XFEM, *see* EXtended Finite Element Method (XFEM)
X-ray diffraction (XRD), 18
X-ray micro computed tomography (μCT), 546, 547, 593, 598
X-ray scattering, 214–215
XRD, *see* X-ray diffraction (XRD)

Yashima (YS) magnetic separator, *see* New York (NY) drum magnetic separator
Yielding characteristics of powder bed, 226–229
Yield stress, 33, 35
Young-Dupre equation, 495
Young-Laplace equation, 211, 213, 214, 419
Young's modulus, 37, 38, 62, 305

Zeolites, 60, 162
Zeolitic water, 193
Zero point charge (ZPC), 332
Zeta (ζ) potential, 86, 89, 528
  electrophoretic particle mobility with, 86, 89
  methodologies for measurements, 89
ZPC, *see* Zero point charge (ZPC)
ZR Fourier descriptors, 23–24



Taylor & Francis eBooks

www.taylorfrancis.com

A single destination for eBooks from Taylor & Francis with increased functionality and an improved user experience to meet the needs of our customers.

90,000+ eBooks of award-winning academic content in Humanities, Social Science, Science, Technology, Engineering, and Medical written by a global network of editors and authors.

TAYLOR & FRANCIS EBOOKS OFFERS:

A streamlined experience for our library customers

A single point of discovery for all of our eBook content

Improved search and discovery of content at both book and chapter level

REQUEST A FREE TRIAL

support@taylorfrancis.com

Routledge
Taylor & Francis Group

CRC Press
Taylor & Francis Group